

PAC

Proceedings of the

2003

Particle Accelerator Conference



DISTRIBUTION STATEMENT A
Approved for Public Release
Distribution Unlimited

Volume 4 of 5
pp. 2159-2834



REPORT DOCUMENTATION PAGE			Form Approved OMB No. 0704-0188	
Public reporting burden for this collection of information is estimated to average 1 hour per response, including the time for reviewing instructions, searching existing data sources, gathering and maintaining the data needed, and completing and reviewing the collection of information. Send comments regarding this burden estimate or any other aspect of this collection of information, including suggestions for reducing this burden, to Washington Headquarters Services, Directorate for Information Operations and Reports, 1215 Jefferson Davis Highway, Suite 1204, Arlington, VA 22202-4302, and to the Office of Management and Budget, Paperwork Reduction Project (0704-0188), Washington, DC 20503.				
1. AGENCY USE ONLY (Leave Blank)	2. REPORT DATE	3. REPORT TYPE AND DATES COVERED Final		
4. TITLE AND SUBTITLE 2003 Particle Accelerator Conference Vol 4		5. FUNDING NUMBERS G		
6. AUTHORS various				
7. PERFORMING ORGANIZATION NAME(S) AND ADDRESS(ES) IEEE 445 Hoes Lane, PO Box 1331 Piscataway, NJ 08855-1331		8. PERFORMING ORGANIZATION REPORT NUMBER		
9. SPONSORING / MONITORING AGENCY NAME(S) AND ADDRESS(ES) Office of Naval Research Ballston Centre Tower One 800 North Quincy Street Arlington, VA 22217-5660		10. SPONSORING / MONITORING AGENCY REPORT NUMBER N00014-04-1-0417		
11. SUPPLEMENTARY NOTES				
12a. DISTRIBUTION / AVAILABILITY STATEMENT DISTRIBUTION STATEMENT A Approved for Public Release Distribution Unlimited			12b. DISTRIBUTION CODE	
13. ABSTRACT (Maximum 200 words) The twentieth biennial Particle Accelerator Conference on Accelerator Science and Technology was held May 12 - 16, 2003 at the Hilton Hotel in Portland, Oregon. The Stanford Linear Accelerator Center and the Lawrence Berkeley National Laboratory organized PAC 2003, and it was held under the auspices of the Nuclear and Plasma Sciences Society of the Institute of Electrical and Electronics Engineers and the Division of Physics of Beams of the American Physical Society. The attendance was 1025 registrants from 21 countries. The Program Committee was co-chaired by Alan Jackson and Ed Lee. The program they arranged had opening and closing plenary sessions that covered the most important accomplishments, opportunities, and applications of accelerators. During the remainder of the conference there were parallel sessions with oral and poster presentations. In addition, there was an industrial exhibit during the first three days. The Proceedings present a total of 1154 papers from the invited, contributed orals, and poster sessions.				
14. SUBJECT TERMS Particle Accelerators and Colliders, Beam Dynamics, Magnets, RF Systems, Synchrotron radiation sources, Free Electron Lasers, Energy Recovery Linacs, Instabilities, Feedback Instrumentation, Pulsed Power, High Intensity Beams, Accelerator Applications, Advanced Accelerators.			15. NUMBER OF PAGES 3571	
			16. PRICE CODE	
17. SECURITY CLASSIFICATION OF REPORT Unclassified	18. SECURITY CLASSIFICATION OF THIS PAGE Unclassified	19. SECURITY CLASSIFICATION OF ABSTRACT Unclassified	20. LIMITATION OF ABSTRACT	

NSN 7540-01-280-5500

Standard Form 298 (Rev. 2-89)
Prescribed by ANSI Std. Z39-1
298-102

PAC 2003

PROCEEDINGS OF THE 2003 PARTICLE ACCELERATOR CONFERENCE

Portland, Oregon U.S.A.
May 12-16, 2003

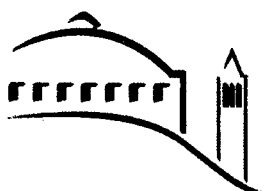
Joe Chew, Peter Lucas, and Sara Webber, editors

Volume 4 of 5

Organized by
Stanford Linear Accelerator Center
Lawrence Berkeley National Laboratory

Held under the joint auspices of
Institute of Electrical and Electronics Engineers
(Nuclear and Plasma Sciences Society)
American Physical Society
(Division of Physics of Beams)

Sponsored by
U.S. Department of Energy
Office of Naval Research
National Science Foundation



20040311 164

ACKNOWLEDGEMENTS

Cover Design: Terry Anderson

Photographs: Edmund Keene Photographers

Funding for these proceedings was provided under DOE Grant No. DE-FG03-01ER41233 by the following U.S. Department of Energy offices:

- Office of High Energy and Nuclear Physics
- Office of Basic Energy Sciences
- Office of Fusion Energy Sciences

This work related to Department of Navy grant N00014-03-1-0417 issued by the Office of Naval Research. The United States Government has a royalty-free license throughout the world in all copyrightable material contained herein.

Funding for student and postdoctoral associate travel to attend the conference was provided by National Science Foundation Grant No. PHY-0225358.

Proceedings of the 2003 Particle Accelerator Conference

Copyright and Reprint Permission: Abstracting is permitted with credit to the source. Libraries are permitted to photocopy beyond the limit of U.S. copyright law for private use of patrons those articles in this volume that carry a code at the bottom of the first page, provided the per-copy fee indicated in the code is paid through Copyright Clearance Center, 222 Rosewood Drive, Danvers, MA 01923. For other copying, reprint, or republication permission, write to IEEE Copyrights Manager, IEEE Operations Center, 445 Hoes Lane, P.O. Box 1331, Piscataway, NJ 08855-1331. All Rights reserved. Copyright ©2003 by the Institute of Electrical and Electronics Engineers, Inc.

IEEE Catalog Number: 03CH37423

ISBN: 0-7803-7738-9

Library of Congress: 88-647453

Additional copies of this publication are available from
IEEE Operations Center
445 Hoes Lane
Piscataway, NJ 08855-1331 USA
+1 800 678 IEEE
+1 732 981 9667 (FAX)
email: customer.service@ieee.org

Volume 4

Final Test Results for the SNS Ring Dipoles

- P. Wanderer, J. Jackson, A. Jain, Y.-Y. Lee, W. Meng, Y. Papaphilippou, C. Spataro, S. Tepikian, N. Tsoupas, J. Wei (BNL)*2159

Initial Test of a Fast-Ramped Superconducting Model Dipole for GSI's Proposed SIS200 Accelerator

- P. Wanderer, M. Anerella, G. Ganetis, A. Ghosh, P. Joshi, A. Marone, J. Muratore, J. Schmalzle, R. Soika, R. Thomas (BNL), W. Hassenzahl (Advanced Energy Analysis, Inc.), M.N. Wilson (Consultant), J. Kaugerts, G. Moritz (Gesellschaft für Schwerionenforschung mbH)*2162

Beam Based Measurements of Hysteresis Effects in Fermilab Main Injector Magnets

- B.C. Brown, D.P. Capista (FNAL)*2165

A New Lambertson Magnet for the FNAL 400 MeV Linac

- J.-F. Ostiguy, H. Glass, D. Harding, J.R. Lackey, W. Robothom (FNAL)*2168

Pulse Octupole Magnet System at the Photon Factory Storage Ring

- T. Miyajima, Y. Kobayashi, S. Nagahashi (KEK)*2171

SPEAR3 Gradient Dipole Core Fabrication

- N. Li, R. Boyce, D. Dell'Orco, D. Ernst (SLAC), X. Wang, N. Xu (Institute of High Energy Physics, Beijing), J. Tanabe (SPEAR3 Project Consultant)*2174

Cost Based Failure Modes and Effects Analysis (FMEA) for Systems of Accelerator Magnets

- C.M. Spencer (SLAC), S.J. Rhee (Stanford University)*2177

Permanent Magnets for Radiation Damage Studies

- J. Spencer (SLAC), J.T. Volk (FNAL)*2180

Magnetic Measurement of the 10 kW, IR FEL 180 Degree Dipole

- K. Baggett, G. Biallas, D. Bullard, J. Dail, D. Douglas, T. Hiatt, M. McCrea (Thomas Jefferson National Accelerator Facility)*2183

Magnetic Modeling vs. Measurements of the Dipoles for the JLAB KW Free Electron Laser Upgrade

- G. Biallas, K. Baggett, D. Douglas, T. Hiatt, R. Wines (Thomas Jefferson National Accelerator Facility), V. Christina, J.W. Rathke, T.J. Schultheiss (Advanced Energy Systems), Y. Luo, D. Newsham, A.V. Smirnov, D. Yu (DULY Research Inc.)*2186

Magnetic Measurement of the 10 kW, IR FEL Dipole Magnets

- T. Hiatt, K. Baggett, M. Beck, G. Biallas, D. Douglas, K. Sullivan, C. Tennant (Thomas Jefferson National Accelerator Facility)*2189

An Adjustable Permanent Magnet Quadrupole Final Focus System for Low Energy Experiments

- J. Lim, P. Frigola, J.B. Rosenzweig, S. Telfer, G. Travish (University of California, Los Angeles), W. Brown, A.M. Tremaine (LLNL)*2192

Canadian Light Source Magnets

- L. Dallin, D. Lowe, J. Swirsky (Canadian Light Source)*2195

Permanent Magnet Quadrupole for Final Focus for Linear Collider

- Y. Iwashita, T. Mihara (Kyoto University), E. Antokhin (BINP), M. Kumada (National Institute of Radiological Sciences (NIRS)), M. Aoki (Sumitomo Special Metal Co., Ltd.)*2198

A Switching Magnet for the IFUSP Microtron

- M.N. Martins, R.R. Lima, M.L. Lopes, A.A. Malafronte, U. Schnitter, J. Takahashi (Instituto de Fisica da Universidade de Sao Paulo)*2201

Measuring Beta Function and Phase Advance in RHIC with an AC Dipole

- M. Bai, S. Peggs, T. Roser, T. Satogata, D. Trbojevic (BNL)*2204

Measurement of Linear Coupling Resonance in RHIC	
<i>M. Bai, F. Pilat, T. Satogata (BNL), F. Schmidt, R. Tom_s (CERN), R. Calaga (State University of New York)</i>	2207
Linear Model for Non-Isosceles Absorbers	
<i>J.S. Berg (BNL)</i>	2210
Linear Design of Combined-Function Ionization Cooling Lattices	
<i>J.S. Berg, H. Kirk (BNL), A.A. Garren (University of California, Los Angeles)</i>	2213
Design of FFAGs Based on a FODO Lattice	
<i>J.S. Berg (BNL), C. Johnstone (FNAL)</i>	2216
End Field Effects in Bend-Only Cooling Lattices	
<i>J.S. Berg, H. Kirk (BNL), A.A. Garren (University of California, Los Angeles)</i>	2219
Linear Coupling Correction with N-Turn Maps	
<i>W. Fischer (BNL)</i>	2222
On-Line Monitoring of the Linear Coupling Resonances for the LHC	
<i>S. Fartoukh, N. Catalan-Lasheras, J.P. Koutchouk (CERN)</i>	2225
Measurement of Sextupolar Resonance Driving Terms in RHIC	
<i>R. Tom_s, F. Schmidt (CERN), W. Fischer (BNL)</i>	2228
Completion of the Sextupole Driving Terms Measurement at the SPS	
<i>R. Tom_s, M. Hayes, F. Schmidt (CERN)</i>	2231
A Technique to Measure Chromaticity Based on the Harmonic Analysis of a Longitudinally Kicked Beam	
<i>R. Tom_s (University de Valencia), G. Rumolo (Gesellschaft für Schwerionenforschung mbH)</i>	2234
Correcting the LHC Beta* at Collision	
<i>W. Wittmer, A. Verdier, F. Zimmermann (CERN)</i>	2237
2002 Nonlinear Optics Measurements and Modelling for the CERN SPS	
<i>F. Zimmermann, G. Arduini, R. Tom_s (CERN), N. Iida (KEK), A. Faus-Golfe (University de Valencia)</i>	2240
Slow Ground Motion Modelling of DIAMOND	
<i>J.K. Jones (Daresbury Laboratory)</i>	2243
Impact of Narrow Gap Undulators on the Advanced Light Source	
<i>D. Robin, C. Steier, W. Wan, A. Wolski (LBNL)</i>	2246
ID Modeling at the ALS	
<i>D. Robin, H. Nishimura, C. Steier, W. Wan (LBNL), Y.K. Wu (Duke University), E. Forest (KEK)</i>	2249
Maxwell-Lorentz Equations in General Frenet-Serret Coordinates	
<i>A.C. Kabel (SLAC)</i>	2252
Global-Beam Based Alignment Method	
<i>A. Terebilo (SLAC)</i>	2255
Generation of Femtosecond Electron Bunches and Hard-X-Rays by Ultra-Intense Laser Wake Field Acceleration in a Gas Jet	
<i>M. Uesaka, T. Hosokai (University of Tokyo), K. Kinoshita, A. Zhidkov (National Institute of Radiological Sciences (NIRS))</i>	2258
Feedforward Correction of the Pulsed Circularly Polarizing Undulator at the Advanced Photon Source	
<i>O. Makarov, B. Deriy, L. Emery, S. Sasaki, R. Soliday, I. Vasserman (ANL)</i>	2261
A Thin Beryllium Injection Window for CESR-c	
<i>Y. Li (Cornell University)</i>	2264

Diagnosis of Optical Errors with a Precision BPM System at CESR <i>M.A. Palmer, D.L. Rubin, D. Sagan, J.C. Smith (Cornell University)</i>	2267
Power Supply Performance Monitoring and Analysis Using Operation Data <i>J. Li, S. Hartman, Y.K. Wu (Duke University)</i>	2270
Status of the Booster Synchrotron for Duke FEL Storage Ring <i>S.F. Mikhailov, M. Busch, M. Emamian, S. Hartman, V. Litvinenko, I. Pinayev, V.G. Popov, G. Swift, P. Wallace, Y.K. Wu (Duke University), N. Gavrilov, Yu. Matveev, D. Shvedov, N. Vinokurov, P. Vobly (BINP)</i>	2273
Challenges for Magnetic Design of a Compact Booster Fed by Single Power Supply <i>S.F. Mikhailov (Duke University)</i>	2276
Feasibility Study of a 2 GeV Lepton Collider at DAFNE <i>G. Benedetti, D. Alesini, M. Biagini, C. Biscari, R. Boni, M. Boscolo, A. Clozza, G. Delle Monache, G. Di Pirro, A. Drago, A. Gallo, A. Ghigo, S. Guiducci, M. Incurvati, C. Ligi, F. Marcellini, G. Mazzitelli, C. Milardi, L. Pellegrino, M.A. Preger, P. Raimondi, R. Ricci, C. Sanelli, M. Serio, F. Sgamma, A. Stecchi, A. Stella, C. Vaccarezza, M. Vescovi, M. Zobov (INFN)</i>	2279
Bunch Pattern By-3 in PEP-II <i>F.-J. Decker, A. Kulikov, M. Sullivan (SLAC)</i>	2282
Injection Related Background due to the Transverse Feedback <i>F.-J. Decker, R. Akre, A. Fisher, R. Iverson, M. Weaver (SLAC)</i>	2285
Lattice with Smaller Momentum Compaction Factor for PEP-II High Energy Ring <i>Y. Nosochkov, Y. Cai, M. Donald (SLAC)</i>	2288
Tracking Simulations Near Half-Integer Resonance at PEP-II <i>Y. Nosochkov, Y. Cai (SLAC)</i>	2291
RF Heating and Temperature Oscillations due to a Small Gap in a PEP-II Vacuum Chamber <i>A. Novokhatski, J. Seeman, M. Sullivan (SLAC)</i>	2294
Progress of the PEP-II B-Factory <i>J. Seeman, M. Browne, Y. Cai, W. Colacho, F.-J. Decker, M. Donald, S. Ecklund, R. Erickson, A. Fisher, J. Fox, S. Heifets, R. Iverson, W. Kozanecki, P. Krejci, A. Kulikov, A. Novokhatski, P. Schuh, H. Schwarz, M. Stanek, M. Sullivan, D. Teytelman, J.L. Turner, U. Wienands, Y. Yan, J. Yocky (SLAC), M. Biagini (INFN), M. Zisman (LBNL)</i>	2297
Design Studies for a 10^{36} Super-B-Factory <i>J. Seeman, Y. Cai, F.-J. Decker, S. Ecklund, A. Fisher, J. Fox, S. Heifets, Y. Nosochkov, A. Novokhatski, M. Sullivan, D. Teytelman, U. Wienands, Y. Yan (SLAC), M. Biagini (INFN)</i>	2300
Improvements in Aladdin Bend Magnet Stability by Reduction of Leakage Currents <i>D.J. Wallace, M. Fisher, K.D. Jacobs, G. Rogers, L. Rowley, M. Thikim, W. Trzeciak (Synchrotron Radiation Center, University of Wisconsin)</i>	2303
Longitudinal Single-Bunch Instabilities for Different Operation Energies at ELETTRA <i>G. De Ninno, M. Danailov, B. Diviacco, F. Iazzourene, E. Karantzoulis, M. Marsi, L. Tosi, M. TrovÀ (Sincrotrone Trieste)</i>	2306
Injection and FEL Lasing with Front End Open at ELETTRA <i>G. De Ninno, K. Casarin, F. Iazzourene, E. Karantzoulis, L. Tosi, G. Tromba, A. Vascotto (Sincrotrone Trieste)</i>	2309
Initial Studies of Longitudinal Dynamics on UMER <i>A. Valfells, B. Beaudoin, S. Bernal, A. Diep, I. Haber, J. Harris, Y. Huo, P.G. O'Shea, B. Quinn, M. Reiser, M. Walter (University of Maryland)</i>	2312
Nonlinear Optimization of a Low Emittance CLIC Damping Ring Lattice <i>M. Korostelev, F. Zimmermann (CERN)</i>	2315

Status of the MAX-III Storage Ring

*G. LeBlanc, A. Andersson, M. Demirkan, M. Eriksson, L.-J. Lindgren, H. Tarawneh, S. Werin (MAX-Lab), B. Anderberg (AMACC, Sweden)*2318

MAX 4, a 3 GeV Light Source

*G. LeBlanc, A. Andersson, M. Bergqvist, M. Eriksson, L.-J. Lindgren, L. Malmgren, H. Tarawneh, E. Wall_n, S. Werin (MAX-Lab), B. Anderberg (AMACC, Sweden), J rgen Larsson (Lund University).....*2321

Bates South Hall Ring Commissioning for Internal Target Experiments

*J.B. van der Laan, D. Cheever, M. Farkhondeh, W.A. Franklin, E. Ihloff, S. Krause, L. Longcoy, C. Tschalaer, E. Tsentalovich, F. Wang, A. Zolfaghari, T. Zwart (MIT-Bates).....*2324

Connection-Oriented Relational Database of the APS Control System Hardware

*D.A. Dohan, N.D. Arnold (ANL).....*2327

Use of a General-Purpose Optimization Module in Accelerator Control

*L. Emery, M. Borland, H. Shang (ANL)*2330

An Operator Training Facility at the Advanced Photon Source

*J.W. Lewellen, S. Pasky (ANL).....*2333

All Digital IQ Servo-System for CERN Linacs

*A. Rohlev, R. Garoby, J. Serrano (CERN).....*2336

Pulsed NMR Magnetometers for CESR

*R.E. Meller, D. Hartill (Cornell University)*2339

Requirements for RF Control of TTF II FEL User Facility

*V. Ayvazyan, K. Rehlich, S. Simrock (DESY)*2342

Antiproton Stacking and Un-stacking in the Fermilab Recycler Ring

*C.M. Bhat (FNAL)*2345

Gated Current Integrator for the Beam in the RR Barrier Buckets

*C.M. Bhat, A. Cadorna, J. Crisp, B. Fellenz (FNAL)*2348

Improvement of Photon Factory Advanced Ring Control System

*T. Obina, A. Akiyama, T. Katoh, T. Kawamoto, I. Komada, K. Kudo, S. Nagahashi, T.T. Nakamura, J. Odagiri, Y. Takeuchi, N. Yamamoto (KEK).....*2351

The LANSCE RICE Control System Upgrade

*S. Schaller, E. Bjorklund, M. Burns, G. Carr, J. Faucett, D. Hayden, M. Lusk, R. Merl, M. Oothoudt, J. Potter, J. Reynolds, D. Romero, F. Shelley, Jr. (LANL)*2354

The Upgrade of HLS Linac Control System

*G. Liu, X. Bao, L. Chen, C. Li, W. Li, J.P. Wang (National Synchrotron Radiation Lab), J. Li (Duke University) ...*2357

Application Programming Structure and Physics Applications

*C. Chu, J. Galambos, W.-D. Klotz, T.A. Pelaia, A. Shishlo (ORNL), D. Ottavio (BNL), C.K. Allen, C.A. McChesney, N. Pattengale (LANL)*2360

SNS Global Database Use in Application Programming

*J. Galambos, C. Chu, E. Danilova, J. Patton, T.A. Pelaia, A. Shishlo (ORNL), W.-D. Klotz (European Synchrotron Radiation Facility)*2363

The EPICS Based Virtual Accelerator - Concept and Implementation

*A. Shishlo, P. Chu, J. Galambos, T.A. Pelaia (ORNL)*2366

Accelerator Control Middle Layer

*A. Terebilo, J. Corbett, G. Portmann (SLAC)*2369

Simulated Commissioning of SPEAR 3 Storage Ring	
<i>A. Terebilo, J. Corbett, D. Keeley, G. Portmann (SLAC)</i>	2372
A New Real-Time Operating System and Python Scripting on Aladdin	
<i>D.E. Eisert, R.A. Bosch, K.D. Jacobs, K.J. Kleman, J.P. Stott (Synchrotron Radiation Center, University of Wisconsin)</i>	2373
Control System for the Superconducting Insertion Devices of NSRRC	
<i>K.T. Hsu, C.K. Chang, J. Chen, S.-Y. Hsu, K.H. Hu, C.S. Hwang, C.H. Kuo, Demi Lee (Synchrotron Radiation Research Center)</i>	2376
Low Level RF System for Jefferson Lab Cryomodule Test Facility	
<i>T. Plawski, T. Allison, J. Delayen, C. Hovater, T. Powers (Thomas Jefferson National Accelerator Facility)</i>	2379
PLC and Linux Based Control System for the CAMD Linac	
<i>P. Jines, E. Anzalone, B. Craft, A. Crappell, M. Fedurin, T. Miller, M. Smith, Y. Wang, T. Zhao (Center for Advanced Microstructures and Devices)</i>	2382
Cross Platform SCA Component using C++ Builder and Kylix	
<i>H. Nishimura, J.L. McDonald, C. Timossi (LBNL)</i>	2385
Design of Control System for SAGA Synchrotron Light Source	
<i>H. Ohgaki (Kyoto University), K. Kudo, H. Toyokawa (National Institute of Advanced Industrial Science and Technology), Y. Iwasaki, S. Koda, T. Tomimasu (Saga Synchrotron Light Source)</i>	2387
SNS Ring and Transport System Magnet Acceptance and Installation Preparation	
<i>S. Tepikian, R. Anderson, M. Hemmer, H. Hseuh, J. Jackson, A. Jain, F. Karl, Y.-Y. Lee, W. McGahern, D. Raparia, R. Savage, J. Tuozzolo, P. Wanderer, J. Wei (BNL)</i>	2390
Laser-Based Alignment System for the J-PARC Linac	
<i>M. Ikegami, Y. Higashi, T. Kato, H. Tanaka, K. Yoshino (KEK)</i>	2393
A Model of ATL Ground Motion for Storage Rings	
<i>A. Wolski (LBNL), N. Walker (DESY)</i>	2396
Design and Operation of the Cryostat for the CESR-c Superconducting Wiggler Magnets	
<i>Y. He, G. Codner, R.D. Ehrlich, Y. Li, V. Medjizade, A. Mikhailichenko, N.B. Mistry, E. Nordberg, D. Rice, D. Sabol, E.N. Smith, K. Smolenski, D. Widger (Cornell University)</i>	2399
The Pilot-Runs of the Helium Cryogenic System for the TLS Superconducting Cavity	
<i>F.Z. Hsiao, J.C. Chang, S.H. Chang, J.R. Chen, T.C. King, H.C. Li, M.C. Lin, Ch. Wang (Synchrotron Radiation Research Center)</i>	2402
Design of Cryogenic System for Several Super-Conducting Modules at National Synchrotron Radiation Research Center	
<i>T.C. King, J.C. Chang, S.H. Chang, J.R. Chen, F.Z. Hsiao, H.C. Li (Synchrotron Radiation Research Center)</i>	2405
Techniques for Synchronization of X-Ray Pulses to the Pump Laser in an Ultrafast X-Ray Facility	
<i>J. Corlett, L. Doolittle, R. Schoenlein, J. Staples, R. Wilcox, A. Zholents (LBNL)</i>	2408
Bunch Purity Evolution during APS Storage Ring Top-up Operations	
<i>A.H. Lumpkin, T. Toellner, B.X. Yang, C.Y. Yao (ANL)</i>	2411
The Feasibility of OTR Imaging of High-Intensity Proton Beams at FNAL	
<i>A.H. Lumpkin (ANL), V. Scarpine (FNAL)</i>	2414
Recent Characterizations of Electron Beams from the APS Linac	
<i>A.H. Lumpkin, W.J. Berg, M. Borland, J.W. Lewellen (ANL)</i>	2417
Initial CTR-Based Bunch Length Measurements of Linac Beams Following the APS Bunch Compressor	
<i>A.H. Lumpkin, W.J. Berg, M. Borland, J.W. Lewellen, N.S. Sereno (ANL)</i>	2420

X-Ray Imaging of the APS Storage Ring Beam Stability Effects: from the Alaskan Earthquake to Undulator Field Changes	
<i>A.H. Lumpkin, L. Emery, B.X. Yang, C.Y. Yao (ANL)</i>	2423
Super-Conducting Resonator as Beam Induced Signal Pickup	
<i>R.C. Pardo, B.E. Clifft, P.N. Ostroumov, S.I. Sharamentov, G.P. Zinkann (ANL)</i>	2426
Beam Position Monitor Systems for the SNS LINAC	
<i>J. Power, L. Day, M.A. Plum, M. Stettler (LANL)</i>	2429
Split Scattering Effects in a Well Aligned Pepper Pot	
<i>J.G. Power (ANL)</i>	2432
Advanced Photon Source Booster Synchrotron Beam Position Monitor Upgrade and Applications	
<i>N.S. Sereno, F. Lenkszus, Robert M. Lill (ANL)</i>	2435
Tune System Applications at the APS	
<i>C.Y. Yao, L. Emery, K. Harkay (ANL)</i>	2438
AGS Booster Beam Position, Tune, and Longitudinal Profile Data Acquisition System	
<i>K.A. Brown, L. Ahrens, F. Severino, K.S. Smith, M. Wilinski (BNL)</i>	2441
Spallation Neutron Source Ring Diagnostics	
<i>P. Cameron, J. Brodowski, P. Cerniglia, R. Connolly, J. Cupolo, C. Dawson, C. Degen, A. DellaPenna, D. Gassner, R. Gonzalez, M. Grau, J. Gullotta, L. Hoff, A. Huhn, M. Kesselman, C.J. Liaw, J. Mead, R. Sikora, G. Smith, K. Vetter, M. Wilinski (BNL), M.A. Plum (LANL), S. Assadi, W. Blokland, C. Diebele, D. Purcell, T.J. Shea (ORNL), R.L. Witkovar (TechSource, Inc.)</i>	2444
Spallation Neutron Source Beam Loss Monitor System	
<i>D. Gassner, P. Cameron, C. Mi (BNL), R.L. Witkovar (TechSource, Inc.)</i>	2447
Design and Testing of the New Ion Chamber Loss Monitor for SNS	
<i>D. Gassner (BNL), R.L. Witkovar (TechSource, Inc.)</i>	2450
Beam Current Monitor Calibrator for the Spallation Neutron Source	
<i>M. Kesselman, C. Dawson, G. Smith (BNL)</i>	2453
Electro-Optic Longitudinal Electron Beam Diagnostic at SDL	
<i>H. Loos, A. Doyuran, J.B. Murphy, J. Rose, T. Shaftan, B. Sheehy, Y. Shen, J. Skaritka, X.J. Wang, Z. Wu, L.H. Yu (BNL)</i>	2455
A High Dynamic-Range Beam Position Measurement System for ELSA-2	
<i>P. Balleyguier, D. Deslandes, Ph. Guimbal (French Atomic Energy Commission), H. Borrión (University College)</i>	2458
Upgrades to the Digital Receiver-based Low-Intensity Beam Diagnostics for CERN AD.	
<i>M.E. Angoletta, D. Belohrad, L. Bojtar, A. Findlay, M. Ludwig, F. Pedersen (CERN), O. Marquersen (TERMA A/S, Radar Systems)</i>	2461
OTR Studies for the High Charge CTF3 Beam	
<i>T. Lefevre, E. Bravin (CERN), C. Vermare (French Atomic Energy Commission)</i>	2464
Measurement of Beam Position Using Highly-Damped Accelerating Structures	
<i>J. Prochnow, E. Jensen, W. Wuensch (CERN)</i>	2467
Cavity Mode Related Wire Breaking of the SPS Wire Scanners and Loss Measurements of Wire Materials	
<i>F. Roncarolo, F. Caspers, B. Dehning, E. Jensen, J. Koopman, J.F. Malo (CERN)</i>	2470

System Level Implementation of Beam Position Monitors with Local Data Processing Capability for the Cornell Electron Storage Ring	
<i>M.A. Palmer, J. Dobbins, B.Y. Rock, C.R. Strohmman (Cornell University), J.R. Moffitt (The College of Wooster)</i>	2473
Design of OTR Beam Profile Monitors for the TESLA Test Facility, Phase 2 (TTF2)	
<i>K. Honkavaara, A. Brenger, R. Fischer, D. Nalle, K. Rehlich (DESY), L. Cacciotti, M. Castellano, L. Catani, A. Cianchi, G. Di Pirro, M. Raparelli, R. Sorchetti (INFN)</i>	2476
BPM and Orbit Correction Systems at the Duke Storage Ring	
<i>Y.K. Wu, J. Li, V. Litvinenko, P. Wang (Duke University)</i>	2479
A Physics Based Control System for the Duke Storage Ring	
<i>Y.K. Wu, S. Hartman, S.F. Mikhailov (Duke University)</i>	2482
The SNS Linac Wire Scanner System	
<i>M.A. Plum, W. Christensen, R.E. Meyer Sr., C.R. Rose (LANL)</i>	2485
Performance of a Beam Monitor in the Fermilab Tevatron Using Synchrotron Light	
<i>H.W.K. Cheung, A. Hahn, A. Xiao (FNAL)</i>	2488
Measurement of Proton and Anti-proton Intensities in the Tevatron Collider	
<i>S. Pordes, J. Crisp, B. Fellenz, R. Flora, A. Hahn, T.S. Meyer, A.V. Tollestrup (FNAL), W. Blokland (ORNL)</i>	2491
Digital Down Conversion Technology for Tevatron Beam Line Tuner at FNAL	
<i>W. Schappert, E. Lorman, V. Scarpine (FNAL), M.C. Ross, J. Sebek, T. Straumann (SLAC)</i>	2494
Measurements of the Longitudinal and Transverse Beam Loss at the Tevatron	
<i>A.V. Tollestrup, M.E. Binkley, B.M. Hanna, V.A. Lebedev, R. Moore, V. Shiltsev, R. Tesarek, R. Vidal (FNAL)</i>	2497
Study of a Low Impedance Beam Position Monitor for Short Bunches	
<i>D. Alesini, B. Spataro, C. Vaccarezza (INFN), C. D'Alessio, A. Mostacci, L. Palumbo (University of Rome)</i>	2500
Improved SR Extraction Chamber for KEKB LER SR Monitor	
<i>J.W. Flanagan, S. Hiramatsu, H. Ikeda, K. Kanazawa, T. Mitsuhashi (KEK)</i>	2503
Construction of SR Monitor for Photon Factory Advanced Ring	
<i>T. Mitsuhashi, M. Tadano (KEK)</i>	2506
Beam Position Measurement Using Linac Microstructure at the KEK Booster Synchrotron	
<i>T. Miura, Y. Irie, Y. Sato, H. Someya (KEK)</i>	2509
Beam Position Measurements at Los Alamos: Isotope Production Facility and Switchyard Kicker Upgrade	
<i>J.D. Gilpatrick, D. Barr, D. Martinez, J.F. O'Hara, R.B. Shurter, M. Stettler (LANL)</i>	2512
A Multiwire Proportional Chamber System for Monitoring Low Momentum Beam in Accelerators	
<i>R. Merl, F. Gallegos, C. Pillai, B.J. Sanchez, F. Shelley, A. Steck (LANL)</i>	2515
High Speed Epics Data Acquisition and Processing on One VME Board	
<i>R. Merl, F. Gallegos, C. Pillai, F. Shelley (LANL)</i>	2518
Halo Measurements of the Extracted Beam at the Los Alamos Proton Storage Ring	
<i>T. Zaugg, M. Borden, A. Browman, D. Fitzgerald, R.J. Macek, R. McCrady, T. Spickermann (LANL)</i>	2521
Beam Imaging Diagnostics for Heavy Ion Beam Fusion Experiments	
<i>F.M. Bieniosek, W. Ghiorso, L.R. Prost (LBNL)</i>	2524
A Second Beam-Diagnostic Beamline for the Advanced Light Source	
<i>F. Sannibale, D. Baum, N. Kelez, T. Scarvie (LBNL), K. Holldack (BESSY)</i>	2527

Development of a Longitudinal Density Monitor for Storage Rings <i>W. Turner, J.-F. Beche, J. Byrd, P. Datte, S. De Santis, P. Denes, M. Placidi, A. Ratti, V. Riot, R. Schoenlein, M. Zolotorev (LBNL)</i>	2530
DARHT-II Energy Analyzer <i>A.C. Paul, S. Hawkins, J. McCarrick, J. Sullivan, J.A. Watson, G. Westenskow (LLNL), W. Nexsen (Johnston Controls), S. Eylon, T.J. Fessenden (LBNL)</i>	2533
Progress on a Smith-Purcell Radiation Bunch Length Diagnostic <i>S. Korbly, A.S. Kesar, M.A. Shapiro, R.J. Temkin (MIT Plasma Science and Fusion Center)</i>	2536
Beam Diagnostic System for High Intensity Proton Linac at KAERI <i>S.J. Park, Y.S. Bae, J.Y. Huang, W.H. Hwang, S.H. Nam, J.H. Park (Pohang Accelerator Laboratory), Y.S. Cho, B.H. Choi, J.M. Han, S.H. Han (Korea Atomic Energy Research Institute)</i>	2539
Improved Results from the Gas Scattering Energy Spectrometer on the ISIS RFQ Test Stand <i>J.P. Duke, D.J.S. Findlay, A.P. Letchford, J. Thomason (Rutherford Appleton Laboratory)</i>	2542
Very High Resolution RF Cavity BPM <i>M.C. Ross, J. Frisch, L. Hendrickson, D. McCormick (SLAC), V. Vogel (BINP), H. Hayano, J. Urakawa (KEK)</i> ...	2545
RF Cavity BPM's as Beam Angle and Beam Correlation Monitors <i>M.C. Ross, J. Frisch, D. McCormick (SLAC), H. Hayano (KEK)</i>	2548
Bunched Beam Cleaning System of SPring-8 Booster Synchrotron <i>T. Aoki, K. Fukami, N. Hosoda, T. Ohshima, M. Shoji, K. Tamura, H. Yonehara (SPring-8)</i>	2551
Beam Position Monitoring System for the 1.5 GeV Transport Line of NSRRC <i>K.H. Hu, J. Chen, K.T. Hsu, C.H. Kuo, Demi Lee, C.J. Wang (Synchrotron Radiation Research Center)</i>	2554
Functionality of the Digital Beam Position Monitor Test-Bed in NSRRC <i>C.H. Kuo, J. Chen, K.T. Hsu, K.H. Hu (Synchrotron Radiation Research Center)</i>	2557
Synchrotron Light Interferometer at Jefferson Lab <i>P. Chevtsov, A. Freyberger, R. Hicks (Thomas Jefferson National Accelerator Facility), J.-C. Denard (SOLEIL)</i> ..	2560
Development of a BPM Lock-in Diagnostic System <i>R. Dickson (Thomas Jefferson National Accelerator Facility)</i>	2563
Large Dynamic Range Beam Profile Measurements <i>A. Freyberger (Thomas Jefferson National Accelerator Facility)</i>	2565
Tunneling Ionization Bunch Length Monitor for the Ultrarelativistic Compressed Electron Beams <i>A. Murokh (University of California, Los Angeles)</i>	2568
Design and Testing of a Fast Beam Position Monitor <i>B. Quinn, B. Beaudoin, S. Bernal, A. Diep, M. Glanzer, J. Harris, M. Holloway, D. Lamb, W.-T. Lee, P.G. O'Shea, M. Quirus, M. Reiser, A. Valfells, M. Walter, R. Yun (University of Maryland)</i>	2571
Time Resolved Emittance Measurement in the University of Maryland Electron Ring <i>M. Walter, S. Bernal, I. Haber, R.A. Kishek, D. Lamb, H. Li, P.G. O'Shea, B. Quinn, M. Reiser, M. Snowel, A. Valfells (University of Maryland)</i>	2574
Alignment of Components at the University of Maryland Electron Ring <i>M. Walter, S. Bernal, A. Diep, M. Glanzer, I. Haber, J. Harris, R.A. Kishek, D. Lamb, W.-T. Lee, H. Li, P.G. O'Shea, B. Quinn, M. Quirus, M. Reiser, A. Valfells (University of Maryland)</i>	2577
Emittance Measurement by Using Duo Image Pattern of Cherenkov Radiation <i>J. Chen, Y. Ding, S. Quan, B. Zhang, K. Zhao (Peking University), R. Geng, A. Gu (Princeton University)</i>	2580

Filling Pattern Measurement in the LNLS Storage Ring	
<i>S.R. Marques, H.J. Onisto, P.F. Tavares (Laboratório Nacional de Luz Sincrotron, Brazil)</i>	2583
Multichannel Single-Shot Transient Signal Measurements with an Optical Fiber Recirculating Delay Line Loop	
<i>Y. Yin, A. Chen, G. Chen, X.Z. Wang, W. Zhang (YY Labs, Inc.)</i>	2586
Compensation of Nonlinear Resonances in the Presence of Space Charge	
<i>A. Fedotov, G. Parzen (BNL)</i>	2589
Application of Envelope Instability to High-Intensity Rings	
<i>A. Fedotov (BNL), I. Hofmann (Gesellschaft für Schwerionenforschung mbH), H. Okamoto (Hiroshima University), R.L. Gluckstern (University of Maryland)</i>	2592
Spill Structure in Intense Beams	
<i>J. Glenn, M. Blaskiewicz, K.A. Brown, E. Raka, J. Ryan (BNL)</i>	2595
Electron-Cloud Mitigation in the Spallation Neutron Source Ring	
<i>J. Wei, M. Blaskiewicz, J. Brodowski, P. Cameron, D. Davino, A. Fedotov, P. He, H. Hseuh, Y.-Y. Lee, H. Ludewig, W. Meng, D. Raparia, J. Tuozzolo, S.Y. Zhang (BNL), N. Catalan-Lasheras (CERN), R.J. Macek (LANL), M. Furman (LBNL), A. Aleksandrov, S. Cousineau, V. Danilov, S. Henderson (ORNL), M. Pivi (SLAC)</i>	2598
On Emittance Evolution in the Extraction System of High-Current Electron and Ion Sources	
<i>J.-M. Lagniel, P. Balleyguier, D. Guilhem, J.-L. Lemaire, N. Pichoff, M. Prom_ (French Atomic Energy Commission)</i>	2601
Resistive-Wall Wake for Non-Ultrarelativistic Beams	
<i>F. Zimmermann (CERN), K. Oide (KEK)</i>	2604
Effects of Space Charge on Decoherence in Ion Beams	
<i>G. Rumolo, O. Boine-Frankenheim, I. Hofmann, Y. Liu (Gesellschaft für Schwerionenforschung mbH), A. Al-Khateeb (Yarmouk University)</i>	2607
Space Charge Effects during the Injection Period of the KEK PS Main Ring	
<i>S. Igarashi, T. Miura, E. Nakamura, Y. Shimosaki, M. Shirakata, K. Takayama, T. Toyama (KEK)</i>	2610
Challenge of Benchmarking Simulation Codes for the LANL Beam-Halo Experiment	
<i>T.P. Wangler, R.W. Garnett, W.P. Lysenko (LANL), J. Qiang (LBNL)</i>	2613
High Brightness Potassium Ion Gun for the HIF Neutralized Transport Experiment (NTX)	
<i>S. Eylon, E. Henestroza, P.K. Roy, S.S. Yu (LBNL)</i>	2616
Final Focus System for High Intensity Beams	
<i>E. Henestroza, F.M. Bieniosek, S. Eylon, P.K. Roy, S.S. Yu (LBNL)</i>	2619
Neutralized Transport of High Intensity Beams	
<i>E. Henestroza, A. Anders, S. Eylon, P.K. Roy, W. Sharp, S.S. Yu (LBNL), D.V. Rose, D.R. Welch (Mission Research Corporation), P. Efthimion, E. Gilson (Plasma Physics Laboratory, Princeton University)</i>	2622
Non-Intercepting Diagnostic for the HIF Neutralized Transport Experiment	
<i>P.K. Roy, S. Eylon, R. Hannink, E. Henestroza, J. Ludvig, D. Shuman, S.S. Yu (LBNL)</i>	2625
Magnetic Lattice for the HIF Neutralized Transport Experiment (NTX)	
<i>D. Shuman, S. Eylon, E. Henestroza, P.K. Roy, W. Waldron, S.S. Yu (LBNL), T. Houck (LLNL)</i>	2628
Analytical Study of Envelope Modes for a Fully Depressed Beam in Solenoidal and Quadrupole Periodic Transport Channels	
<i>S.M. Lund (LLNL), B. Bukh (LBNL)</i>	2631

Influence of Conducting Plate Boundary Conditions on the RMS Envelope Equations Describing Intense Ion Beam Transport	
<i>S.M. Lund (LLNL), B. Bukh (LBNL)</i>	2634
Realistic Modeling of Chamber Transport for Heavy-Ion Fusion	
<i>W.M. Sharp, D.A. Callahan, D.P. Grote, M. Tabak (LLNL), E. Henestroza, S.S. Yu (LBNL), D.V. Rose, D.R. Welch (Mission Research Corporation), P.F. Peterson (University of California, Berkeley)</i>	2637
Reverted Resonant "Wakefield"	
<i>E.S. Masunov (MEPhI), A.V. Smirnov (DULY Research Inc.)</i>	2640
Three-Dimensional Modeling of Intense Bunched Beams in RF Accelerators and Sources	
<i>R. Bhatt, C. Chen, M. Hess (MIT Plasma Science and Fusion Center)</i>	2643
Beam Halo Formation and Loss Induced by Image-Charge Effects in a Small-Aperture Alternating-Gradient Focusing System	
<i>J. Zhou, C. Chen, B.L. Qian (MIT Plasma Science and Fusion Center), S. Eylon, E. Henestroza, S.S. Yu (LBNL)</i>	2646
Initial Experimental Results of the Small Isochronous Ring (SIR)	
<i>J. Rodriguez, F. Marti, E. Pozdeyev (National Superconducting Cyclotron Laboratory)</i>	2649
SNS Linac Commissioning - Transverse Matching	
<i>D. Jeon (ORNL), J. Stovall (LANL)</i>	2652
Recent Results from the Paul Trap Simulator Experiment	
<i>H. Qin, R.C. Davidson, P. Efthimion, E. Gilson, R. Majeski (Plasma Physics Laboratory, Princeton University)</i>	2655
Drift Compression and Final Focus of Intense Heavy Ion Beam	
<i>H. Qin, R.C. Davidson (Plasma Physics Laboratory, Princeton University), E.P. Lee (LBNL), J.J. Barnard (LLNL)</i>	2658
RF Plasma Source for Heavy Ion Beam Charge Neutralization	
<i>P. Efthimion, R.C. Davidson, E. Gilson, L. Grisham (Plasma Physics Laboratory, Princeton University), B.G. Logan, S.S. Yu (LBNL)</i>	2661
Simulating Accelerator Structure Operation at High Power	
<i>V. Ivanov, C. Adolphsen, N. Folwell, L. Ge, A. Guetz, K. Ko, Z. Li, C.-K. Ng, J.W. Wang, M. Wolf (SLAC), M. Weiner (Harvey Mudd College), G. Schussmann (University of California, Davis)</i>	2664
A Modified QuadScan Technique for Emittance Measurement of Space Charge Dominated Beams	
<i>C.G. Limborg, S. Gierman (SLAC), J.G. Power (ANL)</i>	2667
Calculation of the Maximum Stored Beam Current Considering the Phase Noise of a Generator RF Signal	
<i>L.H. Chang, M.C. Lin, G.H. Luo, Ch. Wang (Synchrotron Radiation Research Center)</i>	2670
Space-Charge-Dominated Phenomena in the UMER Source Region	
<i>I. Haber, S. Bernal, R.A. Kishek, P.G. O'Shea, B. Quinn, M. Reiser, Y. Zou (University of Maryland), J.-L. Vay (LBNL), A. Friedman, D.P. Grote (LLNL)</i>	2673
Large Diffuse Halos in Time-Dependent Space-Charge Potentials with Colored Noise	
<i>C.L. Bohn (Northern Illinois University and Fermilab), I.V. Sideris (Northern Illinois University)</i>	2676
Main Regularities of Particle Redistribution in Space Charge-Dominated Beam Transport and Bunching	
<i>B.I. Bondarev, A.P. Durkin (Moscow Radiotechnical Institute)</i>	2679
Angular Momentum Measurement of the FNPL Electron Beam	
<i>Y. Sun, K.-J. Kim (University of Chicago), K. Desler, D. Edwards, H. Edwards, M. H€ening, P. Piot, J. Santucci (FNAL), S.-H. Wang (Indiana University), S.M. Lidia (LBNL), N. Barov, D. Mihalcea (Northern Illinois University), R. Tikhoplav (University of Rochester)</i>	2682

Multiple Beam Interaction Studies in Heavy Ion Fusion	
<i>D.R. Welch, D.V. Rose (Mission Research Corporation), S.S. Yu (LBNL), C.L. Olson (Sandia National Laboratories)</i>	2685
Observation of Coherent Microwave Transition Radiation in the APS Linac	
<i>G. Decker, X. Sun (ANL)</i>	2688
RHIC Transverse Injection Damping	
<i>A. Drees, P. Cameron, R. Michnoff, C. Montag, M. Wilinski (BNL)</i>	2691
RHIC Electron Detector Signal Processing Design	
<i>J. Gullotta, D. Gassner, D. Trbojevic, S.Y. Zhang (BNL)</i>	2694
Multi-Million-Turn Beam Position Monitors for RHIC	
<i>T. Satogata, P. Cameron, P. Cerniglia, J. Cupolo, C. Dawson, C. Degen, J. Mead, K. Vetter (BNL)</i>	2697
Waveguide Mode Reflectometry for Obstacle Detection in the LHC Beam Pipe Including Signal Attenuation	
<i>T. Kroyer, F. Caspers (CERN)</i>	2700
Tune Measurement Methods of the Tevatron	
<i>C.Y. Tan, P. Lebrun, X.L. Zhang (FNAL)</i>	2703
The SNS Laser Profile Monitor Design and Implementation	
<i>S. Assadi, A. Aleksandrov, W. Blokland, A. DeCarlo, C. Deibele, P. Gibson, W. Grice, M. Hechler, T. Hunter, J. Kelly, P. Ladd, G. Murdoch, J. Pogge, K. Potter, D. Purcell, T.J. Shea, D. Stout (ORNL)</i>	2706
Design of an Optical Diffraction Radiation Beam Size Monitor at SLAC FFTB	
<i>Y. Fukui, D. Cline, F. Zhou (University of California, Los Angeles), M. Tobiyama, J. Urakawa (KEK), P.R. Bolton, M.C. Ross (SLAC), R. Hamatsu, P.V. Karataev, T. Muto (Tokyo Metropolitan University), A.S. Aryshev, G.A. Naumenko, A.P. Potylitsyn (Tomsk Polytechnic University)</i>	2709
Measurement of Electron Beam Divergence Using OTR-ODR Interferometry	
<i>R. Fiorito, P.G. O'Shea, A.G. Shkvarunets (University of Maryland)</i>	2712
A New Tool for Beam-Life Research at HLS Storage Ring	
<i>Yuxiong Li, Juexin Li, W. Li, Zuping Liu (National Synchrotron Radiation Lab)</i>	2715
New Design of the TESLA Interaction Region with $l^* = 5$ m	
<i>J. Payet, O. Napoly (CE Saclay)</i>	2718
Optimum Choice of RF Frequency for Two Beam Linear Colliders	
<i>H. Braun, D. Schulte (CERN)</i>	2721
Progress in the Design of a Damped and Tapered Accelerating Structure for CLIC	
<i>J.-Y. Raguin, I. Wilson, W. Wuensch (CERN)</i>	2724
Main Linac Emittance Growth and Luminosity in Future Linear Colliders	
<i>D. Schulte (CERN)</i>	2727
Bunch-to-Bunch Energy Stability Test of the Nb Prototypes of the TESLA Superstructure	
<i>H. Schlarb, V. Ayvazyan, P. Castro, R. Kammering, S. Schreiber, J. Sekutowicz, S. Simrock, M. Wendt (DESY), M. H��ening (FNAL), M. Ferrario (INFN)</i>	2730
Intra-Bunch-Train Luminosity Optimisation for the TESLA Linear Collider	
<i>N. Walker (DESY), D. Schulte (CERN), G.R. White (Queen Mary College, University of London)</i>	2733
Simulations of the Static Tuning for the TESLA Linear Collider	
<i>N. Walker (DESY), D. Schulte (CERN)</i>	2736

Comparison of the TESLA, NLC and CLIC Beam-Collimation System Performance	
<i>A. Drozhdin, N.V. Mokhov (FNAL), W. Kozanecki, O. Napoly (CE Saclay), D. Schulte, F. Zimmermann (CERN), N. Walker (DESY), G. Blair (Royal Holloway College), L. Keller, T. Markiewicz, T. Maruyama, T.O. Raubenheimer, A. Seryi, P. Tenenbaum, M. Woodley (SLAC)</i>	2739
CTF3 Prototypes: Design, Tests and Measurements	
<i>A. Ghigo, D. Alesini, C. Biscari, R. Boni, A. Clozza, G. Delle Monache, A. Drago, A. Gallo, F. Marcellini, C. Milardi, C. Sanelli, M. Serio, F. Sgamma, A. Stecchi, A. Stella, M. Zobov (INFN), R. Corsini, L. Rinolfi (CERN)</i>	2742
Harmonic Cavities for the NLC Damping Rings	
<i>A. Wolski, S. De Santis (LBNL)</i>	2745
Study of Near-Field Vibration Sources for the NLC Linac Components	
<i>F. Asiri, F. Le Pimpec, A. Seryi (SLAC)</i>	2748
Capture and Polarization of Positrons in a Proposed NLC Polarized Positron Source	
<i>Y.K. Batygin, J.C. Sheppard (SLAC)</i>	2751
A Test of NLC-Type Beam Loading in the SLAC Linac	
<i>F.-J. Decker, T.O. Raubenheimer, A. Seryi, J.L. Turner, M. Woods, J. Yocky (SLAC)</i>	2754
Implementation of Dynamic Misalignments and Luminosity Stabilization	
<i>L. Hendrickson, T. Himel, T.O. Raubenheimer, A. Seryi, P. Tenenbaum, M. Woodley (SLAC), D. Schulte (CERN)</i>	2757
Optimized Wakefield Suppression & Emittance Dilution-Imposed Alignment Tolerances in X-Band Accelerating Structures for the JLC/NLC	
<i>R.M. Jones, Z. Li, R.H. Miller, T.O. Raubenheimer (SLAC)</i>	2760
Energy Dispersion Compensation and Beam Loading in X-Band Linacs for the JLC/NLC	
<i>R.M. Jones, C. Adolphsen, V.A. Dolgashev, R.H. Miller, J.W. Wang (SLAC)</i>	2763
A Recipe for Linear Collider Final Focus System Design	
<i>A. Seryi, M. Woodley (SLAC), P. Raimondi (INFN)</i>	2766
Long Term Stability Study at FNAL and SLAC Using BINP Developed Hydrostatic Level System	
<i>A. Seryi, R. Ruland (SLAC), A. Chuprya, A. Erokhin, M. Kondaurov, A. Medvedko, V. Parkhomchuk, E. Shubin, S. Singatulin (BINP), J. Lach, D. Plant, V. Shiltsev (FNAL), A. Kuznetsov (Novosibirsk State University)</i>	2769
Wigglers and Single-Particle Dynamics in the NLC Damping Rings	
<i>M. Venturini, A. Wolski (LBNL), A. Dragt (University of Maryland)</i>	2772
A Lattice with Larger Momentum Compaction for the NLC Main Damping Rings	
<i>M. Woodley, T.O. Raubenheimer, J. Wu (SLAC), A. Wolski (LBNL)</i>	2775
Feedback on Nanosecond Timescales: Fast Feedback Simulations	
<i>G.R. White (Queen Mary College, University of London)</i>	2778
Form-Factor for a Target Used for Positron Generation with Undulator Radiation Conversion	
<i>A. Mikhailichenko (Cornell University)</i>	2781
Pulsed Undulator to Test Polarized Positron Production at SLAC	
<i>A. Mikhailichenko (Cornell University)</i>	2784
The Technical Realisation of RF Kickers for CLIC Test Facility CTF3	
<i>E. Plawski, A. Kucharczyk, S. Kulinski (Institute for Nuclear Studies, Poland)</i>	2787
Development of Room Temperature Accelerating Structures for the RIA	
<i>N.E. Vinogradov, P.N. Ostroumov, E. Rotela, S.I. Sharamentov, S. Sharma, G.P. Zinkann (ANL), J.W. Rathke, T.J. Schultheiss (Advanced Energy Systems), D.L. Schrage (LANL)</i>	2790

AGS Upgrade to 1-MW with a Super-Conducting Linac Injector	
<i>A.G. Ruggiero, J. Alessi, D. Raparia, T. Roser, W.T. Weng (BNL)</i>	2793
Study of a 10-MW Continuous Spallation Neutron Source	
<i>A.G. Ruggiero, H. Ludewig, S. Shapiro (BNL)</i>	2796
Results of the IPHI Drift Tube Linac's Hot Model CW Tests	
<i>P.-E. Bernaudin, G. Congretel (CE Saclay), P. Balleyguier (French Atomic Energy Commission), A. Fontenille, E. Froidefond, M. Fruneau, D. Marchand, M. Planet, J.-C. Ravel (LPSC Grenoble)</i>	2799
Beam Dynamics Studies in SPIRAL II Linac	
<i>R. Duperrier, D. Uriot (CE Saclay), N. Pichoff (French Atomic Energy Commission), P. Bertrand, B. Bru, A. Savalle, F. Varenne (Grand Accelérateur National d'Ions Lourds), J.L. Biarrotte (Institut de Physique Nucl_aire d'Orsay), J.-M. De Conto, E. Froidefond (LPSC Grenoble)</i>	2802
Instabilities Study and Implications for the RIA Project	
<i>R. Duperrier (CE Saclay), D. Gorelov (National Superconducting Cyclotron Laboratory)</i>	2805
A SCRF Linac as a FEL Driver and Storage Ring Injector	
<i>J. Rose, J.B. Murphy, B. Podobedov, T. Shafan, B. Sheehy, X.J. Wang, L.H. Yu (BNL)</i>	2808
Beam Dynamic Calculations for the Superconducting COSY Injector Linac	
<i>A. Lehrach, H. Jungwirth, R. Maier, R. Toelle (Forschungszentrum Juelich)</i>	2811
Debuncher Developing for H and D Beams Injection into COSY Ring	
<i>Y. Senichev, R. Maier, R. Stassen, R. Toelle, N. Vasyukhin (Forschungszentrum Juelich)</i>	2814
The RFQ-Injector for COSY-SCL	
<i>K.-U. Kuehnelt, A. Schempp (Institut fur Angewandte Physik), A. Schnase, R. Toelle (Forschungszentrum Juelich), C.P. Welsch (Max-Planck-Institut fuer Kernphysik)</i>	2817
Design of a Superconducting CH-Cavity for Low- and Medium Beta Ion and Proton Acceleration	
<i>H. Liebermann, H. Podlech, U. Ratzinger, A. Sauer (Institut fur Angewandte Physik)</i>	2820
The Frankfurt Funneling Experiment	
<i>J. Thibus, I. Mueller, N. Mueller, A. Schempp, H. Zimmermann (Institut fur Angewandte Physik)</i>	2823
Cold-Model Tests of an Annular Coupled Structure for Upgrade of a J-PARC Linac	
<i>H. Ao (Japan Atomic Energy Research Institute), V. Paramonov (Institute for Nuclear Research, Moscow), N. Hayashizaki (Tokyo Institute of Technology)</i>	2826
Low Power Test of RFQ Mock-up Modules at 175MHz for IFMIF Project	
<i>S. Maebara, T. Imai, T. Morishita, M. Sugimoto, H. Takeuchi (Japan Atomic Energy Research Institute), M. Saigusa, S. Sazawa (Ibaraki University)</i>	2829
Development of a Low-Energy Proton Accelerator System for the Proton Engineering Frontier Project (PEFP)	
<i>J.M. Han, Y.S. Cho, B.H. Choi, S.H. Han, J.H. Jang, K.K. Jeong, Y.J. Kim, H.J. Kwon, H.H. Lee, J.H. Na, M.Y. Park, K.T. Seol (Korea Atomic Energy Research Institute)</i>	2832

FINAL TEST RESULTS FOR THE SNS RING DIPOLES*

P. Wanderer[†], J. Jackson, A. Jain, Y.-Y. Lee, W. Meng, Y. Papaphilippou[#], C. Spataro,
S. Tepikian, N. Tsoupas, J. Wei, BNL, Upton, NY 11973-5000, USA

Abstract

To meet the performance parameters of the Spallation Neutron Source (SNS) for high beam intensity with low losses, the compact accumulation ring will contain 32 sector dipoles with 1.44 m effective length and a large aperture, 170 mm. The magnets are built from potted coils and machined pieces of solid iron. When first assembled, the dipoles met the requirements for field uniformity but the rms variation of the integral transfer function (ITF) was much larger than design at both fields of interest, 1.11 T·m and 1.33 T·m, corresponding to proton energies of 1.0 GeV and 1.3 GeV respectively. Based on initial measurements, shims have been added to the return legs or poles, as appropriate, in order to bring the rms variation of the 1.0 GeV ITF to the specification, 0.01%. The value of the ITF rms variation at 1.3 GeV for the shimmed magnets is 0.033%. Sorting the magnets has significantly reduced the load on the correctors due to this ITF variation.

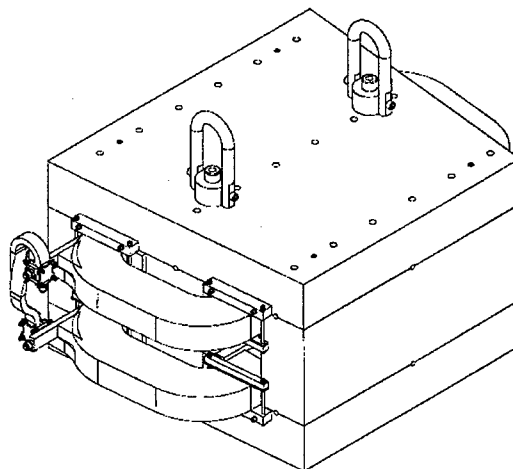


Figure 1: SNS Ring Dipole

1 INTRODUCTION

The Spallation Neutron Source (SNS) is under construction at Oak Ridge National Laboratory [1]. The SNS accumulator ring [2] will contain 32 sector dipoles. To accommodate the high intensity proton beam, the magnet aperture is large. The dipoles are being characterized over the energy range 0.8 to 1.3 GeV to allow for operation over a range of injection energies. The magnets were fabricated at Brookhaven National Laboratory (BNL), using coils and machined iron parts purchased from industry. The yokes are machined from solid 1006 steel. Other parameters of the magnets are given in Table 1. A drawing of the magnet is shown in Fig. 1. This paper reports magnetic measurement results from all 32 dipoles. Measurements of the first 16 dipoles have been published previously [3].

Table 1: Magnet Parameters

Effective length, m	1.44
Gap, mm	170
Pole width, mm	450
B_0 at 1.0 GeV (1.3 GeV), T	0.77 (0.925)
I_{op} at 1.0 GeV (1.3 GeV), A	4398 (5408)
$\int B \cdot dl$ at 1.0 GeV (1.3 GeV), T·m	1.11 (1.33)

* SNS is managed by UT-Batelle, LLC, under contract DE-AC05-00OR22725 for the U.S. Department of Energy. SNS is a partnership of six U.S. national laboratories: Argonne, Brookhaven, Jefferson, Lawrence Berkeley, Los Alamos, and Oak Ridge.

[†] wanderer@bnl.gov

[#] now at ESRF, Grenoble, France

2 FIELD QUALITY REQUIREMENTS

For the individual magnets, there are field quality requirements for the integral field and for the region near the axial center of the magnet, where the field is two-dimensional. (The requirement applies to the integral field after the linear variation of the integral dipole field with horizontal position due to the sector ends is subtracted.) In both cases, the requirements call for 0.01% uniformity across an aperture of ± 100 mm at the horizontal midplane. Field uniformity near the axial center of the magnet was achieved by locating steel strips 5.19 mm high and 40 mm wide at the edges of the poles. Uniformity of the integral field was achieved by adjusting the amount of steel at the corners of a yoke of the prototype dipole in an iterative process that utilized both three-dimensional calculations and measurement.

For the group of magnets, the rms variation of the integral field is to be less than 0.01%. After measurement, the magnets are disassembled in order to install the vacuum chamber, so magnet assembly must be reproducible to 0.01% in order to assure that the field measurements correctly represent the installed magnets. The six yoke sections (poles, top and bottom plates, side plates) are pinned and bolted to obtain this reproducibility.

3 MAGNETIC FIELD MEASUREMENTS

The integral fields in production dipoles are measured with a rotating coil 2.49 m long and 163.8 mm in diameter. Tangential sense windings are mounted on the coil [4]. At 1.0 and 1.3 GeV, measurements are made at

the center of the magnet aperture and at positions 50.8 and 101.6 mm on both sides of center. The regions covered by the coil at these positions overlap, providing considerable redundancy in the data. For a sector magnet, accurate horizontal placement of the measuring coil is essential. (A horizontal displacement of 0.76 mm changes the integral field by 0.01%.) This is accomplished by a precision magnet stand and a computer controlled coil translation stage. In addition, optical survey is used to locate fiducials on the coil with respect to the magnet fiducials. The survey data are then used to correct the magnetic measurements for any errors in the coil position. The short-term variation (i.e., noise) of the integral measurements is $\sim 0.002\%$. The reproducibility of the measurements is $\sim 0.01\%$ when the magnets are removed from and reinstalled on the test stand. The absolute accuracy of the integral field measurement is estimated to be $\sim 0.03\%$.

To obtain reproducibility of the hysteresis, the magnets were ramped to 4834 A (5408 A) for 1.0 GeV (1.3 GeV) operation. Following this cycle, the magnets were ramped up to the same high current. Measurements were then made on the down-ramp.

The as-built dipoles did not meet the specification of a 0.01% standard deviation in the integral transfer function (ITF) due to variations in the pole gap, as well as apparent variations in the iron properties. The dipoles were shimmed to meet the specifications. A target mean value was established based on the measurements of a few early dipoles. For all the subsequent dipoles, a preliminary measurement was carried out at 1.0 GeV excitation and a shim was installed, if necessary, either in the return leg position (to reduce the ITF) or under the upper pole (to increase the ITF). Most magnets were shimmed to within $\pm 0.02\%$ of the target value on the first attempt. A few magnets remained outside this margin (which corresponds to the shim resolution of 25 μm) after the first shimming. These magnets were reshimmied.

Initially, the shim thickness was determined based on

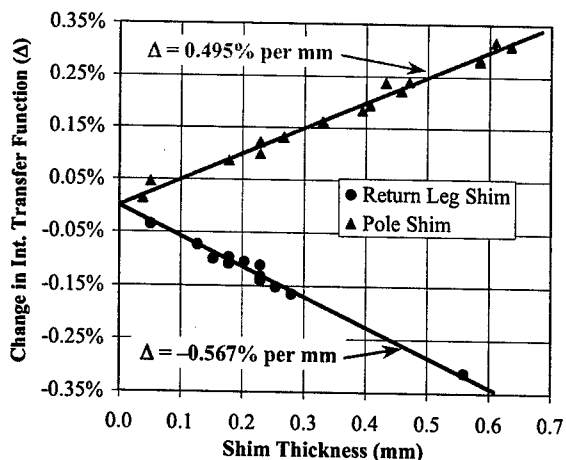


Figure 2: Change in Integral Transfer Function as a function of shim thickness in the pole and the return leg.

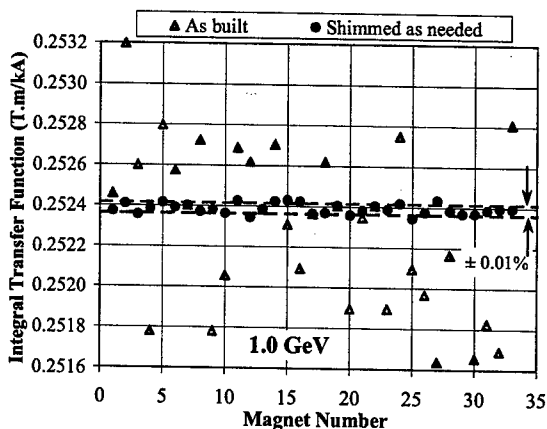


Figure 3: Integral dipole field at 1.0 GeV before (triangles) and after (circles) shimming.

the nominal pole gap and the amount of correction required. As data on more shimmed magnets became available, an empirical relation between the shim thickness and the change in the ITF was established (see Fig. 2). This empirical relationship was used in the later part of the program for a more accurate shimming. A small difference was observed between the sensitivities for the return leg and pole shims. This difference is perhaps due to different levels of iron saturation in the pole and return leg regions.

Integral field measurements of the 32 magnets, at the central position, before and after shimming, are shown in Fig. 3. Before shimming, the rms variation of the integral field was 0.165%; after shimming, it is 0.01%. At 1.3 GeV, shimming reduced the rms variation from 0.089% to 0.033% (Fig. 4). Local dipole correctors will be used to correct the orbits. To minimize the load on these correctors, the dipoles will be sorted based on their integral field at 1.3 GeV. Magnets with high and low integral fields will be placed 360 degrees in phase advance (two full cells) apart.

With the measuring coil at the central position,

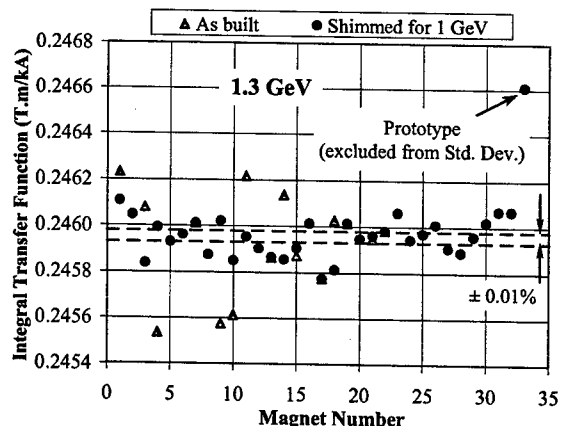


Figure 4: Integral dipole field at 1.3 GeV before (triangles) and after (circles) shimming.

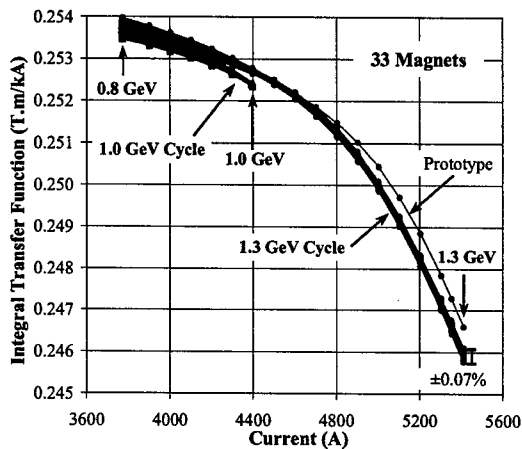


Figure 5: Excitation curves for operation at 1.0 GeV and 1.3 GeV.

excitation curves for operation at 1.0 and 1.3 GeV were measured, down to 0.8 GeV. Fig. 5 shows the excitation curves in the two cases.

An alternate way to represent the field quality of the magnets is to give the harmonic decomposition of the field. Table 2 (Table 3) summarizes the integral harmonics in the magnets at the central position of the

Table 2: Integral harmonics in the 17D120 dipoles in 10^{-4} units at 80 mm (1.0 GeV operation)

Harmonic	Normal		Skew	
	Mean	Std. Dev.	Mean	Std. Dev.
Quadrupole	-105.04	0.28	-0.26	0.95
Sextupole	0.16	0.43	-0.02	0.49
Octupole	2.05	0.15	-0.05	0.32
Decapole	1.14	0.20	0.00	0.11
Dodecapole	0.06	0.09	0.00	0.16
14-pole	-0.30	0.12	-0.02	0.10
16-pole	0.15	0.07	0.00	0.10
18-pole	-0.08	0.11	0.00	0.06
20-pole	-0.04	0.05	0.01	0.09
22-pole	-0.18	0.13	0.00	0.03

Table 3: Integral harmonics in the 17D120 dipoles in 10^{-4} units at 80 mm (1.3 GeV operation)

Harmonic	Normal		Skew	
	Mean	Std. Dev.	Mean	Std. Dev.
Quadrupole	-103.66	0.29	-0.19	1.01
Sextupole	-6.28	0.41	-0.02	0.53
Octupole	2.48	0.16	-0.03	0.32
Decapole	-0.45	0.20	0.00	0.11
Dodecapole	0.08	0.10	0.00	0.16
14-pole	-0.49	0.12	-0.02	0.10
16-pole	0.15	0.07	0.00	0.10
18-pole	-0.07	0.11	0.00	0.06
20-pole	-0.04	0.05	0.01	0.09
22-pole	-0.17	0.13	0.00	0.03

measuring coil at 1.0 GeV (1.3 GeV) excitation. It is important to note that the integral measurements of two harmonics are affected by the magnet taper, which produces an apparent normal quadrupole of -105 units ($\sim 1\%$) and an apparent normal octupole of ~ 2 units. A three-dimensional calculation shows that the apparent values of these harmonics are -107 and $+1.96$ units respectively, in reasonable agreement with the measured values. The harmonics are essentially unchanged by the shimming. Both 2-D and 3-D calculations were performed to show that changes in harmonics due to the shims are negligible. Typical harmonic changes are less than 0.1 unit. The normal sextupole increases from 0 to 6 units between 1.0 and 1.3 GeV, the result of saturation. The ~ 1 unit variation of the skew quadrupole may be the result of top-bottom differences in the taper of the yoke.

The three-dimensional calculation also allows us to evaluate the difference between the harmonics measured by the (straight) integral coil and those along the curved path of a proton. Except for the normal quadrupole and normal octupole as discussed above, the harmonics integrated along the trajectory of the protons are expected to be within 1 unit of those measured by the rotating coil. The integral normal quadrupole and the normal octupole for the curved path differ from the straight path value by 99.4 units and 2.7 units respectively.

4 CONCLUSIONS

The 32 ring dipoles for the Spallation Neutron Source have been measured and found to meet the field quality tolerances. When shimmed, the magnets meet the 0.01% tolerance on the rms variation of integral dipole field at 1.0 GeV. The rms variation at 1.3 GeV, 0.033%, will be compensated by sorting. The integral fields are uniform across the good field region of $x = \pm 100$ mm within 0.01%, except for a residual quadrupole, estimated at ~ 6 units due to the magnet taper.

5 ACKNOWLEDGEMENTS

We acknowledge useful discussions with G. Danby, S. Henderson, J. Galambos, and T. Hunter of SNS.

6 REFERENCES

- [1] N. Holtkamp, "Status of the SNS," PAC03 (These proceedings).
- [2] J. Wei et al, "Low-loss design for the high-intensity accumulator ring of the Spallation Neutron Source," Phys. Rev. ST-AB 3, 080101 (2000).
- [3] P. Wanderer et al., "The SNS Ring Dipole Magnetic field Quality," Proc. EPAC 2002, p. 1317.
- [4] See, for example, A. Jain, "Harmonic Coils," in Proc. CERN Accelerator School on Measurement and Alignment of Accelerator and Detector Magnets, CERN 98-05, p. 175-218 (1998).

INITIAL TEST OF A FAST-RAMPED SUPERCONDUCTING MODEL DIPOLE FOR GSI'S PROPOSED SIS200 ACCELERATOR *

P. Wanderer[†], M. Anerella, G. Ganetis, A. Ghosh, P. Joshi, A. Marone, J. Muratore, J. Schmalzle, R. Soika, R. Thomas BNL, Upton, NY 11973-5000, USA

J. Kaugerts, G. Moritz, GSI, Darmstadt, Germany

W. Hassenzahl, Advanced Energy Analysis, Piedmont, CA 94611 USA

M. N. Wilson, consultant, 33 Lower Radley, Abingdon OX14 3AY, UK

Abstract

Gesellschaft für Schwerionenforschung (GSI) has proposed a large expansion of the existing facility in Darmstadt, Germany. The proposal includes an accelerator, SIS200, with rigidity of 200 T·m that utilizes 4 T superconducting dipoles ramped at 1 T/s. An R&D program including both the superconductor and the magnet is directed at achieving the desired ramp rate with minimal energy loss. The RHIC arc dipoles, with 8 cm aperture, possess adequate aperture and field strength but are ramped at only 1/20 of the desired rate. However, for reasons of speed and economy, the RHIC dipole is being used as the basis for this work. The superconductor R&D has progressed far enough to permit the manufacture of an initial cable with satisfactory properties. This cable has been used in the construction of a 1 m model magnet, appropriately modified from the RHIC design. The magnet has been tested successfully at 2 T/s to 4.38 T.

1 INTRODUCTION

This paper reports the successful initial test of a 1m fast-ramped superconducting model dipole built as part of the magnet R&D program for the new accelerator facility that will be built at the Gesellschaft für Schwerionenforschung (GSI) in Darmstadt, Germany [1]. The magnet was designed to meet specifications for the SIS200 accelerator: 4 T central field, 1 T/sec ramp rate [2,3]. Because the RHIC arc dipoles [4] can operate at 4 T, GSI and BNL are working together on a model magnet program based on the RHIC design. Use of the RHIC cross-section has enabled the work to take advantage of much of the RHIC design and tooling and some of the RHIC magnet components, thereby getting the effort off to a fast start. However, it has been necessary to make significant modifications to the magnet design, especially the superconductor, to build a magnet that can ramp 20 times faster than RHIC and have much lower eddy current energy losses.

2 SUPERCONDUCTOR

The strand for the first dipole (GSI001) is made from leftover NbTi strand from the RHIC program (2.25 Cu:SC ratio, $J_c = 2900 \text{ A/mm}^2$ at 5 T, 4.2 K, 0.648 mm wire diameter, 6 μm filament diameter, 13 mm twist pitch). The twist-pitch of the GSI001 strand is 4 mm. The extra twist reduced the wire diameter slightly ($\sim 13 \mu\text{m}$) with minimal impact ($< 5\%$) on the critical current. The cable parameters that determine the energy loss are the resistance between adjacent strands, R_a , and the resistance between crossing strands, R_c [5]. In the cable used in this magnet (GSI#004), R_c was increased compared to RHIC values by inserting two 25 μm -thick, 8 mm wide stainless steel cores into the cable as it was formed. To allow for some current sharing, R_a was decreased by coating the strands with Staybrite (Sn with 4% Ag). Without cores, cables made from Staybrite coated strands (e.g., LHC) have $R_c \sim 20 \mu\Omega$. The cables used in this magnet have $R_c = 60 \text{ m}\Omega$, more than a factor of a thousand higher. The measured value of R_a is much lower, 64 $\mu\Omega$, so eddy current effects are dominated by currents flowing between adjacent wires. (This value of R_a was determined using the standard method. Detailed measurements reveal that R_a actually varies by as much as a factor of ~ 1000 between the wide and narrow sections of the cable. The effects of this variation introduce some uncertainty into the calculation of energy loss [6].)

The cable has standard RHIC insulation: two wraps of Kapton®, each 25 μm thick, with 50% overlap of each wrap, and a polyimide-based heat-set adhesive on the outside of the inner wrap and on both sides of the outer wrap. This provides substantial impedance to the flow of helium between the interior of the cable and the reservoir just outside the coil. To allow more rapid heat exchange, a laser was used to cut away about 25% of the insulation on the thin edge of the insulated cable (Fig. 1). The holes in the insulation were precisely made so that the coils could be wound and cured without developing turn-to-turn shorts. Turn-to-turn standoff voltages of 1.1 kV were observed for both the straight section and end regions of a test coil that was cut in half and collared. This is less than the nominal test condition, $> 2 \text{ kV}$, for RHIC coils but sufficient for the SIS200 application.

*Work supported by US DOE under contract DE-AC02-98CH10886 and GSI.

[†] wanderer@bnl.gov



Figure 1. Cable inner edge.

3 MAGNET CONSTRUCTION

Where feasible, magnet components were made from insulators rather than metals. In the GSI magnet (Fig. 2), the three wedges used in the coil to control field quality were G11 rather than Cu. The cable is $\sim 25 \mu\text{m}$ thicker than the RHIC cable, resulting in a cured coil (32 turns) that is oversize by 0.9 mm. The G10 end pole spacers and Ultem® coil end saddles were modified to take account of the oversize cable. The shims placed between the coil and the pole were made of G11 and reduced in thickness to compensate for the oversized coil.

The coils were collared with Kawasaki high-Mn stainless steel collars. (The collars were designed for the LHC D2/D4 IR dipoles, also made using a variation of the RHIC arc dipole design [7].) As a handling aid, collars are assembled into 15 cm-long packs before being placed on the coils. G10 tubes were used to assemble these packs. It was possible to replace the brass keys used to lock the collars around the coils with G11 everywhere except for 2 cm at the nonlead end, where brass was used. At the lead end of the magnet, the collars have a larger inner diameter because of the radial space needed to bring the lead at the pole of the coil beyond the end of the coil. For the GSI magnet, the brass pieces used to fill this volume were halved in thickness and doubled in quantity, and the pieces of brass were insulated from one another.

The yoke laminations were 0.5 mm thick and punched from low coercivity steel ($H_c = 31 \text{ A/m}$) with 3.3% Si added. The laminations were coated with B-stage epoxy and glued into blocks 254 mm long. Five blocks make up a half yoke. Each half yoke is supported against axial motion by three stainless steel rods that run through holes

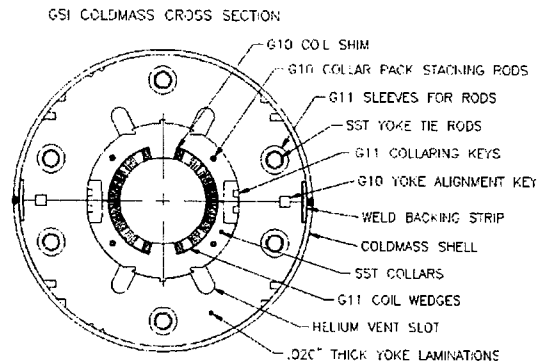


Figure 2. Cross section of the cold mass.

in the yoke and restrain the yoke with stainless steel nuts insulated from the yoke by G10 washers. G10 tubes are placed around the stainless steel rods to insulate the rods from the yoke. The two yoke halves are aligned with respect to one another with G10 alignment keys at the yoke midplane. The yoke is held together by welding a stainless steel shell around it. There is a welding backup strip at the midplane but the strip is not welded to the yoke.

In RHIC magnets, quenches at high ramp rate are likely to originate in the "ramp" section of the cable, at the end of the pole turn of the coil, where the cable is filled with solder to keep it rigid as it is moved by G10 fixtures to a larger radius so that it can be brought past the end of the coil and spliced to the cable from the other coil. The splice between the two coils halves is itself a possible source of quenching. However, the high value of R_c in the cored cable was judged to be sufficient to prevent such quenching in this magnet, so this region of magnet construction was the same as for RHIC dipoles.

The magnet was constructed so that helium axial flow would be forced along the coil inner radius, for maximum cooling. All other axial flow paths were blocked either by plugs or vents. Vents (reed valves), located at each end of the yoke, will open under pressure to allow helium to escape during a quench. (These features will be tested when the magnet is tested at GSI in supercritical helium. BNL testing is in pool boiling.) The magnet has no beam tube in it. Standard RHIC construction is used to restrain the axial motion of the coil.

4 QUENCH TEST RESULTS

The magnet was tested in pool boiling helium (4.5 K nominal). It was initially operated at the RHIC ramp rate, 0.053 T/s (Fig. 3). The sixth and last quench at this ramp rate was at 7.76 kA (4.38 T central field), approximately equal to the short-sample limit of the cable and $\sim 10\%$ above the 4 T design. A different power supply was used for quenching at high ramp rate. It was found that both the magnet and this supply could ramp at 2 T/s, twice the design. Quench testing was carried out at this ramp rate because it reduced the DC heating of the power supply

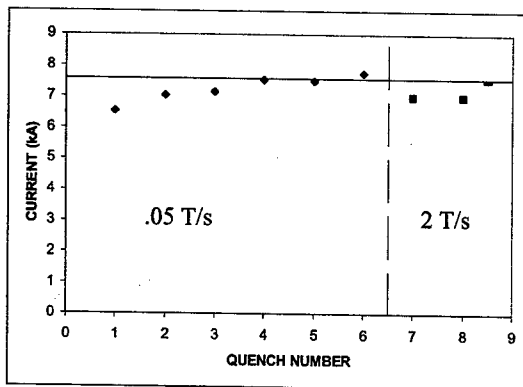


Figure 3. Quench history, showing six quenches at 0.05 T/s, followed by two at 2 T/s, then stable operation at 7.5 kA. The horizontal line indicates the estimated short-sample limit of the magnet.

leads, one of the power supply operational limits. The initial part of the program to measure energy losses was to cycle the magnet to 7000 A. It quenched a few moments after reaching 7000 A the first two times it was ramped to this current. Subsequently it was ramped numerous times to currents as high as 7500 A (the limit of the supply) at 2 T/sec without quenching. Thus, the magnet has substantially exceeded the quench current and ramp rate goals of the GSI design.

5 FUTURE PLANS

Work on the energy loss measurement is still underway and will be published at a later time.

Since this work was initiated, the energy of the accelerator has been increased 50%. The design value of the dipole central field has been increased, to 6T, a value beyond that which can be readily achieved in a magnet built with a single layer coil. Consequently, future plans for BNL/GSI work now focus on establishing design principles for such magnets.

The highest priority is the measurement of the magnetic fields during the 1 T/s ramp. Development of the new type of measurement system needed for this is underway. The present magnet will be tested in supercritical helium at GSI. The addition of ventilation holes to the inner edge of the cable is expensive, and at least one magnet should be built and tested to determine whether this venting is necessary. The use of two cores in the cable became necessary when holes in cable made with a single core

were found in the core near the keystone cable's narrow edge at the places where the wires crossed. Making cable with two cores is more difficult than making them with one core, so some further development was undertaken, resulting in the successful production of cable with a single core but no holes. To reduce losses further, strand with 3.5 mm filaments has been ordered.

6 CONCLUSIONS

A model magnet for the GSI SIS200 superconducting accelerator has been rapidly built using many components from the BNL RHIC arc dipoles. It has been successfully ramped at 2 T/s, forty times higher than the RHIC ramp rate and twice the design goal, to 4.38T, above the 4 T design field.

7 REFERENCES

- [1] Gesellschaft Fur Schwerionenforschung, "An International Accelerator Facility for Beams of Ions and Antiprotons," Conceptual Design Report, November 2001.
- [2] G. Moritz et al, "Towards Fast-Pulsed Superconducting Synchrotron Magnets," Proc. 2001 Particle Accelerator Conf. (Chicago IL, June 18-22, 2001), p. 211.
- [3] G. Moritz, "Superconducting Magnets for the 'International Accelerator Facility for Beams of Ions and Anti-protons' at GSI," Proc. 2002 Applied Superconductivity Conf., (Houston TX, Aug. 4-9, 2002).
- [4] M. Anerella et al., "The RHIC Magnet System," Nucl. Instrum. Meth. A 499 (2003) pp. 280-315.
- [5] M. N. Wilson et al, "Design Studies on Superconducting Cos θ Magnets for a Fast Pulsed Synchrotron," IEEE Trans. Appl. Superconductivity, Vol. 12, No. 1 (March 2002), p. 313 [MT17].
- [6] M. N. Wilson et al, "Cored Rutherford Cables for the GSI Fast Ramping Synchrotron," Proc. Proc. 2002 Applied Superconductivity Conf., (Houston TX, Aug. 4-9, 2002).
- [7] J. Muratore et al., "Test Results for Initial Production of LHC Insertion Region Dipole Magnets," Proc. 2002 European Particle Accelerator Conf. (Paris, June 3-7, 2002), p. 2415.

BEAM BASED MEASUREMENTS OF HYSTERESIS EFFECTS IN FERMILAB MAIN INJECTOR MAGNETS

B. C. Brown* and D. P. Capista, Fermi National Accelerator Laboratory[†], Batavia, IL 60510, USA

Abstract

Operation of the Fermilab Main Injector is sensitive to magnetic field differences due to hysteretic effects. Measurements using the beam are reported with various current ramps. This will provide magnetic field information for accelerator operations with better ramp control than is available from magnet test facility data. This makes possible improved low field reproducibility with mixed 120 GeV and 150 GeV operation of the Main Injector.

OPERATIONAL CONSIDERATIONS

The Fermilab Main Injector is a multipurpose synchrotron designed for injection at 8 GeV and extraction at 8, 120 or 150 GeV. Protons and antiprotons are accelerated to 150 GeV for injection to the Tevatron by accelerating them in opposite directions. Protons are accelerated to 120 GeV and extracted in a single turn for antiproton or neutrino production and resonantly extracted for experiments in the fixed target area. Ramps are initiated by a time line generator capable of synchronizing the Main Injector with the Tevatron and other Fermilab machines. Figure 1 shows a time line with typical ramp profiles for Main Injector dipole current. This figure shows cycles for antiproton production and one cycle for transfer of protons to the Tevatron. The Fermilab physics program requires changes in the mix of these required cycles as often as many times per day. Conditions with no 120 GeV cycles and conditions with no 150 GeV cycles are both experienced.

The acceleration ramps are specified by requesting momentum vs. time and using a model of the magnetic field response to specify current vs. time[1] based on the measured magnetic fields[2]. The power supply system uses measurements of the current, not the field achieved, for controlling the magnet current ramps. Tune control is achieved in a similar fashion[3]. If the field achieved is sufficiently matched to the specification, the RF feedback will accommodate small momentum errors. If the ramps are sufficiently reproducible, tune changes can be programmed to achieve the desired tune. It was expected that some adjustments of the ramp details would be required to match the current ramps to the required magnet response through use of changes in the hysteresis.

Measurements of the hysteresis properties of the Main Injector magnets were carried out at the Fermilab Magnet Test Facility. However, the power supply system used for these measurements had only unipolar voltage drive so the downramp current changes were limited to those achieved

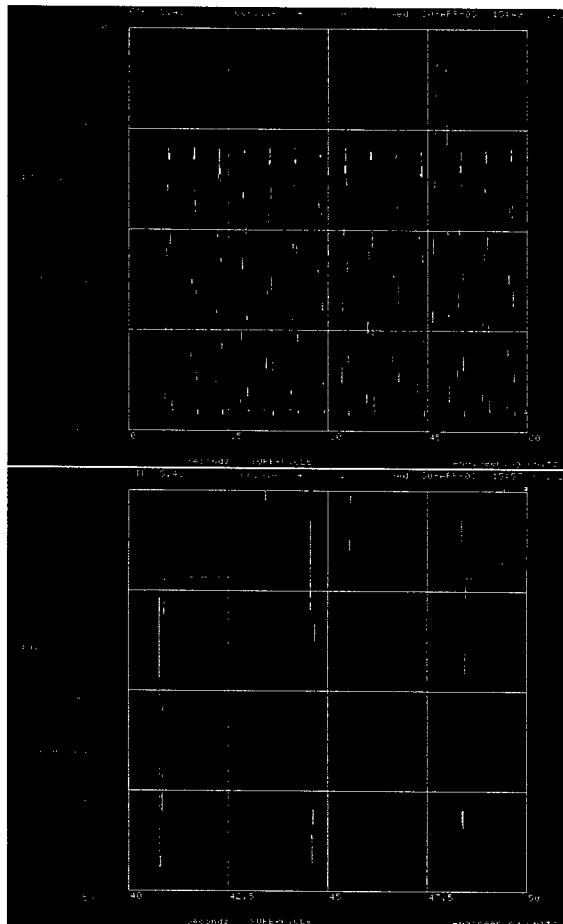


Figure 1: Main Injector Dipole magnet current vs. time in seconds in typical operation. Upper figure shows full scale with many 120 GeV ramps and a single 150 GeV ramp. Lower figure expands scale to show reset current following 120 and 150 GeV ramps. The injection porch requires a current just above 500 A.

with the inductive and resistive load attached. Even in laminated magnets, eddy current effects would be expected to modify the fields achieved. Thus, we expected and have found that the hysteresis depends on the downramp ramp rate in addition to the dependence on peak and reset currents. We carried out studies during commissioning to determine suitable ramps to attempt to match the injection fields achieved after 120 and 150 GeV ramps. This study extends those measurements using improved software and a larger variety of ramps.

* bcbrown@fnal.gov

[†] Operated by Universities Research Association Inc. under Contract No. DE-AC02-76CH03000 with the United States Department of Energy.

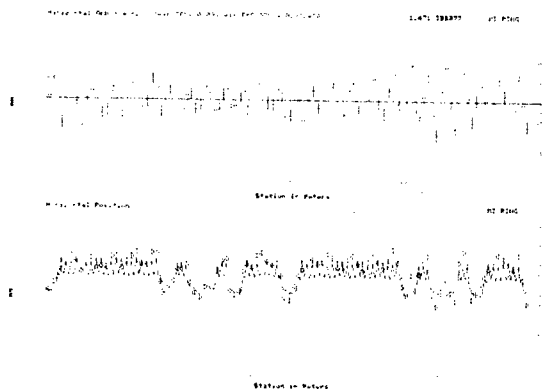


Figure 2: Orbit on standard 120 GeV ramp following a ramp with 130 GeV peak and standard -300 GeV/sec downramp. Reference orbit taken on standard 120 GeV Ramp following another standard 120 GeV ramp. The lower plot shows the measured orbit difference and that calculated for a difference of $dp/p = -0.82 \times 10^{-3}$. The upper plot shows the difference between measured and calculated orbits.

MEASUREMENTS

Ramp Specification

To specify the ramp properties that we control for hysteresis measurements, we consider the following ramp segments: injection porch, upramp, flattop, downramp, and reset. The reset portion extends the downramp below the injection momentum to allow a portion of the transition from hysteresis curve of downramp type[2] toward the upramp curve. Since the approach to the upramp is exponential, if the reset is sufficiently low, the injection field changes will depend linearly on small reset differences.

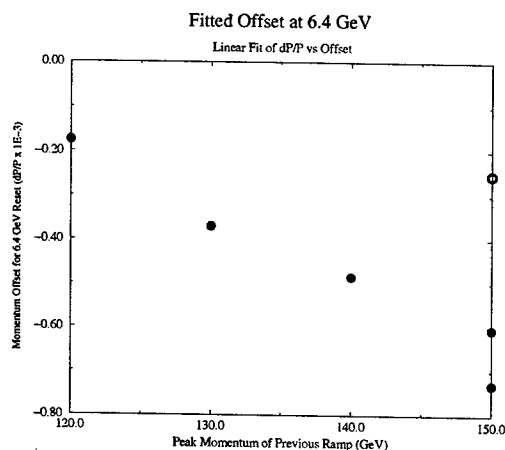


Figure 3: Momentum Offset at 6.4 GeV Reset vs. Peak of Previous Ramp for ramps with standard -300 GeV/sec downramp. Open circle for -150 GeV/sec downramp.

The desire to ramp quickly limits the reset to values well above zero.

Measurement Technique

Since we currently operate many 120 GeV antiproton production cycles for each 150 GeV cycle, we concentrate on making the 150 GeV cycle reset appropriate to allow the next 120 GeV cycle to experience the same injection field as those on 120 GeV cycles which follow other 120 GeV cycles. Using the I90 Application Program[4], the closed orbit of the injected beam is measured after injection into fixed rf buckets prior to initiation of rf feedback. The beam is injected into fixed frequency rf buckets so the closed orbit is set by the rf frequency and the magnetic field, not by the injected beam momentum. Analysis of the orbit in terms of fractional momentum error is accomplished within the program. To avoid issues of Beams Position Monitor (BPM) offsets, each data set is compared with a reference set obtained on a typical 120 GeV acceleration cycle. Some measurements show orbit differences which are completely dominated by the momentum error term which in turn reflects changes in the mean value of the bend field. Others additionally show some effects of dipole magnet-to-magnet variations and tune differences or other focusing effects. The average BPM error is sensitive to the momentum offset and independent of tune or other errors which are reflected in the RMS BPM error. By adjusting the momentum error input to the program until the average BPM error is zero, one can find the momentum offset which describes a data set.

Data and Analysis

Figure 2 shows results from analysis of a typical orbit difference measurement. The fitted pattern of the beam

Table 1: Fit Momentum Errors for 6.4 GeV Reset from linear fit of offset vs reset for sets of ramps with various peak currents. Where downramp rate is not shown it includes segments other than those in the ramps used for standard operation.

Reset GeV/c	dp/p $\times 10^{-3}$	downramp rate GeV/c/sec
150	-0.605	-300 GeV/s
130	-0.142	
100	-0.886	
50	-0.416	
27	-0.057	
150	-0.731	-300 GeV/s
140	-0.485	-300 GeV/s
130	-0.370	-300 GeV/s
120	-0.175	-300 GeV/s
100	-2.927	-300 GeV/s
150	-0.253	-150 GeV/s

position differences is characteristic of the Main Injector lattice with regions of regular cells interspersed with regions designed to provide zero dispersion. We interpret the fractional dp/p error described by the program as due to a hysteretic change in the bend field at the standard injection current.

For a set of peak currents, measurements were taken using a range of reset currents. The fractional momentum error vs. requested reset momentum was fit to a straight line and the fit momentum offset for a 6.4 GeV reset (that used prior to the 120 GeV cycle reference orbit) was obtained. In Figure 3 we show these offsets for measurements with peak currents 120 - 150 GeV where the downramp matched the standard operational downramp with -300 GeV/sec maximum slope. Also shown is the fit result for a 150 GeV peak ramp with -150 GeV/sec downramp.

To display the linear dependence of the fractional bend field error (as measured by the orbit dp/p) on reset momentum, we subtract the fitted offset at 6.4 GeV reset from the data set and plot it vs. requested reset momentum. We show the full range of our measurements in the lower plot of Figure 4 while the upper plot expands the scale. We see that ramp-to-ramp variations up to $\pm 0.2E-03$ are typical. The fitted dp/p at 6.4 GeV for this data are shown in Table 1. Included are several sets of data with different downramps and data with peak current below the 120 GeV comparison ramp.

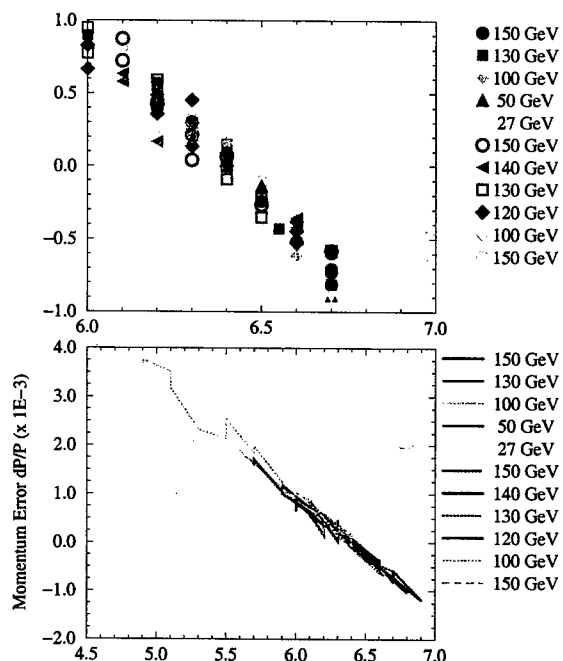


Figure 4: Fractional momentum error of following 120 GeV ramp vs. reset for various peak momenta. Final 150 GeV set used slow downramp. Offset at 6.4 GeV reset subtracted.

CONCLUSIONS

We have shown that Main Injector dipole fields at the standard injection current vary in the expected (approximately linear) fashion as a function of a reset current on the previous ramp cycle. For conditions similar to the standard 150 GeV operation mixed into the 120 GeV antiproton production cycles, we find a regular pattern in which the the offset of dp/p for a 6.4 GeV/c reset changes by about 4×10^{-4} between 120 GeV and 150 GeV ramps. The 150 GeV ramps experience a more negative momentum offset than 120 GeV ramps. Interpreted as a change in the field this corresponds to 0.4 Gauss out of the 1000 Gauss injection field. The remanent field of Main Injector dipoles is about 22 Gauss so peak field changes modify the remanent by about 1.8%. We interpret this to indicate that the higher peak field sets a remanent field which is lower. This then requires a higher reset momentum (less of a transition required).

The consistency among measurements provides evidence that this control of the reset allows one to modify the hysteretic portion of the injection field. Nevertheless, the values obtained in this study are different than have been found optimal for operational ramps which we interpret to imply that additional details of the ramps (dI/dt , flattop time...) may also affect the hysteretic remanent field. At present, control of the reset value at the end of each ramp provides adequate control of the injection field in mixed 120 and 150 GeV operation.

It had been observed that timelines with only 150 GeV ramps required changes of ≈ 6 MeV/c in the injection field compared with those with only 120 GeV ramps. Resets for both ramps had been set to 6.7 GeV/c. In October 2002 the reset for the 120 GeV ramps was set to 6.4 GeV/c and injection was tuned up for that value. Examination of the results in Figure 4 would suggest this would create a change of about 8×10^{-4} (7 MeV/c). We note that these injection currents no longer have to be changed when making this timeline change.

REFERENCES

- [1] B.C. Brown *et al.* Design for Fermilab Main Injector Magnet Ramps Which Account for Hysteresis. In *Proceedings of the 1997 Particle Accelerator Conference, Vancouver, B.C., Canada, 12-16 May 1997*, page 3245. IEEE, 1998.
- [2] B. C. Brown. Hysteresis Study Techniques and Results for Accelerator Magnets with Unipolar Current Excitation. In *Proceedings of the 1999 Particle Accelerator Conference, New York*, page 3315. IEEE, 1999.
- [3] G. Wu *et al.* Tune Control in the Fermilab Main Injector. In *Proceedings of the 1999 Particle Accelerator Conference, New York*, page 714. IEEE, Piscataway, N.J. 08855-1331, 1999.
- [4] M. J. Yang. A Beamline Analysis Program for Main Injector Commissioning. In *Proceedings of the 1999 Particle Accelerator Conference, New York*, page 723. IEEE, Piscataway, N.J. 08855-1331, 1999.

A NEW LAMBERTSON MAGNET FOR THE FNAL 400 MeV LINAC

J.-F. Ostiguy*, H.D. Glass, D.J. Harding, J. Lackey, W. Robotham
Fermi National Accelerator Laboratory, Batavia, IL 60510, USA †

Abstract

A new Lambertson magnet has been constructed for use at the downstream end of the Fermilab 400 MeV Linac. To reduce costs, the core is composed of laminations left over from the Main Injector dipoles with a round hole through one pole face. In contrast with more conventional Lambertson designs, the magnet is excited by two coils located above and below the field region. The integrated transverse fringe field at the end of the field-free region is minimized using a pole piece extension with 75% packing factor followed by a thick flux return plate. The relatively low packing factor prevents saturation of the extension by the return flux while preserving the odd longitudinal symmetry of the transverse flux distribution. Measurements show better than an order of magnitude reduction of the integrated transverse field, in good agreement with simulations.

INTRODUCTION

In this paper, we present the design rationale and the result of simulations and measurements performed on a new magnetic septum magnet of the Lambertson type. This magnet will be located at the downstream end of the Fermilab 400 MeV linac. By default, the linac H^- beam circulates through the field-free region of the magnet, into a spectrometer magnet and finally, to a beam dump. For injection into the Booster synchrotron, the beam is first kicked vertically into the bending region of the Lambertson and then horizontally into an injection stripping chicane.

Historical Background

In 1993, the Fermilab Linac was upgraded from 200 to 400 MeV by replacing the last four tanks of the original drift-tube Linac (which provided acceleration from 116 to 200 MeV) with 805 MHz side-coupled cavities (four times the original frequency). Raising the Booster injection energy reduced emittance growth by providing a reduction in space-charge tune-shift and improvements in magnetic field quality by reducing the relative importance of remanent magnetization and eddy currents. Coincidentally with commissioning of the upgraded linac, production of new dipole magnets for the Main Injector had just begun. Because of a tight schedule and a desire to minimize costs, a DC Lambertson magnet was built using readily available Main Injector dipole laminations. Since the beam circulating through the field-free region is directed to a dump, minimum attention was paid to end field effects beyond the ad-

dition of crude shielded extensions. Not surprisingly, it was later found that despite the presence of these extensions, the dipole kicks experienced by the beam in the end regions remained substantial enough to steer the beam away from the dump. Dipole correctors were installed; however, both operationally and from a safety point of view, they are somewhat of a nuisance because the excitations need to be carefully readjusted following every shutdown. A decision was made to build an improved version of the magnet, with the constraint that the lamination geometry should not be modified.

DESIGN CONSIDERATIONS

Lambertson magnets are typically used for extraction in high energy machines. For this application, the normally circulating beam traverses a field-free region, basically an opening carved into one of the poles of a dipole magnet. At extraction, an upstream pulsed kicker magnet moves the beam vertically (horizontally) into the dipolar field region (i.e. the so-called bending region) where it is deflected horizontally (vertically) into an extraction beamline. In practice, kicker magnets have limited strength, and the magnetic septum needs to be as thin as possible. The minimum thickness is obviously limited by saturation which causes penetration of the flux into the field-free region. To retard the onset of saturation, the field free region opening often has a characteristic V-shaped notch to take maximum advantage of the smaller diameter of the (higher energy) extracted beam.

The Lambertson magnet described in the paper is used for injection. The field-free opening has a simple 44.5 mm (1.75 in) diameter circular shape to accommodate a 5 mm-mr (95%) beam. At 400 MeV, kicker strength is less of an issue and the magnetic septum has a minimum thickness of 5.56 mm (0.219 in). Furthermore, since the beam makes only a single pass through the field-free region, field quality requirements are not as stringent as they would be for a storage ring.

An important consideration for Lambertson magnets is the effect of fringe field in the end regions. Magnetic flux lines originating from the opposite pole have a tendency to terminate on the interior of the field-free opening since it is at the same magnetic potential as the pole it is carved into. If no special measures are taken, a strong transverse magnetic field is present at the extremities of the field-free region. Since this field has an asymmetric and nonlinear dependence on radial offset, its presence can lead to serious perturbations. To mitigate fringe field effects, two approaches are possible. The obvious one is a complete suppression of the fringe field. This can be accomplished

* ostiguy@fnal.gov

† Work supported by the US Department of Energy under contract number DE-AC02-76CH03000.

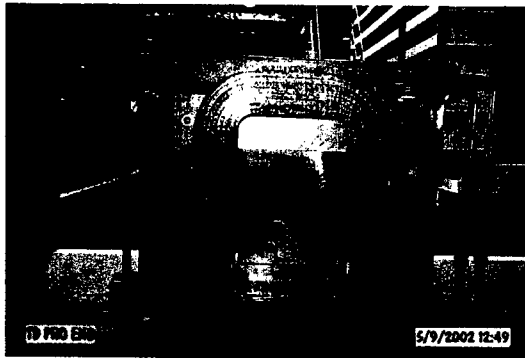


Figure 1: View of an extremity with the end plate removed.

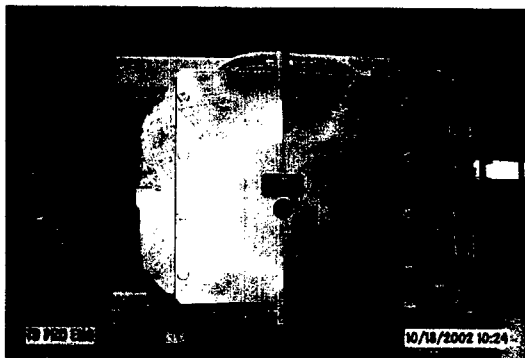


Figure 2: Shield plate at the lead-end extremity.

by making the surface of the pole containing the field-free region completely flat, extending it a few gap lengths beyond the end of the other pole and by providing a high permeability path for the flux to return before it reaches the edge of field-free aperture [3]. The second possibility is to force the magnetic field in the end regions to be predominantly longitudinal [1, 2]. This can be done by placing a thick shield (a steel plate which mirrors the field-free opening) at a small distance away from the end of the magnet. The flux leaves one of the poles and enters the shield at



Figure 3: Shield plate at the non lead-end extremity.

normal incidence; it then circulates around the openings and back into the opposite pole. If the plate permeability is high, its surface is a magnetic equipotential and the field vanishes downstream from it. In the gap between the end of the field-free region and the corresponding opening in the shielding plate, the magnetic field has a transverse component. However, the latter possesses an odd longitudinal symmetry with respect to the center of the gap. In practice, this symmetry becomes more exact as the distance between the pole end and the shielding plate is reduced, the relevant dimension being the thickness of the septum. Making the gap very small is generally not an option because it increases the flux circulating through the shield and saturates it, rendering it ineffective. To preserve both the odd longitudinal symmetry of the transverse magnetic field and to avoid saturation of the shield plate, the space between the end of the field-free region and the plate can be filled with (magnetically) loosely packed laminations.

Because it was not possible to modify the existing magnet core, the second approach was selected. Magnetic shielding plates were built out of solid 7.6 cm (3 in) thick steel. To allow for in-tunnel assembly and disassembly, each plate is made out of two pieces approximately of the same size, horizontally joined together. At both magnet extremities, the field-free pole is extended by 9.8 cm (3.850 in) using alternating laminations of 1.5 mm (0.0598 in) steel and 0.5 mm (0.020 in) G-10, yielding a 75% packing fraction. The shielding plate mechanically rests on the end of the extension.

SIMULATIONS AND MEASUREMENTS

To model the magnet and optimize the shield thickness and the packing factor of the field-free pole extension, we used OPERA3D [4], a standard FEM magnetostatics code. Only one end was modeled, assuming a somewhat simplified end plate geometry very similar to that of the entrance plate (lead-end). Note that the exit plate geometry is somewhat different due to the large bend angle (9.9 deg) and the need to accommodate vacuum connections and other neighboring hardware. The shielding plate geometries are shown in Figures 2 and 3. To gain some confidence and as a reference to assess the effectiveness of the end effect mitigation scheme, we first measured and modeled a bare rectangular end as shown in Fig. 1. The results are presented in Fig 4. Following a few iterations (both computational and experimental) a satisfactory geometry was attained. It is likely that further optimization could lead to even better performance, but this was not pursued. Figure 5 shows contours of the magnetic field magnitude in a shielding plate which does not have sufficient thickness. The area where saturation occurs (in red) indicates the importance of providing enough width. When the plate is not magnetically equipotential, a characteristic long transverse field tail is produced. Figure 6 shows measured (using a Hall probe) and computed transverse magnetic field at the end of the field-free region for the final geometry (the origin coincides

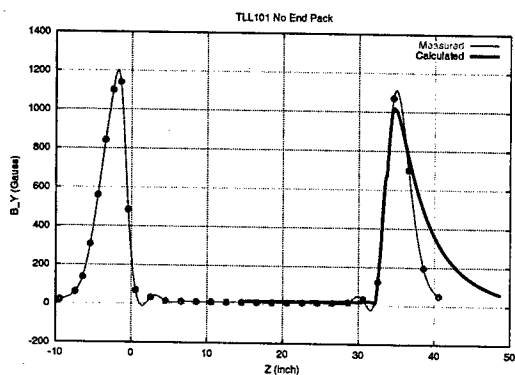


Figure 4: Measured transverse magnetic field in absence of endpacks. The integrated magnetic field is 240 G-m. The calculated field is also shown for comparison.

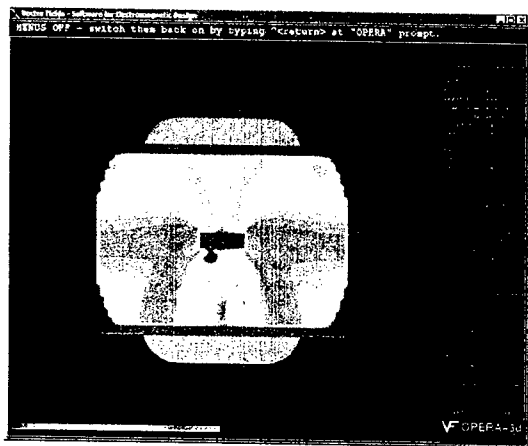


Figure 5: Calculated flux magnitude distribution in the shielding plate, assuming a field-free extension of 4.125 in, 75% packing factor and a plate thickness of 0.75 in.

with the surface of the shielding plate). At the center of the field-free region, the field is almost exclusively longitudinal. At ± 0.375 in vertical offset, a pattern resulting from the curving of the field lines near the edges of the circular aperture is observed. The odd symmetry is nearly perfect in the direction away from the septum and a little bit worse in the opposite direction. Compared with a simple rectangular end, the measured integrated transverse field strength is reduced by a factor of 12 i.e. from 240 to 19 G-m.

DISCUSSION AND CONCLUSION

Reduction of fringe-field effects at the extremities of the field-free region of a Lambertson magnet is a common problem. The strategy presented in this paper allows one to reduce the magnitude of the transverse field perturbation by one and possibly up to two orders of magnitude. However, a longitudinal component of roughly the same amplitude as the uncorrected transverse one remains. In applications

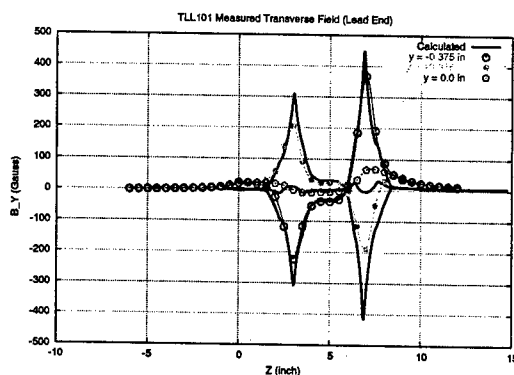


Figure 6: Transverse magnetic field in the field-free region measured at different radial offsets.

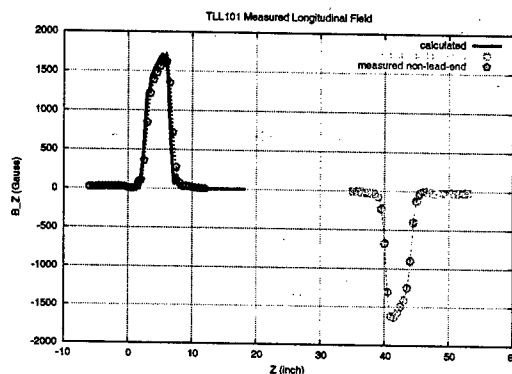


Figure 7: Measured longitudinal magnetic field in the field-free region. The calculated field is also shown for comparison.

where the beam normally circulates through the field-free region, the presence of this longitudinal component may introduce small amounts of transverse coupling and focusing whose impact on beam dynamics needs to be quantified and taken into consideration.

REFERENCES

- [1] J.-F. Ostiguy and D.E. Johnson, "3D End Effects in Iron Septum Magnets", Proceedings of the 1995 Particle Accelerator Conference, Dallas, TX, pp. 1349-1351
- [2] D.E. Johnson et al., "Design and Magnetic Measurements of the Fermilab Main Injector Lambertson", Proceedings of the 1997 Particle Accelerator Conference, Vancouver, Canada, pp. 3272-3274
- [3] N. Tsoupas et al., "Design and B-Field Measurements of a Lambertson Injection Magnet for the RHIC Machine", Proceedings of the 1995 Particle Accelerator Conference, Dallas, TX, pp. 1352-1354
- [4] OPERA, Vector Fields Ltd, Oxford, UK

PULSE OCTUPOLE MAGNET SYSTEM AT THE PHOTON FACTORY STORAGE RING

Tsukasa Miyajima*, Yukinori Kobayashi and Shinya Nagahashi,
High Energy Accelerator Research Organization, Tsukuba 305-0801, Japan

Abstract

In order to study a dynamical property of a vertical instability, we have developed a pulse octupole magnet system. The magnet can be operated with magnetic field rise and fall time of around 1.2msec, respectively. The maximum integrated field strength reach up to 2600T/m². We measured the dynamical behavior of the vertical instability using the pulse octupole magnet for a multi-bunch beam of 400mA. We found that the growth time of the instability was longer than the suppression time.

INTRODUCTION

In the Photon Factory Storage Ring, a vertical instability is observed in a multi-bunch operation mode. The instability can be suppressed by DC octupole magnetic field in routine operation. It seems that the instability is caused by ion trapping effect, the operating parameters in routine operation are near the threshold of it, and Landau damping caused by octupole field is suppressed the instability [1].

In order to study the dynamical behavior of the instability, we developed a pulse octupole magnet system which can produce the octupole field with rise and fall time of around 1.2msec. We installed the magnet system in the PF-ring, and have made a detailed study. In this paper, we describe the design performance, the results of magnetic field measurement and preliminary results of a measurement for the behavior of the instability.

PULSE OCTUPOLE MAGNET SYSTEM

The pulse octupole magnet system can provide a octupole magnetic field with rise and fall time of around 1.2msec, respectively. The principal parameters are given

Table 1: Principal parameters of the pulse octupole magnet system.

Parameter	Value
Maximum field gradient (peak)	11700 T/m ³
Maximum peak current	±100A
Maximum peak voltage	±285V
Bore diameter	80 mm
Core length	0.20 m
Effective length	0.22 m
Self inductance	3.34 mH

*E-mail address: tsukasa.miyajima@kek.jp

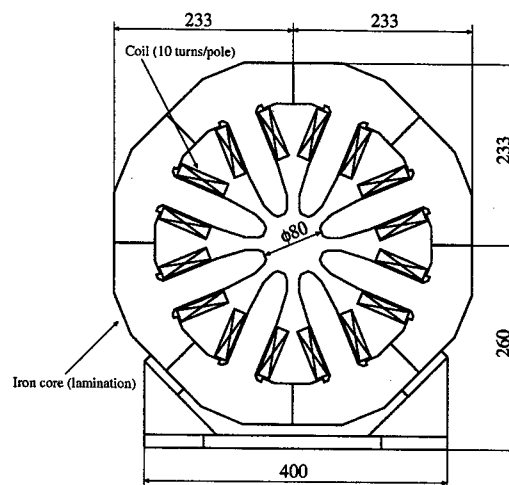


Figure 1: Cross sectional view of the pulse octupole magnet.

in Table 1. It consists of a magnet, a ceramic duct and a power supply.

Pulse Octupole Magnet

The pulse octupole magnet was designed by the use of a computer code POISSON to realize the maximum field gradient of 11700 T/m³ at the excitation current of 1000A-turns and the self inductance of about 3mH. In order to realize the high field gradient, the bore diameter of the magnet was designed to be 80mm. To reduce the in-



Figure 2: Photograph of the pulse octupole magnet installed in the PF ring.

ductance, it was determined that the turn number of the coil was 10 turns/poles, then the calculated inductance was 3.24mH, and the measured inductance was 3.34mH.

Cross sectional view and photographs of the pulse octupole magnet are shown in Fig. 1 and 2. The iron core is made of the 0.5mm thick silicon steel lamination and the length of the iron core is 0.2m.

Ceramic Duct

A ceramic duct, as shown in Fig. 3, was adopted to avoid problems of the eddy currents. In order to reduce a beam coupling impedance, inner-side of the duct was coated with Ti of 5 μ m thick. The coating was connected with the both ends of Fe-Ni-Co flange(see Fig. 3). The duct caused no problems in both single and multi bunch operation. The temperature of the duct was not raised practically, when a single bunch beam of 70mA was stored.

An absorber was placed at upper side of the pulse octupole magnet in order to prevent the synchrotron radiation from impinging on the duct.

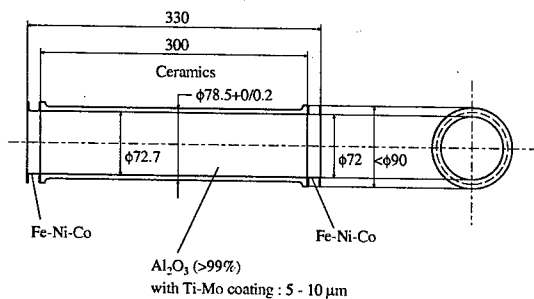


Figure 3: Ceramic duct coated Ti-Mo.

Power Supply

Since the inductance of the magnet is about 3mH, to excite the magnet with 1.2msec to maximum current of 100A, the power supply must output maximum voltage of about 280V. In order to realize the magnetic field rise and fall time of around 1.2msec, the power supply was designed to be maximum current of 100A and maximum voltage of 285V.

FIELD MEASUREMENT

The field measurement of the pulse octupole magnet was performed using two method: a harmonic coil method for static magnetic field and hall sensor for pulse magnetic field.

DC Octupole Field

The static field measurement of the pulse octupole magnet was performed using DC power supply and a harmonic coil that consisted of the long coil to measure integrated

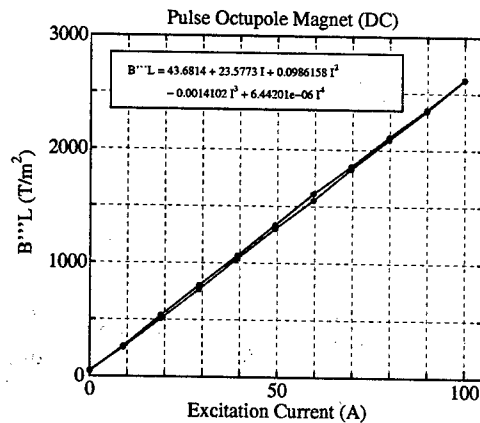


Figure 4: Excitation curve of pulse octupole magnet.

field and the short coil to measure center field. Fig. 4 shows the excitation curves of the integrated octupole field. The maximum integrated field was 2623T/m² and the maximum field gradient of the magnet center was 11695T/m³ at the excitation current of 100A. The effective magnetic length, which was calculated from the measured value of the center and the integrated field, was 0.22m.

Pulse Octupole Field

The response of the pulse magnetic field was measured using a hall sensor. The sensor was set at $x = -30$ mm(horizontal plane) and $y = 0$ mm(vertical plane) inside the magnet. The pulse signal of set current consists of the magnetic field rise up time of 1.2msec, flat top time of 2.4msec and fall down time of 1.2msec. In order to investigate the effect of eddy current, the field measurement was performed under two conditions: with a test aluminum duct of 15 μ m thick inside the magnet and with out the duct. The response of the magnetic field at the excitation current

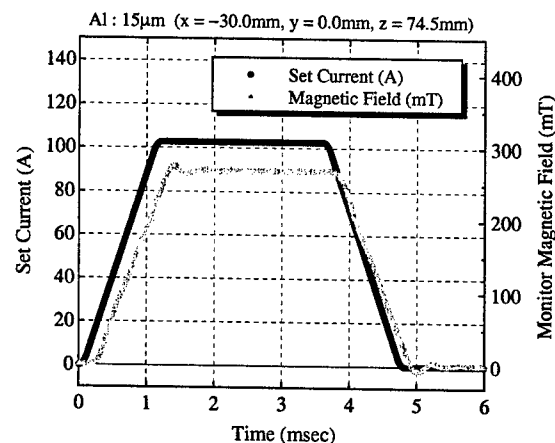


Figure 5: The response of the pulse octupole magnet.

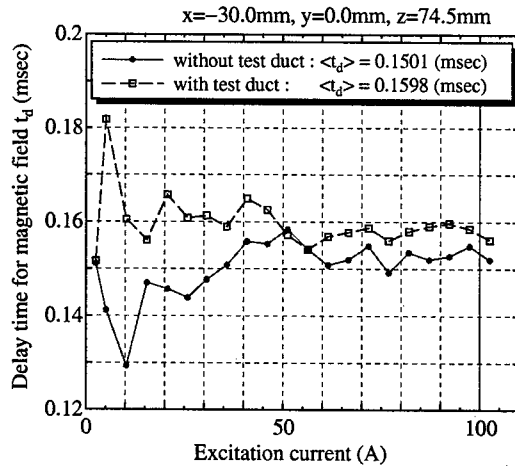


Figure 6: Measured delay time of the pulse octupole field from the set current signal with and without the test aluminum duct of 15 μ m thick. The set current signal is shown in Fig. 5.

of 100A with the test aluminum duct is shown in Fig. 5. The measured magnetic field was delayed about 0.16 μ sec from the set signal. The delay time with and without the test aluminum duct is shown in Fig. 6.

MEASUREMENT OF BEAM INSTABILITY

In order to measure the behavior of the beam instability when the pulse octupole field is excited, we measured the beam spectrum from a button-type electrode using real-time spectrum analyzer. We set the ring parameter in the vicinity of the threshold of the instability suppression. Under this condition, the instability was suppressed when only the pulse octupole magnet was excited.

Fig. 7 shows the beam spectrum in the vicinity of the second harmonic of the rf frequency f_{rf} when we excited the pulse octupole magnet at 100A. The beam current was 400mA with 280 bunches. Fig. 8 shows power of the vertical instability at $2f_{rf} - f_{rev} + f_{\beta y}$, where f_{rev} and $f_{\beta y}$ are the revolution and the vertical betatron frequency, respectively. After excitation of the magnet, the power spectra of the instability decreased, namely, the instability was suppressed. After 50msec, the instability was grown slowly compared with to suppress it.

SUMMARY

We developed the pulse octupole magnet system at the Photon Factory storage ring. The magnet system satisfied design performance: the rise and fall time of the magnetic field was 1.2msec and the maximum integrated octupole field strength reached 2600T/m². We obtained preliminary results of a measurement for the dynamical behavior of the instability. We will study the dependence of the instability on beam current and fill pattern of the bunch train.

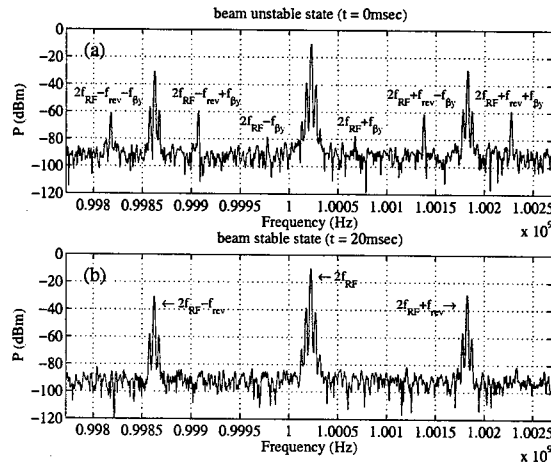


Figure 7: Beam spectrum from a button-type electrode when the pulse octupole magnet was excited at 100A. The beam current was 400mA with 280 bunches. (a) The spectrum when the vertical instability was excited at $t = 0$ msec in Fig. 8. (b) The spectrum when the instability was suppressed at $t = 20$ msec.

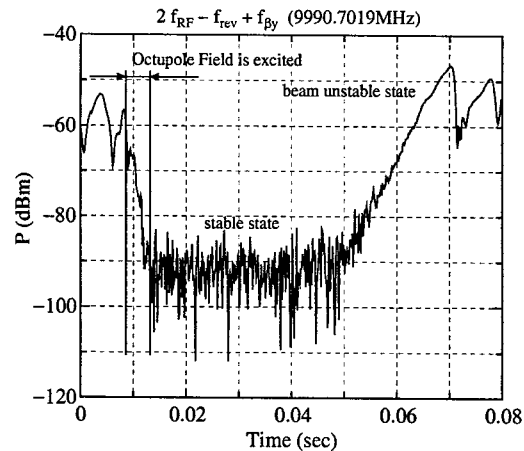


Figure 8: Power of the vertical instability at $2f_{rf} - f_{rev} + f_{\beta y}$. The pulse octupole magnet was excited at 100A from $t = 8$ msec to 12.8msec.

ACKNOWLEDGMENTS

The author wish to express their gratitude to Y. Hori, Y. Tanimoto, S. Asaoka and T. Uchiyama for remodeling the ring for the installation of the pulse octupole magnet.

REFERENCES

- [1] Y. Kobayashi, *et al.*, "Measurement of the Beam Decoherence due to the Octupole Magnetic Fields at the Photon Factory Storage Ring", EPAC98, Stockholm, June 1998.
- [2] L. Walckiers, "The Harmonic-Coil Method", CERN 92-05, p.138.

SPEAR3 GRADIENT DIPOLE CORE FABRICATION

N. Li, J. Tanabe, R. Boyce, D. Dell'Orco, David Ernst, SLAC, USA
X. Wang, N. Xu, IHEP, China

Abstract

Traditional means of core fabrication are to glue the laminations or weld them to form the yoke structure. These means result in good yoke assemblies for shorter (<0.6 meter) magnets. However, because of weld distortions or mechanical strength limitations, welding and/or gluing techniques result in cores with poor mechanical precision or limited mechanical strength for longer cores. The SPEAR3 gradient dipole magnets are up to 1.45 meters long and require distortions of <0.05 mm. Therefore, the SPEAR3 gradient dipole core design incorporated an assembly technique, originally devised for the PEPI Insertion quadrupoles and later adapted for the ALS gradient magnets. This technique involves fabricating a rigid frame for the core, precisely stacking and compressing the laminations using hydraulic jacks and granite surfaces and straight edges, and fixing the laminations in the frame by filling the grooves between the laminations and frame using steel loaded epoxy. Although this technique has been used in the past, it has never been fully described and published. This paper is written to provide a detailed description of the procedure and to present measurement data demonstrating the mechanical precision and stiffness of the resulting product.

CORE CONFIGURATION

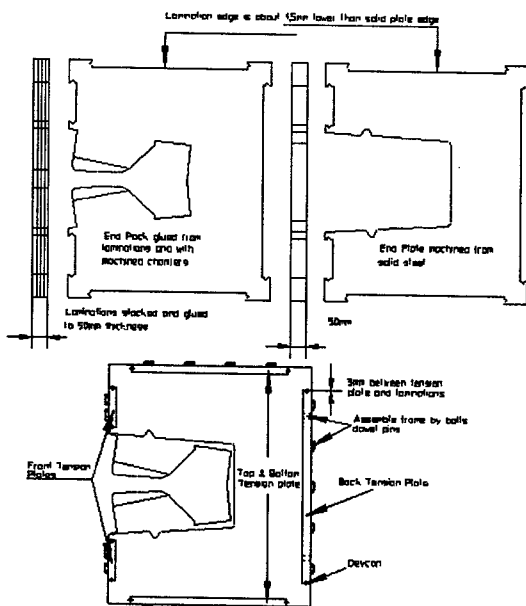


Figure1. SPEAR3 Gradient Dipole Core Configuration

As shown in figure1 above, the laminated dipole core consists of a rigid box frame which is assembled from

five tension plates and two solid end plates. The tension plates are bolted and dowel pinned to end plates. After the laminations are stacked and compressed in the frame, steel loaded epoxy is injected into the grooves, permanently fixing the laminations in the frame. The frame is designed to take all the bending and twisting stresses due to the weight of the laminations and the points of support.

CORE STACKING

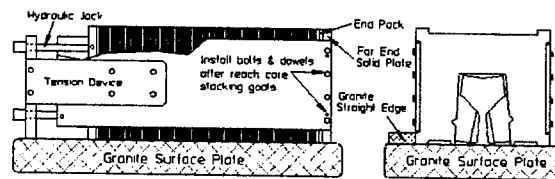


Figure2. Dipole Core Stacking

As shown in the figure 2 above, two side tension plates (top and bottom plates) are assembled to one of the end plates of the core and tension device. The laminations and the second end pack are then stacked inside of this frame assembly and indexed to granite surface and granite straight edge to ensure straightness of the core. The laminations are periodically flipped about their axes in order to maintain mechanical symmetry. Several compression stages are required as the length is built up. During the intermediate compression stages, adjustment of hydraulic jacks' extension is required. The final end pack and solid end plate are then installed and the whole assembly is compressed until the core required length and packing fraction is achieved. Bolts and dowels are finally installed. The final hydraulic pressure is chosen to achieve the following goals: a. the laminations are brought up "metal to metal"; b. the laminations, which are slightly warped, are flattened; c. compression is continued until the packing fraction is no less than 97.5%. Excessive compression will cause laminations to move laterally and cause the final core to exceed the straightness and flatness specification. Figure 3 below shows the actual compression pressure achieved during SPEAR3 dipole 109D-31 core assembly.

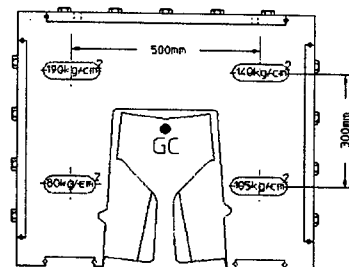


Figure3. Stacking Compression

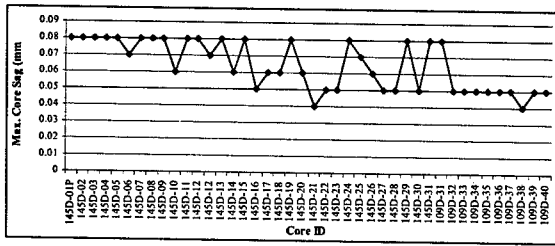


Chart2. Dipole Core Max. Sag Measurement Result

CONCLUSION

Considering the length and size of SPEAR3 gradient dipole, the achievement of the mechanical tolerances of 40ea SPEAR3 gradient dipoles is very impressive. Also, from the practical and cost point of view, Devcon application is easier to perform and results in straighter cores than the traditional welding methods. As long as the core squareness has been reached by the end of the stacking, it will not deform during epoxy cure. The traditional welding process would require highly skilled welders and careful weld sequencing to avoid thermal distortions. Even if low distortion welding sequences are developed, they can be difficult to reproduce with different welders. The technique of Devcon application is relatively easy to learn by inexperienced technicians. What he/her needs to do is just to strictly follow the written specifications step by step; a consistent result will be achieved each time.

One dipole 145D-09 dropped out the truck accidentally during in site transfer at SLAC, all six coils were damaged. This accident gave us a unique opportunity to test the stiffness of Devcon bonded core. 145D-09 was sent back to IHEP for repairs. IHEP inspector re-measured the core when receiving the damaged 145D-09. From chart 1 one can see that the perpendicularities (tolerance #2 and #4 in figure6) stayed the same as it was, the flatness of surface B (tolerance #3 in figure6) slightly increased about 0.025mm, the parallelism (tolerance #1 in figure6) jumped about 0.2mm. These measurement results showed that the core squareness was well preserved under severe impact, and demonstrated that the bonding between laminations and tension plates were very strong. IHEP installed new coils to dipole 145D-09 and used the old core. Chart3 showed the magnetic field uniformity measurement of 145D-09 before and after repairs. One can see that the magnetic field quality after repairs were identical to the original measurements.

As summarized above, we believe that a steel loaded epoxy - Devcon application is a mature, economical and easily learned procedure for longer magnet core fabrication. The mechanical precision and structural rigidity are good and robust.

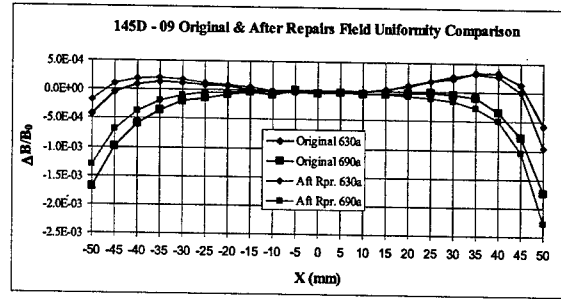


Chart3. Dipole 145D-09 Magnetic Field Quality

REFERENCES

- [1] SSRL Engineering Note M337 "Gradient Dipole Magnet Core Assembly Devcon Epoxy Application Procedure"
- [2] SSRL Engineering Note M308 "Gradient Dipole Magnet Core Assembly Procedure"
- [3] SSRL Engineering Note M409 "Resolution of the Problems Occurred in SPEAR3 Magnet Production"
- [4] SSRL Engineering Note M354 "Mechanical Quality of SPEAR3 Magnets Built at IHEP, China"

COST BASED FAILURE MODES AND EFFECTS ANALYSIS (FMEA) FOR SYSTEMS OF ACCELERATOR MAGNETS*

Cherrill M. Spencer, SLAC, Menlo Park, CA 94025

Seung J. Rhee, Dept. of Mechanical Engineering, Stanford University, Stanford, CA 94305

Abstract

The proposed Next Linear Collider (NLC) has a proposed 85% overall availability goal, the availability specifications for all its 7200 magnets and their 6167 power supplies are 97.5% each. Thus all of the electromagnets and their power supplies must be highly reliable or quickly repairable. Improved reliability or repairability comes at a higher cost. We have developed a set of analysis procedures for magnet designers to use as they decide how much effort to exert, i.e. how much money to spend, to improve the reliability of a particular style of magnet. We show these procedures being applied to a standard SLAC electromagnet design in order to make it reliable enough to meet the NLC availability specs. First, empirical data from SLAC's accelerator failure database plus design experience are used to calculate MTBF for failure modes identified through a FMEA. Availability for one particular magnet can be calculated. Next, labor and material costs to repair magnet failures are used in a Monte Carlo simulation to calculate the total cost of all failures over a 30-year lifetime. Opportunity costs are included. Engineers choose from amongst various designs by comparing lifecycle costs.

INTRODUCTION

There is worldwide consensus that a high-energy, high-luminosity, electron-positron linear collider, operating concurrently with the Large Hadron Collider, is necessary to explore and understand physics at the TeV scale. The linear collider (LC) is envisioned as a fully international project, thus there will be only one LC to serve the world particle physics community and it must meet its luminosity goal through a guaranteed availability over a 30 year lifetime. Therefore every LC component must be highly reliable and/or quickly repairable.

One viable manifestation of a 1TeV LC is the Next Linear Collider (NLC), based on normal conducting X-band cavities. The facility is roughly 32 km in length and uses about 70,000 components of which 7200 are magnets and 6167 are power supplies. We have developed a set of analysis procedures for engineers to use to decide how much money to spend on improving the availability of any LC component through design changes. The LC will not be built if it is "too expensive", we must find an appropriate balance between performance, reliability and cost. This paper uses the magnets and power supplies of the NLC to illustrate some useful modifications to the Failure Modes and Effects Analysis (FMEA) risk-

identifying technique, which involve life cycle costs, from design to operation.

PROBLEMS WITH TRADITIONAL FMEA

A team of engineers following the traditional FMEA process consider all the possible failures modes of a system component, from design through operation, identify all their causes, and rank their severity, expected frequency and likelihood of detection. A multidisciplinary team at SLAC carried out a FMEA of a standard SLAC electromagnet [1] and identified 10 design changes that would improve its reliability. A prototype NLC quadrupole that incorporated most of these changes was fabricated in 2000 [2] and has been run for about 10,000 hours since without any failures. The degree of risk of each failure is represented by the product of these 3 ranked indices, called the Risk Priority Number (RPN). But inconsistent definitions result in questionable risk priorities, and the use of failure modes rather than cause and effect fault chains inhibits ones understanding of the true causes of failures [3]. Furthermore traditional FMEA ends with the calculation of RPNs, the team does not consider the consequences of the failures in terms of costs. They do not check that their design changes for avoiding failures cost less than the failures [4].

LIFETIME COST: A MEASURE OF RISK

Risk contains 2 basic elements (1) chance, measured by probability, and (2) consequence, measured by cost. A new methodology has been developed to overcome these shortcomings, it is called "Life Cost-based FMEA" [3,4]. It measures risk of failure in terms of cost. Cost is a universal language understood by engineers without ambiguity. Expected failure cost is defined as the product of the probability of a particular failure and the cost associated with that failure. Lifetime failure cost is the sum of all the expected costs for all failure scenarios at all stages of a system component's life: design, manufacture, installation, and operation. The probability of a failure can be characterized as the frequency of such failures in a system containing multiple components, e.g. in an accelerator with 4965 water-cooled magnets there will be 9 water leaks a year that cause a severe enough magnet failure to bring down the beam. The cost of each water leak includes labor costs to detect it, repair it and get beam running again, which are proportional to the times these tasks take, and the costs of parts that have to be replaced, e.g. a piece of *Synflex* hose with fittings carrying cooling water.

Work supported by Department of Energy contract DE-AC03-76SF00515

In order to be confident in one's expected failure costs, it is best to measure failure rates and typical fixing times using historical data on systems of components similar in design to the ones you are doing a FMEA on. The next part of this paper describes how we have used the SLAC accelerator failure database (CATER) to make predictions about the availability of the NLC electromagnet and power supply (PS) system. Availability is defined as the average ratio of the time a component or system is usable to the total amount of time it is needed. It is calculated as the ratio of the Mean Time Between Failures (MTBF) to the sum of MTBF and the Mean Time To Repair (MTTR).

ESTIMATE FAILURE OCCURRENCE RATES FOR NLC MAGNETS & PS

Our premise is that the design of the NLC magnets and PS, their fabrication techniques, installation and repair procedures will be very similar to those used at SLAC over the past 35 years, therefore they will have the same failure modes occurring at the same rates as SLAC failures. The methodology described here was developed by considering SLAC magnets and PS and predicting for NLC magnets and PS, but it is applicable to any accelerator component that may fail and abort the beam.

Find MTBF & Availability of SLAC Magnets

We scoured the CATER database to find all magnet and switching PS failures in any beamline at SLAC which brought down the beam in the 5 year period 1997 to 2001. We categorized failures by magnet type: solid wire or water cooled and PS type: "small" : <12A, <0.5KW and "large": >12A,>0.5KW. We carefully counted how many magnets and PS were running in each beamline, and established how many hours each beamline was scheduled to run in that 5 years, thus we calculated number of magnet hours = no. magnets x no. running hours. Then we calculated the MTBF for any one magnet in that beamline. = no. magnet hours / no. failures reported. Table 1 shows the data for water cooled magnets for selected beamlines.

Details of each failure in CATER yielded the total time the beam was down, which we called the time to repair, TR, and particulars on the failure so we could place each one into a specific failure scenario, e.g. water leak from split hose leading to coil overheating, or turn to turn coil short due to damaged insulation.

We found these failures: 70 water cooled magnets, 6 solid wire magnets, 92 large PS and 70 small PS in the stated period. Each failure took a different amount of time to detect, i.e. to realize which component's failure had brought down the beam, and to repair. The TRs of 23 "water leak" failures ranged from 1 to 32 hours, these ranges must be accounted for when one calculates the predicted costs of failures for the NLC. The mean time to repair, MTTR, for a certain category of failures is calculated by dividing their total repair time by the number of failures, this is 10 hours on average for SLAC water cooled magnets. To calculate the average SLAC water cooled magnet's MTBF we summed the magnet running hours from 15 beamline runs (=80,383,136 hrs) and divided that by the 70 failures to give 1,148,331 hours. Then the availability of one "average" SLAC water cooled magnet is $1,148,331 / (1,148,331 + 10) = 0.99999127$.

Predict Availability of System of NLC Magnets.

To calculate the availability of a system of N equivalent components in series, one raises the availability of one component to the Nth degree. In the 2001 NLC configuration, there will be 4965 water cooled magnets. If we built them without any effort to improve their MTBF or MTTR over an average SLAC magnet their availability would be 0.9576. By the same process, we predict the 2202 solid wire magnets in NLC would be 0.9988 available, leading to an overall magnet availability of $0.9576 \times 0.9988 = 0.9565$, which is less than the required 0.975. By the same process, we predict the overall availability of the 6167 power supplies that will power the NLC magnets to be 0.9279, less than the required 0.975.

In other words, we cannot design, build and repair the NLC magnets and PS just the same as we have SLAC magnets if they are to meet our NLC availability goals. We choose to do a "Life Cost-based FMEA" to identify those failure scenarios that would be most costly to the project if not prevented. These will be the types of failures we will tackle first as we develop strategies to increase MTBF and decrease MTTR and thus improve availability.

Estimate Failure Occurrences and Frequencies.

We assume the NLC will run 9 months (=6480 hours) out of every year for 30 years, during the other 3 months preventative maintenance will be done on all components.

Table 1. Measuring Availability of Water Cooled Magnets at SLAC, 1997-2001. Selected beamlines

Dates Line Ran	Beam Line	Run Hours	No. of Magnets	Magnet Hours	No. of # Failures	MTBF (hr)	TR (hr)	MTTR (hr)	Availability 1 Mag	PPM
5/1/97 - 6/8/98	SLC	8828	2302	20,322,056	32	635,064	469.5	14.67	0.999976898	23.1
	HER	918	1240	1,138,320						
1/12/00 - 10/31/00	PEP II	6624	2602	17,235,648	7	2,462,235	34.6	4.94	0.999997993	2.0
	BSY/FFTB	2196	198	434,808						
	BSY/A-Line	630	520	327,600						
1/10/01 - 12/31/01	PEP II	7411	2602	19,283,422	7	2,754,775	37.9	5.41	0.999998035	2.0
	BSY/FFTB(e+)	2795	198	553,410	2	276,705	3.05	1.53	0.999994489	5.5
	BSY/A-Line	820	520	426,400						

Table 2. Life Cost-Based FMEA Table for Some Water Cooled Magnet Failures

Failure Scenario	Ultimate Effect of Failure	Input										Output		
		Origin	Detection Phase	Re-occurring	Frequency	Detection Time	Fixing Time (hr)	Delay Time (hr)	Recovery (hr)	Quantity	Part Cost (\$)	Labor Cost (\$)	Material Cost (\$)	Opportunity Cost
Too many loads on water circuit	Magnet overheats, is turned off	Oper	Oper	30	0.01	0.5	4		4.5	1	50	180	15	33,750
Conductor Sclerosis (hole gets too small)	Magnet overheats, is turned off	Oper	Oper	30	0.5	1	8		9	1	1,250	18,000	18,750	3,375,000
Water passage is blocked due to foreign object	Magnet overheats, is turned off	Oper	Oper	30	2	1	4		5	1	50	38,400	3,000	7,500,000
Damaged (crimped) coil	Shorted coil, magnet won't turn on	Inst	TR	1	4	0.5	2		0	1	1,250	1,280	5,000	
Water sprayed onto the coil	Shorted coil, magnet is turned off	Oper	Oper	30	3	2	8		10	1	50	38,400	1,500	7,500,000
LCW hose fails, water not cooling coil	Magnet overheats, is turned off	Oper	Oper	30	3	2	5.5		7.5	1	50	83,700	4,500	16,875,000
Water fitting or braze connection fails	LCW not reaching coil overheats etc	Oper	Oper	30	1	2	4.5		6.5	1	50	23,700	1,500	4,875,000
Loose Jumpers	Excessive heat lead to melting temp	Mfg	Test	1	4	0.5	2.5		0	1	100	1,560	400	
Poor terminal connection design	Excessive heat lead to melting temp	Des	Test	1	0.01	1	8		0	40	100	494	44	
Bad terminal installation	Excessive heat lead to melting temp	Inst	TR	1	4	0.5	2.5		0	1	100	1,560	400	
Poor thermal contact: thermal switch & cond	Magnet destroyed	Inst	Oper	1	1	0.5	4		4.5	1	11,000	600	11,000	112,500
Human Error - Magnet missing	Forgot to put back magnet	Oper	Oper	30	0.4	0.5	2.5		3	1		4,440		900,000
Out of tolerance dimensions	Insulation Failure	Des	Proto	1	0.3	0.5	4		0	1	1,250	180	375	

Subtracting the 0.9576 availability from 1 and multiplying the result by 6480 hours gives you the predicted downtime of the 4965 water cooled magnets per year, 274.9 hours; dividing this by the MTTR of 10 hours gives you the number of water cooled magnet failures per year in the NLC = 27.4, we call this the number of occurrences per year, or frequency. Using the information on the 70 magnet failures we found in SLAC's failure database we calculated the availabilities and hence the frequencies for many different types of magnet failure, which enabled us to complete a long FMEA table of all possible failure scenarios, a small part of which is shown in Table 2.

PREDICT EXPECTED FAILURE COSTS

Besides failures that occur during accelerator operations we also accounted for errors designers might make while designing a magnet, which would result in a failure when the magnet was first turned on while being tested in QC, for problems that might happen while a magnet was being installed, which would result in a later failure during operation. We gave educated estimates of such scenarios' frequencies and how many hours of labor it would take to recover. Failures that both originated and were detected during operations were assumed to continue to re-occur for 30 years, all others re-occurred just once. The values quantifying these various parameters are in the columns under "input" in Table 2. The lifetime costs associated with each failure scenario are calculated as explained below and the median costs in US dollars are shown in the columns under "output" in Table 2.

Calculate Expected Failure Costs.

$$\text{Labor Cost} = \text{Frequency} \times \{ [\text{Detection Time} \times \text{Labor Rate} \times \# \text{ of operators}] + [\text{Fixing Time} \times \text{Labor rate} \times \# \text{ of operators}] + \text{Delay Time} \times \text{labor rate} \times \# \text{ of operators} \} \times \text{Re-occurring} \quad (1)$$

$$\text{Material Cost} = \text{Frequency} \times \text{Re-occurring} \times \text{Quantity} \times \text{Cost of Part} \quad (2)$$

The "Recovery" time has a strong influence on the failure costs, it is the sum of the other 3 listed times. It is used through an "Opportunity" cost, which is the cost incurred

when a failure inhibits the main function of a system and prevents any creation of value; e.g. the beam is down and no luminosity is being accumulated. What to set this cost to per hour continues to be debated, we have used 3 values: \$10,000, \$25,000 and \$50,000 per hour. All of them far exceed what any technician earns in an hour, so it is vital to minimize the recovery time to reduce costs.

We use a Monte Carlo simulation to estimate the possible range of failure costs. It is misleading to use only an average repair time, for e.g., when a wide variation has been observed. So triangular distributions with minimum, mode and maximum values were used for frequency, all times, and parts costs. We simulated the design, fab and installation stages plus 30 years of operations of all the NLC magnets and PS 5000 times to find the distributions of lifecycle failure costs, the maximum being over \$1B.

CONCLUSIONS

In order to reach the NLC magnet system availability goals, we established we must both cut the repair time for water cooled magnets in half and run the large PSs in a redundant mode: 2 PS in parallel, ready to power magnets at all times. Such actions would yield an availability of 0.962, exceeding the goal of 0.95, and a worst-case lifecycle failure cost of \$339M. The cost-based FMEA described here will continue to be used by NLC engineers to guide their engineering of all aspects of the NLC.

REFERENCES

- [1] Paul Bellomo, Carl E. Rago, Cherrill M. Spencer, Zane J. Wilson, "A Novel Approach to Increasing the Reliability of Accelerator Magnets", IEEE Trans Appl. Superconductivity, 10 (1), (2000) p. 284
- [2] C.E.Rago, C.M.Spencer, Z. Wolf, G.Yocky, "High Reliability Prototype Quadrupole for the NLC", IEEE Trans Appl. Superconductivity, 12 (1), (2002) p.270
- [3] S.Kmenta, K.Ishii, "Scenario-Based FMEA: A Life Cycle Cost Perspective", Proc. ASME Design Engineering Technical Conf. Baltimore, MD, 2000
- [4] S.J.Rhee, K.Ishii, "Life Cost-Based FMEA Incorporating Data Uncertainty.", Proc. ASME Design Engineering Technical Conf, Montreal, 2002

PERMANENT MAGNETS FOR RADIATION DAMAGE STUDIES

James Spencer and SLAC MMG*, SLAC, Menlo Park, CA 94025, USA
James Volk, FNAL, Batavia, IL 60510, USA

Abstract

Permanent magnetic (PM) devices have many current and potential applications based on advantages in size, cost and simplicity but they suffer from uncertainties related to environmental and damage effects. One missing ingredient is a magnet designed to explicate demagnetization effects as a function of the principal magnetic characteristics of the device, the material, the blocks and their fab procedures – all of which need to be independently varied while minimizing the induced radioactivity from testing. We describe such a magnet and the measurements on it and its blocks and discuss the parameters of most interest as well as the constraints that motivate this choice.

INTRODUCTION

In the next linear collider (NLC), PM devices such as solenoids, multipoles, undulators and wigglers could have important uses if the limits of their stability to differing high radiation environments could be established. This work is part of a broader proposal[1] to determine the types and levels of radiation to be expected and the susceptibility of PM material to radiation damage from these. A major goal is to obtain a general interpretation applicable to any PM device. For this, we have developed an unconventional magnet that is simple and easy to test and modify.

We discuss the magnet, defined as more than one PM block, that can't be used for conventional applications but allows a good comparison between the key ingredients thought to be important in radiation damage mechanisms by simply changing the magnet gap or the block material or its characteristics such as intrinsic coercivity H_{ci} .

PROBLEM DESCRIPTION/SITUATION

Demagnetization and especially radiation damage has been of interest in our field for over twenty years[2, 3, 4, 5, 6, 7] with a broad array of approaches. A physically realistic but qualitative picture has the Curie temperature T_c being exceeded in some volume followed by remagnetization in the local, residual field at that location. This implies a natural hierarchy in terms of nominal T_c values: $\text{Sm}_2\text{Co}_{17}$ (800°) > SmCo_5 (700°) > $\text{Nd}_{2-x}\text{Fe}_{14}\text{B}$ (300°) where x represents substitution of other rare-earths such as Dy, Pr or Tb that are known to improve H_{ci} . Tests are open-circuit yet assume fixed load-lines and permeances. Conclusions are mostly empirical with curious omissions e.g. no discussion of characteristics such as stabilization temperatures T_s , tests with thermal neutrons nor any post radiation activations[8].

* SLAC's Magnetic Measurements Group is headed by Zachary Wolf.

Initially, Brown et al. [2] looked at SmCo but did not measure or control the temperature. Later, Brown and Cost[3] observed that higher Dy or Tb contents resulted in higher H_{ci} in NdFeB (with very high linear correlation 0.96) as well as greater radiation resistance (RR) with high correlation (0.87) and thus, a good correlation between RR and H_{ci} (0.78). They controlled temperature but didn't specify T_s . They suggested a radiation induced, nucleation of domain reversals from processes that exceed the domain nucleation energy barrier.

Zeller[4] argued, from the known loss of magnetization with temperature or P_c , that the dominant mechanism was loss of coercivity as opposed to loss of remanence based on macroscopic Pandira simulations. Varying H_c and then B_r , he obtained shapes consistent with his field scans and argued that NdFeB demagnetizes worse than other alloys based on its lighter elements B and O gaining significantly greater recoil energy from knock-on collisions.

Kahkonen et al.[5] proposed this as well and appeared to verify it with 20 MeV protons. They indicated, without comment, that the demagnetization had a $\cos\theta$ dependence if θ is the angle between \vec{M} and the particle velocity \vec{v} . This implies that the particle's path is unaffected by the B field and is understood by remembering that the material is crystalline. They noted their model was premature but this was the first quantitative attempt that suggested tests.

Okuda et al.[6] used electrons and Co^{60} γ 's and showed that $\text{Sm}_2\text{Co}_{17}$ was better in all respects except the B_r ratio of 1.12 for the samples tested. Nearly complete remagnetization after irradiation suggested little structural change consistent with Ref's [2, 3].

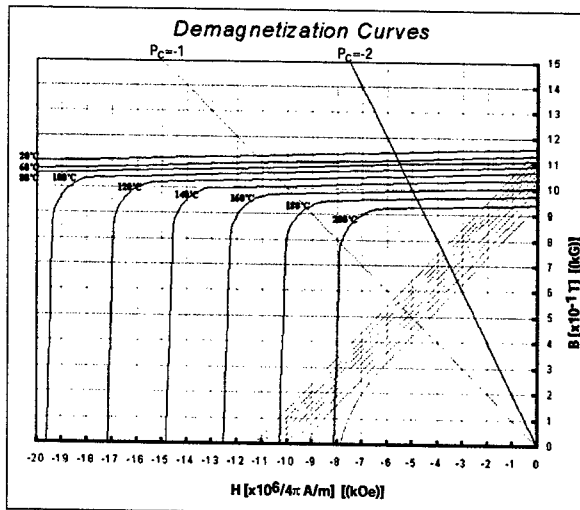


Figure 1: Shin-Etsu N34Z material indicating reversible, thermal behavior up to 200°C for permeances $|P_c| > 0.5$.

Most recently, Ito et al.[7] used 200 MeV protons to test consensus on the effects of H_{ci} and P_c on RR and that “flux loss cannot be attributable to structural change” but that mechanisms are not fully understood. For samples with the same $P_c=0.5$, Sm_2Co_{17} was better than the best Nd sample in all respects except for the B_r ratio of 1.07 even when the Nd had double the coercivity H_{ci} . Their Nd materials were similar to ours such as shown in Fig. 1.

Nomenclature and Conclusions

People have consistently tried to explain RR in terms of a few “simple” properties of a block and its material such as $P_c=B/H$. This is a signed quantity that is not unique in sign or magnitude for many block operating conditions[9]. Similarly, neither it nor the load line it describes is ever unique, even for unloaded, open circuit blocks or magnet assemblies. Still, models[5] assume that every demagnetization is followed by a remagnetization in the opposite direction due to self fields.

While several experiments appear to provide consensus, there are discrepancies. For example, it is interesting to compare *all* available charged hadron data for NdFeB. This includes 106 MeV deuterons and several proton energies from 20-500 MeV[2, 4, 5, 7]. For comparable values of H_{ci} and P_c , one finds the damage hierarchy: $p > d > n > e > \gamma$. Similarly, high energy protons are worse than low[7] - at least $p(200 \text{ MeV}) > p(20 \text{ MeV})$ where the authors note “the reason is not clear” and “more detailed studies are needed”. We agree[10].

There is another serious discrepancy. If one assumes that radiation and ionization loss promotes nucleation of reversed domains[3], one might expect electrons to cause more damage than ions if only radiative losses from bremsstrahlung were relevant:

$$\sigma_i^{rad} \sim \alpha Z^2 (z_i r_i)^2 \ni r_i = r_e \left[\frac{m_e c^2}{m_i c^2} \right] \text{ [cm}^2/\text{nucleus]}. \quad (1)$$

Clearly, ionization and atomic excitation dominate for ions and much of the electron data as well since $E_e < E_c$ - the critical electron energy for the material. Thus, over these energies, one can use the Bethe Bloch equation. This gives $p(\text{LowE}) > p(\text{HiE})$ but also $d(106 \text{ MeV}) > p(200 \text{ MeV})$. The maximum energy of knock-on electrons goes as $2m_e c^2 (\beta\gamma)^2$ reaching $\approx 1.4 \text{ MeV}$ for 500 MeV protons. This model is inconsistent with the data but consistent with no structural damage.

The model where the primary cause is recoil of Boron atoms from Coulomb scattering is intriguing because B is much less prevalent and has a much lower Coulomb cross section than the other components $\propto (Z_A z_i / T_R)^2$ where T_R is the reduced kinetic energy. However, it has a larger “Curie radius” that can be comparable to or larger than the grain size. However, if we extend this model to other incident channels, we expect $\sigma(p) > \sigma(n)$ from the larger Coulomb size but the damage is much greater for protons[3, 7] than expected. Nonetheless, from the maximum energy transfer, we expect: $d > p > n > e > \gamma$

at *fixed* energy and comparable conditions as well as $p(\text{HiE}) > p(\text{LowE})$. Thus, we have some simple but distinct models where only the latter gives any qualitative agreement. All suggest a much higher limit on truly irremedial radiation damage that should be tested - especially with thermal neutrons that can produce structural changes from reactions such as $B^{10}(n, \alpha)Li^7$.

MAGNET DESCRIPTION

Under certain qualifying caveats, conventional PM dipoles should be less susceptible followed by undulators, wigglers, and quadrupoles due to variations in \vec{M} of the blocks *and* variations in \vec{H}_{ext} i.e. their differing load lines throughout each type of block and magnet[9]. This is clear from Fig. 2 and explains our choice of an asymmetric quadrupole magnet with simple dipole geometry - shown here for a large gap magnet $G \geq l_x, l_y, l_z$ of the PM blocks.

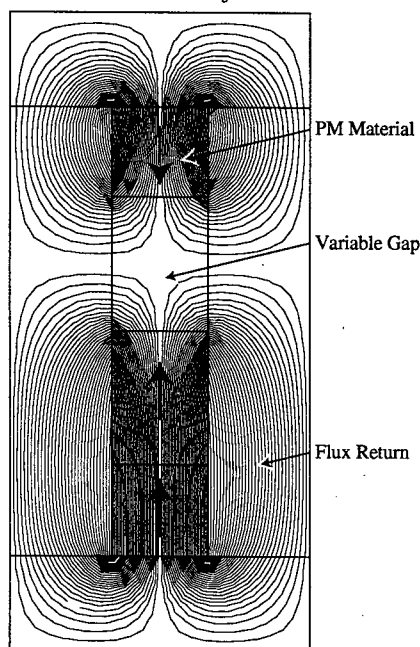


Figure 2: Schematic layout showing magnetization vectors.

In this case, the load-line of the lowest block is far into the first B-H quadrant (from the field of the adjacent, larger block and circuit) and is nearly the same throughout the block while its matching partner at the top has material that is clearly in the second quadrant as does the larger block. As the gap is decreased, the difference increases - making the upper one more susceptible to damage. Going further, some material can be driven past the knee (Fig. 1), H_{cb} and H_{ci} where “irreversible” but not unremediable effects, with or without radiation, are expected. Most of this depends on the magnetic circuit rather than the block dimensions or even the material. This is one reason we measured the block magnetizations several times after initial assembly and disassembly. Clearly, the closed circuit material is too bulky in Fig.3 but this suggests a typical setup.

MAGNETIC MEASUREMENTS

For magnets such as shown in Fig. 2, we have made and measured several variants. For activation analysis, $G=2,3,5$ & 7 mm with block sizes $l_z=9$ mm, $l_x=5.9$ and $l_y=6.8,9$ mm. The finished OD, for a pneumatic rabbit, is 9 x 9 x 30 mm. Some field scans along z are shown in Fig. 3 for the 2(M1) and 7(M3) cases. The effective magnetic length $(\int B_y dz)/B_y^{peak}$ of M3 is $L_z \approx 9$ mm.

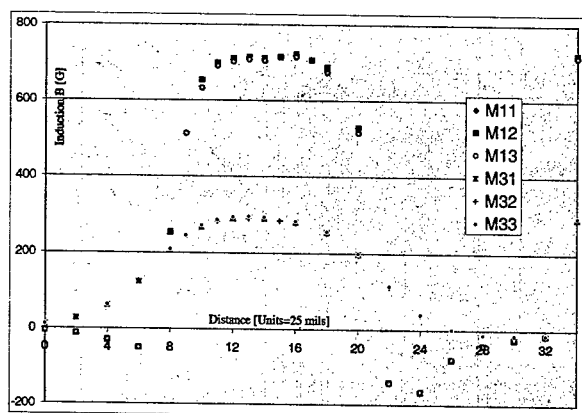


Figure 3: Typical mid-plane scans for the 2 and 7 mm gaps.

The peak field for each scan is shown at position 34 ($34 \times 25 = 0.85$ in) and in Table 1 as Mid as well as along the top and bottom poles for the same probe orientation.

Table 1: Some Peak Field Values

Gap[mm]	Top	Mid [kG]	Bot
2 (M1)	1.185	0.7211 ± 0.0041	+0.722
3 (Ref)	2.880	0.6788 ± 0.0024	-1.557
5 (M2)	3.976	0.5109 ± 0.0025	-2.880
7 (M3)	4.344	0.2932 ± 0.0026	-3.262

Table 2 gives some block measurements. The larger blocks are now at top and bottom (Fig. 2). Easy axis angle errors are large but repeatability is good for such small blocks.

Table 2: Magnetization measurements for the M3 blocks

Block #	M_x [G]	M_y [T]	M_z [G]
10 (top)	81.7	1.1343 ± 0.0012	-584.8 ± 38.9
2 (mid)	-411.7	1.0627 ± 0.0027	187.6 ± 3.11
6 (bot)	27.0	1.1300 ± 0.0002	-68.0 ± 57.9

IRRADIATION PROGRAM [1]

UC Davis has two facilities[1] that could be invaluable in providing the missing information on hadron damage. The McClellan Nuclear Reactor Center (MNRC) provides a number of areas for irradiating samples with neutron fluxes up to 4.5×10^{13} n/cm²s. The radiation test beam at the Crocker Nuclear Laboratory (CNL) cyclotron provides protons of up to 63 MeV spread over a rather uniform beam spot 7 cm in diameter. A typical central flux is 4.2×10^9 protons/cm²s (0.56 kRad/s (Si)). The laboratory can also produce deuteron and neutron (60 MeV) beams. Thus, both facilities are of great interest for this application.

ACKNOWLEDGMENTS

The authors thank Roger Carr, Hobey DeStabler, Dave Pellett as well as Jose Alonso, Cherrill Spencer and the MNRC staff for discussions and the members of SLAC's Magnetic Measurements Group. This work was supported by the U.S. Department of Energy under contracts DE-AC03-76SF00515 and DE-AC02-76CH03000.

REFERENCES

- [1] Maxwell Chertok, David E. Pellett(PI), James E. Spencer, James T. Volk and Zachary R. Wolf, "Radiation Damage Studies of Materials and Electronic Devices Using Hadrons", LCRD Proposal, August 2002.
- [2] R.D. Brown, E.D. Bush, Jr., and W.T. Hunter, "Radiation effects on samarium-cobalt permanent magnets", LANL Rep. LA-9437-MS, July, 1982. R.W. Blackmore, *IEEE Trans. Nucl. Sci.*, NS32(1985)3669.
- [3] R.D. Brown and J.R. Cost, "Radiation-Induced Changes in Magnetic Properties of Nd-Fe-B Permanent Magnets", *IEEE Trans. Magnetics* 25(1989)3117-3120. See also: J.R. Cost, R.D. Brown, A.L. Giorgi, J.T. Stanley, *IEEE Trans. Magnetics* 24(1988)2016.
- [4] A.F. Zeller, "Radiation Damage Mechanisms in NdFeB Magnets", 11th Int'l. Workshop on Rare-Earth Magnets, October, 1990. Also, A.F. Zeller and J.A. Nolen, 9th Int'l. Workshop on Rare-Earth Magnets, October, 1987.
- [5] O-P.Kahkonen, S.Makinen, M.Talvitie, H.Rajainmaki, M.Manninen, "Temperature Dependence of Irradiation-Induced Magnetic Flux in Nd₂Fe₁₄B Permanent Magnets", *Europhys. Lett.*, 12(1990)413. Also: O-P Kahkonen, S. Makinen, M.Talvitie, M.Manninen, "Radiation Damage in Nd-Fe-B Magnets: Temperature and Shape Effects", *J. Phys. Cond. Mat.*, 4(1992)1007.
- [6] S. Okuda, K. Ohashi, N. Kobayashi, "Effects of electron-beam and γ -ray irradiation on the magnetic flux of Nd-Fe-B and Sm-Co permanent magnets", *Nucl. Inst. Meth.*, B94(1994)227. For bremsstrahlung see: Henry B. Luna, Xavier K. Maruyama et al., "Bremsstrahlung Radiation Effects in Rare Earth Permanent Magnets", *Nucl. Inst. Meth.*, A285(1989)349.
- [7] Yoshifumi Ito, et al., "Magnetic flux loss in rare-earth magnets irradiated with 200 MeV protons", *Nucl. Inst. Meth.*, B183(2001)323).
- [8] This is understandable because the information on x may be proprietary and activation for trace elements may create handling problems. Still, such information suggests thermal neutrons are important: see G. Gross et al., "Experience with the SLC Permanent Magnet Multipoles", EPAC'94, London, June 1994 and Ref. [3].
- [9] M. Baltay et al., "Comparison of SmCo and NdFeB in PM Multipoles", PAC'87, Washington, D.C, March 1987.
- [10] Blackmore's data at 500 MeV[2] shows another problem because it implies $p(200 \text{ MeV}) > p(500 \text{ MeV})$. While cross sections decrease with energy, the energy transfer increases e.g. $T_{ion}^{Max}(500) \approx 30 T_{ion}^{Max}(20)$ for B, Fe and Co ions while $T_{ion}^{Max}(B) \approx 4.5 T_{ion}^{Max}(Fe, Co)$ making usual "displacement" damage hardly vary while the observed damage should.

MAGNETIC MEASUREMENT OF THE 10 KW, IR FEL 180 DEGREE DIPOLE*

K. Baggett[†], G. Biallas, D. Bullard, J. Dail, D. Douglas, T. Hiatt and M. McCrea
Thomas Jefferson National Accelerator Facility, Newport News, Virginia

Abstract

A family of large bending dipoles has been magnetically measured to support the 10 kW IR-FEL upgrade. This upgrade will allow for a wider wavelength range and an increase in the machine energy to operate between 80 MeV/c and 210 MeV/c. The dipole magnets allow the beam to bend 180 degrees over a 1 meter radius. The requirements for these magnets include varying field strengths, large horizontal apertures and parts in 10,000 field homogeneity as well as setability of core and integrated field. This paper will describe the process involved in measuring and achieving these requirements.

1 INTRODUCTION

A 10 kW infrared free-electron laser is being constructed at the Thomas Jefferson National Accelerator Facility. The pi bend dipoles (GY) are located at the two arcs of the new transport system. Each has a bend radius of 1 meter and bend angle of 180 degrees. They are designed to handle varying field strengths (0.27T to 0.71T) required to operate the machine between 80 MeV/c and 210 MeV/c. Included in the pi bend dipole are two sets of trim coils used for beam path length adjustment. Tight specifications on the magnet setability and the integration of trim coils into the magnet required an exploration of hysteresis procedures to ensure core field setability.

Twenty-two bending dipole magnets make up six dipole families required to run the accelerator. The GY dipoles are included in the arc string along with the GQ and GX dipoles and use a current shunt to compensate for small core field deviations between the GY and other dipole families [1].

2 SETUP, CALIBRATION, & ACQUISITION

The GY dipoles were designed with stringent field requirements shown in Table 1 [2]. The GY was primarily set and configured for the nominal operating energy of 145 MeV/c. All integral measurements were made using Group 3 Hall probes calibrated against Metrolab NMR probes. A total of four probes were read for each

measurement, 2 Hall Probes and 2 NMR probes, with the analysis done using Microsoft Excel.

Table 1. Dipole excitation error tolerances (rms.)

Constraint	Tolerance
Accuracy of core field	2.5×10^{-4}
Core Field Uniformity	1.0×10^{-4}
Accuracy of integrated field	2.5×10^{-4}
Integrated Field Uniformity	1.0×10^{-4}

The initial mechanical inspection of the magnet revealed delamination of the electrical grade steel, Purcel gap faceplates. These plates were subsequently stripped from the magnet, cleaned up, and reglued to the magnet pole face. Afterward, the pole face flatness was measured to be flat within ± 80 microns.

2.1 Hardware Set Up

A measurement stand adapted from the DY dipole, used in the original Jefferson Lab FEL Demo, was modified to accommodate the larger GY dipole shown in Figure 1 [3]. The stand consisted of a 25 mm aluminum plate mounted to a granite table, made level and coplanar with the magnet's bottom pole face. The 1 meter wheel, used for the original DY measurements, was used to move the probes circumferentially through the magnet. The wheel, which could be split into four sections, was fed through the magnet using wheel guides mounted on the aluminum plate. The wheel guides were used to align the wheel radially with the magnet from survey data taken with a three dimensional Faro portable CMM machine. This system alleviated the need to split the magnet to install the measurement system.

An aluminium probe holder was used to align Hall and NMR probes to the magnets radius. The Hall probes were placed 10 cm apart at the outsides of the probe holder. NMR probes were positioned 1.67 cm inside, adjacent to each Hall probe. The probe holder was first positioned at the inmost radial position for the first data run. For six additional runs the probe holder was moved outboard 1.67 cm allowing the Hall probes to take data over the entire 20 cm good field region. This method allowed overlapping data sets to be taken at several positions including along the magnet center line, confirming data repeatability in any given set of measurements to $\sim 0.02\%$.

* This work supported by DOE Contract DE-AC05-84ER40150, the Office of Naval Research, Air Force Research Laboratory, the Commonwealth of Virginia and the Laser Processing Consortium
[†]baggett@jlab.org

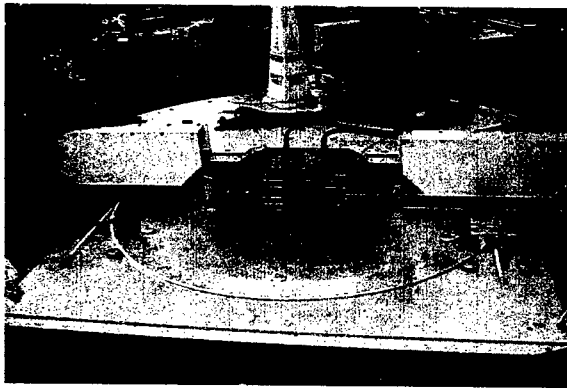


Figure 1: GY Measurement Stand

2.2 Probe Position Calibration

Circumferential positional information was taken from a scale on the wheel as the wheel was rotated through the magnet. Calculations were then made in the analysis spreadsheet to account for scale inaccuracies, scale offset from probe positions, and differing arc distances with respect to radial probe position. This calibration sequence allowed for accurate positional data collection throughout the magnet.

2.3 Hall Probe Calibration

NMR probes, which provide absolute field information at the 10^{-5} level, were used to calibrate the Hall probe by stacking the respective Hall probe on top of its normally adjacent NMR probe. The probe stacks were then positioned in the circumferential centre of the GY. Hall and NMR values were recorded in 15, five-amp increments. Due to the extreme operating range of the GY, a current range specific to each momentum was used for calibration. A linear fit was then made for the 15 data points taken for each of the respective Hall-NMR combinations. This difference was plotted on the ordinate, against the Hall probe readings along the abscissa. The slope and offset of these respective fits were applied to each Hall probe's data readings. Field integral readings between both hall probes, along the 1 meter radius, matched to $\sim 0.01\%$ with the respective calibrations applied but only matched to $\sim 0.15\%$ without the calibrations applied.

2.4 Data Taking

Hall probes provided an effective method to collect core field and integral data because of their large field range. As transverse data sets are taken, NMR probes positions overlapped with Hall probe positions providing an efficient method to back check core field data accuracy.

Circumferential integral measurement runs were taken at the seven radial locations through the magnet for 80, 145 and 210 MeV/c momenta.

Table 2. Circumferential Step increment.

Circumferential Positions (cm)	Step Inc (cm)	Probe Location with respect to Magnet
-40 to -10	1.0	Outside Magnet
-10 to 10	0.2	Enter
10 to 30	1.0	Trim Coil Slot
30 to 284	5.0	Good Field Region
284 to 304	1.0	Trim Coil Slot
304 to 324	0.2	Exit
324 to 354	1.0	Outside Magnet

The measurement sequence began with the wheel rotated to the zero point on its scale. The entrance measurements were made by moving the probe holder along a slot built into the wheel tangent to the 1 meter radius and normal to the magnet entrance for a distance of 30 cm. The probe holder was then locked to the wheel and the wheel was rotated incrementally through the magnet to the magnet exit position. Exit measurements were taken identically to the entrance measurements. Probe data was collected using varying step increments to increase the precision of the integral. Table 2 shows the varying circumferential step increments used while measuring the magnet.

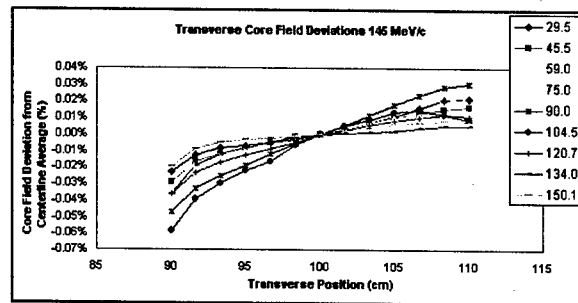


Figure 2: Transverse Core Field Deviation 145 MeV/c

Table 3. GY Parameters

Characteristic	Minimal	Nominal	Maximum
Momenta (MeV/c)	80	145	210
Field (kg)	2.6685	4.8367	7.0049
Set Current (amps)	83.87	152.30	222.78
Hysteresis Current (amps)	Max	118.69	226.01
	Min	6.43	6.44
Shunt Values (%)	1.09%	0.85%	-0.12%

3 RESULTS

The results showed a linear deviation in transverse core field of 0.005% per cm at 145 MeV/c shown in Figure 2. This deviation amounts to nearly 0.1% over the 20 cm good field region, causing the magnet to be out of specification by a factor of 10 [4].

Transverse integral measurements were consistent with the transverse uniformity measurements, showing a 0.1% deviation over the 20 cm good field region. To correct for this, an existing quadrupole trim magnet will be used as a simple and eloquent fix to counter the focusing effects of this deviation.

Integral measurements also showed a -0.596% difference in measured field integral relative to the design integral at the 1meter radius. It is impossible to make this shortage in field integral up by using the adjustable field clamps on the GY, so four 0.9525 cm steel plates were attached to the ends of the magnet to increase the field integral, without affecting core field. A current shunt will be used to correct for the deviation between the GY magnet and other magnets along the arc string operating together on a common power supply. Current parameters and shunt values are listed in Table 3. Final measurements show the field integral matching the design to 0.005% with the core field matching to -0.014%. Similar results were obtained at 80 and 210 MeV/c showing the field integral matching to -0.069% and 0.139% and the core field matching to -0.015% and -0.033% respectively. Table 4 shows the uniformity of the core field and Table 5 shows the uniformity of the integral across the good field region.

Table 4. Deviations from Design Core Field

GY001 Core Field Uniformity			
Radial Position (cm)	80 MeV/c	145 MeV/c	210 MeV/c
90	-0.031%	-0.053%	-0.069%
100	-0.015%	-0.014%	-0.033%
110	0.000%	-0.007%	-0.028%

Table 5. Deviations from Design Field Integral

GY001 Bdl Uniformity			
Radial Position (cm)	80 MeV/c	145 MeV/c	210 MeV/c
90	-0.044%	0.033%	0.177%
100	-0.069%	0.005%	0.139%
110	-0.051%	-0.005%	0.114%

Final analysis of the field integral showed a deviation 0.06% across the good field region for all three momenta. Figure 3 shows the deviation from uniformity across the 20 cm region. Additionally, tests using the path length correcting trim coils built into the pole face of the magnet verify their ability to easily vary the field integral within

the range of the deviation. Trim coil effects on the GY design integral are shown in Figure 4.

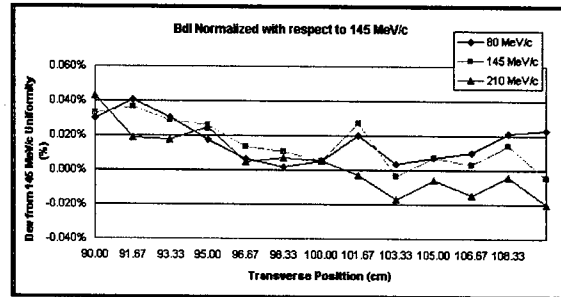


Figure 3: Field Integral Uniformity with respect to 145 MeV/c

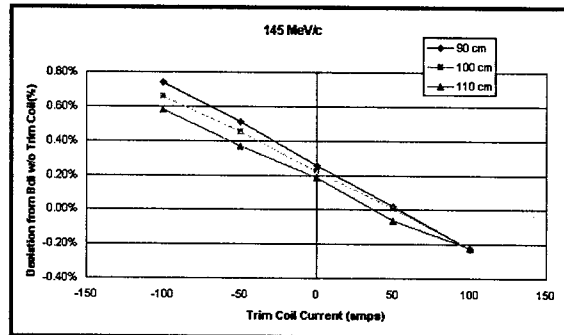


Figure 4: Integral Deviations using Trim Coils

4 CONCLUSIONS

The adapted measurement stand proved to be an effective tool in the collection of core and integrated field data throughout the range of the magnet. The data obtained lead to the implementation of several solutions allowing the magnet to sufficiently meet specifications. Notably, the discrepancy between core and integrated field was solved by the addition of face shim and the slope in the transverse field will be corrected by use of a quadrupole trim magnet.

5 REFERENCES

1. T. Hiatt, et al., "Magnetic Measurement of the 10 kW IR-FEL Dipole Magnets", These Proceedings.
2. D. R. Douglas, "GY Field Homogeneity Evaluation", Jefferson Lab Tech Note #01-042, 2001
3. K. Tremblay, et al, "Magnetic Measurement of the Pi Bend Dipole Magnets for the IR-FEL at the Thomas Jefferson National Accelerator Facility", PAC Proceedings, 1999
4. D. R. Douglas, "Some Features of the FEL Upgrade Pi-Bends", Jefferson Lab Tech Note #01-024, 2001.

MAGNETIC MODELING VS MEASUREMENTS OF THE DIPOLES FOR THE JLAB 10 KW FREE ELECTRON LASER UPGRADE*

G. H. Biallas[#], K. Baggett, D.R. Douglas, T. Hiatt, R. Wines

Thomas Jefferson National Accelerator Facility, 12000 Jefferson Blvd. Newport News VA 23606

T.J. Schultheiss, V.A. Christina, J.W. Rathke

Advanced Energy Systems, Inc. 27E Industrial Blvd., Medford, NY 11763

A. Smirnov, D. Newsham, Y. Luo, D. Yu

DULY Research Inc. 1912 MacArthur Street, Rancho Palos Verdes, CA 90275-1111

Abstract

Magnetic measurements of the six families of dipoles for the infrared Free Electron Laser Upgrade at the Thomas Jefferson National Accelerator Facility (Jlab) are compared to the magnetic models on which their design is based. The magnets were designed in parallel by three organizations. They used ANSYS, Radia or Opera 3D as a 3D magnetic modeling program. Comparison of the discrepancies between model and magnet measurement is presented along with analysis of their potential causes. These dipoles operate in two field ranges. The Injector/ Extractor Dipoles operate around 0.05 T and the Arc Dipoles and Optical Chicane Dipoles operate between 0.22 to 0.71 T. All magnets are required to meet core field and field integral flatness to parts in 10^4 over their "good field" region.

Table 1: Dipole Family Characteristics

Designator -Use	Qty.	Effective Length	Core Field
		m	T
GV - Injection/ Extraction	6	0.21	0.045 - 0.061
GU - Injection/ Extraction	2	0.43	0.045 - 0.061
GW - Optical Chicane	4	0.42	0.223 - 0.592
GX - Arc Bend	4	0.894	0.222 - 0.584
GQ- Arc Reverse Bend	4	0.917	0.222 - 0.584
GY- Arc Pi (180°) Bend	2	3.14	0.267 - 0.711

1 INTRODUCTION

Dipole magnets requiring core fields and field integrals to be uniform to parts in 10,000 require a marriage between magnetic modeling and final adjustment during magnet testing. This paper discusses how closely six families of dipoles matched their design models and the methods used to make the magnets usable.

Twenty-two dipoles are required for the injection, extraction, optical chicane and arcs (Table 1) of the 10 kW IR Free-Electron Laser Upgrade [1] at the Thomas Jefferson National Accelerator Facility (Jefferson Lab). The dipoles run at relatively low fields ranging from 0.05 to 0.7 Tesla. Two sets of 180° "Bates Lab" arcs with three families of dipoles (designated GQ, GX, GY) form the arcs of the racetrack beam path. An additional family (GW) of four dipoles transport the beam around one FEL resonator mirror. These four families operate between 0.16 and 0.71 T. Two low field (0.05 T) families (GU, GV) reside in the injection and extraction lines.

We used the window frame with Purcell gap system dipole style of the IR Demonstration FEL [2] as the starting point for designs. We modeled the dipoles using computer models making use of faster computers and smaller grids than had been used in the past to resolve fields in 3D to the part in 10^5 level.

*Work supported by the US DOE Contract #DE-AC05-84ER40150, the Office of Naval Research, The Air Force Research Laboratory, the Commonwealth of Virginia, and the Laser Processing Consortium.
Email: biallas@jlab.org

We took care to build the magnets to match the magnetic models. The primary item to match is precision gap. We obtained gap uniformities at the part in 10,000 level (7 μ m). This tolerance is at the limit of achievement at skilled machine shops by machining or grinding). A gap-measuring instrument, using a Starrett distance measuring instrument, with 0.25 μ m resolution and electronic read-out enabled this difficult measurement.

The next item we attempted to match to the model is the iron in the core. The magnet cores are made of solid 1006 steel while all field clamps and some auxiliary core parts of the GYs are made of 1018 steel. Families of magnets were made of 1006 steel from the same melt. All 1006 had solution annealing in vacuum at 965 C before final machining. All manufacturers were cautioned to not leave magnetic footprints on pole surfaces from lifting or chucking magnets. Finally, all magnets were run on hysteresis loops at the operations ramp rate to a maximum current above the set point and then set to running current in order to standardize residual fields.

All magnets have field clamps that minimize stray field. Field clamp adjustability in the beam direction also provides ability to adjust the effective length by about 0.5%.

The core field and field integral tolerances for these magnets are the same as the corresponding dipoles of the IR Demo and are repeated in detail elsewhere at this conference. [3] Basically, core fields and field integrals are to match to 1 part in 1000 within a family and core field and integral for any one magnet should be uniform within a few parts in 10,000 over the good field region. All but

one family met these tight magnetic specifications over their required field ranges. (See section 5 for an explanation of the exception) Two families matched the models beautifully. The remainder required one or more adjustments at the Magnet Measurement Facility at Jefferson Lab. [3,6] The injection and extraction dipoles were accepted for a single momentum of 9.2 MeV/c. The recirculation magnets were characterized at core field levels corresponding to 80, 145 and 210 MeV/c with 145 MeV/c as the baseline.

2 INJECTION AND EXTRACTION DIPOLES (GU/GV)

DULY Research designed the two families of window frame style injection and extraction dipoles [4] using the 3D program Radia. The dipoles were designed at a maximum field of 0.061 T, 10 % over the field required for nominal 10 MeV/c operation.

The small dipole (GV) was the most difficult magnet to model of all dipoles because it is short, has a large gap in relation to its length and is a 20° wedge. At the narrow part of the good field region, the magnet length is the same as the gap. Characteristic end field fall-offs within the gap from both ends of the magnet superpose. The resulting droop in the core field on the narrow side makes it difficult to obtain field flatness to parts in 10,000 over the good field region. DULY found that using the mu metal Purcell gap system [2] was not effective for flattening the field. DULY Research invented a trim coil system as a solution to this problem. DULY also incorporated a method to adjust out the non-linear field integral gradient across the good field region seen in their models.

The large injection/ extraction dipole (GU) is nominally double the magnetic length of the GV and much simpler. The GU was able to use the Purcell gap system developed for the IR Demo to flatten the core field and didn't require the trim coil.

Results: DULY's trim coil system worked to make the core field flat over the good field region. However, the current is 7 % higher than predicted. In addition, we found that the magnetic wedge angle (field integral gradient) of this 20° wedge magnet is not constant with excitation. Therefore we picked the momentum the injector was set at in the IR Demo (9.2 MeV/c) as a single operating point. We adjusted the angle of the field clamps to bring the integral gradient to a 20° wedge at the core field for this momentum. Additional measurements provided the field clamp positions for other excitations. The field integrals were smaller than predicted. Since the magnet is a wedge and we had excess width to the good field region, we shifted the wider side of the magnet transverse to the beam centerline to obtain the specified field integral on beam centerline. We found that magnetic shim material on the inside of the field clamps on either side of beam centerline corrected a problem of field integral gradient nonlinearity. The magnet was ramp rate sensitive so all testing was done at ramp rate used for operations.

The modeling of this low field magnet where much of its core is running in saturation was particularly challenging in view of the high fringe fields and non-uniformity for magnetic flux distribution [4]. Using the adjustable trim coils together with the adjustments and accommodations discussed earlier, this magnet family has the best conformance to specification.

Results on the GU magnet showed that the model was correct in its uniformity predictions but the field integral was 2% long. We shortened the pole tips by machining the end faces.

Since the GV's and GU were to be run on the same power supply, we added a variable shunt around the GU magnet that permits matching the magnets.

3 OPTICAL CHICANE DIPOLE GW

The Jlab Engineering Group modeled the GW dipole as a window frame style rectangular pole magnet with Purcell gap system using Opera 3D. All magnet values measured as predicted, matching the GX/GQ magnets.

4 BEND/REVERSE BEND DIPOLES GX/GQ

Advanced Energy Systems Corp. (AES) modeled the GX & GQ magnets using ANSYS. [5] Micrometric steps in the pole tips at the ends and corners shaped the fields to meet uniformity requirements. The magnets are "H" style to allow optical pipes through the return legs of the yokes.

The GX has a large wedge angle (39.4°) and a small good field region (10.2 cm). The pole is enlarged in one region for a second beam path at half field. When half the coil turns are powered, the magnet is a switch, sending beam to the UV branch. The Reverse Bend Magnet (GQ) has a small wedge angle (10.4°) with larger good field region (25.4 cm). Both families are similar enough to be powered in series with no shunt.

Results: The GQ core field and field integral uniformity at 145 and 210 MeV/c matched the model's profile. Field uniformity at 80 MeV/c operation was only obtained by using a reduced current hysteresis loop. In addition, field integral was 0.91% short. We rectified this by adding magnetic shims to lengthen the poles. The field integral gradient was not linear near the centerline. We rectified this by adding 0.75 mm shims to the inside center of the field clamps. The Bend Magnet (GX) matched the model (including the half field "switch" mode) well enough in all respects to meet specification.

5 PI (180°) BEND GY

AES designed the Pi Bend as a window frame style with Purcell gap system using ANSYS. [5]. Modeling indicated factors of 3 to 4 improvement in field uniformity with the system. The magnet has additional coils built into either end of its poles, making the pole portions into path length correctors (designated GG coils).

Results: Unlike the model, the first magnet exhibits quadrupole at the part in 1000 level and sextupole at the parts in 10,000 level. [6] (Perhaps due to an over-current

powering at the start of measurement which we never cancelled by degaussing.) We will compensate for these errors using adjacent multipole trim magnets. Field integral was short by 0.61%. We rectified this by adding 1 cm shims to the pole end faces.

6 SUMMARY AND CONCLUSIONS

Three D modeling and test resulted in dipoles that qualified for installation. Modeling provided excellent design guidance for obtaining field uniformity as well as far more accurate effective lengths than obtainable with 2D modeling. The GW and GX families qualified directly. The GQ and GY ANSYS models predicted effective lengths within 1% at intermediate fields. For low field magnets, Radia's length prediction was 2 % high for the GU and its current prediction for the highly saturated GV was 7% low. All out-of-tolerance conditions were recoverable using adjustments, shims, pole end machining, shunts and (as a

last resort) corrector magnets. We had provisions for all of these measures built into the magnets or available to us.

7 REFERENCES

- [1] D. Douglas, et.al. "A 10 kW IRFEL Design For Jefferson Lab", Proc. PAC2001, Chicago, June 2001.
- [2] G. Biallas, et.al. " Making Dipoles to Spectrometer Quality Using Adjustments During Measurement ", Proc. PAC1999, New York, (1999).
- [3] T. Hiatt, et.al. "Magnetic Measurement of the 10 kW, IR FEL Dipole Magnets". Proc. PAC2003, Portland, (2003).
- [4] D. Newsham, et. al. "Wedge-shaped, Large-aperture, Dipole Magnet Designs for the Jefferson lab Facility Upgrade", Proc. PAC2003, Portland, (2003).
- [5] T. Schultheiss, et al. "Magnetic Analysis of the Arc Dipoles for the JLAB 10 kW Free Electron Laser Upgrade", FEL'02, Argonne, IL, Sep. 2002.
- [6] K Baggett, et.al., "Magnetic Measurement of the 10 kW, IR FEL 180 Degree Dipole". Proc. PAC2003, Portland, (2003).

MAGNETIC MEASUREMENT OF THE 10 KW, IR FEL DIPOLE MAGNETS*

T. Hiatt[†], K. Baggett, M. Beck, G. Biallas, D. Douglas, K. Sullivan and C. Tennant
Thomas Jefferson National Accelerator Facility, Newport News, Virginia

Abstract

Magnetic measurements have been performed on several families of dipoles for the 10 kW IR-FEL presently under construction at the Thomas Jefferson National Accelerator Facility. The requirements for these magnets include varying field strengths, large horizontal apertures and parts in 10,000 field homogeneity as well as setability of core and integrated field. Measurements were made to quantify the magnets according to these requirements and to determine the hysteresis protocol, ramp rate dependence, and field clamp settings that are used. This paper will describe the results of these measurements and the procedures used to accomplish them.

1 INTRODUCTION

A 10 kW infrared (IR) free electron laser (FEL) upgrade is under construction at the Thomas Jefferson National Accelerator Facility. The arc dipoles in this machine must handle beam momenta from 80 MeV/c to 210 MeV/c, while the injection and extraction dipoles must handle beam momenta from 8 MeV/c to 11 MeV/c. The dipoles were designed to meet several critical specifications to ensure maximum machine performance and setability. Some of the dipole design parameters are shown in Table 1. The nominal operating momentum for the GU and GV dipoles is 9.2 MeV/c and for the remaining dipoles the nominal is 145 MeV/c.

2 DESIGN REQUIREMENTS

The accelerator required a total of 22 bending dipoles comprising six different families, five of which are wedge shaped. This put constraints on the reproducibility of the magnets and on the accuracy of the core and integrated field. Each arc string, injection string or extraction string will be powered in series using a separate power supply. These strings link several families of dipoles. Both arc strings link the GY, GX and GQ dipoles. The first arc string also links the GW dipoles from the optical chicane region. The strings in the injection and extraction regions will power GV and GU dipoles. Out of tolerance core fields or field integrals could lead to undesirable steering

and focusing effects. Excitation tolerances for the dipoles are listed in Table 2 [1].

Variable shunts across the GY, GW and GU magnets will be used to adjust core field strength to maximize magnet performance. The shunts will be able to operate up to a maximum current of 10 amps. The actual shunt values for each family by region are shown in Table 3.

Table 1. Dipole Design Parameters

Style	Momentum Range (MeV/c)	Core Field Range (kG)	Effective Length (cm)	Good Field Region (cm)
GU	8-11	0.445 - 0.612	43.43	7.62
GV	8-11	0.445- 0.612	21.00	7.62
GX	80-210	2.22-5.84	91.75	10.16
GQ	80-210	2.22-5.84	89.48	25.4
GW	80-210	2.23-5.92	42.18	7.62
GY	80-210	2.67-7.11	314.16	20.32

Table 2. Dipole error tolerances (rms)

Parameter	Relative Error Tolerance
Core Field Accuracy#	0.1%
Transverse Field Integral and Core Field Flatness	0.01%
Field Integral Accuracy#	0.1%
Reproducibility	0.01%
#GY Relative Error Tolerance is 0.025%	

3 MAGNETIC MEASUREMENTS

The dipoles were required to qualify, by meeting the specifications in Table 2, at their nominal operating momentum. However additional effort was expended to qualify them over their entire range.

All FEL dipoles were measured using a Group 3, Hall effect probe on the magnet measurement Stepper Stand [2]. This stand was used to measure core and integrated field as well as transverse integral and core field flatness. A Stepper Stand measurement of the GX dipole is shown in Figure 1.

* This work supported by DOE Contract DE-AC05-84ER40150, the Office of Naval Research, Air Force Research Laboratory, the Commonwealth of Virginia and the Laser Processing Consortium

[†]hiatt@jlab.org

Table 3. Dipole Shunt Values

Region	Momentum (MeV/c)	Shunted Magnet	Shunt Value (%)
Injection	9.2	GU	6.95
Extraction	9.2	GU	7.84
1 st Arc	145	GY	Not Available
Optical Chicane	145	GW	0.87
2 nd Arc	145	GY	0.85

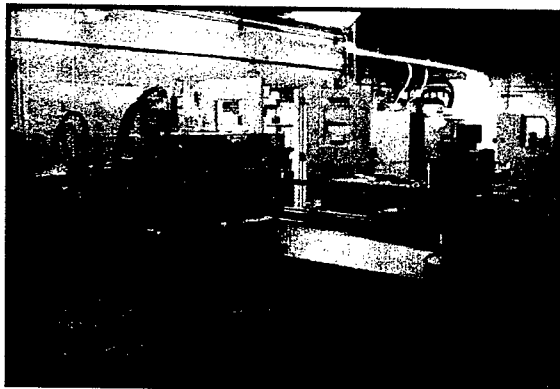


Figure 1. GX Dipole on Stepper Stand

The standard measurement procedure set the magnet's core field within 0.02% of the nominal design momentum after factoring out an estimated 0.20% vacuum chamber field contribution [3]. Transverse profiles were conducted to ensure that the core field was uniform across the required good field region of the magnet. Once field uniformity was confirmed, multiple straight through integral measurements were taken at different transverse locations across the magnet. These integral measurements were used to adjust the design field integral at the nominal centerline to match the design core field of the magnet by the use of adjustable field clamps [4]. The required field integral gradient was obtained by adjusting the field clamps angular position with respect to the pole ends. Once the magnets were satisfactorily qualified, the field clamps were pinned to the magnet core pieces to permanently secure their positions.

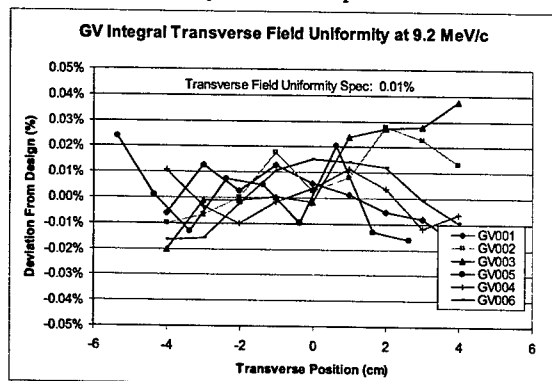


Figure 2. GV Integral Transverse Uniformity

3.1 Hysteresis and Ramp Rate Protocol

A current setting protocol was established to set the current for the main coils that started from a maximum current, specific to a given momentum and magnet family, standardizing the magnets residual field. A ramp rate of 5 amps/sec, +/- ~0.5 amp/sec was used to mimic the characteristic of the string power supplies. Magnets were run through one hysteresis loop using specific minimum and maximum current values for a given momentum, then set to the operating current from the maximum hysteresis current.

The exception to this procedure was the GV magnet, which used two power supplies for a given excitation. The trim coil for the GV dipoles was set to a ramp rate of ~1 amp/sec and operated on a bipolar 10 amp hysteresis loop.

3.2 The GV Injection/Extraction Dipole

The GV produced the least uniform field of the various families of dipoles. It has a wedge angle of 20° and is only 3.4 inches wide at its narrow end. In order to meet the dipole design specifications the magnet employed a trim coil that wrapped around the return legs of the magnet. When powered, the trim coil locally increased flux through the return legs to the point of saturation. This saturation effectively caused the field on one end of the dipole to excessively bulge resulting in a uniform transverse core field [5].

In order to meet the absolute field integral design requirements, these magnets were shifted transversely from the nominal centerline, taking advantage of the magnet's wedge shape to increase or decrease the field integral proportional to the transverse offset.

The GV proved to be the most labor intensive magnet to bring into specification due to the nature of its wedge shape and a combination of trim coil and field clamp adjustments. However, these adjustments allowed the magnet to be precisely tuned, and produced the nicest transverse integral uniformity, shown in Figure 2, of all the FEL upgrade dipoles.

3.3 The GU Injection/Extraction Dipole

Once the GU magnet was set to the appropriate core field, the integrated field was found to be 2% higher than the design. This difference was too large to correct using the adjustable field clamps, and the effect of the magnet's 2.9° wedge angle was not powerful enough to make shifting the magnet from the nominal center line plausible. To reduce the field integral the magnet pole face was shaved by 0.29 cm in order to reduce the integrated field so that it matched the core field. The integrated field was fine tuned by shifting the magnet from the nominal centerline, in the same manner as the GV dipoles.

3.4 The GW IR Chicane Dipole

The GW dipoles used in the IR optical chicane, were the least troublesome of the six families of dipoles, and was the only family that did not have a wedge shape.

Once the first magnet was qualified, the remaining magnets were identically set up and qualified with no exceptions, and were the first magnets installed in the accelerator.

These dipoles were measured on the translating coil stand as well as the Stepper Stand. Results between the two measurements have validated the ability of the Stepper Stand to confirm transverse field integral flatness. As a result only four GW magnets and one GQ magnet was measured on the translating coil stand.

3.5 The GX Bend Dipole

The 39.4° GX dipoles will be used to direct the electron beam to and from the ultra violet (UV) bypass. The switching will be engaged by physically changing the power lead configuration. UV operations will use half the coil package while IR operations will use the full coil package. Characterization in both configurations was made, but only the IR configuration will be discussed here.

Transverse core field measurements fell within specification, but a significant nonlinearity was found in the straight through integral measurements taken transversely across the magnet. An interesting characteristic about this magnet was that the electron beam is bent so extremely that straight through integral measurements sampled areas of field that the beam will not encounter. The good field region was specified normal to the beam orbit, not along a straight line about the nominal center line. For this reason straight line integrals could not be used to quantify the magnet's transverse field integral uniformity. Straight through integrals were used however, to quantify the field integral along the nominal centerline. To ensure the magnet met the design specification for all constraints, a grid of field readings was taken inside the magnet. These readings were compared to finite element models used to design the GX dipoles and were successfully qualified at 80 and 145 MeV/c [6].

3.6 The GQ Reverse Bend Dipole

Straight through field integrals for the 10.4° GQ reverse bend dipoles were significantly deficient across various excitations. To increase the integral of the GQ dipoles, a face shim system, 0.419 cm (0.165 in.) thick, was added to the magnet end faces to extend the poles adjacent to the magnet gap on the front and back of the top and bottom core plates. In order to meet the transverse field integral uniformity requirement, 0.478 cm (0.188 in.) thick shims were used to locally manipulate field in order to change the field integral to meet specification. These shims were bolted to the inside of each of the field clamps at the magnet centerline. The effect of these shim systems was only quantified at 80 and 145 MeV/c. The GQ was ultimately qualified using the same methods as the GX [7].

Further, this magnet is also used as a corrector dipole, designated GF. The GF was measured at 10 amps

and found to produce a field integral of 1244 G-cm, which was consistent with the design field integral of 1000 G-cm.

4 CONCLUSIONS

To date all IR FEL arc dipoles have been measured except for the GY dipoles, though the first GY should be completed within days of this writing [8]. All dipoles have sufficiently passed their magnet measurement qualifications. Due to scheduling priorities the GV and GU magnets were qualified only at 9.2 MeV/c and the remaining arc dipoles were qualified only at 80 and 145 MeV/c. Integrated and core field measurements have suggested the necessary shunt settings to optimize each string's magnetic performance. If it is found that the magnets are not performing to a satisfactory level, or if extrapolation does not adequately predict magnet performance for arc dipole operations at 210 MeV/c, additional measurements will be performed.

5 REFERENCES

- [1] D. Douglas and G. Biallas, "DC Field Quality Characterization of FEL Upgrade Dipoles", JLAB-TN-02-041, 24, September 2002.
<http://www.jlab.org/~douglas/FELUpgrade/technote/JLABTN02041.pdf>
- [2] T. Hiatt, "Automated Stepper Stand Mechanical Calibration", Unpublished Report. 30, January 2001.
<http://www.jlab.org/MagTest/Documentation/StepperStand/StepperCommissioning/AutomatedStepperStandMechanicalCalibration.doc>
- [3] T. Hiatt, et. al. "Vacuum Chamber Contributions to 10 kW FEL Dipole Field Maps", JLAB-TN-03-007, 17, March 2003.
- [4] J. Karn, et. al. "Magnetic Measurements of the Prototype Dipole for the IR-FEL at the Thomas Jefferson National Accelerator Facility", Proc. PAC1997.
- [5] G. Biallas, et. al. "Magnetic Modeling vs. Measurements of the Dipoles for the JLab 10 kW Free Electron Laser Upgrade", published in these proceedings.
- [6] D. Douglas, et. al. "Performance Qualification of 3F Region GX/GQ Dipoles", JLAB-TN-03-015, 26, April 2003.
- [7] Ibid.
- [8] K. Baggett, et. al. "Magnetic Measurements of the 10kW, IR FEL 180 Degree Dipole", published in these proceedings.

AN ADJUSTABLE PERMANENT MAGNET QUADRUPOLE (PMQ) FINAL FOCUS SYSTEM FOR LOW ENERGY EXPERIMENTS

J. Lim*, P. Frigola, J. B. Rosenzweig, S. Telfer, G. Travish,
UCLA PBPL Department of Physics & Astronomy, Los Angeles, CA. 90095

W. Brown, A. Tremaine, LLNL, Livermore, CA. 94550

Abstract

The final focus system for the Thomson X-ray scattering experiment termed PLEIADES (Picosecond Laser-Electron InterAction for Dynamic Evaluation of Structures) at LLNL demands ultra-high field gradient quadrupoles in order to focus initially small beams to 10-20 μ m spot sizes. The scheme present here circumvents limitations due to chromatic aberrations and space-charge effects in this relatively low energy (<100MeV) system. The final focus scheme is based on an ultra-high gradient (≥ 300 T/m) quadrupole which employs the Halbach 16-piece, permanent magnet design. Use of this optimized geometry, NdFeB material, and a small (5mm) bore allows the desired field gradient, and a few cm focal length, to be achieved. The adjustability of the focusing system is obtained by changing the relative longitudinal positions of sub-component focusing and defocusing magnets on precision movers. We present the results of RADIA 3D design simulations, and also discuss the results of beam dynamics simulations of the PLEIADES system using the tracking code.

INTRODUCTION

PLEIADES (Picosecond Laser Electron InterAction for Dynamic Evaluation of Structure) is a next generation Thomson x-ray source facility at LLNL (Lawrence Livermore National Laboratory) which expected to produce x-ray flux between 10^7 - 10^8 photons at pulse durations of 100fs to 5ps long[1]. The maximum production of x-rays depends on short duration electron bunch generated by a photo-injector, and the new installation of high performance beam optics for a tightly focused small transverse beam size at the Thomson interaction zone. The standard UCLA electromagnetic quad triplet (≤ 15 T/m) currently installed at the facility gives a final beta function of 13.5mm; this corresponds to a rms spot size of about 67 μ m. Achieving a spot size of even smaller scale at the interaction point is done with a strongly magnetized permanent magnet based quadrupole magnets. An immediate advantage of permanent magnet quadrupole over the standard quadrupole is in miniaturization of design without reduction of magnetic field strength. On the other hand standard quad's field strength has a linear proportionality dependence on physical size, or (current density)⁻¹.

We have devised a quad which is an asymmetric triplet configuration. TRACE 3D code is used to simulate beam

transport of 30-60MeV, normalized emittance of 10mm-mrad, and beta function of 7mm/mrad. The lattice configuration is proved to be working well as shown later in the simulation results.

16-PIECE HALBACH PMQ MODEL

Magnet Design

We adopted a design initially proposed by Halbach[2]. The design of a PMQ consists of 16-piece magnet blocks put together to form a cylinder of 10mm in length, 2.5mm in bore radius and 7.5mm in outer radius. A slanted side view of a complete assembly of a PMQ is illustrated in Fig. 1. Also shown in the figure on the right-hand side is the magnetic easy-axis direction in each magnet block piece which rotates by 22.5° angle from one magnet block to the next. The remnant magnetic field of each Neodymium Iron Boride (NdFeB) magnet is set to $B_r=1.2$ T. These final magnet physical parameters are chosen to obtain a desired high field gradient $B'\geq 300$ T/m in the 3D magnetostatics modeling.

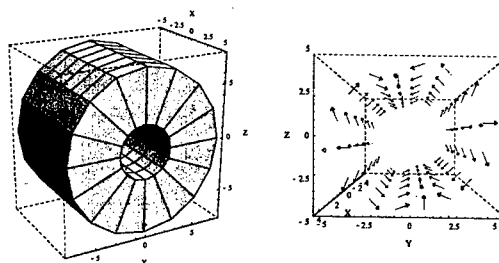


Fig 1: 16-piece Halbach PMQ illustrated on left. Magnetic easy-axis directions illustrated (red arrows) on right.

3D Modeling: Radia

A freely available magnetostatics computation software code termed Radia[3] was used in 3D modeling and numerical analysis of a 16-piece Halbach PMQ. Radia provides easy-to-define functions to easily create a sophisticated virtual model, and its capability to interface with Mathematica® allows one to easily do post-numeric analyses.

The desired field strength of $B'=318.3$ T/m is obtained after a series of trial-and-error computations are carried out. The magnetic field gradient plotted in the bore region exhibited a linear behavior as shown in Fig. 2. Near the bore surface we encounter non-linear fields, and we suspect this is because magnetic field symmetry is broken

*jlim@stout.physics.ucla.edu

Work supported by LLNL Grant No. LS03-001.

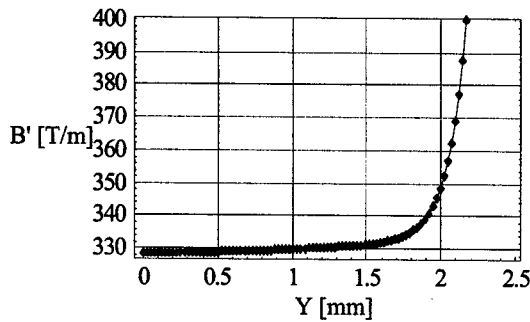


Fig 2: Magnetic field gradient B' plotted in the bore region.

as one moves close to the magnet bore surface where higher magnetic multipole moments are no longer small perturbations. As can be seen from Radia results, significantly large integrated sextupole and dodecapole fields are found at a reference radius of 2mm.

Generally the fringe field is simply neglected by assuming B_z field to be a step function with a constant nonzero field within and zero outside of PMQ. This is to be replaced when one considers a short fringe field extending away from two ends of a PMQ. Fortunately, Radia can automatically define the fringe field components into our PMQ model. For our chosen physical input parameters, we obtained an effective magnetic length (l_{eff}) of 10.23mm. The magnetic field plotted in axial direction is shown in Fig. 3. An deviation in focal length of PMQ due to magnetic length difference, $\delta l = l_{eff} - l$, is defined by

$$|\delta f| = \frac{1}{K \cdot l^2} \delta l \quad (1)$$

where K is the quadrupole focusing strength. For $K = 1.9 \times 10^3 \text{ m}^{-2}$ (50MeV, 318.3T/m), $l = 10\text{mm}$ and $\delta l = 0.23\text{mm}$, a focal length deviation of $\pm 1.2\text{mm}$ is expected.

Design Tolerance

So far we have described an ideal PMQ model where design imperfection is not factored into our modeling. However, we need to find out the performance of our magnet design in the presence of fabrication and assembly errors.

Possible mechanical and magnetic imperfections are easily defined into the Radia 3D modeling of PMQ and showed the robustness of our PMQ. Allowing tolerances of $\pm 1\%$ and $\pm 0.1^\circ$ in mechanical and magnetic values, we obtained the new magnetic field gradient 320.9T/m and the magnetic effective length 10.07mm, or respectively $\pm 0.8\%$ and $\pm 1.2\%$ in deviations from the ideal model.

When 16 magnets are pieced together to form a PMQ, these magnets will mutually try to influence magnetization characterizations. Such mutual magnetic influence can in fact change the overall magnetic properties of a PMQ. In Radia, magnetic relaxation of the PMQ due to inter-magnetic field interactions among 16 magnet block is shown to be almost negligible: the

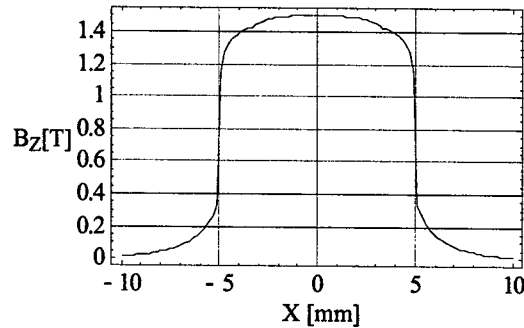


Fig 3: Magnetic field is plotted in the PMQ axis direction.

absolute average in change of magnetizations in 16 magnet blocks is $3 \times 10^{-3}\%$.

Magnet Material Properties

High performance permanent magnet materials are known to be available in current market in large quantities such as Neodymium Iron Boride (NdFeB), Samarium Cobalt (SmCo) and Ferrite (Fe_2O_3). Particularly NdFeB is suitable for our application for its high-performance magnetic properties, machineability, strong material characteristic and availability of low-cost high-grade magnet material. In contrast, SmCo is generally known to be weaker in B_r by 25%, extremely brittle and more expensive than NdFeB. Key magnetic properties of NdFeB (grade 35SH) are listed in Table 1[4].

Radiation hardness of NdFeB magnet compound seems to exhibit a moderate level of resistant against magnetic degradation[5]. At PLEIDEAS facility, magnets will be operated at constant room temperature which is significantly below our maximum operation temperature of 160°C , and B_r loss to due temperature fluctuation is expected to be below a loss rate of $0.10\%/^\circ\text{C}$. The summary of remanence loss due to irradiation sources are as follow: the exposure of 69Mrad of ^{60}Co γ -ray irradiation doses resulted in no remanence loss, 1.5% remanence loss is observed after direct hit by a total of 25 pulses of 82MeV electron beams, and the most remanence loss is observed in NdFeB by Bremsstrahlung source at a dose of 0.45Grad induced 2% minimum up to 14% maximum in loss[5]. We expect to minimize a remanence loss by placing lead based collimators before and after the PMQ final focus system. Also, a high internal coercivity of NdFeB material helps to reduced remanence loss. A further detail study of radiation induced remanence of our NdFeB PMQ system is warranted in the future.

Table 1: NdFeB Grade 35SH Properties

B_r (Gauss)	12,200
H_c (Oersteds)	11,700
H_{ci} (Oersteds)	26,000
Max. Energy (MGOe)	36
Temp. Coeff. Of B_r ($\%/^\circ\text{C}$)	-0.10
Max. Op. Temp. ($^\circ\text{C}$)	160
Density (lb/in^3)	0.271

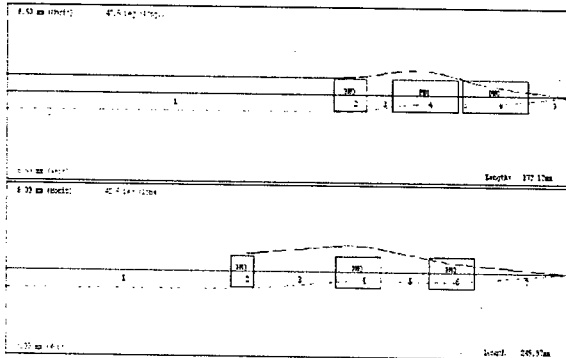


Fig. 4: TRACE3D simulation of 30MeV (Top) and 60MeV (Bottom) beam bunches transporting through PMQ final focus system.

FINAL FOCUS BEAM TRANSPORT SIMULATIONS

PMQ Triplet Final Focus System Layout

Our PMQ asymmetric final focus system consists of three permanent magnets arranged in Focus-Defocus-Focus (FODO) lattice configuration. The first PMQ is 1cm long and the second and third PMQs are 2cm long. Increase in physical length of PMQ effectively changes magnetic field gradient and effective magnetic length of a longer PMQ: 326.5T/m and 20.07mm.

TRACE 3D Simulation

TRACE 3D simulation results showed the tunability of focusing strength of PMQ final focus system. In practice tunability is achieved through varying drift space lengths with linear translators. The initial electron beam parameters entering the first PMQ are shown in Table 2. For 60MeV beam energy, the optimum focusing is achieved for drift space lengths of 36.52mm, 21.50mm and 41.84mm. The final transverse β functions obtained from the simulation are both 1.41mm. The adjustability of PMQ system for a different beam energy setting is also demonstrated in the simulation. For 30MeV, beam parameters are assumed to be the same as before for 60MeV. The optimum focusing is achieved for drift space lengths of 7.79mm, 1.40mm and 12.92mm. The transverse final β functions are 0.50mm and 0.49mm. The TRACE3D simulation plots of 30 and 60MeV beams are shown in Fig. 4.

Conclusion

3D modeling of the PMQ with Radia demonstrated a high magnetic performance based on 16-piece Halbach permanent magnet quadrupole (PMQ) of ≥ 300 T/m and $B'l_{eff} \approx 3$ T integrated magnetic field. And the beam transport simulation of PMQ final focus triplet system with TRACE 3D demonstrated a viability of linear translator mechanical device scheme to control effectively the focusing strength of PMQ final focus system: control of individual PMQ position with linear translator device. We have also shown in Radia that our PMQ had a

Table 2: Initial electron beam parameters

Beam energy	59.2MeV
σ_E	0.2%
σ_t	4ps
$\epsilon_{x,y}$	10mm-mrad
α_x	0.124
α_y	0.146
β_x	6.56mm/mrad
β_y	6.48mm/mrad
Beam charge	250pC

minimum error in its magnetic characteristics under presences of mechanical and magnetic tolerances of $\pm 1\%$ and $\pm 0.1^\circ$. Remanence loss due to radiation bombardment is moderately low as detail experimental results showed[5]. We also expect a temperature fluctuation to incur no remanence loss. But we will need a future plan to study systematically both of these factors in our PMQs.

REFERENCES

- [1] A. Tremaine, *et. al.*, "Ultrafast Materials Probing at PLEIADES, a Subpicosecond Thomson X-ray Source at the LLNL Electron Linac", Linac 2002, Gyeongju, Korea, TH416.
- [2] K. Halbach, NIM 169 (1980) 1.
- [3] http://www.esrf.fr/machine/groups/insertion_devices/Codes/Radia/Radia.html.
- [4] http://www.magnetsales.com/Magnet_Design.htm.
- [5] H. B. Luna, *et. al.*, NIM A285 (1989) 349.

CANADIAN LIGHT SOURCE MAGNETS

L. Dallin, D. Lowe, J. Swirsky, Canadian Light Source, University of Saskatchewan, 101 Perimeter Road, Saskatoon, Saskatchewan, S7N 0X4, Canada

Abstract

Magnets for the Canadian Light Source (CLS) storage ring have been designed and constructed. Magnets include gradient dipoles, quadrupoles, sextupoles, orbit correctors, injection septum and kickers. The compact CLS lattice requires strong focusing and consequently field gradients approach the upper limit of conventional magnet technology. Magnets have been manufactured by industry at a variety of locations. Prototypes have been developed and measured and meet the requirements set out in the magnet specifications. A description of the CLS quadrupole, sextupole and corrector magnets and magnet measurement results will be presented.

DIPOLE MAGNETS

The CLS [1] requires 24 gradient dipole magnets. These magnets were built at TESLA Engineering in Storrington, U.K. and are described in ref. [2].

QUADRUPOLE MAGNETS

The CLS requires three families of quadrupole magnets. Two families have the same design. The third family has the same design but is about 50% longer. Parameters are given in Table 1.

Table 1 Quadrupole Design Parameters.

Name	QFA/QFB		QFC		
#Magnets	48		24		
Field (max)	22.2		22.2		T/m
Length	0.170		0.253		m
Aperture Ø	0.065		0.065		
Coils	4 Inner	4 Outer	4 Inner	4 Outer	
Turns / coil	69	35	69	35	t
Current	87.50		87.50		A
Amp turns	9100		9100		A-t
Conductor (per magnet)					
area	4.76 ²		4.76 ²		mm ²
cooling Ø	3.19		3.19		mm
length	180	108	226	130	m
resistance	220	132	276	159	mΩ
Voltage	19.2	11.5	24.1	13.9	V
Power	1.68	1.01	2.11	1.21	kW
ΔT of water	8.00	3.48	11.1	4.55	°C
Water flow	3.0	4.2	2.7	3.8	L/m
	0.80	1.1	0.72	1.0	GPM

Pole tips are designed to minimize the multipole content of the magnets. Details of the geometry are given in ref. [3]. The sum of the higher order harmonics, inside a radial good field region of $r < 30\text{mm}$, were required to satisfy the relationship:

$$-0.002 < \frac{\sum_{n=3}^{\infty} r^{n-1} \int B_n(l) dl}{r \int B'(l) dl} < 0.002 \quad (1)$$

where $B'(l)$ and $B_n(l)$ are the quadrupole field and the n^{th} harmonics along the magnet axis (l).

The quadrupoles have a top yoke and a bottom yoke as shown in figure 1. The yokes are joined by two non-magnetic end plates with an open-side construction that allows for a vacuum chamber with an antechamber for the passage of synchrotron light.

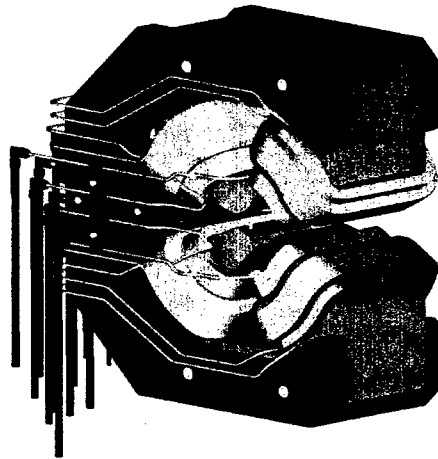


Figure 1. Isometric View of the Quadrupole Design.

The quadrupole magnets were built by SigmaPhi in Vannes, France. One of the finished magnets is shown in figure 2. The quadrupole is shown mounted on one of the CLS magnet girders. The stainless steel end plates also supply a precision interface to the machined girder for alignment.

All magnets from all three families were measured at SigmaPhi with a rotating coil assembly. Although a few of the magnets had higher order harmonics outside the specification defined in eq. (1), the average value of higher harmonics was much better than specified. Subsequent modelling of the CLS lattice with the "as-built" magnets indicated an improved lattice performance compared to the original harmonic estimates.

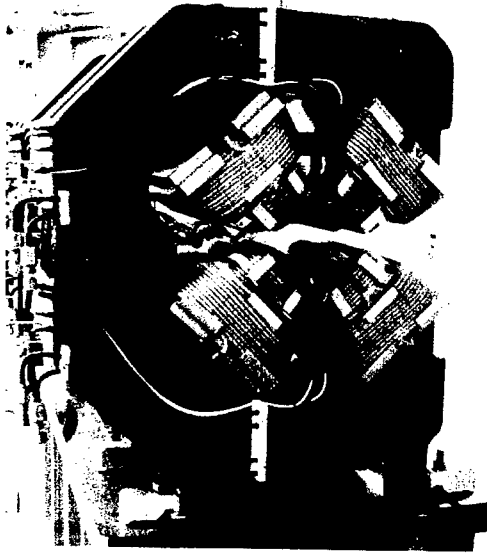


Figure 2. Fabricated Quadrupole Magnet.

For an example, the average harmonics for the QFA family of quadrupoles is shown in Table 2. In the table $I_{n/2}$ is the integrated gradient strength of the n^{th} harmonic relative to the integrated quadrupole gradient (I_2) in units of $\text{m}^{(n-2)}$. Tilt indicates the rotation (skewness) of the harmonic in mrad [tilt = $\tan^{-1}(\text{skew}/\text{normal})/(n-1)$].

Table 2: Measured Harmonics for Family QFA

n	3	4	5	6	7
$I_{n/2}$	0.0535	5.31	1.25E2	1.49E4	1.22E6
tilt	-297.4	-15.3	1.97	3.98	1.58
n	8	9	10	11	12
$I_{n/2}$	2.65E8	6.18E10	3.55E13	3.21E15	1.12E18
tilt	21.78	-9.34	-2.10	2.59	6.70

SEXTUPOLE MAGNETS

The CLS requires two families of sextupoles, Family 1 has 24 magnets and family 2 has twelve. The yokes, mechanical assembly and sextupole field requirements for each family are the same. Family 1 also has separate coils for each of X-corrector, Y-corrector and skew quadrupole functions. Family 2 has extra coils for skew quadrupoles. The sextupole parameters are given in table 3.

Details of the geometry are given in ref. [3]. The sum of the higher order harmonics, inside $r < 30$ mm, were required to satisfy:

$$-0.01 < \frac{\sum_{n=4}^{\infty} r^{n-1} \int B_n(l) dl}{r^2 \int B_3(l) dl} < 0.01 \quad (2)$$

where B_3 is the sextupole field. Similar, but more relaxed, requirements were specified for the corrector and skew quadrupole fields.

Table 3: Sextupole Design Parameters

# Magnets	36	
Field (max)	267.8	T/m ²
Length	0.192	m
Aperture \emptyset	0.078	m
Coils	6	
Turns/coil	36	t
Max Current	117.5	A
Amp turns	4230	A-t
Conductor area	4.76 ²	mm ²
cooling \emptyset	3.18	m
length	144	m
resistance	175	m Ω
Voltage	20.6	V
Power	2.42	kW
ΔT of water	8.0	°C
Total Flow	4.36	L/min
	1.15	GPM

The sextupoles, also manufactured at SigmaPhi have a construction similar to the quadrupoles as shown in figure 3. Non-magnetic end plates support three yoke pieces each containing two poles in an open-sided assembly. The plates also serve as an interface to the girders. One of the finished family 1 sextupoles is shown in figure 4.

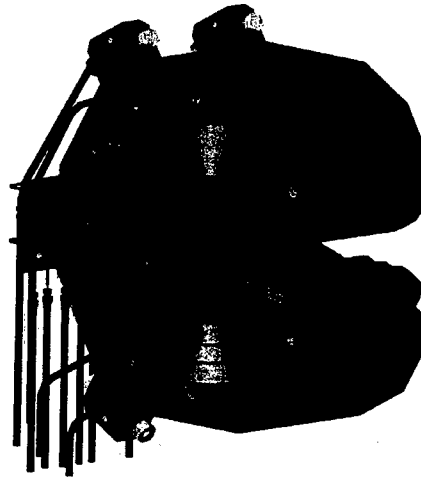


Figure 3. Isometric View of the Sextupole Design.

On average, the sextupole magnets also met the specs defined by eq. (2.). The analysis for the family 1 sextupoles is given in table 3, where the relative strengths, $I_{n/3}$ are now w.r.t the sextupole strength I_3 .

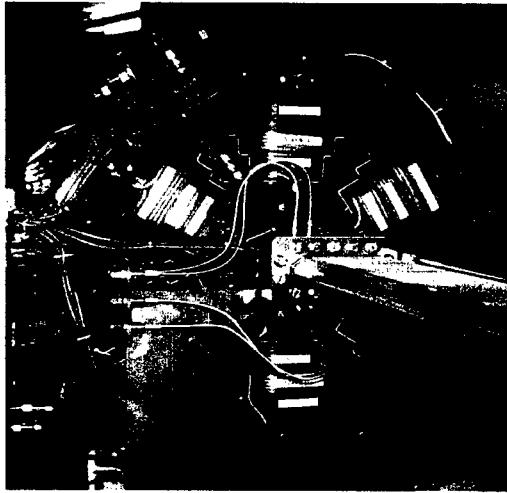


Figure 4. Fabricated Sextupole Magnet (Family 1)

Table 4: Measured Harmonics for Family 1 Sextupoles

n		4	5	6	7
$I_{n/3}$		0.0533	4.47	2.17E2	3.01E4
tilt		69.64	99.92	-25.85	23.40
n	8	9	10	11	12
$I_{n/3}$	9.51E6	1.23E9	4.03E11	8.61E13	2.74E16
tilt	-15.03	-7.95	0.02	-7.62	35.23

ORBIT CORRECTORS

The CLS requires 24 combined horizontal/vertical orbit correctors. The corrector parameters are given in table 5 and details of the design are given in ref. [4]. The correctors were built at Budker Institute in Novosibirsk, Russia. A schematic of the corrector is shown in figure 5 and the finished magnet in figure 6. The two coils on the right drive the vertical field while two sets of coils are used to drive the horizontal field. The harmonic content of the fields was required to satisfy conditions, similar to the sextupole correctors.

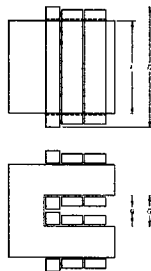


Figure 5. Corrector Schematic.

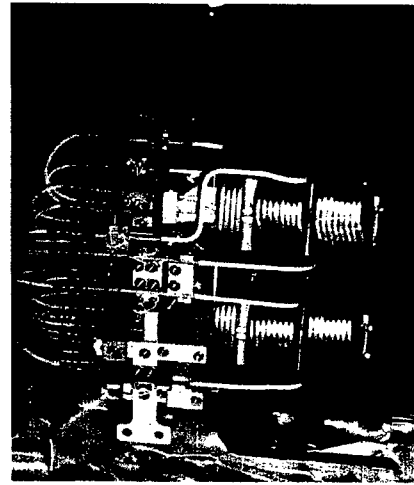


Figure 6. Fabricated Corrector Magnet.

Table 5. Orbit Corrector Design Parameters

# Magnets	24			
Yoke length	0.150			m
Gap (yoke) G	0.108			m
Gap (coils) g	0.044			m
X or Y kick	1.4			mrad
Field B_y	0.090			T
Field B_x	0.090			T
Coil Function	B_y	B_x		
# Coils	2	2	2	
Turns	24	39	36	t
Current	180	180	180	A
Amp turns	4320	7020	6480	A-t
Conductor area	6.48 ²	6.48 ²	6.48 ²	mm ²
cooling Ø	3.18	3.18	3.18	mm
length	34.574	49.964	46.334	m
resistance	18.7	27.0	25.0	mΩ
Voltage	3.36	4.86	4.5	V
Power	605	874	810	W
ΔT of water	3.28	5.96	5.29	°C
Total flow	2.65	2.12	2.20	L/min
	0.7	0.56	0.58	usGPM

REFERENCES

- [1] L. Dallin, "The Canadian Light Source", these proceedings.
- [2] L. Dallin et al, "Gradient Dipole Magnets for the Canadian Light Source", EPAC 2002, p. 2340.
- [3] L. Dallin, CLS tech. note 5.2.31.2 Rev. 0 - "Synchrotron Light Source Magnets", Feb. 11, 2001.
- [4] L. Dallin, CLS tech. note 5.2.31.4 Rev. A - "XY Orbit Correctors", May 30, 2000.

PERMANENT MAGNET QUADRUPOLE FOR FINAL FOCUS FOR LINEAR COLLIDER

Y. Iwashita[#], T. Mihara, Kyoto University, Kyoto, Japan
 E. Antokhin, BINP, Novosibirsk, Russia
 M. Kumada, NIRS, Chiba, Japan
 M. Aoki, Sumitomo Special Metal Co.,Ltd., Osaka, Japan

Abstract

Strong Permanent Magnet Quadrupole Lens is one of the candidates as the final focus lens for the linear collider, because of its compactness and less power consumption, while one drawback is its fixed strength. The total strength of a lens can be changed by rotating subdivided pieces separately. Some issues on such a system will be discussed.

INTRODUCTION

High magnetic field generation as high as 4.45T has been demonstrated without superconducting technology. It is based on the modified Halbach's configuration [1,2,3,4], which introduces saturated iron poles to the original configuration to enhance the magnetic field strength[5,6,7]. This situation is explained in Fig. 1, whose left figure shows the original Halbach's configuration. The operating point of the circled region in the figure is far in the first quadrant in B-H curve (see right figure in Fig. 1). Even plain soft iron can generate higher magnetic flux density than any known permanent magnet at such operating point. By replacing permanent magnet material in the region with soft iron, the magnetic field density increases even with such simple case (see Fig. 2). One can optimize the dimensions to obtain more effect from this technique. Fig. 3 shows the fabricated magnet that has achieved the 4.45T magnetic flux density and the calculated field density. The magnetic flux density is expected to become higher when we cool down it more.

Same technique can be applied to a quadrupole magnet and can generate higher magnetic field gradient than a

Modified Halbach's magnet.

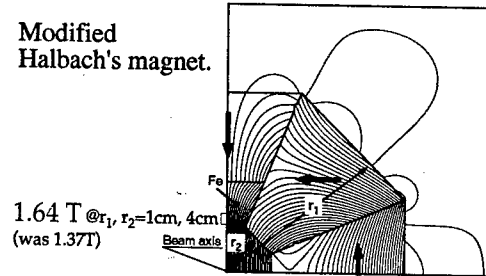
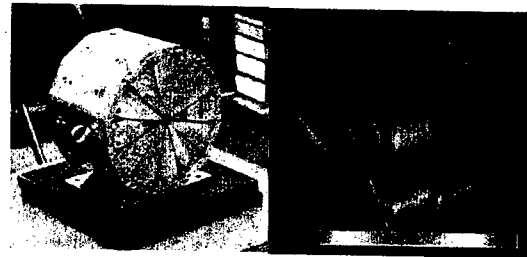


Fig. 2 Modified Halbach's configuration.



Achieved 4.45T @ -29°C (3.9T @ room temperature)

Fig. 3 4.45T permanent magnet dipole.

plain electromagnet. This feature may have advantage in the linear collider field since it needs rather stronger magnetic field gradient. A structure of a test quadrupole magnet using the saturated iron is reported in this paper. The measured data is also presented.

QUADRUPOLE

Fig. 4 shows the flux plot of the designed permanent magnet quadrupole calculated by PANDIRA. The field strength and gradient are also shown in the figure. The

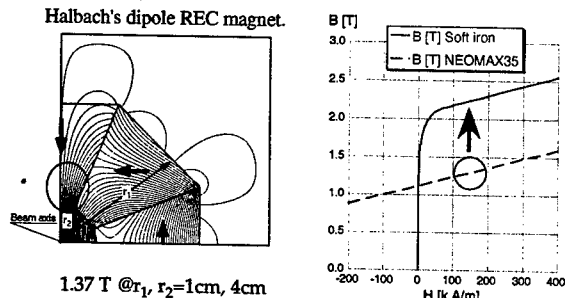


Fig. 1 Left: original Halbach's configuration can generate 1.37T in the bore. Right: The operating point of the region marked by the circle in the left figure is far in the first quadrant of the B-H curve, where plain soft iron is stronger than permanent magnet.

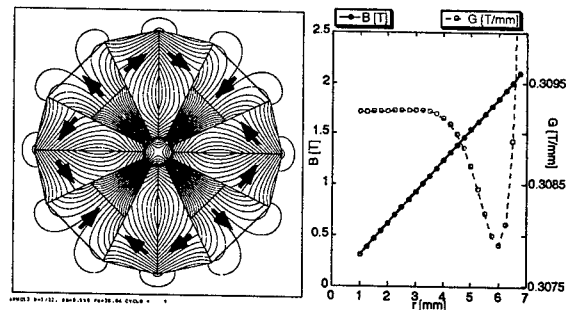


Fig. 4 Permanent Magnet Quad with saturated iron.

field gradient is calculated as 0.3T/mm. The inner diameter and outer diameter are $\phi 14$ mm and $\phi 100$ mm, respectively. It is segmented into 12 trapezoidal sections and inner parts of four of them are replaced by soft iron material. The outer diameter of the SUS case is $\phi 130$ mm, which can leave the space for outgoing beam after the interaction point when the crossing angle of the two colliding beam is set to 0.02 radian assuming that the distance between the interaction point and the edge of the quadrupole is 3.5m. The beam separation increases towards the far end of the 2m-length quadrupole lens.

The 3D calculation is performed on the geometry shown in Fig. 5. The total length is 10cm and that of the iron poles are 9cm. Both the ends of the iron poles are capped by permanent magnet pieces, which push the flux in and reduces the fringing field. Fig. 6 shows the calculated results of the field gradients along the axis. This figure also shows the cases when the iron poles are not used and when the iron poles are extended till the ends. It shows the effect of the saturated iron in the PMQ application. Although the integrated gradient is the strongest in the case of full length iron pole, it exhibits longer fringing field and slightly less peak gradient at the center ($z=0$) and thus we adopted the former option to demonstrate both the strong focal strength and the high gradient. Fig. 7 shows the assembled PMQ where the endplate is removed. The extra small magnets are glued on the endplates and are not shown.

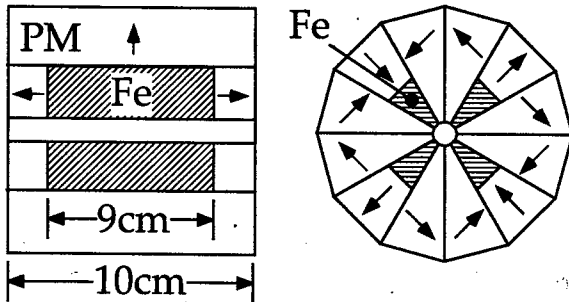


Fig. 5 3D configuration of the PMQ. The iron poles are 1cm shorter and replaced by permanent magnets pushing the flux inside to reduce the fringing field.

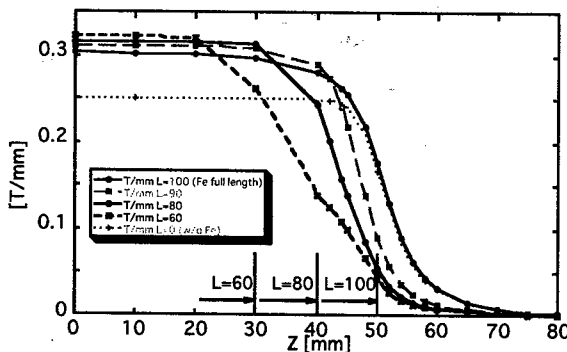


Fig. 6 Calculated field gradient along the axis.

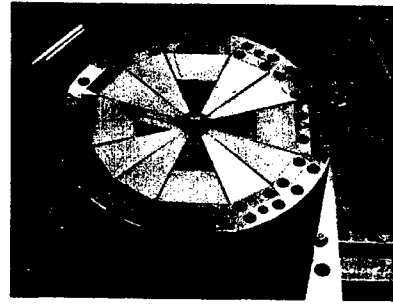


Fig. 7 The PMQ with saturated iron.

MEASURED RESULTS

The magnet was shipped to SLAC and kindly measured by them. The magnet was placed on V-blocks and the integrated field was measured by a rotating coil[8] (see Fig. 8). The measured integrated field gradient was 28.5 [T] while the calculated value was 29.7 [T] for full length. About 5% difference seems reasonable within our experience. Harmonics components are shown in Fig. 9. The dipole component comes from misalignment of the magnet center against the coil axis. Other components except $n=2,6,10,\dots$, which are inhibited by the rotation symmetry, have somewhat larger amplitudes.

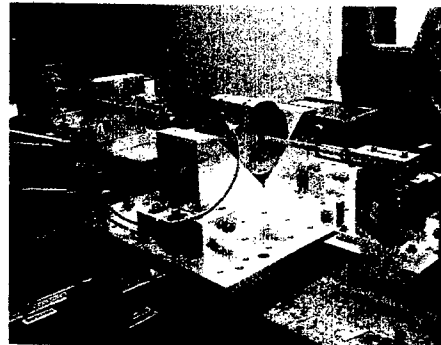


Fig. 8 Magnetic field measurement setup at SLAC.

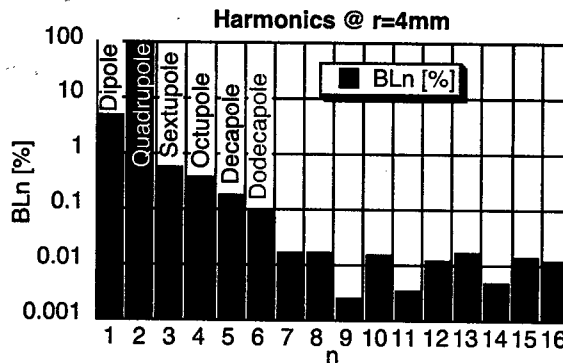


Fig. 9 Harmonics components. Except quadrupole ($n=2$) and dodecapole ($n=6$) components are larger than expected.

ADJUSTABILITY

The adjustability of the focal strength down to 25% is required for a calibration run with 1% resolution. The focal strength adjustments on the PMQs have been realized by adjusting a rotation angle of each separated PMQ in a system such as a triplet, while this scheme introduces skew components. Because the skews have to be strictly inhibited in the linear collider application, this scheme is not directly applicable. The full 90 degree rotation, however, just switches the focus Q to defocus Q and vice versa. Thus, the 2-m length quadrupole lens will be divided into ten 20-cm units and each unit will be divided into four different PMQs with binary way (see Fig. 10). When a smallest PMQ that has 0.5% focal strength of the total system flips 90 degree around its axis, the total focal strength changes 1%. One issue for such scheme is that the mechanical rotation may cause a magnetic center movement. Magnetic force between each PMQ may increase such effect, which can be reduced by putting a space with reduction of the packing factor. For shorter PMQs, the saturated iron technique may not be applicable because they are too short to keep the operating point high. This may make the total length longer.

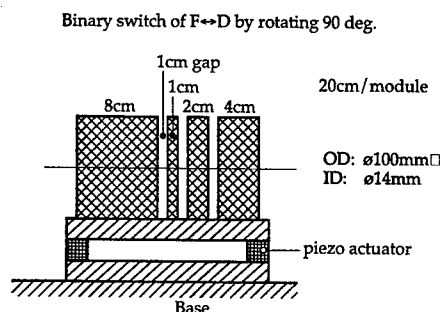


Fig. 10 Binary stepwise PMQ unit. Each PMQ can be flip 90 degree around its axis.

We are also investigating another way to adjust the focal strength (see Fig. 11). There are two PMQs; inner PMQ and outer PMQ. The outer PMQ is nothing but a normal PMQ with a large bore hole. The inner PMQ has iron poles instead of magnets. After we flip the outer ring (left to right figure), the field gradient in the bore decreases down to a few %. The inner PMQ can be fixed, while the outer PMQ rotates. One drawback is larger torque needed to rotate. This may be reduced when the

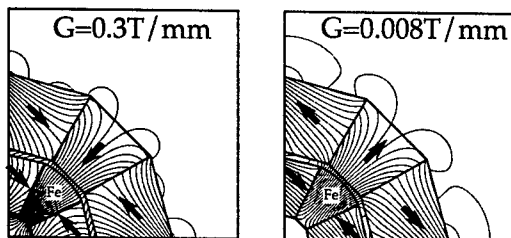


Fig. 11 Double ring scheme.

dynamic range is kept small. Thus the magnets of the inner PMQ will be fixed on the rigid iron poles that has full 20-cm length (Fig. 12). Longitudinally separated outer PMQ should have less sensitivity on the center movement when they rotate because they are far from the axis.

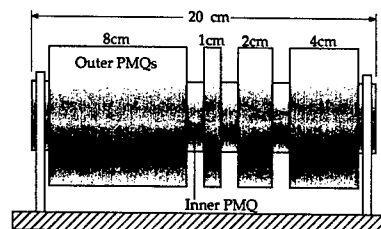


Fig. 12 Alternative way of the focal strength adjustment.

CONCLUSION

The permanent magnet quadrupole with saturated iron demonstrated the fairly high magnetic field gradient compared with the conventional one. The measured gradient agrees with calculated one within 5% difference. The higher harmonics components are observed in spite of the rotational symmetry, which is under investigation. We are preparing a measurement apparatus such as a heater and a temperature controller for temperature dependence.

In order to avoid a skew component while adjusting the focal strength, binary switch scheme will be adopted. A mechanical system for the adjustment of the focal strength is under investigation.

ACKNOWLEDGEMENT

The authors would like to express their sincere thanks to SLAC people, especially Dr. C. Spencer for taking the magnetic field measurement data.

REFERENCES

- [1] K.Halbach, IEEE, Trans., NS26(1979),3882
- [2] K.Halbach, NIM,169(1989) 1
- [3] K.Halbach, NIM,187(1981) 109
- [4] K.Halbach, NIM,198(1982) 213
- [5] CERN Courier(International journal of high energy physics), Magnet becomes more compact volume 41,number 7,september 2001,page 9
- [6] M. Kumada, T. Fujisawa, Y. Hirao, M. Endo, M. Aoki, T. Kohda, Y. Iwashita, Bolshakova, R. Holyaka, "Development of a Model 4 Tesla Dipole Magnet", pac2001, June, 18-22, 2001, Chicago
- [7] M.Kumada, T.Fujisawa, Y.Hirao, M.Endo, M.Aoki, T.Kohda, Y.Iwashita, Bolshakova, R.Holyaka, "Development of high field permanent magnets", MT17 (International magnet technology conference), 9/24-28,2001,Geneve
- [8] C.E. Rago, C.M. Spencer, Z. Wolf, "High Reliability Prototype Quadrupole for the Next Linear Collider", 17th InternationalMagnet Technology Conference

A SWITCHING MAGNET FOR THE IFUSP MICROTRON

M.L. Lopes¹, J. Takahashi¹, R.R Lima¹, A.A. Malafronte¹, M.N. Martins¹, U. Schnitter²

¹Laboratório do Acelerador Linear

²Departamento de Física Nuclear

Instituto de Física da Universidade de São Paulo, CP 66318, 05315-970, São Paulo, SP, Brazil

Abstract

In this work we present the design of a Switching Magnet for the IFUSP Microtron beam line. A configuration with azimuthal symmetry was adopted in order to comply with the boundary conditions of the accelerator building and to ease the machining process. The distribution and uniformity of the magnetic field are presented, as well as the project and construction of the vacuum chamber.

INTRODUCTION

The Laboratório do Acelerador Linear (LAL) of the Instituto de Física da Universidade de São Paulo is building a continuous wave (cw) electron race-track microtron (RTM). The IFUSP RTM [1-8] is a two-stage microtron that includes a 1.8 MeV injector linac feeding a five-turn microtron booster that increases the energy to 5 MeV. The main microtron delivers a 31 MeV cw electron beam after 28 turns. The maximum current of the beam is

50 mA. The Lab will have two main beam lines, one serving the photon tagger (bremsstrahlung monochromator), and the other dedicated to the production of X-rays by coherent bremsstrahlung as shown in Figure 1. This work describes the characteristics and design of the magnet that was built to perform the switching between these two lines.

Due to the distribution of the equipment in the experimental hall, the switching magnet must deviate the beam in angles of $\pm 90^\circ$ relative to the main pipeline that comes from the accelerator hall. The magnet should be able to deviate the beam independently of the energy, that may vary from 5 to 31 MeV. Besides that, we wanted the magnet as compact as possible, but avoiding field strengths too close to the saturation of the iron (< 2 T).

The chosen configuration was that of an "H" dipole, with cylindrical symmetry. Figs. 2 and 3 show two views of the adopted design. The main characteristics of the magnet are summarized in Table 1.

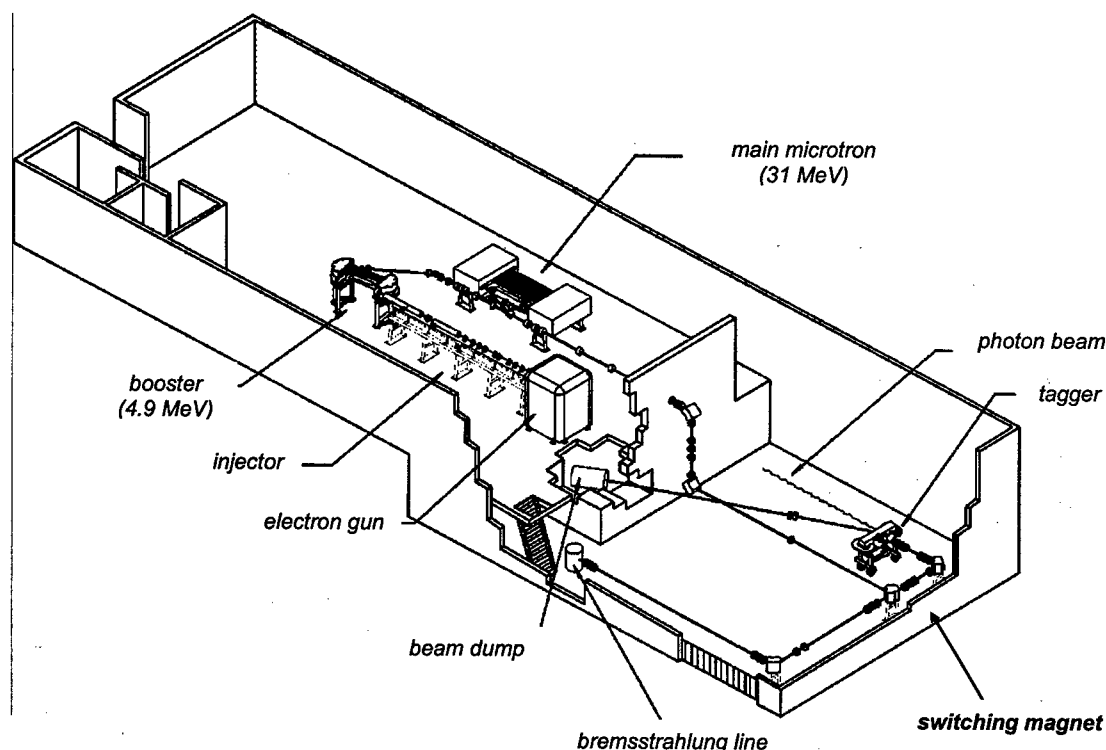


Figure 1: Isometric view of the accelerator in the accelerator building.

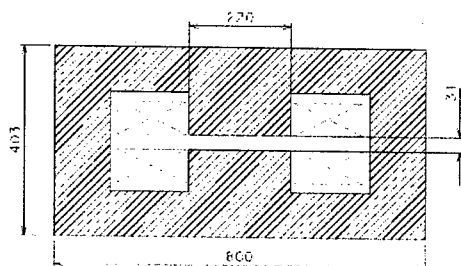


Figure 2: Cross section of the adopted design. Measures in mm.

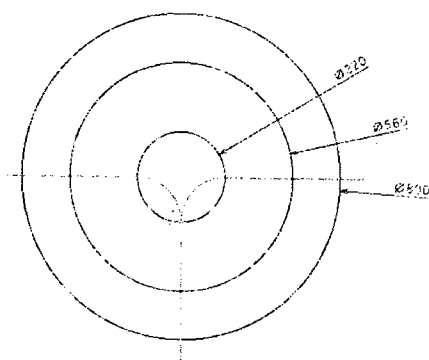


Figure 3: Top view of the magnet. Measures in mm.

Table 1: Magnet Specifications

Radius of curvature of the beam	0.11 m
Pole face diameter	0.22 m
Magnet diameter	0.80 m
Number of coils	2
Operating field @ 31 MeV	0.955 T
Operating field @ 5 MeV	0.166 T

THE MAGNET

Magnetic Design

The dimensions of the switching magnet were chosen in order to keep the magnet as compact as possible, but avoiding field strengths too close to the saturation of the iron (< 2 T). So we set the pole face radius in 0.11 m, because this gives an operational magnetic field of approximately 1 T for a 31 MeV beam. The final design was defined by simulations on the POISSON [9] and FEMM [10] codes, used to solve 2D magnetostatics problems. Figure 4 shows the field profile along a diameter of the magnet. The vertical lines indicate the pole face limits. Figure 5 shows a contour plot of the 2D relative field distribution over the mid-plane of the magnet. The advantage of this geometry is that the fringe fields are very small compared with field in the pole face region.

Mechanical Construction

The magnet was built with 1010 steel in three parts: two discs and a spacer ring. Each of the discs presents a deep channel to house one of the coils. The spacer ring is responsible for the gap. It also presents four ports for beam passage (3) and instrumentation (1). The ports are mounted with 19-mm pipes terminated with CF-25 vacuum flanges, in order to connect the magnet to the beam line.

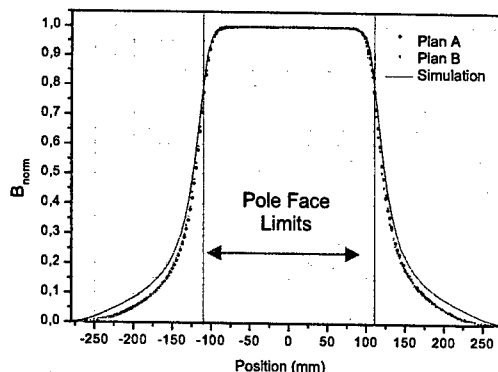


Figure 4: POISSON simulation results of the relative magnetic field along a diameter contained in the mid plane of the magnet (line) and the experimental data (dots). The vertical lines indicate the pole face limits.

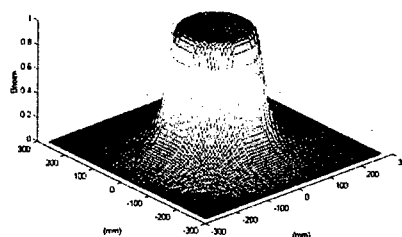


Figure 5: The relative magnetic field distribution over the mid plane.

The whole transport line is kept under high-vacuum. In the case of the switching magnet, in order to keep the gap as small as possible, we decided to use the magnet structure as part of the vacuum chamber. Figure 6 illustrates the system. The internal region of the ring is evacuated. Two brass covers were necessary to isolate the coils from the evacuated region, preventing, this way, virtual leaks proceeding from the coils.

A 4 mm groove was made in each of the iron discs to place the respective brass cover. It is also used for the gasket, which is made of a tin wire (99.7% purity) with a diameter of 1 mm. Figure 7 shows the final aspect of the switching magnet.

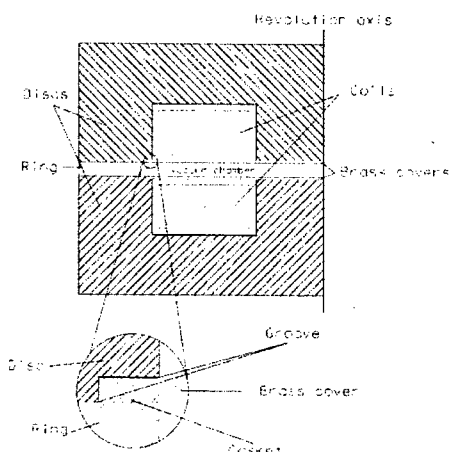


Figure 6: Details of the vacuum chamber design.

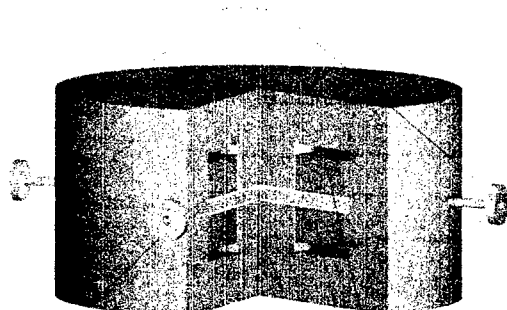


Figure 7: View of the assembled magnet.

RESULTS

For the magnetic characterization of the magnet, we used a Hall probe mounted on an automatic scanning system, operating with a step size of 2.52 mm. The measurements were made along a diameter contained in the mid plane of the magnet. The data acquisition was made in a PC with an analog to digital converter (ADC) board.

Figure 4 shows the results of the magnetic field mapping. We have mapped two different diameters (Plan A and Plan B in the figure), with good agreement between them. We can see that the experimental data agree with the results of the POISSON simulation. A magnetic field uniformity of 10^{-3} was achieved within a 0.16 m-diameter circle centered in the pole face region. The measured field is actually better than the simulated profile, since it falls faster outside the pole face region. This ensures that most of the bending is done in the pole face region.

The leak detection test evidenced that there were no leaks greater than 10^{-9} mbar.l.s⁻¹ (for helium). The

chamber was easily evacuated with a high-vacuum pumping system (mechanical plus ionic pumps), allowing the connection of the magnet to the rest of the beam pipeline without restrictions.

ACKNOWLEDGMENTS

We would like to thank Dr. Jack Tanabe for his helpful suggestions concerning the geometry.

Work supported by FAPESP and CNPq.

REFERENCES

- [1] The IFUSP racetrack microtron, J. Takahashi, Y. Miyao, M.N. Martins, J.M. Machado, A.A. Malafronte, J.C.A. Alcon, J. Marini Jr., A. Bonini, em Proceedings of the Third European Particle Accelerator Conference, editado por H. Henke e P.J. Genaz, Editions Frontières, França, 1992, Vol. 1, pages 429 to 431.
- [2] Plunger frequency control of the side-coupled accelerating structure for the IFUSP Microtron, em Proceedings of the 1997 Particle Accelerator Conference, <http://www.triumf.ca/pac97/papers/pdf/4P038.PDF>.
- [3] The design of the IFUSP main racetrack microtron accelerator end magnets, L.R.P. Kassab, J. Takahashi, M.N. Martins and P. Gouffon, em Proceedings of the 1998 European Particle Accelerator Conference, <http://www.cern.ch/accelconf/e98/papers/TUP45G.PDF>.
- [4] Vacuum system for the accelerating structure of the IFUSP Microtron, J. Takahashi, M.N. Martins, L. Portante, R. da R. Lima and F.T. Degasperi, in Proceedings of the 1999 Particle Accelerator Conference, <http://accelconf.web.cern.ch/AccelConf/p99/PAPERS/TUA125.pdf>.
- [5] The Gun Control System of the IFUSP Microtron, A.A. Malafronte, J. Takahashi, A.L. Bonini and M.N. Martins, Nucl. Instrum. and Methods A390, 423-425(1997).
- [6] Magnetic Field Correction of the IFUSP RTM Booster-End Magnets, L.R.P. Kassab, P. Gouffon and M.N. Martins. Nucl. Instrum. and Methods A404, 181-184(1998).
- [7] The end magnets of the IFUSP race-track microtron booster, L.R.P. Kassab, P. Gouffon, M.N. Martins and J. Takahashi, Part. Accel. 59, 75-92(1998).
- [8] Design of the main racetrack microtron accelerator end magnets of the IFUSP, L.R.P. Kassab, M.N. Martins, J. Takahashi, and P. Gouffon, Phys. Rev. Special Topics - Accelerators and Beams 2, 032401(1999).
- [9] L.M. Young and J.H. Billen LANL Poisson/Superfish codes for the PC, (1996).
- [10] D. Meeker, Finite Element Method Magnetics User's Manual, (2001).

MEASURING BETA FUNCTION AND PHASE ADVANCE IN RHIC WITH AN AC DIPOLE *

M. Bai, S. Peggs, T. Roser, T. Satogata, D. Trbojevic
Brookhaven National Laboratory, Upton, NY 11973, USA

Abstract

High energy hadron collider operation requires accurate measurements of the beta functions and phase advances, to check the linear optics and to locate gradient errors. During the RHIC 2003 run, two AC dipoles with vertical and horizontal magnetic field [1] were used to measure the linear optics at storage and at injection energies. The two AC dipoles are set up to adiabatically induce sizable coherent oscillations at a frequency close to the betatron frequencies. The beta functions and phase advances are then calculated from the 1024 turn-by-turn measurements available from all the RHIC BPMs (Beam Position Monitors). Because the coherent excitation is adiabatic, the beam emittance is preserved after the measurement. The algorithm is discussed in this paper, and experimental results are presented.

INTRODUCTION

During both the RHIC FY 2003 deuteron-Au run and polarized proton run, $\beta^* = 1$ m optics were used to maximize the luminosity. A set of beta function measurements were carried out by using the two RHIC AC dipoles to check the linear optics.

In linear accelerator, an AC dipole can be used to adiabatically generate a sustained transverse coherent oscillation without sacrificing the beam emittance [2]. The driven coherent oscillation at location s is given by

$$z(s)(i) = \frac{B_m L}{4\pi B\rho\delta} \sqrt{\beta(s)\beta_0} \sin(2\pi\nu_m i + \phi(s)) \quad (1)$$

where $z(s)$ is the transverse coherent oscillation amplitude at location s , $B\rho$ is the magnetic rigidity, $B_m L$ is the amplitude of the integrated AC dipole oscillating field strength, $\phi(s)$ is the phase at location s , $\beta(s)$ is the beta function at location s , i is the turn number, and β_0 is the betatron function at the AC dipole. δ is the separation between the intrinsic betatron tune ν_z and the AC dipole tune ν_m ,

$$\nu_m \equiv \frac{f_m}{f_{rev}}, \quad (2)$$

where f_m is the AC dipole oscillation frequency and f_{rev} is the beam revolution frequency. Hence, the ratio of the square root beta functions at two different locations is equal

* The work was performed under the auspices of the US Department of Energy

to the ratio of the coherence amplitudes at these two locations. The phase difference between the two locations is the true phase advance only if the AC dipole is not in-between.

In general, the transverse oscillation at two different locations s_1 and s_2 is given by

$$\begin{pmatrix} z_2 \\ z'_2 \end{pmatrix} = M \begin{pmatrix} z_1 \\ z'_1 \end{pmatrix} \quad (3)$$

where $z_{1,2}$ is the transverse position of the beam, $z'_{1,2}$ is the transverse angle of the trajectory. M is the transfer matrix between the two locations and

$$M = \begin{pmatrix} m_{11} & m_{12} \\ m_{21} & m_{22} \end{pmatrix} = \begin{pmatrix} \sqrt{\frac{\beta_2}{\beta_1}}(C + \alpha_1 S) & \sqrt{\beta_1 \beta_2} S \\ \frac{\alpha_1 - \alpha_2}{\sqrt{\beta_1 \beta_2}} C - \frac{1 + \alpha_1 \alpha_2}{\sqrt{\beta_1 \beta_2}} S & \sqrt{\frac{\beta_1}{\beta_2}}(C - \alpha_2 S) \end{pmatrix} \quad (4)$$

where $S = \sin \phi_{12}$, $C = \cos \phi_{12}$, $\beta_{1,2}$ are the beta functions at location s_1, s_2 , $\alpha_{1,2} = -\frac{\beta'_{1,2}}{\beta_{1,2}}$ and ϕ_{12} is the phase advance between the two locations and [3]

$$\frac{1}{\beta_1} \left(\frac{C}{S} + \alpha_1 \right) = \frac{m_{11}}{m_{12}} \quad (5)$$

Assuming that the turn by turn coherent oscillation is measured at three beam position monitors 1, 2 and 3 with phase advances in between of ϕ_{12} and ϕ_{23} , the beta function at BPM 1 is given by

$$\beta_1 = \beta_1^m \sqrt{\frac{\beta_2/\beta_1}{\beta_2^m/\beta_1^m} \frac{\sin \phi_{12}^m}{\sin \phi_{12}}} \quad (6)$$

where β_1 is the measured beta function at BPM 1, β_1^m is the model beta function at BPM 1, ϕ_{ij} is the measured phase advance between BPM i and BPM j where $i, j = 1, 2, 3$, and ϕ_{ij}^m is the model phase advance between BPM i and BPM j .

RHIC LINEAR OPTICS MEASUREMENT

In RHIC, transverse coherent betatron oscillations were adiabatically excited by the horizontal (or vertical) AC dipole. The amplitude of the AC dipole magnetic field was ramped up in 10,000 turns. It was then kept at constant for 2,000 turns for one to take the turn-by-turn beam position data and then ramped down to zero in another 10,000 turns. Since the coherent oscillation was adiabatically excited, the frequency spectrum of this driven oscillation is

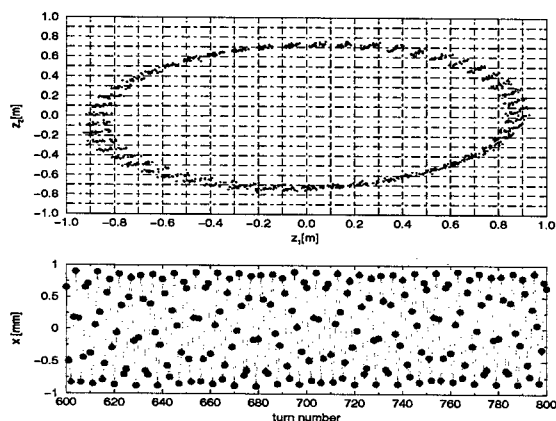


Figure 1: The bottom figure shows the vertical turn-by-turn beam position data in the middle of the arc. The black solid circles are the measured turn-by-turn beam position data and the open diamonds are the fitted turn-by-turn data. The phase plot at the top is the 1024 turn data at the BPM and the BPM next to it.

dominated by the frequency of the AC dipole. Thus, the coherent oscillation amplitude z_m and phase ϕ can be obtained by fitting the turn by turn beam position data by

$$z(i) = z_{m1} \cos(\nu_m 2\pi i) + z_{m2} \sin(\nu_m 2\pi i) \quad (7)$$

where $z(i)$ is the horizontal(or vertical) position of i^{th} revolution turn. The amplitude z_m and phase ϕ of the coherent oscillation are given by

$$z_m = \sqrt{z_{m1}^2 + z_{m2}^2}, \quad (8)$$

and

$$\phi = \arctan\left(\frac{z_{m2}}{z_{m1}}\right). \quad (9)$$

Fig. 1 shows the typical turn-by-turn vertical coherent oscillation at a BPM located in the arc area, and the phase plot represented by using the 1024-turn BPM data of two adjacent BPMs. The spread of the data points in the phase plot is about 0.1 mm and is about same level of the noise on the BPM turn-by-turn signal.

In RHIC, there is a total of 492 physical BPMs distributed around each ring. Among them, 84 are dual-plane BPMs. The vertical BPMs are located at every defocusing quadrupoles, and the horizontal BPMs are located at focusing quadrupoles [4]. 1024 turns of beam position at each BPM were collected with the AC dipole oscillating at a fixed frequency and fix amplitude. The amplitude and phase of the coherent oscillation driven by the AC dipoles at each beam were extracted using Eq. 8 and Eq. 9. The phase difference between any two BPMs is the phase advance in between, and the beta function at each BPM around the ring can be obtained by using Eq. 6. Fig. 2 is a typical example of the measured beta functions and phase advance at storage energy in the RHIC Yellow ring

with 1 m β^* at IP 8 and 2 m β^* at IP 6, IP 10 and IP 2. Compared with the model optics, the rms deviation of the measured phase advances and beta functions from the predicted value is about 12% in the arc area and larger in the interaction area.

In order to provide enough aperture around the RHIC beam abort area at injection, a lattice with $\beta^* = 10$ m at all IPs was used at injection. At storage energy, a lattice of 2 m β^* at IP 6, IP 10 and IP 2 and 1 m β^* at IP 8 was used [5]. In RHIC, three quadrupoles (triplet) were placed next to the D0 magnet in the interaction region for achieving the desired small β^* (beta function at interaction point) [6]. Normally, the beta function at the triplets grows considerably when the β^* gets squeezed down and any gradient error in the triplet quadrupoles then gets amplified and can result in beta function waves through the whole lattice. Fig 3 shows the measured beta function wave with the two different lattices. The larger beta wave of the $\beta^* = 1$ m lattice than the one of the $\beta^* = 10$ m lattice indicates the effect of the triplets effect.

CONCLUSION

The horizontal and vertical AC dipole magnets were commissioned during the RHIC FY 2003 run to measure the beta functions and phase advances at injection as well as at store. Several measurements were done in both Blue ring and Yellow ring to confirm the beta functions at the RHIC interaction point of lattices with different β^* lattices.

ACKNOWLEDGEMENT

The authors would like to thank Dr. Johannes van Zeijts for the fruitful discussions. The authors would also like to thank L. Hoff, V. Ponnaiyan, J. Piacentino and B. Oerter on the constructing the control hardware and software. The authors would also like to thank P. Oddo, J. Delong, T. Russo, D. Lehn, T. Curcio and other engineers for their help.

REFERENCES

- [1] M. Bai, *et al*, *RHIC AC Dipole Design and Construction*, Proceedings of the 2001 Particle Accelerator Conference, p. 3606 (June 2001).
- [2] M. Bai *et al*, *Physical Review E*, 5 (1997).
- [3] Castro-Garcia P., *Luminosity and Beta Function Measurement at the Electron-Positron Collider Ring, LEP*: Doctoral Thesis, Geneva, 1996.
- [4] T. Satogata, *et al*, *RHIC Beam Instrumentation*, Nuclear Instruments and Methods in Physics Research A 499 (2003) 372-387
- [5] T. Satogata *et al*, *Linear Optics Measurement and Correction in the RHIC 2003 Run "Optics"*, Proceedings of the 2003 Particle Accelerator Conference (May 2003).
- [6] *RHIC Design Manual*, April 1998.

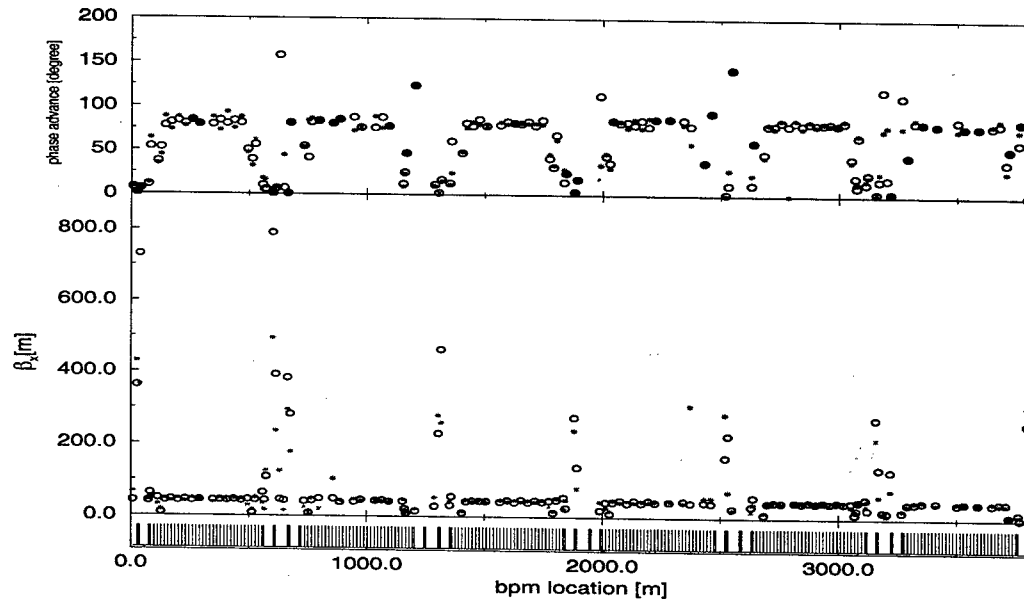


Figure 2: The bottom plot is the schematic layout of dipoles in the RHIC lattice showing 6 IPs. The stars in the middle plot are the horizontal betatron functions at all the available yellow BPMs measured at the RHIC Au storage using the vertical AC dipole. The open circles represent the horizontal beta functions predicted by the RHIC model. In the plot at the top, the stars are the horizontal phase advances between every two adjacent yellow BPMs measured at the Au storage energy. The open circle represents the corresponding phase advances predicted by the RHIC model. Because of the missing BPMs, the algorithm assigns the predicted phase advance to a BPM if the one next to it is missing.

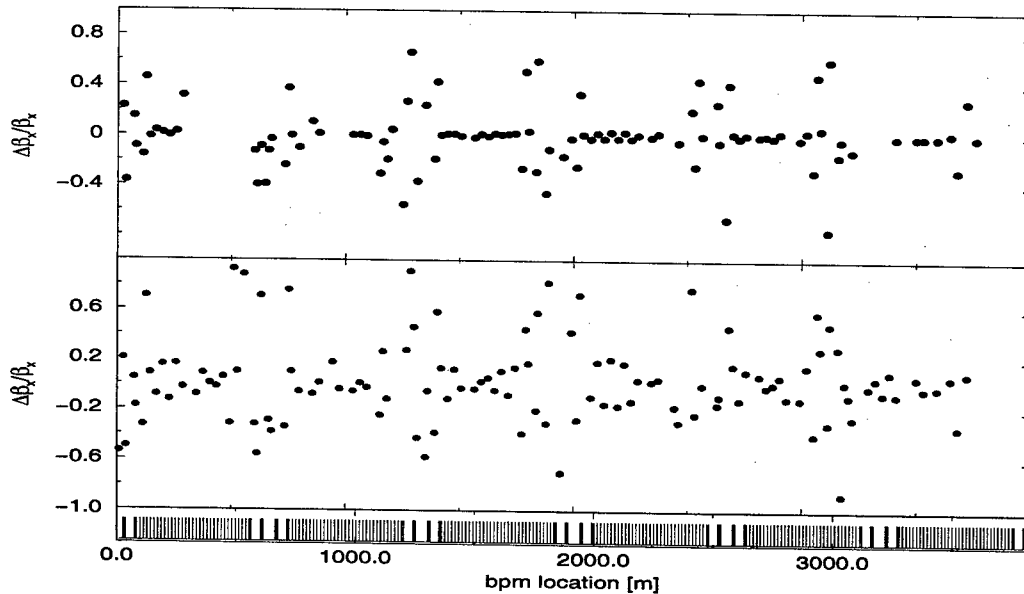


Figure 3: The bottom plot is the schematic layout of dipoles in the RHIC lattice. The stars in the middle plot and top plot are the differences of the measured horizontal beta functions and the beta functions in the model normalized of the predicted beta functions at all the available yellow BPMs measured at RHIC Au storage energy and injection energy.

MEASUREMENT OF LINEAR COUPLING RESONANCE IN RHIC *

M. Bai, F. Pilat, T. Satogata

Brookhaven National Lab., Upton, NY 11973, USA

R. Tomas, F. Schmidt

CERN, CH-1211 Geneva 23, Switzerland

R. Calaga

State University of New York, Stony Brook, NY 11794, USA

Abstract

Linear coupling is one of the factors that determine beam lifetime in RHIC. The traditional method of measuring the minimum tune separation requires a tune scan and can't be done parasitically or during the acceleration ramp. A new technique of using ac dipoles to measure linear coupling resonance has been developed at RHIC. This method measures the degree of coupling by comparing the amplitude of the horizontal coherent excitation with the amplitude of the vertical coherent excitation if the beam is excited by the vertical AC dipole and vice versa. One advantage of this method is that it can be done without changing tunes from the normal machine working points. In principle, this method can also localize the coupling source by mapping out the coupling driving terms throughout the ring. This is very useful for local decoupling the interaction regions in RHIC. A beam experiment of measuring linear coupling has been performed in RHIC during its 2003 run, and the analysis of the experimental data is discussed in this paper.

INTRODUCTION

In a circular accelerator, the linear 4x4 one-turn transfer matrix T for the two-dimensional phase space (x, x', y, y') can be represented by four 2x2 sub-matrices M, m, n and N

$$T = \begin{pmatrix} M & m \\ n & N \end{pmatrix} \quad (1)$$

where M and N are the standard transfer matrices in the (x, x') phase and (y, y') phase space. The off-diagonal sub-matrices m and n represent the coupling between the two transverse planes. In a perfect accelerator with no coupling, $m = n = 0$.

In general, the one turn matrix T can be diagonalized by an canonical transformation

$$T = R U R^{-1} \quad (2)$$

where U is the one-turn transfer matrix for the two decoupled transverse phase spaces (u, u', v, v') [1] and

$$\begin{pmatrix} x \\ x' \\ y \\ y' \end{pmatrix} = R \begin{pmatrix} u \\ u' \\ v \\ v' \end{pmatrix} \quad (3)$$

*The work was performed under the auspices of the US Department of Energy

where R is the transformation matrix between (x, z, s) and (u, v, s) .

$$R = \begin{pmatrix} \gamma I & C \\ -C^+ & \gamma I \end{pmatrix} \quad (4)$$

Here I is the 2x2 unitary matrix and C^+ is the symplectic conjugate matrix of the 2x2 matrix C

$$C = \begin{pmatrix} c_{11} & c_{12} \\ c_{21} & c_{22} \end{pmatrix}, \quad (5)$$

and $\gamma^2 + |C| = 1$. When the C matrix is zero, there is no coupling between the two transverse planes, and one can use C to characterize the strength of the linear coupling.

A technique to measure C by exciting beam at its eigen-tunes was developed at CESR [2]. Unlike CESR, an AC dipole was used in RHIC to adiabatically excite the beam at the vicinity of the eigen-tune instead. This technique has been used to measure the beta functions and phase advances in RHIC [4], and also in the AGS to overcome intrinsic spin resonances [3].

Without losing generality, we assume that the horizontal ac dipole (vertical field) is used to adiabatically excite a sizable coherent excitation nearby the horizontal tune Q_x . The horizontal AC dipole integrated field $\Delta B_y L$ is

$$\Delta B_y L = \Delta B_{ym} L \cos \nu_m \theta. \quad (6)$$

where ΔB_{ym} is the amplitude of the oscillating field, Q_m is the tune of the AC dipole field and θ is the azimuthal angle. In the absence of linear coupling, a horizontal betatron oscillation at location s is excited with amplitude of

$$x(s) = \frac{\Delta B_{ym} L}{4\pi B\rho\delta_x} \sqrt{\beta_0\beta(s)} \quad (7)$$

and no coherent excitation is excited in the vertical plane. Here, $B\rho$ is the magnetic rigidity, $\delta_x = |Q_m - Q_x|$ is the distance between the AC dipole driving tune Q_m and horizontal betatron tune, β_0 is the beta-function at the AC dipole and β_s is the β -function at location s . With linear coupling, the vertical coherent excitation is no longer zero. To derive the size of the coherent excitations in the two transverse planes due to an horizontal AC dipole, we first project the horizontal deflection from the AC dipole into the (u, v) coordinate where the motions in the (u, u')

plane and (v, v') are decoupled, i.e

$$\begin{pmatrix} \delta u \\ \delta u' \\ \delta v \\ \delta v' \end{pmatrix} = \begin{pmatrix} 0 \\ \gamma \delta x' \\ -c_{12} \delta x' \\ c_{11} \delta x' \end{pmatrix}. \quad (8)$$

where $\delta x'$ is the deflection of the horizontal ac dipole. The coherent excitations in the (u, u') and (v, v') are given by

$$u = \frac{1}{4\pi\delta_u} \gamma \delta x' \cos Q_m \theta \quad (9)$$

$$v = \frac{1}{4\pi\delta_v} \sqrt{c_{12}^2 + c_{11}^2} \delta x' \cos Q_m \theta \quad (10)$$

where $\delta_v = |Q_m - Q_v|$ and $\delta_u = |Q_m - Q_u|$. Q_v and Q_u are the two eigen-tunes of the transverse free betatron oscillation. For weak coupling,

$$Q_u \simeq Q_x \quad (11)$$

$$Q_v \simeq Q_y \quad (12)$$

$$\delta_u \simeq \delta_x \quad (13)$$

$$\delta_v \simeq \delta_y. \quad (14)$$

In general, $\sqrt{c_{11}^2 + c_{12}^2}$ is small for weak coupling and δ_x is much smaller than δ_y because the horizontal AC dipole drives the beam close to the horizontal tune. Hence, the coherent excitation in the (v, v') space can be neglected. Transforming the driven coherent excitations in the (u, v) coordinate back to the normal geometric (x, y) coordinates using Eq. 3, the transverse coherent excitations at location s are

$$x(s) = \gamma \frac{\sqrt{\beta_x}}{4\pi\delta_x} (\gamma \delta x') \cos(Q_m \theta + \chi) \quad (15)$$

$$y(s) = \frac{\sqrt{\beta_y}}{4\pi\delta_x} (\gamma \delta x') (c_{22} \cos(Q_m \theta + \chi) + c_{12} \sin(Q_m \theta + \chi)) \quad (16)$$

where χ is the phase between the AC dipole and the location s , and

$$\bar{C} = \begin{pmatrix} \frac{1}{\sqrt{\beta_u}} & 0 \\ \frac{\alpha_u}{\beta_u} & \sqrt{\beta_u} \end{pmatrix} C \begin{pmatrix} \sqrt{\beta_u} & 0 \\ -\frac{\alpha_u}{\beta_u} & \frac{1}{\sqrt{\beta_u}} \end{pmatrix} \quad (17)$$

Hence,

$$\sqrt{\frac{\beta_y}{\beta_x}} \frac{1}{\gamma} \sqrt{c_{22}^2 + c_{12}^2} = \frac{y_{amp}}{x_{amp}} \quad (18)$$

Similarly, the ratio of the horizontal coherent excitation amplitude to the vertical coherent excitation amplitude is

$$\sqrt{\frac{\beta_x}{\beta_y}} \frac{1}{\gamma} \sqrt{c_{11}^2 + c_{12}^2} = \frac{x_{amp}}{y_{amp}} \quad (19)$$

when the beam is adiabatically excited by a vertical AC dipole nearby the vertical tune.

EXPERIMENT DATA

The experiment was carried out in the RHIC blue ring with deuteron beam at injection energy. The linear coupling was corrected to $\delta Q_{min} \sim 0.001$ at injection for the normal operation using three RHIC skew quadrupole families distributed about 120° apart [5]. During the experiment, the coupling strength was measured with different skew family 1 strengths. The vertical (horizontal) AC dipole was used to adiabatically induce coherent oscillation nearby the vertical tune (horizontal tune). 1024-turn BPM (Beam Position Monitor) data in both planes were acquired at all the available RHIC BPMs in the arc areas. The amplitude of the coherent oscillation was calculated by fitting the turn by turn betatron oscillation data with a sinusoidal waveform [4].

Fig. 1 is a typical set of data of the measured coherent amplitudes in the two transverse planes due to a vertical ac dipole excitation. Due to the β -function variations along the arc, the coherent amplitude also varies with the β -function and the solid line is the average of the measured amplitude within one arc area.

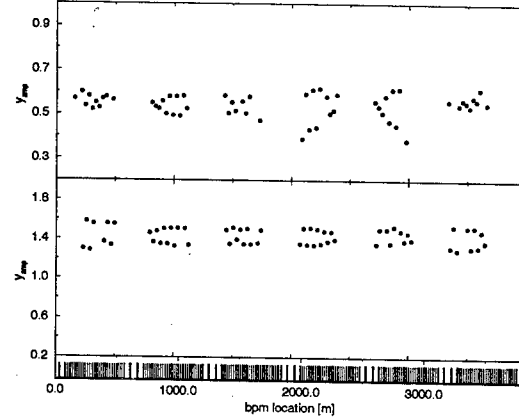


Figure 1: The plot at the bottom is the RHIC lattice. The top plot shows the measured amplitude of the horizontal coherent excitation when the coherent excitation was excited by a vertical AC dipole with skew quad family 1 trim value set to 0.005. The amplitude of the corresponding vertical coherent excitation amplitude at each BPM is shown in the middle plot.

Fig. 2 shows the measured coupling strength. The bottom plot is the measured $\sqrt{c_{11}^2 + c_{12}^2}$ with the vertical AC dipole and the top plot shows the $\sqrt{c_{22}^2 + c_{12}^2}$ with the horizontal ac dipole. Both measurements consistently show a linear dependence on the skew quadrupole family strength. Both data also show that the minimum of the measured coupling strength occurs at zero trim strength in skew quadrupole family 1. This is consistent with the fact that the coupling was well compensated at injection during normal operations.

- [5] F. Pilat *et al.*, *Coupling measurements and correction at RHIC*, Proceedings of the 2002 European Particle Accelerator Conference (June 2002)

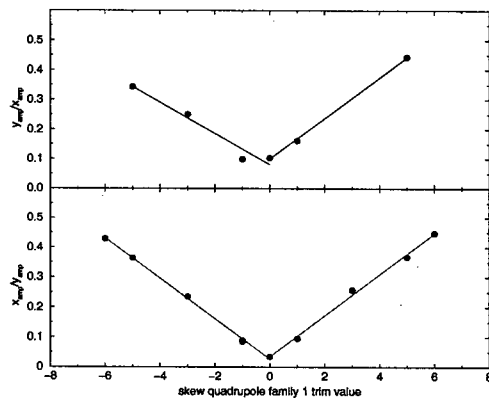


Figure 2: The top plot is the measured $\sqrt{c_{22}^2 + c_{12}^2}$ with the horizontal AC dipole as a function of the trim value of skew quadrupole family 1. And the bottom plot shows the measured $\sqrt{c_{11}^2 + c_{12}^2}$ with the vertical AC dipole with different skew quadrupole family 1 trim value settings.

CONCLUSION

The method of using driven betatron oscillations to measure the linear coupling resonance was tested during the RHIC FY03 dAu run. It demonstrated that the amount of the coupling can be characterized by the ratio of the amplitude of the horizontal (vertical) oscillation driven by an vertical AC dipole and the amplitude of the corresponding coherent excitation amplitude in the vertical (horizontal) plane. Since this technique does not require changes of the machine working point and is parasitic to the normal machine operation, it can also be used to measure the linear coupling along the RHIC acceleration ramp.

ACKNOWLEDGEMENT

The authors would like to thank Dr. W. Fischer for the fruitful discussions. The authors would also like to L. Hoff, V. P. J. P and B. Oerter on the constructing the RHIC AC dipole control hardware and software. The authors would also like to thank P. Oddo, J. Delong, T. Russo, D. Lehn, T. Curcio and other engineers for their help.

REFERENCES

- [1] D. A. Edwards, L. C. Teng, *Parameterization of Linear Coupled Motion in Periodic Systems*, IEEE Trans. Nucl. Sci. 20, 3 (1973).
- [2] D. Sagan *et al.*, *Betatron phase and coupling measurements at the Cornell Electron/Positron Storage Ring* Physical Review ST-AB, 3 (2000)
- [3] M. Bai *et al.*, *Overcoming Intrinsic Spin Resonances with an rf Dipole*, Physical Review Letters 80, 4673(1998).
- [4] M. Bai *et al.*, *Measure Betatron Functions and Phase Advances in RHIC with AC Dipole*, Proceedings of the 2003 Particle Accelerator Conference (May 2003)

LINEAR MODEL FOR NON-ISOSCELES ABSORBERS

J. Scott Berg*, Brookhaven National Laboratory, Upton, NY 11973, USA

Abstract

Previous analyses have assumed that wedge absorbers are triangularly shaped with equal angles for the two faces. In this case, to linear order, the energy loss depends only on the position in the direction of the face tilt, and is independent of the incoming angle. One can instead construct an absorber with entrance and exit faces facing rather general directions. In this case, the energy loss can depend on both the position and the angle of the particle in question. This paper demonstrates that and computes the effect to linear order.

INTRODUCTION

Ionization cooling can be achieved in the transverse direction with a straight cooling channel. However, in the longitudinal direction, one generally gets heating. Energy straggling leads to further heating in the longitudinal plane. To achieve 6-D cooling, one must couple the transverse motion with longitudinal motion. One method to achieve this is to use a triangular cross-section absorber in a location with dispersion. Particles with higher energy then go through a larger length of absorber and lose more energy, thus reducing the energy spread. Unfortunately, this occurs at the cost of an increase in transverse beam size [1]. This process is often referred to as "emittance exchange."

Existing computations have only considered triangular wedges with equal face tilts. The entrance and exit faces of the absorber can be tilted rather generally. This will give an energy loss dependence on transverse coordinates which is different from what occurs when the face tilts are equal and in the same plane. This paper calculates the linear transfer matrix for such a wedge absorber.

First, the path length in the absorber is calculated for general face angles. The computation is first done in the case where the faces are tilted in the same plane, to give a more intuitive picture of what is going on, followed by formulas for more general face tilts. This calculation is then used to find the transfer matrix through the absorber. Finally, possible uses of more general face angles are discussed.

GEOMETRIC LENGTH CALCULATION

The energy loss (ignoring stochastic effects) in the absorber is proportional to the distance that the particle travels through the absorber. Thus, to calculate the effect of the absorber, we will calculate the length of the particle trajectory that is inside the absorber. We further assume that the

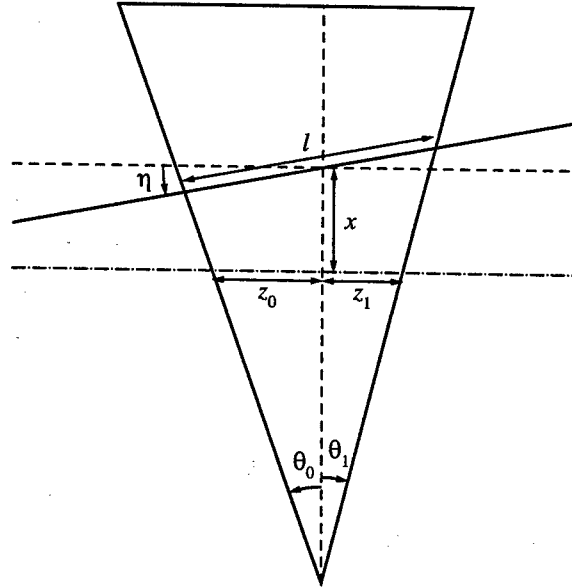


Figure 1: Planar absorber geometry.

particle trajectory is straight: i.e., there are no electromagnetic fields acting on the particle. First, we compute a case where the plane in which the absorber faces are tilted from vertical is the same for both cases. This becomes a one-dimensional problem, and helps give an understanding of what is going on. We then do the computation for a more general case.

Fig. 1 gives the parameters for the one-dimensional problem. The length of the path inside the absorber is

$$l = \left(\frac{L}{\tan \theta_0 + \tan \theta_1} + x \right) \frac{\cos \eta \sin(\theta_0 + \theta_1)}{\cos(\eta - \theta_0) \cos(\eta + \theta_1)}, \quad (1)$$

where $L = z_1 + z_2$. To linear order in x and η , this is

$$l = L + x(\tan \theta_0 + \tan \theta_1) + \eta L(\tan \theta_1 - \tan \theta_0) \quad (2)$$

If $\theta_0 = \theta_1$ (i.e., the absorber cross-section is an isosceles triangle), to linear order, the path length (and thus the energy loss) does not depend on the incoming particle angle, but does depend on the transverse position. This is the situation that has been analyzed in the past. On the other hand, if $\theta_0 = -\theta_1$ (i.e., the faces are parallel but the absorber is tilted), the path length does not depend on the incoming particle position, but it does depend on the incoming particle angle.

In the more general situation, we describe the absorber by its entrance and exit planes. We describe these planes as passing through a point p_i and having a unit normal u_i , where $i = 0$ for the entrance plane and $i = 1$ for the exit

*Supported by US Department of Energy contract DE-AC02-98CH10886

plane. The particle trajectory is described as line passing through a point \mathbf{x}_0 with a unit tangent vector \mathbf{t} . We can calculate the path length within the absorber in terms of these coordinates and vectors as

$$l = \frac{(\mathbf{p}_1 - \mathbf{x}_0) \cdot \mathbf{u}_1}{\mathbf{t} \cdot \mathbf{u}_1} - \frac{(\mathbf{p}_0 - \mathbf{x}_0) \cdot \mathbf{u}_0}{\mathbf{t} \cdot \mathbf{u}_0} \quad (3)$$

We can compute this length to linear order. The coordinates of these vectors are (see Fig. 1):

$$\mathbf{x}_0 = (x, y, 0) \quad (4)$$

$$\mathbf{t} = \left(\frac{p_x}{p}, \frac{p_y}{p}, \frac{\sqrt{p^2 - p_x^2 - p_y^2}}{p} \right) \quad (5)$$

$$\mathbf{p}_0 = (0, 0, -z_0) \quad (6)$$

$$\mathbf{p}_1 = (0, 0, z_1) \quad (7)$$

$$\mathbf{u}_0 = (\sin \theta_0 \cos \phi_0, \sin \theta_0 \sin \phi_0, \cos \theta_0) \quad (8)$$

$$\mathbf{u}_1 = (-\sin \theta_1 \cos \phi_1, -\sin \theta_1 \sin \phi_1, \cos \theta_1). \quad (9)$$

TRANSFER MATRIX

One can easily compute the transfer matrix to lowest order in the relative energy loss in the absorber. In this case, only the path length in the absorber matters. First, compute the evolution of the transverse momenta, as well as the evolution of the energy deviation ignoring the face angles. The equations of motion are

$$\frac{d\mathbf{p}_\perp}{ds} = -\kappa_\perp \mathbf{p}_\perp \quad \frac{d\delta}{ds} = -\kappa_\parallel \delta \quad (10)$$

$$\kappa_\perp = \frac{1}{\beta pc} \frac{dE}{dx} \quad \kappa_\parallel = \frac{d}{dE} \left(\frac{dE}{dx} \right), \quad (11)$$

and their solution is

$$\mathbf{p}_\perp(s) = \mathbf{p}_\perp(s_0) e^{-\kappa_\perp(s-s_0)} \quad (12)$$

$$\delta(s) = \delta(s_0) e^{-\kappa_\parallel(s-s_0)}. \quad (13)$$

Imagine a sequence of planes with normal $\mathbf{u}(z)$ and passing through the point $(0, 0, z)$. Using Eq. (3), the integrated path length to linear order in $\mathbf{x} = (x, y)$ and \mathbf{p}_\perp/p (where the \perp subscript refers to the transverse coordinates) from an arbitrary point to the plane at z is a constant plus

$$z - \mathbf{x} \cdot \frac{\mathbf{u}_\perp}{u_z} - z \frac{\mathbf{p}_\perp}{p} \cdot \frac{\mathbf{u}_\perp}{u_z}. \quad (14)$$

We will parameterize \mathbf{u} by η according to

$$\mathbf{u} = \frac{u_0 \sin(\xi - \eta) + u_1 \sin \eta}{\sin \xi} \quad \mathbf{u}_0 \cdot \mathbf{u}_1 = \cos \xi. \quad (15)$$

η will vary from 0 to ξ while z varies from $-z_0$ to z_1 . The definition of the exact relationship between η and z will be left to later. We then have

$$\frac{dl}{dz} = 1 - \frac{\mathbf{p}_\perp}{p} \cdot \frac{\mathbf{u}_\perp}{u_z} - \left(\mathbf{x} + z \frac{\mathbf{p}_\perp}{p} \right) \cdot \frac{u_{z0} \mathbf{u}_{\perp 1} - u_{z1} \mathbf{u}_{\perp 0}}{u_z^2 \sin \xi} \frac{d\eta}{dz}. \quad (16)$$

Now define

$$\frac{d\eta}{dz} = k u_z^2 \quad (17)$$

for some constant k . Then

$$\frac{d}{dz} \left(\frac{\mathbf{u}_\perp}{u_z} \right) = k \frac{u_{z0} \mathbf{u}_{\perp 1} - u_{z1} \mathbf{u}_{\perp 0}}{\sin \xi} \quad (18)$$

meaning that

$$\frac{\mathbf{u}_\perp}{u_z} = k \frac{u_{z0} \mathbf{u}_{\perp 1} - u_{z1} \mathbf{u}_{\perp 0}}{\sin \xi} z + \mathbf{c} \quad (19)$$

for a constant vector \mathbf{c} . Applying the known boundary conditions,

$$\frac{\mathbf{u}_\perp}{u_z} = \frac{\mathbf{u}_{\perp 0}}{u_{z0}} \frac{z_1 - z}{L} + \frac{\mathbf{u}_{\perp 1}}{u_{z1}} \frac{z + z_0}{L}. \quad (20)$$

We can then write

$$\begin{aligned} \frac{dl}{dz} = 1 - \frac{\mathbf{x}}{L} \cdot \left(\frac{\mathbf{u}_{\perp 1}}{u_{z1}} - \frac{\mathbf{u}_{\perp 0}}{u_{z0}} \right) \\ - \frac{\mathbf{p}_\perp}{p} \cdot \left[\frac{z_1 \mathbf{u}_{\perp 0}}{L u_{z0}} + \frac{z_0 \mathbf{u}_{\perp 1}}{L u_{z1}} + \frac{2z}{L} \left(\frac{\mathbf{u}_{\perp 1}}{u_{z1}} - \frac{\mathbf{u}_{\perp 0}}{u_{z0}} \right) \right] \end{aligned} \quad (21)$$

Now, use Eq. (12), giving

$$\begin{aligned} l = L - \mathbf{x} \cdot \left(\frac{\mathbf{u}_{\perp 1}}{u_{z1}} - \frac{\mathbf{u}_{\perp 0}}{u_{z0}} \right) - \frac{\mathbf{p}_{\perp 0}}{p \kappa_\perp L} \cdot \left[\right. \\ \left. 2 \left(\frac{1 - e^{-\kappa_\perp L}}{\kappa_\perp} - z_0 - z_1 e^{-\kappa_\perp L} \right) \left(\frac{\mathbf{u}_{\perp 1}}{u_{z1}} - \frac{\mathbf{u}_{\perp 0}}{u_{z0}} \right) \right. \\ \left. + \left(\frac{z_1 \mathbf{u}_{\perp 0}}{u_{z0}} + \frac{z_0 \mathbf{u}_{\perp 1}}{u_{z1}} \right) (1 - e^{-\kappa_\perp L}) \right]. \end{aligned} \quad (22)$$

The change in δ is simply $\kappa_\parallel l$, and one can then directly read off the matrix elements.

DISCUSSION

First of all, adjusting the absorber geometry simply to keep the sum of the tangents of the face angles constant will not leave the performance of a cooling channel invariant, unless there happens to be no angular dispersion at the location of the absorber. In fact, at a point where there is both angular and positional dispersion, one may get improved performance by adjusting the face angles separately.

One could even consider a lattice with only angular dispersion and no positional dispersion at the absorbers. This could not be easily done in a ring (if one bends in the same direction all the time, one tends to have nonzero positional dispersion), but could be done in a "snaking" configuration where subsequent cells bend in opposite directions, and thus the lattice is straight over larger scales.

There are several reasons one might want to do this. First of all, a lattice that does not form a ring allows one to adiabatically vary lattice parameters, thus maximizing the cooling performance as the beam changes. One may be especially interested in doing this for a collider to maximize the

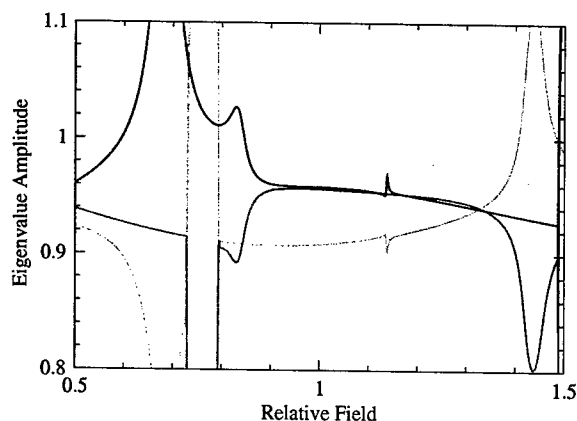


Figure 2: Super-FOFO lattice with bends all in same direction and isosceles wedges. Absolute value of eigenvalues plotted versus field relative to a reference field.

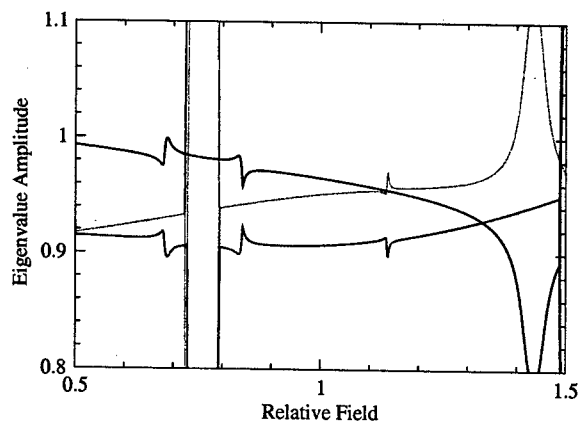


Figure 3: Super-FOFO lattice where bending in one cell is opposite to the bending in the next, and the absorbers are tilted slabs. Plots are as in Fig. 2.

luminosity one achieves. In addition, one avoids the difficulties with injection and extraction.

These considerations apply to any lattice that does not form a ring. The advantage of having only angular dispersion versus positional dispersion at the absorber may lie in the effect of energy straggling. When the energy changes in energy straggling, the betatron amplitude will change since the closed orbit changes. Since the beta function at the absorber is small (whereas the dispersion is not necessarily), energy straggling with positional dispersion will lead to large betatron amplitude changes relative to the beam size. If instead there is angular dispersion at the absorber, energy straggling leads to smaller relative betatron amplitude changes due to the large angular spread at that point. This has the potential to substantially improve the performance of these cooling lattices. This has not been tested in real lattices at this point.

Example

As an example, consider a "Super-FOFO" lattice [2], modified by adding bending as in [3]. A similar lattice has been proposed for achieving 6-D cooling, and shows excellent performance [4, 5]. Fig. 2 shows the absolute value of the eigenvalues as a function of the field strengths for standard isosceles wedges and a lattice where all bends bend in the same direction (giving dispersion at the absorber). This is equivalent to considering the dependence of the eigenvalues on the reference momentum. If the absolute value of all the eigenvalue is less than 1, then the beam will be cooled in all planes. One is able to achieve 6-D cooling over a rather large range of reference momenta.

Figure 3 shows the eigenvalues for a tilted slab in a lattice that has angular dispersion at the absorber. Note that in this case as well, one is able to achieve 6-D cooling over a rather large range of reference momenta. Also note that the wedge angles are steeper than those required for the case with conventional wedge absorbers.

CONCLUSIONS

The energy loss in an absorber with generally placed planar faces has been calculated to linear order in the transverse coordinates. This allows one to calculate eigenvalues for a cooling channel with these rather general wedges. An example was constructed where a cooling channel was constructed with angular dispersion at the absorbers, and parallel-face tilted absorbers were used. Linear performance (without multiple scattering) of that cooling channel was shown to be comparable to that of a channel constructed with more conventional wedges. Such a channel may have multiple scattering performance that is better than a wedge-based 6-D cooling channel.

Further work should incorporate general face orientations into simulation codes such as ICOOL [6]. One can then simulate and optimize proposed 6-D cooling lattices by orienting absorber faces more generally.

REFERENCES

- [1] David Neuffer, *Part. Accel.* **14**, 75 (1983).
- [2] Eun-San Kim *et al.*, report MUC-NOTE-COOL-THEORY-0036, <http://www-mucool.fnal.gov/notes/notes.html> (unpublished).
- [3] J. Scott Berg, in *Proceedings of the 2001 Particle Accelerator Conference*, edited by P. Lucas and S. Webber (IEEE, Piscataway, NJ 2001), p. 145.
- [4] J.S. Berg, R.C. Fernow, R.B. Palmer, MUC-NOTE-COOL-THEORY-0239, <http://www-mucool.fnal.gov/notes/notes.html> (unpublished).
- [5] R.B. Palmer, MUC-NOTE-COOL-THEORY-0250, <http://www-mucool.fnal.gov/notes/notes.html> (unpublished).
- [6] R. Fernow, computer program ICOOL, <http://pubweb.bnl.gov/people/fernow/icool/readme.htm> (unpublished).

LINEAR DESIGN OF COMBINED-FUNCTION IONIZATION COOLING LATTICES

J. Scott Berg, Harold Kirk, Brookhaven National Laboratory*, Upton, NY 11973, USA
Alper Garren, University of California Los Angeles, USA

Abstract

Ionization cooling lattices simultaneously require small beta-functions at the absorber and large energy acceptances to be effective. Simultaneously achieving these goals as well as having a good dynamic aperture requires that the lattice be relatively compact. If one wishes to avoid solenoids, one choice for creating such a lattice is to use combined-function magnets. These magnets can simultaneously focus in both planes, allowing one to achieve a low beta in both planes with a minimum number of magnets. In this paper we explore the design of lattices which contain only combined-function bending magnets using a thin-lens approximation, showing how to optimally achieve the requirements for muon cooling.

INTRODUCTION

Ionization cooling is needed in most scenarios for muon-based accelerators such as neutrino factories and muon colliders. Cooling rings have been proposed as a cost-effective means for cooling in all six phase space dimensions [1, 2, 3]. Cooling rings have traditionally used solenoids, but it is not absolutely necessary to do so.

Since one must bend and focus in the cooling ring, it is logical to use combined-function bends in a non-solenoid cooling ring. For the simple designs here, symmetry will dictate that one chooses the magnet gradients to focus equally in both planes. Thus, all analyses here will be done in a single plane.

For a combined-function bend which focuses equally in both planes, the integrated focusing strength F is

$$F = \frac{Bc\theta}{2pc/q}, \quad (1)$$

where B is the dipole component of the field, θ is the bending angle, p is the momentum, q is the particle's charge, and c is the speed of light. Note the inverse dependence of F on momentum.

There are two parameters that are of importance in a cooling lattice: the energy bandwidth (should be large) and the beta function at the absorber (should be small). They compete with each other: when the energy bandwidth increases, so does the maximum beta function. The energy bandwidth is described by the half-width of the relative momentum spread Δ :

$$\Delta = (p_{\max} - p_{\min}) / (p_{\max} + p_{\min}), \quad (2)$$

*Supported by US Department of Energy contract DE-AC02-98CH10886

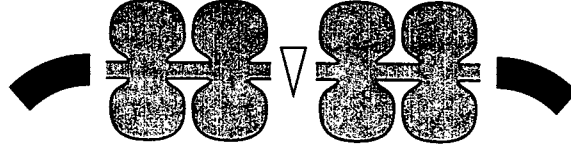


Figure 1: Layout with one bend per cell.

where p_{\min} and p_{\max} are the minimum and maximum momentum respectively. It is also useful to define a reference momentum to be

$$p_{\text{ref}} = (p_{\max} + p_{\min}) / 2 \quad (3)$$

In these calculations, the change in the closed orbit is ignored. As the closed orbit changes, the focusing strength in the combined function bend will change. In particular, a bending magnet that focuses equally in both planes at the reference energy does not do so off-energy.

ONE BEND PER CELL

If there is only one bend per cell, as shown in Fig. 1, and the cell length is L , then the beta function at the absorber is

$$L \sqrt{\frac{1 - LF/4}{LF}}. \quad (4)$$

This lattice is unstable when $LF > 4$; thus, there is a momentum threshold below which the lattice is unstable. The lattice is stable for arbitrarily large momentum. The maximum β -function at the absorber occurs at the largest momentum within the passband. Thus,

$$\beta_{\max} = 2L \sqrt{\frac{2\Delta}{1 - \Delta}} \quad \Delta = \frac{\beta_{\max}^2}{8L^2 + \beta_{\max}^2}. \quad (5)$$

The required magnetic field is

$$B\theta = \frac{2}{Lc} \frac{p_{\text{ref}} c}{q} (1 - \Delta) \quad (6)$$

$$= \frac{2}{c} \frac{p_{\text{ref}} c}{q} \frac{8L}{8L^2 + \beta_{\max}^2} = \frac{2}{Lc} \frac{p_{\min} c}{q}. \quad (7)$$

Note that if β_{\max} is much less than L , then the energy acceptance is very small. Thus, this is probably not an optimal configuration for a cooling ring.

TWO BENDS PER CELL

Now, consider a lattice with two bends per cell, as shown in Fig. 2. Symmetry considerations dictate that the two

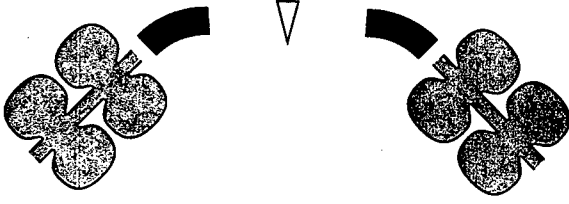
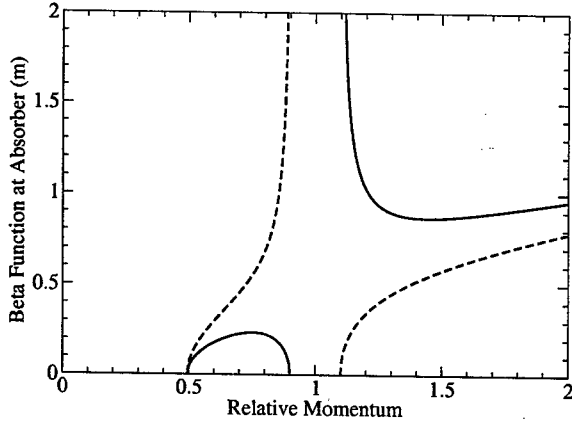


Figure 2: Layout with two bends per cell.


 Figure 3: Beta as a function of momentum. The solid line is for $L_A = 0.9$ m and $L_R = 1.1$ m, and the dashed line is for $L_A = 1.1$ m and $L_R = 0.9$ m.

bends be identical. The beta function at the absorber is

$$\frac{L_A}{2} \sqrt{\frac{\left(\frac{2}{L_A} - F\right) \left(\frac{2}{L_A} + \frac{2}{L_R} - F\right)}{\left(\frac{2}{L_R} - F\right) F}}, \quad (8)$$

where L_A is the length of the drift containing the absorber, and L_R is the length of the other drift (presumably containing RF).

As a function of momentum, the β -function has two zeros, when $F = 2/L_A$ and when $F = 2/L_A + 2/L_R$. There are two poles, when $F = 0$ and $F = 2/L_R$. There are thus two passbands: from the $F = 2/L_A + 2/L_R$ to the larger of $2/L_A$ and $2/L_R$, and from the smaller of $2/L_A$ and $2/L_R$ and 0. These passbands are given in terms of F , but they are equivalent to passbands that are determined by the momentum. One passband is unbounded in momentum, and the other is a bounded region of momentum. The bounded region can either have zeros at both ends or a zero at one end and a pole on the other, as shown in Fig. 3. If the bounded region has an infinite β -function at one end, then the unbounded region will have a zero in the beta function β -function at the low momentum end, and will go to infinity as the momentum goes to infinity. Thus, the β -function gets large in either region. However, if the β -function is zero on both sides of the bounded region (it cannot be zero on both sides of the unbounded region), it will have a maximum value in that region. As can be seen in Fig. 3, one can

achieve a lower maximum beta by running in this bounded region with zeros of the beta function on both ends of the region. The peak β -function can be written in terms of Δ as

$$\begin{aligned} & \frac{L_R - \sqrt{L_R^2 - L_A^2}}{2} \\ &= \frac{L_A}{2} \left(\frac{1 - \Delta}{2\Delta} - \frac{\sqrt{1 - 2\Delta - 3\Delta^2}}{2\Delta} \right) \\ &= \frac{L_R}{2} \left(1 - \frac{\sqrt{1 - 2\Delta - 3\Delta^2}}{1 - \Delta} \right). \quad (9) \end{aligned}$$

Inverting this equation gives

$$\Delta = \frac{\sqrt{\beta_{\max}(L_R - \beta_{\max})}}{L_R + \sqrt{\beta_{\max}(L_R - \beta_{\max})}}. \quad (10)$$

Note that the maximum Δ is 1/3 (giving an energy acceptance of a factor of 2), and occurs when $\beta_{\max} = L_R/2$. The relationship between the lengths is

$$L_A = L_R \frac{2\Delta}{1 - \Delta} = 2\sqrt{\beta_{\max}(L_R - \beta_{\max})}, \quad (11)$$

or inverting,

$$\Delta = \frac{L_A}{2L_R + L_A}. \quad (12)$$

Finally, the field strength required is given by

$$B\theta = \frac{2}{cL_R} \frac{p_{\text{ref}} c}{q} \frac{1 - \Delta^2}{\Delta} \quad (13)$$

$$= \frac{8}{c} \frac{p_{\text{ref}} c}{q} \frac{L_R + L_A}{L_A(2L_R + L_A)}. \quad (14)$$

As one reduces β_{\max} relative to L_R , the energy acceptance decreases, and the field required in the bending magnets increases.

EXAMPLE

Let's say that a 1 m drift is needed for the RF, and the maximum desired beta function at the absorber is 0.25 m. The reference momentum for the lattice is 200 MeV/c.

With only one bend per cell, the energy acceptance of this lattice is less than 1%. This is unacceptable for a cooling lattice. If there are two bends per cell, the energy acceptance is $\pm 30\%$. The length of the absorber straight is 0.87 m. $B\theta$ is about 4 T; if we have 8 bends in the ring, this corresponds to bending fields of 5.1 T, and correspondingly lower if one uses fewer bends. The length of this bend is about 10 cm. Using 4 bends gives a 2.6 T field with 41 cm bend lengths.

The required magnet apertures are difficult to determine, since the beta functions go to infinity as the ends of the momentum passband; an energy cutoff must be introduced because of that, or the ellipsoidal beam distribution must be taken into account.

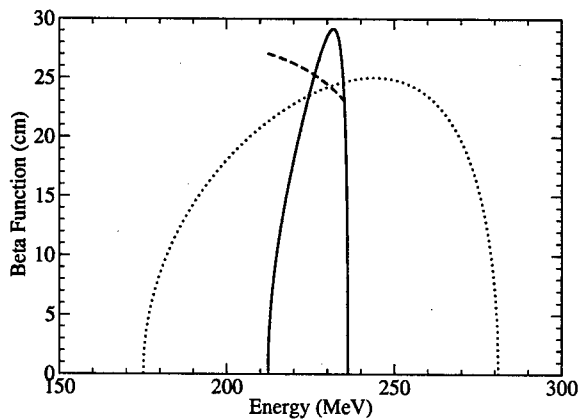


Figure 4: Beta function at the absorber as a function of energy for combined-function magnets with linear midplane field dependence. The dotted line is the thin-lens model, the solid line is β_x , and the dashed line is β_y .

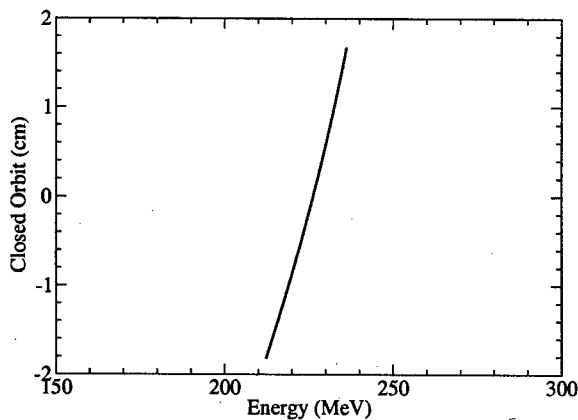


Figure 5: Closed orbit as a function of energy at the absorber side of the magnet for combined-function magnets with linear midplane field dependence.

Thick Magnets

Now, instead of using a thin-lens model, use thick combined-function bends. If we use a bend whose field is linear in the midplane, we get the beta functions shown in Fig. 4. Note the substantially reduced energy acceptance from the linear model. The reason for this reduced energy acceptance is the closed orbit variation with energy (see Fig. 5). When the closed orbit is at a larger radius, the vertical focusing is increased since the length of the orbit in the magnet is longer, but the horizontal focusing is decreased since the geometric contribution to focusing is reduced due to the larger radius of curvature.

One can try to correct the chromaticity by adding a sextupole component to the magnets. The optimal way to do this is to use a magnet which maintains equal focusing in both planes at all positions in the magnet: a magnet whose

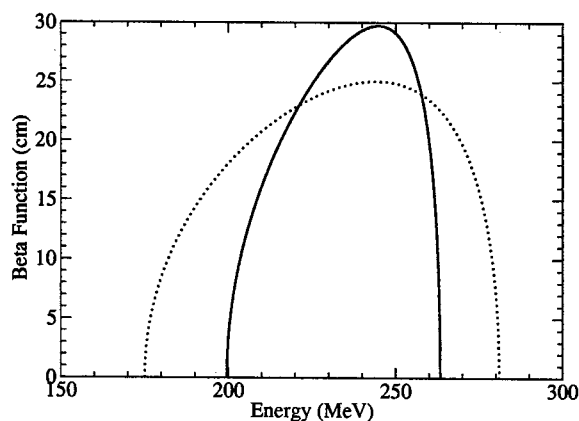


Figure 6: Beta function at the absorber as a function of energy for power law midplane field dependence. The dotted line is the thin-lens model; the solid line is for the actual magnet (both planes).

midplane field is

$$B(x) = B_0 (1 + x/\rho)^{-1/2}. \quad (15)$$

Figure 6 shows the beta functions at the absorber in this case. The energy acceptance has been greatly improved from Fig. 4, but is still not as large as the linear model suggests. Nor should one expect improvement from here: since the beta functions are identical in the two planes, changing the sextupole component would likely make the linear resonances in one plane closer together, while moving them further apart in the other plane.

CONCLUSIONS

A thin-lens model can be used to approximately design and predict the qualitative behavior of a simple cooling ring using only combined-function bending magnets. Probably the most important use of this is to predict the parametric dependence of and interrelationship between performance parameters for such a cooling ring.

A simple design with aggressive lattice parameters seems to be a bit unrealistic: the magnets are very short, and the ring circumference is very low as well. With less ambitious lattice parameters (a relaxed beta function, for instance), the lattice may end up being more realistic.

This paper doesn't look at the dynamic aperture of these lattices: the use of highly nonlinear magnets may have a negative impact on that.

REFERENCES

- [1] V. Balbekov, MUC Note 246 (2002).
- [2] J.S. Berg, R.C. Fernow, and R.B. Palmer, MUC Note 239 (2002).
- [3] Harold G. Kirk *et al.*, in *Proc. of the APS/DPF/DPB Summer Study on the Future of Particle Physics (Snowmass 2001)*, ed. N. Graf, eConf C010630, M101 (2001).

DESIGN OF FFAGS BASED ON A FODO LATTICE

J. Scott Berg*, Brookhaven National Laboratory, Upton, NY 11973, USA
 Carol Johnstone†, Fermilab, Batavia, IL, USA

Abstract

An FFAG is a lattice with fixed magnetic fields that has an extremely wide energy acceptance. One particularly simple type of FFAG is based on a FODO lattice, where both quads can be combined-function bending/quadrupole magnets. The spaces between the combined-function magnets are left open for RF cavities and other hardware. This paper describes a general method for creating lattice designs for this type of lattice which gives the lattice optimal properties for an FFAG accelerator. The properties of this lattice as a function of input parameters are explored. The use of sextupoles to improve lattice properties is also explored.

INTRODUCTION

There has been great interest in recent years in a neutrino factory or muon collider which would accelerate muons to energies in the 20–50 GeV range. Since muons decay, acceleration must be rapid, with an average gradient of at least 1 MV/m. Accelerating systems are a major component of the cost of these machines. A linac accelerating to the full energy would be extremely costly. Cost savings can be achieved by using some form of recirculating acceleration, in which the muons pass through the cavities multiple times. It is at best difficult to design a fast-ramping synchrotron for these lower energies, since it would be challenging to increase the magnetic fields at the rate at which one would like to accelerate the beam. This is especially true because of the large beam emittances that one typically deals with in muon-based machines, since larger magnet apertures lead to larger stored energies, increasing the power that must be delivered to ramp the magnets.

Most studies to this point have proposed CEBAF-style recirculating accelerators for muon acceleration. The accelerator has a racetrack shape, with two linacs connected by a series of arcs. The beam enters a different arc on each pass, depending on its energy. The primary difficulty with these machines is related to the multiple arcs. The switchyard connecting the linac to the several arcs becomes very complex, and it therefore becomes difficult to have more than a few arcs (4 in typical designs). This prevents a further reduction in cost by having more turns in the accelerator and therefore a smaller amount of RF in the linacs.

These considerations have led to the proposal of performing acceleration using a fixed-field alternating gradient (FFAG) machine. Instead of having a separate arc for

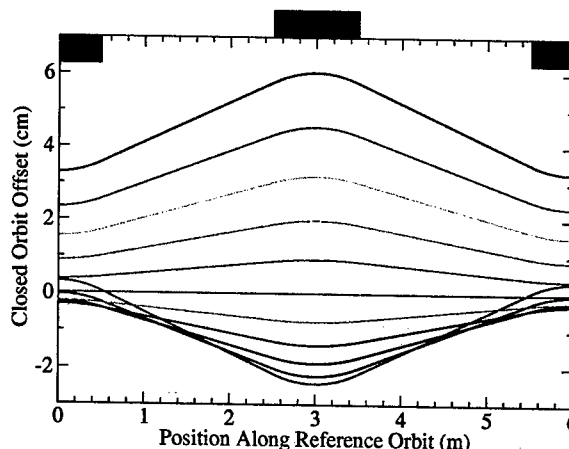


Figure 1: Closed orbits at various energies in a FODO FFAG lattice. Energies are from 10 GeV (bottom center, magenta) to 20 GeV (top center, red). Position of magnets are also shown at the top. The tune at 10 GeV is 0.3.

each energy, these machines avoid the switchyard by having a single arc which accepts the entire range of energies over which one wishes to accelerate.

The traditional type of FFAG is the scaling FFAG. In this machine, the tunes and momentum compaction are independent of energy, and the closed orbits at different energies are geometrically similar to each other. In recent years non-scaling FFAGs have been proposed [1], which don't meet these criteria, yet still accept a wide range of energies. This paper describes some advantages of "non-scaling" FFAGs over scaling FFAGs.

This paper describes how to design a FFAG lattice based on a FODO cell. The FODO cell in this case consists of two combined-function (gradient bend) magnets. Figure 1 shows the closed orbits at various energies in such a lattice.

OPTIMIZATION

A FODO lattice with two combined-function magnets has 7 free parameters: the drift space between magnets (same on both sides), two magnet lengths, two dipole field components, and two quadrupole field components. One adjusts these parameters to achieve a design which is optimum in some sense.

Tunes

One must not allow the tune of a single cell to reach a half-integer or integer. In a scaling FFAG, this is achieved

*Supported by US Department of Energy contract DE-AC02-98CH10886

†Work Supported by the US Department of Energy contract DE-AC02-76CH03000

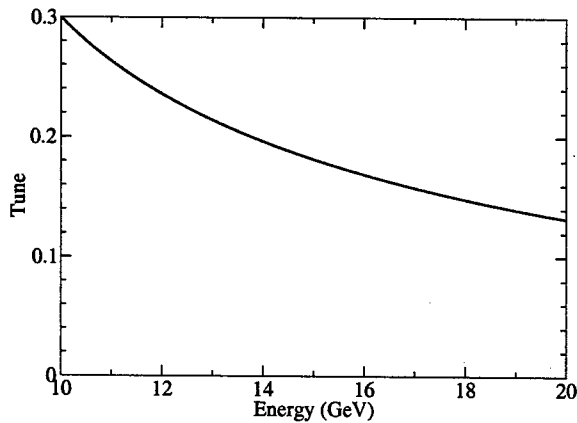


Figure 2: Tune as a function of energy in a FODO FFAG lattice.

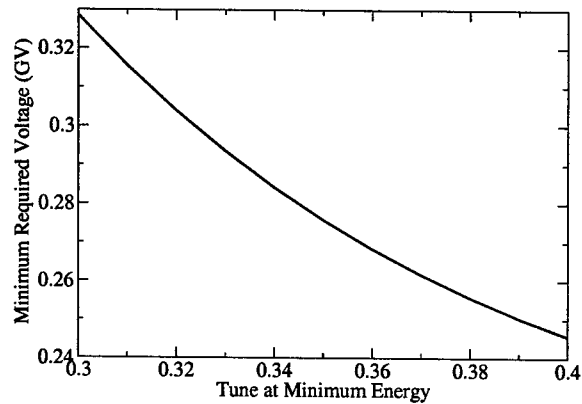


Figure 4: Minimum required voltage as a function of the tune at the lowest energy.

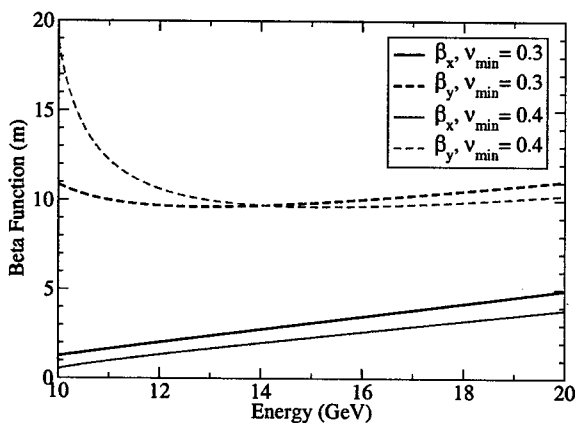


Figure 3: Beta functions as a function of energy at the center of the defocusing quadrupole, for two different tunes at the minimum energy.

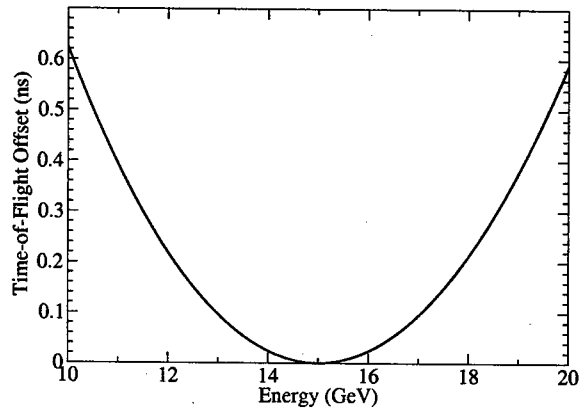


Figure 5: Time-of-flight as a function of energy in a FODO FFAG lattice.

by having a constant tune. In a FODO cell, if the lattice is stable, the tune is below 0.5. The tune increases with decreasing energy, as seen in Fig. 2, until one reaches the half-integer resonance; the lattice is unstable at energies below that point. Thus, at the lowest desired energy, the tune is set to a value safely below 0.5, and this is generally sufficient to have tunes below 0.5 over the entire energy range. Since we are accelerating very rapidly, one is less concerned with nonlinear resonances, since the tune will not remain near any particular value for a very long time.

A good choice for the tunes at the lowest energy is 0.3. This may seem to be quite far from 0.5, but in practice the tune rises very rapidly as the energy decreases. To get a finite energy acceptance at injection, to insure that one's design holds up once end fields are other nonlinearities are included, and to keep the beta functions at injection reasonable (see Fig. 3), it is essential to keep sufficiently far from the half integer resonance at injection. The minimum required voltage (see next subsection and Fig. 4) and

the closed orbit swing improve when that tune is raised, so one does not want to make that tune too low.

Time-of-Flight Variation

Secondly, one wants to make optimal use of the installed RF. It can be demonstrated that there is a minimum amount of RF voltage that must be installed in an FFAG accelerator to achieve a desired energy gain [2]. This minimum requirement comes about because the time-of-flight depends strongly on energy. Because of the rapid rate of acceleration, the relatively high frequencies we desire to use, and the large amount of installed voltage, it is impractical to shift the RF phase to keep the RF synchronized with this time-of-flight variation. The time-of-flight variation therefore prevents one from staying at the peak of the RF crest, and this leads to the minimum RF voltage requirement. One advantage of the non-scaling FODO lattice over a scaling lattice is the parabolic shape of the time-of-flight as a function of energy (see Fig. 5), compared to the roughly linear behavior in the scaling lattice. This leads to a lower minimum required RF voltage for a given lattice scale.

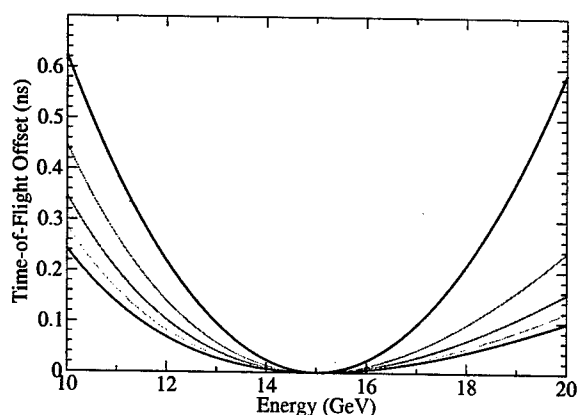


Figure 6: Time-of-flight variation with energy for increasing (top to bottom) sextupole strength.

To minimize the total time-of-flight range if the variation is parabolic in energy, it is clearly optimal to place the minimum of the parabola at the central energy. Thus, this is a constraint in the optimization process.

The time-of-flight range for a single cell is approximately proportional to the square of the bending angle in the cell. Since the minimum required RF voltage is proportional to the time-of-flight range for the entire ring [2], that voltage must be approximately inversely proportional to the number of cells in the ring. Thus, there is a cost optimum if the RF voltage that is actually installed is related to this minimum requirement, since the arc cost will be proportional to the number of cells.

Furthermore, the time-of-flight range is approximately proportional to the cell length. Thus, reducing the cell length would presumably lead to a reduced RF cost.

Since the time-of-flight is very quadratic as a function of energy, one would expect to be able to reduce it by adding sextupole components to the magnets. Figure 6 demonstrates that this is in fact the case. However, these sextupole components may have a negative impact on the dynamic aperture; this has not been examined as yet.

Magnet and RF Considerations

The cost of magnets and the cost of the RF systems are the dominant costs in an FFAG accelerator. While one would like to keep the magnets short to keep the cell lengths short, magnet costs increase as their pole tip fields increase, and there are technological limitations as to how high the fields can be. Furthermore, very short magnets become dominated by end effects and the associated nonlinearities. These field constraints and/or cost optimizations effectively provide two more constraints in the optimization.

The drifts in the lattice must be at least long enough to accommodate an RF cavity. Due to the high peak power requirements for room-temperature RF, one would prefer to use superconducting RF. The field from the magnets at

superconducting RF cavities must not cause the cavities to quench. This requires an additional separation between the cavities and the magnets to allow the field to fall off. If the cavities are cooled before the magnets are powered, then the field at the cavities can be as high as 0.1 T [3]. However, before the cavities are cooled, the field must be around 10^{-5} T. Thus, one must insure that there is no residual magnetization remaining when the magnets are powered off. These considerations determine how much space must be left between the cavities and the magnets, and therefore what the minimum drift length in the FODO cell can be.

Since beta functions (and therefore magnet apertures) will be smallest when the cell length is the least, and since the time-of-flight variation is less when the cell length is least, one generally chooses the drift length to be the minimum allowed for the purposes of installing RF cavities.

Other Considerations

A cost-optimal design may not turn out to be what one wants to use due to muon decays. Thus, if an optimized design turns out to have too many decays, one may instead optimize the system to have the maximum tolerable decay.

A final concern is beam loading in the RF cavities. The beam generally extracts energy from the RF cavities far too quickly to be replaced. Thus, a design requiring an extremely large number of passes will not work well since too much stored energy will be extracted from the cavities. Thus, it may turn out that the desired solution is to have a certain maximum number of turns. Furthermore, this consideration precludes running cavities at very low voltages to try to minimize peak power requirements.

CONCLUSIONS

It is straightforward to design a FODO-based nonscaling FFAG to specified constraints using nonlinear fitting and optimization techniques. Design constraints that are required to insure that the FFAG operates properly have been described. Parametric dependence of some performance parameters on input constraints have been described. The plots in this paper required the creation of several dozen lattices, all of which were done in less than an hour of CPU time on a three-year old PC, using code that was written specifically for this purpose. Thus, one can easily conceive of performing a cost optimization of an FFAG lattice design, based on some model of magnet and RF costs.

REFERENCES

- [1] C. Johnstone and S. Koscielniak, in *High Intensity and High Brightness Hadron Beams*, Weiren Chou *et al.*, eds. (AIP, Melville, NY, 2002) p. 207.
- [2] J.S. Berg, in *Proceedings of EPAC 2002, Paris, France*, T. Garvey *et al.*, eds. (EPS-IGA and CERN, Geneva, Switzerland, 2002), p. 1124.
- [3] M. Ono *et al.*, in *9th Workshop on RF Superconductivity*, edited by Sue Harper. LANL preprint LA-13782-C.

END FIELD EFFECTS IN BEND-ONLY COOLING LATTICES

J. Scott Berg, Harold Kirk, Brookhaven National Laboratory*, Upton, NY 11973, USA
Alper Garren, University of California Los Angeles, USA

Abstract

Cooling lattices consisting only of bends (using either rotated pole faces or gradient dipoles to achieve focusing) often require large apertures and short magnets. One expects the effect of end fields to be significant in this case. In this paper we explore the effect of adding end fields to a working lattice design that originally lacked them. The paper describes the process of correcting the lattice design for the added end fields so as to maintain desirable lattice characteristics. It then compares the properties of the lattice with end fields relative to the lattice without them.

INTRODUCTION

In designing a beamline, the magnets are modeled by having a certain ideal field profile within the body of the magnet which ends abruptly when one exits the magnet. There is one exception to this, which is the a dipole magnet with a pole face that is not perpendicular to the design orbit at the entrance and/or exit to the magnet. In this case, the magnet is modeled as having a simple linear transfer matrix at each end of the magnet.

Maxwell's equations require that real magnets have fields which vary more smoothly at the entrance and exit of the magnet. The ideal field profile now smoothly changes from it's nominal value in the magnet body to zero at a point outside the "ideal" magnet body. When this is considered for dipole and quadrupole magnets, the field strengths generally must be corrected slightly to restore the expected linear behavior of the machine.

Often of greater importance are the nonlinear fields that are induced by the non-constant longitudinal profile of the desired fields. These fields cat strongly affect the chromaticity, dynamic aperture, and other characteristics of the lattice.

In this paper we look at the effect of these endfields on a ionization cooling lattice consisting solely of dipoles [1]. These lattices focus either with edge focusing or by using gradient dipoles. The goal of such a lattice is to have a low beta function (generally less than 1 m) at the absorber over very large energy acceptance (as much as a factor of 2).

TWO EXAMPLES

We describe two example lattices, and show the effect that end fields have on these lattices. The effect of end fields in all cases are estimated using COSY Infinity's [2] default fringe field model.

*Supported by US Department of Energy contract DE-AC02-98CH10886

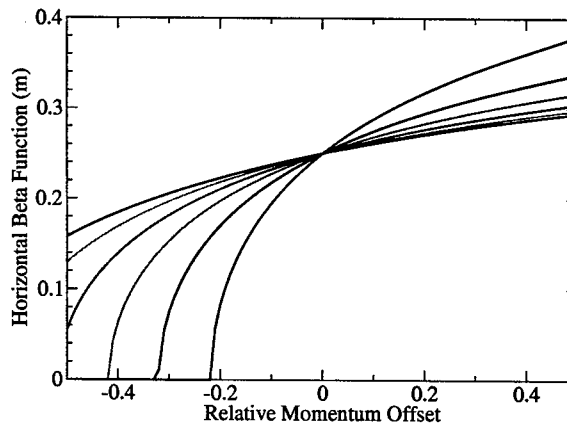


Figure 2: Horizontal beta functions for the compact edge-focused lattice as a function of the fringe field extent. The red curve (most horizontal) is for no fringe field, subsequent curves (going down on the left and up on the right) correspond to increments in the aperture (and therefore increments of the fringe field extent) of 2 cm per step, up to a maximum of 10 cm for the magenta curve.

Compact Edge-Focused Lattice

Our first example is an edge-focused lattice which is designed to have a very low beta function (25 cm) and is therefore very compact (see the top lattice in Fig. 1). Due to the fairly large initial transverse emittance in the beam, the desired magnet aperture is 21 cm. The magnet length is only 40 cm, so the fringe fields give a significant perturbation to the beam behavior. To achieve sufficient focusing, the bend angle must be fairly large: we use 90° bends.

Figure 2 shows the effect of adding the fringe fields to the magnets. As the length of the fringe fields increases (corresponding to an increasing aperture), a linear resonance at the low energy end begins to come closer to the reference energy. The magnet parameters are re-adjusted when the fringe fields are added so that the tunes and beta functions at the reference energy remain the same as they were without the fringe fields.

Figure 2 only shows the horizontal beta functions for up to a 10 cm aperture in the magnets. At 21 cm, the energy acceptance is even worse, and the beta functions get even larger, as can be seen in Fig. 3. Instead of simply trying to restore the linear parameters to their values without the fringe fields, one can instead modify the lattice to attempt to restore the lattice performance. Figure 3 also shows the results of this attempt. The beta functions have been restored to near their original values, and the energy accep-

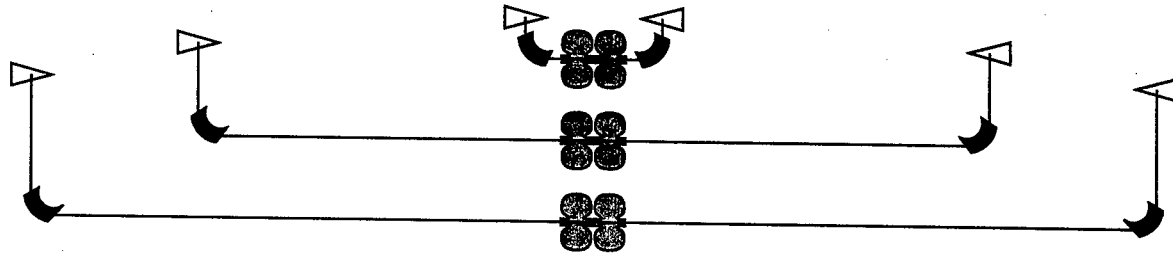


Figure 1: Compact edge-focused dipole cooling lattice. Top is the original lattice design. Below that is the lattice after adding finite-length end fields and restoring the linear behavior of the lattice. Bottom is after trying to restore the lattice performance.

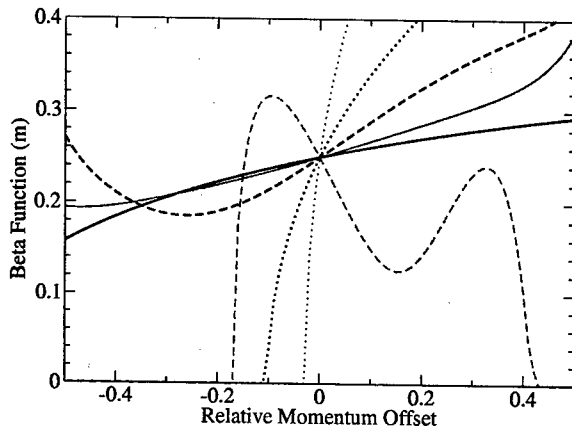


Figure 3: Horizontal and vertical beta functions at the absorber for the compact edge-focused lattice. Black lines are in the horizontal plane, grey lines are in the vertical. The solid lines are with no fringe fields, the dotted lines are with fringe fields corresponding to a 21 cm aperture, and the dashed lines are after changing the linear lattice parameters to restore good performance to the lattice.

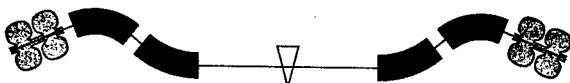


Figure 4: Layout of combined-function lattice.

tance has been improved.

Unfortunately, the modifications that were made to the lattice to compensate for the fringe field effects required a substantial lengthening of the lattice, as shown in Fig. 1. This means that the beta functions at the magnets will be substantially larger, and therefore require a larger aperture. The fringe fields will need to be lengthened further to take this into account.

Combined-Function Lattice

Figure 4 shows the layout of a combined-function cooling lattice with reverse bends to make it less compact than the previous lattice. This lattice has a larger beta function

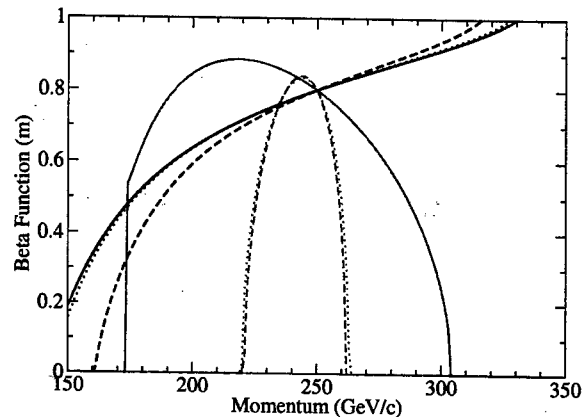


Figure 5: Beta functions at the absorber for the combined-function lattice. Black lines are in the horizontal plane, grey lines are in the vertical. The solid lines have no fringe fields, the dotted lines have fringe fields from a 1 cm aperture, and the dashed lines have fringe fields from a 10 cm aperture.

than the previous lattice: around 75 cm instead of 25 cm. The magnets are 1 m long.

Figure 5 shows the beta functions for this lattice as a function of energy for three cases: no fringe fields, very short fringe fields, and longer fringe fields. Note that even for very short fringe fields, there is a substantial effect on the vertical beta function and the energy acceptance. In fact, the effect on the vertical beta function is almost independent of the length of the fringe fields. There is a much weaker effect on the horizontal beta functions, but that effect does not appear suddenly as soon as the fringe fields are added.

This effect can be understood by considering the mechanism for linear edge focusing in a dipole. If the pole face is rotated so it is not perpendicular to the reference orbit, there is a vertical focusing force whose integral is independent of the length of the fringe field. When there is a nonzero derivative of the dispersion at the end of a bending magnet, the pole face is rotated with respect to the closed orbit off-energy. There is thus a vertical focusing which is linear

REFERENCES

- [1] Harold G. Kirk *et al.*, in *Proc. of the APS/DPF/DPB Summer Study on the Future of Particle Physics (Snowmass 2001)*, ed. N. Graf, eConf C010630, M101 (2001).
- [2] K. Makino and M. Berz, *Nucl. Instr. Meth. A* **427**, 338 (1999).

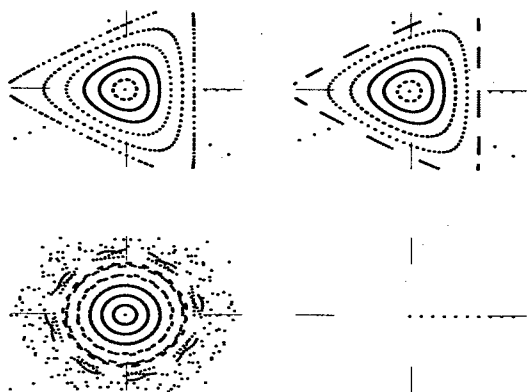


Figure 6: Tracking in the for the combined-function lattice. Top row is horizontal, bottom is vertical. Left is without fringe fields, right is with short fringe fields.

in the energy deviation, and whose integrated strength is independent of the length of the fringe fields. There is no such effect in the horizontal plane.

The relative insensitivity of this lattice to the fringe field profile as compared to the edge-focused lattice is probably related to the relatively short length of the magnets in the edge-focused case, compared to the longer magnets here. For a short magnet, the field profile is almost completely dominated by the ends, whereas for a long magnet, the ends form more of a perturbation to the field profile. The nonlinearities from the ends are also smaller relative to the integrated strength of the magnet when the magnets are longer.

Figure 6 shows the results of tracking with and without fringe fields. The vertical dynamic aperture decreases substantially when the fringe fields are added, while there is little effect in the horizontal plane.

ANALYSIS AND CONCLUSIONS

We have shown that for dipole-based cooling lattices, the magnet endfields affect the performance of the ring very strongly. One cannot design a lattice without endfields and expect it to perform even closely to its design performance after the end fields are added. Restoring the lattice performance to its original state often looks nearly impossible, or at the very least requires drastic changes to the lattice.

This effect is most likely so strong in cooling lattices due to the low beta functions that they require. Since the lowest order contribution from the end fields is a longitudinal field, the beam must make a large transverse angle with respect to the pole face to see a substantial effect. The low beta functions create that large transverse angle.

Endfields must be included at the very beginning of the design stage for a dipole-based cooling lattice if one expects to get even a remotely accurate picture of the performance of the lattice.

LINEAR COUPLING CORRECTION WITH N -TURN MAPS*

Wolfram Fischer†, Brookhaven National Lab, Upton, NY 11973, USA

Abstract

The linear one-turn map of a storage ring contains coupling information on which a correction algorithm can be based. In principal, the one-turn matrix can be fitted from turn-by-turn data of beam position monitors after a kick was applied. However, the so obtained coupling information often sinks into the noise floor. The signal-to-noise ratio of the coupling information can be greatly enhanced by fitting maps for larger turn numbers N , equal to half the beat period. With the so obtained N -turn map an automated global coupling correction is possible without the need for a tune change. This is demonstrated for the Relativistic Heavy Ion Collider where the algorithm is implemented for operational use at injection.

1 INTRODUCTION

Linear coupling [1–3] can make it impossible to set tunes to values close to the coupling resonance $Q_x = Q_y$. These tunes are desirable since the resonance density in this area is low. A widely used method to measure global linear coupling, is to move the tunes until the minimum tune separation $\Delta Q_{min} = |Q_x - Q_y|_{min}$ is reached [1]. A coupling correction is then performed by scanning skew quadrupole corrector settings to minimize ΔQ_{min} . This approach is slow, can lead to beam losses, and cannot be practically applied during an energy ramp. The decoupling method presented here overcomes all these shortcomings. It is based on N -turn maps, fitted from turn-by-turn data after a transverse kick was applied. Based on fitted N -turn maps the minimum tune approach ΔQ_{min} and skew corrector settings to minimize this quantity can be obtained without a tune change. The algorithm lends itself to full automation and allows a coupling correction within seconds. An implementation at RHIC is shown.

2 MATRIX DESCRIPTION

We denote by $\vec{z} = (x, x', y, y')^T$ the 4-vector with the positions and slopes at a certain observation point in the ring (see Fig. 1). The linear one-turn map M transforms the 4-vector \vec{z}^i at turn i into the 4-vector \vec{z}^{i+1} at turn $i + 1$ via

$$\vec{z}^{i+1} = M\vec{z}^i. \quad (1)$$

The 4×4 matrix M can be written in terms of 2×2 matrices as

$$M = \begin{pmatrix} A & B \\ C & D \end{pmatrix}. \quad (2)$$

The machine is said to be globally decoupled if $B = 0$, which implies $C = 0$. If the linear coupling is caused by a number of small sources, rather than a few large ones, global decoupling at any observation point will usually lead

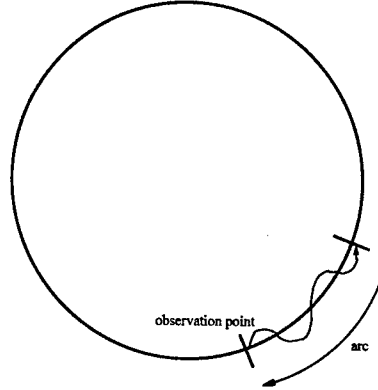


Figure 1: Observation point at the beginning of an arc and beam trajectory in the arc.

to a machine that is almost globally decoupled at any other observation point [3].

We denote by (Q_A, Q_D) the eigentunes of the map (2), and also use the quantities $\mu_{A,D} = 2\pi Q_{A,D}$. The eigentunes can be determined with good precision from turn-by-turn data by filtering, Fourier transformation, and interpolation [4]. The minimum tune approach is then [3]

$$\Delta Q_{min} = \frac{\sqrt{\det |C + \bar{B}|}}{\pi(\sin \mu_A + \sin \mu_D)} \quad (3)$$

where $\bar{B} = -SB^T S$, and S is the symplectic form. Global decoupling amounts to manipulations that result in $\det |C + \bar{B}| = 0$. Note that the sign of $\det |C + \bar{B}|$ is negative on sum resonances and positive on difference resonances [3].

For weak coupling, the largest elements of the matrices B and C can be more than an order of magnitude smaller than those of the matrices A and D . We now consider a N -turn map and chose the turn number N such that the values of the sub-matrices B_N and C_N in the multi-turn map

$$M^N = \begin{pmatrix} A_N & B_N \\ C_N & D_N \end{pmatrix}, \quad (4)$$

are maximized. With coupled motion energy is exchanged between the transverse planes with the beat frequency. To observe the maximum effect of the energy transfer from one plane to the other, one has to wait for half the beat period. This can be seen in Fig. 2 (a) and (b). The optimum N is thus approximately

$$N \approx \frac{1}{2|Q_A - Q_D|} = \frac{\pi}{|\mu_A - \mu_D|}. \quad (5)$$

The coupling information can also be obtained from the N -turn map since [5]

$$C + \bar{B} = (C_N + \bar{B}_N) \times \frac{\cos \mu_A - \cos \mu_D}{\cos(N\mu_A) - \cos(N\mu_D)}. \quad (6)$$

* Work supported by US DOE, contract No DE-AC02-98CH10886.

† Wolfram.Fischer@bnl.gov

ΔQ_{min} can then be computed with Eq. (3). Based on the obtained value for $C + \bar{B}$, skew correctors can be set so that $\det[C + \bar{B}] = 0$ when the correctors are included. This will be shown in Sec. 4.

3 CONSTRUCTION OF A N-TURN MAP

We assume that m consecutive turns of a 4-vector $\vec{z} = (x, x', y, y')^T$ were fitted from turn-by-turn orbit data after a transverse kick. For weak coupling this can be done in a robust way, using a number of beam position monitors in an arc [5]. For the N -turn map one has

$$\vec{z}^{k+N} = M^N \vec{z}^k. \quad (7)$$

To fit the matrix elements of M^N the function

$$\chi^2(M^N) = \sum_{k=1}^{m-N} \sum_{i=1}^4 \left(z_i^{k+N} - \sum_{j=1}^4 M_{ij}^N z_j^k \right)^2 \quad (8)$$

is minimized. Introducing the two 4×4 matrices S^a and S^b with elements

$$S_{ij}^a = \sum_{k=1}^{m-N} z_i^{k+N} z_j^k \quad \text{and} \quad S_{ij}^b = \sum_{k=1}^{m-N} z_i^k z_j^k, \quad (9)$$

the minimization of $\chi^2(M^N)$ leads to the direct solution

$$M^N = S^a (S^b)^{-1} \quad (10)$$

In an implementation the condition $\det S^b \neq 0$ needs to be checked, and the direct solution of Eq. (10) may not be the best way to solve the problem numerically [6].

4 LINEAR COUPLING CORRECTION

We assume that the eigentunes $Q_{A,D}$ were obtained from a Fourier transform of turn-by-turn data, and the matrix

$$K = C + \bar{B}, \quad (11)$$

from a N -turn map with Eq. (6).

For a correction algorithm we work in a coordinate system, in which the linear motion is represented by circles in phase space. The transformation into the new coordinate system

$$\tilde{\vec{z}} = \mathfrak{B} \vec{z} \quad (12)$$

is provided by the matrix

$$\mathfrak{B} = \begin{pmatrix} \mathfrak{B}_x & 0 \\ 0 & \mathfrak{B}_y \end{pmatrix} \quad \text{with} \quad \mathfrak{B}_x = \begin{pmatrix} \beta_x^{-1/2} & 0 \\ \alpha_x \beta_x^{-1/2} & \beta_x^{1/2} \end{pmatrix} \quad (13)$$

and similar for \mathfrak{B}_y [3]. The matrix \mathfrak{B} is computed at the observation point. The matrix \tilde{K} can be written as

$$\tilde{K} = \mathfrak{B}_y C \mathfrak{B}_x^{-1} + \mathfrak{B}_x \bar{B} \mathfrak{B}_y^{-1}. \quad (14)$$

We denote by μ_x^i the horizontal phase advance from the observation point to the skew quadrupole i , and use

$$\begin{aligned} S_x^i &= \sin \mu_x^i, & C_x^i &= \cos \mu_x^i, \\ S_x^i &= \sin(\mu_x - \mu_x^i), & C_x^i &= \cos(\mu_x - \mu_x^i). \end{aligned} \quad (15)$$

In the new coordinate system we have for a number of weak skew quadrupoles [3]

$$\tilde{C} = \begin{pmatrix} \sum k_i \sqrt{\beta_x^i \beta_y^i} S_y^i C_x^i & \sum k_i \sqrt{\beta_x^i \beta_y^i} S_y^i S_x^i \\ \sum k_i \sqrt{\beta_x^i \beta_y^i} C_y^i C_x^i & \sum k_i \sqrt{\beta_x^i \beta_y^i} C_y^i S_x^i \end{pmatrix} \quad (16)$$

and a similar expression for \tilde{B} . The strength k_i is the inverse focal length f_i of skew quadrupole i . Assume a corrector family has the same skew corrector strength k_1 in all correctors and results in

$$\tilde{K}^1 = k_1 (\tilde{C}_1 + \tilde{B}_1). \quad (17)$$

where the elements in \tilde{C}_1 and \tilde{B}_1 were divided by k_1 . For a global coupling correction we want to minimize the quantity

$$\chi(k_1) = \det[\tilde{K} + k_1 \tilde{K}^1]. \quad (18)$$

It follows

$$k_1 = -\frac{\mathfrak{K}_1}{2 \det \tilde{K}^1} \quad (19)$$

with

$$\mathfrak{K}_1 = \tilde{K}_{11} \tilde{K}_{22}^1 - \tilde{K}_{12} \tilde{K}_{21}^1 + \tilde{K}_{11}^1 \tilde{K}_{22} - \tilde{K}_{12}^1 \tilde{K}_{21}. \quad (20)$$

In principal two correctors or families are sufficient to correct linear coupling globally (unless their matrices \tilde{K}^1 and \tilde{K}^2 are linear dependent). After the first strength k_1 has been found, the second strength k_2 can be found with Eqs. (19) and (20), by replacing k_1 by k_2 , \tilde{K}^1 by \tilde{K}^2 , and \tilde{K} by $\tilde{K} + k_1 \tilde{K}^1$.

5 APPLICATION AT RHIC

The above described algorithm for global linear coupling correction has been implemented within the RHIC injection optimization application. After beam is injected, turn-by-turn data are automatically acquired from 12 beam position monitors in the horizontal and 12 monitors in the vertical plane. 1024 turns are recorded in each of the beam position monitors while the beam exhibits injection oscillations. The application has access to an online machine optics model, and can read and set skew corrector strengths [7].

In a test the ΔQ_{min} computed from the N -turn maps was compared with the ΔQ_{min} obtained by bringing the tunes together [5]. Good agreement could be demonstrated over a ΔQ range sufficiently large to cover operation (both RHIC tunes are kept between 0.2 and 0.25).

As an example for a coupling measurement and correction we show the first test of the algorithm in operation, performed in the RHIC Blue ring with deuteron beam. In Fig. 2 (a) and (b) the beam oscillation in the horizontal and vertical plane following the injection are shown. The beating is clearly visible.

From the measured eigentunes, the optimum turn number N is determined with Eq. (5). We get $N = 67$ and the fitted N -turn map is

$$M_{\text{before}}^{67} = \begin{pmatrix} -0.01 & 2.75 & -2.28 & -13.18 \\ -0.02 & 0.49 & -0.17 & -1.40 \\ -1.02 & 22.29 & 0.13 & 1.84 \\ 0.02 & -1.31 & -0.04 & -0.23 \end{pmatrix}. \quad (21)$$

from which $\Delta Q_{min} = 0.0064$ is obtained.

RHIC has three families for global decoupling, due to the six-fold symmetry of the machine. Two of those families are selected to minimize the coupling. The predicted ΔQ_{min} after correction is 0.0003 (see Fig. 2 (a)). A nonzero prediction is a sign of measurement errors in the N -turn map, or a mismatch between the optics model and

the machine. The correction can be implemented by pressing a single button in the application.

The result of the coupling correction is shown in Figs. 2 (c) and (d). The recoherence after 650 turns is due to synchrotron motion and nonzero chromaticity. 650 turns are a synchrotron period. After correction, we have

$$M_{\text{after}}^{122} = \begin{pmatrix} -0.26 & -11.77 & 3.62 & 4.49 \\ 0.01 & -0.40 & 0.06 & 0.29 \\ 0.19 & -5.62 & -0.17 & -1.23 \\ 0.05 & 2.65 & 0.22 & 0.30 \end{pmatrix} \quad (22)$$

and ΔQ_{\min} is reduced to 0.0023. Note the reduction in the matrix elements M_{14} and M_{32} . The ΔQ_{\min} reached by the correction was confirmed by a tune measurement after moving the tunes together. In operation it was found that the coupling correction cannot significantly improved beyond $\Delta Q_{\min} = 0.002$. This is consistent with the $\Delta Q_{\min} = 0.0011$ predicted for the next correction.

6 SUMMARY

A method for global coupling measurement and correction is presented that is based on N -turn maps fitted from turn-by-turn beam position data. N is chosen so as to maximize the signal-to-noise ratio of the coupling information. By using more than two monitors per plane the robustness is increased and the effect of random errors in beam position monitors is ameliorated. No tune change is needed for either the measurement or the correction. The method is implemented for operation as part of the injection optimization application at RHIC. It allows a global coupling correction within seconds after the turn-by-turn data are acquired. The method may be used in situations other than injection, when turn-by-turn data of free beam oscillations can be acquired.

7 ACKNOWLEDGMENTS

The author thankful for discussions and help to: M. Blaskiewicz, C.J. Gardner, J.-P. Koutchouk, A. Luccio, T. Satogata, F. Schmidt, T. Roser, R. Talman, S. Tepikian, and J. van Zeijts.

8 REFERENCES

- [1] D. Rubin, "Measurement and diagnosis of coupling and solenoid compensation", in "Handbook of accelerator physics and engineering" edited by A.W. Chao and M. Tigner, World Scientific (1999).
- [2] D.A. Edwards and L.C. Teng, "Parameterization of Linear Coupled Motion in Periodic Systems", IEEE Trans. on Nucl. Sc. 20, 885 (1973).
- [3] L. Schachinger, R. Talman, "Manual for the Program TEAPOT", Appendix G (1996).
- [4] R. Bartolini et al., "Tune Evaluation in Simulations and Experiments", Part. Acc. 52 147 (1995).
- [5] W. Fischer, "Robust linear coupling correction with N -turn maps", submitted to Phys. Rev. ST Accel. Beams (2003).
- [6] W.H. Press et al., "Numerical Recipes in C", 2nd ed., Cambridge University Press (1992).
- [7] J. van Zeijts, "Model driven ramp control", ICALEPCS 2001 (2001).

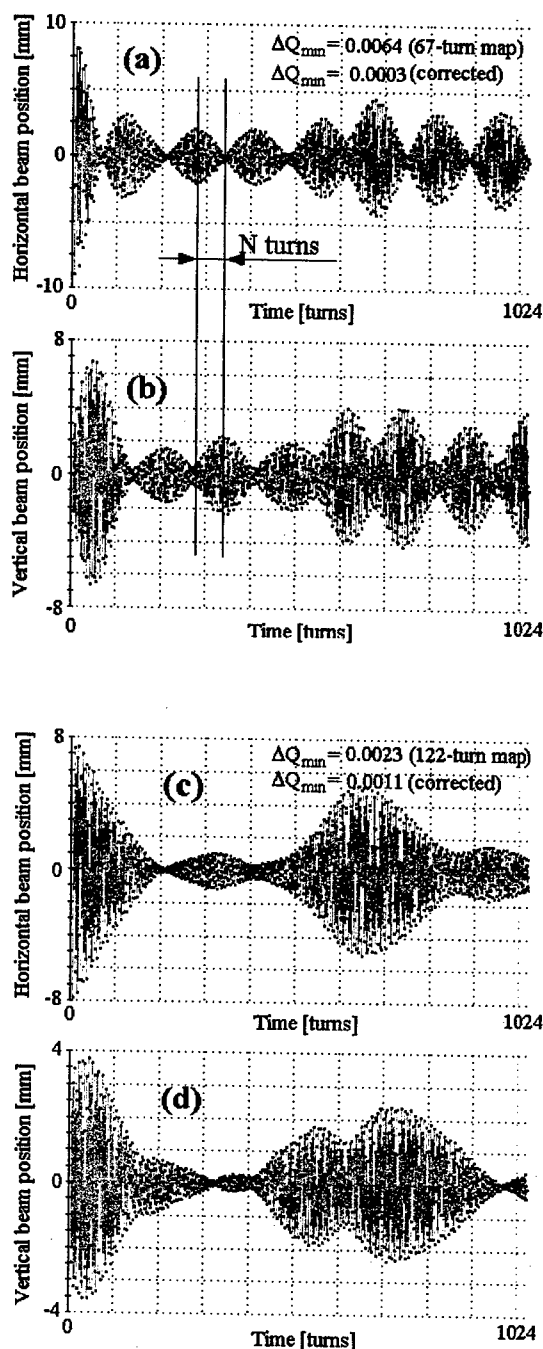


Figure 2: Turn-by-turn signals before and after a coupling correction at injection. In part (a) and (b) the horizontal and vertical injection oscillations are shown before a coupling correction. Part (a) also shows the computed ΔQ_{\min} and the predicted ΔQ_{\min} after a coupling correction. Parts (c) and (d) show the situation after the computed corrector values were applied.

ON-LINE MONITORING OF THE LINEAR COUPLING FOR THE LHC

N. Catalán Lasheras, S. Fartoukh, J.P. Koutchouk, CERN, Geneva, Switzerland

Abstract

Before correction, the difference coupling coefficient in LHC is expected to reach $|c_-| \approx 0.2$ at injection and vary by 30 to 40% from injection to top energy. These high values arise mostly from the field imperfections in the superconducting dipoles, the feed-down from the parasitic sextupoles and the strongly-focused low- β insertions. A measurement method which lends itself to continuous monitoring and active feedback is therefore investigated. Our approach is based on the beam response to an excitation in the other plane (coupling BTF). The analytical approach [1] shows that a proper measurement protocol allows extracting the global and local complex coefficients of both the difference and sum coupling resonances. In order to prevent any emittance blow-up, the beam is excited at small amplitude outside its eigen-frequencies with smooth transitions (AC-dipole principle). A first experiment in the SPS [2] confirms the approach and its robustness.

INTRODUCTION

Betatron coupling causes an oscillation in one plane to be transferred to the other plane. This transfer depends not only on the excitation of the linear coupling resonances but as well on the local tilt of the eigen-modes and, to a lesser extent, on the perturbation of the β -functions. This paper presents first the beam response to a sinusoidal excitation in the presence of coupling. It is used to define measurement protocols yielding the coupled β -functions and the global and local coupling coefficients. The systematic errors in the methods are analysed. First experimental results using a non-nominal set-up are presented.

BEAM TRANSFER FUNCTION (BTF) IN TWO DIMENSIONS

At a given abscissa $s_0 \equiv 0$ of the lattice and at each turn n , the beam is assumed to be excited by a dipolar oscillating force of the form

$$\begin{pmatrix} \Delta x'(n) \\ \Delta y'(n) \end{pmatrix} \equiv \cos(2\pi Q_D n + \phi) \times \begin{pmatrix} x'_D \\ y'_D \end{pmatrix}, \quad (1)$$

with x'_D and y'_D being the amplitudes of the AC kick, ϕ its phase with respect to the beam at turn $n = 0$ and Q_D a frequency given in tune units (i.e. normalized to the revolution frequency). We expect a response at the drive frequency, varying linearly with the excitation amplitude in the approximation of harmonic oscillators (i.e. linear optics approximation). Using complex notations and according to Ref. [1], the beam response can be written as follows:

$$\begin{pmatrix} x(n; s) \\ y(n; s) \end{pmatrix} = e^{2i\pi Q_D n + i\phi} \times \mathcal{A}(Q_D; s) \begin{pmatrix} x'_D \\ y'_D \end{pmatrix}, \quad (2)$$

where

- s denotes the curvilinear abscissa around the ring taking

the AC-dipole as the origin. $x(n; s)$ and $y(n; s)$ are the horizontal and vertical oscillations of the beam at turn n and abscissa s .

- $\mathcal{A}(Q_D; s)$ is a complex 2×2 matrix which, at the first order in the strength of the skew quadrupole errors of the lattice, is given by

$$\mathcal{A}(Q_D; s) \equiv \begin{pmatrix} \mathcal{A}_{xx}(Q_D; s) & \mathcal{A}_{xy}(Q_D; s) \\ \mathcal{A}_{yx}(Q_D; s) & \mathcal{A}_{yy}(Q_D; s) \end{pmatrix}, \quad (3)$$

with

$$\begin{cases} \mathcal{A}_{xx}(Q_D; s) \stackrel{\text{def}}{=} -\frac{\sqrt{\beta_x(0)\beta_x(s)}}{4} [\mathcal{A}_x^+ e^{i\mu_x(s)} - \mathcal{A}_x^- e^{-i\mu_x(s)}] \\ \mathcal{A}_{yy}(Q_D; s) \stackrel{\text{def}}{=} -\frac{\sqrt{\beta_y(0)\beta_y(s)}}{4} [\mathcal{A}_y^+ e^{i\mu_y(s)} - \mathcal{A}_y^- e^{-i\mu_y(s)}] \\ \mathcal{A}_{\pm, y}^{\pm} \stackrel{\text{def}}{=} \frac{e^{i\pi(Q_D \mp Q_{x,y})}}{\sin[\pi(Q_D \mp Q_{x,y})]}, \end{cases} \quad (4)$$

$$\begin{cases} \mathcal{A}_{xy}(Q_D; s) \stackrel{\text{def}}{=} \frac{\pi}{8} \sqrt{\beta_y(0)\beta_x(s)} \times \\ \left\{ \mathcal{A}_y^+ [\mathcal{A}_x^+ C_- (Q_x - Q_D; s) e^{i\mu_x} - \mathcal{A}_x^- C_+ (Q_x + Q_D; s) e^{-i\mu_x}] + \right. \\ \left. \mathcal{A}_y^- [\mathcal{A}_x^- C_- (Q_x + Q_D; s) e^{-i\mu_x} - \mathcal{A}_x^+ C_+ (Q_x - Q_D; s) e^{i\mu_x}] \right\} \\ \mathcal{A}_{yx}(Q_D; s) \stackrel{\text{def}}{=} \frac{\pi}{8} \sqrt{\beta_x(0)\beta_y(s)} \times \\ \left\{ \mathcal{A}_x^+ [\mathcal{A}_y^+ C_- (-Q_y + Q_D; s) e^{i\mu_y} - \mathcal{A}_y^- C_+ (Q_y + Q_D; s) e^{-i\mu_y}] + \right. \\ \left. \mathcal{A}_x^- [\mathcal{A}_y^- C_- (-Q_y - Q_D; s) e^{-i\mu_y} - \mathcal{A}_y^+ C_+ (Q_y - Q_D; s) e^{i\mu_y}] \right\}, \end{cases} \quad (5)$$

$$C_{\pm}(q; s) \stackrel{\text{def}}{=} c_{\pm} - 2ie^{-i\pi q} \sin(\pi q) c_{\pm, <}(s). \quad (6)$$

- $\beta_{x,y}(s)$ are the β -functions at abscissa s (beam observation), $\mu_{x,y} \equiv \mu_{x,y}(s)$ are the betatron phase advances from $s = 0$ (AC dipole location) to s , $Q_{x,y}$ denote the betatron tunes, the coefficients $c_{\pm, <}(s)$ are the $(1, \pm 1)$ linear resonance driving terms integrated from $s = 0$ to s ,

$$c_{\pm, <}(s) = \frac{1}{2\pi} \int_0^s ds_1 \sqrt{\beta_x(s_1)\beta_y(s_1)} K_{\text{skew}}(s_1) e^{-i[\mu_x(s_1) \pm \mu_y(s_1)]},$$

and $c_{\pm} \equiv c_{\pm, <}(s=C)$ represents the usual sum and difference coupling coefficients.

The beam is now assumed to be excited in one of the two transverse planes, say in the vertical plane (that is $x'_D \equiv 0$ in Eq. (1)). According to Eq. (2), the Fourier transform of the beam signal at the excitation frequency Q_D is given by

$$\begin{cases} \hat{x}(Q_D; s) \equiv \frac{1}{N} \sum_{n=0}^{N-1} x(n; s) e^{-2i\pi Q_D n} \stackrel{N \rightarrow \infty}{\approx} \frac{y'_D}{2} e^{i\phi} \mathcal{A}_{xy}(Q_D; s) \\ \hat{y}(Q_D; s) \equiv \frac{1}{N} \sum_{n=0}^{N-1} y(n; s) e^{-2i\pi Q_D n} \stackrel{N \rightarrow \infty}{\approx} \frac{y'_D}{2} e^{i\phi} \mathcal{A}_{yy}(Q_D; s), \end{cases} \quad (7)$$

N being the number of turns used for the BPM acquisition.

MEASUREMENT PROTOCOL FOR THE β -FUNCTIONS

The “direct” transfer function \mathcal{A}_{yy} is most sensitive to the β -function. The term \mathcal{A}_y^+ is dominant when the excitation frequency Q_D lies in the vicinity of the vertical betatron tunes. Starting from Eq. (4), \mathcal{A}_{yy} may be re-expressed

by a dominant term and an "error" $\epsilon(s)$:

$$\mathcal{A}_{yy}(Q_D; s) = -\frac{\sqrt{\beta_y(0)\beta_y(s)} [1 + \epsilon(s)]}{4 \sin[\pi(Q_D - Q_y)]} e^{i\pi(Q_D - Q_y) + i\mu_y(s)} \quad (8)$$

$$\text{with } \epsilon(s) \equiv -\frac{\sin[\pi(Q_D - Q_y)]}{\sin[\pi(Q_D + Q_y)]} e^{2i\pi Q_y - 2i\mu_y(s)} \quad (9)$$

Combining Eq.'s (7) and (8) and assuming $\epsilon = 0$, we get

$$\beta_y(s) = |\hat{y}(Q_D; s)|^2 / K^2 \quad (10)$$

$$\text{with } K \stackrel{\text{def}}{=} \frac{y'_D}{8 |\sin[\pi(Q_D - Q_y)]|} \sqrt{\beta_y(0)}. \quad (11)$$

We now assume that the β -beating measured at the BPM's has no systematic component, i.e.

$$\frac{1}{N_{BPM}} \sum_{j=1}^{N_{BPM}} \frac{\beta_y(s_j)}{\beta_y^{(0)}(s_j)} \approx 1,$$

with N_{BPM} being the number of available BPM's and $\beta_y^{(0)}(s_j)$ the nominal vertical β function at BPM number j . Combining the above condition with Eq. (10), we get

$$\frac{1}{N_{BPM}} \sum_{j=1}^{N_{BPM}} \frac{|\hat{y}(Q_D; s_j)|^2}{\beta_y^{(0)}(s_j)} = K^2, \quad (12)$$

leading to an estimate of the β -function at BPM number i :

$$\beta_y(s_i) \approx \frac{N_{BPM} |\hat{y}(Q_D; s_i)|^2}{\sum_{j=1}^{N_{BPM}} |\hat{y}(Q_D; s_j)|^2 / \beta_y^{(0)}(s_j)}. \quad (13)$$

Neglecting the contribution $\epsilon(s)$ induces an intrinsic measurement error of the order of

$$\frac{\Delta\beta_{x,y}}{\beta_{x,y}} \sim |\epsilon| \sim \frac{\sin[\pi(Q_D - Q_{x,y})]}{\sin[\pi(Q_D + Q_{x,y})]} \sim 4 - 8\%,$$

using the SPS experiment parameters $Q_{x,y} = 0.18/0.15$ and $Q_D = 0.19/0.13$. The function $\epsilon(s)$ (Eq. (9)) oscillates at twice the betatron frequencies and therefore cannot be disentangled from a real β -beating.

This systematic error can be suppressed by exciting the beam at two distinct frequencies [1], preferably on both sides of the betatron tune. The data processing requires the knowledge of the phase ϕ (Eq. (1)) of the AC dipole excitation with respect to the beam, not accessible at the time of the experiment.

MEASUREMENT PROTOCOL FOR THE LINEAR COUPLING

As shown in Eq. (5), the coupling transfer function \mathcal{A}_{xy} can be split into two well-distinct components. Assuming the machine to operate close to the coupling resonance, i.e. $Q_x - Q_y \ll 1$, and the excitation frequency to lie in the vicinity of the vertical betatron tune, the main contributions is the one proportional to the amplitude $\mathcal{A}_y^+ \propto 1/\sin[\pi(Q_D - Q_y)]$:

$$\begin{aligned} \mathcal{A}_{xy}(Q_D; s) &\approx \frac{\pi}{8} \sqrt{\beta_y(0)\beta_x(s)} \mathcal{A}_y^+ \times \\ &\left[\bar{\mathcal{A}}_x^+ C_-(Q_x - Q_D; s) e^{i\mu_x(s)} - \bar{\mathcal{A}}_x^- \bar{C}_+(Q_x + Q_D; s) e^{-i\mu_x(s)} \right] \\ &= \frac{\pi}{8} \times \frac{e^{i\pi(Q_x - Q_y)} \sqrt{\beta_y(0)\beta_x(s)} e^{i\mu_x(s)}}{\sin[\pi(Q_D - Q_y)] \sin[\pi(Q_D - Q_x)]} \times \\ &\quad [C_-(Q_x - Q_D; s) + \lambda(s) \bar{C}_+(Q_x + Q_D; s)], \end{aligned} \quad (14)$$

$$\text{with } \lambda(s) \equiv -\frac{\sin[\pi(Q_D - Q_x)]}{\sin[\pi(Q_D + Q_x)]} e^{-2i\pi Q_x - 2i\mu_x(s)}. \quad (15)$$

Combining Eq.'s (7) and (14) and assuming $\lambda = 0$, we get

$$\hat{x}(Q_D; s) \approx \frac{\pi K \sqrt{\beta_x(s)} e^{i\phi + i\pi(Q_x - Q_y) + i\mu_x(s)}}{2 \sin[\pi(Q_D - Q_x)]} C_-(Q_x - Q_D; s), \quad (16)$$

$$\text{or } |C_-(Q_x - Q_D; s)| = \frac{2 |\sin[\pi(Q_D - Q_x)]|}{\pi K \sqrt{\beta_x(s)}} |\hat{x}(Q_D; s)|, \quad (17)$$

with K the calibration factor defined in Eq. (11) and estimated via the relation (12), and $\beta_x(s)$ as measured following the previous section.

Under the approximation $\lambda(s) = 0$, note that both the phase and the modulus of the coefficient $C_-(Q_x - Q_D; s)$ could be determined thanks to the relation (16). Nevertheless, this would again require that the phase-shift ϕ of the excitation w.r.t. to the beam is well-known at turn $n = 0$.

If the coupling errors are random around the machine or localized but spaced by $\mu_x \sim \mu_y \sim \pi$ in both transverse planes (which was the case for the SPS when the skew quadrupoles were switched on to generate coupling), the sum and difference resonance driving terms are of the same order of magnitude and therefore the sum coupling resonance induces a measurement error of the order of

$$\frac{\Delta|C_-|}{|C_-|} < \frac{|\Delta C_-|}{|C_-|} \sim \frac{|\Delta C_+|}{|C_+|} = |\lambda| = \left| \frac{\sin[\pi(Q_D - Q_x)]}{\sin[\pi(Q_D + Q_x)]} \right|.$$

With the betatron tunes of the SPS $Q_{x,y} = 0.18/0.15$ and a beam excitation in the vertical (resp. horizontal) plane at a frequency of $Q_{D,y} = 0.13$ (resp. $Q_{D,x} = 0.19$), we get

$$\frac{\Delta|C_-|}{|C_-|} \lesssim 19\% - 14\%, \text{ which is significant.} \quad (18)$$

As explained in Ref. [1], to get rid of this measurement error, the coupling transfer function $\mathcal{A}_{xy}(Q_D; s)$ must be measured at two consecutive BPM's, say BPM j and $j + 1$, under the condition that the sources of coupling between these two BPM's remains negligible (e.g. two BPM's spaced by a simple drift), that is

$$C_{\pm}(q; s_j) \stackrel{\text{def}}{=} c_{\pm} - 2ie^{-i\pi q} \sin(\pi q) c_{\pm}(s_j) \approx C_{\pm}(q; s_{j+1}),$$

leading to

$$\int_{s_j}^{s_{j+1}} ds' \sqrt{\beta_x(s')\beta_y(s')} K_{\text{skew}}(s') e^{-i[\mu_x(s') \pm \mu_y(s')]} \ll c_{\pm}.$$

The data processing however requires the knowledge of the betatron phase advance between the AC dipole and the two BPM's, which turns out to be accessible if and only if the phase ϕ (Eq. (1)) of the AC excitation is known. As said previously this quantity was not available at the time of experiment and the perturbation $\lambda(s)$ was neglected in the off-line analysis.

MEASUREMENT RESULTS ON THE CERN SPS

Measurements were carried out at three excitation levels of the SPS skew quadrupole chain corresponding to $|c_-| = 0.005, 0.01$ and 0.015 . For each excitation level, the closest tune approach was measured and the beam responses to an excitation in the horizontal plane at $Q_{D_x} = Q_x + 0.01$ and subsequently in the vertical plane at $Q_{D_y} = Q_y - 0.02$ were recorded over 1000 turns. The oscillation amplitude was of the order of one σ . Due to the impossibility of measuring the phase ϕ and the absence of two consecutive BPM's separated by a drift, the cancellation of the systematic errors $\epsilon(s)$ and $\lambda(s)$ was not carried out.

The β -functions are calculated per Eq. (13) and shown in Fig. 1 together with the MAD model. The error bars are estimated from the reproducibility of the measurements (three different sets of multi-turn data taken in each case). The measured β -beating is of the order of $\pm 20 - 30\%$ peak to peak. It should be real since significantly higher than the " β -beating like" systematic error $\epsilon(s)$ introduced in Eq. (9) and estimated at 5-10%. As expected, the β -functions is weakly dependent on coupling at this level. A few BPM's are either wrong or badly calibrated.

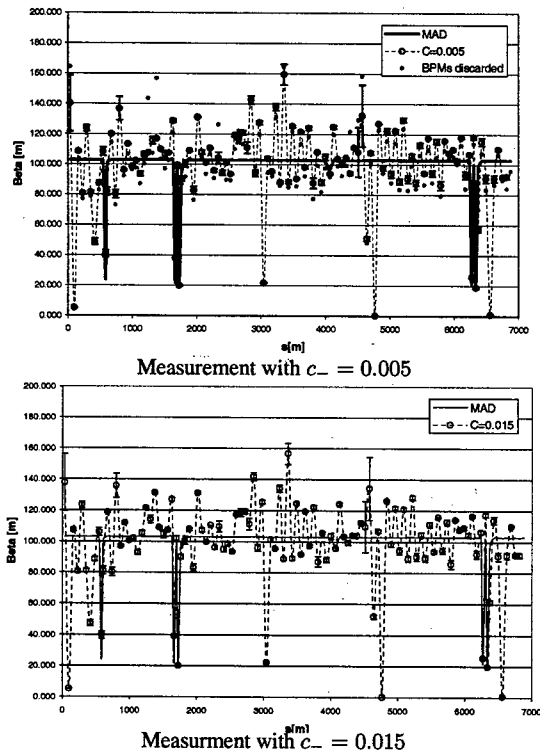


Figure 1: β -functions measured in the SPS for two different values of the difference coupling coefficient c_- .

The local coupling parameters $C_-(Q_{x,y} - Q_{D_{x,y}}; s)$ measured from Eq. (17) are shown on figure Fig. 2. Given the cell phase advance of $\pi/2$, the observed beating from

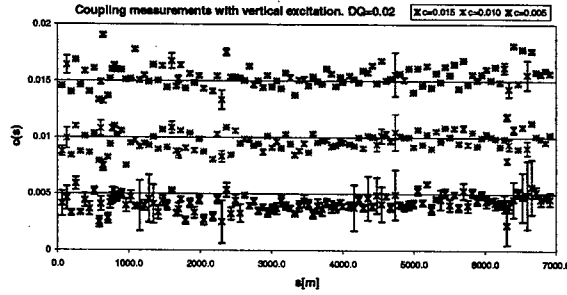


Figure 2: Local coupling coefficient $|C_-(Q_D - Q_x)|$ versus machine azimuth for three excitation levels of the skew quadrupoles measured by the closest tune approach.

BPM to BPM is consistent with the expected systematic error $\lambda(s)$ given in Eq. (15). In principle, this systematic error must cancel when averaged over all BPM's of the ring. In addition, the average of the local coupling parameters $C_-(Q_{x,y} - Q_{D_{x,y}}; s)$ is close to the global coupling coefficient with an estimated bias of less than 15% (Eq. (6) which vanishes for vanishing coupling). The random error on the average is found much below the 10^{-3} level, showing an excellent agreement with the closest tune approach.

The local coupling parameter should in principle exhibit a jump at each coupling source. In the SPS, the six different skew quadrupoles are all in phase. Following Eq. (6), the expected jump amplitude does not exceed $2\pi q |c_-|/6 \lesssim 0.05 |c_-|$ for $q \equiv Q_{x,y} - Q_{D_{x,y}} = 0.04 - 0.05$, that is a factor 3 to 4 below the local measurement error $\lambda(s)$ estimated in Eq. (18). Finally, contrary to the β -functions, it can be proven and it is indeed observed by comparing Fig.'s 1 and 2, that badly calibrated BPM's do not affect the measurement of the local coupling coefficients $C_-(q; s)$.

CONCLUSION

The on-line coupling measurement reached a relative accuracy of 15% due to expected systematic errors and of a few 10^{-4} due to other errors. The latter is our expectation when two BPM's separated by a drift and the synchronization between excitation and observation are available. The measurements, each over 1000 turns, caused no measurable emittance blow-up. The method appears thus well suited for a continuous monitoring and feedback on the difference coupling resonance. Given the large natural coupling in LHC and its anticipated fast variations, this possibility may become essential to prevent a confusion of the beam diagnostics, e.g. of the tune feedback in case the tunes would cross. A second application is the monitoring in real-time of local coupling, notorious to be relevant at the feedback systems, the collision points and/or the cleaning insertions.

REFERENCES

- [1] S. Fartoukh, CERN-SL-2002-059-AP, 6 Dec 2002.
- [2] N. Catalán Lasheras et al., CERN/AB MD Note to be published.

MEASUREMENT OF SEXTUPOLAR RESONANCE DRIVING TERMS IN RHIC

W. Fischer, BNL, F. Schmidt and R. Tomás, CERN

Abstract

Theory predicts that resonance driving terms can be determined by harmonic analysis of BPM data recorded after applying single kicks. In recent experiments at the CERN SPS this technique has been successfully applied to measure coupling and sextupolar resonance terms around the ring. A similar experiment has been carried out in RHIC, BNL, to prove the feasibility of this measurement in this more complex machine. Promising results of the experiment are presented, including a direct measurement of sextupolar resonances and a comparison to the model.

INTRODUCTION

The turn-by-turn single particle motion in normalised coordinates to first order in the non-linearities is given by [1]

$$\begin{aligned} \hat{x}(N) - i\hat{p}_x(N) &= \sqrt{2I_x} e^{i(2\pi\nu_x N + \psi_{x0})} \\ &- 2i \sum_{jklm} j f_{jklm} (2I_x)^{\frac{j+k-1}{2}} (2I_y)^{\frac{l+m}{2}} \\ &\times e^{i[(1-j+k)(2\pi\nu_x N + \psi_{x0}) + (m-l)(2\pi\nu_y N + \psi_{y0})]} \end{aligned} \quad (1)$$

where I_x and I_y are the horizontal and vertical actions, ψ_{x0} and ψ_{y0} are the horizontal and vertical initial phases, ν_x and ν_y are the horizontal and vertical tunes including the amplitude dependent detuning and the factors f_{jklm} are the generating function terms. These are related to the Hamiltonian terms h_{jklm} by the following expression,

$$f_{jklm} = \frac{h_{jklm}}{1 - e^{-i2\pi[(j-k)\nu_x + (l-m)\nu_y]}} \quad (2)$$

Note that the term f_{jklm} drives the resonance $(j-k, l-m)$. The Hamiltonian terms are defined by the following expansion of the non-linear Hamiltonian,

$$\begin{aligned} H &= \sum_{jklm} h_{jklm} (2I_x)^{\frac{j+k}{2}} (2I_y)^{\frac{l+m}{2}} \\ &\times e^{-i[(j-k)(\psi_x + \psi_{x0}) + (l-m)(\psi_y + \psi_{y0})]}, \end{aligned} \quad (3)$$

where ψ_x and ψ_y are the horizontal and vertical angle variables. Eqs. (1) and (2) suggest that a FFT of the turn-by-turn complex signal can be used to measure the generating function and the Hamiltonian terms. The spectral line $(1-j+k, m-l)$ depends only on the term f_{jklm} . By line (m, n) we mean the spectral line with frequency $m\nu_x + n\nu_y$. To illustrate these relations the third order resonance is studied. The Hamiltonian and the generating function terms driving the third order resonance are h_{3000} and f_{3000} respectively. The spectral line produced in the horizontal motion by this resonance is therefore $(-2, 0)$. In

a real machine the complex signal is constructed from two pick-ups with 90° phase advance. If the phase advance between the two pick-ups is not exactly 90° a linear transformation can be applied to the data from both pick-ups to obtain the corresponding set of data with 90° of phase advance. Only one pick-up cannot be used to measure resonance driving terms unambiguously since the spectral lines (m, n) and $(-m, -n)$ cannot be disentangled.

The Hamiltonian and the generating function terms depend on the longitudinal location where they are calculated. To understand how they vary along the ring the values of a Hamiltonian term at both sides of a source of non-linearity are compared. Prior to this element the term is h_{jklm}^1 and after it is h_{jklm}^2 . The non-linearity contributes to the first case with the quantity k_{jklm} and to the second case with the quantity $e^{-i2\pi[(j-k)\nu_x + (l-m)\nu_y]} k_{jklm}$ because the element has moved to the end of the lattice. Therefore the relation between the two Hamiltonian terms is expressed as

$$h_{jklm}^2 = h_{jklm}^1 + (e^{-i2\pi[(j-k)\nu_x + (l-m)\nu_y]} - 1) k_{jklm}, \quad (4)$$

the equivalent relation between the generating function terms is given by

$$f_{jklm}^2 = f_{jklm}^1 - k_{jklm}. \quad (5)$$

These relations state that the amplitude of these terms changes abruptly at the location of the sources. Their amplitudes remain constant along sections free of sources. This feature is very important since it allows the localisation of multipolar kicks. Applications of this feature in the CERN SPS can be found in [2] and [3].

In a real machine the beam is not a single particle but a particle distribution and processes like the beam decoherence change the Fourier spectrum of the turn-by-turn motion. The effect of the decoherence due to amplitude detuning has been described in [2]. The relevant conclusion is that the spectral line $(m, 0)$ of a decohered signal is reduced by a factor of $|m|$ compared to the single particle case. In particular, the two spectral lines $(-2, 0)$ and $(2, 0)$, produced by sextupolar fields, from the decohered motion are decreased by a factor of 2 compared to the single particle case. In order to compare the results from the experiment to single particle simulations the corresponding factor is applied to the experimental results.

DESCRIPTION OF THE RHIC MODEL

The tracking program SixTrack [4] is used for the analysis. The RHIC tracking model is constructed from an ideal lattice, characterized by a β -function of 10 m at all interaction points. This configuration was used in the experiment. Magnetic field errors are introduced in the arc dipoles and

quadrupoles. At injection, these field errors dominate the dynamic aperture.

For the dipoles, cold measurements at 660 A in 58 magnets are used to determine the average and rms values for the geometric field errors [5, 6]. The dipole current at injection is 470 A. Normal and skew components are measured up to 22-poles. The measured mean and rms values are used to assign random errors in the lattice. Mean and rms values for the sextupole component, dominated by persistent currents, are determined in a separate measurement, and also used to assign random errors in the lattice.

For the quadrupoles, only geometric errors are considered. Mean and rms values are measured in 380 magnets at 30 A and room temperature. A good correlation is found between warm and cold measurements in these magnets [5, 6]. No additional persistent current error contributions are included in the quadrupoles.

Tunes and chromaticities are set to the values observed in the experiment. Closed orbit errors are disregarded. In the experiment one interaction region sextupole corrector was changed to excite the third order resonance.

DESCRIPTION OF THE EXPERIMENT

The measurement of resonance driving terms was carried out in gold operation at injection. Relevant parameters are displayed in Tab. 1. In all cases the transverse injection oscillations of a single bunch were observed turn-by-turn. The horizontal oscillation amplitude was varied by changing the strength of the injection septum. The oscillation amplitudes were increased in steps until most of the beam was lost in the injection process. 12 beam position monitors (BPMs) in either plane recorded 1024 turns after the injection.

Five sets of data were taken. In each set the horizontal oscillation amplitude was varied. The first set was taken with the unchanged machine. For the other sets, the single interaction region sextupole was powered to 0.09, 0.03, -0.03 and -0.09 m^{-2} respectively. This sextupole should drive first and third order resonances.

The sextupole that was changed in the experiment is at a location with lattice functions $(\beta_x, \beta_y) = (143 \text{ m}, 50 \text{ m})$. For comparison, the 72 focusing arc sextupoles are at locations $(\beta_x, \beta_y) = (45 \text{ m}, 11 \text{ m})$ with a strength of $+0.18 \text{ m}^{-2}$; 72 defocusing arc sextupole are at locations $(\beta_x, \beta_y) = (11 \text{ m}, 44 \text{ m})$ with a strength of -0.39 m^{-2} . The arc sextupoles correct for the natural chromaticities of $(\xi_{x,n}, \xi_{y,n}) = (-55, -57)$ and the persistent current chromaticities $(\xi_{x,b_2}, \xi_{y,b_2}) = (-38, +36)$ [7].

EXPERIMENT VERSUS MODEL

Sextupolar fields introduce three spectral lines in the Fourier spectrum of the horizontal motion: $(-2,0)$, $(2,0)$ and $(0,0)$. The first one is related to the third order resonance and the other two are related to the first order resonance. An example of the Fourier spectrum obtained from the experimental data and using the SUSSIX [8] code is shown in

Table 1: Machine and beam parameters for the experiment.

parameter	unit	value
ring	...	Yellow
specie	...	Au ⁷⁹⁺
relativistic parameter γ	...	10.52
ions per bunch N_b	10^9	0.1 – 0.7
norm. emittance, 95% $\epsilon_{x,y}$	μm	≈ 10
tunes (ν_x, ν_y)	...	(28.223, 29.235)
chromaticities (ξ_x, ξ_y)	...	$\approx (-2, -2)$
sext. strength $K_2 L(\text{MAD})$	m^{-2}	from -0.09 to 0.09

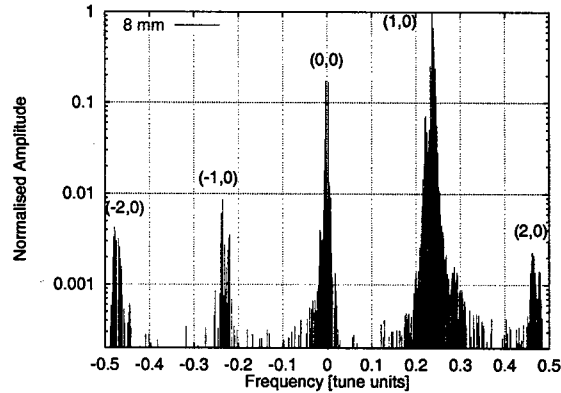


Figure 1: Fourier spectrum of the complex signal from pick-ups *yo5-bh10* and *yo5-bh12* for the unchanged RHIC and for an oscillation amplitude of 8 mm. The label (m,n) means that the frequency is equal to $m\nu_x + n\nu_y$.

Fig. 1. In this figure the tune line and the three sextupolar spectral lines are seen plus the spectral line $(-1,0)$ which is due to quadrupolar and octupolar resonances.

To measure the spectral line $(0,0)$ the closed orbit previous to the excitation of the betatron motion is needed. Since in this experiment the betatron motion was excited by injecting with a certain transverse angle, the reference closed orbit is not known. Therefore the line $(0,0)$ cannot be measured. The spectral lines $(-2,0)$ and $(2,0)$, normalised to the tune line, are proportional to the oscillation amplitude and to the resonance terms h_{3000} and h_{1200} respectively, as derived from Eq. (1). For the different sets of data the normalised amplitude of either spectral line is plotted versus the normalized betatron amplitude $a_x/\sqrt{\beta_x}$. The betatron amplitudes have been measured from the first turns of the BPM data. A beta function of 48 m has been assumed at the BPMs to compute the single particle emittance, which is twice the action I_x . Only the data coming from two of the pick-ups could be systematically used for all the different settings. In Fig. 2 the normalised amplitude of the spectral line $(-2,0)$ coming from these BPMs is plotted versus the oscillation amplitude for the five different settings of the interaction region sextupole. The experimental values have been multiplied by the decoherence factor of two to compare to the curves predicted by the model. There is a good agreement except for the case with -0.09 m^{-2} . To measure the first order resonance the previous procedure

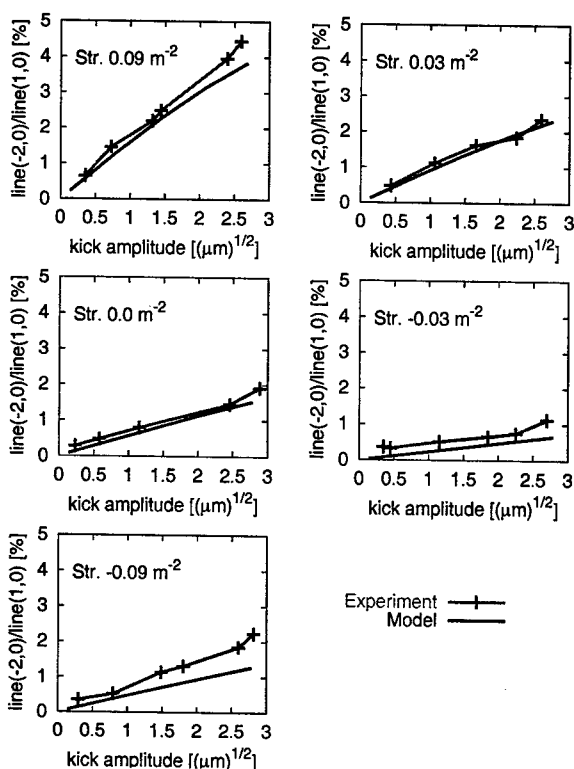


Figure 2: Measurement of the third order resonance. The normalised amplitude of the spectral line $(-2,0)$ is plotted versus horizontal betatron amplitude for five different strengths of the sextupole. Experimental results are multiplied by the decoherence factor of 2 and predictions from the model are shown.

is followed for the spectral line $(2,0)$. The resulting plots are shown in Fig. 3. There is a good agreement for the cases with positive and zero strength. The agreement not as good for the cases with negative strength. In one case (see Fig. 3) disagreement between experiment and model is only at large amplitudes.

CONCLUSIONS

For the first time we were able to demonstrate that sextupole driving terms can be measured in RHIC, an operational superconducting machine. We measured two types of horizontal sextupole resonances in a RHIC experiment and successfully compared them with model calculations of that machine. This opens the possibility of monitoring and correcting the nonlinear content of an operational accelerator. In conjunction with an AC dipole, currently being installed in RHIC, one can use this technique continuously from injection, through the ramp, and on flat top. By using BPMs around the whole machine, one can determine driving terms as function of the longitudinal positions and identify locations of strong non-linear errors or incorrectly powered magnets.

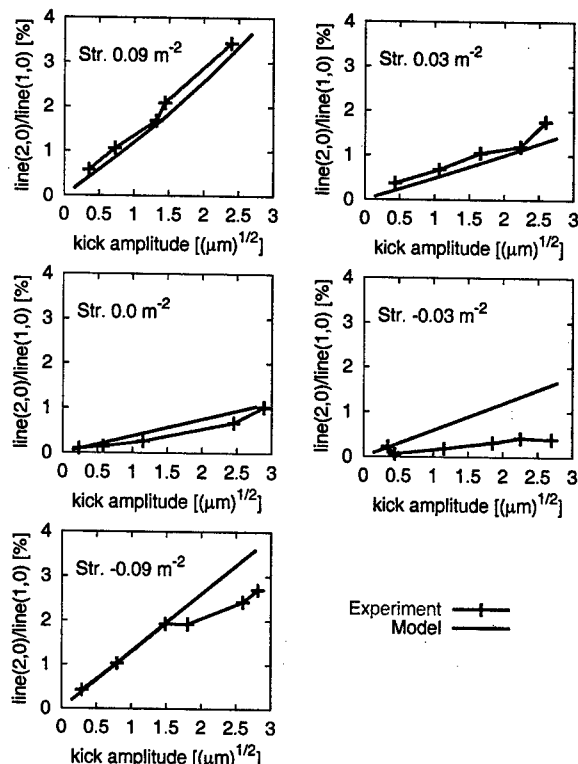


Figure 3: Measurement of the first order resonance. The normalised amplitude of the spectral line $(2,0)$ is plotted versus horizontal betatron amplitude for five different strengths of the sextupole. Experimental results are multiplied by the decoherence factor of 2 and predictions from the model are shown.

ACKNOWLEDGMENTS

The authors are thankful to A. Jain, S. Tepikian, and J. van Zeijts for support in the preparation of the RHIC model. F. Pilat assisted in the measurements. We are grateful to T. Satogata for his support in the data analysis.

REFERENCES

- [1] R. Bartolini and F. Schmidt, LHC Project note 132, Part. Accelerators. 59, pp. 93-106, (1998).
- [2] F. Schmidt, R. Tomás, A. Faus-Golfe, CERN-SL-2001-039-AP Geneva, CERN and IPAC 2001.
- [3] M. Hayes, F. Schmidt, R. Tomás, EPAC 2002 and CERN-SL-2002-039-AP Geneva, 25 Jun 2002.
- [4] F. Schmidt, CERN SL/94-56 (AP) Update March 2000.
- [5] M. Anerella et al., "The RHIC Magnet System", BNL MDN-610-20, to be published in NIM (2001).
- [6] A. Jain, private communication (2002).
- [7] W. Fischer, A. Jain, and S. Tepikian, Phys. Rev. ST Accel. Beams 4, 041002 (2001).
- [8] R. Bartolini and F. Schmidt, CERN SL-Note-98-017 (AP).

COMPLETION OF THE SEXTUPOLE DRIVING TERMS MEASUREMENT AT THE SPS

F. Schmidt, M. Hayes and R. Tomás, CERN

Abstract

This paper represents the completion of the series of sextupole driving terms measurements in the SPS which started in June 1998. The following two items have been missing from earlier reports on these studies: measuring two dimensional resonances and the resonance phase. The possible dependence of these terms on collective effects was studied. Lastly, the experiment was performed at two different energies of 26 and 80 GeV, to suppress energy dependencies. Comparisons to the tracking model show excellent agreement, proving that this technique is ready for other machines.

INTRODUCTION

In previous experiments [1] and [2] a beam based method to measure resonance driving terms has been established. These terms are measured from the Fourier analysis of beam data after applying a transverse kick. This technique has its origin in the pioneering study described in [3] and the improvement of the Fourier transform algorithm [4]. A complete description of the relation between the Fourier spectrum of the single particle motion and the resonances was provided in [5].

In a real machine the beam is not a single particle but a particle distribution and processes like the beam decoherence change the Fourier spectrum of the turn-by-turn motion. The effect of the decoherence due to amplitude detuning has been described in [1]. The relevant conclusion is that the spectral line (m,0) of a decohered signal is reduced by a factor of |m| compared to the single particle case. In order to compare the results from the experiment to single particle simulations the corresponding factor is applied to the experimental results.

During this experiment measurements were performed at different intensities and different energies to investigate any dependence on these parameters.

SEXTUPOLAR RESONANCE TERMS

In order to find an appropriate observable related to the phase of the resonances an insight into the properties of the phases of the spectral lines follows. From the equation of motion given in [5] the amplitude and phase of the spectral line $(1-j+k, m-l)$ are given by the following complex quantity,

$$-2ijf_{jklm}(2I_x)^{\frac{j+k-1}{2}}(2I_y)^{\frac{l+m}{2}}e^{i[(1-j+k)\psi_{x0}+(m-l)\psi_{y0}]}, \quad (1)$$

where $I_{x,y}$ are the transverse actions. The term f_{jklm} is defined as the sum over all the non-linear elements of the same type, i.e.

$$\sum_j k_j e^{i[(-j+k)\psi_{xj}+(m-l)\psi_{yj}]}, \quad (2)$$

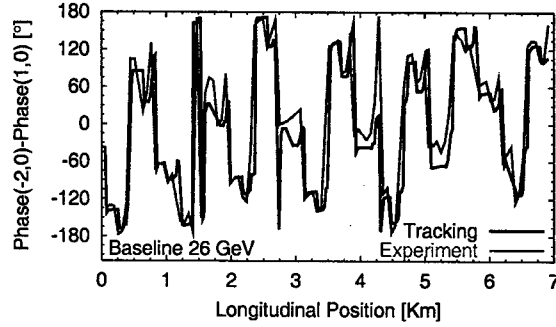


Figure 1: Phase of the line (-2,0) minus the phase of the line (1,0) versus longitudinal position from experiment and model for the baseline machine at 26 GeV.

where k_j contains all the factors as beta functions and strengths. The change in the phase of the spectral line $(1-j+k, m-l)$ over a region free of sources is now computed. Let the betatron phases change by $\Delta\psi_x$ and $\Delta\psi_y$ over this region. Then all the ψ_{xj} and ψ_{yj} change by $-\Delta\psi_x$ and $-\Delta\psi_y$ respectively. The change in the phase of the spectral line is given by the sum of the change of the phase of the term f_{jklm} plus the change of the phase of the exponential part of eq. 1, which yields

$$(j-k)\Delta\psi_x + (l-m)\Delta\psi_y + (1-j+k)\Delta\psi_x + (m-l)\Delta\psi_y = \Delta\psi_x. \quad (3)$$

This means that the phase of any spectral line from the horizontal motion changes by the same amount, $\Delta\psi_x$, over a region free of non-linear sources. In particular this is obvious for the horizontal tune line. Therefore, the following observable remains constant along sections free of non-linear sources for any m and n,

$$\text{Phase}(m, n) - \text{Phase}(1, 0), \quad (4)$$

where $\text{Phase}(m, n)$ represents the phase of the spectral line (m,n). This observable changes abruptly at the location of the non-linear sources as can be seen from [2]. The use of this observable in conjunction with the amplitude of the spectral line allows the unambiguous localisation of non-linear fields. In figure 1 this observable as measured from one single file is plotted together with the model prediction versus the longitudinal location for the baseline machine at 26 GeV. It has to be mentioned that a constant quantity had to be added to the experiment values to meet the model prediction, due to a different origin of the phases. The amplitude of the corresponding driving term f_{3000} is shown in figure 2 together with the prediction from the model. Both, phase and amplitude, show a good agreement.

As in previous years measurements were also done with the eight extraction sextupoles powered to (+ + + + - -

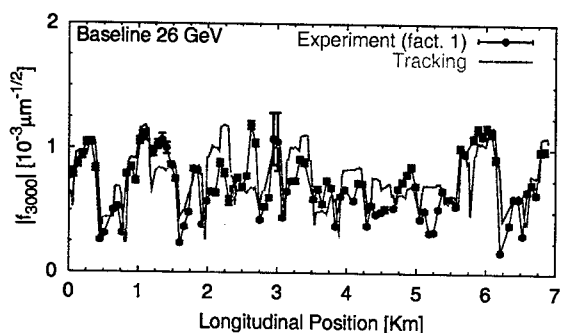


Figure 2: Amplitude of f_{3000} versus longitudinal position from experiment and model for the baseline machine at 26 GeV. The blue line is used to connect the experimental points.

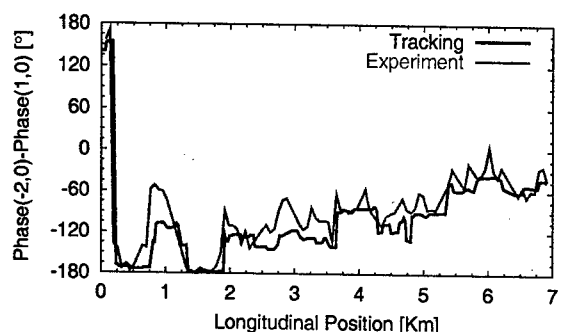


Figure 3: Phase of the spectral line $(-2,0)$ minus the phase of the spectral line $(1,0)$ versus longitudinal position from experiment and model for SPS with the extraction sextupoles powered to $(+ + + + - - - -)$ 30 A at 26 GeV.

—) 30 A. In figure 3 the phase of the spectral line $(-2,0)$ minus the phase of the spectral line $(1,0)$ is plotted versus the longitudinal position for experiment and model. The overall agreement is again good but the curve from the measurement is clearly more rough than the one from the model.

Sextupoles also introduce non-linear coupling, the horizontal component of the magnetic field is proportional to the product of the transverse coordinates xy . This monomial introduces, among others, the term h_{0120} in the Hamiltonian, which drives the resonance $(1,-2)$ and contributes to the vertical motion, $h_y^-(N)$, with the following quantity,

$$-4if_{0120}(2I_x)^{\frac{1}{2}}(2I_y)^{\frac{1}{2}}e^{i[-(2\pi\nu_x N + \psi_{x0}) - (2\pi\nu_y N + \psi_{y0})]} \quad (5)$$

By virtue of this equation the term h_{0120} introduces the spectral line $(-1,-1)$ in the vertical turn-by-turn motion. After normalising to the amplitude of the vertical tune the amplitude of this spectral line is $4|f_{0120}|\sqrt{2I_x}$. This quantity is linear in the horizontal kick. For this reason $|f_{0120}|$ is measured by performing a linear fit. The data acquired for the baseline machine was not decohered therefore it can be directly compared to the single particle model. In figure 4 the amplitude of the generating function term f_{0120}

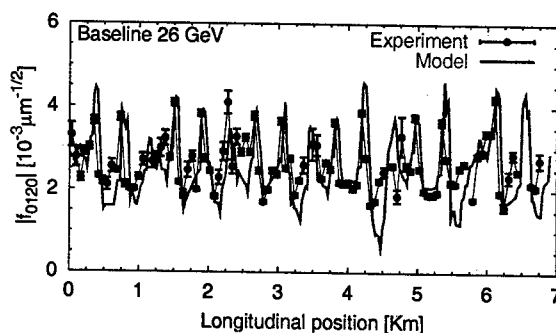


Figure 4: Amplitude of f_{0120} versus longitudinal position from experiment and model for the baseline machine at 26 GeV.

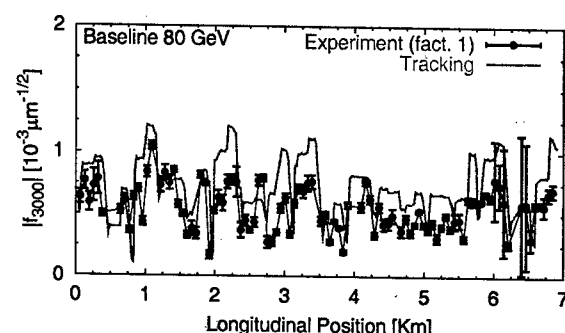


Figure 5: Amplitude of f_{3000} versus longitudinal position from experiment and model for the baseline machine at 80 GeV. The blue line is used to connect the experimental points.

is plotted versus the longitudinal location together with the model. The agreement seems to be better than that obtained for the term f_{3000} , figure 2.

Next are the measurements done at the SPS at 80 GeV. In figure 5 the amplitude of the term f_{3000} is plotted versus the longitudinal position from experiment and tracking model for the baseline machine. To assess any energy effect this is to be compared to the case at 26 GeV shown in figure 2. The level of agreement between model and experiment is similar at the two different energies. For this reason energy effects seem to be not relevant.

In figure 6 the phase of the spectral line $(-2,0)$ minus the phase of the spectral line $(1,0)$ is plotted versus the longitudinal position for experiment and model. The level of agreement is similar when compared to the 26 GeV case, figure 1.

Measurements were also done with the extraction sextupoles powered to $(+ + + + - - - -)$ 100 A. Since the energy is around 3 times larger than the previous 26 GeV, the current in the sextupoles has to be increased by a similar factor to obtain a similar strength. In figure 7 (Top) the amplitude of the generating function term f_{3000} is plotted versus the longitudinal position together with the model. A factor two is applied to the data in order to restore the effect of decoherence. Model and measurements show large

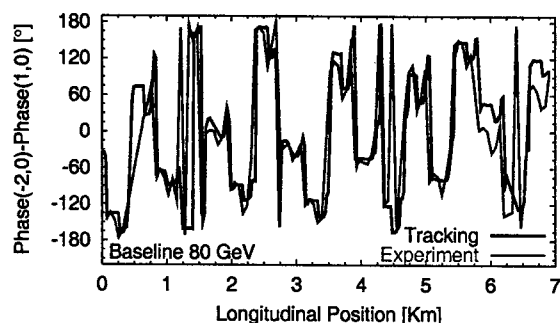


Figure 6: Phase of the spectral line (-2,0) minus the phase of the spectral line (1,0) versus longitudinal position from experiment and tracking model for the baseline machine at 80 GeV.

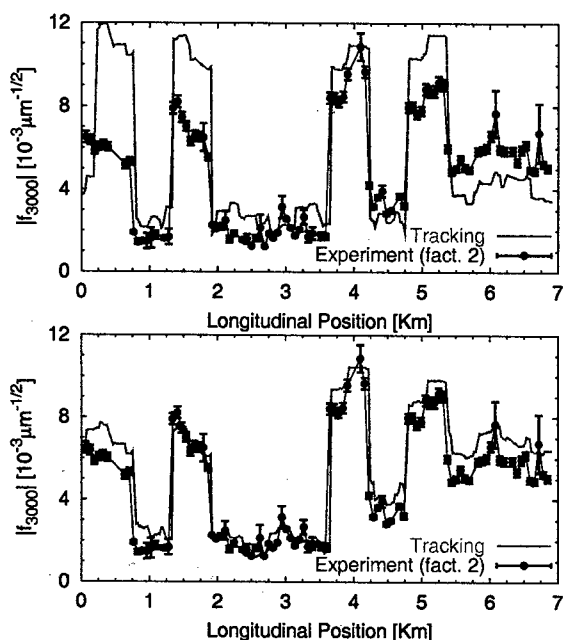


Figure 7: Amplitude of f_{3000} versus longitudinal position from experiment and model at 80 GeV. The vertical lines denote the position of the extraction sextupoles. Top: model with 8 sextupoles. Bottom: model with 7 sextupoles

discrepancies. Looking at the location of the first extraction sextupole a clear discrepancy is observed. Whereas the model predicts a large change of the amplitude of this term, the measurement gives a constant value in that region. We therefore suspected that this particular extraction sextupole was not connected. A comparison of the data with this new model without the first sextupole shows an excellent agreement, figure 7 (bottom). This hypothesis of a disconnected sextupole has been positively confirmed via the SPS alarm system [6], which reported a failure of this sextupole. The successful detection of a mispowered sextupole is an illustration of how this method will help in the commissioning of the LHC.

The effect of the beam intensity on the measurement of

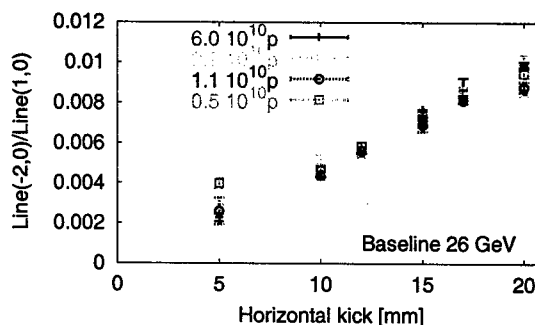


Figure 8: Normalised amplitude of the spectral line (-2,0) versus kick amplitude for the four intensity settings.

the resonance driving terms is now discussed. These terms might depend on the beam intensity due to space charge and impedance effects [7]. During the experiment the beam intensity was changed to different values in the range from 0.5×10^{10} to 6×10^{10} protons. In figure 8 the normalised amplitude of this spectral line averaged over all pick-ups is plotted versus kick amplitude for the four different intensities. For the majority of the kicks the differences remain inside the error bars. No local discrepancies in the resonance terms were observed around the ring.

CONCLUSION

For the first time the phase of the resonance terms has been measured around the ring. A very useful phase-observable has been defined which allows the unambiguous localisation of non-linear sources when used in conjunction with the amplitude of the resonance. The resonance (1,-2) has been also measured for the first time. By using this technique a sextupole that by accident was not powered was identified. Lastly, we have demonstrated that neither a change of energy nor of intensity has significant influence in measuring the resonance driving terms.

ACKNOWLEDGMENTS

We thank G. Arduini, F. Calderini and N. Gonthier for providing the information on the SPS alarm system used in this report. We also thank R. Jones for the careful adjustment of the BPM system.

REFERENCES

- [1] F. Schmidt, R. Tomás, A. Faus-Golfe, CERN-SL-2001-039-AP Geneva, CERN and IPAC 2001.
- [2] M. Hayes, F. Schmidt, R. Tomás, EPAC 2002 and CERN-SL-2002-039-AP Geneva, 25 Jun 2002.
- [3] J. Bengtsson, CERN 88-05, (1988).
- [4] J. Laskar et al., *Physica D* **56**, pp. 253-269 (1992).
- [5] R. Bartolini and F. Schmidt, LHC Project note 132, Part. Accelerators. 59, pp. 93-106, (1998).
- [6] G. Arduini, F. Calderini and N. Gonthier, private communication.
- [7] Question raised by Alex Chao in the LHC MAC held on November 2000.

A TECHNIQUE TO MEASURE CHROMATICITY BASED ON THE HARMONIC ANALYSIS OF A LONGITUDINALLY KICKED BEAM

G. Rumolo, GSI, R. Tomás, Uni. of Valencia

Abstract

Recently a method to measure chromaticity has been proposed by applying a transverse and a longitudinal kick to the beam. Assuming a Gaussian bunch in the 6-dimensional phase space, analytical expressions were derived, which relate the synchrotron sidebands to the machine chromaticity. To assess limitations and extensions of this technique, a more realistic accelerator model is considered including dispersion, transverse non-linearities and second order chromaticity, which modify the Fourier spectrum. Tracking and analytical studies are performed to describe these effects.

INTRODUCTION

The standard procedure for measuring the machine chromaticity is based on changing the beam energy and central orbit via frequency modulations of the radio frequency system. The chromaticities are then inferred by the variation of the machine tunes. The above procedure tends to be lengthy and perturbs the normal machine operation. Nevertheless a recent study has shown that by using a phase locked loop tune meter the performance of this method can be largely improved [1]. Various alternative techniques to measure chromaticity have been proposed during the last years. Two remarkable ones are described in [2], [3] and [4]. The first one uses the phase difference between the oscillations of the head and the tail of the bunch. The second one consists in modulating the radio frequency phase and measuring the induced tune modulation.

In [5] yet another method to determine the chromaticity is proposed by measuring the amplitude and phase of the synchrotron sidebands of the transverse motion after simultaneously applying a longitudinal and a transverse kick. The analytical expression obtained in this paper for the amplitude of the synchrotron sideband of order q , i.e. with frequency given by $Q_x + qQ_s$, is expressed as

$$AMP(q) = e^{-\varsigma^2} |I_q(\varsigma^2 - i\varsigma k)|, \quad (1)$$

where $\varsigma = Q'_x \sigma_\delta / Q_s$, Q'_x is the chromaticity, σ_δ is the momentum spread and k is the longitudinal kick in sigma units. This expression holds for a Gaussian bunch matched to the bucket, i.e. $\sigma_\delta = \sigma_z \frac{Q_s}{\eta R}$, η being the slippage factor and R the machine radius. To obtain this expression a linear motion was assumed both in the longitudinal and the transverse planes and only first order chromaticity was considered. The above equation shows that by applying the longitudinal kick the amplitudes of the synchrotron sidebands are linear (first non vanishing order) in the chromaticity. The sign of the chromaticity is contained in the phase of the sidebands.

To assess limitations and extensions of this technique a more realistic accelerator model is considered in this article including dispersion, transverse non-linearities and second order chromaticity. A Gaussian bunch matched to the bucket will be assumed for the derivations. Macroparticle simulations using the HEADTAIL [6] code are also performed.

CONSIDERING DISPERSION AND NON-LINEARITIES

The most relevant effect of non-linearities is the fact that they produce amplitude detuning and, as a consequence, the decoherence of the beam oscillations after a transverse kick. In this paper we assume that the amplitude detuning is low enough to ensure the resolution of the synchrotron sidebands in the Fourier spectrum of the transverse motion. This condition is normally desirable in the normal operation of an accelerator.

The transverse dynamics of a particle in presence of chromaticity, dispersion and non-linearities is approximated by assuming that the energy oscillations are much slower than the transverse oscillations. The equation describing the transverse motion is obtained by directly introducing the time dependence of the energy in the expressions derived for a constant energy. Therefore the most relevant contributions to the dynamics are those produced by the feed down from the non-linear fields due to the dispersion offset. In general, the contribution of all the feed down fields to the transverse motion can be taken into account by introducing chromatic Twiss parameters in the following way,

$$\begin{aligned} Q &= Q_0 + Q'_0 \delta + \frac{1}{2} Q''_0 \delta^2 + \dots \\ \beta &= \beta_0 + \Delta\beta_1 \delta + \dots \\ D &= D_0 + D_1 \delta + \dots \end{aligned} \quad (2)$$

where β represents the betatron function and D the dispersion function. In the first place we describe the Fourier spectrum of the motion considering only the first chromatic order of Twiss parameters. In the following section the effect of Q'' will be studied. The single particle position as function of the turn number is given by taking into account all the former quantities in the following way,

$$\begin{aligned} x(s, N) &= |a| \sqrt{1 + \frac{\Delta\beta_1}{\beta_0}(s)\delta(N)} \\ &\times \cos(2\pi(Q_x + \Delta Q_x(N))N + \phi_x) \\ &+ D_0(s)\delta(N) + D_1(s)\delta^2(N), \end{aligned} \quad (3)$$

where $\delta(N)$ is the relative momentum deviation as function of the turn number,

$$\delta(N) = \delta \cos(2\pi Q_s N) + z \frac{Q_s}{\eta R} \sin(2\pi Q_s N), \quad (4)$$

δ and z being the initial longitudinal coordinates and $\Delta Q_x(N)$ is the integral of $Q'_x \delta(N)$ from the turn 0 to the turn N divided by N . It can be deduced from the above equations that the chromatic beta beating modifies the synchrotron sidebands and the orbit oscillates with the frequencies Q_s and $2Q_s$ due to the dispersion and the chromatic dispersion. The contribution of sextupoles to the chromatic beta beating is produced by the quadrupolar feed down due to the dispersion at the sextupole and is expressed as

$$\frac{\Delta\beta_1}{\beta}(s) = \int_s^{s+C} ds' \frac{K_2(s') D_0(s') \beta_0(s')}{2 \sin(2\pi Q_x)} \quad (5)$$

$$\times \cos(2\pi Q_x - 2|\phi_x(s') - \phi_x(s)|),$$

where K_2 is the sextupole strength. The contribution of sextupoles to the chromatic dispersion is produced by the dipolar feed down due to the dispersion at the sextupole and is expressed as

$$D_1(s) = \frac{\sqrt{\beta_0(s)}}{4 \sin(\pi Q_x)} \int_s^{s+C} ds' \sqrt{\beta_0(s')} K_2(s') \quad (6)$$

$$\times D_0^2(s') \cos(\phi(s') - \phi(s) - \pi Q_x).$$

Contributions from other multipoles can be similarly computed. The motion of the centroid is obtained by averaging the single particle motion over the initial bunch density, i.e.

$$\bar{x}(s, N) = \int_{-\infty}^{\infty} d\delta \int_{-\infty}^{\infty} dz \rho(\delta, z) x(s, N), \quad (7)$$

where $\rho(\delta, z)$ is the longitudinal density of the Gaussian bunch displaced in the z axis by k sigmas. To solve this integral the chromatic beta beating is assumed to be much smaller than one and the square root of Eq. (3) is expanded up to first order. To obtain the centroid motion the following integrals are needed,

$$\int_{-\infty}^{\infty} d\delta \int_{-\infty}^{\infty} dz \rho(\delta, z) \delta(N) e^{i2\pi \Delta Q_x(N)} = \sigma_\delta (k + i\zeta) \quad (8)$$

$$\times \sin(2\pi Q_s N) e^{(\zeta^2 - i\zeta k)(\cos(2\pi Q_s N) - 1)},$$

$$\int_{-\infty}^{\infty} d\delta \int_{-\infty}^{\infty} dz \rho(\delta, z) \delta(N) = \sigma_\delta k \sin(2\pi Q_s N),$$

$$\int_{-\infty}^{\infty} d\delta \int_{-\infty}^{\infty} dz \rho(\delta, z) \delta^2(N) = \sigma_\delta^2 [1 + k^2 \sin^2(2\pi Q_s N)].$$

The frequencies and amplitudes of the different spectral lines arising in the Fourier spectrum of $\bar{x}(s, N)$ are given in table 1. It is particularly interesting to note that the fundamental spectral line Q_x is not affected by the chromatic Twiss parameters and that the amplitude of the sideband $Q_x + |q|Q_s$ is different from that of $Q_x - |q|Q_s$. This difference is linear in the chromatic beta beating, the longitudinal kick and the chromaticity. Therefore this difference can be used to determine the sign of the chromaticity, provided

Frequency	Amplitude
$Q_x + qQ_s$	$e^{-\zeta^2} \bar{a} \left I_q(\zeta^2 - i\zeta k) + \frac{\Delta\beta_1}{4i\beta} \sigma_\delta (k + i\zeta) \right $ $\times [I_{q-1}(\zeta^2 - i\zeta k) - I_{q+1}(\zeta^2 - i\zeta k)]$
Q_s	$\frac{1}{2} D_0(s) \sigma_\delta k$
$2Q_s$	$\frac{1}{4} D_1(s) \sigma_\delta^2 k^2$

Table 1: Frequencies and amplitudes of the different spectral lines produced by dispersion and sextupolar fields.

that the chromatic beta beating is known or a calibration is done using another method for determining the chromaticity. Likewise, if the chromaticity is known the chromatic beta beating could be measured around the ring.

In order to verify the achieved expressions a macroparticle simulation has been performed using a model of the CERN SPS. One sextupolar kick at a dispersion region has been introduced in the HEADTAIL code. The value of the dispersion was chosen to be the average dispersion at the SPS sextupoles, $D = 2.24$ m. The strength of the sextupolar kick was chosen to reproduce the chromatic beta beating at the start of SPS, $K_2 L = -0.254564$ m⁻². Second order chromaticity was well corrected by means of a phase space rotation and chromaticity is $Q' = -0.279$. The simulation was performed for a longitudinal kick of one sigma, $\sigma_\delta = 0.00248$ and the synchrotron tune is $Q_s = 0.005$. In Fig. 1 a comparison of the Fourier spectrum obtained from the simulation and the prediction from the model is shown. Although a relevant discrepancy is found for the second order sidebands the first order sidebands are well described by the model. This means that second order chromatic Twiss parameters should be considered to properly describe second and higher order synchrotron sidebands. Simulation and model agree with remarkable precision concerning D_1 , as appears from the spectral line with frequency $2Q_s$. This is a very relevant quantity that contains the local non-linear information in a similar way as the resonance driving terms do. It is evident from the figure how important higher orders are, since data were acquired at a dispersion free region but yet lines with Q_s and $3Q_s$ are observed. We can conclude that using the first order synchrotron sidebands of all the BPMs around the ring this technique can provide not only chromaticity but also chromatic beta beating and local non-linear information.

Second order chromaticity

This section studies the effect of the second order chromaticity in the Fourier spectrum of the centroid motion. An analytical expression for the turn-by-turn centroid position is derived considering first and second order chromaticities but not any chromatic Twiss function. The tune shift $\Delta Q_x(N)$ is given by the integral of $Q'_x \delta(N) + Q''_x \delta^2(N)/2$ from the turn 0 to the turn N divided by N , giving the fol-

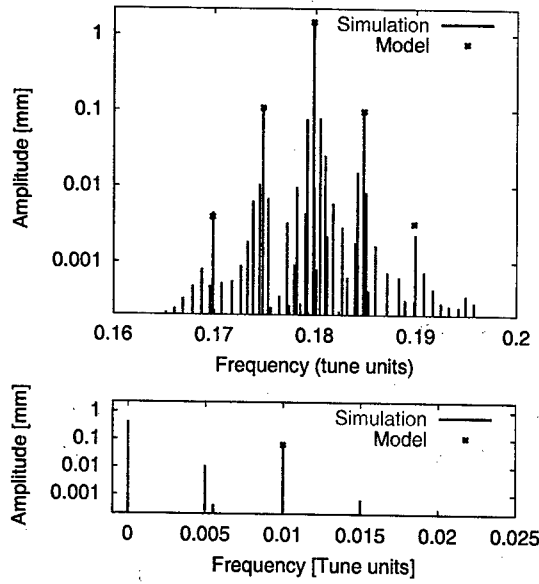


Figure 1: Fourier spectrum of the simulated turn-by-turn motion together with the prediction from the model. Top: Tune and synchrotron sidebands. Bottom: Offset and multiples of Q_s .

following expression,

$$\frac{Q'_x}{2\pi Q_s N} \left[\delta \sin(2\pi Q_s N) - z \frac{Q_s}{\eta R} (\cos(2\pi Q_s N) - 1) \right] + \frac{Q''_x}{4\pi N} \left[\frac{\delta^2}{2} \left(N + \frac{\sin(4\pi Q_s N)}{4\pi Q_s} \right) + \frac{\delta z}{\eta R 4\pi} (1 - \cos(4\pi Q_s N)) + \frac{z^2 Q_s^2}{2\eta^2 R^2} \left(N - \frac{\sin(4\pi Q_s N)}{4\pi Q_s} \right) \right].$$

The centroid position $\bar{x}(s, N)$ is computed as in Eq. (7) with the above tune shift and it is obtained by taking the real part of the following expression (up to a proportionality constant):

$$\frac{-\zeta(k+i\zeta) \left[(i+\zeta_2 N) (\cos(2\pi Q_s N) - 1) + \frac{\zeta_2}{2\pi Q_s} S(N) \right] + F(N)}{e^{1-2i\zeta_2 N + \zeta_2^2 \left[-N^2 + \frac{\sin^2(2\pi Q_s N)}{4\pi^2 Q_s^2} \right]} + i2\pi Q_s N} \sqrt{1 - 2i\zeta_2 N + \zeta_2^2 \left[-N^2 + \frac{\sin^2(2\pi Q_s N)}{4\pi^2 Q_s^2} \right]}$$

$S(N)$ and $F(N)$ being

$$\begin{aligned} S(N) &= \sin(2\pi Q_s N) - \sin(4\pi Q_s N)/2 \\ F(N) &= -ik^2 \left(i + \zeta_2 N + \zeta_2 \frac{\sin(4\pi Q_s N)}{4\pi Q_s} \right) / 2, \end{aligned} \quad (9)$$

where $\zeta_2 = \pi Q'' \sigma_s^2$. This equation shows that for large N the oscillation amplitude is damped proportionally to $1/(\zeta_2 N)$. This effect increases the width of the synchrotron sidebands. The analytical description of the Fourier spectrum is too complicated to be usable. To illustrate this a

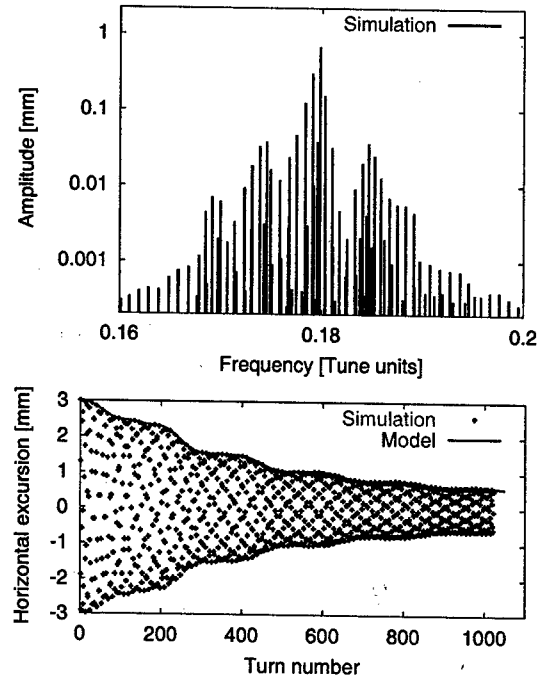


Figure 2: Fourier spectrum and centroid position in presence of first and second order chromaticity from the simulation and from the analytical formula.

simulation has been performed with the same SPS model as above but with $Q' = -0.279$, $Q'' = -150$ and without the sextupolar kick. The turn-by-turn centroid position and the Fourier spectrum obtained from the simulation and the analytical formula are shown in Fig. 2. The first synchrotron sidebands can still be used to estimate Q' although a larger Q'' would completely distort the Fourier spectrum.

CONCLUSIONS

It has been demonstrated that for small amplitude detuning and second order chromaticity the proposed technique can be used to measure chromaticity and to obtain information concerning chromatic Twiss functions and nonlinearities. It probably remains important to study the effect of the non-linearity of the longitudinal phase space motion and collective effects.

REFERENCES

- [1] S. Tepikian et al., EPAC 2002, Paris, France.
- [2] D. Cocq et al. 8th Beam Instr. Workshop BIW' 98, Stanford.
- [3] S. Fartoukh and R. Jones, CERN-LHC-Project-Report-602.
- [4] O. Brüning et al., CERN-SL-2002-037-AP and EPAC 2002.
- [5] G. Rumolo, et al., CERN-SL-2002-049 (AP).
- [6] G. Rumolo, F. Zimmermann, CERN-2002-001.

CORRECTING THE LHC β^* AT COLLISION

W. Wittmer[♣], A. Verdier[◇], F. Zimmermann[◇]

[♣] CERN, Geneva, Switzerland and University of Technology Graz, Austria

[◇] CERN, Geneva, Switzerland

Abstract

To correct the β^* at the main collision points (IP1 and IP5) simultaneously for the two counterrotating proton beams in the Large Hadron Collider (LHC), a set of specific quadrupoles in the non-common part of the machine is used. Due to the antisymmetric optics, several quadrupoles on each side of the insertion have to be employed. The change of β^* is accomplished by incrementing the quadrupole gradients. This set of increments is referred to as β^* tuning knob. The increments were calculated by rematching β^* in a range of $\pm 20\%$ about the nominal value. Linear curves were fitted to the variation of increments to construct a linear tuning knob. This was done for each plane using MAD 8 [1] and repeated with MAD X [2]. The linear behaviour and the orthogonality of the knobs were investigated for the LHC lattices V6.2 and V6.4. Different field errors were introduced in the lattice and the correction efficiency of the knobs was studied.

1 INTRODUCTION

In LHC operation the beam sizes of the two beams have to be corrected. Two orthogonal knobs can correct each plane independently. To form these knobs, a set of quadrupoles, which are located on each side of the IP in the insertion, are available. From these quadrupoles a knob is constructed so that a specific strength change ΔK is assigned to each, which we refer to as knob vector, so that the β^* is changed. To scale the β^* the knob vector $\Delta \vec{K}$ is multiplied with a variable m which acts as the actual knob. The two knobs should have the following characteristics within a variation of $\pm 20\%$: be orthogonal in the x- and y- plane, create no beta beating in the rest of the ring, scale linearly with β^* , not change other constraints (e.g. dispersion, crossing angle), be able to correct the β^* independently of the source of the error and be simple for operation.

The performance of the knobs has to be tested. Therefore, both knobs, when varied over their nominal range, must meet the conditions of the different criteria described above. If this is the case a second stage of testing is started. Various errors are introduced in the lattice and the knobs are used to correct them. This is done step by step to see to which types of errors the knobs can be applied.

2 CALCULATING β^* TUNING KNOBS

The design of the LHC insertion is asymmetric and the beams pass through the inner triplet (Q1–Q3 left and right

from the IP) in a common beam pipe off center of the magnetic field axis. Therefore the magnets of the inner triplet cannot be used to correct the effects of errors outside of the triplet, as the two rings are different. The closest magnets that can be used are Q4 left and right of the IP. There are further three quadrupoles upstream (Q5–Q7) which can be used without any restriction. Q8 to Q13 can also be used, but, as part of the dispersion suppressor, not without restriction. Because of the asymmetric β -functions, the different phase advances and the need to correct both planes, there is no single pair of quadrupoles that can do the correction for either of the planes without changing the other plane's β -function. The position of the different tuning quadrupoles and the dipoles separating and combining the two beams is shown in Fig. 1.

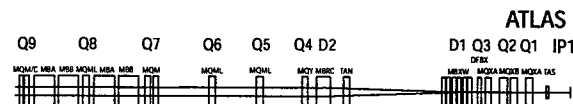


Figure 1: Position of the different magnets on the left side of IR1 and parts of the dispersion suppressor.

Using Q4–Q9 and Q13 scaled to the same relative ΔK as Q9, left and right of the IP, a tuning knob was constructed with MAD8. The version of the lattice file for the LHC was collision optics V6.2. A detailed description of the calculation can be found in [5].

Recently, the crossing angle and other minor changes were re-introduced in the LHC lattice with version V6.4. Also the new version of MAD, MAD X, was defined as the new standard to simulate the LHC lattice. MADX is described in [2]. Therefore, the performance of the knobs had to be reviewed for this new modelling environment and compared to earlier results with MAD 8 and V6.2 [5]. The effect of the knobs on the closed orbit in presence of the nominal crossing angle was investigated, in particular the position and slope at the IP.

To distinguish between sources of changes coming either from the change of the lattice or from the crossing angle the characterisation was repeated twice, with crossing angle on and off, respectively. The vertical crossing angle has a negligible influence on the changes of $\Delta\beta_x^*$, $\Delta\beta_y^*$, $\Delta\alpha_x^*$, $\Delta\alpha_y^*$, Q_x , Q_y , D_x^* , D_y^* , X^* , pX^* at the IP as a function of $\Delta\beta_x^*$ and $\Delta\beta_y^*$ for a variation of $\pm 20\%$. Therefore, only the results with crossing angle on are summarized in Table 1. The vertical crossing angle results in a noticeable variation of vertical orbit Y^* and slope pY^* at the IP.

Table 1: Changes of $\Delta\beta_x^*$, $\Delta\beta_y^*$, $\Delta\alpha_x^*$, $\Delta\alpha_y^*$, Q_x , Q_y , D_x , D_y , X^* , Y^* , pX^* , pY^* as a function of $\Delta\beta_x^*$ and $\Delta\beta_y^*$ for $\pm 20\%$ changes in the presence of a vertical crossing angle ($\pm 150 \mu\text{rad}$) for V6.4.

VAR	β_x^* β_y^*	+20% +20%	+20% -20%	-20% +20%	-20% -20%
$\Delta\beta_x^*/\%$		1.9	1.7	-2.6	-0.5
$\Delta\beta_y^*/\%$		3.7	-3.7	2.4	1.5
$\Delta\alpha_x^*/[1]$		$4.54E-2$	$1.39E-2$	$2.00E-2$	$5.64E-2$
$\Delta\alpha_y^*/[1]$		$-4.43E-2$	$-6.73E-2$	$1.22E-2$	$5.43E-2$
$\Delta Q_1/[1]$		-0.009	0.003	0.001	0.014
$\Delta Q_2/[1]$		-0.009	-0.009	0.009	0.015
$\Delta D_x^*/[m]$		$2.78E-3$	$3.88E-3$	$-3.40E-3$	$-2.36E-3$
$\Delta D_y^*/[m]$		$4.19E-4$	$1.66E-4$	$3.29E-4$	$-5.10E-4$
$\Delta X^*/[m]$		$4.15E-11$	$8.27E-11$	$3.40E-11$	$6.38E-11$
$\Delta Y^*/[m]$		$2.85E-6$	$2.47E-6$	$-2.30E-6$	$-2.79E-6$
$\Delta pX^*/[1]$		$1.51E-10$	$1.27E-10$	$1.12E-10$	$2.26E-10$
$\Delta pY^*/[1]$		$3.91E-6$	$4.61E-6$	$-2.89E-6$	$-5.14E-6$

The responses of $\Delta\beta_x^*$ and $\Delta\beta_y^*$ show a slightly degraded behaviour due to the lattice change from version V6.2 to V6.4. The behaviour of $\Delta\beta_y^*$ is shown in Fig. 2.

The changes of $\Delta\alpha_x^*$, $\Delta\alpha_y^*$, ΔD_x^* , ΔD_y^* , ΔX^* , ΔpX^* , ΔpY^* , ΔQ_1 and ΔQ_2 , are acceptable for adjustments in operation. However, for changes in $\beta_{x,y}^*$ of $\pm 20\%$ the change of Y^* (the vertical position at the IP) exceeds $\pm 10\%$ of the nominal beam size as shown in the left plot of Fig. 3. This effect is under investigation.

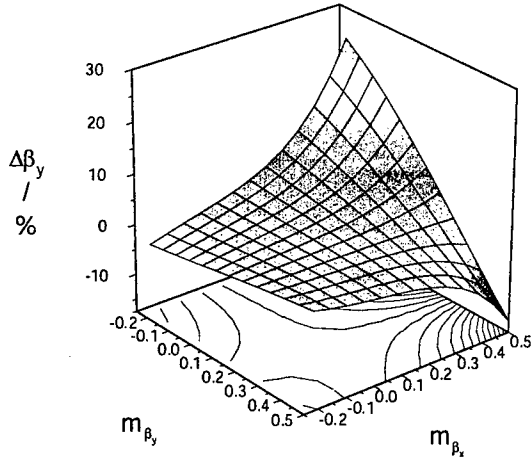


Figure 2: Orthogonality behaviour of the β_x^* knob. $\Delta\beta_y^*$ is shown as a function of $m_{\beta_x^*}$ and $m_{\beta_y^*}$ ($\Delta\beta_y^* = f(m_{\beta_x^*}, m_{\beta_y^*})$). To only see the change of β_y^* created by the β_x^* knob, $\Delta\beta_y^*$ is normalized as following: $\Delta\beta_y^* = (\beta_y^* - \beta_{y0}^*)/\beta_{y0}^*$, where β_y^* is the actual value and β_{y0}^* is the value if only the knob vector for β_y^* is applied. The ranges on the x and y axes are $(+100/-50)\%$. Computation was done for version 6.4 using MADX.

The orthogonality behaviour ($\Delta\beta_x^* = f(m_{\beta_x^*}, m_{\beta_y^*})$, $\Delta\beta_y^* = f(m_{\beta_x^*}, m_{\beta_y^*})$) of both knobs is different, where the two variables $m_{\beta_{x,y}^*}$ denote the knob settings. The reason for this is the antisymmetric lattice as mentioned before. Due to technical and design reasons, the lattice is not

strictly asymmetric. Also the phase advance is not antisymmetric around the IP. All these small differences contribute to the different behaviour of the two planes because a change of the β -function at the IP is related to these variables as follows:

$$\Delta\beta^* = \frac{\beta^*}{2 \sin(2\pi Q)} \oint \beta(s) \Delta K(s) \cos(2|\Delta\mu| - 2\pi Q) ds.$$

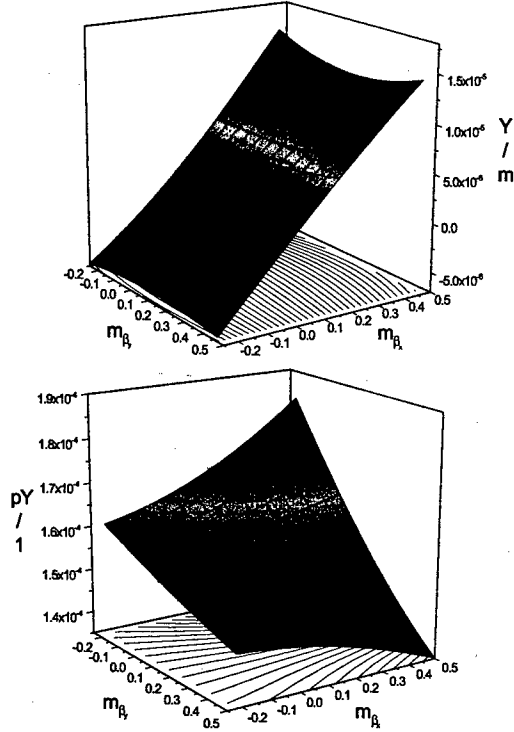


Figure 3: Influence of the knob vectors on Y and the crossing angle pY at IP1. On the x and y axes the values of the scaling factor for the knob m_{β} for both planes, m_{β_x} and m_{β_y} , are shown within a range of $(+0.5/-0.25)$ with 0.1 units corresponding to 0.1 m. On the z axis the vertical position and slope at the IP, Y^* and pY^* , are shown. The computation was done for LHC version 6.4 using MADX.

In addition, the dispersion ΔD and β functions have to be monitored around the ring. A change in either of these functions will cause a change at the other IPs which should be avoided. The β function in the x plane does not change around the ring, when the knob is varied, except in the region of IP1, due to the variation of the tuning quadrupoles around IP1. In the plane where the correction is to be applied the beta function through the region between KQ13L and KQ13R is changed to create the needed change of β^* . This also introduces changes of β in the other plane with the difference that there β^* is kept constant.

For the dispersion the situation is similar, but different from that without crossing angles. With the vertical crossing angle in IP1 introducing dispersion in the vertical plane dispersion in both planes is to be controlled, even if there is

no cross talk between the planes. So far no critical changes of the dispersion around the ring have been observed.

The changes in the lattice between V6.2 and V6.4 and the new simulation program could be the reason for a slightly degraded behaviour of the knobs. This is being studied.

3 TESTS

To test the behaviour of the knobs, errors were introduced into the lattice. A preliminary correction was applied, i.e., orbit correction for b1 field errors, and b3, b4, b5, a2, a3 correction with corrector spool pieces, based on magnetic field measurements. Then the tuning knobs were applied and their effect was observed. To obtain a diversified result, demonstrating for which type of error the knobs work, a test program is followed containing various different types of magnets, fields and errors.

In previous work [5] errors were introduced in the arc dipoles MB and arc quadrupoles MQ. As error field types b1 to b11 were applied. For all cases the β^* values at IP1 could be corrected. Results for errors in all the magnets were summarized in [5]. In these studies no crossing angle was included, and the simulations were performed with lattice version V6.2 and MAD 8.

To test the knobs in the presence of the crossing angle, version V6.4 with MAD X had to be used. Therefore, two test series were performed, one with and one without the crossing angle active. The results are similar in both cases, so that only the results from the test series with active crossing angle is shown in Table 2. The test series were constructed in the same way as in [5] except that no dipole errors were applied for technical reasons.

Table 2: Results from the test run with systematic and random errors of the field error types b2 to b11 in the arc quadrupoles MQ with lattice version V6.4 and MAD X.

	mean value	rms	max neg	max pos		tk appl max pos	tk appl max neg
$\Delta\beta_x^*$	-1.5E-3	1.23E-2	-3.11E-2	1.88E-2	β_x	5.0E-1	5.0E-1
$\Delta\beta_y^*$	3.6E-3	1.39E-2	-2.08E-2	3.16E-2	β_y	5.0E-1	5.0E-1
ΔD_x^*	-8.0E-5	1.41E-3	-4.28E-3	1.99E-3	D_x	2.1E-2	-
ΔD_y^*	1.9E-5	5.57E-5	-1.06E-4	1.04E-4	D_y	1.0E-2	-
ΔQ_1^*	64.3115	1.17E-2	-2.25E-2	2.77E-2	Q_1	64.338	64.285
ΔQ_2^*	59.3215	1.18E-2	-1.82E-2	2.99E-2	Q_2	59.350	59.302
ΔX^*	2.7E-8	4.73E-7	-7.60E-7	1.42E-6	X	7.0E-8	-4.2E-5
ΔY^*	2.6E-8	4.54E-7	-9.27E-7	1.08E-6	Y	2.6E-6	-6.1E-6
ΔpX^*	-5.9E-8	1.25E-6	-3.68E-6	2.22E-6	pX	7.3E-6	-1.0E-5
ΔpY^*	1.2E-7	7.41E-7	-1.28E-6	7.18E-5	pY	7.2E-5	-4.8E-7

Columns two and three in Table2 show the mean and rms value of the changes between the introduction of the errors and the application of the tuning knobs, column four the maximum negative, column five the maximum positive change out of sixty different seeds and columns seven and eight the resulting maximum positive and negative final values of β_x^* , β_y^* , D_x^* , D_y^* , Q_x^* , Q_y^* , X^* , Y^* , pX^* , pY^* over 60 random seeds after the tuning knobs were applied.

To visualize the correction efficiency the actual correction $\beta_0 + \Delta\beta_e$ is plotted over the to be corrected β_e value. In such a plot, all perfectly corrected seeds lie on the diagonal. This is shown in Fig.4 (left plot) for errors generated in the

arc quadrupoles. The right plot refers to errors generated in the insertion triplet. In the latter case, if the resulting errors in β^* exceed a value of $\approx \pm 25\%$ the knobs fail to work, especially for positive $\Delta\beta$ values.

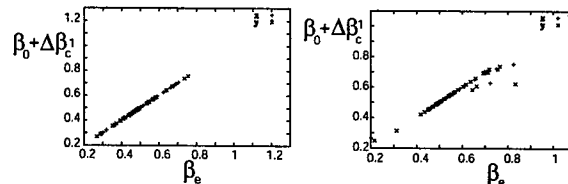


Figure 4: Correction efficiency for errors generated in the arc quadrupoles (left plot) and in the insertion triplet quadrupoles (plot right). The corrected seeds lie on the diagonal. Imperfectly corrected seeds lie off diagonal. The errors of the MQ's were enlarged compared to those expected by a factor of 7. This was done in order to better compare the corresponding correction efficiency with that for errors generated by the insertion triplets.

4 CONCLUSION AND THANKS

So far the characteristics of the calculated tuning knobs are within the given boundaries, except for the changes of the position Y with a maximum of 17% of σ_y for 20% changes in β^* . Normal and skew field error types in the arc dipoles and quadrupoles can be corrected with these knobs. The same optics errors generated in the inner triplet quadrupoles cannot be corrected if the β^* change is larger than $\approx 20\%$. This is not too surprising, since triplet errors change the transfer matrices between the knob quadrupoles on either side of the IP. So far the introduction of crossing angles in the lattice shows no major problem except for the induced change in the orbit at the IP. The action of the knobs in the presence of a closed orbit distortion due to field errors in the magnets will be investigated in the future. Finally beam beam effects and the reaction of the knobs to these will complement the picture of the behaviour of the knobs. We thank M. Hayes, O. Bruening and T. Risselada for comments and informations.

5 REFERENCES

- [1] H. Grote and F. C. Iselin, 'The MAD program version 8.4: User's reference manual,' CERN-SL-90-13-AP-REV.2.
- [2] F. Schmidt, et al., MAD X homepage: <http://slap.web.cern.ch/slap/premiereversion.htm>
- [3] N.J. Walker et al., 'Gloal Tuning Knobs for the SLC Final Focus,' SLAC-PUB-6207,(PAC 93)
- [4] Y. Nosochkov, P. Raimondi, T.O. Raubenheimer, A. Seryi, M. Woodley 'Tuning Knobs for the SLC Final Focus,' SLAC-PUB-9255, (EPAC 2002)
- [5] W.Wittmer 'Luminosity Optimisation by Adjusting LHC β^* at Collision.' <http://icfa-nanobeam.web.ch/icfa-nanobeam/paper/wittmer.pdf>

2002 NONLINEAR OPTICS MEASUREMENTS AND MODELLING FOR THE CERN SPS

G. Arduini, R. Tomas, F. Zimmermann, CERN, Geneva, Switzerland;
A. Faus-Golfe, IFIC-Univ. de Valencia, Spain; N. Iida, KEK, Japan

Abstract

In 2002, nonlinear chromaticity, coupling, amplitude-dependent detuning, chromatic phase advance, resonance driving terms, and off-energy orbits were measured in the CERN SPS at 26 GeV/c. The optics model has been updated by adjusting the strengths of nonlinear field errors in the dipoles and quadrupoles, so as to reproduce the measured nonlinear chromaticity. We compare the field errors deduced in 2002, measuring over a larger momentum range, with those found in 2001 and 2000. The resolution is improved by averaging over all turn-by-turn position monitors in the ring instead of using a single dedicated pick up ('tune meter'). Computations using two different optics codes, MAD and SAD, indicate the sensitivity to matching algorithm and magnet representation. To validate the nonlinear optics model, the predicted tune shifts with transverse amplitude, driving terms of low-order resonance, etc., are compared with direct measurements.

INTRODUCTION

Given the tight emittance budget for the SPS as LHC injector, a precise model of the nonlinear SPS optics is desirable, especially at the injection momentum of 26 GeV/c. Since 2000 we are pursuing an experimental program aimed at establishing a fast and reliable procedure by which the SPS optics model can be updated from a fast measurement. Simultaneously, we are exploring experimental techniques that will be important for the commissioning of the LHC itself. The precursor studies of 2000 and 2001 were reported in [1] and an application to the full SPS cycle in [2]. The optics model is based on the measured nonlinear chromaticity. In 2002 we explored its sensitivity to the momentum range and to the choice of tune signal. We also compared model predictions and measurements locally, as a function of position around the ring, and we applied two different optics codes to cross-check the results. In this paper we highlight these new developments.

NONLINEAR CHROMATICITY

In the SPS, the measured betatron tunes, Q_x and Q_y , show a strongly nonlinear dependence on the relative momentum offset, δ . The latter is varied by changing the rf frequency. The two measurements of 2002 are displayed in Fig. 1. The different pictures show two different beam signals, i.e., either from the 'tune meter' pick-up or from about 2×110 beam-position monitors (BPMs), together with various fits and model predictions. The linear, quadratic and cubic components of the two chromaticities are defined as

$$Q_{x,y} = Q_{0,x,y} + Q'_{x,y}\delta + \frac{1}{2}Q''_{x,y}\delta^2 + \frac{1}{6}Q'''_{x,y}\delta^3, \quad (1)$$

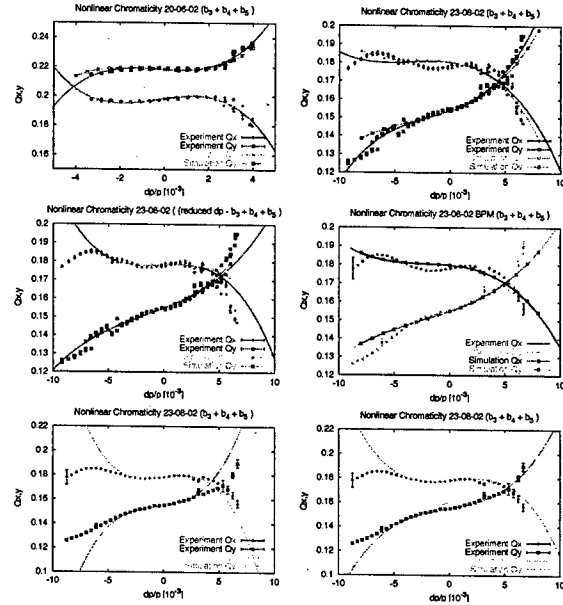


Figure 1: Measured and predicted horizontal and vertical tune versus momentum offset, for the experiment on 20th June 2002 (top left) and on 23rd August 2002 (others); with fit over $\delta = -0.009/0.007$ (top right); $\delta = -0.005/0.005$ (centre left); again $\delta = -0.009/0.007$ (centre right); $\delta = -0.003/+0.003$ (bottom left); $\delta = -0.005/+0.0055$ (bottom right). The bottom row was matched for $K_{5a} \neq K_{5b}$ using SAD; the other four with $K_{5a} = K_{5b}$ using MAD. The data in the first three plots are from a dedicated application ('tune meter'), the last three were obtained by averaging over all BPMs.

and can be obtained by a fit. Table 1 summarizes the coefficients found in 2002. The table also indicates the δ interval.

To construct an SPS optics model with identical nonlinear chromatic behavior, we add sextupolar and decapolar field errors in the two types of dipole magnets (called MBB and MBA) and octupole errors in the two types of quadrupoles [1]. We then determine the strength of these field errors so as to achieve best agreement with the 6 linear and nonlinear chromatic coefficients. We distinguish between the sextupole errors in MBB and MBA, but often assume that the decapole errors are the same. This is done to avoid a degeneracy problem when fitting with MAD. In SAD fits, we kept the distinction between the two types of errors, which we denote by K_{5a} and K_{5b} (a similar notation is used for the other types of errors). Our procedure assumes that all magnets have the same systematic error

and that the nonlinear fields arise from the regular cells.

Table 1: Linear and nonlinear chromatic coefficients obtained from a polynomial fit of the measured betatron tune as a function of rf frequency.

2002 MDs $\mp \delta$ fit	Q_{0x} Q_{0y}	Q'_x Q'_y	Q''_x Q''_y [10 ⁻²]	Q'''_x Q'''_y [10 ⁻⁵]	R^2_x R^2_y
20/06/2002 -0.003/0.004	0.1982 0.2181	2.3 -0.8	-6.0 6.0	-18.0 18.0	0.87 0.95
23/08/2002 -0.009/0.007	0.1804 0.1537	-0.7 2.2	-6.0 4.0	-2.4 2.4	0.76 0.98
-0.005/0.005	0.1780 0.1547	0.3 2.4	-0.6 2.0	-3.0 1.20	0.81 0.96
23/08/2002 -0.009/0.007 (BPMs)	0.1797 0.1574	-0.5 2.2	-3.4 1.8	-1.1 1.8	0.75 0.98

In Table 2 we compare the 2002 field errors with those of the two previous years. In 2000 a single measurement was performed, in the later years several. The error quoted reflects the rms spread over the measurements of one year. The last column gives the average and spread over all years. We observe a significant fluctuation, which is partly caused by different SPS cycles, and, thus, related to actual changes in the remanent fields. However, a large variation is observed even between measurements of the same year and for the same cycle.

Table 2: Matched multipole components for linear and nonlinear chromaticity measurements in 2000, 2001 [1] and 2002 using MAD, and assuming $K_{5a} = K_{5b} (= K_5)$.

element	dipoles	quadr.	dipoles
MDs	K_{3a} K_{3b}	K_{4f} K_{4d}	K_5
units	10 ⁻³ [m ⁻²]	10 ⁻¹ [m ⁻³]	[m ⁻⁴]
2000	1.4 -0.8	0.8 -2.6	-5.8
2001	1.2 ± 0.3 -3.0 ± 0.5	1.1 ± 0.1 -0.8 ± 2.3	-20 ± 4
2002	0.6 ± 0.2 -2.5 ± 0.1	-0.2 ± 0.1 -1.5 ± 0.8	-12 ± 12
total	1.0 ± 0.3 -2.1 ± 0.8	0.5 ± 0.5 -1.6 ± 0.8	-12 ± 6

A possible reason for the variation are differences in the momentum range. This is supported by the various curves and pictures in Fig. 1 (the last five pictures of which show the same experimental data fitted over different momentum ranges with two different programs), and also by Table 3, which confirms a strong dependence of the fitted chromatic coefficients on the momentum interval considered. Table 4 displays the associated multipole errors. In particular, the higher-order errors K_{4d} , K_{5a} and K_{5d} are not well constrained and vary dramatically with the fit range.

Table 3: Linear and nonlinear chromatic coefficients obtained from a polynomial fit to the experimental data on 23rd August 2002, for different δ ranges.

23/08/02 $\mp \delta$ fit	Q_{0x} Q_{0y}	Q'_x Q'_y	Q''_x Q''_y [10 ⁻²]	Q'''_x Q'''_y [10 ⁻⁵]
-0.003/ +0.003	0.1780 0.1547	1.27180 1.40673	0.7 4.3	-8.7 7.7
-0.005/ +0.005	0.1779 0.1548	1.04863 1.78427	1.2 2.2	-5.4 3.0
-0.0045/ +0.005	0.1779 0.1549	0.89959 1.68147	1.9 -0.5	-4.9 2.7
-0.005/ +0.0055	0.1779 0.1549	0.88922 1.66710	1.9 0.6	-4.8 3.4

Table 4: Matched multipole components from linear and nonlinear chromaticity measurements on 23rd August 2002 for different fit intervals of δ and $K_{5a} \neq K_{5b}$.

element	dipoles	quadrupoles	dipoles
23/08/02	K_{3a} K_{3b}	K_{4f} K_{4d}	K_{5a} K_{5b}
$\mp \delta$ fit			
units	10 ⁻³ [m ⁻²]	10 ⁻¹ [m ⁻³]	[m ⁻⁴]
-0.003/ +0.003	0.841 -2.61	0.38 -1.76	-10.0 -29.9
-0.005/ +0.005	0.831 -2.71	0.39 -0.84	-8.6 -6.1
-0.0045/ +0.005	0.782 -2.65	0.42 0.39	-7.78 -5.77
-0.005/ +0.0055	0.778 -2.65	0.44 -0.13	-6.55 -10.74

VALIDATION

Once the nonlinear optics is constructed, we compare its predictions for various optics parameters (other than chromaticity) with direct measurements. A primary test is the detuning with amplitude. Figure 2 shows an example, where the agreement is good for the vertical tune. The residual discrepancy for the horizontal tune decreases if the δ range of the fit is narrowed. Hence, the global behavior of the SPS optics is fairly well reproduced by our model.

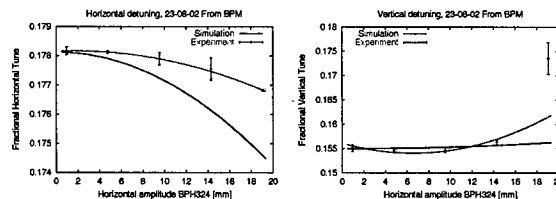


Figure 2: Predicted tune shift vs. horizontal amplitude in mm (at $\beta_x \approx 100$ m) compared with measurement using BPM data.

Figure 3 displays measurements and predictions for

the off-momentum 3rd-order resonance driving term f_{3000} [5, 6] at all BPMs around the SPS. The prediction in the left picture includes the fitted multipole errors; in the right picture it does not. The agreement is better, but not perfect, if the fitted multipole errors are taken into account, which supports our hypothesis of distributed errors.

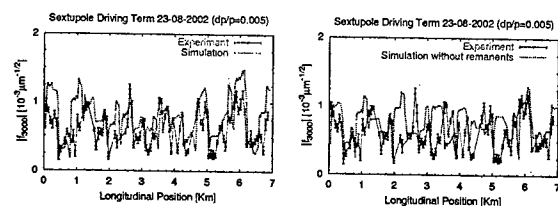


Figure 3: Amplitude of f_{3000} versus the longitudinal position measured at $\delta = 0.005$, and the prediction with (left) and without (right) the fitted multipole errors.

For the octupolar driving term f'_{4000} [5, 6], the simulation (including the fitted multipole errors) and measurement are compared in the left picture of Fig. 4. Except for the first experimental peak at the beginning of the ring, the agreement between model and experiment is consistent within the error bars.

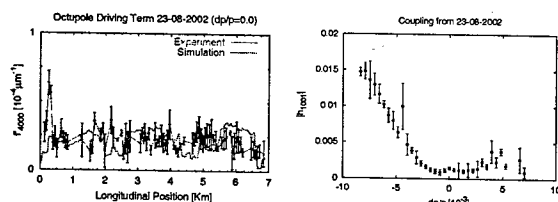


Figure 4: Left: measured and predicted amplitude of the term f'_{4000} versus longitudinal position at $\delta = 0.0$; right: measured coupling resonance driving term versus δ .

From turn-by-turn beam positions recorded after horizontal kick excitation, we can also infer the horizontal betatron phase advance between BPMs. Measuring for two different values of δ and computing the difference at every BPM yields the chromatic phase advance around the ring. Figure 5 compares this with the model prediction. Again, including the fitted errors improves the agreement.

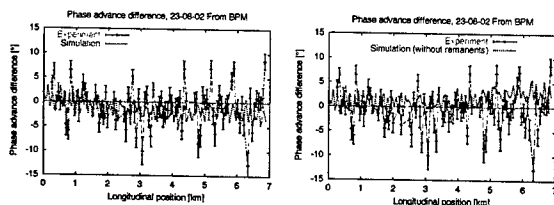


Figure 5: Measured and predicted phase advance differences for $\delta = 0.0$ and 0.005 vs. longitudinal position with (left) and without (right) the fitted multipole errors.

COUPLING & ORBIT

We also measured the strength of the linear coupling as a function of the energy deviation. The coupling was inferred from the secondary spectral lines, as described in [5]. The result is shown in the right picture of Fig. 4. For negative δ , the dependence is almost linear, but for positive δ the coupling stays small and fairly constant. If this dependence is caused by a progressive distortion of the vertical closed orbit, when the vertical tune approaches the integer resonance as a result of the momentum deviation, the vertical orbit should roughly vary as $1/[\sin(\pi Q_y)(1 + \delta)]$. This is indeed the case, as shown in the left picture of Fig. 6 for a single BPM. Plotting the fitted slope (i.e., the slope of the line in the left picture) for all the BPMs of the ring, we obtain the right picture. The number of oscillations coincides with the integer tune.

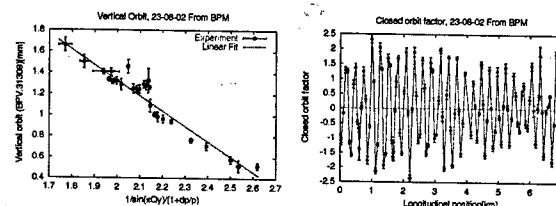


Figure 6: Left: vertical closed orbit vs. $1/[\sin(\pi Q_y)(1 + \delta)]$ at BPV.31309; right: fitted slope ("closed orbit factor") at all BPMs versus the longitudinal location.

CONCLUSIONS

As in previous years, in 2002 the nonlinear optics model of the SPS was updated from the measured nonlinear chromaticity. Compared with earlier measurements the momentum range was widely increased. We simultaneously sampled the turn-by-turn beam position at all BPMs around the ring, which gives a better resolution and also provides many complementary optics informations. And we applied two different optics codes for the fits. The nonlinear multipole components obtained using MAD and SAD are consistent, except for one of the two octupole errors (K_{4d}) and for the decapoles. These are the multipoles which also are most sensitive to the momentum range of the fit. To validate the model, its predictions were compared with various complementary optics measurements, such as the detuning with amplitude, resonance driving terms, and chromatic phase advance. In general, the fitted nonlinear field errors improve the agreement between predictions and measurements, even locally around the ring.

REFERENCES

- [1] G. Arduini, et al., CERN SL Note 2001-030 MD; SL Note 2001-049 MD; and Proc. EPAC 2002, Paris, p. 1220.
- [2] J. Wenninger, CERN SL-Note-2002-041 OP.
- [3] H. Grote, F.C. Iselin, CERN/SL/90-13 (AP).
- [4] K. Oide, et al., <http://acc-physics.kek.jp/SAD/sad.html>.
- [5] R. Tomas, PhD thesis, U. de Valencia 2003.
- [6] R. Bartolini, F. Schmidt, Part. Acc. 59, p. 93 (1998).

SLOW GROUND MOTION MODELLING OF DIAMOND

J. K. Jones, ASTeC, Daresbury Laboratory, Warrington WA4 4AD, UK

Abstract

The need for high stability in third generation light sources has produced strict requirements on the design of the foundations. The specification for the concrete floor stability is a critical task, which can have a major cost impact. A careful assessment of the effects of slow ground motion on the accelerator is therefore required. This paper presents the results of simulations using various ground motion models for the DIAMOND storage ring and the booster synchrotron. The modelling is implemented in flexible manner through the use of a Mathematica to MAD interface. This interface provides various high level functions such as access to an SVD algorithm, which provides effective correction of the closed orbit distortions, the implementation of motion on girders and the statistical analysis and graphical presentation of results.

INTRODUCTION

The DIAMOND project consists of a 3GeV electron storage ring with a full-energy booster synchrotron injector [1]. The storage ring is designed with an aggressive 2.7nm-rad emittance, with an emittance ratio of 1%. Under such conditions the long-term stability of the electron beam is essential to maintaining good photon beam quality for users. The stability of the electron beam is generally separated into two regimes; stability over timescales of a few seconds or less, and stability over the timescale of a few seconds to a few months. The most destructive and unpredictable effect on the stability in the longer timescale regime is that due to the motion of the ground underlying the accelerator complex. In the initial phases of machine construction and operation, ground motion due to settling of the newly loaded ground will be dominant. After this time, experience from many accelerators shows that the magnitude of the ground motion decreases to a constant magnitude that continues for the life of the accelerator.

Assuming a perfectly aligned accelerator initially and excluding the short term effects of creep, misalignment of accelerator elements relative to the design orbit grows with time by a random walk process, this is the basis of the ATL model. The misalignment of accelerator elements resulting from this eventually leads to limitations on the operation of the machine, for example because of limits on maximum corrector strengths used to compensate for this. Once the magnitude of ground motion induced displacement of elements is sufficiently large, a re-survey and re-alignment of the accelerator back to some, possibly different, nominal required orbit is undertaken. The frequency of this re-alignment is directly influenced by the rate of growth of element misalignments the

sensitivity of the accelerator to such motions, and the corrector strength available.

Since it is only differential motion of accelerator elements that are problematic, the electron beam sensitivity to ground motion vibrations can be reduced by use of a single cast floor, thus increasing the correlated element motion and reducing the differential motion.

The use of girders to mount accelerator elements leads to locally correlated motion. Although girder assemblies can amplify the effects of ground motion in some frequency ranges, in the slow ground motion regime the correlated motion reduces the harmful differential motion of the magnetic elements.

Analytic models can be used to assess the effects of slow ground motion on the alignment of the accelerator and the effect on electron beam properties. Several of these models have been used to assess the effects of slow ground motion on the DIAMOND storage ring and booster synchrotron. In the case of the DIAMOND accelerators however, re-survey and re-alignment intervals have been specified, from which the maximum allowable motion of the magnetic elements and so the floor can be specified. The simulations must therefore produce a specification for floor stability that is required so that ground motion does not limit the machine performance within the specified re-alignment interval.

METHODS FOR SIMULATING GROUND MOTION

Pure simulation tools for analysing the floor motion of DIAMOND can be split into two regimes; the effects of (a) plane wave motion and (b) diffusive motion. However, at a specific instance in time a diffusive model can be thought of as a superposition of many planar waves of differing phases and amplitudes. Plane wave motion is then a specific case of a diffusive motion model.

The two methods used for modelling the DIAMOND floor are (a) diffusive motion ATL model, and (b) planar wave Fourier and Gaussian model. These are described below.

ATL Diffusive Motion Model

The ATL model for ground motion is based on empirical evidence collected at many different sites around the world. The ATL model can be thought of as a first order expansion of the real ground motion. This model describes the diffusive or Brownian motion that unconnected points on the ground (or structures attached to the ground) undergo which are uncorrelated and act as a low intensity baseline to the regular (in time and space) motion due to propagating waves in the upper Earth's

crust. According to this empirical model, the variance of the relative motion of two points scales as the product of the spatial and temporal interval between measurements. The proportionality constant A gives the magnitude of the motion, and may be different at every site as it depends strongly on local ground conditions. The value of A is usually given in $\mu\text{m}^2/(\text{m.s})$, although this can be converted to a σ value of ground motion in $\mu\text{m}/10\text{m}/\text{year}$, which is preferred by the project architects.

Applying the ATL model to a circular accelerator is a non-trivial task. Previous work on modelling ATL ground motion was applied to the linear accelerator case. The method for application of ATL to the circular accelerator case has been derived by N. Walker and A. Wolski [2], and is based around the use of co-variant matrices. In essence, the method overcomes the linear distance problem by applying a magnitude of motion to each point based on its variance to every other point in the accelerator. Representative ATL motion can be seen in Figure 1.

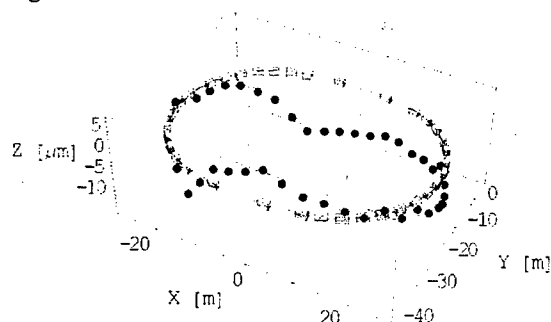


Figure 1: Representative ATL motion over 6 months, with an A factor of $10^{-7} \mu\text{m}^2/(\text{m.s})$, in the DIAMOND booster synchrotron. Quadrupole positions are highlighted as blue points

Due to the diffusive nature of the ATL model, short range differential motion can develop to be unrealistically large, although it is semi-bounded by the magnitude of the A proportionality constant. To ensure a more realistic distribution of motion to the elements, it is important to apply the motion to the magnet girder assemblies. This limits the differential motion between adjacent elements whilst still allowing long range differential motion to occur. It is also a triviality to ensure that the magnets are rotated upon the girders.

Fourier and Gaussian Motion Models

Modelling the slow ground motion as either a Fourier or Gaussian distributed error is useful for the situations where floor deformations are correlated over long distances.

Relative motion of accelerator elements can be decomposed into a set of Fourier harmonics, with the lowest order harmonic being a tilt in the machine axis. By analysing these harmonics individually one can see the relative effects on the accelerator of different frequencies of ground motion. This can then be compared to known

ground motion at the chosen site, giving an insight into the realistic sensitivity of the machine.

Gaussian distributed errors are a special case of applied ground motion, that deals only with the case of localised deformations in the underlying ground. A Gaussian distributed error can apply in superposition with other ground motion errors.

Both of these error distributions are shown in Figure 2.

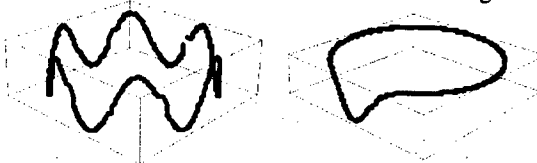


Figure 2: 6th order Fourier distributed error (left) and a 120m wide Gaussian distributed error (right) around the DIAMOND storage ring.

COMPUTER SIMULATIONS

All of the simulations of ground motion modelling are performed through the Mathematica programming environment. A flexible interface to the MAD accelerator code [3] has been written that allows a close integration with the Mathematica environment. Within this Mathematica-to-MAD package, lattices can be defined and modified, using the functions internal to Mathematica. All of the mathematical modelling of ground motion errors is performed within Mathematica, and then the element displacements are written to a MAD deck and the effects on the lattice dynamics calculated.

By using the high-level functionality of Mathematica environment, it becomes trivial to apply element displacements to sets of elements on girders, and to ensure that the girder is tilted and rotated as required. This enables a much more realistic error model to be applied to the accelerator.

The interface between MAD and Mathematica allows functionality to be added to the MAD program without the need to modify the original source code. SVD correction of the closed orbit error is one such functionality that has been added. By using MAD to calculate the BPM response matrices, the mathematical functions within Mathematica then make it easy to invert the matrix and to enable powerful manipulation of the results. The original lattice can then be re-written with newly redefined corrector strengths, and MAD used to calculate the new closed orbit.

As all of the lattice information, and the results of simulations, is available within the Mathematica environment, visualisation of data becomes much simpler. Operations that require basic lattice information, such as lengths or strengths, can be accessed without the need to call MAD, and can be accessed without user intervention. This automation greatly simplifies the analysis of data and can also allow increased complexity of models without a proportional increase in effort.

STORAGE RING MODELLING

The DIAMOND storage ring has two correction schemes. The first is for the fast motion of the beam, and features 96 combined horizontal and vertical corrector magnets, two located either end of each long straight section. The second scheme is used to address all motion occurring over periods of greater than seconds, including slow ground motion. The slow correction scheme consists of 168 combined correctors, located in the sextupole magnets. The slow corrector magnets have a specified maximum deflection of 0.8mrad. Previous work has shown that 0.3mrad of this specification should be allowed to correct static alignment tolerances of magnets upon the magnet girder assemblies. With some contingency, this leaves 0.3mrad available for slow ground motion correction.

The results of applying varying magnitudes of ATL-like ground motion on the storage ring is shown in Figure 3.

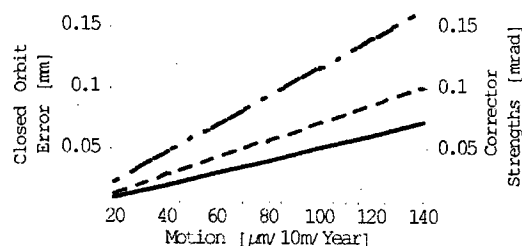


Figure 3: Corrector strength requirements (dashed) and closed orbits at the dipole (solid) and insertion devices (dot dashed) source points in the DIAMOND storage ring under the influence of varying magnitudes of ATL-like ground motion.

The results in Figure 3 show large electron beam offsets at the photon source points. Since this offset is corrected, further minimisation of the electron beam motion at these points would increase the closed orbit error in the rest of the machine, potentially leading to decreased lifetime effects. The diffusive motion inherent in the evolution of these errors would also require an undesirable number of realignments of optical components. For these reasons a specification of 120 $\mu\text{m}/10\text{m}/\text{year}$ for the storage ring floor motion has been chosen.

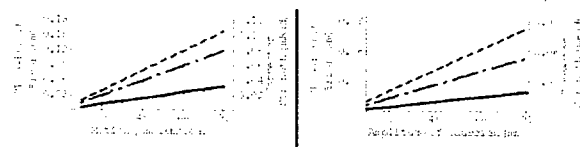


Figure 4: Corrector strength requirements (dashed) and closed orbit at the dipole (solid) and insertion devices (dot-dashed) in the DIAMOND storage ring under the influence of Fourier (left) and Gaussian (right) ground motion.

With the Fourier and Gaussian error models, the storage ring lattice is more sensitive to Fourier errors. This is shown in higher corrector requirements.

The analysis, shown in Figure 4, leads to a ground motion specification of 100 $\mu\text{m}/10\text{m}/\text{year}$ based upon residual closed orbit error specifications.

BOOSTER MODELLING

The DIAMOND booster synchrotron includes 22 horizontal and 22 vertical steering magnets, with 22 combined H/V BPMs.

Currently the booster apertures include an allowance of up to 1.4mm for the effects of ground motion and other factors not already included. The ground motion effects are directly influenced by the choice of dynamically ramped correctors, or static correction. In the case of static correction at injection energy, closed orbit errors at 3GeV will be significantly larger, and therefore floor specifications much tighter.

Inclusion of the effects of ATL, Fourier and Gaussian errors gives a specification for the allowable ground motion of greater than 500 $\mu\text{m}/10\text{m}/\text{year}$ with dynamic correction. With only static correction this drops to much less than 100 $\mu\text{m}/10\text{m}/\text{year}$, and leads to an increase in the defined booster apertures. This can be partly overcome by performing re-alignment of the machine more often than the 6 month interval the specification currently calls for.

CONCLUSIONS

Due to the strong-focusing nature of the DIAMOND storage ring, the contribution of slow ground motion on the degradation of beam optics is considerable. The accelerator floor plays an important role in damping the underlying ground motion and so has significant effects in determining the interval between re-survey of the machine, and so the absolute long term stability of the electron and photon beams. Modelling of the floor motion as diffusive random displacements has lead to a floor specification that should enable the DIAMOND storage ring to operate within its long term stability goals for the specified 6 monthly periods between re-alignments.

The requirements on the booster floor motion are less stringent than the storage ring. The main limitation is the requirement to maintain less than 1.4mm of closed orbit error, due to aperture restrictions. Under the assumption of dynamically ramped correctors the specification given is consistent with a 6 monthly re-alignment of the machine.

REFERENCES

- [1] V P Suller, "Status Of The Diamond Light Source Project", EPAC'02, Paris, June 2002.
- [2] Andrzej Wolski, Nicholas Walker, "A Model of ATL Ground Motion for Storage Rings", these proceedings.
- [3] H. Grote and F.C. Iselin, "The MAD Program", CERN/SL/90-13 (1995).

IMPACT OF NARROW GAP UNDULATORS ON THE ADVANCED LIGHT SOURCE*

D. Robin[†], C. Steier, W. Wan, A. Wolski, LBNL, Berkeley, CA, 94720 USA

Abstract

In low emittance synchrotron light sources the main source of beam loss is intrabeam or Touschek scattering. In most cases the Touschek scattered particles get lost on the vacuum chamber with the narrowest vertical gap. The particles reach the vertical chamber from either diffusion or coupling of the particle motion from the horizontal to the vertical plane. The beam lifetime can be very sensitive to the size of the vertical chamber that can limit the dynamic momentum aperture. The reduction in lifetime limits the minimum size of the chamber that can be installed in the ring. In this paper we examine the effect of the size of the vertical apertures on the beam lifetime at the ALS under various different machine conditions. We show that there are conditions where one can make the beam lifetime much less sensitive to the size of the vertical aperture.

INTRODUCTION

Third generation light sources have been very successful. Nearly all have met and are exceeding their brightness performance expectations. In some cases the brightness delivered is several orders of magnitude higher than the design values. There are several reasons for this. The three main ones are that the facilities are operating with larger currents, smaller emittances (both horizontal and vertical) and beta-functions, as well as insertion devices with smaller vertical gaps. Still there is interest in increasing the brightness further. In particular for the ALS the interest is increasing the brightness for photon starved experiments such as photon-in photon-out and diffractive imaging experiments. There is also interest in extending the range of undulator radiation to higher energy. Presently undulator radiation is being used up to 2keV but with small period narrow vertical gap permanent and superconducting magnet devices it will be possible to extend the spectrum to much higher energies.

Of concern is that smaller gap vacuum chambers required for these insertion devices will increase the loss rate of the particles. Already with the existing chambers, it is known that most of the particle loss occurs on the narrowest gap chamber. The chamber is located in a region where the full gap is 8.9 mm with a beta-function of 5.1 m. Also experimental tests using vertical scrapers to further limit the physical aperture have shown that the lifetime can be strongly dependent upon the size of the vertical aperture [1]. It is desirable to operate in a region where the

lifetime is less sensitive to the aperture. In this paper we investigate several different operational modes where the lifetime has markedly different dependence upon the size of the vertical aperture.

LIFETIME VERSUS GAP

Using a vertical scraper, one can measure the dependence of the lifetime on gap. Lets look at three different cases:

1. High-Coupling,
2. Low-Coupling, and
3. Eta-Wave.

In all three cases the ring was filled with 24 mA with 1.5 mA/bunch. In the High-Coupling case the vertical emittance is increased to 2% of the horizontal emittance by powering one family of skew quadrupoles to excite the linear coupling resonance. In the Low-Coupling case 18 skew quadrupoles are adjusted to correct the vertical emittance to 0.35% of the horizontal. In the Eta-Wave case the 18 skew quadrupoles are used to correct the coupling then 12 skews are used to introduce a vertical dispersion wave (i.e. Eta-Wave) without exciting the coupling resonance to increase the vertical emittances to 2% of the horizontal emittance [3] (i.e. emittances for blue and red cases are equal). The results are plotted in Fig. 1.

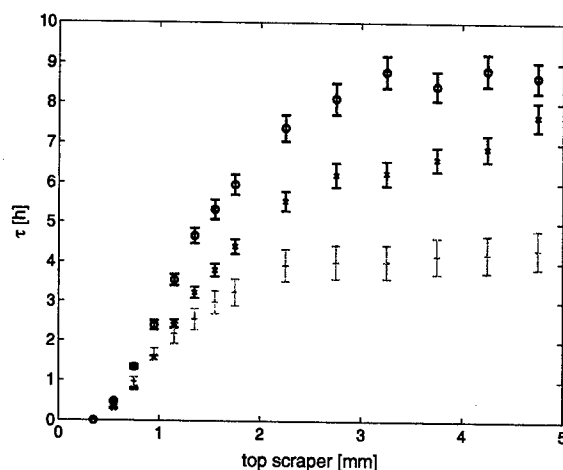


Figure 1: Lifetime versus vertical scraper for High-Coupling (red), Low-Coupling (green), and Eta-Wave (blue).

There is a marked difference in the dependence of lifetime on scraper position for the three cases. When the scraper is out at 5 mm, the lifetime of the High-Coupling

* This work was supported by the Director, Office of Energy Research, Office of Basic Energy Sciences, Materials Sciences Division of the U.S. Department of Energy, under Contract No. DE-AC03-76SF00098.

[†] DSRobin@lbl.gov

case is 8 hours and the Eta-Wave case is 9 hours. The difference is due to the larger dynamic momentum aperture of the Eta-Wave lattice. The lifetime of the Low-Coupling lattice is about 4 hours. The reduction in lifetime is expected due to the higher density of the Low-Coupling case. One sees that the High-Coupling case is much more sensitive to the position of the scraper and the Low-Coupling case is the least sensitive. In fact in the Low-Coupling case the lifetime is only impacted by the scraper at scraper values less than 2 mm. Also the Eta-Wave case is much less sensitive to the position of the scrapers. Earlier theoretical studies of the Swiss Light Source [4] showed similar dependencies.

Analysis

In the ALS the lifetime is strongly limited by Touschek scattering. After a particle is scattered, the energy of the particle changes. If this happens in a region of nonzero dispersion the energy change results in a horizontal oscillation. This can then result in an increase in the vertical motion through resonance excitation and particle diffusion. If the vertical motion is large enough, the particle will collide with the chamber. An illustration of this process is seen in Fig. 2 where a particle is launched with an initial offset of 12 mm horizontally, 1 mm vertically, and an energy offset of $\delta = 2\%$ and tracked turn-by-turn with synchrotron oscillations and damping. In the figure one sees periods of rapid growth to large vertical amplitudes. At one point the particle reaches an amplitude larger than 4 mm which is the size of the vacuum chamber. To calculate the momentum aperture it is necessary to know how much energy can that particle gain or lose and still remain in the ring after a particle undergoes a Touschek scattering.

Another way [1, 5] to illustrate the effect of Touschek scattering is to plot the Amplitude versus energy at one point in the ring (e.g. the injection point) for a particle scattered at some point s in the ring. This is shown in Fig. 2. If the particle changes energy it will increase its amplitude. At the injection point the induced amplitude would be $\sqrt{\frac{H(s)}{\gamma(inj)}}\delta$ where $H = \gamma\eta^2 + 2\alpha\eta\eta' + \beta\eta'^2$. Next the particle will undergo synchrotron oscillations and slowly damp back to zero. During this time the particle may encounter a region of large diffusion causing the particle to become lost. To predict the size of the momentum aperture, it is necessary to map out all the regions that the particle may encounter after a given energy and amplitude change and to determine the largest energy change where no dangerous regions are encountered.

In order to understand the difference in the three cases, simulations were made on models fitted with measured response matrices [6, 7]. Using the fitted models the particles were tracked using a symplectic integrator [8, 9]. In addition we used a post processor [10] to compute the frequency maps. Because we were interested in the Touschek lifetime particles were launched at the injection point with various different initial amplitudes in x and δ , and a small fixed vertical amplitude in y of 0.05 mm and tracked with-

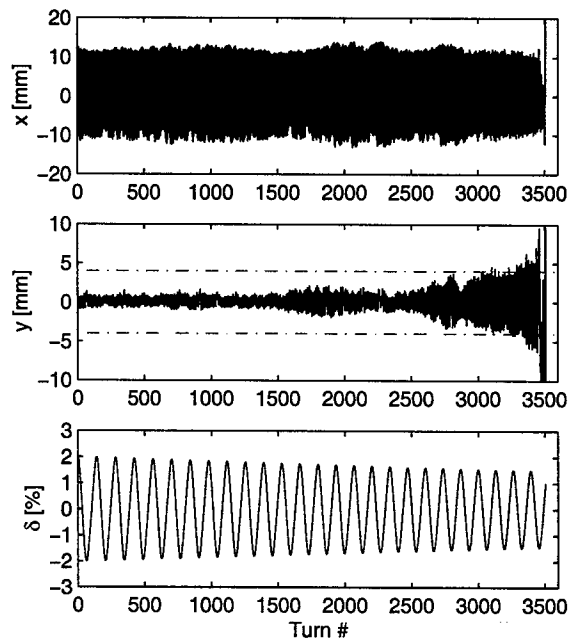


Figure 2: Simulation of the horizontal (top), vertical (middle), and longitudinal (bottom), position versus turn number of a particle which was launched with initial coordinate of $x = 12\text{mm}$, $y = 1\text{mm}$, and $\delta = 2\%$.

out synchrotron oscillations or damping for 1024 turns or until lost. A $\pm 4\text{mm}$ aperture was included in the simulation.

In Fig. 4 the initial coordinates of the particles that survived are plotted for all three cases. All initial conditions that survived are plotted in color and those that did not are not plotted. The color indicates the maximum vertical amplitude that a particle reached in the 1024 turns. Red corresponds to 4 mm, yellow to 2.5 mm and blue is less than one mm. Also on the plot the induced amplitudes are plotted as red lines. In each plot there are two sets of red lines. The steeper ones correspond to the induced amplitude for particles that get scattered in the arcs and the flatter lines correspond to particles that get scattered in the straight [1].

What determines the momentum aperture in the arcs and the straights is the maximum area inside the lines in where the motion can stably damp back to the closed orbit. One sees that the High-Coupling case in Fig. 4, is very different from the other two. In particular there is a loss region near $\delta = 0.02$ which in the High-Coupling case is wider and collapses rapidly if we limit the aperture. If one decreases the aperture from 4 mm to 3 mm for instance, the maximum δ reduces to about 0.018 due to this region. However this region does not strongly effect the other two cases until one reduces the gap further to about 2 mm. Also on the negative δ the aperture is reduced with respect to the other two cases from about 0.024 to 0.022 at 4mm for particles scattered in

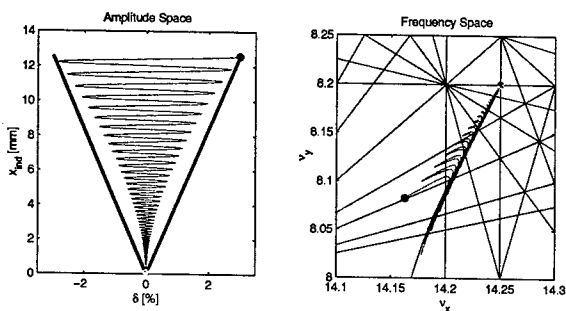


Figure 3: Particle motion in Amplitude (left) and Frequency space (right) after undergoing Touschek scattering

the arcs and that boundary is more sensitive to reducing the vertical aperture than the other two cases. In the High-Coupling case, the aperture starts to further reduce for a vertical aperture of about 2 mm whereas it reduces at 1 mm for the other two cases.

Using a frequency analysis post processor, we then can determine what is the cause. In all cases the region at $\delta = 0.02$ is determined by the linear coupling resonance which is more dangerous for the High-Coupling case. On the negative δ side the restriction are a number of resonances intersecting near $\nu_x = 14.15$ and $\nu_y = 8.075$ with the third order coupling resonance $\nu_x - 2\nu_y = -2$. Again the effect of these resonances as a function of gap is stronger for the High-Coupling case.

SUMMARY

These studies show that one can minimize the reduction of lifetime with vertical gap by controlling the beamsizes with vertical dispersion rather than exciting the linear coupling resonance. With the Low-Coupling and Eta-Wave cases it is possible to reduce the half gap to 2.5 mm without impacting the lifetime. There is good agreement of the measured lifetime versus vertical gap and tracking studies. Frequency analysis of the tracking data suggests that the reduction of lifetime with gap in the High-Coupling case is due to strong excitation of linear and nonlinear coupling resonances.

REFERENCES

- [1] C. Steier et al., Phys. Rev. E 65, 056506 (2002)
- [2] D. Robin et al., Phys. Rev. Lett., 85, pp. 558, (2000)
- [3] C. Steier et. al., "Coupling Correction and Beam Dynamics at Ultralow Vertical Emittance in the ALS", Proceedings of this meeting.
- [4] M. Boege, and A. Streun, in *Proceedings of the 18th Particle Accelerator Conference*, New York, 1999 (IEEE, Piscataway, NJ, 1999), 2430.
- [5] A. Nadji, et al. in *Proceedings of the 17th Particle Accelerator Conference*, Vancouver, 1997 (IEEE, Piscataway, NJ, 1997), 1517.
- [6] D. Robin, J. Safranek, and W. Decking, Phys. rev. ST Accel. Beams 2, 044001 (1999).
- [7] J. Safranek, Nucl. Instr. & Methods, A388, 27 (1997)
- [8] R. Ruth, IEEE Trans. Nucl. Sci., 30, 2669 (1983).
- [9] A. Terebilo, in *Proceedings of the 19th Particle Accelerator Conference*, Chicago (IEEE, Piscataway, NJ, 2001), 1692.
- [10] J. Laskar, in *Proceedings of 3DHAM95 NATO Advanced Study Institutes*, S'Agaro, 1995 (Kluwer Academic Publishers, Dordrecht, The Netherlands, 1999), 134.

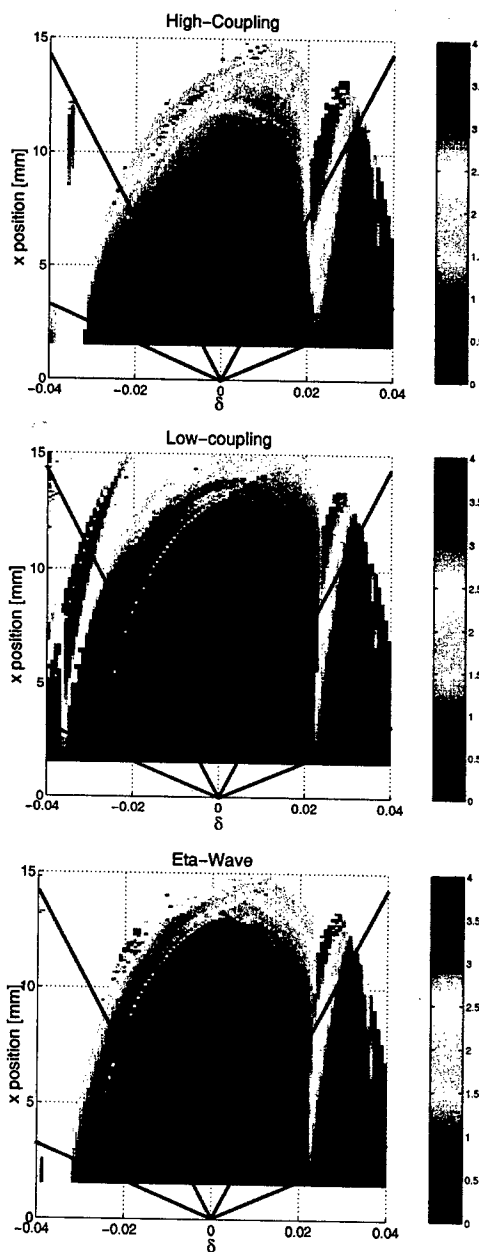


Figure 4: Off energy dynamic aperture for the High-Coupling, Low-Coupling, and Eta-wave versus gap.

ID MODELING AT THE ALS*

Weishi Wan, Hiroshi Nishimura, David Robin, Christoph Steier, LBNL, Berkeley, CA 94720, USA

Ying Wu, Duke University, Durham, NC 27708, USA

Etienne Forest, KEK, Tsukuba, Japan

Abstract

At the Advanced Light Source there are several projects being proposed that will require high field insertion devices. It is important that these devices do not significantly impact the performance of the machine. In particular they should not degrade the beam lifetime or injection efficiency. It is known that high field devices with large field roll off can impact the beam lifetime. It is therefore important to model the effect of the insertion devices including both transverse and longitudinal field roll off. In this paper we present the result of tracking studies using an explicit symplectic integrator with both transverse and longitudinal field roll off. The simulations show where sufficiently large field roll off will impact the beam lifetime.

INTRODUCTION

Due to the ever increasing number of insertion devices used in light sources, the impact of their presence on the beam dynamics becomes more and more of an issue. The problem is made more pronounced by the higher magnetic field and smaller gap of the up coming devices. Most existing insertion devices affect the beam mainly through linear focusing in the vertical plane. The change of phase advance between nonlinear elements (primarily sextupoles) causes change in the strengths of resonances excited. As a result, both injection efficiency and beam lifetime can be affected. Recent experience at SSRL shows that the octupole like component generated by the horizontal roll off of the field can have dramatic effects on the beam dynamics [1]. Since then the issue of horizontal field roll off has attracted more attention both from accelerator physicists and magnet designers.

The Femtoslicing project, currently under construction at the Advanced Light Source (ALS), requires two new insertion devices to be incorporated into the storage ring [2]. One of the design criteria is that the device should be "transparent" from the point of view of the beam. With no exception, the effect of the horizontal field roll off is the main question to be answered. The most economical way to answer this question and optimize the design is to develop simulation tools that takes into account all important effects of the insertion device on the beam dynamics. To this end, a symplectic integrator developed recently is adopted [3]. Together with an adequate field model and existing tools such as frequency map analysis, the designs of both insertion devices have been validated by the simu-

lation results. Furthermore, a case that horizontal significantly reduced dynamic aperture has been identified.

Following the introduction, we outline the setup of the simulation tools and the approach we take to study beam dynamics at the ALS. The simulation results are shown in the following section. Summary and acknowledgment are presented in the last section.

SIMULATION TOOLS

Over the years, frequency map analysis has been applied to the ALS and hence been verified by experimental data [4, 5]. As a result, frequency map analysis has become one of the standard tools for simulations on single particle dynamics. Until recently, the insertion devices has been modeled as a sequence of alternating dipole magnets, where the effect of the horizontal field roll off is not taken into account. As mentioned in the previous section, it is necessary to include this effect in the model if the design of an insertion device is to be validated before procurement order is placed. The newly developed symplectic integrator for insertion devices meets the demand perfectly [3]. The main assumption of the model is the paraxial approximation, which leads to a Hamiltonian that can be separated into solvable parts. It has been implemented in the code PTC [6] using the harmonic representation of the field.

In order to take advantage of the existing model quickly, the lattice of the ALS storage ring was imported into the code PTC and the frequency map analysis was performed separately. Since most of the simulation tools are integrated in the MATLAB environment, the symplectic integrator in PTC was soon rewritten in C and incorporated into the MATLAB based code Accelerator Toolbox [7]. This allowed us to add the new model of insertion devices directly to the existing infrastructure that does the tracking and the frequency map analysis in a integrated way. Comparison between the two versions of the model showed agreement up to the machine precision.

SIMULATION RESULTS

As mentioned in the introduction, two new insertion devices will be built for the Femtoslicing project. One is a wiggler with the period of 11.4 cm and the peak field of 1.9 T (named W11), placing an existing wiggler with the period of 16 cm (W16). The other one is an undulator whose period is 3 cm and peak field is 1.5 T (U3). Based on the success of W16 at the ALS and the lesson of the BL11 wiggler at SPEAR, the designers of these new insertion devices sought to keep the horizontal roll off small, as shown in Figure 1. The goal of the simulation is to de-

* Work supported by the Director, Office of Energy Research, Office of Basic Energy Science, Material Sciences Division, U.S. Department of Energy, under Contract No. DE-AC03-76SF00098

side whether these insertion devices significantly affect the beam dynamics and, if not, what is the safety margin of the designs.

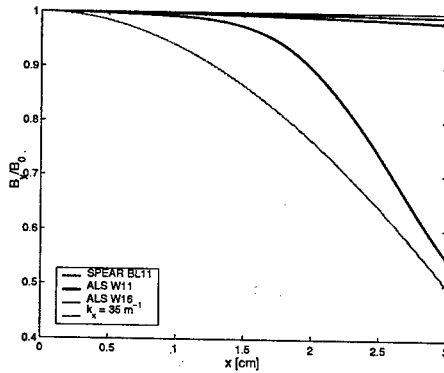


Figure 1: Horizontal field roll off of various insertion devices

The simulations are done using a lattice that is close to normal operating conditions. Random gradient errors are introduced to mimic errors in the real machine. Random skew quadrupole errors are used to reproduce $\sim 2\%$ coupling which is the way to maintain desired beam lifetime during user operations. Physical apertures, ± 30 mm horizontally and ± 4 mm vertically, are placed at the center of the injection straight and those of the insertion devices. Beta beating induced by the insertion devices is largely compensated by two families of quadrupoles nearby. In case of U3, two families of skew quadrupoles are adjusted to produce the vertical dispersion bump required during the operation of the Femtoscaling beamline [2]. The horizontal and vertical tunes are 14.25 and 8.20, respectively; the horizontal and vertical chromaticities are 0.4 and 1.4. In order to perform frequency map analysis, both synchrotron radiation and synchrotron oscillations are off.

Both longitudinal and horizontal roll off are modeled by a Fourier series with only one harmonic (Fig. 2). It is also clear that the vertical roll off is more severe than the real field which makes the simulation more pessimistic than reality. Since $k_y^2 = k_x^2 + k_z^2$ and $k_z \gg k_x$, the vertical roll off is dominated by the longitudinal roll off. When 8 harmonics are used to model the longitudinal roll off, relative error of the vertical roll off is below $3E-4$ up to 4 mm. As a benchmark, this model of 8 harmonics (fitted to the data of W11) was used once in the simulation and no appreciable difference in the beam dynamics was found. Since U3 has a much shorter period, the difference should be even smaller. Figure 3 and 4 show the effect of W11 on the beam dynamics. On-momentum frequency map analysis shows the dynamic aperture, which is important for injection. In case of ALS, injection orbit is about 8 mm off the design orbit horizontally. Figure 3 shows that the presence of W11 will not affect injection efficiency. Off-momentum frequency map analysis shows the momentum acceptance, hence the beam lifetime, because beam lifetime is mainly determined

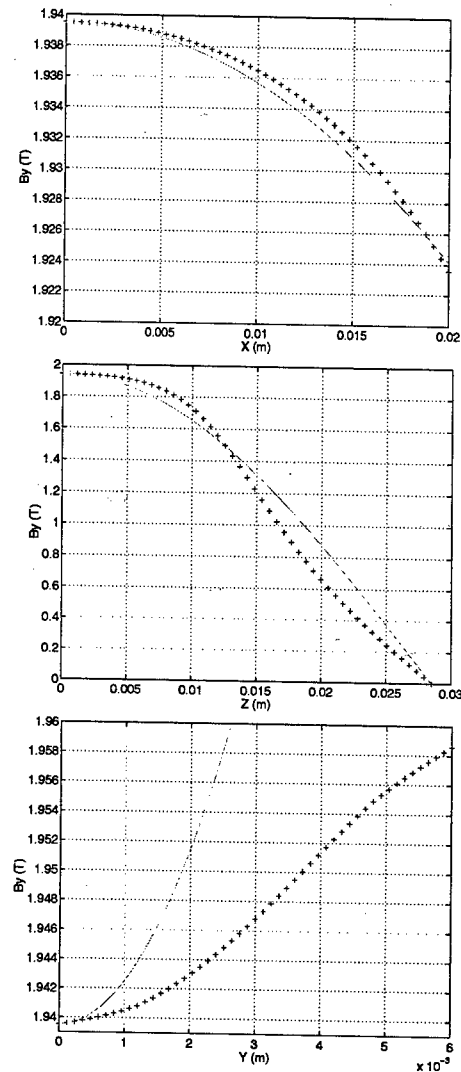


Figure 2: One harmonic field model for W11. The model for U3 looks qualitatively the same.

by Touschek scattering [2]. Figure 4 shows that momentum aperture is slightly worse with W11 on. Simulation of W11 with no horizontal roll off shows the same reduction in momentum.

In order to decide the safety margin of the horizontal roll off, several cases were studied with different k_x . No difference was found between the nominal case which $k_x = 6.3 \text{ m}^{-1}$ and the ones that $k_x = 7 \text{ m}^{-1}$ and 8 m^{-1} , respectively. When k_x is set to be 35 m^{-1} , comparable to that of BL11 (Fig. 1), dynamic aperture is reduced to about 6 mm (see Fig. 5).

Similar studies were done on the impact of U3. Even more so, the effect of the insertion device on the beam dynamics is hardly detectable.

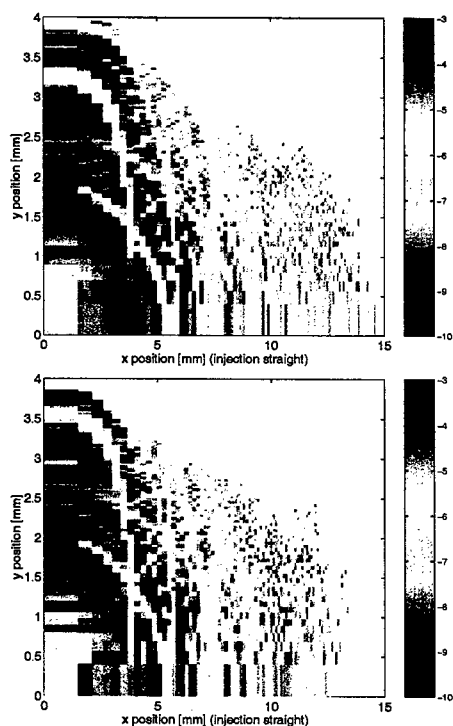


Figure 3: On-momentum frequency map analysis with the wiggler on (top plot) or off (bottom plot)

SUMMARY

A newly developed symplectic model for insertion devices has been used in studying beam dynamics issues. This model was successfully rewritten in C and integrated into the existing MATLAB based simulation tools. Design of two upcoming insertion devices were evaluated and validated from the beam dynamics point of view. A by-product of the study is that a rather straightforward way of modeling the field of planer insertion devices was found. Both the longitudinal and the horizontal roll off are fitted by a Fourier series. The product of the two series represents the field in the midplane. Using the standard harmonic representation, the off-plane expansion is done through the relation $k_{yij}^2 = k_{xi}^2 + k_{zj}^2$. The result is that, for W11, the error is below 30 Gauss at $x = 2$ cm and $y = 4$ mm.

The authors would like to thank S. Marks and S. Prestemon for providing field data and S. Marks, S. Prestemon, R. Schlueter and R. Schoenlein for stimulating discussions.

REFERENCES

- [1] J. Safranek, C. Limborg, A. Terebilo, K. I. Blomqvist and P. Elleaume, "Nonlinear Dynamic in a SPEAR Wiggler", Phys. Rev. ST Accel. Beams **5**, 010701 (2002).
- [2] Christoph Steier, *et al.*, "Accelerator Physics Challenges of the FS-Slicing Upgrade at the ALS", these proceedings.
- [3] Y. Wu, *et al.*, "Symplectic Models for General Insertion Devices", in *Proc. 2001 Particle Accel. Conf.*, 459 (2001).

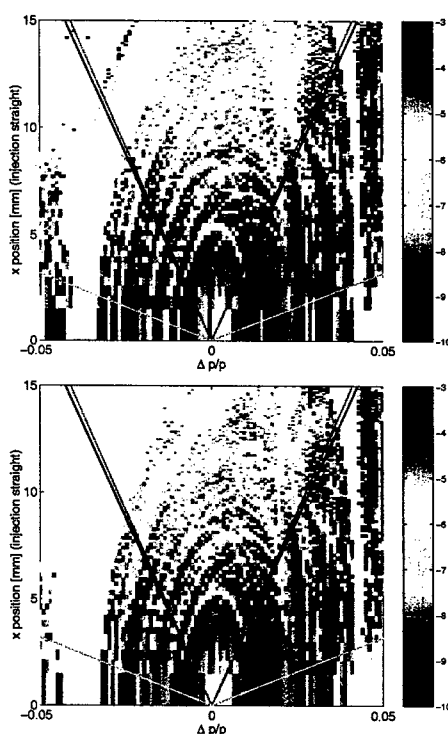


Figure 4: Off-momentum frequency map analysis with the wiggler on (top plot) or off (bottom plot)

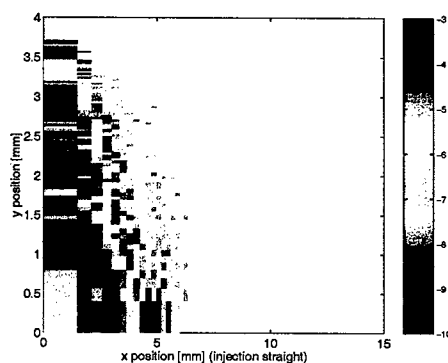


Figure 5: On-momentum frequency map analysis with the wiggler on and with vere horizontal roll off

- [4] D. Robin, C. Steier, J. Laskar and L. Nadolski, "Global Dynamics of the Advanced Light Source Revealed through Experimental Frequency Map Analysis", Phys. Rev. Lett. **85**, 558 (2000).
- [5] Christoph Steier, *et al.*, "Measuring and Optimizing the Momentum Aperture in a Particle Accelerator", Phys. Rev. E **65**, 056506 (2002).
- [6] E. Forest, F. Schmidt and E. McIntosh, "Introduction to the Polymorphic Tracking Code", KEK Report No. 2002-3, 2002 (unpublished).
- [7] A. Terebilo, "Accelerator Toolbox for MATLAB", SLAC-PUB-8732, 2001 (unpublished).

MAXWELL-LORENTZ EQUATIONS IN GENERAL FRENET-SERRET COORDINATES

Andreas C. Kabel*

Stanford Linear Accelerator Center, Stanford, CA, USA

andreas.kabel@slac.stanford.edu

Abstract

We consider the trajectory of a charged particle in an arbitrary external magnetic field. A local orthogonal coordinate system is given by the tangential, curvature, and torsion vectors. We write down Maxwell's equations in this coordinate system. The resulting partial differential equations for the magnetic fields fix conditions among its local multipole components, which can be viewed as generalization of the usual multipole expansion of the fields of magnetic elements.

MOTIVATION

The problem at hand came about while implementing a generalized co-moving coordinate system in TraFiC4 [1], which, in the generalized case, is curvilinear and non-orthogonal.

The usual approach to describing the field content of magnetic elements in accelerator physics is the expansion in multipoles. This is based on the fact that the magnetic field in vacuum can be derived from a potential obeying Laplace's equation; assuming a symmetry along one axis, it reduces to the two-dimensional Laplace equation, which is solved by analytic functions of a complex variable.

Strictly speaking, this approach is only admissible in straight section, where the co-moving coordinate system is cartesian. In curved sections, one has to use curvilinear coordinates, and the Laplace operator changes its shape, leading to a different set of solutions.

Furthermore, the transformation to curvilinear changes the equation of motion, introducing inertial forces.

In this paper, we write down the Maxwell-Lorentz equations for the case of an external purely magnetic field in a coordinate system co-moving on the orbit induced by the external field. We describe that orbit in terms of its local curvature and torsion; the Laplace and Lorentz equations are given to all orders in this frame, Laplace's equation is solved for two special cases.

FRENET-SERRET COORDINATES

We consider the orbit particle in the usual description of an accelerator. Ignoring energy changes, its trajectory is completely determined by its initial conditions and the external magnetic field.

We use the arc length s to parametrize its trajectory $\vec{r}(s)$. Then, we define the usual local dreibein by the Frenet field

frame:

$$\vec{E}_s := \vec{t}(s) = \vec{r}'(s)$$

$$\vec{E}_x := \vec{n}(s) = \frac{1}{k} \vec{t}'(s)$$

$$\vec{E}_y := \vec{b}(s) = \vec{t}(s) \times \vec{n}(s)$$

where k is the curvature. We also introduce the torsion

$$w = \frac{1}{k^2} \det(\vec{r}', \vec{r}'', \vec{r}''')$$

We express all quantities in the coordinate system spanned by \vec{E}_i , i.e. a vector \vec{R} is decomposed as $\vec{R}(s, x, y) = \vec{r}(s) + x\vec{n}(s) + y\vec{b}(s)$.

The magnetic field is scaled such that

$$\vec{t} = \vec{t} \times \vec{B}$$

i. e., we absorb charge and energy into the field.

After some algebra, we find

$$\vec{B}_y = -k$$

$$\vec{B}_s = -w \quad (1)$$

$$\vec{B}_x = 0$$

where the index labels components with respect to \vec{E}_i and barred quantities are values on the trajectory.

THE EQUATIONS OF MOTION

We now look at a particle with trajectory $\vec{x}(t) = x(t)\vec{n}(s(t)) + y(t)\vec{b}(s(t)) + \vec{r}(s(t))$, where the coordinate s is implicitly defined by $\vec{t}(s(t)) \cdot (\vec{r}(s(t)) - \vec{x}(t)) = 0$. The equations of motion for the coordinates x, y, s read:

$$\dot{x} = v_x + yw\dot{s}$$

$$\dot{y} = v_y - xw\dot{s}$$

$$\dot{s} = \frac{v_s}{1 - kx}$$

and

$$\ddot{x} = a_x + x(\dot{s}^2(w^2 + k^2)) + 2\dot{y}w\dot{s} + yw\ddot{s} + (yw' - k)\dot{s}^2$$

$$\ddot{y} = a_y - 2\dot{x}w\dot{s} + yw^2\dot{s}^2 - xw'\dot{s}^2 - xw\ddot{s}$$

$$\ddot{s} = \frac{a_s + 2\dot{x}k\dot{s} + (xk' - ywk)\dot{s}^2}{1 - kx}$$

where v_i and a_i are the components of the particle's velocity and external acceleration.

*Work supported by Department of Energy contract DE-AC03-76SF00515.

Putting in the Lorentz equation with magnetic fields B_i , we have

$$\begin{aligned} a_x &= (\dot{y} + xw\dot{s})vB_s - \dot{s}(1 - kx)vB_y \\ a_y &= (1 - kx)vB_x - (\dot{x} - yw\dot{s})vB_s \\ a_s &= (\dot{x} - yw\dot{s})vB_y - (\dot{y} + xw\dot{s})vB_x \end{aligned}$$

where $v = v_s^{\text{Orbit}}$. The expressions for the second derivatives of the coordinates contain centrifugal (proportional to x, y) and Coriolis (proportional to $\dot{x}, \dot{y}, \dot{s}$) and higher-order terms. They reduced to small quantities ($O(v - v_s), O(kx)$) by the Lorentz force for the values given in (1).

THE OFF-ORBIT MAGNETIC FIELD

We are now interested in the external components of the acceleration. They are given by the external magnetic field; they can, however, not be arbitrary as the magnetic field has to fulfill Maxwell's equations. To find the conditions for b_x, b_y, b_s , we write down the metric tensor for the curvilinear coordinate system defined above:

$$g_{ik} = \begin{pmatrix} h^2 + w^2(x^2 + y^2) & -wy & wx \\ -wy & 1 & 0 \\ wx & 0 & 1 \end{pmatrix}_{ik}$$

(where $x_1 = s, x_2 = x, x_3 = y$ and $h = 1 - k(s)x$ with

$$\det g = (1 - kx)^2$$

The inverse is

$$g^{ik} = h^{-2} \begin{pmatrix} 1 & wy & -wx \\ wy & h^2 + w^2y^2 & -w^2xy \\ -wx & -w^2xy & h^2 + w^2x^2 \end{pmatrix}^{ik}$$

The coordinate region we are interested is free of currents, so the magnetic field is the gradient of a potential Φ with $\Delta\Phi = 0$. We express Laplace's operator in curvilinear coordinates; we find the following Laplace operators for the cases of vanishing torsion and constant curvature; constant curvature and torsion; and arbitrary curvature and torsion, resp.:

$$\begin{aligned} \Delta_{k,0} &= h^{-2}\partial_s^2 + \partial_x^2 + \partial_y^2 - k/h\partial_x \\ \Delta_{k(s),0} &= \Delta_{k,0} + xh^{-3}k'(s)\partial_s \\ \Delta_{k,w} &= \Delta_{k,0} + wh^{-3}(2[ky + h(y\partial_x - x\partial_y)]\partial_s + \\ &\quad w[-y\partial_y + h(x^2\partial_x^2 - 2xy\partial_x\partial_y + y^2\partial_y^2)]) \\ \Delta_{k(s),w(s)} &= \Delta_{k,w(s)} + xh^{-3}k'(s)\partial_s \quad (2) \end{aligned}$$

Note that the s derivative of the torsion does not enter the equations.

The magnetic field is

$$B^i = g^{ik}\partial_k\Phi$$

so Φ has to fulfill the conditions

$$\begin{aligned} \partial_s\Phi &= -w \\ \partial_x\Phi &= 0 \\ \partial_y\Phi &= -k \end{aligned}$$

at the origin of the local system.

Obviously, the usual analyticity property of the solutions is lost for nonvanishing curvature.

Constant Curvature

Let us solve the constant curvature case first. We notice that the partial differential equation separates, i. e.

$$\Psi(s, x, y) = \psi_s(s)\psi_x(x)\psi_y(y)$$

We notice that $\psi(s) = \text{const}$ because of the vanishing torsion of the orbit. $\psi_y(y)$ has to be a function fulfilling

$$\psi_y''(y) = \mu\psi_y(y)$$

and

$$(1 - kx)\psi_x''(x) - \mu(1 - kx)\psi_x(x) - \psi_x'(x) = 0$$

which is solved by Bessel functions

$$\psi_x = c_1 J_0\left(\sqrt{-\frac{\mu}{k^2}}(1 - kx)\right) + c_2 Y_0\left(\sqrt{-\frac{\mu}{k^2}}(1 - kx)\right)$$

so

$$\begin{aligned} \Psi(s, x, y) &= \int d\mu (c_{1,y}(\mu)e^{-\mu y} + c_{2,y}(\mu)e^{\mu y}) \\ &\quad \left[c_{1,x}(\mu) J_0\left(\sqrt{-\frac{\mu}{k^2}}(1 - kx)\right) \right. \\ &\quad \left. + c_{2,x}(\mu) Y_0\left(\sqrt{-\frac{\mu}{k^2}}(1 - kx)\right) \right] \end{aligned}$$

This, of course, is just the well-known radial solution of Laplace's equation in cylinder coordinates [2].

Constant Curvature and Torsion

This case corresponds to an infinitely extending helical orbit. The differential equation is given by line 2 of (2). We make a separation Ansatz $\psi(s, x, y) = -ws + \varphi(x, y)$. The resulting differential equation for φ reads

$$\begin{aligned} (\partial_x^2 + \partial_y^2 - k/h\partial_x + \\ w^2h^{-3}(2[h(x\partial_y - y\partial_x) - ky] + \\ h(x^2\partial_x^2 - 2xy\partial_x\partial_y + y^2\partial_y^2)))\varphi(x, y) = 0 \end{aligned}$$

This equation is not solvable in closed form (the coordinate system is not one of the ones in which the Laplace equation is known to be separable[2]), we can, however, obtain a recursion relation for coefficients in a power series

$\varphi(x, y) = \sum_{m,n} a_{m,n} x^m y^n$. After some tedious work, and one obtains

$$\begin{aligned} & a_{m-3,n+2}k(w^2 + k^2)(n+1)(n+2) + \\ & - a_{m-2,2+n}(w^2 + 3k^2)(n+1)(n+2) + \\ & - a_{m-1,n}k(-k^2(m-1)^2 + w^2(m-1)(2n+1)) + \\ & 3a_{m-1,2+n}k(n^2 + 3n + 2) + \\ & a_{m,n}(k^2(-3m^2 + 2m) + w^2(m+n+2nm)) + \\ & - a_{m,2+n}(n+2)(n+1) + \\ & a_{1+m,-2+n}kw^2(m^2 - 1) + \\ & a_{1+m,n}k(3m+1)(m+1) + \\ & - a_{2+m,-2+n}w^2(m+1)(m+2) + \\ & - a_{2+m,n}(m+1)(m+2) = -2w^2k\delta_{m,0}\delta_{n,1} \quad (3) \end{aligned}$$

where the rhs term comes from the separation Ansatz. The initial conditions are $a_{0,0} = 0$ (a global gauge fixing), $a_{1,0} = 0$, $a_{0,1} = -k$. Note that there are special cases of the recursion relation for $m \leq 3$ or $n \leq 3$, they are (using the initial conditions)

$$\begin{aligned} & a_{2,0} + a_{0,2} = \\ & ka_{1,1} - 2a_{2,1} - 6a_{0,3} + w^2k = \\ & - 2a_{1,2} + 8ka_{2,0} - 6a_{3,0} + 6ka_{0,2} = \\ & 4w^2a_{1,1} + 18ka_{0,3} + 8ka_{2,1} - 6a_{3,1} - 2k^2a_{1,1} - 6a_{1,3} = \\ & - 6k^2a_{0,2} + 6ka_{1,2} - 12a_{4,0} - 2w^2a_{0,2} - \\ & 10k^2a_{2,0} + 2w^2a_{2,0} - 2a_{2,2} + 21ka_{3,0} = \\ & - 3kw^2a_{1,1} - 18k^2a_{0,3} + 21ka_{3,1} - 6w^2a_{0,3} - \\ & 12a_{4,1} + 7w^2a_{2,1} - 10k^2a_{2,1} - 6a_{2,3} + k^3a_{1,1} + 18ka_{1,3} = 0 \end{aligned}$$

and, for $p > 0$

$$\begin{aligned} & w^2pa_{0,1+p} - kw^2a_{1,-1+p} + ka_{1,1+p} + w^2a_{0,1+p} - \\ & 6a_{0,3+p} - 5a_{0,3+p}p - a_{0,3+p}p^2 - 2w^2a_{2,-1+p} - 2a_{2,1+p} = 0 \\ & 3w^2pa_{1,1+p} + 18ka_{0,3+p} + 15ka_{0,3+p}p + 3ka_{0,3+p}p^2 + \\ & 8ka_{2,1+p} - 6a_{1,3+p} - 5a_{1,3+p}p - a_{1,3+p}p^2 - \\ & 6a_{3,1+p} + 4w^2a_{1,1+p} - 6w^2a_{3,-1+p} - 2k^2a_{1,1+p} = 0 \\ & - 2kw^2pa_{1,1+p} - 5w^2a_{0,3+p}p - w^2a_{0,3+p}p^2 + \\ & 3ka_{1,3+p}p^2 + 15ka_{1,3+p}p - 15k^2a_{0,3+p}p - 3k^2a_{0,3+p}p^2 + \\ & 5w^2pa_{2,1+p} - 3kw^2a_{1,1+p} + 3kw^2a_{3,-1+p} - a_{2,3+p}p^2 - \\ & 5a_{2,3+p}p - 6w^2a_{0,3+p} - 10k^2a_{2,1+p} + 21ka_{3,1+p} + \\ & 18ka_{1,3+p} + 7w^2a_{2,1+p} + k^3a_{1,1+p} - \\ & 18k^2a_{0,3+p} - 6a_{2,3+p} - 12w^2a_{4,-1+p} - 12a_{4,1+p} = 0 \end{aligned}$$

$$\begin{aligned} & - kw^2pa_{1+p,0} + k^3a_{1+p,0}p^2 + w^2a_{2+p,0}p + \\ & 16ka_{3+p,0}p + 3ka_{3+p,0}p^2 - kw^2a_{1+p,0} + 2k^3pa_{1+p,0} + \\ & 2kw^2a_{-1+p,2} - 3p^2k^2a_{2+p,0} - a_{4+p,0}p^2 - 7a_{4+p,0}p - \\ & 2w^2a_{p,2} + 6ka_{1+p,2} - 10k^2a_{2+p,0} - 6k^2a_{p,2} - 12a_{4+p,0} + \\ & 2w^2a_{2+p,0} + k^3a_{1+p,0} + 2k^3a_{-1+p,2} + 21ka_{3+p,0} - \\ & 11k^2pa_{2+p,0} - 2a_{2+p,2} = 0 \\ & - 3kw^2pa_{1+p,1} + 16ka_{3+p,1}p - 3kw^2a_{1+p,1} + 2k^3pa_{1+p,1} - \\ & 11k^2pa_{2+p,1} - 3p^2k^2a_{2+p,1} + 6kw^2a_{-1+p,3} + k^3a_{1+p,1}p^2 + \\ & 3w^2a_{2+p,1}p + 3ka_{3+p,1}p^2 - a_{4+p,1}p^2 - 7a_{4+p,1}p + \\ & 18ka_{1+p,3} - 6w^2a_{p,3} + 6k^3a_{-1+p,3} - 10k^2a_{2+p,1} + \\ & k^3a_{1+p,1} - 12a_{4+p,1} - 18k^2a_{p,3} + \\ & 21ka_{3+p,1} + 7w^2a_{2+p,1} - 6a_{2+p,3} = 0 \\ & - 3kw^2a_{1,1} - 18k^2a_{0,3} + 21ka_{3,1} - 6w^2a_{0,3} - 12a_{4,1} + \\ & 7w^2a_{2,1} - 10k^2a_{2,1} - 6a_{2,3} + \\ & k^3a_{1,1} + 18ka_{1,3} = 0 \end{aligned}$$

(3) can be viewed as a generalization of the multipole Ansatz for helical orbits. Of course, setting $w = k = 0$ we obtain the recursion relation valid for harmonic functions in x, y , namely $(n+1)(n+2)a_{m,2+n} + (m+1)(m+2)a_{2+m,n} = 0$. Obviously, the complexity of the power series prescription limits its usefulness.

Planar Undulator

Here, we have vanishing torsion and a periodic curvature $k(s) = \kappa \exp(-i\lambda s)$. We substitute $k(s)$ for s and obtain, after separating off the harmonic y dependence as $\partial_y^2 \psi = -\mu \psi$, where $\mu = 0$ due to the boundary condition $w = 0$

$$(-\lambda^2 k(\partial_k + h k \partial_k^2) + h^2 \partial_x h \partial_x) \psi(k, x) = 0 \quad (4)$$

Again, a solution is only possible in terms of a power series in terms of x and k , similar as above. We obtain the recursion relation

$$\begin{aligned} & a_{m-1,n-3}(m-1)^2 - a_{m-1,n-1}\lambda^2(n-1)(n-2) - \\ & a_{m,n-2}m(3m-1) + \lambda^2 a_{m,n}n^2 + \\ & a_{m+1,n-1}(3m+1)(m+1) - \\ & a_{m+2,n}(m+1)(m+2) = 0 \quad (5) \end{aligned}$$

, as well as special cases for small m, n and for initial conditions, which will not be given here for lack of space.

REFERENCES

- [1] A. Kabel. Particle tracking and bunch population in trafic4 2.0. 2003. this conference.
- [2] Philip McCord Morse and Herman Feshbach. *Methods of theoretical physics*. 1953.

GLOBAL BEAM-BASED ALIGNMENT METHOD

A. Terebilo, SLAC, 2575 Sand Hill Rd. Menlo Park, CA 94025 USA

Abstract

This paper presents an algorithm for orbit centering in the quadrupole magnets developed specifically for the early commissioning stage of SPEAR3 light source. During commissioning many factors can reduce the effectiveness of simpler beam-based alignment techniques. Our method is more tolerant towards inaccurate optics model, undetected large alignment errors, systematic errors and faults in the BPM system.

INTRODUCTION

Beam Based Alignment (BBA) techniques estimate the beam offsets with respect to the centers of magnets, most commonly quadrupoles, in an accelerator lattice. BBA uses measured changes in the beam position in response to static changes or periodic modulation of magnet strength. The two well-known approaches to BBA are: model-based and empirical zero-response search. Model-based techniques are prone to error due to the difference in the optics of the used model and the real machine. This difference is caused in part by the unknown orbit offsets in sextupole magnets, which creates normal and skew quadrupole terms not accounted for in the model. The method proposed here greatly improves the model-based approach by extracting additional information about the optics distortion from the same orbit response data.

METHOD

The method is based on finding an equivalent (computer) model of a storage ring that produces the same orbit shifts in response to physical quadrupole shift and tilt as the machine in response to a change in the quadrupole strength.

Analytical solution

Using the analytical results and notation of [1] the shift in the closed orbit around the ring $\delta\bar{x}_s = (\delta x \ \delta x' \ \delta y \ \delta y')^T$ as a result of changing the strength Δk of one quadrupole is:

$$\delta\bar{x}_s = M_{s \leftarrow m} [I - M_m]^{-1} \delta\Delta\bar{x}_m \quad (1)$$

Where M_m is the one turn transfer matrix. Subscript m denotes quantities at the midpoint of the quadrupole. $M_{s \leftarrow m}$ is the transfer matrix to a location s in the ring. Vector $\Delta\bar{x}_m = (\Delta x_m \ \Delta x'_m \ \Delta y_m \ \Delta y'_m)^T$ describes the transverse position and angle orbit offset with respect to the quadrupole center.

$$\underline{\delta} = \Delta k l \begin{bmatrix} 0 & \frac{\sigma^-}{k} & 0 & 0 \\ -\sigma^+ & 0 & 0 & 0 \\ 0 & 0 & 0 & \frac{\sigma_h^-}{-k} \\ 0 & 0 & -\sigma_h^+ & 0 \end{bmatrix} \quad (2)$$

Assuming a horizontally focusing quadrupole, positive k

$$\sigma^\pm = \frac{l\sqrt{k} \pm \sin(l\sqrt{k})}{2l\sqrt{k}}, \quad \sigma_h^\pm = \frac{l\sqrt{k} \pm \sinh(l\sqrt{k})}{2l\sqrt{k}} \quad (3)$$

The interpretation of (1) is particularly simple when there is no coupling between x and y planes. In the uncoupled case for the horizontal shift

$$\delta x_s = \delta_s^\theta \theta_m + \delta_s^\Delta \Delta_m \quad (4)$$

Transverse offset Δx gives rise to the first term, which is a familiar orbit perturbation due to a dipole error:

$$\delta_s^\theta = \sqrt{\beta_m \beta_s} \frac{\cos(|\Delta\phi_{s \leftarrow m}| - \pi\nu)}{2\sin(\pi\nu)} \quad (5)$$

Angular offset $\Delta x'$ generates the second term:

$$\delta_s^\Delta = \sqrt{\frac{\beta_s}{\beta_m}} \frac{\alpha_m \cos(|\Delta\phi_{s \leftarrow m}| - \pi\nu) - \sin(|\Delta\phi_{s \leftarrow m}| - \pi\nu)}{2\sin(\pi\nu)} \quad (6)$$

$$\theta_m = -\Delta k l \sigma^+ \Delta x_m \quad \Delta_m = \frac{\Delta k}{k} l \sigma^- \Delta x'_m \quad (7)$$

Equivalent model

It is possible to approximate the Δk response of a real storage ring as an orbit change in an *equivalent model*. In order to show this, we examine the differential orbit changes in response to two types of model perturbations that can be easily implemented in most accelerator optics codes.

When a quadrupole is shifted by ξ in x , the propagation of particle is given by

$$\begin{pmatrix} x \\ x' \end{pmatrix}_e = G_x \begin{pmatrix} x \\ x' \end{pmatrix} + [I - G_x] \begin{pmatrix} \xi \\ 0 \end{pmatrix} = G_x \begin{pmatrix} x \\ x' \end{pmatrix} + \xi D_\xi \quad (8)$$

$$D_\xi = \begin{pmatrix} 1 - \cos(l\sqrt{k}) \\ \sqrt{k} \sin(l\sqrt{k}) \end{pmatrix} \quad (9)$$

$$G_x = \begin{bmatrix} \cos(l\sqrt{k}) & \frac{1}{\sqrt{k}} \sin(l\sqrt{k}) \\ -\sqrt{k} \sin(l\sqrt{k}) & \cos(l\sqrt{k}) \end{bmatrix} \quad (10)$$

The other type of model perturbation involves derivative kicks of $\pm\theta$ at the quadrupole ends. This leads to

$$\begin{pmatrix} x \\ x' \end{pmatrix}_e = G_x \begin{pmatrix} x \\ x' \end{pmatrix} + \theta D_\theta \quad (11)$$

$$D_\theta = \begin{pmatrix} -\frac{1}{\sqrt{k}} \sin(l\sqrt{k}) \\ 1 - \cos(l\sqrt{k}) \end{pmatrix} \quad (12)$$

Note that the second type of perturbation does not exactly correspond to a physical tilt of the quadrupole, only in the thin lens approximation.

Comparing (1) with the closed orbit solution for the model

$$\begin{pmatrix} \delta x_s \\ \delta x'_s \end{pmatrix} = M_{s \leftarrow m} [I - M_m] g^{-1} D \quad (13)$$

where g is the transfer matrix for one-half of the quadrupole, and observing that

$$g^{-1} D_\xi = \begin{pmatrix} 0 \\ 2\sqrt{k} \sin\left(\frac{l\sqrt{k}}{2}\right) \end{pmatrix} \quad (14)$$

$$g^{-1} D_\theta = \begin{pmatrix} -\frac{2}{\sqrt{k}} \sin\left(\frac{l\sqrt{k}}{2}\right) \\ 0 \end{pmatrix}$$

it is easy to see that orbit shifts from perturbations D_ξ and D_θ are the same as (5) and (6) when

$$\xi = -\frac{1}{4} \left(\frac{\Delta k}{k} \right) \frac{l\sqrt{k} + \sin(l\sqrt{k})}{\sin\left(\frac{l\sqrt{k}}{2}\right)} \Delta x_m \quad (15)$$

$$\theta = -\frac{1}{4} \left(\frac{\Delta k}{k} \right) \frac{l\sqrt{k} - \sin(l\sqrt{k})}{\sin\left(\frac{l\sqrt{k}}{2}\right)} \Delta x'_m$$

Determination of offsets

We write the orbit shift observed at M points caused by changing a single quadrupole q as a column vector

$$\delta \bar{Z}_q = (\delta x_1 \quad \dots \quad \delta x_M \quad \delta y_1 \quad \dots \quad \delta y_M)^T_q \quad (16)$$

We can minimize the difference $\|\delta \bar{Z} - \delta \tilde{\bar{Z}}\|$ between the measured $\delta \bar{Z}$ and the model $\delta \tilde{\bar{Z}}$ computed as

$$\delta \tilde{\bar{Z}}_q = \frac{\partial \tilde{\bar{Z}}_q}{\partial \xi_x} \xi_x + \frac{\partial \tilde{\bar{Z}}_q}{\partial \xi_y} \xi_y + \frac{\partial \tilde{\bar{Z}}_q}{\partial \theta_x} \theta_x + \frac{\partial \tilde{\bar{Z}}_q}{\partial \theta_y} \theta_y + c_q \bar{Z}_\eta \quad (17)$$

where $\frac{\partial \tilde{\bar{Z}}}{\partial \xi_{x,y}}$ and $\frac{\partial \tilde{\bar{Z}}}{\partial \theta_{x,y}}$ are computed differential shifts

from model perturbations ξD_ξ (8) and θD_θ (11), ξ , θ , and c are free parameters,

$\delta \bar{Z}_\eta$ is the measured dispersion to account for the energy shifts associated with kicking the orbit transversely.

In SPEAR3 optics the effect of angular offset (6) is small and the systematic error in determining the position optics by using

$$\delta \tilde{\bar{Z}}_q = \frac{\partial \tilde{\bar{Z}}_q}{\partial \xi_x} \xi_x + \frac{\partial \tilde{\bar{Z}}_q}{\partial \xi_y} \xi_y + c_q \bar{Z}_\eta \quad (18)$$

instead of (17). In this case the error can be estimated as

$$\frac{\alpha_m}{\beta_m k} \frac{\sigma^-}{\sigma^+} \frac{\Delta x'}{\Delta x} \text{ is } < 1\% \text{ for all quadrupoles}$$

When the above procedure is applied to each quadrupole *independently* it will introduce systematic errors in the determined offsets due to the optics differences between the real storage ring and the model. It is possible to avoid this systematic error by turning the problem into a least squares minimization of $\delta \bar{Z} - \delta \tilde{\bar{Z}}$ for all quadrupoles simultaneously at the same time varying the model parameters, most importantly the quadrupole and skew-quadrupole term in model sextupoles.

We form a vector of orbit shifts in response to the changes of Δk in all quadrupoles:

$$\delta \bar{Z} = \begin{pmatrix} \delta \bar{Z}_1 \\ \vdots \\ \delta \bar{Z}_N \end{pmatrix} \quad (19)$$

and minimize the difference between the measured and model values:

$$\delta \bar{Z} - \delta \bar{Z}^{(0)} = A \begin{pmatrix} \Delta \bar{\xi}_x \\ \Delta \bar{\xi}_y \\ \Delta \bar{c} \\ \Delta \bar{k}_{Norm} \\ \Delta \bar{k}_{Skew} \end{pmatrix} \quad (19)$$

where $\bar{Z}^{(0)}$ is a vector formed from the zero-iteration solutions of (18) for individual quadrupoles. A is the design matrix of the least squares problem, whose columns are numerical derivatives of $\delta \bar{Z}$ with respect to varied parameters:

$$\bar{A}_i = \left. \frac{\partial \bar{Z}}{\partial p_i} \right|_{(0)} \quad (20)$$

SIMULATION RESULTS

Simulated BBA using the proposed method was carried out for SPEAR3. Realistic alignment errors of 200 μm r.m.s. transverse shift and 500 microradian r.m.s. roll in all magnets were introduced in addition to 1 μm BPM noise.

Figure 1 shows the true orbit position offsets in quadrupoles compared with the offset predicted by a zero-iteration fit (18) and the least-squares solution (19)

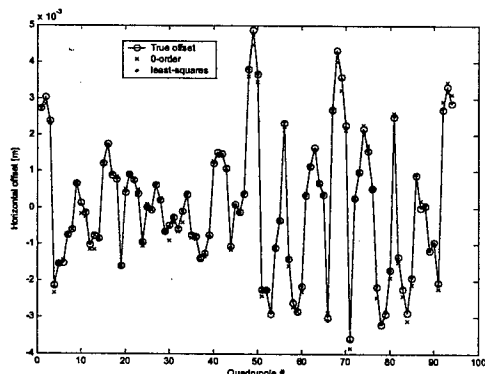


Figure 1: Real and predicted orbit offsets.

Figure 2 compares errors in the offset determination of the zero-iteration solution and the least squares solution.

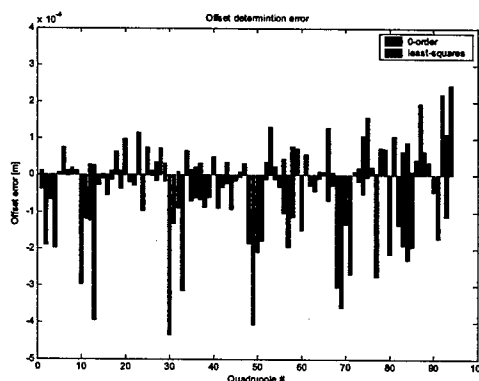


Figure 2: Error of the offset determination

DISCUSSION

The proposed method is practically useful during commissioning because the time consuming calculation of design matrix A is done *prior* to the measurement of all quadrupole Δk -response. The only computer-intensive operation to be performed during BBA procedure is finding the least squares solution of (19) through the singular value decomposition of A .

The proposed technique is an extension of the idea behind the powerful response matrix analysis method [2]. When this idea is applied to a BBA problem, changes in quadrupole strength Δk act as corrector magnets.

REFERENCES

- [1] G. H. Hoffstaetter, F. Willeke, Phys. Rev. ST Accel. Beams Vol. 5, 102801 (2002)
- [2] J. Safranek, "Experimental determination of storage ring optics using orbit response measurements", Nucl. Inst. and eth. A388, 27 (1997)

GENERATION OF FEMTOSECOND ELECTRON BUNCHES AND HARD-X-RAYS BY ULTRA-INTENSE LASER WAKE FIELD ACCELERATION IN A GAS JET

M. Uesaka, T. Hosokai, K. Kinoshita¹⁾, A. Zhidkov¹⁾
 Nuclear Engineering Research Laboratory, University of Tokyo
¹⁾ National Institute of Radiological Sciences, Japan

Abstract

Femtosecond electron beams and hard x-rays with $\lambda \sim 0.1$ nm may find various applications in biology, chemistry, and microelectronics giving a new time-scale probe analysis. Such short electron beams can be produced in the wake field acceleration by short relativistically intense laser pulses and then Thomson scattering of a second laser pulse can serve for efficient generation of very short x-rays with use of such electron beams.

INTRODUCTION

We study experimentally with 12 TW, 50 fs Ti:sapphire laser set-up and numerically through a multidimensional particle-in-cell simulation two mechanisms of generation of femtosecond electron bunches in gas jet suitable for efficient Thomson scattering. The first is the LWFA of electrons injected due to wave-breaking on a shock-wave produced by a laser prepulse in a He gas-jet. This mechanism allows us to produce a narrow-coned electron bunch with duration around 40 fs. Results of measurements agree well with two-dimensional hydrodynamics and particle-in-cell simulations. Such a beam can scatter up to 10^9 photons per pulse in 1° cone. Spectrum of scattered light is discussed. Because of large energy spread of electrons in a bunch, the x-ray spectrum is broad. To overcome this problem another mechanism, self-injection of plasma electrons, is proposed and studied numerically. The self-injection of plasma electrons which have been accelerated to relativistic energies by a laser pulse moving with a group velocity less than the speed of light appears when $a_0 \geq \sqrt{2}(\omega/\omega_{pe})^{2/3}$ where a_0 is normalized laser field. In contrast to the injection due to wave-breaking processes, self-injection allows extraction of a beam-quality bunch of energetic electrons. This injection is also expected to be useful in generation of very short pulse, ~ 10 fs, electron beams with the charge ~ 100 pC. The diameter of such a beam in a gas jet after acceleration is only 5-10 μm that makes possible the production of high-brightness hard-x-rays with few percent energy spread by using contrary propagating laser pulses. The efficiency and spectrum of such x-rays are calculated and discussed.

EXPERIMENTAL SET-UP

An intense and ultra-short laser pulse has been focused on helium gas (see Fig. 1). In order to form a spatially localized gas column, to suppress the transverse expansion into vacuum due to the thermal and fluid motion of the injected gas, a supersonic pulsed gas

injection has been used as a target. The pulsed gas jet has been produced by a device consist of an axially symmetric Laval nozzle and a solenoid fast pulse valve. The nozzle was designed to provide the Mach number $M=4.2$ at the exit of the nozzle. It has a 2.0 mm inner diameter at the exit. The typical experimental set-up is shown in Fig.1. The nozzle with the pulse valve

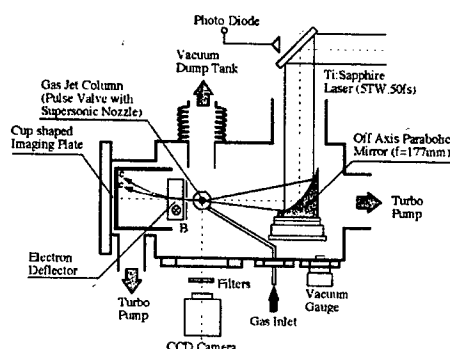


Fig.1 Experimental set-up.

was placed inside the vacuum chamber. The pulse valve was driven for 5 ms a shot at a repetition rate of 0.2 Hz. The stagnation pressure of the valve is varied from 5 to 20 atm. With these pressures the density at the exit of the nozzle ranged from 7×10^{18} to $3 \times 10^{19} \text{ cm}^{-3}$.

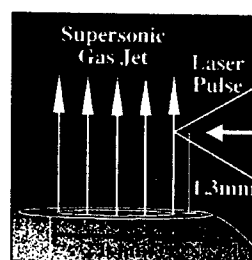


Fig. 2 Supersonic gas jet and laser focus position.

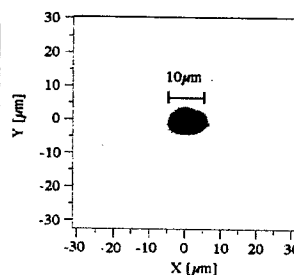


Fig. 3 Image of the laser focal spot at the target.

The 12TW Ti:Sapphire laser system based on CPA technique generated up to 600 mJ, 50 fs laser pulses at fundamental wavelength of 790 nm with 10 Hz repetition rate. The laser power at the target in the vacuum chamber was up to 5TW. As shown in Fig.2, the p -polarized laser pulse with diameter of 50 mm was delivered into the vacuum chamber through a vacuum laser transport line and was focused on the front edge of helium gas jet column at the height of 1.3 mm from nozzle exit with an $f/3.5$ off-axis parabolic mirror (OAP). Fig. 2 gives side-

view of the interaction region obtained by the CCD camera, and illustrates the gas jet and the focus point. Fig. 3 shows a typical image of a laser focal spot at the target position. The spot size was $7.5 \mu\text{m}$ in full width at $1/e^2$ of maximum. The maximum laser intensity on the target was estimated as 10^{19} W/cm^2 so that the laser parameter a_0 exceeded 2.0.

SELF-INJECTION IN LWFA

Injection of electrons for their further acceleration is a crucial part of LWFA [1]. Usually for LWFA, the injection of a high quality electron beam from a RF accelerator is assumed [2]. In other schemes, two or several laser pulses are employed for the injection [3]. Such schemes require highly precise synchronization between the wake-field and the injection. Moreover, though the LWFA, particularly, allows the production of an ultra-short electron bunch ($\sim 10 \text{ fs}$), which is necessary for probe-analysis of matter [4], the schemes based on an external injection hardly be applied for this. Another way for electron injection exploits an injection produced by the laser pulse itself, so-called 'self-injection'. A short laser pulse consists of a short ($\sim 50\text{--}100 \text{ fs}$) intense part, main pulse, and a long ($\sim 2\text{--}10 \text{ ns}$) pedestal which is usually called as a prepulse and a post pulse. The intensity of the prepulse varies from 10^{-5} down to 10^{-7} from that of the main pulse. Self-injection schemes can exploit both parts of the laser pulse. The prepulse can be used to form a proper condition for the wave-breaking injection of electrons to the wake-field while the main pulse can produce injection by itself due to relativistic effects.

If the Raleigh length, L_R , for the laser pulse is short enough, the prepulse can form a cavity with a shock wave in the front of laser propagation. In contrast to the plasma channel produced by long Raleigh length laser beam [5], the length of the cavity is determined by this small L_R , because the energy is deposited in the plasma mostly near the focus point $x=0$ as $W(x) \sim 1/(1+(x/L_R)^2)$. For low intensity laser pulse, the electron temperature, T_e , can be estimated via the collisional absorption mechanism, $dT_e/dt = \Delta\epsilon v_{ei}(1\text{eV})/T_e^{3/2}$, where $\Delta\epsilon = 2\pi^2 I / m\omega^2$ the energy acquired by an electron in a collision; v_{ei} the frequency of electron-ion collisions. For intensity $I=10^{13} \text{ W/cm}^2$ and ion density $N_i=3 \times 10^{18} \text{ cm}^{-3}$ (in the cavity) and pulse duration $\tau=2 \text{ ns}$, $T_e=150 \text{ eV}$. If $X=C_s \tau > L_R$, where C_s the ion sound speed, a shock wave can be formed in the plasma. If the shock wave relaxation depth $\Delta x \sim (M/m)^{1/2} l_i$ (M is the ion mass, l_i the ion free path) less than the plasma wave wavelength λ_{pi} , the strong wave-breaking of wake-field produced by the main pulse there can be a good source of injection. For temperature $T_e \sim 150 \text{ eV}$ in a He gas-jet, the ion sound speed is $C_s \sim 5 \times 10^6 \text{ cm/s}$ and $X \sim 100 \mu\text{m}$ so that the effect appear for the laser pulse with the Raleigh $L_R < 100 \mu\text{m}$. The shock wave can be generated in get with $\omega_{pi} l_i (M/m)^{1/2} / 2\pi > 1$ that gives $N_i > 5 \times 10^{18} \text{ cm}^{-3}$. The density gradient at the shock wave is steep and effective wave-breaking is appeared [6].

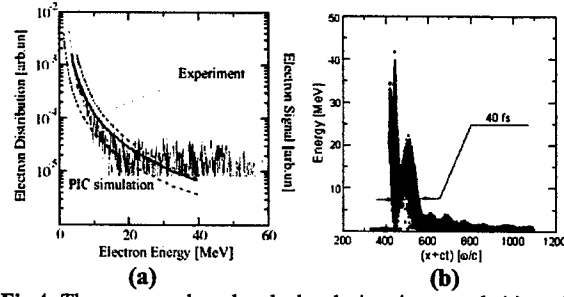


Fig.4 The measured and calculated time-integrated (a) and spatial (b) energy distribution of electrons in the bunch for the laser power of 4TW.

In order to obtain the energy distributions of the electrons, a magnetic electron deflector was set in the laser axis behind the jet (as shown in Fig.1). The bottom plate of the cup is used as an electron detector. The magnetic field between the magnets is mapped out with a Hall probe and the maximum field strength reaches 300 mT. That has an entrance aperture of 2.0 mm with an acceptance solid angle of 1 msr. With this set-up, the energy distribution of the ejected electrons up to 40 MeV can be detected. Measured distribution of narrow-coned electrons is shown in Fig.4. The distribution agree well with that obtained in 2D particle-in-cell calculation. This energy distribution is Maxwell-like with the effective temperature $T_h \sim 10 \text{ MeV}$, and the maximal energy we observed is 40 MeV. The electrons with energy from 10 to 40 MeV constitute a bunch with duration of 40 fs in PIC simulation. The calculated charge of electron bunch is 0.7 nC/1J . In Fig.4b the spatial distribution of accelerated electrons obtained from PIC simulation shows the bunch duration is 40 fs!

The wave-breaking is initially a stochastic process that provokes rapid randomization in energy of accelerated electrons. This makes such kind of injection sometimes inefficient and usually very sensitive to plasma parameter changes. A mechanism of electron injection originating from the relativistic character of the laser-plasma interaction can be applied to improve the energy spread of accelerated electrons.

Along with the common wake-field, a relativistically intense laser pulse moving in an under-dense plasma with group velocity less than the light speed generates additional electrostatic wave, which has a group velocity close to the group velocity of the laser pulse from the linear theory. This wave comes from electrons temporally trapped and accelerated directly by the laser pulse forming a bunch at the front of the laser pulse. This bunching of electrons creates a potential difference, potential cavity [6], behind the laser pulse due to the evacuation of electrons. The number of electrons in this bunch is limited by repulsion; the repealed electrons are accelerated to energy equal the potential difference in the cavity and, thus, can be efficiently injected for further acceleration if proper matching condition occurs. However this injection, which can be considered as a self-

injection, contends with injection after wave-breaking. At low plasma density, the self-injection produces efficient acceleration with a low energy spread while at high density, wave-breaking dominates producing a Maxwellian distribution of energetic electrons with an effective temperature. Propagating in under-dense plasma with the group velocity, v_g , an intense laser pulse can accelerate plasma electrons, which are in the rest at the beginning, up to the energy $\varepsilon_{e\max} = mc^2 a_0^2 / 2$, where $a_0 = eE/mc\omega$ with E the laser electric field, and ω the laser frequency. If the velocity of such electrons exceeds the group velocity of the laser pulse, these electrons can be trapped and move with the pulse forming an electrostatic wave. The matching condition can be written in the following form, $\gamma_{\text{cmax}} = a_0^2 / 2 = \gamma_g = 1 / (1 - v_g^2/c^2)^{1/2} \sim \omega \gamma_g^{1/2} / \omega_{\text{pl}}$ where ω_{pl} is the plasma frequency and $\tilde{\gamma}_e \sim \sqrt{1 + a_0^2 / 2}$ is the electron quiver energy. The potential difference, $\Delta\phi$, produced by electrons directly accelerated by the laser at the front of the pulse cannot exceed the ponderomotive potential $mc^2 a_0^2 / 2$. As a result, the length of the cavity behind the laser pulse is $d = \lambda_0 a_0 / 2\pi$. At this distance behind the laser pulse the repealed electrons acquire energy $\varepsilon = |\Delta\phi|$ and, moving with the group velocity, are further accelerated in the cavity. For mono-energetic acceleration, d must exceed the pulse length $c\tau$, where τ is the pulse duration. The maximal energy finally acquired by such an electron is $E_{\text{max}} = (a_0 / 2\pi) E_{\text{max}}^{\text{WF}}$, where $E_{\text{max}}^{\text{WF}}$ is the corresponding maximal energy in acceleration by longitudinal plasma wave.

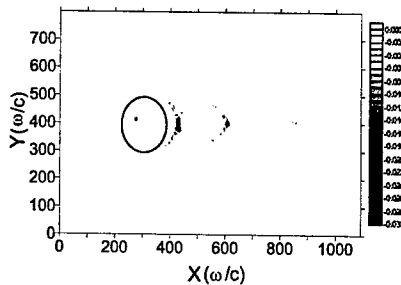


Fig.5 The spatial distribution of normalized density of electrons in the gas-jet of density, $N_e = 10^{19} \text{ cm}^{-3}$, at $\omega t = 4000$ for $I = 10^{20} \text{ W/cm}^2$; $X = x + ct$

Results of 2D simulation displaying the formation of the electrostatic wave are shown in Fig.5. One can see a clear cavity structure in electron density after the pulse propagates 0.5 mm in the plasma though there is no wave-breaking of the plasma wave. The transverse size of the first bunch in the rear of the first cavity is about $10 \mu\text{m}$. The energy distribution of electrons in the bunch after the pulse past 1 mm and 2 mm in the plasma are shown in Fig.6. The both distributions have a peak that corresponds to electrons accelerated after the self-injection. The energy spread is 5% in both cases although energy spread in the pedestal increases considerably. Formal calculation of the emittance in the bunch gives that of $0.1 \pi \text{ mm mrad}$

at total charge $Q \sim 100 \text{ pC}$.

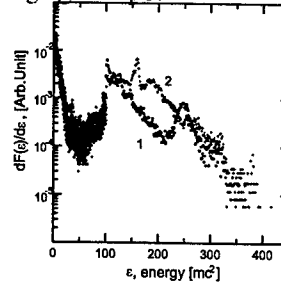


Fig.6 Electron energy distribution in 2D PIC simulation; $I = 10^{20} \text{ W/cm}^2$, $\tau = 20 \text{ fs}$, $\omega t = 6000$ (a) $\omega t = 12000$ (b) at the plasma density $N_e = 10^{19} \text{ cm}^{-3}$

THOMSON SCATTERING

Moving through the laser pulse, a relativistic electron transforms the laser light to X-rays. The total number of photons produced by an electron strongly depends on the intensity of the scattered light and can be found from simple equation, $dn/dt = \sigma I / h\omega$, where $\sigma \sim \pi r_e^2 = \pi e^4 / (mc^2)^2$ electron cross-section, n the number of x-ray photons. For the laser pulse with total energy 1 J, $\lambda \sim 1 \mu\text{m}$, and focus spot $\sim 10 \mu\text{m}$ $-W = 1 \text{ MJ/cm}^2$ that gives $n \sim 2-3$. Electron bunch, 40 fs, 100 pC, can produced 10 keV x-rays in 1° with 10^9 photons and duration $\sim 30 \text{ fs}$. A typical spectrum of scattered signal is given in Fig. 7 for $a_0 = 2$ [2]

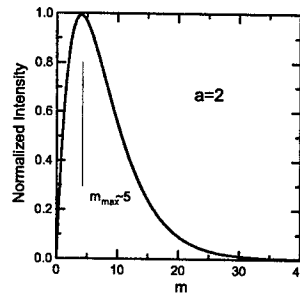


Fig. 7 Typical spectrum of scattered x-rays [2].

The maximum frequency is $\omega - m\omega_0 \gamma_0^2 / (1 + a_0^2)$ with γ_0 the energy of accelerated electrons.

REFERENCES

- [1] T. Tajima and J. Dawson, Phys. Rev. Lett., **43**, 267 (1979); K. Nakajima et al., Phys. Rev. Lett. **74**, 4428 (1995); F. Dorchies et al., Phys. Plasmas **6**, 2903 (1999).
- [2] D. Umstadter et al., Science **273**, 472 (1996); Phys. Rev. Lett. **76**, 2073 (1996); Phys. Rev. Lett., **90**, 055002 (2003)
- [3] E. Esarey, R.F. Hubbard, W.P. Leemans, A. Ting, and P. Sprangle, Phys. Rev. Lett. **79**, 2682 (1997); IEEE Trans. Plasma Sci., **24**, 252 (1996)
- [4] M. Uesaka, et al, Phys. Rev E **50**, 3068 (1994); Radiation Physics and Chem. **60**, 303(2001); Nucl. Instr. Meth. Phys. Res. A **455**, 148 (2000); Phys. Rev. ST Accel. Beams **5**, 041301 (2002)
- [5] V. Malka, et al., Phys. Plasmas **8**, 2605 (2001); Science, **298**, 1600 (2002); Phys. Plasmas **6**, 2903 (1999); Phys. Plasmas **7**, 3009 (2000)
- [6] T. Hosokai, et al., Phys. Rev. E **67**, 036407 (2003); A. Zhidkov, et al, Phys. Rev. Lett. (in press)

FEEDFORWARD CORRECTION OF THE PULSED CIRCULARLY POLARIZING UNDULATOR AT THE ADVANCED PHOTON SOURCE*

L. Emery[†], I. Vasserman, Oleg Makarov, Boris Deriy, Shigemi Sasaki, Robert Soliday,
Argonne National Laboratory, Argonne, IL 60439, USA

Abstract

A circularly polarizing undulator capable of switching the polarization very rapidly was installed at the Advanced Photon Source. The net magnetic field perturbation is characterized in both planes by a transient orbit motion, which lasts about 30 ms, and a DC orbit shift. In addition, multipole magnetic moment errors are present. The correction system consists of small dipole and multipole correction magnets at the ends of the undulator, a multichannel arbitrary function generator (AFG) to program the corrector magnet current triggered on the polarization change event, low-level software to load and interpolate the AFG waveforms, and high-level software running on a workstation to determine the optimum AFG waveforms for the dipole correctors. We rely on the existing real-time feedback system to acquire the orbit transient and to automatically generate a close approximation of the required corrector waveforms. A choice of deterministic correction or trial-and-error manual adjustments of the wave forms is available in the high-level software.

INTRODUCTION

A circularly polarizing undulator (CPU), designed and built by the Budker Institute of Nuclear Physics, was installed at the Advanced Photon Source storage ring in May 2001. The 2.4-m long, 12.8-cm period, 34-pole electro-magnet CPU has a set of vertical and horizontal coils that produce an internal helical trajectory in the electron beam for production of circularly polarized photons. A switching circuit in the vertical field coil power supply produces a trapezoidal-shaped current pattern with short transients (5-10 ms) and arbitrarily long DC parts, thus alternating the photon polarization between right-circular (RCP) and left-circular (LCP) with a small gap in the photon throughput, making this undulator a uniquely efficient device for polarization studies. The first stage of commissioning covered fixed polarization (DC modes) operation, which produced first light for users on August 1, 2001. In November 2001, we started commissioning of the more complex alternating polarization (AC mode) operation, which required the integration of several systems; this was completed in March 2003.

This paper will describe what needed to be done to commission the DC and AC modes, including some implementation details such as hardware designs, organization of

data, use of existing storage ring systems, machine studies, and low-level and high-level software design.

The requirements for CPU operation are that the stored beam properties be minimally affected during operation. In general, insertion devices (IDs) cause small but measurable angular and position displacements of the beam orbit and some weak high-multipole moments. The field perturbations are dependent on the main coil current and the polarization mode. In addition, a short-lived transient in these fields occurs at the switching of polarization. Extensive magnetic measurement of the on-axis CPU field components were made at several main coil currents for the various modes. This data were used initially for the feedforward correcting channels. Since the CPU has very strong nonlinearities, especially during transients, and the fields are very sensitive to misalignment, we expected to have to make additional beam-based corrections after the CPU was installed in the storage ring. Though the slowly varying components of the angular and position displacements can be corrected by the real-time orbit feedback (RTFS) and the DC orbit correction (DC OC) systems at the APS, we strove to correct all measurable CPU perturbations.

MULTIPOLE CORRECTOR MAGNETS

The present correction system consists of four channels to compensate the first and second field integrals of both planes (two dipole magnets at the upstream end and two more at the downstream end). Additional channels were implemented for correcting higher-order multipole components: the normal quadrupole, skew quadrupole, and skew octupole field components [1].

The initial part of the commissioning plan called for making a complete magnetic characterization with no correction, then to repeat the bench measurement with correction turned on to confirm the tuning of the CPU.

The seven channels of corrector magnet currents are programmed by a multichannel arbitrary function generator (AFG) with a sampling rate of 1 kHz and a depth of 128 points. In the AC mode, the AFG produces alternating waveforms for each transition synchronized to a switching pulse (i.e., one waveform for RCP → LCP and a different waveform for LCP → RCP). On the last point of the AFG, the corrector current freezes until the next trigger. In DC modes, the AFGs produce a constant waveform and is updated when the CPU set point is changed. An EPICS IOC dedicated to the CPU handles the updating of AFG waveforms from stored tables of correction data specific to each operating mode. The tables are linearly interpolated at the CPU set point value and the resulting wave-

* Work supported by U.S. Department of Energy, Office of Basic Energy Sciences under Contract No. W-31-109-ENG-38.

[†] emery@aps.anl.gov

forms are sent to the AFGs. The waveform data tables are loaded into the IOC from self-describing data set (SDDS) protocol-compliant [2] data files.

The use of SDDS files in managing the corrector waveform data was crucial. Briefly, SDDS datasets are files with headers that describe the structure and contents of the data in terms of names, units, and data type. The data itself is typically one or more instances of data pages, which are tables accompanied by parameters and multidimensional arrays. Access to data in SDDS files is *by name only*, which is the key feature for a robust protocol. A suite of data processing and display tools that work with SDDS files helps integrate data from various systems, which is the case here.

The data for configuring DC mode compensation is contained in a single file. Each data page of the file corresponds to a different polarization mode and contains a table of CPU main coil currents and the seven multipole corrector magnet currents. For AC mode configuration, one file for each corrector magnet is required because of the extra time dimension. Each data page corresponds to a particular CPU current set point with a table of time index and waveforms for the RCP and LCP states.

MEASUREMENT AND CORRECTION OF ORBIT PERTURBATION

It turns out that the dipole corrections based on the magnetic measurements did not correctly compensate the dipole perturbation for both DC operation and AC operation. We were not surprised by this since we knew of some CPU misalignments in the vertical plane (by 250 microns) due to inaccuracies in the manufacture of the poles. We proceeded to make beam-based measurements of the dipole perturbations to apply as feedforward correction. For the DC modes, the normal and skew quadrupole correction was confirmed with tune measurement and beam size measurements, respectively, while the skew octupolar correction was difficult to confirm. In any case, we found no effect on the beam lifetime from the octupole magnet operating at full range. For the AC modes, the latter three corrections would be difficult to confirm, so we left the correction from the initial magnet measurement as is.

DC Modes

The measurement and correction of the fields for DC mode operations required no extraordinary setup. We configured our existing system of DC orbit correction with the four CPU dipole correctors acting as the only correctors, while the CPU was ramping slowly between predetermined set points. The recorded values of the correctors were then written to the DC-mode operations compensation file. Occasionally one corrector reached its range limit at some CPU set point, in which case we continued orbit correction with the remaining corrector of that plane. Even though the compensation will not be perfect, the perturbation would be minimized, leaving the regular DC OC to make up the

difference in user operations.

Figure 1 shows the difference between the initial correction based on the magnetic measurements and the final correction for the four dipoles in RCP mode. For the initial correction, the curves for the two vertical correctors were set the same because the magnetic measurement could not definitely detect a second integral perturbation. The final correction definitely displays a second integral correction for both planes.

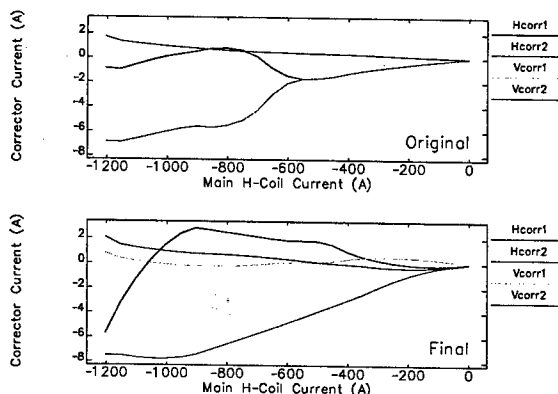


Figure 1: Original and final RCP mode correction of dipole fields.

AC Mode

The measurement and correction of the fields for AC mode operations required a more complicated setup because of the extra time dimension. Briefly, we use the transient orbit data to make changes to the dipole compensation waveforms. We needed to integrate several data sets, signals, and systems: the original waveforms from magnetic measurements, a timing signal, RTFS data acquisition system, a special RTFS correction matrix configuration, a GUI application for manual or automatic waveform feedback, a new Tcl/Tk widget for waveform display and tweaking, a SDDS data file structure to facilitate waveform operations, and the RTFS for rms orbit measurement.

The RTFS has access to almost all orbit data at a sampling rate of 1.5 kHz. The RTFS data acquisition can be triggered by the 2-Hz rate injection timing signal. To get synchronization between RTFS and CPU transition, the CPU switching circuit was connected to a trigger sequence derived from the same timing signal. The RTFS was set up for data acquisition with the loops open, otherwise the orbit would not truly reflect the magnetic filed perturbation.

It turned out that we could utilize the powerful RTFS to do some of the mathematical work. The data from the beam position monitor (BPM) system is actually transformed in real time into "corrector error" signals by multiplying the orbit data vector with rows of the RTFS correction matrix. The corrector error signals are the amount of current that would be commanded to the RTFS correctors (one per sector) to correct the global orbit for that time step, assuming unity gain. Even with the loops open, the matrix calculation

goes on indefinitely. The correctors error signals from the upstream and downstream RTFS correctors (regular storage correctors) are the most relevant ones because they are the closest to the CPU. Since the RTFS correctors are not at the same location of the CPU dipoles, additional modification of the corrector error signals was sought. For a time, we ran the flexible RTFS with a correction matrix that had phantom RTFS correctors at the locations of the CPU dipoles. The corrector error signal would then correspond to exactly the required correction for the CPU correctors. In practise, however, the solutions were too noisy to use, mainly because the first and second integral correction components were solved simultaneously, the second integral solution being very sensitive to input error. Until we find a way to reduce the noise, we'll adopt the default correction matrix used for operations, which is less accurate but nevertheless permitted a convergence in tuning.

The next step was to make a change to the corrector waveform based on the orbit readback. We have the option of using the readback waveforms to calculate a change in the CPU dipole waveforms, or simply edit part of the CPU dipole waveforms in an attempt to change some visible features of the readback waveforms. At a given CPU current set point, there are eight waveforms to adjust, two waveforms for each of the four dipole magnets.

Finally, the data of the new waveforms for the given CPU set point were inserted into the four corrector SDDS files that had been loaded in the IOC. Tens of iterations were typically required for correcting perturbations for one CPU set point.

Graphical User Interface

A Tcl/Tk application was written to facilitate the control and processing steps for the AC mode correction described above. The application sets up the RTFS for acquiring the particular data required, collects the data over many CPU pulses, averages the data over several pulses, separates the orbit transients belonging to the RCP and LCP portions of cycle, and writes the data to a file in a selected working directory. The original version of the application did a deconvolution of the CPU corrector time response (7 ms) from the orbit transient and a transfer matrix multiplication to obtain the angle corrections required at the CPU correction locations. This method had the potential of converging to the right waveforms quickly, but had the noise problems mentioned earlier that the deconvolution itself worsened. In the later version of the application, the deterministic approach was replaced with a "manual" search approach. A waveform Tcl/Tk widget was designed specifically for displaying the orbit data and the corrector waveform data in adjacent frames. Each point of the corrector waveform can be selected by the mouse and moved vertically to change the value. After editing is completed, the waveform can be saved in an archival SDDS file, and uploaded to the IOC. Any archival waveform data can also be recalled and uploaded to the IOC. Preset plots of the RTFS and corrector

waveform data are available.

Figure 2 shows an example of the orbit perturbation data before any correction, corresponding to a 250 μm orbit. After correction (not shown), the remaining perturbation is reduced to about 7 μm of orbit (0.1 A in the scale of Figure 2) and lasts about 15 ms.

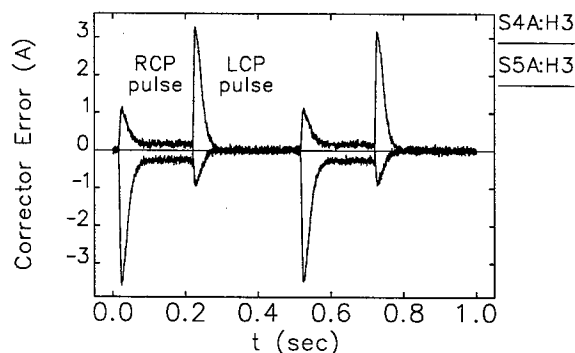


Figure 2: Orbit data for uncorrected CPU at 260 A.

USER OPERATION

We stop iterating the dipole corrector waveforms when the remaining orbit error doesn't appear to be correctable anymore. The remaining uncorrected errors occur just after the switch time, are short lived (5-15 ms), and are of small amplitude. The overall figure of merit for the quality of correction is the rms orbit calculated by the RTFS when the RTFS loops are closed. Because the RTFS correction bandwidth is about 50 Hz, we don't expect the remaining pulse-like errors to be corrected by the RTFS, though the DC-level error would be.

We decided arbitrarily that the acceptable increase in the rms orbit error (for 30 Hz BW) was to be 20% from its base level of 1.1 μm in the horizontal plane and 0.9 μm in the vertical plane. Because the rms error depends on the pulsing period, we have restricted the pulsing period to a minimum of 2 seconds. The measured rms orbit errors for the full operating range of the CPU varies from 1.1 μm to 1.3 μm in the horizontal plane and 0.9 μm to 1.3 μm in the vertical plane. The CPU set points most used by the user have rms orbit errors 1.2 μm and 0.9 μm in the horizontal and vertical planes, respectively.

REFERENCES

- [1] S. Sasaki, I. Vasserman, and E. Trakhtenberg, "Planar Electromagnetic Multipole Correctors for CPU," 2001 PAC, Chicago, Illinois, 2447 (2002).
- [2] M. Borland, "A Self-Describing File Protocol for Simulation Integration and Shared Postprocessors," 1995 PAC, Dallas, Texas, 2184 (1996).

A THIN BERYLLIUM INJECTION WINDOW FOR CESR-C*

Yulin Li†, Laboratory for Elementary-Particle Physics, Cornell University, Ithaca, NY 14853, USA

Abstract

The e^+e^- collider CESR is expanding its beam energy range to below 2 GeV for the planned Charm Physics Program. The original 5 GeV injection beam lines consisted of two 0.025-mm thick titanium windows, separated by a helium line at atmospheric pressure. The beam injection efficiency at low energies is reduced dramatically due to excessive emittance growth from multiple scattering in the Ti windows. The Ti windows were replaced with 0.075-mm thick beryllium windows to restore injection efficiency at low beam energies. This paper describes the design and construction of the Be windows. Finite-element analysis was used to determine the minimum Be window thickness able to support atmospheric pressure across 24-mm diameter aperture. The Be window housing is a cylinder consisting of two stainless steel tubes (SST) vacuum brazed to each end of a copper ring. The Be window is subsequently vacuum brazed to the copper ring at a lower braze temperature. The SST ends of the window assembly provide mechanical strength and protection to the fragile window, and facilitate welding of the window assembly to the injection vacuum chambers. Injection efficiency close to 70% was achieved with the beryllium injection windows in CESR.

As a part of CESR-c conversion program [1] in optimizing luminosity performance in beam energy range of 1.5 to 2.5 GeV, the titanium windows are replaced with thin beryllium ones, to reduce excessive emittance growth due to multiple scattering [2]. This paper describes the construction of the thin beryllium windows.

WINDOW DESIGN

The beryllium window assembly is designed with the following requirements. First, it must provide reliable mechanical performance to handle both a static differential pressure between the atmospheric helium and the vacuum, and occasional pressure cycling when either the CESR or the Synchrotron vacuum system is vented for maintenance. Secondly, it needs to provide a required 24-mm beam aperture. Furthermore, the window housing need to be thin enough so that to allow the injecting beam to be brought close to the stored beam in CESR.

Deflection and stress across a 24-mm diameter beryllium foil are calculated under atmospheric pressure using finite element analysis (FEA) for two commercially available thicknesses, namely 0.050 mm and 0.075 mm. A beryllium thickness of 0.075-mm was chosen based on the FEA results.

INTRODUCTION*

At CESR, the injected electron or positron beam from the boost ring, the Synchrotron, are merged into the stored beam in CESR via a pulsed electro-magnet, the septum, as shown in Figure 1. The beam passage channel in the septum is filled with pure helium at atmospheric pressure. Two thin metallic windows at each ends of the septum provide vacuum separation between the helium space and the CESR and the Synchrotron vacuum systems.

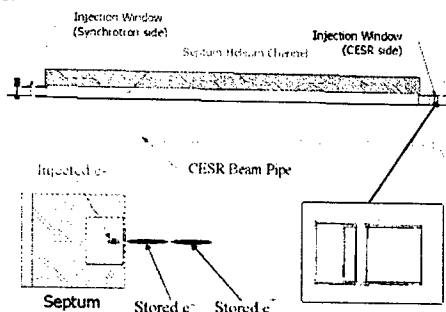


Figure 1. CESR Injection (vacuum) layout

The windows made of 0.025mm thick titanium were used when CESR was running at beam energy ~ 5 GeV.

WINDOW CONSTRUCTION

The beryllium window assemblies are made through a two-step vacuum furnace braze.

The first step produces the window housing, as shown in Figure 2. The window housing consists of a copper ring sandwiched between two stainless steel (SST) tubes. The SST tubes at the ends provide mechanical strength and protection to the fragile window, and make it much easier to weld to the stainless flange on the CESR injection vacuum chamber. The parts are vacuum brazed at 955°C with BAu-4 (82%Au-18%Ni, or Nicro®) alloy wires. Two grooves in the base SST tube and the copper ring serve as brazing alloy retaining "wells" to ensure reliable joints among the parts. The housing is completed by machining away the grooves after the vacuum braze and a successful leak checking.

The 0.075 mm (0.003") thick beryllium disk (Brush-Wellman, Electrofusion Grade IF-1) is vacuum brazed onto the copper ring of the window housing using Bag-18 (60%Ag30%Cu10%Sn) alloy at 718°C, with the braze joint arrangement shown in Figure 3. The beryllium disk is brazed on both sides to enforce the very narrow joint.

Due to brittleness of the thin beryllium disk and the braze joint, extreme care must be taken to avoid sudden pressure changes cross the window aperture, either during pumping down or venting to atmospheric pressure. This is specially the case for the first pumping down of the window assembly after the second vacuum braze.

* Work supported by the National Science Foundation

† yl67@cornell.edu

Because the beryllium disk is flat at this state, quick evacuation from one side of the window induces sudden deflection across the beryllium disk that may result in failure of the beryllium disk or/and the braze joint. To avoid the failure, the brazed window assembly was evacuated very controlled fashion, using a setup as illustrated in Figure 4, to slowly form a stable curved state. The beryllium disk experiences much less mechanical stress from the atmospheric pressure at this curved form.

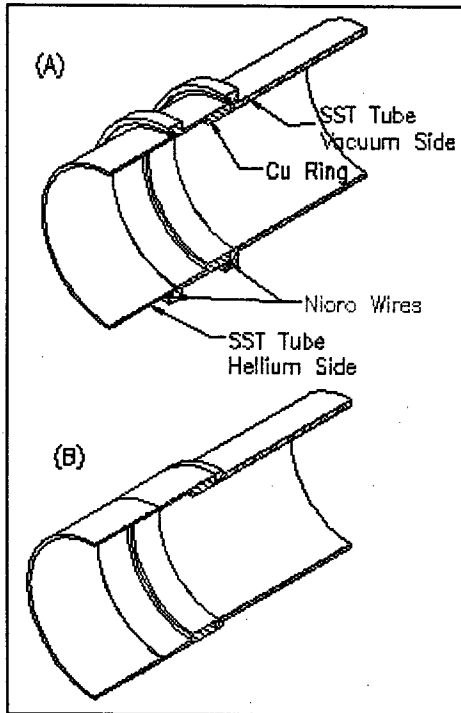


Figure 2: Vacuum braze of the beryllium window housing (a)Braze arrangement, (b)Finished housing.

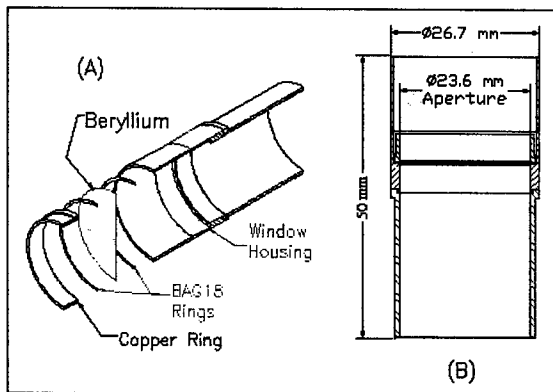


Figure 3: Vacuum braze of the beryllium window (a)Braze arrangement, (b)Finished window assembly

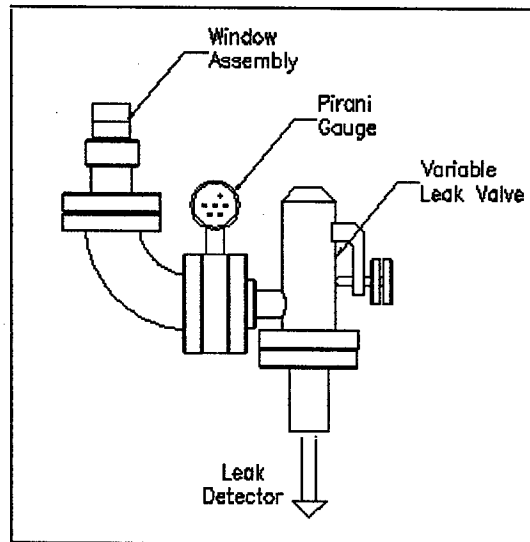


Figure 4: Setup for forming the beryllium window and leak checking. The pumping down rate (<1 torr/sec) is controlled by the opening of the variable leak valve, and monitored by a Pirani vacuum gauge.

CONCLUSION REMARKS

During a short accelerator shutdown in September 2002 (when a prototype CESR-c super-conducting wiggler magnet was installed in CESR), the titanium injection windows for the electron beam were replaced with the new beryllium windows. This led to an estimated a factor of 2.6 reduction [2] in the electron beam emittance growth from multiple scattering in the injection windows. Machine studies before and after the injection window replacement showed expected improvement in the electron beam injection efficiency, as listed in Table 1. During a 4-month long shutdown starting in March 2003, the titanium injection windows for the positron beam will also be replaced with the 0.075mm thick beryllium windows. Similar improvement in the CESR positron injection efficiency is expected for the CESR-c operations.

Table 1. Comparison of the Measured Electron Beam Injection Efficiencies between Ti- and Be- Windows [3]

0.025mm Ti Windows		0.075mm Be Windows	
η_{\max}	η_{τ}	η_{\max}	η_{τ}
38%	13%	69%	56%

Notes: η_{\max} is maximum injection efficiency disregarding beam lifetime; η_{τ} is injection efficiency with reasonable beam lifetime

ACKNOWLEDGEMENT

The author would like to thank Neil Sherwood for his very helpful suggestion in the braze joint design, and for

carrying out the vacuum furnace braze of the beryllium windows described in this paper.

REFERENCES

- [1] D. Rice, "CESR-C – A Frontier Machine for QCD and Weak Decay Physics in the Charm Region," Proc. of EPAC 2002, p. 428
- [2] D. Rubin, "Multiple Scattering in Injection Channel", CON 02-01, LEPP, Cornell University, Ithaca, NY 14853, USA
- [3] A. Temnykh, private communication

DIAGNOSIS OF OPTICAL ERRORS WITH A PRECISION BPM SYSTEM AT CESR

J. C. Smith, M. A. Palmer, D. L. Rubin, D. C. Sagan*
Cornell University, Ithaca, NY 14853, USA

Abstract

In the Cornell Electron Storage Ring (CESR) multi-bunch beams of electrons and positrons share a common vacuum chamber and guide field. A new precision beam position monitor system, with bunch-by-bunch measurement capability, is now in operation in one sector of the CESR ring including the interaction region (IR). Two of our position monitors are located 67cm on either side of the interaction point (IP) within the 1T experimental solenoid. By measuring the relative positions of electron and positron bunches at these detectors we can obtain information about the displacement of the beams at the collision point with an anticipated resolution on the order of the vertical beam size. The measurement of the dependence of beam trajectories at these IR beam position monitors (IRBPMs) on changes in the ring steering elements provides a powerful diagnostic of guide field errors in the interaction region.

INTRODUCTION

The pretzeled orbits [1] associated with multibunch operation of CESR place the counter-rotating beams off axis in most of the quadrupoles, skew quadrupoles, sextupoles, etc. As a result, skew quadrupoles affect closed orbits differentially for the two beams, and tuning to reduce coupling is complicated by feed down. A new BPM system is capable of precise and nearly simultaneous differential measurement of electron and positron positions near the IP. The relative positions are measured with the requisite resolution to keep the beams in collision. In addition, the dependence of the positions on steering elements outside the IR yields precise determination of coupling parameters.

INTERPOLATION FROM IRBPM TO IP

The transverse phase space coordinates of a trajectory at element i_2 in a ring are given by the transfer matrix [2] M from i_1 to i_2 and the particle's position at i_1 :

$$\mathbf{x}_{i_2} = \mathbf{M}_{1 \rightarrow 2} \cdot \mathbf{x}_{i_1} \quad (1)$$

Given position measurements at two detectors, and the transfer matrix that propagates the trajectory from one to the other, the orbits are uniquely determined, including at the collision point. Systematic effects are minimized by measuring and mapping electron and positron orbit difference, $\Delta \mathbf{x} = \mathbf{x}_{e+} - \mathbf{x}_{e-}$. The relative positions at the IP are obtained by solving the following system of equations:

$$\Delta \mathbf{x}_{ip} = \mathbf{M}_{e \rightarrow ip} \cdot \Delta \mathbf{x}_e \quad (2)$$

$$\Delta \mathbf{x}_w = \mathbf{M}_{e \rightarrow w} \cdot \Delta \mathbf{x}_e \quad (3)$$

where \mathbf{x}_e and \mathbf{x}_w and \mathbf{x}_{ip} are the phase space coordinates at the detector just to the east of the IP, just to the west, and at the IP respectively. Between the two IRBPMs are permanent magnet final focus quadrupoles immersed in a 1T solenoidal field for which the mapping is well known. Given the transfer matrices in this region, the determination of the relative IP beam positions and crossing angles is limited only by the resolution of the difference measurement at the IRBPMs.

X-Y COUPLING AT IRBPMs

The positron and electron beams in CESR travel in a pretzel orbit. This pretzel orbit serves to separate the beams at multiple parasitic crossing points around the ring and to establish the horizontal crossing angle at the IP. The experimental solenoid introduces strong x-y coupling in the interaction region so horizontal displacement of the beams in the arcs produces vertical displacement in the IR. This coupling can be parameterized using normal mode coordinates and the \bar{C} -matrix [3].

The motion of the normal mode that reduces to the horizontal in a region in which there is no coupling, is given at any BPM by

$$x = A_x \sqrt{\beta_x} \cos n\nu_x \quad (4)$$

$$y = -A_x \sqrt{\beta_y} [\bar{C}_{22} \cos n\nu_x + \bar{C}_{12} \sin n\nu_x] \quad (5)$$

where A_x is the overall amplitude, β_x and β_y are the beta functions at the BPM, ν_x is the normal mode tune, and n is the turn number. By measuring the change in vertical orbit at the IRBPMs due to a change in the horizontal pretzel amplitude, for example by adjustment of the horizontal electrostatic separators, these coupling errors can be determined with good resolution. We take advantage of the difference measurement ($x_{e+} - x_{e-}$) to reduce systematic errors. A similar analysis can be performed using vertical kickers in the ring.

Coupling errors in CESR have traditionally been measured and corrected by taking synchronous phase measurements around the ring and comparing the measurements to the model lattice [4]. Then we adjust machine quadrupoles and skew quadrupoles to minimize the difference between measured and design phase and coupling. This measurement is performed by exciting a beam normal mode with a shaker and monitoring the relative phase and amplitude at each of the BPMs around the ring. It requires that the beam be very nearly centered in all of the beam detectors. Therefore, the separation pretzel is turned off and there is only one beam in the machine. Ideally we would measure coupling corresponding to pretzel trajectories with beams in collision. Guide field nonlinearities and misalignments

* Work supported by the National Science Foundation

introduce pretzel dependent coupling errors that are not accessible by the traditional measurement technique. The coupling measurement based on position dependence in the IRBPMs can yield high resolution about the closed orbits that correspond to colliding beam conditions.

NEW IRBPM DESIGN

A new BPM readout system has been designed and installed in one sector of the CESR ring including the IR [5]. The system is capable of measuring the beam positions of individual bunches and, when operating in its highest precision mode, can cycle between bunches at $\sim 100\text{Hz}$. The system's large bandwidth allows us to resolve counter-rotating bunches at the IRBPMs which pass by at intervals as short as 6 ns. This capability opens up the possibility of monitoring and correcting the trajectories of colliding bunches. In machine studies conditions, we have obtained differential measurements between electron and positron bunches with a resolution of approximately $6\mu\text{m}$ at the IRBPMs. The system's resolution is limited by ADC and front-end nonlinearities, gain variations between the four independent channels that read out the beam buttons, the timing resolution with which we can digitize the peak of the button signal, and electronic cross-talk between the signals from the most closely spaced bunches.

IRBPM COUPLING MEASUREMENTS

The horizontal separators that generate the pretzel predominantly excite the a or horizontal normal mode. If there is no coupling at the four kickers then the a -mode and x -mode are equivalent and the vertical displacement at the IRBPMs is given by equation 5. Because there is in general finite coupling at the horizontal kickers, the b -mode is excited as well. Therefore, the actual x and y displacement at the IRBPMs is

$$x = A_a \gamma \sqrt{\beta_a} \cos n\nu_a + A_b \sqrt{\beta_a} (\bar{C}_{11} \cos n\nu_b - \bar{C}_{12} \sin n\nu_b) \quad (6)$$

and similarly for y . Although the coupling at the kickers is small, the contribution to the change in vertical position due to the b -mode excitation is comparable to the vertical coupling to the a -mode at the IRBPMs so the b -mode contribution cannot be ignored.

The horizontal crossing angle is proportional to the kicks on the 4 horizontal separators that produce the pretzel. The dependence of vertical position versus the horizontal separator kicks is given by

$$\frac{\partial y}{\partial \alpha} = \frac{\sqrt{\beta_{det}}}{-2 \sin \pi \nu} \sum_{k=1}^4 \left(\bar{C}_{22} \sqrt{\beta_{ak}} \frac{\partial \theta_k}{\partial \alpha} \cos \psi_{ak} + \bar{C}_{12} \sqrt{\beta_{ak}} \frac{\partial \theta_k}{\partial \alpha} \sin \psi_{ak} \right) + \Phi \left(\frac{\partial A_b}{\partial \alpha} \right) \quad (7)$$

where the last term represents the component of the slope due to the excited b -mode and $\psi_{ak} = \phi_{aBPM} - \phi_{ak} - \pi \nu_a$. Typical Twiss parameters for one of the IRBPMs yield (in $\mu\text{m}/\text{mrad}$)

$$\frac{\partial y}{\partial \alpha} = 1554 \bar{C}_{22} + 1666 \bar{C}_{12} + \Phi \left(\frac{\partial A_b}{\partial \alpha} \right) \quad (8)$$

With an anticipated IRBPM resolution of a few microns, variation of crossing angle by 1 mrad gives a resolution on \bar{C}_{22} and \bar{C}_{12} of ~ 0.001 . (The typical colliding beam crossing angle is $\sim 3\text{mrad}$.) The resolution of the traditional synchronous phase measurement is 0.01.

A useful characterization of the coupling is in terms of the slope of the measured positions at the IR detectors versus crossing angle. The measured slope is then compared with the machine model. As an example we consider the coupling introduced by vertical misalignment of the ring sextupoles. We misalign all of the ring sextupoles according to a Gaussian distribution defined by $\sigma \sim 200\mu\text{m}$ and with a 2σ cutoff. We can compute both the change in \bar{C}_{12} at all of the beam detectors, and the change in the slope of y versus θ^* at the IRBPMs. We find that the change in \bar{C}_{12} is of order 0.01 and just about at the resolution limit of the synchronous coupling measurement. But the change in slope corresponds to position changes of $28\mu\text{m}$ for $\theta^* \sim 1\text{mrad}$. With a position resolution of about $6\mu\text{m}$, the change in slope due to the coupling introduced by the sextupole misalignment is easily measured.

Coupling Correction using Skew Quadrupoles

To improve the quality of our model of machine coupling we propose to complement the traditional synchronous phase measurement data with measurements of the response matrix at the IR beam position monitors. The CESR ring includes 12 pairs of skew quadrupoles distributed symmetrically around the ring. We find that we can fit position data and phase and coupling data simultaneously with suitable adjustment of the corrector skew quadrupoles. A Levenberg-Marquardt optimization routine is then used to adjust the skew quadrupoles so that the CESR ring model reproduces the measurements. We plan to load the computed skew quadrupole strengths into CESR and then iterate the process. A similar technique, based exclusively on the synchronous phase data [4] has proved quite successful correcting optical errors in the machine arcs, but not so in the IR where, because of the very strong focusing and complicated solenoid compensation, additional constraints are required.

As an example of the leverage of the position measurement in resolving coupling errors we first make a synchronous measurement of phase and coupling around the ring. A comparison of the data \bar{C}_{12} and fitted model is shown in Figure 1. The model is based on a fit to the measured coupling data, using skew quadrupoles as fit parameters. After completing the coupling measurement, and without changing machine conditions, we measure the ver-

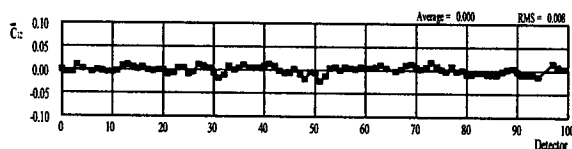


Figure 1: Difference between measured and modeled \bar{C}_{12} . The fit is based on the measured coupling \bar{C}_{12} data.

tical position at the IRBPMs versus crossing angle by varying horizontal separator strengths. The data for the west IRBPM is shown in Figure 2. Meanwhile we can predict the position dependence based on the machine model that was used to predict the coupling parameters \bar{C}_{12} shown in Figure 1. The inconsistency of the prediction and the measurement is clear.

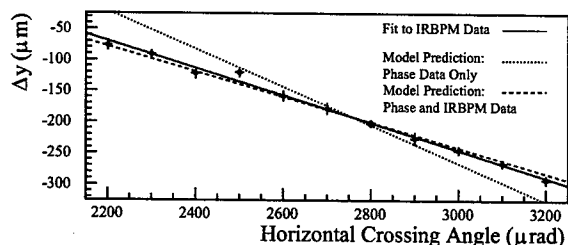


Figure 2: Data points indicate measured differential (positron minus electron) vertical position versus horizontal crossing angle. The solid line is a fit to the data. The dashed line is the model prediction based on a fit to both coupling data and position data. The dotted line is the model prediction based on a fit only to coupling data.

The next step is to try to find a new model that reproduces the position dependence as well as the coupling data. We fit to position data and coupling data simultaneously, again using skew quadrupoles as fit parameters as shown in Figure 2. Note the excellent agreement with the data. The difference between predicted and measured coupling data is shown in Figure 3. The fit of modeled to measured data in Figure 3 is as good as the fit in Figure 1. But the model used in Figure 3 also reproduces the position data. Evidently, the measurement of position at the IR detectors can be used to remove the degeneracy in the modeled machine coupling and to reduce coupling errors at the collision point.

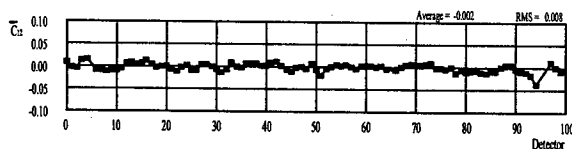


Figure 3: Difference between measured and modeled \bar{C}_{12} . The fit is based on the measured coupling \bar{C}_{12} data and the IRBPM position dependence.

Measured dependence of vertical position at the IR detectors on horizontal excitation of kickers helps remove the uncertainty in the coupling in the interaction region. We plan to extend the measurement and fitting procedure to include dependence of horizontal position on vertical excitations so that we can remove the remaining degeneracy in the machine model. With a unique model of the coupling optics we can systematically remove the optical errors in the interaction region that limit performance.

COLLISION ASSURANCE

Having corrected the coupling we would like to develop the capability to monitor relative displacement of the beams at the IP by interpolation from the pair of IRBPMs. As described above, it is straightforward to extrapolate horizontal and vertical position differences measured at the detectors to the interaction point. The measurement resolution of the detectors at present is about $6\mu\text{m}$ which corresponds to an uncertainty of also about $6\mu\text{m}$ in the relative positions at the IP or about one and a half times the vertical beam size ($\sigma_y^* \sim 4\mu\text{m}$). We expect that with better understanding of the systematics and implementation of improvements to the electronics described above, that a resolution of a fraction of the beam size can be obtained.

CONCLUSIONS

The traditional method of synchronous phase measurement for characterizing optics in CESR lacks the resolution to adequately identify transverse coupling errors at the collision point. The measurement requires a single beam on axis, rather than along the design pretzel trajectory. In addition, because only one element of the coupling matrix is measured, the fitted model is degenerate. The new high resolution beam position monitors yield a measurement of the response matrix with an order of magnitude better resolution and the redundancy necessary to remove this degeneracy. We anticipate that the new system will give a unique determination of the coupling in the IR.

The authors would like to thank the CESR operations group for their support of this work.

REFERENCES

- [1] S. B. Peck and D. L. Rubin, Proc. of the 1999 IEEE Part. Accel. Conf., p.285.
- [2] D. Edwards and L. Teng, IEEE Trans. Nucl. Sci. **20**, 3(1973).
- [3] D. Sagan and D. Rubin, Phys. Rev. ST Accel. Beams **2**, 074001(1999).
- [4] D. Sagan *et al.*, Phys. Rev. ST Accel. Beams **3**, 092801(2000).
- [5] M.A. Palmer, *et al.*, Proc. of the 2001 IEEE Part. Accel. Conf., p.1360.

POWER SUPPLY PERFORMANCE MONITORING AND ANALYSIS USING OPERATION DATA *

J. Li†, Y.K. Wu, S. Hartman

FEL Lab, Duke University, Durham, NC 27708, USA

Abstract

Magnet power supplies are critical components of a storage ring. The performance of power supplies directly impacts the stability and reliability of the storage ring operation. There are several type of DC power supplies in Duke FEL storage ring. The performance data of power supplies can be collected in a non-interruptive manner by an EPICS archiver or by a MATLAB program. MATLAB based tools have been developed to analyze the power supply data collected during the operation. Careful evaluation of data allows us to identify a power supply with degraded performance and provide a reference to perform preventive maintenance.

INTRODUCTION

The Duke storage ring was designed to accommodate a variety of FELs [1]. There are several type of DC power supplies used to power dipole, quadrupole, sextupole, and corrector magnets. The performance of these power supplies directly impacts the stability and reliability of the storage ring operation. For example, a bad power supply may change the transverse tune, chromaticity, and orbit of the stored beam. So it is important to pay enough attention to these power supplies. The efforts that we have made to improve the performance of power supplies include the following two parts: (1) modifying and tuning power supplies to meet their specifications [2]; (2) maintaining power supplies' performance for operation. In this paper, we will present the method to monitor the performance of the power supplies.

Two kinds of tools are used to log the performance data of the Duke storage ring power supplies. One is the EPICS archiver [3] which has been configured to log the set and readback current of power supplies in a non-interruptive manner. It usually works at a relatively low sampling rate. The sampling rate can be chosen to meet the real operation need. For performance reason, the archiver will be automatically disabled during ramping. Another tool is a MATLAB based tool, "srmonitor", which we have developed to log data at a higher sampling rate. It logs not only the power supply data but also other important parameters of the storage ring. This tool is usually used in machine studies. For example, it can monitor the stability of power supplies and the beam orbit with a fixed lattice, as well as log the ramping data for further analysis.

* Research supported by DoD MFEL program as managed by the AFOSR, grant F49620-001-0370.

† jing@fel.duke.edu, 1-919-660-2677 (phone)

POWER SUPPLY PERFORMANCE ANALYSIS

To analyze the performance of power supplies, we have developed a set of MATLAB based tools. These tools are used to read data from the EPICS archiver, convert the data to the MATLAB format, and analyze them. The data are analyzed by computing the difference between readback and set current of each power supply and the peak-to-peak value of this difference (see Eq. 1).

$$\begin{aligned}\Delta I &= I_{\text{set}} - I_{\text{read}} \\ \Delta I_{PP} &= \max(\Delta I) - \min(\Delta I)\end{aligned}\quad (1)$$

where I_{set} and I_{read} are set and read back currents respectively, ΔI is their difference, and ΔI_{PP} is the difference between maximum and minimum ΔI .

The power supplies of Duke FEL storage ring can be divided into two groups. The first group of power supplies, such as corrector and quadrupole trim supplies, usually work at a relatively low or near zero current level. The ΔI_{PP} is used as the performance merit for this type of supplies. Another group of power supplies, such as dipole and quadrupole supplies, usually work at a relatively high current level. For this type of power supplies, the normalized peak-to-peak value is calculated for performance as follows:

$$\Delta I_{NPP} = \frac{\Delta I_{PP}}{I_{\text{set}}}$$

The performance of each group of power supplies is usually plotted in separate bar charts: (1) main magnet supplies, including dipole and quadrupole supplies; (2) quadrupole trim supplies; (3) orbit corrector supplies. The difference between readback and set current of each power supply is also plotted as a function of time for detailed analysis.

The power supply performance has been analyzed weekly. To cover a wide energy range of operation in the entire week, the largest peak-to-peak performance of each power supply is plotted on the bar chart for the worst case scenario analysis.

The measured power supply performance is sometimes distorted by the accuracy of the control and readback system. For example, the Walker supplies powering straight section quadrupoles are read by a 14-bit CAMAC SAM ADC with auto-gain which has a relative accuracy of 300 ppm. The specification of power supply and the measurement accuracy of the control/readback system are listed in Table 1.

Table 1: Power Supply Specification and Measurement System Accuracy at 1 GeV

Magnet Family	Power Supplies	peak-to-peak Spec.	Meas. Accuracy
Dipole	PEI	50 ppm	< 20 ppm
Arc Quad.	Bruker	50 ppm	< 20 ppm
SS Quad.	Walker	100 ppm	300 ppm
Orbit Trim	Corrector	2 mA	< 1 mA
Quad. Trim	Corrector	2 mA	~ 1 mA

Fig. 1 and Fig. 2 show the logged data of main magnet and horizontal orbit corrector supplies on Dec. 13, 2002 at 700 MeV. With the exception of one Walker supply, all power supplies seem to be operating normally within the limits of the measurement system.

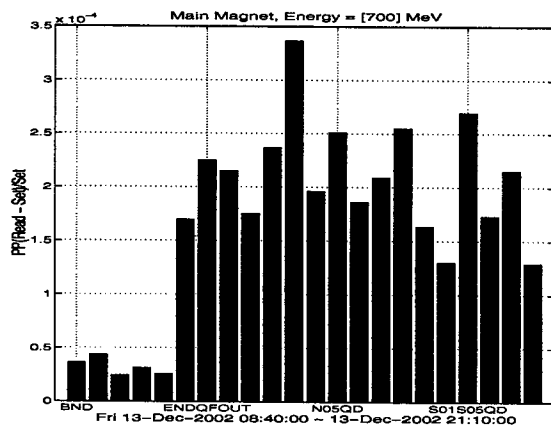


Figure 1: Peak-to-peak values of main magnet supplies. The first supply is PEI, followed by 4 Bruker and 17 Walker supplies.

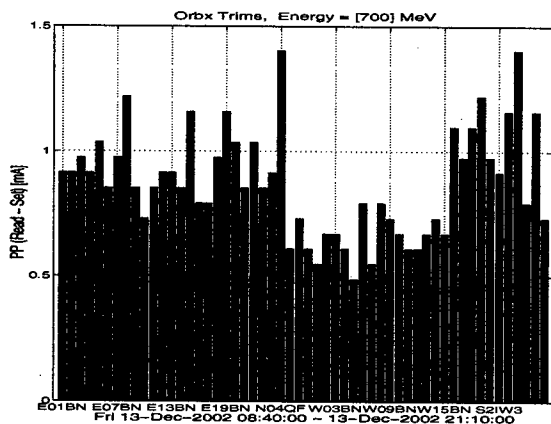


Figure 2: Peak-to-peak values of X orbit correctors.

To reveal the problem of a misbehaving power supply, the detailed performance data is plotted as the function of

operation time. As an example, when analyzing the data on Feb 18, 2003, we found the normalized peak-to-peak value of the PEI supply powering the dipole magnets was 90 ppm which was about twice of its specification. Plotting the difference between the readback and set current, we found that it varied by 30 mA (see Fig. 3). This problem was reported and has been investigated.

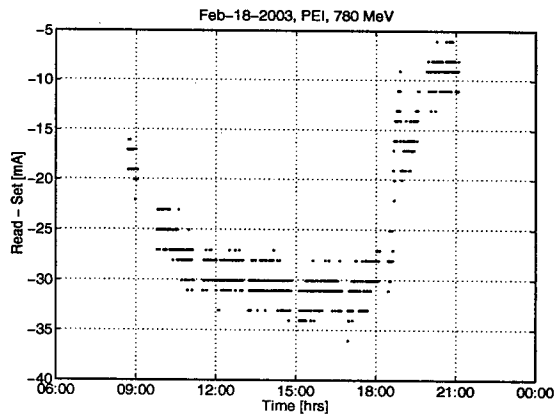


Figure 3: Performance of dipole magnet supply (PEI). The difference between the readback and set current varied by about 30 mA.

OTHER ANALYSIS BASED ON THE ARCHIVED DATA

Besides for power supply performance analysis, the logged data can also be used to characterize the ramping performance and orbit stability.

Ramping Analysis

There are several operation modes for the Duke storage ring, most of which need energy ramping after injection. The control system is developed based on physics quantities. The energy ramping can be carried out by stepping the energy knob [4]. The "srmonitor" has been used to log the ramping data (see Fig. 4). Since the energy ramping is a relatively fast procedure, the sampling rate for "srmonitor" is chosen as 1 Hz. Using the logged data, the following effects can be studied:

- missed current setpoints during energy ramping;
- the accuracy that readback tracks the setpoint;
- the overshoot at the end of ramping;
- lifetime and orbit stability during ramping.

For example, from Fig. 4, we can see there are no missed points during the ramping, and the the readback tracks the setpoint well. The current dependency is more than linear after 800 MeV, indicating that the field begin to saturate.

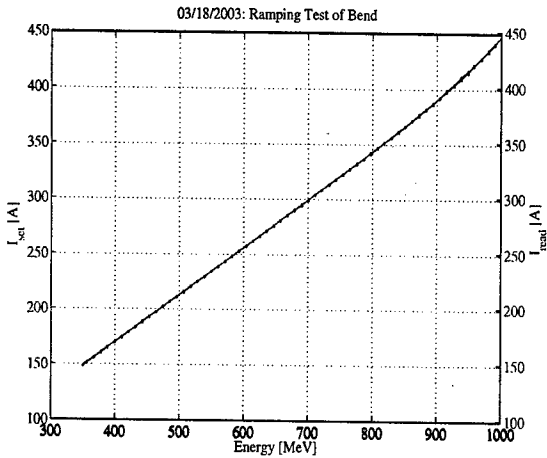


Figure 4: Performance of dipole supply during ramping

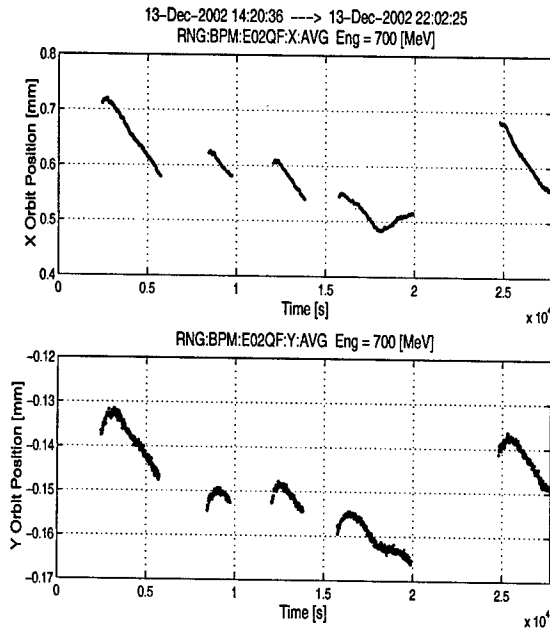


Figure 5: Orbit stability at BPM E02QF without orbit feedback.

Orbit Stability Monitoring

Using the logged data, the orbit reproducibility and stability during operation can be analyzed. The following is an example of such analysis using the orbit data at BPM E02QF (see Fig. 5). The data were logged with a fixed storage ring lattice without orbit feedback. For this BPM, the worst orbit reproducibility among all fills was about 180 μm horizontally and 20 μm vertically. During the run after refill, the max orbit drift was about 140 μm horizontally and 16 μm vertically. It is worth pointing out that part of the orbit drift was due to the current dependency of BPM readings. This problem is been investigated and will be re-

solving soon [5].

CONCLUSION

Several misbehaving power supplies have been found by analyzing the logged data using these tools. The results have been reported for maintenance reference. Besides for the analysis of power supply performance, the tools can also be used to do a variety of analysis, which are also very useful to improve the performance of the ring.

ACKNOWLEDGMENTS

We would like to thank V. Litvinenko for his encouragement and support.

REFERENCES

- [1] S.F Mikhailov, V.N. Litvinenko, Y. Wu, Proceedings of the 2001 Particle Accelerator Conference, Chicago, P3528.
- [2] Y. Wu, V. G. Popov, S. Hartman, et al, "Improving Power Supply Performance for the Duke Storage Ring", these Proceedings.
- [3] EPICS Channel Archiver, <http://lansce.lanl.gov/lansce8/Epics/Archiver/doc/default.htm>
- [4] Y.K. Wu, S.Hartman, S.F Mikhailov, "A Physics Based Control System for Duke Storage Ring", these proceedings.
- [5] Y.K. Wu, J. Li, P. Wang, "BPM and Orbit Correction Systems at the Duke Storage Ring", these proceedings.

STATUS OF THE BOOSTER SYNCHROTRON FOR DUKE FEL STORAGE RING*

S.Mikhailov[#], V.Litvinenko, M. Busch, M. Emamian, S.Hartman, I.Pinayev, V.Popov, G.Swift, P.Wallace, Y.Wu, FEL Laboratory, Duke University, Durham, NC 27708, USA

N.Gavrilov, Yu. Matveev, D.Shvedov, N.Vinokurov, P.Vobly
Budker Institute of Nuclear Physics, Novosibirsk, Russia

Abstract

In this paper we present current status of the Booster Synchrotron for the Duke FEL storage ring. The Booster which is recently under design, fabrication and construction, will provide full energy injection into the storage ring at energy from 0.3 to 1.2 GeV. The Duke storage ring FEL (SR FEL) operates in lasing mode with 193-700 nm wavelength range. The geometry of the Duke SR FEL provides for interacting head-on collision of e-beam and FEL photons. This mode of operation is used to generate intense beams of γ -rays from 2 MeV to about 200 MeV (currently from 2 MeV to 58 MeV). Generation of γ -rays with energy exceeding 20 MeV causes the loss of electrons, which will be replaced by injection from the Booster operating in a top-off mode. The paper presents design and status for elements of magnetic system and vacuum system, as well as design and parameters of fast extraction kicker with 11 nS pulse duration. All these element are designed and will be fabricated by Budker Institute of Nuclear Physics, Novosibirsk, Russia.

BOOSTER LATTICE AND DESIGN

The Duke Booster synchrotron is relatively compact 31.9 m circumference machine with race-track shape (fig.2). Two arcs are separated by 6.24 m straight sections accommodating RF cavity, injection and extraction kickers and septum magnets. The total circumference of the machine is exactly 19 RF wave lengths of the storage ring. Since the initial reported version of design [1] we increased the length of the straight sections by one RF wave each. RF frequencies of the main Duke storage ring and the Booster are identical. Two additional defocusing quads were also added into the straight sections. These modifications allowed us to relieve aperture constrains for single kick vertical injection and extraction [2].

The lattice of the Booster consists of 6 effective triplets, two of them, those in the middle of the arcs, have a virtual defocusing quads made by vertically focusing dipole edges. Lattice is optimized for the fast 11 nS pulse kicker providing for the single bunch extraction [2]. One of the major requirements for the magnetic design was fitting the Booster into existing storage ring room to avoid cost extensive building construction.

The shortest operation cycle is 2.5 sec (Fig.1) which is determined by maximum required average extraction rate from the Booster to the storage ring of up to 4-5 nC/sec. Therefore, the ramp of energy from injection $E=0.27$ GeV

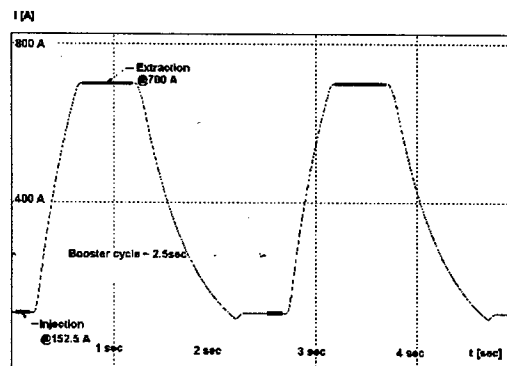


Figure 1: Booster shortest operation cycle $T=2.5$ sec.

to extraction of up to $E=1.2$ GeV has to be as short as 0.5-0.8 sec.

MAGNETIC SYSTEM

Magnetic system of the Booster includes 12 bending magnets with parallel edges, 8 focusing and 8 defocusing quadrupoles, injection and extraction septum magnets of Lamberson type, 4 focusing and 4 defocusing sextupoles for chromaticity correction, 4 strong (10 and 12 mrad) vertical trim dipoles producing a local orbit bump prior to injection and extraction, and four weak (up to 2 mrad at $E=1.2$ GeV) horizontal trim dipoles for injection and extraction orbit correction. All the bending dipoles and quadrupoles of the Booster are fed by single power supply [2] with maximum current $I=700$ A for $E=1.2$ GeV (Fig.1). There is also vertical orbit trim in each quad and horizontal orbit trim in each bending dipole. The maximum strength of those trims at $E=1.2$ GeV is 1.75 mrad for the vertical in quads and 10.5 mrad for the horizontal in the dipoles.

There are three quadrupole families, two focusing (QF1 and QF2) and one defocusing (QD). Parameters of the quads are listed in Table 1. The aperture of the quads is $D=50$ mm. The required variety of the quad strengths is provided by combination of three types of coils and two

Table 1: Parameters of Booster quadrupoles

Type	Qt y	Turns per pole	L_{eff} [cm]	L_{core} [cm]	$E=1.2$ GeV	
					G_{max} [T/m]	$K1$ [m ⁻²]
QF1	4	10	0.151	0.146	27.62	6.901
QF2	4	7			19.54	4.882
QD	8	3	0.131	0.125	8.37	2.092

*Supported by the Dean of Natural Sciences, Duke University

[#]smikhail@fel.duke.edu

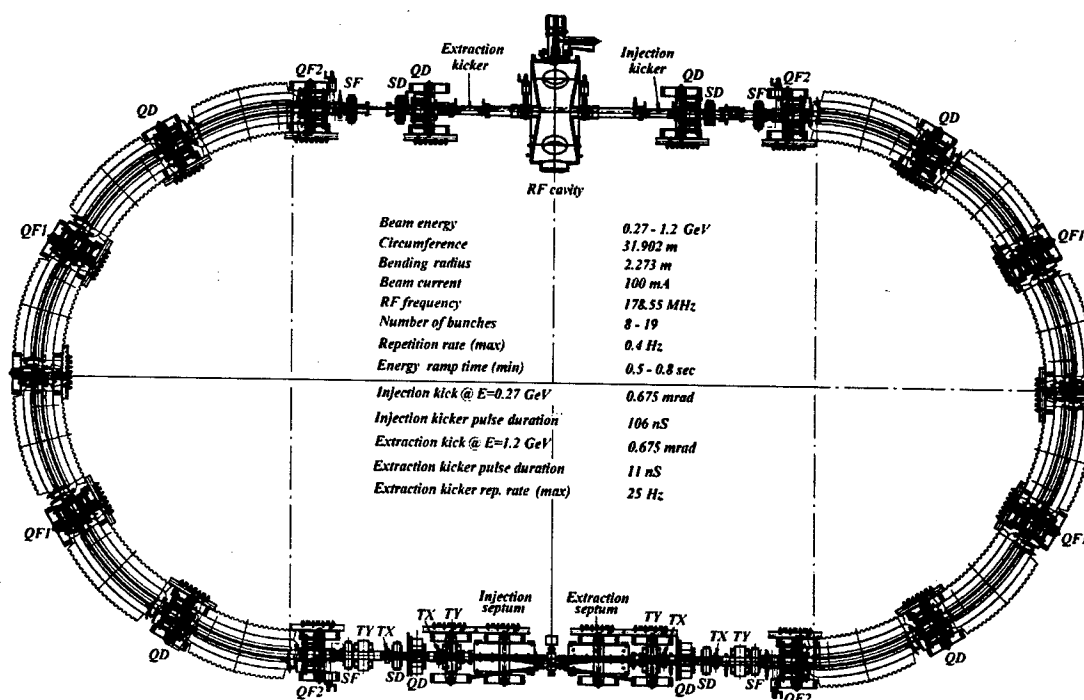


Figure 2: Layout and parameters of the Booster synchrotron

types of cores. The coils have the same shape but different number of turns (10, 7 and 3 for QF1, QF2 and QD respectively). The cores are the same in cross section and different in length (see Table 1). Besides of the vertical orbit correction coils (120 turns per pole, $I_{max}=6$ A) each quad also has gradient correction of up to $\Delta G/G_{max}=3.5\%$ for QF1 (40 turns per pole, $I_{max}=6$ A).

The core of the quads is made of Stabocor 940-50A low carbon/low silicon laminated steel with 0.5 mm thick laminations. The poles are shimmed to minimize 2D harmonic contents to be within $|b_n/b_2| < \pm 5 \times 10^{-5}$ for $n=6, 10, 14$, and 18 at $R_n=2.4$ cm for any current up to $I=700$ A. A comprehensive end chamfer, optimized for the minimum integral harmonic content ($|\int b_n ds / \int b_2 ds| < \pm 3.6 \times 10^{-4}$, $n=6, 10, 14$, and 18, at $R_n=2.4$ cm, for the quads of all types at any current up to $I=700$ A), also provides against 3D edge saturation during the fast ramp of current.

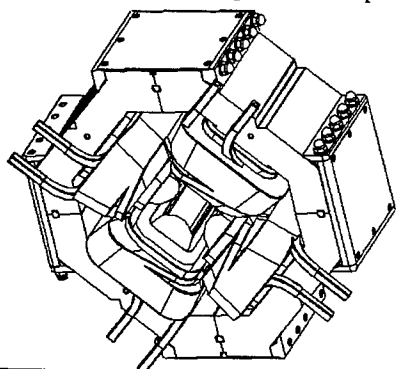


Figure 3: General view of QF1 quadrupole.

The bending dipoles have maximum field $B_{max}=1.76$ T at $E=1.2$ GeV in 27 mm gap and effective magnetic length $L_{eff}=1.19$ m. Each dipole has a trim coil capable of correction up to $\Delta B/B_{max}=2\%$ (60 turns per pole, $I_{max}=6$ A). For the end chamfers we accepted the shape developed for a dipole designed for 10 Hz operation cycle [3]. To fabricate the dipole cores we use 1 mm thick laminations of Stabocor 1500-100SG low carbon steel.

Stabocor steel is produced with a layer of glue on the sheets. To fabricate the parts of the core for both quads and dipoles their laminations are stacked in fixtures under specific pressure and then baked out. This makes the core practically solid, so that its parts may be machined, drilled, etc. The stacking factor for the magnetic simulations was assumed to be 0.98.

The other magnetic elements, such as septum magnets, sextupoles and trim dipoles are solid, their capability of fast field ramping is tested. We re-use existing sextupoles ($D=60$ mm) and weak dipole trims (72 mm gap).

Simulations and optimization for all the magnetic elements of the Booster have been done with the use of MERMAID 3D code [4].

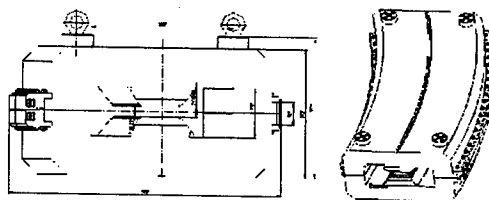


Figure 4: General view of the Booster dipole (core).

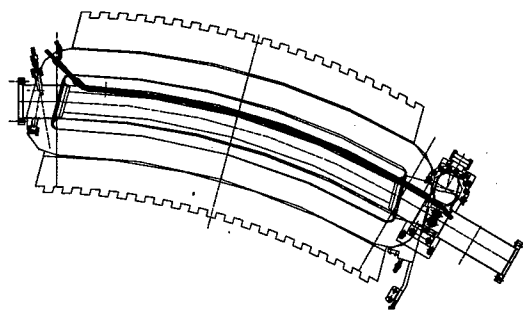


Figure 5: Arc periodic vacuum chamber (dipole & quad).

VACUUM SYSTEM AND KICKERS

The Booster has a stainless steel vacuum chamber. The arc chamber consists of 6 identical pieces (dipole & quad chambers). The dipole part of that periodic piece (Fig.5) is fabricated of 3" OD pipe with 0.049" thick wall. Stay clear area in the dipole is an ellipse of 107x24.5 mm.

Each periodic piece of the arc chamber accommodates a vacuum pump. In the arcs we install 6 NMD-0.1 (100 l/sec) and 6 PVIG-100/160 Russian ion getter pumps [5]. The latter are equipped with a TSP module. We also install nine 20 l/sec Varian pumps in the straight sections.

The calculations of the vacuum pressure distribution along the Booster ring showed that at injection $E=0.27$ GeV, 100 mA beam current, initially we can expect maximum pressure $\sim 1.5 \cdot 10^{-6}$, and after few weeks of SR cleaning it will drop down to $\sim 2 \cdot 10^{-9}$. The corresponding life time determined by the scattering on the residual gas initially may be expected as low as 4-5 sec, however after the SR cleaning it should increase up to 50 min.

One of the most challenging part of the Booster project is the single bunch extraction kicker with 11 nS pulse duration. The prototype of such a kicker has been fabricated and successfully tested, the design of real kickers is finished. Fig.6 plots their cross section. The use of novel pseudo-spark thyatron type commutators for the

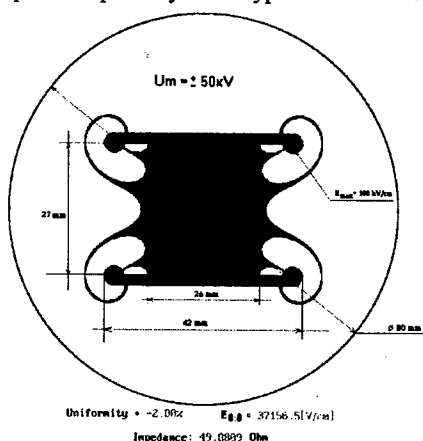


Figure 6: Extraction kicker for the Booster. Blue color shows 2 % homogeneity region. Vacuum pipe OD=80 mm.

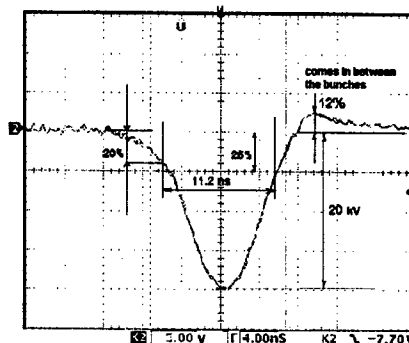


Figure 7: Extraction kicker pulse obtained with the use of fast pseudo-spark commutators (thyatrons)

kicker drivers is suggested instead of spark gaps commonly used for the very short pulses. The pseudo-spark commutators easily cover the entire voltage range required for the energy range 0.27-1.2 GeV. Fig. 7 shows the pulse shape measured on the kicker driven by the pseudo-spark commutators.

CONCLUSIONS

The design of the magnetic elements and the arc vacuum chamber of the Booster is finished and their fabrication started. Design of the vacuum chamber for the straight sections and design of the magnet supports with cooling pipes are to be finalized. Existing RF system from the storage ring will be used for the Booster after replacement by new RF with HOM damping. The disassembly of that existing RF system and installation of the new one into the storage ring is planned for February – April 2003. Booster main power supply is recently under construction and testing. Magnetic elements will arrive to Duke along with the vacuum chambers, kickers and magnet supports in May 2004. We plan to start the installation of the Booster on Summer – Fall 2004 and commission it during first half of 2005. The entire project, including modification of the north straight section of the storage ring for the injection from the booster, installation and commissioning of new linac-to-booster and booster-to-ring transfer lines, shall be completed in 2005 – 2006.

REFERENCES

- [1] S.F.Mikhailov, V.N.Litvinenko, P.Morcombe, G.Swift, N.A.Vinokurov, N.G.Gavrilov, Yu.G.Matveev, D.A.Shvedov, "Project of Booster Synchrotron for Duke FEL storage ring", Proc. of the 2001 Part. Acc. Conf., Chicago, 2001, p. 3525-3527.
- [2] S.Mikhailov, "Challenges for magnetic design of a compact Booster fed by single power supply", this proceedings.
- [3] Baryshev Yu.V., Dikansky N.S., Mikhailov S.F., et al., "LEB Dipole and Quadrupole Prototypes for SSC", Proc. of 1994 European particle accelerator conf. EPAC'94, London, 1994, Vol.3.- p.2223-2225.
- [4] Mermaid, the 2D/3D code for magnetic design, © A.N.Dubrovinn, Novosibirsk, Russia.
- [5] <http://www.pryzma.ru>

CHALLENGES FOR MAGNETIC DESIGN OF A COMPACT BOOSTER FED BY SINGLE POWER SUPPLY *

S.F.Mikhailov[#], FEL Laboratory, Duke University, Durham, NC 27708, USA

Abstract

In design of full energy Booster injectors, commonly used in the modern accelerator facilities, there is a tendency of avoiding saturation of the magnetic elements in order to avoid losses associated with tune change during the energy ramp. Typical maximum field in the bending magnets of the modern Booster projects of 1.0-1.4 T results in the large circumference. For 0.27-1.2 GeV full energy Booster injector for the Duke FEL storage ring, recently under design and fabrication, there was an ultimate goal to fit it into existing storage ring room to avoid cost extensive building construction. Therefore, the Booster ring has to be compact, therefore the maximum field in the bending magnets was accepted 1.76 T. With a different level of saturation in the bending magnets, focusing and defocusing quadrupoles it was not possible to avoid a tune change with the energy rise. However, the ratio of saturation levels for the elements was optimized to avoid crossing of any significant resonance while ramping through the entire energy range. The lattice was simulated for different energies based on the results of 3D calculations of the magnetic elements with the use of MERMAID 3D code [1]. Another challenging part of the design was supplying all the dipoles and quadrupoles by single power supply.

BOOSTER LATTICE

A fast Booster-shynchrotron providing for a full energy top-off injection is commonly accepted in nowadays an integral part of any modern accelerator facility, specifically for SR facility. The one for the Duke FEL storage ring was proposed in the year 2000 as a part of the DOE proposal to improve drastically performance of the High Energy γ Source (Hi γ S) at Duke [2, 3].

The Booster will provide for top-off replacement of up 4 nC/sec of electron loss while producing intensive γ -rays beam of high energy. Extraction energy must be variable within 0.3-1.2 GeV range. Existing 270 MeV linac will be injector for the Booster. The RF frequencies of the Booster and the storage ring are identical. The odd ratio of the harmonic numbers of the ring and the Booster 64/19 provides for extraction of individual bunch from any bucket of the Booster into selected RF buckets of the storage ring. The lattice is optimized for the fast 11 nS pulse kicker providing for the single bunch extraction. The value of that kick has to be as low as possible. Thus, we have chosen vertical single kick symmetrical injection/extraction scheme with $\beta_y \approx 25$ m (Fig.2) at the location of the kickers and septum magnets. $Q_y \approx 1/2$ allows to install them in the opposite straight sections.

Table 1: Main parameters of the Booster (at 1.2 GeV)

Maximum beam energy [GeV]	1.2
Injection energy [GeV]	0.27
Average beam current [mA]	100
Circumference [m]	31.902
Bending radius [m]	2.273
RF frequency [MHz]	178.55
Number of bunches	8 - 19
Shortest operation cycle [sec]	2.5
Energy rise time, min [sec]	0.5 - 0.8
Beam emittance ϵ_x, ϵ_y [nmrad]	350/ 15
Maximum β_x, β_y, η_x [m]	25.4/9.4/1.4
Betatron tunes Q_x/Q_y	2.43/ 0.46
Momentum compaction factor	0.153
Natural chromaticity C_x/C_y	-1.7/ -3.7
Damping times τ_x, τ_y [mS]	3.16/ 1.58
Energy loss per turn [KeV]	80.7
Energy spread $\sigma E/E$	$6.8 \cdot 10^{-4}$
Magnetic System:	
Dipoles (G=2.7 cm): ea./ B_{max} [T]/ L_{eff} [m]	12/ 1.76/ 1.19
Quadrupoles (D=5.0 cm):	
QF1: ea./ G_{max} [T/m]/ L_{eff} [m]	4/ 27.6/ 0.151
QF2: ea./ G_{max} [T/m]/ L_{eff} [m]	4/ 19.5/ 0.151
QD : ea./ G_{max} [T/m]/ L_{eff} [m]	8/ 8.4/ 0.131
Supplied by the same current I_{max} [A]	700
Sextupoles (D=6.0 cm):	
SF: ea./ B''_{max} [T/m ²]/ L_{eff} [m]	4/ 100/ 0.098
SD: ea./ B''_{max} [T/m ²]/ L_{eff} [m]	4/ 70 / 0.098

We have originally planned a single turn injection [4], though stacking is also considered. The orbit is pre-distorted prior to the kick by strong vertical trim dipoles located in the injection/extraction straight section and providing for 10 mm local orbit bump at septum magnets. The pre-distortion of the orbit relieves vertical aperture constraints associated with 27 mm dipole gap (~24 mm stay-clear). The kick value required for the injection/extraction is 0.675 mrad. The designed repetition rate for the extraction kicker is up to 25 Hz.

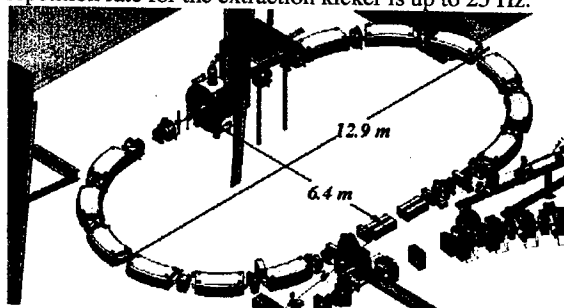
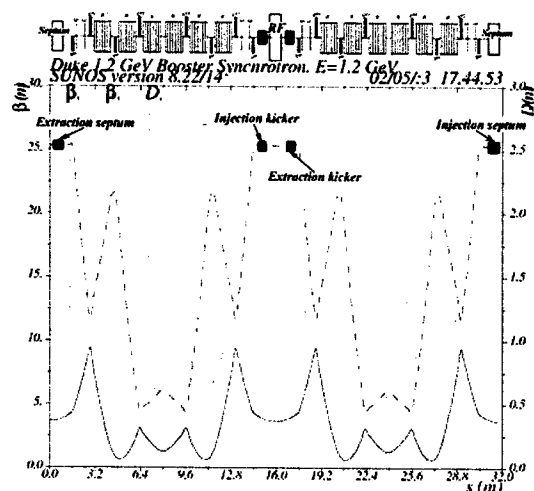


Figure 1: Layout of the Booster synchrotron in the North-East corner of the Duke FEL storage ring building.

*This work is supported by the Dean of Natural Sciences, Duke University
*smikhail@fel.duke.edu


 Figure 2: β -function and dispersion in the Booster ring.

MAGNETIC DESIGN

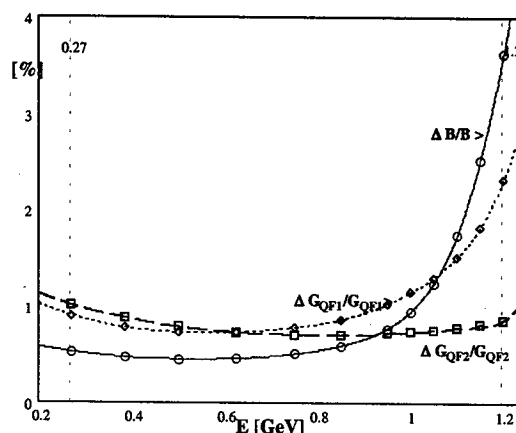
Use of single power supply for all magnets

To obtain required injection rate for the designed stored beam current the Booster must have 2.5 sec operation cycle. The energy has to ramp through the entire energy range 0.27-1.2 GeV within 0.5-0.8 sec. This is fast enough to consider supplying of all bending magnets and quads by the same power supply in order to avoid the current synchronization problems. Minimization of a variety of the quad families is a major concern in the lattice design of a ring fed by single power supply. In the Booster we use only two focusing and one defocusing families (see Table 1). Out of cost-saving and robustness consideration, the bending dipole has been constrained to be rectangular type. The required variety of the quad strengths is provided by combination of three types of coils and two types of iron cores. The coils have the same shape and different number of turns (10, 7 and 3 for QF1, QF2 and QD respectively). The cores are the same in cross section and different in length (146 mm for QF1, QF2 and 125 mm for QD).

All the dipoles and quads are laminated and have extensive end chamfers optimized both for the harmonic content and for the fast ramp [4, 5].

Cure of non-linearity of the magnets

The major cost-saving requirement of fitting the Booster into existing storage ring room (Fig.1) imposes strong limitation on its circumference and, therefore, on the bending radius of the dipoles. On the other hand, we tried to make possible an efficient full range energy ramp without any trimming, only by ramping the main current. From some level of the maximum field in the dipole in becomes simply impossible. The maximum of 1.76 T was found as a good compromise. The saturation of the poles at this field still significantly effects the lattice. Fig. 3 shows a relative effective "loss" of the field and gradient


 Figure 3: Effective "loss" of field/gradient in the core of the dipole and quadrupoles $\Delta B_{eff}/B$, $\Delta G_{eff}/G$ vs. energy.

in the core of the dipole and quadrupole magnets due to the finite permeability of the iron. The effective "loss" is determined taking into account an additional saturation of the magnet edges. For example, for dipole it is $\Delta B/B = 1 - \int B ds / B_{\mu=\infty} L_{effinj}$, where $B_{\mu=\infty}$ is the field calculated for the infinite permeability of the iron and L_{effinj} is effective magnetic length at injection energy. Significant saturation effect in the dipole appears from $B \approx 1.4$ T which in our case corresponds to $E = 0.95$ GeV. From that point the lattice starts rapidly changing. Fig.4 plots calculated drift of the betatron tunes on the energy ramp from 0.27 GeV to 1.2 GeV for all quads and bending magnets fed by the same current with no trims on. As one can see, the tune point makes a zigzag around a small spot at the beginning of the ramp and then, from the level of $E = 0.95$ GeV, starts rapidly floating along a straight line. The change of the tunes directly results from different level of saturation of bending magnets, focusing and defocusing quads. Designing all the magnetic elements with the same level of is possible in principle but absolutely unpractical because of huge difference in their strength and effective length. However, the ratio of their saturation levels is optimized so that the tune change is reasonable and the tunes do not cross any significant resonance through the entire energy range. To find an optimum, we studied dependency of the tune change ΔQ_{xy} on the effective saturation of the dipole and QF1 quad considering QF2 and QD practically linear. We observed that the total tune drift distance is approximately proportional to the non-linearity of the field loss in the dipole, while direction of the drift is determined by the ratio of effective saturation levels of the dipole and QF1 (Fig.5). The range $\Delta G_{QF1eff}/G_{QF1} \approx 1.8-3.9\%$ was found relatively "safe". Thus, we accepted $\Delta G_{QF1eff}/G_{QF1} = 2.4\%$ for the QF1. This allows some safety margins for the uncertainty of the magnetic properties of the iron and its packing factor.

Though the Booster is designed with sufficient number and strength of trims in the magnets anyway [5], this approach relieves the requirements on the synchronization of the trim currents during the energy ramp.

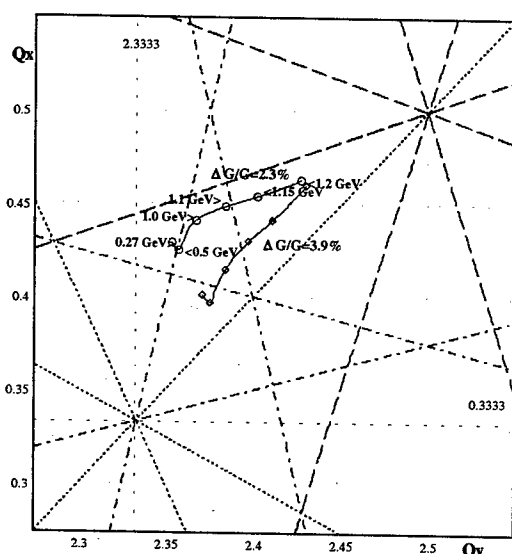


Figure 4: Drift of the betatron tunes during energy ramp 0.27-1.2 GeV with all the quads and bending magnets fed by the same current without trims. The upper curve (o) is for $\Delta G_{FIeff}/G_{FI}=2.3\%$ and the lower curve (◊) for 3.9%.

Compensation of chromaticity

Significant saturation of the dipole at the field higher than 1.4 T also causes nonlinear growth of sextupole component distributed along the dipole (body sextupole). Fig.6 shows dependency of the normalized integrated body sextupole along with the edge sextupole appearing at the ends of the dipole. This latter is almost constant over the entire range and determined by geometry of the dipole edge. Initial level of $K2L_{body}$ at low energy is pre-set by the pole shims to compensate $K2L_{edge}$ at injection. The growth of $K2L_{body}$ results in a growth of non-compensated chromaticity from $C_x/C_y = -1.5/-3.8$ at $E=0.27$ GeV to $C_x/C_y = -6.4/+16.5$ at $E=1.2$ GeV. The lattice is also optimized for favorable locations of the sextupoles

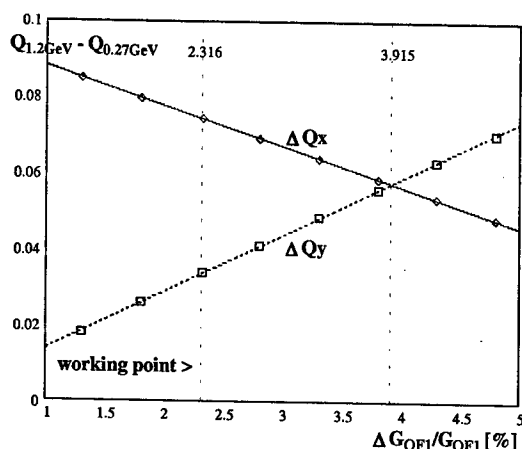


Figure 5: Tune change between $E=0.27$ GeV and 1.2 GeV for different effective level of saturation in the QF1 quad.

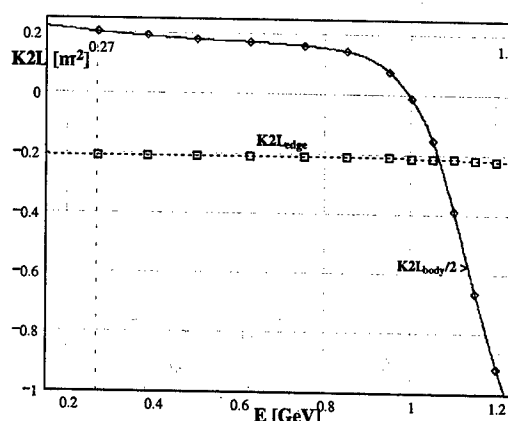


Figure 6: Integrated normalized sextupole in the bending dipole $K2L = \int B'' dl / B \rho$ vs. energy. $K2L_{edge}$ is contribution of the fringe field and $K2L_{body}$ is body sextupole.

where they need a minimum strength to compensate chromaticity within entire energy range. This allows us to re-use existing solid yoke sextupoles to be driven only for 1/8 of their nominal strength. Sextupole component induced by the eddy currents in the vacuum chamber of the dipoles during a fast linear ramp shall be compensated by pre-setting the sextupoles to small constant levels.

CONCLUSIONS

We found that 1.75 T maximum field in the bending magnets is a reasonable compromise for a compact Booster without pre-determined use of the trims for the tune change compensation. Certainly, there are a number of uncertainties not allowing us to design a Booster on a paper without further corrections. Among those we have to mention magnetic properties of the iron, staking factor for the laminated core, their variation, random and systematic, from magnet to magnet, mechanical imperfection of assembly, residual fields, etc. Thus, the model of the Booster based upon the results of magnetic simulations shall be corrected after the fabrication and magnetic measurements of the real magnets.

REFERENCES

- [1] Mermaid, the 2D/3D code for magnetic design, © A.N.Dubrovin, Novosibirsk, Russia.
- [2] HfS proposal to the US Department of Energy, Technical Description, September 2000.
- [3] V.Litvinenko, "Performance upgrade to the High Intensity γ -ray Source at Duke University", this proceedings.
- [4] S.F.Mikhailov, V.N.Litvinenko, P.Morcombe, G.Swift, N.A.Vinokurov, N.G.Gavrilov, Yu.G.Matveev, D.A.Shvedov, "Project of Booster Synchrotron for Duke FEL storage ring", Proc. of the 2001 Part. Acc. Conf., Chicago, 2001, p. 3525-3527.
- [5] S.Mikhailov, V.Litvinenko, M. Busch, N.Gavrilov, et al. "Status of the Booster synchrotron for Duke FEL storage ring", this proceedings.

FEASIBILITY STUDY OF A 2 GeV LEPTON COLLIDER AT DAFNE

G. Benedetti, D. Alesini, M. E. Biagini, C. Biscari, R. Boni, M. Boscolo, A. Clozza, G. Delle Monache, G. Di Pirro, A. Drago, A. Gallo, A. Ghigo, S. Guiducci, M. Incurvati, C. Ligi, F. Marcellini, G. Mazzitelli, C. Milardi, L. Pellegrino, M. A. Preger, P. Raimondi, R. Ricci, C. Sanelli, M. Serio, F. Sgemma, A. Stecchi, A. Stella, C. Vaccarezza, M. Vescovi, M. Zobov
LNF-INFN, Frascati, Italy

Abstract

While the main advances in the Standard Model probing require the construction of very high-energy colliders, many open questions still remain which can be answered by exploring low and medium energy regions. In this framework we are investigating the possibility of upgrading the ϕ -factory DAFNE [1] from the energy of 1.02 GeV c.m. up to the neutron-antineutron threshold (about 2 GeV c.m.) using the existing systems and structures. The luminosity required by the experiments for a light quark factory is of the order of few $10^{31} \text{ cm}^{-2} \text{ s}^{-1}$, easily achievable in the particle factory era. The very first results of the feasibility study are presented.

ENERGY UPGRADE OF THE FRASCATI FACTORY: GENERAL PROJECT

In the discussion about the future plans for the Frascati e^+e^- factory, one of the possibilities the DAFNE team is considering is the upgrade of the collider energy for new experiments up to about 2 GeV c.m. The hypothesis called DAFNE2 (Double Annular Frascati e^+e^- factory for Nice Experiments at 2 GeV) is aimed at the measurement of the form factors of the nucleon and the QCD excited states in

Table 1: DAFNE2 Parameters

Energy E_0	1.0 GeV
Luminosity L	$1 \cdot 10^{32} \text{ s}^{-1} \text{ cm}^{-2}$
Circumference C	97.69 m
Emittance ϵ	$0.5 \cdot 10^{-6} \text{ rad m}$
Coupling $\kappa = \epsilon_x / \epsilon_y$	0.009
Beta functions at IP β_x^* / β_y^*	1.5 / 0.025 m
Crossing angle at IP θ_x^*	$\pm 15 \text{ mrad}$
Bunch width at IP σ_x^* / σ_y^*	0.95 / 0.008 mm
Bunch natural length σ_z	13.9 mm
Linear tune shift ξ_x / ξ_y	0.014 / 0.024
Betatron tunes ν_x / ν_y	5.15 / 5.21
Momentum compaction α_c	0.009
Number of bunches	30
Particles per bunch	$3 \cdot 10^{10}$
Beam current I_{tot}	450 mA

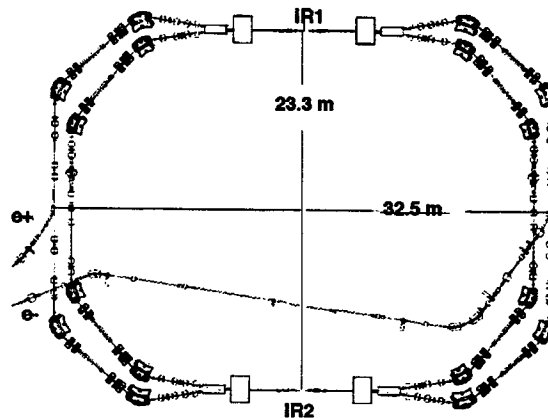


Figure 1: Main Rings layout.

the 1.2 to 2–2.5 GeV c.m. energy range [2]. This experimental program can be realized with the FINUDA [3] detector at a solenoid field of 0.3 T.

DAFNE2 can use without any change the DAFNE injection system (linac, damping ring and transfer lines) at 0.51 GeV and the two Main Rings with limited changes in the hardware to reach 1–1.25 GeV per beam.

Design Parameters

The experimental luminosity requirements are not critical for DAFNE2. This allows choosing the machine parameters with enough freedom, exploiting our commissioning know-how. We have worked out new parameters at the beam collision energy of 1 GeV.

Choosing an emittance $\epsilon = 0.5 \cdot 10^{-6} \text{ rad m}$ compatible with the ring aperture, a vertical beta function at the Interaction Point (IP) and a coupling factor already achieved, the linear tune shift is $\xi_x / \xi_y = 0.014 / 0.024$, below the limit achieved by DAFNE.

The horizontal crossing angle at the interaction point is $\pm 15 \text{ mrad}$, corresponding to a Piwinsky's angle:

$$\phi = \theta_x^* \frac{\sigma_z}{\sigma_x^*} = 0.22$$

which has already been exceeded in the existing factories.

The chosen number of bunches is 30 so that, leaving the harmonic number $h = 120$ unchanged, we can inject both electrons and positrons out of collision and collide the two beams by performing a RF phase jump [4] after having ramped the beam energy to 1 GeV.

Once fixed such parameters (Table 1), a luminosity of $1 \cdot 10^{32} \text{ s}^{-1} \text{ cm}^{-2}$ is straightforward to achieve with 15 mA per bunch and a total current of 0.45 A.

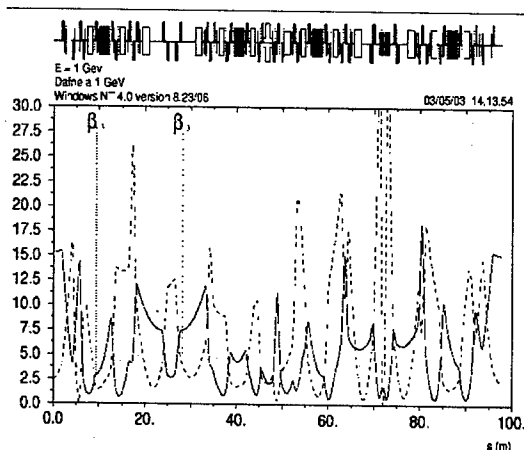


Figure 2: DAFNE2 ring beta functions calculated by MAD.

MAIN RINGS

The design of the two collider Main Rings is unchanged (Figure 1): two different rings for positrons and electrons with two 10 m long Interaction Regions where the opposite beams travel in the same vacuum chamber. Four wigglers per ring are installed in the arcs. The existing vacuum chamber is reused.

The experiment FINUDA is in the Interaction Region 2 (IR2) and in the opposite Interaction Region (IR1) two quadrupole doublets are installed: a lattice already used when only the KLOE detector was installed [5].

More study has to be done on the energy ramping, to be performed keeping the betatron tunes constant.

Optics

The main optical features at 1 GeV are (Figure 2):

- Only one low beta insertion in IR2, where the experimental detector is housed and the positron and electron beams collide at a horizontal angle of ± 15 mrad.
- In IR1, four FDDF quadrupoles allow to separate the two beam trajectories with a vertical bump of ± 1 cm.
- Horizontal and vertical beta functions in the four achromat arcs, where the dispersion is higher, are separated to correct both horizontal and vertical chromaticities with chromatic sextupoles.
- The horizontal beta function and the dispersion are shaped in such a way that the natural emittance does not change from 0.51 to 1 GeV as explained in the next section.

Interaction Region 2

The low beta insertion is realized with four FDDF quadrupoles housed inside the experimental detector (Figure 3). Since they must be powered for variable beam energy, the only solution to fit them inside the detector is developing superconducting quadrupoles as for example at upgraded HERA [6]. Two further doublets outside the detector are realized with conventional quadrupoles.

The FINUDA solenoid field integral of $0.3 \text{ T} \times 2.4 \text{ m}$ at the collision energy rotates the beam by an angle of 6° around the longitudinal axis. The coupling at the Interaction Point and outside IR2 is corrected with the rotating frame method [7]: each quadrupole is rotated around its longitudinal axis following the rotation of the beam and two compensating solenoids $0.36 \text{ T} \times 1 \text{ m}$ provide cancellation of coupling outside the IR. The solenoid fields and the quadrupole rotation angles are fixed. At the injection energy of 0.51 GeV the non vanishing coupling from mismatched quadrupole rotation angles can be useful to have a long beam lifetime during ramping and can be controlled with the skew quadrupoles in the ring.

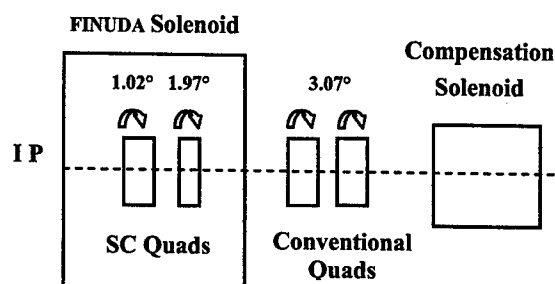


Figure 3: half Interaction Region 5 m long layout: from the Interaction Point (IP) to the splitter magnet.

Synchrotron Radiation and Emittance

The synchrotron radiation loss per turn depends on the energy and on the bending radius in dipoles as:

$$U_0 = C_\gamma \frac{E^4}{2\pi} \oint \frac{ds}{\rho^2}$$

The wigglers are useful at the injection energy to increase synchrotron radiation and decrease damping times. From 0.51 to 1 GeV the wiggler field is kept constant, since it is already near saturation and the synchrotron radiation from the energy increase is high enough to improve damping times (Table 2).

The emittance in electron storage rings depends on the second power of the energy according to:

$$\varepsilon = C_q \gamma^2 \frac{\langle H / |\rho|^3 \rangle}{J_x \langle 1 / \rho^2 \rangle}$$

and to have constant emittance at different energies the dispersion invariant:

$$\mathcal{H} = \gamma_x D^2 + 2\alpha_x D D' + \beta_x D'^2$$

is fairly reduced by changing the Twiss parameters in the arcs when the energy goes from 0.51 to 1 GeV.

Table 2: Energy loss with and without wigglers

without / with Wigglers		0.51 GeV	1 GeV
U_0	(keV/turn)	4.3 / 9.3	64.0 / 83.5
τ_x	(ms)	68 / 40	11 / 8.6
τ_E	(ms)	41 / 31	5.0 / 3.5

Table 3: RF System and Bunch Parameters

RF peak voltage V_{RF}	250 kV
RF frequency f_{RF}	368.26 MHz
Energy loss $U_{rad}+U_{paras}$	83.5 + 6.5 KeV/turn
RF power $P_{beam}+P_{wall}$	40.5 + 17.5 kW
Synchr. frequency f_{syn}	11.7 kHz

Magnets

Eight dipoles are installed in each ring: four 0.99 m long magnets with a 40.5° bending angle and four 1.21 m long with a 49.5° angle. The bending field in present magnets at 0.51 GeV is 1.2 T and the maximum field is 1.7 T, insufficient to reach 1 GeV: new stronger dipoles are needed.

The existing vacuum chamber puts constraints on the dipole geometry. With a different shape of the polar shoe, the same gap height and 10% longer magnets, we expect to achieve the needed field of 2.2 T with a $\Delta B/B = 2 \cdot 10^{-4}$ field quality in the ± 3 cm range, using a ferromagnetic alloy with higher saturation limit to realize the DAFNE2 dipoles. More work and simulations are in progress to study the features and the quality of such magnets.

Existing quadrupoles and sextupoles allow doubling the ring energy, some quadrupoles reach saturation, but we assume to avoid it with further optics optimisation.

RF Parameters and longitudinal bunch distribution

The DAΦNE RF cavity cooling system can withstand a maximum accelerating field of 350 kV, corresponding to a RF power loss of 35 kW on the cavity walls, while the maximum RF power the klystron can supply is 150 kW. The RF power to be delivered to the beam is given by $P_{beam} = V_{loss} I_{beam} \approx 40.5$ kW, assuming 90 keV/turn of total losses (including the parasitic ones). Since the required accelerating voltage is 250 kV corresponding to a RF wall dissipation of ≈ 17.5 kW, the existing RF system is completely compatible with the required specifications.

Bunch lengthening has been estimated by performing a multiparticle tracking. Using the impedance estimates and corresponding wake fields calculated for the present vacuum chamber [8] in the turbulent microwave threshold calculations and in the bunch lengthening simulations, the rms bunch length increases from the natural value of 13.9 mm (Figure 4) to only 15.9 mm at 15 mA per bunch, while the energy spread remains constant indicating that the microwave instability threshold is not reached at the nominal bunch current.

Lifetime and background

Background and beam lifetime at DAΦNE are strongly dominated by Touschek scattering [9]. Touschek lifetime is a complicated function of machine parameters: at the larger energy and RF voltage of DAFNE2 it will be less critical than at the present energy. In fact with the

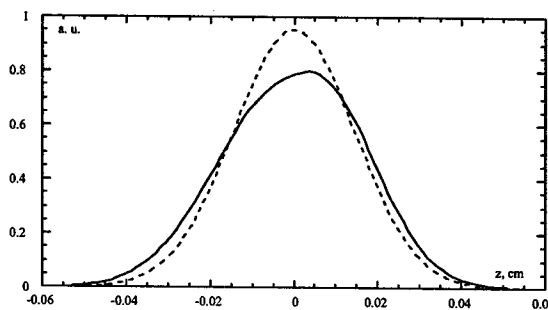


Figure 4: Charge density bunch distribution at zero current (dashed line) and at 15 mA/bunch (solid line).

parameters in Tables 1 and 3 τ_{lout} comes out to be 650 min as calculated by MAD with longitudinal acceptance dominated by RF. Further quantitative simulations will be done with the programs developed and used for DAΦNE that consider the physical aperture of the vacuum chamber along the rings.

Vacuum System

Present layout can withstand the new configuration. In fact in DAFNE2 (0.45 A and 1 GeV) synchrotron radiated photon flux is $1.8 \cdot 10^{20}$ phot/s corresponding to a power of 38 kW, while the existing vacuum chamber is designed for a synchrotron radiation power of 50 kW.

Feedback System

No change is needed for the transverse feedback if the betatron tunes stay constant during the energy ramping. The longitudinal feedback can follow the synchrotron frequency variation in a large range with eight synchronizable filters. Timing is not critical with a synchronous RF phase up to 100 ps (the RF phase is 70 ps at 250 kV).

REFERENCES

- [1] G. Vignola and DAΦNE Project Team, "DAΦNE: The first Φ-Factory", EPAC'96, Sitges, June 1996.
- [2] R. Baldini, "Unknown for ever?", Accelerator Division-LNF seminar, Frascati, January 2003, www.lnf.infn.it/acceleratori/
- [3] The FINUDA Collaboration, "FINUDA, a detector for nuclear physics at DAΦNE", LNF Internal Note LNF-93/021, May 1993.
- [4] A. Gallo et al., "Operational Experience with the DAΦNE Radio Frequency Systems", PAC'99, New York, Nov. 1999.
- [5] C. Biscari, "Detuned Lattice for Main Rings", DAΦNE Technical Note L-32, 2001.
- [6] B. Parker and al., "Superconducting Magnets for use inside the HERA ep Interaction Regions", EPAC'98, Stockholm, June 1998.
- [7] M. Bassetti et al., "Solenoidal field compensation", 14th ICFA Beam Dynamics Workshop, Frascati, Oct. 1997.
- [8] M. Zobov et al., KEK Proceedings 96-6, August 1996 (A), pp. 110-155.
- [9] M. Boscolo et al., "Simulations and Measurements of the Touschek Background at DAΦNE", EPAC'02, Paris, June 2002.

BUNCH PATTERN BY-3 IN PEP-II*

F.-J. Decker, A. Kulikov, M. Sullivan, SLAC, Stanford, CA 94309, USA

Abstract

After a long 4-month down time where additional RF was installed and heating problems addressed, the PEP-II B-factory should be capable of delivering about 1.5 times the currents. This can only be done by going to more bunches from a full by-4 pattern to either a partly filled by-3 or by-2 pattern. The by-2 pattern has parasitic crossings, so the by-3 pattern is the next candidate. Heating issues from the different higher order modes, especially in the longitudinal and transverse feedback structures are a concern. Effects from an electron cloud seem to be still visible in the by-3 and by-2 pattern.

1 INTRODUCTION

Figure 1 shows a typical by-3 bunch pattern with short bunch trains of 10 bunches out of 12. We fill up to bucket number 3400 out of 3492 giving us about 940 bunches. The details in the pattern are mostly caused by electron cloud effects (or possibly phase transients). The train length, the beginning after the abort gap, the first bunches of the train, and the timing for the beam position monitors (BPMs) have to be carefully chosen.

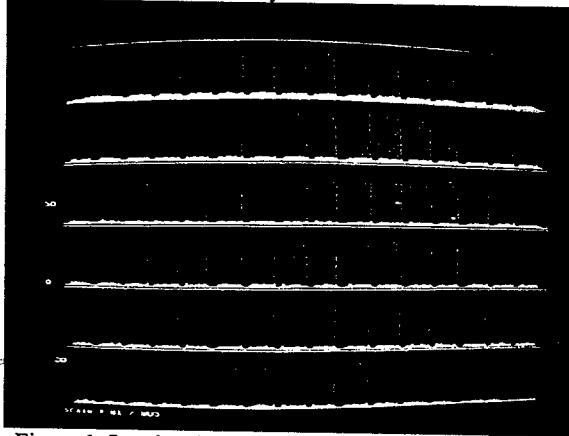


Figure 1: Luminosity per bunch for typical by-3 pattern.

When we first switched from the by-4 to the by-3 pattern excessive vacuum activity was observed which scrubbed out after a few days (Fig. 2, top).

2 PATTERN DETAILS

2.1 Train Length

The initial switch went to a full by-3 pattern, then the number of bunches got reduced by moving to trains of 30 out of 32 and then trains of 28 giving about 1000 bunches

(Fig. 2, bottom). With 28 or later 26 bunches in a train the luminosity dropped down about 15% over that length, making shorter bunches more attractive. So we went to 9 and 10 bunches out of 12 keeping the number about constant (see Fig. 1). Even shorter bunch trains of 5 out of 6 (see Fig. 3) were not successful, since the luminosity was 5% lower, probably caused by too many "first" bunches in a train.

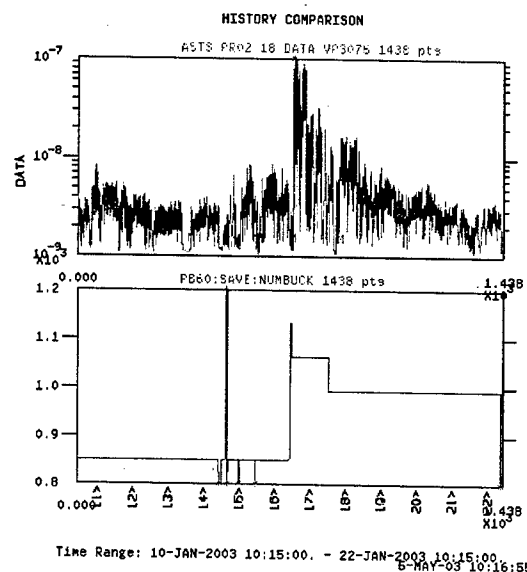


Figure 2: Pressure activity (top, in Torr) and number of bunches (bottom) when going from by-4 to a by-3 pattern.

2.2 First Bunch in Train

The first bunch in a train has often a different lifetime in the Low Energy Ring (LER). This can be easily seen as less bunch current at the end of a coast, when the overall current decayed from 1700 mA to 1300 mA or about -25% while the first bunches lose 40%. It is a difference when there are 2 or 3 bunch spaces free (3 worse), but there is also a difference when there is only one bunch missing (as in all cases of Fig. 3), but there is another gap close by.

A gap causes the LER bunch to be less blown up in x from less electron cloud, which gives it less beam-beam tune shift causing it to be more near a resonance and having therefore less lifetime [1]. There are two successful ways to improve this situation at different times. To increase the tune spread a lower charge in the LER train's first bunch can help its lifetime, since it loses charge anyway faster. Sometimes the opposite is true and less HER current in the first bunches helps.

*Work supported by Department of Energy contract DE-AC03-76SF00515.

Fill Ratios & Luminosity

04/06/2003 20:47:44

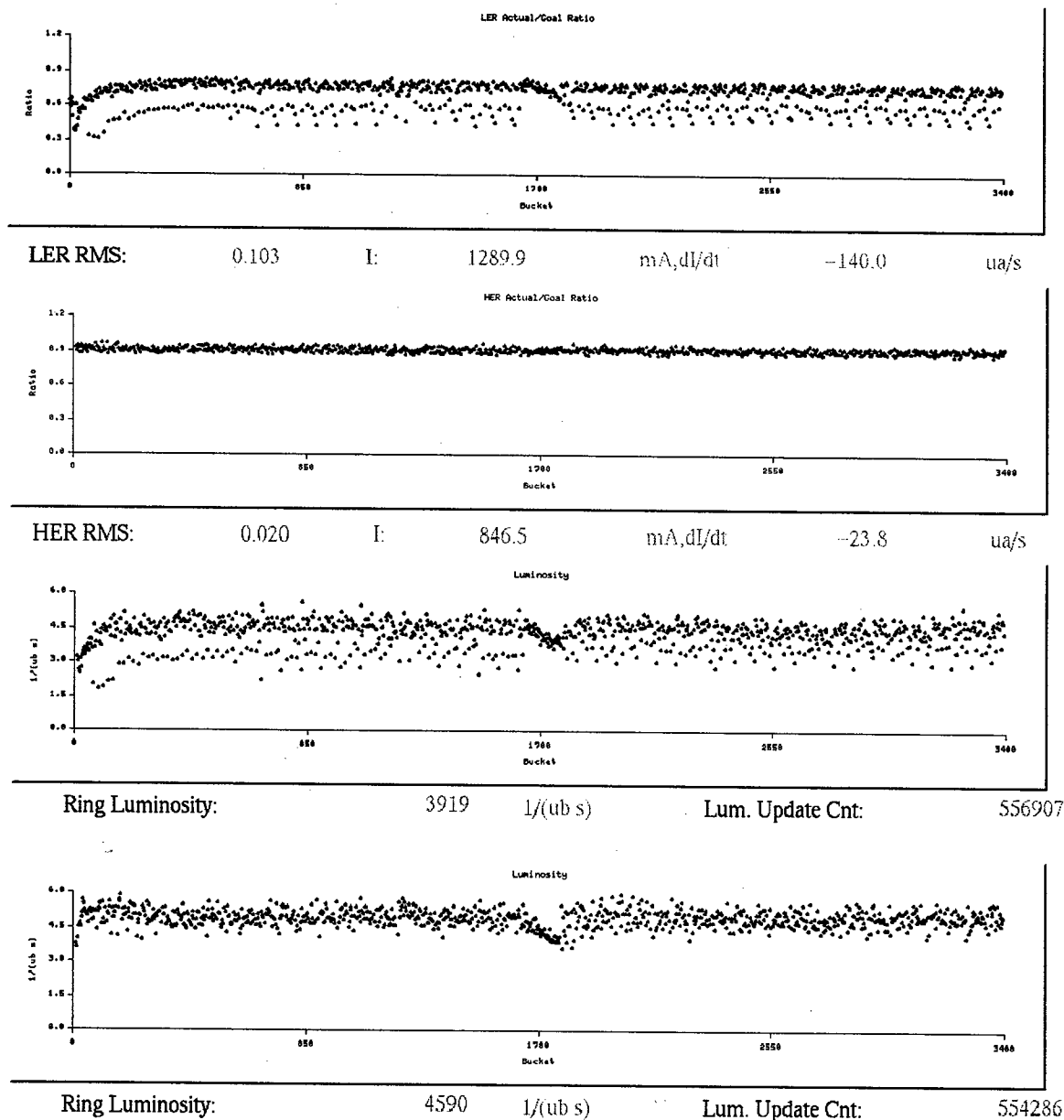


Figure 3: Special by-3 pattern with short trains of 5 bunches out of 6 (till bucket 585), and then every 4th train the middle of the 5 bunches is removed. A straight by-3 part is around bucket 1700±70. The top shows the LER bunch current after coasting for 45 min, next is the HER current with no change and the luminosity. The bottom shows the initial luminosity, when the currents were flat, indicating a drop induced by the electron cloud.

2.3 First Bunches after Abort Gap

The problem gets of course more serious after the abort gap where all or most the electron cloud should be gone. Here helps a longer current ramp from 70 to 100% [2,3], or we tried to "preload" the chamber with an electron cloud by filling a few bunches in the LER before the first colliding bunch. In Fig. 4 six bunches are filled before the

colliding bunches. This help only a little, but when we filled every bucket (by-1) instead of a by-3 distance, the next colliding bunches were stable. Later we had to reduce this line density to a by-2 distance since the longitudinal feedback system had trouble to keep these bunches stable. We probably still need to increase the number of not colliding LER bunches.

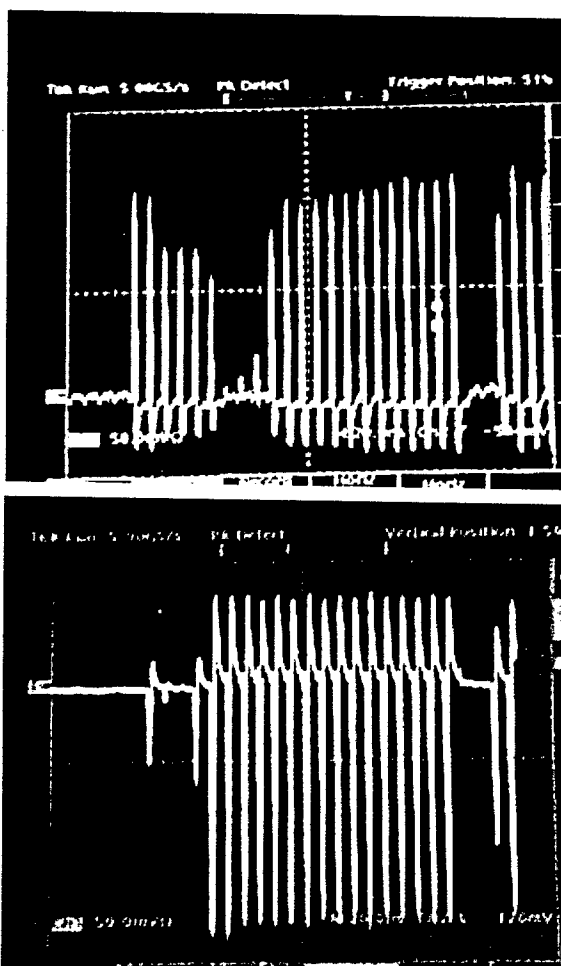


Figure 4: BPM intensity signals of first few bunches in LER (top) and HER (bottom), (20ns/div).

2.4 Close to $\frac{1}{2}$ Integer Tune

Recently we moved the x-tune close to the half integer (0.52) and achieved nearly a 20% luminosity improvement. Since then the behaviour is quite different the currents stay flat (except in the very front), while the luminosity at the end of a coast down shows a lower value of about 15%.

3 BY-2 PATTERN

Since we already see a 15% luminosity loss for long by-3 trains it might be necessary to look at a by-2 pattern before we reach a full by-3 pattern.

Two scenarios with very long trains of about 50 bunches, and very short "trains" of two bunches were studied. The first shows the typical 20-25% luminosity loss after the first few (5-10) bunches (Fig. 5), while the second case showed a very interesting behaviour (see Fig. 6). The first buckets of the duplets have the same high luminosity, while the luminosity of the second ones drops about 50% over 25 duplets, or 320 ns. Then it is constant

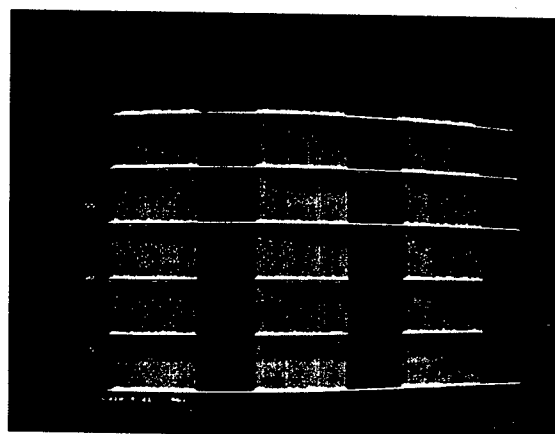


Figure 5: By-2 pattern with long trains show about a 25% luminosity drop.

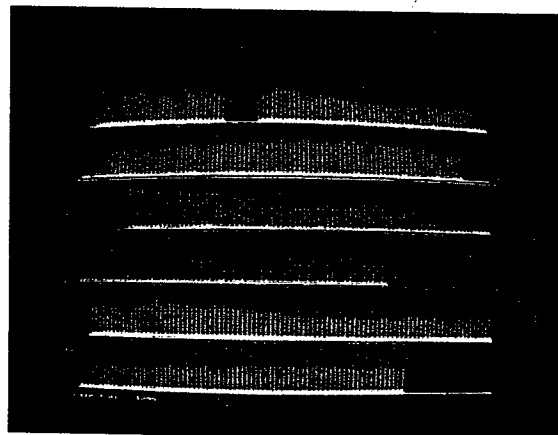


Figure 6: By-2 pattern with short "trains" (2,4,2,4...) shows only a luminosity loss for the second bunch.

except for after an empty bucket with number 585 (beginning of second row in Fig. 6). The luminosity slowly grows to nearly 75% before it starts dropping down again faster.

4 SUMMARY

Besides the rough number of buckets, gaps in the detailed pattern help to avoid the built-up of an electron cloud. But this causes different tunes, and therefore lifetimes or even beam loss. Most effects can be reduced by adjusting the size of the gaps and the intensity of the following bunch.

5 REFERENCES

- [1] R.L. Holtzapple, et al., "Observation of Beam Size Flip-Flop in PEP-II", EPAC02, Paris, June 2002.
- [2] F.-J. Decker et al., "Increasing the number of Bunches in PEP-II", EPAC02, Paris, June 2002.

INJECTION RELATED BACKGROUND DUE TO THE TRANSVERSE FEEDBACK*

F.-J. Decker, R. Akre, A. Fisher, R.H. Iverson, M. Weaver, SLAC, Stanford, CA 94309, USA

Abstract

The background in the BaBar detector is especially high during injection, when most components are actually having reduced voltages. The situation is worse for the beam in High Energy Ring (HER) when the LER beam is present. It was found that the transverse feedback system plays an important role when stacking more charge on top of existing bunches. Lowering the feedback gain helped and it was realized later that the best scenario would be to gate off the feedback for only the one bunch, which got additional charge injected into it. The explanation is that the blown-up, but centered, original HER bunch plus the small injected off-axis bunch (each with half the charge) would stay in the ring if not touched, but the feedback system sees half the offset and wants to correct it, therefore disturbing and scraping the blown-up part.

1 INTRODUCTION

The background in BABAR from PEP-II can have many different reasons. Offsets in the six phase space dimensions come to mind first (x, x', y, y', E, ϕ). These are generally tuned for best injection rate and low background. The next order (matching) and other not anticipated effects are described in this paper.

2 LATTICE MISMATCHES

2.1 Injected Beam

Increasing the beam size at the injection septum by changing the betatron function from 35 m to 70 m, the very high betatron region near the interaction point (IP) was reduced from 2400 m in Fig. 1 to 1200 m. This helped to reduce injection background.

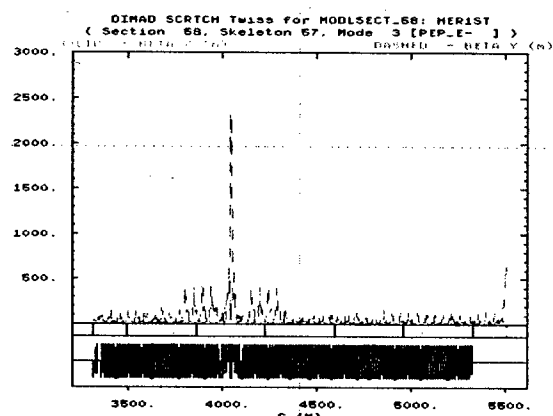


Figure 1: Mismatching the injected beam reduced the high betatron region near the IP ($z = 4000\text{m}$) into half.

*Work supported by Department of Energy contract DE-AC03-76SF00515.

2.2 Mismatch between Injection Bump Kickers

For injection a few hundred ns long part of the stored beam is kicked nearly 20 mm, so close to the septum that the lifetime starts to degrade. If the kickers have different strengths or the phase advance between them is not 180° , the bump is not closed and an oscillation results. Figure 2 shows the stored beam orbit at the septum. The beam position monitor (BPM) indicates a 16 mm bump, but then in the following turns the beam oscillates by about ± 1 mm. This is about only 6% of the bump, but two times the beam size in y .

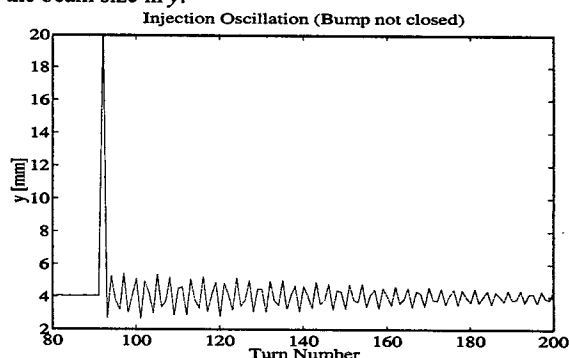


Figure 2: Injection oscillation due to a not perfectly closed bump.

To figure out whether it is the kicker strength or the phase advance in between, the first oscillation is plotted versus z or BPM number in Fig. 3. The offset at the kicker is caused by about 11° less phase advance than 180° .

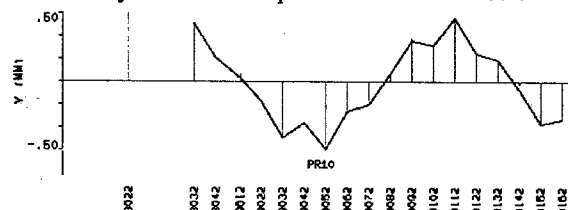


Figure 3: Oscillation due to non-closed bump, indicating offset at kicker (near BPM 8032). The septum is to the left, around it BPMs read 5.7, 16.7 and 6.7 mm.

3 BACKGROUND SIGNALS

3.1 Top Offs

A top off into PEP-II can be as fast as 3 min (Fig. 5). Besides the injection rate, background signals from SVT-diodes are typically monitored. They roughly distinguish the induced background coming mainly from HER or LER. To get more information other signals like from the calorimeter (EMC) and trigger rate are monitored.

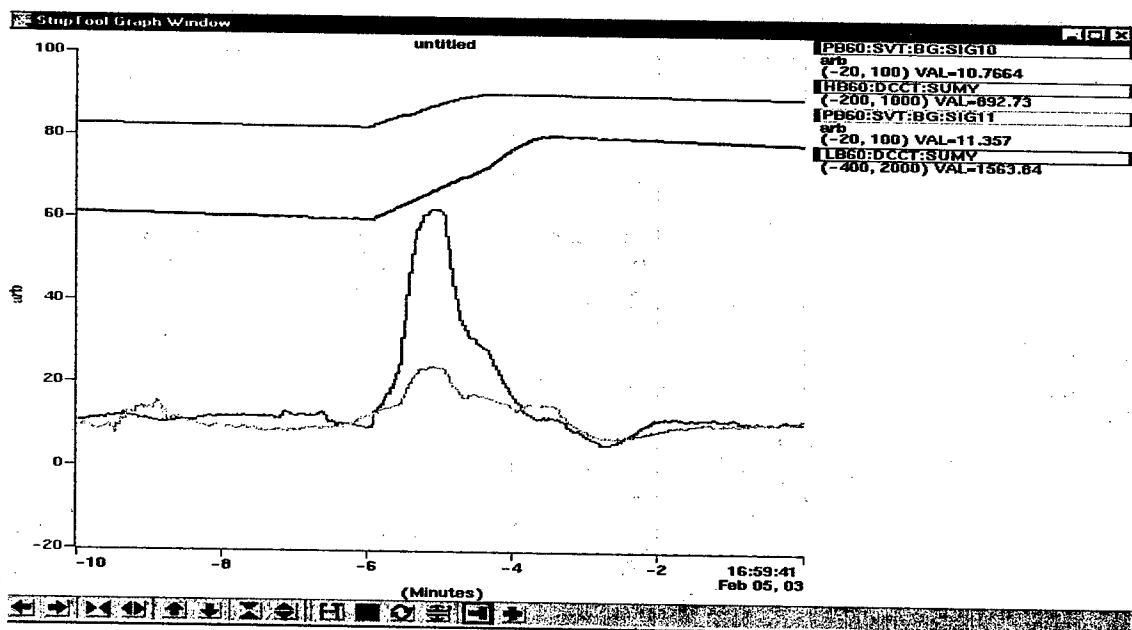


Figure 4: Three minutes top off injection. The top two lines show the HER and LER currents, then background signals SIG10 for HER and SIG11 for LER.

3.2 Electromagnetic Calorimeter

The BaBar electromagnetic calorimeter provides detailed information on backgrounds during injection. This detector consists of 6580 Th-doped CsI crystals, each readout by a pair of photodiodes. The photodiode response is amplified, shaped, and digitized at 3.72 MHz. The resulting readout stream is split onto two paths, one path to the BaBar trigger electronics and another to an intermediate buffer in the calorimeter readout boards where up to 256 samples (68.8 μ s) can be processed after a trigger decision. The BaBar trigger system generates trigger decisions from input on the first path, and a timestamp is recorded from a counter based on the PEP-II 476 MHz clock divided by 8.

The single-cluster trigger times ($E > 100$ MeV) are compared with the times of individual injection shots. This data source has small deadtime (2.7 μ s per trigger) and runs in parallel to the normal BaBar data acquisition. On the other hand, during periods of abnormally high backgrounds in HER injection the trigger system can suffer inefficiency from detector saturation effects.

An example of background trigger timing with respect to HER injection is shown in Fig. 5. Background trigger rates are typically heightened for the first 30 μ s after injection and then rise again over the next 3 - 5 ms. The trigger rates fall over a time scale of roughly 5 ms. Finer analysis of the timing confirms that the additional triggers occur at intervals of 7.34 μ s, the revolution period of the injected bunch. The injection backgrounds also depend upon the progress into a fill. Figure 6 displays the injection backgrounds for both the LER and HER when filling from 0 to maximum current. A Fourier transform of the background trigger timing, also in Fig. 6, shows a

distinct contribution from synchrotron oscillations. The observed HER synchrotron oscillation frequency drift could be from time-lacking of the HER RF cavity tuners.

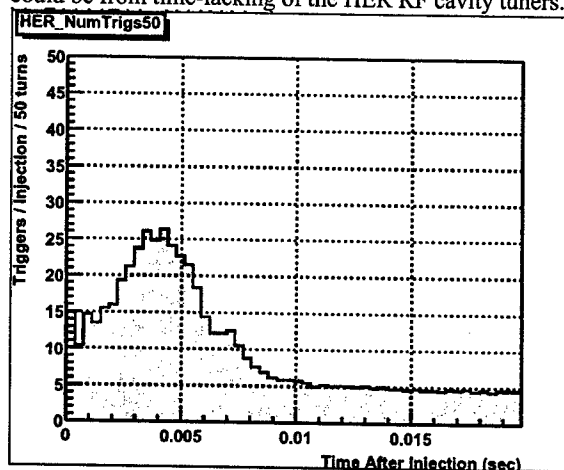


Figure 5: Calorimeter triggers show a large background increase several ms after an injection.

The second calorimeter readout path can be used to obtain unbiased sampling at well-defined times using the PEP injection timing signal and a programmable delay generator. This data includes the detector response magnitude and its sampling is immune to detector effects associated with high backgrounds. Figure 7 shows an example of the calorimeter energy measurements accumulated over several scans of the 7 ms period following an injection. The LER synchrotron oscillation component is observed to be a greater exposure contribution than indicated by the trigger analysis.

LER

HER

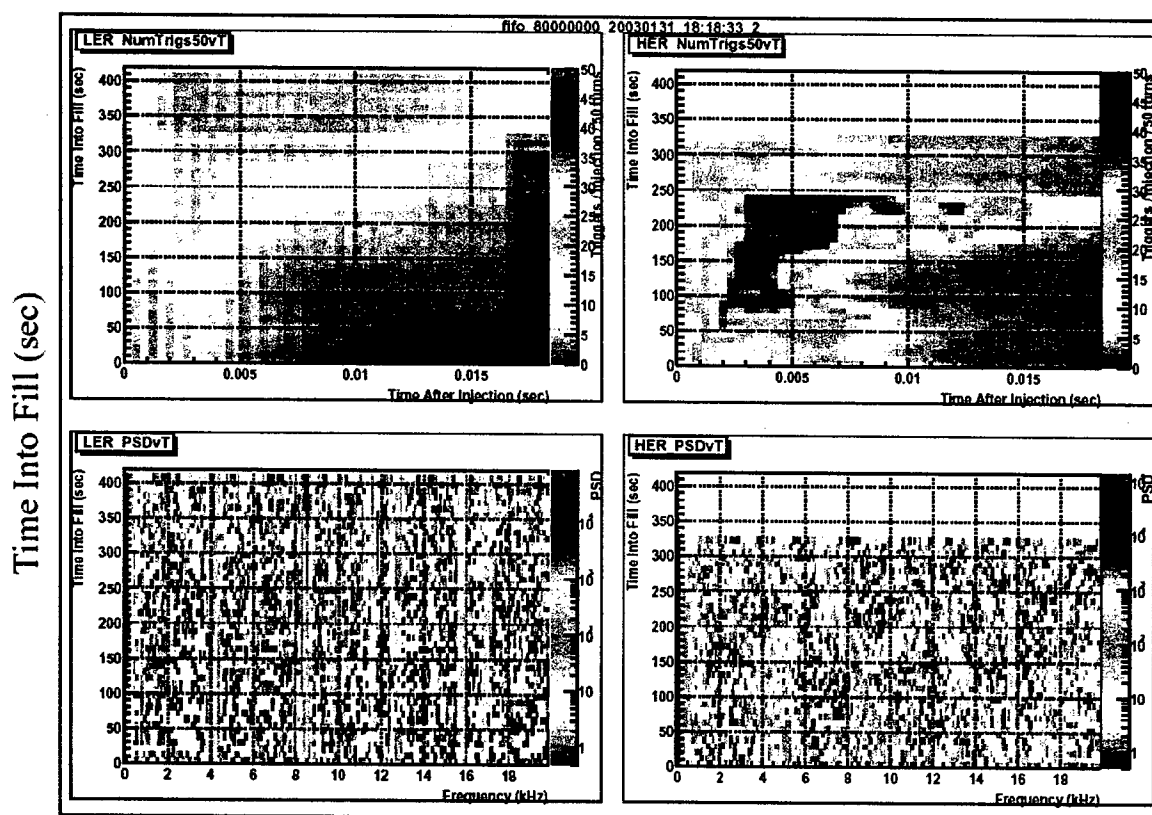


Figure 6: Injection backgrounds increase as a fill progresses. The period from 0 to 240 seconds consists of large charge quanta injection into the HER and LER at 15 Hz each. The period from 240 to 320 seconds uses small charge quanta injection into the HER. The period from 320 to 410 seconds includes 30 Hz injection into the LER.

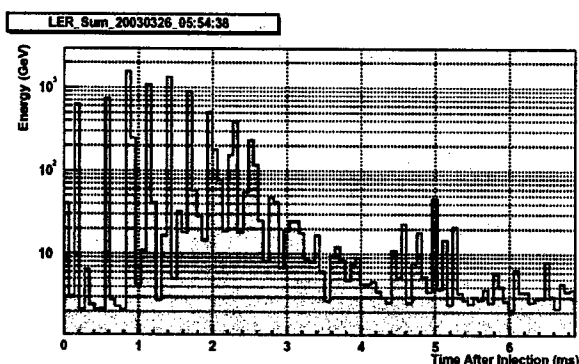


Figure 7: Calorimeter background energy measurements during the 7 ms following an injection. The energy scale is averaged per injection.

4 POSSIBLE FIXES

First offsets and sizes (1st and 2nd order effects) need to be tuned. Speeding up the HER low level RF feedback system, which controls the tuners, should

eliminate the shift of the synchrotron tune lines. The tricky part is the long lasting (>5ms) background from Fig. 5, which is faster than the damping time (40 ms). Since the observed effect with the fast transverse feedback system (described in the abstract), we are planning to gate off the feedback only for the bunch with additional injected beam for about 30 ms. The current set up should be able to do this up to 1 ms which seems too short. The 30 ms fits good compared with a 30 Hz injection (= 33.33 ms), so we plan to have no feedback on only one bunch at a time and hope that the injected beam is filamented enough that it does not represent any offset, which the feedback wants to fix.

5 REFERENCES

- [1] R.L. Holtzapple, et al., "Observation of Beam Size Flip-Flop in PEP-II", EPAC02, Paris, June 2002.
- [2] F.-J. Decker et al., "Increasing the number of Bunches in PEP-II", EPAC02, Paris, June 2002.

LATTICE WITH SMALLER MOMENTUM COMPACTION FACTOR FOR PEP-II HIGH ENERGY RING *

Y. Cai, M.H.R. Donald, Y. Nosochkov, SLAC, Menlo Park, CA 94025, USA

Abstract

At present, the PEP-II bunch length and vertical beta function β_y^* at the Interaction Point (IP) are about of the same size. To increase luminosity, it is planned to gradually reduce β_y^* . For the maximum effect, bunch length has to be also reduced along with β_y^* to minimize luminosity loss caused by the hourglass effect at IP. One of the methods to achieve a smaller bunch length is to reduce momentum compaction factor. This paper discusses a lattice option for the High Energy Ring, where the nominal 60° cells in four arcs are replaced by 90° cells to reduce momentum compaction factor by 30% and bunch length by 16%. The increased focusing in 90° cells results in 40% stronger arc quadrupoles and 150% stronger arc sextupoles due to reduced dispersion and larger chromaticity. Tracking simulations predict that dynamic aperture for this lattice will be ≥ 10 times the rms size of a fully coupled beam for a horizontal emittance of 30 nm and $\beta_y^* = 1$ cm. The lattice modification and results of simulations are presented.

INTRODUCTION

One of the methods to increase luminosity at PEP-II [1] is to reduce a vertical beta function β_y^* at the Interaction Point (IP). The current plan is to reduce β_y^* from the present value of 12.5 mm to 9 mm this year, and to ~ 5 mm within the next few years.

Due to a finite bunch length σ_s , particle interactions occur over distance $-\sigma_s/2 < s < \sigma_s/2$ from IP. Because of angular divergence $\propto 1/\sqrt{\beta_y^*}$, beam size increases with distance s from IP according to: $\sigma_y(s) = \sigma_y^* \sqrt{1 + s^2/\beta_y^{*2}}$. As a result, contribution to luminosity is gradually reduced with distance from the beam waist at IP. This so-called "hourglass" effect can be analytically estimated and translated into a luminosity reduction factor due to a finite bunch length [2]. For flat beams with equal beam size and emittance, this factor depends only on one parameter β_y^*/σ_s and is shown in Fig. 1.

At present, the bunch length and β_y^* at PEP-II are about of the same size. According to Fig. 1, this corresponds to 14% of luminosity loss due to the hourglass effect. If β_y^* is reduced from the current 12.5 mm to 9 mm and then to 5 mm without changing σ_s , luminosity loss would increase to 21% and 35%, respectively. One can conclude, therefore, that for maximum PEP-II luminosity at lower β_y^* , bunch length has to be reduced as well.

Among other parameters, the equilibrium bunch length depends on the total accelerating rf-voltage V , momentum

*Work supported by Department of Energy contract DE-AC03-76SF00515.

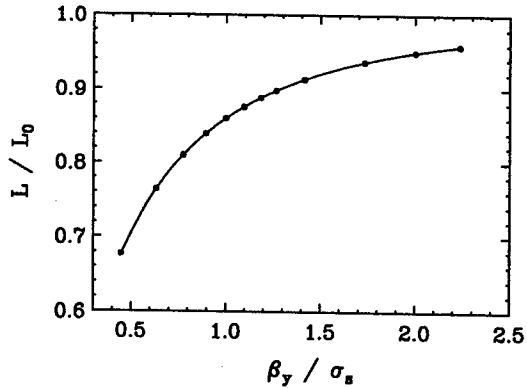


Figure 1: Luminosity reduction factor due to the hourglass effect for flat beams.

compaction factor α and bending radius ρ as

$$\sigma_s \propto \sqrt{\frac{\alpha}{V} \cdot \frac{\langle 1/\rho^3 \rangle}{\langle 1/\rho^2 \rangle}}, \quad (1)$$

where $\langle \rangle$ denote an average in the machine [3]. The PEP-II upgrade to increase rf-voltage for a smaller bunch length is being implemented. However, the bunch length is a relatively slow function of V , therefore many rf-cavities would be needed for a large reduction of β_y^* . To help reduce the bunch length, a reduction of momentum compaction factor may be considered.

The momentum compaction factor is defined by dispersion function η_x and bending radius ρ according to

$$\alpha = \left\langle \frac{\eta_x}{\rho} \right\rangle, \quad (2)$$

where η_x depends on ρ and quadrupole focusing. A change of bending properties or magnet locations is not considered in this paper since it would require a modification of machine geometry. Therefore, for a fixed bending, a smaller momentum compaction factor could be achieved by reducing the average dispersion in bends by means of a stronger quadrupole focusing. Such optics modification is discussed below for the PEP-II High Energy Ring (HER) with $\beta_x^*/\beta_y^* = 50/1$ cm.

LATTICE MODIFICATION

Layout of the HER is shown in Fig. 2. The lattice consists of six arcs with periodic 60° cells and six straight sections with various matched optics for the Interaction Region (IR), injection, rf-cavities, and tune and coupling correction. The HER nominal dispersion function is shown in Fig. 3, where IP is in the middle at $s \approx 1100$ m. Modulation of η_x in the four arcs farthest from IR is introduced to

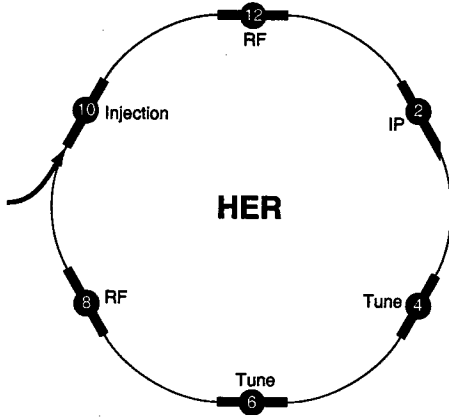


Figure 2: Top view of the High Energy Ring.

increase the HER horizontal emittance to 48 nm, while in the two arcs near IR it is caused by special β bumps for the IR sextupoles. Because in the four arcs this perturbation is a free betatron motion around the periodic η_x , it does not change the average dispersion $\langle \eta_x \rangle$ and bunch length, but increases $\langle \eta_x^2 \rangle$ for a higher emittance. In the straight sections, dispersion is canceled by dispersion suppressors.

The most contribution to momentum compaction factor in HER comes from dispersion in the arcs. A simple way to reduce $\langle \eta_x \rangle$ is to increase phase advance in the periodic arc cells. The effect of phase advance per cell μ_c can be estimated using a thin lens approximation. This method gives the following well-known equations for the extreme (\pm) values of β and η_x , and the quadrupole integrated strength $K_1 L$ in the arc FODO cell:

$$\beta^\pm = L_c \frac{1 \pm \sin(\mu_c/2)}{\sin \mu_c}, \quad (3)$$

$$\eta_x^\pm = \frac{L_c^2}{8\rho} \frac{2 \pm \sin(\mu_c/2)}{\sin^2(\mu_c/2)}, \quad (4)$$

$$K_1 L = \frac{4 \sin(\mu_c/2)}{L_c}, \quad (5)$$

where L_c is a cell length. For an estimate of the average values of β and η_x in the arcs, one could use the following approximation:

$$\langle \beta \rangle \approx \frac{\beta^+ + \beta^-}{2} = \frac{L_c}{\sin \mu_c}, \quad (6)$$

$$\langle \eta_x \rangle \approx \frac{\eta_x^+ + \eta_x^-}{2} = \frac{L_c^2}{4\rho \sin^2(\mu_c/2)}. \quad (7)$$

Below, a modification of HER optics for a lower momentum compaction factor is considered, where phase advance in the four arcs farthest from IR is increased from 60° to 90° per cell. The other two arcs contain some of the IR sextupoles and skew quadrupoles to compensate the detector solenoid and non-linear chromaticity. In order to maintain the original IR optics and local correction, these two arcs were not changed.

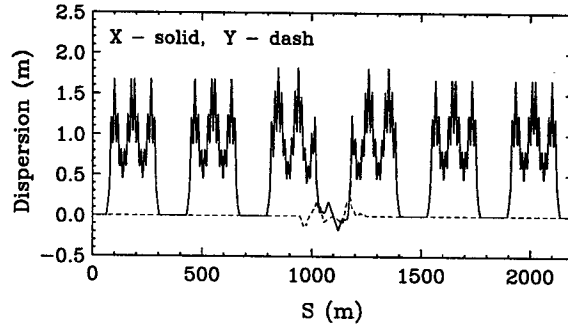


Figure 3: Dispersion in the nominal HER.

Since the maximum β functions are about the same in 60° and 90° cells, physical aperture acceptance will not be reduced by this modification. As in 60° optics, the 90° cells naturally provide $-I$ transformation between arc sextupoles to help compensate the third order sextupole aberrations. Also, the first order chromatic perturbation of β function is naturally suppressed in 90° lattice.

According to Eqn. 7, the average dispersion in 90° arc is reduced by a factor of 2 compared to 60° lattice. Consequently, the momentum compaction factor in four 90° and two 60° arcs is reduced by a factor of $\frac{2}{3}$ compared to the 60° value. From Eqn. 3-5, disadvantages of 90° cells are a factor of $\sqrt{2}$ stronger quadrupoles, a factor of $\sqrt{3}$ larger linear chromaticity per cell and a factor of $2\sqrt{2}$ stronger sextupoles ($K_2 \propto K_1/\eta_x$).

To maintain the original non-dispersive optics in the injection, tuning and rf-cavity sections, quadrupole focusing in dispersion suppressors designed for 60° arcs was appropriately adjusted to match the straight sections to the new β functions and reduced dispersion in 90° arcs. One complication was related to the original design of arc sextupoles, where each of the four arcs has 12 SF and 12 SD sextupoles to correct linear chromaticity. Ideally, the same family sextupoles should have identical lattice functions to minimize residual sextupole aberrations. But in the HER, 2 SF and 2 SD sextupoles in each arc are extended into the dispersion suppressors which have different optics compared to the arcs. In the original 60° design, lattice functions at the above 4 sextupoles were made reasonably close to the periodic values in the arcs. It has been found particularly important to keep this property in the 90° modification as well. It was verified that a large change of β functions at these sextupoles could reduce dynamic aperture to unacceptable level. This is caused by an increase of the third order sextupole geometric aberrations if they are not sufficiently compensated due to breakdown of optical periodicity and $-I$ transformation at the 4 sextupoles.

The resultant dispersion in HER with four 90° arcs is shown in Fig. 4. In this option, a periodic dispersion without modulation is used in the 90° arcs, while dispersion in the two arcs near IR is not changed. Some of the HER global parameters for the original 60° and modified 90° lattice with $\beta_x^*/\beta_y^* = 50/1$ cm are shown in Table 1, where the

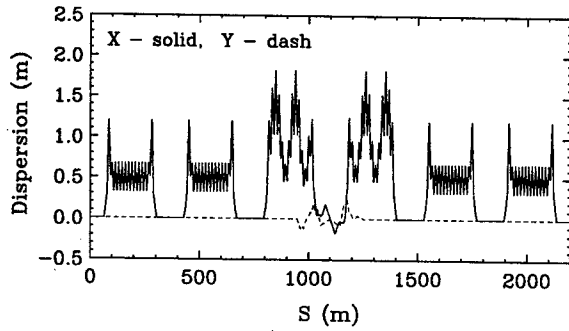

 Figure 4: Dispersion in HER with reduced α .

Table 1: HER parameters for 60° and 90° lattice.

μ_c	α [10^{-3}]	ϵ_x [nm]	ν_x / ν_y	ν_s	ξ_x / ξ_y
60°	2.41	48	24.569 / 23.639	0.045	-44 / -71
90°	1.69	30	28.569 / 29.639	0.038	-56 / -81

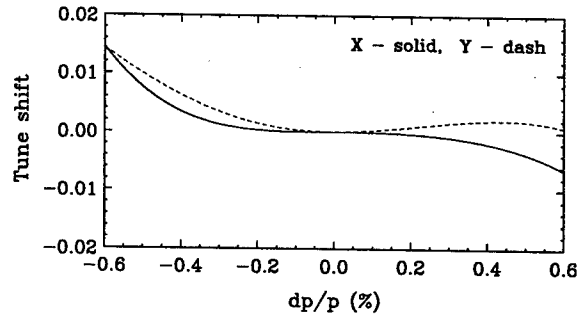
total voltage of $V = 14$ MV was used.

Momentum compaction factor is reduced by 30% in the 90° modification, therefore the bunch length is expected to decrease by 16%. The reduced dispersion in 90° arcs results in a smaller horizontal emittance ϵ_x in this option. A modulation of η_x may be introduced to increase the emittance. For the same rf-voltage, synchrotron tune ν_s is also reduced by 16% since it scales as $\sqrt{\alpha V}$. If the voltage is increased for a smaller bunch length, ν_s could be restored.

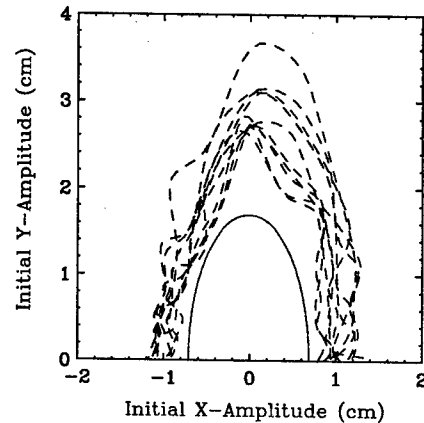
Naturally, the stronger quadrupole focusing in 90° arcs increases the HER betatron tune ν_x / ν_y and linear chromaticity ξ_x / ξ_y . Quadrupole strength increases by 42% in the 90° arcs, and the SF, SD sextupoles become stronger by a factor of 2.3 and 2.5, respectively, compared to 60° design. The large increase in strength may require an upgrade for some of these magnets.

Optics and compensation schemes of the Interaction Region have not been changed in this modification. The IR sextupoles provide correction of the non-linear chromaticity generated in the final quadrupole doublets near IP. It has been important to verify that compensation of non-linear chromaticity has not been affected by arc modifications. Indeed, calculation of betatron tune and β^* in the 90° lattice versus relative momentum deviation $\frac{\Delta p}{p}$ showed a negligible change of non-linear chromaticity compared to the original optics. This confirms that the IR chromaticity correction is, indeed, local. Tune shift in the modified HER is shown in Fig. 5 for the range of $-10\sigma_p < \frac{\Delta p}{p} < 10\sigma_p$, where σ_p is the *rms* relative energy spread in the beam, and linear chromaticity is set to zero.

Finally, tracking simulations have been performed to verify dynamic aperture for the HER with 90° arcs and $\beta_y^* = 1$ cm. Simulations have been done using LEGO code [4] for 10 different combinations of random field and alignment errors, and $\pm 8\sigma_p$ synchrotron oscillations. Compensation of beam orbit, linear chromaticity, coupling and


 Figure 5: Tune shift vs. $\frac{\Delta p}{p}$ in HER with reduced α .

tune were simulated in LEGO prior to tracking. The resultant dynamic aperture at the injection point is shown in Fig. 6, where the 10 dash lines represent different error settings. The area inside a dash line corresponds to a particle stable motion. This dynamic aperture exceeds 10σ depicted by a solid line, where σ is the *rms* size of a fully coupled beam at injection with $\epsilon_x = 30$ nm and $\epsilon_y = \epsilon_x/2$. This dynamic aperture should be sufficient for beam operation. We conclude, therefore, that 90° optics in HER for a lower momentum compaction factor may be considered as an option for a shorter bunch length.


 Figure 6: Dynamic aperture in HER with reduced α .

CONCLUSION

It has been shown that momentum compaction factor in HER can be reduced by 30% by increasing phase advance per cell from 60° to 90° in four arcs. The resultant dynamic aperture exceeds 10σ and is considered adequate. The expected reduction of bunch length in this option is 16%.

REFERENCES

- [1] PEP-II Conceptual Design Report, SLAC-418, 1993.
- [2] M.A. Furman, SLAC-ABC-41-REV, 1991.
- [3] H. Wiedemann, "Particle Accelerator Physics II", Springer-Verlag, 1995.
- [4] Y. Cai, *et al.*, SLAC-PUB-7642, 1997.

TRACKING SIMULATIONS NEAR HALF-INTEGER RESONANCE AT PEP-II *

Y. Cai, Y. Nosochkov, SLAC, Menlo Park, CA 94025, USA

Abstract

Beam-beam simulations predict that PEP-II luminosity can be increased by operating the horizontal betatron tune near and above a half-integer resonance. However, effects of the resonance and its synchrotron sidebands significantly enhance betatron and chromatic perturbations which tend to reduce dynamic aperture. In the study, chromatic variation of horizontal tune near the resonance was minimized by optimizing local sextupoles in the Interaction Region. Dynamic aperture was calculated using tracking simulations in LEGO code. Dependence of dynamic aperture on the residual orbit, dispersion and β distortion after correction was investigated.

INTRODUCTION

PEP-II [1] has been operating at the betatron tune ν_x/ν_y close to 24.569/23.639 in the High Energy Ring (HER) and 38.649/36.564 in the Low Energy Ring (LER). These working points were selected experimentally for a reliable machine performance, good luminosity and beam lifetime. However, the beam-beam simulations predict that luminosity can be increased by operating betatron tune very close and above the half-integer resonance. Fig. 1 shows the LER tune diagram with synchro-betatron resonances up to the 4th order and a contour plot of the single bunch luminosity. Calculation of luminosity was done using the beam-beam code developed at SLAC [2] which has been recently upgraded to the three dimensional version.

The difficulty of operating close to half-integer resonance comes from enhancement of the resonance effects on betatron motion. It is well known that perturbation of β function created by focusing errors depends on tune ν as

$$\frac{\Delta\beta}{\beta}(s) = \frac{1}{2 \sin 2\pi\nu} \oint \beta(l) \Delta K_1(l) \cos 2\phi(s, l) dl, \quad (1)$$

where μ is phase advance, $\phi(s, l) = \pi\nu - |\mu(s) - \mu(l)|$, and ΔK_1 is a focusing error created mainly by quadrupole field imperfections, horizontal orbit at sextupoles, and momentum error. Close to half-integer resonance, growth of $\Delta\beta/\beta$ comes from the resonance term $[\sin 2\pi\nu]^{-1}$ which behaves as $1/\Delta\nu$ when distance to the resonance is as small as $\Delta\nu \ll 1/2\pi$. On the other hand, orbit and dispersion are not excited by the half-integer resonance.

For significant enhancement of luminosity, fractional value of horizontal tune should be in the range of $[\nu_x] \approx .51$. At this working point, enhancement of $\Delta\beta_x/\beta_x$ in HER and LER due to the resonance term in Eqn. 1 would be a

* Work supported by Department of Energy contract DE-AC03-76SF00515.

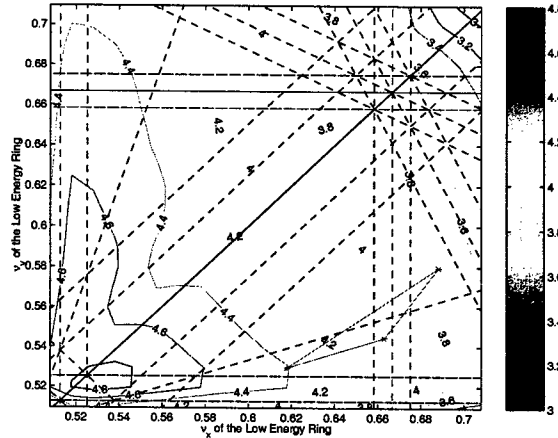


Figure 1: Single bunch luminosity scan [$10^{30} \text{ cm}^{-2} \text{ s}^{-1}$].

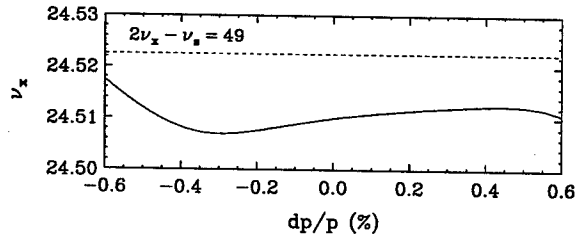
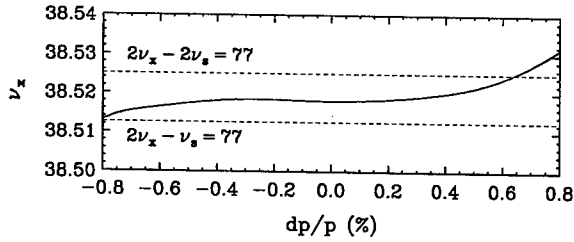
factor of 6.7 and 12.8, respectively, compared to the present tune. Without compensation, the large β growth may significantly increase amplitude dependent non-linear aberrations and reduce dynamic aperture and beam lifetime.

More resonance effects are generated by the synchrotron sidebands of the half-integer resonance: $2\nu_x + m\nu_s = n$, where ν_s is a synchrotron tune, and m, n are integers. In the LER, where $\nu_s = 0.025$, the 1st and 2nd synchro-betatron resonances occur at $[\nu_x] = .5125$ and $.525$, while in HER with $\nu_s = 0.045$ the 1st sideband is at $[\nu_x] = .5225$. Tracking simulations will show that the sidebands have a strong effect on dynamic aperture, therefore working tune should be chosen reasonably far from them. In addition, variation of tune with synchrotron momentum oscillations should be minimized to avoid crossing with these resonances.

Optimization of PEP-II lattice near half-integer resonance and analysis of dynamic aperture are discussed below. The optics with $\beta_x^*/\beta_y^* = 50/1.25 \text{ cm}$ at the Interaction Point (IP) is used.

LATTICE OPTIMIZATION

PEP-II has two tuning sections which can be locally adjusted to change betatron tune without affecting the rest of machine optics. Initially, only these sections were modified to move the horizontal tune closer to half-integer, and vertical tune to $[\nu_y] \approx .61$ as suggested by beam-beam analysis. But tracking simulations showed that dynamic aperture was not sufficiently large with machine errors and synchrotron momentum oscillations of up to $\pm 8\sigma_p$, where σ_p is the rms value of relative momentum spread $\frac{\Delta p}{p}$ in the beam. Analysis of chromaticity indicated that non-linear variation of horizontal tune with momentum needs to be

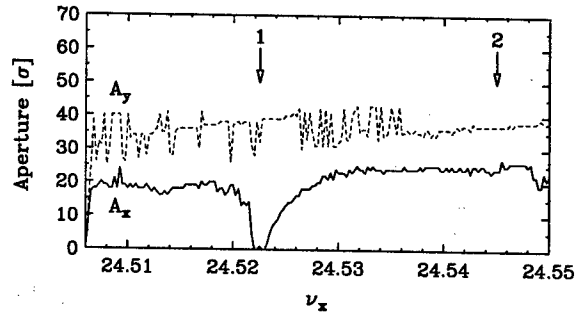
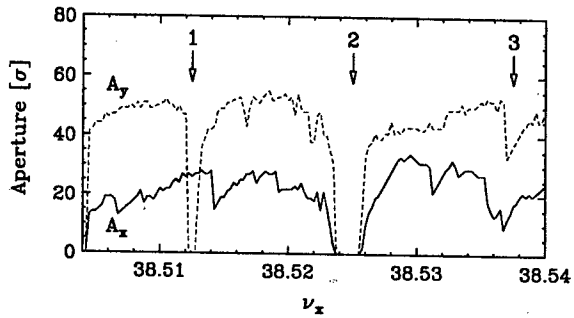

 Figure 2: HER horizontal tune vs. $\frac{\Delta p}{p}$ at $\nu_x = 24.51$.

 Figure 3: LER horizontal tune vs. $\frac{\Delta p}{p}$ at $\nu_x = 38.518$.

further reduced to avoid crossing with the synchro-betatron resonances.

In PEP-II, the most contribution to non-linear chromaticity is generated in the final quadrupole doublets near IP. This chromaticity is compensated by the Interaction Region (IR) sextupoles located in the same phase with the doublets. Variation of strength of these sextupoles allows to compensate quadratic dependence of tune on $\frac{\Delta p}{p}$, and a small adjustment of sextupole phase advance helps reduce the higher order variation.

Minimum of the second order chromaticity was achieved by reducing strengths of the IR sextupoles correcting horizontal chromaticity. Further improvement in LER resulted from reduction of horizontal phase advance between the IR horizontal sextupoles and IP by 5° . For correction of the machine linear chromaticity, strength of the global sextupoles was increased to compensate for the weaker IR sextupoles. Because the adjusted IR sextupoles in LER have a non-zero design orbit, the reduced sextupole strength created a feed-down effect of linear focusing and coupling. This small perturbation was compensated by a slight adjustment of the IR magnet strengths.

The optimized horizontal tune for momentum range of $-10\sigma_p < \frac{\Delta p}{p} < 10\sigma_p$ is shown in Fig. 2, 3, where the working point is $\nu_x/\nu_y = 24.51/23.61$ in HER and $38.518/36.61$ in LER. The straight dash lines depict the half-integer synchrotron sidebands. In HER, a positive linear chromaticity $\xi = +1$ was used in Fig. 2 to counteract the negative slope of non-linear tune variation. Due to the large synchrotron tune, it was possible to place the HER working point below the 1st synchrotron sideband without crossing with the resonance lines. In the LER, synchrotron tune is a factor of 2 smaller while energy spread is 25% larger, therefore the closest to half-integer working point was chosen between the 1st and 2nd sidebands.


 Figure 4: HER dynamic aperture without magnet errors vs. ν_x at $\nu_y = 23.61$. Synchrotron sidebands: 1) $2\nu_x - \nu_s = 49$, 2) $2\nu_x - 2\nu_s = 49$.

 Figure 5: LER dynamic aperture without magnet errors vs. ν_x at $\nu_y = 36.61$. Synchrotron sidebands: 1) $2\nu_x - \nu_s = 77$, 2) $2\nu_x - 2\nu_s = 77$, 3) $2\nu_x - 3\nu_s = 77$.

DYNAMIC APERTURE SIMULATIONS

Calculations of dynamic aperture were performed using tracking simulations in LEGO code [3]. First, dependence of aperture on betatron tune near half-integer resonance was investigated for lattice without magnet errors, but with synchrotron momentum oscillations of $\pm 8\sigma_p$. The resultant horizontal tune scan is shown in Fig. 4, 5 for HER and LER, where dynamic aperture is normalized by the *rms* size of a fully coupled beam.

The HER horizontal dynamic aperture vanishes in the vicinity of the main half-integer resonance $2\nu_x = 49$ and its 1st sideband. In LER, the strongly affecting resonances are $2\nu_x + m\nu_s = 77$ with $m = 0, -1, -2, -3$. Naturally, the working tune should be chosen reasonably far from these resonances. The following scenarios for more and less aggressive horizontal tune ν_x near half-integer were investigated in the simulations:

1. HER: 24.51, LER: 38.518.
2. HER: 24.529, LER: 38.529.

Dynamic aperture scan versus vertical tune was performed for the first scenario of ν_x and the range of $[\nu_y]$ from .55 to .64. It showed that dynamic aperture gradually reduces as $[\nu_y]$ becomes closer to $[\nu_x]$ and the working point approaches the crossing of half-integer and coupling resonances. Based on this scan, the vertical fractional tune of $[\nu_y] = .61$ was chosen for these simulations. A lower ν_y may be considered for further luminosity enhancement.

Secondly, tracking simulations with field errors, misalignment and $\frac{\Delta p}{p} = \pm 8\sigma_p$ synchrotron momentum oscillations were performed for the selected working points. For statistics, ten different settings ("seeds") of random machine errors were used in each tracking. Perturbation of beam orbit, linear chromaticity, betatron tune and vertical dispersion was compensated using realistic correction schemes in LEGO. Since distortion of β function becomes more sensitive to focusing errors near half-integer resonance, a special correction of $\frac{\Delta\beta}{\beta}$ was implemented in LEGO. It uses MICADO method to find the most effective quadrupoles to minimize β perturbation.

Due to the greater effect of errors near half-integer resonance, a better machine correction is needed to maintain acceptable dynamic aperture. To verify tolerance to various errors, simulations were performed for different levels of machine correction. It has been confirmed that beam orbit should be decreased for an acceptable dynamic aperture. The better orbit correction reduces the feed-down focusing errors in sextupoles as well as residual dispersion in the machine. On the other hand, correction of vertical dispersion did not significantly affect dynamic aperture in the observed range of residual *rms* $\Delta\eta_y$ from ~ 70 to 5 mm.

As expected, the simulations confirmed that compensation of $\Delta\beta/\beta$ is required in the first scenario, where ν_x is closer to the resonance. Typically, $\Delta\beta/\beta$ was corrected to the *rms* level of $< 5\%$. In the second scenario, at $[\nu_x] = .529$, correction of β function was less important, although it helped to improve cases with small aperture. Table 1 summarizes the observed approximate levels of *rms* orbit and $\Delta\beta_x/\beta_x$ for acceptable dynamic aperture.

Table 1: Tolerances on *rms* orbit and $\Delta\beta_x/\beta_x$.

	HER		LER	
$[\nu_x]$.529	.510	.529	.518
orbit (mm)	1	1	0.4	0.2
$\Delta\beta_x/\beta_x$ (%)	25	5	25	5

The resultant dynamic aperture in HER at $\nu_x/\nu_y = 24.51/23.61$ for a good level of correction is shown in Fig. 6 at the injection point. Stable particle motion corresponds to the area inside the dash lines which represent 10 different seeds of random machine errors. The solid half-ellipse, shown for reference, is the 10σ size of a fully coupled beam at injection with emittance $\epsilon_x = 48$ nm and $\epsilon_y = \epsilon_x/2$. In this simulation, the residual *rms* orbit, dispersion and β distortions after correction were: 0.27/0.31 mm, $\Delta\eta = 31/8$ mm and $\Delta\beta/\beta = 1.9/1.5\%$ in x/y planes, respectively. Linear chromaticity was set to +1 to minimize non-linear tune variation with momentum.

The LER dynamic aperture at $\nu_x/\nu_y = 38.518/36.61$ is shown in Fig. 7 at the injection point. The solid half-ellipse corresponds to 10σ size of a fully coupled beam at injection with emittance $\epsilon_x = 24$ nm. The residual *rms* orbit, dispersion and β distortions after correction were: 0.20/0.23 mm, $\Delta\eta = 23/9$ mm and $\Delta\beta/\beta = 2.4/2.5\%$ in x/y planes, respectively. Linear chromaticity was set to

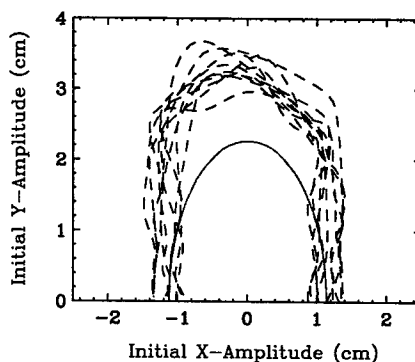


Figure 6: HER dynamic aperture at $\nu_x/\nu_y = 24.51/23.61$.

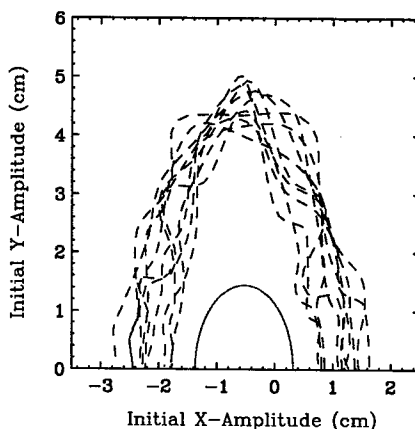


Figure 7: LER dynamic aperture at $\nu_x/\nu_y = 38.518/36.61$.

zero in this case.

Implementation of the tune near half-integer resonance has been recently performed at PEP-II. The working point was successfully moved to $\nu_x/\nu_y = 24.52/23.63$ in HER and 38.52/36.57 in LER. After the necessary machine adjustments luminosity has been improved by $\sim 15\%$ to the new record of $6.1 \cdot 10^{33} \text{ cm}^{-2} \text{ s}^{-1}$.

CONCLUSION

Beam-beam simulations performed for PEP-II predicted an enhancement of luminosity for a betatron tune near a half-integer resonance. Horizontal fractional tune of .52 has been recently implemented at PEP-II and $\sim 15\%$ luminosity gain has been achieved. Particle tracking simulations showed that an improved machine correction is needed for acceptable dynamic aperture at $[\nu_x] = .51$ in HER and .518 in LER. This requires a minimization of non-linear chromaticity and tighter correction of orbit and β_x distortions. At $[\nu_x] = .529$, a looser orbit correction may be used while compensation of $\Delta\beta_x$ may not be necessary.

REFERENCES

- [1] PEP-II Conceptual Design Report, SLAC-418, 1993.
- [2] Y. Cai, *et al.*, Phys. Rev. ST Accel. Beams 4, 011001 (2001).
- [3] Y. Cai, *et al.*, SLAC-PUB-7642, 1997.

RF HEATING AND TEMPERATURE OSCILLATIONS DUE TO A SMALL GAP IN A PEP-II VACUUM CHAMBER

A. Novokhatski^{**}, J. Seeman and M. Sullivan, SLAC, Stanford, CA 94309, USA

Abstract

Wake fields excited in a small gap of a vacuum chamber by ampere beams can have enough amplitude to heat the chamber. The electric component of these fields can be above the arcing limit. Usually flange connections in a vacuum chamber contain a vacuum gasket and an inner RF gasket. If a small gap occurs between the RF gasket and flange surface, wake fields can heat the flanges. The flanges are usually made of stainless steel, which efficiently absorbs RF power. Some flanges consist of two parts (like a vacuum valve flange) and are mechanically connected but have poor thermal contact. A temperature rise can lengthen the inner part of the flange and make firmer the thermal contact to the outer part of the flange. The heat will then flow to the outer part of the flange, which is air and water-cooled. This cooling lowers the flange temperature and the thermal contact becomes poor again. This "quasi" periodic mechanism can explain the nature of temperature oscillations observed at several locations in PEP-II, the SLAC B-factory.

INTRODUCTION

During the 2001 PEP-II run [1] an unusual behaviour of the valve body temperature was observed in the low energy (positron) ring, in region 2. A high positron current elevated the temperatures on different vacuum chamber elements like bellows and vacuum valves. Mainly the temperatures, measured by thermocouples, varied monotonically in accordance with the positron current. However, thermocouples placed on vacuum valve 2175 showed oscillations of temperature with a period of 3-8 minutes. The amplitude of the oscillations was of the order 5-20 degrees Fahrenheit. The oscillations happened from time to time, when the positron current reaches 1000 mA level and more. A typical temperature oscillation is shown in Fig. 1.

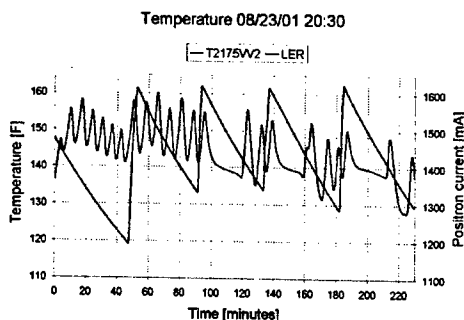


Figure 1: Vacuum valve temperature and positron current.

Work supported by Department of Energy contract DE-AC03-76SF00515.
^{**}nov@SLAC.Stanford.edu

The red curve (more rapidly oscillations) presents the signal from the thermocouple attached to body of the vacuum valve. The green curve (slow function) shows the time dependence of the positron current during several top-offs. This unusual behaviour of the temperature cycling initiated the wake field study of very small gaps to understand the RF heating.

WAKE FIELDS AND RF HEATING

It was supposed that the gasket (RF gap ring), which is placed in the connection between the vacuum valve and the vacuum chamber, could have dimensions that are incorrect thereby producing a very small gap.

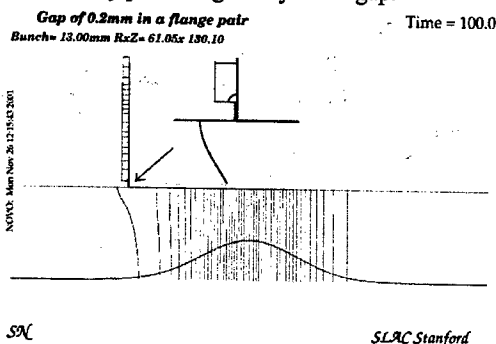


Figure 2: Electric force lines of the field excited by a bunch, travelling in the vacuum chamber with a small gap.

It was suspected that the gap size could be of order of the 100 microns. Flange connection has also a vacuum (main) gasket, which is situated at a larger radius. The positron beam through a small gap could excite a cavity formed by the flange sides and these gaskets.

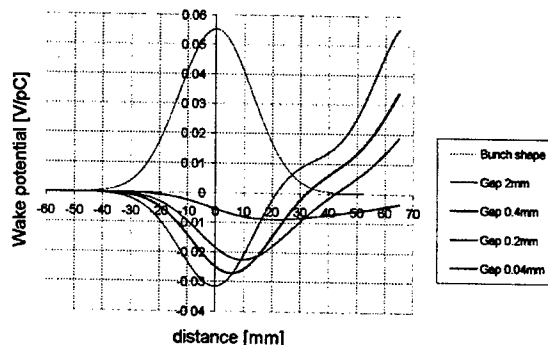


Figure 3: Wake potentials for a bunch length of 13mm for different gap sizes.

The vacuum gasket is a round ring of radius 60.2mm, while the RF gap ring has an elliptical shape with half

axes 25mm and 42.5mm. Wake field calculations were performed for an azimuthally symmetric model of the vacuum chamber for the radii equivalent to the half axes. Code named "NOVO" [2] was used for the calculations, as only this code has the required resolution for such small gap sizes, like 100 micron or less. Wake field calculations for a gap size of 40 micron needs 20 million mesh points. A picture of the electric force lines of the fields excited by the bunch passing a gap is presented in Fig. 2. The gap size is 200 microns and the bunch length is 13mm. Wake field potentials are shown in Fig. 3. Loss factor dependence upon the gap size for different radii is shown at Fig. 4.

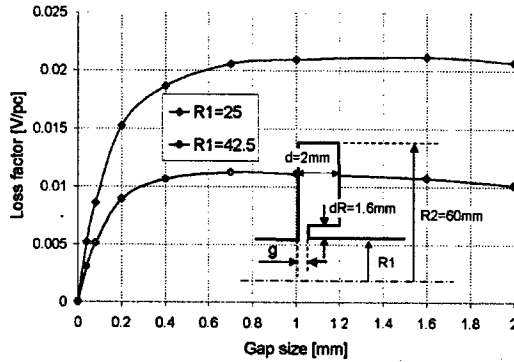


Figure 4: Loss factor as a function of the gap size.

It can be seen that the loss factor is almost constant but vanishing quickly at the gap size of 100-200 microns. The RF power P dissipated in the flanges wall can be estimated as half of the beam power loss (assuming that the other half part propagates in the vacuum chamber)

$$P = 0.5 \times K \times \frac{I^2}{Nf_{rev}}$$

K is the bunch loss factor, I is the positron beam current, N is the number of bunches in the beam, f is the revolution frequency. This estimation gives an RF power of 100-200 W for a gap of 200 microns and $I=1600$ mA, $N=728$, $f=136$ kHz.

In addition to the RF heating, the amplitude of the electric fields that are excited in the gap, can be high enough to exceed the breakdown level. Results of calculations for the electric field amplitude in the gap are shown in Fig. 5. The amplitude increases when the gap size goes down.

The behaviour of the loss factor and the corresponding electric field with the gap size can be easily understood from a simple model of an equivalent LC circuit. In this model we consider a gap to be an additional capacitor, then the total capacitor is

$$C = C_{LC} + C_{gap}$$

According to the geometry (Fig. 3) we can estimate the capacitors to be:

$$C_{LC} \sim \frac{R_2^2 - R_1^2}{8d} \quad C_{gap} \sim \frac{R_1 d R}{2g}$$

with a loss factor which is inversely proportional to the total capacity

$$K \sim \frac{1}{C} \sim \frac{1}{C_{LC}} \frac{g}{g + 4d \frac{R_1 d R}{R_2^2 - R_1^2}} \sim \frac{g}{g + 0.12}$$

Here the gap size is measured in millimetres.

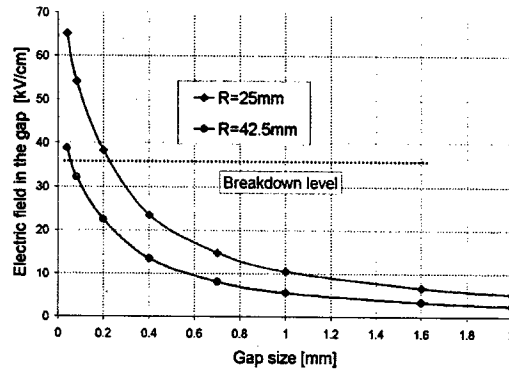


Figure 5: Amplitudes of the electric field in the gap for different gap sizes.

The derived formula says that the loss factor changes when the gap becomes of order of 120 microns. A good comparison of the loss factor with this analytical estimation can be seen from the Fig. 6.

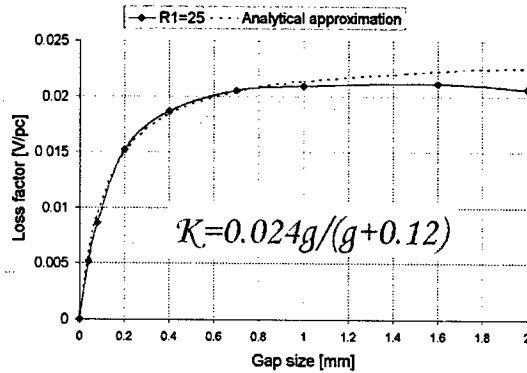


Figure 6: Comparison of the calculate values for loss factor K with the analytical approximation.

This model also gives an estimation of the amplitude of the electric field in the gap

$$E = \frac{V}{g} \sim \frac{1}{\omega C g} \sim \frac{1}{\sqrt{g(g + 0.12)}}$$

So the amplitude of the electric field is inversely proportional to the square root of the gap size. This means that the gap size must be very near zero to avoid any kind of breakdowns. It is interesting to note that these

calculations and predictions for possible breakdowns in the gap were performed before the time when the vacuum chamber flanges were disconnected and traces of the breakdowns tracks were actually observed. Fig. 7 presents a photo of the disconnected flanges and a gap ring. Traces of breakdowns can be easily seen by discolorations on the stainless steel flange at the right. After replacing the ring with one that has the proper size, the RF heating and the temperature oscillations stopped.



Figure 7: Photo of the disconnected flanges and RF gap ring.

TEMPERATURE OSCILLATIONS

We have studied different models to understand how the temperature oscillations could occur. Here we discuss one model. A vacuum valve flange consists of two stainless steel parts, as it shown at Fig. 8. Parts are connected through a circular ring and radial gaps could be from both sides of the ring. When the inner part of the flange is heated, as was discussed before, the size of these gaps decreases with the temperature and thermal contact is improved. The heat energy flows to the outer flange part, which is cooled though with a fan and a copper water-cooled disk. The temperature then goes down and the radial opens up once again..

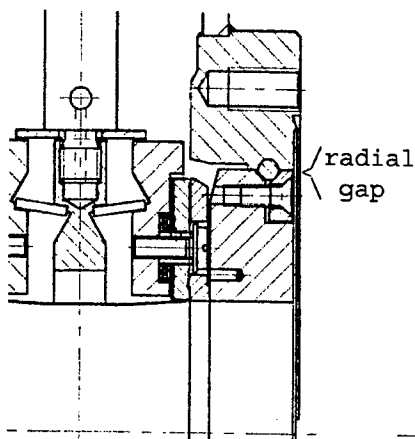


Figure 8: Vacuum valve flange geometry.

This process is demonstrated in Fig. 9, where the results of a two-dimensional simulation are presented.

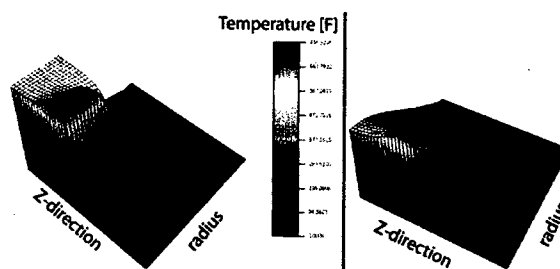


Figure 9: Temperature distribution in the vacuum valve flange connection for different stages of the thermal contact. Maximum temperature is achieved at the inner edge of the stainless steel vacuum valve flange.

The left figure shows the temperature distribution at the time when the gap size is large and the thermal contact is small. The right figure shows the temperature distribution at the time when the gap size is small. Comparison of the simulated and measured temperatures is presented at Fig.10.

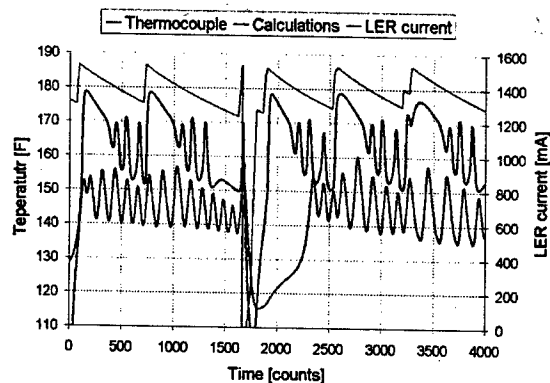


Figure 10: Comparison of the simulated temperature oscillations (blue middle curve) and measured temperatures from the thermocouple (red down curve) with the positron beam current (green upper curve) as a function of time.

The theoretical prediction is in good qualitative agreement with the temperature behaviour. Additional geometry details are needed for better agreement. As it was discovered, the period of oscillation depends upon the distance between the radial gap and the cooled flanged part.

ACKNOWLEDGEMENTS

The authors wish to thank all the PEP-II staff for their help and very fruitful discussions.

REFERENCES

- [1] J. Seeman et al., "PEP-II Status and Future Plans", EPAC2002, Paris, France, 2002, p.434.
- [2] A. Novokhatski, "Code 'NOVO' for wake field calculations", in preparation.

PROGRESS OF THE PEP-II B-FACTORY *

J. Seeman, M. Browne, Y. Cai, W. Colacho, F.-J. Decker, M. Donald, S. Ecklund, R. Erickson, A. Fisher, J. Fox, S. Heifets, R. Iverson, W. Kozanecki, P. Krejcik, A. Kulikov, A. Novokhatski, P. Schuh, H. Schwarz, M. Stanek, M. Sullivan, D. Teytelman, J. Turner, U. Wienands, Y. Yan, J. Yocky, SLAC, Stanford, CA 94309, USA;
M. Biagini, INFN, Frascati, Italy; M. Zisman, LBNL, Berkeley, CA 94720, USA

Abstract

PEP-II is an e^+e^- B-Factory Collider located at SLAC operating at the Upsilon 4S resonance. PEP-II has delivered, over the past five years, an integrated luminosity to the BaBar detector of over 131 fb^{-1} and has reached a luminosity of $6.11 \times 10^{36} / \text{cm}^2 / \text{s}$. Steady progress is being made in reaching higher luminosity. The goal over the next several years is to reach a luminosity of at least $2 \times 10^{34} / \text{cm}^2 / \text{s}$. The accelerator physics issues being addressed in PEP-II to reach this goal include the electron cloud instability, beam-beam effects, parasitic beam-beam effects, high RF beam loading, shorter bunches, lower betay*, interaction region operation, and coupling control. A view of the PEP-II tunnel is shown in Figure 1.

The present parameters of the PEP-II B-Factory are shown in Table 1 compared to the design. The present peak luminosity is 204% of design and the best integrated luminosity per month is 7.4 fb^{-1} that is 225% of design. The best luminosity per month is shown in Figure 2. The integrated luminosity over a month is shown in Figure 3 and the total integrated luminosity in shown in Figure 4.

The progress in luminosity has come from correcting the orbits, adding specific orbit bumps to correct coupling and dispersion issues, lowering the beta y* in the LER, and moving the fractional horizontal tunes in both rings to just above the half integer (<0.52).

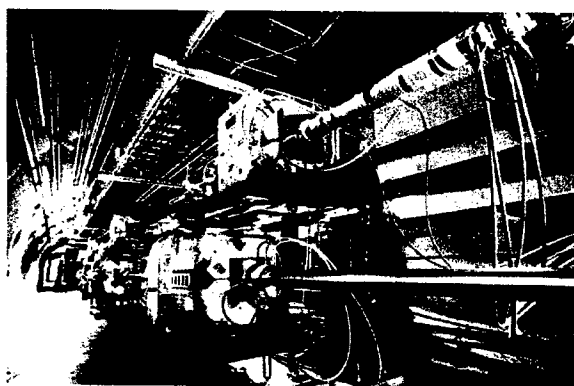


Figure 1 View of the PEP-II tunnel.

*Supported by US DOE contracts DE-AC03-76SF00515 and DE-AC03-76SF00098.

**seeman@slac.stanford.edu

Table 1: PEP-II May 2003 Parameters.

Parameter	PEP-II Design	PEP-II Present
Energy (GeV)	3.07x9	3.1x8.97
HER Vertical tune	23.64	23.57
HER Horizontal tune	24.62	24.516
LER Vertical tune	36.64	36.63
LER Horizontal tune	38.57	38.509
HER current (mA)	750	1100
LER current (mA)	2140	1750
Number of bunches	1658	939
Ion gap (%)	5	2.6
HER RF klystron/cav	5/20	7/24
HER RF volts (MV)	14.0	11.5
LER RF klystron/cav.	2/4	3/6
LER RF volts (MV)	3.4	3.2
β_y^* (mm)	15-25	11
β_x^* (cm)	50	35
Emittance (x/y) (nm)	49/2	21 to 49/3
σ_z (mm)	11	12
Lum hourglass factor	0.9	0.84
Crossing angle(mrad)	0	<0.5
IP Horiz. size Σ (μm)	222	150
IP Vert. Size Σ (μm)	6.7	6.8
HER Horizontal ξ_x	0.03	0.075
HER Vertical ξ_y	0.03	0.060
LER Horizontal ξ_x	0.03	0.065
LER Vertical ξ_y	0.03	0.048
Lumin. ($\times 10^{33} / \text{cm}^2 / \text{s}$)	3.00	6.11
Int. Lum/month (fb^{-1})	3.3	7.4
Integ. Lumin. (fb^{-1})	100 (for CP)	131

1 RUN 3 STATUS

PEP-II has been providing colliding beams for the BaBar detector since May 1999 [1-8]. The present run started in November 2002 and will end in June 2003. There will be a two month down this summer with beam starting again in September 2003. During the recent run, colliding beams occupied 70% of the time, 20% for repairs, and 10% for machine development and accelerator physics studies. About 87% of the data logged by BaBar was on the Upsilon 4S resonance and 13% off-resonance about 40 MeV lower. PEP-II has scanned the Upsilon 3S, shown in Figure 5. The highest luminosity in PEP-II is $6.11 \times 10^{33}/\text{cm}^2/\text{s}$ with the corresponding parameters listed in Table 1. The horizontal beam size of the LER is enlarged at this peak luminosity by about 20%. Also, the vertical beam size of the HER is enlarged by about 20% at the peak luminosity. Both increases are due to the beam-beam effect. 365 pb^{-1} has been delivered in 24 hours. The present delivered luminosity to BaBar is 131 fb^{-1} .

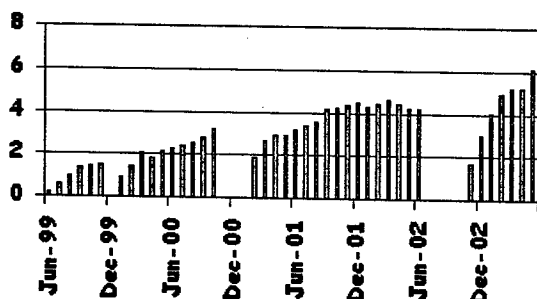


Figure 2 Peak luminosity each month since May 1999. The peak luminosity has reached $6.11 \times 10^{33}/\text{cm}^2/\text{s}$.

PEP-II Monthly Integrated Luminosity

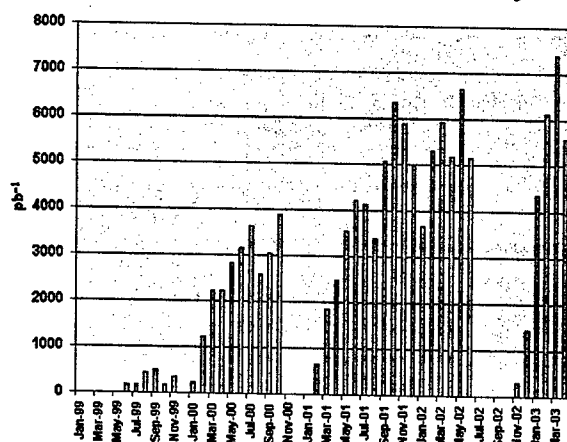


Figure 3 Integrated luminosity per month. In March 2003 PEP-II deliver 7.4 fb^{-1} and BaBar logged 7.2 fb^{-1} .

2 BEAM-BEAM INTERACTION

At low currents, the luminosity increases as the product of the electron and positron bunch charges. At higher currents the LER-x and HER-y beam sizes enlarge due to beam-beam and, perhaps, electron cloud effects in LER, thus, reducing the luminosity increase with current. The HER and LER bunch charges are appropriately balanced to produce near equal beam-beam effects. If there is a miss-balance, flip-flop effects can occur. The horizontal tunes of both rings were recently moved to just above the half integer (~ 0.52) and an immediate increase of about 20% in luminosity occurred. In order to move the LER to the half integer, the horizontal beta beats in the LER had to be fixed. Moving close to the half integer makes the beta beats worse. A computer algorithm (MIA) was created and recently has been made to work. The beta beats in the LER are below 10%. The HER still needs additional work and will be worked on soon.

Total PEP-II Delivered Luminosity

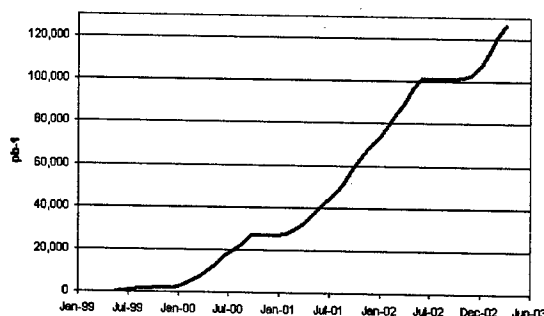


Figure 4 Total delivered integrated luminosity to BaBar by PEP-II. 131 fb^{-1} was delivered by May 2003.

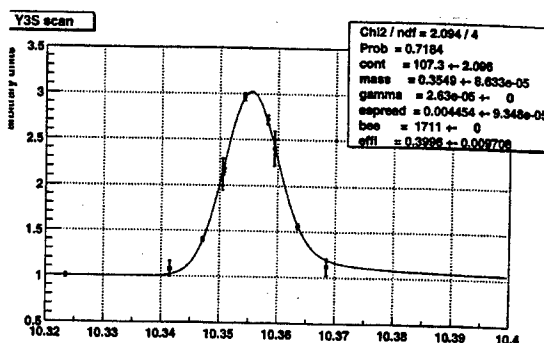


Figure 5 Energy scan of the Upsilon 3S resonance in November 2002.

Recently, PEP-II has been operated with bunches every three RF buckets but with mini-gaps after about 10 to 11 bunches to allow easy bunch number changes and to reduce small ECI effects. A plot of the bunch luminosity over the whole train is shown in Figure 6. There are no obvious signs of ECI over the train. With two bucket spacing, there are signs of electron cloud effects and

parasitic beam-beam effects. To help reduce the ECI effects in the By-2 pattern, stronger solenoids will be added to the LER straight sections this coming summer. The parasitic crossing beam-beam effects are largest in the vertical plane where the vertical betas are much larger than the horizontal betas at the parasitic collisions displaced 63 cm from the IP on both sides. As the betay* is lowered the parasitic effects will become stronger. The exact limit of this effect is under study.

Beam-beam parameters from 0.048 to 0.075 are now routinely achieved in PEP-II that far exceed our design goal of 0.03.

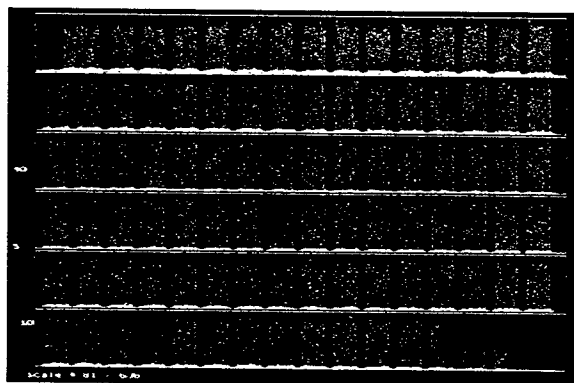


Figure 6 Bunch luminosity along the train with every 3th RF bucket filled and a 2.6% ion gap at the end of the train. There are mini-gaps of about 5 RF buckets.

3 INTERACTION REGION HEATING

At the interaction point of PEP-II there is a Be chamber surrounded by a precision silicon strip detector SVT of BaBar. The Be chamber is double-walled with water cooling between. At present, the water removes about 1 kW of HOM and I²R heat load. This 60 cm long chamber is connected to the nearby B1 dipole magnet chamber with a two convolution bellows on each end. In the summer of 2002, the IR support tube was removed and extra cooling of air and water added, new temperature instrumentation was added to the Be chamber bellows, a new Q2 crotch chamber with lower HOM generation was installed, and new higher power Q2 bellows were installed. The increased power capability of a factor of four to five should allow a factor of about four increase in luminosity. During recent operation, the new cooling techniques have performed according to specification.

4 FUTURE PLANS

PEP-II has an upgrade plan that is leading towards a luminosity of greater than 2×10^{34} in FY2006. Combining the equations for luminosity and the vertical beam-beam parameter, one derives the traditional luminosity scaling

$$L = 2.17 \times 10^{34} (1+r) \xi_y \left(\frac{EI}{\beta_y^*} \right) \text{ cm}^{-2} \text{ sec}^{-1} \quad (1)$$

equation with r the y to x aspect ratio (~ 0.02), E the beam energy, I the beam current, and β_y^* the vertical beta at the collision point. In order to get a factor of four above the present luminosity (to 2×10^{34}), the currents will be raised about a factor of two, the tune shifts increased about 10% and β_y^* reduced from 12 mm to about 7 mm. The number of RF stations in the LER will be increased from three to four in order to achieve about 3.6 A. The number of RF stations in the HER will be increased from seven to eight allowing a current of 1.6 A. The β_y^* can be decreased to about 7 mm using the present IR quadrupole configuration but with extra permanent magnet quadrupole slices replacing some B1 dipole slices. Somewhat increased backgrounds are expected that are under study. The chromatic corrections will be more difficult but early tests indicate an acceptable dynamic aperture. To achieve near 4×10^{34} the β_y^* must be lowered to about 5 mm and additional RF stations added to the HER and LER. In order to shorten the bunches, to reduce the hourglass effects, lower alpha lattices would be needed in the HER and LER or higher harmonic RF cavities to increase the effective RF voltage. The details of the 4×10^{34} upgrade will be evaluated in the next few months.

5 ACKNOWLEDGMENTS

We wish to thank the Operations Group for their help.

6 REFERENCES

- [1] J. Seeman *et al.*, "Status and Future Plans of the PEP-II B-Factory," EPAC 2002, Paris, June 2002.
- [2] Y. Cai *et al.*, "Search of the Gold Orbit with a New Steering Algorithm," PAC 2003, Portland.
- [3] U. Wienands *et al.*, "Betatron-function measurement in lattices with 90° sections," EPAC 2002, Paris.
- [4] Y. Cai *et al.*, "Build up of the Electron Cloud with Different Bunch Patterns in the Presence of a Solenoid Field," PAC 2003, Portland.
- [5] Y. Cai *et al.*, "Tracking Simulations near the Half-Integer Tune at PEP-II," PAC2003, Portland.
- [6] F.-J. Decker *et al.*, "Bunch Pattern By-3 in PEP-II," PAC2003, Portland.
- [7] Y. Nosochkov *et al.*, "Lattice with a Smaller Momentum Compaction Factor for PEP-II HER," PAC2003, Portland.
- [8] P. McIntosh *et al.*, "An Over-Damped Cavity Longitudinal Kicker for the PEP-II LER," PAC 2003, Portland.

DESIGN STUDIES FOR A 10^{36} SUPER-B-FACTORY *

J. Seeman**, Y. Cai, F.-J. Decker, S. Ecklund, A. Fisher, J. Fox, S. Heifets, Y. Nosochkov,
A. Novokhatski, M. Sullivan, D. Teytelman, U. Wienands, Y. Yan
SLAC, Menlo Park, CA 94025, USA
M. Biagini, INFN, Frascati, Italy

Abstract

A Super B Factory, an asymmetric e^+e^- collider with a luminosity of $10^{36} \text{ cm}^{-2}\text{s}^{-1}$, can provide a sensitive probe of new physics in the flavor sector of the Standard Model. The success of PEP-II and KEKB in producing unprecedented luminosity with unprecedently short commissioning time has taught us about the accelerator physics of asymmetric e^+e^- colliders in a new parameter regime. It appears to be possible to build on this success to advance the state of the accelerator art by building a collider at a luminosity approaching $10^{36} \text{ cm}^{-2}\text{s}^{-1}$. Such a collider would produce an integrated luminosity of 10,000 fb^{-1} (10 ab^{-1}) in a running year. Design studies are underway to arrive at a complete parameter set based on a collider in the PEP-II tunnel but with an upgraded RF system (perhaps a higher frequency) and an upgraded interaction region [1-6].

1 DESIGN CONSTRAINTS

The construction and operation of modern multi-bunch e^+e^- colliders have brought about many advances in accelerator physics in the area of high currents, complex interaction regions, high beam-beam tune shifts, high power RF systems, controlled beam instabilities, rapid injection rates, and reliable uptimes (~95%).

The present successful B-Factories have proven that several design concepts are valid. 1) Colliders with asymmetric energies can work. 2) Beam-beam energy transparency conditions are weak. 3) Interaction regions with two energies can work. 4) IR backgrounds can be handled. 5) High current RF systems can be operated (2 amps x 1 amp). 6) Beam-beam parameters can reach 0.06 to 0.9. 7) Injection rates can be good and continuous injection is feasible. 8) The electron cloud effect (ECI) can be managed to a small effect. 9) Bunch-by-bunch feedbacks at the 4 nsec spacing work well.

In addition to the above lessons learned, new techniques can be employed [1,3]. A) The beam lifetimes will be low so continuous injection will be needed. B) Continuous injection will be used to push the beam-beam parameter to higher values than can be tolerated when long lifetimes are required. C) Much higher currents are needed and the vacuum chamber and feedbacks must be made to match. D) Bunch-by-bunch feedbacks will need to operate at the

1 nsec scale, down from the present 4 nsec time. E) Much shorter bunches will be needed; on the order of 2 mm. F) Higher-power vacuum chambers and HOM tolerant chambers will be needed. The use of expansion bellows will need to be minimized or a high-power design developed. G) Very low vertical beta functions at the interaction of about 1.5 to 2.5 mm will be needed. H) Special chromaticity corrections will be needed. I) Every technique to reduce the wall plug power will need to be used. For example, reducing the energy asymmetry to reduce synchrotron radiation, increase the vacuum chamber bores to reduce resistive wall effects,, and increasing the RF cavity bores to reduce HOM losses.

2 PARAMETERS

The design of a $10^{36} \text{ cm}^{-2}\text{s}^{-1}$ e^+e^- collider combines a natural extension of the design of the present B Factories with a few new ideas and special circumstances to allow improved beam parameters to be achieved. The luminosity L in an e^+e^- collider that has a limited vertical tune shift ξ_y with flat beams ($r=0.02$) is given by the standard expression

$$L = 2.17 \times 10^{34} (1+r) n \xi_y \left(\frac{EI_b}{\beta_y^*} \right) \text{ cm}^{-2}\text{sec}^{-1} \quad (1)$$

where I_b is the bunch current (amperes), n is the number of bunches, E is the beam energy (GeV), and β_y^* is the vertical beta function (cm) at the collision point. The luminosity gain of the Super B Factory comes from the increase of the beam currents by about a factor of eight, lowering β_y^* about a factor of five, and increasing the beam-beam tune shifts about 25%. The resulting gain is about a factor of 50 over that of the present B Factories when they are upgraded to about $2 \times 10^{34} \text{ cm}^{-2}\text{s}^{-1}$ over the next few years. In addition, due to continuous injection with the luminosity always near the maximum, the integrated luminosity per unit time of the Super B Factory is expected to increase another 20 to 30% over the present machines. The parameters of a representative $10^{36} \text{ cm}^{-2}\text{s}^{-1}$ e^+e^- collider are listed in Tables 1 and 2 for different RF frequencies. These parameters were chosen after balancing beam dynamics effects, technology limits, luminosity performance, and SLAC site AC power issues. The PEP-II tunnel is an excellent site for this collider. The SLAC power substation can provide 140 MW if needed.

The beam energies are 8 GeV for the high-energy ring and 3.5 GeV for the low-energy ring. Lowering the high-energy ring energy from 9 GeV reduces the synchrotron

*Supported by US DOE contract DE-AC03-76SF00515.

**seeman@slac.stanford.edu

radiation load on the RF system. The e^+ and e^- may be exchanged if need be as either particle can be stored in either ring using the versatile SLAC injector. The linac can provide low emittance beams with 80 Hz of electrons and 20 Hz of positrons. The remaining 20 Hz will be used to generate positrons at the production target.

3 RF FREQUENCY SELECTION

Two RF frequencies for the Super *B* Factory have been studied: 476 MHz as in the present PEP-II and 952 MHz. At the higher frequency, more bunches (about 6900) can be stored, thereby reducing single bunch effects and higher order mode losses at the high total current. Industry has the ability to make cw 952 MHz klystrons at the MW level needed for this accelerator. RF cavities at 952 MHz can be made with a similar design to the PEP-II style copper cavities, using improved HOM dampers and with additional storage cavities to help reduce longitudinal multi-bunch instabilities.

In the Super *B* Factory, the single bunch currents are a factor of two higher than those of PEP-II or KEKB; the total current is increased by a factor of eight, but there are four to eight times as many bunches. Furthermore, the bunch lengths are about five times shorter. These short high-charge bunches lead to increased single bunch effects; Higher-Order-Mode (HOM) losses and resistive wall losses that have to be minimized in each ring, see Figure 1. HOM losses in the RF cavities will be reduced by opening the beam channel through the RF cavities

about 50%. The resistive wall losses of the short bunches in the vacuum chambers will be reduced by a factor of two by increasing the vacuum chamber radius.

4 INTERACTION REGION

The interaction region is being designed to leave the same longitudinal free space as that presently used by *BABAR* but with superconducting quadrupole doublets as close to the interaction region as possible, as shown in Figure 2. A crossing angle is used to separate the two beams as they enter and leave the interaction point. The overall interaction region is shorter than for PEP-II, allowing a shorter detector if that is advantageous [6].

Recent work at Brookhaven National Laboratory on precision conductor placement of superconductors in large-bore low-field magnets has led to quadrupoles in successful use in the interaction regions for the HERA collider in Germany [7]. A minor redesign of these magnets will work well for the Super *B* Factory.

The beams must have a crossing angle at the collision point to avoid parasitic crossing effects; the anticipated crossing angle is ± 12 to 17 mrad. Short bunches are also needed to avoid the geometrical hour-glass effects that could reduce the luminosity during collisions. The short Super *B* Factory bunches are made by providing extra over-voltage in the RF system and by a high phase-advance quadrupole lattice in each ring.

The low beta functions at the collision point will make

Table 1 Super B Factory Parameters with 476 MHz RF.

Parameter	LER	HER
Energy (GeV)	3.5	8
RF frequency (MHz)	476	476
Vertical tune	72.64	56.57
Horizontal tune	74.52	58.52
Current (A)	11.0	4.8
Number of bunches	3450	3450
Ion gap (%)	1.2	1.2
HER RF klystron/cav	22/44	18/36
HER RF volts (MV)	29	24
β_y^* (mm)	2.2	2.2
β_x^* (cm)	15	15
Emittance (x/y) (nm)	27.5/0.4	27.5/0.4
σ_z (mm)	2.5	2.5
Lum hourglass factor	0.82	0.82
Crossing angle(mrad)	15	15
IP Horiz. size (μ m)	64	64
IP Vert. size (μ m)	0.9	0.9
Horizontal ξ_x	0.15	0.15
Vertical ξ_y	0.15	0.15
Lumin. ($\times 10^{34}/\text{cm}^2/\text{s}$)	50	50

Table 2 Super B Factory Parameters with 952 MHz RF

Parameter	LER	HER
Energy (GeV)	3.5	8
RF frequency (MHz)	952	952
Vertical tune	72.64	56.57
Horizontal tune	74.52	58.52
Current (A)	15.5	6.8
Number of bunches	6900	6900
Ion gap (%)	1.2	1.2
HER RF klystron/cav	32/64	25/50
HER RF volts (MV)	43	33
β_y^* (mm)	1.5	1.5
β_x^* (cm)	15	15
Emittance (x/y) (nm)	19.5/0.19	19.5/0.19
σ_z (mm)	1.75	1.75
Lum hourglass factor	0.8	0.8
Crossing angle(mrad)	15	15
IP Horiz. size (μ m)	54	54
IP Vert. size (μ m)	0.5	0.5
Horizontal ξ_x	0.15	0.15
Vertical ξ_y	0.15	0.15
Lumin. ($\times 10^{34}/\text{cm}^2/\text{s}$)	100	100

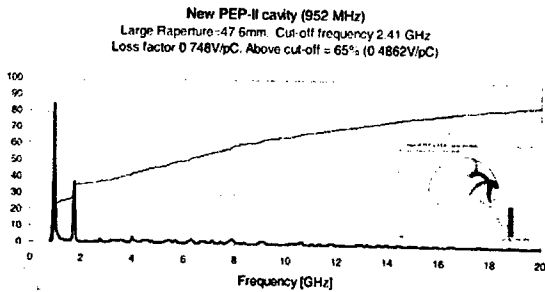


Figure 1 HOM calculation for a 952 MHz PEP-II style RF cavity with an increased bore.

the ring chromaticity high. Correcting the chromaticity is the task of sextupole magnets, but sextupoles reduce the dynamic aperture of the storage ring. Due to the naturally reduced lifetimes of the beams, the dynamic aperture and the resulting vacuum system do not have to be designed for lifetimes of hours, only for one hour, thus, reducing costs.

The increases in the beam-beam parameters from the present 0.06 to 0.09 range to 0.15 will be achieved by operating just above but very close to the half-integer horizontal tune where standard, but strong, dynamic beta effects occur. Also, pushing the transverse tunes closer to specific resonances allows a higher tune shift and more luminosity but with shorter beam lifetimes. Both techniques have been successfully demonstrated at the present B Factories.

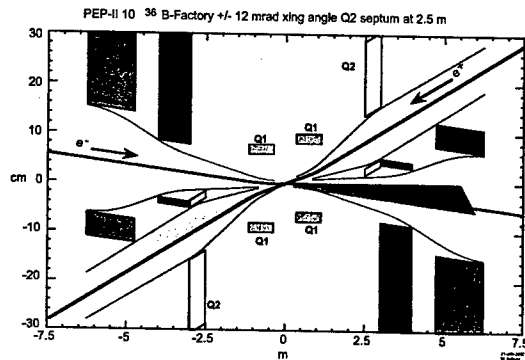


Figure 2 Interaction region for a Super B-Facility. Note the first quadrupole is at 30 cm from the interaction point. This first quadrupole will have a quadrupole, x and y dipole, solenoidal, and skew quadrupole windings.

5 POWER SCALING

The power required by a collider is the sum of a site base plus RF sources. With a Super B-Facility, there will be an overall base level due to the SLAC campus (~15 MW), the linac running for PEP-II at 30 Hz (~8MW), The PEP-II magnets (~7 MW), the linac running for LCLS (~10 MW), and SPEAR (~5 MW) for a total of about 40 MW.

The total RF power is the sum of the cavity wall losses, beam synchrotron radiation, beam resistive wall losses, beam higher order mode losses (HOM), and AC distribution inefficiencies. The AC transformers and high

voltage power supplies are about 90% efficient. The RF klystrons are about 65% efficient. For beam stability control, the klystrons do not run at full power which reduces their efficiency to about 50%. The RF power losses to the cavity walls are 70 to 100 kW depending on the voltage. The synchrotron radiation losses are minimized by reducing the energy asymmetry of the B-Facility to 3.5 x 8 GeV and by adding dipoles to the low-energy ring to reduce the effective bending radius. The vacuum chamber bores are enlarged to reduce the resistive wall losses that go inversely with the chamber size. The HOM losses are reduced by going to a higher RF frequency with more bunches but same total current.

The total power of a Super-B Facility at the SLAC site as a function of luminosity is shown in Figure 3. If the site power is limited to 120 MW that is within the range of the incoming power lines, then a luminosity of about 5×10^{35} luminosity is possible at 476 MHz and 1×10^{36} at 952 MHz.

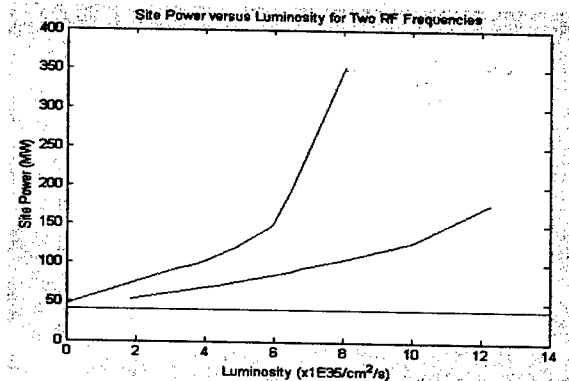


Figure 3 Site power scaling for two RF frequencies The upper curve is for 476 MHz and the lower curve 952 MHz. The power above the 40 MW horizontal line is from the overall PEP-II RF system. The currents increase with the luminosity and, thus, increase the power usage.

6 REFERENCES

- [1] J. Seeman, "Initial Parameters for a $10^{36}/\text{cm}^2/\text{s}$ Luminosity e^+e^- B-Facility," SLAC-PUB-8787, March 2001.
- [2] J. Seeman, "Higher Luminosity B-Factories," PAC 2001, Chicago, p. 305.
- [3] J. Seeman, "Prospects on Future Higher Luminosity e^+e^- Colliders," ICFA e^+e^- Factories Workshop, Ithaca, New York, October 2002.
- [4] P. Burchat et al, "Physics at a 10^{36} e^+e^- B-Facility," Snowmass, July 2001.
- [5] S. Henderson et al., "Lepton Colliders Working Group Report," Snowmass, July 2001.
- [6] M. Sullivan, "Interaction Region Upgrades of e^+e^- B-Factories," PAC, Portland, May 2003.
- [7] B. Parker et al., "Superconducting Magnets for use inside the HERA ep Interaction Regions," PAC 1999, New York, p. 308.

IMPROVEMENTS IN ALADDIN BEND MAGNET STABILITY BY REDUCTION OF LEAKAGE CURRENTS*

D. J. Wallace[#], M. Fisher, K. D. Jacobs, G. Rogers, L. Rowley, M. Thikim, W. Trzeciak
Synchrotron Radiation Center (SRC), Stoughton, WI 53589, USA

Abstract

For 800 MeV operation of the Aladdin Synchrotron Storage Ring, 730 amps of current flow through the 12 bend magnets in series. The bend magnet field coils are cooled by water which is in intimate contact with the copper coils. The elastomer hoses which deliver this water had up to 103 VDC between the coils and the electrically grounded plumbing. This configuration induced an electrolytic reaction which produced and deposited cuprous oxide on the inner walls of the hoses. The electrical resistance of the hoses was significantly reduced and leakage currents as high as 833 mA flowed to ground. This missing and changing bend magnet current resulted in significant horizontal electron orbit changes. When the deposits were large, additional deposits occurred quickly and tripped off the bend magnet power supply, resulting in lost photons for the storage ring users.

We have electrically isolated the cooling water hose manifolds and lengthened some hoses. This minimized leakage currents to ground, slowed recontamination of new hoses and reversed contamination in badly contaminated hoses. These improvements have resulted in improved storage ring orbit stability (and thereby improved photon beam stability), less electrochemistry on the copper coils, and better operations reliability.

BACKGROUND

At the SRC we have recently commissioned a reduced-emittance lattice (LF15) [1], with a significantly reduced σ_x of $\sim 200 \mu\text{m}$. Therefore, a reasonable target for horizontal electron beam position stability would be $\sim 20 \mu\text{m}$ at the bend magnet source points. Attempts to achieve this beam stability demand requisite levels of both mechanical and electrical stability.

The 12 bend magnets in the Aladdin storage ring are shown in Figure 1. A closed loop system, with deionized, high resistivity ($\sim 6 \text{ Mohm cm}$) water, cools the copper coils which produce the magnetic fields. For each bend magnet top half or bottom half, cooling water flows from a grounded 4.5 inch diameter supply pipe through an elastomer hose, ~ 32 inches long and 1 inch in diameter, to a metal supply manifold. This manifold distributes the water through 9 elastomer hoses, each ~ 15 inches long and 0.5 inch in diameter, to 8 copper field coils and a power lead. After the water passes through the internal cooling channels in the coils, it flows to a metal return manifold through 9 similar hoses. The water continues to a grounded 4.5 inch diameter return pipe. The metal

supply and return manifolds were originally grounded. The intent of this system was to provide cooling water and electrical isolation of the field coils by using the insulating elastomer hoses and high resistivity water. We observed significant leakage currents and modified this system after additional measurements and preliminary testing.

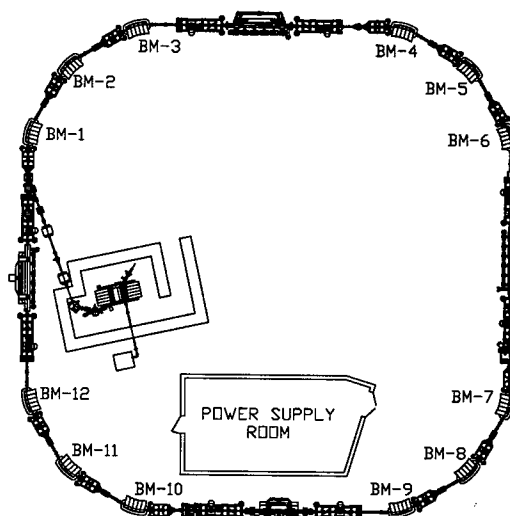


Figure 1. Aladdin storage ring with bend magnets (e.g., BM-10) and power supply room.

The Aladdin storage ring normally operates at 800 MeV and by request at 1 GeV. At the beginning of the current path, the voltage between the field coils and the grounded distribution manifolds was $\sim 103 \text{ VDC}$, for 800 MeV operation ($\sim 147 \text{ VDC}$ for 1 GeV operation). This voltage decreased proportionally around the storage ring to $\sim 8.4 \text{ VDC}$ at bend magnet 9. At these voltages new, clean, elastomer hoses should prevent significant leakage currents between the copper coil sets and the cooling manifolds.

The current through the 12 Aladdin bend magnets is 730 A for 800 MeV operation (1017 A for 1 GeV operation). This current begins at a Transrex power supply. The current enters the circuit at bend magnet 10, in the top set of coils, and proceeds clockwise around the ring through the series of 12 top coil sets. At the end of the top coil series (bend magnet 9) the current continues through the 12 bottom coil sets in series, in reverse order from 9 back to 10. This series circuit of top and bottom coil sets is intended to produce identical and stable currents and fields in the magnets, resulting in a stable electron beam orbit. For safe and proper power supply

* Work supported by the U.S. National Science Foundation under Award No. DMR-0084402

[#] Danwallace@src.wisc.edu

operation there is a ground fault current detector halfway around the circuit, after the top series of coils, with an established shutdown limit of 250 mA. It should be noted that this detector monitors only the net imbalance in leakage currents, with positive, top coil leakage currents being offset by negative, bottom coil leakage currents.

LEAKAGE CURRENT PROBLEMS

In 1997, 98 and 99 there were a minimum of 5 unplanned and uncontrolled bend magnet power supply shutdowns per year. These were due to excessive ground fault currents from electrical leakages in the cooling water hose system. The fault correction involved determining which magnet's hoses were "bad" and replacing all the hoses for that magnet. These shutdowns interrupted machine operation and the experimental programs which depend on the photons generated by the electron beam. The fast shutdown of these large currents also placed additional magnetic and mechanical stress on the magnet cores, possibly leading to observed lamination separations.

After careful analysis of the interactions among the cooling water hoses, the copper field coils and the applied bend magnet voltages, we determined that an electrolytic reaction was removing copper from inside the coils. This reaction created copper oxides and deposited them on the inside of the insulating elastomer hoses. Sufficient internal coatings eventually built up allowing the hoses to become significant leakage paths. The worst observed

leakage of 833 mA from the top manifolds of bend magnet 11 tripped the ground fault detector during 1 GeV operation. This leakage occurred across a 135 VDC drop.

The leakage currents were also found to seriously affect the position of the electron beam in each bend magnet. Obviously, any current leaking to ground from hoses decreased magnetic fields in that magnet and in each sequential bend magnet in the ring. Furthermore, changing leakage currents result in changing electron beam positions. During 800 MeV operation, increases in leakage currents of 38 mA were observed in one magnet over 5 hours. During 1 GeV operation, increases of 225 mA were observed over 8 hours. Since any change in leakage changes the electron orbits, the source position and the trajectory angle of the photon beam would also change.

Figure 2 shows a plot of the ground fault detector current (lower continuous trace) and the horizontal beam position in bend magnet 10 (upper disconnected points) as a function of time. This data covers 2 months of normal storage ring operation with the global feedback system [2] providing real time position corrections. It is clear that the ground fault detector current was changing and in some cases changing very quickly on the left half of the plot. The horizontal photon beam position moved by more than 160 μm , which is clearly beyond our position stability target of 20 μm . The main contribution to these leakage currents was bend magnet 11 with an individual leakage current larger than 800 mA.

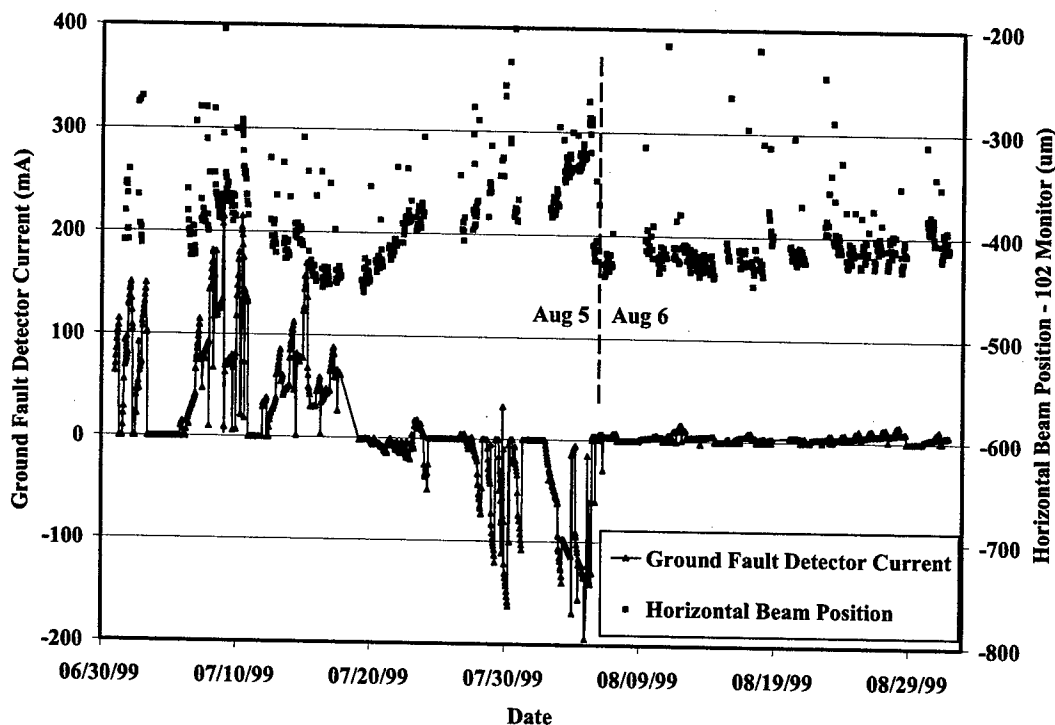


Figure 2. Ground fault detector current and horizontal beam position at monitor 102 during Aladdin ring operation.

The leakage currents from a particular bend magnet were found to be directly proportional to the applied voltage, for a constant level of internal contamination. It was also found that magnets (10, 11 and 12) with higher voltage drops across the cooling hoses developed contamination more quickly and developed higher leakage currents. Since the voltage drops during 1 GeV operation were 43% higher, significantly higher rates of contamination occurred during those operating conditions.

MINIMIZING LEAKAGE CURRENTS

An electrolytic reaction can be minimized by reducing the voltage across the electrodes. This was done in this situation by ungrounding the supply and return water manifolds for each half of each bend magnet. This was accomplished by inserting 6 concentric pieces of PVC pipe around each manifold in the appropriate places to electrically isolate the manifold from ground. When this was done the manifolds floated to a voltage based on the cumulative resistance of the 9 small hoses relative to the high resistance of the larger, 32 inch long hose. This is basically a voltage divider circuit. In bend magnets 10 and 11 respectively the voltage drops at 800 MeV, from the field coils to the manifolds, have been reduced from 103 VDC to 6 VDC and from 96 VDC to 5 VDC. Furthermore, the added high, series resistance of the 32 inch long elastomer hose reduced all leakage currents by more than a factor of 100.

Since the isolated manifolds floated up in voltage (142 VDC is worst case, at bend magnet 10, at 1 GeV), it was necessary to shield personnel from manifold contact. This was done with bent plexiglass shields and insulating pipe foam. A test point wire was also attached to each manifold to allow monitoring of leakage currents and hose contamination.

RESULTS

Between July and November of 1999, the cooling manifolds on the bend magnets with the worst leakage currents were electrically isolated to test the new system. The remaining manifolds were electrically isolated in November of 2001. Immediately after isolating manifolds with badly contaminated hoses and high leakage currents, hoses "cleaned up" due to the reduced voltage drop. When the top supply manifold on bend magnet 11 was isolated, that leakage current decreased from 612 mA to 25 mA over 4 days. Test measurements over the last 3 years with manifolds temporarily regrounded show individual leakage currents remain below 40 mA, even during 1 GeV operation. (The added series resistance of the longer hose further reduces actual leakage to less than 0.4 mA.)

On August 5, 1999 the extremely high leakage currents at bend magnet 11 tripped the ground fault detector and shut down the ring. At midnight between August 5 and 6, the cooling manifolds on bend magnet 11 were electrically isolated in an attempt to correct this problem without changing the contaminated hoses. This point in

time is marked in Figure 2 by the vertical dashed line. It is clear that the ground fault detector current was significantly reduced and the horizontal beam position became much more stable after manifolds were isolated. Since August 6, 1999 there have been no bend magnet power supply shutdowns due to ground faults. The smaller changes in beam position after August 6 are due to leakage currents from the remaining 10 bend magnets with grounded manifolds.

Recently, known leakages at bend magnet 12 and at bend magnet 1 were separately imposed on a stable LF15 electron orbit by temporarily grounding the cooling manifolds. Changes were monitored by our recently updated optical beam position monitoring system. With the global feedback system off, a leakage current of 100 mA caused a 45 μ m beam position shift. The manifold isolation system reduces leakages and their effects by a factor of over 100. The resulting beam position shifts, from the present level of current leakage, is less than 0.4 μ m. This is well within the position stability target of 20 μ m. Changes were also monitored with the global feedback system on. Beam shifts were further reduced by a factor of 6 with global feedback.

CONCLUSION

Gains realized by isolating bend magnet cooling manifolds:

- Direct monitoring of leakage currents and hose contamination is possible.
- Voltage drops and leakage currents between the magnet coils and the cooling manifolds are significantly reduced.
- Bend magnet coils receive proper current resulting in correct electron beam orbits.
- Electron orbit stability is improved providing more stable photon beams.
- Electrolytic damage to the copper magnet coils is reduced along with hose contamination.
- Storage ring reliability is improved.

We gratefully acknowledge the assistance and patience of Mike Green and other SRC staff in the implementation of these machine upgrades.

REFERENCES

- [1] K.D. Jacobs, et al., "Commissioning Low Emittance Beam at Aladdin", these proceedings.
- [2] K.J. Kleman, "High Precision Real Time Beam Position Measurement System", Proc. of the 1989 P A C, Chicago, IL, pp. 1465-1467.

LONGITUDINAL SINGLE-BUNCH INSTABILITIES FOR DIFFERENT OPERATION ENERGIES AT ELETTRA

G. De Ninno*, M. Danailov, B. Diviacco, F. Iazzourene, E. Karantzoulis, M. Marsi, L. Tosi, M. Trovò

Sincrotrone Trieste, Area Science Park, Trieste, Italy

Abstract

The ELETTRA storage ring is currently operated over a wide electron-energy range (0.75-1.5 GeV and 2-2.4 GeV). This paper reports on measurements performed in order to characterize the longitudinal beam stability when the machine is operated in the low-energy range in single-bunch filling mode.

INTRODUCTION

Instabilities of different nature may affect electron beams circulating in a Storage Ring (SR) [1], [2] and cause severe limitation in the performances of devices dedicated to exploitation of Synchrotron Radiation or to Free Electron Laser (FEL) operation. The origin of such instabilities can be traced back either to the electromagnetic wake field which is generated by the interaction between the electron beam and its environment (e.g vacuum pipe, low-gap chambers, discontinuities, etc.) and re-acts on the electrons perturbing their motion, or to external perturbations (e.g. line-induced modulations, mechanical vibrations, etc.). The presence of the instability may manifest in different ways. For example, the so-called saw-tooth regime is currently observed on many SR [3]; in this case the beam evolution is characterized by a periodic fast blow-up of the energy spread and bunch length followed by a damping. In other cases, the effect of the instability is less dramatic and simply manifests in a smooth increase of the beam energy spread and bunch length with current [1].

Longitudinal instabilities can be basically grouped in two classes: the fast ones, which are characterized by coherent (or pseudo-coherent) oscillations at frequencies close to the synchrotron frequency (and its harmonics) and the slow ones, whose typical frequencies range from 50 to few hundred Hz. Since coherent synchrotron oscillations represent the "natural" beam response to kick-like external perturbations, slow-frequency instabilities often induce high-frequency ones.

The ELETTRA SR is currently operated over a wide electron-energy range. The high-energy multi-bunch operation mode (2-2.4 GeV), which is characterized by a better beam stability (the synchrotron damping being more effective), is the standard one for experiments requiring high fluxes. An increasing interest is being manifested in the operation mode where the machine is run in few-bunch filling mode at relatively low energies (0.75-1.5 GeV). In fact, this low-energy domain is well suited both for FEL operation

[4], [5] and for experiments exploiting the time structure of synchrotron radiation.

IMPEDANCE AND SINGLE-BUNCH MEASUREMENTS

During the first year of commissioning (1993-94) it was possible to store in the ELETTRA storage ring more than 60 mA in single bunch and more than 700 mA in multi-bunch. According to calculations performed in the same period, the longitudinal broad band impedance was < 0.5 (measured < 0.5) Ω and the transverse one < 200 (measured 130) $\text{k}\Omega/\text{m}$ giving a tune shift with current of about 0.12 ± 0.02 kHz/mA [6].

Since then, many new installations took place, the most serious from the impedance point of view being the replacement of straight section vacuum chamber with low gap ones. With each new installation a broad band transverse impedance increase of about 0.1 $\text{kHz}/\text{mA}/\text{installation}$ has been measured. An even greater increase [7] has been measured when Aluminum chambers with NEG (Ti, Va, Zr) sputtered material was used [8]. Although since 1994 the transverse impedance increased by about a factor 12, this did not affect the multi-bunch operating mode. However, a great reduction of the maximum stored current and of the beam stability has been observed when the machine is operated in single-bunch mode. The theoretical transverse mode coupling threshold is now at about 14 mA/bunch [7] whereas in 1994 was above 40 mA. No clear change of the longitudinal effective impedance, that was $Z \simeq 0.2\Omega$, has been measured until 2000. Recent measurements [7] of bunch length versus single bunch current have been performed using a double sweep streak camera: Figure 1 shows the bunch length increase detected at the end of 2002 together with the reduction of the maximum current stored in a single bunch indicating an impedance of 0.32 Ω , i.e. a change of 50%.

The biggest contributors to the longitudinal impedance are the main rf-cavities and, although since 2000 there was installed a longitudinal kicker as a part of a longitudinal multi-bunch feedback (spring 2002) and a third harmonic super-conducting cavity (autumn 2002), this change cannot be attributed solely to the increase of the cut-off frequency being now above 3.5 GHz.

Figures 2 and 3 show the behaviour of the bunch length and of the energy spread, as a function of the beam current, when ELETTRA is operated at 0.75, 0.9 and 1.5 GeV. Measurements of energy spread are based on

* giovanni.deninno@elettra.trieste.it

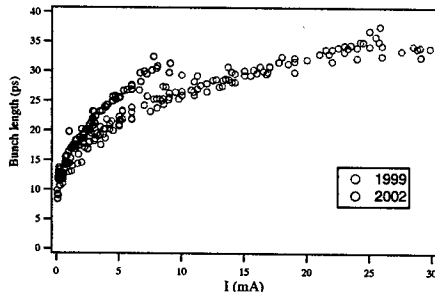


Figure 1: Bunch length as a function of the beam current (single bunch). Measurements performed in 1999 and 2002 at 0.9 GeV. Data have been acquired over the whole current range by means of a double sweep streak camera. The absolute error on each point is about 2 ps.

the analysis of the spectrum of the spontaneous radiation emitted by the FEL optical klystron, as reported in [9].

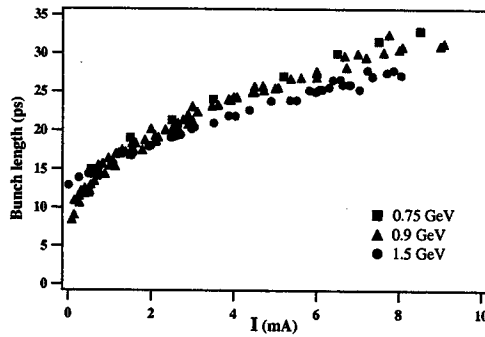


Figure 2: Bunch length as a function of the beam current (single bunch) at 0.75, 0.9 and 1.5 GeV. Data have been acquired by means of a double sweep streak camera. The absolute error on each point is about 2 ps.

It is worth pointing out that while the natural bunch length and energy spread at 1.5 GeV are larger than the corresponding values at 0.9 GeV (in agreement with theory), the trend is reversed already at relatively small values of the beam current (roughly 1 mA). This result confirms that the effect of the microwave instability is reduced when the energy is increased. The curve of the energy spread at 1.5 GeV in Figure 3 shows the transition between the potential well distortion (pwd) regime [10], in which an increase of the bunch length is observed (Figure 2) while the energy spread stays almost constant, and the microwave instability regime [11], characterized both by an "anomalous" bunch lengthening and by an increase of the energy spread. The current threshold, I_{th} , i.e. the so-called Boussard parameter [12], is given by

$$I_{th} \propto \frac{E \sigma_{e,0}^3 \alpha^2}{Z_n / n} \quad (1)$$

where E is the nominal electron-beam energy, $\sigma_{e,0}$ the

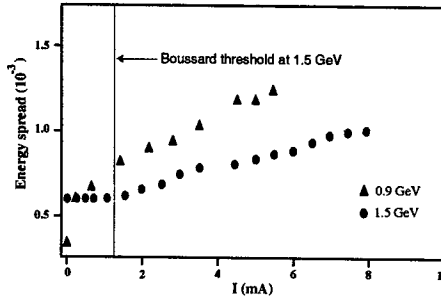


Figure 3: Beam energy spread as a function of the beam current (single bunch) at 0.9 and 1.5 GeV. The natural (i.e. close-to-zero current) values at 0.9 and 1.5 GeV are $0.36 \cdot 10^{-3}$ and $0.6 \cdot 10^{-3}$, respectively.

natural energy spread, α the momentum compaction factor and Z_n the broad band impedance (n being the harmonic of the revolution frequency). The previous relation shows that a suitable modification of the beam optics could allow to extend the current range in which ELETTRA is operated in pwd regime, possibly improving the the FEL performance.

SINGLE-BUNCH INSTABILITIES

As a general remark, it is important to point out that while the behaviour of the bunch length as a function of the beam current has been found well reproducible, the same does not hold when the stability is regarded on a temporal scale of the order of few synchrotron period (tens of μ s) or larger. Although a slight misalignment of the machine may have its influence, this lack of reproducibility seems mainly due to the presence of non-systematic effects, such as a 50 Hz perturbation (and its harmonics), whose origin has not been for the moment fully clarified. This slow instability may manifest in different ways, e.g. as a "kick" (Figure 4) or as a continuous modulation (Figure 5), and it can be at the origin of fast synchrotron-like instabilities.

In most cases, the center of mass of the electron bunch has been found subject to synchrotron oscillations (Figure 4b), the amplitude of which is found to be both energy and current independent. A recurrent mechanism which is at the origin of these oscillations is shown in figure 4a: the study of the beam evolution on a long (several ms) temporal scale shows the occurrence of a kick that excites the beam every 20 ms; the synchrotron oscillations represent the "natural" beam response to the perturbation. Figure 5c shows that, once excited, the synchrotron oscillations relax with a characteristic time (less than 10 ms) much shorter than the synchrotron damping time, which is around 86 ms for the case shown in Figure 4.

As it has been previously mentioned, the 50 Hz perturbation (or its harmonics) may also manifest itself as a continuous modulation. In this case, as it is shown in Figure 5, the beam centroid tends to follow the dynamics of the

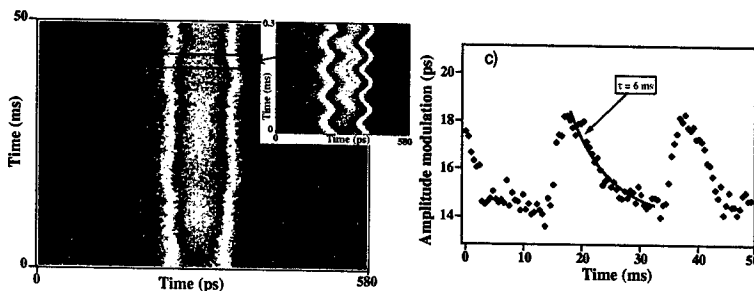


Figure 4: Figure a): streak camera image of the electron beam at 0.9 GeV (0.5 mA). Along the vertical axis one can follow the evolution in time of the temporal beam distribution while a horizontal cut provides the beam distribution profile. Figure b): zoom along the vertical axis of figure a) allowing to visualize the beam dynamics on a temporal scale of the order of few synchrotron periods. Figure c): Evolution of the amplitude of the synchrotron oscillations (observed in figure b)) as obtained by the analysis of Figure a).

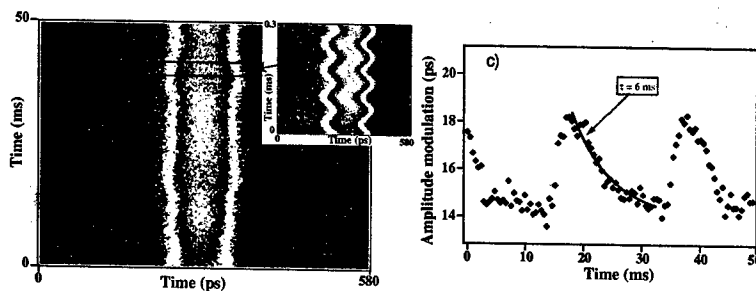


Figure 5: Figure a): streak camera image of the electron beam at 0.9 GeV (6 mA). Figure b): Evolution of the position of the beam center of mass of as obtained by the analysis of Figure a).

instability.

CONCLUSIONS AND PERSPECTIVES

Continuous measurements carried out at ELETTRA allow to characterize the evolution of the electron beam quality when the SR is operated in the single-bunch, low-energy configuration. The study of the single-bunch configuration is to be considered as propedeutic to the few-bunch operation mode which is, in turn, suitable for a number of application exploiting the time structure of the synchrotron radiation. The study points out the existence of non-trivial phenomena, such as the coupling between a slow (50 Hz) perturbation and fast synchrotron-like instabilities. The origin of this non-systematic perturbation will be the topic of a future dedicated analysis.

REFERENCES

- [1] J.L. Laclare, *CERN Report* **85-19** (1985) 377.
- [2] A. W. Chao, *Physics of collective Beam instabilities in High Energy Accelerators*, Wiley, New York (1993).
- [3] Brandt et al, *Proceedings EPAC 1992* 345.
- [4] R.P. Walker et al., *Nucl. Instr. and Meth. A* **429** (1999) 179.
- [5] G. De Ninno et al., in press on *Nucl. Instr. and Meth. A*.
- [6] E. Karantzoulis et al., *Proceedings EPAC 1994* 602.
- [7] E. Karantzoulis et al., *Phys. Rev. ST Accel. Beams* **6** (2003) 030703.
- [8] E. Karantzoulis and L. Tosi, *ELETTRA Internal Note* ST-TN 03/04 (2003).
- [9] G. Dattoli et al. *Nucl. Instr. and Meth. A* **471** (2001) 403.
- [10] J. Haissinski, *Il Nuovo Cimento B* **18** (1973) 72.
- [11] G. Dattoli and A. Renieri, *Nucl. Instr. and Meth. A* **375** (1996) 1.
- [12] D. Boussard, *CERN LABII* **75-2** (1975).

INJECTION AND FEL LASING WITH FRONT END OPEN AT ELETTRA

K. Casarin, G. De Nino, F. Iazzourene, E. Karantzoulis, G. Tromba, L. Tosi, A. Vascotto,
ELETTRA, Trieste, Italy

Abstract

In view of the construction of the new full-energy injector at ELETTRA, radiation dose measurements have been performed to study the scenario of beam losses in top-up regime and to explore potential conditions of radiation hazard for personnel. Measurements of gamma and neutron radiation fields have been carried out in the experimental hall varying the injection efficiency while a beamline front-end was open. In this context, FEL lasing experiments were performed while in injection mode. The collected data as well as future developments are presented and discussed.

PRELIMINARY STUDY OF DETECTOR RESPONSE

During injection with front-end open, two ionisation chambers (see Fig.1) produced by PTW Freiburg (model 32002 - volume 1000 cm³ and model 32003 - volume 10000 cm³) were placed inside the ring and the front-end hut to measure radiation yield.

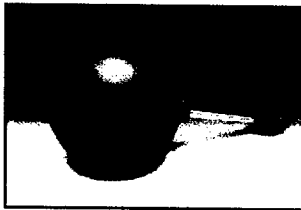


Figure 1: PTW chamber.

The response of these detectors to high intensity pulsed radiation fields was previously investigated to obtain their response curves and to evaluate the saturation level beyond which they start to significantly underestimate the dose rate.

With this goal in mind the detectors were placed at different lateral distances with respect to the linac beamstopper, and integrated doses were measured at various currents with the beam hitting the beamstopper itself, as shown in Fig.2.

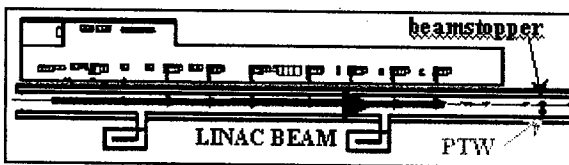


Figure 2: Layout of experiments performed to investigate PTW response to high intensity pulsed radiation fields.

The Linac beam was operated at 900 MeV with a repetition rate of 10 Hz and a pulse length of 70 nsec; the pulse amplitude was varied according to needs. Results are shown in Figs. 3a and 3b.

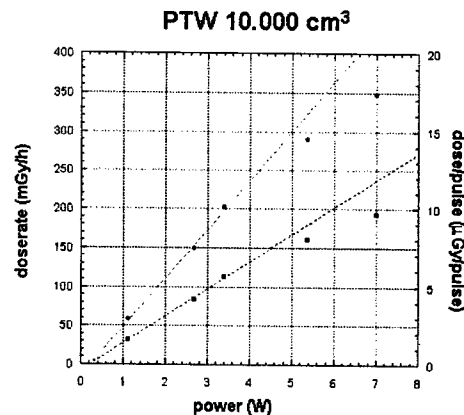


Figure 3a: Response of the 32003-PTW ionization

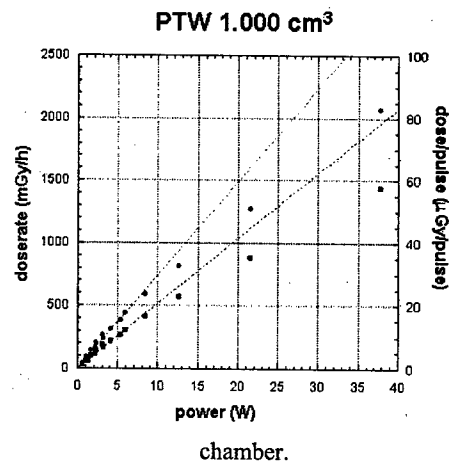


Figure 3b: Response of the 32002-PTW ionization chamber.

The response of the 32003-PTW ionization chamber can be considered linear up to a beam power of about 5 W (dose rate \approx 300 mGy/h), whereas for the 32002-PTW ionization chamber this limit is reached at 10 W (dose rate \approx 700 mGy/h).

INJECTION WITH FRONT-END OPEN.

The great advantage of operating the future new injector of Elettra in top-up mode is that the beam current will be kept constant within 0.1% to 1% of the maximum level.

Safety issues related to injection with open photon shutters and beamstoppers have to be considered in order to design an appropriate safety system and radiation monitoring network [1]-[7]. Preliminary experiments have been carried out to evaluate the radiation levels produced outside the shielding when the beam is injected with one of the beamlines open.

The beamline used for this experiment was the FEL/Nanospectroscopy beamline, the first encountered by the beam after injection. It is an optical-klystron (i.e. two undulators separated by a dispersive section) beamline with an aluminium low gap (14 mm internal aperture) vacuum chamber that can be used, in conjunction with its back-end, at 0.9 to 1.5 GeV to drive a Free Electron Laser (FEL).

Machine behaviour was studied during normal injection conditions. Furthermore, in order to study possible beam loss scenarios during inefficient injection, controlled "bumps" were applied to the beam in the straight section upstream of the operating beamline, to force partial or total beam losses close to the beamline front-end (FE). These bumps consisted of vertical shifts of the beam parallel to the vacuum chamber axis, so as to reduce the local vertical acceptance.

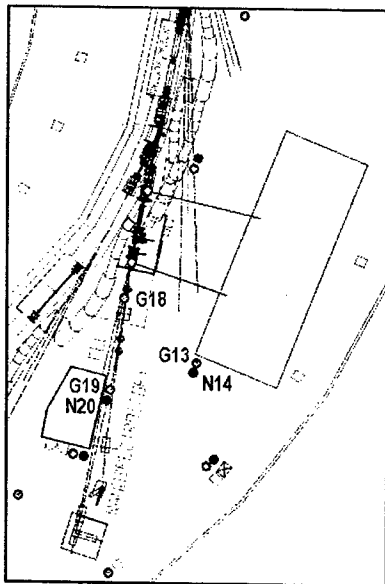


Figure 4: Layout of beamline area showing the positions of gamma (green circles) and neutron (red circles) monitors and PTW chambers (yellow circles). The readings of labelled monitors (G=gamma, N=neutron) are shown in Table 5. Unlabelled monitor readings were comparable with the natural radiation background and are not reported.

During all these experiments, radiation measurements were performed in the machine tunnel close to the front-end, and inside the beamline hutch using the PTW chambers described above. A radiation survey in the experimental hall was carried out by means of environmental Silena gamma/neutron monitors [7] and portable dosimeters.

The layout of the beamline area with the positions of the monitors and ionization chambers is shown in Fig.4. Tables 5a and 5b list the data from PTW chambers and from the gamma/neutron monitors obtained during the experiments both with an efficient injection (no bump) and applying 1 to 4 mm bumps.

bump	PTW measurements (mSv/h)			portable monitors (μSv/h)
	injection efficiency	inside ring	inside FE hutch	outside FE hutch door
Ø mm	77%	9.8	2.07	< 1 γ, n
1 mm	71%	11.3	2.5	< 1 γ, n
2 mm	53%	28.5	8.5	8 γ + 5 n
3 mm	47%	79.2	25.0	30 γ + 23 n
4 mm	8 %	223.4	79.8	50 γ + 36 n

bump	Silena gamma /neutron monitors measurements (μSv/h)				
	G18	G19	N20	G13	N14
Ø mm	0.13	0.10	/	0.10	0.20
1 mm	0.50	0.10	0.12	0.18	0.22
2 mm	1.10	0.10	0.22	0.30	0.50
3 mm	5.30	0.20	0.90	1.30	1.20
4 mm	11.60	0.40	1.70	2.30	2.30

Table 5a and 5b: Data from PTW chambers, portable dosimeters and environmental gamma and neutron monitors (γ=gamma, n=neutron, G=gamma, N=neutron).

Results of the survey outside the hutch (reported in tables 5) demonstrate that radiation detected in the experimental hall in the forward direction is significantly lower than the one measured laterally, next to the door.

This is due to the fact that consistent shielding (25 cm of lead) was placed downstream of the first mirror of the beamline to shield against the products of gas bremsstrahlung during conditioning of the aluminium vacuum chamber. The lateral 5 cm lead wall, present for the same reason, was not always sufficient to shield from losses produced during inefficient injection (2 to 4 mm bumps).

Similar measurements performed as described above, but with the front-end closed, also showed that, under worst conditions, radiation fields were one order of magnitude less than the corresponding data taken with the front-end open.

FEL MEASUREMENTS

A preliminary set of experiments were carried out to study the effect of the storage ring FEL on the instability threshold that limits the maximum current that can be injected in a single bunch.

During their motion, the electrons interact with the ring environment. This interaction manifests itself as an electromagnetic wake field that acts on the electrons and may perturb their stability. The microwave instability [8] is one of the mostly likely observed. It may limit the maximum current that can be stored in a single bunch and leads to an increase of energy spread with consequent anomalous bunch lengthening [9, 10].

In a SR based FEL, like ELETTRA [11, 12], the electron beam is recirculated many times in an optical cavity where it radiates coherently. The multipass interaction of the beam with the radiated power, stored in the optical cavity, induces bunch lengthening and energy spread that cause the FEL to saturate [13].

On this basis, one can argue that longitudinal instabilities and FEL dynamics are competing non-linear mechanisms generating noise, since both effects are based on the increase of the electron beam energy spread and bunch length [14]. In fact, the competition between the two processes can be traced to the mutual feedback between the respectively induced electron beam effects, that can lead to the collapse of one of the other growing effect. If, for example, the laser is able to develop, the instability is completely counteracted even though ready to grow again when, for any reason (for example due to an external perturbation), the laser is switched off.

In this context, one can expect that beam injection when the laser oscillation is established may lead to a higher threshold for the instability that limits the maximum single bunch current. The preliminary set of experiments confirms this trend: the instability threshold turned out to be shifted to 12 mA per bunch while the maximum current stored in the absence of the FEL (identical machine conditions) was 10 mA. This result is in good agreement with the same kind of measurements performed at Duke, where an increase of the single-bunch current of more than 20 % has been found when the machine is operated in a top-up regime and in the presence of the FEL oscillation [15].

More systematic experiments, as well as a dedicated theoretical analysis aimed at modelling the FEL interaction with the instability responsible for the single-bunch current limitation are foreseen in the near future.

SUMMARY

Results obtained from a set of systematic measurements performed during injection with a front-end open have shown that, if the injection efficiency is over 70%, the radiation levels outside the beamline hutch are within the limits provided for unclassified areas. When, however, the beam is forced to be lost along the beamline low-gap vacuum chamber inside the ring, radiation doserates increase significantly.

These experimental results are useful because they help in predicting the radiation fields detectable inside the experimental hall if, during top-up injection, the electrons bunches are not correctly injected inside the ring and are lost along the ring vacuum chambers. Further experiments will be performed to investigate other possible beam loss scenarios (i.e. changing the status of injection kickers or applying different kinds of corrections to the beam orbit to study the beam loss distribution). All the results will be taken into account in designing an appropriate safety system and radiation monitoring network for the new injector.

The top-up regime also revealed itself to be very interesting for FEL operation. A preliminary set of experiments seems to confirm that injecting while the laser oscillation is established leads to a higher threshold for the instability that limits the maximum single bunch current. The possibility of increasing the maximum current compatible with FEL oscillation is an important improvement in the performance of the source in terms of maximum extractable power.

REFERENCES

- [1] P. Berkvens, "Injection with front-end open at the ESRF", 2nd International Workshop on Radiation Safety at Synchrotron Radiation Sources, 2002.
- [2] PK Job, "Experiences in radiation safety during the top-up operation at the Advanced Photon Source", 2nd International Workshop on Radiation Safety at Synchrotron Radiation Sources, 2002.
- [3] A. Ludeke et al., Proceedings of EPAC 2002, 602, Paris, France.
- [4] L. Emery, M. Borland, Proceedings of PAC 1999, 200, New York.
- [5] L. Emery, M. Borland, Proceedings of PAC 1999, 2319, New York.
- [6] L. Emery, M. Borland, Proceedings of PAC 1999, 2939, New York.
- [7] K. Casarin, G. Tromba, A. Vascotto, "The new full energy injector for the Elettra light source", 2nd International Workshop on Radiation Safety at Synchrotron Radiation Sources, 2002.
- [8] G. Dattoli and A. Renieri, Nucl. Instr. and Meth. A, 375 (1996) 1.
- [9] G. Dattoli et al., Nucl. Instr. and Meth. A, 471 (2001) 403.
- [10] G. De Ninno et al., these Proceedings.
- [11] R.P. Walker et al., Nucl. Instr. and Meth. A, 429 (1999) 179.
- [12] G. De Ninno et al., Nucl. Instr. and Meth. A, in press.
- [13] A. Renieri, Il Nuovo Cimento, 35 (1979) 161.
- [14] R. Bartolini et al., Phys. Rev. Lett., 87 (2001) 134801.
- [15] V. Litvinenko, Private communication.

INITIAL STUDIES OF LONGITUDINAL DYNAMICS ON UMER*

J. R. Harris#, A. Valfells, B. Beaudoin, S. Bernal, A. Diep, I. Haber, Y. Huo, B. Quinn, M. Reiser, M. Walter, P.G. O'Shea, Institute for Research in Electronics and Applied Physics, University of Maryland, College Park, MD 20742, USA

Abstract

The University of Maryland Electron Ring (UMER) is a small-scale experiment on space-charge dominated beams. The 100 ns, 10 keV electron beam fills up nearly one-half of the ring circumference. Here we review two models for the evolution of such beams, and present some initial results of measurements of longitudinal beam expansion for two initial line charge profiles.

1 INTRODUCTION

The University of Maryland Electron Ring (UMER) is a compact, low-energy transport system built to study the physics of space-charge dominated beams [1,2]. The beam is produced by a 10-keV electron gun with current adjustable from 550 μ A to 100 mA. This allows UMER to operate in both the transverse emittance dominated and transverse space-charge dominated regimes. UMER is designed with operating parameters that allow it to serve as a model system for beams of very high intensity in a strong focusing lattice such as those for spallation neutron sources or heavy ion inertial confinement fusion (HIF) drivers [3].

Longitudinal space-charge effects are an area of particular interest for both UMER and HIF. In UMER, the beam initially fills half the ring. Longitudinal space-charge forces will cause the beam to expand, ultimately filling the entire ring and making extraction impossible. For HIF, certain designs call for longitudinal compression of the beam to increase the beam density delivered to the target [4]. For both projects, an improved understanding of longitudinal effects is needed, including both free expansion and beam compression.

To this end, we are conducting a detailed study of longitudinal dynamics in UMER. Here we describe two models for the longitudinal behavior of space-charge dominated beams and report the initial results of longitudinal experiments on drifting beams.

2 THEORY

2.1 Longitudinal Envelope Equation

The most general description for the longitudinal behavior of beams is the longitudinal envelope equation (LEE) [5-10]. For a space-charge dominated beam with no focusing, the LEE becomes

$$\ddot{z}'' = \frac{K_L}{5\sqrt{5}\tilde{z}^2}. \quad (1)$$

Here \tilde{z} is the RMS length of the beam, K_L is the longitudinal generalized perveance, and the primes denote differentiation with respect to s , the distance traveled from the cathode. The generalized longitudinal perveance is given by

$$K_L = \frac{3}{2} \frac{gN}{\beta^2 \gamma^5} \frac{q^2}{4\pi\epsilon_0 mc^2} \quad (2)$$

where N is the total number of particles in the bunch, m is the mass of the electron, q is the charge of the electron, and ϵ_0 , c , β , and γ have their customary meanings. The geometry factor g is given approximately by

$$g \approx \alpha + 2 \ln\left(\frac{b}{a}\right) \quad (3)$$

where b is the radius of the beam pipe, a is the radius of the beam, and α is a constant that is variously cited as 0 [11], 0.5 [12], 0.67 [5], or 1 [5].

The LEE is derived for a beam with a parabolic line charge density. However, in longitudinal theory the parabolic line charge density serves the same role that the K-V distribution serves in transverse theory. That is, the parabolic beam can be taken as an equivalent line charge density for a beam with the same number of particles, the same emittance, and the same RMS length [9]. Therefore the LEE may describe the evolution, in an RMS sense, of any beam.

2.2 One-Dimensional Cold Fluid Model

A second theory to describe the longitudinal evolution of beams is the one-dimensional cold fluid model (CFM). The CFM applies only to beams which are totally space-charge dominated. In the CFM, the longitudinal evolution of a beam is given by the one-dimensional continuity equation

$$\frac{\partial \lambda}{\partial t} + \frac{\partial}{\partial z} v \lambda = 0 \quad (4)$$

and the momentum equation [12]

$$\frac{\partial v}{\partial t} + v \frac{\partial v}{\partial z} \approx - \frac{qg}{4\pi\epsilon_0 m \gamma^5} \frac{\partial \lambda}{\partial z}. \quad (5)$$

Here λ is the local line charge density, z is the position in the rest frame of the beam, v is the local particle velocity in the rest frame of the beam, and t is time. Note that the momentum equation is the Euler equation for compressible fluid flow [13], with the pressure term

replaced by $\frac{q}{m\gamma^3} E_{sz}$, where

*This work supported by the U.S. Department of Energy
#harrisjr@wam.umd.edu

$$E_{sz} = \frac{-g}{4\pi\epsilon_0\gamma^2} \frac{\partial\lambda}{\partial z} \quad (6)$$

is the expression for the longitudinal space charge force in the beam in the limit of slowly varying λ , and $m\gamma^3$ is the longitudinal effective mass [5]. In the special case of a beam with an initially rectangular line charge profile, these equations can be solved to describe the longitudinal erosion of the beam [14]. This erosion occurs through the propagation of a shock wave from each end of the beam towards the center at the speed of sound in the beam [4,10],

$$c_0 = \sqrt{\frac{qg\lambda_0}{4\pi\epsilon_0 m\gamma^5}} \quad (7)$$

As the shock wave passes a particle, it is accelerated, eventually reaching its escape velocity $2c_0$. The resulting line charge and velocity distributions for the leading edge of the beam are

$$\lambda(z,t) = \left(\frac{2}{3} \pm \frac{1}{3} \frac{z-z_0}{tc_0} \right)^2 \lambda_0 \quad (8a)$$

and

$$v(z,t) = \frac{2}{3} \left(\frac{z-z_0}{t} \mp c_0 \right) \quad (8b)$$

Here λ_0 is the initial line charge density of the rectangular pulse, z is the location in the beam with $z=0$ at the beam center, z_0 is the initial location of the front or rear edge of the beam, and t is the time measured from $t=0$ when the beam is created. The upper sign is used when considering erosion of the flat top from its rear edge, and the lower sign is used when considering erosion of the flat top from its leading edge. Equations (8a) and (8b) are only valid so long as the forward-traveling shockwave and the rear-traveling shockwave have not met. Once they meet, the flat top has been eliminated and the beam is "all ends." After this time, the shock waves which caused the flat top to erode begin to overlap, and the resulting nonlinear equations cannot be solved exactly. An approximate solution is given in Ref. [4].

3 EXPERIMENTS

3.1 General

UMER is still under construction at this time, so the initial longitudinal measurements were taken using the existing portions of the machine, including the straight injection section (~1.5 m long) and 180° of arc of the ring. The total length of the existing sections used for longitudinal measurements is 7.54 m from the cathode to the last current monitor. The beam pipe radius in UMER is 25.4 mm, while the average beam radius in the ring's quadrupole focusing channel is 5.3 mm for the 24-mA beam and 9.5 mm for the 85-mA beam.

Measurements of the beam line charge profile were made using one Bergoz fast current transformer (FCT) and one fast beam position monitor (BPM) in the injection section, nine additional fast BPMs placed every 64 cm around the existing portions of the ring, and a second Bergoz FCT 48 cm after the last BPM. (During the actual experiment, the BPM at 5.78 m downstream from the cathode was not available.) The BPMs used for these measurements are designed to act as fast current monitors as well as to detect beam centroid position, and have a measured resolution (10%-90% rise time) of 1.7 ns [15]. An improved energy analyzer is currently under development and will be included in UMER in the near future [16].

3.2 Expansion of Rectangular Beam

The standard initial beam profile produced in UMER is a rectangular pulse with length of 100 ns and rise time of approximately 2 ns produced by thermionic emission from a dispenser cathode. As a test of the CFM, the rise time of the beam was measured for 85-mA and 24-mA beams as they traveled through the existing 7.54 m of beam line. The 20%-80% rise time was used to limit the effects of detector circuit ringing on the measurement. The measured rise times were then compared to those predicted using Eq. (8a) (Fig. 1).

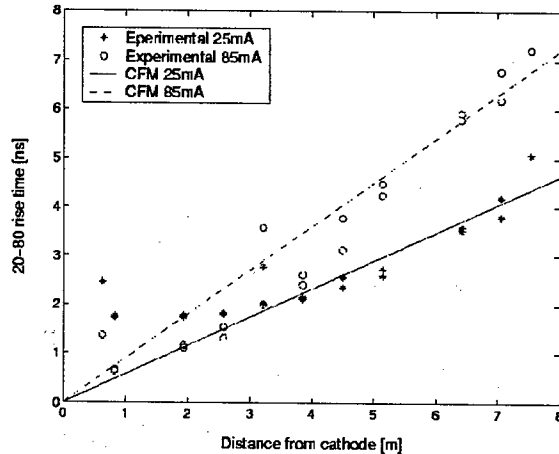


Figure 1: Increase in rise time of rectangular beam with distance from cathode for 85-mA and 24-mA beams.

For both current levels the increase of the rise time with distance from the cathode followed the linear trend predicted by Eq. (8a) after the beam had traveled through approximately half the existing transport line. For the 24-mA beam the observed rise time remained constant at 1.7 ns over the first 3 m of beam line. This may suggest that the expansion predicted by Eq. (8a), which assumes an initial perfect rectangular beam, is obscured by the ~2-ns initial beam rise time associated with the limitations of the gun and pulser. It is also possible that the beam rise time in this region is smaller than the BPMs or FCTs can detect. The 85-mA beam closely follows the expected linear trend after traveling 4.5 m from the cathode.

Before this point, the measured rise time is less than expected. The source of this discrepancy is unknown at this time.

A least-squares fit was made to the rise time data, assuming linear expansion beginning at the origin. Only data taken far from the cathode where the rate of increase was linear was included ($s > 4.5$ m for 85 mA, $s > 3.9$ m for 24 mA). These fits were compared with the expected rate of increase of the 20%-80% rise time based on Eq. (8a) in order to determine the value of the geometry factor g . The resulting values were $g = 2.82$ for the 85-mA beam, and $g = 4.25$ for the 24-mA beam. This gives $\alpha = 0.85 \pm 0.25$ for the 85-mA beam and $\alpha = 1.12 \pm 0.25$ for the 24-mA beam, and an average value of $\langle \alpha \rangle = 0.985 \pm 0.25$.

3.3 Expansion of Photoemission Beam

The UMER gun was designed for use with a dispenser cathode operating as a thermionic emission source. Recent work at Maryland has investigated the use of dispenser cathodes as photoemission sources [17]. As a byproduct of this research, UMER has been modified by the addition of an adjustable mirror inside the first diagnostics chamber, which allows the cathode to be illuminated from outside the beam pipe with laser light. The laser used on UMER is an Nd:YAG laser with some of its light shifted into the green with external nonlinear crystals. The laser pulse is 4.5 ns long, and Gaussian in profile. This allows us to produce short beams of Gaussian line charge profile in addition to longer rectangular pulses.

The longitudinal expansion of a 24 mA peak current beam was measured with the same FCTs and BPMs used to study the expansion of the rectangular beam. The averaged measurements at each location are plotted in Fig. 2.

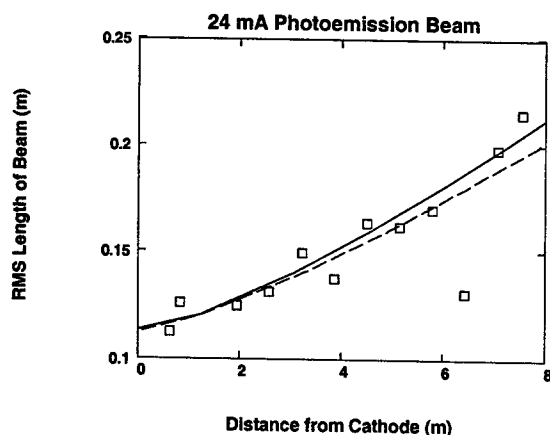


Figure 2: Increase in length of photoemission beam with 24 mA peak current. Curves are calculated from LEE using measured initial slope and length of beam. Solid curve is for $\alpha = 1$ and dashed curve is for $\alpha = 0$.

Also shown in Fig. 2 are theoretical expansion curves calculated from the LEE assuming two values for α . The initial beam length and initial rate of increase used to generate these curves were taken from experiment.

4 CONCLUSIONS

Initial experiments have commenced to study the longitudinal behavior of space-charge dominated beams in UMER. These experiments show expansion of beams with rectangular and Gaussian line charge profiles in the absence of focusing which is in agreement with the CFM and the LEE, respectively. Initial measurements of the constant α suggest its value is approximately one.

REFERENCES

- [1] Online: <http://www.ireap.umd.edu/umer/>
- [2] S. Bernal et al., "Beam Transport Experiments over a Single Turn at the University of Maryland Electron Ring (UMER)," these proceedings.
- [3] P.G. O'Shea et al., *Laser Part. Beams* (2002), 20, 599-602
- [4] D. D.-M. Ho, S.T. Brandon and E.P. Lee, "Longitudinal Beam Compression for Heavy-Ion Inertial Fusion," *Particle Accelerators*, 1991, Vol. 35, pp. 15-42.
- [5] M. Reiser, *Theory and Design of Charged Particle Beams*, Ch. 5.
- [6] L. Smith, et al., *ERDA Summer Study of Heavy Ions for Inertial Fusion: Final Report*, LBL-5543, Appendix 6-4, December 1976.
- [7] David Neuffer, "Extensions of the Longitudinal Envelope Equation," *FERMILAB-TM-1993*, April 1997.
- [8] Frank J. Sacherer, *IEEE Trans. Nucl. Sci.* 18, p. 1105, 1971.
- [9] M. Reiser, Personal Communication, 19 Aug. 2001.
- [13] H.W. Liepmann and A. Roshko, *Elements of Gasdynamics*, Wiley, New York, 1967.
- [12] A. Faltens, E.P. Lee, and S.S. Rosenblum, *J. Appl. Phys.* 61 (12), 15 June 1987, p. 5219
- [14] G. Emanuel, *Analytical Fluid Dynamics*, CRC, Boca Raton, 2001.
- [10] Dunxiong Wang, *Experimental Studies of Longitudinal Dynamics of Space-Charge Dominated Electron Beams*. Doctoral Dissertation, University of Maryland, 1993.
- [11] I. Haber, et al., "Maryland Transport Experiment Comparison to Theory and Simulation." *Space Charge Dominated Beams and Applications of High Brightness Beams*. Ed. S.Y. Lee. AIP: Woodbury, N.Y. 1996
- [15] B. Quinn, et al., "Design and Testing of a Fast Beam Position Monitor," these proceedings.
- [16] Y. Cui, et al. "Experimental Study of Energy Spread in A Space-Charge Dominated Electron Beam," these proceedings.
- [17] D. Feldman, et al., "Development of Dispenser Cathodes for RF Photoinjectors," these proceedings.

NONLINEAR OPTIMIZATION OF A LOW EMITTANCE CLIC DAMPING RING LATTICE

Maxim Korostelev and Frank Zimmermann
CERN, Geneva, Switzerland

Abstract

The CLIC damping ring design is optimized to produce a beam with ultra low emittances. The lattice for such a machine requires a small value of the optical functions, a large number of compact arc cells and, for the chromatic correction, strong sextupoles, that introduce significant nonlinearities, decreasing the dynamic aperture. In this paper, the nonlinear optimization of the damping ring lattice is described.

CLIC LATTICE DESIGN

The Theoretical Minimum Emittance (TME) lattice [3, 4, 5, 6, 8, 9] is most suitable for the low emittance compact arc cell needed for the damping ring of CLIC [1]. The length of a cell is important since the damping time is directly proportional to the ring circumference. Comparing the minimum emittance of the TME lattice with the minimum emittances produced by three other lattice types (Double Focusing Achromat, Triplet Achromat Lattice, Triple Bend Achromat) [10] for a fixed bending angle θ , we obtain the following ratios:

$$\frac{\epsilon_{DFA}^{min}}{\epsilon_{TME}^{min}} = 3, \quad \frac{\epsilon_{TAL}^{min}}{\epsilon_{TME}^{min}} = 12, \quad \frac{\epsilon_{TBA}^{min}}{\epsilon_{TME}^{min}} = \frac{7}{3}.$$

The energy for the CLIC damping ring was chosen as 2.42 GeV. At lower energy (for example 1.98 GeV), the intrabeam scattering (IBS) is much stronger. The IBS growth time is proportional to γ^6 , while the damping time is inversely proportional to γ^3 .

A TME arc cell of the CLIC damping ring comprises four quadrupoles and a combined function bending magnet. The two arcs of the ring are connected by long dispersion-free straight sections that include RF cavities, FODO cells with damping wigglers, and injection/extraction sections. The design parameters of the damping ring are presented in Table 1.

At the exit of the main linac, the horizontal emittance $\gamma\epsilon_x$ should not exceed 680 nm, and the vertical emittance $\gamma\epsilon_y$ be smaller than 10 nm. However, downstream of the damping ring some additional emittance dilutions are expected both in the linac and in the bunch compressors.

The values of the equilibrium transverse beam emittances ϵ_x, ϵ_y , rms energy spread σ_δ , and rms bunch length σ_s were computed for the proposed damping ring design by a step-wise integration in time, using the Bjorken-Mtingwa formalism [11] for the IBS growth rates.

LINEAR AND NONLINEAR PROPERTIES

-I Transformer

Sextupoles introduce both second order geometric aberrations and chromatic aberrations. If two thin-lens sextupoles of equal strength are placed at the entrance and exit

Table 1: List of CLIC damping ring parameters.

Parameter	Symbol	Value
Nominal ring energy	γmc^2	2.424
No. of bunches stored	N_{train}	9
Ring circumference	C	357.2 [m]
Number of cells	N_{cells}	96
Extracted hor. emittance at IBS	$\gamma\epsilon_x$	620 [nm]
Extracted vert. emittance at IBS	$\gamma\epsilon_y$	8.7 [nm]
Extracted long. emittance at IBS	$\gamma mc^2 \epsilon_t$	4319 [eV × m]
Extracted energy spread at IBS	σ_δ	1.36×10^{-3}
H. betatron tune	Q_x	72.85
V. betatron tune	Q_y	34.82
Betatron coupling	$\epsilon_{y0}/\epsilon_{x0}$	2.1%
Field of bending magnet	B_a	9.32 [kG]
Length of bending magnet	L	0.545 [m]
Phase advance per arc cell	μ_x/μ_y	$210^\circ/90^\circ$
Field of wiggler	B_w	17.64 [kG]
Momentum compaction	α_p	0.731×10^{-4}
Energy loss per turn	U_0	2.1916 [MeV]
RF frequency	f_{rf}	1500 [MHz]
RF voltage	V_m	3.0 [MV]
Revolution time	T_r	1.191 [μ s]
Harmonic number	h	1786

of a $-I$ transformer the geometric aberrations introduced by the two sextupoles exactly cancel each other. A perfect cancellation of the geometric aberrations produced by the sextupoles would be to place separate $-I$ transformers of sextupole pairs in such a way that they do not interfere with each other. In reality, the finite length of the sextupoles compromises this cancellation. For example, consider the 1-D motion through a pair of thick sextupoles both of strength S and length L , separated by a $-I$ transformer between the entrance of the first and the second sextupole. In Lie algebra notation [7], the map of the complete two-sextupole system is

$$M = e^{if} \cdot e^{-\frac{1}{2}Lx'^2} \cdot E$$

where f denotes the linear ($-I$) transformation between the entrances of the two sextupoles. The error map E is

$$E = e^{\frac{1}{6}S^2L^3x^4 + O(L^4)}.$$

The dominating term in the error map is of the order $O(L^3)$, and it looks like an octupole term.

Second-Order Achromat

In our case, non-interlaced $-I$ transformers with thin sextupoles are impossible to realize, because there is not enough space available to arrange them. The small beta and dispersion functions require a sufficient number of strong

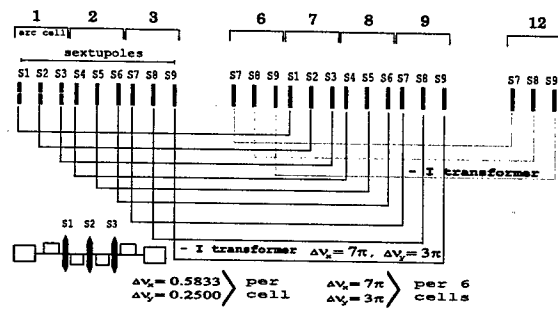


Figure 1: Second-order achromat of the damping ring.

sextupoles in order to correct the large horizontal and vertical chromaticities.

According to Brown's 1st theorem [12, 13], if a lattice consists of n identical cells with $n > 3$ and has a total phase advance $2\pi m$, all second-order geometric aberrations are cancelled. The uncorrected geometric aberrations introduced by the crosstalk of interlaced $-I$ sextupolar transformers are of third and higher order.

In the proposed damping ring design [9], interlaced sextupole pairs are used for the chromatic correction. Nine families of sextupoles were chosen, located in 3 adjacent arc cells, as it is shown in Fig. 1 (three families for the vertical motion and six families for the horizontal motion).

The damping ring comprises two arcs, each of which consists of 48 cells. At the given number of TME arc cells, it is possible to tune the phase advance of the cell from 180° degree to a maximum value of 284° degree, keeping the cell length less than 2.5 m. Taking into account IBS, a larger phase advance per cell reduces the final emittances and also the average values of betatron and dispersion function over the cell. But it increases the strength of the sextupoles, which induces strong nonlinearities and consequently limits the dynamic aperture. Tuning the phase advance by variation of quadrupoles strength, drift length, and gradient field of bending magnet, the natural chromaticities can be minimized. However, to achieve a sufficient beta split at the location of the sextupoles is complicated, due the required short length of the arc cell.

The horizontal and vertical phase advances per cell were chosen as 210° and 90° degree [2], respectively. Such phase advances meet second-order achromat requirements and also provide acceptable emittances. Three adjacent arc cells form a super-period. By imposing the $-I$ transformation conditions over 6 cells (cancellation between first and seventh cell, 2nd and 8th, 3rd and 9th, 6th with 12th, etc.) for both vertical and horizontal motion, the total phase advance over four identical super-period cells is a multiple of 2π . The X and Y phase advances over 12 arc cells with repetitive symmetry are $7 \times 2\pi$ and $3 \times 2\pi$, respectively, that is a first order transfer matrix equal to unity in both transverse planes. Thus, a second-order achromat using the interlaced $-I$ transformers is assembled, which provides a cancellation of all second-order geometric aberrations.

Chromatic Correction

The first and second order chromatic terms are corrected by matching the strengths of 9 sextupole families. Without chromatic correction the natural first order chromaticities ξ_x and ξ_y are -115 and -124 for the horizontal and vertical plane, respectively. The chromaticity contribution of the two very long straight sections is $\Delta\xi_x \approx 23\%$ and $\Delta\xi_x \approx 30\%$.

The D-sextupole is placed between the two identical defocusing quadrupoles where the beta split is maximum. There are only two possible location of F-sextupoles for the proposed arc cell. First position is between the bending magnet and the focusing quadrupole. The second one is between the focusing and defocusing quadrupoles. At the first option, the strength of F and D sextupoles is 32% and 25% respectively less than in second option. However, the first option of sextupole placement gives significant tune shift with amplitude that limits dynamic aperture. Thus,

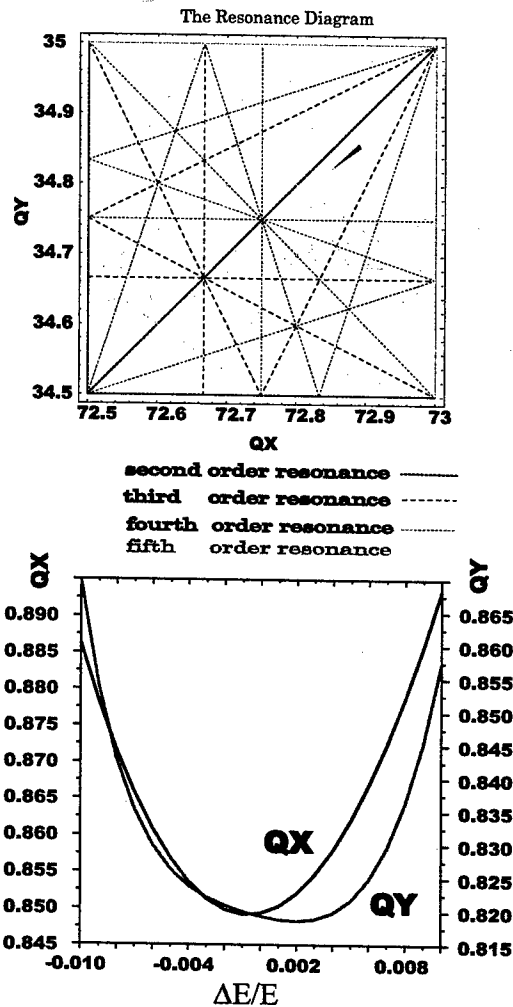


Figure 2: The tune shift versus momentum deviation (bottom) and the same on a resonance diagram (top).

the second option was chosen.

In fact, the strengths of all horizontal sextupole families are nearly equal, with a difference of less than one percent. The same is true for the vertical families. In the case of only two families, the second order chromatic aberrations for the vertical and horizontal motion are not exactly equal to zero, but $\partial^2 Q_x / \partial \delta^2 = 16$ and $\partial^2 Q_y / \partial \delta^2 = 143$ still not significantly contributing to the tune shift with momentum deviation.

The strengths of the chromatic sextupoles are considerable (but their pole-tip fields do not exceed a value of 2 T, which we considered a reasonable upper bound). The tune shift over a large momentum range of $\pm 1\%$ is shown in Fig. 2. A low periodicity of the damping ring results from the two long straight sections. The working point for zero momentum offset was chosen as $Q_x/Q_y \rightarrow 0.85/0.82$. The working point can be shifted by changing the FODO cell phase advance, while the arc phase advance should be kept fixed.

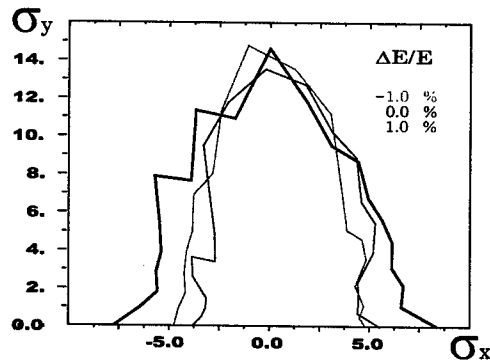


Figure 3: The dynamic aperture of the injected beam, as determined by particle tracking over 1000 turns.

Dynamic Aperture

To enhance the dynamic aperture, harmonic sextupoles can be installed in the non-dispersive sections[14]. In our present lattice, two families of harmonic sextupoles are used. Each consists of eight sextupoles, which are located in the wiggler sections. By means of the harmonic sextupoles, the dynamic aperture is increased about two times, so that its value now corresponds to about six rms beam sizes for an on-momentum particle, as it is shown in Fig. 3. Strengths and positions of the harmonic sextupoles were chosen empirically by particle tracking. The dynamic aperture might be further improved by increasing the number of harmonic-sextupole families and, possibly, by adding some octupole correctors which may cancel third-order terms resulting from crosstalk.

OUTLOOK

The final equilibrium emittances obtained by the present damping-ring lattice have been estimated via numerical integration. The longitudinal emittance is 5% below the specification. The two transverse emittances are smaller than

those required at the end of the CLIC main linacs, but the horizontal emittance exceeds the original target value [1] by 38% (620 nm compared 450 nm), which is due to IBS.

Recently, the dynamic aperture of the ring has been optimized by means of 9 families of chromatic sextupoles, consisting of interleaved $-I$ pairs, and 2 additional harmonic families. It now exceeds 5–6 rms beam sizes at injection. The momentum acceptance of the lattice surpasses $\pm 1\%$.

In the future, we plan to investigate the following three items: (1) the effect of alignment errors and beam-based tuning on the dynamic aperture, (2) the optimum choice of the emittance ratio, representing linear betatron coupling between the horizontal and vertical plane, which is an external input to the emittance computation, and (3) the potential for a transverse emittance reduction by increasing the length of the wiggler.

We would like to thank D.Kaltchev for help and his contributions.

REFERENCES

- [1] R. Assmann et al., G. Guignard (ed.), "A 3-TeV e^+e^- Linear Collider Based on CLIC Technology," CERN-2000-008 (2000).
- [2] D. Kaltchev, "Private Communication".
- [3] L. Teng, S.Y. Lee, "Theoretical Minimum Emittance Lattice for an Electron Storage Ring," (1991).
- [4] J.P. Potier, L. Rivkin, "A Low Emittance Lattice for the CLIC Damping Ring," CERN-PS-97-020 (1997).
- [5] J.P. Potier, T. Risselada, "Fundamental Design Principles of Linear Collider Damping Rings, with Application to CLIC," EPAC 2000, Vienna, CERN-PS-2000-037-LP, CLIC-NOTE-439 (2000).
- [6] P. Emma, T. Raubenheimer, "Systematic Approach to Damping Ring Design," Phys. Rev. ST Accel. Beams 4, 021001 (2001).
- [7] A. Chao, "Lecture Notes on Topics in Accelerator Physics," SLAC, March (2001).
- [8] J.M. Jowett, T. Risselada, F. Zimmermann, H. Owen "Damping Rings for CLIC," PAC2001, Chicago (2001).
- [9] M. Korostelev, F. Zimmermann, "Optimization of CLIC Damping Ring Design Parameters," EPAC 2002 Paris (2002).
- [10] A. Ropert, "High Brilliance lattice and the effects of ID," CERN Accelerator School, 6-13 April (1989).
- [11] J.D. Bjorken, S.K. Mtingwa, "Intrabeam Scattering," Part. Accel. 13, 115-143 (1983).
- [12] K. Brown, "A Second Order Magnetic Optical Achromat," SLAC-PUB-2257 (1979).
- [13] K. Brown, R. Servrancks, "Applications of the Second-Order Achromat Concept to the Design of Particle Accelerators," Proc. PAC95, p. 2288 (1995).
- [14] A. Wolski, "Optimisation Of The Dynamic Aperture Of The DIAMOND Storage Ring Lattice," EPAC 2000 Vienna (2000).

STATUS OF THE MAX-III STORAGE RING

G. LeBlanc, Å. Andersson, M. Demirkan, M. Eriksson, L-J. Lindgren, H. Tarawneh, S. Werin,
MAX-lab, Sweden

B. Anderberg, AMACC, Sweden

Abstract

The MAX-III storage ring[1] is a 700 MeV machine intended to provide UV and IR radiation. The novel magnet design provides a compact lattice. The magnetic measurements of the first cell will be presented and compared with calculations.

INTRODUCTION

A 700 MeV storage ring for synchrotron radiation is being built at MAX-lab. The ring is optimized for the UV spectral region and will also provide IR radiation. The lattice is compact, with combined function magnets. The magnets are integrated into the support structure providing for ease of alignment. The magnet structure is designed with 2D/3D magnetic field programs and the results are compared with measurements on the first prototype magnet structure.

The ring has 8 cells. Space constraints have led to a compact ring with only two families of magnets, a quadrupole and a bending magnet. The lattice parameters are given in table 1.

Table 1: Lattice Parameters

Horizontal tune	3.80
Vertical tune	2.85
Energy	700 MeV
Horizontal emittance	13 nm rad
Ring circumference	36 m
Momentum compaction factor	0.033
Dispersion in straight sections	0.46 m
Periodicity	8
Straight section length	2.45 m

The magnet structure is complex in the way that all magnets share the same yoke. Cross-talk between the different magnet families within the cell is studied with a 3D magnetic field code. The magnetic lengths for different multipoles are calculated and the final pole face profiles are corrected to give the right integrated strengths.

THE MAGNET BLOCK

The magnet is solid iron and the bending magnet poles, coil slots, and surfaces for quadrupole poles are machined out of a block. The quadrupole poles are made separately and bolted to the block, which serves as the return yoke. The bending magnet has an integrated gradient and specially formed ends to give a sextupole component. Pole-face windings are used to control both the quadrupole and sextupole components of the magnetic field. The quadrupoles have an integrated sextupole component, as well as separate coils to adjust it.

Additional coils on the quadrupole poles will be used for orbit correction.

The desired magnetic components are calculated using the hard edge model for the magnetic lengths. Figure 1 shows the lower half of the magnet block. The design magnet parameters are shown in table 2, where the chromaticity is set to 1 in both planes.

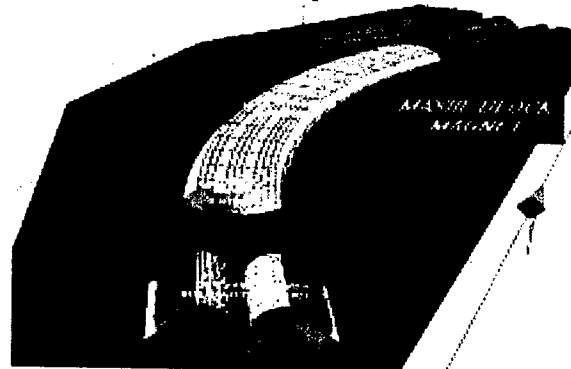


Figure 1: Lower half of a magnet block.

Table 2: Design Magnet Parameters

Bending Magnet		Quadrupole	
L	1.25 m	L	0.2 m
ρ	1.59 m	---	---
B	1.46709 T	---	---
K	3.52277 T/m	K1	13.9862 T/m
S*L	-8.73085 T/m	S	30.72434 T/m ²

CALCULATIONS

Bending Magnet

Initially, the pole profile for the bending magnet is designed using a 2-dimensional program[1]. The program is used to form the edges to give the final field components and reduce higher order multipoles. The resulting field is shown in figure 2.

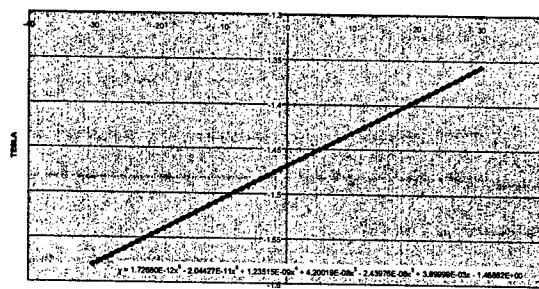


Figure 2: Field in the bending magnet.

The residual field, containing higher order multipole components, is shown in figure 3.

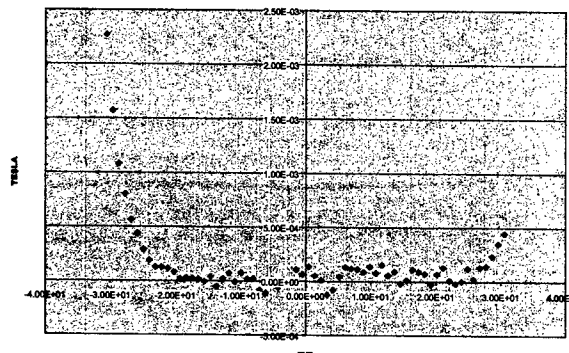


Figure 3: Residual multipoles in the bending magnet.

The bending magnet end is formed to give one of the sextupole components of the structure. The integrated sextupole field is calculated in RADIA[2]. The result is shown in figure 4.

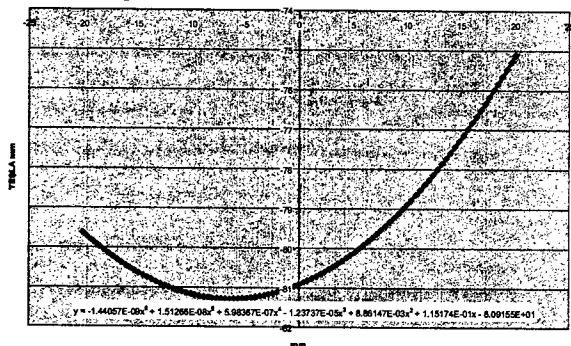


Figure 4: Integrated sextupole field in the bending magnet.

Magnetic Lengths

From the calculations shown, we determine the magnetic lengths. The dipole and gradient fields at the midpoint of the magnet, together with the integrals over the model magnet makes it possible to extract the magnetic lengths for different multipoles. The values for the bending magnet are:

- Dipole length: $L_{\text{dip}} = 1249.6$ mm
- Gradient length: $L_g = 1198.0$ mm

These lengths are compared to the hard edge length 1250 mm. By varying the mechanical length, the dipole length can be adjusted. The deviation in the gradient length is corrected by increasing the gradient value until the integrated strength equals the lattice value as previously described.

Sextupole Component

The pole end is formed to give the desired integrated sextupole strength and the other multipoles are minimised. The result is shown in figure 3. The residual fields correspond to less than 1 gauss at ± 20 mm in the bulk field. The integrated sextupole field is $S \cdot L_s = 8.9$ T/m.

Quadrupole

The calculations for the quadrupole with integrated sextupole component are similar to that of the bend-section. The results for the extracted multipoles of the quadrupole are:

- Mechanical length = 170 mm
- Quadrupole length = 200 mm
- Sextupole length = 190 mm

Corrections due to Cross-talk

The integration of several magnetic elements in a single block gives rise to coupling between the magnetic circuits. In the present design, we have found that the return flux from the bending magnet gives rise to a small dipole and sextupole component in the quadrupole region. In these calculations the magnet model is simplified due to the large memory requirements for the detailed model. The cross-talk effect was calculated in the simplified version of the cell as shown in fig.5.

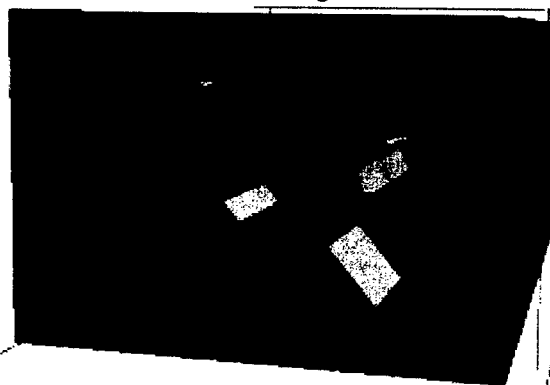
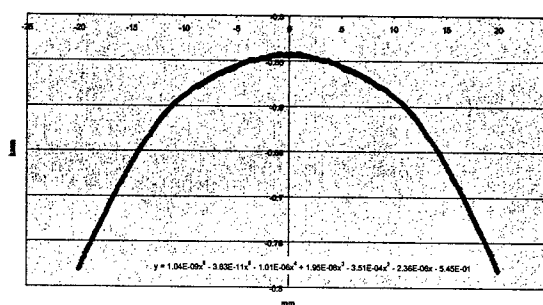


Figure 5: Simplified model used for cross-talk calculations.

The resulting integral field in the quadrupole region due to the return flux from the bending magnet field is shown



in figure 6.

Figure 6: Integrated field in quadrupole region.

The main component that needs to be corrected for is that part that goes through the quadrupole poles. For the prototype cell, the sextupole component is corrected for with the number obtained from these calculations. The normal corrector magnets will correct for the small dipole component of the cross-talk field.

A polynomial fit of the integral gives the sextupole strength, $S^*L = -0.35\text{T/m}$. For an effective sextupole length of 190mm for the quadrupole, the integrated sextupole component should be corrected by $0.35/0.19 = 1.84\text{T/m}^2$. The cross-talk sextupole component is of the opposite sign of the designed sextupole component, so this value is added to the initial value.

Results of Model Simulations

Table 2 compares the design values for the bending magnet field with those achieved in the model after correcting for the magnetic lengths of the different components.

Table 2: Comparison of design and model values for bending magnet.

Bending Magnet: 1.46709 T, 1250 mm designed		
	Design	Model
K^*L_K	$3.52 \cdot 1.25 = 4.4\text{ T}$	$3.67 \cdot 1.198 = 4.397\text{T/m}$
S^*L	8.73 T/m	8.9 T/m

Table 3 compares the design values for the quadrupole field with those of the model after correcting for magnetic lengths, and cross-talk from the bending magnet.

Table 3: Comparison of design and model values for quadrupole.

Quadrupole: 13.99 T/m, 200 mm designed		
	Design	Model
S^*L_S	$30.7 \cdot 0.2 = 6.14\text{ T/m}$	$32.32 \cdot 0.19 = 6.14\text{ T/m}$
Cross-talk: $1.85\text{ T/m}^2 \rightarrow 34.17 \cdot 0.19 = 6.49\text{ T/m}$		

PROTOTYPE MEASUREMENTS

The prototype magnet was measured with a high quality Hall probe system. Measurements were made in the symmetry plane. The measurements start far outside the bending magnet and extend into the bend section where fields are stable.

When analysing the data in the measured field map it was found that the sextupole component decreases further into the magnet. This unexpected behaviour is caused by holes for mounting the pole-face windings to the pole. Since the initial value from the pole curvature is higher than designed, the extra holes for the pole-face windings can be used to trim the sextupole component to the design value. The behaviour of the integrated end sextupole component is shown in figure 7.

The cross-talk field from the bending magnet was measured in the quadrupole region outside the bending magnet. It turns out that the measured field is not as strong as was calculated in the model. An explanation could be that there are several cuts in the yoke that could not be included in the model calculations.

The quadrupole was mapped in the same way as the bending magnet.

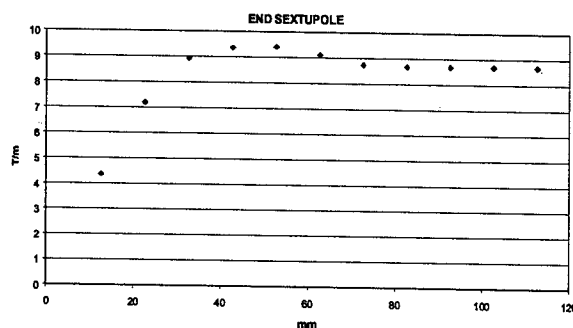


Figure 7: End sextupole in the bending magnet.

RESULTS

Table 4 shows the results of the magnetic measurements of the prototype MAX-III magnet fields. The values obtained from the model are in parentheses.

Table 4. Measured components of the bending magnet and quadrupole fields.

Bending Magnet			
	B	Gradient	Sextupole
Strength	1.467 T (1.467)	3.79 T/m (3.67)	-----
Integrated strength	1.842 Tm (1.836)	4.53 T (4.40)	9.4-8.7 T/m (8.9)
Magnetic Length	1.254 m (1.250)	1.194 m (1.198)	-----
Quadrupole			
	Gradient		Sextupole
Strength	13.98 T/m (13.98)		34.8 T/m ² (33.9)
Integrated strength	2.78 T (2.80)		6.59 T/m (6.44)
Magnetic Length	0.199 m (0.200)		0.185 m (0.190)

CONCLUSIONS

The measured magnetic field values for the prototype MAX III cell agree well with the designed values. The 3D code RADIA turns out to be a good tool for designing complex structures. The cross-talk seems to be overestimated in the code, but in this case the model had to be simplified since the real yoke contains a lot of cuts that could not be modelled. The holes for fitting the pole-face windings in the bending magnet poles provided an excellent way to trim the value of the end-sextupole component. The strength of the pole-face windings of $\pm 10\%$ for all components is much more than is needed to reach the design values for the cell.

REFERENCES

- [1] G. LeBlanc et.al. "MAX-III, a 700 MeV Storage Ring for Synchrotron Radiation", EPAC2000, Vienna.
- [2] D. Meeker; <http://members.aol.com/dcm3c>.
- [3] <http://www.esrf.fr/machine/support/ids/public/>.

MAX 4, A 3 GEV LIGHT SOURCE

Greg LeBlanc, Åke Andersson, Marlene Bergqvist, Mikael Eriksson, Lars-Johan Lindgren, Lars Malmgren, Hamed Tarawneh, Erik Wallén, Sverker Werin, MAX-lab, Lund University, Sweden
Bengt Anderberg, AMACC, Sweden
Jörgen Larsson, Atomic Physics, Lund University, Sweden

Abstract

A proposal for a new synchrotron light source, MAX 4, is presented. The main components are two identical storage rings operated at different electron beam energies and equipped with superconducting insertion devices. Small beam emittances will yield high brilliance radiation over a wide spectral range.

A small horizontal emittance is achieved by using a large number of cells with gradient dipoles flanked by horizontally focusing quadrupoles. A small magnet aperture allows strong gradients in dipoles and strong sextupole components in quadrupoles. This results in an equilibrium emittance on the order of 1 nmrad. A full-energy injector, enabling top-up operation, will be a 3 GeV S-band linac with an energy doubling system. This opens up the possibility to produce short, intense radiation pulses, coherent as well as spontaneous.

INTRODUCTION

The aim of the MAX 4 conceptual design study is to define a high-performance facility succeeding the existing MAX facility during the next decade. Since some of the design work remains to be done, some of the parameter values given in this report might be subject to changes.

The backbone of the MAX 4 facility consists of two similar storage rings operated at different electron energies. One ring will be placed just above the other and rotated half a super-cell to distribute the beamlines from the insertion devices (ID) evenly. This solution, compared to a single, larger ring, gives us the possibility to cover a wider spectral range with high brilliance radiation. It also provides a sufficient number of straight sections for insertion devices and fits in a smaller building. The insertion devices will be the primary light sources.

The bunches in the storage rings will be stretched by a harmonic cavity system. The elongation of the electron bunches limits the resistive wall effect, increases the Touschek lifetime and reduces the heating of the cold bores in the superconducting insertion devices. Time-resolved experiments will be carried out at the linac, which is superior to the storage rings in this respect.

As an injector, a linear accelerator is chosen. The linac is optimised for coherent radiation production and fulfils the specification for topping up injection. The field of coherent radiation generation is now developing quickly and much experience is now gained at the first generation of FELs. New ideas for critical elements are currently being developed. We feel it is a bit premature at this stage to exactly define the coherent radiation sources at MAX 4 that should go in operation one decade from now.

THE STORAGE RINGS

Design Philosophy

The storage rings are designed to take advantage of the features of superconducting undulators, which offer a short period length with a high K-value. The main consequences for the rings are:

- The small undulator period opens up the possibility to use a large number of periods. A small electron beam emittance is needed to take advantage of this, especially when utilising the higher harmonics.
- Small lattice magnet apertures suffice; the ring admittance is defined by the small undulator gaps. A small magnet aperture is in fact a necessity for creating the small beam emittance in a ring of small size since strong multipole magnets can be introduced.
- The small gap undulators and the small beam emittance make it necessary to spend some effort on beam lifetime issues. Even if a topping up injection method is foreseen, the rings must have a decent beam lifetime to restrict the injection repetition rate and the radiation background.

Magnet Lattice

A very simple basic cell consisting of a dipole magnet flanked by horizontally focusing quadrupoles is used. The vertical focusing is taken care of by the dipole gradient, which also reduces the horizontal emittance. The chromaticity correcting sextupole components are introduced in the shape of the quadrupoles and by discrete sextupoles flanking the dipoles. An octupole component is also introduced in the quadrupole magnets to increase the dynamic aperture.

Each ring consists of twelve super-cells. Each super-cell consists of five basic cells plus matching-sections. This lattice results in a very small equilibrium emittance, which is further reduced by the damping effect of the strong insertion devices. The emittance for the X-ray ring is approximately 1 nmrad with five superconducting undulators. The emittance of the soft X-ray ring is a factor of four smaller.

The small aperture size allows for strong multipole magnet. A compact lattice results in smaller betatron functions, which gives a good admittance-aperture relation.

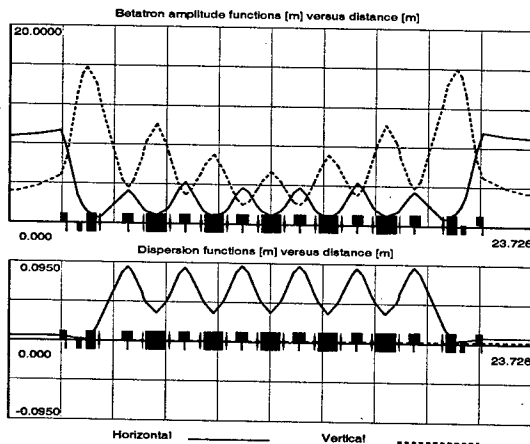


Figure 1. Magnet lattice.

The lattice functions of one of the 12 super-cells in each ring are seen in fig. 1. The main parameter values are given in table 1.

Table 1. Ring parameter values.

	X-ray Ring	Soft X-ray Ring
Circumference	285 m	285 m
Operating energy	3 GeV	1.5 GeV
Current	0.5 A	0.5 A
Energy loss/turn	770 keV	50 keV
Hor. emittance	1.2 nmrad	0.3 nmrad
Q_h	26.6	26.6
Q_v	9.6	9.6
Hor. admittance	17 μ rad	17 μ rad
Vert. admittance.	1.2 μ rad	2.8 μ rad
Energy acceptance	4 %	4 %
Straight section length	4.6 m	4.6 m
RF	100 MHz	100 MHz
Touschek lifetime	30 h	42 h
El. scattering lifetime	131 h	73 h
Bremsstrahlung lifetime	195 h	195 h
Total lifetime	21.7 h	23.4 h

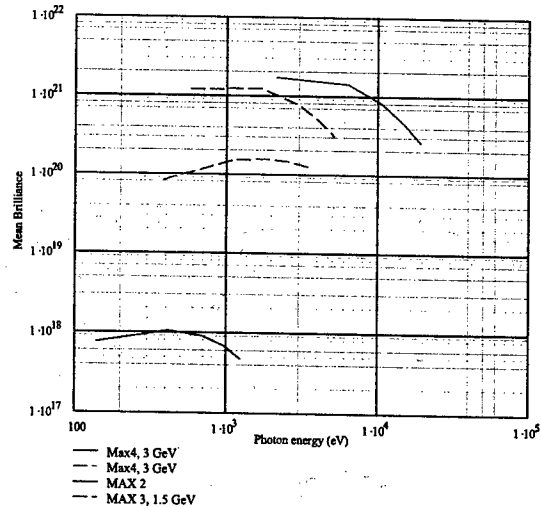
Magnet Design

The magnet system is of the MAX III kind[1]. The magnets are machined out of solid iron blocks resulting in an integrated girder-magnet design.

Radiation Performance

The operation of two storage rings at different electron energies and with very small electron beam emittances

results in a high brilliance over a wide spectral range. The calculated brilliance for the two rings is shown below. The brilliance of the MAX 2 ring, being a high performance ring today, is shown as a comparison.



Brilliance MAX 4 and MAX 2

Figure 2. Brilliance

Insertion Devices

As mentioned above, the insertion devices, and especially the small gap superconducting ones, define the ring design. The following devices were used for the brilliance calculations above.

Table 2. Parameter values of the SC undulator

	X-ray ring	Soft X-ray ring
Period length	13 mm	16 mm
Full gap	4 mm	6 mm
Nr. of periods	250	200
Maximum K	2.2	2.2

Dynamic Aperture and Beam Lifetime

The dynamic aperture calculated is larger than the vacuum chamber aperture, which is sufficient for injection and for the beam lifetimes calculated.

For the beam lifetime calculations, the same gas composition and pressures as measured in MAX II are used. The Touschek life-time is increased by Landau cavities as already used in MAX II[2]. The Touschek life-time is surprisingly high in the soft X-ray ring taking into account the low electron energy and the very small emittance. This result can however be explained by the combination of a high momentum acceptance and the limited transverse momentum.

RF System

A 100 MHz RF system, similar to the systems now being introduced into the MAX II and MAX III rings[3], will be used. This low frequency is chosen to get a large bucket height at relatively low RF power.

Table 3. RF system

	X-ray ring	Soft X-ray ring
Operating frequency	100 MHz	100 MHz
Cavity shunt impedance	3.4	3.4
Nr. of cavities	10	4
Transmitter power	30 kW	30 kW
RF voltage	1.6 MV	0.5 MV
Nr. of transmitters	20	4
Harmonic nr.	5	5
Nr. of harm cavities	2	1
Bunch length without harm. system	1.4 cm	1.9 cm
Bunch length with harm. system	9.7 cm	9.8 cm

THE MAX 4 LINAC

Design Philosophy

The MAX 4 linear accelerator will be used as injector for the two storage rings. Even in the topping up mode, only a very small fraction of the linac capability will be used. The linac can thus be used also as an electron source for a free electron laser (FEL) system.

At the first glance, the two missions of the linac might seem contradictory. The figure of merit of the injector is stability and re-producability while the FEL electron source demands flexibility. We are now investigating the possibility to introduce multiple electron guns and pre-programmed modulators to fulfil the demands for both modes of operation.

Linac System

The building blocks of the MAX 4 linac will be similar to those now used at the MAX injector[4]. In the MAX 4 case, however, one station consisting of a modulator, klystron and SLED cavities feeds two linac structures.

The endpoint energy of 3 GeV can be reached with 15 units, each consisting of one klystron feeding 2 linac sections. By installing 17 units, some redundancy is offered.

Table 4. Injector Linac

Endpoint energy	3 GeV
Total length	300 m
Repetition rate	10 Hz
Frequency	3 GHz
Nr. of klystron stations	17
Klystron power	35 MW
Nr. of linac structures/klystron	2
Structure length	5.2 m
Energy gain/station	200 MeV

Coherent Radiation Generation

Several coherent radiation generators can be considered. A classical SASE FEL is contemplated but

we are also investigating other schemes such as that shown in figure 3.

One interesting version is to use a HG laser as the seed. This laser has the following interesting properties:

- An energy range up to 30-40 eV with a power of a few kW. This power is sufficient to dominate over the spontaneous radiation.
- The ability to deliver very short pulses. The amplified radiation will be a replica of this time structure plus the slippage time.
- The radiation is close to the Fourier limit.
- A terawatt laser drives this HG laser. The repetition rate is thus limited to some kHz.

A 600 MeV electron bunch is sufficient to operate a FEL amplifier at 40 eV. A 6 m long undulator is needed to reach saturation with powers in the GW range. The next step is to guide the bunched beam into an undulator tuned to a harmonic of the seed laser to generate coherent radiation in the 100 eV range. The 600 MeV beam originates from an electron gun positioned three linac stations downstream the linac exit.

The radiation from the harmonic radiator mentioned above is then used as a seed for the next step, acting on an electron bunch of higher energy. This bunch originates from another electron gun placed i. e. 10 klystron stations upstream the linac exit and has an energy of 2 GeV. This FEL is then tuned to the output of the first FEL and the 2 GeV bunch is fed into a harmonic radiator to generate harmonics of the first laser.



Fig.3. Cascaded optical klystron scheme.

ACKNOWLEDGEMENT

The funding from the Knut and Alice Wallenberg foundation has initiated the work on the conceptual design for the MAX 4 facility.

REFERENCES

- [1] G. LeBlanc et.al. "MAX-III, a 700 MeV Storage Ring for Synchrotron Radiation" EPAC 2000, Vienna
- [2] Å. Andersson et. al., 'The MAX II Synchrotron Radiation Storage Ring', Nucl. Instr. and Meth. A 343 (1994) 644-649.
- [3] Å. Andersson et.al, "The 100 MHz RF System for MAX-II and MAX-III", EPAC 2002, Paris
- [4] B. Anderberg et.al., "The 500 MeV Injector for MAX-lab Using a Recirculated LINAC", Epac 2000, Vienna

BATES SOUTH HALL RING COMMISSIONING FOR INTERNAL TARGET EXPERIMENTS *

J. B. van der Laan, D. Cheever, M. Farkhondeh, W.A. Franklin, E. Ihloff, S. Krause, L. Longcoy, C. Tschalaer, E. Tsentalovich, F. Wang, A. Zolfaghari and T. Zwart

MIT-Bates Linear Accelerator Center, Middleton, MA 01949

Abstract

In 2003, the installation and commissioning of the Bates Large Acceptance Spectrometer Toroid (BLAST) came in its final state. The South Hall Ring (SHR) commissioning has been dynamically integrated in this process to provide high quality electron beams under BLAST experimental conditions. The design goal of 80 mA stored high polarization beams is met routinely. Results of beam development for the BLAST commissioning runs in 2002 and 2003 are presented. New developments in beam diagnostic and spin manipulation are also presented.

INTRODUCTION

The commissioning of the BLAST spectrometer and the Internal Target (IT) physics program at Bates started in the spring of 2002 and continued through December. The commissioning resumed in April 2003, is nearing completion and the first measurement of physics asymmetry in e-p elastic scattering with polarized beam and polarized target is beginning. At 850 MeV, stored current of 140 mA peak is routinely achieved. The vacuum in the ring has continuously improved through synchrotron radiation, resulting in lifetimes of 50 minutes.

Longitudinal beam polarization at the IT is maintained with a Siberian snake spin rotator. For the first time, strong depolarization effects caused by non-linear spin resonance were observed and the vertical betatron tune was adjusted accordingly to avoid these resonance lines for maintaining full polarization. The high (~70%) polarization from the polarized source is then preserved during the lifetime of the beam. In collaboration with the University of Michigan, a spin flipper with a high flipping efficiency was installed and commissioned [1]. New developments of beam diagnostics, spin manipulation and polarized electron injector are presented.

SOUTH HALL RING

Figure 1 schematically shows the South Hall Ring with the BLAST IT area marked. On the opposite side of the BLAST area in the ring, a 180-degree Siberian snake fully preserves the longitudinal electron polarization at the IT region. A laser backscattering Compton polarimeter located upstream of the IT area measures beam polarization continuously [2]. An RF-driven spin flipper downstream of the IT area provides the capability for

multiple reversal of the electron spin during each storage cycle. An atomic beam source (ABS) has been incorporated into the BLAST IT area for providing windowless high purity polarized hydrogen and deuterium targets for e-p and e-d nuclear scattering. The ABS system is now fully operational with the presence of the BLAST magnetic field. These results were obtained with a 15 mm diameter and 40 cm long IT storage cell and with the presence of both the BLAST magnetic field and the ABS magnetic holding field. Two sets of slits are used to minimize beam halo and experimental backgrounds as indicated by the particle tracking wire chamber systems in BLAST. This beam optimization was further developed with signals from a set of 4 beam quality monitors (BQM) consisting of phototubes symmetrically positioned around the beam pipe immediately downstream of the IT area. A strong correlation was shown between this signal and the signal to noise ratio in the wirechambers.

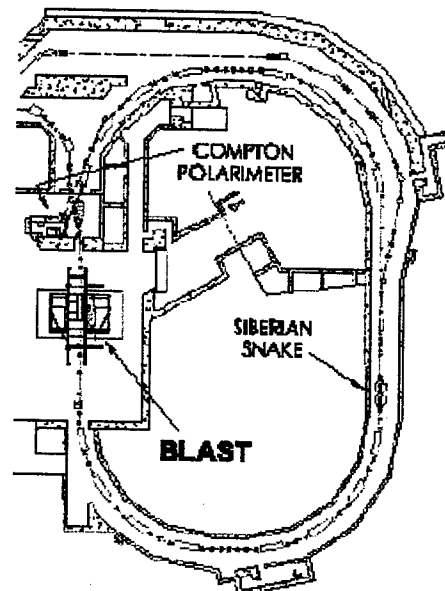


Figure 1: The Bates South Hall Ring with internal target area (BLAST)

BEAM CURRENT AND LIFETIME

The design goal of the BLAST experiments requires an average current of 80 mA and lifetimes longer than 30 minutes. These goals were met in the 2002

commissioning period. The peak stored current was 150 mA, with the snake magnets on and the target cell in.

The installation of the ABS at the IT area and a small aperture spin flipper in the fall of 2002 limited the maximum stored currents to below 100 mA. Ion trapping and possible multi-bunch instabilities intensified inferior vacuum conditions and deterioration of the ring impedance was considered as the primary causes of the lower stored currents for that period.

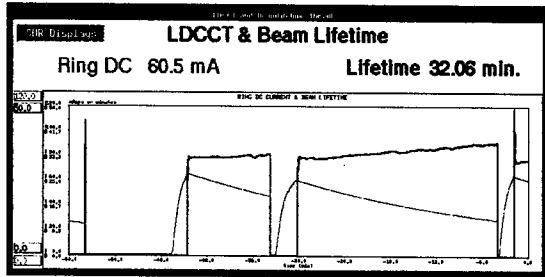


Figure 2: Typical fills for the experiment commissioning.

During the 2002 winter shutdown for ABS tests, the extraction septum magnets were removed to improve vacuum and impedance in that region. This resulted in a significant increase of maximum storage current from 150 mA to more than 200 mA. The maximum current was further increased to 300 mA by overcompensating the negative horizontal chromaticity. These high current results were obtained with the presence of the full magnetic fields of the Siberian snake and BLAST and the ABS holding field. An operational upper limit of 150 mA was put in effect to prevent damaging the synchrotron radiation monitor view ports from unprecedented radiation power for this ring and to provide practical long lifetimes for the present BLAST runs. Vacuum conditions are not yet optimal, but will improve gradually over time with more integrated charge in the ring. Typical ring filling cycle and beam lifetime are shown in figure 2.

BEAM POLARIZATION

The operating betatron tune was originally set to suppress vertical beam oscillations caused by ion trapping [1]. The Compton polarimeter beam polarization studies in 2002 revealed the presence of depolarization effects at high stored currents. Detailed study of polarization and betatron tunes indicated depolarization effects caused by non-linear spin resonances. The depolarization occurs only when beam current reaches a certain threshold that causes a significant enlargement of the beam size. A "safe" betatron tune operation zone is then chosen, to avoid both spin and betatron resonances. The margins in the resonant free area should be adequately large to accommodate both tune shifts and spreads in the operating current range. Under these conditions, full

longitudinal polarization can then be maintained with the Siberian snake at currents well above 50 mA.

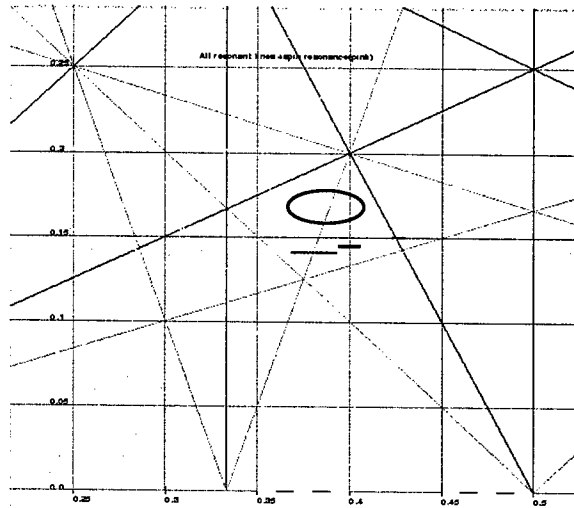


Figure 3: Tune diagram. The Oval area is the operating set point that maintains full polarization at high maximum currents and good lifetimes.

The resonances lines are defined by $3\nu_y + \nu_s = 0.5$, $3\nu_y + 2\nu_s = 0.5$ and $2\nu_x - \nu_y \pm \nu_s = 0.5$ respectively and are seen in Figure 3 below and left of the marked oval area. Our operating tune point is located between the betatron and spin resonance lines, the oval area in Figure 3. The indicated lines just below that area are the points where a drop in polarization was observed. Figure 4 shows the polarization for different vertical tune set points.

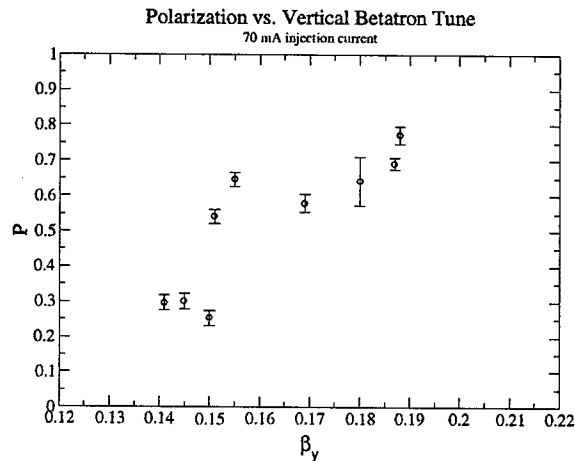


Figure 4: Measured beam polarization as a function of the vertical betatron tune.

Further study of non linear spin resonant and its effects on beam polarization is underway.

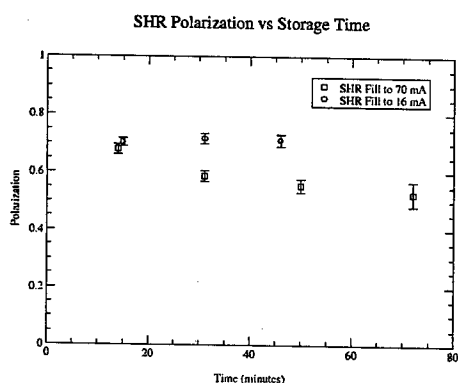


Figure 5: Polarization during a fill. A good tune working point ensures conservation of the polarization for a long enough time for the experiment (> 10 minutes)

BEAM DIAGNOSTIC AND SPIN FLIPPER IMPROVEMENTS

Tune measurement

An electrical betatron oscillation driver is used for measuring the beam tune on a 3 GHz spectrum analyzer. With this setup, at currents higher than about 80 mA, it becomes increasingly difficult to accurately measure the horizontal betatron tune. A frequency scanner in combination with an RF amplifier used on a ion clearer generates much better frequency response from the beam. The beam size is monitored by imaging synchrotron light on a CCD camera with framegrabber. Maximum changes in beam size of up to $100 \mu\text{m}$ were observed during a non-destructive frequency scan through the betatron resonance of the beam that has a 1 mm diameter. Work is in progress to develop a method for reproducible and routine measurements of the betatron tune.

Spin flipping

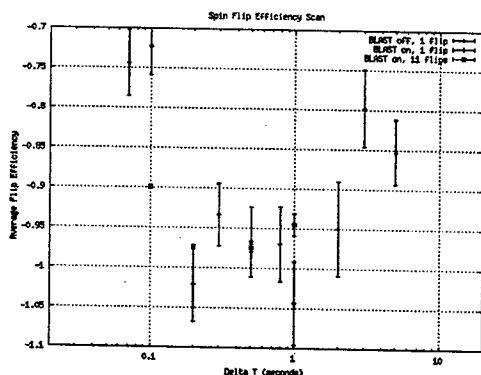


Figure 6: Polarization after a spin flip. Data are taken with and without the magnetic field from the BLAST toroid. The polarization of the data point with the smallest error bar was measured after 11 consecutive spin flips.

Spin flipping was demonstrated in the South Hall Ring in 2001 [1]. A new RF dipole with an impedance matched aperture has been built and tested. The spin direction can be reversed with an efficiency of greater than 99%. (Figure 5)

PRE-PREBUNCHER

The high stored currents in the ring are achieved by stacking multiple 1-2 mA pulses from the linac. However higher injection currents may have the advantages of both a shorter fill time and a higher stored peak current. This will particularly impact at low energies where high repetition rate injections are not be feasible.

The maximum available peak current from the polarized source is constrained by the effective Quantum Efficiency of the photocathode and the maximum laser power. When the maximum peak current from the source falls below the required peak current, the photocathode is heat cleaned and activated during which no beam is available.

The standard design of the S-band Bates linac with chopper - prebunch cavities combination has a capture efficiency of about 1/3 from the source to the linac. Any improvement in this capture efficiency leads to an increase in the duration between activations.

An additional prebunching cavity has been built and installed. PARMELA calculations show an increase of the capture efficiency from 33% to 58%. At present, 50% efficiency has been reached, as shown in Figure 8.

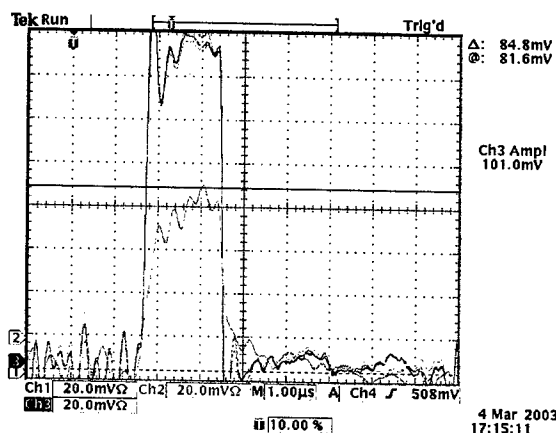


Figure 8: Peak currents at the polarized source, the chopper, and at the end of the linac. As seen there are no losses up to the chopper, and capture efficiency is 50%.

REFERENCES

- [1] V.S. Morozov et al. PRST Ab 4, 104002 (2001)
- [2] G.T. Zwart et al. IEEE Proc. PAC2001, 3597

CONNECTION-ORIENTED RELATIONAL DATABASE OF THE APS CONTROL SYSTEM HARDWARE*

N. D. Arnold and D. A. Dohan

Argonne National Laboratory, Argonne, IL 60439, USA

Abstract

After the flurry of activity to construct, commission, and begin routine operation of a large user facility, the focus must then turn to long-term reliability. Key concerns include a full inventory of all installed devices, sufficient spares, quick identification of a failed device, and accurate documentation to minimize the number of system experts needed for routine maintenance.

This paper describes the Visual Connection Configuration Tool (VCCT) used in creating a searchable schema of all control system hardware. A framework is provided for identifying each installed device and its connection to the control system. The schema provides numerous benefits over a simple inventory list, such as:

- an immediate visualization of information flow through the system,
- intuitive documentation of input/output controller (IOC) hardware, subnet links and nodes, and
- a common presentation for easier cross training and maintenance.

The paper will also describe the mechanisms used to automatically populate much of the database by "discovering" the hardware through the EPICS databases and start-up scripts. Future work, such as extending the device definition to include wiring information will also be discussed.

INTRODUCTION

The Advanced Photon Source has been an operational facility since 1995. Although beam availability exceeding 97% has become the norm, there is continued emphasis on maintaining and reducing the mean time to repair and increasing the mean time between failures. Therefore, accurate and up-to-date documentation of all control devices and their configuration is imperative. Due to frequent upgrades, system enhancements, and the inevitable loss of personnel, maintaining up-to-date documentation for over 240 IOCs is difficult to achieve with conventional approaches that rely on "revision controlled drawings." This paper describes a central, searchable database of the control system devices installed at the APS, which promotes accuracy and provides online accessibility of the currently installed hardware configuration.

* Work supported by U.S. Department of Energy, Office of Basic Energy Sciences, under Contract No. W-31-109-ENG-38.

DISCOVERING INSTALLED DEVICES

In the EPICS control system architecture [1], accelerator applications, or 'databases' are developed by instantiating 'records' from a relatively small palette of record types. Each record type is made up of a set of named 'fields,' whose values are configured during the process of building an application. These fields, available to external applications, are often referred to as process variables, or PVs. The granularity in the EPICS record structure permits one to 'inspect' database code and to graphically display the application logic.

Record types that obtain data from (or write data to) external hardware use a standard hardware address protocol to specify input and output connections. Hardware addresses normally begin with the '#' character, followed by a series of character/value pairs to fully designate the appropriate field bus parameters. Each field bus type has a different pattern in the hardware addressing scheme. In the following EPICS code snippet:

```
record(ai,"L3:DG5:aDelayAI") {  
  field(DESC,"Chan A Delay")  
  field(DTYP,"DG535 Delay Generator (GPB)")  
  field(INP,"#L1 A15 @3")  
}
```

the DTYP field indicates that a DG535 device is connected to the control system, and the hardware address pattern indicates that it is a GPIB device. By parsing this record, one infers the existence of the GPIB daisy chain (link 1) and a GPIB scanner device, which provide the data path from the DG535 to the IOC.

Another source of device information is the EPICS 'dbior' report. From the following partial report:

```
ioclic2> dbior  
Driver: drvDNbug  
DirectNet PLC via BUG at #L0 N12 P0 S1  
DirectNet PLC via BUG at #L1 N21 P0 S1
```

one can infer the existence of two DirectNet PLC devices, connected via two BitBus links (links 0 and 1), to a BitBus VME scanner.

The entire set of EPICS records in the APS control system has been put into a PV relational database, using the Oracle RDBMS [2]. Using this exhaustive source of record/field data, an extensive data-mining process was undertaken to "discover" the APS control equipment referenced by PVs. Other sources of device information can be found in configuration statements within the start-up scripts. Using these tactics and a few heuristic rules about standard devices (e.g., every VME chassis has a

power supply), it was possible to automatically "discover" approximately 75-85% of installed devices.

DEFINING A CONNECTION HIERARCHY

Physical information originating in an external sensor follows a deterministic path from the sensor to a specific IOC. This deterministic path of data flow implies a hierarchy of device connections with each device having a parent device and <potentially> several children devices. This connection orientation forms the heart of the VCCT data model and provides dramatically more information than a simple device inventory list.

Device Types

For the purpose of this paper, a "device type" is defined as a unique type of unit replaceable hardware component (e.g., card, chassis, instrument, CPU, etc.) installed at the APS as part of the control system. A device type may support information flow (e.g., a VME ADC card, a serial link, VME backplane, etc.), provide power to other components (e.g., a replaceable power supply), or simply house other equipment (e.g., an electronic enclosure).

To manage the wide range of devices at APS, each of the device types is formally described in a device type table. Unique device names are assigned to each device type, so that users interacting with the system may use only device names defined in the device type table.

Several attributes defined for each device type are quite common and need not be discussed here (e.g., manufacturer, form factor, description, function). Two particular attributes, however, are critical to the connection-oriented model applied here.

Device Interfaces

The fact that each device is defined by its connection to the control system requires device attributes related to its

connection. Each device type has an attribute 'Interface Required' (IFR) that determines the types of parent devices the device can connect to. A complementary attribute, the 'Interface Provided' (IFP), restricts the types of child devices that may be connected to a device. Each device type may have more than one IFR or IFP. For a valid connection, one of the device's IFRs must match at least one of the IFPs of the potential parent device. As a simple example, it is not possible to plug an Allen-Bradley I/O card into a VME chassis because the IFR needed by the A/B cards does not match any of the IFPs exported by the VME chassis.

A helpful question that assists in working with this connection scheme is to ask for each device "What does it plug into?" (its IFR) or "What can plug into it" (its IFP).

Device Table of Device Instances

Each device installed at the APS is an instance of one of the defined device types. To date, 13,384 devices have been identified and entered in VCCT. Additional attributes required to fully describe an installed device (a device instance) include its location, serial number, logical number (used by software to identify a particular device), and physical slot (a physical slot number or position in a daisy chain). To track the connection-oriented hierarchy, a parent-id attribute is required that is a reference to another device that is this device's parent. Each device supplies data to (or receives commands from) or supplies power to its parent device.

Many of the device attributes are optional and are placeholders until valid data may be entered.

The Physical Data Model for VCCT shown in Figure 1 illustrates the relationship between the device_table, and the device_type_table and its related tables.

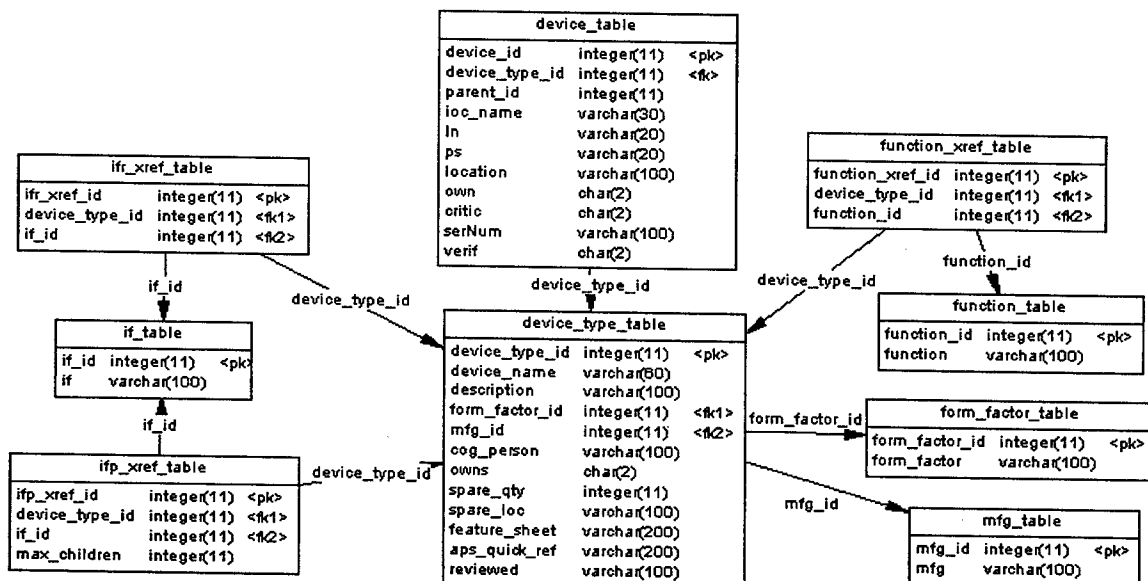


Figure 1: VCCT Physical Data Model.

DEVTREE

The data mining process was successful in 'discovering' the vast majority of the APS control system equipment. To provide the ability to manually complete, update, and display the device hierarchy, a graphical user interface (GUI) tool 'DevTree' was developed. DevTree was developed in Java to allow for platform independence. For the initial implementation, the physical data model shown in Figure 1 was implemented using a flat file for each IOC, to minimize collisions between multiple user editing sessions (see the following section for plans on using MySQL).

DevTree allows the user to interact with the connection hierarchy much like a file system hierarchy. Figure 2 shows an example of the DevTree display GUI.

If a device is selected in the connection hierarchy, then details of its location, logical number, physical slot, etc.

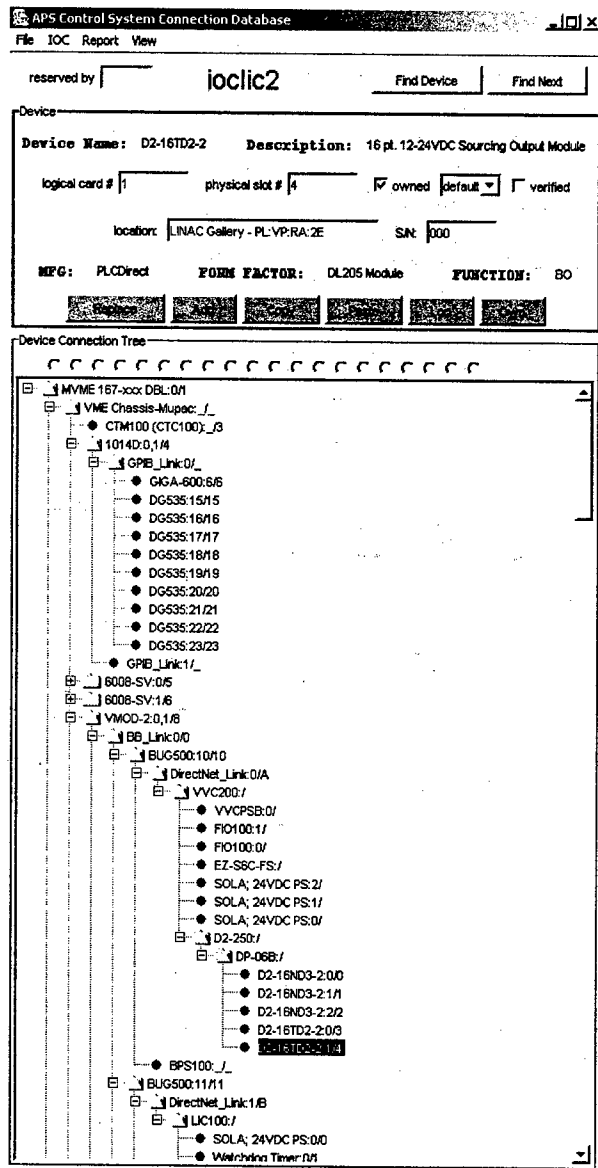


Figure 2: VCCT Graphical User Interface.

are shown in the top panel. The user readily sees all the devices that share any backplane or field bus daisy chain and can immediately observe the data flow from the IOC to the instrument. Branches may be expanded or collapsed to adjust the view as desired.

When the user wants to add a device to the hierarchy, only those device types whose IFR matches the selected device's IFP will be displayed. This minimizes configuration errors by not allowing inconsistent connections (e.g., you cannot plug a VXI board into a VME chassis). A string entry field is provided to filter the list of choices should it be too long.

FUTURE PLANS

- DevTree is now used exclusively to maintain the searchable control equipment inventory. An effort is in progress to convert VCCT to using a relational database. The MySQL database has been set up using the physical data model of Figure 1, and the VCCT flat file data has been imported into the relational database. This information will greatly enhance the accessibility of the data for more advanced reporting and searching.
- Working with the connection hierarchies has revealed that devices actually belong to three hierarchies at once: control flow, power, and housing. Work is in process to better define this tri-hierarchy schema, which will lead to a more thorough device definition.
- Discussion has begun to extend this idea to allow full documentation of interdevice wiring.
- We recognize that the connection-oriented hierarchy has the potential to allow tracing of a fault from a PV to the device where the information flow is broken. Another GUI tool that interacts with this database, the PV database, and live PV data (via Channel Access) to provide this feature has been envisaged.

CONCLUSION

Maintaining accurate information on more than 13,000 installed devices in the APS control system presents a huge challenge. Implementing a connection-oriented approach to defining installed equipment has made significant progress in addressing this problem. The convenience of a GUI tool (DevTree) to maintain this hierarchy promotes wide cooperation and accurate entries. This groundwork promises a huge payback as more tools are developed to take advantage of this data.

REFERENCES

- [1] L.R. Dalesio, M.R. Krammer, A.J. Kozubal, "EPICS Architecture," ICALEPCS 1991 Proceedings, C.O. Pac, S Kurokawa, and T. Katoh, Eds., (ICALEPCS, KEK, Tsukuba, Japan, 1991), pp. 278-282.
- [2] D. A. Dohan, "Decision Support System for the APS Control System," ICALEPCS 2001, San Jose, November 2001, pp. 271-273 (2002).

USE OF A GENERAL-PURPOSE OPTIMIZATION MODULE IN ACCELERATOR CONTROL*

L. Emery[†], M. Borland, H. Shang, Argonne National Laboratory, Argonne, IL 60439, USA

Abstract

The SDDS EPICS toolkit has recently been enhanced by the addition of a general-purpose optimizer. The tool `sddsoptimize` is easily configured and has features that make it robust. The `sddsoptimize` program has been incorporated in many new Tcl/Tk applications used for various Advanced Photon Source tune-up operations, such as injection tune-up for the storage ring, coupling minimization of the storage ring, and the automatic phasing of the linac.

INTRODUCTION

The development of high-level software for operations and machine physics measurements at the Advanced Photon Source (APS) has progressed steadily since the start of operations. The foundation of our software is the robust self-describing data set (SDDS) file protocol [1], and the accompanying SDDS Toolkit of applications. In addition an SDDS-compliant EPICS toolkit [2] acts as the intermediary between the EPICS control system and SDDS-protocol data files.

A generic optimization program `sddsoptimize` has been added to the EPICS toolkit. The ability to do optimization complements the generic feedback tool `sddscontrollaw`, with both applications handling the set of adjustment problems likely to be seen in accelerators. The features of `sddsoptimize` and recently added features of `sddscontrollaw` are covered in reference [2].

A feedback process relies on several readbacks being (at least approximately) linearly dependent on a set of actuators. Using a correction matrix to evaluate new set points for the actuators, feedback usually takes a few steps to converge. In optimization, there is only one readback (or a sum of squares of readbacks), there is no matrix to give an initial direction for actuator changes, and the readback is most likely a nonlinear function of the actuator changes. As a result, one can expect the optimization process to take many more steps to converge, especially with a large number of variables. This is a drawback, but there is no other choice in these cases.

As mentioned earlier, feedback and optimization are applicable to separate sets of problems. However, a feedback problem with one or two variables can be formulated into an optimization problem if the convergence time is not an issue. Optimization obviates a correction matrix and its configuration files are easier to maintain.

In accelerators, optimization is usually done manually or with software written for a particular optimization prob-

lem. This approach may cost tune-up time (e.g., inefficient tweaking) and effort (maintenance of customized software). As far as we know, no one has written an optimization control system application that is configurable for any problem. In this paper we will list the features of `sddsoptimize` and give examples of its use at the APS.

FEATURES

The optimization criterion is the rms value of one or more EPICS process variables (PVs), or else the value obtained by running a script. In the former case, the PVs are listed in an SDDS file with optional values for weights, target values, and tolerances. In the latter case, the measurement script can be used to perform more general operations, which may or may not involve accessing PV values. The variable PVs are listed in an SDDS file as well with a range defined by lower and upper limits data. Setting the values of control variables can be replaced by running a "variable script" (given by the `varScript` option) so that the program can effectively set PVs in an arbitrarily complicated fashion, or even perform optimizations that do not involve PVs. There are no obvious IOC calls if both variable and measurement scripts are provided.

Two optimization methods are provided: Simplex and successive 1D optimization (also called 1D scan). Simplex is a multidimensional minimization method that requires only function evaluations. It is frequently the best method if the computational burden is small. By default, our Simplex method makes explicit use of a one-dimensional minimization algorithm as a part of the computational strategy, since this often will make the optimization proceed faster; this can be disabled in cases where it is found not to help. The successive 1D scan method allows minimizing of the target with respect to each parameter separately and in turn. The main disadvantage is that if the optimal changes of the parameters are mutually dependent, this method may converge very slowly toward the minimum. Nevertheless, it runs efficiently when the variations are quasi-independent.

The program performs minimization by default and will perform maximization if the "-maximize" option is given.

`sddsoptimize` can be used to adjust knob PVs, which are predefined linear combinations of PVs. Examples are knobs for orbit bumps or ganged timing control for a set of kicker magnets.

The control variables for readback and variables are specified by SDDS files. The knobs PVs are configured by SDDS files.

To make the optimization robust, a series of validity tests on PV values are implemented by means of an additional SDDS file containing the names of PVs and their corre-

* Work supported by U.S. Department of Energy, Office of Basic Energy Sciences under Contract No. W-31-109-ENG-38.

[†] emery@aps.anl.gov

sponding limit values. The optimization is suspended if one of the tests fails. This can be used to avoid processing invalid data and to terminate the program if it adjusts settings beyond a safe or reasonable range.

The optimization can be stopped at will by the user using ctrl-c (i.e., the UNIX SIGINT signal). The best settings obtained so far will then be implemented before the program terminates.

sddsoptimize optionally logs settings and results to an SDDS file. This file can be used to view results during or after an optimization and also to set up a new optimization.

APPLICATIONS

We have configured several instances of sddsoptimize for various optimization problems at APS. They are usually wrapped within a customized graphical user interface (GUI) that uses standardized Tcl/Tk widget libraries. The controls available on the GUIs are: an entry for the log file directory, a button to set up the accelerator condition, a button to start optimization, and a button to plot the progress of optimization. For simplicity, most of the optimization parameters in the GUI are hard-coded. However, where flexibility is required, some parameters are available for modification in the GUI. A pop-up window displays the output of sddsoptimize with an abort button.

Averaging of the readbacks is used in all cases, as the simplex search algorithm is sensitive to noise. Several cycles of optimization is recommended to ensure that noise does not cause a false minimum.

Maximizing Injection Efficiency

The efficiency is particularly difficult to optimize at APS since the available aperture of the storage ring (SR) is relatively small, the booster beam is relatively large, and the trajectory in the transfer line jitters to some degree. The optimization problem is that of steering with unknown aperture coordinates and beam absolute positions (at least to the accuracy desired). If we had a beam position monitor (BPM) in the transfer line where the aperture is smallest, then a feedback process would be used to reproduce the trajectory there.

A measurement script calculates an average efficiency from the charge stored in several pulses divided by the total charge injected. The variable PVs are the two SR septums and a pure x-coordinate "Entrance" knob that uses the last two horizontal plane correctors of the transfer line. Though Simplex optimization finds the best direction for the variables after testing many directions, we occasionally help the method by creating knobs that might speed up the search initially. In this case, the first SR septum PV variable was replaced with an "Exit" knob that has the two SR septum PVs combined to give a pure x-coordinate at the end of the downstream septum. The aperture is known to be small there, so an adjustment of the trajectory at that aperture is thought to make the optimum search efficient.

The optimization usually finds a peak rather than a broad optimum. Depending on the SR lattice, one may obtain a peak efficiency as low as 80% (for the low-emittance lattice). Figure 1 shows an example of optimization of the injection efficiency for the low-emittance lattice. Some of the actuator set points produce a bad result. This is necessary in the optimization process, as negative directions for the simplex are found and excluded.

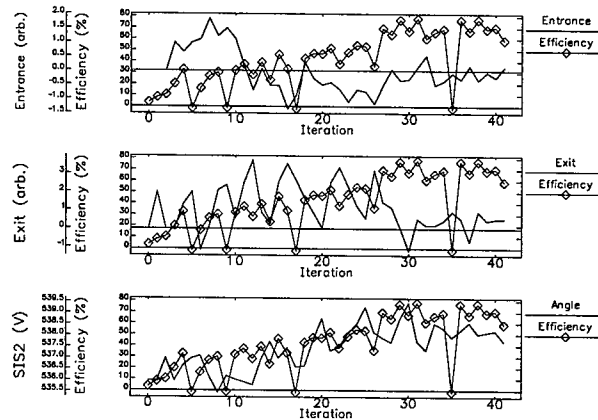


Figure 1: Injection efficiency optimization. Two variables "Entrance" and "Exit" are knobs mentioned in the text. The downstream septum is named S1S2 in the control system and functions as a trajectory-angle adjustment.

The injection optimization is done during the machine studies period that precedes top-up operation. The injection rate is 2 Hz, so the optimization proceeds relatively quickly. The optimization has not been implemented during top-up operation yet, given the low repetition rate of injection (once every two minutes), and the possible long periods of low efficiency when the variables are searching for the best path. If the injection efficiency during top-up operation drops significantly, we presently do a 1D tweaking on one septum to prevent getting too far from reference set points.

SR Beam x - y Coupling Minimization

SR beam x - y coupling minimization uses measurements of the vertical beam size of the X-ray pinhole beam image as readbacks. Knobs for sine and cosine harmonics of ten skew quadrupoles are the variables.

Note that minimizing the coupling could be handled by a complicated feedback process where coupling matrix elements at various points around the ring would be measured with several experiments. However, we already know the knobs selected have the largest influence on the x - y coupling. Because optimization is faster, we selected this method to minimize the coupling. Figure 2 shows a good example of coupling reduction during optimization.

On-Axis Injection Set-Up

To set up on-axis injection for some machine physics experiments, the kickers are adjusted so that the first-turn

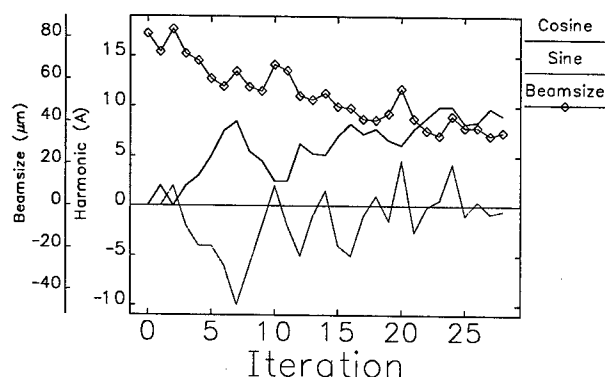


Figure 2: Coupling minimization.

trajectory coincides with the closed orbit. The readbacks are the BPM readbacks in the horizontal plane, sampled on the first turn and averaged for 32 injections. The range of sectors of BPMs is selectable from the GUI. Limiting the range of BPMs was useful when a local perturbation was present and sectors downstream of the perturbation needed to be ignored. The variables are the two injection kickers downstream of the injection area.

A feedback could have accomplished the same thing, since the BPM readbacks are linearly dependent on the kicker strength. However, this would have required a lattice-dependent linear correction matrix for each lattice type, which implies extra maintenance on trajectory configuration files. The implementation for optimization happens to be simpler in this case, and the optimization files work for all lattices. Figure 3 shows an example of trajectory correction starting with the kickers in a nominal accumulation configuration that produced an rms of 8 mm, and finally converging with an rms of 0.5 mm.

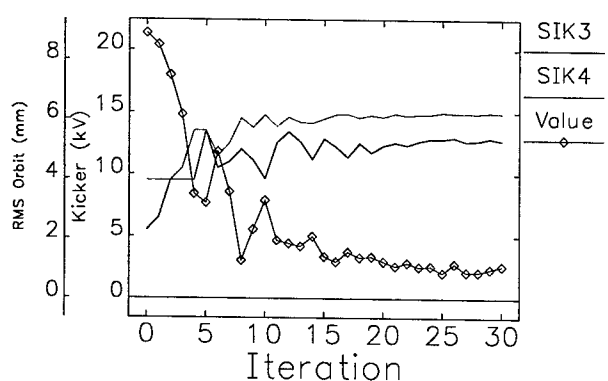


Figure 3: Steering the first-turn trajectory on axis.

Injection Closed-Bump Set-Up

A closed bump is created by a set of four symmetrically-placed kickers in the injection area. A closed bump optimization is required to make best use of the SR aperture at the septum, i.e., bring the stored beam as close as possible to the septum wall without losing particles.

The closed bump condition is obtained by minimizing

the betatron amplitude caused by the kickers' pulses. A script reads the turn-by-turn history of a selected BPM, calculates an amplitude, and averages over many pulses. The first kicker of the group is fixed by the user setting the overall amplitude of the bump. The variables of the optimization are the two downstream kickers. The second kicker is essentially equivalent to the third one, and both are equalized in amplitude after an optimization cycle.

Booster-to-SR rf Phase Adjustment

Booster-to-SR rf phase adjustment is optimized for centering the injected beam in the rf bucket. A script downloads BPM turn-by-turn history and determines the amplitude of the data. The variable is an rf phase PV.

Beam-Based Optimization of rf Phase and Power in the APS Linac

The injector has a four-magnet-chicane bunch compressor after the first set of accelerating structures. A fluorescent screen at the center of the chicane allows viewing of the linac beam energy and energy spread. A Tcl/Tk application was written that periodically inserts the screen and then runs `sddsoptimize` to reduce the energy spread while keeping the energy constant using `sddscontrolaw`. The application was found to be robust and is quick enough to run between top-up events and thus keep the upstream part of the linac properly phased. We also envision using it as part of the start-up procedure to obviate the need for manual rf phasing by operators.

Maximizing Capture Efficiency of the Particle Accumulator Ring

Another injector application is to maximize capture efficiency of the particle accumulator ring (PAR), which is downstream of the linac. The PAR is sensitive to energy drift in the linac. We have found that this is not completely compensated by restoring the trajectory, even though we have BPMs in dispersion regions and allow the feedback to change rf power levels. Hence, a Tcl/Tk application was written that uses `sddsoptimize` to adjust the power and phase in the last linac structure, along with the set points for the trajectory feedback. At present, this is a work in progress, as we find the algorithm does not always result in an improvement, probably due to the amount of noise in the readbacks.

REFERENCES

- [1] M. Borland, "A Self-Describing File Protocol for Simulation Integration and Shared Postprocessors," 1995 PAC, Dallas, Texas, 2184 (1996).
- [2] H. Shang et al., "New Features in the SDDS-Compliant EPICS Toolkit," these proceedings.

AN OPERATOR TRAINING FACILITY AT THE ADVANCED PHOTON SOURCE*

J.W. Lewellen[†], S. Pasky, ANL, Argonne, IL 60439, USA

Abstract

The Advanced Photon Source (APS), a premier third-generation synchrotron radiation source, presently operates in top-up mode during most user run time. During top-up mode, charge is injected into the storage ring at approximately 2-minute intervals to stabilize the stored beam current to within 0.1%. Top-up mode requires the dedicated use of the entire APS injector system, severely limiting time available for operator training.

The APS injector test stand (ITS) is presently configured to operate a ballistic bunch compression (BBC) rf gun, which uses three independently powered and phased rf cavities, and either a thermionic cathode or a photocathode. Operation of the BBC gun requires cavity phasing and input rf power selection analogous to the operation of a high-energy linac. In conjunction with the ITS beamline components (quadrupoles, dipoles, diagnostics, correctors), this provides an effective analog to the APS linac. Operators can therefore practice accelerator tuning and control methods with a live beam and real components, rather than simulations, while top-up operation is ongoing.

INTRODUCTION

For some time, the Advanced Photon Source has been operated primarily in top-up mode during user studies. During top-up, charge is injected into the storage ring once every two minutes, to maintain a stable circulating beam current. This eliminates the varying heat load on user optics associated with stored beam current decay and subsequent refills, providing for more stable operation and constant, maximum flux operation. Top-up has also allowed the APS to operate using lower emittance, higher average brilliance lattices, with associated shorter stored-beam lifetimes, to further improve user operations.

Top-up operation comes with a price, however, both in terms of machine maintenance requirements and in terms of injector availability for other uses. During top-up mode, the entire APS injector complex must essentially run continuously. Therefore, there are greater than usual demands upon operational reliability and performance. There is also very little time to fix injector faults before the stored beam current is impacted significantly.

This paper deals with the other measure of top-up costs: injector availability for non-storage-ring injection, specifically with regard to operator training time.

APS TRAINING REQUIREMENTS

Operators at the APS are required to be knowledgeable about four separate accelerators: the linac, the particle accumulator ring (PAR), the booster synchrotron, and the storage ring. (The PAR is slated for long-term obviation; however, it will remain in use for the next year at least.)

Operator training can be conducted only when the storage ring is not in top-up mode and the APS is not in a shutdown. Eight-hour and 2-day studies periods are alternately scheduled on a weekly basis, however, these are most often dedicated for machine repair and verification, and machine physics studies.

There are typically 2 to 3 weeks of non-top-up storage ring operations scheduled every 3-month run period during which operator training time can reasonably be scheduled. This time, however, is in high demand also for injector maintenance, free-electron laser operation, and studies related to future operational requirements of the APS. Therefore, a means of providing operator training time during top-up operation is increasingly important.

FUNDAMENTAL ELEMENTS

An accelerator operator training facility should be able to recreate all of the fundamental aspects of generating, transporting, diagnosing, and using a particle beam.

For the APS, in many respects the most complex machine to operate correctly is the linac. It is the only non-circulating machine in the APS injector complex, and as a result, many of the controls and operating systems are somewhat different from the remainder of the APS accelerators. The linac is also the most in-demand accelerator for studies during non-top-up periods.

LINAC SURROGATES

A good linac simulator would certainly be a feasible means of providing operator training; however, there are several limitations to this approach. These include response time, construction time, and operator buy-in.

All of the physical features appearing in the APS linac have analogs in various simulation codes such as *elegant* [1] or *PARMELA* [2]. Even with a fast computer, the response time of these codes to changes in the input deck is not, generally speaking, as rapid as the response of a real accelerator to a similar change. There must also be a method for wrapping the simulation code, including inputs and outputs, into an analog of the actual control system, to foster both familiarity and the causal relationship with the actual linac control system.

Wrapping the required features into a graphical interface that mirrors the behavior and response of the actual APS control system, however, would take the dedicated

* This work is supported by the U.S. Department of Energy, Office of Basic Energy Sciences, under Contract No. W-31-109-ENG-38.

[†] Lewellen@aps.anl.gov

attention of a number of programmers and physicists. While certainly feasible, this would consume scarce resources for what is essentially a single-purpose program. Finally, even a very good training program could elicit the "videogame effect." That is, the operators know it is not real; this can lead to a lack of interest, among other effects.

Instead, we propose that the APS injector test stand (ITS) can serve as a reasonable analog to the APS linac for training purposes. The ITS contains most of the elements found within the APS linac and all the essentials for learning the fundamentals of accelerator operation. Perhaps most importantly, the presently installed electron gun consists of three rf cavities, each with its own independent rf port. This allows independent adjustment of the gradient and phase in each cell, directly analogous to separate tanks or sectors in a high-energy linac.

Other components of the ITS line are common linac elements: quadrupoles, steering correctors, gate valves, dipoles, current monitors, Faraday cups, and viewscreens. A CAD-generated layout of the test stand is shown in Figure 1. In fact, the only element present in the APS linac that is missing an analog in the ITS is a beam position monitor (BPM). We plan to install a BPM in the ITS to permit the testing of new BPM electronics, however, so this will be addressed shortly.

The use of the ITS as an operator training facility has two additional advantages. First, operators may be shown the physical layout at any time, to permit an immediate comparison between the reality of the hardware versus its

representation in the control system. Such an understanding can be valuable when attempting to remotely diagnose fault conditions. Second, if an operator is so inclined, he or she can participate in the active injector research program taking place in the test stand.

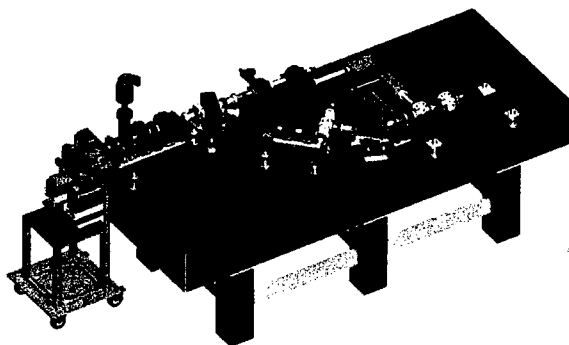


Figure 1: Injector test stand physical beamline layout.

CONTROL SYSTEMS

The ITS control system [3] is based on EPICS, as are all accelerators in the APS complex. This effectively leverages the wide variety of component control screens, hardware drivers, and higher-level software in use throughout the remainder of the APS accelerator complex. It also helps ensure that the "look and feel" and response of the ITS control system is similar to that of the rest of

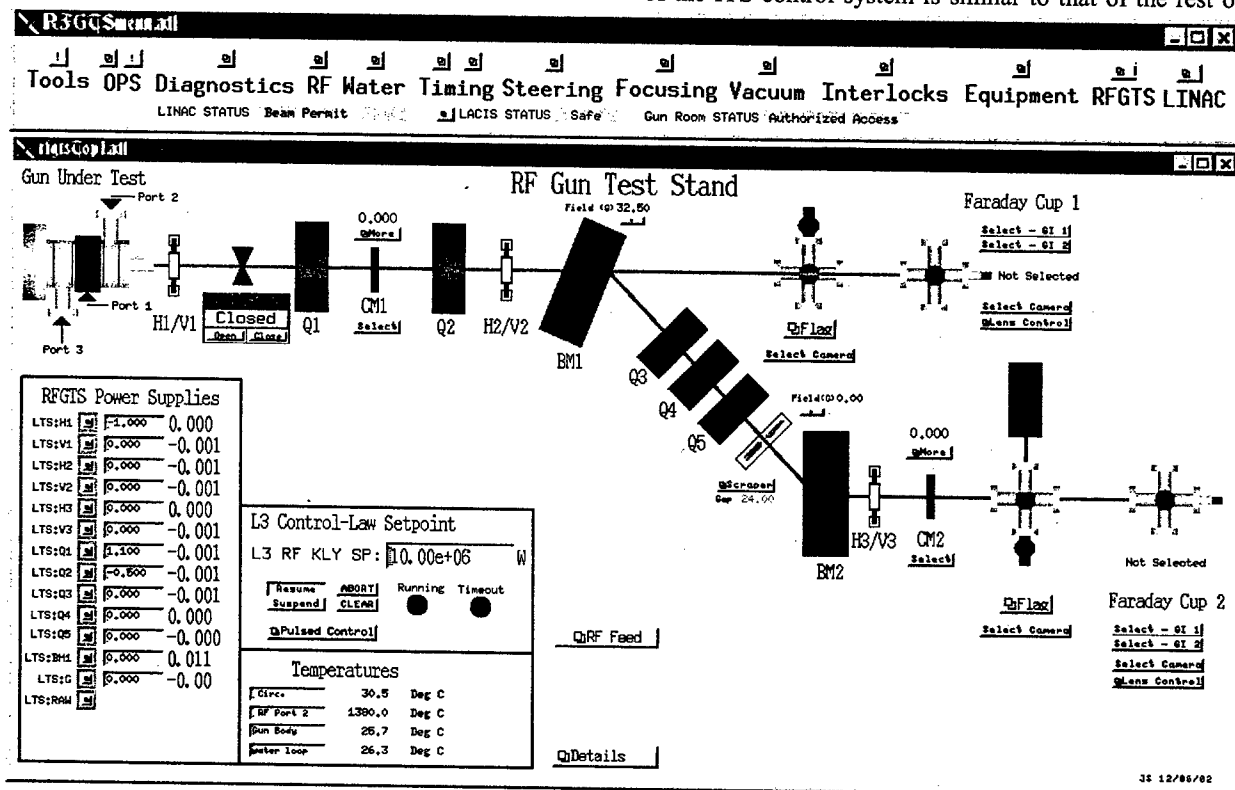


Figure 2: Injector test stand control and facilities screens.

the APS. The ITS control system does not rely on APS operational hardware, however, meaning that faults or error conditions within the ITS will not affect the operation of the APS itself.

The top-level control screens for the ITS are shown in Figure 2. The layout of the beamline screen is chosen to mirror the actual device layout, as is done with the main APS accelerator. The facilities panel also mimics the layout and content of the APS linac.

The rf control system for the ITS [4] is, by necessity, different from that of the linac. Instead of individual klystrons for each linac sector, the ITS uses two variable power dividers, two phase shifters, and three circulators to provide isolated rf power feeds to three separate ports. The ITS rf power distribution control screen is shown in Figure 3.

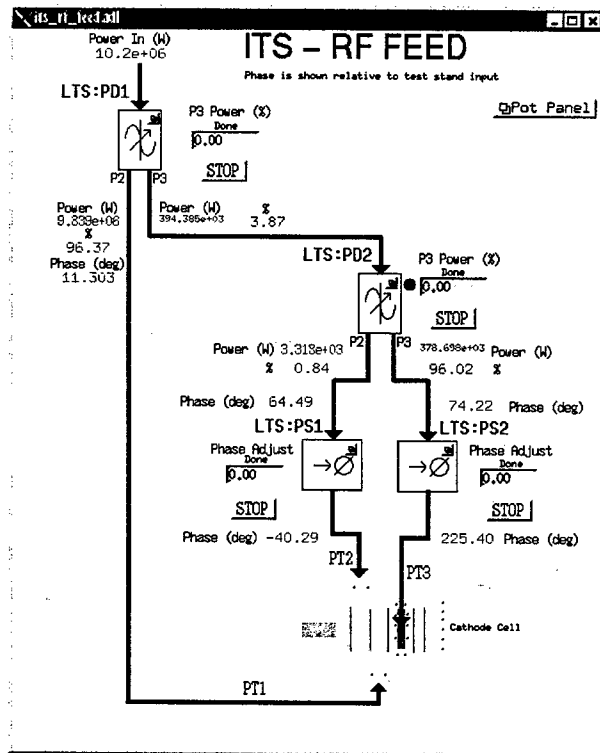


Figure 3: ITS rf power feed control screen.

Whenever possible, the individual component control panels, such as those for flags, power supplies and vacuum systems, use exactly the same template files as those for the APS linac.

CONCLUSIONS

The APS injector test stand is currently operational, and commissioning has begun on the 2.5-cell ballistic compression rf gun. Although it is intended primarily for use as a research laboratory, the test stand will also serve as an operator training facility. Advantages include similarity of the control system to the APS as a whole, similarity of tuneup procedures to the APS linac, easy access for operator orientation and familiarization, and the ability to permit operators to actively participate in an ongoing research program.

ACKNOWLEDGEMENTS

Many people have contributed to the planning, construction, and operation of the Advanced Photon Source injector test stand; the authors in particular wish to thank Ned Arnold, Steven Berg, Debra Briddick, William Berg, Robert Dortwegt, George Goeppner, Aaron Lopez, John Maclean, and Wayne Michalek.

This work is dedicated to the memory of Kevin Beczek.

REFERENCES

- [1] The *elegant* program (source and binaries) and manual can be obtained from the APS Operations Analysis Group website:
<http://www.aps.anl.gov/asd/oag/oaghome.shtml>
- [2] J.H. Billen and L. Young, "PARMELA," Los Alamos document LA-UR-96-1835 (user's guide for version 3.30, revised 27 March 2003).
- [3] J.F. Maclean and N.D. Arnold, "The Advanced Photon Source Injector Test Stand Control System," Proceedings of the 8th International Conference on Accelerators and Large Experimental Physics Control Systems (ICALEPCS 2001), San Jose, CA, pp. 98-100 (2001).
- [4] A. Grelick et al., "The High Power S-Band Feed Subsystem for the Advanced Photon Source (APS) Injector Test Stand," Proceedings of the 2001 Particle Accelerator Conference, pp. 1393-1395 (2001).

ALL DIGITAL IQ SERVO-SYSTEM FOR CERN LINACS

A. Rohlev, J. Serrano, R. Garoby, CERN, Geneva, Switzerland

Abstract

A new VME based system has been developed and built at CERN for the servo loops regulating the field in the linac accelerating structure. It makes use of high speed digital IQ detection, digital processing, and digital IQ modulation. The digital processing and IQ modulation is done in a single PLD. The system incorporates continually variable set points, iterative learning, feed forward as well as extensive diagnostics and other features well suited for digital implementations. Built on a single VME card, it will be first used in the energy ramping RF chain of the CERN Heavy Ion Linac (linac 3) and later for upgrading the present proton linac (linac 2). This system serves also as a prototype for the future Superconducting Proton Linac (SPL). The design principle and the experimental results are described.

INTRODUCTION

The needs for field regulation in the accelerating structures of modern Linacs determine the design and capabilities of the low level control systems. The means to handle large transient beam loading (large beam current and high cavity impedance) favors the use of IQ sampling and processing over amplitude and phase. The need for a high accuracy and low drift control system calls for digital rather than analog electronics. The advantages of easy remote maintenance and diagnostics also favor a digital implementation. Lastly, the need for sophisticated flexible control algorithms, such as feed forward and learning, practically necessitates the digital, programmable, domain. For these reasons the present development of the CERN Low Level Control Card (LLCC) has focused on an all digital, IQ system centered around the flexible functionality of a high density FPGA. The goal of the present development is the demonstration of the potential technology to be implemented in a series of products used to upgrade the servo systems of conventional Linacs.

CONTROL BOARD DESCRIPTION

Figure 1 shows a simplified block diagram of the CERN LLCC board. There are three control loops: the main cavity control loop, an embedded klystron control loop, and an embedded feed forward iterative learning loop. The main control loop uses a standard architecture that takes the sampled cavity RF signal and compares it to a set point. The resulting error signal is processed by a PI filter and then modulated to the RF frequency which drives the klystron. The embedded klystron loop functions to eliminate low frequency (< 2 kHz) phase and gain variation in the klystron which degrade the control margins of the main loop. This control loop compares the

intended klystron drive signal to the actual drive signal as sampled from a directional coupler following the klystron. Since large phase rotations are expected in the klystron, the control must be done in polar coordinates in order to maintain loop stability. Thus the I and Q input signals must first be converted to amplitude and phase. The actuator for the klystron control loop is a 2x2 rotation matrix that scales and rotates the I and Q klystron drive signals. The feed forward iterative learning loop attempts to cancel repetitive errors that lie outside the bandwidth of the main control loops' PI filter [1]. Finally, the reflected signal from the directional coupler is also measured. This signal along with the forward and cavity signals allow for the measurement and subsequent control of the cavity resonance frequency.

The three input channels are identical and use the same digital IQ demodulators. The input RF at 202.56 MHz is first down converted to 20.256 MHz and filtered. The resulting IF signal is sampled with a 14-bit ADC at four times the IF frequency, or every 90° . This results in a stream of consecutive I and Q values in the form: I, Q, -I, -Q, I...[2]. When this data is de-multiplexed and sign reversed it results in a 40.512 MHz stream of I and Q values.

The output channel driving the klystron is a digital IQ modulator followed by a high speed DAC, reconstruction filter, up converting mixer, RF filter and amplifier. The FPGA incorporates the digital IQ modulator in which the I and Q control signals are multiplied by $\cos(\theta nT)$ and $\sin(\theta nT)$ respectively then summed. The value of the angle θ is determined by the speed of the FPGA. A small angle will result in lower sidebands in the output IF signal after reconstruction but comes at the price of higher processing speed. The resulting signal, $I\cos(\theta nT) + Q\sin(\theta nT)$, is the IF drive to the klystron in digital form. In the LLCC the sine and cosine values are tabulated for ten points on the unit circle (every 36°) and the effective multiplication is done at 202.56 MHz. This results in an output frequency of 20.256 MHz. The actual multiplication in the FPGA is done at half that rate (101.28 MHz) but in two parallel data streams. This can be done because the output DAC (AD9755) has two data ports and internally multiplexes that data at the full 202.56 MHz rate. Figure 2 shows this 10-step, 20 MHz output sine wave as formed by the DAC. A 20.256 MHz band pass filter following the DAC is used to reconstruct the output IF signal which is then up converted, filtered and amplified to become the 202.56 MHz RF drive to the klystron.

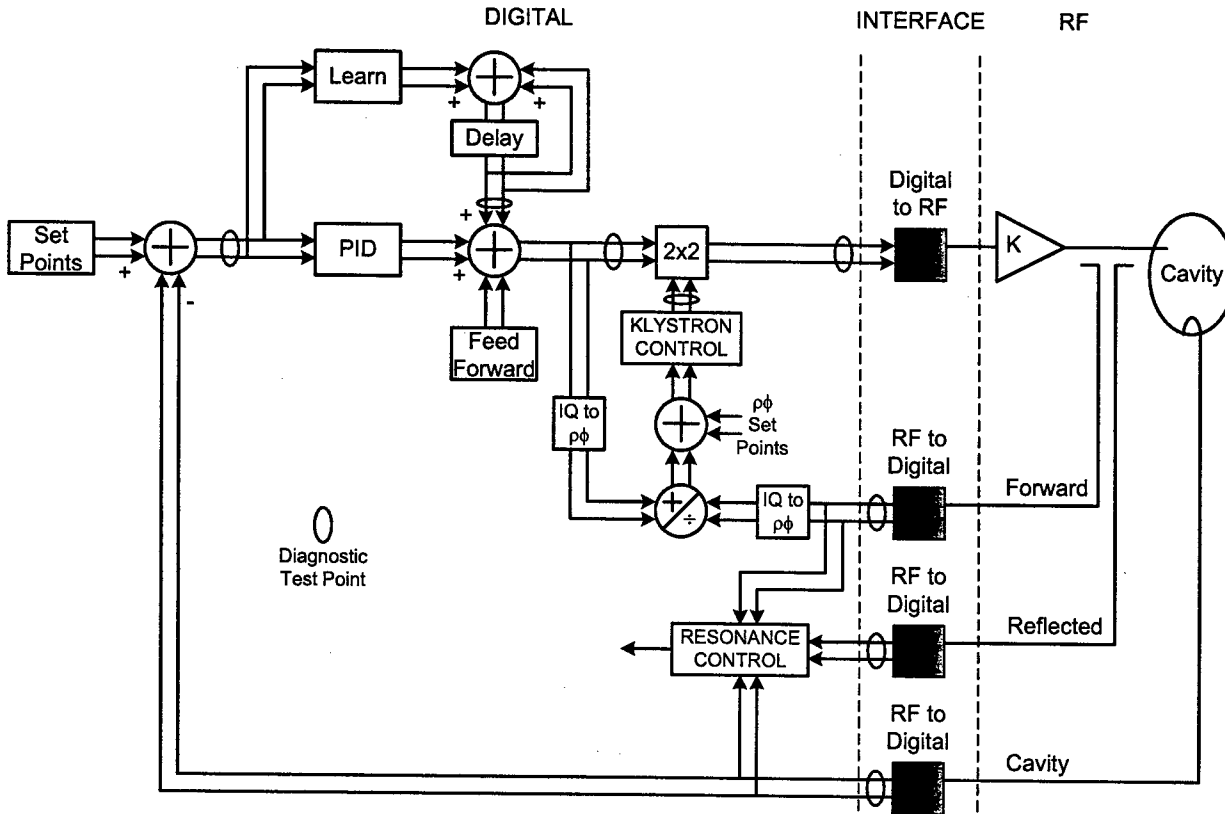


Figure 1: Block diagram of CERN low level control card

All of the control and logic functions for all three loops on the LLCC are done on a single FPGA (Xilinx XC2V2000). All of the input channels, as well as having identical analog front ends, have an identical 'digital' front end. The 14-bit 80 MHz I,Q,-I,-Q,I...data stream coming out of the ADC's is split and alternately sign reversed in the FPGA to form the parallel 40 MHz I and Q data streams. This data is then rotated and scaled with a 2x2 matrix such that $I_{OUT} = I_{IN}\alpha\cos(\phi) - Q_{IN}\alpha\sin(\phi)$ and $Q_{OUT} = I_{IN}\alpha\sin(\phi) + Q_{IN}\alpha\cos(\phi)$. The values of α and ϕ are used to calibrate for fixed gain and phase variations on each channel.

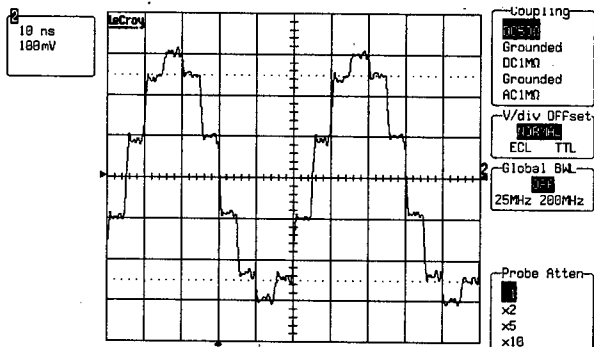


Figure 2: A 10-step, 20 MHz, output sine wave formed by the FPGA IQ modulator driving the output DAC.

After rotation and scaling the data is passed through a digital low pass filter. This filter is a third order

Butterworth with a cut off frequency of 10 MHz. At this point the data from each channel is ready for use.

Data from all three channels is used in the resonance control algorithm. The 'forward' data is also used for the klystron control loop. The 'cavity' data is used for the main control path.

The I and Q set points in the main control loop are fed from an asynchronous on-board RAM. The RAM is 256k x 16-bit (4MB) which is sufficient capacity for 3.3 ms of data at the full 40 MHz rate. The use of a RAM, rather than fixed values, allows for modulation of the set-points during the turn-on phase of each pulse in order to avoid excessive overshoots in the error signal.

A feed-forward signal can be added following the PI filter from an identical on-board 4MB RAM. This signal is used to cancel the effects of fixed errors that occur beyond the bandwidth of the loop. Alternatively this input can also be used to test the klystron and cavity response when the feedback loop is open. Finally there are two other 4MB RAMs used in the iterative learning loop.

The LLCC board has both analog and digital diagnostic capabilities. Each input channel as well as the output channel has a high speed SPDT RF switch as the leading component. The switch is controlled by the FPGA and

allows test inputs to be used on any or all of the input channels. The test port of the output channel can be connected to any of the input channels and the loop can be closed without the klystron or cavity. This function can be used to check the operation and calibration of the input and output channel between pulses. The digital diagnostic capabilities consist of four 4MB RAMs identical to the ones used in the control loops. These RAMs can record I and Q data during the pulse from any 4 of 8 locations in the digital data path. These locations are: the cavity error signal, the klystron loop output signal, the final drive signal, the iterative learning signal, the drive signal before klystron correction, and finally each of the three input signals after they have been scaled and filtered. The FPGA internally multiplexes these signals to the RAMs which record the data during the pulse. After the pulse the data can be sent via the back plane to be plotted or stored. The same data buses feeding the RAMs also go to 4 dual-channel 40 MSPS DACs whose outputs are available on the front panel. Through these DACs the diagnostic signals can be observed with an oscilloscope.

EXPERIMENTAL RESULTS

The LLCC board has not yet undergone extensive tests, however two parameters have been tested: the minimum group delay from input to output, and the channel to channel isolation. The minimum group delay was measured by having the simplest possible function in the FPGA. This function is to sort the input IQ stream from the sampling ADC and then send this IQ data directly to the output modulator. There is no rotation, filtering or processing. For the purpose of this test the signal path from input to output was: input at the RF frequency, down conversion (to 20 MHz), IF filtering, IQ sampling (at 80 MHz), IQ de-multiplexing (in the FPGA), IQ modulating (again in the FPGA), reconstruction filtering, up conversion, and finally filtering and amplification at the RF frequency. The total group delay for this process, as measured with a network analyzer at the RF frequency is 408 ns. Figure 3 shows the same results as measured with an oscilloscope. The upper trace is the pulsed input RF, the lower trace is the output RF envelope. The time scale is 100 ns/div. Each of the three analog band-pass filters contribute about 75 ns of delay. These filters have a full bandwidth of 20 MHz. The delay of the A to D conversion is 4 cycles at 80 MHz, 50 ns. The delay through the FPGA for de-multiplexing and modulating the IQ signal is 112.5 ns. The delay of the output DAC is approximately 15 ns.

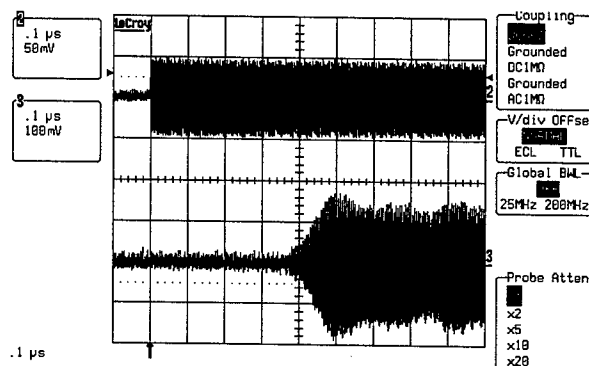


Figure 3: RF envelope of the pulsed input (upper trace) and output (lower trace). 100 ns/div time scale.

The channel to channel isolation was measured by first injecting an RF signal into the 'Cavity' input channel which produced an output signal in the manner described above. The output power was measured to be +13 dBm. The same signal was then injected into the 'Forward' input channel which is physically the closest to the 'Cavity' and should therefore present the largest degree of coupling. The 'Forward' channel was fully powered and sampled, except that its sampled I and Q values were not fed to the output modulator as with the 'Cavity' channel. The output power in this case was measured to be -55 dBm. The difference between the two levels is taken to be the isolation, which is 68 dB.

CONCLUSION

An all new digital low level cavity control system has been designed and built at CERN. The control system is centered around a single high speed FPGA and uses the latest in high speed conversion electronics to both sample the input signals and create the corrected output drive signal. The system, built on a single VME board, has three identical input channels and one output channel. The system has extensive diagnostic capabilities made possible through the use of on-board RAMs and signal multiplexing in the FPGA. Other RAMs allow for set point modulation, feed-forward, and iterative learning in the control algorithm. While extensive tests have not yet been performed on the board, the minimum input to output latency has been measured to be 408 ns, and a channel to channel isolation of 68 dB has been observed.

REFERENCES

- [1] S.I. Kwon, Y.M. Wang, and A.H. Regan, 'SNS Superconducting cavity modelling and linear parameter varying gain scheduling controller (LPV-GSC) and PI controller syntheses', Technical Report LANSCE-5-TN-00-013, LANL, June, 2000.
- [2] Ziomek, C. and Corredoura, P., 'Digital I/Q Demodulator', PAC'95, 1995

PULSED NMR MAGNETOMETERS FOR CESR*

R. E. Meller, D. L. Hartill, LEPP, Cornell University, Ithaca, NY 14853, USA

Abstract

The Cornell Electron Storage Ring (CESR) has recently begun an operating program spanning a wide energy range, from 1.5 to 5.4 GeV. Wide-range magnetometers are necessary for accurate control of the bending fields. These have been implemented using the principle of pulsed nuclear magnetic resonance (NMR). The required field range has been achieved by using a high impedance preamplifier in the field probe to isolate the detection coil, and resonating the coil with high-ratio tuning diodes. A probe installed in a CESR standard bend magnet has been operated continuously from 350 to 2450 gauss using water as the resonance medium, and a second probe in a high field bend magnet has been operated from 860 to 6725 gauss, also using water.

INTRODUCTION

When a nucleus with a magnetic moment is placed in a magnetic field, the nucleus will preferentially align with the magnetic field in the state of lowest energy. If the nuclear magnetic moment is then displaced from alignment, the nucleus will gyrate at the Larmor frequency in the same manner as a torqued gyroscope. The Larmor frequency is determined only by the field strength and the magnetic moment of the nucleus, which is a precisely known constant. The gyrating magnetic moment can be detected with a coupling coil and an RF receiver, and hence, the magnetic field strength can be determined as accurately as RF frequency can be measured. If the magnetic nuclei are contained in an isotropic liquid, such as protons in water, then NMR magnetometry is also independent of probe orientation.

Steady-state NMR

The traditional method of NMR magnetometry [1] involves continuously exciting the nuclei with a steady-state RF signal through a coupling coil with a field axis perpendicular to the main magnetic field. The excitation field will periodically torque the magnetic moments away from alignment, and when the excitation frequency passes through the Larmor frequency, the nuclei will respond resonantly. If the coupling coil has been electrically resonated with an external capacitor, then the nuclear magnetic resonance will cause an absorption dip in the Q of the resonant circuit. This method requires modulation of the excitation frequency or the main magnetic field to reveal the absorption dip. If the magnetic field is not uniform over the excited volume, then the contained nuclei will have a spread

of Larmor frequencies, and the absorption dip will become broad and difficult to resolve.

Pulsed NMR

A more efficient method of NMR magnetometry [2] involves exciting the nuclei to maximum gyration with a short, high-intensity RF pulse, and then detecting the magnetic gyration at the Larmor frequency, the so-called free induction, directly with the coupling coil. In this case, magnetic field nonuniformity will be manifest as the decoherence decay of the free induction. The optimum excitation pulse has a total impulse which rotates the nuclear magnetic moments by 90 degrees from their equilibrium orientation. This method can be further enhanced by the spin-echo technique: Even if the nuclear spins have decohered, an additional excitation pulse of twice the total impulse as the original can be applied. This rotates the nuclear spins by 180 degrees around the axis of the excitation field. This is equivalent to inverting the main magnetic field, which is in turn equivalent to time reversal of the Larmor motion. Hence, the nuclear spins will recombine to form a spin-echo pulse. This pulse is twice as wide as the free induction pulse, and furthermore occurs long after the transmitter transients have died away. These advantages make the pulsed NMR method more reliable and simpler to implement than the steady-state NMR method. The basic time sequence of pulsed NMR is shown in Figure 1.

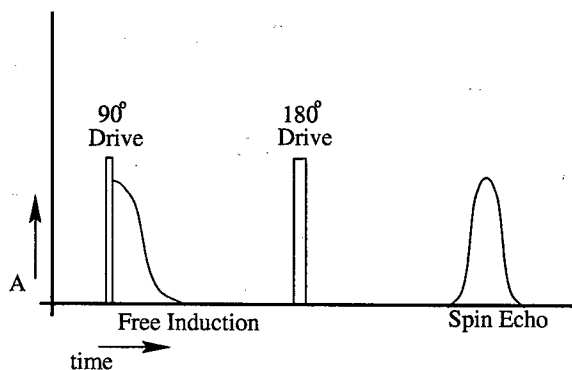


Figure 1: Pulsed NMR signals.

Accurate magnetic field measurement with the pulsed NMR technique requires that the drive pulses be much shorter than the detected pulses. When the width of the drive pulse becomes comparable to the decoherence time, the spectrum of the drive signal begins to overlay the distribution of nuclear frequencies and conceal the natural frequency response. Since the drive pulses are constrained to a given total impulse, their width is inversely proportional

* Work supported by the National Science Foundation

to the transmitter amplitude. Hence, the uniformity of the magnetic field is not an issue as long as sufficient transmitter power is available.

TECHNIQUE

Probe and Preamp

The resonance medium used is protons in water. In pure water, the time for thermal equilibration of the nuclear moments is greater than 2 seconds. This limits the rate at which field measurements can be taken because the measurement completely disrupts the aligned nuclear moments, and a polarized population must be reestablished in order to make another measurement. For this application, 10^{19} /ml cupric ions were added to the water to increase the magnetic coupling of the protons to thermal fluctuations of the liquid. This makes a measurement rate of 10 Hz practical. The doped water is placed in a 1/4" glass tube with the coupling coil wound solenoidally around the tube. Figure 2 represents the schematic of the probe and preamplifier, where L1 is the coupling coil inductance.

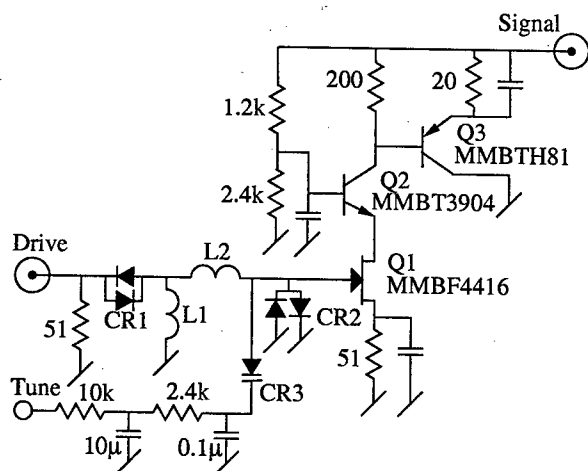


Figure 2: Probe and preamp.

The coupling coil is usually made to be part of a high-Q resonant circuit, since the amplitude signal-to-noise ratio of the detector is proportional to \sqrt{Q} . The largest possible tuning range is achieved if the capacitor is implemented as a high-ratio tuning diode with no additional parasitic capacitance. Hence, the drive switching diodes CR1, CR2, and the cascode-configured JFET Q1 are chosen to minimize parasitic capacitance. The measured tuning ranges are consistent with a total parasitic capacitance of 8 pF. The air-core inductor L2 is included to isolate CR3 and Q1 from the high-amplitude drive pulse. The diode array CR1 switches the drive pulse into the circuit, and CR2 prevents the JFET Q1 and the tuning diode CR3 from becoming forward biased. Therefore, the drive pulse simply drives both L1 and L2 in parallel. When the drive pulse ends, both CR1 and CR2 turn off and thereafter contribute only a small par-

asitic capacitance, and the resonant circuit of L1, L2, and CR3 returns to full Q of approximately 100. Since the detected signal is very small, the tuning diode CR3 bias can be reduced all the way to zero to get the maximum capacitance range. The circuit parameters for the normal field and high field probes are shown in Table 1.

Table 1: Probe parameters

probe	normal field	high field
L1	5.6 μ H	1.7 μ H
L2	2.2 μ H	0.7 μ H
CR3	3 \times MV7404	MV7404
C_{min}	35 pF	18 pF
f_{max}	9.6 MHz	24.2 MHz
C_{max}	840 pF	280 pF
f_{min}	1.96 MHz	6.10 MHz

The gain of the preamplifier depends on the transconductance g_m of Q1 and the current gain β of Q3, but at low frequencies it is typically > 10 . The signal level increases with frequency, since the greater magnetic field increases the polarization of the water sample. Since the preamplifier is located in the magnetic field with the coupling coil, it must be made with substantially nonmagnetic components to avoid corrupting the uniformity of the magnetic field being measured. This poses a significant problem, since steel leads are prevalent in electronic components, particularly on capacitors and diodes. The preamplifier was made entirely with surface mount components. The transistors and diodes in SOT packages are essentially nonmagnetic. The resistors and capacitors have nickel end caps, but the small size minimizes the quantity of magnetic material and allows them to be positioned well away from the resonance capsule.

Receiver

The spin-echo signal is detected by mixing it with a reference frequency derived from an accurate frequency synthesizer. Two channels with a 90 degree phase difference between the references are used to produce sine-like and cosine-like IF (Intermediate Frequency) signals. This allows a signed beat frequency to be reconstructed from a single measurement, and eliminates the need to sweep the reference frequency to determine which side of resonance it is on. The receiver consists of resistor-capacitor filters and common analog integrated circuits. The gain 100 unit is a 733 differential amplifier, and the gain 20 units are implemented with op-amps. Since the reference signals are derived from a programmable logic circuit, it is simple to gate them off while the transmitter is active to reduce the overload recovery time of the op-amps. The receiver block diagram is shown in Figure 3. The +8VDC bias voltage for the probe preamplifier is coupled to the signal input through a ferrite choke.

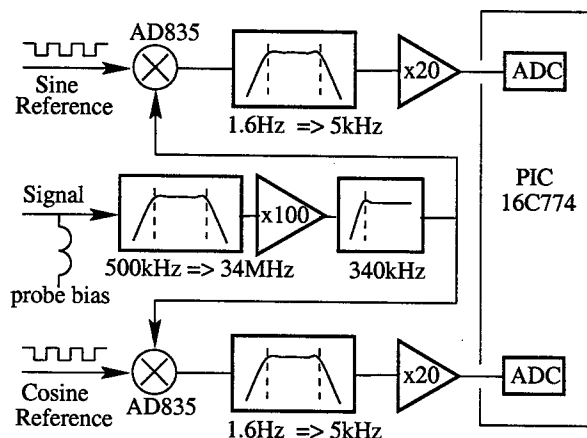


Figure 3: Receiver block diagram.

Transmitter

The transmitter is shown in Figure 4. The 10 volt avalanche diodes are necessary to clamp ringing when the power switching transistors turn off. The output is 20V p-p with a large signal impedance of $2\ \Omega$. Hence, the transmitter is capable of significantly higher output power with a suitable transformer ratio. It is very important to prevent the reference carrier frequency from leaking into the drive when the transmitter is off, as it will capacitively couple through the switching diodes in the probe and overload the receiver. To this end, the transmitter should have a power supply that is completely isolated from other RF circuits.

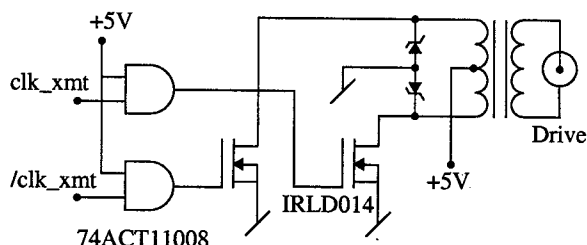


Figure 4: Transmitter.

Frequency Synthesizer

The absolute accuracy of an NMR magnetometer is determined by the accuracy of the frequency synthesizer reference clock. A 20 MHz temperature-compensated crystal oscillator which is specified to 8×10^{-6} absolute accuracy over ten years has been used. This accuracy level is relatively inexpensive, and corresponds to approximately one centigauss in the CESR standard bend magnet. This oscillator is used to clock a direct-digital synthesizer which produces sinusoids up to 1.8 MHz. The sinusoidal reference is then converted to a logic level and multiplied by 64 using a phase-locked loop frequency multiplier circuit similar to the one used for CESR timing [3]. The resulting frequency is divided down in a programmable logic device

to produce the sine and cosine reference signals and the transmitter clock in the appropriate range, up to 28.8 MHz with 40 Hz resolution. This maximum frequency allows field measurements up to 6760 gauss.

Data Processing

All data processing is done with a PIC16C774 8-bit microcontroller. This unit includes a 12-bit analog to digital converter (ADC), and with the maximum clock rate of 20 MHz it can digitize both IF signals at 15 kHz. Each IF signal is sampled 16 times over 1 ms at the peak of the spin-echo. For each sample, the tangent of the phase angle is obtained as the quotient of the two IF amplitudes, and the phase angle itself is obtained from a lookup table. Then a linear least-squares fit is done to the 16 phase measurements, with the beat frequency appearing as the slope of the fit. Frequency tracking is accomplished by shifting the digital synthesizer command by the beat frequency to obtain a zero-beat condition. The digital frequency command is then reported as the magnetic field measurement.

The sampling rate of 15 kHz limits the tracking range to ± 1.5 gauss. Initial capture and recapture are accomplished by sweeping the synthesizer over a range of ± 30 gauss from the last known signal, with 0.5 gauss steps between measurements. This results in reliable resonance capture within 13 seconds.

RESULTS

The instruments described were developed over several months using common and inexpensive components. They require programming with tuning, pulse width, and search frequency data for the magnetic field to be measured. However, having made tables of suitable programming values, the instruments have been completely reliable and attention-free over the entire working field range of the CESR bending magnets.

When the probe is tuned to resonance, the IF signals are 30 dB above thermal and semiconductor noise. The good signal to noise ratio of the spin-echo method has allowed the extension of the measurement range well beyond the probe tuning range, which has facilitated continuous magnetic history measurements of the magnet iron. The 10 Hz measurement rate has revealed both random and periodic noise in the magnet power supplies that was not visible to the steady-state NMR magnetometers which were previously employed.

REFERENCES

- [1] N.Bloembergen, E.M.Purcell, and R.V.Pound, *Phys. Rev.* vol. 73, 679 (1948)
- [2] E.L.Hahn, *Phys. Rev.* vol. 80, 580 (1950)
- [3] R.E.Meller, *Proceedings of the 1997 Particle Accelerator Conference, Vancouver, Canada* (IEEE, Piscataway, NJ, 1999) p.2505

REQUIREMENTS FOR RF CONTROL OF TTF II FEL USER FACILITY

Valeri Ayvazyan, Kay Rehlich, Stefan N. Simrock, DESY

Abstract

During the past years, the experience gained with the operation of RF system at the TESLA Test Facility (TTF)[1] resulted in several modifications and improvements of its design. In addition, as the TTF is converted to become a user facility TTF II for the SASE-FEL during 2004. The electron beam energy will be increased from 250 MeV/c up to 1 GeV/c by installation of 6 TESLA cryo-modules. The RF system include 4 klystrons, each of them will supply RF power to group of cavities (rf gun, module 1, module 2&3, module 4,5&6). This paper presents the performance of the digital RF control at TTF I, commissioning/extension and features of the RF control for the upgrade of the TTF II.

1 INTRODUCTION

At TTF I significant progress has been made on the issues of pulsed operation of superconducting cavities at high gradients with respect to Lorentz force detuning and the associated resonant excitation of mechanical resonances, microphonics, the transients induced by the pulsed beam, and the control of the vector-sum of multiple cavities driven by single klystron.

Considerable experience of RF control at high gradients close to 20MV/m with pulsed RF and pulsed beam has been gained at the TTF. The RF control system employs a completely digital feedback system[2] to provide flexibility in the control algorithms, precise calibration of the vector-sum, and extensive diagnostics and exception handling capabilities. Presently under study is a piezotranslator based active compensation scheme for the time varying Lorentz force detuning which if successful will reduce RF power requirements at gradients >25MV/m considerably and provide improved field stability[3].

The requirements for amplitude and phase stability of the vector-sum a group of cavities are driven by the maximum tolerable energy spread for the TESLA Test Facility. The goal is an rms energy spread of $\sigma_E/E = 10^{-3}$. The requirements for gradient and phase stability are therefore of the order of 10^{-3} and 0.3° respectively.

The amplitude and phase errors to be controlled are of the order of 5% for the amplitude and 20° for the phase as a result of Lorentz force detuning and microphonics. These errors must be suppressed by a factor of at least 40 which implies that the loop gain must be adequate to meet this goal. Fortunately, the dominant source of errors is repetitive (Lorentz force and beam loading) and can be reduced by use of feedforward significantly.

2 RF CONTROL PERFORMANCE FOR THE TTF I

Fast amplitude and phase control is accomplished by modulation of the RF signal to the klystron which will drive group of cavities. Digital I/Q detectors are used for the cavity field, and incident and reflected waves. The RF signals are converted to an intermediate frequency of 250kHz and sampled at a rate of 1MHz (i.e. two consecutive measurements describe I and Q of the cavity field). The cavity field vector defined by I and Q is multiplied by 2x2 rotation matrices to correct for phase offsets and to calibrate the gradients of the individual cavity probe signals. The vector-sum is calculated and corrected for systematic measurements errors. Finally the setpoint is subtracted and the compensator filter is applied to calculate the new actuator setting (I and Q control inputs to the vector-modulator). Feedforward is added from a table in order to minimize the control effort. The feedforward tables are adaptively updated to reflect slow changing parameters such as average cavity detuning, changes in klystron gain, phase shift in the feedforward path, and general changes in operating parameters. The RF control system has been completely integrated into the TTF control system DOOCS[4]. The operation is automated by the implementation of a DOOCS finite state machine server[5], which has access to high level applications. The start up, restart and routine operation of cryo-modules are automated. The state machine process includes loop phase measurement and correction, feedforward and feedback parameter adjustment, beam loading compensation, calibrations, and automatic fault recovery.

The cavities at TTF I have been routinely operated at a gradient of 15MV/m providing a beam energy of 250 MeV/c. The requirements of for amplitude and phase stability have been achieved with feedback only, the stability being verified by beam measurements. The residual fluctuations are dominated by a repetitive component which is further reduced by the adaptive feed forward by about one order of magnitude, thereby exceeding the design goals significantly.

Despite the fact that second bunch compressor is installed between the two cryo-modules all 16 cavities driven by a single klystron. In TTF mode the bunch compressor was by-passed by a straight section and the vector-sum of 16 cavities was controlled. During FEL operation only the vector-sum of the first 8 cavities was regulated in order to maintain stable injection conditions into the bunch compressor. The cryo-modules also were operated in different gradients by changing power balance between the mod-

ules. During the last run each cryo-module was driven by separate klystrons and each cryo-module was controlled by its own feedback loop. Cryo-module 1 at location ACC2 (Module 1*) has been tested at high gradient (close to 25MV/m) with closed feedback loop.

During the initial start-up time the individual cavity gradients and phases relative to the beam are calibrated using beam induced transients. The phases of the incident waves are adjusted to be equal in all cavities by means of motorized tree stub waveguide tuners. The calibration is verified by a measurement of the beam energy. The gradient calibration error was in the range of 3-5%. The measurement of beam induced transients (vectors) is shown in Figure 1 as the difference of the cavity field with and without transient during the beam pulse.

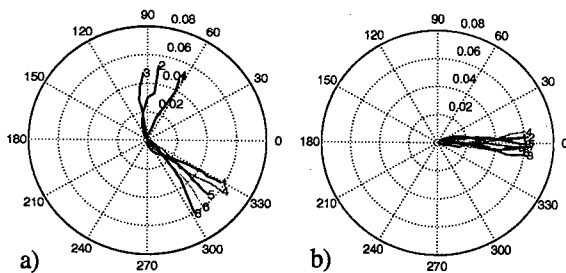
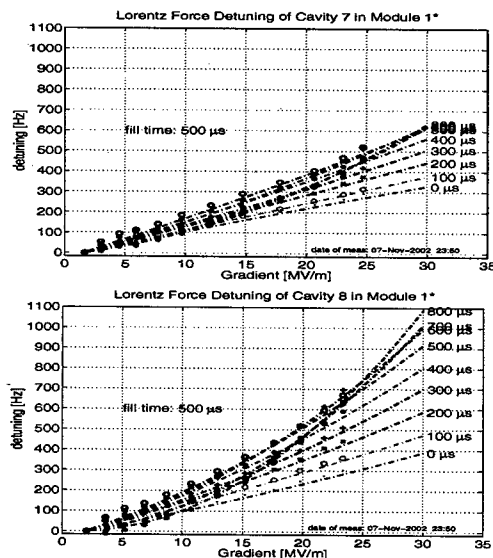


Figure 1: Measurement of beam induced transients at Module 1* a) before and b) after adjustment of cavities phases.



ery will help to maximize accelerator up-time. A thorough understanding of the RF system will allow for operation close to the performance envelope while maximizing accelerator availability. Often the RF control must be fully functional over a wide range of operating parameters such as gradients and beam current. For efficiency reasons the RF system should provide sufficient control close to klystron saturation.

The cavities are limited in their maximum operable gradients by quench, field emission or coupler sparks. Maximum operable gradient can be achieved with proper exception handling.

A cavity quench results in several effects:

- Field breakdown as shown in Figure 3 and resulting change in beam energy gain if the regulation of vector-sum cannot be maintained.
- Increase in cryogenic heatload.
- Increase in incident power to couplers and cavities if feedback gain is high and subsequent increased chance of coupler sparks and quench/field emission in other cavities due to increase of gradient. The beam energy may be constant if sufficient power is available. If cavities are operated in feed forward mode only, the energy gain of the beam will drop especially towards the end of the pulse.

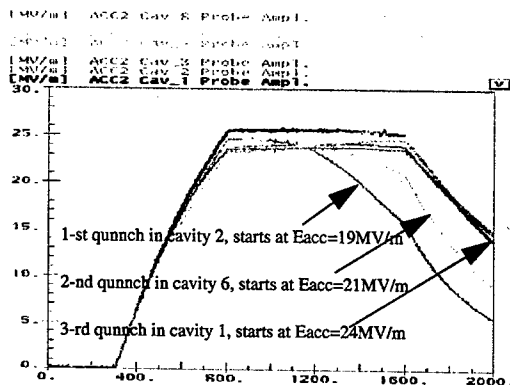


Figure 3: Quench detection during high gradient run at Module 1*.

Several measures can be taken to avoid cavity quench and to achieve desired stability:

- Turn-off klystron if cavity or coupler fault occurs.
- Reduce gradient in rf station where fault occurs.
- Reduce pulse length (rf and beam) if fault occurs.
- Detune cavity in which fault occurs.
- Change loaded Q of cavity in which fault occurs.

The mentioned task requires fast quench detection mechanism which can be implemented by including detuning and loaded Q measurement within DSPs.

3.3 Diagnostics

Diagnostics are required for calibration of gradient and phase with respect to beam, loop phase, incident wave and reflected wave, cavity detuning, loaded Q, etc.

- Loop Phase. The loop phase is determined during open loop operation by comparison of the vector controlling the actuator and the field vector induced in the cavity.
- Gradient and phase. Initial coarse calibration with RF, precise calibration with beam induced transients.
- Detuning and loaded Q. During decay of the cavity field the slope of gradient and phase (with respect to master oscillator) determine detuning and loaded Q.

4 CONCLUDING REMARKS

TTF I RF system was operational more than two years with a basic state machine for automated operation. Pulsed operation of superconducting cavities has been successfully demonstrated and has proven that the phase and amplitude stability requirements can be met even in the case of control of the vector-sum of multiple cavities.

The future developments will be able to make use of advances in electronics. Faster DSPs reduce latency and allow more complex algorithms. Phase and gradient calibration based on beam induced transient can be improved to detect small transients with high precision thereby reducing beam loss in the accelerator when phasing the linac.

The future development plans includes: implement fast quench detection mechanism by including detuning and loaded Q measurement within DSPs; exception detection capability for individual cavities; extensive upgrade of finite state machine by implementation of automatic cavity/module tuning procedure and automated waveguide tuner control; develop robust and fast algorithm for adaptive feed forward; improve hardware diagnostic system by integrating diagnostic system within operational programs.

REFERENCES

- [1] "The Conceptual Design Report for the TESLA Test Facility", Edited by D.A. Edwards, DESY, Hamburg, 1995. <http://tesla.desy.de/TTFReport/CDR/TTFcdrTab.html>
- [2] S.N. Simrock, I. Altmann, K. Rehlich, T. Schilcher, "Design of the Digital RF Control System for the TESLA Test Facility", Proc. EPAC'96, Barcelona, Spain, p.349, 1996
- [3] M. Liepe, W.-D. Moeller, S.N. Simrock, "Dynamic Lorentz Force Compensation with a Fast Piezoelectric Tuner", Proc. PAC'01, Chicago, p.1074, 2001
- [4] G. Grygiel, O. Hensler, K. Rehlich, "DOOCS: a Distributed Object Oriented Control System on PC's and Workstations", ICALEPCS 97, Beijing, 1997
- [5] V. Ayvazyan, K. Rehlich, S.N. Simrock, N. Sturm, "Finite State Machine Implementation to Automate RF Operation at the TESLA Test Facility", Proc. PAC'01, Chicago, p.286, 2001

ANTIPROTON STACKING AND UN-STACKING IN THE FERMILAB RECYCLER RING*

C. M. Bhat,
FNAL, Batavia, IL 60510, USA

Abstract

The Fermilab Recycler Ring (RR) is intended to be used as a future antiproton storage ring for the Run II proton-antiproton collider operation. It is proposed that about 40mA of antiproton beam from the Accumulator Ring will be transferred to the Recycler once for every two to three hours, stacked and cooled. This operation continues for about 10 to 20 hours depending on the collider needs for antiprotons. Eventually, the cooled antiproton beam will be un-stacked from the Recycler and transferred to the Tevatron via the Main Injector. We have simulated stacking and un-stacking of antiprotons in the Recycler using multi-particle beam dynamics simulation code ESME [1]. In this paper we present results of these simulations.

INTRODUCTION

Fermilab has planned to use the Recycler [2] as the main antiproton storage ring in future. The primary goal of the Recycler is to stack in excess of $200E10$ antiprotons, cool and transfer to the Tevatron for proton-antiproton collider operation. The stacking of the antiprotons in the Recycler is carried out on several transfers over 10-20 hrs by extracting them from the Accumulator Ring. Every transfer takes place whenever the stack size in the Accumulator Ring is above about $40E10$. As and when it is needed, the antiprotons in the Recycler will be un-stacked in the form of thirty-six 2.5MHz low emittance intense bunches and sent to the Tevatron via the Main Injector. Both stacking and un-stacking of the antiprotons in the Recycler Ring involve complicated sequences of rf manipulations like de-bunching/re-bunching, squeezing/un-squeezing, cogging, merging/slicing of the beam. These rf manipulations should be carried out in adiabatic fashion to retain emittance.

In this paper we present longitudinal beam dynamics simulations for the stacking and un-stacking of the antiprotons in the Recycler. The simulations have been carried out with an emphasis on preservation of longitudinal emittance at every stage of the rf manipulation. The simulations have been carried out using a 2D-multi-particle beam dynamics Monte Carlo code ESME [1].

The Recycler is an 8 GeV proton/antiproton synchrotron and its lattice is very similar to that of the Main Injector [3]. The *slip factor* of the Recycler is about -0.0086 and the harmonic number $h = 28$ (for 2.5MHz rf system). All beam manipulations in the Recycler are carried out using a broad-band rf system [4] which can

produce barrier buckets of any shape. We use barrier buckets made of rectangular rf pulses (max. pulse height=2 kV and width = 0.908 μ sec) to store the beam. An efficient rf control system has been developed [5] to perform all of the rf manipulations. Presently, the Recycler is being commissioned using the proton beam from the Fermilab 8 GeV Booster. We also had several antiproton stores in the Recycler.

SIMULATIONS

The simulations were carried out in two steps. The first step involves an optimization of individual process like de-bunching of the 2.5MHz bunches in a barrier bucket, re-bunching in to 2.5MHz buckets, squeezing, etc. For example, to study the de-bunching process a train of four 2.5MHz bunches are injected in to matched buckets of the Recycler which are bounded by a barrier bucket of pulse gap of 1.59 μ sec. Next, we optimize the rate at which the 2.5MHz bucket is brought down from 2kV to 0.0kV and how it is brought down – suddenly, linearly or adiabatically. As we expected, by turning off the 2.5MHz rf voltage suddenly gave largest emittance growth. On the other hand, a truly adiabatic process is less practical. An iso-adiabatic de-bunching is developed by combining three linear processes in succession. At present, in the Recycler, we adopt a similar de-bunching technique by bringing down the 2.5MHz rf voltage from 2 kV to 1 kV in 5 sec, from 1 kV to 0.5 kV in the next 5 sec and take 10 sec to go down from 0.5 kV to 0.0 kV. Thus we take about 20 sec for the entire de-bunching process. A similar, but reverse procedure is adopted for re-bunching. Our simulations suggested that we can reduce the de-bunching and re-bunching time at least by a factor of two in the operation without any emittance dilution by bringing down the rf voltage from 2kV to 1kV in 2 sec, 1kV to 0.5kV in next two second and 0.5kV to 0 kV in the final 4 sec. These simulation results have been verified using beam measurements.

Figure 1 shows simulated wall current monitor data (with a relative normalization) and a data from a beam measurement. The figure 1(a)-(c) show a case for four 2.5MHz bunches of beam in the Recycler de-bunched in 8 sec and re-bunched in 8 sec. The corresponding wall current monitor data is shown in figure 1(d). The beam data show that the bunch lengths before and after de-bunching are the same within a few percent.

Similar simulations are performed for different processes to establish optimum operational conditions.

The second step involves the simulations of the entire process of stacking and un-stacking of the beam.

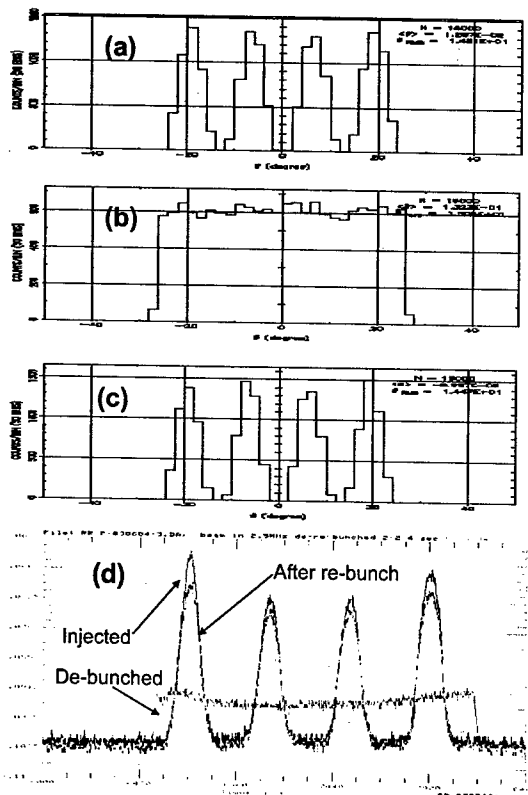


Figure 1. Results of ESME simulations of wall current monitor data. (a) The beam at injection in the 2.5MHz buckets, (b) De-bunched in 8 sec, (c) Re-bunched in 8 sec as explained in the text. (d) Wall current monitor data taken during a beam experiment for similar conditions. The measured bunch lengths before de-bunching and after re-bunching are essentially the same.

Stacking of Pbars

Figures 2 and 3 show the simulations of the entire stacking sequence for three transfers. Fig. 2(a) shows the injection of four 2.5MHz bunches into the Recycler. These bunches are de-bunched and are squeezed symmetrically in a barrier bucket by moving the upstream and the downstream barrier pulses towards the center of the barrier bucket in about 5.25 sec. We used a linear cog rate of the barrier pulse=4.89deg/sec. The phase-space distribution of the beam particles and its projection on the θ -axis after squeeze are shown in Fig. 2(e) and 2(f), respectively. Before the injection of the new group of four bunches the squeezed beam bunch is moved to a new location using the same cog rate (see figure 2(g)).

Similar procedure is repeated for the 2nd and 3rd transfers. A special care is taken while merging the new transfer with the old stack. Here we have investigated two methods of merging. In the first method, we simply cog the second set of fully squeezed bunch towards the old stack. As the head of the moving bucket interferes with the tail of the old bucket, the -ve and +ve barrier pulses start canceling one another at the same time they produce

an increasing non-stable region between them which produces a void in the phase-space area of the final stack. In the second method, the merging of the stacks involves two steps: 1) Bring two buckets as close as possible and reduce the barrier pulse heights adiabatically to zero voltage as shown in figure 3(a) and (c), 2) Squeeze the final stack to get proper dp/p. The simulation suggested that the 1st method introduces a hollow in the middle of the $(\Delta E, \Delta\theta)$ -space of beam particle for the final distribution resulting in a small emittance dilution. On the other hand the 2nd method gives rise to smaller emittance growth.

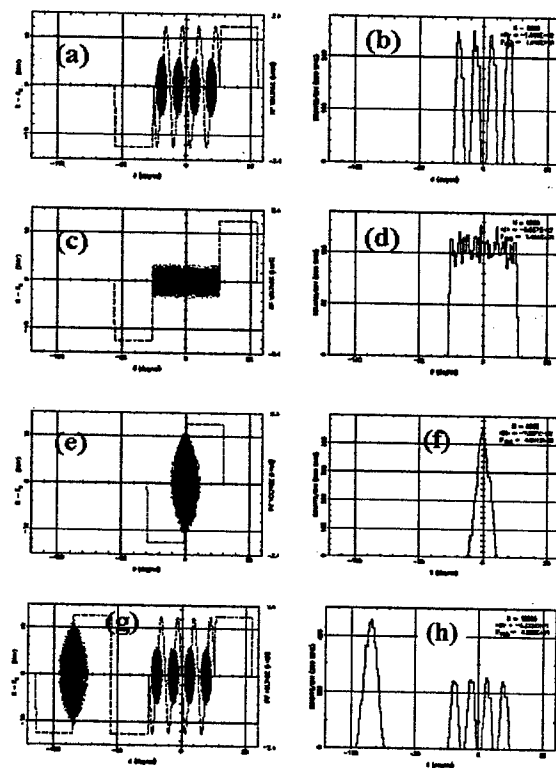


Figure 2. ESME simulations of the beam stacking in the Recycler. The figures (a), (c), (e) and (g) show $(\Delta E, \Delta\theta)$ -phase space distributions of beam particles. The figures on right show their projections on θ - axis (equivalent time coordinate).

In our simulations, we have used a rate of 400 V/sec for reducing the barrier pulse voltage in figure 3(c) and after merging of new transfers the final stack is squeezed by 41.6deg to get dp/p for final stack to be same as that of bunches shown in figure 3(a). Before injecting the next group of four 2.5MHz bunches the final stack of the beam is clogged by 71deg so that the new injection barrier bucket can be grown at the same azimuthal location of the Recycler. We find that stacking of a new injection can be performed in about 33 sec with out any emittance growth (compare this with 105 sec scenario which is in use at the Recycler). Note that, the simulation does not include any rf noise or any other un-wanted mechanism which would give rise to emittance dilutions.

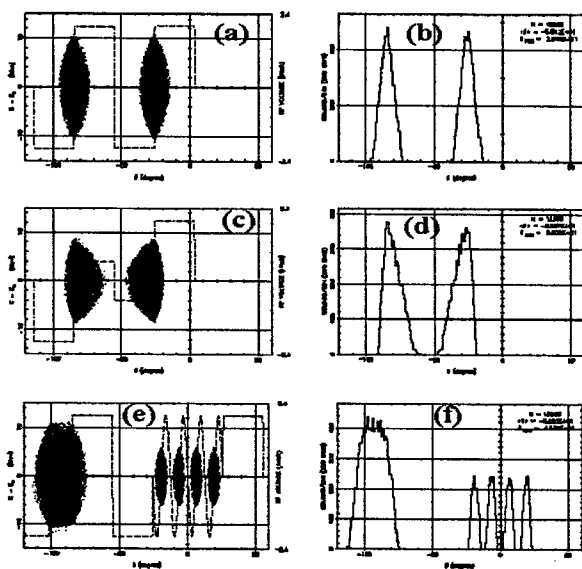


Figure 3. ESME simulations to illustrate a way of merging two stacks (particularly see (c) and (d)). (e) and (f) illustrate a new injection.

Unstacking of Antiprotons

For the simulations of unstacking of the beam we start with the final distribution produced from the previous stacking simulations. The sequences are essentially reversed. The entire process of beam unstacking is shown in Figures 4 and 5. Simulations predicted <5% emittance growth.

In summary, we have carried out simulations for both stacking and un-stacking of antiprotons in the Recycler to establish better operating conditions. We find that the total time required for a beam stacking sequence is about 33 sec, which is about a factor of three smaller than the present operating scenario in use. Special attention should be given to cog rate of the barrier pulses and buckets. A cog rate of 4.89 deg/sec gives <5% emittance growth. We plan to test these results using the beam in the Recycler.

The author would like to thank Jim MacLachlan and John Marriner for many useful discussions in the course of this work.

REFERENCES

- * Work supported by the Universities Research Association, Inc., under contract DE-AC02-76CH03000 with the U.S. Department of Energy.
- [1]. J. MacLachlan, ESME modified to handle beam dynamics in barrier buckets (1996), (private communications)

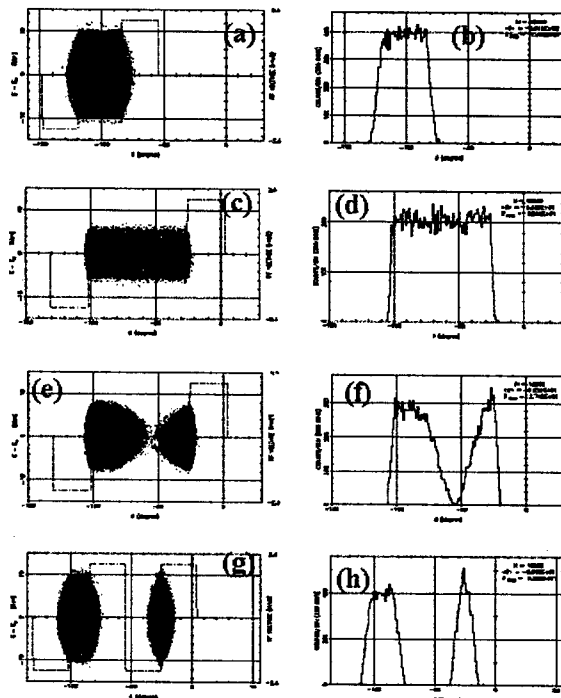


Figure 4. ESME simulations illustrating the beam unstacking sequences.

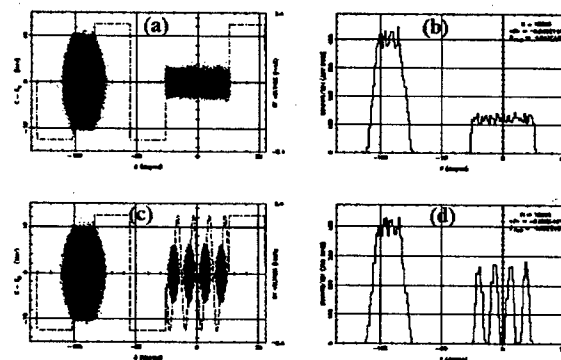


Figure 5. ESME simulations illustrating the beam unstacking sequences.

- [2] "The Fermilab Recycler Ring Technical Design Report" G. Jackson, FERMILAB-TM-1991 (1996).
- [3] "The Fermilab Main Injector Technical Design Handbook" Fermilab Internal Document (1994)
- [4] J.E. Dey and D.W. Wildman, IEEE, Proc. the 1999 Part. Accel. Conf. New York, NY, 869, (1999).
- [5] B. Chase and K. Meisner (private communications, 2003).

GATED CURRENT INTEGRATOR FOR THE BEAM IN THE RR BARRIER BUCKETS

A. Cadorna, C.M. Bhat, J. Crisp, B. Fellenz

Fermi National Accelerator Laboratory (FNAL) *, Batavia, IL 60510, USA

Abstract

At the Fermilab Recycler Ring (RR), the antiproton (pbar) beam will be stored azimuthally in different segments created by barrier buckets. The beam in each segment may have widely varying intensities. We have developed a gated integrator system to measure the beam intensity in each of the barrier bucket. Here we discuss the design of the system and the results of beam measurements using the integrator.

INTRODUCTION

Equipped with a wide-band RF system to create barrier buckets of any shape, the Fermilab RR[1] is an 8GeV permanent magnet antiproton storage ring. These barrier pulse[2] have a 2kV pulse height and a 908nsec pulse width (48, 53 MHz RF buckets). Furthermore, the positions of the barrier pulses are determined by RR LLRF arbs settings[3]. Consequently, during stacking and un-stacking of the beam (protons or anti-protons), they are moving but are fixed during cooling.

The Gated Current Integrator (GCI) measures the proton and antiproton beam intensity in RR barrier buckets during stacking, un-stacking, and storage. GCI aims to accommodate an intensity range of $1E10$ to $4E12$, with 10% or better accuracy at the lower limit and 2% or better at the higher limit.

GCI SYSTEM ARCHITECTURE

The GCI system prototype integrates the total area under a gated wall current monitor (WCM) signal to determine the beam intensity. Essentially, the system can be divided into five basic modules. The first three are shown below.

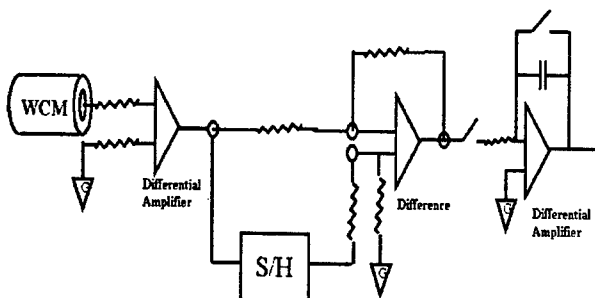


Figure 1 : First 3 stages of GCI system prototype

The first stage receives a WCM signal transmitted over

twin-ax cable. This signal passes through a common-mode choke to filter any additive noise induced over the transmission lines, an impedance matching network to handle cable termination and reflections, and then a differential receiver amplifier. This differential-to-single-ended amplifier is characterized to have a high common-mode rejection ratio (70dB @10MHz). This minimizes the corruption by external noise sources or crosstalk. The amplifier also has tuneable gains to adjust for losses in the transmission lines or for different full-scale intensity ranges.

The second stage addresses the slow drifting baseline shift of the WCM signal. It is composed of a sample-and-hold (S/H) amplifier and a differential amplifier. Due to the rise and fall characteristics of the barrier buckets' separation, 250 nsec is needed to acquire and sample the baseline between integrations. Further, the S/H amplifier is characterized with a slow $0.02\mu V/\mu s$ droop rate, allowing the sampled baseline to be held steadily. Once sample, the baseline is subtracted from the original WCM signal using a differential amplifier. The differential input range of the differential amplifier must accommodate differences between peaks in the beam bunches and the baseline.

Next, this baseline-corrected signal is feed into the integrator in a switched-capacitor configuration. The time constant determined by the feedback resistor and capacitor needs to be much greater than the typical gate width. This minimizes the intrinsic exponential droop error of non-ideal integrators during the hold state. In addition, errors due to noise also vary proportionally to the square root of the gate width. Serving as an input buffer to the A/D converter, this amplifier has a fast settling time (90nsec to 0.1%) as well as a high slew rate (230V/ μ sec uncompensated).

The integrated signal is then passed to the next stage, where is it converted to a digital 16-bit equivalent (A/D) and then back to analog (D/A). With a 250 kHz sampling rate, the A/D acquisition and conversion time is at most 4μ sec. The 16-bit D/A has a bipolar output rate of $\pm 10V$ and has a typical settling time for 1 LSB step is 2.5μ sec.

Finally, the output analog signal is put through a non-inverting unity operational amplifier. This low noise op-amp has a maximum offset voltage drift of $0.1\mu V/^{\circ}C$ and a maximum offset voltage of $25\mu V$ at $25^{\circ}C$. This eliminates the need of external offset voltage adjustments and increases system accuracy over temperature.

* Work supported by the Universities Research Assoc., Inc., under contract number DE-AC02-76CH03000 with the US Dept. of Energy

GCI SYSTEM TIMING

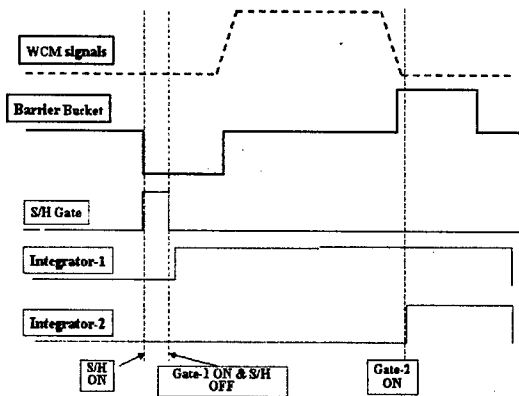


Figure 2 : Timing schematic for various gates

The GCI system prototype requires a set of digital signals from the control system: S/H Gate, Integrator-1, and Integrator-2. Timing schematic for various gates used in RR relative to the barrier rf signals and the beam pulse are shown in figure.1.

S/H Gate is a high pulse trigger control and decides when to sample the baseline. Though it is independent of the other two signals, it is best to sample the baseline just when the integrator is resetting before integration. This will minimize the droop during the hold mode of the S/H amplifier.

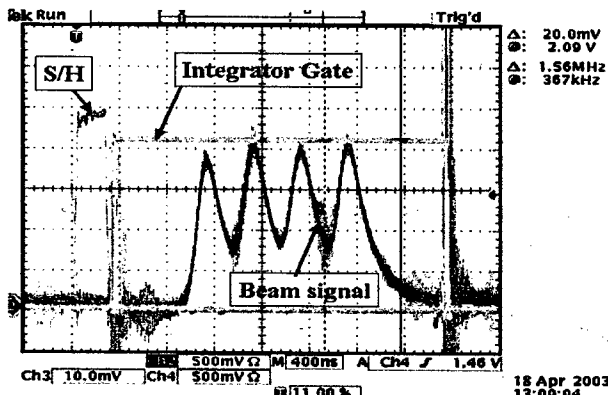


Figure 3 : WCM beam signals and various gates

Integrator-1 and Integrator-2, both high pulses, together control an adjustable integration window. The rising edge of Integrator-1 provides the beginning of the beam integration while the rising edge of Integrator-2 marks the stop of the beam integration. This resulting gate triggers a Altera FLEX 10K field programmable gate array (FPGA) to generate signals controlling the switching action for the integrator's three modes: INTG, which lasts as long as the gate, HOLD, which is after INTG lasting the duration for the A/D conversion, and then RESET, occurring between HOLD and the next INTG.

A timing circuit is also programmed into the FPGA to generate the correct handshaking signals needed to coordinate the A/D and D/A conversions.

Figure 3 shows the scope picture during setting up of various gates to measure the integrated injected beam in to the Recycler Ring. The data shown here is for four 2.5MHz bunches at the time of injection.

GATE SETTINGS IN RR

Exact positions of various GCI gates are highly critical for accurate beam intensity measurements in RR. The RR many have pbar beam in three different regions as shown in figure 4 with different energy spreads. Besides, for optimum use of the RR azimuth space, two barrier pulses may be back to back during storage of the beam. This requirement demands that the ON of S/H-gate must align with beginning of -ve barrier pulse as shown in figure 2. The ON of Integrator-1 is set at 250ns (minimum width of S/H-gate) from the beginning of the barrier pulse. This implies that the present GCI system is capable of measuring the intensity for a beam with maximum $\Delta E < 30.6\text{MeV}$ (assuming the beam is contained in a rectangular barrier of 2kV pulse height and 908ns pulse width).

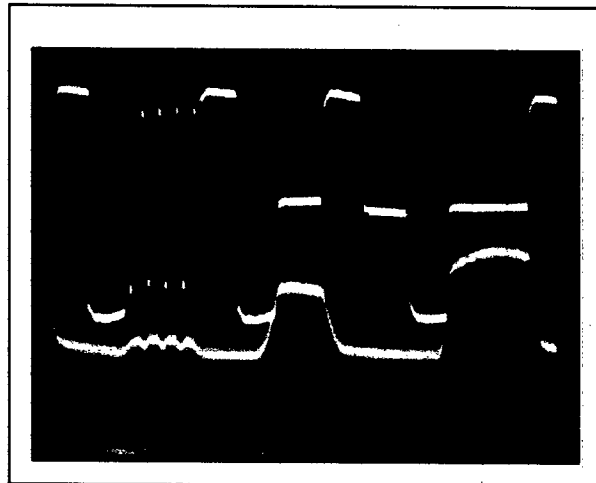


Figure 4 : A typical RR beam segments. RF wave (top trace) and beam segments (bottom trace).

CALIBRATION AND BEAM MEASUREMENTS

The GCI system is calibrated by two methods. The first calibration is carried out on a test stand using an external current source and the corresponding response is measured.

Further calibration is done by recording the GCI response as a function of the Recycler Ring DCCT for the beam in barrier bucket of fixed size. The beam intensity measured using DCCT is known to better than

0.5%. The correlation between DCCT output and the GCI output is shown in figure 5.

We have also recorded the GCI response as a function of DCCT for varied barrier bucket width. This distribution found to be flat for a fixed amount of beam.

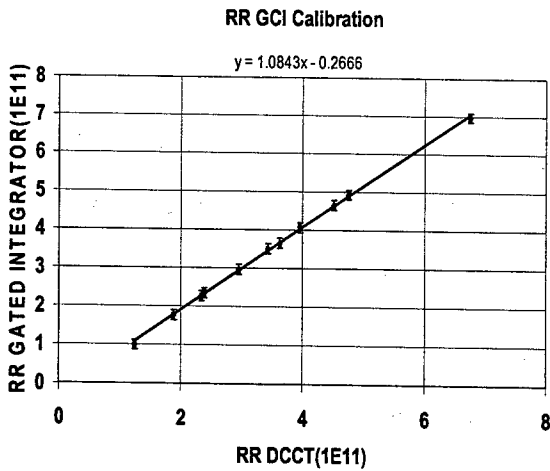


Figure 5 : RR GCI vs RR DCCT response

In future we plan use more than one GCI systems in the RR to measure the stored beam in more than one barrier buckets and the beam in the extraction region. This would help us to measure the injection and extraction efficiencies.

A device similar to this was used to make first measurements of longitudinal emittance of the beam in the RR barrier buckets[4] by reducing the barrier pulse height until the beam area matches with that of bucket area. The GCI is used to find out when the beam start leaking out of the barrier bucket. The results of these measurements lead to further investigation of the Main Injector ramp induced longitudinal emittance growth of the Recycler beam.

Our special thanks are due to J.P. Marriner for his inputs and many useful discussions during the course of this work. We also would like to thank Dallas Heikkinen for his help.

REFERENCES

- [1] "The Fermilab Recycler Ring Technical Design Report" G. Jackson, FERMILAB-TM-1991 (1996).
- [2] J.E. Dey and D.W. Wildman, IEEE, Proc. the 1999 Part. Accel. Conf. New York, NY, 869, 1999).
- [3] Brian Chase and Keith Meisner (private communications, 2003).
- [4] "A first measurement of longitudinal emittance of RR beam", C.M. Bhat, Fermilab- MI Note 287

IMPROVEMENT OF PHOTON FACTORY ADVANCED RING CONTROL SYSTEM

T.Obina, T.Katoh, N.Yamamoto, T.T.Nakamura, J.Odagiri, Y.Takeuchi, K.Kudo, A.Akiyama, S. Nagahashi, T.Kawamoto, I.Komada, High Energy Accelerator Research Organization (KEK), 1-1 Oho, Tsukuba, Ibaraki 305-0801, Japan

Abstract

As a part of the Photon Factory Advanced Ring (PF-AR) upgrading project, the control system is upgraded. Considering the importance to realize the seamless operation between PF-AR, injector linac and KEKB, we decided to adopt EPICS as a basis of the control system. The old control system of the PF-AR was based on the HIDIC mini-computer system and the CAMAC was used as a field-bus. In order to minimize the cost and the work of renewal, we didn't change the device interface layer below CAMAC. A total of 13 EPICS Input/Output controllers (IOCs) are used to replace HIDIC mini computers, and we use the VME modules such as CAMAC crate controller, GPIB interface and the timing synchronization module. The ARCNET driver modules are also used mainly for the control of magnet power supplies. For the archiving of accelerator parameters, we use Channel Archiver, which is one of the EPICS extensions. We have also renewed the accelerator safety control system using the PLC.

INTRODUCTION

The PF-AR, 6.5 GeV electron storage ring for pulsed X-rays, was originally constructed as an injection booster to TRISTAN main ring, and had also been used as a synchrotron radiation source during the intervals of injection to the TRISTAN. The upgrading project of PF-AR [1] which intended to reconstruct the ring as the SR light source was successfully finished as shown in these proceedings [2]. Replacement of the control system with the system reliable and easy for machine operation was the part of the project.

DESIGN CONCEPT

General Description

In the standard model of the accelerator control, the system can be classified into three layers: device interface layer, equipment control layer and presentation layer. Figure 1 show the old control system based on HIDIC mini-computer system which had been used as the TRISTAN control system [3]. In this system, device interface layer which consists of a large number of CAMAC modules were used for input/output signal processing. In order to minimize costs and works of the replacement, device interface layer under CAMAC had not been changed. Because the seamless operation between PF-AR, linac and KEKB is important, we adopt EPICS[4] to realize it. We replaced the HIDIC mini-computer system with EPICS Input/Output Controller

(IOC). The equipment control layer and the presentation layer upgraded using today's standard technologies.

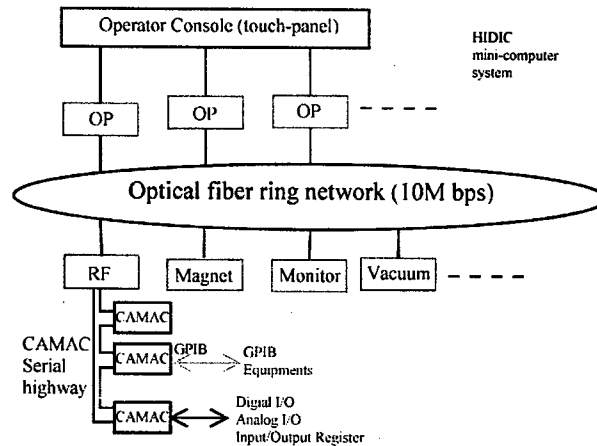


Figure 1: AR control system before the improvement (TRISTAN control system). "OP" denotes the HIDIC mini-computers for control of operator console.

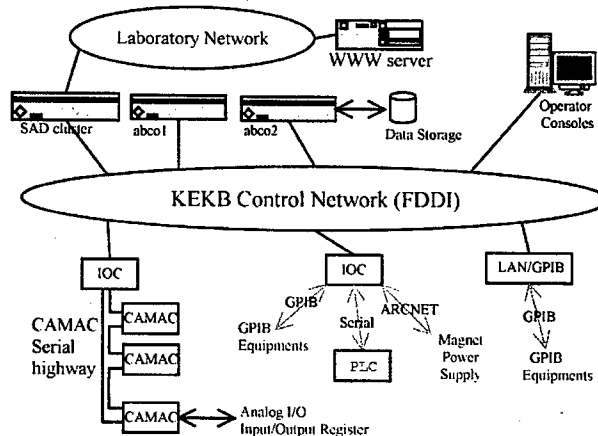


Figure 2: AR control system after the improvement.

Device Interface Layer

We use several kinds of field busses such as CAMAC, RS232, GPIB and ARCNET. The CAMAC modules are mainly used in many groups such as RF, Beam Transport (BT) and Beam Monitor (BM). In these groups, the existing CAMAC serial highway, which has a data transmission rate of 2.5Mbps, are fully used. Many kind of common CAMAC modules were developed for

TRISTAN. For example, we use ADC, DAC, status input gate (SIG), status output register (SOR) and input/output register (AIO). We did not create a new CAMAC module but only re-calibrate or repair the broken modules. ARCNET is used to control the magnet power supplies. We use the same power supply control interface module (PSICM) as KEKB[5].

Programmable logic controllers (PLCs) are used for vacuum control system[6] and for the accelerator safety interlock system. Status of PLC is transferred to the CPU board of EPICS IOC via RS232C. We don't control the PLC from IOC (read-only).

We need to control some GPIB equipments such as digital voltmeters, signal generators or oscilloscopes. In TRISTAN control system, CAMAC-GPIB board controlled the GPIB device. We decided not to use them. Mainly, we use VME-GPIB controller board (National Instruments, NI-1014) or LAN-GPIB interface (Agilent Technologies, E2050A). Driver and device support for EPICS was developed by BESSY[7].

Equipment Control Layer

The location of IOCs distribute at four sub control buildings and the main control building. A total of 13 IOCs are used for PF-AR and connected through FDDI network. Each IOC consists of VME subrack, CPU board (Power PC 750, 64MB memory), CAMAC Serial Driver(VSD 2992), remote access server module (Mitsubishi Electric, DRSJ-01), etc. Some IOC contains the GPIB interface board. Two IOCs for magnet control equip the event trigger module (EVR) which is used to synchronize the trigger of acceleration[8].

A new UNIX server workstation was installed for PF-AR, and the machine is also used for KEKB operation. The specification of the workstation is as follows: 2 CPU, 440MHz PA-8500 processor, 1GB memory, 36GB system disk, 100GB external RAID disk, HP-UX 11 operating system. On the other hand, the SAD [9] cluster machines are extensively used for the modelling or controlling of PF-AR. A number of software was already developed for KEKB operation. Some of them were used with a small modification for PF-AR operation.

Presentation Layer

We use X-terminal or its emulator for the operator consoles. There are eight personal computers (1GHz, Pentium III CPU), five of them are running on Linux operating system with dual-head display board, three of them are Windows 2000 machines with four-head display.

SOFTWARE

General

The TRISTAN control system used NODAL[10] and PCL[11] for software development. We decided to extract the data such information as cabling, however, we don't to translate any programs into new control system. Each working groups developed new programs for machine operation. In order to record the history of many files, we

utilized CVS (Concurrent Versions System) for the management of software.

Although the most of the record types are already developed by EPICS community or KEKB, we must develop several new EPICS record. For example, we modify the existing KEKB BPM record to BPM-AR record. For Magnet control, we add some functions to the KEKB magnet record to support energy ramp-up for PF-AR operation.

EPICS runtime database is created by several methods. For example, database for BPM record is developed by a schematic editor Capfast and then converted to the EPICS database format. In many cases, simple database is written by text editor. Detail of the beam position measurement system is reported in ref. [12].

As for the presentation software, MEDM (Motif-based EPICS Display Manager) and the scripting software such as Python/Tkinter and SAD/Tkinter are mainly used. SAD[9] is a language for accelerator design developed at KEK. For the control of orbit measurement/correction, injection tuning, SAD is very effective because it equips an interface to EPICS channel access protocol. We can measure any accelerator parameters using SAD and can perform the calculation using it. On the other hand, Python language is also used for the application that does not require the lattice parameters.

Oracle database is used to store wiring information and property of magnet power supplies[13]. The data is extracted and converted to EPICS database.

Archive/Retrieval

We adopted the Channel Archiver[14], which is one of the EPICS extensions. The ArchiveEngine programs are running on HP-UX workstation, and almost 9000 records are always monitored and stored to the disk. Amount of daily archive depends on the status of machine operation. Roughly speaking, magnet group and RF group need 100MB/day, and another group is 10-30MB/day.

WWW

A dual Pentium III machine for the WWW server is working. The machine acts as a front-end of CGI interface of Channel Archiver. Due to the security reason, this machine can be accessed only from inside KEK. In order to show the operation status to the outside world, operation information is transferred to another web server machine periodically.

INTERLOCK SYSTEM

Radiation safety system of PF-AR is already built as a part of a KEKB safety system[15]. In order to manage the safety among the beamline safety system, KEKB safety system, linac beam trigger signal and the interlock signal from PF-AR operation system, we installed a new PLC (OMRON). In the old control system, this interlock was made up of many logical circuits installed in NIM modules, however, reliability of the decrepit system was not sufficient. We carefully check the logic and ported

them to a new ladder program on the PLC. The block diagram of this accelerator safety system is shown in Fig.3.

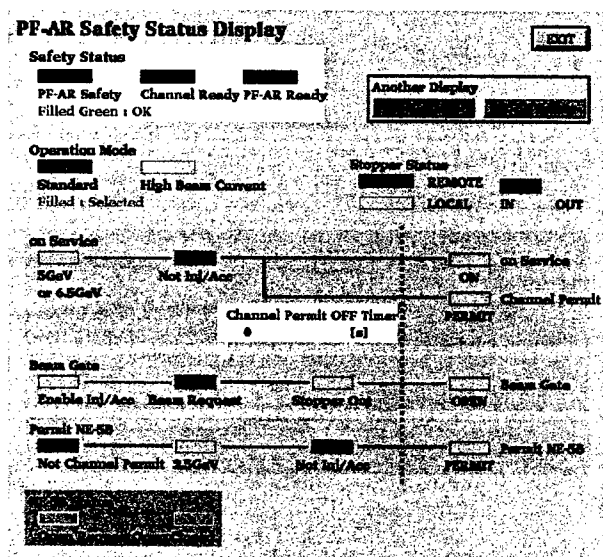
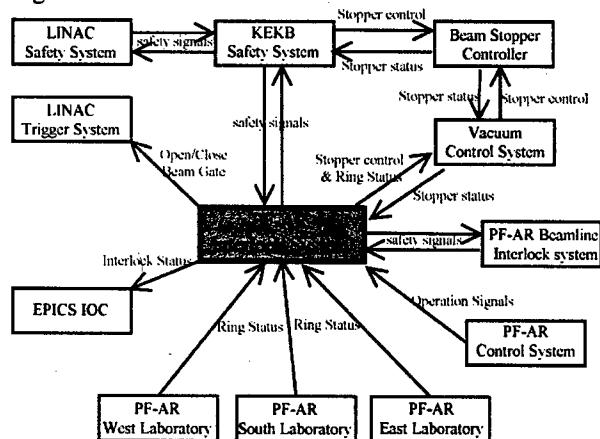


Figure 3: Block diagram of the PF-AR interlock system after the renewal(top) and the example of MEDM display panel(bottom).

SUMMARY AND FUTURE PLAN

Renewal of PF-AR control system was successfully finished. We continue the software development for the stable and reliable operation. Because one of the insertion device dose not have interface to EPICS based system, we

are developing the software for them. This will start operation from the next user run period. Electronic notebook is also an important issue. We must develop more general interface for it.

ACKNOWLEDGEMENT

The authors wish to thank Lifang Zheng (Shanghai Synchrotron Radiation Center) and Ge Lei (Institute for High Energy Physics, Chinese Academy of Science) who developed the BPM measurement system based on EPICS.

REFERENCES

- [1] Photon Factory Activity Report #19(2001)
- [2] T. Miyajima et al., "Present Status of Photon Factory Advanced Ring" in these proceedings
- [3] S-I. Kurokawa, et al., "The TRISTAN Control System", Nucl. Instr. and Meth., A247(1986) 29
- [4] L.R. Dalesio, et al. "EPICS Architecture", ICALEPCS 1991.
- [5] A. Akiyama et al., "KEKB Power Supply Interface Controller Module", Proc. ICALEPCS'97 (1997) p.243
- [6] Y. Tanimoto et al., "Vacuum Systems Renewal for the PF-AR Upgrade" in these proceedings
- [7] GPIB support for EPICS: <http://www-csr.bessy.de/control/SoftDist/gpib/>
- [8] T. Naito et al. "Performance of the Timing System for KEBB", ICALEPCS 99, p.214
- [9] SAD (Strategic Accelerator Design) Homepage: <http://acc-physics.kek.jp/SAD/sad.html>
- [10] M.C. Crowley-Milling, et al. "The NODAL System for the SPS", CERN LAB II-CO/74-2 (1974)
- [11] "PCL (Process Control Language) Manual", Hitachi Limited., JAPAN
- [12] T. Obina et al. "EPICS based beam orbit measurement system for KEK PF-AR", Proc. 2nd Asian Particle Acc. Conf. (2001) p.716
- [13] M. Kaji et al., "Relational Database System in the KEBB Accelerator Control System", Proc. 1st Asian Particle Acc. Conf. (2001)
- [14] Channel Archiver for EPICS: <http://lansce.lanl.gov/lansce8/Epics/Archiver/Default.htm>
- [15] N. Akasaka et al. "KEKB Accelerator Papers", Nucl. Instr. and Meth. A 499(2003)138-166

THE LANSCE RICE CONTROL SYSTEM UPGRADE*

Michael Oothoudt, Stuart Schaller#, Eric Bjorklund, Mary Burns,
Gary Carr, John Faucett, David Hayden, Matthew Lusk, Robert Merl, Jerry Potter,
Jerome Reynolds, Dolores Romero, and Fred Shelley, Jr
Los Alamos National Laboratory, Los Alamos, NM 87545, USA

Abstract

The LANSCE (Los Alamos Neutron Science Center) control system upgrade program continues with the impending replacement of the RICE (Remote Instrumentation and Control Equipment) subsystem. The RICE subsystem upgrade is a challenge because of its technology (late 1960's), number of channels (>10,000), and unique characteristics (all-modules data takes, timed/flavored data takes). The plan is to replace at least the non-timed data and the command portions of the subsystem with Programmable Logic Controllers (PLCs). We discuss motivations, technological challenges, proof-of-principle, and planning. The boundary condition, as usual, is that we must implement these major changes on a running accelerator.

INTRODUCTION

The RICE system was designed before the advent of CAMAC, VME and other standard data acquisition and control busses. The RICE architecture was designed as an integral part of the accelerator facility, with capabilities custom crafted to support hardware in the accelerator. As the years have passed, some readout and control capabilities have been moved to CAMAC and VME, but over 10,000 channels remain in RICE today. Some upgrades to RICE hardware were made in the early 1970's, but few changes have been made since then.

The initial description of the RICE hardware was given at the very first Particle Accelerator Conference in Washington, D.C., in 1965 [1]. For a more in-depth discussion of the RICE system in the context of the history of the LAMPF/LANSCE control system, see [2].

With thirty year old technology comes problems. Many of the discrete components in RICE electronics can no longer be purchased and supplies of spares are dwindling. Plastic connectors are becoming brittle and spares are not available. Calibration capabilities were not built-in, raising questions about year-to-year comparability of settings. Lack of any vendor support means all maintenance and repair must be done in-house. Non-standard electronics means all in-house maintenance people must receive extensive RICE-specific training. Retirement of the original designers and builders of RICE

makes extended re-engineering necessary to understand the reasons for the current architecture and implementation.

A proposal was made in the early 1990s to rebuild the system in standard electronics, providing a complete duplication of RICE capabilities. Declining budgets and high cost, along with the undesirability of an extended accelerator downtime, prevented funding of the effort.

The current proposal takes a different approach. Review of channel usage shows that full RICE capabilities are needed for only about 10% of the channels in the system. A "divide-and-conquer" approach will be used, moving approximately 9,000 "slow control" channels to commercial Programmable Logic Controllers. The remaining 1,200 diagnostic and RF channels that require full RICE capabilities will be implemented in special-purpose VME electronics.

RICE CAPABILITIES

The RICE system provides a wide range of capabilities. This paper deals with the standard capabilities that comprise the slow control functions of the system. This section also describes the RICE features beyond slow control that cannot be implemented in a standard PLC.

Slow Control

Approximately 9,000 channels in the RICE system are not dependent on the instantaneous state of the accelerator and can be read and commanded at a 1 Hz or slower rate. Examples of such channels are binary on/off and analog magnet currents. The RICE system supports this functionality with

- Analog inputs with 11 bits plus sign. Input ranges of $\pm 10V$, $\pm 1V$ and $\pm 100mV$ are allowed.
- Analog raw data, corresponding to the ADC count. Conversion to engineering units is done in the legacy VAX control computers.
- Analog stepper motor controllers, used to provide local analog control and to provide set point control that holds across power outages. While a green-field effort might use DACs, this upgrade will stay with stepper motor controllers to avoid the cost of replacing the stepper motors and the field wiring plant.
- Binary input data, compatible with 0-8.5V low, greater than 14V high, converted down to DTL levels.
- Binary commands.

*This work has benefited from the use of the Los Alamos Neutron Science Center at the Los Alamos National Laboratory. This facility is funded by the US Department of Energy and operated by the University of California under Contract W-7405-ENG-36. Paper LA-UR-03-2758.
#schaller@lanl.gov

- Linked binary commands, allowing an operator to command a single binary channel but issue commands to several channels at the hardware level.
- Local control capability. RICE commands can be locked out locally, allowing work on equipment without possible interference from the control room.

The RICE hardware is organized into "modules." In the linac portion of the system, a RICE module corresponds to the equipment associated with one of the 48 accelerating modules. A typical RICE Module supports 64 analog inputs, 144 binary inputs, 25 analog stepper motor controllers and 48 binary commands. An extension chassis can be used to increase these limits.

High Speed, Gated Acquisition

Sampling beam and RF diagnostics clearly requires high speeds and gating capabilities well beyond that provided by slow control. Furthermore the LANSCE linac runs at 120 pulses per second with a maximum 12% duty factor, requiring the ability to schedule data reads at specific times during the pulses. Finally many different kinds of beam pulses may be accelerated during the one-second repeat cycle of the linac and it is even possible to have two different kinds of beam on a single RF pulse, so it must be possible to schedule reads on specified pulses. In RICE these capabilities are called

- Timed data – schedule the data read at a one microsecond granularity with respect to the start of a $8\frac{1}{3}$ millisecond timing cycle.
- Flavored data – schedule the data read on a pulse with specific beam parameters. Up to 96 parameters can be specified, including the desired beam species (H^+ or H^- or H^+ and H^-), the beam energy, and the beam-chopping pattern (e.g. gaps of 90 ns in the beam every 270 ns for beam intended for the Proton Storage Ring).
- All-modules data – because of the architecture of the RICE (a star configuration), data from all 72 RICE modules are acquired with each read. Thus a single request can read correlated data along the entire length of the linac in a one-microsecond window; 72 individual reads would otherwise be spread over 600 milliseconds. Thus it is possible, for instance, to get a snapshot of all spill monitors along the linac on the same beam pulse.
- Flagged data – a special link to the Fast Protect system flags data read during a pulse with excessive beam spill. Also an all-modules data read can get spill status from all accelerator locations on the same pulse to determine where the spill was.

All channels in RICE, including the slow control and binary channels can be read with these constraints. However, only the 1,200 channels for beam and RF diagnostics can fruitfully use these capabilities. A proposal to deal with these channels is being developed using transient-digitizer technology in VME [3,4].

PROPOSED SLOW CONTROL REPLACEMENT

Commercial PLC systems can readily meet our needs for slow control data. Evaluations at SNS [5] have measured read speeds under EPICS [6] that are well in excess of our needs and in fact may support a 10 Hz update rate for our channel count. This is highly desirable for channels that are controlled by knobs, such as magnet currents.

We propose to replace each RICE module with an Allen Bradley ControlLogix [7] PLC. An EPICS Input-Output Controller (IOC) in a VME crate will be used to control three to six PLCs in a geographical area; connection will be made via Ethernet, with an Ethernet switch used to isolate the IOC-to-PLC traffic from the rest of the network. To replace the slow-control channels for a typical RICE module, a PLC will have three ControlLogix crates containing six analog input modules, two digital input modules, six stepper motor controller units and two digital output modules. There will also be one DAC for diagnostic purposes.

Extra accelerator downtime to install the new hardware is not acceptable. Thus installation will be done during normal maintenance periods and will result in running the accelerator with a mixed RICE/PLC system for several years. With present manpower and other commitments, it is expected that during a normal monthly three-day maintenance period, one RICE Module can be converted. During the yearly three-month extended maintenance periods, it may be possible to do as many as 10 modules. Thus this upgrade will be spread over four to five years if fully funded.

A proof-of-principle test has been done for binary channels. During this year's accelerator operation we expect to run one RICE Module with a full complement of analog and digital PLC modules as a final validation of the plan. Completion of the remaining RICE Modules will depend on funding.

KEEPING THE ACCELERATOR RUNNING

Accelerator operation constraints, as always, mitigate the aggressiveness with which we would like to pursue the RICE upgrade. It is vital that during the course of the upgrade we present operations with an (almost) totally transparent control system interface. Fortunately, we have already had some experience with (almost) seamless integration of new controls.

The RICE hardware is managed by and communicated with through the linac control system (LCS) which runs on a legacy VAX/VMS computers. EPICS applications access the RICE data through "gateway" software which interfaces Channel Access reads, monitors and commands to the LCS data system. Moving RICE channels to a PLC is mostly invisible to EPICS application programs but has significant problems for applications still running on the VAXes. There are approximately 50 legacy applications running on the VAXes, which took 10-25 man-years to

originally develop. Conversion of the applications to EPICS is in progress, but there will be many years when there are significant VAX applications needing to access PLC data. Some of the issues that need to be addressed are:

- Raw data – Many legacy applications were written to acquire and display raw analog data in RICE ADC counts. Many of the operators find that the raw values are more meaningful than the associated engineering values. This problem becomes important for legacy applications, which will have to acquire some data from RICE and some from PLCs which, by EPICS convention, supply only engineering values. As an interim step we are considering for the PLCs that will supply some kind of scaled “raw” values for use by such legacy programs.
- Mixed RICE/PLC – Some legacy programs acquire data via all-modules data reads by explicitly referring to “vector” (or array-based) channels. The vector reads will have to be handled specially if some of the individual channels in the vector are in RICE while others are in PLCs. We plan to have the legacy data acquisition library routines recognize these channels and automatically split them into separate RICE/PLC references, without application modification. (Note that the RICE front-end computer already builds all-modules reads from scalar reads whenever possible.)
- Single channel for command and readback – The EPICS channel naming philosophy calls for separate channels for input and output hardware. The LCS allows input and output channels to be associated in the device database and be referred to with a single name. EPICS applications will be written assuming separate input and output channels. We will provide appropriate extra names for such channels in the LCS database. The EPICS gateways will provide data/command associations for EPICS channels that are commanded by LCS applications.
- Ability to read any channel timed/flavored – The RICE system allowed reading slow-control channels as timed and flavored data for unusual troubleshooting activities. The new system is designed to make it possible to easily move a channel back to RICE if necessary.

EXPERIENCE SO FAR

During a three-day maintenance period RICE binary input/output channels in the RICE module controlling the last accelerating module of the linac were rewired to a PLC. An EPICS IOC was installed to interface the PLC to the remainder of the control system. Control system

software was modified to access these RICE channels through the IOC. The system was tested and a few software problems corrected. The accelerator then ran for a month in production mode with the PLC system. Thus we have high confidence that such upgrades can be done during monthly maintenance periods.

The next step in the upgrade will move all RICE analog and digital slow control channels on the RICE module to a PLC. It is expected that this test will be done during the 2003 production period. Based on the manpower costs for this step we will be able to finalize a budget and possible schedule for upgrading the slow control channels on the remaining RICE modules.

REFERENCES

- [1] T.M. Putnam, R.A. Jameson, and T.M. Schultheis, “The Application of a Digital Computer to the Control and Monitoring of a Proton Linear Accelerator,” *IEEE Trans. Nucl. Sci.*, NS-12 (1965) 21.
- [2] S.C. Schaller, “A LAMPF Controls Retrospective: The Good, the Bad, and ‘It Seemed Like a Good Idea at the Time’,” 1993 Int. Conf. on Accel. and Large Experimental Physics Control Systems, *Nucl. Instr. and Meth. A* 352 (1994) 516-520.
- [3] Rob Merl, Charles Burns, Floyd Gallegos, Chandra Pillai, Fred Shelley, Andy Steck, “A Multiwire Proportional Chamber System For Monitoring Low Momentum Beam In Accelerators,” this conference.
- [4] Rob Merl, Floyd Gallegos, Chandra Pillai, Fred Shelley, “High Speed EPICS Data Acquisition And Processing On One VME Board,” this conference.
- [5] K.U. Kasemir and L.R. Dalesio, “Interfacing the ControlLogix PLC over Ethernet/IP,” *Proceedings of the 8th International Conference on Accelerators and Large Experimental Physics Control Systems*, November 2001, San Jose, CA., THDT002, <http://www.slac.stanford.edu/econf/C011127/proceedings.html>.
- [6] L. R. Dalesio, et al., “The Experimental Physics and Industrial Control System Architecture: Past, Present and Future,” *Proceedings of the International Conference on Accelerator and Large Experimental Physics Control Systems*, 1993, pp. 179-184.
- [7] Rockwell Automation, “ControlLogix Selection Guide,” Publication 1756-SG001A-US-P from <http://www.ab.com>, July 2000.

THE UPGRADE OF HLS LINAC CONTROL SYSTEM

G. Liu*, W. Li, C. Li, J. Li†, L. Chen, X. Bao, J. Wang

National Synchrotron Radiation Lab., P. O. Box 6022, Hefei, Anhui 230029, P. R. China

Abstract

The linac control system of Hefei Light Source (HLS) was initially build in late 1980's, and a concerted effort has been put forth to upgrade it to a new, distributed one based on EPICS. Industrial PC based hardware is widely used as not only IOC but also front-end controller. Besides industrial PC, PLC and single-chip microcomputer are also used as front-end controllers in some subsystems. The software for industrial PC based front-end controller is developed based on vxWorks real-time operating system. The software for PLC and single-chip microcomputer are written with ladder software package and assemble language respectively. PC with Linux operating system and SUN workstation with Solaris operating system are used as operator interfaces. High level control is made up of some EPICS tools and Tcl/Tk scripts.

INTRODUCTION

HLS is a second-generation dedicated synchrotron light source. It consists of a 200 MeV linac, a beam transport line, and an 800 MeV electron storage ring [1]. The linac control system was initially build in late 1980's [2]. Except some subsystems, most of the system were not computerized. In the computerized subsystems, personal computer (PC) and single board computer were used as operator interface and front-end controller respectively. RS232 and RS422 were used for the communication between PC and single board computers. It used a different communication protocol from the storage ring control system which had been upgraded using Experimental Physics and Industrial Control System (EPICS) [3]. For ease of communication with the storage ring control system and operation, a concerted effort has been put forth to upgrade the linac control system to a new, distributed one based on EPICS in the last two years.

In HLS linac, there are a large number of magnet supplies, beam measurement equipment, and devices in vacuum system, accelerating system, and interlock system. All of the devices and equipment need to be controlled and monitored by the control system. The upgrade has performed in several stages. By now, the following subsystems have accomplished:

- Linac magnet power supply control and monitoring;
- Linac vacuum monitoring;
- Linac flag control and monitoring;
- Interlock system;
- Klystron focus power supply control and monitoring;

- Modulator pulse power supply control and monitoring.

HARDWARE

Hardware structure

The "standard model"[4] is used for HLS Linac control system, which consists of operator interface, input/output controller(IOC) and front-end controller. Fig. 1 gives an overview of the hardware structure of HLS linac control system. A SUN workstation and some PCs are used as operator interfaces to perform high level control. Industrial PC based hardware is widely used in HLS linac control

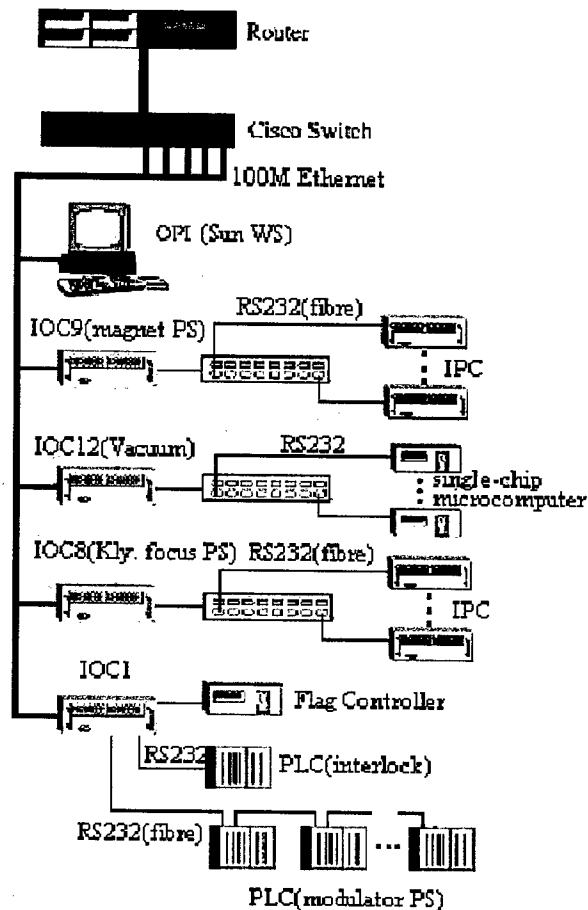


Figure 1: Overview of HLS linac control system.

system. It is used as not only front-end controller but also IOC. Besides PC based hardware, programmable logic controller (PLC) and single-chip microcomputer are also

* gflu@ustc.edu.cn

† Currently works at FEL Lab, Duke University

used as front-end controllers. For example, single-chip microcomputers are used to control and monitor linac vacuum subsystem, and PLCs are used in the interlock system and modulator pulse power supply system. The RS232 serial protocol is used for the communication between IOC and front-end controller. The MOXA's multi-serial card, C168P, is used to add up more serial ports for IOCs. 100M-Ethernet is used for the local area network (LAN) to get high network transport speed. Shielded cable and optical fiber are used for the communication media.

Industrial PC based front-end controller

The industrial PC based front-end controller is mainly used to control and monitor the magnet and klystron focusing coil power supplies. Fig. 2 illustrates its hardware structure which is based on ISA bus technology. Because the specifications of the power supply that are controlled by this type of controller are about 1000 ppm, the 12-bit DAC and ADC cards are used to set and read the power supply current. Relay and digital-in cards are used to control and monitor the power supplies' status respectively. The chan-

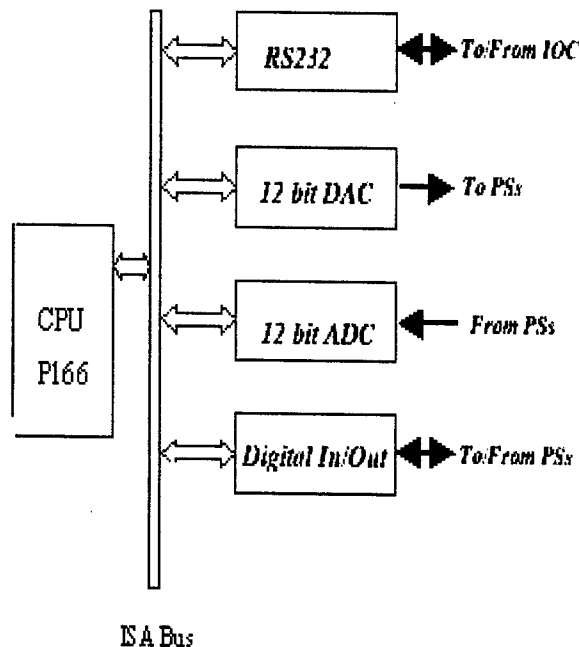


Figure 2: Hardware structure of industrial PC based front-end controller.

nels of these control and monitor cards are determined by the number of power supplies that the controller controlled. To avoid the electro-magnetic interference (EMI) between the controller and the power supplies, optical isolation is adapted in these controllers.

SOFTWARE OVERVIEW

Software of front-end controller

The software for industrial PC based front-end controller has been developed based on VxWorks multi-task mechanism, which consists of three parts (see Fig. 3): communication module, main loop module, and device drivers. The communication module is used to receive/send messages from/to IOC. The main loop module is used to parse the command and data from the message received by communication module and call the corresponding device driver according to the command. It will send messages to the IOC if it gets a read command. The device drivers are used to access the hardware or software channels.

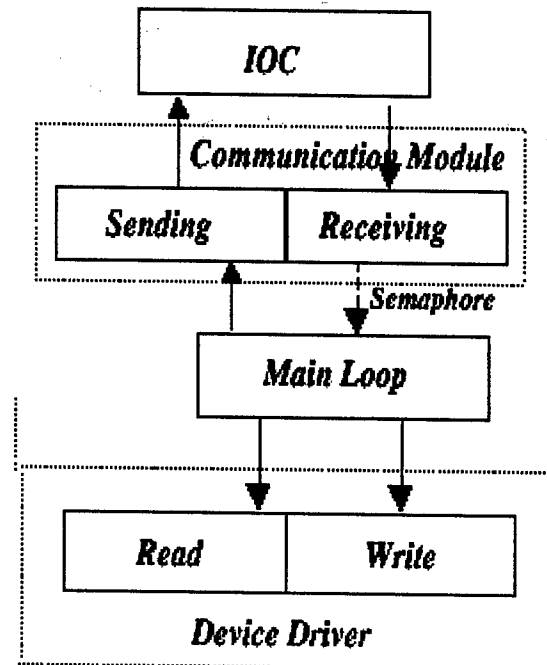


Figure 3: Software structure of industrial PC front-end controller.

The software for PLC is written with ladder software package (LSS), and assemble language is used to develop the software for single-chip microcomputer.

Software of IOC

There are about 1,000 records resident in four IOCs, which made up of the distributed database of the linac control system. The following record types are used: AI, AO, BI, BO, Mbbi (Multi-bit Binary Input), Mbbo (Multi-bit Binary Output), MbbiDirect (Direct Multi-bit Binary Input), MbboDirect (Direct Multi-bit Binary Output), and subroutine. The device support and device drivers for these record type have been developed to access input/output

hardware or field-bus adapter [5]. The state notation language and sequencer are used to perform a number of commands, for example, to interlock and protect the devices.

Some EPICS tools are used for high level control. For example, MEDM is used to edit and manage the control interface screens, Alarm handler (ALH) is used to monitor the alarm status of some devices, for example power supply alarm . status

A number of Tcl/Tk [6] scripts have also been developed to perform high level control, which are used in the routine machine operation and machine study. For example, they are used for the power supply setpoint backup and restore, turning power supplies on and off, magnet cycle, and so on.

CONCLUSION

Most of the subsystems of HLS linac control system have been in operation for a period of time, and the performance is as good as expected. Our experiences have proven that a control system that is build with inexpensive but reliable controllers, for example industrial PC, PLC, and single-chip microcomputer, not only is extremely cost effective but works fine.

REFERENCES

- [1] W. Li, et al, "Upgrade plan for the NSRL control system", ICALEPCS'97, Beijing, China, 1997.
- [2] Rongsheng Xie, "The control system of the Hefei 200 MeV electron linac", Proceedings of the international conference on synchrotron radiation application, Hefei, Chian, 1989.
- [3] Martin Kraimer, "EPICS Input / Output Controller (IOC) Application Developer's Guide", EPICS Documentation on <http://www.aps.anl.gov/asd/controls/epics/EpicsDocumentation>.
- [4] W B. Kuiper, "Issues in Accelerator Proceedings Conference on of International Accelerator and Large Experimental Physics Control Systems", (ICALEPCS 91), Tsukuba, Japan, November 1991, pp. 602-611.
- [5] Philip Stanley, Janet Anderson, Martin Kraimer, "EPICS Record Reference Manual", EPICS Documentation on <http://www.aps.anl.gov/asd/controls/epics/EpicsDocumentation>.
- [6] Brent Welch, "Practical Programming in Tcl and Tk", published by Prentice Hall: ISBN 0-13-182007-9.

APPLICATION PROGRAMMING STRUCTURE AND PHYSICS APPLICATIONS*

C.M. Chu, J. Galambos, W.-D. Klotz[§], T. Pelaia, A. Shishlo, ORNL, Oak Ridge, TN, USA
C.K. Allen, C. McChesney, N. Pattengale, LANL, Los Alamos, NM, USA
D. Ottavio, BNL, Upton, NY, USA

Abstract

The Spallation Neutron Source (SNS) is using a Java based hierarchal framework for application program development. The framework is designed to provide an accelerator physics programming interface to the accelerator, called XAL. Much of the underlying interface to the EPICS control system is hidden from the user. Use of this framework allows writing of general-purpose applications that can be applied to various parts of the accelerator. Also, since the accelerator structure is initiated from a database, introduction of new beamline devices or signal modifications are immediately available for all XAL applications. Direct scripting interfaces are available for both Jython and Matlab, for rapid prototyping uses. Initial applications such as orbit difference, orbit correction and a general purpose diagnostic tool have been developed and tested with the SNS front end. The overall framework is described, and example applications are shown.

INTRODUCTION

The SNS is an accelerator for pulsed, high-intensity neutron production. For general-purpose, high-level accelerator physics applications for SNS commissioning and operation, a Java-based software infrastructure called XAL [1] is designed and implemented. The XAL is a programming framework providing an object-oriented model of an accelerator, interfaces to the SNS control systems for dynamic data and to the SNS global database [2] for static information, interfaces to various external modeling software packages, and a built-in lattice tool [3] mainly for quick, on-line calculation. The entire application software infrastructure is shown schematically in Fig. 1. A subset of the global database is extracted into portable extensible markup language (XML) formatted files which can be any part of the entire accelerator. The communication between the applications and the control hardware is through an EPICS Java Channel Access layer embedded in the XAL. Also, an optional data correlation engine in the XAL ensures the event data collected all occurred within a specified time window, usually the beam pulse width. The framework also provides standard user interface design such as common look-and-feel, Java

logging and user preferences, and on-line help in HTML form. To test the framework and applications without a real accelerator running most of the time, we rely on an accelerator simulator called the virtual accelerator [4] with Trace-3D and PARMILA as model engines and portable channel access server as EPICS data provider. The advantages of this simulator are model-based simulation, and the same data acquisition interface and the same EPICS process variable (PV) settings as been used on the real machine.

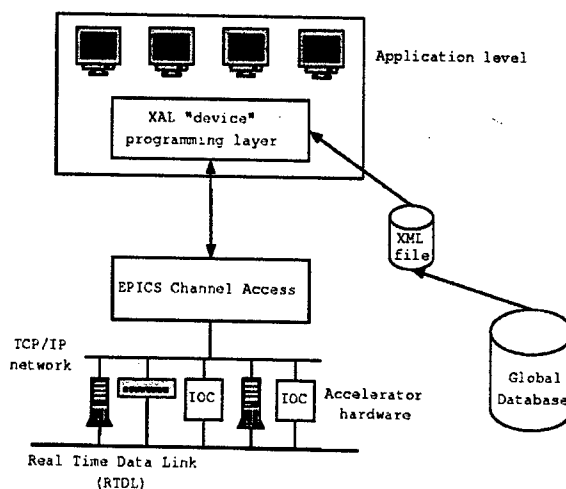


Figure 1: Application software infrastructure.

APPLICATION FRAMEWORK

In Fig. 1, the application framework is represented in the top box plus the connection to the database. A more detail diagram of the framework can be found in Fig. 2. The figure is also a simplified SNS application software design layout. The major parts of this software infrastructure can be categorized in the following subsections.

XAL toolkits

This is the core part of the framework. The framework design is based on hierarchal view of the machine, namely, a tree-like structure with accelerator sequences as branches and accelerator nodes as leaves. However, this physical view of the machine is not quite suitable for accelerator lattice which also contains drift space, split elements for various physics reasons and devices sitting on top of each other. Therefore, a conversion between the machine view and lattice view is introduced in the XAL. The XAL toolkits contain the followings:

* SNS is a collaboration of six US National Laboratories: Argonne National Laboratory (ANL), Brookhaven National Laboratory (BNL), Thomas Jefferson National Accelerator Facility (TJNAF), Los Alamos National Laboratory (LANL), Lawrence Berkeley National Laboratory (LBNL), and Oak Ridge National Laboratory (ORNL). SNS is managed by UT-Battelle, LLC, under contract DE-AC05-00OR22725 for the U.S. Department of Energy.
[§] Also at ESRF, Grenoble, France.

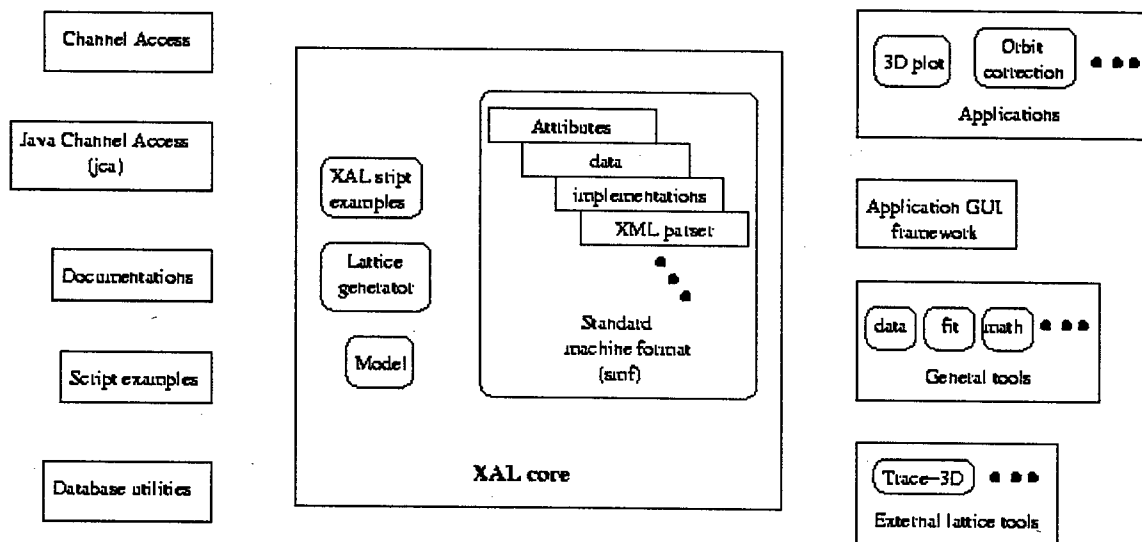


Figure 2: Application framework overview.

- On-line modeling tool providing a quick particle trajectory or envelope calculation. Currently we use external Trace-3D routine as the modeling tool. The on-line modeling tool will replace this external call and increase the flexibility and robustness.
- Standard machine format (SMF) defining an hierarchal view of the accelerator, implementations for various beam-line devices, sets of attributes for both static and dynamic data, and XML parser for file input/output of the accelerator object in XML format.
- Lattice generator providing the conversion between hardware view of the machine (a list of accelerator nodes) and physics view of the machine (lattice elements).
- XAL specific tools such as generating input files with XAL lattice generator for external modeling tools, setting or gathering multiple EPICS PVs.

Channel Access

The communication between XAL applications and accelerator hardware is through channel access. A Java wrapper layer over the native C language libraries provides extra exception handling, thread management and convenient methods for Channel Access. We plan to replace both the wrapper and the Java-to-C library by a pure Java communication protocol in the future.

General Tools

There is a collection of general-purpose tools for applications. These tools can be used independent of XAL. Here is a brief list of the tools:

- Mathematical tools such as elliptical integration.
- Graphical User Interface (GUI) components.
- General polynomial data fitting routine.
- Time correlation for gathering data events within a specified time window. This is a very important requirement for a pulsed machine.

- Standard messaging for saving and passing Java messages.

Database Utilities

As shown in Fig.1, a subset of the global database in XML format is parsed in by applications for initializing accelerator objects. The advantage of this intermediate XML file is portability and providing a hierarchal view of the database. So far we have demonstrated that the lattice generated from the database designed values via the XML file produces the same model result as the original design. Alternatively, direct access from applications to the global database is also possible. The database query and automatic XML generation, and several data validation-check routines are provided.

Scripts and Examples

Scripting language such as Jython can be a quick development or software debugging tool. Also, the Matlab scripting language provides many data analysis tools. Both Jython and Matlab can access XAL by importing their own Java interface libraries. General examples are also provided for quick tutorial purpose. Once a script is proven useful and needs to be more user-friendly, we convert the script to a real Java application.

Application GUI Framework

The idea of using a standard application GUI framework is to try to give every application share the same look-and-feel, so a general user can learn how to use an application more quickly. Also, many GUI components can be re-used in different applications, such as logging service, user-defined preferences, file input and output, etc. This GUI framework can greatly reduce the development time for user interfaces.

As shown in Fig. 3, all the XAL applications will use this GUI framework with common pull-down menus, editing buttons, console output panel, window control and on-line HTML help feature. Application writers can

easily replace or add to any pre-defined feature with customized ones.

Applications

There have been more than a dozen of applications using Java/XAL framework. Examples are orbit display, orbit correction, general-purpose EPICS process variable display, 2-dimensional and 3-dimensional correlation plots, and many other scripts. We also converted some applications originally written in Matlab to XAL-based Java applications for maintenance and improvement purposes. Several applications as examples are discussed in the next section.

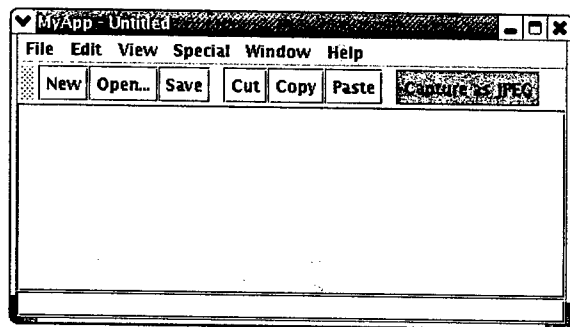


Figure 3: XAL application GUI common look.

APPLICATION EXAMPLES

General Purpose Diagnostic Display

A general purpose beam-line device display application is written for quick device diagnosis purpose. As shown in Fig. 4, the application can display same type of beam-line devices' signals along a given accelerator section as 2-D scattered plot or the same type of PVs versus time as water-fall plot. Plot updating at 5 Hz still maintains reasonable performance. The data plotting package used here and many other applications is JClass version 6.1 [5].

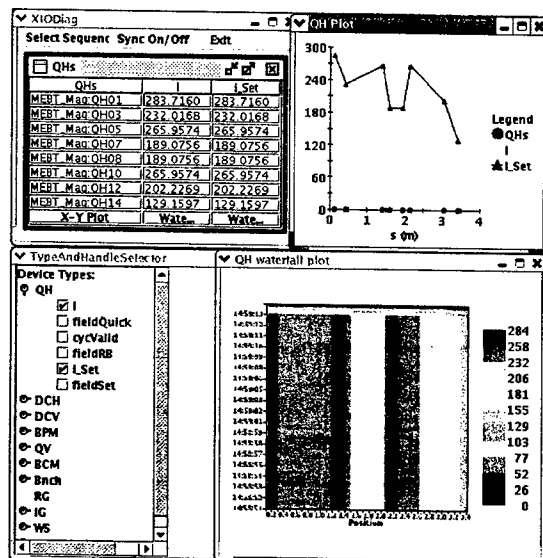


Figure 4: General purpose device display screen snapshot.

Orbit Display

The Orbit display application compares the model-predicted beam trajectory and the beam position monitor (BPM) measured average beam positions. In Fig. 5, the horizontal trajectory differences between before and after a dipole corrector strength change are plotted. The filled circles are model prediction and the squares are BPM measurement. In this particular application, the modeling tool is external Trace-3D Fortran code compiled as a shared library. The initial beam coordinates and momentums for the model are manually settable via user interface.

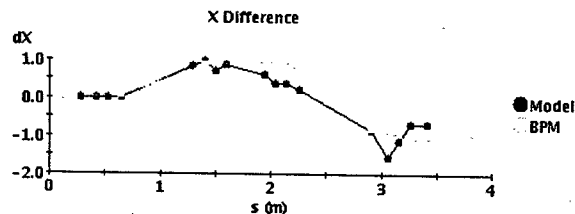


Figure 5: Partial screen snapshot of Orbit Difference Display application.

CONCLUSION

The SNS application framework is in production mode. Many applications using this framework have been tested during the SNS front end commissioning. As the XAL framework becomes more and more stable, we will speed up new application development and convert existing Matlab applications to use this framework. With a common look-and-feel for each application, the end-user will not suffer a steep learning curve. Also, the on-line lattice tool will be tested in the next commissioning period.

ACKNOWLEDGEMENTS

The authors would like to thank the SNS Controls, Diagnostics and Database groups for their great efforts of providing us various hardware and software support. All the other members in the SNS Accelerator Physics group deserve the credit for their valuable suggestions and help. We also thank Dr. N. Malitsky for the original XAL design work.

REFERENCES

- [1] <http://www.sns.gov/APGroup/appProg/xal/xal.htm>.
- [2] J. Galambos, *et al.*, "SNS Global Database Use in Application Programming", these proceedings.
- [3] C. Allen, *et al.*, "A Modular, Online Simulator for Model Reference Control of Charged Particle Beams", these proceedings.
- [4] A. Shishlo, *et al.*, "The EPICS Based Virtual Accelerator - Concept and Implementation", these proceedings.
- [5] <http://java.quest.com/jclass/jclass.shtml>.

SNS GLOBAL DATABASE USE IN APPLICATION PROGRAMMING *

J. Galambos, C. Chu, E. Danilova, A. Shishlo, J. Patton, T. Pelaia, ORNL, Oak Ridge TN, USA,
W.-D. Klotz, ESRF, Grenoble France

Abstract

A global relational database is being assembled to track accelerator components for the Spallation Neutron Source (SNS). As part of this activity, beamline element information is stored for use in high level application programs. A hierarchal accelerator framework is generated from the database and used for initialization of a Java based programming infrastructure. From within this framework input files for beam simulation codes can be generated using either live machine values or design values. The database also includes global coordinates for beamline element alignment, and magnet measurement data. An overview of the table schema and relationships to tables used in other parts of the project are discussed.

INTRODUCTION

The approach of the Spallation Neutron Source (SNS) application programming effort [1] is to write general purpose software which can be applied to any part of the SNS accelerator. To facilitate this, the SNS global database plays an important role as the primary repository for the static data used to configuring applications for a specific parts of the accelerator. In addition to application program configuration, the beamline device information stored in the database is used for other purposes, such as storage of the global coordinates defining the ideal and actual lattice elements positions, design values for magnets and RF, and for external lattice generation.

This paper discusses the general architecture of the beamline device portion of the database. The following sections describe the organization of the beamline device schema, describe some of the ways data is extracted, and show some example applications. There are many other parts of the global database not covered here, particularly related to the equipment aspects. These areas include equipment tracking, maintenance, and calibration data. More detailed information about the SNS global database may be found in reference [2].

DATABASE ORGANIZATION

An important aspect of the SNS global database is its organization around two distinct conceptual components: devices and equipment. A device instance is an abstract component with perhaps some design values. An equipment instance is an actual piece of hardware with a

barcode. Generic information (e.g. design values or position along the lattice) is stored with the device and equipment specific information (e.g. magnet measurement) is stored with the equipment. For example, every magnet has a device record containing its design field, lattice position, etc. There is also a bar-coded piece of equipment that occupies each magnet position. The equipment portion of the magnet database contains the magnet measurement information. A device-equipment association table relates which piece of equipment is installed in a particular device. If a piece of equipment breaks, and is replaced by another, none of the device information changes; only the device to equipment association needs to be modified.

Beamline Devices

Devices are required to be identified by four different predefined pieces: system, subsystem, type and instance. Concatenation of these pieces is the core of the SNS naming convention. The "system" is similar to a primary lattice sequence (e.g. Drift Tube Linac (DTL), Ring, etc.); subsystems include magnets, diagnostic, power supply, etc.; type includes Quad, BPM, RF, etc., and for example "instance" is 1,2,3, etc. Devices include components throughout the accelerator complex, including racks, computer controllers etc. Subsets of the devices are indicated as beamline devices – i.e. components that would normally be found in a modeling lattice file. It is the beamline devices that the application programming is most directly concerned with, and the rest of this paper primarily addresses. But we emphasize that there are no hard boundaries in the global database schema – the application programming configuration also has to access some equipment data. Population and use of the database crosses group administrative boundaries.

Each item that would be treated as an independent element in a typical beam-tracking model is handled as an independent beamline device. For example, in the SNS there are single hardware pieces, each consisting of a quadrupole, a dipole corrector and a BPM. Each of these are treated as three separate beamline devices, all at the same beamline position. Also, each magnetic pole of a magnet assembly is treated as an independent beamline device.

* SNS is managed by UT-Battelle, LLC, under contract DE-AC05-00OR22725 for the U.S. Department of Energy. SNS is a partnership of six national laboratories: Argonne, Brookhaven, Jefferson, Lawrence Berkeley, Los Alamos, and Oak Ridge.

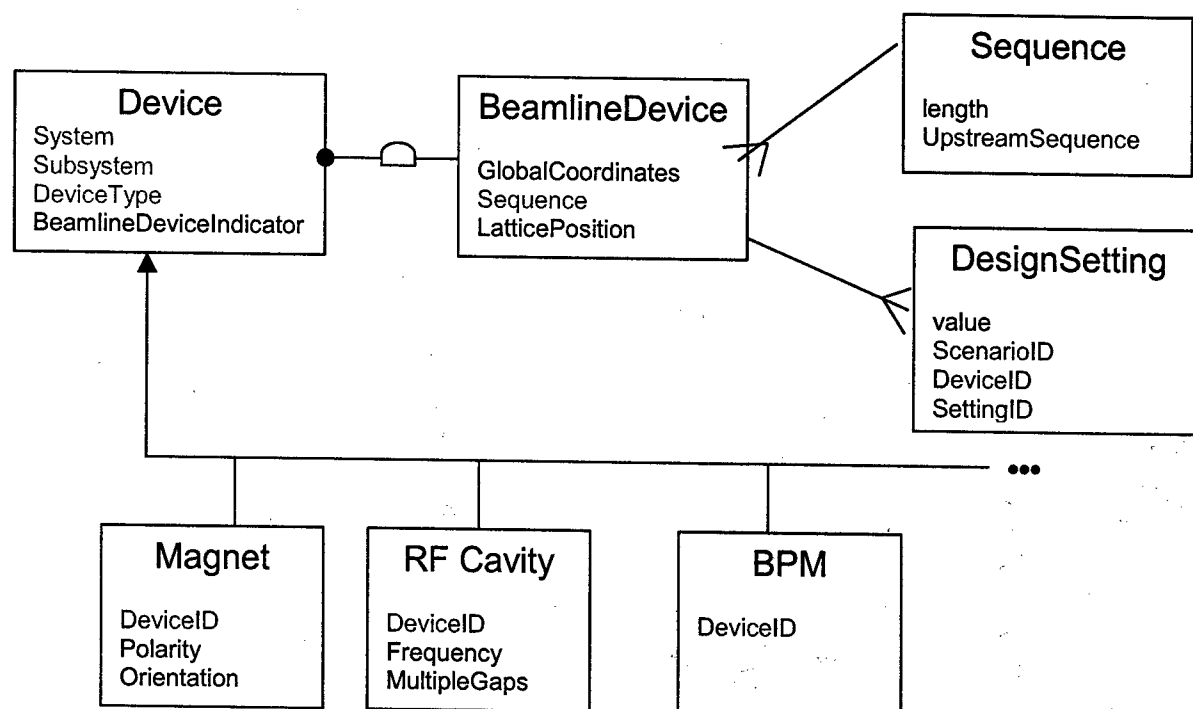


Figure 1. Simplified schematic of the Beamline-device related tables in the SNS global database. Items in red are foreign keys to other table records.

Relationship to XAL Classes

The application-programming framework [2] is Java based and has a class hierarchy describing the accelerator. The SNS database is a relational database (not object oriented), but the table structure is organized to simplify the beamline mapping to the XAL class structure. As shown in Figure 1, beamline device elements belong to a sequence. Information is also stored regarding the beamline device placement within a sequence and which sequences may be concatenated with others. Also, each beamline device has a specified type (e.g. BPM, Magnet, etc.). By using the type identification, proper tables can be found to obtain additional information specific to that device. Also there are tables to hold design values (e.g. baseline field setting for a magnet). Design values have a scenario ID, allowing multiple sets of design values to be stored (but at present, only a single "baseline" set of design values is used).

Connection to the Control System

An important aspect of the application programming framework initialization is relating the beamline devices to the appropriate control system signals. SNS uses the EPICS [3] control system which uses "Process Variables" or PVs to communicate between clients and Front-End

computers. The EPICS PVs are stored in separate tables and used to initialize EPICS setup files (or EPICS "database" files). In the XAL setup procedure, a prescribed subset of the available PVs for each device type are selected and assigned a "handle" that describes their function. For instance we assign the PV that supplies the average horizontal position from a BPM the handle "xAvg". The handle can be used in general actions over a set of devices of the same type.

XML file representation of the XAL accelerator class structure

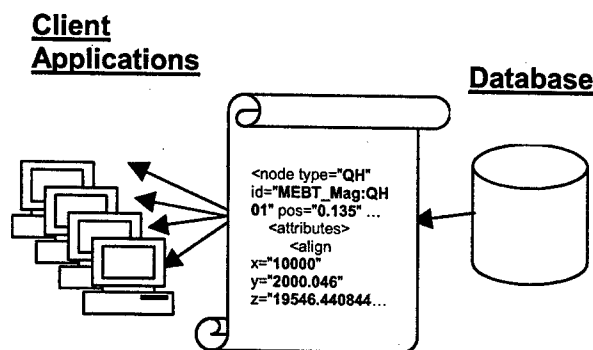


Figure 2. Data flow path from the database to the application programs.

APPLICATIONS

For application programs, the primary use of the database is to acquire the accelerator hierarchy class structure initialization. This is represented schematically in Fig. 2. An XML file is generated by a java-based query, which is subsequently read by client applications on startup. A direct database query from the applications is also possible, but we use the intermediate XML file for reasons of speed and flexibility for quick changes. In the future, a service is planned that will query the database and dynamically provide clients the latest accelerator structure.

Device and Lattice views

Only information about complete physical devices is stored in the database. This view of the accelerator is referred to as the accelerator "data-graph", and is adequate by itself for some applications (e.g. displaying the BPM orbit vs. position). However, for modeling purposes devices must be subdivided and drift spaces between physical elements must be accounted for. This different way of viewing the accelerator is depicted in Fig. 3. The database contains only information about device positions and lengths. All drift space calculation and element splitting is done within the XAL framework. Also depicted in Fig. 3 are views of the "Devices" and "Lattice elements" in XML formats which are used within XAL. This lattice view is used in the XAL online model [4], as well as for creating external model lattice files.

Magnet Families

Another important consideration in configuring the application framework is knowledge of magnet families (on common power supplies) and magnet excitation curve measurements. The mapping of magnets to power supplies is included in the beamline devices tables. Field mapping data is also stored in special magnet measurement tables. This information is associated with specific equipment (as opposed to devices). The

implementation of current to field transformations is to be done at the Front End Controller level (i.e. field information will be available via EPICS). However, the database is being used to provide the necessary field mapping and magnet family information for Front End Controller initialization.

EXPERIENCE

Organization and population of the database has proved to be more labor intensive than originally anticipated. Part of this is due to increasing schema complexity driven by the overlapping needs of diverse groups using the database. At present the beamline elements are roughly halfway populated and the database is being used as the configuration base for the application programs (the SNS accelerator is much less than halfway commissioned now). Even in the initial commissioning stages use of the database to configure applications has proved useful. For example, modification of only a single point to accommodate multiple applications realization that BPM electronics have moved from one device to another. We anticipate the flexibility offered by the use of a database to reap further dividends as SNS moves towards operations.

Acknowledgements

Many thanks to D. O Jeon, E. Tanke, S. Henderson, J. Wang for helping gather data for populating the tables.

REFERENCES

- [1] C. Chu, J. Galambos, T. Pelaia, A. Shishlo, C. Allen, N. Pattengale, "Application Programming Structure and Physics Applications", these proceedings.
- [2] http://it.sns.ornl.gov/mis/MIS_IT.htm
- [3] <http://www.aps.anl.gov/epics/>
- [4] C.K. Allen, C. Chu, J. Galambos, T. A. Pelaia, N. D. Pattengale, "A Modular, Online Simulator for Model Reference Control of Charged Particle Beams", these proceedings.

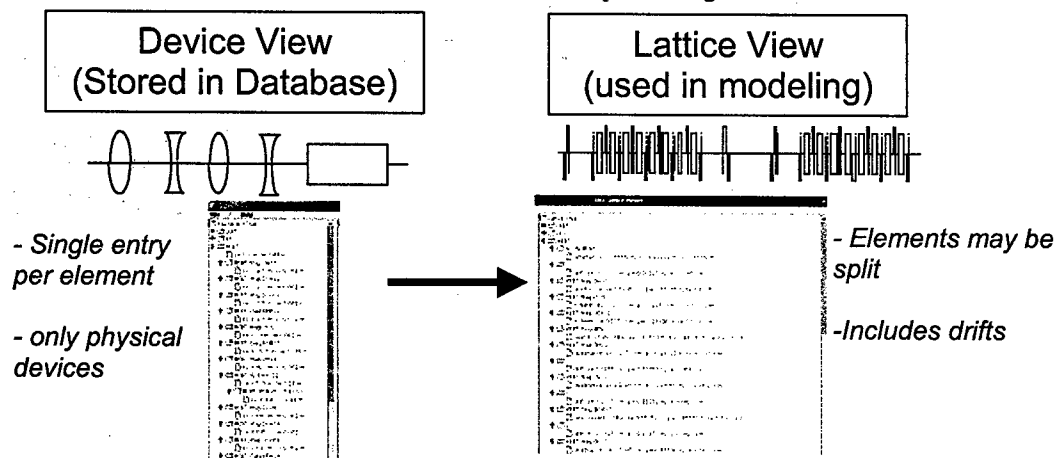


Fig. 3 Schematic of the device view of data abstraction used in the database, and the lattice view abstraction used in setting up modeling sets. The lattice view is constructed within the XAL framework.

THE EPICS BASED VIRTUAL ACCELERATOR – CONCEPT AND IMPLEMENTATION*

A. Shishlo**, P. Chu, J. Galambos, T. Pelaia, ORNL, Oak Ridge, TN 37830, USA

Abstract

A virtual accelerator (VA) concept and an implementation founded on TRACE3D and PARMILA codes are presented. This virtual accelerator is suitable for accelerators with a control system based on EPICS and consists of the EPICS portable channel access server (PCAS), the EPICS client providing communication between a simulation model and PCAS, and the simulation model itself. The virtual accelerators for the SNS linac and experience in using these VAs are discussed.

COMPONENTS OF A VIRTUAL ACCELERATOR

Development of physics applications for an accelerator that does not yet exist presents a nontrivial task (the SNS is an example). In the case of a control system based on EPICS [1] there is an elegant solution facilitating this task. It is possible to create a model imitating the real machine by using the EPICS PCAS and one of the existing simulation programs. This combination of PCAS and a simulation program has been termed the “virtual accelerator” because it looks like a real machine from the EPICS channel access view, operates with real process variable (PV) names, and produces a reasonable response generated by the simulation model. To provide the network communication between the simulation model and EPICS PCAS we need an EPICS channel access client (third part of virtual accelerator). The structure of VA is shown on Fig. 1.

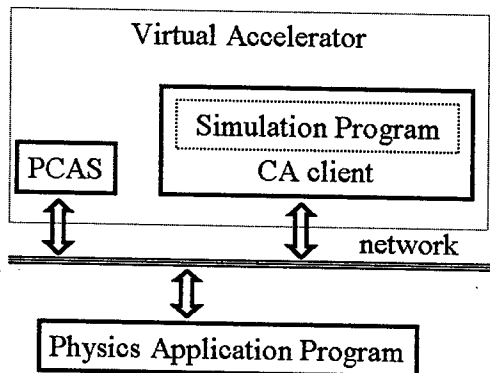


Figure 1. The structure of the virtual accelerator.

A physics application program (see Fig. 1) is a program that is supposed to work with a real machine and communicates only with the PCAS. It is not a part of the

* SNS is managed by UT-Battelle, LLC, under contract DE-AC05-00OR22725 for the U.S. Department of Energy. SNS is a partnership of six national laboratories: Argonne, Brookhaven, Jefferson, Lawrence Berkeley, Los Alamos, and Oak Ridge.

**shishlo@sns.gov

virtual accelerator.

There are certain differences between the real and virtual accelerators. First, the simulation program is not as fast as the real machine, therefore the time delay parameters (if any) in the physics application should be increased. Second, the quality of response is defined by the accuracy of the model in the description of the physics of the real accelerator. An advantage of the VA is that the developers can have as many VAs as they need.

Portable Channel Access Server

The PCAS has been built on the base of the EPICS Release 3.14.1 Portable Server library. For the sake of simplicity PCAS implements only classes related to the synchronous EPICS process variables (PVs) because it is enough for our purposes. It means that our PCAS extends only three abstract base classes from the EPICS channel access server (CAS) library: caServer, casPV, and casChannel. The initialization of the server is performed by using a simple ASCII file that can be prepared by hand or can be generated by the client part of the virtual accelerator. It includes information about EPICS environment variables and the PV's description. In addition to the PV's name the user can specify the lower and upper limits for PV's value, a size for vector PVs, a random error spread for PV's value, and period for applying random errors to simulate noise.

This PCAS has nothing specific for the virtual accelerator and can be used as a usual EPICS portable channel access server.

Simulation Program

A simulation program for the virtual accelerator should meet several criteria:

- It should be reliable in producing the reasonable physical results.
- It has to be fast enough. The calculation time for the considered part of accelerator should be about several seconds. If it is not we cannot talk about interactivity of the model.
- It should be capable to calculate physical values that determine diagnostic signals necessary for the particular physics application program.

At this time, there are two types of VAs. The first type is based on TRACE3D [2], and the second one uses the PARMILA [3] simulation program. These codes are well known and widely used.

Usually the TRACE3D based VA is used to simulate a trajectory of the center of the beam in the SNS linac. TRACE3D code is fast, but it cannot describe beam losses, and so this VA cannot produce diagnostic signals related to the intensity of the beam.

PARMILA is the linac design and beam dynamics simulation code. However, the VA uses its simulation

capabilities only. It is more complex and slower than TRACE3D, but it enables us to simulate the beam position monitor's (BPM) amplitude and phase values, and signals from both the beam current monitors and wire scanners.

CA Client

The CA client part of the virtual accelerator provides exchange of information between PCAS and the simulation code. It gets PV's values from PCAS, transforms them if it is necessary, and puts them as input parameters into the simulation program. After the simulation code finishes calculation, the CA client should extract diagnostic information and put it into the corresponding channel access server's PVs. These actions put into "loop forever" will produce an impression of the live accelerator if the user deals with PVs on the PCAS only. There are two extremely different ways to implement this algorithm.

In the first way the CA client deals with the input and output files of the simulation program only. In the beginning of the calculation loop, the CA client has to prepare the simulation input file with the values corresponding to the PV values from the PCAS at the appropriate places in this file. Then it has to start the simulation program executable file by using the system call. After the simulation code finishes the calculation and dumps output files onto the hard drive, the CA client has to analyze these output files, extract necessary diagnostic information, and put this information into PCAS. This approach does not require any modification in the simulation code, and this is a big advantage of this approach. On the other hand, parsing of the output files can be difficult, and these files may not contain all of the necessary information. For instance, none of the existing simulation programs generates BPM phases and amplitudes.

In the second way the CA client and the simulation code are integrated into one executable and do not use intermediate files for information exchange. For this case, the source code of a simulation program has to be modified to include methods for input data definition and extraction of diagnostic information. These new methods should not interfere with the original source code, so the results of calculations for modified and unmodified simulation programs have to be the same. This approach provides greater flexibility in producing the simulated diagnostic signals, because the CA client has access to all internal information in the simulation code. It enables us to create a new diagnostic method for each of the necessary diagnostic values. The disadvantage of this approach is that the developer should have knowledge about not only input and output files of the simulation program, but also about the details of the program implementation. Therefore, this approach can be used only for a relatively simple simulation code.

In the described virtual accelerators, the second method is used in the VA based on the TRACE3D code and a combination of both methods for the PARMILA based

VA. The different approaches were used because TRACE3D has a very simple structure for input data describing an accelerator lattice and can be easily modified.

TRACE3D CA CLIENT

The structure of the CA client based on the TRACE3D code is shown on Fig. 2.

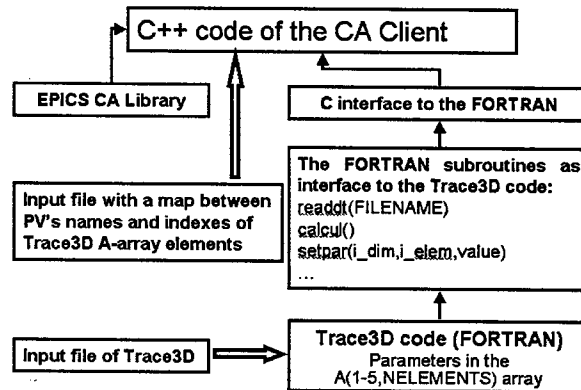


Figure 2. The structure of the CA client and simulation program for the TRACE3D based VA.

As it is said above, the source code of TRACE3D has been modified. The main program has been transformed into the FORTRAN function "calcul" and the part of code that reads the TRACE3D input data has been moved into the "readdt" function. The call of new function that grabs coordinates of the centroid of the beam has been inserted into the main loop of the TRACE3D, which passes through all elements of the accelerator lattice.

A number of new FORTRAN subroutines that work with the TRACE3D data structure were added. They provide the ability to set and read values inside the 2D A-array where TRACE3D keeps all data about the accelerator's lattice elements. Thus, the CA client can synchronize this data with PVs in the PCAS.

There are two files needed to initialize this CA client. The first file is a usual unmodified TRACE3D input file, and the second one is an ASCII map file with PV names for "set" and "read back" variables and indexes of the A-array associated with these PVs. The second file also includes necessary parameters to transform PCAS PV values to the TRACE3D values such as coefficients between current and field strengths for electromagnets.

The algorithm of the calculation cycle of the TRACE3D based CA client is revealed in Fig. 3. In the beginning, it reads data from two input files and initializes the internal structures. Then, it puts initial values into PCAS PVs in accordance with the TRACE3D input file data. Eventually, it starts the main loop of calculations. During this loop, the CA client reads data from PCAS, puts them into the TRACE3D data structure, starts TRACE3D, and places calculated BPM responses into PCAS. There are beam center initial coordinates PVs in PCAS that do not exist in a real accelerator and are

initialized from the TRACE3D input file, but they enable outside applications to change these coordinates without interruption of the VA calculation cycle if necessary.

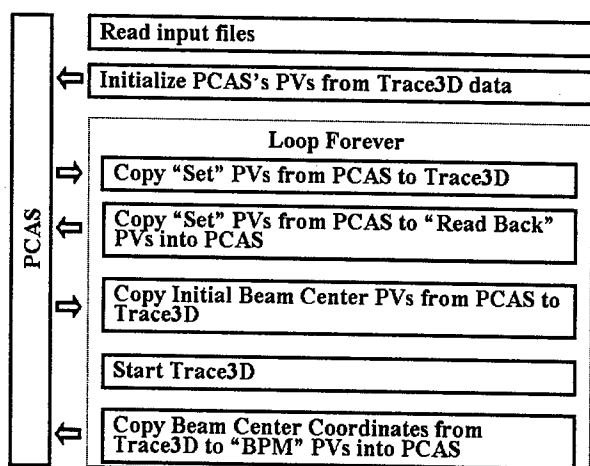


Figure 3. The algorithm of calculations of the TRACE3D based CA client.

Using of the TRACE3D Based CA Client

The TRACE3D based VA is mostly used in the development and debugging of orbit correction application programs. It is very suitable for this purposes, because it is very fast. It takes less than one second to get the beam center trajectory for the SNS MEBT part of the SNS linac that includes about 100 lattice elements.

PARMILA CA CLIENT

The structure of the PARMILA based CA client is similar to the one based on TRACE3D (see Fig. 2.). It includes the modified PARMILA FORTRAN code, additional FORTRAN subroutines providing access to the data about coordinates of macro-particles, and the C interface to the FORTRAN subroutines that enable the CA client to control PARMILA calculations. In either case, one executable file for the CA client is created.

The difference is that the PARMILA based CA client does not work with data structures describing an accelerator lattice directly. Instead, it reads the input PARMILA file with special marks on the places where parameters from PCAS should be placed, keeps this file in memory, at necessary moments edits this file replacing marks by numbers, and dumps the new version of the file onto the hard drive as the new input file for PARMILA. The algorithm of the PARMILA based CA client is shown in Fig. 4. This approach demands minimal changes in the PARMILA source code; only a few lines with calls to the external diagnostic routine were added. This diagnostic routine has access to the inner PARMILA array where the 6D coordinates of the macro-particles are kept. Using this information the diagnostic method calculates average x and y coordinates that are x and y BPM signals, BPM's

amplitudes and phases (the second harmonic of FFT of the longitudinal macro-particles distribution), and the wire scanner signals (the RMS distributions for each of the x and y coordinates).

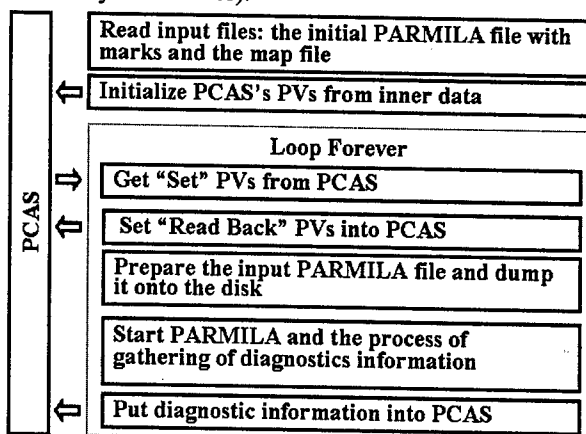


Figure 4. The structure of the CA client and simulation program for the PARMILA based VA.

Using of the PARMILA Based CA Client

The PARMILA based VA provides more realistic simulation of the diagnostic signals, but it is slower than the TRACE3D based one. It takes several or several tens seconds to calculate the propagation of macro-particles through the MEBT. The calculation time depends on the number of macro-particles and the space-charge treatment approach. This VA is used in development and debugging of the RF cavities tuning applications.

SUMMARY

Using EPICS as a base for the control system of an accelerator provides the ability to create realistic simulation software (VA) that can be used instead of the real machine during development of the physics application programs. The combination of the portable channel access server and the accelerator simulation code with the channel access client has been called a "virtual accelerator". These VAs are widely used in application development for SNS and appear to be a useful tool.

ACKNOWLEDGEMENT

Authors thank E. Tanke and S. Aleksandrov (ORNL) for many useful discussions during the VA development.

REFERENCES

- [1] <http://www.aps.anl.gov/epics>.
- [2] D.P. Rusthoi K.R. Crandall. TRACE 3-D Documentation, LA-UR-97-886. LANL, 1997
- [3] Harunori Takeda. PARMILA, LA-UR-98-4478. LANL, 1999.

ACCELERATOR CONTROL MIDDLE LAYER*

J. Corbett, G. Portmann and A. Terebilo, SLAC, Stanford, CA 94309, USA

Abstract

This paper reviews an efficient implementation of the software 'middle layer' that resides between high-level accelerator control applications and the low-level accelerator control system. The middle layer software is written in MATLAB and includes links to the EPICS Channel Access Library. Functionally, the middle layer syntax closely parallels the Family/Index naming scheme used in many accelerator simulation codes and uses the same convention to communicate with both the online machine and the accelerator model. Hence, machine control, machine simulation and data analysis tools are integrated into a single, easy-to-use software package.

INTRODUCTION

As shown in Fig. 1, the *middle layer* provides a set of functions that communicate with machine hardware via the MATLAB Channel Access toolbox MCA [1]. At the heart of the middle layer is a data structure containing *Accelerator Objects* or Families of hardware elements with various attributes: element names, element indices, i/o channel names, unit conversions, etc. The naming scheme mimics the Family/Index convention commonly used in accelerator simulation codes. Hence, the language of simulation codes can be used to communicate directly with either online accelerator components or the model.

The middle layer family definitions are contained in a text file for easy editing. Typical families include dipoles, quadrupoles, sextupoles, correctors and BPMs. An additional *Accelerator Data* structure contains default directory specifications, file names and basic accelerator parameters. Execution of a simple MATLAB script loads both the *Accelerator Object* (AO) and the *Accelerator Data* (AD) blocks into memory - all routines in the middle layer toolbox have direct access to the AO and AD data.

Middle layer *functions* are used to communicate with accelerator hardware and access different family attributes. At present, hardware communications occurs via EPICS Channel Access. In this case, the middle layer provides channel names and keeps track of integer handles for each device thereby buffering the user from detailed Channel Access calls with complicated channel names. Other communication protocols are also possible. The middle layer also accommodates an accelerator model in the MATLAB Accelerator Toolbox (AT) [2,3] or can communicate with a MATLAB model server operating in an EPICS ioc [4]. The ability to switch between 'simulator' and 'online' modes is useful for program development and analysis.

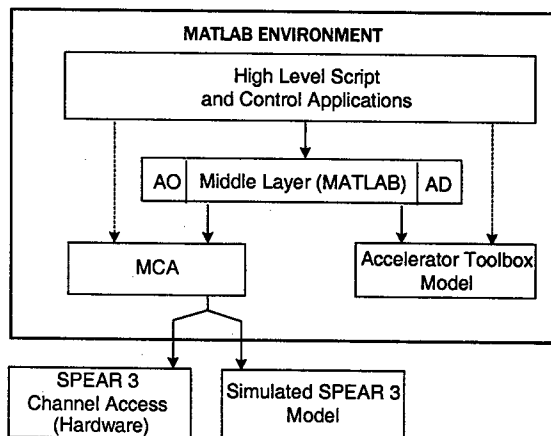


Figure 1: Middle Layer Software Flow Diagram

By design, the middle layer is machine independent - communication with different machines requires the user to reconfigure the *Accelerator Object* file, revise the *Accelerator Data* structure and update the model. Special functions may be required for machine-specific hardware.

USE OF MATLAB

One key feature of our approach to the middle layer is the use of MATLAB. MATLAB provides an active variable workspace, a built-in math library, powerful graphics capabilities and on-going development of new software features. Just as MATLAB can be augmented with commercial 'toolboxes', the Accelerator Toolbox (physics) [2,3], the MATLAB Channel Access Toolbox (EPICS interface) [4] and the Middle Layer Toolbox (controls & data organization) [5] facilitate accelerator simulation and control. All of these functions make use of the array processing capabilities inherent in MATLAB.

At the application level, script-based control sequences and graphical interfaces utilize the middle layer to standardize and simplify programming. At the highest level, MATLAB and the associated toolboxes can be used to control the accelerator - at the Advanced Light Source MATLAB is used for energy ramp, configuration save/restore, global orbit correction, insertion device compensation and beam-based alignment [6]. Response matrix analysis routines are in turn used for accelerator calibration and lattice studies [7]. Several of the high-level ALS functions have been ported to SPEAR 3 and upgraded to the middle layer formalism. Well before SPEAR 3 start-up, the MATLAB tools were used for physics studies and simulated commissioning [8,9].

*work supported in part by Department of Energy Contract DE-AC03-76SF00515 and Office of Basic Energy Sciences, Division of Chemical Sciences.

MIDDLE LAYER NOMENCLATURE

In the EPICS environment each hardware device has a unique set of identifiers or *Process Variables* (PV). Accelerator physicists, however, often think in terms of hardware families (dipoles, quadrupoles) and attributes of the family elements (length, strength, etc). In the middle layer, each family has a nominal set of structure fields (element names, element indices, channel names, etc). Specific hardware elements in a family are referred to by {Family, DeviceList} where DeviceList is an integer doublet {Sector, Index}. A further division of the family structure into *Monitor* and *Setpoint* sub-structures keeps element attributes well organized and fits neatly into the middle layer function architecture. The EPICS setpoint PV names, for instance, are found in Family.Setpoint.Channelnames.

Middle layer *function* names are characterized by a prefix to indicate action: get=[retrieve value]; set=[deposit value]; meas=[measure]; calc=[calculate]. *getsp* retrieves a setpoint, whereas *measchro* measures chromaticity. Step- and ramp- functions are wrappers for the 'set' routine. Wherever possible, functions are written in machine-independent format.

MODES OF OPERATION

Middle layer software can be run in several modes of operation. The *online* mode broadcasts get/set calls to EPICS Channel Access servers. The servers can be connected to live hardware modules or a model server [4]. The *simulation* mode directs get/set calls directly to the local AT model [2,3]. This mode is useful to develop and test control programs prior to deployment and for programs not intended for online use. In practice, get/set calls check if the mode is 'online', 'simulator', 'manual', or 'special.' The 'manual' mode prompts the user for manual data input (e.g. tunes) while the 'special' mode allows the user to define an in-line function to numerically process data.

MIDDLE LAYER FUNCTIONS

The middle layer function toolbox is well established and continues to expand. At present, it contains about 100 functions.

Get and Set Functions

These core functions communicate with Channel Access Servers or the MATLAB Accelerator Toolbox. The two main functions are *getpv* (get EPICS PV) and *setpv* (set EPICS PV). Both functions accept a variety of input formats via the Family/Index convention. Rather general calls are permitted and timing requests are possible. It is important to note that the MCA toolbox communicates with the .val field of an EPICS record. Nevertheless, each *Accelerator Object* family can contain many PV channel names for a given hardware device. A quadrupole magnet family, for instance, can have setpoint, monitor, voltage,

and status PV channel names that refer to the .val field in the associated EPICS records.

Utility Functions

Utility functions allow easy conversion between fields in an *Accelerator Object* family. Examples include *family2common* (convert family name to element common names), *common2dev* (convert common names to numerical device indices) and *common2channel* (convert common names to PV channel names). *getfamilydata* is a particularly important utility function used to access information from an *Accelerator Object* family.

Shortcut Functions

Shortcut functions are designed to reduce number of parameters required in a function call. Examples include *getsp* and *setsp* which communicate with *setpoint* PV's, and *getx/gety* which return horizontal and vertical beam position values. Reference to the channel access handles is performed in the base routines *getpv/setpv*.

Unit Conversion Functions

Unit conversions play an important role in modeling the on-line machine. For this purpose, the middle layer supplies two functions *HW2Physics* (hardware-to-physics) and *Physics2HW* (physics-to-hardware). Both functions accept the Family/Index naming convention but refer to the *Accelerator Object* database to retrieve the numerical conversion algorithm and associated parameters. For SPEAR 3, polynomial current-to-field transfer functions are used for each magnet family. Each individual magnet has an additional numerical scaling factor for detailed modeling applications.

Simulator Functions

These functions *only* communicate with the AT model to return simulated physics parameters. Examples include *getbeta*=(calculate beta functions), *getchro*=(calculate chromaticity) and *getdisp*=(calculate dispersion). MATLAB functions in the AT toolbox can also be used directly to augment the set.

Special Functions

Some devices do not conform neatly with the Family/Index formalism so special functions are created to access the data. An example is *getid/setid* for insertion device gap control. Alternatively, since it is easy to create *Accelerator Object* families, special families can be added for a specific task. The storage ring tunes, for instance, can be represented by a family structure containing fields for the common names, channel access handles and golden tunes. For ramping applications an *Accelerator Object* with every magnet involved in the ramp can be created.

DATA MANAGEMENT

Robust data management for accelerator control and accelerator measurements can be a challenging task. The *Accelerator Objects* framework organizes element names and attributes in a local database. In principle, much of the AO data can be loaded from a master site-wide database if it exists. But this is not always the case - SPEAR 3 studies in MATLAB commenced years before a database was available. The *Accelerator Data* structure contains machine- and middle layer specific data that resides outside of the site-wide database. Examples include calculated physics parameters and directory locations to store measured data.

APPLICATION PROGRAMS

A primary reason for middle layer software is to simplify script construction and high-level application programming. Scripts rely heavily on middle layer software to perform correlated perturb/measure studies. Application programs can be dominated by user-interface software but again benefit from the middle layer for machine control and data handling. In both cases the middle layer buffers the user from detailed Channel Access calls. The middle layer also provides high-level functions for common accelerator physics tasks. Examples include:

- (1) *measresp*mat - measure response matrix
- (2) *getresp*mat - read response data from files
- (3) *measdisp* - measure the dispersion function

SUMMARY

The MATLAB middle layer provides convenient and easy-to-use 'glue' for experimentalists and application programmers to access online hardware, model programs and data analysis tools. In conjunction with the inherent flexibility of MATLAB, the middle layer allows rapid software development and testing. Due to the machine-independent nature of the software, it is readily adapted to other accelerators, particularly storage rings and LINACS which feature magnet families and repetitive cells. In principle, the middle layer can be adapted to other applications in experimental physics and industrial control.

ACKNOWLEDGEMENTS

The authors would like to thank D. Robin, H. Nishimura and C. Steier at the ALS for a fruitful on-going collaboration - many of the original concepts were developed under their watch. We are also grateful to M. Cornacchia, J. Safranek and the SPEAR 3 project for support in this area.

REFERENCES

- [1] A. Terebilo, "Channel Access Toolbox for MATLAB," Proc. of 8th ICALEPCS, San Jose, USA, Nov. 2001.
- [2] A. Terebilo "Accelerator Modeling with MATLAB Accelerator Toolbox," PAC'01, May 2002, pg. 3203.
- [3] A. Terebilo, "Accelerator Toolbox for MATLAB," SLAC-PUB-8732 and www-ssrl.slac.stanford.edu/at/.
- [4] A. Terebilo, "Simulated Commissioning of SPEAR 3," these proceedings.
- [5] G. Portmann, et al, "Middle Layer Software for Accelerator Control", SSRL Internal, Dec. 2002.
- [6] G. Portmann, "ALS Storage Ring Setup and Control Using MATLAB," LBL LSAP Note #248, June 1998.
- [7] J. Safranek, et al, "Linear Optic Correction Algorithm in MATLAB," these proceedings.
- [8] J. Corbett, et al, "Orbit Control Using MATLAB," PAC'01, Chicago, May 2002, pg. 813.
- [9] A. Terebilo, "Global Beam-Based Alignment Method," these proceedings.

SIMULATED COMMISSIONING OF SPEAR 3 STORAGE RING

A. Terebilo, D. Keeley, J. Corbett, G. Portmann, SLAC, Stanford, CA 94309, USA

Abstract

In preparation for the commissioning and operations of SPEAR3 we developed a number of high-level accelerator control applications. We also developed a test platform that simulates the physics of a storage ring. To any application using EPICS Channel Access protocol it appears as a real storage ring: measurable parameters such as orbits and tunes change in response to the changes in the accelerator hardware setpoints.

BACKGROUND

SPEAR3 synchrotron light source will be commissioned soon at SSRL. New EPICS control system software will make most of the existing high-level applications obsolete. It is challenging to commission a new facility with this many new software applications most of which were never tested on a real machine.

Many simple applications such as operator menus, panels, live data and history displays present less of a challenge because they are built using standard EPICS toolkit components and they can be tested against dummy CA servers.

Accelerator physics applications that implement measurement functions or control algorithms are inherently more complex and require *realistic behavior* of the simulated variables in order for the tests to be meaningful.

COMPONENTS

We developed a platform for testing such accelerator physics applications, the Model Server. Figure 1 shows the component diagram of the Model Server.

Portable channel access server

A Basic EPICS portable channel access server (PCAS) [1] serves Process Variables (PV's) commonly used by accelerator physics applications:

- Orbits (Beam Position Monitor readings)
- Corrector magnets
- Magnet setpoints (quadrupoles and sextupoles)
- RF frequency and voltage
- Betatron tunes

Physics Simulator

Physics simulator is a MATLAB [2] program. It uses Matlab Channel Access (MCA) Toolbox [3] to communicate with PCAS. It uses Accelerator Toolbox (AT) [4] to make accelerator physics calculations. We run MATLAB on the same CPU as the PCAS but it is not a requirement since all communications with PCAS go through channel access.

The physics simulator performs the following tasks:

- Maintains connections to PV's in PCAS
- Sets and maintains EPICS monitors on the PV's that may be modified by tested applications
- Maintains an AT model of a storage ring. The model updates when test applications change the values of corresponding PV's on the PCAS
- Periodically computes the close orbits, betatron tunes, synchrotron frequency and posts them to PCAS

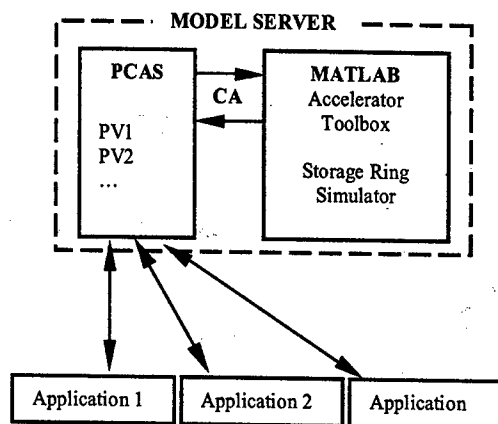


Figure 1: Model server – an application testing platform.

Random noise and systematic errors may be optionally added to computed closed orbits and frequencies. A delay can be introduced beyond the required computation time to simulate processing delays in the control system

Tested applications

An application under test communicates with the Model Server as if it was a real machine. The behavior of orbits and tunes is completely physical.

Most of the SPEAR3 accelerator physics applications are also MATLAB programs that use Channel Access Toolbox, Accelerator Toolbox, and Accelerator Control Middle Layer [5].

REFERENCES

- [1] J. Hill, "Channel Access Portable Server Reference Guide", available at <http://lansce.lanl.gov/lansce8/Epics/>
- [2] www.mathworks.com
- [3] A. Terebilo, "Channel Access Toolbox for MATLAB", Proc. ICALEPCS 2001
- [4] www-ssrl.slac.stanford.edu/at/
- [5] J. Corbett, "Accelerator Control Middle Layer", these proceedings

A NEW REAL-TIME OPERATING SYSTEM AND PYTHON SCRIPTING ON ALADDIN*

D.E. Eisert[#], R.A. Bosch, K.D. Jacobs, K.J. Kleman, J.P. Stott, Synchrotron Radiation Center, University of Wisconsin-Madison, 3731 Schneider Drive, Stoughton, WI 53589-3097, USA

Abstract

We are in the process of upgrading the VME processors on the Aladdin electron-storage-ring control system. The last major redesign of the control system occurred in the mid 1980's. At that time we converted to VME microcomputers and VAX/VMS workstations communicating via Ethernet. This is the second upgrade since then of the VME processor. As upgrades of the Motorola 680x0 processor are no longer available we have decided to switch to the Intel Pentium III. This change allowed us to reconsider our use of the rather primitive μ C/OS kernel and implement a commercial real-time OS. We decided to use QNX primarily as it was a good match to our existing software and was zero cost. In addition to upgrading the CPUs we have also added a new scripting language to our main control application. We used SWIG (Simplified Wrapper and Interface Generator) to create wrapper code for the scripting software. SWIG can create wrapper code for many scripting languages so our initial choice of a scripting language was not critical. We decided to start by using Python due to the many available add-on libraries and the apparent ability to support larger projects. We will discuss our evaluation process and the challenges we encountered.

INTRODUCTION

Our present control system utilizes several generic desktop PCs running Windows 2000, eight VME systems running QNX [1] and ten dedicated power-supply controllers running μ C/OS [2,3]. The network is primarily 100 Mbps switched Ethernet with a 1 Gbps over copper link between the storage ring and the control room. Our new VME processor boards (VMIC 7750) use a 733 MHz Pentium III processor and have 64 MB of Compact Flash storage, 64 MB of SODIMM RAM and dual 100 Mbps Ethernet ports. These boards replaced processor boards based on the Motorola 68030. The dedicated power-supply controllers are built into our dipole and quadrupole power supplies. They were updated with new VME processors based on the Motorola MC68360 in 2000. These controllers are actually the oldest processors in our control system.

The size of our control system is smaller than many facilities [4]. As a result we no longer have a controls group. Several years ago the controls group was trimmed from three staff members down to one. The responsibilities were also reduced and no longer include facility computing and network support. The operations

group supplies staff for cabling and transition panel work as needed by the control system.

REAL-TIME OPERATING SYSTEMS

For the last ten years we have been using μ C/OS for simple task management. It doesn't include any support for networking or memory management. We wrote our own networking software and simple heap management software. Typically our budget is consumed by hardware purchases so we are forced to write our own software or find an open source solution.

While investigating many possible real-time operating systems, we discovered that QNX had recently changed its licensing policy. The software was now offered free for non-commercial use. We verified with their sales department that this new licensing policy allowed us to use QNX free of charge.

Some possible operating system choices included μ C/OS, RTEMS, several versions of real-time Linux and QNX. μ C/OS has served us well but we desired a more complete package. RTEMS appeared to be an improvement over μ C/OS but its support is not as strong as real-time Linux.

The choice was narrowed down between the various real-time Linux systems and QNX. QNX has many advantages for us:

- Drivers are separate from the kernel and they run in their own protected address space. Rebuilding the kernel is not required for every driver change.
- Drivers can be started and stopped independently from the kernel.
- QNX's built-in message passing functions closely matched our existing software's need for interprocess communication.
- QNX has a cleaner implementation of its networking software. Linux switches out of its real-time kernel for network communication.
- QNX has a much shorter learning curve for people unfamiliar with Linux. There is no need to learn how to build the kernel or how to write kernel drivers.

PROCESSOR SELECTION

With the availability of no cost real-time OS's the decision of processor architecture became less important. The decision could now be made based on cost vs. performance. We requested bids for a VME processor board with a Pentium III, Celeron or Motorola MPC750 processor. We also specified some form of on-board flash memory, 100 Mb Ethernet and a PMC expansion site.

* Work supported by the U.S. National Science Foundation under Award No. DMR-0084402.

[#]deisert@src.wisc.edu

Unfortunately it seems that many vendors don't like to respond to the generic bids required by our purchasing department. But we did receive a reasonable selection of low bidders with prices that varied by less than about 10%. The VMIC board with the Pentium III clearly had the most computing power. Other benefits included removable/upgradeable RAM and Compact Flash, two Ethernet controllers and available on-board 32-bit timers.

One concern is that the heat generated by the Pentium III is greater than that generated by the PowerPC processor. VMIC claimed that with proper cooling the Pentium III processor would not have problems. To test this a VMIC board was initially configured to run Windows 2000. A CPU thermal stressing program was downloaded from the Internet. The processor temperature climbed to 50 °C in about 5 minutes. The BIOS was configured to throttle down the processor by 50% at that temperature. In the throttled down state it would cool off and then the BIOS would return the processor to full speed. This cycle would continue indefinitely. Unfortunately the early BIOS must have been configured to set a flag if it reached the throttle down temperature. When attempting to reboot after this test, the board indicated a problem by flashing a LED. VMIC's documentation instructed that the board must be returned to the factory. The service record from the factory only indicated that the BIOS firmware had been updated to fix the flashing LED. This would not be suitable for number crunching but it probably does not represent a problem for real-time control applications.

CODE DEVELOPMENT

The first task in porting our software was writing a driver for the PCI-VME bus interface (Tundra Universe II). At that time VMIC had not written the driver for the latest version of QNX. In fact they suggested they might be interested in supplying the prior version's source code to us if we would update it for them. We declined since the source code was available for a Linux driver. Creating the QNX version did not prove to be an overly ambitious project.

Most OS driver protocols typically require procedures that are similar to the standard file processing functions. These procedure calls allow only a limited number of parameters to be passed. Our original drivers assume that the interface would allow a significant number of parameters to be passed with the function calls. Initially we thought of trying to bypass the built in driver support library and communicate via a lower level raw message format. But one of the many technical articles available on QNX's web site detailed an easy method to extend the driver call to pass the parameters we required.

One of the unique features of our drivers is their ability to be restarted on the fly. When the new driver is started, it requests all of the information needed to restart the driver from the old process. The old driver then exits and the new driver is able to initialize without modifying the contents of the board's registers.

We were concerned that the architecture change would cause byte order problems. The Motorola and Intel processors use different integer byte ordering. The VMIC board has on-board hardware to automatically correct byte order problems. As a result, all but one of our drivers were ported without any special consideration to byte order. The driver that had difficulty was a stepping motor driver that required four byte integers to be written to a byte wide register.

Polling the analog input boards requires several percent of the CPU. This may seem curious at first since the task does not require much processing. Upon further investigation it appears to be caused by bus throughput limitations. Our older 16 bit VME bus can only transfer data at about 1.2 MB per second.

INSTALLATION

The VME processor boards were upgraded over a nine-month period. During that time both the new and old processors were used together in the control system. Normally the processor would be changed during the beginning of a ring development period coinciding with other work on the ring. After initial testing the system would be monitored for the rest of the development period. If no problems were detected, it would remain on the ring during the user period.

One of the VME systems developed problems after installation. Approximately once a week the system will stop servicing interrupt requests on the VME bus. The system is nearly identical to several other systems that do not have this problem. So it may be a very subtle software bug or hardware related problem. The problem is too infrequent to isolate during development periods. The work around is to monitor interrupts in the PCI-VME Tundra Universe driver. When a lockup occurs, a shell script is spawned to kill all of the affected drivers. The drivers are then restarted within in about a second. This is done without losing any of the stored beam. A small delay may occur in some of our feedback loops but it should be nearly impossible for the users to detect. We hope to have this problem fixed soon but the ability of QNX to restart drivers without rebooting is quite impressive.

CONTROL SOFTWARE

The primary program used to operate our facility is called the Page Program. The program is very easy to use and its tabular appearance allows a significant amount of information to be neatly displayed on the screen. Much of its basic look and feel has not changed in over a decade. Operators like the consistency of the user interface. But for many years there have been requests to improve its primitive built-in scripting language. The amount of work involved seemed considerable due to the program's internal dependence on its own scripting language.

We did have another method to develop programs without having to write traditional software. In the mid 1990's LabView had been extended to allow access to the control system. LabView could create great looking GUI

screens and had built in plotting and data analysis. Our beamlines had been using it for years but most staff are reluctant to use it.

THE TOOLS

There are several open source scripting languages to choose from. Tcl/Tk seems to be very popular but the syntax is very similar to shell scripts. Python's syntax looked appealing due to its greater similarities to a traditional programming language [5]. It also appeared to have more libraries, including matrix libraries.

The initial choice of a scripting language soon became irrelevant. SWIG claims to allow applications to be written for most of the popular scripting languages with only minor changes [6]. Being a small facility we only wanted to support one language. SWIG allowed us to initially pick any language we wanted without the risk of making the wrong choice.

EMBEDDING THE LANGUAGE

The first step was to write an extension for Python using SWIG. After only a couple of days most of the common operations were available, such as reading and writing device settings and device database queries. The software was installed on one workstation and a notice was e-mailed to a small group of staff members. The response was immediate and very enthusiastic. Several staff members dropped their current projects and started experimenting with the new software. Another week or two was spent testing, documenting and adding new functions to this extension. The DLL extension was also used to enable control system access for IGOR and MATLAB.

The next step was to replace the primitive scripting in the Page Program. This proved to be quite simple but time consuming due to the number of functions that were created for Python. Redirecting Python error messages posed a slight difficulty. Python documentation explains the procedure but the task could be made a bit more straightforward. It is also possible to create multiple threads in the program all running Python scripts. It was decided to limit the program to only one thread running a Python script due to the possible confusion it could create for the operators.

The final step was to translate all of our existing scripts into Python. The original scripting language was modeled after VAX/VMS's Digital Command Language. It allowed command options to be placed anywhere in the command string. In only a few hours a Python script was written that did the translation. More than 100 scripts were translated to Python in a single afternoon.

IMPLEMENTATION

Surprisingly most of the initial scripts that were written performed operations that were already available in existing software. But eventually these scripts became building blocks for larger measurement operations.

Scripts were written to change lattices, apply quadrupole corrections and start orbit feedback and undulator compensations with the click of a button. Many scripts are so complex that they require several hours to execute. Scripts have also been used to create feed forward control loops for newly installed hardware.

The original work on creating a Python extension proved to be very useful. Initially it was written only to experiment with the scripting language. But it now allows us to spawn Python scripts that are independent from our main control program. It has also been useful for developing new scripts during user periods. Access to the control system is prohibited from most PCs therefore initial debugging can be performed on them without affecting the ring. Access control will be expanded in the future to allow limited real-time access to the control system from these systems.

Excessive reliance on scripting for normal operation could create some problems. Operators could become complacent and would be less likely to notice problems unless the script or other monitoring software detects them. Operators could lose the ability to recover from problems if a routine configuration script fails. Operators need to review the procedures frequently and stay informed about changes to maintain their skills.

CONCLUSION

Replacing our older VME processor boards has brought increased reliability and future expandability. Some staff were disappointed that they did not detect any change after the upgrade. Actually the primary goal of the project was to implement the change without disruption. The initial software was created to be identical to the old system while creating a base of expansion for years to come.

The new scripting software appears to be serving the needs of the accelerator development group. This clearly demonstrates that ease of use is very important to the acceptance of a tool. An added benefit is the ability to distribute software related work across more individuals. The focus of the controls related work can now be more concentrated on supplying tools for the operation and accelerator development groups rather than end user applications.

REFERENCES

- [1] <http://www.qnx.com>
- [2] Jean J. Labrosse, *µC/OS The Real-Time Kernel*, R&D Publications, (1992).
- [3] D. E. Eisert, Fermilab Report CONF-96/069, 851 (1996).
- [4] J. P. Stott and D. E. Eisert, *Nucl. Instr. and Meth. A293*, 107 (1990).
- [5] <http://www.python.com>
- [6] <http://www.swig.org>

CONTROL SYSTEM FOR THE SUPERCONDUCTING INSERTION DEVICES OF NSRRC

Jenny Chen, C.K. Chang, K.H. Hu, Demi Lee, S.-Y. Hsu, C.S. Hwang, C.H. Kuo, K.T. Hsu
National Synchrotron Radiation Research Center
101 Shin-Ann Road, Hsinchu Science-Based Industrial Park, Hsinchu, Taiwan.

Abstract

To enhance hard X-ray production in the 1.5 GeV storage ring of NSRRC to serve the rapidly growing X-ray user community in Taiwan, the storage ring are planed to install up to five superconducting insertion devices. A 6 Tesla superconducting wavelength shifter was installed in mid-2002. A 3.2 Tesla superconducting multi-pole wiggler will be installed in the fall of 2003. The project for the other three multi-pole wigglers is launched. The control system had been implemented to support the operation of the superconducting insertion devices. The control system play a role to coordinate the operation of the main power supply and the trimming power supplies to charge/discharge the magnet and provide interlock protection for the magnet coils and vacuum ducts. A friendly user interface and various application programs are used to support routine operation. Design considerations and details of the implementation are also presented.

INTRODUCTION

The 1.5 GeV storage ring of NSRRC is a low-energy machine. Superconducting insertion devices have been installed to increase the photon flux in the hard X-ray spectral range and thus enhance X-ray production, to meet the increasing requirements of X-ray users. A compact cryogen-free 6 Tesla superconducting wavelength shifter (SWLS) has been constructed because of the limited space in the injection straight section [1]. Plans exist to install four superconducting multi-pole wigglers. One (SMPW6) has a designed field of 3.2 Tesla, a period of 6 cm, and 32 poles; it will be installed in the fourth straight section at downstream of the superconducting RF cavity. The other three multi-pole wigglers (SMPW-A) are planned to install near the second bending magnet of the triple bend achromat sections [2]. The control system for superconducting insertion devices is a VME crate based system. A PowerPC-based VME host module runs a LynxOS real-time operating system. The application programs and user interface of the control system are implemented for the superconducting insertion devices routine operation and data acquisition.

ELEMENTS OF THE SUPERCONDUCTING INSERTION DEVICES CONTROL SYSTEM

The basic elements of a superconducting insertion

devices control system are the cryogenics system monitoring, the liquid level control of the cryogenics system, charge/discharge the magnet, quench detector, interlock logic and operation interface. Figure 1 illustrates the structure of the superconducting insertion devices control system. The cryogenics instruments monitor the parameters of the cryogenics system, including temperature, liquid level, gas pressure and gas flow rate in routine operation. Process controllers regulate the liquid helium (LHe) level and the liquid nitrogen (LN₂) level in the cryostat. The main power supply and the trimming power supplies are coordinated by the control system to charge/discharge the magnet coils. Two correctors can be added to upstream and downstream of the insertion devices to compensate for distortion of the beam orbit. Interlock logic protects the magnet when the coils quench and protects the vacuum ducts from damage by a mis-steered beam. The user interface is provided in the control consoles. Control consoles communicate with the VME host module via the control Ethernet.

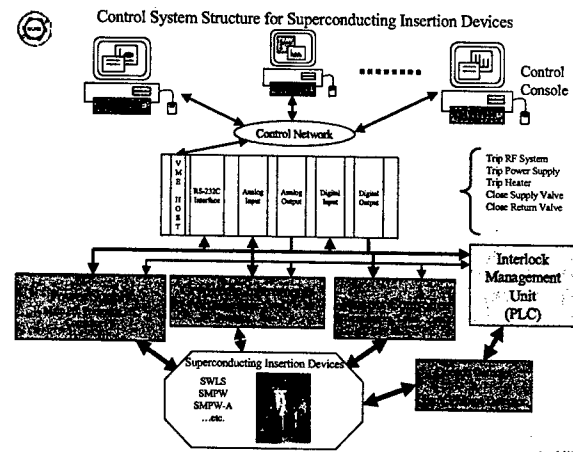


Figure 1. Control system for superconducting insertion devices.

IMPLEMENTATION DETAILS

The control system for superconducting insertion devices adopt standard VME crate running a real-time operating system as a local controller. The crate includes the analog input/output module, the digital input/output module and the RS-232 interface module. The local controller organizes the power supplies, the cryogenics instruments, the process controllers, the quench detector, and the interlock logic. Figure 2 shows the control system for SWLS in the equipment area of NSRRC.

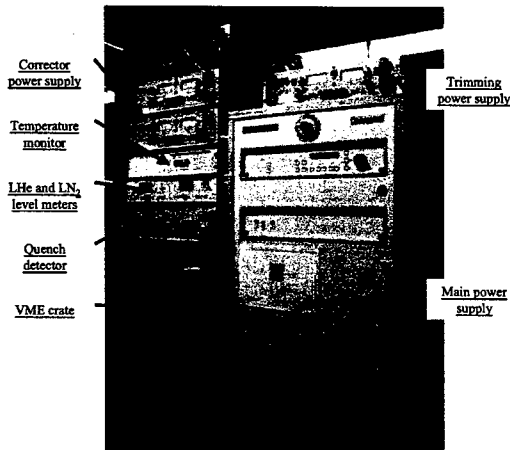


Figure 2. Control system of the SWLS.

Cryogenics Instrumentation

The cryogenics instruments include a temperature monitor, level meters for LHe and LN₂, pressure meters for He gas and N₂ gas, a vacuum gauge, a flow meter of He gas, process controllers and heaters. A LakeShore temperature monitor is used to measure the temperature of the helium space and the vacuum chamber. The SWLS is cryogen-free and the coils are cooled by a cryocooler. The coils of the SMPW6 are soaked in liquid helium to maintain their superconductivity. The cryogenics plant provides LHe and LN₂ to the cryostat of SMPW6. The PID process controllers regulate the LHe and LN₂ levels in the cryostat and the liquid levels are measure by the AMI level meters. The goal is to maintain the level of the liquid and the pressure of the gas at constant values. The heaters in the cryostat are to warm up the magnet and bake out the beam tube.

Power Supply Control

A bipolar main power supply and trimming power supplies are used to charge/discharge the magnet. The output current of the trimming power supply follows the main power supply to nullify the first field integral. If the current is ramping too fast, then the coils will generate excess heat and make increase the temperature. In routine operations, the slow rate of the main power supply of the SWLS cannot exceed 0.6 A/sec, to prevent coils quench.

Quench Protection Circuit

The hardware quench protection circuit is a network of R620 cold diodes and 5 mΩ stainless steel resistors that connects the coils to limit the peak voltage when the coils quench. The diodes do not conduct in the routine operation. When the coils quench, the voltage across the coil will increase quickly. The protection diodes will conduct bypass current. The resistors in series with the diodes assist in dissipating the store energy in the coils. Figure 3 shows the quench protection and detector circuit. A traditionally bridge circuit is used to detect a quench. When the coils of magnets approaches quench, unbalance of the coil arm voltage and the resistor arm voltage lead

the signal of the quench detector to trigger the protection logic in PLC. The voltage signals of the magnet consist of two parts - one is across the charging leads, and the other is across the coils. These signals are available for use in interlock logic.

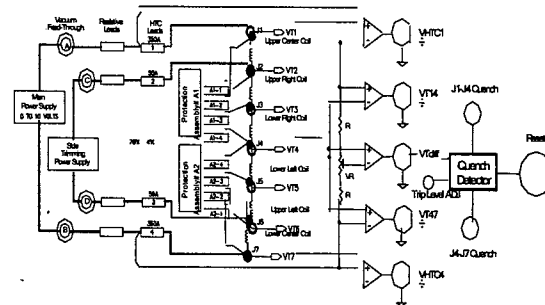


Figure 3. Quench protection and detector circuit.

Interlock Protection

The interlock logic is integrated in a programmable logic controller (PLC) [3]. The PLC collects data on the temperature, the LHe and LN₂ levels and the pressures of the He and N₂ gases in the cryostat, the quench detector and the lead voltage monitor are treated as hardware interlock signals. The protective actions are as follows. When the temperature in the He space exceeds the high limit or the LHe level is below the low threshold or the quench detector triggers the interlock logic, shutting down the power supply. When the pressure of He gas exceeds the high limit, the LHe supply valve is closed and the power supply is shut down. If the temperature of the vacuum chamber exceeds the high threshold, then the control system will shut down the RF system. The software interlock logic is built into the application programs. The power supply stops charging when the temperature in the He space is too high or the LHe level is too low.

USERS' INTERFACE AND APPLICATIONS

Application programs and user interfaces are provided to support routine operation. The user interface of the system for controlling superconducting insertion devices has two pages. On the first page, operators can monitor the statuses of the superconducting insertion devices and set the output current and slew rate of the power supply. Figure 4 shows this page for SWLS. The second page presents the interlock status and the alarm limit. The operator can set the alarm limit and reset the interlock logic on this page. Figure 5 shows the second page of the user interface for SMPW6.

CURRENT STATUS

Installation of SWLS had been done in early 2002. Commissioning has been finished in late 2002. The control system of SMPW6 is being implemented and will complete in June 2003. Preliminary design of the control

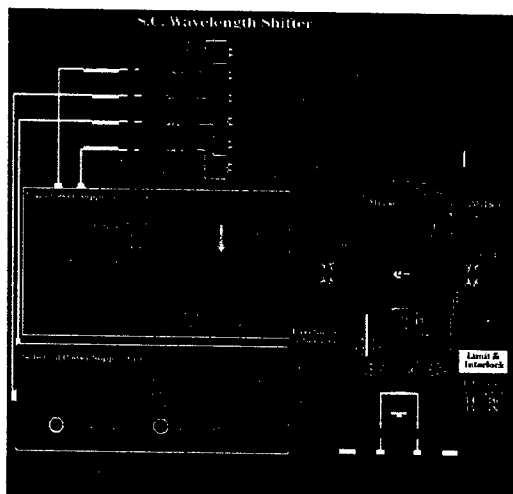


Figure 4. User interface for routine operation.

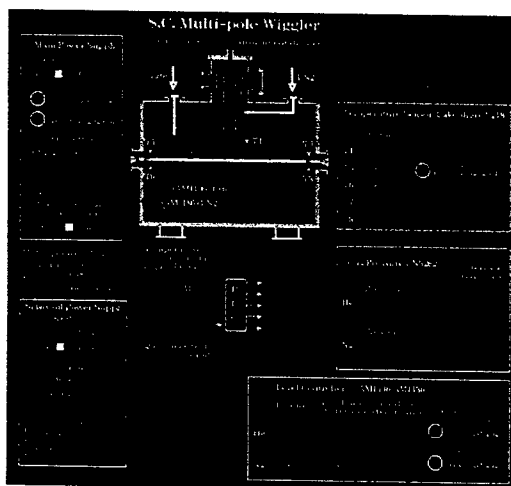


Figure 5. User interface for presenting interlock information.

system for the planned SMPW-A is underway. All superconducting insertion devices share a common structure for ease of maintenance and operation. Following example summary the typical SWLS operation data to demonstrate the basic functionalities of the control system include control, monitoring and archiving.

Operational experiences of SWLS over the past year confirm that the control system is reliable and easy to operate. A procedure for operating the control system has been provided. The top plot of figure 6 shows magnet current of a typical charge/discharge cycle of SWLS. Magnet current charge from 0 A to 230 A need about 15 minutes and the discharge from 230 A to 0 A need about 10 minutes. Magnet current 230 A is corresponding to 5.3 Tesla field strength. The middle plot shows the induced voltage in the magnet coils. The induced voltage varies according to slew rate of the output current. The bottom plot of figure 6 shows that the temperature of magnet bottom near cold head. Figure 7 shows the achieve data record a quench event of SWLS. In the top plot, when the coil quench happen, the bridge circuit is unbalance and

the quench detector triggers the interlock logic. Middle plot shows a quench interlock logic trip the main power supply and the magnet current drop to 0 A within a couple of seconds. The temperature at the cryostat rise drastically due the stored energy of the magnet is dissipated at the quench protection circuitry, which mound inside the cryostat as shown in bottom plot. The cooling capability of the cryocooler is limited, it need about 60 minutes to return to nominal operating temperature.

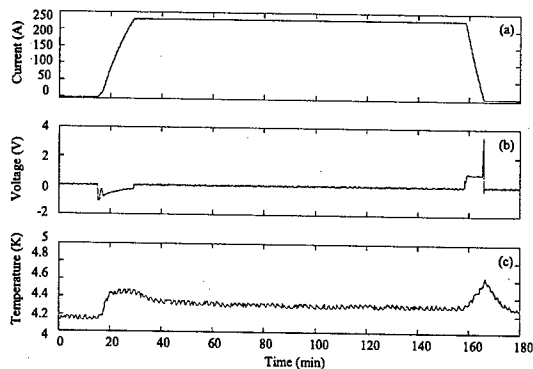


Figure 6. A typical charge/discharge scenario of SWLS.

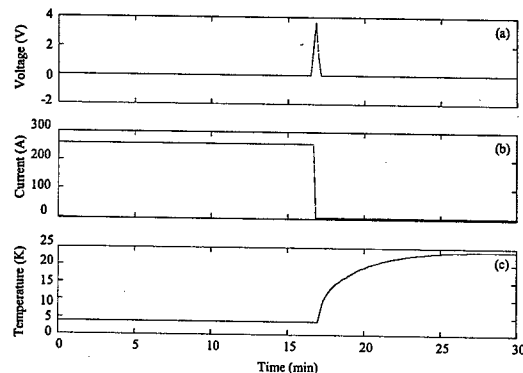


Figure 7. Achieved data record a quench event of SWLS.

SUMMARY

The control system for the superconducting insertion devices is implemented to support the routine operation. Despite there are some difference for the configuration of the magnet, the control system share the same structure. Interlock functions is implemented by a fast scan PLC. The operation experiences from SWLS show the system working well with satisfied performance. Performance and reliability of the control system is improved continuously to ensure smooth operation.

REFERENCES

- [1]. C. S. Hwang, et. al., "Construction and Performance of a Compact Cryogen-Free Superconducting Wavelength Shifter," Proceeding of MT17, Geneva, Swiss, 2001.
- [2]. H. P. Chang, et. al., "Operational Experience of the Insertion Devices and Expectation of the Future Superconducting Wiggles at NSRRC," These Proceeding.
- [3]. <http://www.aromat.com>.

LOW LEVEL RF SYSTEM FOR JEFFERSON LAB CRYOMODULE TEST FACILITY*

Tomasz Plawski[†], Trent Allison, Jean Delayen, Curt Hovater, Tom Powers,
Thomas Jefferson National Accelerator Facility, Newport News, VA, 23606, USA

Abstract

The Jefferson Lab Cryomodule Test Facility (CMTF) has been upgraded to test and commission SNS and CEBAF Energy Upgrade cryomodules. Part of the upgrade was to modernize the superconducting cavity instrumentation and control. We have designed a VXI based RF control system exclusively for the production testing of superconducting cavities. The RF system can be configured to work either in Phase Locked Loop (PLL) or Self Excited Loop (SEL) mode. It can be used to drive either SNS 805 MHz or CEBAF Energy Upgrade 1497 MHz superconducting cavities and can be operated in pulsed or continuous wave (CW) mode. The base design consists of RF-analog and digital sections. The RF-analog section includes a Voltage Control Oscillator (VCO), phase detector, I&Q modulator and "low phase shift" limiter. The digital section controls the analog section and includes ADC, FPGA, and DAC. We will discuss the design of the RF system and how it relates to the support of cavity testing.

INTRODUCTION

The present RF system was designed to control RF signals driving two types of cavities: SNS and CEBAF upgrade in pulsed or CW mode. Table 1 contains the main parameters of these cavities.

Table 1: Cavity Parameters

Parameters	SNS	CEBAF upgrade
Frequency[MHz]	805	1497
Gradient[MV/m]	10.5/12.5	12.5
Mode	pulse/CW for test only	CW/pulse for test only
Loaded Q	7.3E5/7E5	2.2E7
Cavity bandwidth(Hz)	1000	70
Number of cavities /per cryomodule	3/4	8
Number of cells	6	7
Repetition rate/duration	60Hz/1.2ms	cw

* Work supported by the U.S. Department of Energy under contract DE-AC05-84ER40150.

[†] email: plawski@jlab.org

Coplanar Waveguide consists of two slots on a dielectric substrate with the same width

The initial goal of the system was to build a generic, VXI based, remotely and locally controlled card for both 805 and 1497 MHz frequencies. Later, due to problems with finding an appropriate VCO and phase shifter, two separate boards were designed and built. To reduce noise on the board, the analog section is separated from the digital (separated grounds). For all RF paths 50 ohm CPW[#] lines are used.

CONCEPTUAL DESIGN

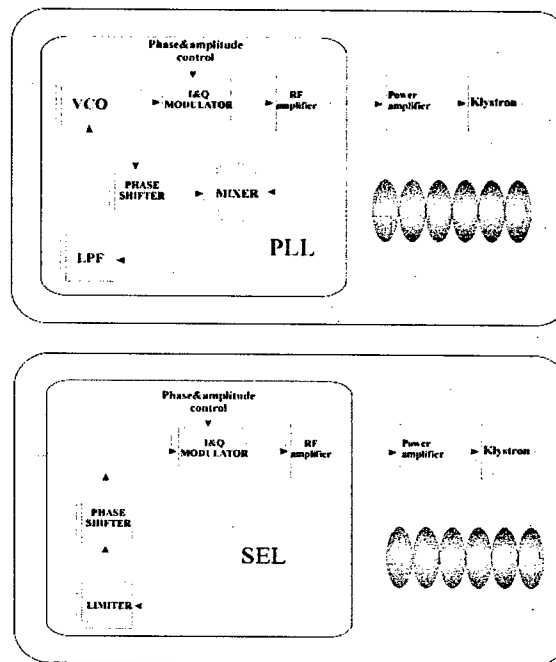


Figure 1: PLL vs. SEL

Unlike a typical RF system where requirements are defined in terms of amplitude and phase stability, the CMTF RF control system has to follow the cavity resonance frequency, which due to high Q_{ext} is particularly susceptible to microphonics and Lorentz forces causing its fluctuations. Two modes can be chosen: Phase Locked Loop (PLL) or Self Exciting Loop (SEL). Fig. 1 shows these two setups. The PLL system requires a frequency source (VCO) and phase detector. The SEL, where loop gain >1 and phase shift is equal $2\pi n$, will oscillate by itself at the cavity resonance frequency. In addition, we have implemented a "low phase shift" limiter to protect the system against saturation and undesired phase shift.

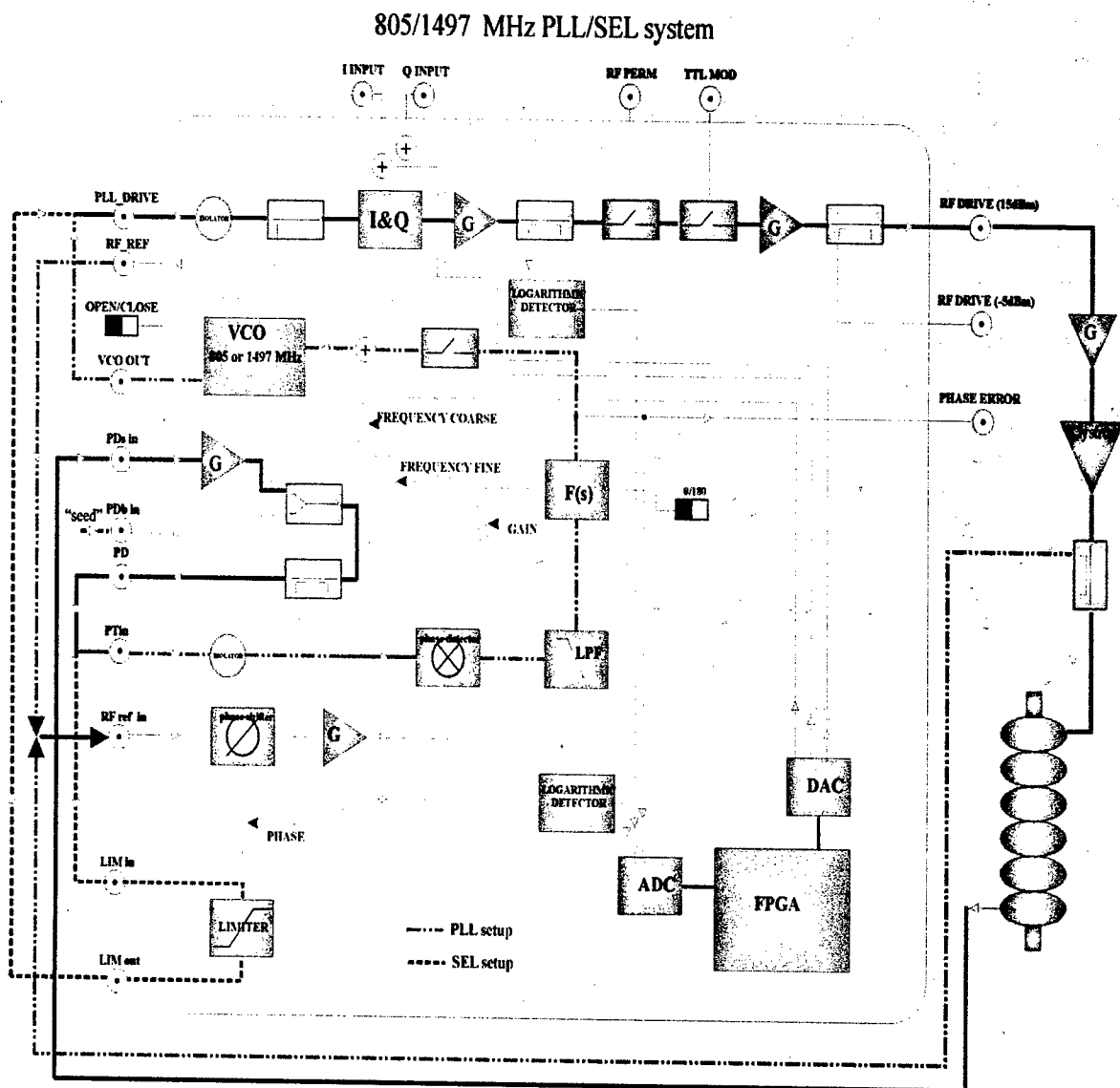


Figure 2: Block diagram of the RF system

RF SYSTEM

A block diagram of the RF system is shown in Fig. 2. Depending on connection "dot-dash or dash line" the two configurations (PLL and SEL) can be established. Amplitude and phase are controlled using I and Q modulation. To lock the system in PLL mode, initial tuning of the VCO frequency, phase, and gain is required. After the system is locked, it can operate in pulse or CW mode. For SEL configuration, the start-up process is statistical in nature and the system can be locked to modes other than π mode. In addition a seed signal can be injected to accelerate the tuning process. The Phase Locked Loop consists of a voltage-controlled oscillator, a phase detector and a low pass filter. For our application

we have chosen two types of VCOs from EMHISER MICRO-TECH:

790-820 MHz/Phase noise @ 10kHz -95dBc
1420-1540 MHz/Phase noise @ 10kHz -80dBc

A passive, double balanced, level 7 mixer was implemented as a phase detector. An active, 1-pole low pass filter reduces loop bandwidth to 30 kHz. The dynamic range and the stability of the PLL setup were improved by implementation of the additional limiter (see Fig. 2). Initial problems with stability and EMI noise observed on the first version of the board were reduced by improved grounding and by replacing microstrip line with CPW. To reduce the cost of production, regular 6-layer FR-4 board was used. The effective dielectric constant of the FR-4 substrate was measured and supplied by the manufacturer. Figure 3 shows measured, forward,

reflected and gradient signals for PLL setup and pulse operation. The system can be switched between pulse and cw, while the lock remains undisturbed. Figure 4 shows measured, forward, reflected and gradient signals for SEL setup and pulse operation. The system can follow changes in resonance frequency even when the cavity is detuned several hundred kHz from the operational frequency. The start-up process is fast enough ($\sim 10\mu\text{s}$) for a 1.2 ms RF pulse.

CONCLUSION

The presented system was successfully tested and commissioned in the CMTF and currently is used in the cryomodule testing process where cavities are tested under strong coupling conditions and for high power pulses. For static and dynamic Lorentz forces measurements different type of AM modulation were used. It is planned to use different RF parts (phase detector, limiter) according to market evaluation to achieve larger dynamic range and better stability of the system.

REFERENCES

- [1] S. N. Simrock, "Achieving Phase and Amplitude Stability in Pulsed Superconducting Cavities", Proceedings of the 2001 Particle Accelerator Conference, Chicago
- [2] C. Hovater, J. Delayen, L. Merminga, and T. Powers, "Proceedings of the 20th International Linac RF Control Requirements for the CEBAF Energy Upgrade Cavities", Proceedings of the 20th International Linac Conference, Monterey, August, 2000 pp. 51852
- [3] K. C. Gupta *and all*, "Microstrip Lines and Slotlines", 1996, Artech House, INC.

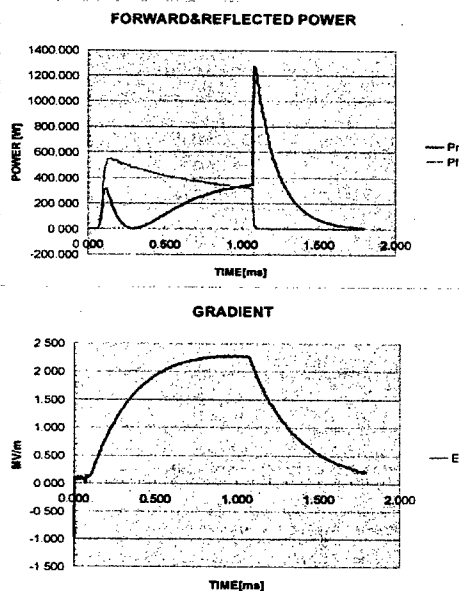


Figure 3. Results from PLL Setup

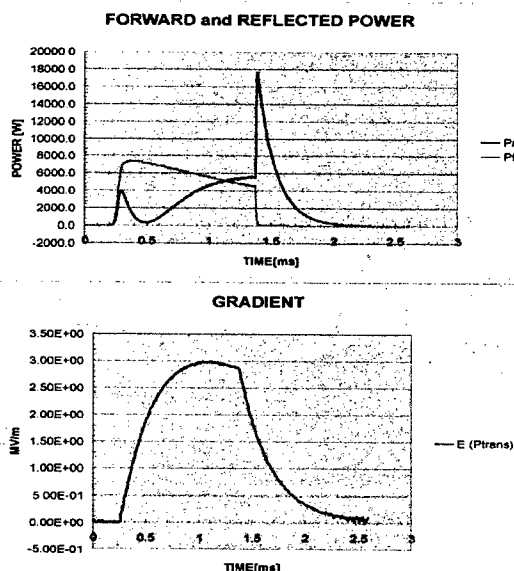


Figure 4: Results from SEL Setup

PLC AND LINUX BASED CONTROL SYSTEM FOR THE CAMD LINAC

P. Jines, E. Anzalone, B. Craft, A. Crappell, M. Fedurin, T. Miller, M. Smith, Y. Wang, and T. Zhao
CAMD, Baton Rouge, LA, USA

Abstract

Louisiana State University Center for Advanced Microstructures and Devices (CAMD) began operations in the fall of 1992. At the time, the facility had separate control systems for the storage ring and Linac. In 1997, CAMD began a control system upgrade project with the goal of producing a single unified control system running on the PC/Linux platform. After completion of the storage ring control system, the Linac control system was designed utilizing AutomationDirect.com PLCs for the real-time components, and PC/Linux for the user interface. The new Linac control system has been completed, and has been operational since July 2002. This paper will discuss the objectives, design, and future upgrade plans for the Linac control system, as well as the experiences with replacing the CGR-MeV VME/OS/9 control system with a PLC/PC/Linux based system.

INTRODUCTION

Efforts to integrate the VME/OS/9 based CGR-MeV Linac control system with the storage ring control system had been difficult. Though OS/9 provided basic TCP/IP capabilities, the third-party control software consumed essentially 100% of the available CPU. Pinging the Linac control system resulted in the expiration of watchdog timers, which in turn lead to a shutdown of the Linac.

The largest problem with maintenance of the system involved documentation and spares. Many components in the system were undocumented or unidentifiable. Efforts to reverse engineer the system had not been successful. Reliability of the system had also become a concern. The components were almost ten years old, and were starting to fail on a regular basis. Luckily, most failures were in known components. However, the sense of impending failure of one of the undocumented or unidentified components forced the control system upgrade to become high priority. Given the inability to reverse engineer these components, CAMD decided to replace the control system instead of attempting to upgrade or integrate it.

The existing VME system was based on a VME computer with custom I/O components. A custom scanner card in the VME crate communicated with the I/O cards via a 50-pin ribbon cable using an in-house protocol. Each I/O card was homogenous in that all digital I/O was a TTL signal, and all analog I/O utilized a 0-10V signal. The cards had a ribbon cable connector on one side, and connected to a 3U Eurocard backplane that handled all incoming and outgoing control signals. The backplane then connected to any signal specific hardware necessary, such as TTL to 24V contact relays or voltage to frequency converters. As all I/O was homogenous at

the Eurocard backplane, this was the point at which the conversion from the old control system to the new PLC system would take place. Special cables were fabricated to connect D-shell DIN-rail breakout boxes to the 96-pin backplane connectors. Using this setup, the new control system could be tested, and the Linac could be reverted to the old control system simply by removing the adapter cables, and reinserting the I/O cards as before.

The timing system was based on yet another undocumented VME card, which provided fiber optic outputs. The source code did not provide a clear description of how the timing was set, so the timing charts had to be measured externally. However, as with the Eurocard backplane connectors, this provided the ideal place to insert the new timing system controls.

HARDWARE DESIGN

The system was architected to be fully distributed so that performance problems could be easily addressed, and additional channels could be added quickly (see Figure 1). The heart of the architecture was separating the interlock code from the code that checked analog signal conditions.

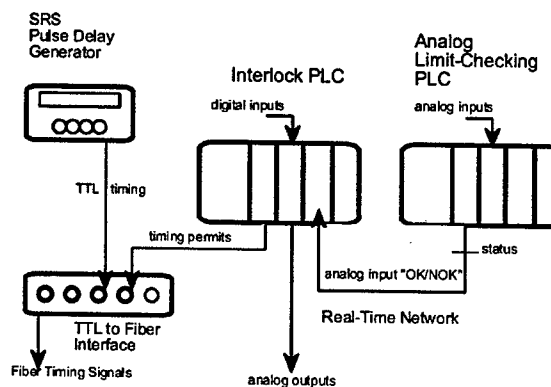


Figure 1: Linac Control System Architecture

One PLC is dedicated to reading analog signals and comparing them against downloaded upper and lower limits. Out of limit conditions are indicated by a digital signal. An input signal is provided that can enable or disable checking of a channel so that an out-of-range condition is not generated if the device is simply turned off as opposed to faulted. With this scheme, performance of the analog limit checking system can be enhanced by splitting the channels into more CPUs as opposed to a single CPU, and the change would be transparent to the rest of the system. Communication with the user interface PC is done thru dual-port memory provided by the H4-ECOM ethernet interfaces.

The second PLC is dedicated to the interlock and control tasks. User requests to turn devices on are inputs to this PLC. If all interlocks and analog signal conditions are met, this PLC does the actual turn on. In the event of a linac problem, it turns off the required devices and latches the fault condition. Ramping of devices is also performed by this PLC. As with the analog PLC, the user interface PC sends commands and receives status information via ethernet.

A third PLC provides control and readback of any signals which are not involved in equipment protection or interlock functions. This PLC has no CPU, but provides only a "dumb" interface directly from ethernet to the I/O.

The timing system consists of Stanford Research Systems DG535 Digital Delay/Pulse Generators, with pulses being converted from TTL to fiber by a dedicated chassis. This conversion system either permits or disables pulses based on input from the interlock PLC.

Lastly, all system digital outputs and permits are fed thru an external watchdog system. This system monitors clock outputs from both the analog limit PLC and the interlock PLC, and will turn off all outputs and permits in the event of the failure of either PLC.

SOFTWARE DESIGN

The CAMD storage ring control system provides a device independent applications programming interface where device specific parameters are stored in a PostgreSQL database [1][2]. Device support for both CPU and EBC based AutomationDirect PLCs and SRS devices were already provided in this system[3]. Therefore, to accommodate the Linac control system at the raw device level, only updates to the database were required.

Individual parameter control was accomplished using the ring control system's generic "magnet pages". These pages utilize channel name patterns to configure the windows. Given a list of "magnet" names, the code searches the database for setpoint, readback, shunt, and on/off channels, and configures the window and code accordingly. To accommodate the Linac, this code needed to be extended to handle upper limit, lower limit, out of range indicators, and alternate names for setpoints and readbacks.

To minimize operator training on the new system, the approach chosen for the main user interface was to "clone" the existing CGR-MeV interface as closely as possible, with a few exceptions (see Figure 2). The original interface provided an "on/off/reset" view of each major Linac subsystem. Only one button from the list of "on", "off", or "reset" was active at any given time. An "off" button of either green or yellow would distinguish between "off/enabled" and "off/disabled" conditions. Buttons would flash to indicate on, off, or reset "in progress" conditions. Buttons, as well as all related parameters on the parameter pages, would turn red on fault conditions.

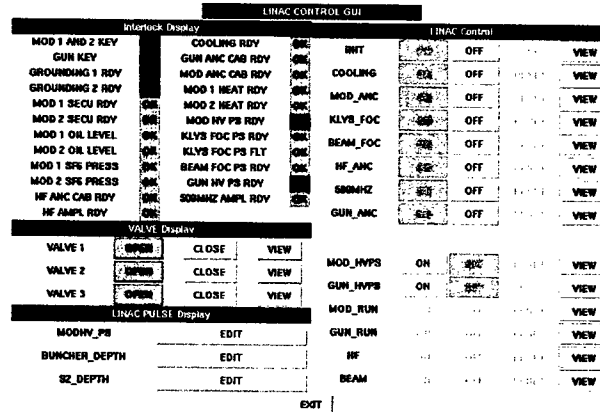


Figure 2: Control System User Interface

While most features of the CGR-MeV interface were kept, some were changed. In the original system, the operator was required to switch between two or three pages to operate the Linac. In the new system, a single window is utilized. A limitation of the original system is that when a fault occurred, the operator had to search thru several pages to find the analog signal that caused the fault. In the new system, the signals are grouped by which ones are utilized by a subsystem's interlock logic. So, if a certain subsystem is faulted, a "View" button launches a window which shows the status of all signals which are related to that subsystem and could cause the fault condition. For subsystems with longer timeouts and warm-up periods, countdown timers were added. One last enhancement to the system involves operator access to parameters such as upper and lower limits, and not-commonly-used parameters. Global access to these parameters resulted in wildly varying linac tunings, and some limits being so large as to be ineffective. Now, these parameters are only available on "Linac Expert" pages, and are under configuration management control.

INSTALLATION AND COMMISSIONING

While the initial shutdown for installation of the Linac control system was planned for one week, most of which was dedicated to ring vacuum activities. To test the Linac with beam required Radiation Interlock System permits that could only be given when the storage ring was searched and secured. This left about three days to commission the new control system with all interlocks in place. To accommodate this schedule, all components of the system had to be tested before the shutdown, leaving only final integration tasks until the last minute.

The first task was to identify all operating voltages and voltage ranges, so that in the event of a control system failure, a known "electrical" state could be recreated. Next was to test the TTL-to-fiber interface, and to verify that the Linac would operate using SRS pulse generators. Since operation of the old and new control systems simultaneously was not possible, this required the "human interlock" approach.

Analog limit checking PLCs were tested channel by channel, with both upper and lower limits, along with

parameter pages and database entries. Documentation and wiring lists were verified as part of this task.

Analog and digital control of the Linac was verified in one of two modes. First, the old control system would be "in charge" of the interlocks, and the new system would "steal" as many signals as were possible. Secondly, the old control system would not be used, and the new control system would rely heavily on the "human interlock" approach.

Finally, by the first day of the shutdown, all systems except the interlock PLC had been verified. As luck would have it, this was the day that the old system finally crashed. Without the option to reverting to the old system, the first days of the shutdown were spent on Linac controls which did not require ring security. Most of the problems encountered were of one of two forms: timing issues or externally disabled hardware.

Timing issues were the first major problem encountered. The solutions were mainly tradeoffs between the length of time waiting for a system to reach a steady state, and how soon to assume it was broken and engage the interlock code.

Most other problems were caused by a history of being unfamiliar with the old Linac control system. Due to the sensitivity of the code, the lack of documentation, and the criticality of the system, no changes had ever been made by CAMD staff to the system. If the system needed to be changed in any way, it was either done by widening the analog limits to almost full scale or "jumping out" external relays. This led to a large number of disabled interlocks, or systems whose real status was "faked" as far as the computer was concerned. While most of the first steps in the Linac turn-on sequence had "faked" inputs, the decision was made to write and test the interlock code as written, so that minimal changes would be required later on when the external problems would be properly fixed and the jumpers removed.

In addition to providing interlocks that verified that systems were on and operating properly, we also identified the requirement to check that systems are actually "off". In addition to externally jumpered signals, we also discovered that the "pull up" and "pull down" status of many signals were incorrect. Bad connections or failed relays caused many conditions to appear as acceptable when, in fact, they were not. Consequently, for the next revision of the design, an extensive review of the electrical signals between the PLC and the devices will be required. Also, alarm capabilities that indicate that "off" commands were sent, but the device is still "on" will be required.

The Linac controls which required ring security were straightforward. The timing system had already been tested with the old system, so the testing was mainly an exercise in determining the proper timing for the warm-up vs. interlock. Scope traces and analog voltages were compared against similar values from the old system as commissioning proceeded, so only mild optimization of

the pulses, timing, and setpoints were required in later stages. Finally, six days into the shutdown, we had Linac beam injected into the storage ring, and were able to begin recommissioning the storage ring after the vacuum intrusion.

RESULTS AND FUTURE PLANS

The performance of the PLC control system is on target. The goal is to detect faults in time to stop the next Linac pulse, occurring at a 10Hz rate. After analyzing the running system, the Interlock and Analog Limit PLCs have average scan times of 12ms and 63ms. The F4-SDN modules provide a real-time network with a transmission time of 32ms, producing a total average time of 107ms. In the scope of the project, these timings were considered adequate for the first phase. Future upgrades could significantly improve this number by upgrading the Analog Limit PLC architecture from a one CPU, two expansion base model to a three independent CPU model.

The PLC system was "spliced in" at a homogenous, standard electrical interface that provided easy integration and the ability to switch back and forth between the old and new systems for testing. However, this method exposed several limitations in the rest of the Linac tunnel, such as hardwired status signals, jumpered out relays, and incorrect "pull up" and "pull down" configurations. As most of these "fixes" were put in place due to a lack of ability to modify the existing system, they can now be fixed properly with the completion of the upgrade.

Linac alarms are now possible. The first critical need is alarms that indicate that "off" commands were successful. As we have seen during commissioning, failures of relays and other hardware between the PLC system and the controlled devices reduce the reliability of the overall system. Wiring and intervening devices should be simplified and corrected as one of the first upgrades. Other planned hardware upgrades include the Linac energy upgrade, the klystron focusing power supply replacement project, and water cooling upgrade project.

Software upgrades that are planned are automated pulse optimization, tuning, and operations procedures such as on, off, and standby modes. Enhanced logging of Linac parameters and waveforms are also planned.

REFERENCES

- [1] B. Craft and P. Jines, 'The GNU Control System at CAMD,' Proceedings of the 1997 ICALEPCS, pp. 194-196, 1997
- [2] P. Jines and B. Craft, 'The GNU Control System at CAMD: Part Two' Proceedings of the 1999 ICALEPCS, pp. 118-120, 1999
- [3] P. Jines and B. Craft, 'PLC Based Upgrades for the CAMD Linac and Storage Ring Control System,' Proceedings of the 2001 ICALEPCS, 2001

CROSS PLATFORM SCA COMPONENT USING C++ BUILDER AND KYLIX*

H. Nishimura, C. Timossi and J.L.McDonald, LBNL, Berkeley, CA 94720, USA

Abstract

A cross-platform component for EPICS Simple Channel Access (SCA) has been developed. EPICS client programs with GUI become portable at their C++ source-code level both on Windows and Linux by using Borland C++ Builder 6 and Kylix 3 on these platforms respectively.

INTRODUCTION

The Advanced Light Source (ALS) control system is migrating from its original x86-based system[1] to an EPICS-based system[2]. To ease the migration of existing applications to EPICS for the application developers, a client API library called Simple Channel Access (SCA) was developed. Subsequently, SCA was packaged as a Java Native Interface and later, using the same interface, as an ActiveX component for the Windows platform (SCAcom [3][4]). This re-packaging makes the underlying SCA a better fit for both the Java environment and for the numerous development tools on Windows: Visual C++, Visual Basic, Borland Delphi/C++ Builder and LabView.

Recently we packaged SCAcom to make it available both to Delphi 6 for Windows and to Kylix 2 for Redhat Linux 7.3. These tools support development of native and portable applications across platforms using a framework called the Component Library for Cross-Platform (CLX) covering advanced GUI, database and network accesses. On Delphi, the ActiveX control SCAcom was imported into a custom CLX component called SCAclx[5]. For Kylix, SCAcom required some re-writing (keeping the same properties and methods) for compiling in gcc instead of importing SCAcom. With the release of Kylix 3, CLX is supported in the Borland C++ environments (C++ Builder 6.0 on Windows 2000 and Kylix 3.0 C++ Builder on Redhat Linux 8.0) extending the access to SCAclx to C++ applications.

SCACLX COMPONENT

CLX: Cross Platform Environment

Component Library for Cross-platform (CLX) is a framework and component library from Borland[6] shared by its development tools Delphi and C++ Builder on Windows and Kylix on Linux. A C++ program developed on Windows, as a CLX application in C++ Builder 6.0 can also be built to run natively on Linux (and visa versa).

* This work was supported by the Director, Office of Energy Research, Office of Basic Energy Sciences, Material Sciences Division, U. S. Department of Energy, under Contract No. DE-AC03-76SF00098

These portable programs can also make use of advanced GUI, database and network accesses routines. By creating a custom CLX component (SCAclx) for channel access, the same source code for channel access client programs can be built to native code for both Redhat Linux and Windows.

Porting SCAcom to SCAclx in C++

The ActiveX control, SCAcom, was built with Visual C++ 6.0. We took the C++ source code of SCAcom and modified it to create a CLX component called SCAclx by using Borland C++ Builder 6.0 on Windows. After confirming its function on Windows, the source code was moved to Linux and recompiled under Kylix 3.0 C++ Builder. At the platform specific level, SCAclx calls the same dynamic-link libraries (DLL) that implements the ActiveX control installed on each Windows machine in the control room. On Linux, SCAclx calls into a shared-object libscacx.a which in turn depends on the channel access and simple channel access libraries sca.a, ca.a and Com.a. Fig.1 shows these layers. Compared to our previous implementation of SCAclx in Delphi, the implementation in C++ was much simpler. In addition to the portability of client programs, the source of SCAclx itself became portable.

<i>Windows</i>		<i>Linux</i>	
<i>Win32</i>	<i>CLX</i>		
Sca ActiveX Control	QSCAclx CLX Component		
SCAcom.ocx		libscacx.so	
SCA.dll		libsca.a	
CA.dll	Com.dll	libca.a	libCom.a

Figure 1: SCAclx and Libraries

Functions of SCAclx

The following members functions and properties have been implemented in SCAclx.

- published property bool GroupCall
- published property bool SetEnabled
- public int Status
- void addInt32Item(AnsiString pvname);
- void addDoubleItem(AnsiString pvname);
- double getDouble(AnsiString pvname);
- int getInt32(AnsiString pvname);
- void setDouble(AnsiString pvname,double value);
- void setInt32(AnsiString pvname,int value);

The property GroupCall is used to turn on or off the group access mode that becomes important when many channels are added. SetEnabled is for the debugging to disable accidental value settings. A data member Status holds the status of the last EPICS call. The group name is taken from the component instance name property therefore it is not included here.

USING SCACLX

Once the newly developed SCACLx component is installed in both development environments, we can develop an EPICS client programs as CLX programs taking advantage of the other features with a provided by CLX components including GUI, database access and networking. (We prefer to develop in the Windows environment since Kylix has more features). The following example was written to demonstrate application portability. It reads and displays 8 vacuum values. We first developed it on Windows(see Fig.2) and rebuilt it on Linux (see Fig.3). Fig.4 shows this application running on Windows and Fig.5 shows it on Linux.

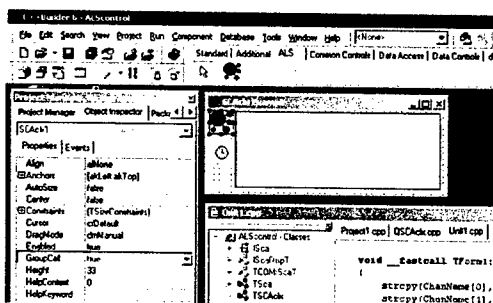


Figure 2: SCACLx on Windows at Design Time

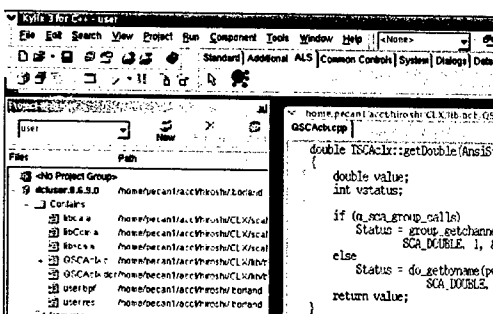


Figure 3: SCACLx on Linux at Design Time

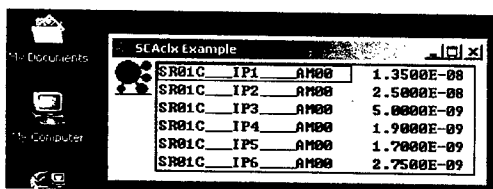


Figure 4: SCACLx on Windows at Run Time

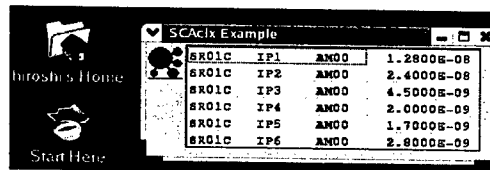


Figure 5: SCACLx on Linux at Run Time

CONCLUSION

The ActiveX component, SCACom, has been ported to as a cross-platform CLX component called SCACLx. This component can now be used to build native Windows and Linux C++ programs. Compared with our previous effort of porting it for the Delphi Pascal, it much simpler in C++. Without using interpreter languages, we can support EPICS client program development in C++ on both Windows and Linux without compromising the robustness and performance

ACKNOWLEDGEMENTS

We express our thanks to A. Biocca and S. James for their support.

REFERENCES

- [1] S. Magyary et al. "The Advanced Light Source Control System", NIM A 293 (1990) 36-43, North Holland. S. Magyary, "Anatomy of a Control System; A System Designer's View", IEEE PAC93, 93CH3279-7, 1811, 1993.
- [2] L.R. Dalesio, et al., "The Experimental Physics and Industrial Control System Architecture", ICALEPCS '93, Berlin, Germany, 1993.
- [3] C. Timossi and H. Nishimura, "Accelerator Control Software Construction Based On Software Components", PAC 1997
- [4] C. Timossi, www-controls.als.lbl.gov/epics/collaboration/sca/win32/JSca/SCA.JSca.html
- [5] C. Timossi, J. McDonald and H. Nishimura, "Experience with ActiveX Control for Simple Channel Access", to be appeared in PCaPAC 2002
- [6] <http://www.borland.com>
- [7] J.L.McDonald, H. Nishimura and C. Timossi "Cross Platform Development Using Delphi and Kylix", to be appeared in PCaPAC 2002

DESIGN OF CONTROL SYSTEM FOR SAGA SYNCHROTRON LIGHT SOURCE

H. Ohgaki[#], Institute of Advanced Energy, Kyoto University, Kyoto, 622-0011, Japan

T. Tomimasu, S. Koda, Y. Iwasaki, Saga Light Source, Tosu, 841-0002, Japan

H. Toyokawa, K. Kudo, National Institute of Advanced Industrial Science and Technology,
Umezono 1-1, Tsukuba, Ibaraki 305-8568, Japan

Abstract

A control system for SAGA Synchrotron Light Source has been designed. The system consists of PC-IOC with off-the-shelf IO devices, console computer, and network. Industrial IO device, FieldPoint (National Instruments) and PLC with Ethernet module (Yokogawa, FA-M3) will be employed as the off-the-shelf IO devices. Ethernet channel access for PC, ActiveX CA, will be used for the network protocol. The server-client applications will mainly be developed by LabView. Field tests for prototype systems have been done in the KU-FEL Linac at IAE, Kyoto University and the storage ring TERAS at National Institute of Advanced Industrial Science and Technology (AIST). Those tests show that the system is suitable for a small-to-medium size control system.

INTRODUCTION

The SAGA synchrotron light source (SAGA-LS) is the light source, which is designed and constructed by a local Japanese government [1]. The construction has been started, and the main components of the light source will be installed during the year 2003. An important issue on this facility is its tightly restricted budget and, hence, the limited number of staff in the facility. Thus, the control system for SAGA-LS should be simple and robust, while inexpensive, easy to develop, maintain and expandable. The use of the off-the-shelf products and PC brings us a solution to this problem.

The PC control system is widely used in many facilities [2] because of a very high cost performance of PC. On the other hand, there are sophisticated and well-established control systems based on workstations, such as EPICS, which have been used in many accelerator facilities. Because a large number of hardware drivers and utility software are available for EPICS system, it is an efficient way to use those resources to design a control system. Since EPICS also runs on a PC-UNIX system, a PC-based EPICS system is one of the solutions. However, it is difficult to modify and expand the EPICS system with the limited number of the staff. Fortunately, the number of the control items of the SAGA-SL is about 500 and there are very few demands for real-time control. So, we designed a Windows PC-based control system which only uses the EPICS channel access (CA). There are many excellent works to develop CA components for the PC-Windows environment [3]. ActiveX CA [4] is one of such component. PC running the ActiveX CA server with off-

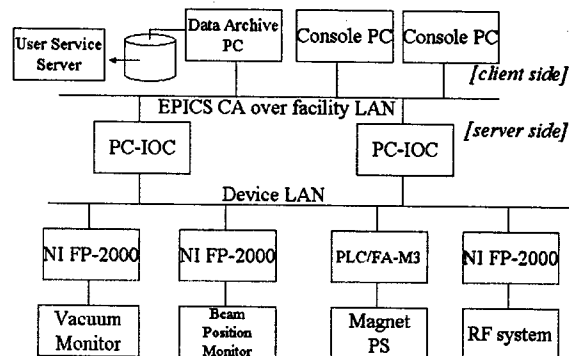


Figure1: Schematic drawing of the SAGA-SL control system

the-shelf IO devices works as a PC IO controller (PC-IOC) [5]. Because the data communication protocol is EPICS CA, we can use the existing EPICS tools and, off course, in-house applications.

In this paper, we will describe the system design and the field tests of the prototype systems in KU-FEL facility [6] at IAE, Kyoto University and in the storage ring TERAS [7] at National Institute of Advanced Industrial Science and Technology (AIST).

SYSTEM DESCRIPTION

The system consists of PC-IOC connected to the off-the-shelf IO devices (CA server), console PC (CA client), and Ethernet LAN. Fig.1 displays the schematic drawing of the system.

PC-IOC

A PC with slot IO cards is a cost effective off-the-shelf IO device [7]. However, there are problems on this configuration: the reliability of the IO card is not so high, and that the system operator has to keep up with the speed of the update of version of the OS and the hardware drivers. So, we chose the industrial IO devices, because the industrial IO device is reliable, and the product lifetime is longer than the PC IO card. Recent industrial IO devices have their Ethernet modules, and this means that we can construct the IOC only with such off-the-shelf devices. Then, the control system will be free from the PC update problem. However, we put PCs between the console computer and the IO device because:

- 1) PC can be used to convert the IO device parameter into the physical one.

[#]ohgaki@iae.kyoto-u.ac.jp

- 2) PC can be used as a local monitor during installation and maintenance.
- 3) PC works as the IOC for GPIB and non-Ethernet devices.

4) The device LAN should be separated from the facility LAN to secure the network.

FieldPoint (National Instruments) is a candidate for the IO devices, because of its reliability and hot plug and play operation. While a severe real-time control is not required for the SAGA-LS, a synchronous control is required for the magnet control of the storage ring during the energy ramping. We will use FA-M3 PLC (Yokogawa Co., Ltd.), which can perform the preloaded ramping pattern via Ethernet command [8], for the magnet IO device.

There will be about ten Windows 2000 PCs for the PC-IOC that are equipped with ActiveX CA servers. The server applications will mainly be developed by LabView (National Instruments).

LAN

The data communication between the PC-IOC (server) and the console PC (client) is done via 100 Mbps LAN, which will be installed in the whole facility (facility LAN). On the other hand, the data communication between the PC-IOC and the IO device is done via 100 Mbps LAN which is locally wired in the machine room (device LAN). Thus, the PC-IOC acts as a gateway machine between two different LANs. The facility LAN is connected to the Internet passing through a router which protects the facility LAN from the outside. The SR users can get the machine status from a data archive system which periodically records the CA Process Variables (PVs). An intra-web server and web browser will be used to extract information from the database. Undulator user will be able to access to the undulator PVs, corrector magnets and tune correction quadrupoles.

Console PC

Since EPICS CA will be used as a communication protocol, both UNIX workstation and PC can be used for the console computer. But we will mainly use Windows PC which has high cost-performance and familiarity for un-trained operators. The ActiveX CA client will be used to access the PVs. Console applications are developed by LabView and some other GUI tools, i.e. Delphi, MS-Visual Basic. The data archive system, which records control parameters and delivers the machine status, will be installed in the system. MS-Access is a candidate of the system. A small look-up table, which stores the latest snapshot of the control devices, is also put in the database.

FIELD TESTS

The prototype systems have been tested in two accelerator facilities, KU-FEL facility and AIST storage ring facility.

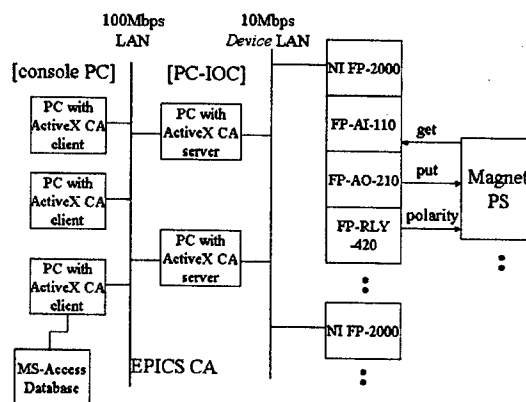


Figure 2: Block diagram of the IAE magnet control system.

KU-FEL facility

KU-FEL is a compact and economical FEL facility in the Institute of Advanced Energy, Kyoto University. The purpose of the KU-FEL is to establish Linac-FEL techniques for industrial and to explore new application fields especially in advanced energy science. The machine is under construction, and the electron beam of 20 ~ 40 MeV will be provided by an S-band linac with an RF gun in this year. A control system using the ActiveX CA has been developed as a prototype system of the SAGA-SL. The system has been installed on a gun cathode, magnets, and vacuum monitors. The block diagram of the IAE magnet control system is shown in fig.2. FieldPoint Ethernet modules (FP-2000) and analog AI/AO modules (FP-AI-110/AO-210) are used as the IO devices. Relay modules (FP-RLY-420) are also used for polarity control of the steering magnets. The number of PVs is about 100. The PV server and PV client applications have been developed by LabView. The 'PV get' frequency of 4 Hz and 'PV put' frequency of 2 Hz are easily achieved by using 200-300 MHz Windows machines connected to 10 Mbps LAN. The maximum transmission rate is almost 250 Hz for one PV channel. These response is enough fast for the daily operation. A data archive system has been installed in the system, and MS-Access database is used for this purpose. LabView database connectivity tools add-on is employed to archive the PVs. The historical trend charts generated by MS-Access are available on any network PCs. The look-up table which shows the latest control parameters for the magnet is also drawn by the MS-Access database.

AIST storage ring TERAS

The storage ring TERAS at AIST is a small synchrotron radiation source. Electron beam is injected by a 300 MeV linac. The storage ring is operated from 200 MeV to 800 MeV depending on the user's request. The electron orbit is sometimes tuned to fit to a specific operation mode. The PC based distributed control system has been

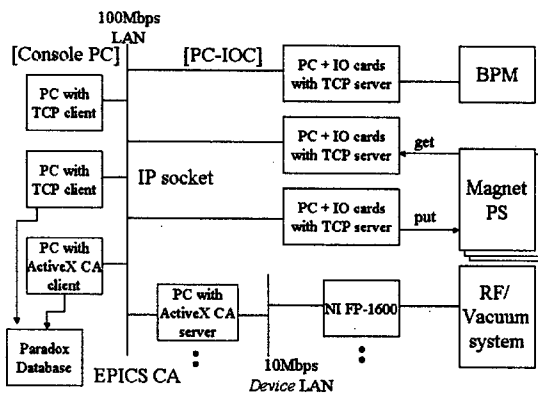


Figure 3: Block diagram of the AIST control system at the present stage.

developed [6]. The system consist of PC-IOC, console PC, and LAN. Figure 3 shows the block diagram of the AIST control system. The PC IO card, which is directly inserted in the PC expansion slot, is used for the IO device. IP socket is used for the client-server communication protocol. Because the system has been developed since 1997, several PCs are already out of date. We have to recalibrate the DAC and ADC on PC IO cards when they are replaced, because low-cost PC IO cards do not certify the AD/DA values, and that process affects significantly the accelerator operation. So, we upgrade the vacuum monitor, and the RF control system using FieldPoint modules. ActiveX CA system has also been tested for the data communication between the server and the client. Two PC-IOCs have been installed with two FP-1600 Ethernet modules. The RF control system has a feedback loop to stabilize the intra-cavity RF power. The updated control system works for 5 Hz feedback-loop which is fast enough for a stable operation of the storage ring. The vacuum monitor runs in 2Hz updating frequency, which is also fast enough for a practical use. A PARADOX database has been used for the original control system because the applications were developed by DELPHI. Since the ActiveX CA is also available in DELPHI, we continuously use the PARADOX for the data archive system.

CONCLUSION

The control system of SAGA-SL has been designed. We will be able to develop a simple and robust control system with a reasonable cost by using ActiveX CA component, LabView programming environment, and industrial IO device. Easy development, maintenance, and expansion of the control system, will also be achieved, at the same time. The total number of control items will be about 500, and most of them do not require the severe real-time control. Thus, the system consists of PC connected to off-the-shelf IO devices (PC-IOC), which

communicates via EPICS CA, console PC, and Ethernet LAN. The prototype systems, which consist of the ActiveX CA and FieldPoint, have been tested in IAE Linac and AIST storage ring. The result of the system test shows enough performance in each facility. So, we will try to use this configuration in the commissioning of the SAGA-SL. However, we will need further tests and discussions about the communication protocol and the database system for the routine operation of SAGA-SL, because the number of the control items is larger than that of these two test facilities. We tried another approach, OPC (OLE for process control), to the network communication. OPC is widely used in industrial field [9]. FieldPoint and FA-M3 have ready-to-use OPC server and we can access to the device directly from network. In a preliminary test of the OPC server with LabView client, we found a very smooth response between them. The other candidate is TACO developed in ESRF [10]. Several accelerator facilities adopt the TACO system [11] and one can develop an appropriate system with the common control resources.

The authors would like to thank H. Nishimura (LBNL) for his helpful advises on this work. A part of this study was financially supported by the Budget for Nuclear Research of the Ministry of Education, Culture, Sports, Science and Technology, based on the screening and counselling by the Atomic Energy Commission. A part of this study was also financially supported by the Budget for the 21st Century COE Program (E-3) of the Ministry of Education, Culture, Sports, Science and Technology.

REFERENCES

- [1] T.Tomimasu et al., "SAGA Synchrotron Light Source Design Report", (2001) in Japanese.
- [2] e.g. P. Duval et al., "Controlling DESY Accelerators with PCs", PCaPAC96,(1996).
- [3] e.g. C. Timossi, http://www-controls.als.lbl.gov/epics_collaboration/sca/win32/readme.txt
- [4] Kay-Uwe Kasemir, <http://lansce.lanl.gov/lansce8/Epics/ActiveXCAServer/default.htm>
- [5] M. Pieck et al., Proc. of the 2001 PAC, Chicago,(2001) p.800.
- [6] T. Yamazaki et al., Free Electron Laser 2001, (2002) II-13.
- [7] H. Ohgak et al., "PC based Control System for Storage Ring TERAS", PCaPAC99,(1999).
- [8] M. Fujita et al., "A CONTROL SYSTEM FOR THE NEW AVF CYCLOTRON AT CYRIC", The 13th Symp. on Acc. Sci. and Tech, (2001) p.106.
- [9] <http://www.opcfoundation.org/>
- [10] A. Gotz et al., "TACO: An object oriented system for PC's running Linux, Windows/NT, OS-9, LymxOS or VxWorks", PCaPAC96,(1996).
- [11] e.g. S. Avsec et al., Proc. of the 1997 PAC, Vancouver, (1997) p.248

SNS RING AND TRANSPORT SYSTEM MAGNET ACCEPTANCE AND INSTALLATION PREPARATION

S. Tepikian, R. Anderson, M. Hemmer, H. C. Hseuh, J. Jackson, A. Jain, F. Karl,
Y. Y. Lee, W. McGahern, D. Raparia, R. Savage, J. Tuozzolo, P. Wanderer, J. Wei
BNL, Upton, Long Island, New York*

Abstract

Installation of the magnets in the SNS-Ring, or any accelerator, requires quality assurance to minimize problems. The geometry of the ring was frozen and the dipole length was adjusted to reflect the measured dipoles magnetic length to aid the installation process. The approach established here is based on the Magnet Acceptance procedures used for RHIC [1]. The magnets are first measured and checked on the bench for mechanical and electrical characteristics, field strength, multipole strengths, survey, etc. Each group performing these measurements determines whether the magnet is within the design specifications. A magnet that passes is accepted. A magnet that fails may be accepted if the problem can be either repaired or reworked and retested to specifications. Such a magnet is classified as a spare or fixed. Furthermore, once accepted, these magnets are assembled into units such as the full half cell assemblies before being shipped for installation. These assemblies have a checkout list as well.

INTRODUCTION

The process of installing magnets in the SNS-Ring (or any accelerator) requires that any problems be identified and resolved. A system of checking is proposed to identify any problems that may arise. A determination of whether this problem is a show stopper and must be fixed or can be handled by simpler means is then addressed. In this paper we discuss our approach. We start with the geometry of the SNS-Ring, then we describe the method used to identify problems.

RING GEOMETRY

Before installing the SNS-Ring, the geometry must be agreed upon and fixed. The geometry consists of the ring dimensions and the coordinates of the center of the ring. Since the geometry of the HEBT and RTBT lines are already established, the SNS-Ring geometry must not be changed.

Ring Dimensions

When the SNS-Ring was originally designed the dipoles were assumed to be 1.5m long. After some dipoles were

* SNS is managed by UT-Battelle, LLC, under contract DE-AC05-00OR22725 for the U.S. Department of Energy. SNS is a partnership of six national laboratories: Argonne, Brookhaven, Jefferson, Lawrence Berkeley, Los Alamos, and Oak Ridge

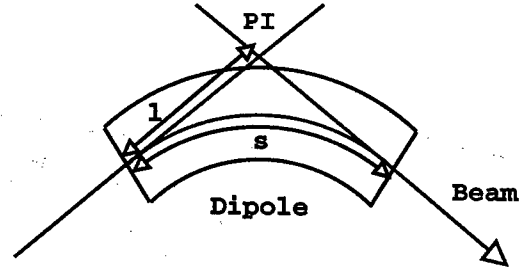


Figure 1: Schematic of the dipole showing the beam direction and the two intersecting tangents (PI). Fixing the PI point freezes the geometry.

built and their lengths measured, the magnetic length was somewhat shorter. We agreed to choose the SD1717 dipole to be the standard. The magnetic length of this dipole is measured to be 1.4407m. Replacing these design magnets with the shorter magnets and adjusting the drift spaces to fix the circumference leads to a change in the geometry.

To fix the geometry the drift spaces about the dipoles must be adjusted differently. Consider the schematic of the dipole shown in Fig. 1. If the length, s , changes and the PI point (Point of tangent Intersection) stays fixed, then the angle must be the same as:

$$s = \rho\theta \quad s_0 = \rho_0\theta$$

where s_0 is the length of the design dipole. The length from either end of the dipole to the PI point is:

$$l = \rho \tan\left(\frac{\theta}{2}\right) \quad l_0 = \rho_0 \tan\left(\frac{\theta}{2}\right)$$

Thus, the change to the drift space length on both sides of the dipole due to a change in the dipole length leads to:

$$\Delta d = l_0 - l = \frac{s_0 - s}{\theta} \tan\left(\frac{\theta}{2}\right)$$

When applied to the SNS-Ring the circumference becomes 248.00612m.

Ring Center

The center for the SNS-Ring is fixed at [2]:

$$North(X) = 10110.611218m$$

$$Vertical(Y) = 2000.000000m$$

$$East(Z) = 20000.000000m$$

This center is determined by the Linac coordinates, HEBT line and the foil position.

QUALITY CHECKS

Several groups are involved with the quality assurance. The Magnet Division measures the performance of the magnets as well as the multipoles. They also check to see if the mechanical center from the Survey Group matches the field center of the magnet. Furthermore, it may be necessary to trim or shim the magnet. The magnets and assemblies must pass tests for the mechanical and electrical systems. The AP (Accelerator Physics) Group sorts which half cell the magnet should go based on reducing optical errors. We ensure that the Survey and Magnet Divisions must send all their data to SNS. In addition, all applicable data (e.g. magnet, surveys, travelers, inspection and test records) are forwarded to SNS. Assemblies must be checked for vacuum leaks and polarity as well. We start with the Magnet checks.

Magnet Checkoff List

The following table shows the checkoff list to determine if the magnet is acceptable. Here we use 'y/n/yc/c' which means 'Yes/No/Yes with comment/Comment'.

Table 1: Magnet check

Column	Description	Response
Mag.Serial	Magnet serial name	
Mag.Type	Magnet description	
DateTime	Date and time of last data entry	
TF1.0OK	Transfer function at 1.0GeV measured	y/n/yc/c
TF1.3OK	Transfer function at 1.3GeV measured	y/n/yc/c
MulOK	Magnet harmonics	y/n/yc/c
MechOK	Mech. test complete	y/n/yc/c
ElecOK	Elec. test complete	y/n/yc/c
SurveyOK	Survey measurement complete	y/n/yc/c
Shim	Is it shimmed?	y/n/yc/c
Trim	Is there a trim?	y/n/yc/c
Sort	Is it sorted?	y/n/yc/c
MagDataTransOK	Magnet data transferred to SNS	y/n/yc/c
SurvDataTransOK	Survey data transferred to SNS	y/n/yc/c
DocOK	Documents complete	y/n/yc/c
HCA	Half-cell assigned	y/n/yc/c
SUMOK	Summary OK for installation	y/n/yc/c

Sometimes a magnet can be accepted but a comment is added such as a particular multipole is greater than 2σ from

the average. In this case the magnet can still be accepted, but may be sorted to a region where that multipole is not critical or this magnet could become a spare. If this turns out to be a problem the magnet may be repaired and then retested. Table 3 shows the results for the first half-cell sent to SNS. Note, at this time the magnet data has not been transferred to SNS yet. The *SUMOK* cannot be given till this is complete

When a set of magnets for making an assembly such as a complete half cell are accepted, the final assembly then undergoes a similar battery of checks.

Assembly Checkoff List

A table for the assembly checkoff list is shown in Table 2. Many of the items are similar to the checkoff items for the magnets. Two differences are the polarity checks and the vacuum checks. The magnet polarity is checked off when the power supply leads produce field directions as defined by [3]. The assembly is checked for vacuum leaks as well.

Table 2: Assembly check

Column	Description	Response
Assemble.Serial	Assembly serial name	
DateTime	Date and time of last data entry	
TypeOK	Verification of the element type and sorting plan	y/n/yc/c
MechOK	Mech. test complete	y/n/yc/c
ElecOK	Elec. test complete	y/n/yc/c
MpolOK	Magnetic polarity checked correctly	y/n/yc/c
SurveyOK	Survey measurement complete	y/n/yc/c
VacuumOK	Vacuum test complete	y/n/yc/c
SurveyDataTransOK	Survey data transferred to SNS	y/n/yc/c
DocOK	Documents complete	y/n/yc/c
SUMOK	Summary OK for installation	y/n/yc/c

After the assemblies checks out, they are sent to SNS. Table 4 gives an example of the results for the first half-cell sent to SNS.

SUMMARY

Before the SNS-Ring can be installed, the geometry must be defined and frozen. This geometry depends on the injection as well as the extraction lines. Since, the measured dipole length was different from the original design, the drift spaces about the dipole had to be changed in order to recover the original design geometry. A prescription for doing this is presented in the ring geometry section.

Table 3: This table shows an example of the acceptance checkoff list for the magnets in the first half-cell for the SNS-ring. The comment: (1) Magnetic measurement made with non-production measurement system.

Column	Dipole	Quadrupole	Sextupole	Corrector
Mag_Serial	13	07	03	004
Mag_Type	17D120	21Q40	21CS26	27CDVM30
DateTime	October 18,2002	October 18,2002	October 18,2002	October 18,2002
TF1.0OK	Y	Y	Y	Y
TF1.3OK	Y	Y	Y	Y
MulOK	Y	Y	Y	YC (1)
MechOK	Y	Y	Y	Y
ElecOK	Y	Y	Y	Y
SurveyOK	Y	Y	Y	Y
Shim	N	N	N	N
Trim	N	N	N	N
Sort	Y	Y	N	N
MagDataTransOK				
SurvDataTransOK	Y	Y	Y	Y
DocOK	Y	Y	Y	Y
HCA	Y	Y	Y	Y
SUMOK				

Table 4: Assembly acceptance example for the first half-cell A1. The comment: (1) Magnet polarity ID for dipole and quadrupole per Tepikian's TN#114

Column	Result
Half_cell	A1
Assemble.Serial	RA1-1
DateTime	Nov 1, 02
TypeOK	Y
MechOK	Y
ElecOK	Y
MpolOK	YC (1)
SurveyOK	Y
VacuumOK	Y
SurveyDataTransOK	Y
DocOK	Y
SUMOK	Y

A plan for pre-installation checks of the SNS-Ring is presented for minimizing problems that may arise. This plan calls for checking each magnet that will be installed. These magnets must be tested to produce the magnetic field required for proper operation of SNS. Furthermore, these magnets must be able to operate at the higher energy of 1.3GeV protons. Along with the field checks there are other checks for each magnet. These magnets must be checked mechanically and electrically. They must be measured by the Survey Group which may uncover other problems that need to be addressed. Additionally, we record whether the magnet was shimmed, has a trim coil and if the magnet was sorted. This information is required if the mag-

net ever needs to be replaced by a spare. Finally, all data concerning these magnets, such as magnetic field measurements, survey measurements and all other documentation must be transferred to SNS. When everything is complete then the summary OK for installation is checked.

Besides each individual magnet, the completed assemblies that are shipped to SNS must pass similar kinds of checks with the following differences. The magnets in the assembly must be verified and follow the sorting plan. The power supply connections must be properly labeled so that the magnets are correctly powered during installation. The beam tube must pass the vacuum tests. Finally, all documentation must be transferred to SNS. Similarly, as with the magnets, when an assembly passes all these tests, the summary OK for installation is checked.

ACKNOWLEDGEMENTS

We would like to thank J. Galambos, S. Henderson, J. Holmes and J. Error from ORNL for their invaluable assistance.

REFERENCES

- [1] J. Wei, et al, Proc. 1995 Part. Acc. Conf. and Internat. Conf. on High-Energy Accelerators Dallas, Texas (May, 1995) 461 - 463. and J. Wei, Proc. 5th European Particle Accelerator Conference, Sitges (Barcelona) (June, 1996) p. 2222.
- [2] J. Galambos, private communication.
- [3] S. Tepikian, C. J. Gardner, SNS TechNote #114 (July, 2002) and W. J. McGahern, SNS TechNote #119 (November, 2002)

LASER-BASED ALIGNMENT SYSTEM FOR THE J-PARC LINAC

Masanori Ikegami, Yasuo Higashi, Kazuo Yoshino,
Hirokazu Tanaka, Takao Kato, KEK, Tsukuba, Japan

Abstract

A laser-based alignment system has been developed for the J-PARC linac. The total length of the linac is about 280 m, and the alignment goal is $\pm 50\mu\text{m}$ transversely. In this paper, the outline of the alignment system is presented together with the feasibility test results with a 50 m test beam line.

INTRODUCTION

The J-PARC (Japan Proton Accelerator Research Complex) accelerator consists of a 400-MeV linac, a 3-GeV RCS (Rapid Cycling Synchrotron), and a 50-GeV synchrotron [1]. The linac is comprised of a 50-keV negative hydrogen ion source, a 3-MeV RFQ, a 50-MeV DTL, a 190-MeV SDTL (Separate-type DTL), and a 400-MeV ACS (Annular Coupled Structure linac). The total length of the J-PARC linac, which includes the straight section of the following beam transport line, is about 280 m. To avoid excess beam loss and beam quality deterioration, an accurate alignment of accelerator components is indispensable for the linac. From this point of view, the alignment goal along the linac is set to $\pm 50\mu\text{m}$ transversely. In addition, it is essential to carefully watch long-term ground motion to maintain the alignment accuracy, considering that the J-PARC facility is to be built on a flimsy ground beside the Pacific Ocean. To meet these requirements, a laser-based alignment system has been developed. Trial-manufacturing of main components and feasibility tests with a 50 m test beam line have been performed. In this paper, the outline of the alignment system is presented together with some preliminary results of the feasibility tests performed with a 50 m test beam line. For detailed description of the system, please refer to the reference [2].

LASER-BASED ALIGNMENT SYSTEM

Concept and key components

The laser-based alignment system is designed based on the KEK-PF linac alignment system[3]. A conceptual drawing of the alignment system is shown in Fig.1. A light source is located at the upstream end of the linac. We adopt a 532-nm DPSS (Diode-Pumped Solid State) laser for the light source. An optical system is placed on a laser stage to make a parallel beam, and we have no other optical component downstream. The laser beam axis is set 700 mm horizontally away from the proton beam axis, and surrounded by an airtight duct to ease the sway by air turbulence. The inner diameter of the airtight duct is 80 mm.

While a vacuum-tight duct is adopted in the KEK-PF linac alignment system, we plan to adopt an airtight duct for easy handling and manufacturing. A feasibility study of the alignment with the laser path in the atmosphere is now underway, using a 50 m test beam line as described later.

The J-PARC linac consists of accelerator components, such as rf cavities, quadrupole magnets, beam monitors, etc. Generally, several accelerator components are placed on an accelerator stand. The relative alignment among these components, which are placed on the same accelerator stand, is performed with the usual optical alignment method using an alignment telescope. Then, accelerator stands are aligned using the laser beam as a reference line. Each accelerator stand has two laser targets at the upstream end and the downstream end. For the laser target, we use quadrant silicon photo-diodes with a diameter of 30 mm. This diameter is larger than the expected diameter of the light spot after propagation length of 280 m.

Each laser target is installed in a box we refer to as a "laser target box". The laser target box has a driving mechanism to turn the laser target away from the laser axis. This feature is essential to enable downstream measurements, because laser targets are supposed to be attached to each accelerator stand. Precise position reproduction is required for the driving mechanism. Four target boxes have been manufactured by way of trial, and position reproduction of less than $\pm 5\mu\text{m}$ has been achieved.

The box is attached to an accelerator stand by an arm. As an example, Fig.2 shows the case where the laser target box is attached to a DTL tank. The laser target position is adjusted using templates as a reference before we install the tank into the accelerator tunnel. Once the target position is adjusted, we can lock the position of the laser target box with respect to the tank. The template is a steel bar

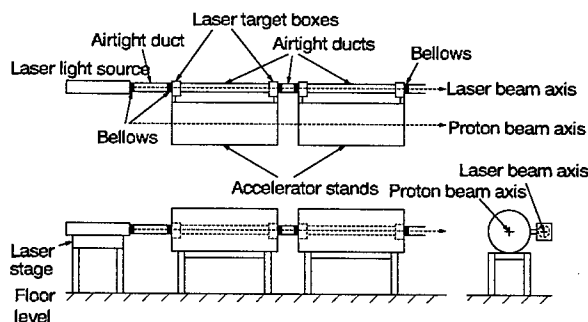


Figure 1: Conceptual view of the laser-based alignment system.

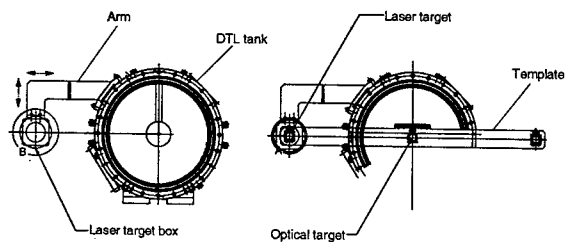


Figure 2: Attachment of a laser target box to a DTL tank.

on which we can mount an optical target and a laser target. These targets are removable with accurate mounting position repeatability. Using two laser targets mounted on two templates attached to the upstream and downstream ends of a DTL tank, we set the reference laser axis for the position adjustment of laser target boxes. An optical target can be mounted on the template, which is used for a relative alignment between a tank and the drift tubes. The attachment of laser targets to other parts, such as SDTL and ACS, is performed in a similar way. The rotation of an accelerator stand around the laser beam axis is avoided by using a level.

In principle, we leave the laser targets attached during beam operation, which enables us to watch the ground motion for a long period of time. However, the laser target can be easily put on and taken off with accurate mounting position repeatability. This feature is required because radiation damage of photo-diodes may be significant in some part of the linac.

After a long period of beam operation, it is necessary to perform re-alignment due to ground motion. As the floor on which the laser stage is placed also moves, the light direction also changes after a long period of time. Then, to enable re-alignment, the stage for the light source should have a mechanism to adjust the light direction to the designated one. The required resolution for the direction control mechanism is extremely high, namely, around $0.1 \mu\text{rad}$. To realize the high-resolution direction control, we have adopted a deformation method. In the laser stage, the optical system is placed on a stack of four aluminum plates, and each plate has a narrow part about which we can bend the plate easily. We elastically deform the plates to change the light direction by pushing the plates with stepping motors. Figure 3 shows a photo of the laser stage installed in the JHF linac accelerator tunnel at KEK. Research and development of the laser stage is now underway.

Setting up the laser axis

This direction control system is expected to be useful in the initial alignment also, because the laser axis should be determined in consistent with the downstream alignment. The downstream beam transport line, to which we refer as L3BT, has arc sections. We plan to use a laser-tracker for the alignment after the first arc section of L3BT. Therefore,

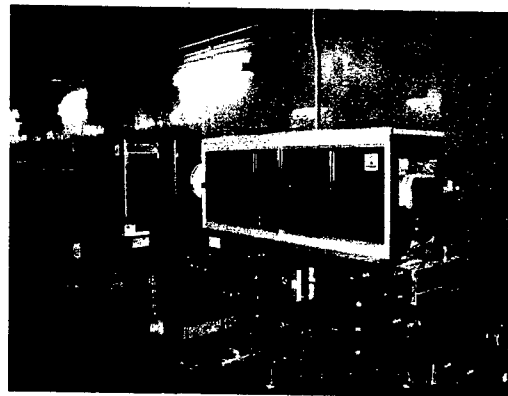


Figure 3: Photo of the laser stage.

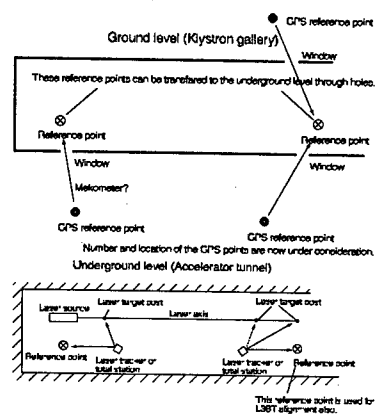


Figure 4: Determining of the laser axis.

we need a connection scheme between these two alignment systems. In addition, we plan to have two reference points in the accelerator tunnel, above which we have penetration holes to enable GPS measurement of the reference points. Using these reference points, we measure the relative position of the linac to other J-PARC facilities, such as the 3-GeV RCS and the 50-GeV Main Ring. We are setting up a GPS measurement network around the J-PARC facility for this purpose. To determine the laser axis using these reference points, we plan to have three secondary reference points (one of them is auxiliary), to which we refer as "laser target post", in the accelerator tunnel. By setting up these laser target posts with a laser-tracker, we can connect two alignment systems consistently. The procedure to determine the laser axis is schematically shown in Fig.4.

EXPERIMENTAL RESULTS WITH A TEST BEAM LINE

To check the feasibility of the laser-based alignment system, we have performed a long-range experiment with a 50 m long test beam line placed in the JHF linac accelerator tunnel at KEK. The main aim of this experiment is to examine the effect of air turbulence.

Before proceeding to the long-range experiment, we per-

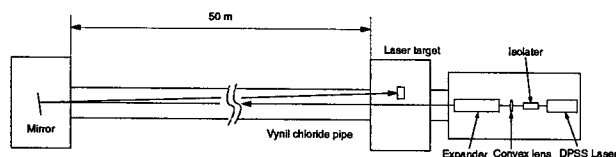


Figure 5: Conceptual view of the experimental setup.

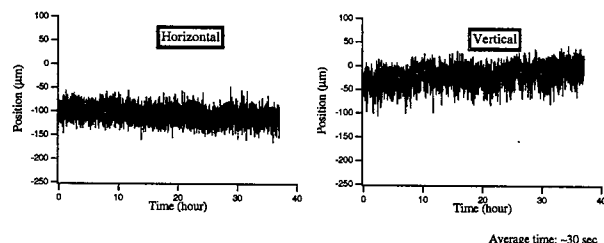


Figure 6: Time evolution of the photo-diode readout in a 50 m experiment.

formed a experiment with much shorter beam propagation length of around 0.3 m to check the fundamental characteristics of the system. In the experiment, we concluded that the spatial resolution of $5\ \mu\text{m}$ can be achieved with the photo-diode, and the effect of the long-time drift of the A/D converter is around $\pm 5\ \mu\text{m}$.

Figure 5 shows the experimental set up of the long-range experiment. At the upstream end, a laser source and an optical system are placed on the laser stage. The optical system used in the experiment is simplified one which consists of a beam expander and an optical isolator, and neither collimator nor optical fiber is included. The laser pathway is surrounded by a temporal air-tight duct made with vinyl chloride to ease the sway by air turbulence. At the downstream end, we have an optical stand on which we place a laser target for 50 m measurements, or a mirror for 100 m measurements. The tunnel is air-conditioned and a cooling-water system for the linac is operated during the measurements. No temperature control is applied for the laser source.

Figure 6 shows the result of a 50 m measurement, in which measured laser-spot position is shown as a function of time. The result for 100 m measurement is shown in Fig.7. It is seen in these figures that the output signal is composed of relatively fast sway component whose period is around or shorter than a few minutes, and slow sway, or drift, component whose period is longer than a few hours. The relatively fast component can be reduced with averaging. In Fig.6, the output signal is averaged over 30 sec, and 2 min in Fig.7.

DISCUSSIONS

We have found in the experiment that the amplitude of the fast sway is roughly proportional to the path-length in this setup, and that we need three- to four-times longer av-

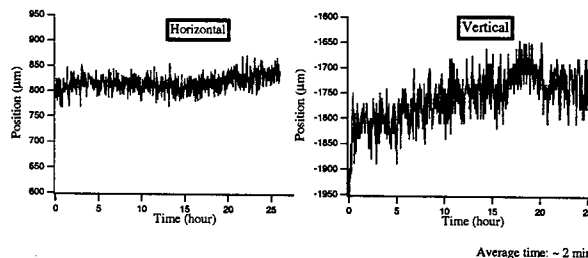


Figure 7: Time evolution of the photo-diode readout in a 100 m experiment.

eraging time to reduce the amplitude to half. It is seen in Fig.6 and Fig.7 that the measurement resolution of less than $50\ \mu\text{m}$ can be achieved except for the vertical direction in the 100 m measurement. We suspect that the 100 m measurement is affected by some instability of the optical stand on which a mirror is placed, because the large-amplitude turbulence suddenly arises in 100 m cases. Because even a slight tilt of the optical stand can affect the measurement in this setting, the system is very sensitive to the stability of the optical stand in the 100 m measurements. To have more conclusive results in 100 m measurements, we need to improve the optical system at the 50 m point.

As mentioned earlier, the fast component of the sway can be reduced by averaging. Contrary, it is difficult to reduce the slow sway or drift component. While the slow component observed in the experiment is within a tolerable level, that in the actual alignment can be more significant considering that the path-length is much longer and the stability may be strongly dependent on the tunnel environment. Therefore, it is urgent to perform further investigation on the cause of the slow component and find a way to reduce it.

ACKNOWLEDGEMENT

We would like to thank F. Naito (KEK), E. Takasaki (KEK), C. Kubota (KEK), T. Ito (JAERI) for helpful discussions. We are deeply indebted to Z. Kabeya (MHI, Mitsubishi Heavy Industries LTD.), S. Kakizaki (MHI), T. Kikuchi (REC, Ricoh Elemex Corp.) and N. Hiramatsu (REC) for the detailed mechanical design of the laser target and the laser target box. We also thank D. Arakawa (KEK) for the design of the low-pass filter unit.

REFERENCES

- [1] Y. Yamazaki, "The JAERI-KEK Joint Project (the J-PARC Project) for the High Intensity Proton Accelerator", in these proceedings.
- [2] M. Ikegami et. al., "Development of a Laser-Based Alignment System for the J-PARC Linac", Procs. 7th International Workshop on Accelerator Alignment, to be published.
- [3] Y. Ogawa, et. al., "Improvement of the Alignment System for the KEK 2.5-GeV Electron Linac", Procs. 1995 PAC, 1995.

A MODEL OF ATL GROUND MOTION FOR STORAGE RINGS*

A. Wolski[#], LBNL, Berkeley, CA 94720, USA
N.J. Walker, DESY, Hamburg, Germany

Abstract

Low emittance electron storage rings, such as those used in third generation light sources or linear collider damping rings, rely for their performance on highly stable alignment of the lattice components. Even if all vibration and environmental noise sources could be suppressed, diffusive ground motion will lead to orbit drift and emittance growth. Understanding such motion is important for predicting the performance of a planned accelerator and designing a correction system. A description (known as the ATL model) of ground motion over relatively long time scales has been developed and has become the standard for studies of the long straight beamlines in linear colliders. Here, we show how the model may be developed to include beamlines of any geometry. We apply the model to the NLC and TESLA damping rings, to compare their relative stability under different conditions.

ATL FOR LINEAR GEOMETRIES

Damping rings for future linear colliders will need to operate with equilibrium vertical emittances of a few picometers (unnormalized). Achieving such highly focused beams will depend on precise alignment of beamline components, particularly the quadrupole and sextupole magnets, and effective steering and coupling correction algorithms. Small movements of the quadrupoles and sextupoles over time will necessitate (possibly invasive) retuning of the ring, and it is important to estimate at the design stage how frequently such tuning may be required. Although movement of magnets and diagnostic components can occur from a variety of causes, for example thermal effects or mechanical stress on the supports, a significant contribution to the motion is expected to come from the ground itself.

Ground motion in a variety of regimes relevant for high energy beamlines has been discussed in some detail by Napoli and Seryi [1]. In this paper, we consider only the slow or diffusive ground motion, which is described by the ATL model:

$$\langle (Y_i - Y_j)^2 \rangle = ATL_{ij} \quad (1)$$

Here, Y_i is the vertical position of the i^{th} beamline component relative to some (conceptual) fixed reference point, T is the time after initial (perfect) alignment, and L_{ij} is the horizontal distance between components i and j . The parameter A is a constant characteristic of the site on which the accelerator is built: "quieter" or "more stable"

sites have lower values of A . The angled brackets indicate an average over an ensemble, or in practice, the mean value over a number of different random seeds. In the original paper [1], the authors considered only the application of this model to linear systems, such as the main linac or beam delivery system of a linear collider. In such a system, it is straightforward to apply the ATL model (1) in a simulation. For a given time step T it is only necessary to start at one end, giving each component a random displacement with respect to the previous component, with the variance of the displacement given by ATL , with L the distance between the components. This generates a "random walk" and one finds that the relative displacement of any two components in the beamline then obeys the ATL model.

Attempting to apply this procedure to a storage ring will result in failure, since L_{ij} becomes the arc length between two components, rather than the direct horizontal distance that is required by the model. The start and end points, for example, will typically be close together, but will have a relative misalignment characteristic of the circumference of the ring, which may be very large.

Since the ATL model is now the standard description for linacs and beam delivery systems in linear colliders [2], it is desirable to be able to apply the same model to describe the motion of components in other parts of the machine, in particular the damping rings, where alignment is an important issue. We therefore describe here a technique for applying the ATL model in a consistent way to beamlines that are not rectilinear.

ATL FOR GENERAL PLANAR GEOMETRIES

Theoretical Analysis

First, we choose a fixed reference point $j=0$. For any component i we can then write:

$$\langle Y_i^2 \rangle = ATL_{i0}$$

Noting that:

$$\langle (Y_i - Y_j)^2 \rangle = \langle Y_i^2 \rangle + \langle Y_j^2 \rangle - 2\langle Y_i Y_j \rangle$$

it then follows that:

$$\langle Y_i Y_j \rangle = AT \cdot \frac{1}{2} (L_{i0} + L_{j0} - L_{ij}) = ATM_{ij} \quad (2)$$

which defines the matrix \mathbf{M} with components M_{ij} . We can write equation (2) in terms of the outer product of the vector \mathbf{Y} (with components Y_i) with itself:

$$\langle \mathbf{Y} \cdot \mathbf{Y}^T \rangle = AT\mathbf{M} \quad (3)$$

*Work supported by the US DOE, contract DE-AC03-76SF00098.
[#]awolski@lbl.gov

Since \mathbf{M} is symmetric, it can be diagonalized by a unitary matrix Λ :

$$\tilde{\mathbf{M}} = \Lambda \cdot \mathbf{M} \cdot \Lambda^T$$

The components of $\tilde{\mathbf{M}}$ are the eigenvalues λ_i of \mathbf{M} :

$$\tilde{M}_{ij} = \lambda_i \delta_{ij}$$

Λ is of course constructed from the eigenvectors of \mathbf{M} . It is important that we choose an orthonormal basis for the eigenvectors, otherwise $\tilde{\mathbf{M}}$ is not diagonal – this is discussed further below. We define the vector \mathbf{V} :

$$\mathbf{V} = \Lambda \cdot \mathbf{Y}$$

By premultiplying equation (3) by Λ and postmultiplying by Λ^T , we see that the components of \mathbf{V} satisfy:

$$\langle V_i^2 \rangle = A T \lambda_i \quad (4)$$

Equation (4) is our result: it is all we need to apply the ATL ground motion model to a general planar geometry. Explicitly, from the distances between the components and a chosen fixed reference point, we construct the symmetric matrix \mathbf{M} , and find its eigensystem. We then generate a set of values with variances given by the eigenvalues of \mathbf{M} , and transform these values using the eigenvectors of \mathbf{M} to find the corresponding vertical displacements of the components. The case of a rectilinear beamline is of course a special case of this general model.

Implementation Issues

We commented above that it is important to choose an orthonormal basis for the eigenvectors of \mathbf{M} . It is easy to show that if the eigenvalues are all distinct, then the eigenvectors of a symmetric matrix are necessarily orthogonal. However, eigenvectors corresponding to repeated eigenvalues may become “mixed” in such a way that they are not orthogonal. In this case, the matrix $\tilde{\mathbf{M}}$ is not diagonal, and the above procedure will fail, since the final result (4) is not correct.

The question then arises, as to which situations will give rise to repeated eigenvalues of \mathbf{M} ? This is a difficult question to answer completely, but in general, repeated eigenvalues are an indication of some symmetry in the system. For example, one finds that if the system consists of N points equally distributed on a circle with the reference point at the center, the eigenvalues occur in $(N-2)/2$ or $(N-1)/2$ pairs according to whether N is even or odd. Moving the reference point away from the center reduces the number of pairs of eigenvalues, and choosing a reference point on the circle renders them all distinct.

Fortunately, where repeated eigenvalues do occur, the above technique can still be applied: it is, however, necessary to ensure that the eigenvectors form an orthonormal basis.

Large accelerators (for example, the TESLA Damping Ring) may consist of many hundreds of components, in which case we need to find the eigensystem of a large

matrix. This is not necessarily an obstacle, since efficient numerical algorithms exist for this task. Also, for a given accelerator design, it is only necessary to perform the eigensystem analysis once. The eigenvalues and eigenvectors can then be saved for application of the ATL model for simulations over different timescales.

EXAMPLES

Regular Grid

To test the technique, it is interesting to apply it to a regular grid of points. In this case, one expects to see the correlation of vertical displacement with distance to show up clearly (or not, in the case of some flaw in the theory or its application). The application is conveniently carried out in any mathematical program capable of an eigensystem analysis of a large matrix. We have used Mathematica [3]: our grid consisted of 25×25 points, with the reference point at the origin. Initially, all points are at $Y=0$. Figure 1 shows that grid after 5, 10, 30 and 50 time steps (the value of A is 5×10^{-4}).

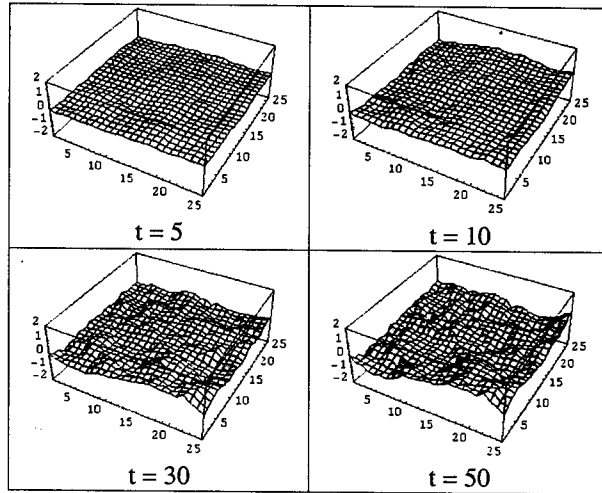


Figure 1: ATL Applied to a Rectangular Grid of Points

Clearly, the displacements of the points on the grid are correlated, with the average relative displacement between two points increasing with the distance between the points.

The NLC Main Damping Rings

For a storage ring, we are generally interested in questions such as the change in the closed orbit and the vertical emittance degradation when the main magnets in the lattice move. It is therefore convenient to have the ATL model integrated into an accelerator simulation code. We have implemented the 2D ATL model into the tracking code MERLIN [4], and applied the model to the NLC Main Damping Rings [5] and the TESLA Damping Rings [6].

Figure 2 shows the effects of ATL ground motion applied to the quadrupoles of the NLC Main Damping Ring over a period of 30 hours, starting from a perfect

alignment. The blue points show the quadrupoles, and the red line shows the closed orbit. The value of A used in the simulation was $4 \times 10^{-6} \mu\text{m}^2/\text{m/s}$. The horizontal scales are in meters, and the vertical scales are in microns.

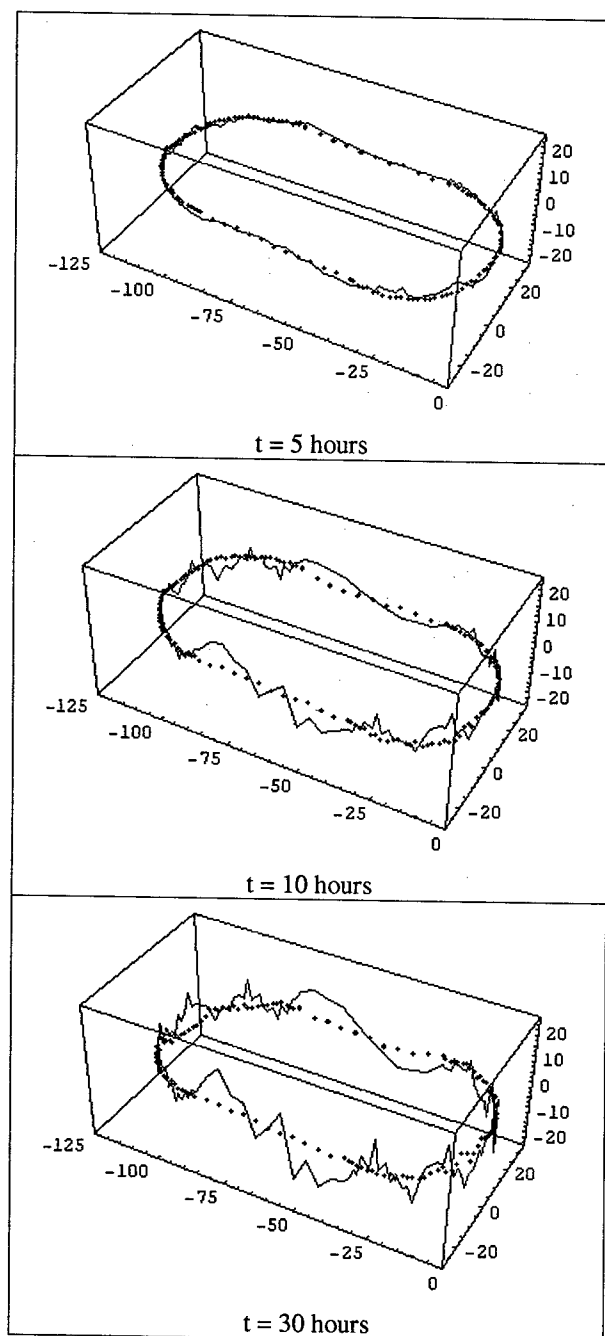


Figure 2: Effect of ATL Ground Motion on the Closed Orbit in the NLC Main Damping Rings

EMITTANCE TUNING

Maintenance of very low vertical emittance over long periods is an important issue for linear collider damping rings, as this has a direct impact on the rate at which the linear collider can integrate luminosity. Although it is expected that low emittance may be maintained to some

extent by a straightforward orbit correction, it is important to know how frequently more invasive tuning procedures may be required.

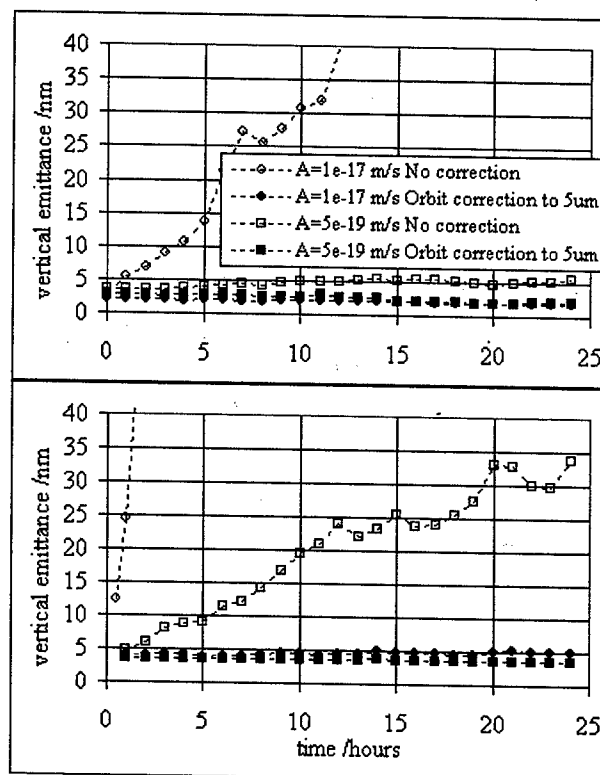


Figure 3: Emittance Growth from ATL Ground Motion in the NLC (top) and TESLA Damping Rings

Figure 3 shows the growth of the normalized vertical emittance from ATL ground motion in the NLC Main Damping Rings and the TESLA Damping Rings. The rings were initially misaligned by applying 50 hours of ATL ground motion to the quadrupoles and sextupoles, followed by a full coupling correction. Without orbit correction, a rapid emittance growth can be seen for $A = 10^{-17} \text{ m/s}$ (NLC and TESLA) and $A = 5 \times 10^{-19} \text{ m/s}$ (TESLA). An orbit correction at half-hourly intervals to $5 \mu\text{m}$ is effective at suppressing the emittance growth.

REFERENCES

- [1] A. Seryi and O. Napoly, "Influence of Ground Motion on the Time Evolution of Beams in Linear Colliders", Phys. Rev. E, 53 p.5323 (1996).
- [2] Second Report of the International Linear Collider Technical Review Committee, 2003.
- [3] Wolfram Research, <http://www.wolfram.com/>
- [4] <http://www.desy.de/~njwalker/MerlinII/index.htm>
- [5] A. Wolski and J. Corlett, "The Next Linear Collider Damping Ring Lattices", PAC'01, p.3795.
- [6] TESLA Technical Design Report, Part II p.137, DESY 2001-011, March 2001.

DESIGN AND OPERATION OF THE CRYOSTAT FOR THE CESR-C SUPERCONDUCTING WIGGLER MAGNETS

Y. He*, G. Codner, R.D.Ehrlich, Y. Li, V. Medjidzade, A. Mikhailichenko,
N. B. Mistry, E. Nordberg, D. Rice, D. Sabol, K. Smolenski, D. Widger
Laboratory for Elementary-Particle Physics, Cornell University, Ithaca, NY 14853, USA
E. N. Smith, Laboratory of Atomic and Solid State Physics, Cornell University

Abstract*

As part of the "CESR-c" upgrade project, a full-scale prototype superferric wiggler module has been installed into the Cornell Electron Storage Ring (CESR) and successfully operated since October 2002. At least eleven more wigglers are to be installed to enable full operation of the CESR-c. The wiggler magnets are chosen to achieve the necessary damping for optimum operation of CESR-c at a beam energy of 1.88 GeV. The wiggler cryostat units are designed to be modular, of fixed length flange-to-flange, so that they can be easily installed and exchanged. The cryostat incorporates several novel features including a suspension system with very low heat leak that prevents any significant motion during cool down, a custom triple cryogenic feedthrough, and a helium vessel made in two halves, each enclosing a half-magnet. This article presents the design, fabrication, and operation of the CESR-c wiggler cryostat.

INTRODUCTION

The conversion program CESR-c will extend CESR operating range to 1.5 GeV through 5.6 GeV [1]. It requires the addition of over 15 meters of wiggler magnets to enhance synchrotron radiation (SR) effects for optimum CESR operation at low energies. The wiggler design is of superferric type [2][3]. The wiggler cryostat units are designed to be modular of fixed length flange-to-flange, so that they can be easily installed or replaced. A full-scale prototype wiggler has been installed into the CESR ring and successfully operated since October 2002. Five more wigglers have been manufactured and tested and are now installed. At least six more wigglers are to be installed to enable full operation of the CESR-c [4].

The cryostat serves to support the cold mass accurately and reliably within the vacuum vessel, to provide all required cryogenic plumbing, and to insulate the cold mass from heat radiated and conducted from the environment. The fact that the cryostat should fit into the tight space available in the existing CESR tunnel while providing maximum wiggler magnetic length makes its design more challenging.

The cryostat is 0.6 m in diameter and 1.725 m in length. It consists of a liquid helium vessel made in two halves, insulation vacuum vessel, thermal shields, helium stack for housing current leads and instrumentation wires, suspension system, cryogenic

plumbing and an integral copper beam-pipe with warm-bore (see Fig. 1, 2).

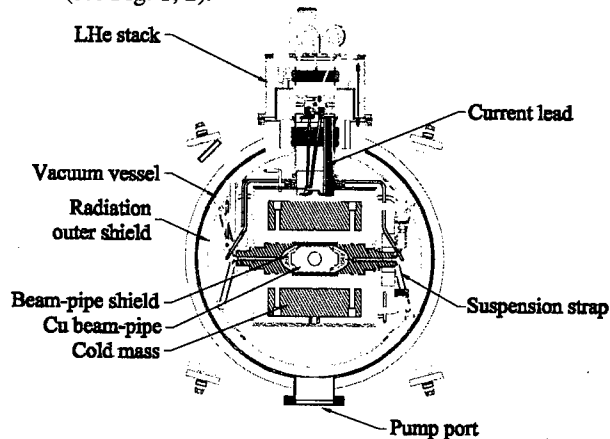


Figure 1: Wiggler cryostat cross-section.

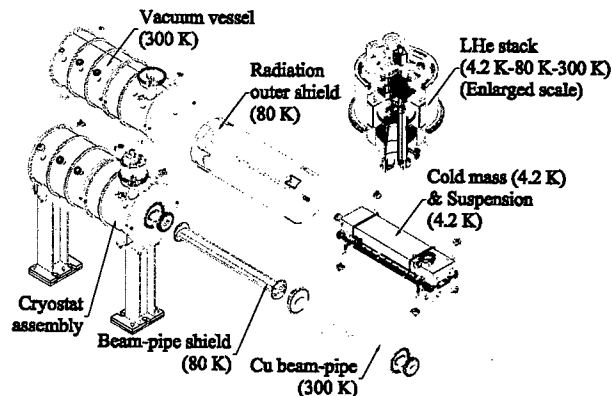


Figure 2: Cryostat assembly with major components.

DESIGN DESCRIPTION

Thermal Design Considerations

In addition to mechanical requirements, the cryostat is designed to minimize heat transfer by radiation and conduction from ambient to the cold mass. The heat transfer to the cold mass directly affects the magnet's operating cost.

The conductive heat leak is minimized by choosing the proper materials for the cold mass support, employing thermal interception at 80 K and providing high vacuum insulation. The radiative heat transfer is reduced by interposing liquid nitrogen cooled thermal shields and wrapping the cold mass with multilayer super-insulation. The thermal load associated with the current leads is reduced by the use of high temperature superconducting

* work supported by the US National Science Foundation
#yh63@cornell.edu

(HTS) current leads below 77 K. The estimated static heat leaks to the stages at 4.2 K and 80 K are summarized in table 1.

Table 1: Static heat leak in cryostat (in Watts)

Components	4.2 K	80 K
Thermal shields	0.35	6.8
Supports	0.05	9.0
Cryogenic feedthrough	0.14	3.2
Current leads	0.17	17.1
LHe stack	0.19	1.4
Total	0.9	37.5

Cold Mass and Suspension System

The magnet has 1.3 m active length with a peak field of 2.1 T. It is made in two halves. Each half-magnet has a mass of about 420 kg cooled in a helium bath. The two halves are connected through interconnecting side tubes for wires and LHe flow.

The cold mass is suspended in a 609 mm diameter vacuum vessel by eight tension straps with four straps at each of the two ends (see Fig. 3). With this suspension scheme the center of cold mass does not move during cool down. The racetrack-shaped straps are made of S-glass fiber in an epoxy matrix. The material has a low conductivity-to-yield-strength ratio. The warm end of the strap is joined to an invar rod through a clevis, which is thermally anchored to the 80 K thermal shield by copper braids. The alignment of the cold mass axis relative to the beam-pipe is performed at room temperature by adjusting nuts on the invar rods from the outside of the vacuum vessel.

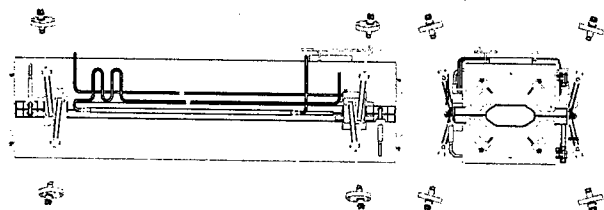


Figure 3: Cold mass suspension system.

Radiation Shields, beam-pipe and interconnection

Radiation shields are interposed to intercept radiative heat transfer between cryostat vessel and cold mass, and between beam-pipe and cold mass. The shields are made of pure aluminum 1100-O with a thermal conductivity of $300 \text{ Wm}^{-1}\text{K}^{-1}$ at 80 K. The outer radiation shield is cooled by liquid nitrogen through stainless steel (SS) tubes which are clamped and glued to provide good thermal contact. The beam-pipe shield is cooled through thermal conduction from the outer shield via end flanges.

The ultrahigh vacuum beam-pipe is made of copper with water cooling channels at both sides to intercept wiggler radiation.

The cold mass, radiation shields and beam-pipe are interconnected at both ends through thermally insulating supports which allow adjustment during assembly and accommodate shrinkage during cool down. At each end, the radiation shield is supported from the cold mass by four tensioned Kevlar straps while the beam-pipe is supported by four fiberglass rods from the shield.

The cold mass, radiation shields and beam-pipe are all wrapped with four to ten layers of multilayer super-insulation made of aluminized Mylar with mesh polyester interlayer.

LHe Stack and Instrumentation

A LHe stack on the top of vacuum vessel houses HTS current leads, instrumentation wires, voltage taps and trim current leads. A liquid nitrogen pot provides an 80 K heat sink for thermal intercept.

A pair of HTS leads is used to deliver the current to the magnet coils. The warm end of the lead is thermally anchored at the LN₂ pot and the cold end at 4 K.

When a magnet quenches, part of the generated heat is transferred into the helium bath and thus the helium pressure is increased. The stack is equipped with a safety relief valve and burst disc to ensure fast discharge of helium due to quench or cryogenic failure.

Thick film 56 k Ω resistors are placed at various locations to monitor the temperature. They are mounted on copper tabs, with leads wrapped several turns around the tab to ensure a good thermal contact.

Two liquid helium level sensors are used, with one in the stack and the other installed in the side tube of the cold mass. A liquid nitrogen level sensor is installed in the stack LN₂ pot at the output of the radiation shield cooling line.

Cryogenic Plumbing

A triple cryogenic feedthrough with LN₂ intercepted vacuum break accommodates LHe input, Helium cold gas return and LN₂ input. The low heat leak compact design allows for a flanged bellows connection in the tight space in the CESR tunnel.

The cryogenic plumbing contains four separate circuits: LHe line; gaseous helium warm return; LN₂ line for shields and LN₂ pre-cooling line for cold mass. They are all made of SS tubing.

The LN₂ precooling circuit is clamped and glued onto 9.525 mm thick copper plates which are thermally bonded between SS support plates of cold mass halves. This line cools the cold mass to 80 K from room temperature and is capped off afterwards. The gaseous helium warm return line serves for cooling down from 80 K to 4.2 K. It is also capped off afterwards. The helium output is then switched to the cold return line which is connected to the refrigerator through the transfer line. The LN₂ precooling line and helium warm return line are anchored at 80 K to minimize 4.2 K heat load during wiggler operation.

Vacuum System

There are two separate vacuum systems in the wiggler module. The cryogenic insulation vacuum provides a high vacuum to avoid heat load by conduction from the environment to the cold mass, while the beam pipe vacuum requires ultrahigh vacuum to provide a good beam lifetime and low background for the experiment.

The insulation vacuum of the prototype wiggler was pumped by a turbomolecular pump. All future wigglers are pumped by diffusion pumps with water cooled baffles. Once the insulation space is pumped to the range of 10^{-4} Pa, LN₂ precooling process can be started. After the system is cooled down, the cryopumping on the large surface of multilayer super-insulation is sufficient for maintaining high vacuum (10^{-6} Pa).

A non-evaporable getter (NEG) pump is connected to the copper beam-pipe to pump gas load induced by wiggler SR and bending magnet SR.

ASSEMBLY AND TEST

Assembly

Vacuum leak checking, including cold shocking of cryogenic subassemblies at 77 K, was carried out throughout the cryostat manufacture process.

The insulation vacuum vessel is constructed in two parts to facilitate cryogenic plumbing connection. The short vessel incorporates all necessary ports for cryogenic plumbing and instrumentation wiring. The long vessel is installed last when all components are assembled and aligned. Finally two 660 mm O-ring sealed flanges are welded onto the beam-pipe to complete the cryostat. The assemble sequence is as below (see Fig. 4):

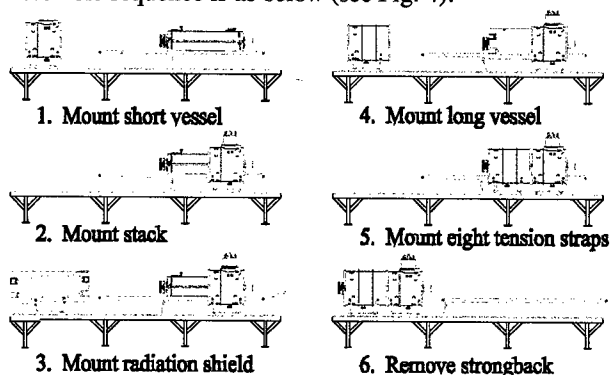


Figure 4: Assembly procedure.

Pre-assembly: Place preassembled unit of beam-pipe shield with beam-pipe on the bottom half of cold mass, and then connect the top half to the bottom half with pre-cooling plates in between;

Step 1 and 2: Slide short vacuum vessel over cold mass and connect cryogenic tubing. Assemble current leads and wires to the cold mass, and then finish stack assembly.

Stage 3, 4 and 5: Install outer radiation shield and connect liquid nitrogen tubing. Slide long vacuum vessel into place, mount all eight tension straps with invar rods.

Stage 6: Remove temporary support from the cold mass. Finish end interconnection, and then weld the vessel end flanges to beam-pipe;

Throughout the assembly optical surveying is used to provide alignment of the magnet to the beam-pipe within 0.1 mm.

Test and Operation

Prior to installation in the CESR tunnel, each wiggler magnet was tested and run above 2.1 T field. Magnetic field quality measurements were performed.

Three proportional pneumatic control valves regulate LHe input, cold helium gas return, and LN₂ input. The input flow of LHe and LN₂ are controlled through level sensors. Helium bath pressure is controlled using helium return valve and a pressure sensor. LHe overpressure or power outage would shut the LHe input valve and the cold return valve.

For protecting the magnet, the power supply current would commence a slow run-down if one of three cryogenically related indications occurs: high He pressure in cold mass; high He pressure in return line; poor insulation vacuum in cryostat. More importantly, quenches cause external switch to open ramping magnet down in ~ 10 seconds.

So far we have completed and tested six wigglers. The prototype was installed into the CESR ring and successfully operated with beam since October 2002. All six wigglers worked well the first time they were cooled down. One to three training quenches occurred to some of them before reaching the target current. It took 48 hours to precool the cold mass to 80 K using the LN₂ precooling line. Then it took five hours and 200 liters of LHe to cool down to 4.2 K and fill up the cold mass. The static LHe evaporation rate is about 1.5 ~ 2.0 l/h. This corresponds to a heat load of 1.0 ~ 1.35 W, close to the budgeted load. When quenches did occur, the maximum pressure in helium bath went up to 1.8 atmospheres in a few seconds with a helium loss of 16 liters.

SUMMARY AND ACKNOWLEDGMENTS

A full-scale superferric wiggler prototype, to enhance synchrotron radiation damping for CESR-c at low energies, has been successfully developed, fabricated and operated in the CESR ring. Five more wigglers have been tested and are now installed. Proper design of the cryostat plays an important role in ensuring reliable wiggler magnet operation.

The authors would like to thank the machine shop and technical support staff at LEPP for their contributions to the manufacture of the wiggler cryostats.

REFERENCES

- [1] D. Rice, Proc. EPAC 2002, p. 428
- [2] A. Mikhailichenko, Proc. PAC 2001, p. 3648
- [3] J. Crittenden et al, PAC 2003, WPAE009
- [4] D. Rice et al., PAC 2003, TOAB007

THE PILOT-RUNS OF THE HELIUM CRYOGENIC SYSTEM FOR THE TLS SUPERCONDUCTING CAVITY

F.Z. Hsiao, H.C. Li, T.C. King, S.H. Chang, Ch. Wang, M.C. Lin, J.C. Chang and J.R. Chen

National Synchrotron Radiation Research Center
Science-Based Industrial Park, Hsinchu 30077, Taiwan

Abstract

At NSRRC the installation of a helium cryogenic system, which is tailor-made for the cooling of TLS superconducting cavity, was finished at the end of October 2002. The cryogenic system had finished its first phase commission work at the end of March 2003. This paper presents the first measurement result of the cryogenic system.

INTRODUCTION

A helium cryogenic system with cooling capacity of 450 W at 4.5 K was set up in National Synchrotron Radiation Research Center (NSRRC) at the end of the year 2002. This helium system is dedicated for the cooling of a 500 MHz superconducting radio frequency (SRF) cavity which is the key item of an upgrade project to enhance the beam current and stability of NSRRC electron storage ring. The cryogenic system is a turnkey system and provided by the Air Liquide Company; its configuration is shown in Fig. 1[1]. The system includes one 315 kW compressor, one 45 kW recovery compressor, one 10 kW refrigerator, one 2000 liter dewar, two 100 m3 gas helium storage tanks, and one 5 m multi-channel transfer line. The distribution valve box is included in the SRF cavity system since the inside control valves regulate the pressure and level of the cryostat. In normal operation the SRF cavity will require a cooling power of 80 W at 4.5 K and a liquefaction rate of 0.18 g/s for the cooling of cavity's wave guide[2].

SYSTEM INSTALLATION

Apparatus of the cryogenic system are installed at three areas, i.e., the platform, the gas yard, and the compressor room. Figure 2 shows the layout of these three areas. The refrigerator, the dewar, and the distribution valve box are located on the platform with 2.8 m height. The liquid helium is drawn off from the dewar and sent to the

distribution valve box through the multi-channel transfer line; the helium is then sent to the cryostat of the SRF cavity via the 6 m flexible transfer line. The space under the platform is reserved for the cavity test before its installation into the storage ring.

The main compressor and its oil removal module, the various frequency driver for the main compressor, the recovery compressor and its oil removal module are installed in the compressor room, which is located in the basement of the utility building. The compressor room is constructed with soundproof wall and vibration isolation floor. A ventilation system is installed to provide the cooling air for the compressor motor and prevent the oxygen-poor condition. All the signals in the compressor room are collected in a cabinet and then sent to the PLC controller on the platform via the PROFIBUS communication protocol.

In the gas yard a nitrogen storage tank with a capacity of 20000 liter is installed and two helium tanks are located nearby. Liquid nitrogen is used for precooling the first heat exchanger of the refrigerator; it is also used for the thermal shielding of the multi-channel line, the distribution valve box, and the cavity cryostat. A local grounding network for pressure transmitters is installed in foundations of the nitrogen tank and the helium tanks. Another grounding network is constructed for the nitrogen tank to prevent a lightning strike.

COMMISSION RESULT

Before filling the grade-A helium into the gas tank, the dry nitrogen gas was flushed into the tank until the dew point of the tank was less than -59°C . The gas tank was then evacuated down to 0.13 mbar from 1 bar and this procedure took 48 hours. After two cycles of purge and pump down, the tank was filled with helium up to 10 bar. The charcoal of the oil removal module was dried using hot nitrogen gas ($\sim 70^{\circ}\text{C}$). It took more than one week for keeping the dew point down to -60°C ; three days were required for the recovery oil removal module. The leakage test for the inner piping of the refrigerator shows a value lower than $1.3\text{e-}8$ mbar-L/sec; the test for the interconnect piping among the compressor, the refrigerator, and the gas tank shows a leakage value lower than $7\text{e-}8$ mbar-L/sec.

The capacity measurement at the dewar after optimizing parameters of the cryogenic system is shown in Fig. 3, where the dewar pressure was kept at 1.3 bar

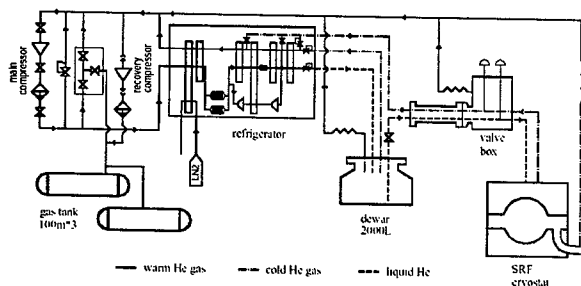


Figure 1: Configuration of the helium cryogenic system.

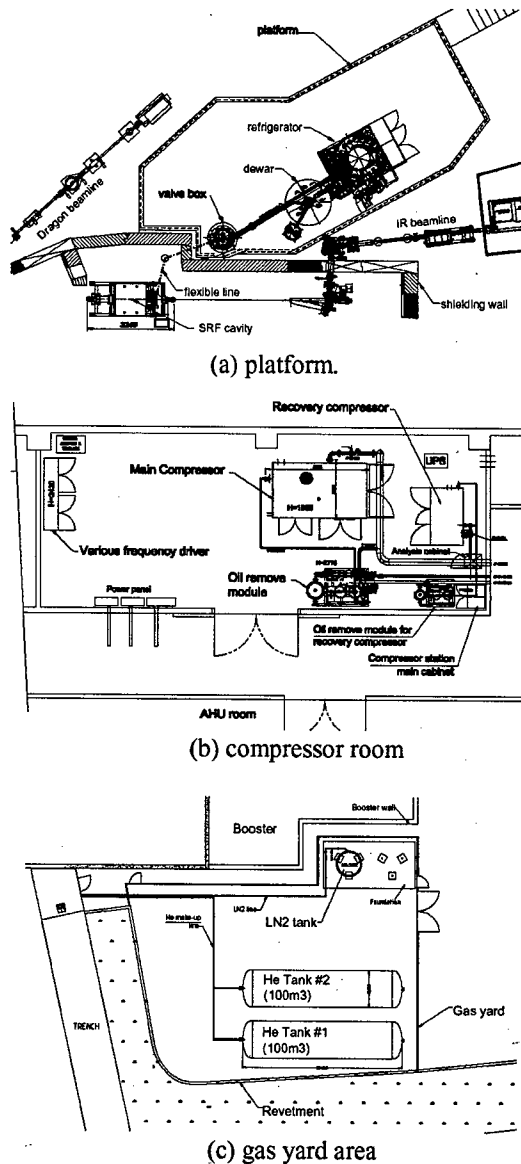


Figure 2: Cryogenic system layout.

(1.25 bar) as liquid nitrogen was (wasn't) used for precooling. In the test of liquefaction mode the dewar level increases 8 % (20.2 %) in 3 hours without (with) liquid nitrogen for precooling; i.e., the system provides liquefaction rate of 60.5 L/hr and 153 L/hr. In the refrigeration mode the system provides a cooling power of 255 W with 10.6 L/hr liquefaction rate without liquid nitrogen and 452 W with 5.6 L/hr liquefaction rate using liquid nitrogen. After linear extrapolation the data from the performance test one can know the system provides cooling power of 309 W (469 W) at refrigeration mode without (with) liquid nitrogen for precooling. The mass flow rates are 24 g/sec (39 g/sec) and 44 g/sec (82 g/sec) respectively during the test at liquefaction mode and refrigeration mode without (with) liquid nitrogen. During commission the system capacity can be automatically turned down either by changing the compressor discharging flow via a frequency driver or adjusting the

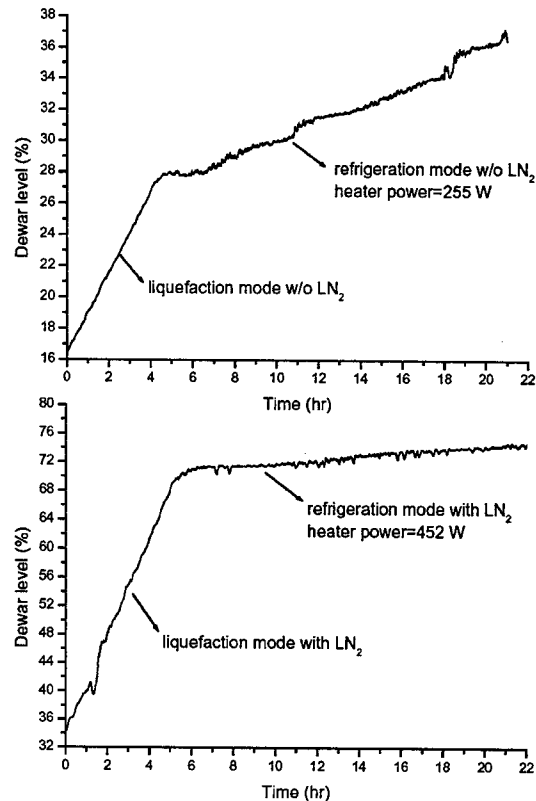


Figure 3: Capacity measurement at dewar.

mass flow in the expansion turbine via its inlet control valve. Table 1 summarizes the design and measured values of the helium cryogenic system. The system provides more capacity than the design value: a larger margin is provided as the system is operated either in refrigeration mode without liquid nitrogen or in liquefaction mode with liquid nitrogen.

Figure 4 shows the result of a stability test, where the test period lasted more than 72 hours. The resulting pressure of the suction line kept at 1.05 bar with ± 2 mbar fluctuation; the dewar pressure kept at 1.38 bar with $\pm 5/3$ mbar fluctuation. These pressure fluctuations are compatible to the ± 3 mbar fluctuation requirement specified from the SRF cryostat. Figure 4 also shows an increase in the mass flow rate during the switch period of the two 80 K cryogenic absorbers. The pressure fluctuation increases when the dewar level is kept at a high value of 85 %, where the level fluctuates up to ± 0.4 % within 16 hours operation.

There happened several times system interrupt due to either the electric power was interrupted or the emergency push button was incidentally touched. Components of the cryogenic system are automatically isolated from each other during those interrupt events. The suction line pressure increases since the refrigerator depressurizes itself as system being interrupted. Each time the safety relief valve of the suction line, which is placed near the oil removal module, acts first due to its lowest setting pressure of 1.5 bar. During system interrupt period the suction line pressure increased up to 1.54 bar, which is lower than the setting pressure of the safety valve in SRF

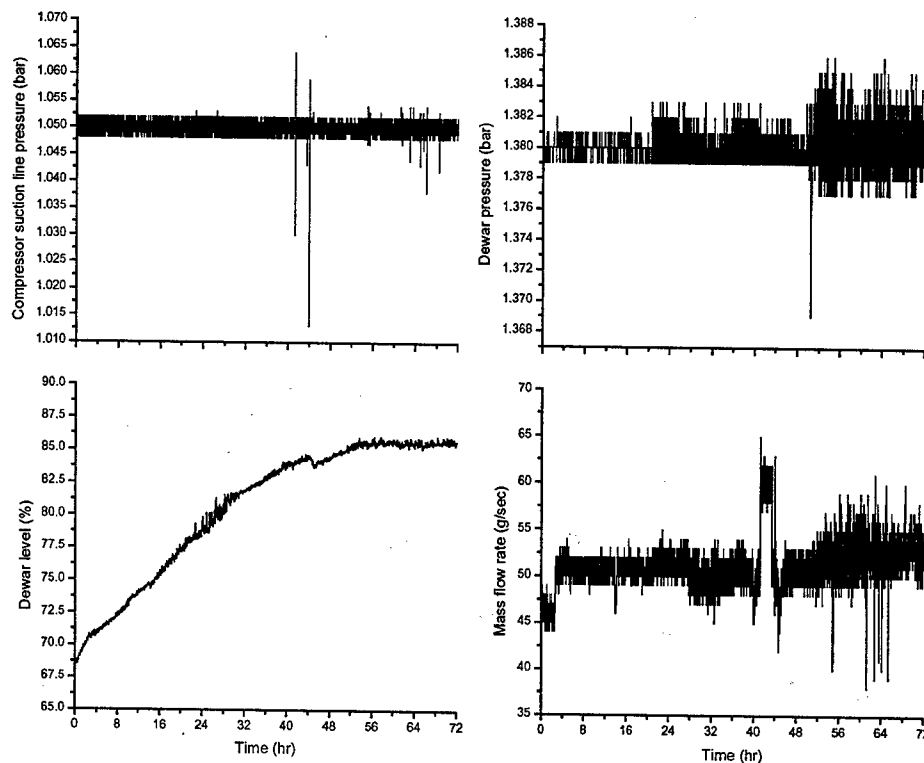


Figure 4: Stability and reliability test.

cryostat; thus the helium loss at cold condition could be prevented.

CONCLUSION

The cryogenic system provides a higher capacity than the specified value. Stability test shows acceptable level of pressure fluctuation at both the dewar and the compressor suction line. This system is ready for providing helium cooling for the operation SRF cavity, which will be installed at NSRRC in the near future.

ACKNOWLEDGEMENT

The authors wish to thank Mr. F. Lepron, Mr. E. Walter, and Miss A. Caillaud from Air Liquid DTA for their effort during the commission of the cryogenic system.

REFERENCE

- [1] F.Z., Hsiao, et al., "The Liquid Helium Cryogenic System for the Superconducting Cavity in SRRC", PAC 2001, Chicago, June 2001, p. 1604.
- [2] "Technical Specification of the Main Cryogenic Plant for a 500 MHz SRF Module," SRRC Technical Report, Nov. 24, 2000.

Table 1: Characteristics of the helium cryogenic system.

Item	Units	Design value				Measurement value			
		Refrigeration		Liquefaction		Refrigeration		Liquefaction	
		w/o LN2	w/ LN2	w/o LN2	w/ LN2	w/o LN2	w/ LN2	w/o LN2	w/ LN2
Cooling capacity	W	255	450	-	-	309	469	-	-
Liquefaction rate	L/hr	-	-	51	115	-	-	60.5	153
Mass flow rate	g/s	51.2	73.9	42.3	59.6	44	82	24	39
Frequency driver	Hz	35	52	30	42	42	57.5	33.2	43.5
Discharge pressure	bar	12.2	15	15	15	15	15	15	15
Suction pressure	bar	1.05	1.05	1.05	1.05	1.05	1.05	1.05	1.05
Suction pressure fluctuation	mbar	+/-3	+/-3	+/-3	+/-3	+/-2	+/-1	+/-2	+/-2
Dewar pressure	bar	1.25	1.3	1.25	1.3	1.25	1.272	1.25	1.25
Dewar pressure fluctuation	mbar	+/-3	+/-3	+/-3	+/-3	+/-1	+3/-2	+/-1	+/-1
Warm turbine speed	Hz	2724	2730	3340	2658	2912	2752	3200	2752
Cold turbine speed	Hz	-	2069	-	-	1842	1963	1846	1990

DESIGN OF CRYOGENIC SYSTEM FOR SEVERAL SUPER-CONDUCTING MODULES AT NATIONAL SYNCHROTRON RADIATION RESEARCH CENTER

T. C. King, F. Z. Hsiao, S. H. Chang, H. C. Li, J. C. Chang, and J. R. Chen

National Synchrotron Radiation Research Center,
Hsinchu Science-Based Industrial Park, Hsinchu, 300 Taiwan, Republic of China

Abstract

National Synchrotron Radiation Research Center (NSRRC) is planning to install two 500 MHz super-conducting radio frequency (SRF) cavities and six super-conducting magnet (SM) modules. For the cryogenic requirements, we are presently constructing a helium cryogenic system. The cryostat properties of the SRF cavities and the SM modules are so different that in our design the cryogenic system has two cryogenic plants (465W or 110 liters per hour @ 4.5 K for every plant), one is for the SRF cavities and the other is for the SM modules. The two plants are independent in normal operation. However, when the cryogenic plant for the SRF cavities shuts down, the other one can be transferred to supply the SRF cavities, and we design a distribution valve box to carry out the transformation.

NSRRC REQUIREMENTS

National Synchrotron Radiation Research Center (NSRRC) is a third-generational 1.5 GeV light source. There are 23 beam-lines now in NSRRC to supply light from IR to hard x-ray for experiments. Initially NSRRC does not have any super-conducting systems. To promote the storage ring, NSRRC is planning to replace the initial conventional radio frequency (RF) cavity by the super-conducting radio frequency (SRF) cavity, and install some super-conducting magnet (SM) modules as hard x-ray beam-line sources.

There are totally two 500 MHz SRF cavities and six SM modules will be installed in the storage ring. Figure 1 shows their locations, where the refrigerators and the liquid helium main Dewars are located on a platform beside the storage ring. The estimated heat leak of these

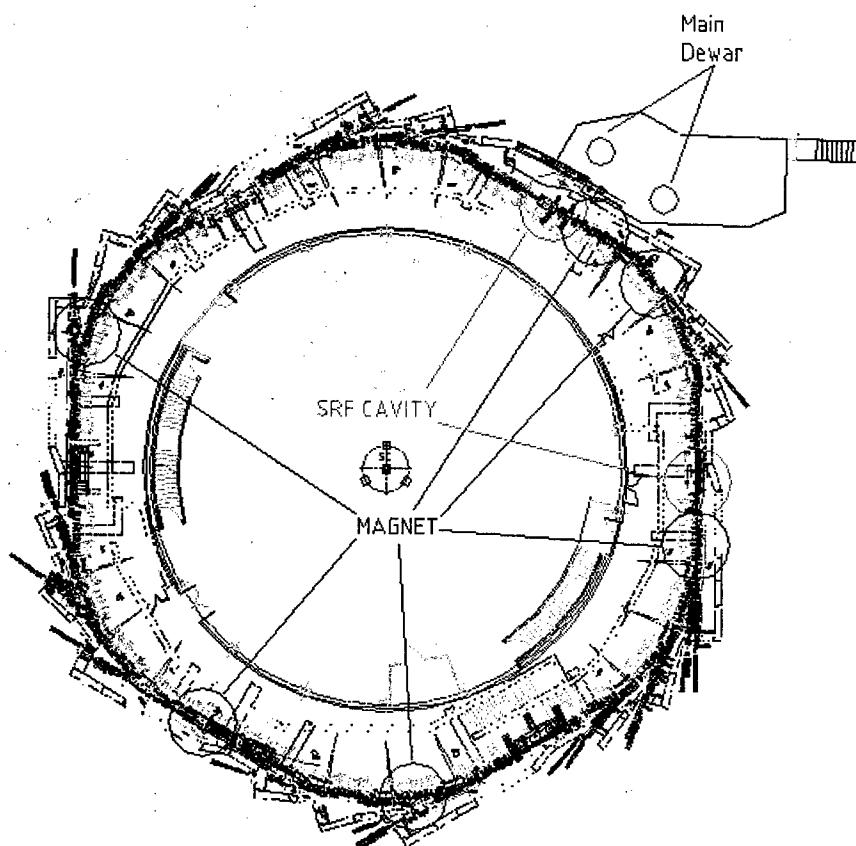


Figure 1: Locations of SRF cavities and SM modules.

super conducting systems, associated valve boxes, and cryogenic transfer lines are shown in Fig. 2. For the cryogenic requirements, we are planning to construct a cryogenic system with two cryogenic plants (herein named MCP1 for SRF cavities and MCP2 for SM modules), and the capacity of every plant is 465W or 110 L/hr @ 4.5 K.

The cryogenic quality demands of the SRF cavities and the SM modules are so different. The SRF cavities ask the pressure fluctuation must be less than 3 mbar and the level fluctuation must be less than 1% in its liquid helium vessel. The SM modules ask the pressure as low as possible, but do not care for the fluctuation of

pressure and level. Besides, the SM modules will sometimes quench and release huge quantity of helium gas in short time. Therefore, the SRF cavities and the SM modules can't be supplied by one cryogenic plant, and in our design the two cryogenic plants must normally operate independently. However, only several beam-lines will shut down if the SM modules shut down, but the storage ring will shut down if the SRF cavities shut down, i.e., about thirty beam-lines will shut down. Hence, we ask the MCP2 can be transferred to supply the SRF cavities when the MCP1 shuts down, and we design a distribution valve box to carry out this transformation.

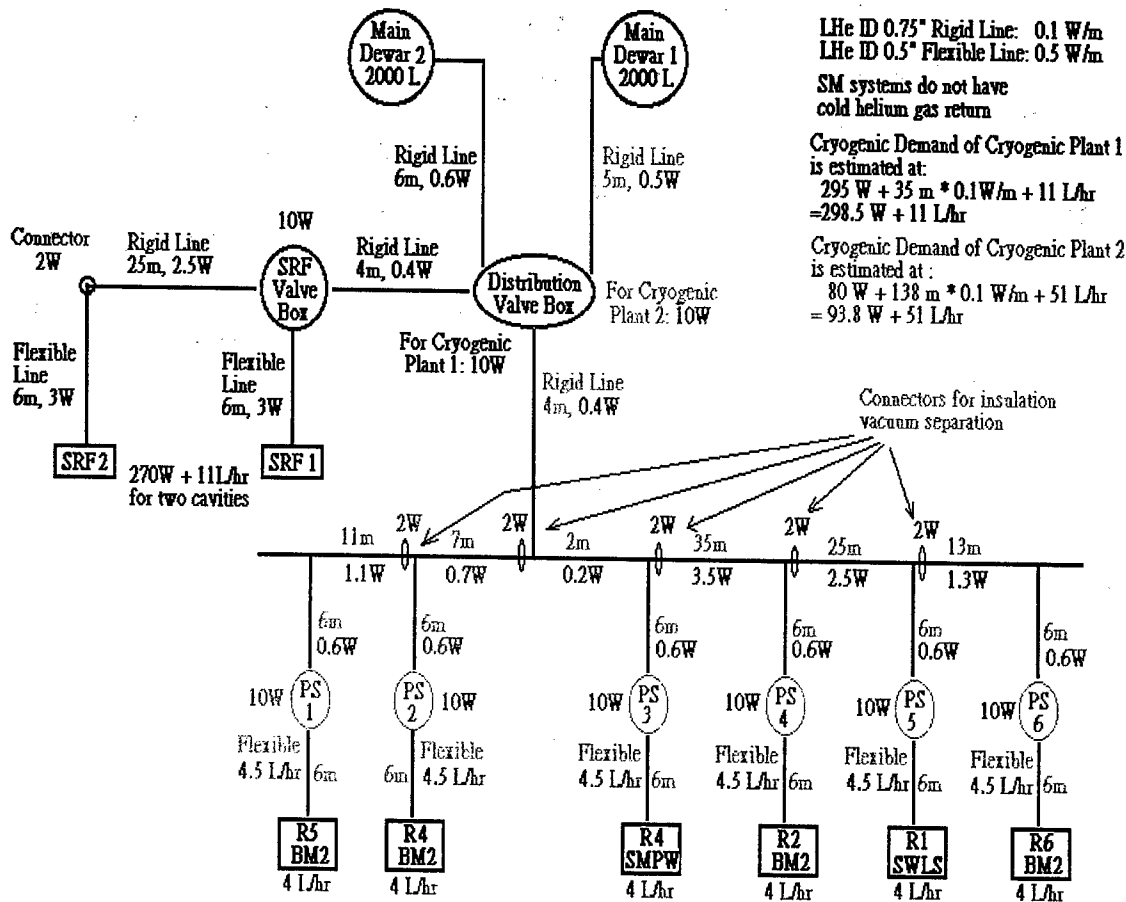


Figure 2: Estimated heat leak of SRF cavities, SM module, and associated valve boxes and piping.

CRYOGENIC SYSTEM

Our cryogenic system is shown in Fig. 3, where the distribution valve box is the key part in our design. In normal operation, the valves V102, VD01, VD02 close, and VD03, VD04, V101, V201 open. That is, the SRF cavities are supplied by MCP1, and the SM modules are supplied by MCP2. When the MCP1 shuts down but we

still want the SRF cavities to operate, we close the valves V101 and VD03, and open the valves V102, VD01 and VD02. Then the SRF cavities get the liquid helium from MCP2, and return the cold and warm gas back to MCP2. In the same time, the thermal release helium gas from MCP1, the SM modules, and their phase separators will also goes back to the MCP2.

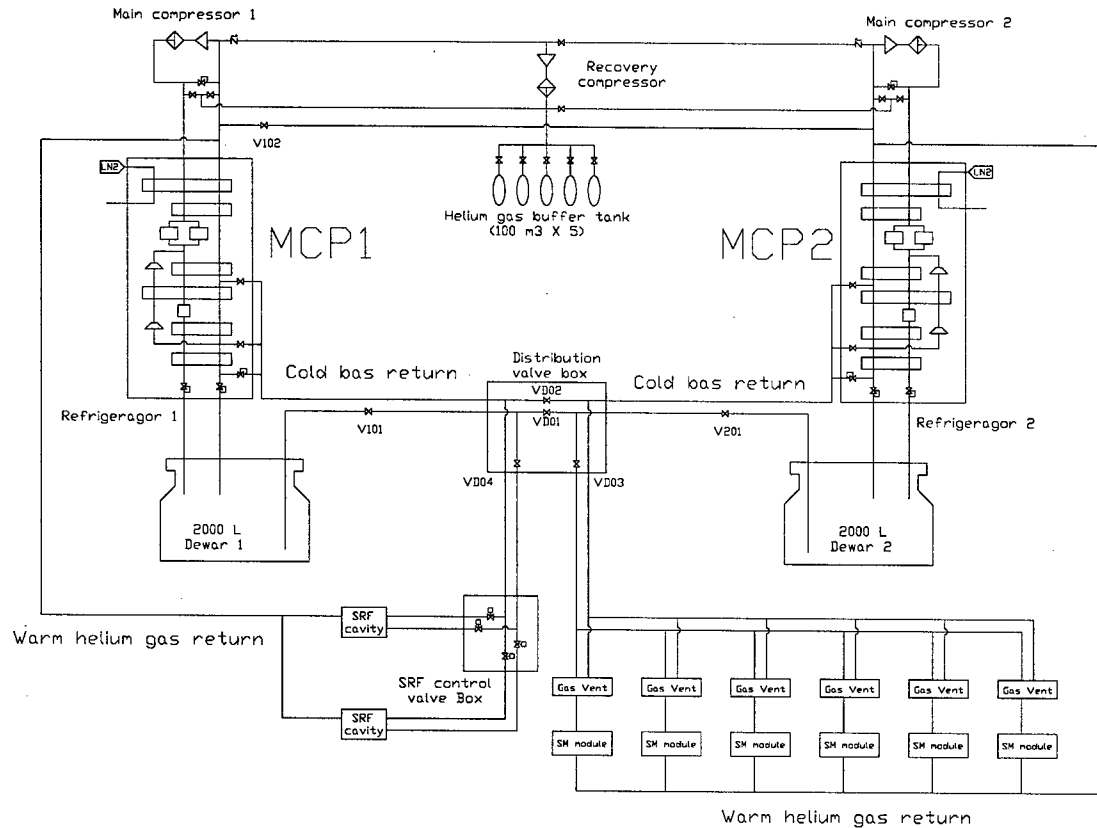


Figure 3: Cryogenic system of NSRRC.

Our design has some advantages. (1) The storage ring can operate if any one of the two cryogenic plants works. This point is very important for us because now our user time is crowded, and we have to avoid any unexpected storage ring shut down caused by the cryogenic system accidents. (2) The cryogenic system for the SRF cavities and the SM modules are isolated. If the SRF cavities and the SM modules are supplied by the same cryogenic plant, the quenches of the SM modules will disturb the pressure of the SRF cavities through the suction line, and the electron beam in the storage ring maybe will run trip. (3) Our design is the simplest way for that MCP2 is the backup of MCP1. Only the distribution valve box is the additional part for the backup function. The two

cryogenic plants can be different capacities, operated by different control systems, and from different vendors. Of cause, our design has some weak points. (1) Two cryogenic plants are more expensive and complex than a large one with the same total capacity. (2) There is additional heat leak (estimated at 20W) from the distribution valve box.

SUMMARY

Now the user time in NSRRC is crowded, and we have to do our best to avoid any unexpected storage ring shut down and electron beam run trip caused by the cryogenic system accidents. The design of NSRRC cryogenic system is based on our special requirements.

TECHNIQUES FOR SYNCHRONIZATION OF X-RAY PULSES TO THE PUMP LASER IN AN ULTRAFAST X-RAY FACILITY*

J. N. Corlett, L. Doolittle, R. Schoenlein, J. Staples, R. Wilcox, and A. Zholents, LBNL, Berkeley, California, USA

Abstract

Accurate timing of ultrafast x-ray probe pulses emitted from a synchrotron radiation source with respect to the signal initiating a process in the sample under study is critical for the investigation of structural dynamics in the femtosecond regime. We describe schemes for achieving accurate timing of femtosecond x-ray synchrotron radiation pulses relative to a pump laser, where x-rays pulses of <100 fs duration are generated from the proposed LUX source based on a recirculating superconducting linac. We present a description of the timing signal generation and distribution systems to minimize timing jitter of the x-rays relative to the experimental lasers.

PRODUCING FS X-RAY PULSES FROM PS ELECTRON BUNCHES

The techniques described here are developed for synchronization of ultrafast x-ray pulses produced in the LUX recirculating linac facility [1,2]. In this recirculating linac-based design, hard x-rays are produced after electron bunches receive a time-correlated vertical kick in a dipole-mode rf cavity. This imparts to the electron bunch a transverse momentum that is correlated in amplitude to longitudinal position within the bunch. The electrons then radiate x-rays in the downstream chain of undulators and dipole magnets, imprinting this correlation in the geometrical distribution of the x-ray pulse. The correlated x-ray pulse is then compressed by use of asymmetrically cut crystal optics to achieve the ultra-short x-ray pulse length. Stability of the x-ray pulse to bunch arrival time at the deflecting cavities is described in [1,3].

A laser-seeded cascaded harmonic-generation scheme produces EUV and soft x-ray pulses [4]. In this process the electron beam is passed through an undulator where a co-propagating seed laser modulates the charge distribution over a short length of the bunch. The imposed modulation results in enhanced radiation at specific wavelengths and a selected wavelength is amplified in a following undulator, tuned to a higher harmonic of the seed laser. The harmonic-generation scheme has been developed and demonstrated at the Brookhaven DUV FEL facility [5]. The process is directly seeded by a laser system, and the seed laser oscillator can also be used to drive the endstation pump laser, resulting in tight synchronization between laser pump and x-ray probe pulses.

MASTER OSCILLATOR

We propose a laser oscillator as master oscillator for the LUX facility, providing optical pulses at ~ 80 Mhz rate to the multiple experimental endstations, the cascaded harmonic generation seed laser, and the rf photocathode laser. In addition, the same master oscillator provides rf signals by use of photodiodes. The optical signals must be transported with fs-scale timing stability over distances of approximately 100 m.

Figure 1 shows the block-diagram of a master oscillator based on a passively modelocked femtosecond laser cavity providing optical pulses of less than 100 fs duration. In essence, this laser is a highly stable comb generator. By illuminating a photodiode with output pulses from this laser, one can generate RF harmonics extending from the fundamental oscillator frequency (cavity frequency = 81.25 MHz, round trip time = 12.3 ns), up to the bandwidth limit of the photodiode (which can extend well into the GHz range). Thus, this laser is a direct source for all the necessary RF signals for the linac and other rf systems. Because the laser is passively modelocked, the phase noise is substantially lower than that of conventional RF oscillators at frequencies above ~ 1 kHz. The dominant phase noise contribution for such lasers originates typically from mirror motion due to environmental acoustics as well as amplitude noise of the pump laser. With advances in stable diode-pump sources, pump laser effects can be largely eliminated. In addition, air turbulence effects are eliminated in hermetically sealed cavities, and in modelocked fiber lasers, both of which are available from commercial vendors. Low frequency acoustic effects and long-term cavity drift can be effectively suppressed by locking the fundamental cavity frequency to a conventional high-stability rf generator by constructing a phase-locked loop as illustrated in Figure 1, in which the laser cavity acts as a voltage-controlled oscillator by modulating the cavity length with a moving mirror attached to a piezoelectric transducer. Thus, a femtosecond laser phase-locked to a stable rf generator provides phase noise levels which match that of the rf generator at low frequencies (DC to ~ 1 kHz), and are substantially better at high frequencies. Table 1 summarizes the essential characteristics for two potential master oscillator laser systems.

* This work supported by the U.S. Department of Energy under Contract No. DE-AC03-76SF00098

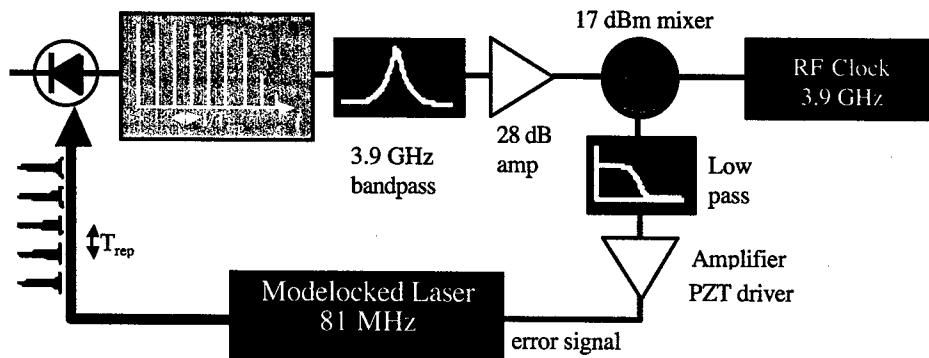


Figure 1. Schematic diagram of an rf-stabilized modelocked laser oscillator

Table 1. Master oscillator laser parameters

Master oscillator laser	Ti:sapphire	Er fiber
Timing jitter	<50 fs	<50 fs
Phase noise	<120 dBc/Hz	<120 dBc/Hz
Pulse duration (fs)	<100	2000
Wavelength (μm)	0.78	1.55
Repetition rate (MHz)	81	81
Average power (W)	~ 1	~ 0.01

TIMING DISTRIBUTION

The optical distribution system must be extremely stable, particularly with respect to path length drift (e.g. a path length drift of only 10 μm corresponds to a time shift of 30 fs). One approach is to use free-propagating beams and mirrors. In this case, pointing stability will require an active position feedback system and hermetically sealed (low vacuum) optical transport lines. A second and currently preferred approach is to use a fiber delivery system. With either approach, active monitoring of the path length stability is assumed. This may be accomplished by back-reflecting a cw reference laser, with interferometric techniques to monitor and control the path length via a piezo-driven variable optical delay line.

One advantage of an optical fiber delivery system is that it completely eliminates any pointing stability problem. However, in a fiber delivery system the nonlinear optical effects and pulse-stretching effects (group-velocity dispersion) must be managed, by propagating sufficiently low pulse energies and by using photonic bandgap fiber in which the group velocity dispersion is balanced by the modal dispersion. Alternatively, by choosing a fiber laser operating at 1.55 μm as the master oscillator laser, one can take advantage of zero-dispersion fiber that is routinely used for telecommunications applications.

Figure 2 illustrates the general layout of the master oscillator and timing systems for a fiber system. The passively modelocked laser oscillator coupled to a high-stability rf generator is the original source for the rf signals required for the linac, as well as the original source of seed laser pulses for laser amplifiers at various

locations in the facility. The photocathode drive consists of a second laser system (oscillator/amplifier combination) that is slaved to the master oscillator. Laser pulses from the master oscillator are distributed via an optical transport system to various beamlines. At the beamline endstations a separate modelocked femtosecond laser oscillator (synchronized to the master oscillator), followed by a power amplifier, provides the pump signal to the sample.

DELAY LINES AND PATH LENGTHS

The path lengths from the master oscillator laser to the various beamline endstations will in general not match the path length of the electron beam and x-rays. Thus, delay lines will be required. These delay lines should be as compact as possible and the length kept to a minimum (~ 1 m) in order to preserve stability. An important point is that the master oscillator laser acts as an extremely stable optical delay line. Beamline users can select any pulse, within a given time window (from the 81 MHz train of pulses) for triggering subsequent sample excitation.

SYNCHRONIZATION OF SYSTEMS

Synchronization of lasers to femtosecond timescales by rf locking at high harmonics in the GHz frequency range has been demonstrated by several groups [6,7,8]. We propose to use similar techniques to ensure synchronization between the master oscillator and all other laser oscillators in the facility. Experimental demonstration of locking lasers to fs stability using ps duration master oscillator pulses is to be demonstrated.

In addition to synchronization of the laser systems, the electrical rf signals in the accelerator will be derived from the optical master oscillator by high frequency photodiodes, commercially available up to 60 GHz bandwidth. Use of low-noise rf signal amplifiers reduces the electrical noise to the inherent Schottky noise in the diode. Rf feedback systems as depicted in Figure 3 control the phase and amplitude of the rf waveforms in the accelerator cavities, to control modulation arising predominantly from microphonics in the superconducting cavities.

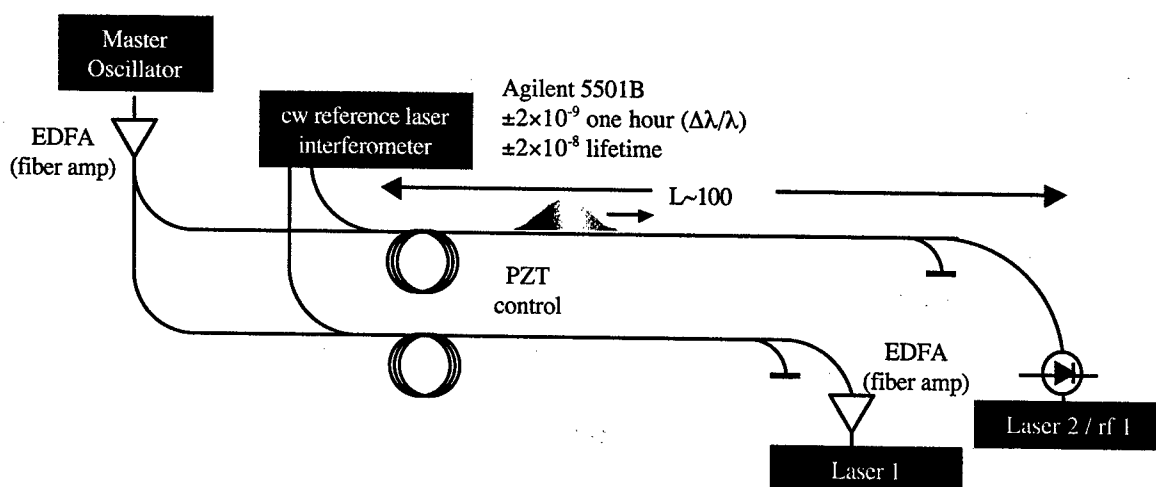


Figure 2. Schematic of fiber distribution network with path length control $\Delta l = \pm 2 \mu\text{m}$, $\Delta t = \pm 7 \text{ fs}$.

DEFLECTING CAVITIES AND PHASE NOISE

The phase of the deflecting cavity voltage with respect to the experimental pump laser is most critical in hard x-ray synchronization in LUX [1,3]. Phase noise from a passively modelocked femtosecond laser is typically superior to rf sources at frequencies above $\sim 1 \text{ kHz}$, and the deflecting cavity loaded bandwidth may be adjusted to allow the cavity phase to follow the low-frequency variations inherent in the laser master oscillator, with minimal residual timing jitter resulting from the laser phase noise. To control the cavity phase and amplitude a system similar to that shown in Figure 3 will be employed. The drive power to control the superconducting cavities, even with loaded bandwidth of 1 kHz , remains in the order of 100 W . Controlling the cavity phase to 0.01° would result in a timing stability of 7 fs . The expected timing jitter for the hard x-ray pulses, including effects of movements in the beamline downstream of the deflecting cavities, is then a few tens of femtoseconds.

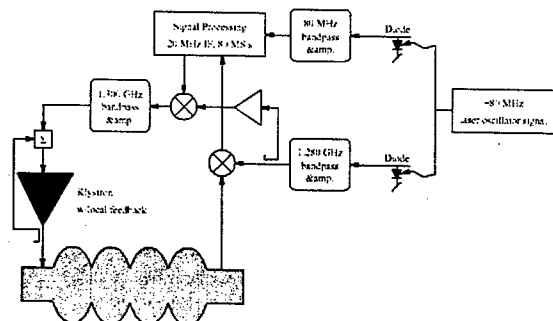


Figure 3. Rf systems control schematic.

ELECTRON BEAM TIMING JITTER

Contributors to the timing jitter in the electron beam include photoinjector laser and rf errors, time of flight

changes in the transport lines due to energy variation from coherent synchrotron radiation emission, and magnet ripple. The lattice design has been carefully developed to control and minimize path length variations as a function of bunch charge, for example [9]. These effects are currently being evaluated to produce a timing jitter budget - our initial estimate is that the jitter in the electron beam with respect to the master oscillator will be approximately $\pm 0.5 \text{ ps}$. This is well within the requirements for overlap of the cascaded harmonic generation seed pulse, and the requirement that the electron beam arrive in the linear region of the rf waveform in the deflecting cavities.

REFERENCES

- [1] J. N. Corlett et al, "Feasibility study for a recirculating linac-based facility for femtosecond dynamics", LBNL formal report LBNL-51766, December 2002.
- [2] J. N. Corlett, et al, "A Recirculating Linac Based Facility for Ultrafast X-ray Science", this conference.
- [3] J. N. Corlett, et al, "Synchronization of x-ray pulses to the pump laser in an ultrafast x-ray facility", Proc. EPAC'02, Paris, France, June 2002.
- [4] W. Fawley et al, "Simulation studies of an XUV/soft x-ray harmonic-cascade FEL for the proposed LBNL recirculating linac", this conference.
- [5] L.-H. Yu et al, "High-Gain Harmonic-Generation Free-Electron Laser", Science **289** 932-934 (2000).
- [6] R. Shelton et al., *Opt. Lett.*, **27**, 312 (2002).
- [7] D.J. Jones et al., *Rev. Sci. Instruments*, **73**, 2843 (2002).
- [8] A. Bartels, S.A. Diddams, T.M. Ramond and L. Hollberg, *Opt. Lett.*, **28**, 663 (2003).
- [9] A. Zholents et al, "Longitudinal phase-space control in the Berkeley Femtosecond X-ray light source", this conference.

BUNCH PURITY EVOLUTION DURING APS STORAGE RING TOP-UP OPERATIONS*

A.H. Lumpkin[†], C.-Y. Yao, B.X. Yang, and T. Toellner
Advanced Photon Source, Argonne National Laboratory
Argonne, Illinois 60439 USA

Abstract

During top-up operations of the Advanced Photon Source (APS) storage ring, a growth of the charge in the buckets on the trailing time side of the target rf buckets was observed in the bunch purity monitor data. This system is based on a photon counting technique that provides sub-ns time resolution with a dynamic range of greater than 10^6 . The satellite bucket growth was related to the number of linac bunches being injected into the particle accumulator ring (PAR) and the adjustment of the 12th harmonic rf cavity phase. Besides measuring this growth in the +3,+1 buckets relative to the 22 singlets targeted during top-up, we also report a special configuration and extended counting period that detected charge at the 10^{-9} level of the target bucket.

INTRODUCTION

The Advanced Photon Source (APS) storage ring serves as a national hard x-ray synchrotron user facility [1]. In addition to the requirements of high brilliance of hard x rays, beam stability at the few-micron rms jitter level, and >95% availability, the bucket purity of the fill pattern is monitored at the one part in a million level. The timing experiment users (e.g., nuclear resonance experiments) request that the adjacent bucket charge/intensity on the trailing time side (+) of the target rf buckets should be less than 10^{-6} of the target bunch. This is particularly relevant when the fill pattern is nominally 1+22 singlets with the 22 singlets spaced by 54 rf buckets (352 MHz rf fundamental). Any charge in the buckets on the late side becomes a background source to the experiments triggered by the target buckets. The bunch purity measurement is done by the standard photon counting system based on a fast x-ray avalanche photodiode (APD), timing electronics, and an analog-to-digital converter (ADC) linked to the EPICS system. Although bunch purity is very stable in our injections done at 12-hour intervals, our system detected a change in the bunch purity of the +1 bucket during top-up operations where single-shot injection occurs every two minutes. We have traced this to the change in the number of linac bunches selected for injection into the particle accumulator ring (PAR) and the adjustments of the PAR 12th harmonic rf phase during top-up. Examples of the bunch purity measurements from a standard fill and the evolution during top-up will be shown.

EXPERIMENTAL BACKGROUND

Some background about the injector and the bunch purity system will now be presented.

APS Injector System

The APS uses an S-band linac to accelerate electrons from the rf thermionic gun. The electron beam macropulse is about 8 ns long and typically includes about 1 nC of charge. The beam energy is 325 MeV at the end of the linac, and this beam is accumulated in the PAR at up to a 30-Hz rate. The number of macropulses can be selected from 1 to 6. The beam is damped in the PAR with the assistance of a 12th harmonic cavity at 117.3 MHz. The beam is extracted at a 2-Hz rate and injected into the injector synchrotron (IS), which ramps the energy up to 7 GeV in a 200-ms time period. Extraction from the booster and injection into the storage ring (SR) also can occur at a 2-Hz rate under standard conditions, such as a fill from zero charge or a fill-on-fill procedure done at 12-h intervals. However, for top-up operations with the 1+22 singlets pattern and low effective emittance of about 2.9 nm-rad, the charge from the injection is added in one shot every two minutes. In order to compensate for the shorter lifetime of the latter fill pattern, ~2.8 nC per shot is needed so more linac bunches are selected to inject into the PAR. Initially there was no procedure to retune the PAR rf for this beam loading change.

The Bunch Purity Monitor

The bunch purity monitor is based on the standard photon counting system [2,3], which uses a fast x-ray APD, timing electronics, a time-to-amplitude converter (TAC), and an ADC linked to the EPICS system. A bunch clock generator built by the APS Controls Group provides a timing reference for each of the buckets targeted for charge in the prescribed fill pattern. A schematic of the system is shown in Fig. 1. X rays emitted by the beam as it transits an upstream dipole magnet are transported through a pinhole aperture to a stainless steel scattering foil. The APD is at 90° to the x-ray beam direction and positioned by a remotely controlled translation stage. The x-ray arrival times are compared in the TAC to these bunch clock signals. The multichannel analysis (MCA) time spectrum is the average of the bucket purity adjacent to each of the targeted singlets. Count rates in the detector of 80 kc/s result in the 10^6 counts in the target peak after 300 s. Due to the PAR's 12th harmonic being one third of the IS and SR fundamental frequency, it is possible for charge to

*Work supported by U.S. Department of Energy, Office of Basic Energy Sciences, under Contract No. W-31-109-ENG-38.

[†]lumpkin@aps.anl.gov

appear in the ± 3 bucket position. The +1 bucket is usually very weakly populated unless there are timing drifts in the 12th harmonic phase.

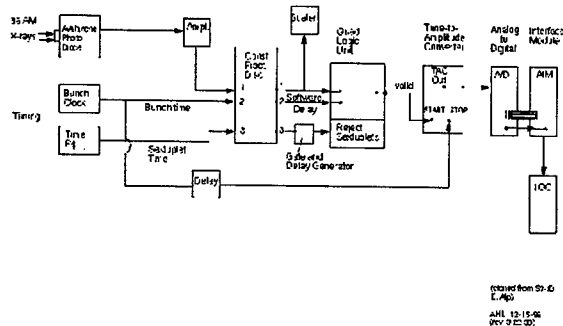


Figure 1: A schematic of the photon counting electronics layout for the bunch purity monitor.

EXPERIMENTAL RESULTS

Top-Up Operations

The initial observations of bucket purity degradation occurred after the top-up operations became routine in the Fall of 2001. The bucket purity was better than 10^{-6} at the +1 and +3 buckets just after filling from zero current to 100 mA, as shown in Fig. 2. However, within eight hours the bucket purity was measurably degraded to about 5×10^{-5} . In a later run this degradation of the +1 and +3 buckets reached the 10^{-5} level after 98 hours as shown in Fig. 3. The nominal operations guideline is to maintain the bunch purity ratio better than 10^{-5} .

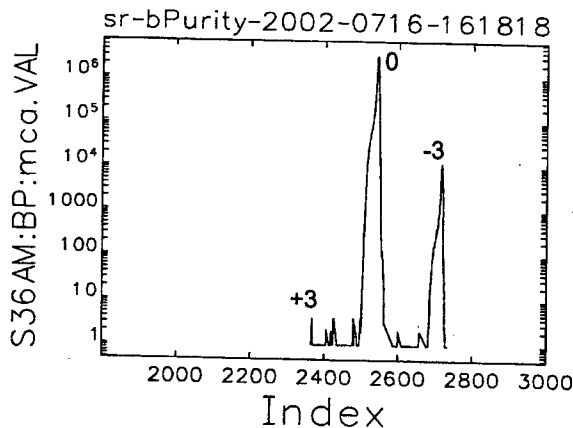


Figure 2: An example of the bunch purity measurement from the MCA showing the dominant signal on the target bucket and the minimal signal on the late time side (left) after the fill from zero current.

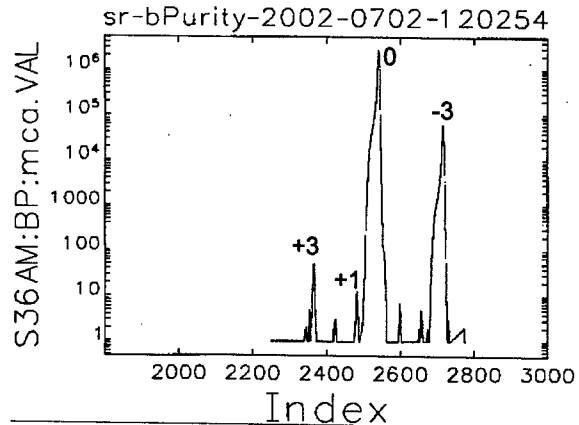


Figure 3: An example of the bunch purity measurement from the MCA after 98 hours of top-up operations. The growth of the +1 and +3 bucket intensity is to a level of about 10^{-5} of the target bucket.

Controlled Experiments

Studies were conducted to investigate the difference in the injection procedure between initial fills and top-up. It was recognized that the initial fill was done by injection only one or two linac macropulses into the PAR, but for top-up the operators switched to three or four linac macropulses. The PAR 12th harmonic rf was usually optimized for the first injection scenario, but not the second. We were able to demonstrate this by dedicated studies with the injector and storage ring on several occasions. We filled the storage ring to 102 mA each time using two, three, four, and five linac bunches selected for injection into the PAR. The two-bunch case is particularly clean as shown in Fig. 4. The four-bunch case is shown in Fig. 5. There is significant +1 impurity at the 10^{-4} level. For the four- and five-bunch cases we obtained a large +1 bucket impurity, which indicates an instability in the PAR rf system (since the 12th harmonic of the PAR is 1/3 of the SR rf frequency). We were also able to clean these impurities by selectively driving the weak bunches into a scraper blade. This test was done partly to develop the capability to clean the impure buckets and partly to demonstrate the signals were bunch-charge related and not electronic noise (see Fig. 6). The 12th harmonic function generator has been changed and retuned to provide better damping of the beam and better phase stability. The growth of the satellite buckets has been reduced during top-up operations with these steps.

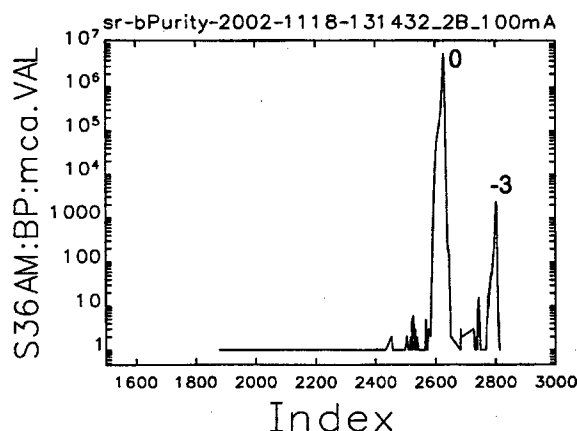


Figure 4: An example of the bunch purity measurement from the MCA using two linac bunches per cycle into the PAR. Bunch purity is nominal.

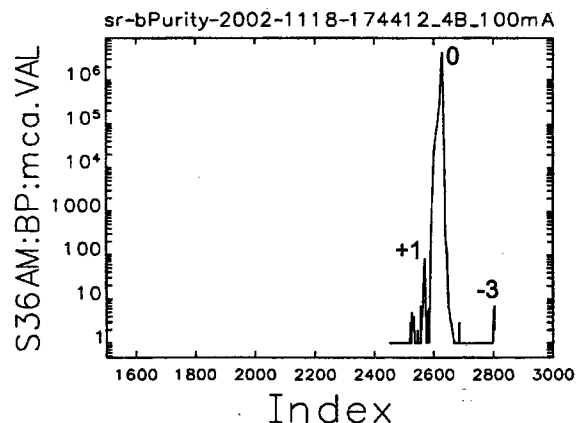


Figure 5: An example of the bunch purity from the MCA using four linac bunches per cycle (1/2 s) into the PAR. Bunch purity is degraded noticeably.

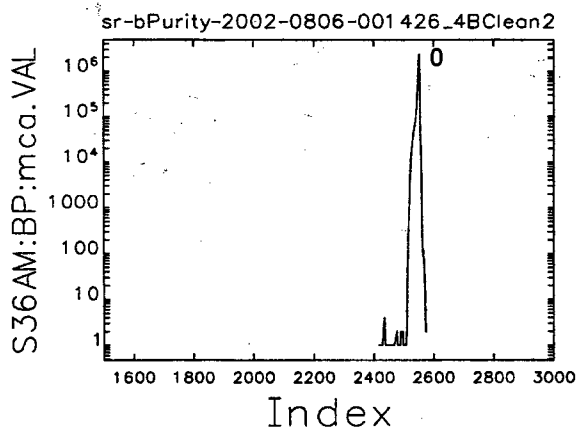


Figure 6: An example of the bunch purity from the MCA after bunch cleaning using a resonantly driven beam oscillation.

Ultrahigh Bucket Purity

During the course of these tests, an additional effect was reported by a user experiment on very small intensities (10^{-9} level) in the satellites 32-36 buckets away from the target singlets [4]. This effect appeared to have some correlation with the +1 and +3 bucket growth. We opened up the pinhole aperture upstream of the APD and moved the detector closer to the scattering foil to obtain count rates of about 500 k per second. We also integrated the MCA data over a 24-hour period. We were able to confirm trace charges in these far away buckets (which are close to one period of the PAR) at the 10^{-9} level as shown in Fig. 7.

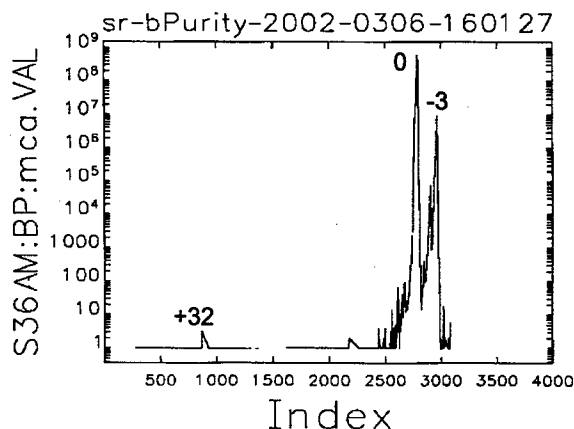


Figure 7: An example of the bunch purity from the MCA with statistics to the 10^9 range. There are a few counts at the +32 bucket position.

SUMMARY

In summary, we have used the bunch purity system to identify a degradation of the bunch purity during top-up operations. Controlled experiments were used to verify their source, and an improved tuning of the PAR's 12th harmonic phase has reduced the effect. We also demonstrated the ability to measure satellite impurity to the 10^{-9} level.

REFERENCES

- [1] J.N. Galayda, "The Advanced Photon Source," Proc. of the 1995 Particle Accelerator Conference, IEEE, Vol. 1, pp. 4-8 (1996).
- [2] J. Revol (ESRF), private communication (May 1998).
- [3] E. Alp and T. Toellner (Argonne National Laboratory), private communication (September 1999).
- [4] W. Sturhahn (Argonne National Laboratory), private communication (March 2002).

THE FEASIBILITY OF OTR IMAGING OF HIGH-INTENSITY PROTON BEAMS AT FNAL*

A. H. Lumpkin and V. Scarpine[†]

Argonne National Laboratory, Argonne, IL USA

[†]Fermi National Accelerator Laboratory

Abstract

The Fermi National Accelerator Laboratory (FNAL) is currently pursuing a number of projects where either beam luminosity for the Tevatron collider (Run II) or proton intensity for neutrino experiments requires careful tracking of beam properties throughout the facility or before a target. The feasibility of using optical transition radiation (OTR) imaging for the proton (or antiproton) beam sizes in transport lines between the rings of the facility has recently been evaluated. Based on comparisons to electron beam results at the Advanced Photon Source (APS) linac and proton results at CERN, the potential of OTR imaging at FNAL looks very encouraging.

INTRODUCTION

Particle-beam diagnostic techniques based on optical transition radiation (OTR) have been demonstrated at a number of facilities over a wide range of beam energy (or Lorentz factor, γ). The preponderance of these measurements has been on electron accelerators where the beams have $\gamma > 10$ and adequate charge ($\sim 10^9$ e⁻) within a 30-ms video camera frame time to produce useable images. The potential for online imaging of proton beams with $\gamma > 10$ at the accelerators at Fermi National Accelerator Laboratory (FNAL) has recently been reviewed. The accelerators at FNAL involve a number of projects where proton beam intensity for the Tevatron collider (currently in Run II) or proton intensity for neutrino experiments requires careful tracking of beam properties throughout the facility or before a target [1]. The feasibility of using OTR imaging for the intense proton beams is evaluated in comparison to electron-beam results at the Advanced Photon Source (APS) linac [2] and proton-beam results at CERN [3]. The scalings on γ and the charge intensity indicate significant levels of OTR will be generated by the generally lower γ , but higher-intensity (5×10^{12} p) proton beams. The signal levels are compatible with standard CCD or CID camera technology. In addition, by using a thin metal screen as the converter foil, a minimally intercepting beam profile capability would be attained.

BACKGROUND

FNAL Complex

The FNAL accelerator complex has evolved during the last decades. Major upgrades have included the

construction of the Tevatron with its superconducting magnet upgrade and the addition of the new Main Injector (MI) ring. The protons from the linac are stacked and ramped to 8 GeV in the booster. A transport line, MI-8, brings the protons to the new MI, which ramps the beam energy to 120 GeV. As can be seen in Fig. 1, the protons are extracted through the P1 line to F0 where they are either switched into the Tevatron or else continue along the P2 line to F17. At F17 the protons are switched to the AP-1 line and directed to the antiproton target. The prototype experiment with OTR is to be done in the AP-1 proton line just upstream of the target. During normal antiproton production, protons are sent to the target in a single 1.6- μ s-long pulse train every 2 to 3 seconds.

OTR Background

Optical transition radiation is generated when a charged-particle beam transits the interface of two media with different dielectric constants (e.g., vacuum to metal or vice versa) [3-6]. The effect is a surface phenomenon that might be simply understood as the collapsing of the electric dipole formed by the approaching beam charge and its image charge in the metal at the surface. As the fields readjust, a burst of radiation is emitted. The expression for the single-particle spectral angular distribution of the number of photons, N_1 , per unit frequency (ω) and solid angle ($d\Omega$) is given by [6,7],

$$\frac{d^2 N_1}{d\omega d\Omega} \approx |r_{\perp, \parallel}|^2 \frac{e^2}{\hbar c \pi^2 \omega} \frac{(\theta_x^2 + \theta_y^2)}{(\gamma^{-2} + \theta_x^2 + \theta_y^2)^2}, \quad (1)$$

where e is the electron charge, \hbar is Planck's constant divided by 2π , c is the speed of light, γ is the Lorentz factor, and θ_x and θ_y are angles relative to the beam direction. The reflectivity of the surface for perpendicular and parallel polarized light is $|r_{\perp, \parallel}|^2$. In this paper we are only dealing with a single-foil, single-particle expression and its product with N_p , the number of particles.

Since it is a surface phenomenon, thin foils are often used as the converter screen to reduce beam scattering and to minimize heat deposition. The latter feature is of particular importance for proton beams due to their higher dE/dx than that of electrons. The radiation is emitted around the angle of specular reflection for backward (vacuum to metal) OTR so that if the foil is at 45° to the beam direction, the radiation is at 90° to the beam direction. This is schematically illustrated in Fig. 2.

* Work supported by U.S. Department of Energy, Office of Basic Energy Sciences, under Contract No. W-31-109-ENG-38.

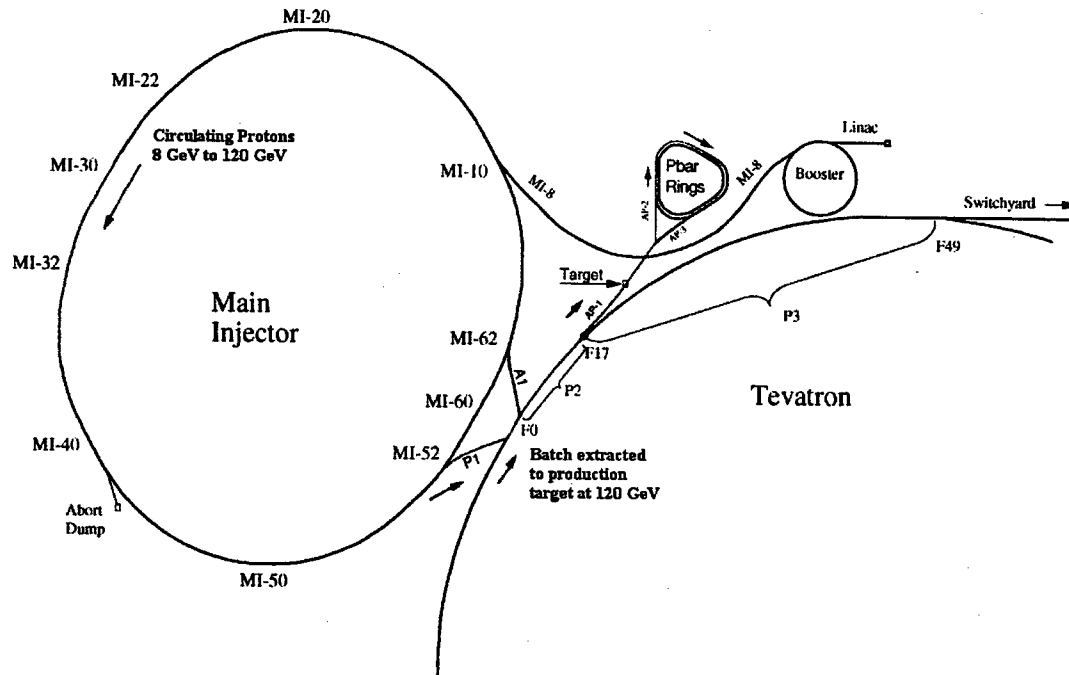


Figure 1: A schematic of the FNAL complex showing the linac, booster, Main Injector, Tevatron, and the transport lines between them.

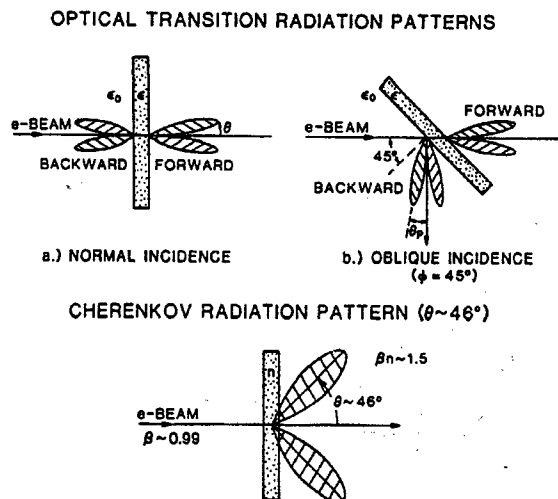


Figure 2: A schematic of the OTR radiation cases for normal incidence and for the foil at 45° to the beam direction. Backward and forward OTR are emitted at the two interfaces. The Cherenkov radiation pattern is shown for comparison.

The basic strategy is to convert the particle-beam information to optical radiation and then to take advantage of imaging technology such as cameras, video digitizers, and image processing programs. These techniques can provide information on transverse position, transverse profile, divergence, beam angle, emittance, intensity, energy, and bunch length. In the case of the proton beam applications, beam position and transverse profile are the two parameters of interest, particularly the latter. As mentioned, the possibility that beam scattering effects are negligible compared to intrinsic beam properties would make this a minimally intercepting technique (potentially online at all times subject to foil survivability).

OTR FEASIBILITY CONSIDERATIONS

Electron Beams

The feasibility of using the OTR techniques for the FNAL proton beams was assessed in part by considering recent experiments at the APS linac. We have performed experiments with electron beam energies from 50 to 600 MeV. The 0.3-nC micropulse from an rf photocathode gun or the 1-nC macropulse from the rf thermionic gun was accelerated and sampled at several beamline stations. Beam imaging was successful for such charges, and beam sizes of about 0.2 mm (σ) were measured [2].

Proton Beams

Since the original work by Jelley with intense proton beams in the 1950s [5], a significant amount of work has been done at CERN beginning with collaborations with L. Wartski in 1984 [3]. The CERN results indicate imaging screens of aluminized mylar or thin Ti foils can survive proton beams of 10^{12} particles and with beam focus sizes of a few mm [8].

Potential FNAL Proton Beam Case

Although several cases have been considered at FNAL, we have recently directed our attention towards a measurement of the 120-GeV proton beams in the AP-1 transport line upstream of the antiproton production target. At this location there was an air gap in the transport line as part of a vacuum isolation of the downstream Be vacuum window and the rest of the beamline. At the air-gap z location the beam is not tightly focused, and the two Ti foil vacuum windows on either end of the gap establish the survivability of foils at this location. A Ti foil in the air gap at 45° to the beam would serve as the OTR converter screen. A mirror and lens system will transport the OTR to the in-tunnel CID camera.

The expected beam properties for the protons are compared to the known electron beam case at APS in Table 1. For comparable γ between the beams, the key particle number of 5×10^{12} for the protons indicates about 10^3 times more light than the electron cases. The camera will be integrating the signal over the 84 bunches of protons in the 1.6- μ s-long pulse train. However, the reflectivity of Ti is less than the Al mirror used in the electron beam case, and the proposed CID camera is less sensitive to light than the CCD technology. These factors reduce the system sensitivity by 50-100, but there still should be a strong video signal. Measurement of individual bunches could be done with a gated, intensified camera.

Table 1: A comparison of OTR imaging for electron beams to 120-GeV proton beams. The application looks feasible in context of signal strength, spatial resolution, and minimally intercepting foils.

Feature	Electrons	Proton
Beam size (σ)	200 μ m	1 mm
Macropulse	8-40 ns	2 μ s
Q (nC)	0.3	800
Particle #	1.8×10^9	5×10^{12}
γ	100-14000	129
Theta peak	10-0.07 mrad	8 mrad

SUMMARY

In summary, the very high-energy proton beams with their high particle intensity are strong candidates to be imaged by OTR techniques. An initial experiment in a transport line is being planned in CY03. Following a successful demonstration, a three-screen emittance measurement and beta-function matching configuration may be installed between the main injector and the Tevatron for both the proton and antiproton transfer lines. This would be used to evaluate and optimize beam conditions in support of Run II. Other possible applications involve the proton transport lines that support the neutrino experiments.

ACKNOWLEDGMENTS

The authors acknowledge the support of K.-J. Kim (APS), W. Schappert (FNAL), R. Webber (FNAL), and S. Pordes (FNAL).

REFERENCES

- [1] The Fermilab Main Injector: Technical Design Handbook, Fermi National Accelerator Laboratory website, <http://www-fmi.fnal.gov>.
- [2] A. H. Lumpkin et al., Nucl. Instrum. Methods, A429, 336 (1999).
- [3] J. Bosser, J. Mann, G. Ferioli, L. Wartski, "Optical Transition Radiation Proton Beam Profile Monitor," CERN/SPS 84-17 (1984).
- [4] I. Frank, J. Ginsburg, J. Phys. USSR 9 353 (1945).
- [5] P. Goldsmith, J. V. Jelley, Phil. Mag. 4 836 (1959).
- [6] L. Wartski, J. Marcou, S. Roland, IEEE Trans. on Nucl. Sci., Vol. 20, No. 3, June 1973.
- [7] D.W. Rule et al., "The Effect of Detector Bandwidth on Microbunch Length Measurements made with Coherent Transition Radiation," Advanced Accelerator Concepts: Eighth Workshop, W. Lawson, C. Bellamy, and D. Brosius, eds., AIP 472, p. 745-754 (1999).
- [8] C. Bovet et al., "The OTR Screen Betatron Matching Monitor of the CERN SPS," Proceedings of the 1999 DIPAC Workshop, May 16-18, 1999, Chester, England, CERNSL-99-050 BI (1999).

RECENT CHARACTERIZATIONS OF ELECTRON BEAMS FROM THE APS LINAC*

A.H. Lumpkin[†], W.J. Berg, M. Borland, and J. Lewellen

Advanced Photon Source, Argonne National Laboratory, Argonne, IL 60439 USA

Abstract

The Advanced Photon Source (APS) facility includes an S-band linear accelerator (linac) that normally provides beam for the injection system of the 7-GeV storage ring. This beam is usually generated by one of two rf thermionic guns or the rf photocathode (PC) gun under special circumstances. When the beams are not required for injection, we may characterize them at a station located at the end of the linac. At this station we have begun a retrofit and upgrade of the optics on the diagnostics table that is outside of the linac enclosures. For beam transverse profiling studies, a CCD camera was used to image the beam spot at the YAG:Ce screen or the optical transition radiation (OTR) screen. In using the quadrupole field scanning technique we demonstrate that the YAG:Ce saturation effect is present under these conditions so that OTR imaging is needed for PC gun beam. A Hamamatsu C5680 streak camera with OTR and a zero-phasing rf technique with an electron spectrometer were used for bunch length measurements of beam from a newly-installed rf thermionic gun. These results will also be presented.

special circumstances. When the beams are not occupied with injection, we may characterize them at several stations along the accelerator. In particular, we report here observations at the end of the linac that were supported by a recent upgrade of the optics on the diagnostics table. The beam transverse profile measurements were performed at 325 MeV using the PC gun beam and both YAG:Ce and optical transition radiation (OTR) screens. We demonstrated that during the quadrupole field scanning techniques used in the emittance measurements, the beam charge areal density crossed the saturation threshold of the YAG:Ce crystal so OTR imaging was needed [1]. We also evaluated the beam bunch length as a function of the scraper position in the alpha magnet associated with the rf thermionic gun. Both a streak camera technique with OTR and the zero-phasing rf technique with an electron spectrometer were used. These measurements clearly showed that a shorter bunch length (albeit with less charge) could be obtained by scraping off the lower energy, later arriving electrons. A preliminary comparison of the results at the sub-ps level is presented.

INTRODUCTION

Interest continues in the characterization of the linear accelerator (linac) beams at the Advanced Photon Source (APS) as components are upgraded or configurations changed. The APS facility includes an S-band linac that normally provides beam for the injection system of the 7-GeV storage ring. This beam is generated by one of two rf thermionic guns or the rf photocathode (PC) gun under

EXPERIMENTAL BACKGROUND

These experiments were performed at the APS using beams accelerated by the S-band linac, which is normally used as part of the injector system for the 7-GeV storage ring. The measurements were performed at the end of the linac at an energy of 325 MeV, the nominal energy for operations. As shown schematically in Fig. 1, either the rf thermionic gun or rf PC gun can be used to provide beam

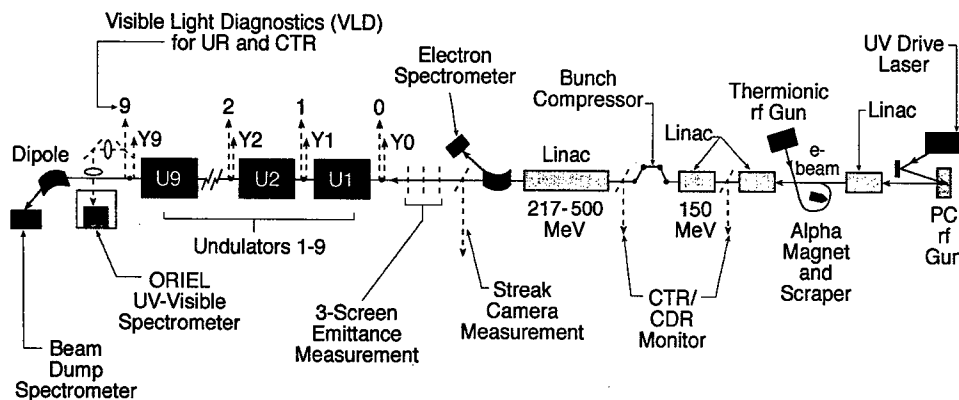


Figure 1: A schematic of the APS linac with its guns, accelerator, and diagnostic locations.

* Work supported by U.S. Department of Energy, Office of Basic Energy Sciences, under Contract No. W-31-109-ENG-38.

[†]lumpkin@aps.anl.gov

to the linac. The thermionic gun system includes an alpha magnet for compression and injection of beam into the linac line. The PC gun beam can be compressed with a chicane bunch compressor as described elsewhere [2].

For the beam transverse profiling experiments, the beam was imaged at the same location indicated for the streak camera in Fig. 1 and just beyond the electron spectrometer. At the time of these experiments a crossed polarizer under EPICS control was added for remote light intensity control in front of the CCD camera that imaged the YAG:Ce screen or OTR screen. The visible light was transported by mirrors and a set of achromat lenses from the linac tunnel to the optics table outside of the radiation enclosure. In the case of the YAG:Ce screen tests, this remote intensity control was used during the quadrupole field scan to balance the video level signals generated. In the case of the OTR tests, the intensity was adjusted by the use of the neutral density filters to avoid the factor of 4 attenuation overhead of the crossed polarizers. The Vicon CCD was operated in the line-locked mode to provide a synchronization with the camera, line-locked linac, and the MaxVideo 200 video digitizer.

For the bunch length measurements, the Hamamatsu C5680 streak camera with OTR and the zero phasing rf technique with the electron spectrometer were used. The locations are shown in Fig. 1. Due to the low charge per micropulse (~30 pC) in the 8-ns-long macropulse from the rf thermionic gun, the streak camera images were taken in synchroscan mode at 119.0 MHz as a 10-shot or micropulse average. However, the Chromox converter screen in the focal plane of the electron spectrometer has a slow time response that averaged the effects of all 25 micropulses in each macropulse. By adjusting the rf accelerator phase in a section upstream of the spectrometer so the micropulse arrived on the maximum slope of the rf cycle, the arrival times of the electrons were encoded as energy differences. The energy plane became a time axis for the micropulses. Our initial experiments with the newly installed gun were to evaluate the effects of the alpha-magnet scraper position on observed micropulse bunch length and to compare the two measurement techniques.

EXPERIMENTAL RESULTS

In this section we will present the results of the transverse and longitudinal beam profiling experiments.

Transverse Beam Profile Results

One of the goals of these beam profiling experiments was to determine if the YAG:Ce converter screen could be reliably used for beam characterizations of the PC gun beam at this location. We rely on beam size measurements based on YAG:Ce screen at 150 MeV after the chicane to evaluate emittance and in the PAR bypass regime. We had previously discovered an effective threshold for saturation, where above certain areal charge densities the screen gives a blurred image [1]. The quadrupole scans were first done with the YAG:Ce screen

and then repeated with the OTR screen. The image intensities were adjusted so that we operated with similar video levels into the video digitizer. The results of the scans are shown in Fig. 2. The YAG:Ce images are systematically a little larger than the OTR images, and this is particularly true at the beam waist. The saturation effect results in an overestimate of the PC gun beam size by a factor of 1.75. This is again a demonstration that tightly focused beams of 300 pC per pulse can exceed the saturation threshold in YAG:Ce crystals, so care must be taken in employing such screens for beam characterizations.

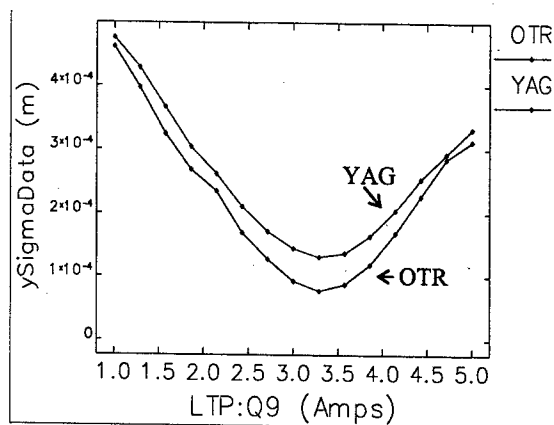


Figure 2: A comparison of beam sizes measured as a function of quadrupole field strength using the YAG:Ce screen and the OTR screen. Smaller beam sizes are observed with the OTR technique at the beam waist.

Bunch Length Measurement Results

Our newly-installed rf thermionic gun (#2) was next evaluated. The macropulse contained about 0.7 nC with the scraper at the out position (reading 9.5 cm). At this position an rms bunch length of about 2 ps was measured by both techniques. An example of the streak image is given in Fig. 3, and a tabulation of results for several images and conditions is provided in Table 1. As the scraper is put further into the beam in the dispersive point of the alpha magnet, the low-energy tail and then the core on the low energy/late time side are trimmed. At the 11.5-cm scraper position a very narrow peak at about the expected streak camera resolution limit of 0.6 ps is observed. There is some evidence of the gun or rf transitioning between conditions that result in two bunch length states. A bandpass filter with 40-nm width was used to reduce the chromatic temporal effects in the streak camera input optics.

Statistical fluctuations seemed reduced in the zero-phasing rf technique data. Evaluations of the bunch length vs. scraper position are shown in Fig. 4. The shortest bunch length calculated at the scraper setting of 11.7 cm is below the streak camera resolution. However, we believe these initial cross comparisons of the two techniques also contributed to the gun characterization.

Table 1: A Tabulation of Preliminary Streak Camera Results versus Alpha-Magnet Scraper Settings

Run #	Scraper Position (cm)	Charge: L5 cm1 (nC)	Raw FWHM (ps)	# Averaged	Raw Estimated σ (ps)
A	9.5	0.7	4.6	1	2.0
A	11.0	0.6	3.0	2	1.3
A	11.3	0.4	2.6	2	1.1
B	9.5	0.8	5.1	6	2.2
B	11.0	0.7	4.1	2	1.7
B	11.5	0.3	3.4	2	1.5
			2.4	3	1.0

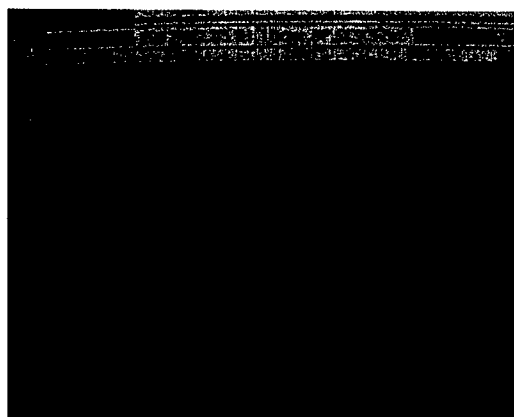


Figure 3: An example of a streak image of the rf thermionic gun beam for a scraper setting of 9.5 cm. The time axis is the vertical axis, and the x-profile is on the horizontal axis.

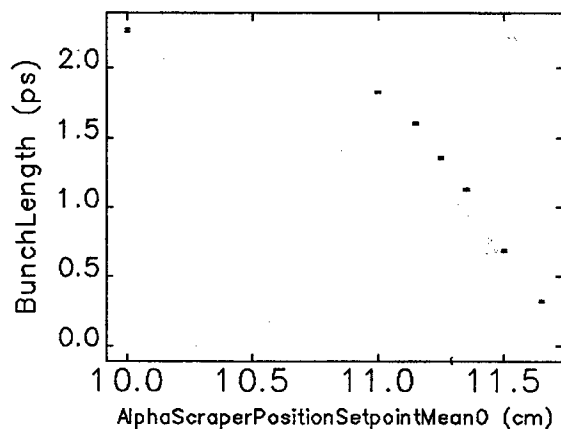


Figure 4: A plot of the measured bunch length using the zero-phasing rf technique vs. the alpha-magnet scraper position.

SUMMARY

In summary, we have used our imaging techniques at the end-of-linac station (sta-5) to determine the limitation of the YAG:Ce screen for small, bright beams at 325 MeV. In addition, we have performed the first bunch length measurements as a function of alpha-magnet scraper position for our new rf thermionic gun. Sub-ps bunch lengths were obtained, although at very low charge per micropulse.

ACKNOWLEDGMENTS

The authors acknowledge the support of O. Singh, G. Decker, and R. Klaffky of the Accelerator Operations Division of APS.

REFERENCES

- [1] A.H. Lumpkin et al., Nucl. Instrum. Methods in Phys. Res. A429, 336-340 (1999).
- [2] M. Borland, J. W. Lewellen, and S.V. Milton, "A Highly Flexible Bunch Compressor for the APS LEUTL FEL," Proc. of the XX International Linear Accelerator Conference (LINAC2000), SLAC-R-561, 863-865 (2001).

INITIAL CTR-BASED BUNCH LENGTH MEASUREMENTS OF LINAC BEAMS FOLLOWING THE APS BUNCH COMPRESSOR*

A. H. Lumpkin,[†] W. J. Berg, M. Borland, J. W. Lewellen and N. S. Sereno
Advanced Photon Source, Argonne National Laboratory, Argonne, IL 60439 USA

Abstract

The interest in generation and characterization of ultrabright electron beams for experiments at the Advanced Photon Source (APS) resulted in the installation of a four-dipole chicane bunch compressor within the linac. Both rf thermionic guns and an rf photocathode (PC) gun can be used to generate the electron beams with ps-regime bunch lengths. The bunch compressor can then be used to produce sub-ps bunches. In support of this initiative, a coherent transition radiation (CTR) bunch length monitor based on a far-infrared (FIR) Michelson interferometer was also installed at a location just downstream of the compressor. It used a room-temperature Golay cell as the FIR detector. Processing of the autocorrelation data indicated that structures shorter than 500 fs were being generated.

INTRODUCTION

The generation and characterization of ultrabright electron beams continues to be of interest to the accelerator community. At the Advanced Photon Source (APS) we have addressed these issues in part by the installation of a four-dipole chicane bunch compressor [1] at the 150-MeV point in the linac and in part by the installation of a bunch length monitor based on coherent transition radiation (CTR) techniques [2,3]. In the cases where the rf photocathode (PC) gun and rf thermionic gun generate ps-long bunches, the bunch compressor can be

used to shorten the bunch to the sub-ps domain. In this domain a FIR Michelson interferometer has been used to detect radiation in the sub-300- μm -wavelength regime and to perform an autocorrelation of that signal so that profile information can be obtained. These experiments were the first at the APS with the device installed after the chicane. Previous results were reported for a 50-MeV location located after the α -magnet of the thermionic gun [3]. A zero-phasing rf technique was also used with the analyzing magnet at the end of the linac to verify that very short bunches were being generated. Both measurement techniques indicate there is a narrow time spike at the leading edge of the pulse that results in the higher peak current at that point.

EXPERIMENTAL BACKGROUND

These experiments were performed at the APS using beam accelerated by the S-band linac, which is normally used as part of the injector system for the 7-GeV storage ring. We have obtained data with both the PC gun, which generates a single micropulse at 6 Hz, and the thermionic gun with an 8-ns-long macropulse. As seen in Fig. 1 the PC gun beam is at the 150-MeV point at the bunch compressor due to the additional accelerator structure available upstream of the thermionic gun location. The guns and linac are described elsewhere [4,5].

The location of the CTR monitor after the chicane compressor is also seen in Fig. 1. The FIR interferometer

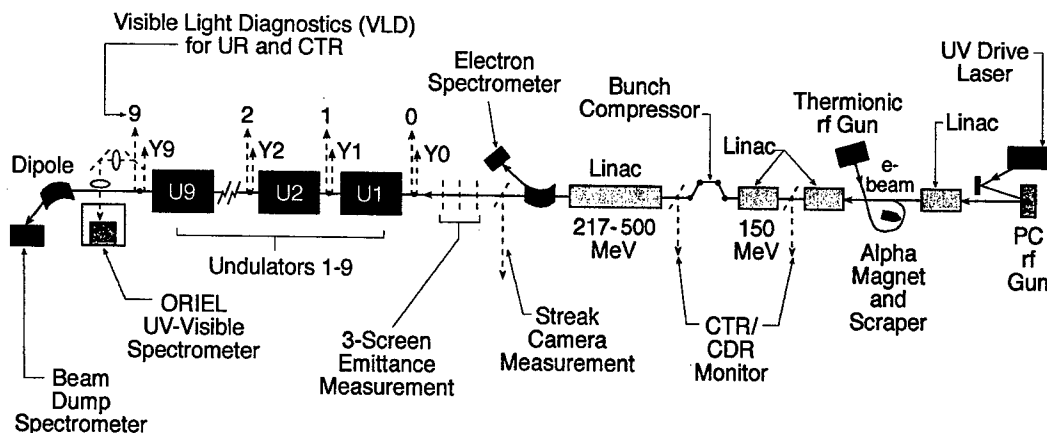


Figure 1: A schematic of the APS linac with bunch compressor, CTR monitor locations, and electron spectrometer indicated.

* Work supported by U.S. Department of Energy, Office of Basic Energy Sciences, under Contract No. W-31-109-ENG-38.

[†]lumpkin@aps.anl.gov

was described in [3]. It is based on the autocorrelation of FIR CTR generated as the charged-particle beam strikes a metal mirror oriented at 45° to the beam direction. This particular interferometer has a novel, compact design using an Inconel-coated beam splitter. A Golay cell, model OAD-7 from QMC Ltd., is used as the FIR detector. Its entrance window transmits well from $20\text{ }\mu\text{m}$ to 1 mm . The moveable arm of the interferometer and the data acquisition are handled via EPICS. The bunch profile was calculated using a fast Fourier transform (FFT) of the autocorrelation followed by an application of the minimal phase approximation of Lai and Sievers [6]. Complementary bunch length measurement information is available at the end of the linac using the rf zero-phasing technique combined with the electron spectrometer (see Fig. 1).

EXPERIMENTAL RESULTS

The electron beam was transported through the bunch compressor with the phasing of the accelerating structure just before the chicane adjusted for the desired energy-time correlation in the beam.

PC rf Gun Results

Without compression the beam was measured using the zero-phasing technique to have a bunch length of $\sim 3\text{ ps}$ (FWHM). For a charge of 200 pC , the beam compression was increased so that the bunch was shorter at $\sim 1\text{ ps}$. Then the compression was further optimized, and the CTR interferometer scan was performed. The processed autocorrelation results indicate a 300-fs FWHM, as seen in Fig. 2. A rephasing of rf was done to lengthen the pulse, and the result is shown in Fig. 3. The intensity profile has shifted out towards the 500-fs regime. The gun was reoptimized at 300 pC and at good compression. Under these conditions another autocorrelation was obtained and processed as shown in Fig. 4. The beam was then transported to the rf zero-phasing test location at the end of the linac, and the bunch length of $0.45 \pm 0.02\text{ ps}$ was determined using maximum power in the last accelerating structure. After rephasing the beam to be on rf crest in L2 (before the compressor) the measured bunch length was $2.2 \pm 0.3\text{ ps}$ (rms), but no CTR signal was detected at this longer bunch length.

Thermionic rf Gun Results

We operated with about 1 nC in 24 bunches from the thermionic gun. This corresponds to about 42 pC/bunch . Two CTR scans were taken, and the shortest result was 290 fs (FWHM). This would imply about 140 A peak current. Figure 5 shows the processed autocorrelation that provides the time profile. The leading edge spike is present as in the data for the PC gun. There appears to be a measurable difference in this spike width from the two gun sources. The data with the single micropulse is narrower than the average of 24 micropulses.

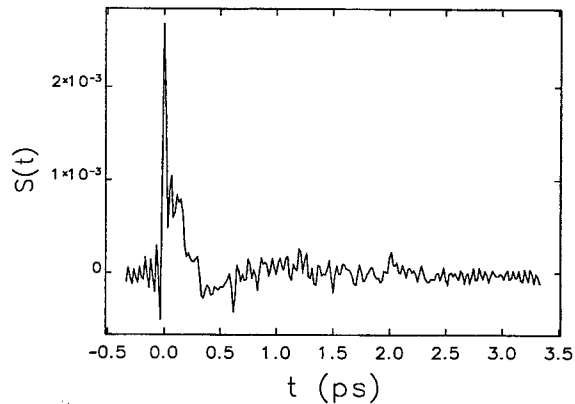


Figure 2: The derived longitudinal bunch profile using the CTR data for the compressed PC gun beam at 200 pC .

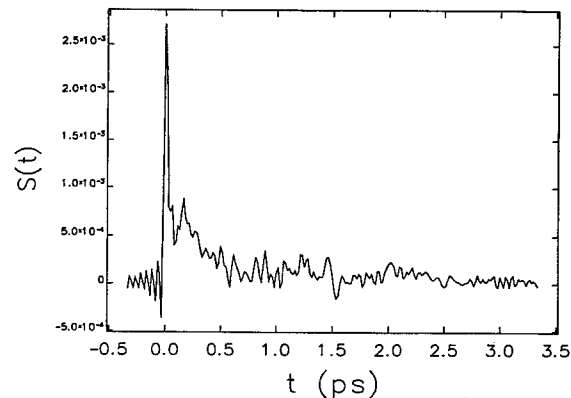


Figure 3: The derived longitudinal bunch profile using the CTR data for the partly dephased beam. Note the increased intensity near 500 fs compared to Fig. 2.

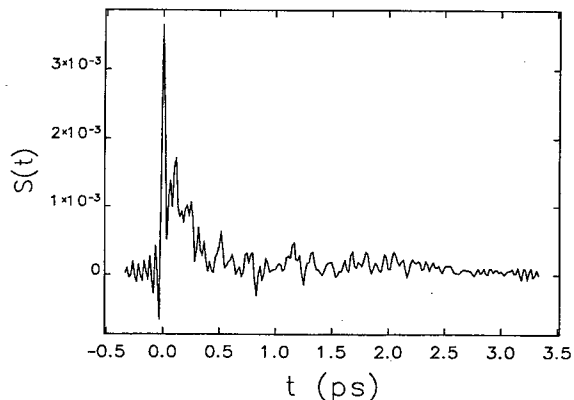


Figure 4: The derived longitudinal bunch profile using the CTR data for the PC gun beam at 300 pC .

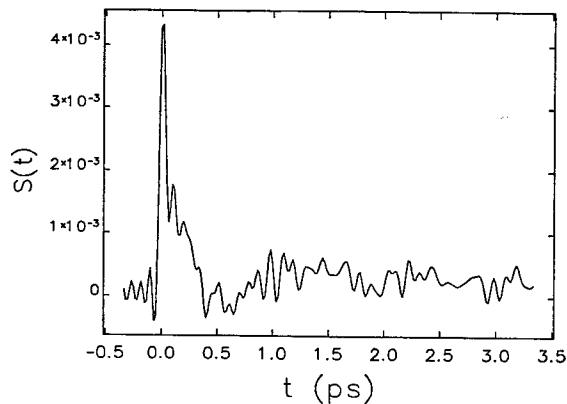


Figure 5: The derived longitudinal bunch profile using the CTR data for the thermionic gun beam.

SUMMARY

In summary we have obtained our initial measurements of the beam following the chicane bunch compressor. Two different gun sources were assessed by the FIR CTR interferometer. The compressed PC gun beam was subsequently used for a number of self-amplified spontaneous emission free-electron laser experiments. A more complete assessment of the CTR system detector efficiencies for various bunch lengths is still warranted.

ACKNOWLEDGEMENTS

The authors acknowledge the support of O. Singh, G. Decker, A. Raugas, R. Gerig, and R. Klaffky of the APS.

REFERENCES

- [1] M. Borland, J. W. Lewellen, and S. V. Milton, in Proc. of the XX Linac Accelerator Conference (e Conf. Menlo Park, CA 2000) p. 863.
- [2] U. Happek, E. B. Blum, A. J. Sievers, Phys. Rev. Lett. 67 (1991) 2962.
- [3] A. H. Lumpkin et al., Nucl. Instrum. and Methods, A475 (2001) 476-480.
- [4] S. Biedron et al., Proc. of the IEEE 1999 Particle Accelerator Conference, New York, NY, pp. 2024-2026 (2001).
- [5] J. W. Lewellen et al., Proc of the 1998 Linac Conference, Chicago, IL, pp. 1288-1290 (2001).
- [6] R. Lai, A. J. Sievers, AIP Conf. Proc. 367 (1996) 31, and references therein.

X-RAY IMAGING OF THE APS STORAGE RING BEAM STABILITY EFFECTS: FROM THE ALASKAN EARTHQUAKE TO UNDULATOR FIELD CHANGES*

A.H. Lumpkin[#], B.X. Yang, C.Y. Yao, and L. Emery

Advanced Photon Source, Argonne National Laboratory, Argonne, IL 60439 USA

Abstract

The Advanced Photon Source (APS) 7-GeV storage ring serves as a national x-ray synchrotron radiation user facility. The stability and beam quality of the electron beam, and hence the photon beams, are monitored continuously by an array of diagnostics. In particular, x-ray imaging techniques are employed in the diagnostics sector of the ring to characterize beam position, size, and emittance. The x-ray synchrotron radiation (XSR) emitted by the electrons as they pass through the field of a dipole magnet is imaged by a pinhole camera. The images are processed by a Datacube MV200 video digitizer, and the results are provided through the EPICS platform. We have detected the effects on the beam ranging from the arrival of shock waves from the Alaskan earthquake of November 3, 2002 to the variation of the undulator fields by the users during their scans. In the latter case, the beam size effects were observed at the submicron level. Examples of beam centroid and size effects will be presented including some due to longitudinal instabilities at elevated stored beam currents.

INTRODUCTION

As a national x-ray synchrotron radiation user facility, the Advanced Photon Source (APS) 7-GeV storage ring must be held to a high performance level [1]. The stability and beam quality of the electron beam, and hence the photon beams, are monitored continuously by an array of diagnostics. The beam orbit stability is predominantly measured by rf beam position monitors (BPMs) [2] while the beam transverse quality issues are assessed by imaging techniques. In particular, x-ray imaging techniques are employed in the diagnostics sector of the ring to characterize beam profile, beam position, and emittance. The x-ray synchrotron radiation (XSR) emitted by the electrons as they pass through the field of a dipole magnet is imaged by a pinhole camera. The images are processed by a video digitizer, and the results are provided through the EPICS platform. Improvements to the system since commissioning have made it possible to detect submicron effects in a 100- μ m beam size. Since the digitizer operates at 30 Hz, we have the potential to see subtle effects in the beam. These have ranged from the arrival of shock waves from the Alaskan earthquake of November 3, 2002, to the variation of the undulator fields during their scans. We noted, in particular, the cycling of

the circularly polarized undulator (CPU) magnetic fields in a run in the Fall of 2002. In addition, we report the beam size effects in the horizontal (dispersive) plane due to longitudinal instabilities encountered during studies at higher stored beam currents such as 120 mA and 200 mA.

EXPERIMENTAL BACKGROUND

The APS facility includes an injector system based on an S-band linac, a particle accumulator ring (PAR) for stacking and damping charge, and an injector synchrotron to ramp the beam energy to 7 GeV plus the 7-GeV storage ring. The storage ring (SR) has an 1104-m circumference and is composed of 40 sectors of a standard lattice. There are a total of 80 dipoles of which 34 are available for x-ray source points and provision for 34 straights for user insertion devices (IDs) and one straight (S35) dedicated for diagnostics of the particle and photon beams. The nominal stored beam current is 100 mA, and this is routinely maintained in top-up operations by one-shot injection of charge every two minutes. The beam stability is monitored by rf BPMs, and the feedback systems reduce the beam jitter to less than 2.5 μ m and 1.5 μ m for the horizontal and vertical components, respectively, in a 20-Hz bandwidth [2].

The beam quality is evaluated by using the XSR emitted as the electrons encounter the magnet field of the S35 dipole bending magnet (BM). The source is imaged at about 0.86 magnification by using an in-vacuum 4-jaw aperture located 9.0 m from the BM source point. The x-ray information is converted to visible light by a YAG:Ce crystal located 16.63 m from the source point. Two mirrors and two lenses are used to image the beam spot onto a CCD camera. A target grid at the plane of the crystal is used to validate the focus of the system and determine the calibration factor of 6.8 μ m/ch and 5.7 μ m/ch for the x and y axes, respectively. The pinhole aperture is typically set at 15 μ m by 15 μ m, and the effective system resolution is about 22 μ m in both planes [3].

The video information is processed by a dedicated Datacube MV200 video digitizer and the results are provided through the EPICS platform. The beam images are fit to a Gaussian profile at the video rate. The beam sizes and positions are process variables that can be tracked and archived. With an independent determination of the beta functions and dispersion at the source point, the beam emittance and coupling factor are also calculated, displayed, and archived. Short-term storage of these values at a 1- to 30-Hz rate is possible. Long-term archives use sampling rates of once per minute.

*Work supported by U.S. Department of Energy, Office of Basic Energy Sciences, under Contract No. W-31-109-ENG-38.

[#]lumpkin@aps.anl.gov

EXPERIMENTAL RESULTS

In the process of daily review of the beam size, position, and emittance data irregular behavior can be noted and targeted for a more detailed analysis as in the first two cases. The third example is from a machine studies case.

Alaskan Earthquake of November 3, 2002

On a quiet Sunday afternoon in November 2002, a beam orbit excursion resulted in limits being exceeded and an abort of the beam for machine protection purposes at about 16:37 hrs. The routine review of the beam motion prior to this loss of beam in Fig. 1 uncovered an unusual pattern/frequency of motion. This centroid motion and a correlated beam size oscillation were also recorded in the fast data logger data of the pinhole images as shown in Figs. 2 and 3, respectively. An inspection of the data shows that the orbit became perceptively noisy several minutes before the beam loss. There were ~11 oscillations at tens of microns amplitude in a 5-minute period just before the beam loss. Since these were not compatible with signatures of betatron motion or rf difficulties, further inquiries were made to explain the beam loss. It was noted that the Fermi Lab Tevatron also had a beam loss at nearly the same time. One of their operators assigned their observed beam motion to the arrival of the shock waves from the Alaskan earthquake of November 3 (initiated at 16:12:41 CST) [4]. We also found some corroborating information on the U.S. Geological Survey web pages for a seismic detector site in Ann Arbor, Michigan [5]. The compressions of our ring circumference by the shock waves were sufficient to be easily detected by our diagnostics. The p-wave took about seven minutes to arrive in the region, but the more significant seismic detector activity started at 16:32.

Undulator Field Variation Effects

Later in the same month we observed again a small, strange variation in the vertical beam size and calculated emittance. The period in this case was about one hour, and the amplitude was about $\pm 0.5 \mu\text{m}$ out of the $43\text{-}\mu\text{m}$ vertical signal. By searching through the process variables for insertion device activity, we noticed the tests of the CPU had involved cycling of the current values and hence fields at this period. A strong correlation in the vertical emittance (beam size) values is seen with this cycling of the magnetic field as determined by a comparison of data shown in Fig. 4 and Fig. 5, the vertical emittance and current readback, respectively. Very little effect was seen in the horizontal emittance.

Detection of Longitudinal Instabilities

Since the x-ray source point is at a dispersive location in the lattice, the energy spread contribution (75 and $45 \mu\text{m}$) to the total observed beam size of 140 or $95 \mu\text{m}$ for the high-emittance and low-emittance lattices, respectively, is a detectable factor. We have commissioned the SR to run stably at 100 mA, but in our

studies for higher currents at 120 and 200 mA we have readily detected the growth of the horizontal beam size due to a presumed longitudinal instability as shown in Fig. 6 (stable) and Fig. 7 (unstable). In these cases the onset of the instability was at the 102- to 103-mA regime, and adjustments were made to the rf cavity temperature set points to reduce the higher-order-mode effects.

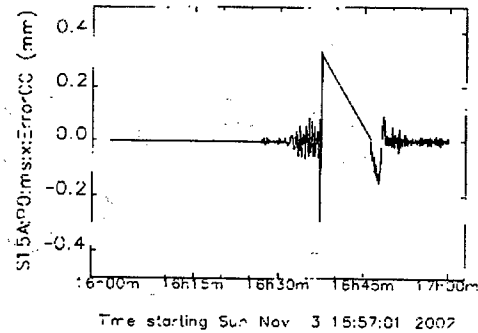


Figure 1: A plot of rf BPM x-position readings at Sector 15 from 1600 to 1700 hours on November 3, 2002. The beam loss was at about 16:37. Beam was restored by 16:50 (fast data logger).

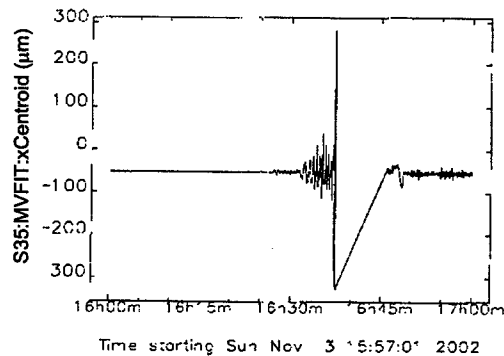


Figure 2: A plot of the x centroid of the pinhole image as processed from Sector 35 from 1600 to 1700 hours on November 3, 2002 (fast data logger).

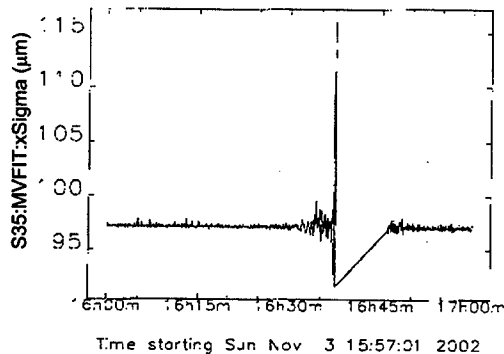


Figure 3: A plot of the x sigma fit results of the pinhole images processed from Sector 35 from 1600 to 1700 hours on November 3, 2002. The oscillations are only a few microns prior to beam loss, but the peaks are aligned with the centroid motion (fast data logger).

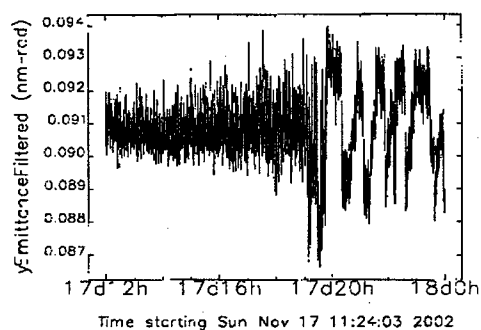


Figure 4: A plot of the y emittance results of the pinhole images processed from Sector 35 from 1200 to 1800 on November 17, 2002. There is a statistically significant beam size oscillation of $\pm 0.5 \mu\text{m}$ with about a 1-hour period.

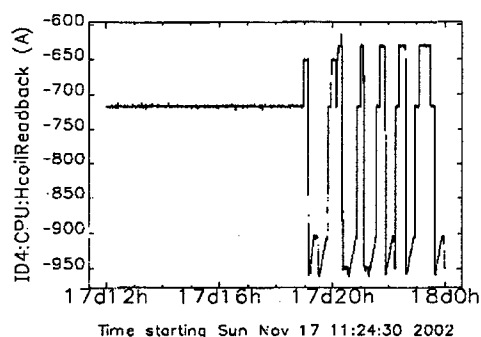


Figure 5: A plot of the Sector 4 CPU horizontal coil readback in A from 1200 to 1800 hours on November 17, 2002. The larger vertical beam emittance/size is correlated with the -650-A value and the smaller value with the -950-A value.

SUMMARY

In summary, the x-ray imaging diagnostics are used not only to validate beam quality, but also to help in identifying the sources of extraneous effects on the beam. These effects ranged from a far-away earthquake to the subtle effects of ID fields varying. The resolution and stability of the diagnostic system have met the challenge. New challenges of supporting lower-emittance lattices with lower vertical coupling are pushing the resolution requirements, so further developments are in the planning stage.

ACKNOWLEDGMENTS

The authors acknowledge the support of O. Singh, G. Decker, and R. Klafky of the Accelerator Operations Division of APS.

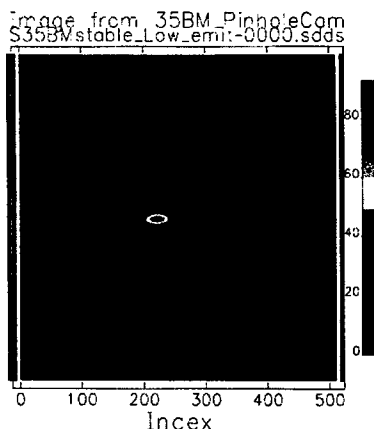


Figure 6: An x-ray pinhole image of the particle beam at S35 in stable condition against a longitudinal instability at 102 mA.

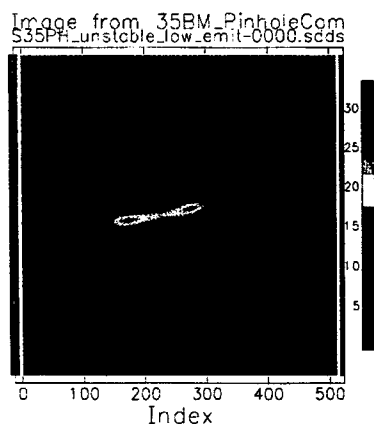


Figure 7: An x-ray pinhole image of the particle beam at S35 in unstable conditions for a longitudinal instability at 103 mA.

REFERENCES

- [1] J.N. Galayda, "The Advanced Photon Source," Proc. of the 1995 Particle Accelerator Conference, IEEE, Vol. 1, pp. 4-8 (1996).
- [2] G. Decker, J. Carwardine, O. Singh, "Fundamental Limits on Beam Stability at the Advanced Photon Source," BIW 1998, AIP Conf. Proc. 451, pp. 237-244 (1998).
- [3] B. Yang, A.H. Lumpkin, L. Emery, and M. Borland, "Recent Developments in Measurement and Tracking of the APS Storage Ring Beam Emittance," BIW 2000, AIP Conf. Proc. 546, pp. 622-630 (2000).
- [4] Tevatron Online Status logbook of November 3, 2002, Fermi National Accelerator Laboratory.
- [5] Information obtained from the U.S. Geological Survey webpage, <http://www.usgs.gov>.

SUPERCONDUCTING RESONATOR AS BEAM-INDUCED SIGNAL PICKUP

S. I. Sharamentov, B. E. Clifft, P. N. Ostroumov, R. C. Pardo, G. P. Zinkann, ANL, Argonne, IL 60439, USA

Abstract

The first demonstration of a superconducting resonator (SCR), installed for beam acceleration, to detect the arrival time of a beam bunch is described. The detecting resonator is operated at very low field level, comparable to the field induced by the beam pulse traversing the cavity so as to maintain an acceptable response characteristic for this high-Q device. Due to this, the RF field in an SCR is always a superposition of a "pure" (or reference) RF and the beam-induced signal. A new method of circular phase rotation (CPR), allowing extraction of the beam phase information from the composite RF field was developed. Arrival time phase determination with CPR is better than one degree for a beam current of 100 nA. The electronics design is described and example data are presented.

INTRODUCTION

Superconducting linear accelerators have become widely popular for the acceleration of all types of charged particles [1,2] due to their high accelerating gradients and low operating costs. The design of these linacs relies on the use of short independently phased cavities with transverse focusing elements interspersed among the resonators. For optimum beam optics, close spacing of the active elements is needed with minimum drift distances. This requirement is especially true in the low-velocity ($\beta \leq 0.1$) accelerator region for heavy-ions with low charge-to-mass ratio (q/m), and so the pressure to minimize the space needed for diagnostics is intense. In existing heavy-ion linacs such as ATLAS, no space has been allocated for diagnostics over ten meter distances. At velocities under 0.05c, beam steering and focusing problems make longitudinal diagnostics cumbersome and can induce distortions in the data unrelated to the actual beam conditions in the early resonators. This problem will be even more acute in SC linacs planned for future large facilities such as the Rare Isotope Accelerator (RIA) [3]. In this paper, we demonstrate for the first time the use of a superconducting resonator, installed for beam acceleration, to detect the arrival time of a beam bunch at the detecting resonator. This is accomplished when the resonator is operating, not as an accelerating cavity, but rather running with a very low field, comparable to the field induced by the beam pulse traversing the cavity. In this mode the information obtained from the detecting resonator can be used to accurately determine the beam-RF phase relationship in an upstream resonator and thereby correctly set that resonator for the proper accelerating mode.

SCR FEATURES AND BEAM PHASE MEASUREMENTS

Very narrow frequency bandwidth and microphonic effect do not allow direct use of the induced RF signal in the SCR for beam phase detection. Similar to the normal SCR application for particle acceleration, beam phase detection requires stabilization of the SCR resonant frequency, which is typically accomplished by means of RF feedback loops. Another way of minimizing microphonics is to decrease the Q value of the SCR. This can be done, for example, by overcoupling an SCR drive port. For the SCR application as a beam phase detector, this method cannot be recommended, however, due to the lower sensitivity. To achieve normal operation of the feedback loops, some initial level of RF field inside the resonator is required. The level of the RF field has to be as low as possible. Otherwise the energy of the incoming beam can be changed due to the interaction between the beam and cavity's RF field. Therefore, unlike "normal" beam phase detectors, the RF field in an SCR is always a superposition of a "pure" (or reference) RF and the beam-induced signal:

$$A_{\Sigma}(t) \exp(i\phi_{\Sigma}(t)) = A_{rf} \exp(i\phi_{rf}(t)) + A_b \exp(i\phi_b),$$

$$\text{with amplitude } A_{\Sigma}(t) = A_{rf} \sqrt{1 + p^2 + 2p \cos(\phi_{rf} - \phi_b)}$$

$$\text{and phase } \phi_{\Sigma}(t) = \arctan \frac{\sin \phi_{rf} + p \sin \phi_b}{\cos \phi_{rf} + p \cos \phi_b}, \text{ where}$$

A_{rf} , ϕ_{rf} are the magnitude and phase of the reference RF field, A_b , ϕ_b are similar parameters for the beam-induced signal, $p = A_b/A_{rf}$ is the relative beam-induced signal magnitude. For small p , the amplitude of the resultant field can be written as

$$A_{\Sigma}(t) \approx A_{rf} (1 + p \cos(\phi_{rf} - \phi_b)).$$

As follows from these equations, neither amplitude nor phase of the resonator RF field can give unambiguous information about beam phase, because both amplitude and phase of the resultant RF field are functions of the reference RF field amplitude A_{rf} and phase ϕ_{rf} . Nevertheless, there is a simple way to extract beam phase information from the resultant RF field. Suppose, we apply a *linear circular phase modulation* to the reference

RF field: $\phi_f(t) = \omega_r t = 2\pi F_r t$, which can be described as a continuous circular rotation of the RF vector with modulation frequency F_r . Then, the magnitude of the resultant RF field will be amplitude modulated with the same frequency F_r , and, relative to the reference signal $\cos \omega_r t$, will be shifted in phase by an angle exactly equal to the beam phase ϕ_b .

Thus, by applying a linear circular phase rotation to the reference RF field, and measuring the phase shift between the resonator's resultant signal magnitude and modulation signal, one can measure the beam-induced signal phase.

ATLAS BEAM PHASE DETECTION SETUP

All beam phase-detection tests were made at the first PII cryostat, which has six superconducting quarter-wave resonators with central frequency 48.5 MHz. Their position numbers are R111, R112...R116. Figure 1 shows a simplified RF diagram of an ATLAS superconducting resonator in normal accelerating mode. The resonator operates in a self-excited mode, with locked amplitude and phase feedback loops. Phase locking is accomplished by means of a voltage-controlled reactance VCX [4].

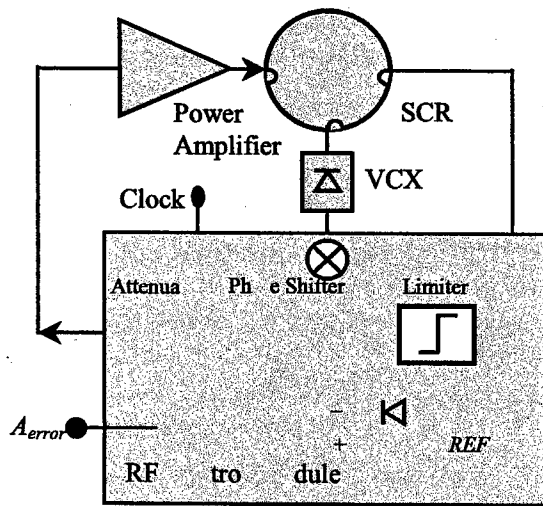


Figure 1. Simplified RF diagram of ATLAS superconducting resonator in normal accelerating mode

The complete experimental setup for using a SCR as a beam phase detector is shown in Figure 2. For low field operation, an additional 40 dB gain preamplifier and a 20 dB attenuator were installed in resonator pick-up line and power amplifier input line. The preamplifier and attenuator allow normal operation of the RF control module and RF power amplifier, while the resonator field is only 1% of the normal accelerating mode. This background field can cause acceleration of the beam in the detecting resonator and affect the effective arrival time in the resonator slightly. For the worst case situation, where the velocity is still very low ($\beta \sim 0.015c$) and the

prior total voltage is low, the observed phase can be perturbed by as much as 2° . For all other cases, this perturbation is less than 0.5° .

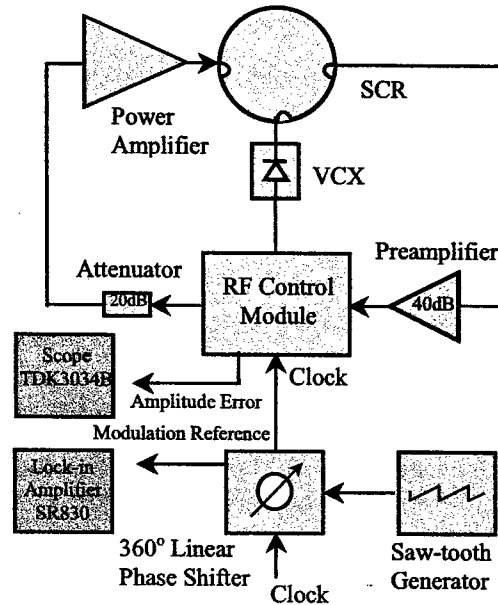


Figure 2. Complete experimental setup for using SCR as beam phase detector.

An external linear phase shifter with 360° range in the master oscillator (clock) line, controlled by a saw-tooth shape signal, provides continuous circular rotation of the reference RF field vector in the resonator, with a 6-7 Hz rate. Because of the interaction between the rotating reference RF field vector and the beam-induced RF vector inside the resonator, an amplitude error signal in the amplitude feedback loop was also modulated. It was found that the amplitude error signal is very convenient to use as the beam phase signal, because it reflects any changes in the resonator's RF field magnitude, and can be amplified to any desired level.

A synchronous detection method was chosen for extracting the beam phase information, because it provides high accuracy phase measurements in a noisy environment, which is typically the case for SCR, due to the high level of microphonics. A Stanford Research Lab SR-830 two-channel lock-in amplifier was used as the synchronous detector, and a Tektronix digital TDK3034B scope was chosen for waveform display. Overall accuracy of the beam phase measurements in the real ATLAS accelerator noise environment is estimated to be better than half a degree.

EXPERIMENTAL RESULTS

The most difficult region of the ATLAS linac to tune with our present surface barrier detector diagnostics is the lowest energy section of the Positive Ion Injector (PII) linac. This is due to steering effects from misalignments as well as asymmetric fields inherent in the resonators and

the relatively long distance (~10m) to the diagnostics region at the end of PII. Therefore, we chose to focus on this very low-velocity region of the linac to develop and test this new system.

First beam phase measurements were made using a $^{20}\text{Ne}^{8+}$ beam in March 2002. Electrical beam current was about 1 μA . Beam was delivered from the ATLAS ECR injector with a velocity of 0.0085c, and bunched to approximately 0.25 ns FWHM by a two-stage bunching system [5]. The idea was to operate a nearby downstream SCR as the beam phase monitor, as described before, and observe the induced signal phase as a function of the RF phase of an upstream resonator. Figure 3 shows experimental data for the cases where resonators R112, R113 and R114 were alternately used as the beam phase monitor, and the first resonator, R111, was turned on with RF field at approximately 3 MV/m. The fact that for all three locations of the beam phase monitor, the measured phase curves have a similar shape, and their minimum corresponds to the same value of R111 phase of 300° , is a confirmation that the measured data were real beam phase data. Another important conclusion from the beam phase data in Figure 3 is that the value of R111 RF phase 300° corresponds to the point of maximum energy gain where the beam and resonator RF relative phase is 0 degrees.

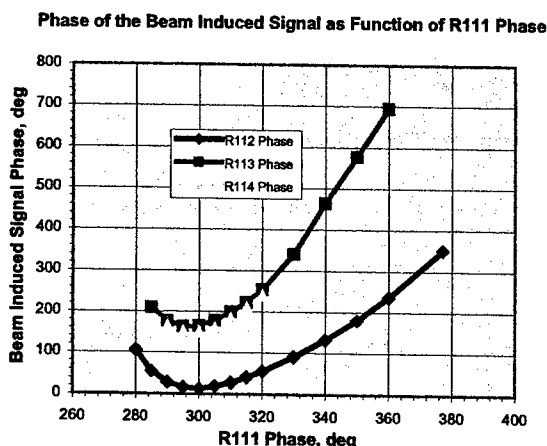


Figure 3. Beam induced signal phase as function of R111 RF phase. Beam phase monitor was placed at three different locations, R112, R113 and R114.

A semi-manual version of this system was then used to 'tune' the first five resonators in the PII linac by sequentially moving the electronics from one resonator to another in order to approximately maintain the velocity match condition and maintain a well bunched beam into the detecting resonator. A wide range of tunes was developed to match beams with charge-to-mass ratio (q/A) from 0.15 to 0.375. In each instance the actual energy gain was determined using a solid-state detector to measure the absolute energy gain from each resonator. In principle, the total phase shift observed at the detecting resonator between the last accelerating resonator in 'on' and 'off' states is the beam transit time change due to the

energy gain given to the beam by that resonator. The energy gain of the beam is calculable within that model and the total beam energy at that point can be determined. The measured total phase shift and the calculated energy of the beam after acceleration are presented in Table I for an $^{40}\text{Ar}^{6+}$ beam. Table I shows data identified by the last accelerating resonator and the detecting resonator. The energy of the ^{40}Ar beam into the first of this set of resonators is 5.5 MeV.

If two resonators are used in detection mode, then the difference in phase contains time-of-flight information, which can be used to obtain the absolute energy directly. A calibration procedure would first need development in order to determine the electronic phase offset between the two detecting resonators.

Table 1. Comparison of Phase-Shift Energy Determination and Solid State Detector Measured Energy.

Resonator Pair (Accel./Det.)	Distance (m)	Total Phase Shift (deg)/(ns)	Energy Out (MeV)	SBD measured energy (MeV)
R113/R114	.540	221/12.7	7.2	7.7
R114/R116	.991	616/35.3	12.6	12.7
R115/R116	.406	104/6.0	16.2	16.5

CONCLUSION

The system described in this paper is now in regular use at the ATLAS facility for tuning the resonators in the lowest energy section of the facility. The system is a significant improvement over the previous diagnostics system located 8 meters downstream from these early resonators. Full integration of the method into the ATLAS control system is now underway. Improved phase sensitivity at higher energy may be possible where the technique can be used at the zero-crossing, 90° , point where the maximum possible phase sensitivity exists. At the low velocities studied in this report, the debunching in that phase region makes the detecting resonator insensitive to the beam bunches.

This work was supported by the U.S. Department of Energy under contract W-31-109-ENG-38.

REFERENCES

- [1] L. M. Bollinger, et al., Nucl. Instrum. and Methods, B79, 753(1993).
- [2] R. L. Custom, "An Overview of the Spallation Neutron Source Project", Proc. of the XX International Linac Conf., August 21-25, 2000, Monterey, CA, p. 321.
- [3] P. N. Ostroumov, J. A. Nolen, and K. W. Shepard, Proceedings of the XX International Linac Conference, August 21-25, 2000, Monterey, CA, p. 1018.
- [4] J. M. Bogaty, B. E. Clift, K. W. Sheppard and G. P. Zinkann, Proceedings of the IEEE Particle Accelerator Conference, 1989, p.1978.
- [5] P. K. Den Hartog, J. M. Bogaty, L. M. Bollinger, B. E. Clift, R. C. Pardo and K. W. Sheppard, Proceedings of the IEEE Particle Accelerator Conference, 1989, p. 545.

BEAM POSITION MONITOR SYSTEMS FOR THE SNS LINAC*

J. Power[†], L. Day, M. Plum, M. Stettler
Los Alamos National Laboratory, Los Alamos, NM 87545

Abstract

The 402.5- and 805-MHz beam position and phase monitors for the Spallation Neutron Source linac are based on standard PC technology. The SNS beam is to be injected into a storage ring with a 1-MHz circulation frequency requiring 650-ns-long minipulses. The injection cycle takes 1 ms and the machine can run at rates up to a 60 Hz. The rf input signals are down converted to 50 MHz and sampled at 40 MHz with 14-bit ADCs to produce I and Q data streams. A custom PCI module has been designed to accept modular digital front end (DFE) and analog front end (AFE) circuit cards. This hardware is installed in a standard rack-mounted 1U computer chassis running Windows® 2000, LabVIEW® and custom DLL software. The system continuously self-calibrates by generating 300-ns long rf pulses which are switched between the AFE inputs and the cables going to the BPM pickups. This provides a TDR-like calibration of the entire system. The system is designed to provide a position and phase resolution of 0.1% of the beam pipe aperture and 0.1 degrees RMS respectively over a 50 μ s period. The design of the system is described as well as the initial performance measuring beam during the commissioning of the SNS MEBT.

INTRODUCTION

One of the primary design principals of the SNS linac BPM system was to take advantage of mainstream

solution. Another design choice was to make the hardware platform modular to simplify the design and testing as well as to provide a more general purpose instrumentation platform for other diagnostics such as beam current monitors.

We chose to build a PCI carrier card which accepts several plug-on modules including an AFE, DFE and clock multiplier. All analog connections are made through the AFE, via patch cables to the back panel of a generic 1U server PC. The timing and trigger signals attach to the standard front panel of the PCI card.

The instrument is a stand-alone device, providing the capability to serve beam position and beam phase measurements over Ethernet without any external controls requirements. In our case data is served via channel access for compatibility with the SNS EPICS-based control system. For the general case the data can be served to any web browser via the standard LabVIEW® tools. This mode is particularly useful for system testing.

ELECTRONICS

The BPM system operates by down converting the four individual BPM lobe signals which are either 402.5 MHz or 805 MHz to an IF of 50 MHz. These IF signals are sampled at 40 MHz to generate the quadrature information that is processed to measure position and phase. The PCI card that accomplishes the more interesting parts of this process is shown in Figure 1.

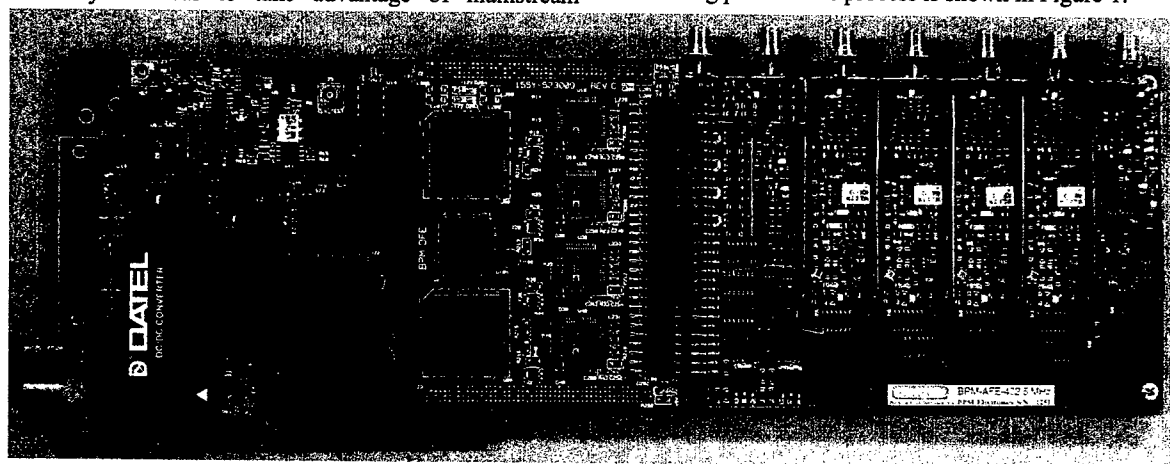


Figure 1. The BPM system PCI card showing the clock multiplier (top left), DFE (center) and AFE (right).

industry standard components and software. Using standard PCs running a Windows® operating system and LabVIEW® instrument software was the obvious

Analog Front End

The AFEs used by SNS were designed and built by Bergoz Instrumentation [1] to our specifications. This module, shown on the right end of the PCI card in Fig. 1, contains four channels of down conversion, a local oscillator distribution chain, and a calibration system.

* Work supported by the Office of Basic Energy Science, Office of Science of the US Dept. of Energy, and by Oak Ridge National Lab.

[†] jpower@lanl.gov

The calibration is made possible by fast-switching networks on the inputs to each down converter channel. A calibration signal, at the same frequency as the beam signals, can be switched to either the input to the down converter, or to the cable connected to the AFE input. The third switched condition is the normal operation one in which the AFE inputs are connected directly to the down converter inputs.

The technique is basically the same as a time domain reflectometer (TDR), except we use a rf burst instead of a step function. This is made possible by using rather long cables between the AFE and the BPM pickups, and by using pickups that have the downstream end of each lobe shorted.

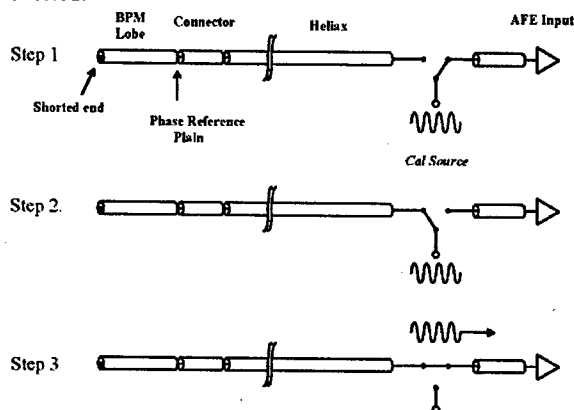


Figure 2. The calibration uses an rf burst to calibrate the down converter chain in step 1, launch a calibration burst down the BPM Helix cable in step 2 and measure the reflected burst in step 3.

The first step in the process is to inject a rf burst into the input of a down converter channel and measure the amplitude and phase of the result. Next is to launch a burst of the same amplitude into the cable connected to the AFE input. This cable has a round-trip transit time of 300 ns, which determines the maximum length of the calibration burst. This burst reflects off of the shorted end of the pick-up and returns to the down converter input, which is switched in at the time of arrival of the reflected pulse. Having measured the amplitude and phase of the reflected pulse, one has enough information to calibrate the system in amplitude and phase through the entire signal path.

The AFE calibrator circuit is carefully adjusted to give the same amplitude and phase of calibration bursts to each channel by tweaking a resistive splitter on the AFE circuit board.

Digital Front End

The DFE has four channels of 14-bit ADCs clocked at 40 MSPS (see Fig. 1). Filters before the ADCs limit the analog bandwidth to about ± 10 MHz. Two FPGAs each process the data from two ADCs to de-convolve the multiplexed quadrature stream created by under-sampling the input at 1.25 times the input period, creating

individual arrays of in-phase and quadrature-phase (I & Q) data. A total of 8 arrays are thus created for the four input channels.

These same FPGAs serve as multiplexers such that raw data and from the ADCs, or preset ramp data may be passed through for testing and de-bugging, instead of the I and Q streams.

A third FPGA is used to generate the timing signals which drive the switches on the front of the AFE for calibration purposes, as well as control the analog gain of the AFE, either 1X or 4X.

PCI Motherboard

The PCI motherboard card is the backbone of our custom hardware. The AFE plugs into the DFE, and the DFE plugs onto the PCI card. The PCI card has eight 256-kB FIFOs, one for each array of data from the DFE. This provides for up to 3.2 ms of data history to be stored for each channel.

One large gate array provides the PCI interface, DMA data transfer for the FIFOs to the PCs memory, timing controls, and a custom 12-bit "L-bus" for control of the DFE.

Three separate power supplies/regulators reside on the PCI card for providing low-noise power to the peripheral modules.

A third clock-multiplier module also plugs onto the top-left corner of the card to generate the differential ADC clocks. This module multiplies the external phase reference of 2.5 MHz up to the required 40 MHz sampling rate. The PLL is serially-programmed to accommodate future reference frequencies such as 10 MHz. The circuit design is based on a LBNL design done by L. Doolittle[2] for their SNS LLRF control systems.

Instrument Packaging

The PCI motherboard and its associated daughter cards are installed in a 1U rack-mounted computer chassis (see Fig. 3). A bracket containing SMA feed-through connectors for the four pick-up lobe inputs, LO drive and calibration drive is attached to the back of the chassis.

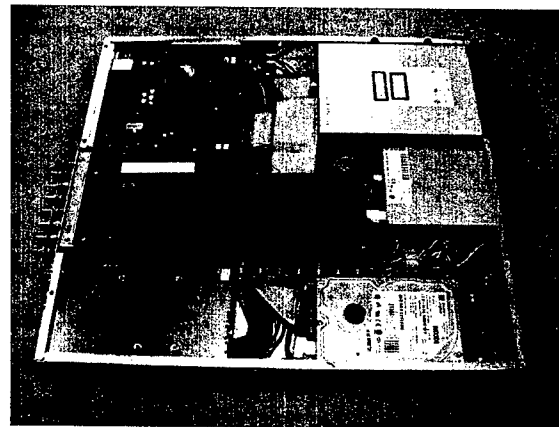


Figure 3. The SNS linac BPM system in a 1U, rack-mounted PC configuration.

The phase reference and trigger signals attach via LEMO® connectors of the PCI card panel.

Additional versions of the BPM instrument have been assembled using a 2U rack-mount chassis, which can accept an additional PCI timing receiver card. This is required for the final SNS facility implementation which uses a complex timing system using both VME and PCI hardware.

PERFORMANCE

Nine BPM systems are currently installed and operational at the SNS facility. Six of the units are prototypes which were used to commission the accelerator front end both at LBNL over a year ago and again at ORNL this year. Three systems are improved, second generation hardware, which will be used for commissioning the first DTL tank shortly.

Performance as Installed

For the SNS linac commissioning, we define the measurement resolutions based on minimum beam pulses of 50 μ s, meaning we average all data for this duration. With this in mind, we ran the new BPM systems as installed, taking data for the equivalent of 1000 beam pulses over about two minutes. This data was analyzed to determine the phase resolution of the measurement.

As installed, the newer systems provide a position measurement resolution of better than 0.1% of the beam pipe radius, and a phase resolution of about 0.6 degrees rms. Figure 3 shows the phase data accumulated in a typical run, from which the RMS measurement resolution is calculated.

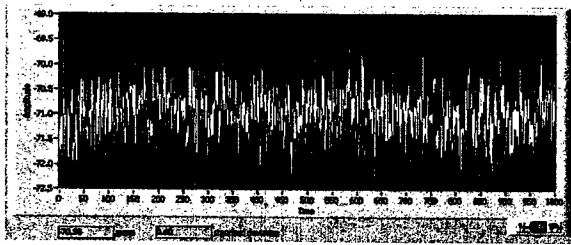


Fig. 3. Data from the equivalent of 1000 beam pulses of 50- μ s duration. The phase resolution is calculated as 0.6 degrees.

Frequency-domain analysis of the amplitude measurement data for a single lobe-channel gives a SFDR of over 70 dB as measured on the bench (see Fig. 4).

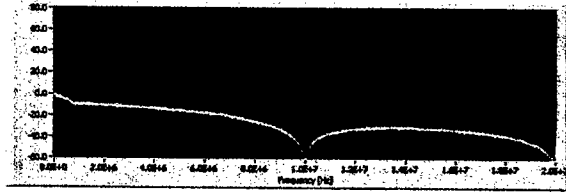


Figure 4. Results of a FFT on 4000 consecutive samples of the amplitude measurement for a single BPM lobe channel. The vertical axis is in db, with 76 being full scale for the ADCs. The horizontal axis is frequency in Hz. The usable dynamic range is about 65 dB.

Issues Needing Further Study

The position-measurement-resolution of the newer systems meets our requirement, but the phase-measurement resolution is not as good as we would like. We currently have a factor of about six higher than our goal. There are technical means of improvement that are being pursued

The phase resolution is primarily a measure of the ADC sampling clock jitter relative to the various rf sources in the system. These include the calibration source, LO source and system reference. Our 0.6-degree resolution is equivalent to 4.2 ns of clock jitter over a bandwidth of a few milli-Hertz to 40 MHz. The high frequency jitter (over 10 kHz) of our clock multiplier VCXO is specified as 1 ns, and substantially lower frequencies are within the PLL loop bandwidth and should be removed. Further study of the jitter of all of our sources is an on-going endeavor.

One expected improvement will be to increase the reference frequency from 2.5 MHz to 10 MHz. We currently use the 2.5 MHz as a hold-over from earlier requirements.

CONCLUSION

We have developed stand-alone beam position and phase measurement instruments based on standard PC hardware and software, with custom-designed PCI cards. The instruments are capable of being communicated with over Ethernet via either EPICS channel access or standard Web browser interfaces. We have achieved a position resolutions of better than 0.1% of the pipe radius and phase resolutions of 0.6 degrees. Further improvement of the phase measurement resolution is being studied.

REFERENCES

- [1] Bergoz Instrumentation, <http://www.bergoz.com>
- [2] Private communication with L. Doolittle, ldoolitt@recycle.lbl.gov

SLIT SCATTERING EFFECTS IN A WELL ALIGNED PEPPER POT

John G. Power, ANL, Argonne, IL, 60439

Abstract: A pepper pot is a device used to measure a medium energy (< 20 MeV) electron beam's transverse emittance by sampling its transverse phase space. This is accomplished by blocking most of the incident electron beam, while allowing small 'beamlets' to pass through openings in a mask. The accuracy of the transverse emittance measured by a pepper pot is limited by several factors including, electrons leaking through the solid region of the mask, the imaging system resolution and dynamic range, scattering, etc. While the noise contributions from the prior quantities can be easily estimated, scattering effects have previously been neglected due to the difficulty in estimating the effect. In this paper, EGS4 simulations are presented to determine the affect of scattering on emittance measurements for an 8 MeV electron beam.

INTRODUCTION

In general, it is difficult to measure the transverse beam emittance directly out of an RF photocathode gun because the emittance is small, the charge is high, and the energy is low, so that the beam is space charge dominated. For this reason, the emittance is usually measured after the RF photoinjector – defined here to be an RF photocathode gun and at least one linac tank – so that the energy of the electron beam is higher, typically greater than 20 MeV. At higher energy, and hence lower space charge, there are several reliable methods for measuring the emittance: (1) The Quad Scan; (2) The Three Screen Method; and (3) OTR-based measurements. However, these three methods cannot easily be applied for the case considered here.

In the traditional quad-scan method, the space charge force is neglected and an exact analytic expression is used to track the beam envelope evolution. However, if the beam is space charge dominated this method fails since the beam envelope evolves under the influence of both emittance and space charge [2, 3]. While the traditional method has been modified to include space charge [2, 4], this method is still not ideal since it is not a single-shot measurement – something that is important for photoelectron beams due to the shot-to-shot fluctuation of the laser. And while the three screen method is limited by the same space charge considerations as the traditional quad scan, OTR-based techniques do not suffer from space charge limitations. However, since the angular distribution of the OTR light at the beam waist depends on both the divergence and the angle energy correlation induced by the quad focusing of the photoelectron beam. Therefore, this technique can be limited by a large energy spread (1%) of the photoinjector. Recently, a promising model has been developed [5] using a technique related to OTR, based on

optical diffraction radiation (ODR-OTR interference) that may overcome even this last limitation.

The pepper pot (and emittance slit) based method does not suffer from the above limitations. However, concerns have been raised that the electron beam may undergo slit scattering as it passes through the pepper pot. The slit scattering process and the degree to which it affects the measured emittance is described in the remainder of the paper.

SLIT SCATTERING

The function of the pepper pot collimator is to stop or scatter away the fraction of the incident electron beam that is intercepted by the plate while letting the non-intercepted fraction of the incident beam pass through the hole. (l.h.s. of Fig. 1). In the case of an ideal pepper pot with one round hole, the non-intercepted beam signal (beamlet) emerges from the hole as a cylinder of charge while the intercepted beam is either stopped. In the real case, however, some of the intercepted beam will enter the plate, undergo a series of interactions, and then re-emerge from it as a source of noise which may affect the measured profile of the non-intercepted signal thus limiting the accuracy of the emittance measurement. In this paper we will examine how this noise affects the measurement of the signal. To keep matters simple, a pepper pot with a single hole is studied.

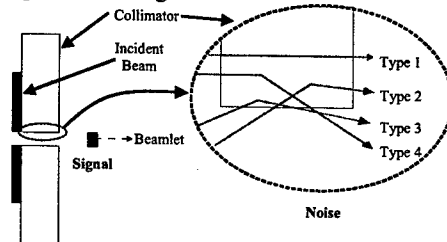


Figure 1: The incident beam strikes a collimator with one hole. The non-intercepted beam is the signal (beamlet) and some of the intercepted beam produces noise (Types 1 -4) in the measurement.

For clarity, we divide the *noise* into four components as shown on the r.h.s. of Figure 1. The first component of the noise (Type 1) is the intercepted beam that enters the front face and exits the back face of the collimator and is termed the *leakage* component. The distribution of the leakage component can be readily estimated from the well known atomic and nuclear properties of the collimator material. The angular and spatial distributions of the leakage component can be obtained from the standard multiple Coulomb scattering formula [6] while the fraction of the intercepted beam that is stopped in the material can be estimated with the stopping distance from the minimum ionizing energy, typically $1 - 2 \text{ MeV cm}^{-2} \text{ g}$.

The other three noise components, taken together, make up the *slit scattered* component. Types 2 and 3 particles start out inside the hole but end up striking the plate due to their initial trajectories, while Type 4 particles initially strike the front face of the collimator but are scattered back into the hole. Unlike for the leakage component, there are no simple formulas to guide one in estimating the slit scattered contribution to the noise.

SIMULATION

The method used to simulate the problem of an electron beam incident on a single collimating hole was as follows: (1) generate an incident beam at the beginning of the pepper pot; (2) transport the incident beam to the end of the pepper pot with an electromagnetic shower code; (3) transport all particles through a drift to the location of the screen; and (4) analyze the output distribution. A user written routine, using the SDDS Toolkit [7], was used to generate the monochromatic incident beam of zero length and the toolkit's Gaussian random number generator was used to populate the angular profiles. The interaction of the incident electron beam with the collimator was modeled with Shower [7] which is a SDDS-compliant interface program to the Monte Carlo electron-photon transport program EGS4 [8]. The propagation of the beam in the drift and the post-processing analysis were done with user written Matlab files.

Electron Beam and Pepper Pot Parameters

This study of slit scattering was motivated by need to measure the emittance of the new 1.5 cell RF photocathode gun at the Argonne Wakefield Accelerator (AWA). This gun was recently RF conditioned to 80 MV/m, on the cathode, corresponding to 12 MW of input power. PARMELA simulations show that with 80 MV/m and a flat-flat laser pulse profile the gun will produce a photoelectron beam with $E = 7.5$ MeV, $Q = 40$ nC, $\epsilon_n = 66$ mm mrad, $\sigma_z = 1.1$ mm (3.7 psec), and $\Delta E/E = 2\%$. At an energy of 7.5 MeV we have $\gamma = 15.6$ so that the geometrical emittance $\epsilon \sim 4.2$ mm mrad. Initially, however, the AWA laser profile will be either Gaussian – Gaussian or longitudinally Gaussian – transversely flat so that $\epsilon_n \sim 100$ mm mrad is a better estimate which means that $\epsilon \sim 6.4$ mm mrad. The plan is to measure the emittance about 50 cm after emittance compensating solenoid where we have a round beam near a waist with $\sigma_{x,y} \sim 5$ mm so that the divergence is approximately $\sigma'_{x,y} \sim 1.5$ mrad. These parameters will be used as basis for the incident beam during the simulation.

Based on the above assumptions about the photoelectron beam, a pepper pot was designed for measuring the emittance. Since slit scattering can be understood by just considering a single hole, the overall hole pattern will not be describe but, instead, discussion will be confined to just a plate with a single hole [Fig. 2].

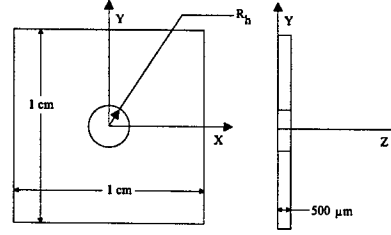


Figure 2: The single hole pepper pot collimator. (Not to scale.)

The parameters used for the pepper pot in this study were a square plate of tungsten (1 cm x 1 cm and 500 μ m thick) with a hole of radius R_h μ m in the center. Using the radiation length, $X_0 = 3.5$ mm and density $\rho = 19.3$ g cm^{-3} of tungsten, we calculate the multiple coulomb scattering of the 7.5 MeV beam from the 500 μ m thick plate to be $\theta_{mcs} = 635$ mrad. The geometry used for this pepper pot (Fig. 2) defines the beginning of the tungsten plate to be at $z = 0$, the exit of the tungsten plate at $z = 500$ μ m, the profile monitor at $z = L$, and the hole radius of R_h .

RESULTS

Shower was used to simulate an initial distribution of electrons incident on the pepper pot described above. This initial distribution is a round, uniformly populated electron beam of radius $R_b = 500$ μ m, with a Gaussian angular distribution of $\sigma'_{x,y} = 1.5$ mrad.

As an example, the total output distribution of particles (electrons, photon, and positrons) located at the back face of a pepper pot with $R_h = 100$ μ m is shown in figure 3. Looking at the profile from this point of view, it is not possible to pick the signal (100 μ m spot) out of the noise (≤ 500 μ m spot). However, by plotting the intensity of the particle distribution along a slice through the middle of the profile (figure 3), a small signal can be observed. In figure 4, this intensity along the center of the slice is shown at four different locations behind the pepper pot (where $z = 0$ is the back face of the pepper pot). The first feature to notice is that there is small, sharply peaked signal sitting on the center of a hill of noise. At the exit of the plate ($z = 0$ in figure 4) the noise hill is rather concentrated ($\sigma_{\text{noise}} \sim 500$ μ m) but quickly spreads out due to its large angular divergence so that by the time it has traveled just 5 mm away, the background noise is just a low level, wide hill.

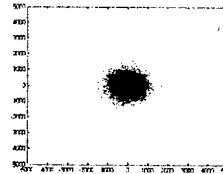


Figure 3: Image of the electrons, photons, and positrons that emerge at the back of the tungsten plate.

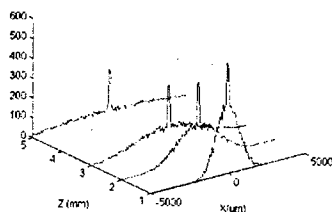


Figure 4: The evolution of the distribution of particles after having passed through the one-hole pepper pot of Fig 2 as a function of distance after the pepper pot.

Calculating the Divergence

Since the main purpose of these simulations was to see how the slit scattered particles affected the measurement of the signal particles at the downstream screen, the next step was to analyze the downstream spot to see if we can extract the initial divergence of the input beam. The procedure used to do this is described next.

For a particular hole radius, R_h , the output distribution was propagated to a downstream screen a distance $L_{\text{screen}} = 50$ cm away. Since the input divergence was manually set to have a Gaussian distribution, the spot on the downstream screen was first projected along the x axis (not sliced) and fit to a Gaussian. From this projection, the 1-sigma beam width of the spot was extracted, which, for the case of a Gaussian, is also equal to the standard deviation of the distribution. The width of the spot due to the divergence of the beamlet is added in quadrature with the r.m.s. width of the pepper pot hole to give the width of the spot at the screen. From this, the divergence is calculated according to,

$$\sigma' = \frac{1}{L_{\text{screen}}} \sqrt{\sigma_{\text{screen}}^2 - \left(\frac{R_h}{2}\right)^2} \quad (1)$$

where σ_{screen} is the spot size at the screen. (Note that while the r.m.s. width of a 1D slit is $R_h / \sqrt{3}$, we are using the r.m.s. width of a projected hole.)

As a typical example, the intensity distribution of the projected beamlet spot for the case of $R_h = 50$ μm and $L_{\text{screen}} = 50$ cm is shown in figure 5. From the fit to this spot the width of the beam at the screen was found to be $\sigma_{\text{screen}} = 738$ μm . Using Eqn. 1, the divergence was calculated to be $\sigma' = 1.51$ mrad, in very close agreement with the divergence of the initial beam distribution.

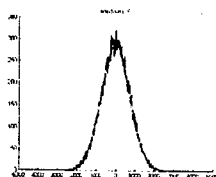


Figure 5: The intensity distribution of the projected beamlet at the screen located 50 cm downstream of the pepper pot.

Table 1: Calculated divergence from the fit as a function of the aspect ratio of the hole for the case of a pepper thickness of $W = 500$ μm .

R_h (μm)	Aspect Ratio = R_h/W (mrad)	Divergence from Fit
10	20	1.49
20	40	1.49
50	99.6	1.51
100	197	1.50
200	381	1.51
500	785	1.49

To determine if the multiple scattering effects depended on the aspect ratio of the hole, a variety of cases were considered. In all cases considered, the thickness of the tungsten plate was held at $W = 500$ μm , while the hole radius was allowed to vary from 10 μm to 500 μm , thus varying the acceptance angle of the hole ranged from 20 mrad to 785 mrad. As shown in table 1, the fitted value of the divergence agrees very closely to the known value of divergence of 1.5 mrad for a wide range of aspect ratios. The small disagreement is due to the statistics from the limited number of macro particles used in the Monte Carlo simulation.

It is worth emphasizing that the simulation results obtained in this section, and shown in figure 3, figure 4, and table 1, include all the sources of flux mentioned in the *SLIT SCATTERING* section above, i.e. leakage flux (type 1), slit scattered flux (type 2-4) and the beamlet signal. However, from these simulation result only two fluxes are apparent, the signal and leakage particles. It is obvious that the slit scattering effect is very small over the range of parameters examined.

CONCLUSIONS

EGS4 based simulations show that the effect of slit-scattering on an 8 MeV electron beam by a well aligned pepper pot, with various hole aspect ratios, is negligible. Thus, the pepper pot is a highly reliable technique for measuring emittance from a photoinjector. In the future, the study will be carried out over a wider range of energies and for misaligned pepper pots.

REFERENCE

- [1] M. Reiser, Theory and Design of Charged Particle Beams (Wiley, New York, 1994).
- [2] J. G. Power, M. E. Conde, Rev. Sci. Inst. 69 1295 (1998)
- [3] S. G. Anderson, et al., Phys. Rev. ST Accel. Beams 5 014201 (2002)
- [4] C. Limborg, these proceedings
- [5] R. Fiorito, these proceedings
- [6] Particle Data Book
- [7] see www.aps.anl.gov for SDDS Toolkit & Shower
- [9] see www.slac.stanford.edu/egs/ for EGS4

ADVANCED PHOTON SOURCE BOOSTER SYNCHROTRON BEAM POSITION MONITOR UPGRADE AND APPLICATIONS*

Nicholas S. Sereno, Frank Lenkszus, Robert M. Lill
Advanced Photon Source/ANL, Argonne, IL 60439, USA

Abstract

The Advanced Photon Source operates in top-up mode, which adds charge to the storage ring every two minutes to maintain the current at 102 ± 1.0 mA. This requires the booster synchrotron to operate efficiently and reliably. The booster BPM system was upgraded to overcome a severe performance limitation due to operation of the receiver at the low end of its input power range. The upgrade provided a 25-dB improvement in overall system gain. This improved dynamic range and resolution, and reduced other systematic errors. The booster BPMs have been used in studies including measurements of ring circumference, synchrotron and betatron tune, and orbit correction. Software feedback corrections of the energy and rf phase errors at injection have been implemented for routine operations using the BPM beam history/DSP-based synchrotron tune measurement. Transverse injection feedback is presently being commissioned. The latest experimental results using the upgraded BPMs will be presented.

INTRODUCTION

The APS booster BPM system is used to provide horizontal and vertical beam position, average beam position, and position history information over a user-selectable number of turns. This information can be obtained over the entire 225 ms it takes the beam to linearly ramp from 0.325 to 7 GeV at the 2-Hz booster cycle rate. Average position information is used to correct the orbit at various time points (energies) up the ramp. Average horizontal orbit position as a function of frequency was used to measure the orbit circumference and dispersion [1]. Orbit correction was used extensively when commissioning new low-emittance booster lattices [1].

Beam history position information is used for time and frequency domain processing to determine synchrotron and betatron tunes at any point up the ramp. The synchrotron tune measurement uses DSP techniques to process the first 256 turns after injection to determine the synchrotron tune for each pulse. The synchrotron tune is then used with feedback to correct the longitudinal phase-space mismatch (energy and phase deviation) that can occur due to rf phase errors and/or booster magnetic field errors. The same DSP techniques are presently being studied to determine betatron tunes as a function of time up the ramp.

*Work supported by U.S. Department of Energy, Office of Basic Energy Sciences, under Contract No. W-31-109-ENG-38.

BOOSTER BPM ELECTRONICS UPGRADE

The APS booster has a circumference of 368 m employing 80 BPMs installed every 4.6 m around the ring. The storage ring and booster both employ identical BPM electronics. The signal processing topology is a monopulse amplitude-to-phase (AM/PM) technique for measuring the beam position in the x and y axes. A logarithmic amplifier channel measures the beam intensity [2]. The signal level into the receiver with 1.0 nC of charge was typically -40 dBm during normal booster operation. This input power level is considered the low end of the receiver dynamic range (+5 to -45 dBm) and performance was severely limited. The booster has an operating range of 0.2 to 10 nC or 34 dB.

The BPM system upgrade block diagram shown in Figure 1 reduced the insertion loss of the original filter comparator as part of the upgrade. The filter comparator provides the sum and difference signals of the four button electrodes in a 10-MHz bandwidth centered at 352 MHz. The original filter comparator used attenuators on the inputs (6 dB) and between the hybrid bridge output and the bandpass filters (2 dB) to attenuate standing waves between components. This technique provided a broadband match at the cost of signal strength. The bandpass filter implemented in this design had an insertion loss of 3 dB.

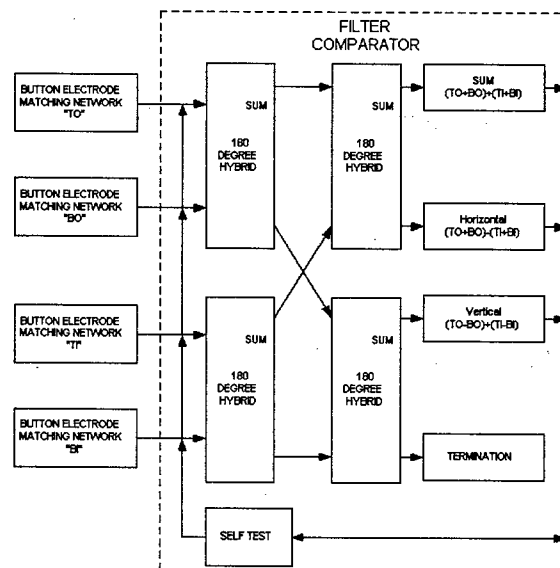


Figure 1: Upgrade block diagram showing schematically the new matching networks feeding signal to the filter comparator.

The upgrade design eliminated the need for pads by carefully matching the components and button pick-up source. The source or button pick-up electrodes have a very poor return loss when measured from the feedthrough side, which results in reflecting 97% of the power. To match the button's impedance ($0.25-75j$ ohm) into 50 ohms, an inductor is placed in parallel with the capacitive electrode. This effectively creates a parallel resonant circuit driven by the image current source. This technique of resonating the capacitive pickup provides a controllable response in a compact electrode design. A similar design was installed in the APS storage ring [3]. The upgrade also moved the critical filtering into the new matching network, which incorporates the 5-pf electrode capacitance into the filter design. When connected to the 10-mm button electrode, the matching network was designed to passively increase the signal power by 15 dB @ 352 MHz with a 20-dB return loss. The matching network has a bandwidth of 10 MHz @ -3 dB power point when connected to the capacitive button electrode. The matching network also provides 40 dB of filtering at the second harmonic (704 MHz). The modified filter comparator has an 11-dB reduction of insertion loss and the signal enhancement realized by the matching network (15 dB) equates to an overall system improvement of 26 dB.

BOOSTER LONGITUDINAL SYNCHROTRON MOTION MEASUREMENT AND CORRECTION

The booster BPM and beam history [4] are used to determine the synchrotron frequency and correct energy and phase (field) errors at injection. The BPM used in this application is located in a region of dispersion. This BPM is configured to provide only horizontal position data on each turn for 256 turns. Synchrotron oscillations can be observed on the beam history on each pulse depending on the level of phase and/or energy errors at injection.

The beam history time-domain data are processed (using DSP techniques) to filter out betatron motion. This filtering is accomplished by subtracting a shifted copy of the beam history waveform from itself. This procedure minimizes betatron oscillations on the processed waveform since the synchrotron oscillation is much slower than the betatron motion. The procedure also zeros the net waveform offset.

The processed time-domain waveform is Fourier transformed. The resulting real and imaginary parts are transformed into amplitude and phase. A peak search is done over a specified range to identify the synchrotron oscillation peak. The frequency, phase, amplitude, and real and imaginary parts at the peak are EPICS process variables that are used for feedback and to characterize the synchrotron oscillation. The real and imaginary components represent cosine- and sine-like synchrotron oscillations. In phase space an energy error (or equivalently a magnetic field error) at injection corresponds to the cosine-like synchrotron oscillation

shown in Figure 2. Similarly, a phase error corresponds to a sine-like oscillation.

The real and imaginary values are used in a feedback loop to control general booster injection energy and phase errors. The actuators that control phase and energy errors in the booster are the rf phase setpoint and the timing of the dipole, quadrupole, and sextupole family ramps. The timing of the magnet family ramps controls the precise field the beam sees when it is injected. Standard feedback is performed based on the program *sddscontrollaw* [5], which uses an inverse response matrix with rf phase setpoint and magnet family ramp timing as actuators and the real and imaginary parts of the synchrotron oscillation as readbacks. The feedback is run continuously during normal booster operation.

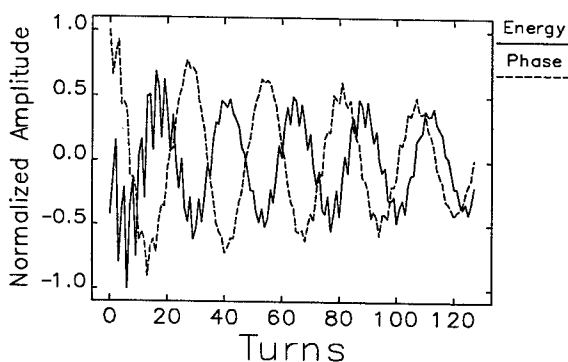


Figure 2: Horizontal BPM beam history data for pure energy and phase errors. One sees that the energy and phase oscillations are 90 degrees in phase apart. The fast ripple remaining on each waveform is residual betatron oscillation not completely removed by the DSP time-domain processing.

BOOSTER CIRCUMFERENCE AND DISPERSION MEASUREMENTS

Booster circumference and (horizontal) dispersion measurements were performed using the upgraded BPMs. The as-built booster circumference does not match precisely one-third of the storage ring (SR) circumference due to "distortion" of the SR lattice, which directs stray radiation away from the X-ray BPM blades [6]. The rf frequency is defined by the SR circumference, resulting in a beam that is horizontally off-axis in the booster at dispersion regions. The circumference measurement was performed by varying the rf drive frequency until the average horizontal orbit in the booster was zero. The difference between start frequency and the frequency where the average orbit is zero is proportional to the deviation of the actual circumference to the ideal circumference (proportionality factor is the known momentum compaction factor). Using this technique, the booster circumference was found to be 1.8 cm too large. This information will be used in the future to realign the booster magnets.

Similarly, the dispersion at the BPMs can be measured by varying the rf frequency and knowing the lattice momentum compaction. This measurement was done and is now a routine application (along with the chromaticity measurement). Figure 3 shows the results for the booster 132-, 109-, and 92-nm-radian lattices. The standard lattice (132 nm-radian) is seen to have zero dispersion in the straight sections. The two lower-emittance lattices show nonzero dispersion in the straight sections as is required since only for the horizontal tune for the standard lattice can there be no dispersion in the straight sections.

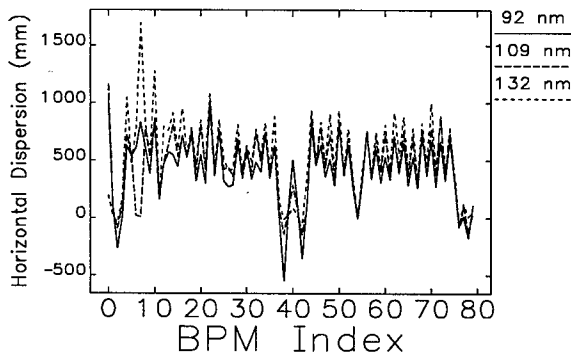


Figure 3: Measured dispersion function for 132-, 109-, and 92-nm-radian booster lattices. Some BPMs with obvious gain problems are observed. One can see that in the straight sections at BPM indexes 0, 40, and 80 the dispersion is (nearly) zero only for the standard, 132-nm-radian lattice. Comparison of the data with theory gives a measure of the BPM gain calibration for each of the different lattices.

CONCLUSION

A total of 80 BPM systems were upgraded in the APS booster. The upgrade was a cost-effective solution since the existing filter comparator was modified. The booster BPM upgrade presented improved single-shot resolution to 20 microns rms, which was an improvement of more than a factor of 50. The 26-dB gain was realized purely passively which saved the cost and complexity incurred with an active amplification solution. Further upgrades of the beam history modules will be investigated in the future.

The upgraded booster BPMs have been used extensively for orbit correction at various energies as the beam is ramped. In addition, the BPM beam histories have been used in an application to correct the phase and energy errors using feedback and a novel DSP-based measurement of the synchrotron oscillation at injection. The DSP processing of the beam history data will be used in the future to measure betatron oscillation as a function of time up the ramp. The BPMs have also been used to measure the booster circumference for realignment purposes and dispersion to characterize new low-emittance booster operating modes.

ACKNOWLEDGEMENTS

The authors wish to acknowledge many valuable discussions with M. Borland and L. Emery regarding synchrotron measurement correction. Thanks to G. Decker for advice on the original booster BPM design specifications.

REFERENCES

- [1] N. S. Sereno, M. Borland, "APS Booster Low Emittance Lattice Commissioning Results," these proceedings.
- [2] E. Kahana, "Design of the Beam Position Monitor Electronics for the APS Storage Ring," Proceedings of the 3rd Accelerator Beam Instrumentation Workshop, AIP Conference Proceedings 252, 235-240 (1992).
- [3] R. Lill, G. Decker, "Advanced Photon Source Monopulse RF Beam Position Monitor Front-end Upgrade," Proceedings of the 8th Accelerator Beam Instrumentation Workshop, AIP Conference Proceedings 451, 318-324 (1998).
- [4] F. Lenkszus, E. Kahana, A. Votaw, G. Decker, Y. Chung, D. Ciarlette, "Beam Position Monitor Data Acquisition for the Advanced Photon Source," Proceedings of the 1993 Particle Accelerator Conference, Washington, D.C., 1814-1816 (1994).
- [5] M. Borland, "Applications Toolkit for Accelerator Control and Analysis," Proceedings of the 1997 Particle Accelerator Conference, Vancouver, BC, Canada, 2487-2489 (1998).
- [6] G. Decker et al., "Reduction of X-BPM Systematic Errors by Modification of Lattice in the APS Storage Ring," Proceedings of the 1999 Particle Accelerator Conference, New York, 2051-2053 (1999).

TUNE SYSTEM APPLICATIONS AT THE APS *

C.Y. Yao, Katherine Harkay, Louis Emery
Argonne National Laboratory, Argonne, IL 60439, U.S.A.

Abstract

The Advanced Photon Source (APS) storage ring is a third-generation X-ray synchrotron radiation user facility. The storage ring tune measurement system consists of signal pickup and beam excitation drive striplines, a network analyzer, and a vector spectrum analyzer. The system has been used for daily tune tracking, beta-function measurement, chromaticity measurement, lattice correction, magnet power supply stability analysis, machine coupling impedance, and observation of beam instabilities. Several software applications were developed to automate the instrument control and data collection processes. We present the current configuration of the tune measurement system, the software tools, and their application at the APS.

SYSTEM DESCRIPTION

The APS storage ring tune measurement system consists of signal pickup and beam excitation drive striplines, an HP4396 network analyzer, and an HP89441 vector spectrum analyzer. Figure 1 shows the block diagram of the system.

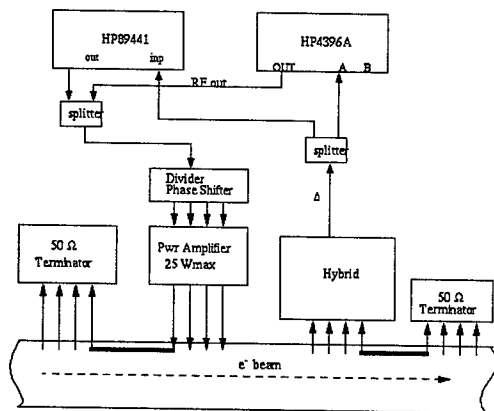


Figure 1: Block diagram of the tune system.

The input signal is connected to the difference signal of a pair of diagonal electrodes of the pickup striplines. The rf source from both the VSA and the NA are summed together to drive the excitation striplines. On/off is controlled remotely through the rf on/off command of each of the analyzers.

The HP89441 VSA is connected to the controls network via standard Ethernet connection. It has an X-window screen for a remote control panel, which can conveniently be called up from any workstation. TCP/IP commands are

used for automatic data acquisition. The HP4396A network analyzer is interfaced to a VME-based IOC. MEDM screens and channel access commands are available for remote control and data acquisition.

STORAGE RING TUNE ARCHIVING

The HP4396 network analyzer is used mainly for routine tune measurement. A Tcl script was developed for this purpose. It is used for daily tune archiving during normal user beam operation and machine studies. Figure 2 shows a tune spectrum plot for the low-emittance lattice.

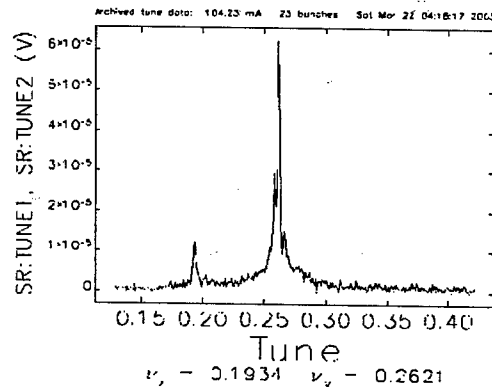


Figure 2: Tune plot of the low-emittance lattice.

The tool also allows one to review the storage ring tune history, which is useful for troubleshooting storage ring lattice problems.

The resolution of the tune readings is estimated to be 0.001.

BETA FUNCTION MEASUREMENT

The beta functions of a storage ring can be measured with different methods. The quadrupole magnets of the APS storage ring are all powered by individual power supplies. This is ideal for measurement of beta functions using the quadrupole field variation method.

The beta function measurement application (see Figure 3) graphically displays all the quadrupole magnets of the storage ring in a matrix. The user can select the quad locations where the beta functions are to be measured and the model machine lattice to use. The script automatically varies each quad and reads the tune spectrum from the VSA. After each measurement, the program adjusts the quad current to restore the tunes to the same value before the measurement. This prevents the lattice from walking away due to magnet hysteresis.

* Work supported by the U. S. Department of Energy, Office of Basic Energy Sciences under contract No. W-31-109-ENG-38.

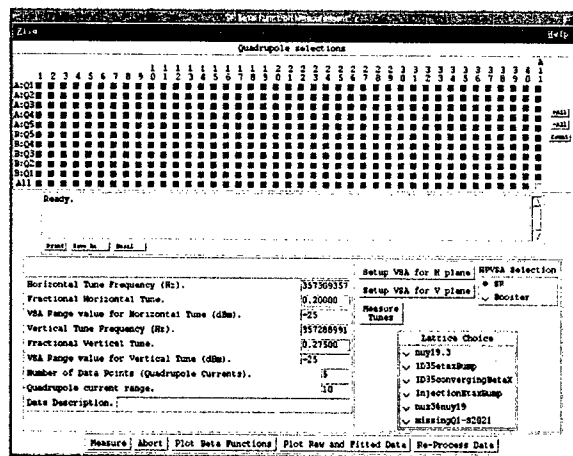


Figure 3: Front page of beta function measurement application.

Fitted results are displayed together with model calculated beta function curves. Figure 4 shows a plot of fitted beta functions.

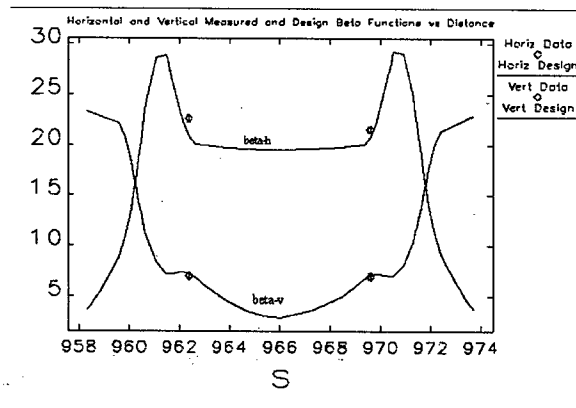


Figure 4: Plot of a fitted and design beta functions.

CHROMATICITY AND DISPERSION FUNCTION MEASUREMENTS

Chromaticity and dispersion function measurements are performed by varying the rf frequency and acquiring tune spectrum waveforms and beam position monitor readings. The chromaticity is calculated from the relationships $\Delta\nu/\nu = \xi \Delta p/p$ and $\Delta p/p = -\alpha^{-1} \Delta f/f$, where ν is the betatron tune, ξ is the chromaticity, p is the momentum, and α is the momentum compaction factor. The rf frequency f is typically varied over the range ± 100 Hz, over which the tune shift is linear. An example chromaticity measurement is shown in Figure 5.

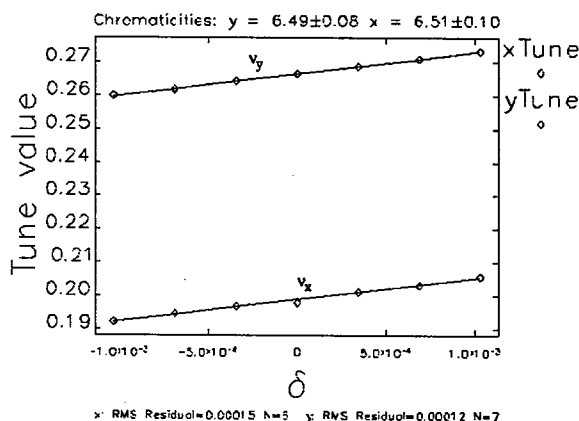


Figure 5: Chromaticity measurement results.

For the dispersion measurement, fitted results are displayed together with model calculated dispersion function curves. Figure 6 shows a plot of fitted dispersion functions.

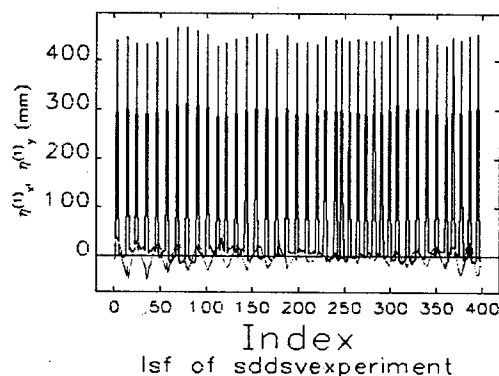


Figure 6: Dispersion measurement results.

TUNE SHIFT MEASUREMENT

In the APS storage ring there are many small-gap insertion device chambers. The contribution to the vertical impedance can be quantified by measuring the tune shift with beam current (tune slope) with the VSA [2]. The measured tune waveforms clearly show the mode merging between the tune and the lower synchrotron sidebands [3]. The transverse mode-coupling instability is avoided with a high positive chromaticity. The total effective impedance computed from the tune slope compares well with that computed from the impedance model [4].

SYNCHROTRON TUNE SPECTRUM

Amplitude modulation of the rf source at the harmonics of the line voltage results in rf noise sufficient to drive the synchrotron frequency, which can be measured using the signal striplines. These data can be archived and are used typically in two ways. First, the intercavity rf phase is adjusted to maximize the synchrotron frequency. Second, the data can be compared with the archive to diagnose

increased rf noise coming from the low-level rf system. Figure 7 shows an example when the rf noise level was elevated. The first indication of problems was an increase in the horizontal beam motion by a factor of two. The noise source was traced to the main frequency synthesizer, which produced 120-Hz amplitude modulation when the AC line voltage was low [5]. The data were acquired at the seventh harmonic of the fundamental rf frequency.

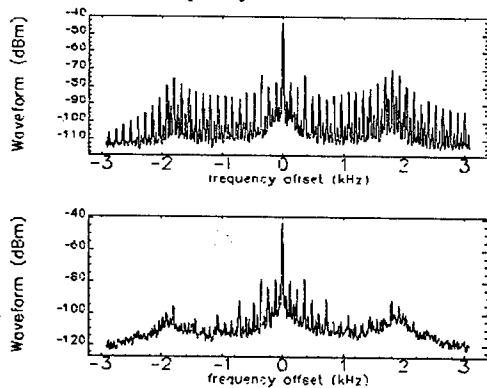


Figure 7: Synchrotron tune spectra, showing elevated (top) and normal (bottom) noise signatures. The synchrotron frequency is 1.8 kHz.

INSTABILITY OBSERVATION

Occasionally, while exploring new operating modes, an intensity-dependent beam instability is observed that is driven by the longitudinal or transverse impedance. Typically, the first observation of unstable beam motion is an apparent emittance blow-up observed on the bending magnet synchrotron radiation photon diagnostics. To identify collective motion, the VSA is used in a passive mode to acquire beam spectra and identify self-driven tune signals. We were able to identify a longitudinal coupled-bunch instability and its driving source to be a TM rf cavity HOM in one of the 16 rf cavities. In Figure 8 the upper trace is the longitudinal spectrum from a stable beam and the lower trace is from an unstable beam. The numbers of the lower trace indicate the phase shift between bunches in unit of $2\pi/3$. Clearly there is a strong mode $2\pi/3$ oscillation on top of the regular mode 0 bunch spectrum. Note the mode 0 spectral harmonics are reduced by $f/54$ due to the bunch fill pattern.

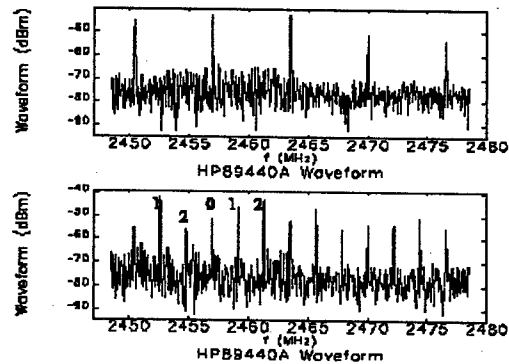


Figure 8: Stable (upper) and unstable (lower) spectra showing longitudinal coupled-bunch instability.

CONCLUSION

The tune measurement system at the APS has played an important role in accelerator operations, lattice measurement, and instability analysis.

ACKNOWLEDGEMENTS

The Beam Diagnostics Group designed and developed the original tune measurement. Michael Borland wrote the dispersion/chromaticity measurement application, and Nick Sereno developed the early version of beta function measurement application. The authors would like to thank Chuck Gold, Jim Stevens, and the operations crews for their support.

REFERENCES

- [1] APS machine studies logbook.
- [2] N.S. Sereno et al., Proc. of 1997 PAC, 1700 (1997).
- [3] K.C. Harkay et al., Proc. of 1999 PAC, 1644 (1999).
- [4] Y.C. Chae et al., "Vertical Coupling Impedance of the APS Storage Ring," these proceedings.
- [5] D. Horan, private communication.

AGS BOOSTER BEAM POSITION, TUNE, AND LONGITUDINAL PROFILE DATA ACQUISITION SYSTEM*

K.A.Brown[†], L.Ahrens, F.Severino, K.Smith, M.Wilinski,
C-AD Dept., BNL, Upton, NY

Abstract

In this paper we will describe a data acquisition system designed and developed for the AGS Booster. The system was motivated by the need to get high quality beam diagnostics from the AGS Booster. This was accomplished by locating the electronics and digital data acquisition close to the Booster ring, to minimize loss of bandwidth in the original signals. In addition we had to develop the system rapidly and at a low cost. The system consists of a Lecroy digital oscilloscope which is interfaced through a National Instruments LabViewTM server application, developed for this project. This allows multiple client applications to time share the scope without interfering with each other. We will present a description of the system design along with example clients that we have implemented.

INTRODUCTION

The AGS Booster has operated since 1991 as a pre-injector of protons and heavy ions into the AGS. Over the past decade the operation of the Booster has evolved such that it now always operates in the linear regions of the magnetic elements. Most recently, though, the Booster was modified to allow for slow extraction of ions to the NASA Space Radiation Laboratory (NSRL). This facility is designed to employ heavy ion beams of many different ion species and at beam energies ranging from 0.04 to 3.07 GeV/nucleon. Many of the modes of operation required by NSRL will be operating the Booster at the limits of the magnets and respective power supplies. In order to allow operating at the highest fields it was necessary to upgrade the tune quadrupole trim power supplies, to provide a larger area of tune space maneuverability. To allow us to experimentally explore these high rigidity regions of the Booster lattice we needed a flexible yet powerful beam diagnostics system, which would provide the highest possible fidelity of information from Beam Position Monitors (BPM) and the Booster wall current monitor. In this report we will describe this system and show examples of its use.

SYSTEM DESCRIPTION AND DESIGN

Figure 1 shows a block diagram of the data acquisition system. The most fundamental component is a Lecroy WaverunnerTM digital oscilloscope. This scope is capable of operating at 1 GSamples/sec, with 2 MSamples/channel

* Work performed under Contract Number DE-AC02-98CH10886 with the auspices of the US Department of Energy.

[†] Email: kbrown@bnl.gov

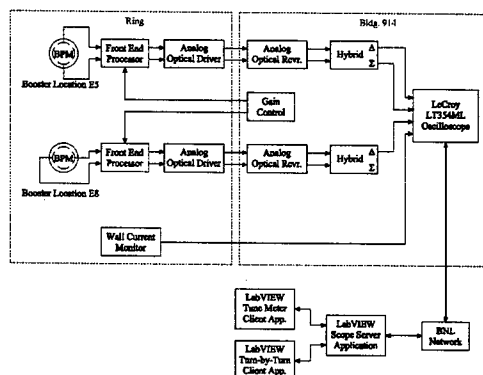


Figure 1: Booster BPM Data Acquisition Block Diagram.

memory depth. This allows sampling the BPM or Wall current monitor signals for as long as 2 msec at 1 nsec resolution. In practice we need only to sample up to 500 μ sec to get good resolution in the betatron tunes.

Hardware Components

The Booster BPM system has been described previously in [1, 2]. Booster BPM's are located in β_{max} locations in the Booster lattice. The system bandwidth range is from 0.05 to 30 MHz. The Booster has two Wall current monitors, one for RF phase loop operation and a second one for diagnostics. The Wall current monitor bandwidth is in the range from about 1 MHz to 1 GHz. The Booster BPM's have the main electronics in the Booster tunnel and use optical fiber links to transmit data to electronics outside the tunnel. The BPM signals are then sent to an RF Hybrid, used as a combiner, to create sum and difference signals. The vertical sum and difference and the horizontal sum are input to the scope. The Wall current monitor signals are connected through high frequency coaxial cables directly to the Booster Main RF controls station. The digital oscilloscope we employ is located in a rack with the Booster Main RF controls.

Software Components

One of the advantages of using the Lecroy digital oscilloscope is the availability of driver modules and interface libraries through the use of National Instruments LabViewTM development environment. Since this system is basically a copy of an existing AGS application [2], we were able to adapt the existing LabView application code

to the new scope and Booster parameters. But we didn't just make a copy of the AGS system. One of the limitations of the AGS system is the application's interface to an oscilloscope directly through a GPIB address. Only one application can communicate and control the scope during a measurement session. To enable the scope to be accessible to multiple simultaneous applications, we built a LabView server and adapted the applications to communicate with the scope through the server. Figure 2 shows the main window for the server application.

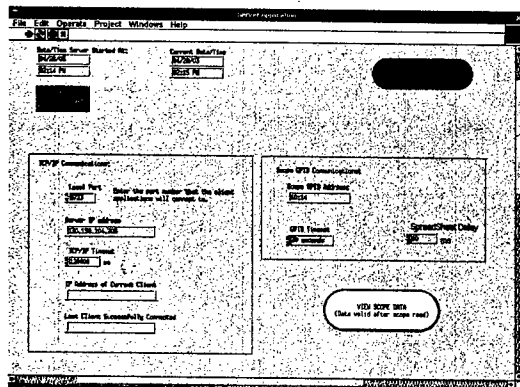


Figure 2: Server Main Window.

Tune Meter Client Even though the tune meter client was adapted from the AGS tune meter, there was still a substantial amount of development required to get the software to work with the new system. The most significant difference in the two systems is the amount of preprocessing that is done in the hardware. For the AGS tune meter system the BPM signals are heavily integrated, such that position information is retained over the period of one turn. The scope, in the AGS case, is clocked on the AGS revolution frequency, so that one sample is taken per revolution. This works well for obtaining a frequency from an FFT/DFT, but limits the amount of information that can be obtained from the BPM signal. In the new system we minimize the amount of processing outside the scope and sample the BPM signals (sum and difference signals) using the scopes internal clock.

In order to perform the same FFT/DFT operation on the data, we have to generate a position per turn array internally and feed that data to the FFT/DFT modules. To do this we have taken advantage of the ability to connect our own code to the LabView application, using the LabView CIN interface. The CIN interface is a mechanism provided by LabView for interfacing external c-code to the application. This allows us to take the BPM sum and difference arrays and use our own algorithms to generate the position/turn. As a benefit of this process we can provide any other information derived from the BPM signals, including integrated intensity, revolution frequency, and bunch length arrays. The problem of generating the position/turn

data requires that we know a few things in advance, such as the RF frequency, the harmonic, and the expected bunch length. This information doesn't have to be exact, but good enough to allow the algorithm to have reasonable starting points. The algorithm begins by looking at just the sum data, to derive the locations and widths of the bunches.

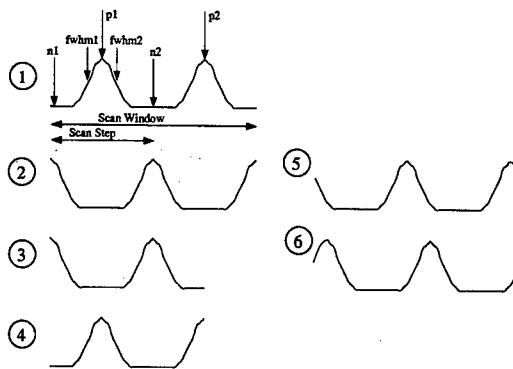


Figure 3: Bunch processing cases.

In figure 3 six cases that must be handled are shown. Since the scope trigger is not synchronous to the bunches, the start of a sample could occur on a bunch or someplace between two bunches. The algorithm cannot assume the data starts in a bunch free region of time. In the figure, case 1 is annotated to illustrate the events and sample windows used in the algorithm. In cases 2, 5, and 6, the data begins on top of a bunch. For these cases the start point must be moved to just after the first partial bunch. In cases 3 and 4 the user defined frequency was set to high and the scan window isn't long enough to contain two full bunches. The user defined frequency cannot be set too low, either, since this risks bunches being interpreted as noise. The algorithm uses a multi-search approach that is adaptive and learns the proper parameters to use as it moves along the bunch train. The first task it must accomplish is to determine where to start and how wide a sample window to use. To accomplish this it uses a user supplied starting frequency and harmonic to set the window to contain two bunches worth of data. It must then search through the first window of data and set a starting point in the region between two bunches. Since it is possible that the signal to noise ratio could be small, especially given 1 nsec sampling, the algorithm performs various permutations to the original data to enhance the bunch data. It does this in an adaptive way, applying only as much filtering and integration as required. To find a bunch the sum data is differentiated to obtain positive and negative slopes of the bunch. This allows determination of whether an edge is rising or falling. Once the starting point is determined the algorithm searches over a sample window of data to find two maximums (labeled p1 and p2 in the figure), separated approximately by a distance determined from the user supplied RF frequency, with each located in the region between a rising and falling edge. The algorithm makes various tests to determine that it is finding reason-

able values. Based on the values of p1 and p2 it searches though the regions between the bunches to find the middle point between the bunches (n1 and n2 in the figure). The algorithm then steps a distance of one Scan Step and repeats the exercise. It scans across the entire data set in this manner. In a second stage the algorithm searches around each maximum for full width half maximum points (fwhm1 and fwhm2 in the figure) and refines the values for the bunch peak locations and the middle points between bunches. Finally, using the knowledge of the bunch positions it scans across the difference data to generate the position/turn array, using the integral of the area between the two fwhm points. The algorithm always adjusts parameters such that it can work its way into case 1.

Turn by Turn Mountain Range Client As with the tune meter application, a LabView application exists for a turn by turn mountain range. In this case the adaption to the new system was more straight forward, since the only change that was needed was to have the application communicate with the server instead of directly to the scope. In fact, the existing AGS application can be used to communicate directly to the scope by simply giving it the correct GPIB/TCPIP address. This application takes a frequency, a harmonic, and an f-dot as variables and produces a mountain range by sampling the wall monitor at the required frequency to get the desired sample size.

RESULTS

Figure 4 shows the data analysis results window of the Tune Meter Client. The beam position/turn is shown above the Fourier transforms for the horizontal and vertical planes. Below the Fourier transforms is a frame for each plane that allows zooming in on the spectrum data.

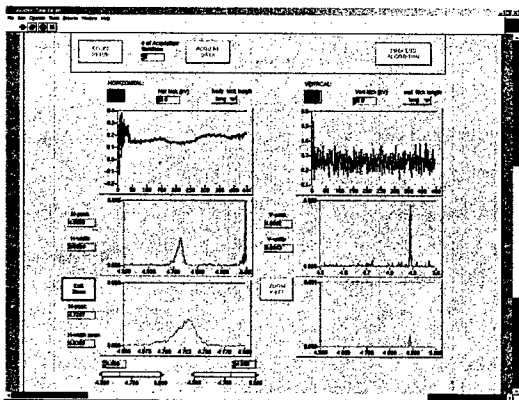


Figure 4: Booster Tune Meter Client.

Figure 5 shows the main window of the Turn by Turn Mountain Range Client. In this case, although the harmonic is 1, two turns of the Wall current monitor are shown per trace. The data shows beam debunching as the accelerating RF is turned off on a zero B-dot porch.

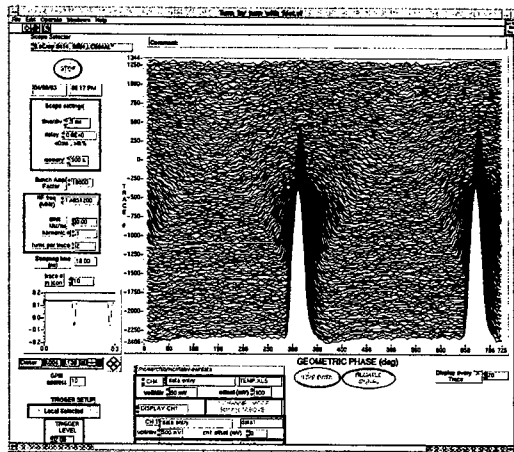


Figure 5: Booster Turn by Turn mountain range client.

FUTURE DEVELOPMENTS

By using a client/server communications architecture we have given ourselves the ability to provide a more general platform for beam diagnostics. To offer more flexibility to the system we are looking into providing a high frequency multiplex, to allow connecting different signals to the digital scope. This would allow selection of which BPM's to view, as well as development of new applications. We are also looking at being able to process the BPM data using fittings. In this case one would want to solve equation 1 [3].

$$X_n = C + Dn + Ae^{\frac{(-n\pi\Delta Q)}{2}} \cos(2\pi n(Q_0 + \frac{n\delta Q}{2}) + \phi) \quad (1)$$

Where C , D , A , Q_0 , ϕ , ΔQ , and δQ , are, respectively; the position of the closed orbit at the BPM; the change in the closed orbit position per turn; the amplitude, tune, and phase of the betatron oscillations; the tune spread of the beam; and the tune shift per turn. n represents the turn number and X_n is the position per turn.

REFERENCES

- [1] D.J.Ciardullo et al, "Design of the AGS Booster Beam Position Monitor Electronics", PAC'91, May 6-9, 1991, San Francisco, CA, p.1431.
<http://accelconf.web.cern.ch/AccelConf/p91/INDEX.HTM>
- [2] W.K.van Asselt et al, "The Tune Meter Systems at the AGS Complex", PAC'91, May 6-9, 1991, San Francisco, CA, p.1273
<http://accelconf.web.cern.ch/AccelConf/p91/INDEX.HTM>
- [3] C.Gardner et al, "Turn-by-Turn Analysis of Proton and Gold Beams at Injection in the AGS booster", PAC'99, March 29-April 2, 1999, New York, NY, p.2063
<http://accelconf.web.cern.ch/AccelConf/p99/PROCS.HTM>

SPALLATION NEUTRON SOURCE RING DIAGNOSTICS*

P. Cameron, J. Brodowski, P. Cerniglia, R. Connolly, J. Cupolo, C. Dawson, C. Degen, A. DellaPenna, D. Gassner, R. Gonzalez, M. Grau, J. Gullotta, L. Hoff, A. Huhn, M. Kesselman, C. Liaw, J. Mead, R. Sikora, G. Smith, K. Vetter, M. Wilinski, BNL, Upton, NY 11973, USA
S. Assadi, W. Blokland, C. Diebele, D. Purcell, T. Shea, ORNL, Oak Ridge, TN, USA
M. Plum, LANL, Los Alamos, NM, USA
R. Witkover, TechSource, Santa Fe, NM, USA

Abstract

Brookhaven is providing the Ring and Transfer Lines Beam Diagnostics for the Spallation Neutron Source (SNS), to be installed at Oak Ridge National Laboratory. The customary diagnostics that will be present include Beam Position Monitors (BPM), Ionization Profile Monitors (IPM), Beam Loss Monitors (BLM), Beam Current Monitors (BCM), Coherent Tune Measurement, and Wire Scanners. An overview of these systems is presented, along with brief discussions of SNS-specific problems that must be addressed, including unprecedented beam power, large dynamic range, a stringent loss budget, space charge, beam halo, and electron cloud. We also present an overview of systems more specifically tailored to address these problems, including Beam-in-Gap measurement and cleaning, two types of incoherent tune measurement, halo monitor, and video monitors for stripping foils and the electron catcher.

OVERVIEW

An overall description of the SNS project and status is available in these proceedings[1], as well as an update on the Ring and Transfer Lines[2]. Additional background information on SNS diagnostics is available in earlier conference[3] and Beam Instrumentation Workshop[4,5] proceedings. An overall layout of SNS Diagnostics is shown in Figure 1.

The SNS Diagnostics team is taking full advantage of the cost and performance advantages offered by the ubiquitous PC platform. With a few exceptions, a typical SNS diagnostic is a rack-mount PC running embedded Windows 2000 or XP, with control of data acquisition and accomplishment of data analysis handled by LabVIEW[6]. Each PC also runs EPICS IOC core, so the PCs appear to be Input-Output Controllers to the EPICS Control System. Whenever possible standard off-the-shelf PCI analog front end/digitizer boards have been used. In the more demanding applications (BPM, BCM, IPM, tune systems) a custom PCI board is used. Timing signals are

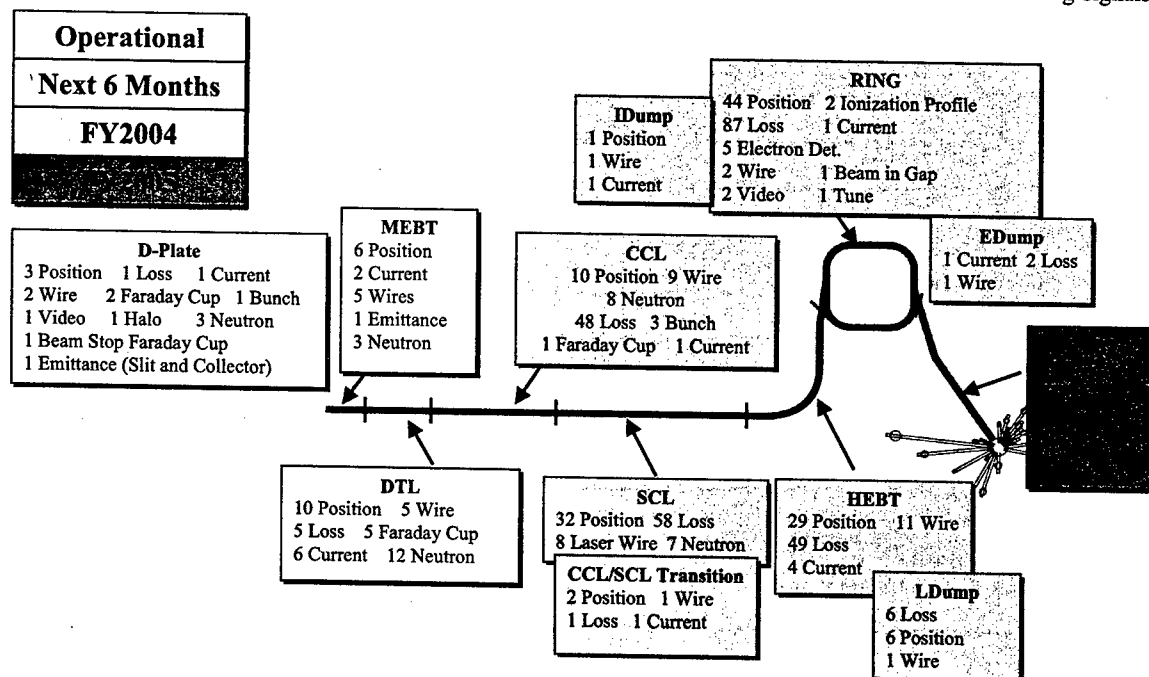


Fig. 1. (color) Layout of the diagnostics in the SNS facility, color-coded to indicate the staged installation dates.

*supported by US Department of Energy

decoded by a standard SNS timing module embedded in a PCI-interfaced FPGA. For systems using the custom PCI AFE/digitizer boards, this gate array is the PCI interface, and also offers the possibility of fast pre-processing.

BEAM POSITION MONITORS

Dual plane 50ohm 250mm long stripline electrodes are located at all quadrupoles. The transfer line striplines are shorted to take advantage of the superior mechanical accuracy offered by that construction. The Ring striplines are open to permit biasing for electron clearing. Apertures vary from 12cm in HEBT to 36cm in the downstream portion of RTBT.

Verification of signal path and calibration of electronics will be accomplished via S21 measurements. Beam-based offset determination (BBOD) will be employed to find BPM electrical centers relative to quad magnetic centers[7]. Log-ratio processing in combination with BBOD opens the possibility of further calibration of the electronics. All Ring and RTBT electronics will be dual-band, with both baseband and 402.5MHz processing.

IONIZATION PROFILE MONITOR

The SNS IPM is an improved version of the IPMs installed[8] in the RHIC ring. Modifications were necessary due to rf coupling to the beam, susceptibility to beam loss, and interference from electrons.

To deal with rf coupling, the microchannel plates were moved outside the beam image-current path and 100dB of rf shielding was added.

Beam loss can cause particle showers to pass through the micro-channel plate and the collector board, generating large background signals. Again, moving all components outside the aperture minimized this problem.

Interference from electrons is handled by extending the IPM's electric and magnetic fields beyond the active volume to prevent electrons created outside from entering. Additionally, the beam pipe in the ring is TiN-coated to suppress electron creation. Finally, the IPM's strong electric field will prevent electron multipacting.

The modified RHIC IPM was tested by scraping beam upstream on the beam pipe wall. As shown in Fig. 2, the profile using the improved IPM is much cleaner than the profile measurement using the unmodified unit.

BEAM LOSS MONITORS

The high average beam power requires that uncontrolled losses be kept very low to allow machine maintenance. The BLM system is designed to detect an uncontrolled loss of 1 part in 10^4 at 1 MW over the full ring and provide a signal to inhibit further injection. Ion chambers (IC) will be used as the detectors to provide the interlock function and multi-turn loss data. Several photomultipliers will provide observation of losses within the bunch. The ICs will be at each quadrupole, the collimators, and key injection and extraction loss points.

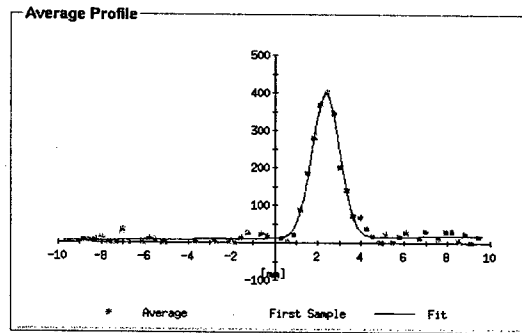
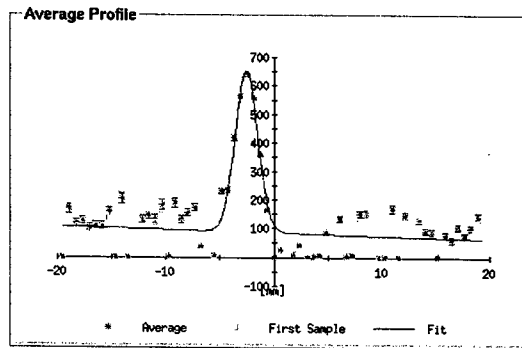


Fig. 2. (color) RHIC IPM measurements before (top) and after (bottom) modifications.

Several movable units may be placed at local hot-spots, for a total of 70 channels.

A new design IC has been developed for the SNS[9], resulting in significantly faster ion transit times and higher dose rate capability. Nominal sensitivity is 70 nC/rad. The system is designed to handle a 10^4 dynamic range. Each BLM signal will be acquired by an individual channel of a 24-bit ADC sampling at 100 KS/sec[10].

The fast BLMs consist of bare photomultipliers, eliminating the problems of radiation darkening and disposal of mixed wastes. Unit-to-unit variation and radiation effects on the window of the tube will require periodic re-calibration and individual HV power supplies. The signals will be integrated over the bunch length and read through digitizer channels of a multi-channel fast digitizer to observe losses within the bunch.

BEAM CURRENT MONITOR

The BCM system is designed to handle the 2×10^{14} circulating protons required for a 2MW beam. Peak current can reach 100A, and care must be taken to prevent transformer core saturation. To achieve 1% accuracy and 0.1% resolution, droop is specified to be less than 0.1% during the 1msec accumulation period, requiring a decay time constant of about 1 second. Rise time is specified at 50ns. A Bergoz® current transformer with rise time <1ns and droop of 0.1%/μs is used. Software[11] compensates for transformer droop and provides the 1 second time constant. The signal is processed by a switched gain amplifier followed by a 7MHz Gaussian Filter. A 5-pole

17MHz Chebyshev filter provides anti-aliasing before digitization at 68MS/s. Charge is calculated for each turn as well as the macro-pulse total. A 100MHz BW output goes to a fast digitizer capable of capturing the edge information.

INCOHERENT TUNE

Incoherent tune will be determined by both dipole and quadrupole beam transfer function measurements. Both systems will employ resonant kickers and pickups. Kicker control and data acquisition and analysis will be accomplished with modified BPM electronics. The objective of the BTF systems is to map the tune footprint, which is large in the SNS Ring as a result of chromaticity and space charge tune depression. Both systems will be similar to an existing system in RHIC[12].

BIG/HALO MONITOR

Gap beam will be vertically kicked onto the collimators for the last 60 to 100 turns of the accumulation cycle by 4.5m long 50 ohm striplines driven by 7KV pulsed, and observed with a gated FBLM. Kick strength and number was determined utilizing particle-in-cell tracking code[13]. Scrapers for BIG tuning and halo observation will be installed adjacent to the IPMs. Kicker control and data acquisition and analysis will be accomplished with modified BPM electronics.

COHERENT TUNE

The BIG/Halo kicker will also be utilized in the coherent tune system. Position signals will come from a dedicated BPM. Kicker control and data acquisition and analysis will be accomplished with independent modified BPM electronics. Both FFT and fit algorithms will be employed. In addition to this independent system, the capability to calculate tune using all ring BPMs will be a part of the Orbit software.

WIRE SCANNERS

The wire scanner mechanisms and electronics are provided by LANL, and are described in detail in ref [14]

VIDEO FOIL MONITOR

Normal operating temperature of the primary stripping foil will be ~2000K, permitting use of a vacuum tube radiation hard video camera, located in a cubby near the injection region. This camera will also be used to confirm the position of the primary foil and monitor its integrity. A second similar camera will be similarly installed to monitor beam profiles at the secondary stripping foil when a phosphor screen is positioned in the beam path. During tuning, a similar phosphor screen can be positioned at the primary stripping foil location. The position and angle of the injected beam can be measured, and beam profile data can be obtained. A third system will

monitor the electron catcher, which is located just below the primary injection stripping foil. Each system will have a multi-position neutral density filter assembly mounted between camera and lens to avoid saturation. The analog video signals will be processed using the NI-PCI-1409 Image Acquisition board, and live video will be available via the network using a video-to-Ethernet converter.

FAST DAQ SYSTEMS

Fast signals from the BLM, BCM, and electron detector systems will be processed by 'PC scopes', utilizing standard commercially available PCI-based digitizers.

CONCLUSION

A full complement of sophisticated diagnostics systems is essential to provide the information needed to commission and operate the SNS. The challenge of integrating these systems and bringing them on-line with limited manpower is being met by utilizing commonality between systems, in both the inter- and intra-laboratory arenas.

REFERENCES

- [1] N. Holtkamp, "Status of the Spallation Neutron Source", these proceedings.
- [2] J. Wei, "Spallation Neutron Source Ring - Status, Challenges, Issues, and Perspectives", these proceedings.
- [3] R. Witkover et al, "Beam Instrumentation for the SNS Ring", proc. PAC1999, New York.
- [4] T. Shea et al, "SNS Diagnostics", BIW2000, Boston.
- [5] M. Plum et al, "Diagnostics Challenges at SNS", DIPAC2003, Frankfurt.
- [6] W. Blokland et al., "Network Attached Devices at SNS", these proceedings.
- [7] R. Talman and N. Malitsky, "Beam-based BPM Alignment," these proceedings.
- [8] R. Connolly et al, "Performance of the RHIC IPMs", PAC2001, Chicago.
- [9] R. Witkover and D. Gassner, "Design and Testing of the New Ion Chamber Loss Monitor for SNS", these proceedings.
- [10] D. Gassner, et al, "Spallation Neutron Source Beam Loss Monitor System", these proceedings.
- [11] M. Kesselman, "SNS Beam Current Monitor Electronics", PAC2001, Chicago.
- [12] P. Cameron et al, "RHIC Third Generation PLL tune System," these proceedings.
- [13] S. Cousineau et al, "SNS Beam-in-Gap Cleaning and Collimation," EPAC2002, Paris.
- [14] R. Hardekopf et al, "Wire Scanner Design for the SNS Superconducting-RF Linac," PAC2001, Chicago.

SPALLATION NEUTRON SOURCE BEAM LOSS MONITOR SYSTEM*

D. Gassner, P. Cameron, C. Mi, R. Witkover[†]
 Brookhaven National Laboratory, Upton, NY, U.S.A.
[†]TechSource, Inc. Santa Fe, NM, USA

Abstract

The Spallation Neutron Source (SNS) [1] being built at Oak Ridge National Laboratory (ORNL) is designed to deliver 1.5×10^{14} protons at 1.0 GeV in one bunch at 60 Hz to a liquid mercury target. To achieve this without excessive activation, an uncontrolled loss criteria of 1 part in 10^4 (~ 1 W/m) has been specified. Measured losses will provide machine tuning data, a beam abort trigger, and logging of loss history. The design of the distributed loss monitor system utilizing argon-filled ionization chambers and photomultipliers will be presented, as well as data from tests with beam.

BACKGROUND

The SNS is being built at ORNL by a collaboration of 6 laboratories, each responsible for specific sections of the accelerator. However, for efficiency and uniformity, controls and some beam instrumentation were handled globally. BNL has responsibility for the beam loss monitoring system for all of SNS. An H-minus ion source injects into a 2.5 MeV RFQ, followed by a Drift Tube Linac (DTL) which accelerates the beam to 87 MeV. The beam then enters a Cavity Coupled Linac (CCL), exiting at 186 MeV. A Superconducting RF Linac (SRF) brings the beam energy to 1 GeV. The High Energy Beam Transport (HEBT) carries the beam to the Ring where it is stripped to protons and accumulated in a single 695 nsec bunch over the 1 msec injection pulse. The bunch is transported via the Ring-to-Beam-Target (RTBT) line to the target. The design pulse beam current in the Linac and HEBT is 38 mA. In the Ring it will increase to more than 40 A at the end of the pulse, for a total of 1.5×10^{14} protons. This high average beam power makes it crucial that uncontrolled losses be minimized through careful design with beam dumps and collimators handling losses in a controlled manner. It is the job of the BLM system to provide data to minimize uncontrolled losses and inhibit the beam when excessive losses occur.

SYSTEM PHILOSOPHY AND DESIGN

Sufficient detector coverage is required to accomplish this goal. To provide full coverage the BNL Linac and AGS Ring uses long argon-filled ion chambers made from hollow, large diameter coaxial cables[2]. The same type

of detectors have been used at ISIS, a machine similar to SNS [3]. A long detector can provide continuous coverage but its length often prevents close coupling to the beam line, lowering response. Since most losses will occur at the beta-max most of the detector receives a much lower exposure, reducing the benefit of the greater length. These cables cannot support high bias voltage, limiting them to low dose rates. For these reasons, smaller, sealed glass ion chambers were designed for the FNAL Tevatron [4] and also used in RHIC [5]. In the SNS HEBT, Ring and RTBT, detectors will be placed at essentially every quadrupole and at other key points. In addition a number of movable BLMs have also been included. Table I shows the distribution of BLMs.

DTL	CCL	SRF
12	28	86
HEBT	Ring	RTBT
59	70	40

Table I. Distribution of BLMs. Total = 295

Ion chambers will be used as the primary detector. Commercial pin-diode BLM [6] are not well suited to the 1 msec beam pulse. PMTs require excessive recalibration and are not practical for a high count distributed system. However, some will be installed to view losses within the bunch. These will be used for only relative time history.

SYSTEM REQUIREMENTS

The SRF cavities can quench if hit by large beam losses over several pulses. At the other end of the scale, even low level losses over extended periods can prevent "hands-on" maintenance. Experience at LAMPF and the PSR, and studies for APT at LANL [7] indicate that a loss of 1 W/m corresponds to about 100 mR/hr. This would be equivalent to a loss of about 0.01% uniformly around the Ring. The system should be able to detect this level with a resolution of 1%. The BLM system must have sufficient dynamic range to detect long-term low level losses, but not saturate during short duration, high level losses.

Experience has shown that the beam-on dose rate can be estimated from the beam-off dose rate by a "rule-of-thumb" multiplier of 1000. Thus 100 mR/hr at 1 foot would imply a beam-on dose rate of 100 R/hr, or, 0.46 R/sec during the 1 msec, 60 Hz beam. This is taken as the 1 W/m low end loss. The upper end limit (1% local loss) is based on the expected losses in the Ring collimators

* Work performed under the auspices of the U. S. Dept of Energy

[8]. This represents a 6-decade range but linearity at the high end is not critical.

The BLM system must generate a beam abort signal for the Machine Protect System (MPS) in less than 10 μ sec. Long term low level losses can activate and damage beamline components. Channels exceeding the 1 W/m loss level for extended periods will be monitored in software resulting in a warning alarm to operations. Losses which exceed the programmable threshold will trigger an inhibit signal sent through the IOC hardware to the MPS.

DETECTOR

SNS will use 295 argon-filled ion chambers as the primary detectors for monitoring beam losses. Argon has the advantage of fast electron transit time compared to slower air filled detectors [9]. The initial choice was an ion chamber designed for the Tevatron, but concerns about saturation at high dose rate and long ion transit time (~ 700 μ sec at 2 kV bias) led to the development of a new ion chamber designed to overcome these limitations [10.] It utilizes a larger inner diameter electrode to significantly decrease the ion transit time and raise the collection efficiency for a 1% local loss.

BLMs mounted near RF cavities may detect X-rays. Measurements at RHIC indicate that this may reach 50 R/hr for a 1 MV gap voltage. This would be at a level comparable to the 1 W/m losses. It is estimated that 3/8-inch of lead would provide sufficient shielding but a study will be done using the SRF cavities to determine if this would reduce the X-rays to an acceptable level. It will also be necessary to determine the effect on the beam loss measurement.

CABLING

Experience with the RHIC loss monitor system has shown that nano-ampere measurements require low tribo-electric cable. Tribo-electric noise comes from friction between the conductors and insulation due to movement, such as vibration, but a low friction coating between insulator and conductors will reduce this significantly. Special cable such as Belden 9054 or 9224 will be used for the signals. Two HV cables (Times Microwave 91421), from separate HV power supplies will connect to alternate BLM's from each rack to provide some coverage in the event of a high voltage short or power supply failure.

ELECTRONICS

The interface to the Controls system will be in VME, with analog signal electronics housed separately in the same rack. Figure 1 shows the system block diagram.

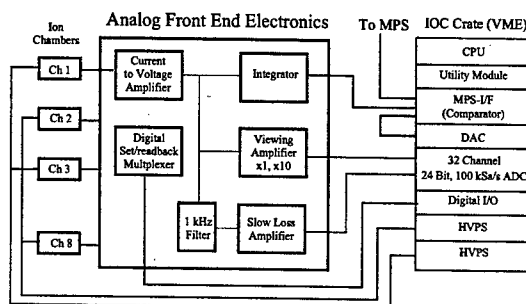


Figure 1. BLM System Block Diagram

ANALOG FRONT END ELECTRONICS

The BLM System must measure beam losses from a 1% local loss (15 kW) down to 1% resolution of a 1 W/m ($\sim 0.01\%$) loss, a dynamic range of over 120dB, or at least 21 bits. In terms of signal current, this corresponds to a range from 324 pA to 486 μ A. Fortunately there is a large difference in bandwidth between the requirements (0.1 Hz to 35 kHz), which can be exploited. The circuit (Figure 2) provides 3 outputs to meet the wideband-wide range data, fast trip, and 1 W/m sensing requirements.

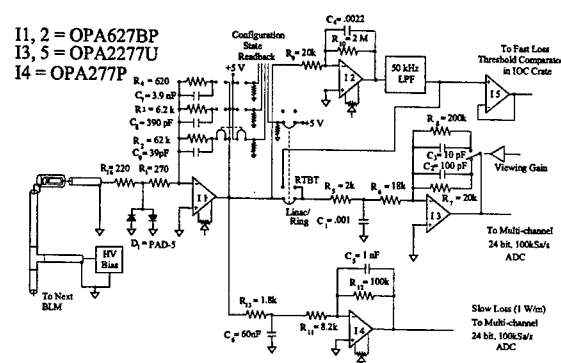


Figure 2. Analog Front End Electronics Schematic

Since the ion chamber is a current source, the transfer gain is set by the feedback resistor while the input resistor only determines the voltage noise gain and input signal risetime. For a typical 100 m cable the 470 Ω input resistor gives about a 5 μ sec risetime. Three jumper selectable gains are provided to allow for lower losses in the linac or higher losses near dumps or collimators. "Viewing Gain" can be set and read back remotely without affecting the beam interrupt or 1 W/m outputs. A 6.2 k Ω feedback resistor puts the signal mid-range for 5 V ADC for a 1% beam loss. For the 35 kHz SNS BW, the 10 pA equivalent noise observed in RHIC with a 10 Hz BW would correspond to 3.7 μ V.

A 1 W/m loss will produce about 200 μ V out of the input stage, roughly an LSB for a 5V, 16-bit (15-bit plus sign) ADC. Another 6 to 7-bits would be needed for 1 % resolution of the 1 W/m loss. The first stage signal is split and passed through a 1 kHz low pass filter, reducing the noise and lowering the peak of fast losses, allowing an additional gain of 10. While a lower cut-off would further reduce the noise it might not allow measurement of the baseline for offset subtraction. The output is applied to a 24 bit, 100 kSa/sec ICS-110B ADC. Testing has shown that it can achieve 18-19 bit resolution but taking over 600 samples provides the required sensitivity.

Experience at LANSCE [11] has shown that integrated dose rather than dose rate should be used for the beam inhibit. The output of the first stage is split again and sent to an integrator. The integrator output is fed to a comparator module in the VME which generates an inhibit for the MPS when the programmable reference is exceeded. The circuit is a "leaky integrator", with a large value resistor to bleed the charge. It is simple and provides a good representation of the pulse dose. Simulations indicate that for the 1 msec pulse the output will reach equilibrium in 3 beam pulses with an error of less than 10% while decaying to under 5% by the next beam pulse. For the RTBT channels the integrator serves a dual purpose. Since impulse losses from the 695 nsec wide RTBT beam pulse would be too narrow for the 100 kSa/s ADCs to acquire through the wideband output, the signal from this integrator will be jumper selected for input to the Viewing Gain stage.

MPS INTERFACE CIRCUIT

The output of the leaky integrator is compared to a computer settable reference voltage to sense excessive loss. The comparator output is applied to an open-collector TTL driver which is used to signal the MPS that the beam should be inhibited. The circuit also passes through a continuity line from the MPS through the AFE module which will alert the MPS if either the MPS interface or AFE module is removed or powered down.

PACKAGING

The 8 channel AFE boards are packaged in 6U, 6hp wide eurocard modules. Four modules are mounted horizontally in a 4U high cardcage. A custom backplane provides a common bus to allow multiplexed readback of the more than 220 digital states by the IOC, using 8 bits. Linear supplies provide clean power. The HV power supplies, ADCs, DACs for the MPS references, Digital I/O modules, and the MPS-I/F modules are located in the VME crates with the control system IOC CPU and support modules.

STATUS

A prototype AFE crate has been fabricated with a hand-wired backplane and tested with an IOC. One 8-channel AFE module has been fully tested. The AFE crate 8-channel AFE module, IOC and 2 detectors have been delivered to the ORNL site for commissioning of the DTL linac section. Another four AFE modules have been built and are being testing. Seven more detectors are being prepared for shipment. An AFE crate is being prepared to accept the PCB backplane when it is completed shortly. This preproduction crate with the 4 AFE modules will be sent to ORNL following testing.

ACKNOWLEDGMENTS

The authors would like to acknowledge the guidance and support provided by Tom Shea and Saeed Assadi of ORNL. R. Shafer and M. Plum of LANL provided valuable insight and discussions regarding a number of topics in this work. The BNL staff includes Chaofeng Mi who built and tested the AFE circuit. Yongbin Leng evaluated the ADC's, John Smith and Larry Hoff have been invaluable in supporting the Controls aspect of this system. Tony Curcio, Paul Ziminski and members of the Instrumentation Group provided enthusiastic cooperation in building, testing and installation of the prototype detectors and circuits.

REFERENCES

- [1] J. Alonso, "The Spallation Neutron Source Project," Proceedings of the 1999 PAC, NY, p. 574 (1999). For current status see <http://www.sns.gov>.
- [2] R.L. Witkover, "Microprocessor Based Beam Loss Monitor System for the AGS," IEEE Trans. Nucl. Sci 26 3313 (1979).
- [3] M. A. Clarke-Gayther et al., "Global Beam loss Monitoring Using Long Ionisation Chambers at ISIS," 4th European Particle Accelerator Conference, London, England, p. 1634 (1994).
- [4] R.E. Shafer et al., "The Tevatron Beam Position and Beam Loss Monitoring Systems," Proc. The 12th Int'l Conf. High Energy Accel., p. 609 (1983).
- [5] R.L. Witkover, R.J. Michnoff and J.M. Geller, "RHIC Beam Loss Monitor System Initial Operation," Proceedings of the 1999 PAC, NY, 1999, 2247 (1999).
- [6] Bergoz Inc, <http://www.bergoz.com>.
- [7] R.A. Hardekopf, "Beam Loss and Activation at LANSCE and SNS," LA-UR-99-6825, Los Alamos National Laboratory, Los Alamos, NM. Sept. 1999.
- [8] Y.Y. Lee, BNL, Private Communication, Oct 2001.
- [9] M. Plum and D. Brown, "Response of Air-Filled Ion Chambers to High Intensity Radiation Pulses," Proceeding of the 1993 PAC, p. 2181 (1994).
- [10] R.L. Witkover and D. Gassner, "Design and Testing of the New Ion Chamber Loss Monitor for SNS," these proceedings
- [11] M. Plum and R. Shafer, Private communications.

DESIGN AND TESTING OF THE NEW ION CHAMBER LOSS MONITOR FOR SNS

R. L. Witkover, TechSource, Inc., Santa Fe, NM
D. Gassner, Brookhaven National Laboratory, Upton, NY 11973

Abstract

An ion chamber beam loss monitor has been designed for the Spallation Neutron Source (SNS). The new detector overcomes concerns with the original design about slow ion collection times and low collection efficiency at high loss rates. Prototypes have been built and tested with static sources and pulsed beams. Commercially made pre-production units have been fabricated and laboratory tested. Details of the design and test results will be presented.

BACKGROUND

Ion chambers (IC's) are the detector of choice at many accelerators for measuring beam loss. Their stability, sample uniformity, flat response over a wide voltage range and sensitivity are strong features. Shafer designed a simple chamber for the Tevatron in 1982[1], which were also used in RHIC at BNL[2]. These have a coaxial 1/4" OD tube inner and 1.5" ID nickel foil outer electrodes in an argon filled glass tube. Testing of the RHIC ICs showed wide sample variations with the preferred bias polarity (electrons collected on the inner electrode). However, when biased with the opposite polarity, unit-to-unit variations were small. Due to schedule demands the non-preferred polarity was used in RHIC. The resulting slower ion signal rise time and earlier saturation were not a problem in RHIC, but would be important concerns in SNS. Recently it was found that a crimp in the outer electrode at the support attachment was the cause of the problem and was eliminated by a simple fix. It is likely that subtle changes in the fabrication technique over the intervening 15 years caused the problem. Tests on 8 samples built with this change showed good reproducibility[3].

The SNS will deliver 10^{14} protons to a liquid mercury target at a rate of 60 Hz. The 1 msec long H-minus pulse will be accelerated through the Linac to 1 GeV. It then is transported in the HEBT to the Ring where it is accumulated in a single 695 nsec proton bunch over approximately 1000 turns. The beam is then extracted and sent down the RTBT line to the target. The Beam Loss Monitor (BLM) system will utilize nearly 300 ICs along the beam path. In the Ring and RTBT the detectors must operate over an intensity range of 10^3 . The dose rate in RTBT even from low percentage losses could be significant due to the short pulse length and high

intensity. While the ICs do not need to resolve the time structure of the bunch (PMTs will be used for that) they must be able to provide a fast beam abort signal to the Machine Protection System (MPS). Subsequent analysis and tests showed that the FNAL ICs, even with the fix, would not satisfy the signal rise time and high dose rate requirements. A new design was needed.

RISE TIME

While electrons are collected in a few microseconds the heavier ions take much longer. At 2000 V the ion collection time for the FNAL IC would be close to 700 μ sec. For a step loss the ion portion of the signal would rise over the 1 msec, and fall with a 700 μ sec tail. While the electron signal would allow a rapid beam abort, the waveform during the pulse would require unfolding.

The positive ion transit time is given by:

$$t = \frac{d^2}{\mu_0 V \left(\frac{P_0}{P} \right)}$$

where:

μ_0 = Ion mobility at STP [$\text{cm}^2/(\text{V}\cdot\text{sec})$]

V = Applied Voltage [V]

P_0 = Atmospheric pressure

P = Working pressure

d = Effective electrode separation [cm] for cylindrical geometry[4]

The transit time can be reduced by decreasing the electrode gap, but the chamber must be lengthened to keep the same sensitivity[5]. By increasing the inner radius to 0.5" the ion collection time at 3 kV bias would be reduced from 560 μ sec to 72 μ sec.

COLLECTION EFFICIENCY

Thomson derived the equations for the collection efficiency in 1899, but they have only been solved for

$$d = \left[(a^2 - b^2) \frac{\ln(a/b)}{2} \right]^{1/2}$$

limited ranges. Using the "equivalent" gap ("d" above), the parallel plate solutions can be applied to cylindrical geometry. Boag and Wilson[6] found a solution assuming second and third order polynomials for the ionization distributions, and steady state radiation. Their result, which gives a good fit for efficiency > 0.7 is given by:

* Work performed under the auspices of the U.S. Dept. of Energy.

$$f = \frac{1}{1 + \frac{\xi^2}{6}} \quad \text{where:} \quad \xi^2 = \frac{\alpha}{ek_1k_2} \frac{P}{P_0} \frac{d^4q}{V^2}$$

e is the electron charge,
 α is the first Townsend recombination coefficient,
 $\alpha = 1 \times 10^{-6}$ [cm³/sec] for Argon
 k_1 is the electron mobility = 1.8 [cm²/(V-sec)]
 k_2 is the ion mobility = 1.3 [cm²/(V-sec)]
 q is the ionization charge density

$$q = \frac{I_{\text{signal}}}{v} \times 3 \times 10^9$$

where I_{signal} is the current generated by beam loss and v is the active volume of the ion chamber. For the FNAL IC, the sensitivity is 70 nA/rad/sec, for a volume of 110 cm³. For a 1 % local loss, the dose rate is 9.2 kRad/sec during the Linac pulse.

The collection efficiency and ion transit time are shown in Figure 1 as a function of inner cylinder radius.

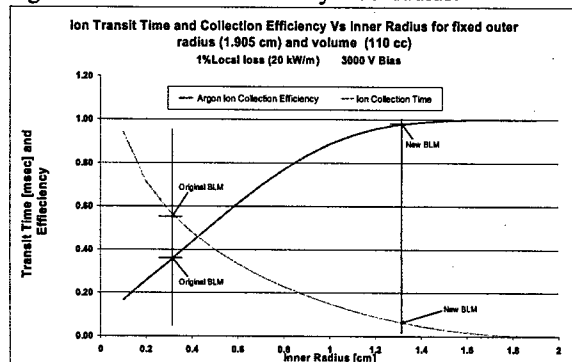


Figure 1: Ion transit time and collection efficiency

This calculation is for continuous radiation, but Boag[7] also found a solution for the pulsed radiation when the loss occurs in a time short compared with the ion transit time. The application is not clear in the Linac and Ring where the pulse length is comparable to the ion transit time for the FNAL chamber. However for the RTBT pulse for a 1% local the calculation gives the efficiency as 21% for the FNAL IC and 60% for the new design.

THE NEW ION CHAMBER DESIGN

Clearly the new design is superior on paper, but careful high voltage design would be required due to the smaller gap. Guard electrodes were used to divert leakage from the HV electrode to ground and define the active region. Voltage gradients have been reduced by rounding the electrode ends. Figure 2 shows the new design. Two prototypes were tested at BNL. The first was filled with Nitrogen at 1 ATM. A second prototype with a higher voltage feedthrough and improved ceramic and guard rings was able to hold 4.5 kV with 1 ATM Argon.

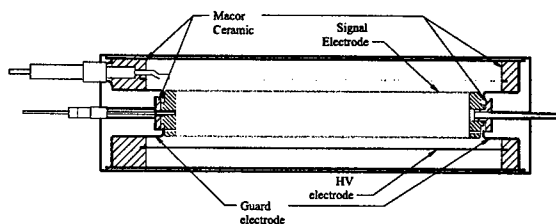


Figure 2: Design of new SNS ion chamber.

TESTS WITH BEAM

An FNAL IC and Prototype 1 were installed after the BNL 200 MeV Linac. Figure 3 shows the results. The larger FNAL IC signals were due to the difference in proximity to the loss and the use of Argon versus Nitrogen. The wide scatter of points was probably due to beam motion since the beam current did not show this variation. The reason positive bias is not preferred is clear. Prototype 1 shows fairly flat response.

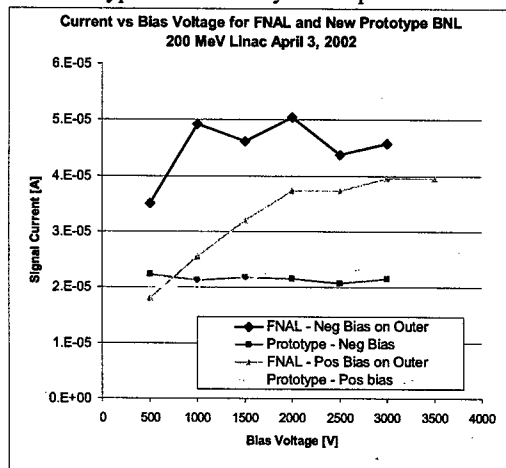


Figure 3: Response of FNAL IC and SNS prototype IC to 200 MeV Linac beam. Approximately 1000 W/m loss.

Figures 4a and 4b show the results using the prototype analog front end (AFE) circuitry designed for SNS[8]. The first stage is a current amplifier with a 35 kHz BW using a Burr-Brown OPA627BM. The slow ion transit time can be clearly seen after the pulse in Fig 4a. This also causes the gradual rise during the pulse. The "noise" during the pulse is modulation of the beam to tailor the stacking in the Booster. The signal from the Prototype ion chamber has a much faster ion collection time, as expected and does not show the rise during the pulse.

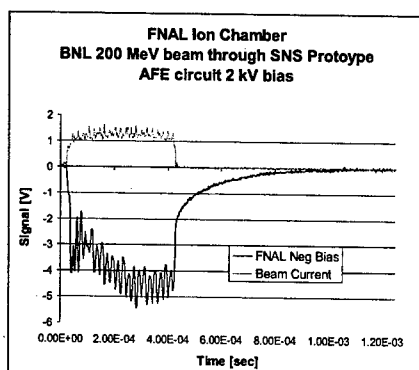


Figure 4a: FNAL IC BNL Linac Beam Test.

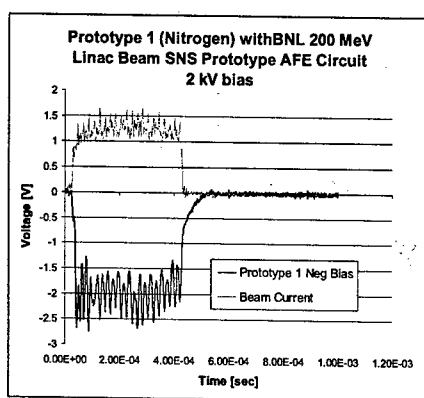


Figure 4b: SNS Prototype IC Linac Beam Test

STATUS

LND Inc.[9] has produced 10 units of the new design based on BNL supplied drawings. Tests indicate that all units reached 5 kV without breakdown and appeared to give the expected sensitivity. A typical calibration scan is shown in Figure 5.

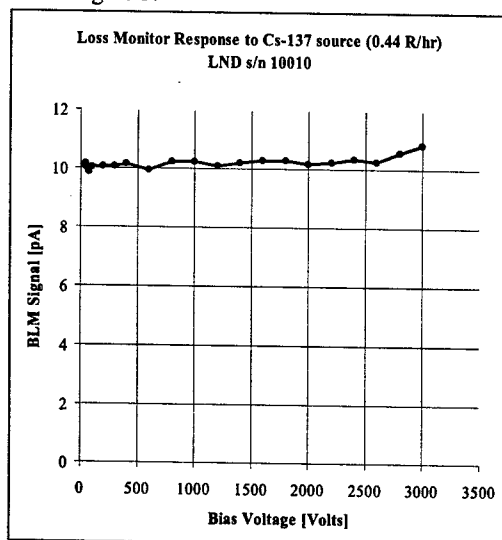


Figure 5: Response of typical new ion chamber.

CONCLUSIONS

A new design ion chamber has been developed for the SNS application which provides significantly faster ion transit times and can tolerate higher dose rate losses than the FNAL IC. Tests with beam confirm the calculations. In addition, the all ceramic and metal construction is likely to be less susceptible to breakage than the glass FNAL chambers. However, the new chambers will be about twice the cost of the FNAL design and may not be justified in all applications. A pre-production run has indicated that they can be successfully manufactured.

ACKNOWLEDGEMENTS

The authors wish to acknowledge the contributions of C. J. Liaw in the mechanical design, Dave Kipp is assembling the prototype chambers and Paul Ziminski in testing the chambers with the cesium source. The prototype circuit used in the beam tests was built and tested by Chaofeng Mi. Anthony Curcio (BNL) was invaluable in the installation and setup of the beam tests.

REFERENCES

- [1] R. E. Shafer, et al., "The Tevatron Beam Position and Beam Loss Monitoring Systems", Proc. 12th Int'l Conf on High Energy Accel., FNAL (1983) p609
- [2] Witkover, R. L., Michnoff, R. J., Geller, J. M., "RHIC Beam Loss Monitor System Initial Operation", Proceedings of the 1999 PAC, NY, 1999, 2247
- [3] Witkover, R. L. and Gassner, D., "Design of an Improved Ion Chamber for the SNS", BIW2002, AIP Conf Proc 648 (2002) p337
- [4] Boag, J. W. in "Radiation Dosimetry, Vol. II", F. Attix, et al, eds., Academic Press (1966), p22
- [5] R. Witkover, "Proposal for a Quasi-Parallel Plate, Cylindrical Geometry Ion Chamber for SNS", November 7, 2001, unpublished
- [6] Boag, J. W. and Wilson, T., "The saturation curve at high radiation intensity", Brit. J. Phys., 3 222-9, (1952) and Loc. Cit (5), p16
- [7] Boag, J. W., "the Dosimetry of Ionizing Radiation", Vol. 2, Ed. By K. R. Kase, B. E. Bjamgard and F. H. Attix, Academic Press, (1987), p 191
- [8] Witkover, R. L. and Gassner, D., "Preliminary Design of the SNS Beam Loss Monitoring System", BIW2002, AIP Conf Proc 648 (2002) p345
- [9] LND, Inc., 3230 Lawson Blvd., Oceanside, NY 11572

BEAM CURRENT MONITOR CALIBRATOR FOR THE SPALLATION NEUTRON SOURCE*

M. Kesselman, C. Dawson, G. Smith, Brookhaven National Laboratory, Upton NY 11973, USA

Abstract

The Beam Current Monitor (BCM) system for the Spallation Neutron Source (SNS) to be installed at Oak Ridge National Laboratory (ORNL) requires an on-line calibrator to assure the system is appropriately scaling current. The calibration system must be able to handle the current range expected in the MEBT, Linac, HEBT, Ring and RTBT. This covers a dynamic range of 35ma to 50 amps. A 10-turn calibration winding has been included in all current transformers. This calibrator must provide adequate flexibility to assure the current transformers are not damaged by failures in the calibrator drive amplifier, and provide better than 1% accuracy with a capability to provide calibrated currents covering the dynamic range. This paper will address the design considerations and resulting design of a suitable calibrator for this system.

1 INTRODUCTION

The BCM system is designed as a network attached PC based instrument. The current sensor is a Bergoz® FCT [1]. It has been specially customized for this application and includes a 10-turn calibration winding. This allows the calibrating current to be 1/10 that of the beam.

A calibration signal generator is included to permit the measurement of a known current prior to each beam cycle. This is necessary to insure that the scale and transformer droop are known accurately enough to maintain the 1% system accuracy.

A large dynamic range is required for the accumulator Ring and RTBT where beam currents can reach 50 Amps. The MEBT, Linac and HEBT will only have 50ma peak beams. To satisfy the MEBT, Linac and HEBT requirement, a low current calibrator will be provided. In the Ring and RTBT the same low current calibrator will be installed but will be connected to a high current driver with two additional current ranges. This approach then, uses the low current calibrator to drive a high current driver housed in the drive bay space in the PC for the systems being used for the Ring and RTBT.

2 TECHNIQUE

To meet the demand of an adjustable current source, capable of high accuracy and stability, a current output DAC2902 has been selected as the basic element. This provides a well-controlled dual current source suitable for

the two channels included in the PC chassis. The DAC is to be preceded by a memory that can be loaded from the higher-level application program and so act as a function generator that can provide a wide selection of calibration waveforms. The DAC2902 can deliver up to 20ma into a 50 Ohm load. For most applications as a calibrator, however, it is intended to run a 5ma, 400 usec pulse. This is equivalent to a 50ma beam current due to the 10-turn calibration winding in the SNS transformers.

2.1 Special Considerations

A number of design features have been included to assure flexibility and safe operation:

- Ground isolated calibration output.
- Current limiting and fuse protection to assure there can be no damage to the transformer in the event of DAC/driver failure.
- Transmission line AC source termination to avoid reflections due to mismatch at the transformer end and high impedance current source end.
- Opto-isolated digital interface and isolated power supplies to maintain galvanic isolation.
- Memory driven waveform to provide flexibility.
- DC fused protection to protect the transformer winding against catastrophic driver failures.
- Careful attention to cabling and shielding to avoid ground loops and shield against pick-up on the calibration winding cabling.

2.2 Prototype efforts

To test the concepts described above, an evaluation board was obtained from Texas Instruments for the DAC2902. Space available for additional components was used to create a simple clocking system to enter a fixed digital value followed by a zero value, thus creating a pulse. This was accomplished using a 555 timer IC. All digital triggering and power was isolated from ground to avoid ground loops. The DC capability was implemented by inhibiting the clock that would return the DAC to zero. The output current was measured by an Agilent 3458A 8-1/2 digit Digital Multi-meter. In this way a 5ma current was easily set digitally.

The pulse obtained from the DAC2902 was isolated from the transformer by a 50 Ohm protection resistor, and AC terminated at the source (0.1 μ F and 82 Ohm) to match a 78 Ohm Twinax cable (Belden 9463). The cable was 500 feet long to simulate estimated wiring and measurements performed on the transformer output. By adjusting the pulse width to 400 μ s, adequate pulse time was available to permit transients, due to the AC coupled termination, to settle and computation of transformer droop time constant and gain to be performed. The

*Work performed under the auspices of the U.S. Department of Energy. SNS is managed by UT-Battelle, LLC, under contract DE-AC05-00OR22725 for the U.S. Department of Energy. SNS is a partnership of six national laboratories: Argonne, Brookhaven, Jefferson, Lawrence Berkeley, Los Alamos, and Oak Ridge

transformer droop is compensated by a special compensation filter described in reference [2]. This is necessary for proper calibration since the FCT has a droop near $0.1\%/ \mu\text{s}$.

The original prototype housed the calibrator in the main section of the PC chassis, where space permitted. The final version is expected to devote one drive bay for this calibrator.

take advantage of all the noise immunity provided by a balanced line. Noise pickup in the calibrate cable, as yet unknown, could cause significant problems in the measurement of the currents due to the fact that it is effectively multiplied by ten (the turns ratio) in the transformer output circuit. As a result consideration is being given to a differential output version of the current pump circuit of Figure 1.

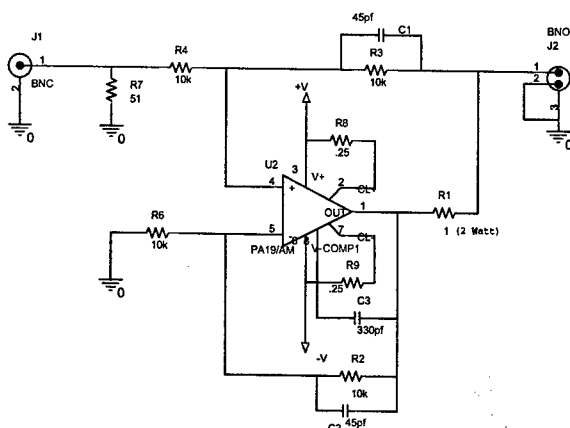


Figure 1: Breadboard of the Improved Howland Current Pump.

3 DRIVER

The prototype described above provides adequate current for the MEBT, Linac and HEBT transformers. To achieve the currents required to calibrate the Ring and RTBT transformers, where actual beam currents will accumulate up to 50 Amps, a current amplifier/driver will be provided.

A circuit has been designed using an APEX PA19A Video Power Operational Amplifier configured in an "Improved Howland Current Pump"[3] as in figure 1. This circuit has been breadboarded and is undergoing tests. So far it appears to offer the rise time, stability and the ability to drive the cable lengths required. Several issues remain however. First the circuit as shown produces an output offset current of around 5 ma. Such a DC offset current in the transformer core has been shown to produce slight errors in the droop measurements and so may need to be carefully zeroed. This might be adequately accomplished with a pot on the board but then over time there is no way to know if the adjustment drifts. It could also be zeroed using the DAC but some additional means of measuring the offset would need to be provided since it does not pass through the transformer. Another possibility being considered is to provide an auto zero feedback in the design to correct for long term drift in this current.

Second, the driver in many cases needs to drive the current pulse along a TwinaX cable up to 100 meters long. The single ended driver shown in Figure 1 is perfectly adequate on the bench, but a single ended drive does not

4 SUMMARY

A calibrator for the SNS BCM system is in the development phase. A prototype low current calibrator has been built and tested. It provides a DC capability for calibration of the calibrator, and utilizes a current output dual 12 bit DAC2902. A driver amplifier design is underway to use the output of the DAC as an input and develop a current of the order of an amp. For the final product, a board will be laid out that contains the function generator, the DAC2902, timing and control interface logic and the necessary ground isolation.

5 REFERENCES

- [1] <http://www.bergoz.com/>
- [2] Martin Kesselman, "Spallation Neutron Source Beam Current Monitor Electronics", PAC2001, June 18-22, 2001, Chicago, IL.
- [3] "Voltage to Current Conversion", APEX Application Note 13. Available at; http://www.apexmicrotech.com/pdf/app_notes/apnote13.pdf

ELECTRO-OPTIC LONGITUDINAL ELECTRON BEAM DIAGNOSTIC AT SDL

H. Loos*, A. Doyuran, J. B. Murphy, J. Rose, T. Shaftan, B. Sheehy,
Y. Shen, J. Skaritka, X.J. Wang, Z. Wu, L.H. Yu,
BNL, Upton, NY 11973, USA

Abstract

The linac at the NSLS Source Development Lab (SDL) provides a high brightness electron beam for the DUV-FEL project with subpicosecond bunch length and several hundred Amperes peak current by means of a photoinjector and a magnetic bunch compressor. Previous diagnostics of the longitudinal bunch dynamics relied on the rf zero-phasing method and measurements of CTR spectra. In order to have a fast and non-intercepting longitudinal diagnostic available, the electro-optic measurement technique has been implemented with its major component, a synchronized 100 fs Ti:Sapphire laser coaligned with the electron beam, already in place as a seed for the FEL. The theoretical temporal resolution for a 100 μm thick ZnTe crystal is limited to about 200 fs and the signal contrast to more than 1%. We present preliminary results of multi-shot scanning measurements and the single-shot diagnostics of the bunch shape as well as its application as a rf-laser jitter monitor.

INTRODUCTION

The DUV-FEL accelerator [1] consists of a photoinjector, four SLAC-type accelerating structures for up to 200 MeV beam energy, a magnetic chicane after the second linac tank compressing the beam to several hundred femtoseconds, and two undulators, a short modulator and NISUS, for self amplified spontaneous emission (SASE) and high gain harmonic generation (HGHG) experiments. The frequency tripled Ti:Sapphire laser for the photo-cathode generates several hundred pC of charge at a repetition rate of up to 10 Hz. A small fraction of the fundamental serves as a seed for the HGHG experiment. The bunch length of the electron beam is regularly determined using a zero-phasing method [2], i.e. accelerating the beam with the last linac tank 90° off crest and measuring the energy spectrum with a magnet spectrometer. However, the observed spikes in the temporal distribution cannot unambiguously be attributed to the time or energy domain with this method. Therefore, as a method based fully in the time domain, an electro-optic detection scheme [3, 4] has been installed, which is nondestructive and provides single-shot measurements to obtain the bunch shape. The induced birefringence in a ZnTe crystal from the Coulomb field of the electron beam is probed with the seed laser, which is synchronized with the electron beam, thus making measure-

ments of both the temporal profile and the timing jitter between electron beam and seed laser available.

ELECTRO-OPTIC DIAGNOSTIC

The experimental set-up is located between the first spectrometer dipole after the accelerator and the modulator magnet of the HGHG experiment, where a temporal and transverse overlap of the electron beam and the seed laser can be established. As shown in Fig. 2, the electron beam bypasses the in-vacuum mirror for the seed laser by using four trim coils. A motor-controlled mount holds both the ZnTe crystal with the out-coupling mirror behind as well as a YAG screen (not shown). Depending on the mount's position, either the ZnTe crystal intercepts the laser with the electron beam passing by, or both the laser and the electron beam can be observed with a CCD camera imaging the YAG crystal. The seed laser and the Coulomb field of the electron beam at the ZnTe-crystal's location are horizontally polarized. For a $\langle 110 \rangle$ -cut crystal with the $[001]$ -axis oriented vertically, the induced phase change is

$$\Delta\varphi = \frac{2\pi n_0^3 r_{41} E_{vac} l}{(1 + \sqrt{\epsilon}) \lambda}, \quad (1)$$

with crystal length $l = 500 \mu\text{m}$, wavelength $\lambda = 800 \text{ nm}$, refractive index $n_0 = 2.853$, dielectric constant $\epsilon = 10.1$, and electro-optic coefficient $r_{41} = 4.04 \text{ pm/V}$. The Coulomb field at distance r is

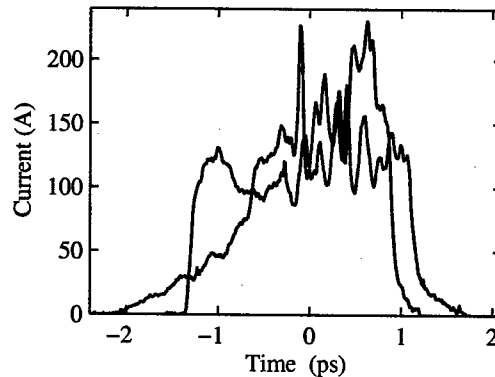


Figure 1: Time profile of the compressed electron beam using zero-phasing method. The two profiles are taken with +90° and -90° phase in the last linac tank.

*loos@bnl.gov

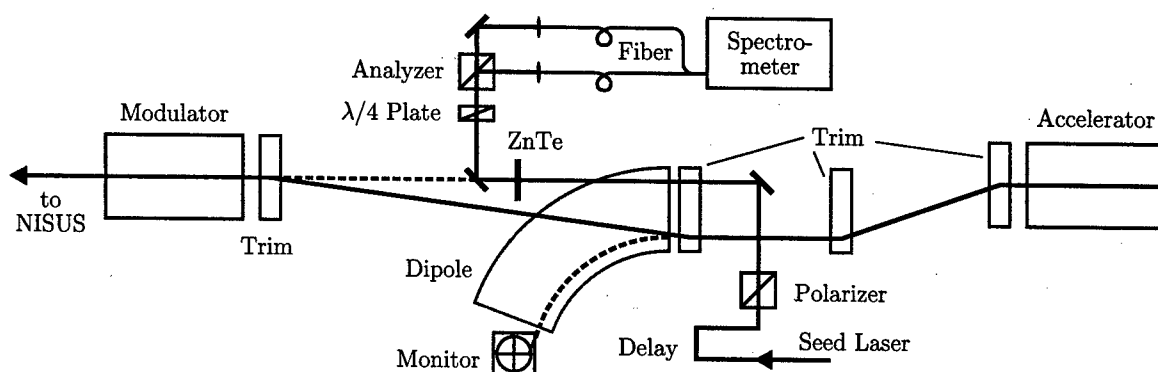


Figure 2: Setup of the electro-optical bunch length measurement placed in the section of the DUV-FEL accelerator between the last accelerating tank on the right and the HGHG modulator on the left.

$$E_{\text{vac}} = \frac{Z_0 I}{2\pi r}, \quad (2)$$

with the time dependent beam current I . The phase change is detected with a $\lambda/4$ plate as compensator and an analyzer cube, whose transmitted and reflected beams are either focused into a pair of photodiodes for the multi-shot experiment or into a pair of fibers and eventually a monochromator with CCD array for the single-shot set-up [5]. With the compensator set to balanced intensities, the asymmetry of the integrated photodiode signals or the spectra becomes

$$A = \frac{S_T - S_R}{S_T + S_R} = \sin(\Delta\varphi + \varphi_0), \quad (3)$$

and φ_0 accounting for any residual birefringence.

SCANNING EXPERIMENT

The accelerator and seed laser were operated at their usual settings for the HGHG experiment with 177 MeV beam energy, a bunch charge of 290 pC, and the seed laser chirped to 5.9 ps (FWHM) for good overlap with the 1 ps long electron bunches. The amplified difference signal of

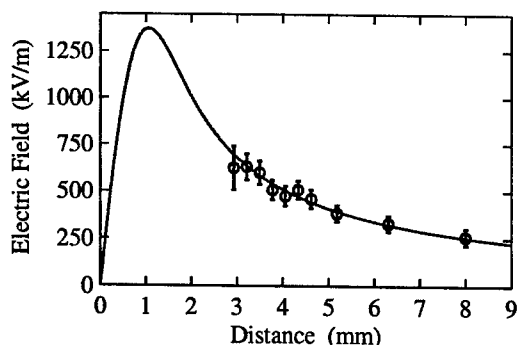


Figure 3: Electric field at maximum temporal overlap for different laser-electron beam distance with theoretical calculation as solid line.

the photodiodes was averaged over 50 bunches for each data point, whereas the sum signal was measured only once. To eliminate electrical noise and background from electrons hitting the crystal, data was also taken with either the seed laser or the electron beam blocked. Figure 3 shows the effective electric field calculated from the signal asymmetry using Eq. (1) for different separations of laser and electron beam. Note that the obtained Coulomb field is reduced, since it is averaged over the much longer laser pulses. The solid curve shows Eq. (2) convoluted with the measured rms beam sizes of 300 μm and 600 μm for electron beam and laser, respectively. To fit the data points, the charge was assumed to be 230 pC, which is not far less than the 290 pC measured in the Faraday cup.

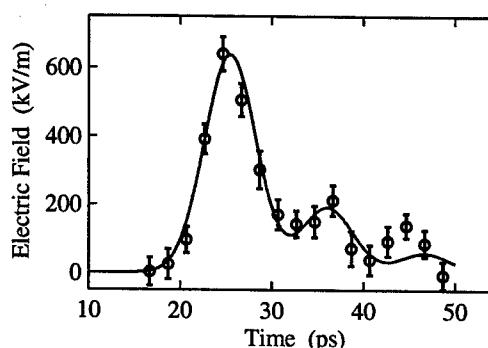


Figure 4: Electric field for different laser-electron beam delay with solid line as theoretical model.

A scan of the seed laser delay relative to the electron beam is shown in Figure 4. The main peak has a FWHM of 6.7 ps which is slightly longer than the laser pulse. The solid curve is a corresponding gaussian distribution with satellites after multiples of 10 ps added, which is the round-trip time of THz waves in the ZnTe crystal. The peak height of the satellites is larger than expected which indicates the presence of trailing wake fields. No electric field ahead of the bunch could be observed.

SINGLE-SHOT EXPERIMENT

The raw spectra, with and without electron beam, from the two multi-mode fibers carrying the transmitted and reflected beams from the analyzer cube, are shown in Fig. 5. Both reference spectra differ significantly from each other and their difference varies with the compensator orientation. This indicates a large wavelength dependent intrinsic birefringence, which partly is stress induced in the ZnTe crystal and partly may originate from a crystalline quartz vacuum window. The static phase is determined from the asymmetry of the reference spectra without electron beam and subtracted from the phase including the electro-optic signal. The resulting current profile using Eqs. (1,2) is shown in Fig. 6 with a delay difference of 1.67 ps between the upper and lower part. The wavelength shift in the signal peak was used to obtain the time calibration to $\eta = (1.25 \pm 0.2) \text{ nm/ps}$ which is close to the chirp in the seed laser of 1.15 nm/ps. The data in the lower part of the figure exhibits the expected single-sided shape of the Coulomb field, whereas each of the data in the upper part contains an additional pre- and post-pulse, which is not yet understood. Therefore, the following discussion only refers to the first set of data.

Considering the temporal resolution of the electro-optic set-up, the rms pulse width of this measurement of $(730 \pm 75) \text{ fs}$ can be compared with the bunch length of $(625 \pm 50) \text{ fs}$ obtained with the zero-phasing method, which has a resolution of tens of femtoseconds. The individual FWHM contributions for the electro-optic method are the intrinsic duration of the Coulomb field in 2.1 mm distance of $\tau_r = r/(\gamma c) = 20 \text{ fs}$, the coherence frequency for the THz waves in the $500 \mu\text{m}$ thick ZnTe crystal of $f_{\text{coh}} = 2.8 \text{ THz}$ which corresponds to a coherence time of $\tau_{\text{coh}} = 210 \text{ fs}$, the resolution due to the chirped detection scheme [5] of $\tau_{\text{BW}} = \sqrt{T\tau_0} = 700 \text{ fs}$ with chirped and unchirped length of $T = 5.2 \text{ ps}$ and $\tau_0 = 130 \text{ fs}$, and the spectrometer resolution $\tau_\lambda = \Delta\lambda/\eta = 190 \text{ fs}$. This combines to a rms reso-

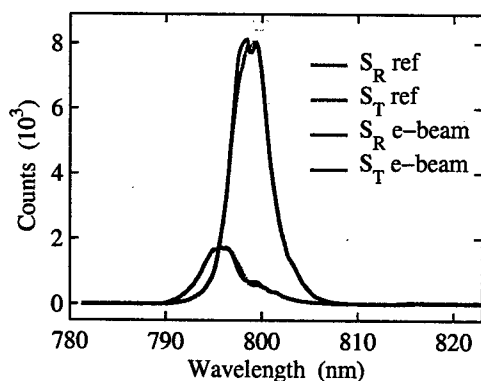


Figure 5: Raw spectra of transmitted (green) and reflected (blue) light. The thick curves are the reference data without beam, the thin curves single-shot spectra with beam.

lution of 320 fs. When applied to the bunch length from the zero-phasing method, this results in an expected rms length of 725 fs for the electro-optic signal, which is within the fluctuations of the actual measured length. The charge can be calculated to $(180 \pm 35) \text{ pC}$ compared to $(290 \pm 15) \text{ pC}$ from the Faraday cup.

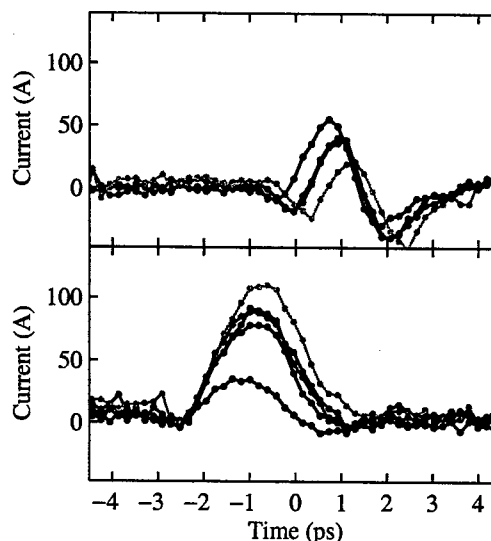


Figure 6: Single-shot electron beam current distribution with 1.67 ps different delay between upper and lower part. The shaded area represents the noise level from spectra without beam.

The single-shot electro-optic method also enables a measurement of the timing jitter between laser and electron beam since the jitter is decoupled from the bunch length. The jitter obtained is 170 fs rms which is of the order of the 200 fs jitter measured between the Ti:Sapphire laser oscillator and the low level RF system.

SUMMARY

A nonintercepting single-shot electro-optic bunch length measurement has been installed at the DUVFEL accelerator and successfully demonstrated results which agree with theory and with results obtained by zero-phasing.

ACKNOWLEDGEMENTS

This work was supported by DOE Contract DEAC No. DE-AC02-98CH10886.

REFERENCES

- [1] W.S. Graves et al., PAC 2001, Chicago, June 2001, p. 2224
- [2] D.X. Wang et al., Phys. Rev. E **57** (1998) 2283
- [3] X. Yan et al., Phys. Rev. Lett. **85** (2000) 3404
- [4] I. Wilke et al., Phys. Rev. Lett. **88** (2002) 124801
- [5] J. Jiang, X.-C. Zhang, IEEE J. Quant. Electr. **36** (2000) 1214

A HIGH DYNAMIC RANGE BEAM POSITION MEASUREMENT SYSTEM FOR ELSA-2

Ph. Guimbal*, P. Balleyguier, D. Deslandes, CEA/DPTA Bruyères-le-Châtel, France
H. Borrión, Electrical and Electronic Engineering Dept., University College, London

Abstract

New beam lines are presently under construction for ELSA, a 18 MeV electron linac located at Bruyères-Le-Châtel. These lines need a beam position measurement system filling the following requirements : small space occupancy, good sensitivity, wide dynamic range (more than 90 dB), high noise immunity, single-bunch/multi-bunch capability. We designed a compact 4-stripline sensor, and an electronic treatment chain based on log-amplifiers. This paper presents the design, cold and hot test results.

INTRODUCTION

The ELSA facility [1] was designed in the late 80's as a test bench for high-power FEL physics and technology. It is now mainly used as a versatile 1-18 MeV electron source or as a picosecond hard X-ray source. In response to this shift in the user's needs, dedicated beamlines are under construction in a new experimental area [2].

In 1988, during design stage, two types of diagnostics were chosen for transverse beam monitoring :

- thin OTR screens (300 nm Al on 8 μ m kapton film)
- button-type or stripline (depending on available space) BPMs

Subsequent ELSA operation showed the limits of these diagnostics :

- OTR screens allow precise measurement of the transverse profile, but are not very sensitive. They were replaced by two-screen systems (like the one described below on fig. 1) with an OTR screen and a scintillator screen (Cr:Al₂O₃ deposited on a thin film).
- the button BPMs (10 mm in diameter capacitive pickups) are not sensitive enough
- the BPM electronic treatment chain is not reliable enough and was specifically designed for FEL operation. Therefore, it can be used only for 14.44 MHz (and 14.44 MHz/n) rep-rate train of bunches.

THE ELSA-2 COMBINED STATION

For these reasons, it was decided to design a new diagnostic station (fig. 1 et 2) with the following constraints:

- all-in-one OTR/scintillator/BPM station to save space and allow easy comparison of OTR and BPM data
- simple design
- high sensitivity BPM

- high dynamic range electronics, compatible with every macropulse structure of the beam, which means any sub-pattern extracted from a 144 MHz train.
- a length equal to a standard 6-way tee (164 mm)

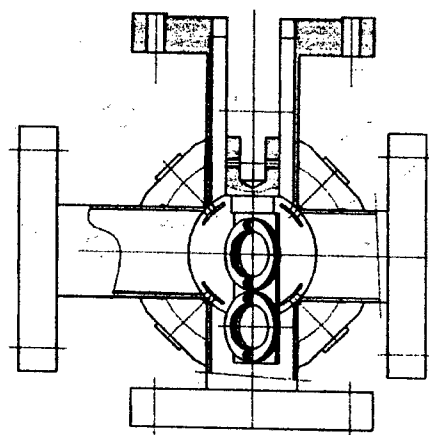


Fig. 1. Schematic drawing of the new diagnostic station combining two screens (OTR and scintillator) and a 4-stripline BPM : transverse view, showing the screens.

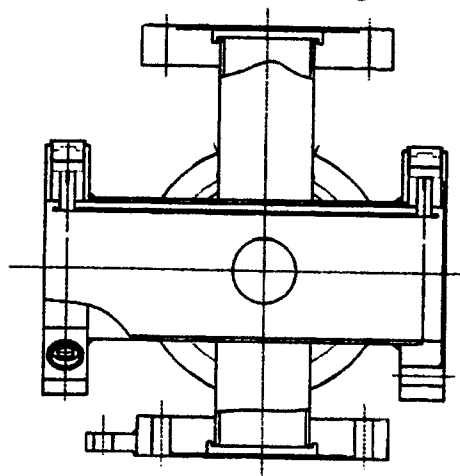


Fig. 2. Longitudinal view, showing the stripline ports.

For the BPM electronics (see details below), we chose a central frequency of 288.89 MHz. The corresponding wavelength (about 1 meter) is much longer than the stripline. In this case, the sensitivity grows with the

*email : philippe.guimbal@cea.fr

stripline length. For that reason, we chose to house the SMA sockets in the flanges. This symmetrical design also offers the opportunity to get a good impedance matching (see figure 3) by putting an external $50\ \Omega$ load at the downstream port.

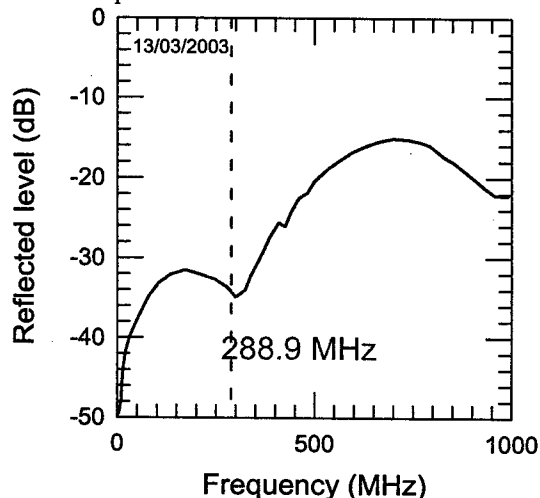


Fig. 3. Measurements show a good impedance matching of the BPM at the working frequency (better than 30 dB return loss).

Compatibility between the screen holder movement and the strips limits the subtended angle of the strips to slightly less than 45° , and imposes their locations at 45° of the horizontal and vertical axis. Numerization and post-processing of the position data will translate these data in the X et Y axis, in accordance with the implementation of the ELSA steerers and quadrupoles.

BPM ELECTRONICS

Because of the wide variety of beam energy, current and transverse dimension and the wide variety of requirements for the realtime bandwidth, numerous schemes have been proposed for BPM electronics in the last decades [3].

Early stage design was strongly influenced by the arrival on market of inexpensive high performance log amplifiers, offering 100 dB dynamic range and 500 MHz input bandwidth.

Our requirements were :

- a macropulse current between 1 and 100 mA
- a position sensitivity of $100\ \mu\text{m}$ (stripline radius $R=27\ \text{mm}$)
- no calibration required after an initial check
- very simple design.

These requirements already imply a dynamic range of more than 80 dB :

- 40 dB for the current range
- 40 dB for the 0.1 mm resolution (to first order : $\Delta/\Sigma=2\ \Delta x/R$)

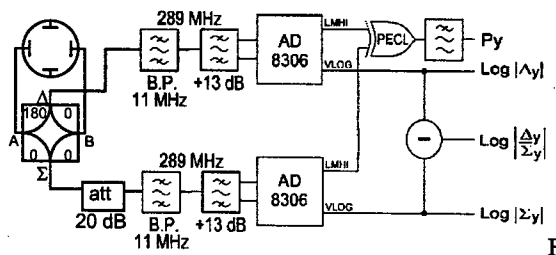


Fig. 4. Scheme of the electronics of one of the two channels of an ELSA-2 BPM.

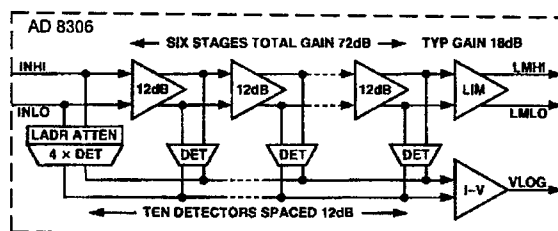


Fig. 5. Functional block diagram of the AD8306 log amplifier (source Analog Devices).

As seen on figure 4, the actual scheme is very simple :

- signals issued from two opposite striplines are carried along two equal-length semi-rigid short cables
- a hybrid Σ/Δ circuit creates the sum and difference, followed by a 20 dB attenuator on Σ channel
- a narrow-band filter at $289 \pm 5\ \text{MHz}$ samples a single harmonic of the signal.
- it is followed by a resonant impedance matching filter for adaptation of the $50\ \Omega$ line to the $1\ \text{k}\Omega$ input of the log amplifier (giving an extra +13 dB gain)
- an AD8306 limiting-logarithmic amplifier (fig. 5) gives two outputs : the logarithm of the envelope with a slope of 20 mV/dB (video bandwidth of 5 MHz) and a limiter output
- $\log(\Delta)$ and $\log(\Sigma)$ signals are treated analogically to extract current and position informations
- limiter outputs of the Δ and Σ channels are phase-compared to tell on which side of the center the beam actually is.

The 4 channels of a BPM are packed on a $70 \times 100\ \text{mm}^2$ electronic board (cf. figure 6) whose design must be very careful from a EMC point of view, not to reduce the dynamic range and log conformance (cross-talk between channels put less constraint than these two points). A box in the accelerator room includes two such circuits (one for each transverse direction). The box is close to the strip line in order to avoid degrading the signal to noise ratio of the Δ/Σ signals.

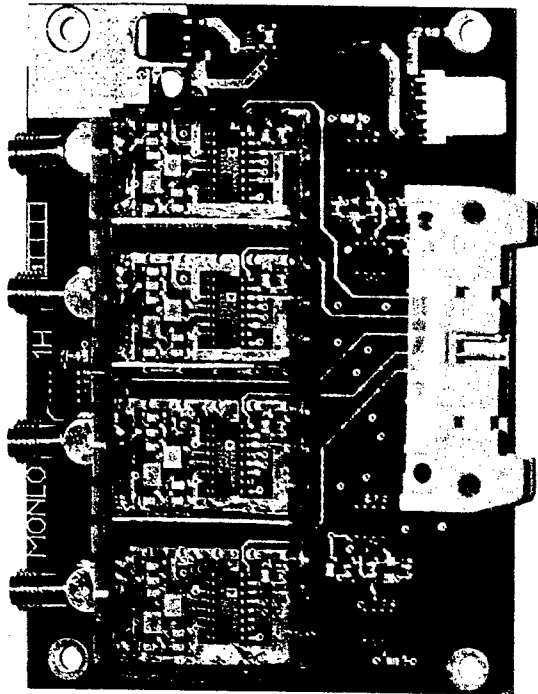


Fig. 6. Top view of the main circuit board

BPM TESTS

Electronic board tests on bench

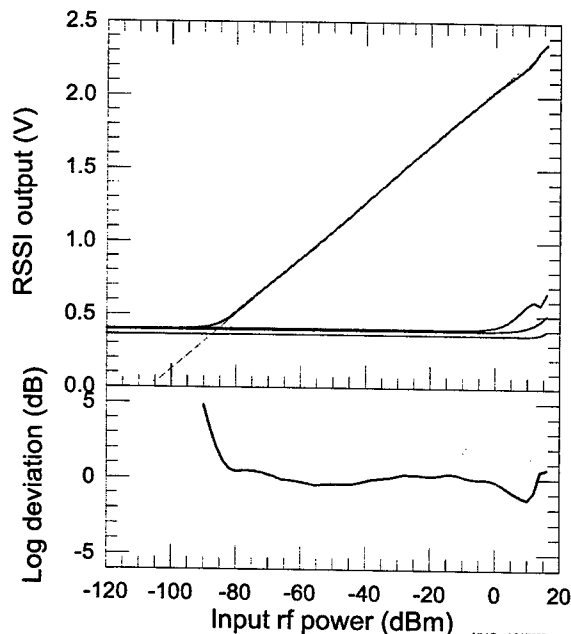


Fig. 7. Log response of the main board.

The slope is 20 dB/m

Measurement of the log output is very close to the AD8306 datasheet. The useful dynamic is more than 95 dB and the log conformance (lower part of fig. 7) shows a

peak-peak deviation slightly above 1 dB on a 80 dB range. Such a performance requires a very high attention paid on the printed circuit layout.

BPM tests on ELSA

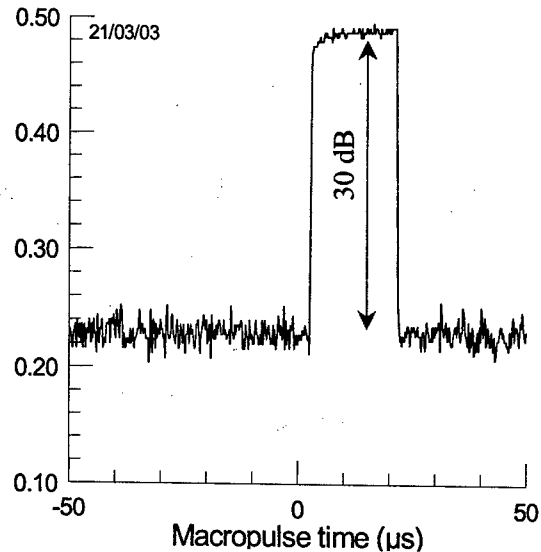


Fig. 8. Response of a Σ channel, on ELSA. The macropulse is 20 μ s long. Vertical scale is in Volts, 10 mV/dB (half the value of the AD8306 slope, because of the 50 Ω termination on scope).

First tests on ELSA (cf. figure 8) showed a BPM sensitivity more than 10 dB above the 1990 stripline design and a minimum current around 0.5 mA for the desired position precision of 0.1 mm, with a real-time bandwidth of 3 MHz.

ACKNOWLEDGMENTS

The authors wish to thank the ELSA team (A. Bayle, A. Binet, A. Bloquet, J.-L. Flament, V. le Flanchec, A. Godefroy and G. Vallart) for their helpful assistance and especially J. Raimbourg, for his contribution to the early design of the system.

REFERENCES

- [1] J.-G. Marmouget, A. Binet, Ph. Guimbal, J.-L. Coacolo, "Present performance of the low emittance high bunch charge ELSA photoinjected linac", EPAC'2002, Paris, June 2002, p. 1795.
- [2] Ph. Guimbal et al., "Status of the ELSA-2 project", EPAC'2002, Paris, June 2002, p. xxxx.
- [3] R.E. Shafer, "Diagnostics for high-brightness beams", Linac'90 proceedings, p. 797

UPGRADES TO THE DIGITAL RECEIVER-BASED LOW-INTENSITY BEAM DIAGNOSTICS FOR CERN AD

M. E. Angoletta, D. Belohrad, L. Bojtar, A. Findlay, M. Ludwig, O. Marquversen[#], F. Pedersen, CERN, Geneva, Switzerland

Abstract

The CERN AD Low-Intensity Beam Multi-Diagnostics (LIMD) has been upgraded as planned since 2001 by adding tune measurements during ramps and plateaus, based on the Beam Transfer Function (BTF) method. This relies on transversally exciting the beam by a deflector and deriving the BTF and coherence function from FFTs of excitation and beam response recorded by digital receivers (DRX). These, continuously tuned to a betatron sideband, pass data to a digital signal processor (DSP) on the DRX board for data processing. The upgrades discussed also include increased longitudinal frequency range, noise reduction measures and digital flags for setup of Data Acquisition (DAQ) and processing parameters.

INTRODUCTION

The Antiproton Decelerator (AD) has been successfully operating for over two years [1]. LIMD [2,3] has been instrumental in the various phases of AD operation. It was recently upgraded to include tune measurement, and to improve its performance by abating parasitic noise from cables and by extending the frequency range covered.

HARDWARE UPGRADES

Figure 1 is a simplified description of the system; many details described in [2,3] are omitted but all the upgrades are indicated. Both NIM and VME crates are located in the AD control room, some distance from the actual Pick-Ups (PU) in the AD Ring Hall. The new components, indicated by a red line, are labelled (a) through (g). The Low Frequency Longitudinal PU (a) (LPULF) expands the detectable frequency range, in conjunction to the original High Frequency PU, LPUHF. The LPULF's response bandwidth is between 0.02 and 3 MHz; its lowest noise level is $2 \text{ pA/Hz}^{1/2}$ in the 0.1-1 MHz range. The outputs of the 2 LPUs are low-pass and high-pass filtered, respectively, and combined by the Summing Unit SU (b) to give a flat frequency response over the (0.02 – 30) MHz bandwidth. Both LPUs are connected to the SU by a 100 m-long, low-attenuation, doubly shielded coaxial cable (c), to minimize parasitic noise. The Cooling Status Unit CSU (d) is an in-house board translating the stochastic/electron cooling voltages into digital values specifying the cooling status (ON/OFF). This information

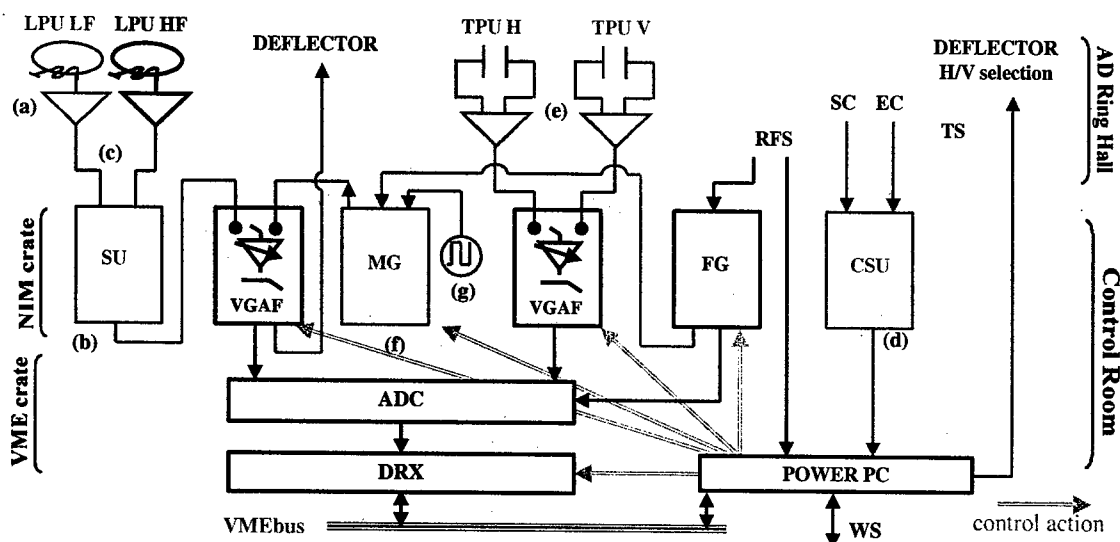


Figure 1: The LIMD system - upgrades are shown in red. Keys: SC – Stochastic Cooling, EC – Electron Cooling, PU – Pick-Up, TPU – Transverse PU, LPU – Longitudinal PU, LF – Low Frequency, HF – High Frequency, TS – Timing System, RFS – Radio Frequency System, SU – Summing Unit, DRX – Digital Receiver Board, VGAF – Variable-Gain Amplifier & Filter, CSU – Cooling Status Unit, MG – M-shaped Noise Generator, FG – Frequency Generator, WS – Workstation.

is used for the proper setup of DAQ and processing parameters by the Real Time Task RTT [2]. The horizontal and vertical (TPUH/V) transversal PUs (e),

[#] Now with TERMA A/S, Radar Systems, 8520 Lystrup, Denmark

now operational, are devoted to tune measurement by the BTF method. They are electrostatic devices, resonant at 5.6 MHz, with a low noise of $1 \text{ pA/Hz}^{1/2}$ between 5.3 and 6.2 MHz [4]. The noise generator MG (f) produces the analogue excitation used for BTF measurements. It is an in-house board that generates an analogue band-limited M-shaped noise signal by filtering the output of a white

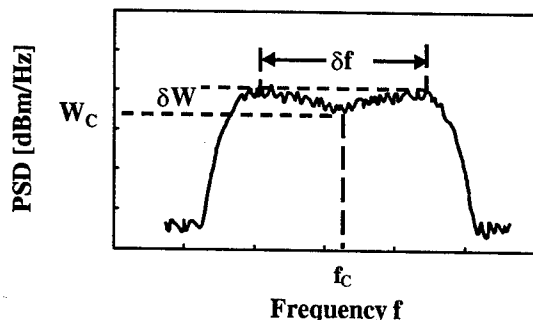


Figure 2: Power Spectral Density PSD vs. frequency f plot for the M-shaped BTF excitation signal. Keys: f_c - central frequency, δf - bandwidth, W_c - central power density level, δW - shoulder height increase.

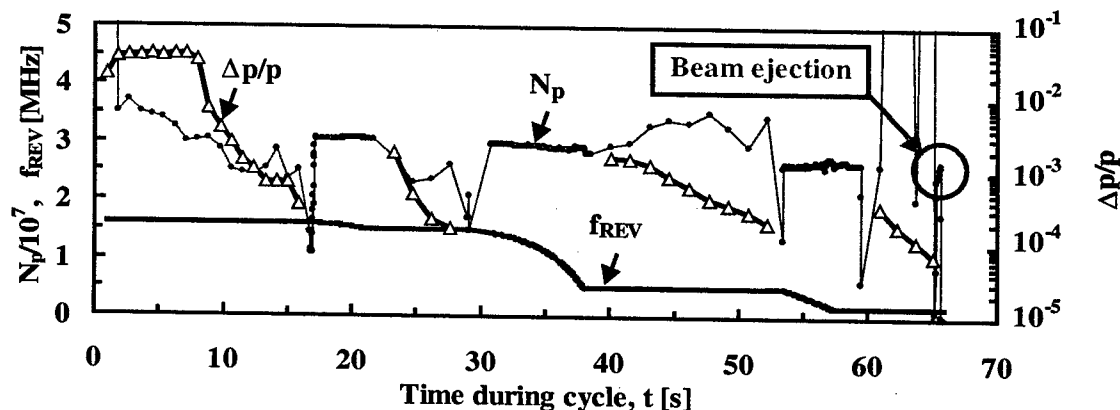


Figure 3: Number of particles, revolution frequency and momentum spread obtained by LIMD during an AD cycle.

noise diode. The board receives as inputs a constant-frequency (f_T) sinewave from a signal generator (g) and the central frequency $f_c = \alpha \cdot f_{REV}$ (Figure 2) from the Frequency Generator FG. Thus f_c tracks the revolution frequency f_{REV} as it varies on the ramps. Actually f_c , a good initial guess of a given betatron frequency (see *BTF Method*), is chosen so as to reside in the TPU low-noise region; typically the $n=4$ harmonic is used in the first ramp. Both α (hence f_c) and the M signal bandwidth δf , as well as the M shoulder height increase δW are user-selected via software. For $\delta f = 0.1 \cdot f_T / (2^m)$, the integer $m = 0, 1 \dots 7$ is user-selected, while δW is varied among -8, -14, -20 and -25 dB. The central power density W_c is constant at -52 dBm/Hz, thus changing δW varies the shoulder height $W_c + \delta W$. The Variable-Gain Amplifier and Filter (VGAF) applies an additional multiplier to the M-shaped noise from MG.

SOFTWARE AND METHODS

Longitudinal DAQ and processing were discussed in [2,3] thus only upgrades are described here; transverse data are detailed for the first time.

Longitudinal Data Software

The RTT running on the PowerPC (Figure 1) has been upgraded to include the readout from the CSU board and the corresponding action. The CSU output is used to adapt the observation window during plateaus to the beam width, which decreases considerably owing to cooling actions (electron/stochastic), thus maintaining sufficient resolution in the computation of the momentum spread $\Delta p/p$ in each plateau. For each plateau, the user can select two different observation windows and the threshold, expressed as percentage of the cooling length, where the window width has to be changed.

Figure 3 plots the number of circulating particles N_p , $\Delta p/p$ and f_{REV} over a whole typical AD cycle. The LPULF upgrade has improved the quality of N_p data while the doubly shielded cabling has lowered the noise level, hence the fluctuations in N_p data during plateaus.

Consequently also $\Delta p/p$ values, that are linked to N_p data, are more reliable. In plateaus three and four between 40 and 65 s of the AD cycle, N_p takes large values; this is an artefact, likely caused by coherent instabilities or noise from RF cavities filtered through the longitudinal BTF. This will be investigated in the upcoming campaign. Finally, the apparently constant $\Delta p/p$ in the first plateau is due to the first observation window bandwidth, which had been left rather large to measure correctly N_p at injection.

Intensity (N_p) Calibration

A particular effort was devoted to the intensity calibration; a crucial task since absolute overall RF gains are difficult to obtain to better than ± 2 dB. The calibration of the intensity, expressed by N_p , is made at ejection against a single pass charge measurement in a calibrated beam transformer recently installed in the ejection line. This approach is convenient since it is always available

during routine operation. The bunched beam intensity measured by LIMD just before ejection (Figure 3) is compared with the extracted beam intensity and is used for calibration assuming a lossless extraction. The calibration factor obtained is used at other f_{REV} on ramps assuming the gains of all elements in the DAQ chain are frequency-independent. This condition is satisfied to ± 0.2 dB from 0.174 MHz to 16 MHz.

LIMD may also be calibrated with protons on 1000-fold higher N_p values, which are measured by a calibrated DC beam current transformer. This is impractical, as it requires complex operations and dedicated machine time; it is therefore scheduled only once, typically at startup.

BTF Method on Transverse Data

At typical AD pbar intensities and low momentum, transverse Schottky signals are too low to produce a useful S/N ratio. The tune is then measured by a variation of the BTF method [5]. Our implementation involves exciting the beam with a band-limited M-shaped noise, by means of a transverse damper deflector, and recording the deflector excitation and the transverse beam response. These are then FFT-processed to yield the tune. In this way it is possible to measure tunes at lower intensities and during the ramps, by keeping the sampling frequency f_s equal to a multiple of f_{REV} . The M-shaped excitation is chosen so as to minimise transverse beam blow-up, by setting f_c very close to a betatron frequency. The beam response is measured by the TPUs, located very close to the beam ejection point and about $3\pi/2$ away (clockwise i.e. for antiprotons) from the transverse deflectors. This method was tested prior to its implementation, on plateaus only; preliminary feasibility results are given in [4]. The LIMD BTF replaces a swept BTF technique that was slow, would only work on plateaus and was only used during the start-up phase.

The user may select up to 10 BTF measurements on a given AD cycle but only one deflector, either horizontal or vertical. The user selects the number of averages the DSP performs, the observation window and its centre via the RTT. This also selects the observation harmonic and sign so that the measurement falls into the low-noise region of the TPU. To avoid exciting unnecessarily the beam, the RTT turns off the excitation when the data acquisition is completed. BTF phase and magnitude, as well as the coherence function are made available to the user, together with PSD of both beam and M noise. The first three contain the information needed to determine the beam tune, which corresponds to the centre of the π phase shift (Figure 4). The coherence function may indicate correlation, or lack of, between excitation and beam response, with a value of 1 for perfect correlation and zero for totally unrelated data. The BTF data are judged acceptable for coherence values close to 1. The TPUH data in Figure 4 are 5 averages of overlapping FFTs at the beginning of the second ramp, with f_{REV} starting at 1.4979 MHz, on the slow wave sideband and 4th harmonic. From a fractional horizontal tune initial guess of 0.45 the measured tune was 0.454. This was a test of the method

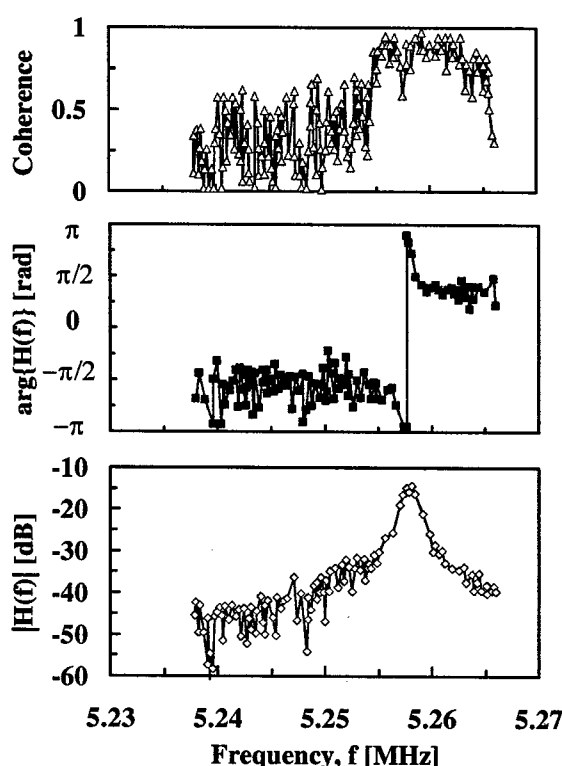


Figure 4: Plot of horizontal BTF phase $\arg\{H(f)\}$, amplitude $|H(f)|$ and coherence function vs. frequency f , showing a π phase shift centred at about 5.25765 MHz.

with a very good initial guess; hence the result is only a small refinement. Poor initial guesses are mastered with larger δf and observation window.

CONCLUSION

LIMD is now ready for full-steam operation. The various diagnostics it includes could be exported to other new systems, for example to Schottky-based diagnostics for CERN's LEIR.

REFERENCES

- [1] P. Belochitskii et al., "Two Years of AD Operation", EPAC'02, Paris, June 2002, p. 317.
- [2] M.E. Angoletta et al., "The New Digital Receiver based System for Antiproton Beam Diagnostics", PAC'01, Chicago, June 2001, p. 2371.
- [3] M.E. Angoletta et al., "Antiproton Beam Parameter Measurement by a New Digital-Receiver-Based System", CERN/PS 2001-016 (BD).
- [4] M.E. Angoletta et al., "Real-time Tune Measurement on the CERN Antiproton Decelerator", DIPAC '01, Grenoble, June 2001.
- [5] J. Borer et al., "Information from Beam Response to Longitudinal and Transverse Excitation", IEEE Trans. Nucl. Sci., NS-26, No. 3, June 1979, p. 3405.

OTR STUDIES FOR THE HIGH CHARGE CTF3 BEAM

E. Bravin and T. Lefèvre, CERN, Geneva, Switzerland
C. Vermare, CEA/DIF, Moronvilliers, France

Abstract

The CTF3 (CLIC Test Facility 3) will produce 1.56μs long intense electron pulses. The unbunched 5.4A beam of the injector will have a transverse beam size ~1mm. After the buncher the current is reduced to 3.5A and the transverse size varies between a few hundred micrometers and one millimetre along the length of the linac. Calculations indicate that these beam parameters will impose an unbearable thermal load for the intercepting screens currently in use (scintillators and aluminium OTR foils). Graphite and SiC have been investigated as possible alternative materials for the OTR radiators. The possibility of replacing scintillating screens with OTR targets at the low energies of the injector has also been considered. A possible limitation in the use of such high temperature radiators has been identified; ions released from the heated target could focus further the beam with the risk of damaging the target itself and/or blowing up the beam. This would also affect the emittance measurement and would hinder any effort to detect head-tail phenomena. This paper gives the results of the theoretical estimations, and of the beam-based experiments.

INTRODUCTION

During the last two decades the use of intense electron beams has been developed, especially for Free Electron Laser studies [1] and X-ray radiography [2]. With current densities of the order of tens of kA/cm² the beam impact destroys or damages any intercepting devices used for beam diagnostics or as Bremsstrahlung X-ray sources. Moreover an instability caused by the interaction of the primary electrons beam with positive ions released by the target when heated up, has been observed [3]. This process has been identified as a time dependant effect that modifies the electron beam size at the location of the target within the beam pulse duration [4].

The CTF3 facility in the nominal phase will produce intense beams [5], 1.56μs long at a repetition rate of 50Hz. The injector delivers a 5.4A average current, which is then reduced to 3.5A after the buncher. Several beam-monitoring devices are foreseen, distributed along the accelerator at 140keV, 20MeV, 60MeV and 180MeV. With beam sizes varying from few millimetres to few hundred of micrometers, the current density can be as high as few kA/cm². The screens will suffer thermal related problems and the measurements will be potentially affected by this ions instability. Concerning beam diagnostics, our main concern is to provide a system, which is robust enough to stand the induced thermal load, and to allow quantitative measurements.

In this paper, thermal calculations are first presented with the aim of determining which material can be used for the CTF3 OTR radiators. Some simulations are performed with the LSP code, developed by Mission Research Corporation [6], in order to estimate the impact of the ion instability on the CTF3 beam. The third part is dedicated to OTR [7] and Black body photon intensities calculations to investigate the light yield of these two processes.

THERMAL ANALYSIS

Assuming an electron beam with a Gaussian spatial distribution, the time evolution of the target temperature can be calculated solving the following equation [8]

$$\frac{\Delta T(r,t)}{\Delta t} = \frac{1}{c_p \rho} \left[\frac{dE}{dx} \rho_e \frac{r^2}{2\sigma^2} N(t) - k \nabla^2 T(r,t) - \frac{2\epsilon\sigma_s}{\delta} (T(r,t)^4 - T_0^4) \right]$$

With σ the electron beam size and $N(t)$ the particle flux. The target is characterized by the thickness δ , emissivity ϵ , specific heat c_p , density ρ and thermal conductivity k . T_0 is the room temperature and σ_s the Stefan-Boltzmann constant. The first term in brackets contains the stopping power, dE/dx , representing the electron energy deposition [9] and is responsible for the heating of the material. The target is cooled by thermal conduction (second term) and Black Body (BB) radiation emitted from the radiator surface (third term).

Electrons traversing matter loose energy by collision (ionization) and by radiation (Bremsstrahlung). If the target is sufficiently thin (~tens of microns), the Bremsstrahlung photons are not re-absorbed by the radiator and then do not contribute to the energy deposition process. For high energies particles, it represents a large fraction of the total energy loss [9]. The collision stopping power does not change sensibly from one material to the other (factor 2 between tungsten and graphite). For electron energies between 100keV and 360MeV, it only changes by a factor less than 2. In the following calculations, the target is supposed to be thin enough (10μm) to neglect the radiative stopping power and to reduce the collision energy deposition, which is much higher for low energies (<100keV). The key parameter for the heat of the screen is the specific heat of the material. An example of the temporal behaviour of the target temperature is displayed on figure 1, considering the interaction of a 140keV, 5.4A, 1mm beam size electron beam and a graphite target ($\epsilon = 0.7$). This calculation assumes a cooled-radiator, which external temperature is kept at 20°C.

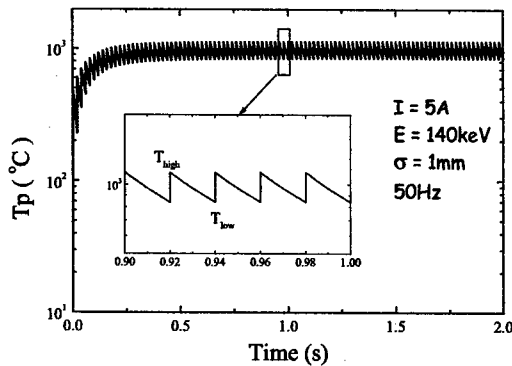


Figure 1: Graphite target temperature versus time

Due to the pulsed nature of the beam (50Hz, 1.56μs) the temperature after a short transition period (~200ms) will cycle between two values here defined as T_{high} and T_{low} , corresponding to the temperatures attained just after and just before the electron pulses as shown in figure 1. In this example, the target is 10μm thick and its temperature oscillates between 778°C and 1003°C. By reducing the repetition rate to 10Hz, T_{high} and T_{low} become respectively, 440°C and 106°C.

The power evacuated via Black Body radiation is given by the Stefan-Boltzmann law:

$$P = 2\pi\sigma^2 \epsilon \sigma_s T^4$$

and it represents only a small contribution to the total thermal balance of the target. In the case represented in figure 1, it amounts to only 65mW compared to the 2.88W deposited by the beam (50Hz). This effect makes the cooling between pulses faster but is almost irrelevant on the maximum temperature attained by the radiator. The cooling by BB radiation would have a more significant effect if using much thinner foils (<μm) in order to minimize the beam energy deposition.

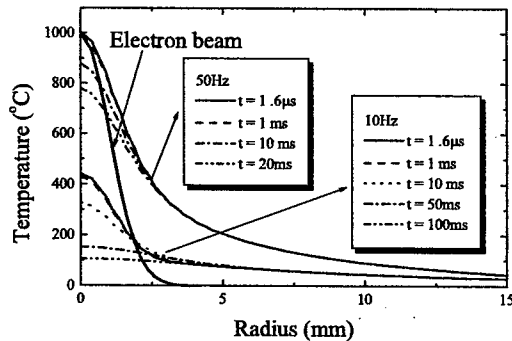


Figure 2: Temperature profile as a function of the radial position at different times in the cycle

On figure 2 the different curves illustrate the time evolution of the temperature profile of the target. Heat exchange is negligible within the pulse duration (μs). The cooling has just started 1ms after the beam pulse

(considering graphite), and 10ms later the temperature in the centre has decreased by 15%. Choosing a high thermal conductivity material allows a faster radial cooling of the target.

Good candidates will have a high fusion temperature, a high specific heat and a high thermal conductivity. The characteristics of the material considered in this analysis are summarized in table 1. On CTF3, even if the beam is focused to a σ equal to 250μm, supposed to be the lower limit, a graphite target can stand the full thermal load reaching temperatures of the order of 2250°C. Beryllium would be slightly better but its use is discouraged due to costs and difficulties of machining.

Table 1: Material characteristics

Material	c_p (J/gK)	K (W/mK)	T_{fusion} (°C)
Be	1.825	190	1287
C	0.7-2.8	140	3527
Al	0.9	235	660
Si	0.7	150	1414
Ti	0.523	22	1668
Mo	0.25	139	2623
W	0.13	170	3422

ION INSTABILITY

The effect of target-emitted ions on the propagation of the electron beam is sketched on figure 3.

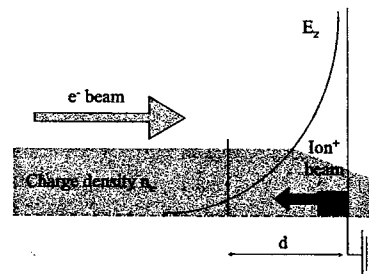


Figure 3: Effect of target emitted ions from the target

Molecules are released from the target by gas desorption of hydrocarbon surface contaminants or water when the material is heated. Ions are produced by direct electron impact ionization with a cross section of the order of 0.1\AA^2 , depending on the electron energy and the nature of the molecule. These ions are then accelerated by the beam space charge potential and propagate along the electrons in the opposite direction. The electric field can be as high as 10MeV/m. This positive ion column partially neutralizes the electron beam charge and modifies the propagation of the primary electrons left with their auto-focusing magnetic force.

Simulations with the code LSP [6] have been done to estimate how important this effect will be. The parameters of the simulation are adjusted, based on the results of recent studies [10]. Two kinds of ions are considered, H^+ 9% and OH^+ 91%. In the simulations, ions are emitted right at the beginning of the pulse. In reality it was shown

that to fit the experimental data, ions should be released after the time needed to heat the target to 400°C. An example of the time evolution of the beam size on the target in the case of the CTF3 injector is shown in figure 5.

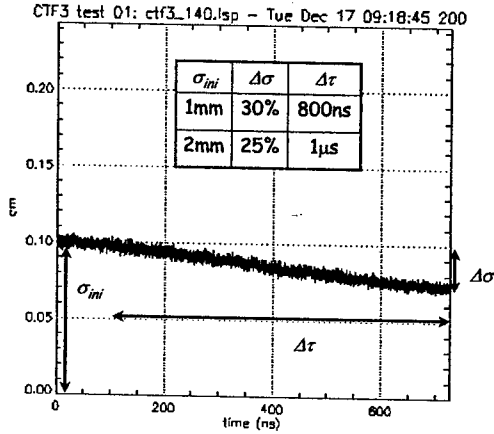


Figure 5: Time evolution of the R.M.S beam size

At 140keV, the beam is continuously focused during the pulse duration. A diminution $\Delta\sigma$ of 30% is expected within 800ns considering nominal conditions. The results summarizes in the table in figure 5 indicate that the smaller the initial beam size (σ_{ini}), the stronger and the sooner the focusing takes place. At 20 MeV, $\Delta\sigma$ is small (< 5% over 1μs) and for electrons of higher energies the effect becomes negligible.

OTR VERSUS BLACK-BODY RADIATION

The CTF3 beam profile monitors are based on the backward OTR emission from a graphite screen. The number of OTR photons emitted by an electron in the wavelength range $[\lambda_a, \lambda_b]$ is given by [7]:

$$N_{OTR} = \frac{2\alpha}{\pi} \left[\left(\beta + \frac{1}{\beta} \right) \cdot \ln \left(\frac{1+\beta}{1-\beta} \right) - 2 \right] \ln \left(\frac{\lambda_b}{\lambda_a} \right)$$

N_{OTR} increases with the beam energy. For non relativistic particles, it is roughly proportional to β^2 , and for high energy particles it behaves like $\ln(2\gamma)$. Moreover the OTR angular distribution [7] can be represented by a cone with a $1/\gamma$ aperture with γ the relativistic factor of the electrons. In consequence, taking into account that the optical system has a finite collection angle ($\sim 1.26 \cdot 10^{-3}$ Sr), only a small part of the OTR light cone would be collected for low energy particles. This calculation must also consider that thermal resistant radiators, like graphite, have low reflectivity (27%) compared to perfect (mirror-like) OTR screens, limiting by the same amount the light intensity produced in the backward OTR.

The number of Black body photons emitted per second in the wavelength range $[\lambda_a, \lambda_b]$ and in 2π sr is given by:

$$N_{BB} = \int_{\lambda_a}^{\lambda_b} \frac{2\pi}{\lambda^4} \frac{2\pi\sigma^2\epsilon}{e^{kT/\lambda} - 1} d\lambda$$

with k the Boltzmann constant, h the Planck constant, and c the speed of light. Thermal calculations have shown that within 10ms the temperature has decreased by 15%. At the same time N_{BB} emitted in the visible range [300, 900] nm has drop by at least one order of magnitude, so that we have considered that the BB photons are emitted only during the first 10ms.

At 140keV, with a typical beam size of 1mm, the maximum temperature is 1003°C. In these conditions $5.3 \cdot 10^8$ N_{BB} photons are collected by our optical system. This value has to be compared with the $1.7 \cdot 10^8$ OTR photons expected in the same conditions.

At 20MeV and for higher energies along the linac, the beam size could be as small as 250μm. The temperature increases up to 2250°C, emitting $6.8 \cdot 10^{11}$ BB photons. The number of OTR photons sent onto the camera will increase significantly with the beam energy. N_{OTR} would be $8.4 \cdot 10^{10}$ at 20MeV, $2.6 \cdot 10^{12}$ at 60MeV and $2.1 \cdot 10^{13}$ at 180MeV.

CONCLUSIONS

The thermal analysis presented in this paper shows that thin foil of graphite must be used as OTR radiator for the CTF3 beam profile monitor.

Simulations with LSP indicate that the ion instability has only a significant effect on 140keV electrons. Even if the beam is over-focused by 30%, there is no risk of damaging the graphite target. Possible cures of this effect are envisaged by direct beam conditioning or laser surface cleaning. Targets will be prepared using a high temperature treatment for outgasing.

At low energy BB radiation is a source of light as intense as OTR. The light spectrum is however quite different. Most of the BB photons are emitted in the red part of the visible range and can be easily suppressed using a blue filter or by gating the camera.

By lowering the repetition rate of the machine to 10Hz, the temperature of the screen can be effectively reduced, eliminating the ion instability and reducing the BB radiation by at least three orders of magnitude depending on the beam parameters.

REFERENCES

- [1] T. Lefevre *et al*, Phys. Rev. Letters 84, (2000), 1188.
- [2] E. Merle *et al*, Proceeding of the of the European Particle Accelerator Conference, Paris, 2649, (2002).
- [3] C. Vermare *et al*, IEEE Trans. Plasma Sci. 27, 1501, (1999).
- [4] D.R. Welch and T.P. Hughes, Laser Particles Beams 16, 285, (1998).
- [5] G. Geschonke *et al*, CERN/PS 2002-008, (2002)
- [6] For more details, see <http://www.mrcabq.com/Services/Particle/index.htm>
- [7] L. Wartski, Thesis, Orsay, (1976).
- [8] E. Bravin, CTF3 note 019, (2001).
- [9] See <http://physics.nist.gov/PhysRefData/contents.html>
- [10] C. Vermare *et al*, Phys. of Plasmas 10, 277, (2003).

MEASUREMENT OF BEAM POSITION USING HIGHLY-DAMPED ACCELERATING STRUCTURES

J. Prochnow, RWTH Aachen, Germany / CERN, Geneva, Switzerland
E. Jensen, W. Wuensch, CERN

Abstract

Active alignment algorithms for linear colliders such as the Compact Linear Collider (CLIC), require measurements of beam positions inside accelerating structures in order to control short and long-range transverse wakefields. Highly-damped accelerating structures offer the possibility that damping waveguides can provide position signals so the accelerating structure itself can be used to make these position measurements. A demonstration of beam position measurement using a 3 GHz slotted iris structure with a dipole mode $Q \approx 16$ was made in CTF II (CLIC Test Facility) and results are compared to computations using HFSS and GdfidL.

INTRODUCTION

The development of multi-bunch accelerating structure for the CLIC main linac is driven to a large extent by strict constraints placed on the long- and short-range wakefields. Beam dynamics simulations have shown that to minimise emittance blow-up along the linac, the amplitude of the transverse wakefield must decrease by two orders of magnitude in the time between bunches in the train. The solution adopted for CLIC structures to achieve this wakefield suppression includes strong damping accomplished via four waveguides coupled to every cell.

The position of the beam inside the structure can be determined from the power in these waveguides generated by the excitation of the lowest order dipole mode in the structure. For this mode, the induced voltage is proportional to transverse beam position and charge. A measurement of the mode's excitation can be used as input to active alignment systems and wakefield minimisation algorithms [1].

The use of heavily damped accelerating structures as beam position monitors has been demonstrated in the experiments described in this report. They also provide benchmarks for the theoretical models developed to describe the coupling of a beam to a heavily damped periodic structure [2]. A confirmation of the simulations by the measurement also gives confidence in the wakefield simulations which were done with the same techniques. The experiment is thus complementary to a direct wakefield measurement such as at ASSET [3]. It is an extension of the ideas presented in [4, 5, 6, 7].

The structure used in the experiment was a 3 GHz Slotted Iris Constant Aperture (SICA) accelerating structure. In both the CLIC main beam accelerating structures [8] and the CTF3 drive beam accelerating structures, SICA [9], damping is achieved by coupling waveguides but the waveguides have a different topology. In the SICA accelerating structure damping is achieved by four slots in ev-

ery iris which extend to double ridged waveguides which are terminated by individual SiC loads. The lowest dipole mode of the SICA has a maximum in the coupling to the beam at 4.3 GHz and a quality factor of about 16. The beam position dependency of this dipole mode was studied experimentally by exciting the structure with the 4 ps, 0.5 nC probe beam of the CTF II [10].

SETUP

The SICA accelerating structure used in this experiment was manufactured for high power tests and consists of four damped and two coupler cells. A drawing of the exploded structure is shown in Fig. 1. In order to measure the dipole mode excitation, the SiC load of one damping waveguide was replaced by an impedance matched transition to coaxial cable to which the read-out electronics was connected. The simulated spectrum of the signal in the damping waveguide shows a resonance with a frequency of 4.25 GHz and a half power width of 205 MHz corresponding to a quality factor of 21. The transition was designed with HFSS to have a better impedance match than the SiC load over four times the bandwidth of the dipole signal. The dipole mode excitation in the two coupling cells was sensed by waveguide directional couplers installed between power couplers and loads that terminated the waveguides. The power couplers and the damping waveguide sense the same polarisation of the dipole mode. A photo of the in-

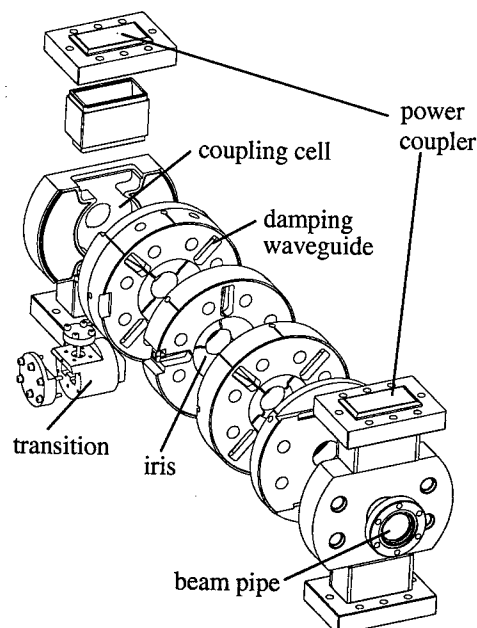


Figure 1: The SICA accelerating structure prototype.

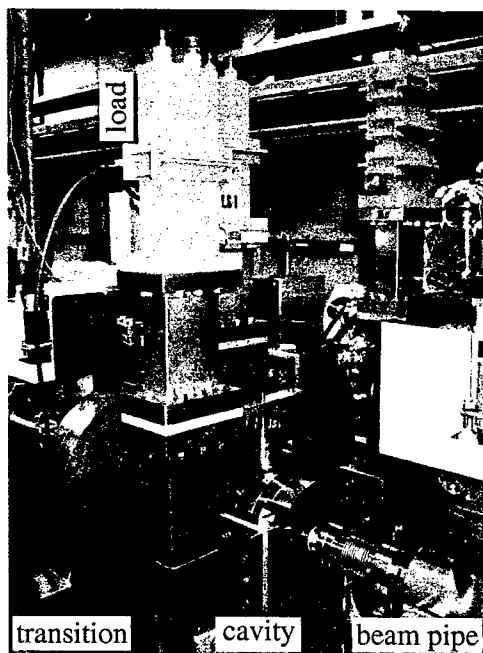


Figure 2: Photography of the accelerating structure installed in the CTF II.

stallation in the CTF II is shown in Fig. 2.

As the cells are so strongly damped (35.9 dB per cell for the lowest dipole mode), the modes do not extend over the whole structure. Therefore measuring the dipole mode at three locations (the two power couplers and one damping waveguide) provided independent position measurements, allowing beam position jitter and measurement resolution to be distinguished. The signals from the two couplers and the damping waveguide were normalised for beam charge variations by a wall current monitor signal.

The beam position dependency of the dipole mode was studied by transversely displacing the beam with a dipole magnet located 1.205 m upstream of the accelerating structure.

MEASUREMENTS

The first measurement was to study the properties of the signal from the damping waveguide in time and frequency domain. The measured time domain signal at the transition from the damping waveguide for a beam offset of 2 mm is shown in Fig. 3. The fast decay of the signal within a few nanoseconds confirms that the damping works well. The Fourier transformation of the signal is shown in the right plot of Fig. 4. The shape of this spectrum was confirmed by measurements with a spectrum analyser. The spectrum shows the dipole mode signal resonance at 4.41 GHz and a second peak at 3.6 GHz caused by the cutoff frequency of the damping waveguide. The whole spectrum was found to be position dependent as expected. The dashed lines are fits with a resonance curve. A quality factor of 33 was found for the dipole mode signal.

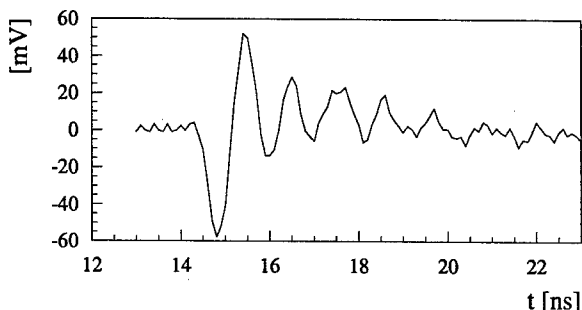


Figure 3: Measured time domain signal from the damping waveguide after mixing with a 3.498 GHz local oscillator.

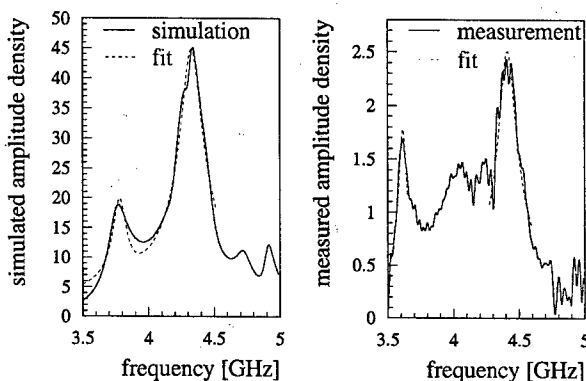


Figure 4: The spectrum of the signal from the damping waveguides after the transition as it was simulated with HFSS (left) and as it was measured (right).

This signal and the ones from the couplers were low pass filtered and mixed down to a DC - 1.5 GHz baseband. The local oscillator signal (3.498 GHz) was generated from the CTF II master clock (249.877 MHz) so that the signals' phase was maintained during the mixing. The wall current monitor and the three intermediate frequency position signals were displayed on a four channel, 3 GHz bandwidth oscilloscope with a sample rate of 10 GS/s. The scope was triggered on the CTF II master clock.

The second measurement was to study the beam position dependency of the signal. The real and imaginary part of the excitation signal both linearly depend on beam position [11]. Fits to these two linear functions provide the parameters for the hyperbolic and arctangent relations of the signal's amplitude and phase respectively. Amplitude and phase of the signal are plotted as a function of beam position in Fig. 5. The representation of the signal in the complex plane is shown in Fig. 6. The error bars equal the r.m.s. value of 100 successive measurements. The measurement is in good agreement with the theoretical curves. The solid curves are hyperbolic and arctangent fits, the dashed curves are the curves derived from the linear fits to the real and imaginary parts. The advantage of the latter is that the parameters of the two linear fits are orthogonal. A mean r.m.s. of $5.7 \mu\text{m}$ was found. Fig. 5 shows that the beam position dependency of the amplitude in the centre of the cavity is weak, however, the beam position information is

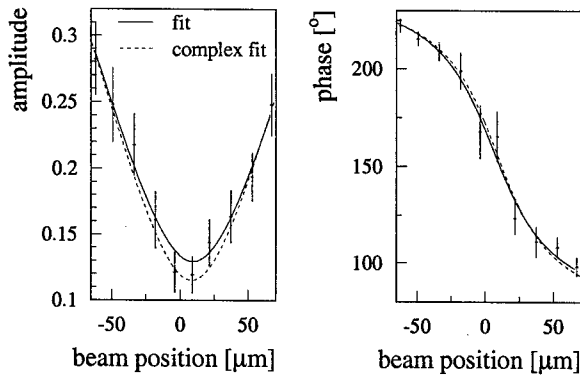


Figure 5: Amplitude (left) and phase (right) of the signal from the damping waveguide as a function of beam position.

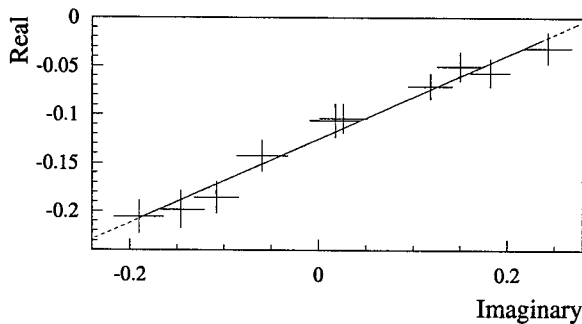


Figure 6: The same data as in Fig. 5 plotted in the complex plane.

contained in the phase which has a strong beam position dependency around the centre.

The same analysis was performed on the signal from the coupler cells. The variations of the beam position signal for unchanged corrector magnet currents have two sources: firstly, the beam position of the CTF II probe beam is known to jitter due to imperfections in the flash-lamp pumped laser which drives the photo-injector. Secondly, there is a noise on the beam position measurements. The coefficient of determination indicates the proportion of variance in one variable explained from knowledge of the second variable. For 100 successive measurements where the beam position signal varied with an r.m.s. of $6\text{ }\mu\text{m}$, the coefficient of determination between the signal from the damping waveguide and from one coupler cell equals 18 %. This means that 18 % of the signal variation are due to real beam position jitter and the rest is caused by limitations of the experiment. Such limitations are likely to be caused by the electronics that was not sufficiently shielded against signals from the CTF II accelerator.

SIMULATIONS

In preparation for the experiment the response of the structure to the excitation with a short bunch was studied with HFSS [12] and GdfidL [13]. The beam leaves a certain voltage in the cavity which results in a certain power in the damping waveguides. In the HFSS simulation, this was

reversed: Power at different frequencies was fed into the structure via the damping waveguide and the voltage calculated by path-integration of the electric field along the particle trajectory. The ratio of the squared voltage and the power provides the impedance as a function of frequency. This spectrum of the signal in the coaxial cable of the transition is shown in the left plot of Fig. 4. The complex sum of two resonance curves was fitted to the spectrum. For the dipole mode signal a resonance frequency of 4.33 GHz and a quality factor of 26.0 was found. The relative deviation of these values compared to the measurements are 1.8 % for the resonance frequency and 24 % for the quality factor.

The GdfidL program calculates the fields in time domain. The spectrum is derived as the Fourier transformation of this signal and was found to agree very well with the result found by HFSS simulations.

More details can be found in [14].

ACKNOWLEDGEMENTS

The authors would like to express their gratitude to the people who aided in practical work and fruitful discussions, especially Claude Achard, Albrecht Böhm, Hans Braun, Nicolas Chritin, Steffen Döbert, Steve Hutchins, Sylvain Leblanc, Erminio Rugo, Ian Wilson.

REFERENCES

- [1] N. Leros, D. Schulte, "Static Beam-Based Alignment of the RF Structures in the CLIC Main Linac", EPAC 2002.
- [2] J.-Y. Raguin et al., "A New Technique to compute Long-Range Wakefields in Accelerating Structures", EPAC 2002.
- [3] C. Adolphsen et al., "An Asset Test of the CLIC Accelerating Structure", CERN/PS 2000-044 (RF), EPAC 2000.
- [4] W. Schnell, "Common-mode rejection in resonant microwave position monitors for linear colliders", CLIC Note 70.
- [5] T. Slaton, G. Mazaheri and T. Shintake, "Development of nanometer resolution C-band radio frequency beam position monitors in the final focus test beam", LINAC 1998.
- [6] V. Balakin et al., "Experimental Results from a Microwave Cavity Beam Position Monitor", PAC 1999.
- [7] C. Adolphsen et al., "Wakefield and Beam Centering Measurements of a Damped and Detuned X-Band Accelerator Structure", PAC 1999.
- [8] J.Y. Raguin et al., "A new damped and tapered Accelerating Structure for CLIC", LINAC 2002.
- [9] E. Jensen, "CTF3 Drive Beam Accelerating Structures", LINAC 2002.
- [10] H.H. Braun, "Achievements and Future Plans of CLIC Test Facilities", HEACC 2001.
- [11] J.P.H. Sladen, W. Wuensch, "Measurement of the Precision of a CLIC Beam Position Monitor", CLIC Note 189.
- [12] <http://www.ansoft.com>
- [13] W. Bruns, H. Büssing, "GdfidL on Clusters of Workstations", EPAC 2002, pp.1619.
- [14] J. Prochnow, "Beam Position Measurement at CLIC", PhD Thesis, to be published, RWTH Aachen, Germany (2003).

CAVITY MODE RELATED WIRE BREAKING OF THE SPS WIRE SCANNERS AND LOSS MEASUREMENTS OF WIRE MATERIALS

F. Roncarolo, CERN/University of Lausanne, Switzerland

F. Caspers, B. Dehning, E. Jensen, J. Koopman, J.F. Malo, CERN, Geneva, Switzerland

Abstract

During the SPS high intensity run 2002 with LHC type beam, the breaking of several of the carbon wires in the wire scanners has been observed in their parking position. The observation of large changes in the wire resistivity and thermionic electron emission clearly indicated strong RF heating that was depending on the bunch length. A subsequent analysis in the laboratory, simulating the beam by two probe antennas or by a powered stretched wire, showed two main problems:

- i) the housing of the wire scanner acts as a cavity with a mode spectrum starting around 350 MHz and high impedance values around 700 MHz;
- ii) the carbon wire used so far appears to be an excellent RF absorber and thus dissipates a significant part of the beam-induced power.

Different wire materials are compared with the classical cavity mode technique for the determination of the complex permittivity in the range of 2-4 GHz. As a resonator a rectangular TE_{01n} type device is utilized.

WIRES HEATING IN THE SPS TUNNEL

During the two last Machine Development periods in the SPS 2002 run, several wires were found broken. Such breaking can be typically related to the wire heating due to some energy deposition by the traversing protons on the wire. Dedicated electronics has been installed in order to have an indication of the wires heating during the LHC type beam injection and ramp in the SPS. In particular a constant current was supplied to the wire and the voltage drop across it was fed to a digital scope together with the difference between the input and output currents. The differential current ($I_{out} - I_{in}$) grow up is due to the wire heating and consequent emission of electrons for thermionic effect. Fig. 1 shows such voltage and differential current evolutions during the SPS cycle with LHC type beam. No scans were performed along this cycle. It is thus evident that the wire heating does not depend on the direct wire-beam interaction.

In particular it is possible to relate the wire heating to the beam intensity (two batches of 72 bunches with $1.1 \cdot 10^{11}$ p/bunch injected in this case) and to the bunch length which is decreasing along the beam ramp to 450 GeV.

The measurements described in the previous section clearly revealed that the bunch length shortening causes a larger wire heating than the beam intensity. Such observations lead the study of possible RF coupling effects between the wire scanner wires and the proton beam travelling inside the wire scanner tank which is acting as a cavity.

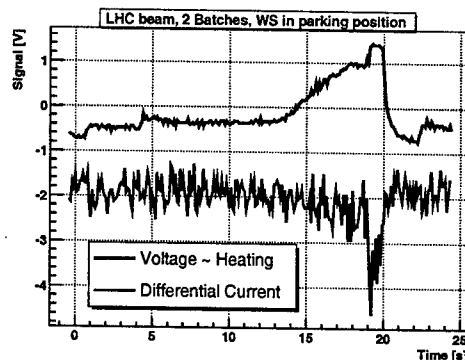


Figure 1: Wire heating due to the LHC beam injection in the SPS (No scan, wire in parking position). The beam energy ramp/bunch length decreasing begin $t=11$ s.

The proton beam circulating in the ring has a frequency spectrum which mainly depends on the bunching structure (bunch length, bunch spacing). The build up of standing waves resonating inside the tank depends on the geometry and the tank materials. If one or more of the modes matches a beam spectral line, a rather large amount of RF power can be transmitted from the beam to the wires.

These hypotheses have been investigated through dedicated laboratory measurements.

LABORATORY MEASUREMENTS

A spare SPS wire scanner tank has been equipped in the laboratory with two probe antennas connected to a Vector Network Analyzer (VNA) in order to simulate the RF modes in the beam spectrum frequency.

Beam-Wire coupling

Two connections to the ends of the wires of the wire scanner are used during normal operation to check the wire integrity (measuring the resistance) or to detect the secondary emission signal. In the laboratory they were applied to estimate the proton beam-wire coupling while simulating the beam with a stretched wire. A $0^\circ/180^\circ$ RF signal combiner circuit has been used to measure the differential signal at the wire ends. One port of the VNA has been connected to one end of the stretched wire, the other one at the combiner output giving the differential signal. Fig. 2 is well describing the effect. The plot gives the S_{21} signal together with the differential signal on the wire scanner wire. Where the frequency peak of the transmitted signal matches a peak of the differential signal, the power present in the cavity can be absorbed by the wire.

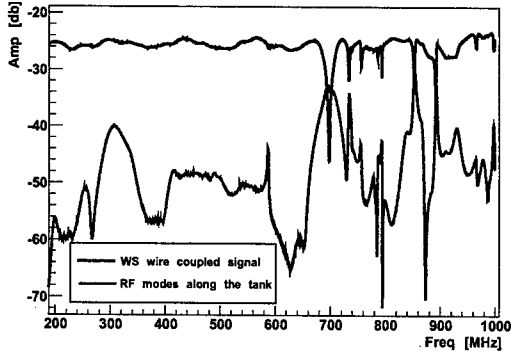


Figure 2: Beam-Wire Scanner coupling

Different configurations have been set up in order to better understand the phenomenon:

- of the wires mounted on the forks, without ferrite tiles inserted
- one copper and one carbon wires mounted and kept in the parking position, without ferrite tiles
- two carbon wires mounted and kept in the parking position, without ferrite tiles
- two carbon wires mounted, the horizontal wire kept in the parking position and the vertical wire in proximity of the beam position, without ferrite tiles
- two carbon wires mounted, the horizontal wire kept in the proximity of the beam position and the vertical wire in the parking position, without ferrite tiles
- none of the wires mounted, nine ferrite tiles inserted in the tank
- one carbon wire mounted, nine ferrite tiles inserted in the tank
- two carbon wire mounted, nine ferrite tiles inserted in the tank

For each measurement the Q factor has been evaluated by mean of the VNA, zooming in the resonance interval. For each resonance the antenna-probes position has been adjusted in order to reach the condition of weak coupling (S_{11} and S_{22} signals minimized to $< .5$ dB) thus allowing the evaluation of the unloaded Q . Fig. 3 shows two of the recorded signals, one with no wires mounted and no ferrite tiles inserted and one with no wires installed and nine ferrite tiles inserted. Fig. 4 summarizes all the quality factors as function of frequency, for all the measurement configurations.

The RF modes damping by inserting the ferrite tiles is evident and suggested such configuration to reduce the power absorbed by the wire scanners wires. The ferrite properties can be found in [2].

WIRE MATERIALS STUDIES

The classical cavity mode technique has been used for the determination of the complex permittivity of different wires in the range from 2-4 GHz. As a resonator a rectangular TE_{01n} type device is utilized. Different materials

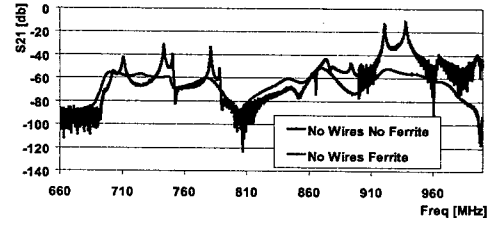
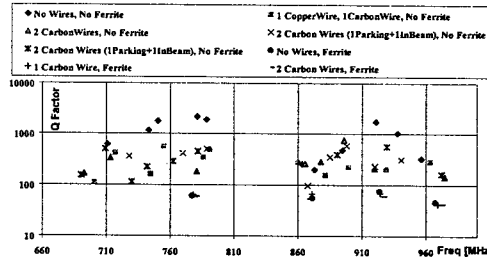


Figure 3: Transmitted signal from one end of the tank to the other using the antenna-probes method


 Figure 4: Unloaded Q factors for all the measurements setups as function of frequency

such as silicon carbide (SiC), carbon and quartz fibers were examined. SiC fibers are an interesting alternative to carbon fibers and their properties had to be investigated, since SiC bulk material is often used as a microwave absorber. The complex permeability can be expressed as

$$\vec{\epsilon} = \epsilon_0 \vec{\epsilon}_r = \epsilon_0 (\epsilon'_r - j\epsilon''_r) \quad (1)$$

from where the loss factor can be defined:

$$\tan \delta_e = \frac{\epsilon''_r}{\epsilon'_r} \quad (2)$$

In the test cavity there are locations, in which either the electric or the magnetic field vanishes. If one puts a sufficiently small sample, which does not disturb the field, in these locations only the magnetic or electric properties of the cavity are influenced by the sample. In both cases the resonance frequency f_r and the quality factor Q are changed. ϵ''_r , ϵ'_r and $\tan \delta_e$ respectively can be found from these changes. [1] provides:

$$\frac{\Delta \vec{f}_r}{\vec{f}_r} = -\frac{\Delta \vec{W}}{\vec{W}} \quad (3)$$

The variables in this equation are complex. $\text{Im}(\vec{f}_r)$ and $\text{Im}(\vec{W})$ describe the losses in the empty cavity, and given the high Q they will be neglected in the following. If the sample is non-magnetic and positioned in a zero-magnetic-field region, which is our case, then \vec{W} and $\Delta \vec{W}$ in Eq. (3) are only calculated from the electrical fields:

$$\frac{\Delta \vec{f}_r}{\vec{f}_r} = \frac{\vec{f}_{r_s} - \vec{f}_{r_e}}{\vec{f}_{r_e}} = \frac{-\epsilon_0 \int_{V_s} (\vec{\epsilon}_r - 1) E(x, \vec{y}, z)_e E(x, \vec{y}, z)_s * dV}{2\epsilon_0 \int_{V_r} E_e^2 dV} \quad (4)$$

The subscripts e and s indicate the empty cavity and the cavity with sample, whilst V_s and V_r are the volumes of the sample and of the resonator. When the electric field is tangential to the surface of the sample and the sample ends on the resonator walls, then the internal field equals the external field:

$$E_e = E_s \quad (5)$$

Given a small volume of the sample:

$$\vec{E}_e(x, y, z) = \vec{E}_{e0} \quad (6)$$

and can be pulled out from the integrals of Eq. (4). The imaginary part of the resonant frequency shift is related to the change in quality factor:

$$\text{Im}(\Delta f_r) = \Delta f_r'' = \frac{f_r}{2} \left[\frac{1}{Q_{Ls}} - \frac{1}{Q_{Le}} \right] \quad (7)$$

Eq. (4) to Eq. (7) lead to the evaluation of the real and imaginary part of the dielectric constant:

$$\epsilon_r' = 1 - \frac{f_{rs} - f_{re}}{f_{re}} \frac{V_r}{2V_s} \quad (8)$$

$$\epsilon_r'' = \left[\frac{Q_{Le}}{Q_{Ls}} - 1 \right] \frac{1}{Q_{Le}} \frac{V_r}{4V_s} \quad (9)$$

and therefore to the characteristic loss factor as defined in Eq. (2). ϵ_r'' can also be deduced from the material conductivity σ and the resonant frequency f according to:

$$\sigma = \omega \epsilon'' = 2\pi f \epsilon'' = 2\pi f \epsilon_0 \epsilon_r'' \quad (10)$$

Experimental Results

In the laboratory fibers of three different materials were considered: Carbon, Silicon Carbide and Quartz. Fig. 5 shows the measurements results as signal intensity versus frequency, around one of the resonating modes with maximum electric field at the sample location. The plot qualitatively proves the RF power absorption of Carbon, and the non-absorption of Silicon Carbide and Quartz. Fig. 5 also includes the results of a numeric simulation and measurement concerning the SiC material which is presently considered as a suitable RF absorber for the Compact Linear Collider (CLIC). A pyramid shaped piece of such material was inserted in the resonator at the same location where the wire scanner wires were placed. The fact that this material is absorbing RF power as shown by the simulation and by the measurements, proved that this is a SiC compound different from the one used for the wire scanners wires.

The insertion of one carbon fiber ($d=36 \mu\text{m}$) is reducing the signal amplitude to a level where the mode frequency is not well defined since the resonance curve is strongly asymmetric. Therefore, for this material, we could not apply Eq. (8). The imaginary part of the dielectric constant was evaluated both from Eq. (9) and Eq. (10). The insertion of 500 SiC fibers ($d=15 \mu\text{m}$) allowed the evaluation of both the real and imaginary part of the dielectric constant by mean of Eq. (8) and Eq. (9). The results for the

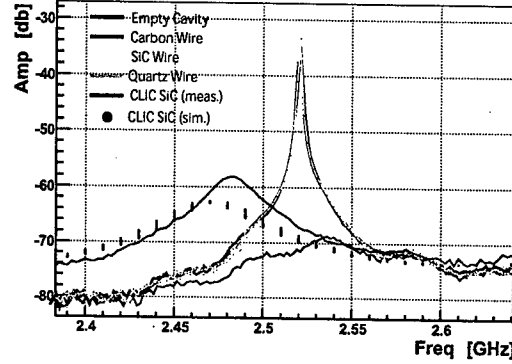


Figure 5: Resonant cavity signal in presence of Carbon, Silicon Carbide and Quartz

TE_{103} are summarized in the table below, together with the available data for the CLIC SiC bulk material [3]. Being Quartz a weakly absorbing material, in order to evaluate ϵ' and ϵ'' one should insert a large number of fibers as it has been done for SiC. However not enough Quartz material was available.

Table 1: Real and imaginary part of the dielectric constant for the TE_{103} mode, at 2.5 GHz.

	ϵ_r'	ϵ_r''
C		
SiC	10.790 ± 0.016	$2.30 \pm 0.05 \cdot 10^5$
SiC (CLIC)	14.4	6.6

CONCLUSIONS

The laboratory measurements investigated the RF coupling nature responsible for the wire breaking in the SPS wire scanners. The wire scanners tanks proved to act as resonant RF cavities in the beam spectrum frequency range. As a cure for the wire heating due to the beam-wire coupling, the SPS wire scanner tanks have been equipped with low outgassing ferrite tiles in order to damp the resonance modes. Carbon, used in the SPS until 2003, provided evidence of RF absorption properties. Therefore the wire material of few monitors were changed from carbon to silicon carbide, which has been characterized as a weakly absorbing material, and will be tested during the 2003 SPS run.

ACKNOWLEDGMENTS

We thank G.Burtin for the useful discussions.

REFERENCES

- [1] E.Nyfors, P.Vainikainen, *Industrial microwave sensors*, Artech House (1989)
- [2] E.Campisi, R.Doolittle, *Proceedings of the Workshop on Microwave-Absorbing Materials for Accelerators* (p.169), Newport News, Virginia, US (1993)
- [3] M.Luong, *Private communication*, CEA-CEN-Saclay, 91191 Gif sur Yvette, France

SYSTEM LEVEL IMPLEMENTATION OF BEAM POSITION MONITORS WITH LOCAL DATA PROCESSING CAPABILITY FOR THE CORNELL ELECTRON STORAGE RING*

M.A. Palmer[†], J.A. Dobbins, B.Y. Rock, C.R. Strohman, Cornell University, Ithaca, NY 14853, USA
J.R. Moffitt, College of Wooster, Wooster, OH 44691, USA

Abstract

We describe the architecture and system-level implementation of a bunch-by-bunch beam position monitoring system for the Cornell Electron Storage Ring (CESR). With this system an individual readout module is supplied for each detector. Each readout module is equipped with its own digital signal processor (DSP) which provides automatic gain and timing control for the acquisition of signals corresponding to particular bunches in the ring. The DSPs also provide local data processing for applications such as multi-turn averaged position information, betatron phase measurements, and bunch-by-bunch tune measurements.

INTRODUCTION

An upgraded beam position monitoring (BPM) system, with bunch-by-bunch readout capability, has recently been installed in one sector of CESR. Electron and positron beams in CESR occupy the same beam pipe and are electrostatically separated into different *pretzel* closed orbits so that collisions occur at a single interaction point. Typical operation is with 9 trains of 4 or 5 bunches in each beam and with a bunch spacing of 14 ns within each train. In order to perform the necessary timing and gain control functions to probe individual bunches at each BPM location, each module is equipped with its own DSP. The presence of the DSP also allows us to perform a number of high level monitoring functions in the readout modules.

Figure 1 illustrates how the BPM modules are connected to the CESR Control System [1] and Timing System [2]. A brief description of operation and performance issues pertinent to the BPM system is presented here.

CONTROL SYSTEM INTERFACE

All command and data transfers to or from a BPM module are initiated from programs running on one of the high-level OpenVMS Alpha Workstations. Data is only moved when it is requested; it cannot be independently pushed up from a BPM module. A program constructs a request packet in the MPM (Multi-Port Memory) system which specifies the desired BPM and either the source (when writing) or the destination (when reading) of the data. Up to 256 32-bit words can be transferred per request. The request packet identity is passed off to the appropriate XBUS processor. The XBUS is a proprietary fieldbus, which transfers data in a byte-serial format (*i.e.*, it is a byte-wide parallel bus with multiple bytes per data transfer).

The XBUS processors are I/O computers which transfer data between the MPM and the accelerator hardware, in this case a BPM module. The XBUS processor receives the request packet and looks up the address of the BPM module. The address specifies the crate and card slot of an SXIO (SERIAL XBUS I/O) card, the channel on the SXIO card where the BPM module is connected, and a register on that channel. BPM modules are connected to SXIO cards with a 1-bit, half-duplex, serial connection. The SERIAL XBUS protocol requires two 16-bit data transfers, of approximately 25 μ sec each, to move each 32-bit data word to or from the DSP. This translates to a 10K word/sec bandwidth limit which is the impetus to place as much data processing capability as possible within the BPM modules.

TIMING SYSTEM INTERFACE

Figure 1 also illustrates how the BPM modules are connected to the CESR precision timing system. An interface card in the timing system distributes a 24 MHz TTL clock signal by way of several coaxial distribution cables around the accelerator. Near each BPM module is a timing cable tap designed to minimize any impedance discontinuity on the coax cable. The circuitry inside each tap converts the TTL clock signal into an LVDS signal which is sent to the BPM module on a twisted-pair cable.

The timing system interface card encodes several pieces of data on the clock signal by means of pulse-width variations. The rising edges of the clocks occur every 42 ns (24 MHz). A data bit of *zero* is encoded by having the falling edge occur 14 ns after the rising edge. A data bit of *one* has the falling edge occurring 28 ns after the rising edge. To keep the DC content of the clock signal constant and to allow for synchronization and error checking, each bit of data is sent normally in one clock period and its complement in the next clock period.

The revolution time of CESR is about 2.56 μ sec. This is equal to 61 periods of the 24 MHz clock. These 61 periods provide for 30.5 bits of data. The first 2.5 bits are used for synchronization and as a turn marker. These bits are encoded as the *illegal* binary data stream of 11101 in 5 clock cycles. Upon receipt of this stream, a turn marker is generated for use by the internal timing system of the BPM module and the remaining 28 bits of BPM data are latched in a register. The first 18 bits are broken into 9 bits of horizontal and 9 bits of vertical shaker phase data. These phase "words" allow betatron phase measurements to be made with the system (see below). The next 8 bits are used as a system-wide command byte for the BPM system. This byte allows us to synchronize operations of all the BPM modules. Typically a control system program will sequen-

* Work supported by the National Science Foundation

[†] map36@cornell.edu

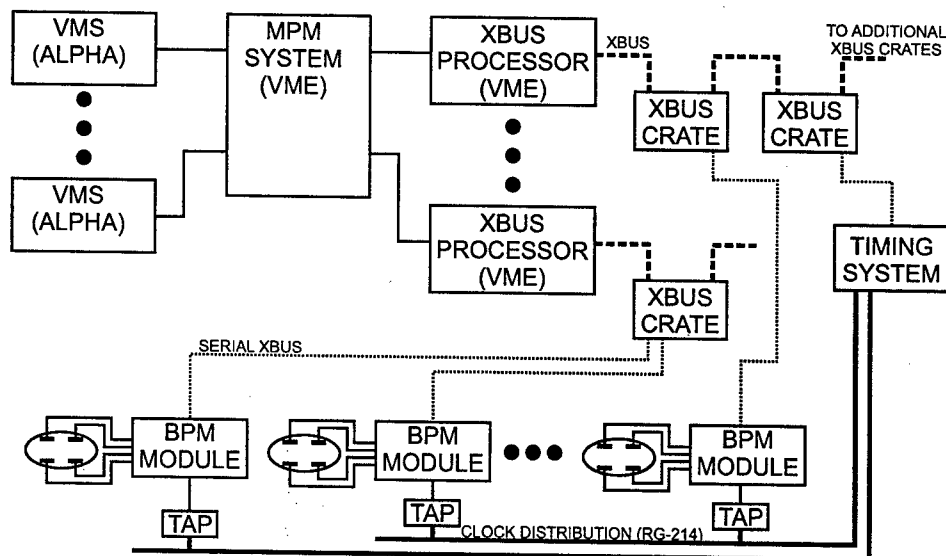


Figure 1: Diagram of the interface between the CESR control system, timing system, and the new BPM system.

tially prepare each BPM module for a measurement, specifying parameters like which bunch to measure and how many turns of data to average. When all of the modules have been programmed, a single command word will be sent on the clock signal. All of the modules will then begin making measurements simultaneously. Due to constraints in the timing system, the command word can be changed at a maximum rate of 60 Hz. The final 2 bits contain hardware trigger information which allows us to synchronize all of the BPM modules to external events. Transitions on the trigger lines are encoded on the clock signal for the next turn so the response to hardware triggers can be very fast. The BPM modules can be configured to take action on individual trigger signals, or on a combination of the pair. To date we have used a 60 Hz line trigger to synchronize measurement with the AC power system and the CESR injection trigger to study transients during injection.

DSP INTERFACE

The front ends of each BPM readout module have been described in detail elsewhere [3]. The digital portion of each module is built around an Analog Devices ADSP-21061 SHARC DSP and an Altera EPF10K30A PLD. The DSP provides 128 KB of memory of which we use 64 KB for code and 64 KB for data storage. A persistent copy of the DSP code is stored in a FLASH memory and is loaded into DSP memory upon reboot. An extensive suite of functions have been programmed for the DSP. These functions fall into four general categories: diagnostic, data acquisition, calibration, and data processing.

The Altera PLD provides the logic for the SERIAL XBUS interface, manages the communications bus on the digital board, decodes the timing system signal, and can reprogram the FLASH memory of the SHARC DSP. An important aspect of having the PLD handle both XBUS communications and the on-board bus is that this allows

the control system to probe the DSP memory irrespective of what state the DSP is in.

DSP Function Suite

The core of the DSP functionality is provided by a set of low level data acquisition routines. These routines set the global timing delay for the readout module to look at a particular bunch, set relative delays between button channels so that each channel digitizes at the peak of the button signal, set each digitally controlled channel gain to optimize the signal levels on each channel, and finally acquire the ADC readings from all four buttons upon request. Considerable flexibility is built into the way in which the ADC data is collected and processed. First, the start of data-taking can be configured to begin at a specified turns delay after any combination of our two hardware trigger bits. A set of data samples, up to our buffer limit of 1024, can then be collected on successive turns or with a specified number of skipped turns between samples. The resulting ADC values for each button can then be stored as is or they can have pedestals subtracted and gain conversions applied before being saved into the data buffer.

In order to obtain the timing information for 90 individual bunches at each BPM location and provide automatic gain control for a large range of signal sizes, an extensive suite of calibration routines is provided in each DSP. Timing calibration begins by putting a single bunch in CESR. Each module then scans its timing offsets until it finds a signal of the correct polarity to within 1 ns. Once the bunch has been located, the known bunch pattern in CESR is used to determine timing offsets for every bunch of that species and these timing offsets are saved to an initialization file. When taking data on specified bunches, a second, more precise timing calibration takes place. A precision calibration algorithm adjusts the overall delay for the module in steps of 17.5 ps. Independent timing delays for each channel, also with 17.5 ps step size, are then scanned and a fit is

carried out to determine the peak of each channel's waveform. Based on this fit each channel's operating delay is then set. The signal waveform from each button is such that timing variations at the 10 ps level lead to a position uncertainty at the few μm level. An additional calibration feature is automatic gain control for each channel on each module. Because bunch currents range from the 100 nA to 10 mA scale in CESR, each module must be able to set its gain level accordingly. In addition, because CESR operates with electrostatically separated beams, the gain control function must be separate for each channel in order to optimize signal-to-noise. The automatic gain control and timing delay calibration functions are tightly coupled because of variations in propagation delay in the variable gain amplifier used in this system.

A number of data-taking options are supported by our DSP code. These include acquiring turn-by-turn data for particular bunches directly, processing turns data in the DSP to provide averaged position and current information for one or more bunches, taking betatron phase measurements, and FFT processing of turns data to provide transverse tune information for specific bunches. In each case a *high-level* DSP routine exists which knows what setup parameters are needed from the control system program and which manages the data acquisition and data processing steps in the DSP.

An example of an application requiring turn-by-turn data is the study of injection transients. The BPM modules start data acquisition a fixed number of turns after a hardware injection trigger. Typically we acquire a full 1024 turn sample for each trigger. Our readout modules are capable of monitoring injected bunches at the 100 nA level.

Averaged position data is used for orbit monitoring and differential trajectory measurements. In this mode, the DSP can cycle through a set of requested bunches, average up to 1024 turns of data for each, and make the resulting mean and RMS information available to the control system. For every turn of data acquired, approximately 2.6 turns are required for on-board processing. This corresponds to a 100 Hz bunch sampling rate for 1024 turn samples.

Betatron phase measurements [4] are made at each detector using the phase information from the horizontal and vertical shakers as encoded on the timing system clock signal. Every BPM module receives new data on every turn. However, due to propagation delays and beam direction, there may be a difference of several turns between when a shaken bunch arrives at a beam detector and when the phase data arrives and is decoded from the clock signal. A calibration procedure was developed which allows us to specify the number of turns of offset between detector data and phase data at each BPM module. Accumulating phase information for 40,000 turns provides a measurement with a few tenths of a degree resolution every 2 seconds.

Good frequency resolution for bunch-by-bunch tune measurements requires a large number of position samples in memory simultaneously. By restricting ourselves to measurements in a single plane and using 16 keywords of

data memory, the DSPs can accumulate 8192 turns of data, calculate either the horizontal or vertical position at each sample time, and then perform an FFT on the data using an *in place* algorithm [5]. The resulting frequency resolution for each bunch is better than 50 Hz.

Monitoring of DSP Memory

In order to monitor operation of the large number of independent processors in this system, we have configured our hardware and software to allow an image of key portions of the memory of each DSP to be maintained in the control system program that services the entire system. To do this, equivalent data structures are defined in both the DSP and control system code. These data structures contain DSP configuration and calibration information, working data, and processed output. Transfer of the data structures between the DSP and the control system is facilitated by a pair of lookup tables for use by the Altera PLD. One table contains the starting DSP address of each structure and the other table contains the size of the structure. These tables are initialized by the DSP code when it starts up. Thus for the control system to access a DSP data structure, it simply has to specify the structure's *tag* (*ie.*, its index in the lookup table) and the entire data structure can be passed as a unit via one or more XBUS packet transfers. On the control system side, a key is maintained for each data structure on each DSP. This key contains the DSP tag for that structure, a set of pointers to the control system copy of each data member, a type specification for each data member, a set of pointers to conversion functions for each, as well as various other supporting pieces of information (*eg.*, read-write permissions). The data conversion functions allow proper handling of complex data types as well translation between IEEE and VMS floating point formats.

CONCLUSION

We have described the system-level implementation of a general-purpose BPM readout system. The system is presently in active use in one sector of the CESR ring and we are continuing to explore and develop its capabilities. We would like to thank the members of the CESR Operations Group for their support in its development.

REFERENCES

- [1] C.R. Strohman and S.B. Peck, "Architecture and Performance of the New CESR Control System", Proc. of the 1989 IEEE Part. Accel. Conf., p.1687.
- [2] R.E. Meller, "Precision Timing Control System", Proc. of the 1997 IEEE Part. Accel. Conf., p.2505.
- [3] M. Palmer *et al.*, "An Upgrade for the Beam Position Monitoring System at the Cornell Electron Storage Ring", Proc. of the 2001 IEEE Part. Accel. Conf., p.1360.
- [4] D. Sagan *et al.*, Phys. Rev. ST Accel. Beams 3 092801(2000).
- [5] Numerical Recipes, W. H. Press *et al.*, Cambridge University Press, 2nd Ed. (1992)

DESIGN OF OTR BEAM PROFILE MONITORS FOR THE TESLA TEST FACILITY, PHASE 2 (TTF2)

K. Honkavaara*, A. Brenger, R. Fischer, D. Nölle, K. Rehlich, DESY, 22603 Hamburg, Germany
L. Cacciotti, M. Castellano, G. DiPirro, M. Raparelli, R. Sorchetti, INFN-LNF, 00044 Frascati, Italy
L. Catani, A. Cianchi, INFN-Roma 2, 00133 Roma, Italy

Abstract

The TESLA Test Facility is being extended to an electron beam energy of 1 GeV to drive a new Free Electron Laser facility. 24 beam profile monitors based on optical transition radiation (OTR) will be used along the linac. Their design is a challenging task, since the system has to measure transverse electron beam sizes from millimeter scale down to 50 μm with a high resolution. This paper describes the design of the beam imaging system, the readout system as well as the mechanical construction.

INTRODUCTION

The TESLA Test Facility (TTF), Phase 1 [1] operated at DESY until November 2002 to perform various tests and experiments related to the TESLA linear collider project [2] as well as to serve as a Free Electron Laser [3, 4]. Presently TTF is being extended to a new Free Electron Laser facility (TTF2-FEL) [5]. In the first stage, five accelerating modules having eight 9-cell superconducting TESLA cavities each are installed, later two more modules can be added. Electron beam energies up to 1 GeV can be achieved. A sketch of the TTF2 linac is shown in Fig. 1.

The requirements for beam profile diagnostics are demanding. Beam profile monitors have to measure transverse electron beam sizes from millimeter scale down to 50 μm (sigma) with a high resolution. These monitors will be based on the use of the visible part of the transition radiation spectrum, i.e. the optical transition radiation (OTR), providing a fast single shot measurement with a linear response. OTR was already used at TTF1 for beam transport optimization and beam characterization [6]. However, in order to meet the more strict requirements of TTF2, several improvements to the old monitor system have been made. The OTR beam profile monitor system is realized, as at TTF1, mainly by INFN-LNF and INFN-Roma 2, in collaboration with DESY.

OTR MONITORS AT TTF2

Totally 27 beam profile monitors will be installed along the TTF2 Linac (Fig. 1). Most of them (24) are equipped with an OTR screen, three monitors in the RF-gun section have Ce:YAG screens. Eight of the OTR monitors are combined with a wire scanner.

*katja.honkavaara@desy.de

Profile monitors have multiple tasks. They provide on-line beam images and profiles to optimize the beam transport through the linac. They are also used for the characterization of the beam: measurements of the transverse beam shape and size, emittance measurements using both the quadrupole scan and the four screen methods, as well as energy spread measurements in dispersive sections. The resolution of the monitor has to be sufficient to measure beam sizes down to 50 μm . In addition the system has to be robust, remote controlled, and have a possibility to change the magnification of the imaging optics and the attenuation of the OTR signal. Furthermore, because TTF2-FEL will serve as a user facility, reliability is an important aspect.

OTR monitors are based on measuring backward optical transition radiation emitted by a screen inserted into the beam with an angle of 45° with respect to the beam direction. A sketch of the monitor is shown in Fig. 2, and the different components are described below. OTR monitors in the bunch compressors have a special design, and they are not discussed in this paper.

VACUUM CHAMBER AND MOVER

A standard OTR vacuum chamber is a 7-way cross having three view ports. Fused silica (DUV-200) is used at the OTR output window because of its radiation hardness and good transmittance at the visible wavelengths. The opposite port is used for alignment purposes and has a normal glass window. The third view port is a small glass window at 45° with respect to the beam direction allowing to illuminate the screen from the front.

Eight of the monitors are combined with a wire scanner providing complementary measurements of the beam profile. Both devices are mounted into the same vacuum chamber. Ideally the screen and the wire should be in the same longitudinal position, but in order to avoid an accidental collision between them, they are separated in the beam direction by 25 mm. In order to have space to the wire scanner actuator, the opposite view port is lacking in these chambers.

An OTR screen is inserted into the beam by a stepper motor actuator. This mover is similar to the movers used at TTF1, but some mechanical parts are redesigned to improve its stability. The moving range is 100 mm, and the absolute screen position is read out by a potentiometer. For compatibility reasons, the motor driver is the same as used for other stepper motors at TTF2.

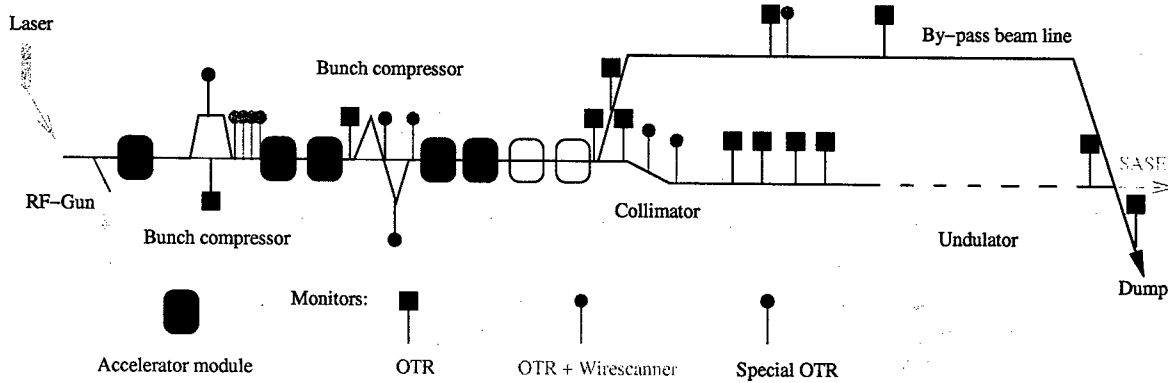


Figure 1: Schematic overview of the TTF2 linac (not to scale). Beam direction is from left to right, the total length is about 250 m. Different beam profile monitors along the linac are indicated.

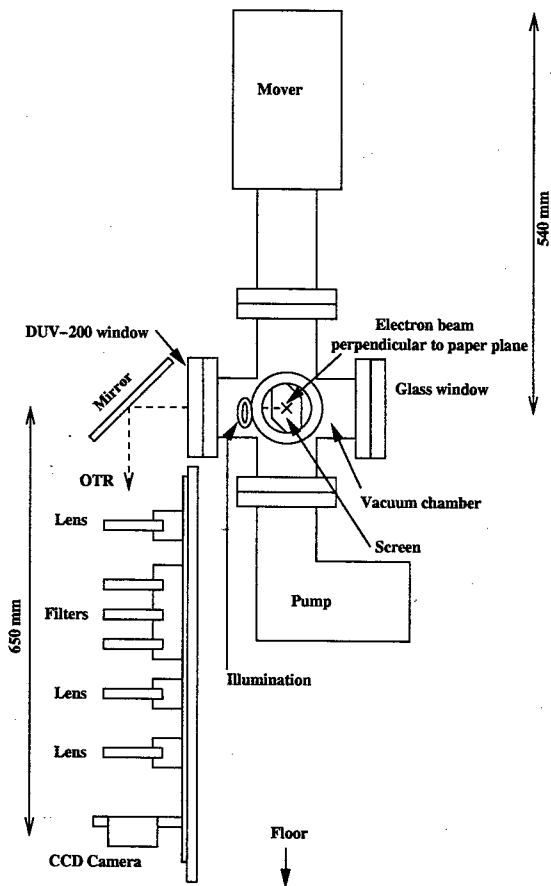


Figure 2: Sketch of a standard TTF2 OTR monitor (not to scale).

SCREENS

At TTF1, kapton foils with an aluminium coating were used as OTR screens. These screens showed cracks in the Al coating after some time of use. Our understanding is that the beam heats the screen and due to different thermal expansion, the Al coating cracks. One silicon screen with

an aluminium coating was used as well. No visible damage is seen on this screen.

At TTF2, due to smaller beam sizes, the charge density on the screen will be even higher than at TTF1. Even if the number of electron bunches per macropulse will be limited to only a few, the charge density on the screen may be sufficient to destroy it even by a single shot. Therefore the screen material has to be carefully selected. So far, two materials, silicon and aluminium, have been studied. Other possibilities are tungsten, titanium and beryllium. According to EGS4 simulations [7] with a round gaussian beam distribution of $\sigma = 50 \mu\text{m}$, a silicon screen stays below its stress limit, when the charge per macropulse is less than about 110 nC. For aluminium the corresponding value is about 10 nC. The light emission efficiency of these two materials has been measured at TTF1: The number of photons detected by the same standard CCD camera was about four times less for polished silicon than for aluminium.

Because of the significant difference in the light emission, it has been decided to mount two screens in all the monitors: a $350 \mu\text{m}$ thick polished silicon screen and a silicon screen with a 40 nm aluminium coating. The size of both screens is 30 mm x 30 mm, and they are mounted on a common screen holder made of stainless steel. Between the two screens, on the same plane, are marks to adjust and calibrate the imaging optics.

OPTICAL SET-UP

A sketch of the optical system used to image the OTR light to the CCD camera is shown in Fig. 2. This system consists of a mirror deflecting the OTR light downwards, three achromatic doublets, three neutral density filters, and a CCD camera. The components are mounted on two rails on a stainless steel plate. The plate will be fixed to the support structure of the linac. The optical system is protected against the stray light, and the CCD camera is shielded with lead to reduce radiation damage.

Both, lenses and filters can be remotely moved transversally in or out of the optical axis. Only one lens is inserted

at any time. Focal lengths of the lenses are 250 mm, 200 mm and 160 mm providing nominal magnifications of 1, 0.38 and 0.25, respectively. The filters have transmission of 10 %, 25 % and 40 %, and any combinations of them can be used. The camera is a digital CCD camera (Basler A301f) with a firewire interface (IEEE1394). The sensor size of the camera is 658 x 494 pixels with a pixel dimension of $9.9 \mu\text{m} \times 9.9 \mu\text{m}$.

The initial adjustment of the optical set-up is done on an optical table. The optical axis is defined with a help of a He-Ne laser and small diaphragms. The correct position of the lenses is searched by automatically measuring the contrast on a calibration target. When the correct position of the lenses and the camera is found, their position is fixed. On the beam line, the distance of the whole system from the screen is adjusted with the help of the marks on the screen holder. The same marks are used to calibrate the magnification.

The resolution of the optical system was studied by measuring the Modulation Transfer Function (MTF). The resolution can be improved significantly by using a diaphragm reducing geometrical aberrations. In order to define the limiting resolution of the system, an edge profile of a black rectangle on the calibration target was taken. A gaussian point spread function (PSF) convoluted with a step function was fitted to the measured profile. From the fit the gaussian width (σ) of the PSF can be determined. A value of $\sigma = 10 \mu\text{m}$ was obtained with a diaphragm of a diameter of 20 mm (magnification of 1). Without a diaphragm, the corresponding value was $\sigma = 30 \mu\text{m}$.

The highest resolution is required when the beam size is expected to be small. This is the case at the high beam energies, in the case of TTF2 after the full acceleration, when the beam energy is of the order of 1 GeV. At high energies OTR is well collimated and therefore the intensity cut by a diaphragm is small. Thus this technique can be used to improve the resolution in the high energy section of TTF2.

READ OUT-SYSTEM

The beam images are captured by digital CCD cameras. All the cameras are connected to a computer running control and acquisition software. This computer acts as a image server controlling the cameras and providing live beam pictures for monitoring, on-line beam profiles and beam widths, as well as high-resolution images for measurements, and low-resolution images for documentation. It also takes care of the communication with the TTF2 control system. A more complete description of the image server is in Ref. [8].

Digital IEEE1394 (firewire) cameras have been chosen, because they offer, at a cost comparable to their analog counterparts, several advantages, like full frame resolution, remote gain and shutter control and a triggered acquisition mode. A further advantage is a simpler cabling topology, because only a firewire link and a trigger are required, no

videomultiplexer nor frame grabber is needed. On the other hand, there is no experience with a large digital camera system. The connection of almost 30 cameras distributed along the linac can be complicated, because the maximum length of standard firewire connections is only about 5 m. One possibility is to use glass fiber optical links and optical repeaters for long distance connections and hubs to connect locally the cameras via firewire links. Another solution is to replace the optical repeaters by compact PC104 computers connected to the image server via a local ethernet. In this solution each computer controls a limited number of cameras. The final solution for TTF2 is still under investigation.

STATUS AND OUTLOOK

All the vacuum components of the beam profile monitors are ready and the mounting of the OTR chambers in the linac will start this summer. The prototype phase of the optical set-up is successfully finished, and the first optical setups will be installed and commissioned soon. The test of the digital camera system continues and the decision of the final solution for the connection scheme will be made within a few months. The complete OTR beam profile monitor system is expected to be in operation early 2004.

ACKNOWLEDGMENT

We like to thank our colleagues at DESY and at INFN for the technical support. Special thanks are due to S. Schreiber for many valuable discussions.

REFERENCES

- [1] TESLA-Collaboration, ed. D.A. Edwards, "TESLA Test Facility Linac - Design Report", DESY Print March 1995, TESLA 95-01.
- [2] R. Brinkmann et al, "TESLA Technical Design Report, Part II The Accelerator", DESY 2001-011, http://tesla.desy.de/new_pages/TDR_CD/PartII/accel.html
- [3] J. Andruszkow et al., "First Observation of Self-Amplified Spontaneous Emission in Free-Electron Laser at 109 nm Wavelength", *Phys. Rev. Lett.* 85 (2000) 3825-3829.
- [4] V. Ayvazyan et al, "Generation of GW radiation pulses from a VUV Free-Electron Laser operating in the femtosecond regime", *Phys. Rev. Lett.*, 88 (2002) 104802.
- [5] "SASE FEL at the TESLA Facility, Phase 2", TESLA-FEL note 2002-01, DESY, June 2002.
- [6] M. Castellano et al, "OTR Measurements for the TTF Commissioning", *Proceedings of DIPAC 1997 - LNF-97/048(IR)* 195, 1997.
- [7] V. Balandin and N. Golubeva, "Survival and Thermal Heating of materials for the OTR Screen at the TTF phase 2", TESLA note in preparation.
- [8] L. Catani, A. Cianchi, G. Di Pirro, "A Beam Image Server For TTF2", *Proceedings of PCaPAC 2002, Frascati (Roma)* October 2002.

BPM AND ORBIT CORRECTION SYSTEMS AT THE DUKE STORAGE RING *

Y. K. Wu[†], J. Li, P. Wang, V. Litvinenko, FEL Lab, Duke University, NC 27708-0319, USA

Abstract

Stable and reliable storage ring operation critically depends on the orbit stability. At Duke, an orbit stability program is well under way to achieve the high level of orbit performance necessary for reliable free electron laser (FEL) and gamma-ray operation. Progress has been made to reduce the current dependency of BPM readings via choice of cables and band-pass filters. Beam based alignment has been carried out to accurately determine the locations of quadrupole centers. A global orbit correction system and a slow orbit feedback system have been developed. Integrated with operation, these systems have demonstrated the ability to significantly improve the overall storage ring performance.

1 INTRODUCTION

The Duke storage ring was first commissioned in 1993 [1] with a minimal set of beam diagnostics. In spite of its rapid successful commissioning, the lack of beam position monitor (BPM) system adversely impacted the high bunch-current operation and subsequent commissioning of the free electron laser (FEL). Purchased from Bergoz, a set of 34 BPM electronics modules were installed in 1999 on the storage ring [2]. The initial operation of the BPM system resulted in limited improvements in the storage ring operation.

The system provided relatively reliable orbit measurements, however, BPM readings were found to be strongly dependent on the beam current. Further investigation indicated that this current dependency was the result of the overloading of BPM electronics due to a high peak voltage. Steps have been taken to address this problem by attenuating BPM pickup signals. Although unfinished, this work has significantly improved orbit readings. The improved BPM system has allowed the development and application of a reliable global orbit correction system. With this system, we are able to store a high single bunch current consistently. In addition, well-corrected vertical orbit has significantly lowered transverse coupling, resulting in improved dynamic aperture and FEL operation. A slow orbit feedback system has also been developed. Its operation in the near future will provide the long-term orbit stability necessary for optimal FEL and gamma-ray operation.

In the following sections, we first report our work on resolving the problem of beam current dependency of BPM readings. We then present the beam-based alignment scheme used to determine quadrupole centers. Finally, we report the development and operation experience

of a global orbit correction system and a slow orbit feedback system.

2 BPM SYSTEM IMPROVEMENTS

The Duke BPM system had been designed to maximize the pickup signals. This decision had resulted in choosing stripline pickup electrodes. Two types of stripline BPM pickups were installed on the Duke ring: arc BPMs with shorter striplines (21.6 mm) and smaller inner radii (17.78 mm) and straight section (SS) BPMs with longer striplines (30.5 mm) with larger inner radii (30.5 mm). Being closer to the electronics modules, arc BPMs were connected with RG223-U cables while straight section BPMs were connected with low loss 1/4" Helix cables. With this configuration, orbit readings from SS BPMs were found to be strongly dependent on the single bunch current (see Fig. 1.a).

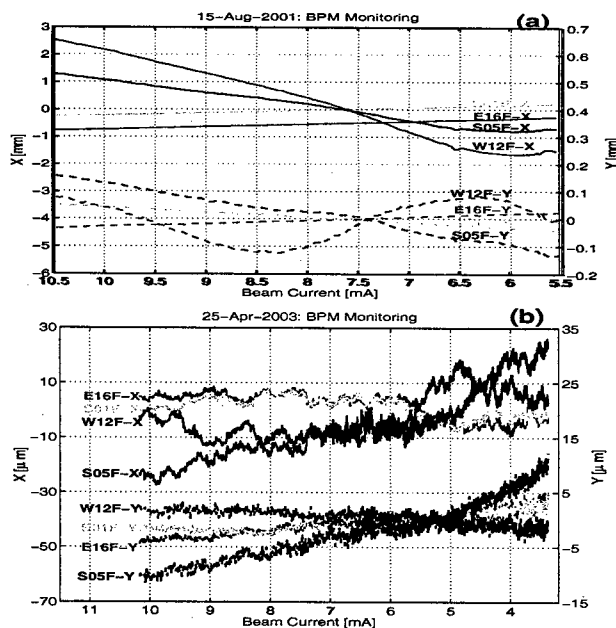


Figure 1: BPM reading variations with the single-bunch current: (a) Helix cables were used for straight section BPMs (including S01QF and S05QF BPMs) while RG223 cables were used for arc BPMs (including E16QF and W12QF BPMs); (b) RG223 cables were used for all BPMs. In addition, 20 MHz band-pass filters were used for E16QF and W12QF BPMs.

The raw BPM pickup voltage was measured at tens of volts level (0-1 GHz), far exceeding the 5 V threshold allowed for the multiplexer in the Bergoz's electronics. The severity of this problem was altered by the type of cables used, for the cable could serve as an effective low pass fil-

* Work Supported by the DoD MFEL Program as managed by the AFOSR, grant F49620-001-0370.

[†] wu@fel.duke.edu, 1-919-660-2654 (phone).

ter in case of RG223 cables. For example, the arc BPM readings were found less dependent on the bunch current (see Fig. 1.a). Further improvements were realized with band-pass filters installed on arc BPMs (see Fig. 1.b). With filters, the small changes in arc BPM readings could be attributed to the real orbit motion during the 1.4 hour test run. The maximum BPM reading variations in various configurations are summarized in Table 1.

BPM & location	Before upgrade (X, Y) [μm]	After upgrade (X, Y) [μm]	Upgrade
S01QF, SS	(4176, 206)	(36, 8)	RG223
S05QF, SS	(2082, 292)	(54, 24)	RG223
E16QF, ARC	(508, 60)	(18, 10)	BP filter
W12QF, ARC	(460, 93)	(16, 9)	BP filter

Table 1: Maximum BPM reading variations. Before upgrade, $I = 10.5$ to 5.5 mA; after upgrade, $I = 10.2$ to 3.3 mA;

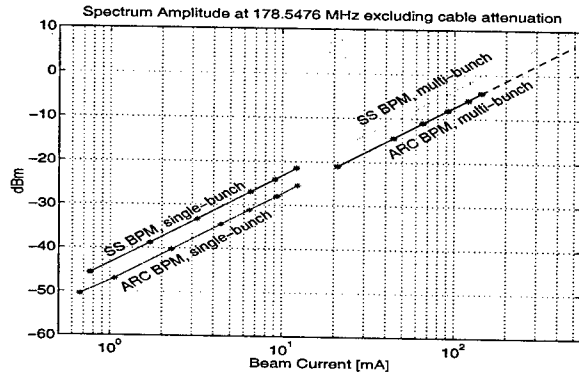


Figure 2: Measured spectrum power at 178 MHz for both shorter striplines (arc BPMs) and longer striplines (straight section BPMs). Two segments of data covering a large current range were collected from single-bunch and multi-bunch runs.

The Duke storage ring operates over a wide beam current range with several bunch patterns: from a few mA to tens of mA in the single-bunch mode and from tens of mA to hundreds of mA in the multi-bunch mode. To achieve optimal BPM operation over such a wide range of currents, it is essential to find a proper combination of cables and filters for BPMs. For example, a large insertion loss due to band-pass filters would limit the usefulness of BPMs at the low current end in the single-bunch operation. The maximum allowed power loss in the cable and filter can be determined from carefully measured power spectra (Fig. 2). We are in the process of finalizing the cable/filter configuration for both types of BPMs.

3 BEAM BASED ALIGNMENT

The desirable closed orbit should go through the centers of quadrupoles. The offset between the quad centers and adjacent BPM centers can be determined using beam based alignment (BBA) techniques. A straightforward

beam based alignment method used in the ALS [3] has been adopted for the Duke ring.

Using this method, a corrector steers the beam orbit in the quad under measurement. For each orbit, the focusing strength of the quad is varied and the difference orbit around the ring is then recorded. The quad center is defined as an orbit in the quad at which the focusing strength adjustment produces no orbit changes around the ring.

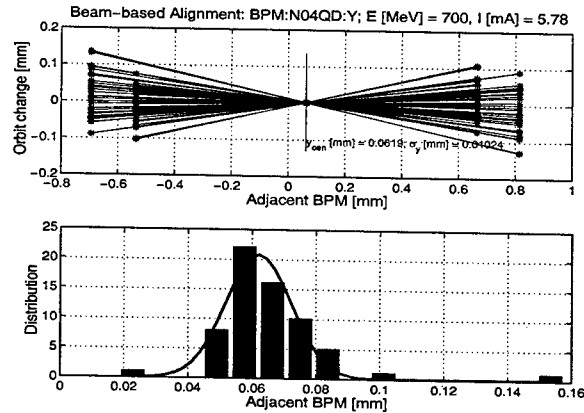


Figure 3: Finding the vertical quad center using a Gaussian fit for quad N04QD, $\beta_y = 12$ m.

Fig. 3 shows the measurement of the N04QD quad vertical center. Each BPM produces its own estimate for the quad center. The distribution of possible quad centers computed using all BPM data is then fitted to a Gaussian form. In this example, the standard deviation of the Gaussian fit is about $10 \mu\text{m}$. Fig. 4 shows the measured quad centers around the ring using a 700 MeV beam. The maximum and average sigmas for arc BPMs are 120 and $70 \mu\text{m}$ respectively with a smaller β -function, $\beta_y = 1.8$ m.

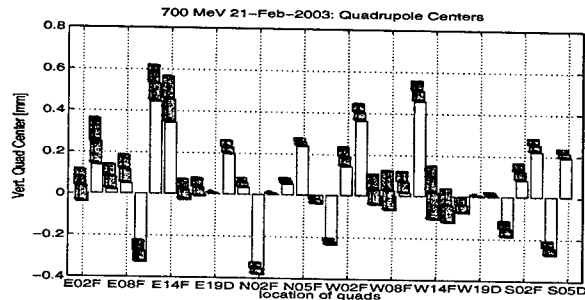


Figure 4: Measured vertical offsets between quad centers and adjacent BPM centers with a 700 MeV beam.

4 GLOBAL ORBIT CORRECTION

Like many high level controls for the Duke ring, the global orbit correction was developed in MATLAB. The correction algorithm is the singular value decomposition (SVD). It utilizes 31 BPMs, 54 horizontal and 25 vertical correctors. With a reasonably updated response matrix, the correction algorithm settles down in 2 to 3 iterations. After the correction, the residual vertical orbit is small: the vertical orbit has a sigma of about $80 \mu\text{m}$ at injection energy

of 274 MeV and a sigma of about 60 μm at 700 MeV at which the BBA is performed.

A well-corrected orbit significantly improves the ring performance. First of all, it helps increase the beam lifetime. Second, by suppressing the skew quad excitation in sextupole elements, a good vertical orbit helps significantly reduce the transverse coupling. For example, when correcting the vertical orbit from 1.2 mm to 0.1 mm (RMS), the vertical β -function is reduced from 20 mm to 4 mm (RMS). Third, a good vertical orbit suppresses the excitation of head-tail instabilities, allowing storage of higher single-bunch current, which is essential for the FEL and Compton gamma-ray operation.

The global orbit correction has been fully integrated with the machine setup and operation. Whenever needed, this tool can be used to correct the orbit drift to maintain a good orbit. This practice has resulted in significant improvement in the reliability of the storage ring operation.

5 SLOW ORBIT FEEDBACK

To achieve a higher level of orbit stability, an active orbit feedback is necessary. A slow orbit feedback system has been developed for the Duke ring via optimization of the global orbit correction program described above. This system is capable of correcting orbit up to 4 times per second. Fig. 5 shows the effectiveness of the slow orbit feedback. First, the orbit feedback system ran for about one hour, maintaining the straight section orbit to less than 10 μm (peak-to-peak). Later, the feedback was turned off and the orbit started to drift with maximum horizontal orbit drift exceeding 100 μm in the next 45 minutes.

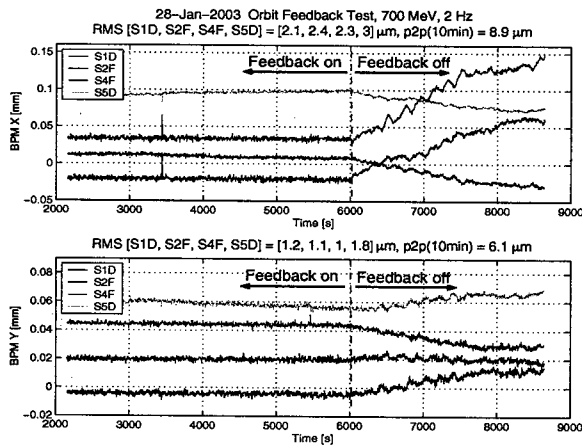


Figure 5: Orbit stability with a slow orbit feedback system. All 4 BPMs are located in the straight section with large β -functions.

It is worth pointing out that the typical beam sizes in the straight section are 300 and 60 μm (RMS) respectively. The ability to maintain orbit stability within 10% of the beam sizes will significantly improve the light source operation and enhance user capabilities. For example, both the FEL and Compton gamma-ray operation requires a good transverse alignment of the optical pulse with the elec-

tron beam orbit in the interaction region. By sustaining a good e-beam orbit continuously, aligning the optical axis with a fixed beam orbit becomes a much easier task. For gamma-ray users, the stable beam orbit angle means a stable on-target gamma-ray energy after the collimator. A higher level of orbit stability also significantly simplifies and improves the two-color biological and chemical experiments using both infrared synchrotron radiation from bending magnets and UV radiation from the FEL.

The orbit feedback has been tested in several operation conditions. Since the feedback system utilizes a fixed response matrix, it is important to find out whether it can maintain its effectiveness when the ring lattice is somewhat changed. The feedback was tested with abrupt orbit changes, lattice tuning, and field strength tuning of the FEL wigglers. The test result indicated that the feedback system was able to adapt to these operation environments.

Our ultimate goal is to allow transparent storage ring operation with the orbit feedback running in the background. Mechanisms have been developed to automatically switch off the feedback during energy and lattice ramping and when there is not enough beam current. In addition, at restart, the feedback system will select and load in an appropriate response matrix suitable for the present lattice. This sophisticated feedback system will be fully commissioned after the current dependence problem of the BPMs is completely addressed.

6 SUMMARY

The current dependency of BPM readings has been found to be caused by overloading BPM electronics with a high peak voltage. Using low-pass cables, this problem has been reduced to a manageable level. Further improvement is expected as the result of an on-going effort to find an optimal configuration of cables and band-pass filters.

The quad centers have been accurately determined using a beam based alignment technique. This work has paved the way for the development of a global orbit correction scheme using SVD. Integrated with operation, the orbit correction system has significantly improved the overall storage ring operation. A slow feedback system is being tested to maintain long-term orbit stability. This system will simplify the light source operation and further improve the light source performance.

We would like to thank I. Pinayev at DFEL for providing reference orbit measurement using his optical BPM and S. Hartman at DFEL for significantly improving the BPM readback system. We also would like to thank Jim Hinkson at GMW for advice and help on resolving the BPM electronics overloading problem.

7 REFERENCES

- [1] V. N. Litvinenko, Y. Wu, B. Burnham, et al., Proc. of PAC95, Dallas, Texas, p. 213 (1995).
- [2] P. Wang, et al. Proc. of PAC99, New York, p. 2099-2101 (1999).
- [3] D. S. Robin, Berkeley National Lab, private communication.

A PHYSICS BASED CONTROL SYSTEM FOR THE DUKE STORAGE RING *

Y. K. Wu[†], S. Hartman, S. F. Mikhailov, FEL Lab, Duke University, NC 27708-0319, USA

Abstract

At the Duke FEL Lab, we have developed a new storage ring control system in terms of the physics quantities of the accelerator. Instead of controlling power supply currents in Amperes, this system controls the effective focusing of magnets. By directly controlling the physics quantities, this control system allows tighter integration of the physics model based high level controls with the EPICS based low-level controls. EPICS events have been extensively used to provide time synchronization during the energy and lattice ramping. This new control system also facilitates the implementation of multiple functions on shared control channels. As a result, the physics based control system simplifies many complex control tasks, improves the beam stability during ramping, and facilitates machine studies. With better understanding of the accelerator, it is possible to fine tune this control system to present users with a virtual accelerator whose operation is independent of the ring energy.

1 INTRODUCTION

The development of modern accelerator control systems has displayed several emerging trends. First, instead of reinventing the wheel, a modern accelerator control system is typically developed based upon a mature and laboratory/industrial standard software infrastructure. The commonly used software infrastructure is Experimental Physics and Industrial Control System (EPICS)[1]. EPICS provides a set of software tools and applications which can be customized to build distributed real-time control systems. Second, the high level controls are developed in a versatile computation environment. The high level physics controls require a flexible programming environment with built-in mathematics and graphics capabilities to allow rapid prototyping, testing, and system integration. An increasing number of accelerator facilities have adopted MATLAB[2] as their preferred software for developing high level controls. Using an interface with the EPICS channel access, MATLAB works seamlessly with the EPICS based control system. Third, the accelerator control system is increasingly integrated with the physics simulation model. The physics model for accelerators has become more accurate in predicting the beam motion thanks to significant advances in accelerator physics in the last decade. For charged particle optics studies, a number of simulation codes have been developed and some of them have been designed with the aim of integrating with the accelerator control system. For example, the PASCAL version of TRACY [3] was developed

as an interactive toolkit for storage ring commissioning and tuning. More recently, Accelerator Toolbox (AT) [4] has been developed as a MATLAB toolkit to allow even closer integration between the physics model and control system.

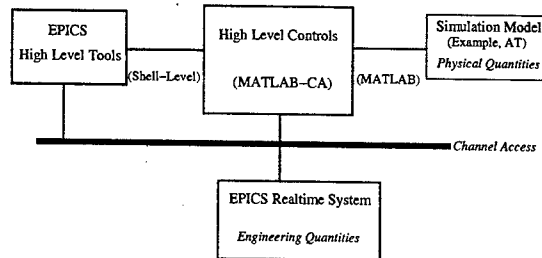


Figure 1: A layout of a typical integrated accelerator control system.

These trends lead to a very flexible but yet very powerful accelerator control system as illustrated in Fig. 1. While MATLAB served as a magic glue for this integrated system, there is an apparent mismatch between the physics model and the the real-time control system. The simulation model works in the physics phase space, for example, using effective focusing strengths for magnets. The real-time control system is typically developed in the engineering space, for example, controlling magnet power supplies in Amperes. The mapping between the focusing strength and the power supply current is typically handled by an add-on high-level program, resulting in a reduced flexibility and efficiency.

Addressing this deficiency, we have recently developed and commissioned a new control system for Duke storage ring based upon the physics quantities. This new approach has simplified many complex operation tasks and resulted in a virtual accelerator directly controlled in the physics space.

2 PHYSICS QUANTITY BASED ACCELERATOR CONTROLS

The physics quantity based control requires accurate measurement data to perform mapping between physics and engineering quantities. For magnet controls, measured magnetic fields data are used to map effective focusing strengths to power supply settings.

The physics quantity based control leads new ways to implement key control functionalities. First, it allows the development of new synchronization methods for energy and lattice ramping. For example, the energy ramping in the storage ring can be achieved by stepping up a single knob, the energy knob, while all necessary power supplies will be updated accordingly in order to maintain the effective focusing for magnets. Second, the physics quan-

* Work Supported by the DoD MFEL Program as managed by the AFOSR, grant F49620-001-0370.

[†] wu@fel.duke.edu, 1-919-660-2654 (phone).

tity based control facilitates the implementation of feed-forward and feedback controls. For example, a corrector magnet control can be split into two soft control channels, one used for closed-orbit correction and the other used in the orbit feedback system. In the following, we will address these issues in detail using the new Duke storage ring control system as an example.

2.1 K-Value to Current Mapping

The most important physics quantities for storage ring operation are the ring energy and effective focusing of dipoles, quadrupoles, and sextupoles. These quantities are also used in the simulation models. In the Duke storage ring control system, the following quantities are controlled directly:

- Ring energy: E [MeV];
- Dipoles, trim controls: K_0 , or θ [mrad];
- Quadrupoles, main and trim controls: K_1 [m^{-2}];
- Sextupoles, main and trim controls: K_2 [m^{-3}];
- Orbit correctors: K_0 , or θ [mrad].

As an example, Fig. 2 illustrates the control of a quadrupole in our system. Changes in either the ring energy or the K_1 -value of a quadrupole will result in the execution of this portion of the control. Magnetic measurement data are analyzed to provide a lookup table to map the product of the energy and K_1 to a proper current setting, which is subsequently set to the power supply. This approach also facilitates the control of more complex magnetic elements. For example, combined function quad-sextupoles are employed in the Duke ring by asymmetrically driving inner and outer quadrupole coils with two different currents [5]. The sextupole field feed-down effects are properly taken into account by mapping the energy, K_1 , K_2 to two power supply currents.

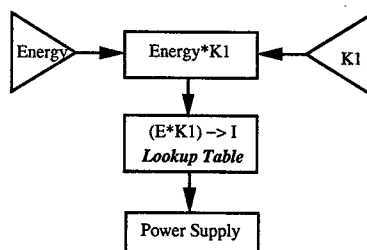


Figure 2: Mapping the energy and K_1 to the current.

Like quadrupoles, the current settings for dipoles, correctors, and sextupoles are properly updated whenever the ring energy and/or relevant K-values are changed. By moving the K-value-to-current mapping down to the lowest level of control in the Input Output Controller (IOC), the mapping efficiency is improved. It also eliminates the potential need to implement multiple copies of the same mapping algorithm on different platforms for high level controls. Most importantly, it allows the lattice ramping to follow the K-value curve instead of the raw current curve, minimizing the tune changes during ramping.

2.2 Energy and Lattice Ramping

Due to the lack of a full energy injector at Duke, most user operations require energy ramping. The energy ramping is performed relatively frequently due to a somewhat short beam lifetime (1–3 hours) in main operation modes. The beam lifetime is limited due to a high peak current in 1-bunch free electron laser (FEL) operation and in 2-bunch gamma-ray operation. In addition to energy ramping, lattice ramping is also commonly performed for FEL wiggler adjustment and lattice tuning. The physics quantity based control leads to a more reliable software based ramping scheme.

Traditionally, the ramping synchronization in a storage ring is provided by either a hardware system or the high-level control software. While providing a high level of synchronization, the hardware based approach is complex, expensive, and less flexible. The software based synchronization is flexible and has been found to be adequate for many storage rings. The downside of this approach is that its timing is less precise and consistent due to performance variations of the local area network, control workstation, and high level software.

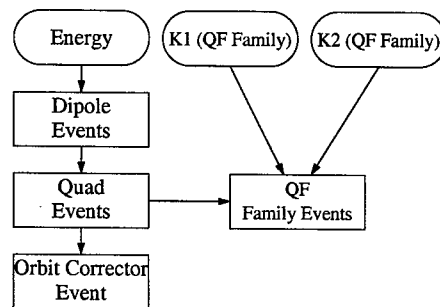


Figure 3: Event-chain in the Duke ring control system.

In contrast, the physics quantity based control facilitates the development of a new type of software based synchronization scheme using EPICS events. For example, an energy event generated by a master IOC is propagated to all related IOCs to signal an energy change. Within an IOC, this event triggers the update of all necessary database records, resulting in ramping relevant hardware. Carried out in the real-time system, the precision of this software based synchronization is significantly improved, especially for the case when all IOCs are connected to a way to minimize the unrelated network traffic.

Fig. 3 shows the actual implementation of the EPICS event-chain for the Duke ring. The event based synchronization is chosen to provide flexibility for updating a large number of channels while minimizing the network traffic. The energy event causes the generation of next-level events to update dipole trims, the main dipole, quadrupoles, etc. This multi-layer event-chain system is very flexible for synchronizing a large number of distributed controls during ramping. For example, using the arc QF event, both the energy ramping and lattice ramping (changes in K_1) can be performed simultaneously.

2.3 Multiple Functions of Shared Controls

In many circumstances, a piece of hardware has to be shared by several high-level systems. For example, a quadrupole or a dipole corrector can be used both in the supervisory control and in the feedback or feedforward control. Fig. 4 demonstrates the shared control of a dipole trim in the Duke ring for the following purposes: (1) compensating for the difference in integrated field strength (feedforward); (2) correcting the closed orbit (supervisory control); (3) performing orbit feedback. Because these three types of control functions are performed in the physics space, a simple sum-join is used to add together the total deflection angle θ_{tot} which is then mapped to the trim current. When operated at 1.0 GeV and above, dipole magnets become highly saturated, resulting in a nonlinear map between the deflection angle and corrector current. The field saturation in the quad-sextupoles is even more complex in the Duke ring. Consequently, without the physics quantity based control, this type of shared controls of a nonlinear device is very difficult to implement in the high-level.

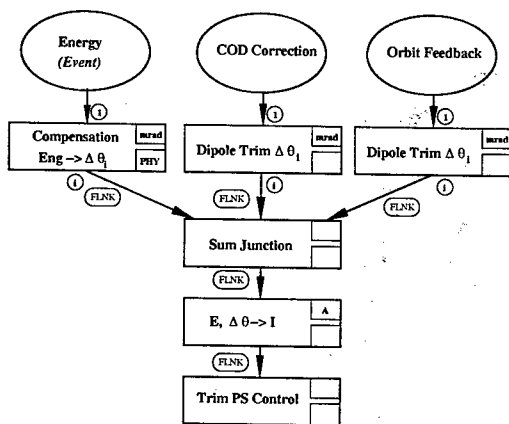


Figure 4: Multiple controls of a shared dipole trim.

3 PERFORMANCE

The present Duke storage ring control system consists of about four thousand EPICS channels. Twelve hundred (1200) of them, concentrated in two IOCs, are associated with the energy and lattice ramping. When optimized, all these channels can be updated at a 5 Hz rate, fully synchronized by the EPICS events. The maximal ramp rate is limited by the IOC CPU load, reaching a peak value of 70% during ramping compared with non-ramping load of about 10%. The ramping IOCs are relatively old computers (MVME167 single board computers) with a 33 MHz CPU. We expect that a higher ramping rate can be achieved using faster IOCs, such as Motorola Power PC boards with 200 MHz to 1 GHz CPUs.

With the physics quantities base control, the stability of beam orbit and beam size has been significantly improved during ramping. The measured beam orbit is shown in Fig. 5 for the energy ramping from 350 MeV to 1 GeV. Horizontally, the maximum and RMS orbit changes are

1.11 mm and 0.24 mm. Vertically, the maximum and RMS orbit changes are 0.54 mm and 0.13 mm.

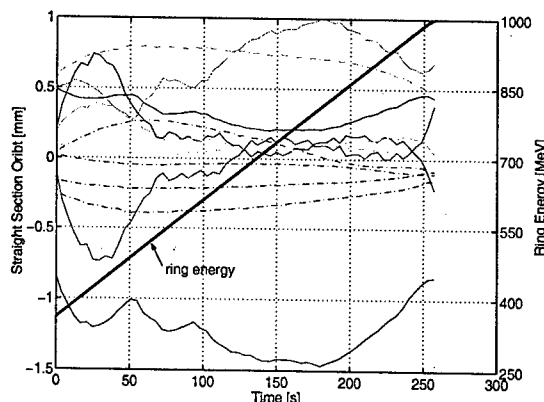


Figure 5: Beam orbit in the wiggler straight section during energy ramping. Solid and dot-dashed lines are horizontal and vertical orbits, respectively.

4 CONCLUSION

We would like to summarize the main benefits of a physics based control system as follows:

- providing closer integration between the simulation model and accelerator control system;
- simplifying and improving the energy and lattice ramping;
- assisting the development of feedback and feedforward systems via shared functional controls;
- allowing independent development of high level controls regardless of the low level details;
- simplifying extrapolating new lattice with different energies using an existing lattice.

These advanced features are great assets in improving the storage ring operation efficiency and reliability and extremely useful in machine studies. With better understanding of the magnetic field hysteresis and saturation, the physics based control can be fine tuned to present the user with an invariant virtual accelerator whose operation is transparent, portable, and independent of the beam energy.

Finally, we would like to thank V. Litvinenko for his encouragement and support and J. Li for his assistance in measuring the control system performance.

5 REFERENCES

- [1] See the APS website, <http://www.aps.anl.gov/epics>
- [2] See the MathWorks website, <http://www.mathworks.com>
- [3] H. Nishimura and J. Bengtsson, LBNL, a tracking code in PASCAL, private communication.
- [4] A. Terebilo, Proc. of 2001 Particle Accelerator Conference, Chicago, p. 3203 (2001).
- [5] V. N. Litvinenko, Y. Wu, B. Burnham, J. M. J. Madey, S. H. Park, Proc. of 1995 Particle Accelerator Conference, Dallas, TX, p.796 (1995).

THE SNS LINAC WIRE SCANNER SYSTEM*

M.A. Plum, W. Christensen, R.E. Meyer Sr., and C.R. Rose,
Los Alamos National Laboratory, Los Alamos, NM 87545

Abstract

The linac wire scanner system for the Spallation Neutron Source (SNS) at Oak Ridge, TN, calls for 5 units in the medium energy beam transport (MEBT), 5 in the drift tube linac (DTL), 8 in the coupled cavity linac (CCL), and 13 in the high energy beam transport (HEBT). The actuators are a custom design fabricated by Huntington Mechanical Laboratories. Four different strokes are required to cover the above areas. The electronics are designed and fabricated by Los Alamos National Laboratory (LANL). In this paper we will discuss the design of the actuators and the electronics, positioning accuracy tests of the actuators, and also show results from beam measurements taken during the MEBT commissioning at Oak Ridge National Laboratory.

OVERVIEW

In the Spallation Neutron Source (SNS) facility, H^- beams will be accelerated to 2.5 MeV in an RFQ, to 87 MeV in a drift tube linac (DTL), to 186 MeV in a coupled cavity linac, and finally to 1000 MeV in a superconducting linac (SCL). The 60-Hz, 1-ms, 36-mA peak-current beam pulses are chopped into 690-ns long segments with a 1 μ s period to give an average current of 1.4 mA and an average beam power of 1.4 MW.

Linac wire scanner systems are installed in the MEBT (5 units), the DTL (5 units), the CCL (8 units), and the HEBT (13 units). Similar actuators but different signal processing electronics are used in the ring and ring-to-target beam transport (RTBT) areas.

A pivoting style of actuator was originally developed [1] for the SCL, but for this portion of the linac it was later decided to install laser profile monitors [2] instead. A large part of this decision was based on the concern of broken wire fragments contaminating the superconducting cavities.

ACTUATORS

The wire scanner actuators in the DTL, CCL, and HEBT areas are based on custom-designed linear actuators from Huntington Mechanical Laboratories, Inc. Three carbon wires, 32 microns in diameter, are mounted to each wire scanner fork to measure the beam profile in three different planes. The wires are offset from each other so that no more than one wire at a time is within ± 2 rms of the beam center. A special collet design, developed at LANL, is used to hold the wires in place with a small amount of tension to accommodate thermal expansion and contraction.

The stroke of the DTL actuators is 6 inches, for the CCL it is 3 inches, and for the HEBT it is 8 inches. The

actuators are fabricated using bellows rated for 50,000 cycles to accommodate the 30,000 cycle estimate of the maximum number of cycles over the 30-year lifetime of the facility. Radiation-hardened coaxial connectors and linear variable differential transformer (LVDT) position read back devices are also used to accommodate the 10^5 Gy estimate of the maximum dose to an actuator over the same facility lifetime.

Each actuator also has a brake and five limit switches. One limit switch at each end is for motion control, two redundant limit switches in series at the retracted end are for the machine protect system, and the last limit switch, at the inserted end, is provided for potential future purposes. Each actuator, including the fork and the collet wire mounts, costs about \$6,500. A photograph of a DTL actuator is shown in Fig. 1.

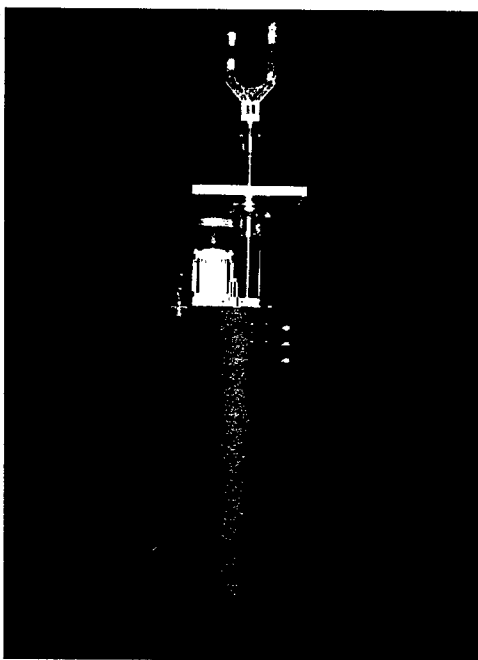


Fig. 1. (color) Photograph of a 6-inch stroke actuator.

Although carbon wires can withstand higher beam intensities than other wire types, the linac duty factor must still be reduced when using the wire scanners. The linac beam parameters are expected to stabilize after about 30 μ s, and so a beam pulse length of about 50 μ s is a minimum requirement for the wire scanner systems. For the nominal beam current of 26 mA average, the carbon wires will remain below the 1225 $^{\circ}$ C temperature limit [3] (needed to avoid signal contamination due to thermionic emission) as long as the beam pulses are less than 50 μ s long and the repetition rate is 10 Hz or less, in all areas

*Work supported by the Office of Science of the US Department of Energy.

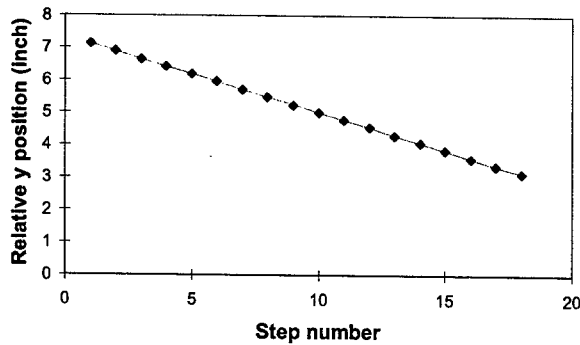


Fig. 2. (color) Measured position of the 6-inch prototype actuator vs. step number.

except the MEBT, where the repetition rate limitation is 1 Hz.

Of course actuator positioning accuracy is a critical component of the accuracy of a beam size or beam position measurement [4]. The SNS requirement is to measure the rms beam size with an accuracy of 10% or better. To meet this requirement, assuming a relative electronic signal processing error of 1%, an absolute signal processing error of 2% of the maximum signal, and no beam jitter, the DTL actuator positioning error should be less than 0.4 mm, and the CCL actuator positioning error should be less than 0.3 mm [4].

We measured the positioning errors of the prototype DTL and CCL actuators by mounting the actuators in the vertical orientation and suspending a 5 kg weight from each actuator to simulate the vacuum load. Each actuator

was moved in a series of equal-length steps by issuing a certain number of pulses to the stepper motor for each step. After each step we used two theodolites to measure the horizontal and vertical positions of an alignment target mounted to the ends of the actuators. Before making any of these position accuracy measurements we cycled each actuator more than 2000 times with the 5 kg weight attached. Shown in Fig. 2 is the plot of the measured actuator position vs. the number of pulses issued to the stepper motor on the 6-inch actuator. The result [5] is an effective positioning accuracy of 0.11 mm for the 6-inch DTL actuator, and 0.15 mm for the 3-inch CCL actuator.

ELECTRONICS

The electronics package consists of an 4.4-cm tall (1U) signal processor chassis, an 8.9-cm tall (2U) driver chassis, and a 17.8-cm tall (4U) rack-mounted PC. A block diagram is shown in Fig. 3.

The signal processor has several functions: 1) it applies a high voltage bias (up to 100 V) to the wire scanner wires; 2) it detects broken wires by sensing a change in the voltage drop due to the 180 k Ω resistors electrically connected to the opposite ends of the signal wires and mounted directly to BNC connectors on the actuators; 3) it ac-couples the wire signals to current-to-voltage converters with three gain ranges; 4) it delivers the 36-kHz bandwidth-limited signals to the National Instruments PCI-6110 data acquisition card in the PC; and 5) it contains a software-controlled built in self test circuit that injects a test pulse into the front end circuitry. The

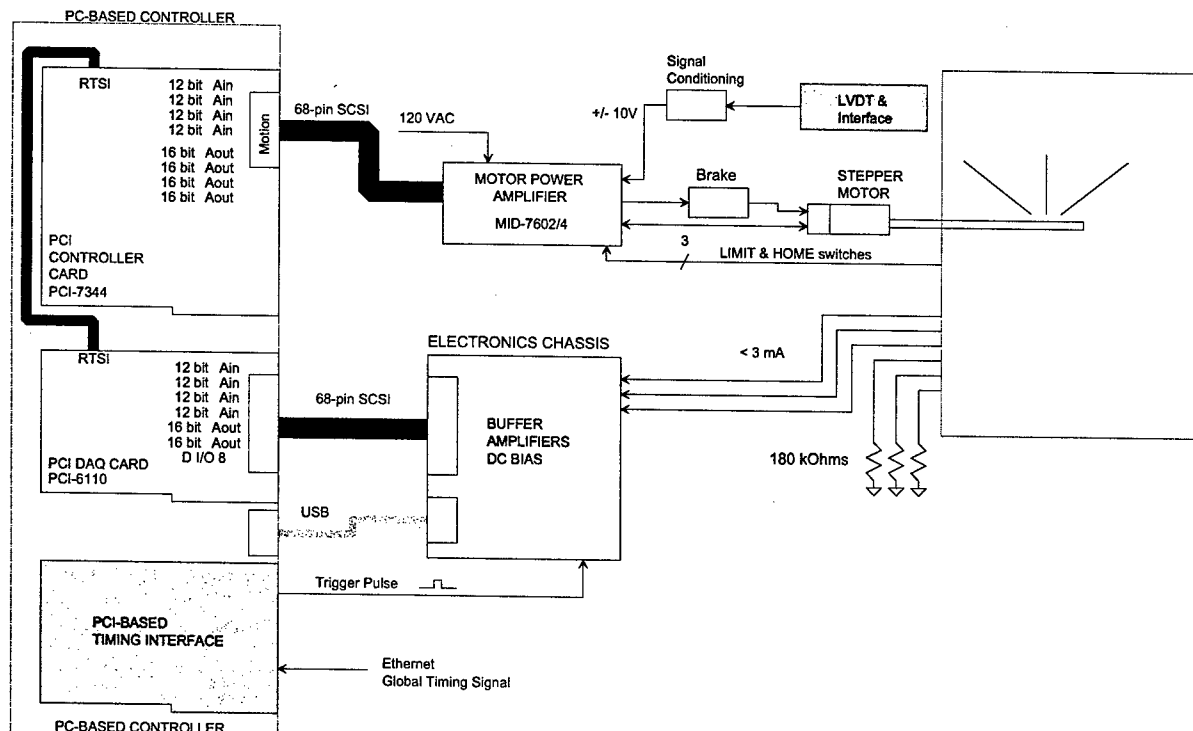


Fig. 3. (color) A block diagram of the linac wire scanner system.

signal processor chassis also employs a LabJack[®] U12 module to monitor critical system voltages and send the results to the PC via a USB port on the PC. Some measured specifications are shown in Table 1, and a photograph of the signal processor chassis is shown in Fig. 4.

Table 1. Signal processor specifications.

Minimum signal	16 nA at high gain
Maximum signal	2.1 mA at low gain
No. gain ranges	3, separated by 18 dB
Linearity	<0.004% of full scale output
Rise/fall time	8 μ s

The driver chassis interfaces to the National Instruments PCI-7344 motion control card in the PC and controls the stepper motor and the brake via the National Instruments MID-7602 stepper motor driver module. The chassis also contains the Macrosensors LVC-2401 signal conditioner for the rad-hard Macrosensors PR-750 series LVDT mounted on the actuator. Although the LVDT linearity specifications are quite good (<0.25% of full range), it does not measure the actuator position as accurately as simply counting the pulses issued to the stepper motor. Its function is therefore limited to checking that the actuator is operating properly.

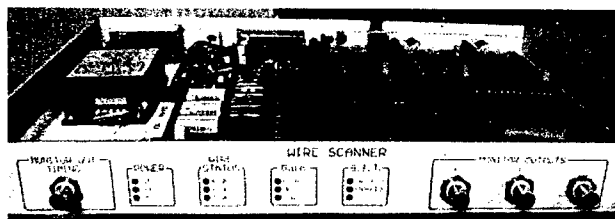


Fig. 4. (color) Photo of the signal processor chassis.

A second type of driver chassis has been designed based on the Phytron CLD 20-24 linear stepper motor driver. The two types of chassis have been designed to be functionally equivalent, however we expect that the linear

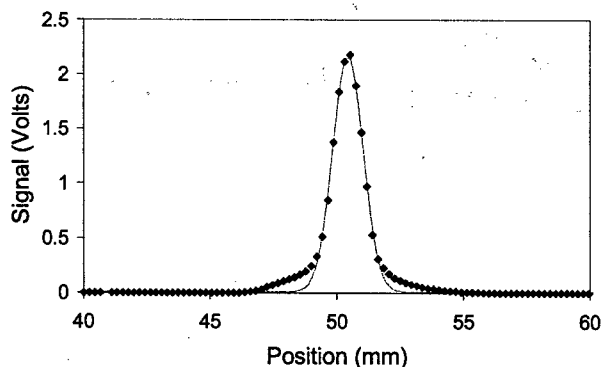


Fig. 5. (color) A sample wire scanner measurement taken in the SNS MEBT.

stepper motor driver will produce less electromagnetic noise than the MID-7602 chopper driver. The two chassis types will be tested in the realistic beam environment during the coming year, and then a down select decision will be made.

The rack-mounted PC contains three PCI cards: 1) a National Instruments PCI-6110, 4-channel, 5-MS/s, 12-bit data acquisition card; 2) a National Instruments PCI-7344 motion control card; and 3) a custom-made PCI timing card to interface to the SNS global timing system. We've chosen to use either embedded Windows 2000 or Windows XP for the operating system, LabVIEW for the data acquisition and motion control software, plus some custom-designed software to allow each PC to appear to the EPICS control system as an Input-Output Controller (IOC).

PERFORMANCE

The electronics were first installed in the MEBT portion of the SNS linac together with the MEBT actuators (not described in this paper) developed by Brookhaven National Laboratory. The first measurements with beam were made in February 2002 at Lawrence Berkeley National Laboratory. A sample profile measurement from the recent Winter 2002-3 commissioning period at ORNL is shown in Fig. 5. The data are smooth and well described by a Gaussian fit to the core of the beam. The measured beam sizes also agree well with optics models of the MEBT and with laser profile measurements made concurrently with the wire scanner measurements.

Two more wire scanner systems, for the first DTL tank and the D-plate, have recently been installed, and in the next year we will install the remainder of the DTL and CCL systems. The HEBT system installations will take place in summer 2004, and this will complete the linac wire scanner system installation.

REFERENCES

- [1] R. Hardekopf et al., "Wire Scanner Design for the SNS Superconducting-RF Linac," Proceedings of the 2001 Particle Accelerator Conference, Chicago, Ill, June 18 - 22, 2001.
- [2] R. Connolly et al., "Laser Beam-Profile Monitor Development at BNL for SNS," proceedings of the 2002 Beam Instrumentation Workshop, Upton, NY, USA, 6 - 9 May 2002.
- [3] J.D. Gilpatrick, private communication.
- [4] M. Plum, W. Christensen, R. Meyer, and C. Rose, "SNS Linac Wire Scanner System: Signal Levels and Accuracy," Proceedings of the LINAC 2002 conference, Gyeongju, South Korea, August 19-23, 2002.
- [5] M. Plum, "SNS Actuator Position Accuracy Tests," Jan. 31, 2003. SNS Tech Note 104050204-TR0001-R00.

PERFORMANCE OF A BEAM MONITOR IN THE FERMILAB TEVATRON USING SYNCHROTRON LIGHT*

H. W. K. Cheung, A. Hahn, A. Xiao, FNAL, Batavia, IL 60510, USA

Abstract

Synclite, the beam monitor in the Fermilab Tevatron using synchrotron light is described. The calibration, monitoring and performance of the system is discussed. Observation of some effects of long range beam-beam interactions seen in the beam monitor will be presented as well as a measurement of DC beam in the Tevatron.

INTRODUCTION

Synchrotron light emitted at the edge of a dipole magnet has a significantly larger intensity in shorter wavelengths than that emitted in a uniform field [1, 2]. Blue light emitted from the ~ 5 cm turn-on region of a Tevatron dipole can be used to measure the 2-dimensional transverse profile of the beam [2, 3]. Synchrotron light emitted by protons (antiprotons) from the upstream edge of a 6 (3) meter superconducting magnet is deflected out of the beam pipe by a movable aluminized flat mirror through a quartz window into a telescope assembly. The light is separated from the particle beam by 2.6 (1.0) cm at the pick-off point.

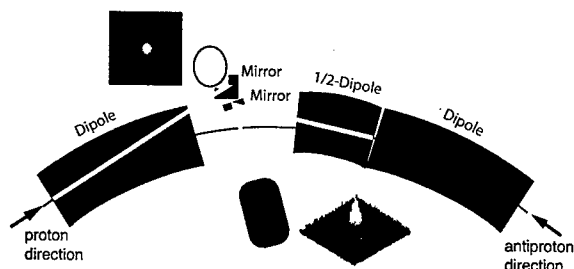


Figure 1: Synclite schematic showing radiation point locations for protons and antiprotons.

The proton and antiproton telescope systems each consist of a single lens and a narrow band blue filter focusing onto the photocathode of a single stage MCP image intensifier. The image on the intensifier phosphor screen is viewed by a CID camera which in turn is captured using a video frame grabber giving an image with 640×480 (horizontal \times vertical) pixels each with 8-bits of intensity data. Each pixel in the proton (antiproton) image corresponds to 57 (83) μm at the object plane. The beam transverse profiles are Gaussian with a sigma of about 0.6 mm, and the diffraction resolution is about 0.2 mm (0.1 mm) in the horizontal (vertical). More details on the physics of the radiation, the Tevatron dipoles and the telescope optical system can be found in earlier reports [2, 3].

* Work supported by the Universities Research Association, Inc., under contract DE-AC02-76CH03000 with the U.S. Dept. of Energy.

Timing and Gain

Both the proton and antiproton beams in the Tevatron are divided into 36 bunches. Each proton (antiproton) bunch contains an average number of about 210×10^9 (25×10^9) particles at the beginning of the store and have the time structure illustrated in Figure 2(b). The bunches are in 3 trains of 12 bunches each where each bunch is separated by 396 ns. The last bunch of one train is separated from the beginning of the next by 2640 ns, these gaps are called the beam abort gaps. Although the CID camera integrates over about 30 ms, the profile for each bunch can be measured by gating the photocathode so that the image intensifier is only sensitive while a particular bunch is illuminating the photocathode.

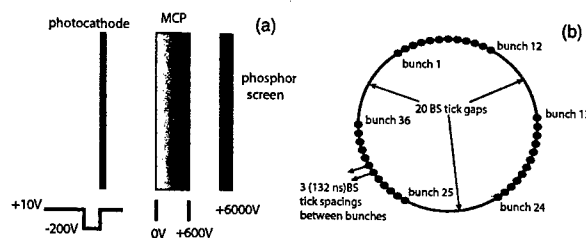


Figure 2: (a) Schematic of image intensifier showing the typical high voltages used; (b) Schematic of beam in the Tevatron illustrating the time structure for the 36 proton bunches. The 36 antiproton bunches have a similar time structure.

The image intensifier consists of a photocathode, microchannel plate and phosphor screen, see Figure 2(a). The gain of the image intensifier varies across its surface. It is calibrated by the use of a UV lamp.

Data Acquisition and Image Analysis

The Synclite system is controlled by a LabVIEW program running on a Mac, and the analysis of the video image is also done within LabVIEW. Sidebands in the image are used as an estimate of the background to give a background subtracted image. The background subtracted image is either fit with a 2-dimensional Gaussian plus a linear background function, or for a faster fit, the data is projected to give vertical and horizontal profiles and then a 1-dimensional Gaussian plus a linear background function is used in the fits. If the transverse profile is elliptical, the full 2-dimensional fit is useful to get the angle of any rotation that might exist.

The measured beam positions, sigmas and the calculated vertical and horizontal emittances are remotely accessible

via Acnet and is also logged into a circular buffer and less frequently into a permanent storage for Shot Data Analysis (SDA) [4].

PERFORMANCE

Calibration and Monitoring

Calibration of the Synclite system is important in getting accurate measures of the beam parameters. The distance scale, image resolution and any rotation in the system must be known. The scale and image resolution can be calculated and measured on the bench. The distance scale and any rotation of the system has also been measured *in situ* by producing closed-orbit 3-bumps. The beam is bumped vertically or horizontally by a calculated amount and the motion of the beam measured in Synclite. Figure 3 shows the data from such a beam study and Figure 4 shows for protons the measured versus calculated expected beam displacements.

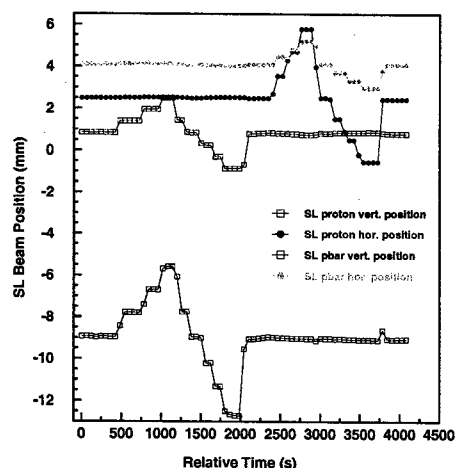


Figure 3: The horizontal and vertical locations of the proton and antiproton beams as measured by Synclite versus time, for the time period when the beams were bumped vertically then horizontally.

The beam bump study results showed that both the proton and antiproton Synclite systems are not rotated with respect to the Tevatron. The proton distance scale obtained by the beam bump study agrees with the expected scale by $\sim 10\%$, which is the expected uncertainty in the lattice functions. On the other hand the antiproton scale was found to be inconsistent.

The image resolution was checked by scraping the beam with a collimator and studying the beam image size as a function of intensity [5]. It was also studied by comparing the beam size as seen by Synclite to that measured in the Flying Wire system [6, 7]. The performance of the proton Synclite system is as expected. However, although the antiproton Synclite system is giving useful results, it has an

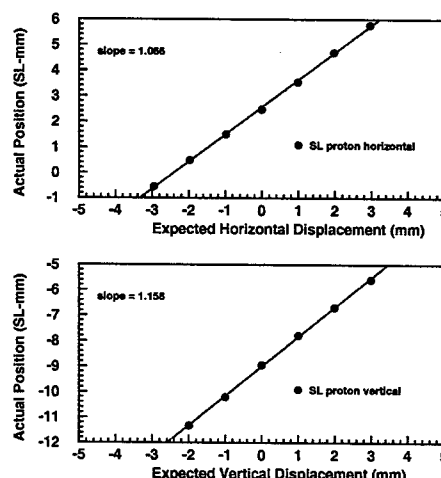


Figure 4: The horizontal and vertical proton beam displacements as measured by Synclite versus the calculated expected displacements.

unexpectedly large resolution, this together with the scale is still under study and must be resolved to improve the performance of the antiproton Synclite system.

Monitoring the status and results of the Synclite system is an important aspect of providing a reliable instrument. The status and results from Synclite are obtained via a Java program and displayed on a web page using an automatically run PERL script [8]. If the Synclite system is down or has incorrect settings, notification emails are sent in addition to a message on the status web page.

Long Range Beam-Beam Effects

The Synclite system can be used to study beam physics. For example one effect of long range beam-beam interactions can be seen in the Synclite measurements. The top plots in Figure 5 show the horizontal positions of all the 36 antiproton bunches averaged over various time periods after the start of a collider store. It can be seen that a 3-fold symmetry is seen where each train of 12 bunches is spread over about $40 \mu\text{m}$. This structure exists because the start of each train interacts with more protons than the end of the train. A similar 3-fold structure is seen in the proton horizontal positions but the 12 bunches of each train are spread over a much smaller range of about $5 \mu\text{m}$. This smaller effect is consistent with the approximately 8–10 times lower antiproton intensities compared to the proton intensities.

DC Beam in the Tevatron

It is known that beam can exist between beam bunches and in the beam abort gaps. Any DC beam is cleaned by the Tevatron Electron Lens (TEL) [9]. The Synclite system has been configured to allow automatic monitoring of any DC beam. A 670 ns gate width timed to look within a beam abort gap is used and the gain is increased by a factor

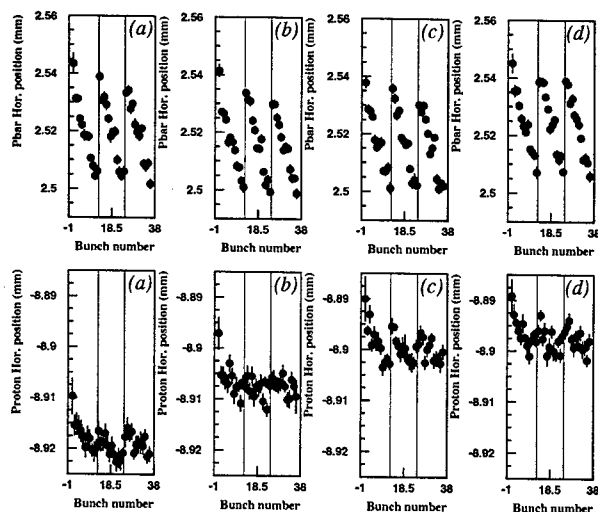


Figure 5: Horizontal positions of each of the 36 bunches for antiprotons (top) and protons (bottom), where (a, b, c, d) give the averaged positions for 0–20, 20–40, 40–60 and 60–80 minutes after the start of collisions for a collider store.

of about 22 by running the MCP in the image intensifier at much higher voltage. Also 100 images are summed to improve S/N since more noise appears when running at high MCP voltages. Typical projections of the background subtracted images are given in Figure 6.

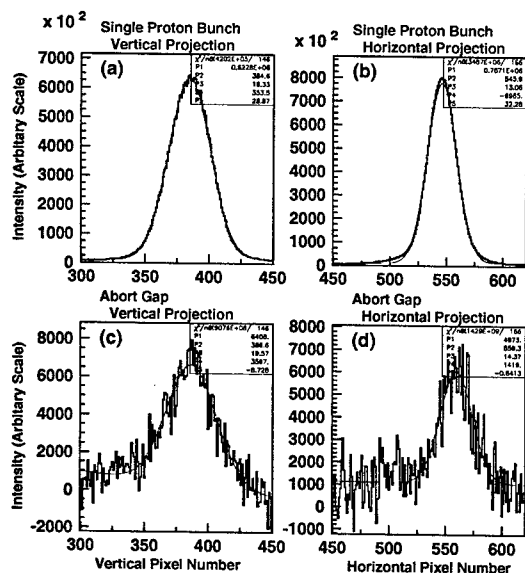


Figure 6: (a,b) Vertical and horizontal projections of the background subtracted image for a single 1.8×10^{11} proton bunch at normal MCP high voltage; (c,d) Vertical and horizontal projections of the background subtracted image for a 670 ns time interval in the beam abort gap. The projections are fit with a Gaussian signal and a linear background function.

With the TEL off, about 6×10^7 protons were observed within the 670 ns window. This is less than $\frac{1}{1000}$ th of the intensity of a single proton bunch. Assuming a uniform DC beam in the Tevatron, this translates to about 2×10^9 protons in total in the DC beam, or about 0.03% of the total number of protons in the 36 bunches. The transverse sigmas of the beam in the abort gap have large uncertainties due to poor S/N. The central location of the DC beam is found to be at the same vertical location as the normal bunches while the horizontal location is 1 mm closer to the Tevatron center. Work is being done to increase the gain and S/N.

CONCLUSIONS

Synclite provides a non-destructive method to measure the 2-dimensional transverse profiles of the high energy beam in the Tevatron. The system is still being calibrated but already interesting beam physics issues can be studied using this instrument.

Acknowledgments

We wish to thank S. Pordes and E. Lorman for their help and efforts on Synclite. We also want to thank P. Lebrun, S. Panacek, T. Bolshakov, K. Genser, A. Slaughter, A. Jansson, V. Shiltsev and the whole SDA team for providing help with the data analysis and easy access to the data.

REFERENCES

- [1] R. Coisson, "Angular-spectral distribution and polarization of synchrotron radiation from a 'short' magnet", *Phys. Rev. A* 20, 1979, pp.524-528.
- [2] A. A. Hahn and P. Hurh, "Results from a Prototype Beam Monitor in the Tevatron Using Synchrotron Light", in 1992 IEEE Particle Accelerator Conference, 1991, pp.1177-1179.
- [3] A. A. Hahn and P. Hurh, "Results from an Imaging Beam Monitor in the Tevatron Using Synchrotron Light", in 15th Int. Conf. on High Energy Accelerators, Ed. by J. Rossbach, Hamburg, Germany July 20-24 1992, pp.248-253, *Int. J. Mod. Phys. A (Proc. Suppl.)* 2A, 1993.
- [4] A. Slaughter *et al.*, "Store Data Analysis for Run II in the Fermilab Accelerator Complex", TPPB071, these proceedings.
- [5] A. Jansson *et al.*, "Collimator Scans to Measure Tevatron Emittance", Tevatron beam study report, Jan. 21, 2003, Beams-docdb-393.
- [6] W. Blokland *et al.*, "A new Flying Wire System for the Tevatron", PAC'97.
- [7] A. Slaughter *et al.*, "Tevatron Run II Luminosity, Emittance and Collision Point Size", TPPB070, these proceedings.
- [8] <http://home.fnal.gov/~cheung/synclite/>
- [9] X. Zhang *et al.*, "The Special Applications of Tevatron Electron Lens in Collider Operation", TPPB076, these proceedings.

MEASUREMENT OF PROTON AND ANTI-PROTON INTENSITIES IN THE TEVATRON COLLIDER*

S. Pordes, W. Blokland,[†] J. Crisp, B. Fellenz, R. Flora, A. Hahn, T. S. Meyer, A. Tollestrup, FNAL, Batavia, IL 60510, USA

Abstract

This paper describes the techniques used to measure the intensities of the proton (p) and anti-proton (\bar{p}) beams in the Tevatron collider. The systems provide simultaneous measurements of the intensity of the 36 proton and 36 anti-proton bunches and their longitudinal profiles.

INTRODUCTION

Accurate measurement of the intensity of the proton and the anti-proton beams is a basic requirement of the Tevatron instrumentation. The proton and anti-proton fluxes enter directly into a calculation of the luminosity provided to the experiments and the life-times of the different beams can give information on the mechanisms for beam loss. Since the proton and anti-proton fluxes enter into the luminosity with equal status, it is desirable to measure them with comparable relative precision even though the anti-proton intensity is typically only 10% of the proton intensity. A DCCT[1] provides a measure of the total current circulating in the machine but does not distinguish between proton and anti-proton contributions to this current. The individual bunch intensities are measured using a high bandwidth Resistive Wall-Current Monitor installed in the F11 section of the Tevatron where the arrival time of proton and anti-proton bunches is separated by 200 ns.

BASIC TECHNIQUE

The design and construction of the Resistive Wall-Current Monitor and its connections (cabling) to the outside world are described in detail in ref[2]. The essential features of the RWCM for our purposes are

- the RWCM has a calculated resistance of 1.288 ohms;
- the RWCM is transformer coupled with a low end cut-off at about 3 kHz and an upper limit at several GHz;
- the RWCM is connected to the measuring electronics in the outside world by 320 ns of 7/8 inch Andrews HeliaxTM cable.

Figure 1 shows a schematic of the two measurement systems attached to the Resistive Wall Current Monitor. One system, the F(ast) B(unch) I(ntegrator), integrates the RWCM output during gates corresponding to the beam passage times; it presently takes two turns of the Tevatron to acquire its data, making 18 bunch measurements and taking a baseline sample in each abort gap (21 measurements)

* work performed under DOE contract no. DE-AC002-76CH03000

[†] now at ORNL

each turn. Intensities are reported for both single-bucket and 5 bucket wide gates to give a measure of satellites around the main bunch. The other system, the S(ampled) B(unch) D(isplay), passes the RWCM signal to a 2GHz, 8 bit sampling oscilloscope[3]. A measurement consists of two full turns of data (42,000 samples), one sweep triggered by the proton marker and one triggered by the anti-proton marker: the resulting waveforms are analyzed to yield both the intensity and the longitudinal profile of each proton and anti-proton bunch. Because the anti-proton intensities are typically 10% or less of the proton intensities, both systems use separate channels for protons and anti-protons and set the anti-proton channel to have higher sensitivity; the FBI further uses separate electronics for the single and multiple bucket readings. The FBI can operate at a few hundred Hz; the SBD returns bunch intensities and longitudinal profiles at about 0.5 Hz, dominated by the oscilloscope readout time.

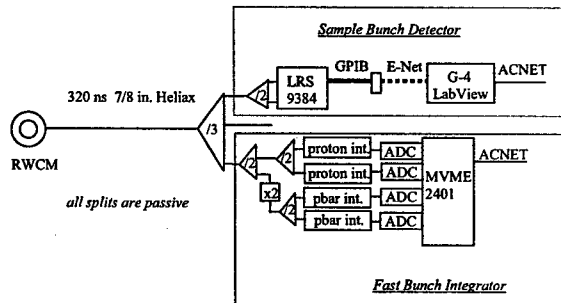


Figure 1: Schematic of FBI and SBD.

ISSUES

Cable Effects

Measurements of the cable[2] show an attenuation in db of $4.26\sqrt{f/\text{GHz}}$; this is consistent with the manufacturer data and a model where the frequency dependence is due to the skin effect. The accompanying dispersion of the RWCM signal along the 320 ns of cable is such that - almost independent of the beam shape - about 4.5% of the original signal arrives after the RF bucket containing the beam. The dispersion must also be accounted for when measuring the bunch-length.

Baseline Effects

Since the RWCM is transformer coupled, after a few turns, the net signal over a complete turn is zero. This

means that the output baseline shifts. The shift is proportional to the beam intensity and can be estimated by noting that the protons (the dominant current) produce signals in 36 of the 1113 RF buckets; the average 'unoccupied' bucket will have a 'signal' of opposite sign and of magnitude $\sim 3\%$ (36/1113) of the average proton bunch. For the protons, the baseline sampling thus produces an upward correction of about 3%. For the anti-protons, which as mentioned, are typically $\sim 10\%$ of the proton intensity, the baseline sampling is responsible for $\sim 30\%$ of the reported \bar{p} intensity.

CALIBRATION

There are two approaches available to calibrate the FBI and SBD - one is a quasi-absolute technique and one is based on comparison with the DCCT. The first involves taking the RWCM resistance as a given and applying a known pulse into the RWCM output cable to calibrate the FBI and SBD electronics. This is limited in principle by the accuracy of the pulser and requires transformer coupling and a proper simulation of the bunch structure and intensities to allow the baseline shift its full effect. Calibration using the DCCT as reference is based on the equation $DCCT = p_{true} + \bar{p}_{true} = PRWCM \times (1 + \frac{PRWCM}{PRWCM}) \times CAL$ where CAL is the calibration factor to be applied to the device looking at the RWCM signal. This approach requires no knowledge of the RWCM resistance and only the relative gains of the proton and anti-proton channels, not their absolute value. A small (few %) correction does have to be made for satellites and any other out of the bucket beam all of which is seen by the DCCT but not by the SBD or FBI.

F(ast) B(unch) I(ntegrator)

The FBI is used as a fast response system. The system calibration is harder to maintain in principle because 4 independent integrators are used to provide the single bucket, multi-bucket, proton and anti-proton measurements. The software to allow all measurements to be made on two integrators and to reduce the baseline issues by removing the amplifier in front of the anti-proton channel is in process. Figure 2 shows a comparison of the FBI and the SBD intensities recorded during a recent store. The plot is drawn such that the FBI and SBD should lie on top of each other - the agreement is quite good except for the anti-proton intensity at the beginning of the store. Examination of the FBI anti-proton baseline sample shows that it does not have the required proportionality to the total beam current probably because of some saturation in the electronics from the proton pulses and this may be responsible for the discrepancy. At present, the accuracy of the FBI is adequate for operations and we have concentrated on understanding the SBD as the device likely to give the more accurate measurement.

The S(ampled) B(unch) D(isplay)

Figure 3 shows one proton and one anti-proton bunch as recorded by the SBD. The darker trace is the proton channel,

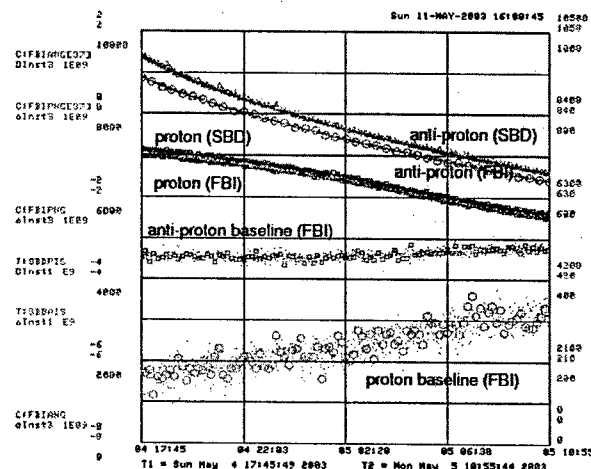


Figure 2: Comparison of FBI and SBD measurements

nel, the lighter trace is the anti-proton channel; the oscilloscope baseline is offset to be able to use the full dynamic range. The proton channel shows a small pulse (the anti-proton bunch) on the left and the proton bunch at the right; the anti-proton channel shows the anti-proton bunch at the left and the proton bunch, which saturates, at the right. The time displacement between a given bunch as seen by the two channels is due to the timing difference of the proton and anti-proton markers. The satellites on the proton bunch are clearly visible in the anti-proton channel, as is the dispersion on the tail.

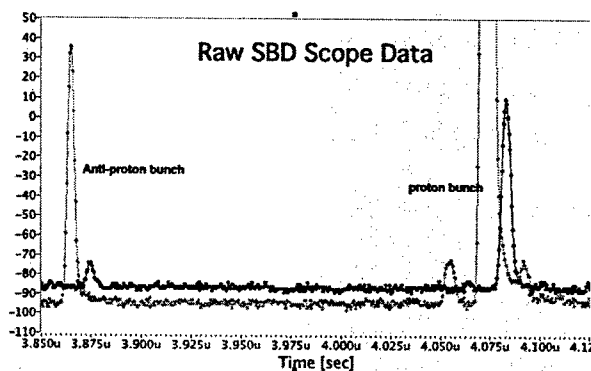


Figure 3: An SBD display of one proton and one anti-proton bunch

SBD Baseline Analysis

The intensity reported by the SBD is quite sensitive to the baseline determination - an error of 1 count in the baseline is about 4% in intensity. After some experimentation, a histogramming technique has been adopted where the data from a sweep are histogrammed and a parabola is fit through the most common datum and its neighbors on either side. A typical data set is shown in figure 4.

Unlike algorithms based on sampling parts of the turn where no beam is expected, this process is robust at all

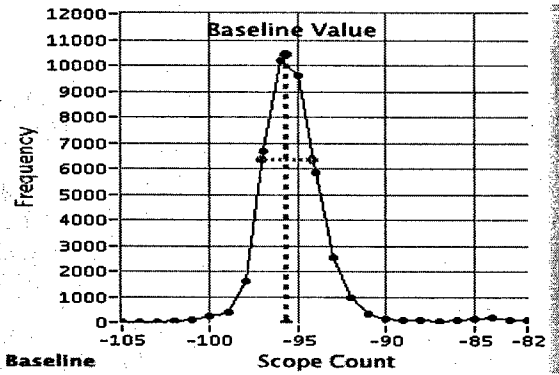


Figure 4: A baseline histogram showing the peak (the baseline) and the effective input noise

times including during cogging operations and the values it produces are good to a fraction of a count. The dispersive tail from the proton pulses tends to give a baseline which is slightly too high on the anti-proton channel; this contributes an $\sim 1\%$ underestimate of the \bar{p} intensity. A larger correction is due to the effect of the dispersion shifting part of the signal outside the RF bucket (see figure 5).

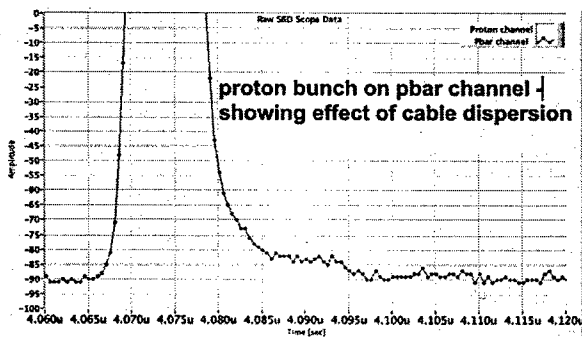


Figure 5: A proton bunch as seen on the anti-proton channel; note the dispersion on the trailing edge

Dispersion Compensation

The SBD was originally designed to provide a measurement of the longitudinal profile and while the effect of the dispersion on the intensity measurement could be corrected by a fudge factor, there is considerable interest in recovering the true input signal. The transfer function of the cable is linear and causal which means that (within the bandwidth of the measurement) it is in principle possible to recover the original signal provided one knows the transfer function. A compensating software filter has been developed based on the cable model - for details see ref[4] - and is applied to the data read from the scope. The filter as currently deployed has 77 taps corresponding to two RF buckets sampled at 2GHz and is applied to each input datum (starting from the 78th). Figure 6 shows the FIR filter - 'now' is at the right.

The form of the FIR can be understood in that any portion of the output at a given time is due to the signal at that time plus some fraction of earlier components of the signal

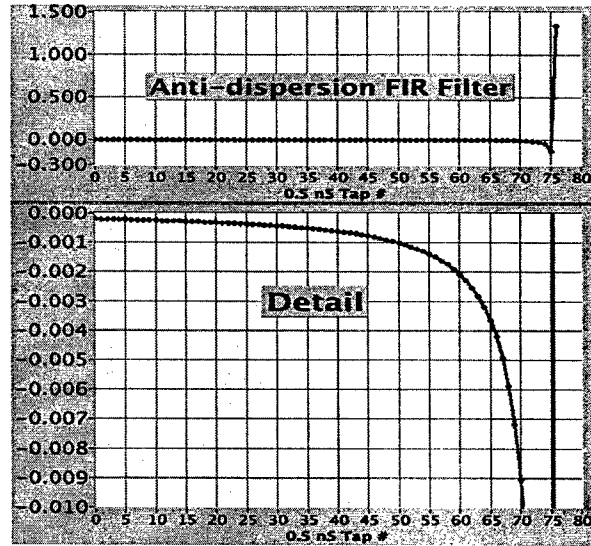


Figure 6: The dispersion compensation filter.

which have dispersed into the present; the FIR enhances the immediate portion and subtracts appropriate fractions of the earlier components. Figure 7 shows the effect on an anti-proton bunch. The performance is quite satisfactory.

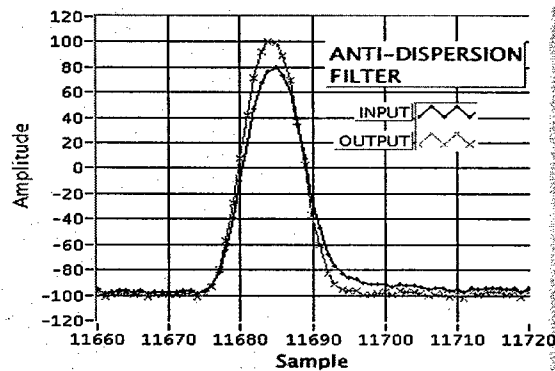


Figure 7: A bunch before and after the FIR filter

SUMMARY

Two systems are available at the Tevatron to measure individual proton and anti-proton bunch intensities with an accuracy of a few percent. A software FIR filter to compensate for cable dispersion has been implemented in the 2 GHz sampling system and recovers the input signal for both intensity and longitudinal profile measurements.

REFERENCES

- [1] R.C. Webber, AIP Conf. Proc. 333, Beam Inst. Workshop, Vancouver, 3-23 (1994).
- [2] J. Crisp and B. Fellenz, Fermilab TM-2208, 2003
- [3] Lecroy Research Systems, 9384
- [4] A. Tollestrup, FNAL Beams Document Database Note 601 (2003).

DIGITAL DOWN CONVERSION TECHNOLOGY FOR TEVATRON BEAM LINE TUNER AT FNAL

W. Schappert, E. Lorman, M. Ross[†], V. Scarpine, J. Sebek[†], T. Straumann[†]

FNAL, Batavia, IL 60510

[†]SLAC, Stanford, CA 94309

Abstract

Fermilab is presently in Run II collider operations and is developing instrumentation to improve luminosity. Improving the orbit matching between accelerator components using a Beam Line Tuner (BLT) can improve the luminosity. Digital Down Conversion (DDC) has been proposed as a method for making more accurate beam position measurements. Fermilab has implemented a BLT system using a DDC technique to measure orbit oscillations during injections from the Main Injector to the Tevatron. The output of a fast ADC is down-converted and filtered in software. The system measures the x and y positions, the intensity, and the time of arrival for each proton or antiproton bunch, on a turn-by-turn basis, during the first 1024 turns immediately following injection. We present results showing position, intensity, and time of arrival for both injected and coasting beam. Initial results indicate a position resolution of ~20 to 40 microns and a phase resolution of ~25 ps.

Introduction

In order to preserve transverse emittance, it is important to match the ideal beam trajectory between synchrotron machines [1]. The Tevatron BLT is used to measure orbit oscillations during injections of protons and antiprotons from the Main Injector into the Tevatron. Digital Down Conversion (DDC) has been proposed as a method for making more accurate beam position measurements [2][3]. Fermilab has implemented a prototype BLT system using a DDC technique in software to measure orbit oscillations during injections.

The DDC BLT system measures the x and y positions, the intensity, and the time of arrival for each proton or antiproton bunch, on a turn-by-turn basis, during the first 1024 turns immediately following injection. Antiprotons are transferred into the Tevatron in 9 injections of 4 bunches each while protons are transferred in 36 single bunch injections.

The BLT System

The BLT consists of two pairs (horizontal and vertical) of bi-directional strip-line pickups installed in the Tevatron F0 interaction region. Each plate of a strip-line is 1.0 m long by 60 wide, mounted at a distance of 41 mm from the mechanical center of the beam pipe. Each strip-

line has a measured sensitivity of 0.65 db/mm. As the beam passes through the BLT it induces capacitive signals on the plates. The difference between the signals on the plates is sensitive to the position of the beam. The time of arrival of the pulses is sensitive to longitudinal oscillations of the beam. Signal cables are connected to both ends of each pickup to measure the bi-directional beams. Protons induce signals on the downstream cables while antiprotons induce signals on the upstream end. The strip-lines have ~30-db directionality and the proton signal is much larger than the antiproton signal, so some of the proton signal is seen on the antiproton side of the strip-line. Since the proton and antiproton signals are separated in time by about 190 ns, the proton signal does not contaminate the antiproton signals.

Analog Processing

The plate signals are transported from the accelerator to the BLT electronics, amplified and digitized using a 100 MHz 12-bit Struck Model SIS3300 digitizer. The digitizer is clocked with a 106 MHz TTL level square wave synchronized to the 53 MHz Tevatron RF. The digitizers are triggered prior to the arrival of each bunch signal by an accelerator beam event signal. Thirty-two samples are collected for each bunch on each turn for the first 1024 turns.

The 19 ns doublets produced by bunches passing between the pickups are too fast to be directly digitized using a 100 MHz ADC. To adequately sample the waveform from the strip-lines, the pulse is stretched in time using a ringing filter. To avoid systematic effects, the ringing must damp before the next bunch arrives, and the impulse response of the filters on the A and B channels must also be well matched.

Digital Signal Processing

The sampled ringing waveform is frequency-shifted to base-band by multiplying by a complex exponential oscillating at the resonant frequency of the pulse-stretching filters. The base-band conversion effectively rectifies the pulse along some direction in the complex plane. The real part contains the rectified waveform while the imaginary part contains a rapidly oscillating waveform that will filter to zero. The complex envelope of the signal could be extracted by low-pass filtering the base-banded waveform.

Instead of low-pass filtering, the base-banded waveform is matched-filtering, i.e. the waveform is correlated with a reference signal corresponding to the envelope of the expected signal. The peak amplitude of the output of the matched-filter provides the optimal linear estimate of the amplitude of a known signal in the presence of noise. The reference signal for the matched-filter is shown in Figure 1. The real and imaginary parts and the magnitude of the simulated signal following matched-filtering are shown in Figure 2.

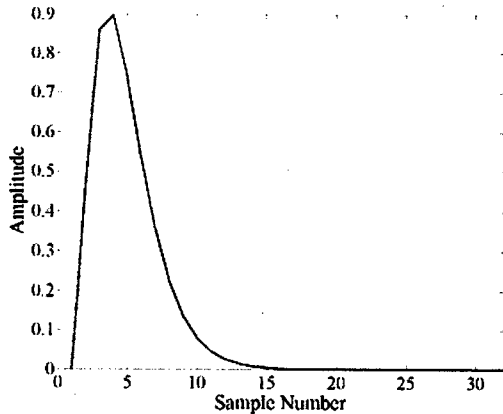


Figure 1. Matched-filter reference waveform.

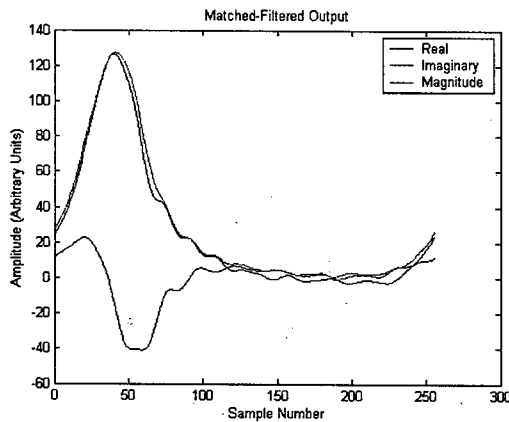


Figure 2. Output of the Matched-Filter.

The transverse position of the beam is estimated by taking the ratio of the difference between the peak amplitudes of the processed signals from the A and B plates divided by the sum of the peak amplitudes:

$$x = 26.7 \text{ mm} \frac{A_{Peak} - B_{Peak}}{A_{Peak} + B_{Peak}}$$

The conversion constant of 26.7 mm has been determined prior to the installation of the strip-lines by scanning a pulsed wire across the aperture.

The phase of the matched-filtered signal contains information about the time of arrival of the doublet relative to the trigger. With each successive pulse, the time of arrival of the pulse relative to the trigger is systematically delayed. As the time of arrival changes, the

power in the signal moves from the real component into the imaginary component and back again. The phase of the peak of the filtered signal provides an estimate of the time of arrival of the doublet. Each of the four pickups in the BLT provides an independent measurement of the time of arrival of the bunch.

The relative time of arrival of the pulse measured by each pickup is estimated by dividing the phase of the peak amplitude by 2 times the resonant frequency of the pulse stretching filters:

$$t = \frac{1}{2 f_{Filter}} \tan^{-1} \frac{\text{Im } A_{Peak}}{\text{Re } A_{Peak}}$$

An overall time of arrival for each bunch is obtained by averaging the time of arrival measured by each of the four pickups.

Performance

Figure 3 and Figure 4 show the horizontal, vertical positions for the four antiproton bunches of as a function of turn at injection. Both the horizontal and vertical positions show rapid variations characteristic of betatron oscillations. The horizontal position also shows the slower variations associated with synchrotron oscillations.

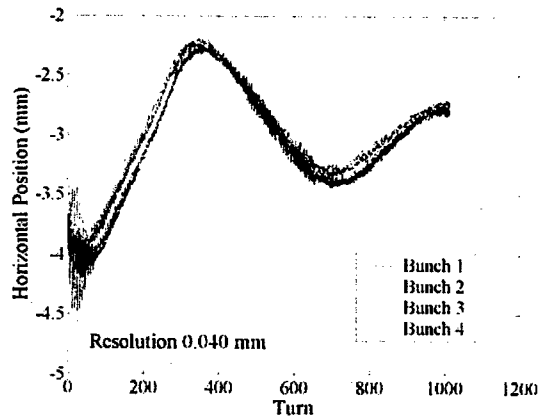


Figure 3. Horizontal positions following injection.

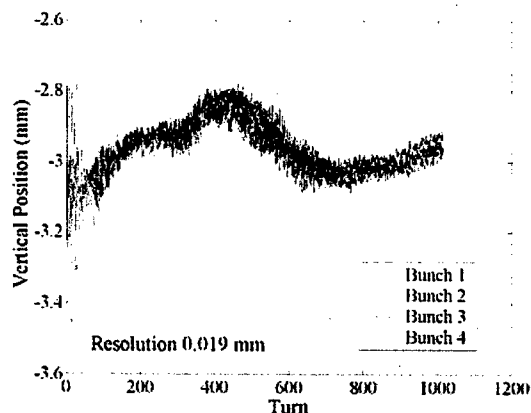


Figure 4. Vertical positions following injection.

Fourier transforms of the horizontal and vertical position measurements are shown in Figure 5 and Figure 6 respectively. Both distributions show clear peaks associated with the tunes of the Tevatron. The noise floor of the Fourier transform provides a model-independent estimate of the position resolution of the measurement. The horizontal and vertical resolutions estimated in this way are 0.040 mm and 0.019 mm respectively.

Figure 7 shows the time of arrival for each of the four antiproton bunches calculated from the phase of the processed signals. For each bunch, the time of arrival has been calculated by averaging the time determined by each the four plates (Horizontal A and B, and Vertical A and B). The noise floor of frequency spectrum of this time series corresponds to a resolution of ~ 25 ps.

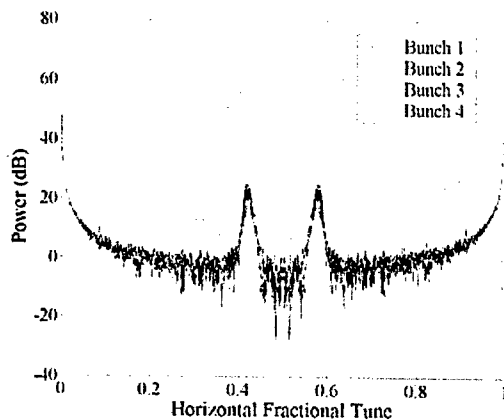


Figure 5. Horizontal tunes at injection.

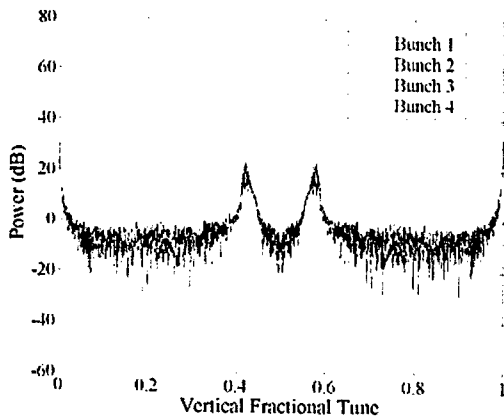


Figure 6. Vertical tunes at injection.

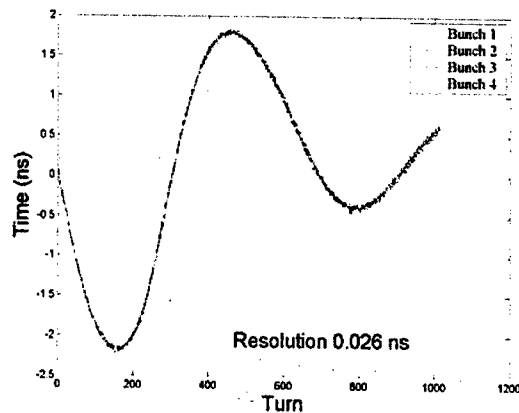


Figure 7. Relative time-of-arrival following injection.

Summary

We have used digital signal processing to measure the orbit oscillations during injections from the Main Injector to the Tevatron. The system measures the x and y positions, the intensity, and the time of arrival for each proton or antiproton bunch, on a turn-by-turn basis, during the first 1024 turns immediately following injection. We are able to measure the transverse position of the beam to a precision of ~ 20 to 40 microns per turn. We are able to measure the time of arrival of the bunch to a precision of ~ 25 ps per turn.

Acknowledgements

The authors acknowledge the support of J. Crisp (FNAL).

References

- [1] D. A. Edwards and M. J. Syphers, *An Introduction to the Physics of High Energy Accelerators*, John Wiley and Sons (1993), pp 221-238.
- [2] G. Vismara, "Signal Processing for Beam Position Monitors" AIP Conference Proceedings 546 (2000) 36.
- [3] R. Ursic, "Digital Receivers Offer New Solutions for Beam Instrumentation" Proceedings of the 1999 Particle Accelerator Conference (1999) 2253.

MEASUREMENTS OF THE LONGITUDINAL AND TRANSVERSE BEAM LOSS AT THE TEVATRON

A. V. Tollestrup, M. E. Binkley, B. M. Hanna, V. Lebedev, R. Moore, V. Shiltsev,
R. Tesarek, R. Vidal., FNAL, Batavia, IL 60510, USA

Abstract

Measurements of the transverse and longitudinal beam losses during a Tevatron store will be presented. The measurements utilize scintillation counters to monitor the nuclear interactions of the 1 TeV halo particles with a scraper that is located near the beam. If the particles are in time with the primary bunches, they are assumed to come from transverse perturbations inducing large betatron oscillations. Particles lost longitudinally drift around the ring due to synchrotron radiation and become asynchronous with respect to the bunches. A pulsed electron lens is then used to induce large betatron oscillations that extract these particles onto the scraper. The resulting nuclear interactions in the scraper are recorded by a gated scintillating counter system. The counting rates from the two channels provide an online measurement of the two types of beam loss. Known beam loss due to interactions at the IP and to nuclear collisions in the residual gas can be subtracted which then exposes the underlying losses from longitudinal and transverse instabilities.

OVERVIEW

When the Tevatron is in the colliding mode, the luminosity decreases over time due to the loss of particles from the beams or due to emittance blow up of the bunches[1]. For instance, the collision of protons and pbars removes particles and is the main source of pbar loss. Interaction of the beam particles with the residual gas in the vacuum chamber can both remove particles by nuclear collisions and scatter particles thru coulomb scattering. Intra beam scattering will increase both the longitudinal and transverse emittances and can cause particle loss from the bucket. And finally beam-beam interaction at the points where the bunches come near each other on their separate helices can cause losses. The instrumentation used to detect and monitor these beam losses is described below. Methods for monitoring the emittance increase are described elsewhere [2]

Current Monitoring

The total DC beam in the machine is monitored by a high precision current transformer, DCT, which in a typical store measures a total beam of about 1 E13 particles with a digitizing error of 1.25 E9 particles and is used to check the calibration of other instruments. There are 36 proton and 36 par bunches in the machine and their separate intensities are measured by resistive wall current monitor, SBD, described elsewhere in these proceedings

[3]. The absolute calibration of the SBD is checked against the DCT.

Once the intensities of the proton and pbar beams are known as a function of time, they can be differentiated to give the particle loss per second. A plot showing the loss rate of p current in Store 2424 is shown as the solid curve in Fig. 1.

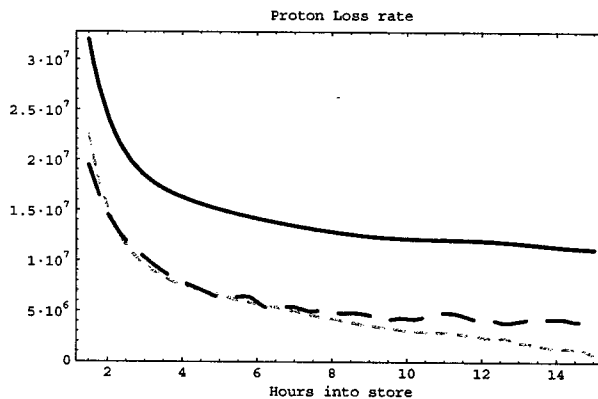


Fig. 1 Loss rate in protons/sec. vs. time in hours near the start of Store 2424. The solid curve is the total proton loss rate. The dotted curve is the loss rate after subtracting the losses due to luminosity, diffusion from the RF bucket, and collisions with the residual gas. The dashed curve is 25 times the E0LTOT counter rate.

Nuclear Interactions in the Vacuum Chamber Gas

The simplest loss to calculate is that due to nuclear interactions in the vacuum chamber. The measurement is made with a small emittance proton beam injected onto the central orbit and accelerated to 980 GeV/c. All loss mechanisms under these conditions are calculated to be small except for the nuclear interactions. The life time measured under these conditions is between 600 and 1000 hours and is a upper limit on the loss rate due to residual gas. The limited accuracy is a reflection of the limited time spent on runs of this type. In what follows we will use 600 hours.

Since the total cross section is known for the various elements, it is possible to relate gas concentration to lifetime. Table 1 gives this calculated relation between residual pressure (room temperature) and gas type for a fixed life time of 1000 hours using cross sections from Drozhdin [4] and making a small correction for coherent scattering at angles so small that they are not intercepted by the collimators. It is interesting to note that except for He there is little A dependence as the effect of Argon being monatomic is nearly cancelled by the cross section

increase with A. The gas composition in the Tevatron can be measured in the warm regions, but is unknown inside the magnets which are at liquid He temperature. Assuming the gas is some mixture of the three heavy gasses, the 600 hour lifetime corresponds to pressure of $5 \cdot 10^{-9}$ torr (room temperature equivalent).

Table 1

Gas	He	N ₂	O ₂	Ar
Pressure, Torr	$1.4 \cdot 10^{-9}$	$3.19 \cdot 10^{-10}$	$2.92 \cdot 10^{-10}$	$3.17 \cdot 10^{-10}$

The second effect of residual gas, which is proportional to Z^2 , is to increase the emittance of the beam by Coulomb scattering. This effect is minimized by making lifetime measurements at 980 GeV/c.

Transverse Losses

Losses in the transverse direction (called transverse losses in this paper) arise from particle betatron amplitude increasing to the point that it exceeds the machine aperture. In order to remove beam halo, there is a complex system of scrapers [5] in the machine that scrape in both the vertical and horizontal direction. A scintillation counter, E0LTOT that observes nuclear interactions of protons with the innermost scraper has been installed. This scraper is positioned at the start of each store to be at the edge of the circulating beam, and thus any subsequent growth of the transverse size will be reflected in the interaction rate increasing as recorded by the scintillation counter. The counter is ungated and records the total rate of protons hitting the scraper. Most of the lost protons are in coincidence with the 36 bunches (see below) and thus this counter primarily monitors the transverse loss rate and it correlates well with the background observed in the CDF and D0 detectors. A similar arrangement for the pbars exists, but uses background counters at CDF that are gated to be sensitive to particles arriving from the pbar direction. Neither of these systems is an absolute monitor of the loss rate, and they are only roughly calibrated.

Longitudinal Losses

Losses in the longitudinal direction (losses from the RF bucket) can arise from intrabeam scattering and from noise on the RF voltage [6] which excites synchrotron oscillations. At the end of acceleration, the injected beam is well confined inside of a phase space ellipse of 4 eV-sec whereas the RF bucket area is about 11 eV-sec. As the time duration of the store increases, stochastic processes cause the bunch length to grow and finally some particles cross the separatrix. At 980 GeV/c, a free proton loses about 9.5 eV / turn and slowly spirals inward until it hits the collimator in about 1000 seconds. As it drifts inward, it also drifts around the ring and thus losses from the bucket generate a ring of charge in the machine whose total intensity is a function of the distance between the edge of the bucket and the nearest collimator. Conversely, the proton and pbar bunch structures consist

of 36 bunches arranged in three groups of 12 equally spaced by 21 RF buckets and the three groups spaced by 140 buckets. These larger gaps are used for injection and extraction of the beam.

Early in the commissioning, it was found that a few E9 drifting protons could be stored in the machine in this manner. Since they are non synchronous, they were not handled properly by the abort system and a significant fraction would reach the SC dipoles and cause a quench. An electron lens system [7], TEL, is used to limit the accumulation of protons lost from the bucket. It is gated on in the abort gaps and causes large betatron oscillations to develop for any protons passing by. These protons in a few turns develop a large enough amplitude to be intercepted by the collimator and are detected by the E0LTOT Scintillation counter. A second output from this counter is gated in coincidence with the abort gaps passage and thus measures the intensity of the protons that are in the abort gaps.

A histogram of the time distribution of counts relative to a turn marker for the E0LTOT counter is shown in Fig. 2. The transverse losses in coincidence with the bunches are clearly seen, and in the middle of the abort gap one sees the effect of the TEL cleaning out protons. The 18.8 ns RF structure is seen because of the radial change due to the spiraling particles drifting in and out of phase with the RF voltage.

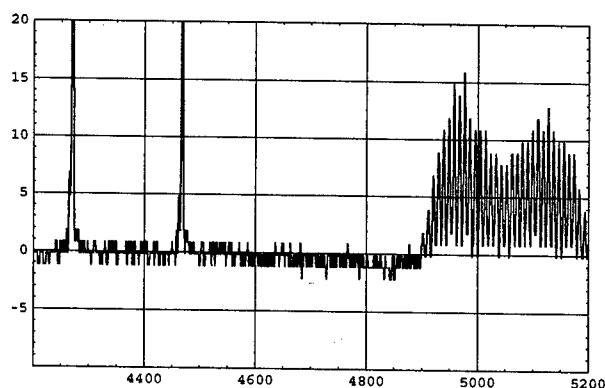


Figure 2. A histogram of the counts in the E0LTOT counter. The time bins are 2 ns and only a fraction of a turn is shown. To the left are two proton bunches and on the right are the counts caused by the TEL extracting protons that have drifted into the abort gap.

The counting rate in the abort gap can be calibrated so that it gives an online measurement of the bucket losses. The procedure is to measure the slope of the DCT output which is proportional to the total charge loss in the machine. The TEL is then switched off. This removes the mechanism by which protons lost from the bucket are removed from the machine. They are still lost from the bucket, but they continue to circulate and so are measured by the DCT. The change in slope of the DCT output then measures the RF bucket loss and can be used to calibrate the counter.

Results

Fig. 3 shows a graphical summary of these measurements on a single store, 2424. The luminosity loss is shown and calculated from the L measured at CDF and D0. The loss due to gas in the vacuum chamber is obtained using a 600 hour lifetime and should be considered an upper limit. The losses from the RF bucket are given by the E0LTOT counter gated on the abort gap and are very small at the beginning as the protons are very well contained in the bucket. As the run progresses the longitudinal emittance grows and protons start to diffuse out of the bucket. The three losses just mentioned do not add up to the total losses shown in Figure 1 as a dotted curve. The difference between this sum and the total losses represent transverse losses from all causes and as such they should be measured by the E0LTOT counter. The rate from this counter scaled by 25 is shown as the dashed curve in Fig 1. The agreement in shape of the two curves suggests that this interpretation is correct.

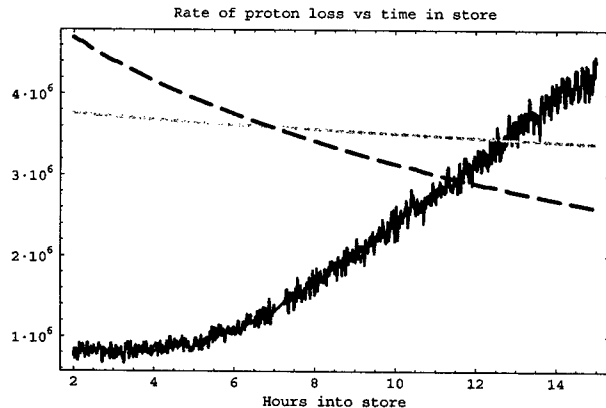


Figure 3. The proton loss rate in store 2424. The dotted curve is due to residual gas losses. The dashed curve is calculated from the measured luminosity at CDF and D0. The curve increasing to the right is obtained from the measured abort gap losses.

Although the accuracy of these measurements is not high, they do furnish on line information and guidance for each store and are also recorded in a data base for later detailed analysis. They provide a good monitor of the various loss mechanisms in the machine and have helped elucidate the physical process occurring in the machine.

The pbar behavior is interesting in contrast. The residual gas interactions and other loss mechanisms seem to be small. A loss plot for the pbars is shown in Fig. 4. The main loss is from the pbar-p interactions. There is a slight error in the absolute values used for some of the constants that result in the sum being greater than the total pbar loss rate. In any case, it is apparent that losses in the pbar bunches are primarily due to the luminosity. One method of increasing the luminosity is to increase the pbar bunch intensity, and so behavior similar to that observed in the proton case can be anticipated.

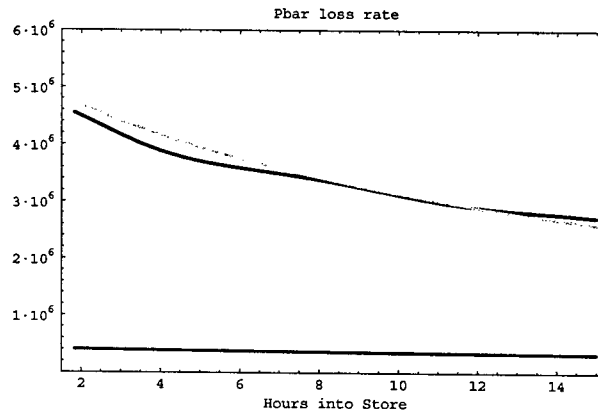


Figure 4. The top black curve is the total pbar loss rate. The top green/grey curve represents the loss due to pbar-p interactions, and the bottom curve is loss in the residual gas.

Although the accuracy of these measurements is not high, they do furnish on line information and guidance for each store and are also recorded in a data base for later detailed analysis. They do provide a good monitor of the various loss mechanisms in the machine and have helped elucidate the physical process occurring in the machine.

REFERENCES

1. P. Lebrun, et al, Observations on the Luminosity Lifetimes, emittance growth factors and Intra-Beam Scattering at the Tevatron, PAC 2003 paper TPPB067
2. H.W.K.Cheung, et al, "Performance of a Beam Monitor in the Fermilab Tevatron Using Synchrotron Light" PAC 2003, paper WPPB036
3. S. Pordes et al, "Measurement of Proton and Antiproton Beam Intensities in the Tevatron" PAC 2003 paper WPPB038
4. A.I. Drozhdin, et al, "Backgrounds in the Tevatron Collider Detectors due to Nuclear Elastic Beam-Gas Scattering", PAC 2003 paper TPPB056
5. D. Still, et al, "The Tevatron Halo Removal Collimator Systems PAC 2003 paper FPAB033.
6. J. Steimel et al, "Effects of RF noise on the longitudinal emittance growth in Tevatron" PAC 2003 paper MOPA008
7. X. Zhang, et al, "The Special Applications of Tevatron Electron Lens in Collider Operation", PAC 2003 paper TPPB076

This work was supported under US DOE Contract DE-AC02-76CH03000

$$\frac{R}{Q} = \frac{4\omega_r \mu A^2 \alpha_E^2}{(1 - 2\alpha_E(1 + Q)A^2)^2 + (1 - 2\alpha_E A^2)^2} \quad (6)$$

where ω_r and Q_0 are the resonant angular frequencies and the quality factor of the TE₁₁₁ mode; α_E is the electrical polarizability of the single slot and the A coefficient is given by the following integral:

$$A = \frac{\omega_r L \tilde{J}_1(b)}{b\pi c} \left[\int_0^L \frac{L\pi}{2} \left(k_i^2(\tilde{J}_1)^2 r + \frac{(\tilde{J}_1')^2}{r} + \frac{k_i^4 L^2}{\pi^2} (\tilde{J}_1')^2 r \right) dr \right]^{\frac{1}{2}} \quad (7)$$

with $\tilde{J}_1(r) = J_1(k_r r) - Y_1(k_r r) J_1'(k_r b) / Y_1'(k_r b)$, the prime denote the total derivative with respect to the argument and $k_i = \sqrt{(\omega_r/c)^2 - (\pi/L)^2}$.

Considering the prototype dimensions, one obtains the values of ω_r , Q_0 and R/Q reported in Table 2 (first column).

The value of the normalized power $P_{th}^{(0)} / Q_0 \tilde{I}_n^2$ as a function of r_0 for $\phi_1 = 0$ is plotted in Fig. 2 and compared with the simulation and measurement results (described in the next section). In Fig. 3 the same quantity is plotted as a function of ϕ_1 for $r_0 = 0.6$ mm.

Table 2: theory, simulations and measurements results

	THEORY	HFSS	MEAS
ω_r [GHz]	3.78	3.74	3.74 (tunable)
Q_0	9600	9100	3500
R/Q [mΩ]	36	31	39

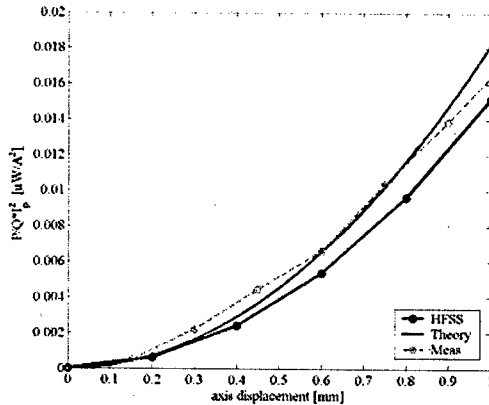


Figure 2: $P^{(0)} / Q_0 \tilde{I}_n^2$ as a function of r_0 for $\phi_0 = 0$.

3 SIMULATION RESULTS

To compare the analytical results with the numerical simulations, we have studied the coupling impedance of the cavity for the TE₁₁₁ mode as a function of the transverse displacement r_0 and ϕ_1 . We have, therefore, calculated the longitudinal shunt impedance of the mode (R_s) for different axial positions, using the Eigenmode Solver of HFSS.

The HFSS model is shown in Fig. 4 with the obtained E field lines. It is only 1/8 of the structure with proper

magnetic and electric boundary conditions on the symmetry planes. The average dissipated power in the cavity corresponding to the TE₁₁₁ mode is given by:

$$P_{Sim}^{(0)} = \frac{1}{2} R_s (\phi_1, r_0) \tilde{I}_n^2 \quad (8)$$

The value of $P_{Sim}^{(0)} / Q_0 \tilde{I}_n^2$ is plotted in Figs. 2-3 and compared with the analytical and measurement results. From the previous plot it is possible to verify that it is possible to write the eq. (8) in the form:

$$P_{Sim}^{(0)} \cong \frac{1}{2} \frac{R}{Q} Q_0 \cos(\phi_1)^2 r_0^2 \tilde{I}_n^2 \quad (9)$$

The values of ω_r , Q_0 and R/Q obtained by the simulations are reported in Table 2 (second column).

If the cavity is coupled through a small probe to an external load, then the average dissipated power in the system is still given by eq. (5) or (9) but with Q_0 replaced by the loaded Q_L . The average power dissipated in the load ($P_{Ext}^{(0)}$) is related to the power dissipated in the cavity by:

$$P_{Ext}^{(0)} = P_{cav}^{(0)} \beta / (1 + \beta) \quad (10)$$

where β is the coupling coefficients between the probe and the cavity mode TE₁₁₁ and it can be obtained from reflection measurement at the probe port.

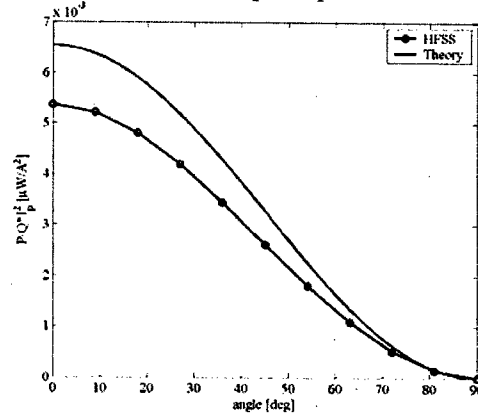


Figure 3: $P^{(0)} / Q_0 \tilde{I}_n^2$ as a function of ϕ_1 for $r_0 = 0.6$ mm.

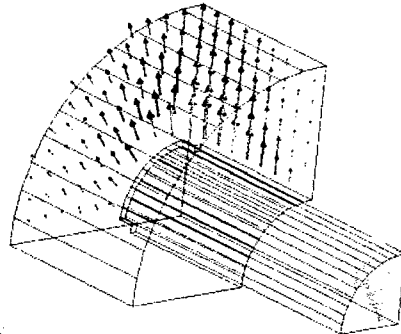


Figure 4: HFSS model with E field lines.

4 PROTOTYPE MEASUREMENTS

Wire measurements have been performed on the aluminum prototype shown on Fig. 5. An antenna probes the signal in the cavity.

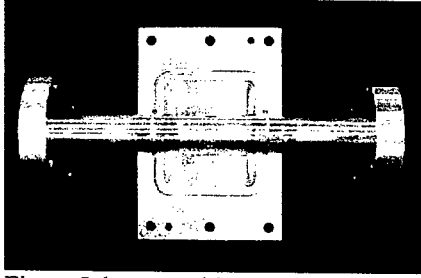


Figure 5: beam position monitor prototype.

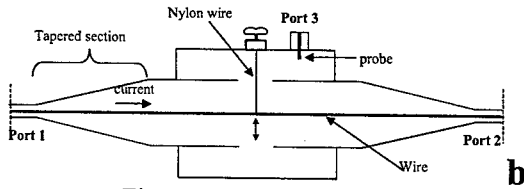
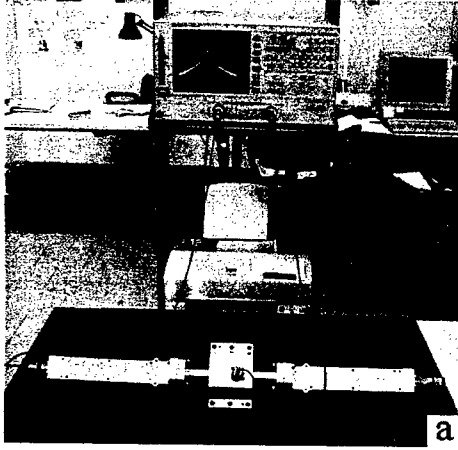


Figure 6: measurement setup

The measurements setup is shown Fig. 6a and schematically represented in Fig 6b. The wire has a radius of 1.5 mm. In order to minimize reflections at the ports 1 and 2 we have inserted two tapered sections that match the 50 Ω impedance of the Network Analyzer with the $\sim 114 \Omega$ impedance of the wire in the beam pipe. To excite the dipolar mode TE_{111} the wire inside the beam pipe has been properly displaced from the axis of the beam pipe. To this purpose, a thin nylon wire has been connected to the wire in order to displace it from the beam pipe axis in a controlled way and to excite the polarity ϕ_0 . The measured transmission coefficient S_{21} and S_{31} are shown in Fig. 7 for a displacement of the wire of ~ 1.5 mm.

The average dissipated power in the cavity is given by:

$$P_{cav}^{(0)} = P_{Ext}^{(0)} \frac{(1+\beta)}{\beta} \cong \frac{1}{2} Z_c \frac{|S_{31}(\omega_r)|^2 (1+\beta)}{|S_{21}(\omega_r)|^2 \beta} \tilde{I}_n^2 \quad (11)$$

The plot of $P_{cav}^{(0)} / Q \tilde{I}_p^2$ as a function of r_0 is reported in Fig. 2. It is clear that $P_{cav}^{(0)}$ can be written in the form (5) or (9) and the equivalent R/Q is reported in Table 2. The Q factor of the resonant mode is lower than the theoretical one because of RF losses in the mechanical contacts. Similar considerations than those developed in [6] can be

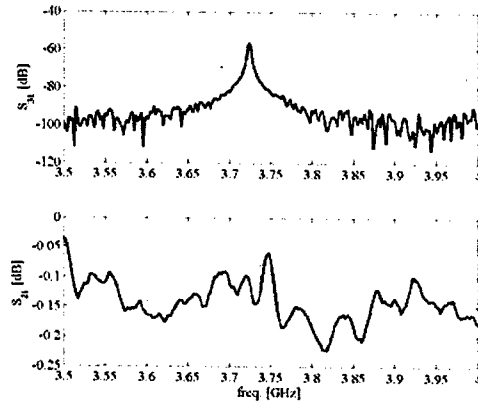
done from the point of view of the induced errors in the measurement setup.

By the system of equations (4) it is possible to calculate the position of the bunches in the beam pipe when the b.p.m is inserted in the accelerator, by the formulae:

$$\begin{cases} r_0 = \frac{\sqrt{P_{Ext}^{(\pi/2)} / P + P_{Ext}^{(0)} / P}}{\tilde{I}_n} \\ \phi_1 = \pm \arctan \left(\sqrt{\frac{P_{Ext}^{(\pi/2)}}{P_{Ext}^{(0)}}} \right) \pm \pi \end{cases} \quad (12)$$

where the calibration coefficient \underline{P} is given by:

$$\underline{P} = \frac{1}{2} Z_c \frac{|S_{31}(\omega_r)|^2}{|S_{21}(\omega_r)|^2} \frac{1}{r_0^2} \quad (13)$$


 Figure 7: measured transmission coefficients (S_{12} , S_{31}).

5 CONCLUSIONS

A novel bunch position monitor has been described. Measurements on an aluminium prototype have been compared to the theoretical and numerical expectations of the power dissipated by the first dipolar mode in the cavity. The compare shows a good agreement between theory and simulations especially considering the mechanical differences between the prototype and the ideal structure. These results confirm the potential application of this device as a beam position monitor. The very low coupling impedance of the device and the possibility of calibration by simple wire measurements make the device hopefully usable in the accelerator machines.

6 REFERENCES

- [1] S. De Santis and L. Palumbo, *Phys. Rev. E*, vol 55, pp. 2052-2055, 1997.
- [2] C. D'Alessio, *Tesi di Laurea*, Univ. "La Sapienza", 2002.
- [3] <http://www.ansoft.com>
- [4] F. Caspers, in *Handbook of Accelerator physics and engineering*, pp. 570-574, World Scientific, 1999.
- [5] A. Hofmann, "Beam Instabilities", CERN 95-06, Geneva, 1995.
- [6] D. Alesini et al., *Proc. of EPAC 2002*, pp. 1834-1836, Paris

IMPROVED SR EXTRACTION CHAMBER FOR KEKB LER SR MONITOR

J.W. Flanagan, S. Hiramatsu, H. Ikeda, K. Kanazawa and T. Mitsuhashi
KEK, Oho 1-1, Tsukuba, Ibaraki 305-0801 Japan

Abstract

We have recently replaced the synchrotron light extraction chamber for the KEKB Low Energy Ring (LER) SR monitor. The beam pipe was changed to copper to minimize resistive-wall heating, and the optical apertures were made as small as permitted by light extraction requirements in order to reduce HOM power leakage. The new chamber shows almost none of the heating problems of the old chamber, and previous problems with the orientation of the extraction mirror changing due to heat expansion of the beam pipe have been essentially eliminated. The design and performance of the new chamber are presented.

HISTORY OF OLD CHAMBER

The original LER synchrotron radiation extraction chamber was installed in the ring in 1998 prior to the initial commissioning. The design employs a cylindrical vacuum chamber through which runs a segment of beam pipe.[1] Both chamber and beam pipe are made of stainless steel. The water-cooled beryllium extraction mirror is mounted in a notch in one side of the beam pipe at a 45-degree angle. RF contact fingers are used to mate the mirror to the edges of the notch.

Opposite from the extraction mirror are two titanium-coated windows mounted in the wall of the beam pipe. One window is directly across the pipe from the extraction mirror in the synchrotron light path. The other window is located next to the first one and is used for observation of the mirror surface and to check the proper seating of the RF fingers around the mirror. The interior windows are coated with a thin layer of titanium (0.5 microns) to minimize disturbance to surface currents in the wall, however the windows are not vacuum sealed. Sealed windows are located on the outer chamber on axes extending from the mirror and through the inner windows.

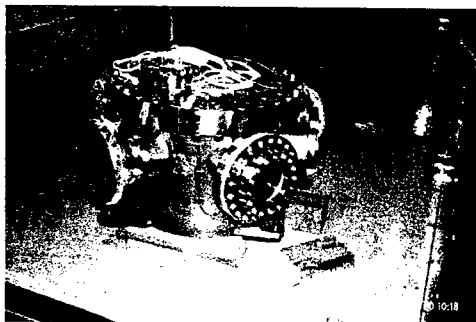


Figure 1: Original chamber, exterior view.

The original chamber exhibited heating problems at high

beam currents. A measurement of the temperature of the interior beam-pipe temperature at the middle of the chamber showed temperatures in excess of 200 degrees even at relatively low maximum beam currents of 700 mA in the LER (see Fig. 2). An analysis of the wall-current heating in the stainless steel chamber walls showed that at 700 mA the expected temperature rise would be about 175 degrees, which added to the ambient tunnel temperature of 25 degrees explains the observed temperature rise. At a beam current of 2000 mA, the expected temperature rise would be a catastrophic 500 degrees.

In February of 2002, after about 10,000 heating cycles (beam current cycles) of the beam pipe, the welds attaching the mounting frame for the windows to the beam pipe failed, due to the thermal-expansion stress. The rest of the Spring 2002 run was completed without the windows present, until the new chamber was installed in the summer.

Upon inspection of the windows, it was found that the titanium coating had largely evaporated away, indicating that the windows had not been providing an effective RF seal. The exterior of the enclosing chamber had exhibited a temperature rise with beam current of 35 deg, up to 60 deg, which may have indicated the leakage of HOM power from the beam pipe windows. Further evidence of this phenomenon was provided when leads to thermocouples inside the beam chamber began arcing to the chamber walls.

Besides structural problems due to heating, the expansion and contraction of the beam-pipe caused the extraction mirror to be moved, which threw the optical axis out of alignment. This problem was corrected for by the implementation of an optical-axis feedback loop, wherein the position of the SR interferogram on the camera CCD face was held constant by continuously adjusting the horizontal and vertical orientations of a movable mirror mounted just outside the extraction chamber.[2] The compensation angles as a function of changing beam current during typical physics runs are shown in Fig. 3. The maximum peak-to-peak excursions in the vertical direction reached 1 milliradian, which if uncorrected would have rendered the interferometer (located 30 meters downstream of the extraction mirror) unusable.

FEATURES OF NEW CHAMBER

The new chamber is shown in Figures 6, 7 and 8. The most significant change was to make the beam pipe out of copper, except for a section of beam pipe outside the containment chamber connecting to a flange which was made of copper-plated stainless steel. The greater conductivity

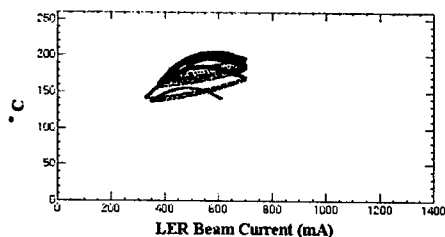


Figure 2: Old beam-pipe temperature dependence on beam current.

of copper compared to stainless steel reduces the resistive heating from wall currents, and the higher heat conductance of copper helps dissipate what energy does get deposited and prevent the temperature build-up seen in the stainless-steel chamber.

In the case of stainless steel, a 1 A beam current at 4-bucket, or 8 nsec, spacing, will induce 20 W of heating in the walls. Without full-surface cooling, this heat deposition would generate a temperature gradient of 140 degrees/10 cm along the beam pipe wall. Copper, with its greater conductivity and thermal conductance was estimated to generate only 3.5 degrees/10 cm, a negligible temperature rise. Switching to copper was considered easier than redesigning the cooling system.

Measurements of the temperature of the inside beam pipe wall show that the temperature rise has in fact been reduced by two orders of magnitude as seen in Fig. 4.

MAFIA simulations indicated that at full current poten-

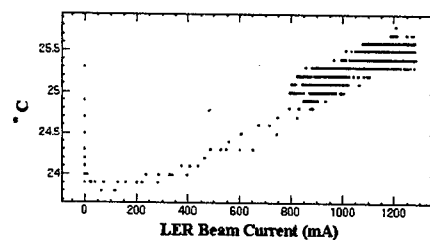


Figure 4: New beam-pipe temperature dependence on beam current.

tially problematic levels of HOM power could be expected to leak from the extraction apertures in the inner beampipe used in the original design. The decision was made to reduce all apertures as much as possible while remaining compatible with light-extraction needs.

The inner light-extraction window was replaced by a smaller aperture. The light-extraction port in the outer chamber was also reduced in radius to minimize the leakage of HOM power to the movable mirror assembly located just outside the outer chamber window. A free-space gap was maintained between the beam pipe and the outer chamber in order to dissipate as much of the HOM power inside the outer chamber as possible, before reaching the final light-extraction port.

Since the titanium coating had not proven effective, the quartz windows were eliminated. The observation port was eliminated entirely, a simplification enabled by changing the way the extraction mirror is mounted. Previously the

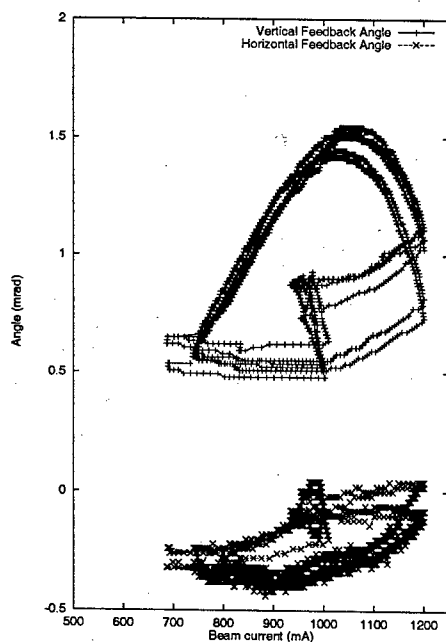


Figure 3: Optical-axis feedback correction angles dependence on beam current with old chamber.

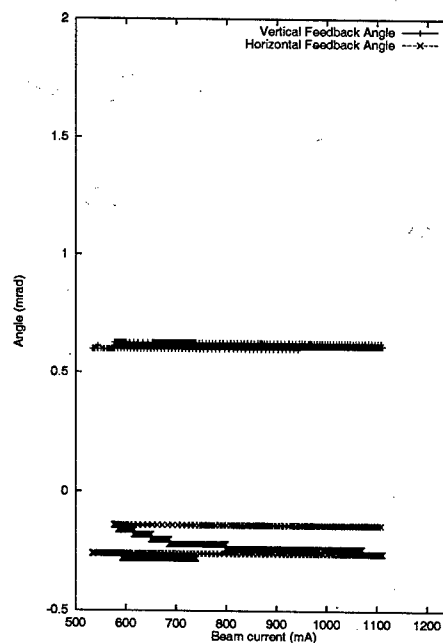


Figure 5: Optical-axis feedback correction angles dependence on beam current with new chamber.

mirror was suspended from a micrometer stage mounted on the lid of the chamber, necessitating fine-tuning of its seating after the lid had been shut. Now the mirror is mounted from the bottom of the chamber, so its seating can be checked while the lid of the outer chamber is still open, eliminating the need for the observation port to check the mirror seating from the outside of the chamber.

The thermocouple leads for monitoring the internal beam pipe temperature are encased in a grounded sheath and carefully routed to avoid any possibility of arcing from leaking HOM fields. In addition, mounting flanges (see Fig. 7, lower right corner) are provided in the ceiling and floor of the outer chamber as locations in which to mount SiC absorbers should they prove necessary. However, as the outer chamber temperature shows negligible temperature rise with beam current, such absorbers have proven unnecessary.

PERFORMANCE

Due to the reduction of the beam-pipe temperature rise, the motion of the mirror as a function of beam current has been greatly reduced. The optical axis feedback compensation angles for the new chamber are shown in Fig. 5. Comparison with Fig. 3 shows that the optical axis alignment drift has been greatly reduced, to the point that the operation of the feedback loop is no longer required. This has made setup of stable optical beamlines for SR studies much easier.

The HER SR chamber is of a similar design to the original LER one, and exhibits the same heating and optical-axis drift problems. Therefore we will be replacing the HER chamber with one similar to the new LER chamber during the summer 2003 shutdown period.

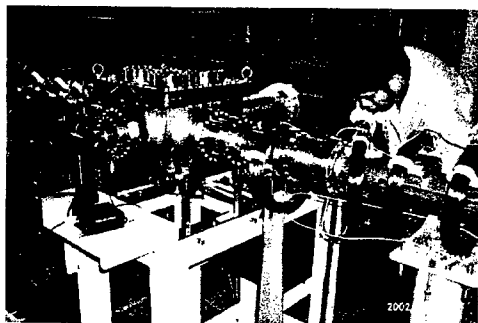


Figure 6: Installation of new LER synchrotron radiation extraction chamber.



Figure 7: Inside of new LER synchrotron radiation extraction chamber, showing light extraction aperture in beam-pipe (center).

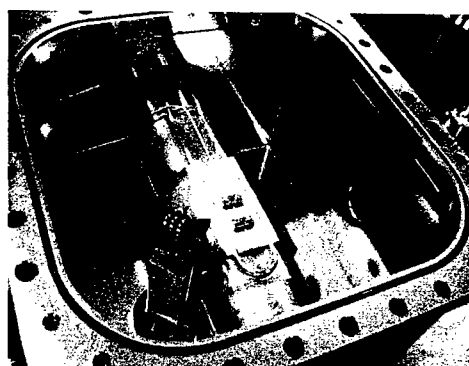


Figure 8: Inside of new LER synchrotron radiation extraction chamber, showing extraction mirror (lower left) and light-extraction aperture in outer chamber wall (middle right).

tem at KEKB," Proceedings of the Second Asian Particle Accelerator Conference, Beijing, China (2001) pp. 639-641.

REFERENCES

- [1] M. Arinaga et al., "KEKB beam instrumentation systems," Nuclear Instruments and Methods in Physics Research A 499 (2003) pp. 100-137.
(SR extraction-mirror system described on p. 124.)
- [2] J.W. Flanagan, S. Hiramatsu, H. Ikeda, and T. Mitsuhashi, "Improvements to Automated Beam-size Measurement Sys-

CONSTRUCTION OF SR MONITOR FOR PHOTON FACTORY ADVANCED RING

T. MITSUHASHI[#] and M. TADANO

High Energy Accelerator Research Organization, Oho, Tsukuba, Ibaraki, 305-0801 Japan

Abstract

An optical diagnostics system using visible synchrotron radiation has been installed in the PF advanced ring. This system is capable of imaging measurements, SR interferometry measurements, and longitudinal profile measurement via streak camera. The interferograms are processed automatically, and the results of beam size measurements are displayed on a CRT panel for the continuous real-time measurements of beam size. Some free ports are also available for performing machine studies.

INTRODUCTION

The Photon Factory Advanced Ring (PF-AR) was originally constructed as a booster for the TRISTAN project. The ring was partially used as an X-ray source. The ring has been upgraded, and reborn as a dedicated pulse X-ray source [1]. In the upgrade project, several systems (vacuum ducts, BPM, etc.) were improved in order to achieve a good performance as a dedicated SR source. Since monitoring the beam profile or beam size using synchrotron radiation improves the efficiency of the commissioning of the ring, we decided to construct a new synchrotron radiation (SR) beam monitor system by the use of as a part of the upgrade project of the PF-AR. In this paper, it is described that design and construction of the new SR monitor for PF-AR.

SR EXTRACTION AND OPTICAL PATH TO MONITOR HUT

The visible part of SR beam radiated from the NW5-bending magnet is extracted by a water-cooled beryllium mirror. A metal O-ring-sealed optical glass window is used to separate the ultra high vacuum of the ring and the outside air [2]. Downstream of the extraction mirror, the SR beam is divided into two beams by a beam splitter. Since the focusing system doesn't need intense beam, we supply 2% of the total beam to the focusing system (beam line No.1). The remaining 98% of the beam is supplied to the SR interferometer, streak camera and the other instruments for machine studies (beam line No.2). The SR beams are relayed to the end of the optical path by several mirrors. The total length of the optical path is about 19m and closed by aluminum tubes and boxes (not evacuated) to reduce the turbulence effect

of the air. The mirrors in the beam lines are aligned by an auto-collimation method using a He-Ne laser. The outline of the arrangement of optical paths is shown in Fig 1. At the end of the optical path, the SR monitor hut is set on the ground floor.

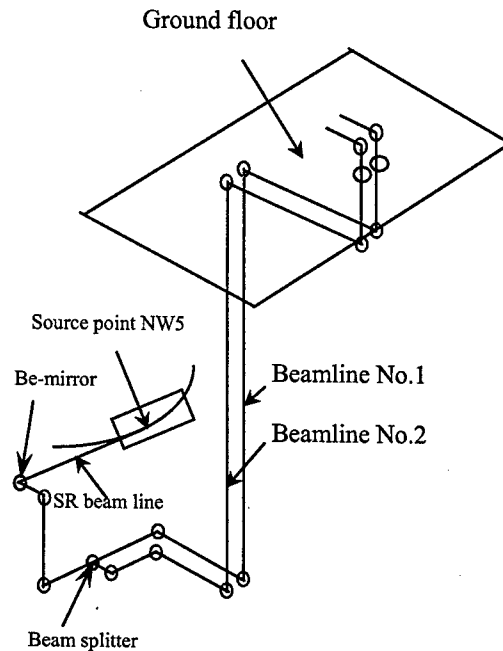


Figure 1 : Outline of optical path.
Circles denote flat mirrors.

IMAGING SYSTEM FOR PROFILE MEASUREMENT

A conventional beam profile monitor based on a focusing system [3] is set at the end of beam line No.1. A typical image of the beam profile is shown in Fig 2. This profile is observed at a beam energy of 6.5GeV and a beam current of 50mA.

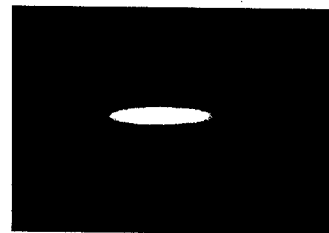


Figure 2 : An example of observed beam profile taken at
50mA, 6.5GeV.

[#]toshiyuki.mitsuhashi@kek.jp

SR INTERFEROMETER FOR MONITORING BEAM SIZE

The SR interferometer is used to monitor the beam size. Two independent SR interferometers are set at the end of branch beamline No.2 for measurements of both vertical and horizontal beam sizes. We use an aplanatic Fizeau type double-slit SR interferometer for the horizontal beam size measurement [4] as illustrated in Fig 3.

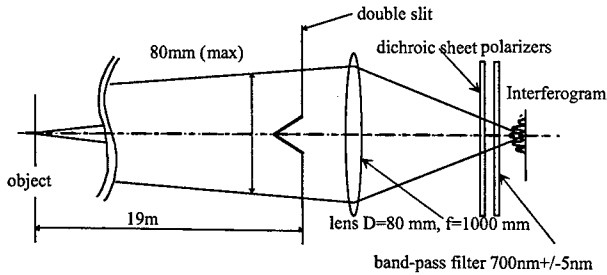


Figure 3: Aplanatic Fizeau type double-slit SR interferometer for the horizontal beam size measurement.

For the vertical beam size measurement, we use a nonaplanatic Michelson type SR interferometer [4] as illustrated in Fig 4.

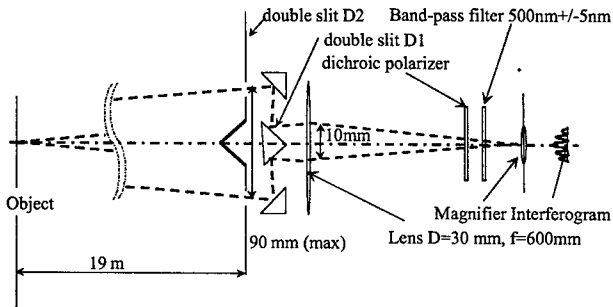


Figure 4: Nonaplanatic Michelson type SR interferometer for vertical beam size measurement.

By this design, the interferogram is given by,

$$I(y, D_2) = (I_1 + I_2) \cdot \left[\frac{\sin\left(\frac{\pi \cdot a \cdot y}{\lambda \cdot f}\right)}{\frac{\pi \cdot a \cdot y}{\lambda \cdot f}} \right] \cdot \left\{ 1 + \gamma(D_2) \cdot \cos\left(k \cdot D_1 \cdot \left(\frac{y}{f} + \psi\right)\right) \right\}$$

where D_2 denotes the separation of the double slit, and D_1 is the fixed separation between the two rays [4]. With this configuration of the SR interferometer, the spatial frequency of the interferogram is a function of D_1 and the modulation of the interferogram is a function of D_2 . Since we can choose a fixed small separation of D_1 , and a movable large separation of D_2 in this configuration, we can easily measure the modulation of the interferogram in the vertical small beam size measurement.

OBSERVATION OF WAVEFRONT DISTORTION AND CALIBRATION OF SR INTERFEROMETER

To observe the thermal deformation of the beryllium extraction mirror, we set the Hartmann-screen type wavefront sensor next of the extraction mirror [5]. We used a 100-hole square-array screen. The hole diameter is carefully optimized by diffraction analysis at the observation point in the hut. Since, a hole smaller than 1mm gives a spread projection pattern, we adopt a 1mm hole diameter. This hole gives a Fraunhofer-like diffraction pattern and has a sharp peak in the center. The interval of the holes should be also small to have a sufficient number of sampling points on the wave front, but not so small that the interference fringe pattern between surrounding holes stands out. We use a hole interval of 5mm. The square-array screen is fixed on a moving stage, and is removed from the beamline during operation of the instruments.

In the SR interferometer measurement, the actual separation of the double slit of the interferometer is changed by deformation of the mirror. To find the ideal separation between the two rays at the location of the double slit, we use a single-hole screen. We can probe the paths of two ideal rays by scanning the single-hole screen in the plane which is perpendicular to the optical axis as illustrated in Fig 5.

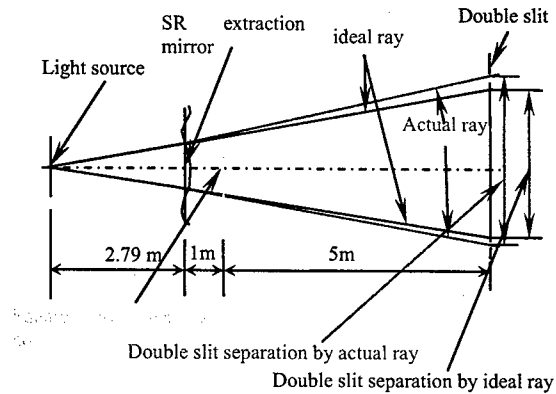


Figure 5: Setup to find the ideal separation of double slit by scanning a single-hole screen.

AUTOMATIC BEAM-SIZE MEASUREMENT SYSTEM

Using a Gaussian beam profile approximation, we can measure the RMS beam size from one measurement of visibility from an interferogram [4], which is measured at a fixed separation of the double slit. The RMS beam size σ_{beam} is given by ,

$$\sigma_{beam} = \frac{\lambda \cdot R}{\pi \cdot D} \cdot \sqrt{\frac{1}{2} \cdot \ln\left(\frac{1}{\gamma}\right)}$$

where γ denotes the visibility, which is measured at a double slit separation of D and R is the distance between the beam source point and the double slit. To find the visibility γ from the interferogram, we use the standard Levenberg-Marquart method for non-linear fitting [6]. After processing of the interferogram, the results are displayed on a CRT panel. Figure 6 shows an example of the display panel. The interferogram, best fit curve and beam size trend graphs are shown in the panel.

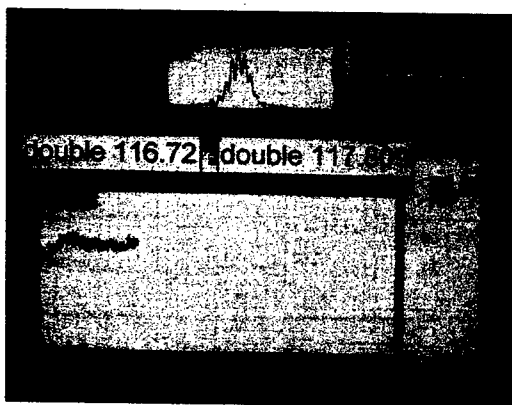


Figure 6: Display panel for automatic beam size measurement. This example shows a panel for vertical beam size measurement.

PORTS FOR MACHINE STUDIES

We prepared some extra ports for machine studies at beam line No.2. White, monochromatic ($\Delta\lambda/\lambda$: 10^{-1} to 10^{-5}), and polarized beams are available for optical measurements. Two of the machine study ports are always occupied by a streak camera and a fast gated camera. By combining these two instruments, we are capable of measuring the instantaneous transverse and longitudinal beam profiles simultaneously.

REFLECTIVE OPTICS FOR STREAK CAMERA

In the time-domain measurement using the streak camera, it is important to design an incidence optical system which has an optical path difference (OPD) as small as possible. In ordinary use of the streak camera such as for a laser, the incident light is almost monochromatic. Because we need an intense light pulse for the streak camera, we prefer to avoid using a band-pass filter, instead using white light. For this reason, we designed incident optics using reflective optics which have no chromatic aberration. Figure 7 shows an illustration of incident optics based on reflective optics. The design of the incident optics consists of two stages; the first stage is a Cassegrain-type objective [7] and the second stage is Offner-type relay system [7].

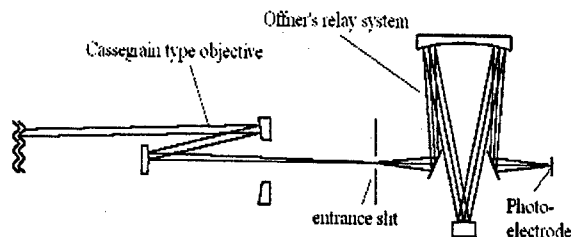


Figure 7 Illustration of incident optics design based on the reflective optics.

The Cassegrain type objective makes an image of the beam on the entrance slit of the second stage. The light is sampled at the entrance slit then relayed onto the photo electrode of the streak camera by the Offner-type relay system. A photograph of the Offner-type relay system with the streak camera is shown in Fig 8.

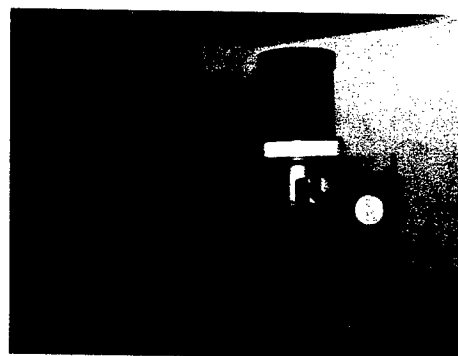


Figure 8: A photograph of the Offner-type relay system with the streak camera. The cover of the Offner-type relay system is opened to show the inside.

REFERENCES

- [1] Photon Factory Activity Report #19, part A, p.60, (2001).
- [2] T. Mitsuhashi, K. Kanazawa and S. Hiramatsu, Proc. 13th Symposium on Accelerator Science and Technology, p.387,(2001).
- [3] T. Mitsuhashi and M. Katoh, Proc. 5th European Particle Accelerator Conference, p.1669, (1996), Sitges (Barcelona).
- [4] T. Mitsuhashi, "Beam Profile and Size Measurement by SR Interferometer" in Beam measurement, Ed. by S. Kurokawa et.al., pp399-427, World Scientific(1999).
- [5] I. Ghozeil "Hartmann and other screen tests" in Optical shop testing, Ed. By D. Malacara ,pp367-396,Wiley-International (1992).
- [6] J.W. Flanagan, S. Hiramatsu and T.Mitsuhashi, Proc. 7th European Particle Accelerator Conference, 1714, (2000),Vienna (Austria).
- [7] L. Mertz, "Excursions in Astronomical Optics", 1996, Springer.

BEAM POSITION MEASUREMENT USING LINAC MICROSTRUCTURE AT THE KEK BOOSTER SYNCHROTRON

Takako Miura*, Hirohiko Someya, Yoshihiro Sato and Yoshiro Irie
KEK, 1-1, Oho, Tsukuba, Ibaraki, 305-0801, Japan

Abstract

The position information of the most recently injected beam from the linac is obtained by picking-up the signal of the harmonic component of the beam, if the bunch structure disappears during one turn due to the momentum spread. The experiment for 201MHz pickup was performed in the KEK booster ring, and is compared with the simulation. The possible application of this method to the 3GeV rapid cycling synchrotron in the Japan Proton Accelerator Research Complex (J-PARC) is also addressed.

1 INTRODUCTION

In the KEK 500MeV booster synchrotron, 40MeV H⁺ beams from the 201MHz linac are injected by multiturn process during 40 μ s or less. The beam dilutes in a longitudinal direction due to the momentum spread as,

$$\Delta T/T = (\alpha - 1/\gamma^2) \Delta P/P, \quad (1)$$

where, T is the revolution period, α the momentum compaction factor, γ the Lorentz gamma, and P the momentum. The evolution of the bunch structure in the ring is shown in Fig.1, where the micro-bunches are injected every 5 ns with $\Delta P/P$ of ± 0.35 % and bunch length of ± 35 deg at the linac output. Figure 2 shows the harmonic components of bunches. It is clearly seen that the harmonics fade away very quickly during turns. It is then suggested that, if the beam position monitor (BPM) picks up these harmonics, the position information of the most recently injected beam can be obtained irrespective of the positions of the previously injected beams.

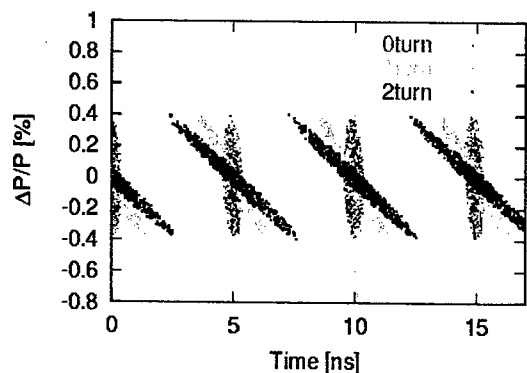


Figure 1: Bunch structures during subsequent turns in the KEK booster ring.

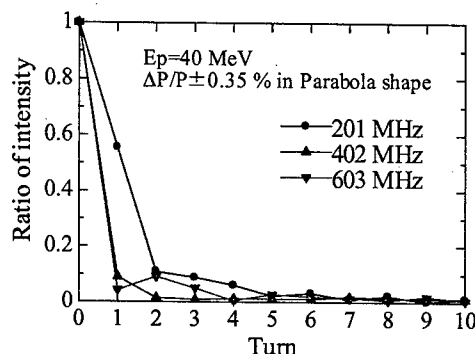


Figure 2: Evolution of each harmonic component during turns. The signal intensity is normalised to 0th-turn value.

2 EXPERIMENTS

2.1 EXPERIMENTAL SETUP

The KEK booster is a rapid cycling synchrotron (RCS) at 20Hz repetition, the circumference of which is 37.7 m and the revolution period at injection about 445 ns. The injection is performed by charge exchange method using a carbon stripping foil. The BPM is an electrostatic type and has 4 electrodes [1], which is located 3.6 m downstream of the stripping foil. The pickup signals are fed into an isolation transformer and transferred through coaxial cables to the central control room. The typical pulse height of the raw signal is several milli-volts. These were inputted to an oscilloscope with a 2GHz sampling rate, and then transferred to a PC where the FFT calculations were performed over each 445ns time range. The harmonics used to calculate the position is 201MHz because the signals of higher harmonics are too small. The conversion to the position from the 201MHz amplitude is given by

$$x = k(R - L)/(R + L), \quad (2)$$

where R and L is the signal from the right and left electrode, respectively, k the conversion coefficient to position. The k -value of this study is 19.84 mm.

In order to compare the beam positions with and without the presence of the circulating beam, the extraction bump magnet is provided downstream the BPM, which kicks the beam out so as to prevent the further excursion. At the 40MeV beam-transport line, the momentum analyser system is available to observe the momentum distribution of the incoming H⁺ beam.

*takako.miura@kek.jp

2.2 EXPERIMENTAL RESULTS

In order to check the performance of the BPM, the injected beam was kicked by a horizontal steering magnet located at the 40MeV beam-transport line. The beam position versus the steering magnet current is shown in case that the extraction bump is ON. The error bars in the figure indicate the fluctuations in the consecutive five measurements. As expected, linear dependence is obtained.

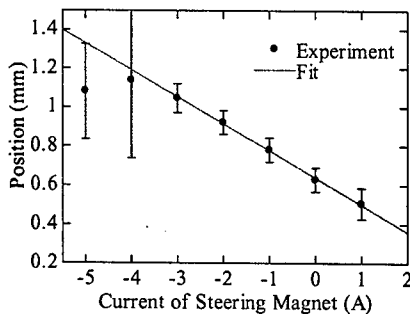


Figure 3: Steering current vs. position response. Line is fitted above the current -3 Amps.

Figure 4 shows the comparison of the signals in the horizontal plane with the extraction bump magnet On and Off. It is clear that the electrode signals and thus the beam positions are different each other, which implies that the 201MHz component survives more than one revolution in the ring.

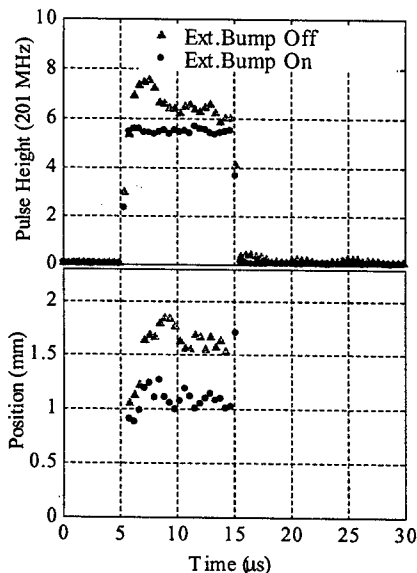


Figure 4: Experimental results of the sum signal of horizontal electrodes (top) and the position (bottom).

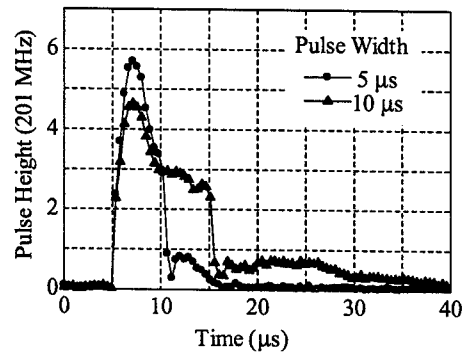


Figure 5: Experimental results of the sum signals with RF Off.

As shown in Fig.5, the bump of 201MHz component appeared after the injection end. Such bumps can be thought as re-bunching in the ring. The data was taken when the RF system of the ring is turned off for simplicity.

3 ANALYSIS

Parameters in the simulation are the central energy, and the shape and width of the momentum spread of the injected beam. Typical momentum distribution is shown in Fig.6. The output of the velocity monitor in the 40 MeV line was used to determine the central energy of the beam. The influence of RF or the space charge effect was not included: space charge effect for one revolution is about 8.8 KeV, which is much smaller than the typical energy spread of the bunch, 274 KeV. In calculation, bunches are injected by multi-turn injection in the same manner as the practical beam injection. The time and the output signals of the BPM are recorded and accumulated. After the end of tracking calculation for all particles, the 201MHz component is picked up by FFT, and then the position information is deduced. Figure 7 shows the calculation result which compares to Fig.4. The initial values for (x, x') were given so as to reproduce the experimental position with the extraction bump On. General trend of the calculation agrees well with the experiment.

Figure 8 shows the calculation which produces the 201MHz bump after the injection end. A square momentum distribution with $\pm 0.3\%$ spread is assumed although this distribution is slightly different from that in Fig.6: it should be noted that the operating condition of the linac during the course of this experiment was not always stable. The momentum distribution might be changing.

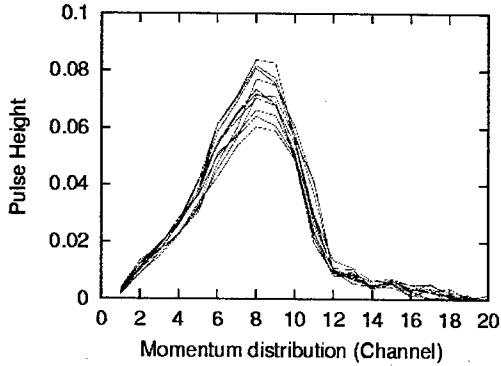


Figure 6: Momentum distributions by the analyser magnet system in the 40MeV line. Each line is obtained in every 0.8 μ s. $\Delta P/P = 0.0735\%$ /channel.

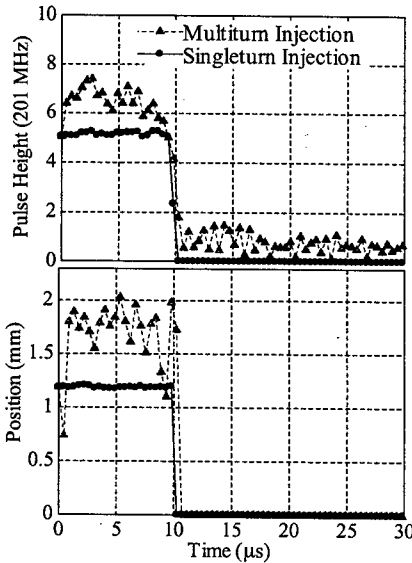


Figure 7: Results of simulation for Fig.4. The data of momentum analyser was used in the simulation.

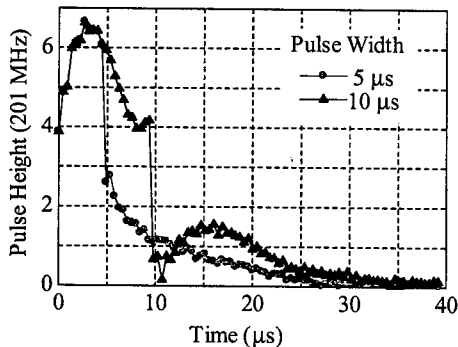


Figure 8: Simulation of re-bunching which compares to the experiments in Fig.5. A square momentum distribution with $\pm 0.3\%$ spread is employed.

4 APPLICATION TO J-PARC

In the 3GeV RCS of the J-PARC, painting injection which forms a uniform density distribution in the real space is planned[2]. In order to precisely control such a process, a realtime monitoring system of the injected beam is foreseen. Parameters of the beam and the RCS are: fundamental frequency of the micro-bunches from the 400MeV linac is 324MHz, the micro-bunch length $\pm 17\text{deg}$ with $\Delta P/P \leq 0.1\%$ at the stripping foil, the circumference 348m, and the momentum compaction factor 0.001197. The evolution of each harmonics in the RCS is shown in Fig.9. Since the bunch length at the foil is short, the intensity of the higher harmonics is high enough to be observed. If the BPM's, which are based upon the 3rd harmonics, are distributed in the ring, the phase coordinates of the most recently injected beam can be deduced because almost no 3rd harmonics survives over one turn as can be seen in the figure.

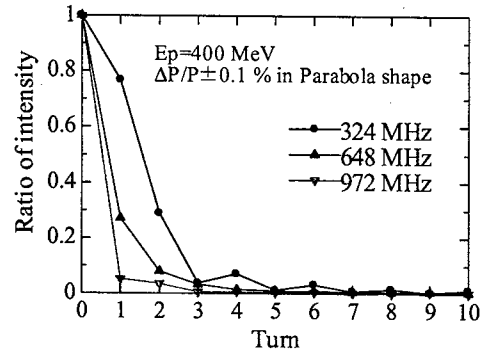


Figure 9: Evolution of each harmonic component in the J-PARC RCS. The signal intensity is normalised to 0th-turn for each harmonic frequency.

5 SUMMARY

The study of the beam position monitor in the KEK booster ring is in progress which observes the fundamental frequency of the linac beam. The agreement between the experiment and the simulation is reasonably well although the simulation showed evolution of the harmonics is quite sensitive to the momentum distribution of the injected beam. The application of this method to the J-PARC 3GeV ring seems promising in order to realtime monitor the painting injection process if the BPM's are based upon the 3rd harmonic component of the 400MeV linac beam.

REFERENCES

- [1] H.Someya, D.Arakawa, J.Kishiro and I.Yamane: Proceedings of the meetings ICANS-XIII and ESS PM4, PSI proceedings 95-2, pp.740-744.
- [2] I.Sakai et al: this proceeding.

BEAM POSITION MEASUREMENTS AT LOS ALAMOS: ISOTOPE PRODUCTION FACILITY AND SWITCHYARD KICKER UPGRADE*

J. D. Gilpatrick, D. Barr, D. Martinez, J. F. O'Hara, R. B. Shurter, M. Stettler, LANL, Los Alamos, New Mexico, USA.

Abstract

The Los Alamos Neutron Science Center (LANSCE) is installing two beam lines to both improve operational tuning and provide new capabilities. The Isotope Production Facility (IPF) will provide isotopes for medical purposes by using the H^+ beam spur at 100 MeV and the Switchyard Kicker Upgrade (SYK) will allow the LANSCE 800-MeV H^- beam to be rapidly switched between various beam lines within the facility. The beam position instrumentation for both of these beam lines uses a micro-stripline beam position monitor (BPM) with a 50-mm or 75-mm radius. The cable plant is unique in that it unambiguously verifies the operation of the complete position instrumentation. The processing electronics use a log ratio technique with error correction such that it has a dynamic range of -12 dBm to -85 dBm with errors less than 0.15 dB within this range. This paper will describe the primary components of these measurement systems and provide initial data of their operation.

IPF AND SYK BEAM LINES

The LANSCE facility is constructing an IPF to provide radioisotopes for diagnosis and treatment of diseases [1]. This spur beam line starts at the 100-MeV transition region of the accelerator and transports H^+ beam to a target area where samples may be irradiated and safely handled. The new beam line contains eight BPMs used to diagnose the beam's position throughout the transport and verify the beam's placement on the target/sample region during either a 10-kHz raster or static operation.

At the end of the 800-MeV LANSCE accelerator, a switchyard directs the beam to either Line D or to Line X [2]. Line D contains such facilities as the Lujan Neutron Scattering Center and Line X contains such facilities as the Proton Radiography and Ultra Cold Neutron Projects. Prior to the installation of the upgraded switchyard kicker beam line, a lengthy process was required to reconfigure the switchyard beam line in order to transport the beam to either Lines D or X. With the completion of the SYK, LANSCE can now simultaneously provide H^- beams to both beam lines by rapidly switching between them using fast kickers located in the new SYK. Three additional BPMs, located in the new SYK, provide beam position information to the facility operators.

Table 1 summarizes key operational requirements of the position measurements for IPF and SYK (a more complete table is in reference [3]). While for IPF and SYK, the beam species are of opposite signs, many

measurement parameters are either the same or very similar, e.g. bunching frequency of 201.25 MHz and data acquisition rate of <10 Hz. However, note the IPF H^+ beam does not have any chopped structure in it, resulting in lower IPF bandwidths requirements for measuring rastered beams. Also note the dynamic range of the both types of signals is larger than the macropulse beam current range would indicate. This range difference is due to the amount of additional range required to cover off-centered beam conditions at either the highest or lowest beam currents. The SYK chopping structure for the various experimental beam lines can be quite complex. If allowed, these chopped-beam structures could further broaden the SYK BPM dynamic range requirements. However, it was decided that monitoring the position of these chopped beams was unnecessary as long as there was a non-chopped tuning beam available.

Table 1: Overall position measurement requirements.

Parameter	IPF	SYK
Macropulse Length (ms)	0.05 to 1	0.15 to 1.2
Chopped Beam Rate (MHz)	N/A	2.8 & 5.6
Chopped Beam DF (%)	N/A	22 to 56
Macropulse Pulse Beam Current (mA)	16.5 to 0.1	13 to 0.1
Base Bandwidth (kHz)	15	~2500
Position Precision/Accuracy (% of pipe radius)	0.3/~3	0.25/~2
Beam Pipe Radius (mm)	50.4, 76.2	50.4
Position Measurement Dynamic Range (dB)	63	70

BPM BEAMLINE COMPONENTS

A previous paper details the BPM's mechanical construction and mapping of the IPF BPMs, this paper only briefly discusses the SYK BPM's characteristics [3]. Fig. 1 and 2 show a SYK BPM and its associated beam line components in picture and schematic form. The SYK BPMs were characterized to have a 0.627 dB per mm sensitivity and typical offsets < +/- 0.1 mm. The sensitivity is within 5% of the theoretical 0.661 dB per mm. Since the SYK and IPF BPMs have feed-throughs at both the downstream and upstream end of each of the four electrodes, a unique method of measurement operation is performed to monitor the BPM's condition during beam operation. As shown in Fig. 2, there is a completely

* Work supported by the U.S. DoE, Defense Programs and the U.S. DoE, Energy Research.

unambiguous signal path for power measurements to and from the processor module through each BPM electrode.



Figure 1. A SYK BPM (oriented vertically in figure) is shown with its associated verification hardware.

The 20-dB attenuators in each electrode signal path provide both additional RF divider leg isolation and 50- Ω termination for the BPM electrode downstream ports. The typical round trip attenuation is 36 dB \pm 1 dB and with an injection signal power of -25 dBm, the resulting verification power measurements are performed at -61 dBm. Since the components in this loop are linear, a single mid-dynamic-range power measurement for each cable/electrode loop path is sufficient to determine the health of the any of the serial components within the loop. If a cable is inadvertently crimped or a BPM electrode is injured to the point of losing its 50-ohm characteristics, the total loop attenuation will change. With the help of a software process, this attenuation measurement is performed on an hourly basis in-between beam pulses so that facility operators always have a quantitative method of detecting BPM and cable health.

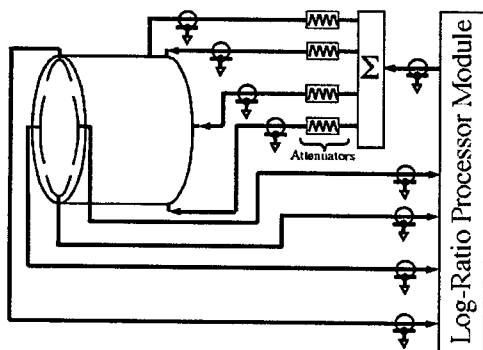


Figure 2. This simple block diagram shows the verification test hardware.

LOG-RATIO ELECTRONIC PROCESSOR

The log-ratio electronics used in this VXI-crate-based processor module has a digital motherboard with on-board digital signal processor (DSP) daughter cards, wide-bandwidth analog-front-end (AFE) circuitry that uses a logarithmic amplifier in each of the four channels, and an on-board 201.25-MHz oscillator on a calibrator daughter card. Fig. 3 shows a simplified schematic of the AFE and calibrator daughter cards. Since all of the components in the calibrator circuitry are solid-state devices, the multi-

step calibration process can be accomplished in the 8.3 ms between beam pulses.

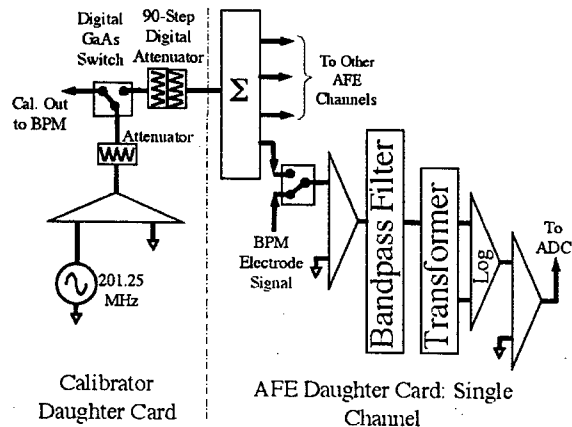


Figure 3. Simplified functional block diagram of the AFE and calibrator daughter cards.

Fig. 4 shows the result of the calibration circuit changes. The deterministic and systematic calibrator errors are subtracted from each of the AFE channels during the software calibration procedure. The error bars, typically <0.1 dB, represent the random errors and uncertainty of the calibrator output signal power.

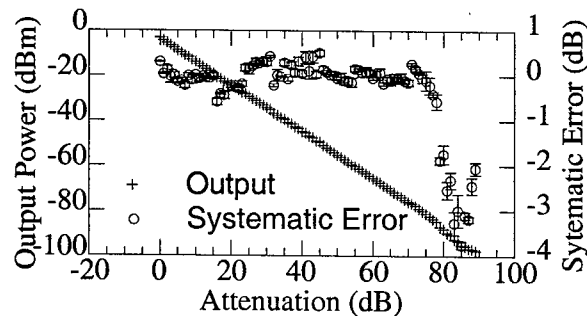


Figure 4. Displayed is a calibrator output signal power and its systematic error as a function of dynamic range.

The present AFE circuitry measures very low-power signals with a wide bandwidth. A Temex 201.25-MHz band-pass filter was placed between the input transformer to the Analog Devices AD8307 log amplifiers and a GALI-52 Mini-Circuits pre-amplifier. Since the 201-MHz harmonic-signal power was lower than initially expected, the band-pass filter was placed to reduce the broadband digital noise finding its way into the log-amp input and not to limit higher harmonic signal power to the preamplifier. These 4.5-MHz-bandwidth filters also have short rise and fall times, typically 76- and 132-ns respectively, providing sufficient bandwidth to measure various chopped-beam conditions in the SYK beam line.

Fig. 5 shows the result of two subtracted module channels, resulting in the log-ratio process, prior to a 90-dB software calibration using the circuitry shown in Fig. 3. The data labeled "Pre-Cal Error" are the residual deterministic errors from a pure logarithmic function.

These errors are primarily due to the log-amp's logarithmic non-conformity and minor thermal variations and are subtracted out during the calibration routine. The Pre-Cal errors are shown for a centered-beam and an off-centered beam condition. The data are plotted as a function of input signal power, in dBm, where a 1 mA current will occur at approximately -55 dBm. Also plotted in Fig. 5 are the random error data, the ultimate limitation to the calibration process and measurement precision. Note that an axis is calibrated to within a <0.15 dB from approximately -12 to -85 dBm. In terms of positional error and beam current applied to the 50-mm IPF and SYK BPMs, this is equivalent to a <0.25-mm-rms error over a ~20 to 0.1 mA current range.

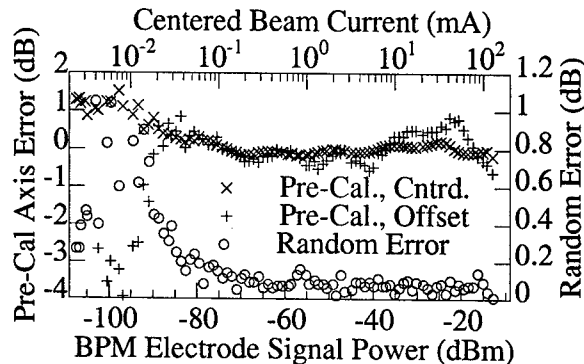


Figure 5. This graph shows the systematic errors prior to and the random errors after a software calibration.

POSITION MEASUREMENT SOFTWARE

The calibration procedure is controlled with a personal computer input/output controller (PCIOC). This procedure uses the same calibrator daughter-card signal-source shown in Fig. 3 that the verification measurement uses but in this case, digital-controlled step attenuators are used to step through a 90-dB range. This procedure was first described in a previous paper [5].

A National Instruments LabVIEW virtual instrument (VI) software process continuously runs on the PCIOC that performs the calibration and verification procedures, repeating on an approximate hourly basis. Upon receiving a timing signal through each VXI processor module, the VI acquires the digital information from the four channels' analog-to-digital converters (ADC) via the digital signal processor (DSP) daughter cards after it has "armed" the DSPs to perform the acquisition [5]. These data are then calibrated by addressing a specific memory location in a 4096 location RAM look-up table (RAMLUT) that contains the correct calibrated data (in counts) on the digital signal processor (DSP) daughter cards. These RAMLUTs remove the systematic "Pre-Cal Errors" for each of the four-processor channels. After the calibration has been completed on all four processor channels, opposite-electrode calibrated-signal powers are then digitally-subtracted to produce a calibrated log-ratio signal for a single axis. Since both IPF and SYK are pulsed beam facilities, a separate timing signal between beam pulses initiates the calibration and verification sub-

VI. This calibration process loads a RAMLUT while another previously loaded RAMLUT is used to provide calibrated position information. After the calibration RAMLUTs have been filled, loaded, and applied to incoming data, another sub-VI switches the appropriate GaAs RF switches in the AFE and Calibrator daughter cards so that the verification procedure checks the health of the cables and BPM electrodes as described earlier.

Finally, the VI serves the data via a portable channel access sub-VI written to interface with the accelerator control system, EPICS (Experimental & Physics Industrial Control System) [6]. The VI, first implemented for the low energy demonstration accelerator at Los Alamos, also allows the facility operators to initiate an "on-demand" calibration procedure and verification test, however, for the "on-demand" verification test to be accurate, the beam through the BPM is turned off.

SUMMARY

This paper describes a beam position instrumentation presently installed in the LANSCE IPF and SYK beam lines. The measurement system uses 50- and 75-mm radius micro-stripline BPMs, an unambiguous verification process that monitors the measurement system's beam-line-hardware health, and an automatic calibration process that removes deterministic and thermal errors on a periodic basis without operator intervention. It has a dynamic range of > 73 dB as defined by errors that are <0.15 dB (or <0.25 mm). Even with this wide dynamic range, the instrumentation bandwidth has been measured to be > 2.5 MHz.

REFERENCES

- [1] R.C. Heaton, E.J. Peterson, "Construction of a New Isotope Production Facility," pp. 112 - 115, LANSCE Activity Report 2001, LA-13943-PR, December, 2001.
- [2] D.H. Fitzgerald, M.S. Gulley, "LANSCE Switchyard Kicker Project," pp. 124 - 125, LANSCE Activity Report 2001, LA-13943-PR, December, 2001.
- [3] J. F. O'Hara, et al., "The Mechanical Design and Preliminary Testing Results of Beam Position Monitors for the LANSCE Isotope Production Facility and Switchyard Kicker Projects.," BIW2002, Upton, NY, May, 2002.
- [4] R. Shurter, et al., "Analog Front-End Electronics For Beam Position Measurement On The Beam Halo Measurement," PAC2001, pp.1369-1371, Chicago, IL, June, 2001.
- [5] D. Barr, et al., "Upgrade To Initial BPM Electronics Module And Beamline Components For Calibration Of The LEDA Beam Position Measurements," PAC2001, pp.1369-1371, Chicago, IL, June, 2001.
- [6] K.U. Kasemir, et al., "Integrating LabVIEW into a Distributed Computing Environment," ICALEPCS 2001, San Jose, CA. LA-UR-01-5905.

A MULTIWIRE PROPORTIONAL CHAMBER SYSTEM FOR MONITORING LOW MOMENTUM BEAM IN ACCELERATORS*

Rob Merl[#], Floyd Gallegos, Chandra Pillai, Fred Shelley, Benjamin J. Sanchez, Andy Steck
Los Alamos National Laboratory, Los Alamos, NM 87545, USA

Abstract

A diagnostic is being developed at the Los Alamos Neutron Science Center (LANSCE) for the purpose of identifying low momentum beam tails in the linear accelerator. These tails must be eliminated in order to maintain the transverse and longitudinal beam size. Instead of the currently used phosphor camera system, this instrument consists of a Multi Wire Proportional Chamber (MWPC) front end coupled to an EPICS compliant VME-based electronics package. Low momentum tails are detected with a resolution of 5 mm in the MWPC at a high dispersion point near a bending magnet. While phosphor is typically not sensitive in the nano amp range, the MWPC is sensitive down to about a pico amp. The electronics package will process the signals from each of the MWPC wires to generate an array of beam currents at each of the lower energies. The electronics will have a wideband analog front end, active anti alias filter, and high-speed analog to digital converter for each wire. Data from multiple wires will be processed with an embedded digital signal processor and results placed in a set of VME registers. An EPICS application will assemble the data from these VME registers into a display of beam current vs. beam energy (momentum) in the LANSCE control room. This display will update at least once per second, but will be a representation of the real time signal processing results from the electronics package.

INTRODUCTION

Beam from the linear accelerator is transported to

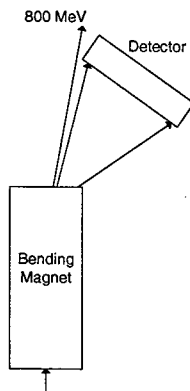


Figure 1: Position of detector with respect to bending magnet.

several different experimental areas by a set of bending

*Work supported by the US Department of Energy

[#]merl@lanl.gov

magnets in the LANSCE switchyard.

Optimally, beam entering the switchyard should be at 800 MeV when the accelerator is properly tuned. Before accelerator tuning is complete, there are often unwanted beam components at energies below 800 MeV that need to be removed. These low energy components are bent in a radius that is too tight to allow them to continue to the experimental areas and fall out and hit a beam stop. The lower the energy, the tighter the bending radius is. The low momentum detector is placed between a bending magnet and a beam stop so it can measure the magnitude spectrum of beam currents over a range of unwanted low energies.

IONIZATION CHAMBER

The chamber is constructed using 1/4" G-10 fiberglass for its frames. It has an active area of 300 sq. cm. (50 cm x 6 cm). There is one frame with wires (64 gold plated tungsten of diameter 20 micron) stretched at 5 mm spacing and two frames with 1 mil aluminum foil on either side of the signal frame for high voltage. The whole assembly is enclosed in an aluminum box with 1 mil aluminum windows covering the active area of the detector. The gas is a mixture of argon-methane (90-10). The signal wires (twisted pair) are connected to a vacuum tight connector attached to the box. The signals from each wire indicate a particular energy beam tail that has to be minimized to achieve an optimum tune for the accelerator. The signals from the wires are fast enough to identify the loss across the macro-pulse of the beam.

SIGNAL

Data is taken from each detector wire to construct a spectrum of beam currents over a range of beam energies from 350 MeV to 750 MeV. Each wire corresponds to a particular unwanted energy component. The wire's relationship to that energy depends on its position in the detector. A sketch of the detector appears in figure 2 [1].

When protons are incident on one of these wires, a current is produced according to equation 1.



Figure 2: Detector

$$I = \frac{N \cdot \Delta E \cdot 1.6 \times 10^{-19}}{I_p} \quad (1)$$

Where I is the current produced in amperes and N is the number of protons per second that are associated with the wire. ΔE is the energy lost in the detector and has been calculated to be 15 eV through a LANDAU simulation [2]. I_p is 12 eV, the ionization potential of argon and 1.6×10^{-19} is the charge of a proton. When 10^6 protons are incident on a wire, a current of 0.2 pA is produced which is amplified due to the effect of the ionization chamber by 10^9 [3]. The result is a current of about 0.2 mA, which is readily measurable.

Figure 3 shows part of a typical signal produced in one of these wires when terminated into 50Ω. The electronics package must integrate this signal over time so that the beam current incident on the wire can be computed.

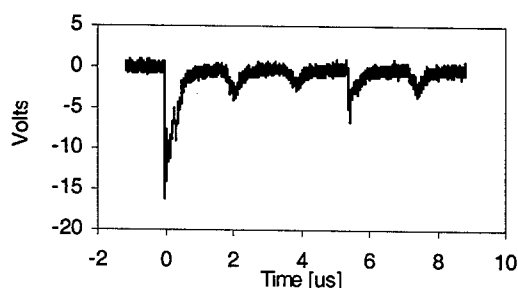


Figure 3: First 8 μs of raw signal from a single detector wire.

This signal is typically 625 μs long, corresponding to the length of the LANSCE beam gate. However, gates as long as 1 ms must be supported. Beam gates occur at a maximum rate of 120 Hz at LANSCE, which means that the electronics package has $(1/120\text{Hz} - 1\text{ ms}) = 7.3\text{ ms}$ to recover from a beam gate.

BANDWIDTH

In figure 4, a frequency analysis of the raw signal reveals three prominent peaks at 559 KHz, 1.1 MHz, and 1.47 MHz.

The electronics must then be sufficiently fast to capture this information. The analog front end has a bandwidth that has been limited to 10 MHz using a 2-pole anti-aliasing filter. The output of that filter is sampled at 50 MHz.

Another bandwidth consideration is that of the EPICS control system in which this instrument will be used. Operators in the LANSCE control room will see their EPICS-based displays update at frequencies between 1 and 10 Hz. This instrument must bridge the bandwidth gap between the 50 MHz data collection and the relatively slow update rate of the control room displays without losing data. It must also do this in real time, meaning the displays in the control room must look "alive" all the time

so that control room operators are comfortable using the instrument [4].

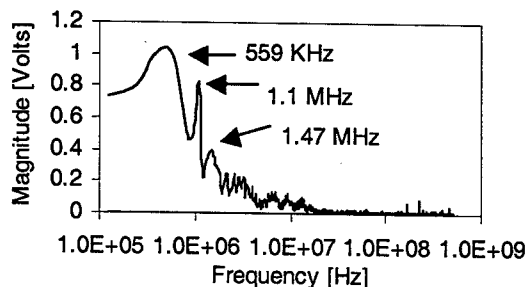


Figure 4. Frequency components of input signal.

ARCHITECTURE

Data that is sampled at 50 MHz at the front end of the instrument is processed in two stages so that a useful, low bandwidth result can be presented to the EPICS control system. At each stage the signal is processed in a way that reduces its bandwidth without discarding information about the signal.

Each wire in the detector has a dedicated section of electronics called the "front-end" associated with it. In the front-end, data is processed by analog and digital hardware to compute an integral at the full sample rate of 50 MHz. However, the signal that is being operated on lasts for less than 1 ms and has a repetition rate of 120 Hz. This means that processed results can flow out of the front end at 120 Hz, which is at a much slower rate than the 50 MHz input data.

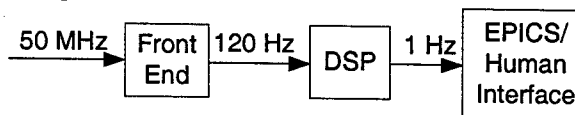


Figure 5. Data processing stages.

The 120 Hz signal is processed further in a DSP before it is presented to EPICS. When the signal is processed in the first stage, a result in Volt-second units is computed. That result has to be converted into charge in Coulombs and then averaged over time for a beam current result in Amperes. The averaging operation reduces the bandwidth of the signal to less than 1 Hz. EPICS can then properly handle this in real-time. A block diagram showing the data flow through the two bandwidth-limiting stages appears in figure 5.

ELECTRONICS

The electronics package consists of a 6U VME board coupled with mixed signal front-end boards suited to the low momentum detector application. The front-end electronics is the mixed signal front-end card and its associated dedicated hardware. There are eight front-ends on each 6U VME card. Since this instrument needs to support 64 wires with 64 front-ends, eight VME cards are required.

Each board has an embedded floating-point digital signal processor (DSP) and a VME interface, which is implemented in a field programmable gate array (FPGA). This FPGA contains only the VME interface, but since just a fraction of its resources are utilized, it could be configured as a hardware coprocessor to the DSP for applications with another type of instrument. The eight front-ends, the DSP, and the VME interface are connected to each other with board wide data, address, and control buses. A block diagram of the VME board architecture is shown in figure 6.

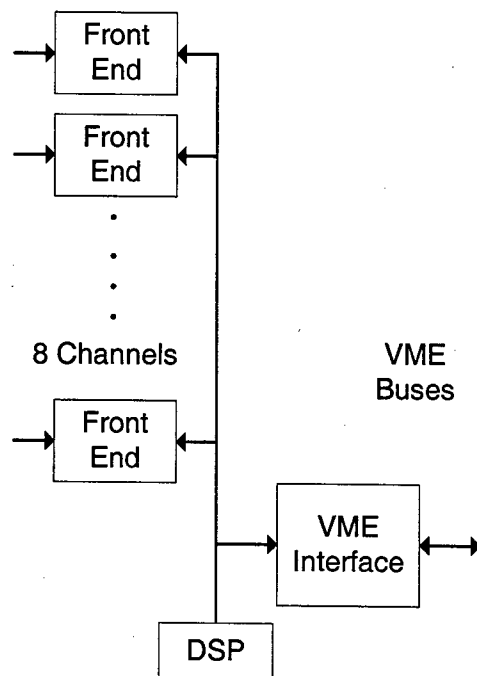


Figure 6. VME board architecture block diagram.

Front End Card

A block diagram depicting the relationship between the front-end card and the VME board is shown in figure 7. The signal from each wire is processed first by the section labeled "analog FE". This is the analog front end, consisting of a two-stage amplifier and a low pass anti-alias filter. The front-end card has on board a 10-bit analog to digital converter (ADC) that is configured to sample at 50 MHz, but can run at speeds up to 200 MHz for other applications [5].

VME Board

The digital hardware for the front end is implemented on the VME board. The underlying VME board accepts eight front-end cards and provides processing support using dedicated FPGAs and one board wide DSP. This board also has first-in-first-out (FIFO) memories to buffer high-speed data so that the raw waveform can be transferred from this instrument to a display in the control room if required.

Although the FPGA dedicated to each front-end is currently configured to be a fixed-point integrator, it may be configured differently for other applications. The digital integrator processes data from the ADC in real time. The integrator can handle signals up to 0.8 μ V-seconds while the measured worst case integral from a real signal is about 0.3 μ V-seconds.

OPERATOR INTERFACE

Result data from this instrument will be in the form of a magnitude spectrum graph of beam current vs. beam momentum. The graph will show how many protons / second are incident on each of the detector wires. The graph will update at up to 10 Hz, for a "live" look. Data transfer from the VME card to the operator's computer screen will be fast because only 64 processed results need to be sent, but not any raw data.

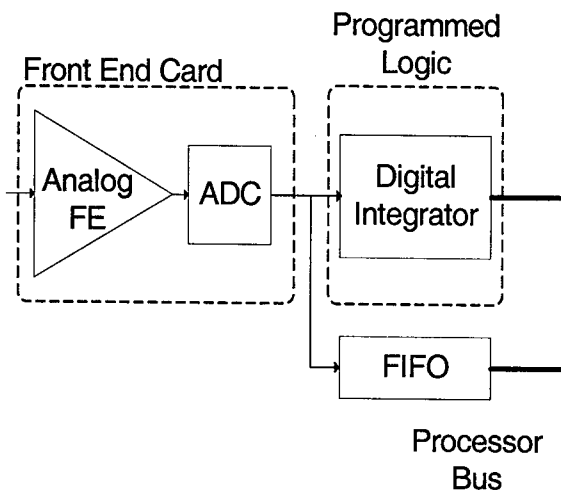


Figure 7. Block diagram of front-end electronics.

REFERENCES

- [1] Jim Witt, Los Alamos National Laboratory, private communication.
- [2] L. Landau, "On the Energy Loss of Charged Particles by Ionization", J. Physics. 8:201, 1944
- [3] T. Ferbel, "Frontiers in Physics", Addison-Wesley, Reading MA, 1987.
- [4] Mark McMillen, Los Alamos National Laboratory, private communication.
- [5] R. Merl, F. Gallegos, C. Pillai, F. Shelley, "High Speed Epics Data Acquisition And Processing On One VME Board", PAC 2003, Portland OR, May 2003.

HIGH SPEED EPICS DATA ACQUISITION AND PROCESSING ON ONE VME BOARD*

Rob Merl[#], Floyd Gallegos, Chandra Pillai, Fred Shelley, Los Alamos National Laboratory, Los Alamos, NM 87545, USA

Abstract

A custom VME board is being designed at the Los Alamos Neutron Science Center (LANSCE) for high-speed signal acquisition and processing. While it is desirable to design around the EPICS / VME platform, it can be difficult to process high-speed signals with long record lengths. The relatively slow data path between the IOC and the general-purpose computer makes real time computations impossible. Commercial VME processor boards can be used, but the data must still flow over the VME backplane in lieu of other traffic. This custom board is designed to overcome this problem by acquiring and processing the signal in one place, with the processed result presented at the VME interface instead of the raw data. The board consists of multiple front-end signal conditioners / digitizer cards plugged into the foundation 6U VME board with an embedded digital signal processor (DSP). The DSP is programmed in C to process the raw signal any way the user wants before writing results into a VME register map. The present front-end conditioner / digitizer cards are being designed with the LANSCE low momentum detector in mind, but other variations on this card could be developed. The architecture is flexible enough to deploy in many accelerator applications.

INTRODUCTION

Powerful, low cost digital signal processors (DSPs) and field programmable gate arrays (FPGAs) have made it feasible to design a single hardware platform from which many accelerator instruments may be launched. Since these devices are reconfigurable / reprogrammable, the same circuit board that is used with a low momentum detector [1] today can be redeployed as part of another diagnostic in the future.

It has been recognized that the application of a single VME board to various accelerator applications might require conflicting analog front-end specifications. To solve this problem, the board has been designed to accept up to eight analog and mixed signal front-end plug in cards. These cards have analog amplifiers, filters, analog to digital converters (ADCs), and perhaps other unanticipated circuitry for future instrument applications.

ARCHITECTURE

The platform was designed to work with the EPICS control system as it exists at LANSCE [2]. In this case, the LANSCE control room operators and scientists are faced with controlling the accelerator through EPICS

displays that update at a 1 Hz to 10 Hz sample rate. At the same time an effective DSP-based accelerator instrument must sample information at rates in the tens of MHz. This bandwidth gap is compensated for with processing capability on the VME board so that high-speed data from an instrument can be reduced in hardware and presented to EPICS as a low bandwidth result. This allows an instrument to have a real-time control room display that looks "alive".

Otherwise, digitized data would have to be transferred from front-end digitizers to a commercial processor in the VME crate or over the network to a general-purpose computer in the control room. Neither of these options is desirable because these techniques require processing of data offline in batches and would not result in real-time update of displays.

VME Board

The VME board is a 6U size module that accepts up to eight custom analog / mixed signal front-end cards. A dedicated ALTERA 20K100E FPGA and a 64Kx18 FIFO support individual front-end cards. These blocks of front-end hardware are linked by a common bus to an Analog Devices ADSP-21161N floating point DSP. Another FPGA that contains a VME interface links this board wide bus to the VME bus. A 25 MHz clock is distributed board-wide and then multiplied by phase locked loops in the DSP and FPGAs. An architectural block diagram appears in figure 1.

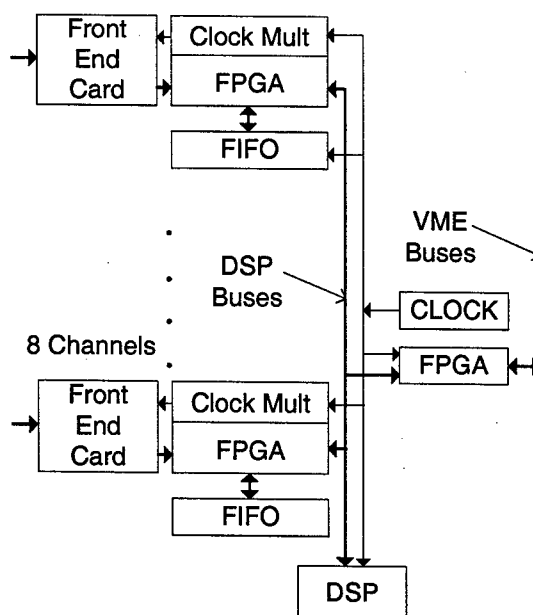


Figure 1: VME board architecture.

*Work supported by the US Department of Energy

[#]merl@lanl.gov

APPLICATIONS

There are 28 bits of configurable I/O between the front-end card and the FPGA. The FPGA can boost the board wide clock up to 200 MHz for use within the FPGA and front-end card electronics. There is a clock output from the FPGA to the front-end card for use as an encode signal for an ADC and other digital hardware.

The embedded DSP operates at a core frequency of 100 MHz. The processor can execute between 1 and 4 floating-point instructions in a single 10 ns cycle.

The VME interface is implemented in an Altera 20K30E FPGA. This FPGA is less than 10% utilized with the VME interface hardware and may be used as a reconfigurable hardware coprocessor for the DSP.

Not shown in figure 1 is a board wide hardware trigger from the front panel.

Front-End Cards

Two types of front-end cards have been designed. The *fast front-end card* is capable of digitizing at rates between 50 MHz and 200 MHz using a 10-bit Analog Devices AD9410 ADC. A two-stage amplifier and 2 pole anti alias filter condition the signal before it is digitized. The analog section of the card has shown a fairly flat response up to 40 MHz on the test bench with its over all gain set to 20. The card accepts a clock from the VME board to set its digitization rate. In order to achieve this speed, it needs two digital output buses, each running at half the full sample rate. The user has the freedom to adjust the amplifier gain, filter cutoff frequency, and ADC conversion rate to suit a particular application.

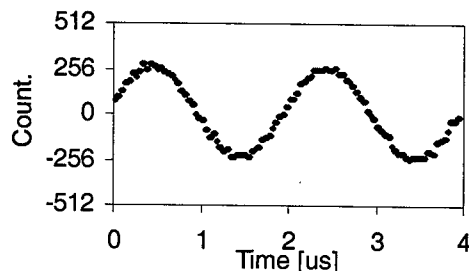


Figure 2: Digitized (measured) test waveform.

The fast front-end card has been prototyped in the lab and tested end-to-end using a waveform generator to supply an input signal and a logic analyzer to acquire the digital data at the back end. The measured data captured with a logic analyzer is shown in figure 2. Here the card was configured with a gain of 40 and a 10 MHz filter cutoff frequency. The ADC was clocked at 50 MHz and a 10 mV, 500 KHz input signal was applied. The figure shows a clearly reconstructed digital version of the input signal. Noise is less than 1 mV.

A second *medium speed* front-end card can digitize at speeds up to 10 MHz with 14 bits and has a programmable amplifier that conditions the signal before it reaches the ADC. The gain can be set with the programmable I/O between the VME board and this front-end card.

The linear accelerator at LANSCE supports several experimental areas at the same time. It does this by multiplexing beam pulses intended for different destinations. Diagnostic instruments are often required to de-multiplex beam data depending on the destination for each beam pulse. The beam pulse destination is locally referred to as its *flavor* [3]. This board supports timed and flavored data with board wide hardware and software triggers from the LANSCE master timing system.

Low Momentum Detector

The platform is first being applied to the LANSCE Low Momentum Detector. This is a diagnostic used during tuning to identify low momentum tails in the linear accelerator. This is done by examining the output of a multi-wire proportional chamber placed at a high dispersion point near a bending magnet. Fast pulses are produced on each of these wires when beam is incident on them. These pulses have to be processed into a spectrum of beam current vs. momentum for display in the LANSCE control room.

When integrated, the pulses are proportional to the number of protons incident on each wire. Integrals then must be averaged over time to convert results in Coulomb units into beam current in Amperes.

Scientists in the control room will want to see an EPICS display with a real-time spectrum of beam current vs. beam momentum as they tune the accelerator. They will use this "live" picture as feedback when they manually adjust accelerator controls in an attempt to remove unwanted beam components. Occasionally they may want to see the beam structure by viewing a waveform record containing the raw digitized data.

This VME board is applied to the low momentum detector problem by assigning a fast front-end card to each of the wires in the detector so that pulses can be digitized at 50 MHz. The digital data is integrated at the full sample rate in the dedicated FPGA and then averaged in the DSP to compute the measured beam current in each wire of the detector. The FIFO memory retains the last 64K samples that have been digitized. Normal processing may be suspended to transfer the FIFO contents to an EPICS display. An architectural block diagram showing this specific configuration appears in figure 3.

The FPGA associated with each front-end card is configured with two digital integrators, one for each output bus of the AD9410 ADC. Analysis with Matlab / SIMULINK using real input data has shown that a 20-bit result bus is sufficiently wide for this application.

When operated at capacity, the LANSCE accelerator has a 120 Hz beam pulse repetition rate. This means that results may be transferred out of the digital integrators at this rate, effectively reducing the bandwidth of the data stream from 50 MHz to 120 Hz without discarding any information.

120 Hz, however, is still out of band for EPICS and the data must be averaged over time anyway to convert from Coulombs to Amperes. The DSP collects these results at

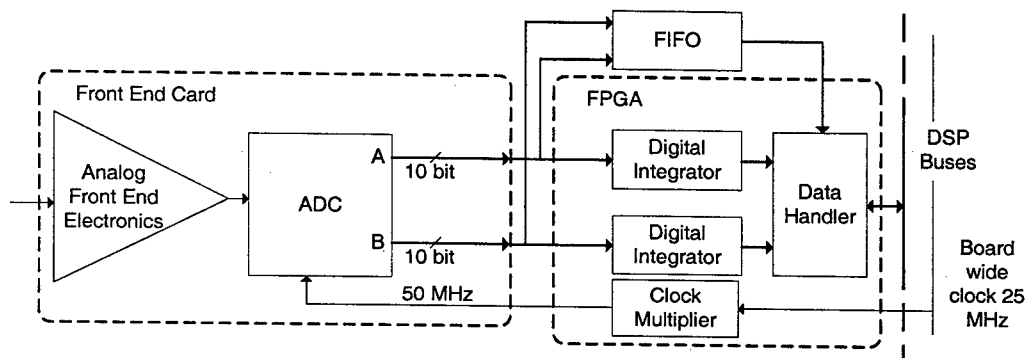


Figure 3: Application specific configuration of the FPGA with the fast front-end card.

120 Hz, computes averages for each wire, and low pass filters the result to further reduce the bandwidth to less than the EPICS update rate.

Control room operators will also need to see current spikes on their displays that may occur with durations too short to be observed with even the fastest EPICS update rate. The DSP will be programmed to detect these spikes in real-time and hold them long enough to be effectively reported through EPICS.

In figure 3, a data handler is shown designed into the FPGA. This is an interface between the front-end electronics and the DSP. It orchestrates the flow of data between the ADC, FIFO, integrators, and the DSP bus.

HARP

A new Isotope Production Facility (IPF) is being commissioned at LANSCE. The transport line to the IPF will require beam position diagnostics. A HARP is a diagnostic used to determine the beam centroid that uses horizontal and vertical wires in the beam.

For the HARP, configuration and programming of this VME board will be similar to the low momentum detector application. In this case, the DSP may also be programmed to partially compute the beam centroid before with the final result is computed by software running in the IOC.

Beam Loss Monitoring

Beam loss monitoring generally involves threshold discrimination and then counting pulses [4]. Count totals are averaged over time to produce a beam loss rate at various locations in the accelerator. One of the front-end cards that have already been designed may be immediately applied to threshold detection. Counting can be done on the associated FPGA. In this case the threshold could be adjusted automatically under the control of the DSP. Additionally, a new front-end card could be developed to convert the raw analog pulses directly into the digital domain without an ADC.

Beam Position Monitoring

The floating point DSP used on this board lends itself to the Δ / Σ type computation common in beam position monitoring (BPM) applications. Depending on the nature

of the BPM, one of the existing front-end cards could be used, or an RF front-end card could be developed [5].

REFERENCES

- [1] Rob Merl, Charles Burns, Floyd Gallegos, Chandra Pillai, Fred Shelley, Andy Steck "A Multiwire Proportional Chamber System For Monitoring Low Momentum Beam In Accelerators," this conference.
- [2] L. R. Dalesio, et al., "The Experimental Physics and Industrial Control System Architecture: Past, Present and Future," Proceedings of the International Conference on Accelerator and Large Experimental Physics Control Systems, 1993, pp. 179-184.
- [3] Michael Oothoudt, Stuart Schaller, Eric Bjorklund, Mary Burns, Gary Carr, John Faucett, David Hayden, Mathew Lusk, Robert Merl, Jerry Potter, Jerome Reynolds, Dolores Romero, and Fred Shelley, Jr, "The LANSCE Rice Control System Upgrade," this conference.
- [4] "A Cerenkov Radiation Detection System For The Advanced Photon Source Storage Ring," A. Pietryla, W. Berg, R. Merl, PAC2001, Chicago, IL. June 2001.
- [5] R. McCrady, LANL, private communication.

HALO MEASUREMENTS OF THE EXTRACTED BEAM AT THE LOS ALAMOS PROTON STORAGE RING*

A. Browman, M. Borden, D. Fitzgerald, R. Macek, R. McCrady, T. Spickermann, T. Zaugg[#]
Los Alamos National Laboratory, Los Alamos NM, 87545

Abstract

The spatial beam density distribution beyond 2.5 to 3 standard deviations of the beam center is an important property for understanding the relatively small fractional losses of high intensity beams at the Los Alamos Proton Storage Ring (PSR) and transport lines to the neutron production target. This part of the distribution (sometimes referred to as beam halo) is not well determined by the LANSCE-standard wire scanner system nor is it yet reliably predicted by the simulation codes. To significantly improve the experimental determination of the beam halo, an improved wire scanner has been developed, tested and installed in the extraction line. To enhance the signal-to-noise ratio, an amplifier consisting of a wide dynamic-range, integrating amplifier, sample-and-hold circuit, log amplifier and line driver is located near the beam line [1]. Offset errors at the input of the amplifiers are actively cancelled and timing gates are derived from a single input pulse. We will describe the prototype instrument, discuss our encouraging test results and report our experience with the instrument in the PSR extraction line.

INTRODUCTION

Efforts are underway to increase the extracted beam from the Los Alamos Proton Storage Ring (PSR) from the present 5 to 6 $\mu\text{C}/\text{pulse}$ (100 to 120 μA) beam. However, losses in the extraction line increase non-linearly with increasing beam currents, and at ~ 8 to 10 $\mu\text{C}/\text{pulse}$, appear to be the limiting factor. To study the beam loss mechanisms, it is important to be certain of beam location and size in the extraction beam line. Data from the LANSCE-standard wire scanner (WS) measurements show that the core of the beam fits nicely inside the 5-inch-diameter pipe at the test location, but the present wire scanner system provides little data on possible beam "halos". The standard wire scanner amplifier is located in instrumentation racks more than a hundred feet from the beam line. The overall profile resolution of this wire scanner measurement is limited to three orders of magnitude. The new amplifier design has extended profile feature-resolution across six orders of magnitude.

DESIGN CONSIDERATIONS

The extracted beam from the PSR is a triangle-shaped, ~ 270 nsec pulse with a dynamic range of nanocoulombs

to 10 μC charge per pulse at up to 20 Hz pulse rate. The 4-mil, biased, silicon-carbide wire has a secondary emission coefficient of approximately 2%. Peak secondary emission currents from the wire range from a few micro amps to 10 milliamps corresponding to a peak (integrated) charge on the wire of a fraction of 1 pC to 2 nC. The environment in PSR is such that a terminated cable located at a normal diagnostics station shows approximately 1 mV_{rms} noise.

The wide dynamic range of the WS signal coupled with the inherent noise environment of PSR suggests that some part of the necessary signal processing should be accomplished near the scanner. We have chosen to measure the average beam profile by integrating the WS signal. The effective capacitance of the measurement includes wire capacitance of ~ 150 pF and other miscellaneous capacitance for a total of 220 pF. Locating the integrator near the beam line has the added advantage, in addition to the minimization of the effect of the previously noted cable pickup noise, of increasing the S/N ratio as compared to long cable runs. The improved S/N characteristics acquired as a result of amplifier location are purchased at the expense of increased exposure of the electronics to radiation fields. The use of linear amplification to achieve five orders of magnitude in signal resolution translates to a tenth of a millivolt in ten volts and implies use of a 16-bit D/A converter. Both of these implications are challenging to implement, particularly given the above-noted PSR noise environment. As an alternative solution, we have chosen to process the integrated signal using a transimpedance logarithmic converter. The log amplifier allows the use of standard 12-bit A/D converters for signal processing with a single bit corresponding to 2.5 mV of signal. For simplicity, the integrator, the S/H and the log amplifier are also located near the beam line on a single printed circuit board. Three gain selections are available, implemented by the discrete selection of the integrating capacitance with a gain of 1 defined, in this report, as the selection of the largest integrating capacitance. Noise suppression is enhanced in the measurement by minimizing the integration time, limiting circuit bandwidth, background subtraction, and auto zeroing techniques. A description of the amplifier will follow the presentation of measurements.

BEAM MEASUREMENTS

The capability of the WS and amplifier response was tested over a range of extracted currents. Figure 1 shows the profiles of two scans of a 3.6- μC beam with amplifier gains of 1 and 10 using the new wire scanner amplifier.

*Work conducted at the Los Alamos National Laboratory, which is operated by the University of California for the United States Department of Energy under contract W-7405-ENG-36.

[#]tzaugg@lanl.gov

(For consistency in this report, data with a gain of 1, 10 and 100 are shown respectively in red, blue and green.) The semi-log plot shows log-amplifier input current as a function of scanner position in mm. A scan consists of seventy-five samples taken across the beam line with each sample an average of four beam pulses. The baseline noise scans (no extracted beam) for these two gain settings are also shown in the figure. Amplifier saturation is evident in the figure for the gain at 10. The choice of gains for the two scans was deliberately chosen to demonstrate the maximum output of the amplifier and also to allow comparison of the linearity of the amplifier over the same range of currents for two gain settings. The log amplifier has an internal intercept current of 100 pA, but a 1 nA offset current has been generated in the circuitry and sets the minimum measured signal current.

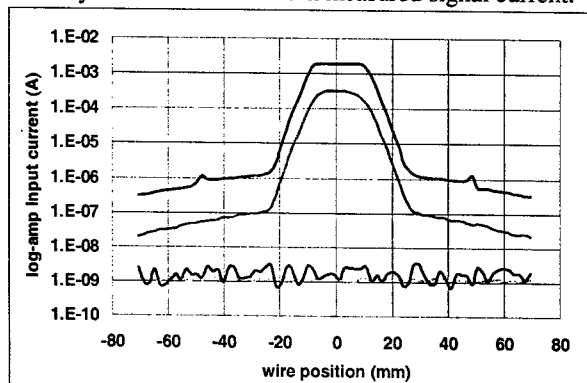


Figure 1: Profiles of a 3.6 μC beam taken with gains of 1 (red trace) and 10 (blue trace) are shown in the chart. Baseline scans without extracted beam were also taken at these gains to demonstrate amplifier noise characteristics.

A “halo” is apparent on the beam more than three orders of magnitude below the peak. The nature of this “halo” has not yet been determined. The wire is biased at -500 V for all of the reported data. Future efforts to increase the bias to greater than -5 kV will be made to explore the nature of this “halo.”

It is apparent that the combined core of the beam and its “halo” do not represent a Gaussian distribution. Nonetheless, a Gaussian fit of the gain=1 data can be made and is shown as the solid blue line in Figure 2. The variance of the function is 49.26. The red crosses in the figure mark the measured data. While the nature of the “halo” and its profile are not presently known, it can be reasonably assumed to also have a normal distribution. A fitting function consisting of the sum of two normal functions was generated; function f_A ($\sigma_A=7.016$) primarily describes the core of the beam, and function f_B ($\sigma_B=40.733$), represents the contribution of the wings of the beam. Function f_A is very similar to the original normal function discussed previously, differing only in a slight change in the value of the deviation. The result of the addition of functions f_A and f_B is shown as the solid black trace in Figure 2.

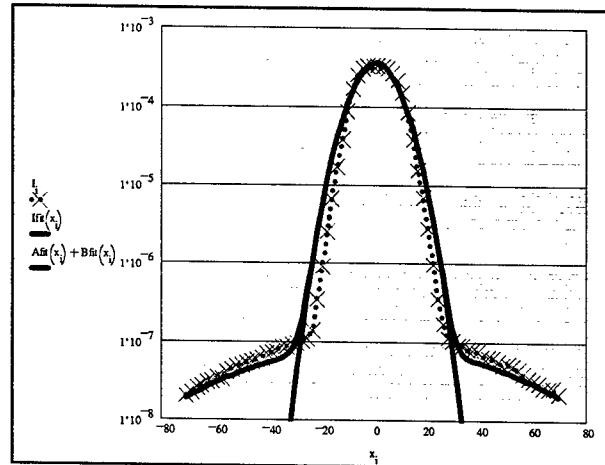


Figure 2: A normal function shown in solid blue has been fit to the data (red x's). A sum of two normal functions is shown in solid black. The x-axis is scaled as scanner position in mm's and the y-axis is log-amp input current in Amps.

The mid range of the amplifier can be demonstrated by reducing the extracted beam an order of magnitude and taking two scans with amplifier gains of 10 and 100. The results are shown in Figure 3 along with “no beam” scans at the same gains.

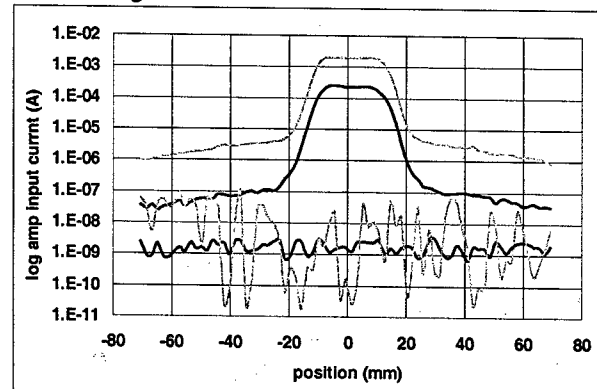


Figure 3: Profiles of a 0.36 μC beam taken with gains of 10 (blue trace) and 100 (green trace) are shown in the chart. Baseline scans, scans with no extracted beam, were also taken at these gains to characterize measurement noise.

At gain=10, the amplifier is again saturated at peak signal levels. The noise limit of the circuit is readily apparent when the gain is set to 100. Peak noise currents are two orders of magnitude above the offset current baseline for this gain. The increased noise is a function of the increased bandwidth at the higher gain.

Finally a scan of a 2 nC “single shot” beam, produced by accumulating beam in the PSR for a single turn followed by normal extraction timing, is shown in Figure 4. The plot shows some evidence of the beam being hollow. The wings of the beam, if they exist at this extraction current, are obscured by the noise.

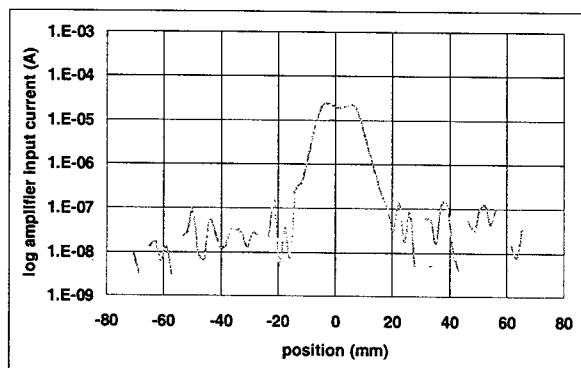


Figure 4: Profile of a "single shot" beam taken with gain of 100. Increased averaging of the samples will likely aid in the ability to resolve "halo" at low beam currents.

AMPLIFIER DISCUSSION

A block diagram of the amplifier is shown in Figure 5. The 1st stage consists of an integrator with relay-selectable capacitors of 10 pF, 100 pF and 1000 pF generating the three gains referred to as 100, 10 and 1. The integrator and its buffer amplifier are actively reset by a low-bandwidth feedback loop. The feedback loop bandwidth is also relay-selected along with the gain to maintain a consistent control for the three gain settings.

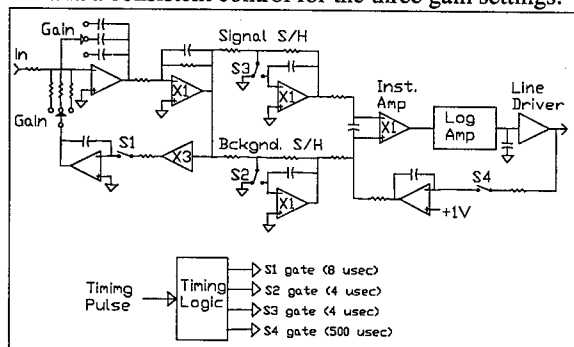


Figure 5: Block diagram of the amplifier.

In addition to providing auto-zero cancellation of the integrator's input offset current and voltage and cancellation of bias supply leakage currents through the coupling capacitor, the feedback loop allows suppression of low-frequency noise components such as 60 Hz pickup. The auto-zero function is removed by switch S1 during a 10 μ sec window around the beam time, and the feedback loop amplifier maintains the last correction voltage just prior to the integrating period.

Two sampling amplifiers acquire data during the integrating period using switches S2 and S3. The "background" sample occurs early in the window before the beam arrives and the "signal" sample occurs shortly after the beam appears. The relative timing between the switch gates is reasonably insensitive to adjustment error. The sampled signals are acquired on a holding capacitor

at the input to an instrumentation amplifier. The instrumentation amplifier drives the transimpedance logarithmic amplifier, an Analog Devices AD8304, followed by a line driver. The bandwidth of the log amp varies as a function of input current from 10 kHz to 10 MHz. A low pass filter at the output of the log amplifier reduces the overall bandwidth to 1 kHz.

The linearity of the log amplifier is challenged at high and low input currents. The AD8304 requires a current source as an input driver to attain the manufacturers promised 160 dB (100 pA to 10 mA) range and log conformance less than 0.1 dB from 1 nA to 1 mA. The original design was implemented with a current source at the input to the log amp, but circuit issues and unexpected time constraints forced the removal of the current driver and resulted in measurement inaccuracy for currents somewhat less than 100 nA during beam line operations. The specific nature of the measurement inaccuracy, an effect of increasing dynamic input impedance of the log amp as input current falls, is well understood and has been corrected in the latest version of this circuit. Measured data as reported in this document has been corrected using a calibration curve generated in a careful test at the bench.

A second active feedback loop is used around the combination of the instrumentation amplifier, the log amp and the line driver. The dominant pole of the feedback loop is fixed at 1.59 Hz. Switch S4 removes the loop control during the log settling and A/D converter sample acquisition time. A one-volt source in the feedback loop is used to set the 1 nA offset current to the log amp.

Timing for the four switches is provided by a single master timer pulse with individual switches driven by pulses derived from the master timer pulse and fixed in time by on-board circuits.

SUMMARY

To significantly improve the experimental determination of the beam halo in the extracted beam from the Los Alamos Proton Storage Ring, an improved wire scanner has been developed, tested and installed in the extraction line. To enhance the signal-to-noise ratio, an amplifier consisting of a wide dynamic-range, integrating amplifier, sample-and-hold circuit, log amplifier and line driver is located near the beam line. Errors at the input of the amplifiers are actively cancelled and timing gates are derived from a single input pulse.

REFERENCES

- [1] A. Browman, memo reports on wire scanner design to R. Macek, 7/8/2001 (macek72) and 9/19/2001 (macek75) available on the web at <http://lansce2-serv.atdiv.lanl.gov/browman/CY2001>.

BEAM IMAGING DIAGNOSTICS FOR HEAVY ION BEAM FUSION EXPERIMENTS*

F.M. Bieniosek[#], L. Prost, W. Ghiorso, LBNL, Berkeley, CA 94720, USA

Abstract

We are developing techniques for imaging beams in heavy-ion beam fusion experiments in the HIF-VNL in 2 to 4 transverse dimensions. The beams in current experiments range in energy from 50 keV to 2 MeV, with beam current densities from <10 to 200 mA/cm^2 , and pulse lengths of 4 to 20 μs . The beam energy will range up to 10 MeV in near-future beam experiments. The imaging techniques, based on kapton films and optical scintillators, complement and, in some cases, may replace mechanical slit scanners. The kapton film images represent a time-integrated image on the film exposed to the beam. The optical scintillator utilizes glass and ceramic scintillator material imaged by a fast, image-intensified CCD-based camera. We will discuss the techniques, results, and plans for implementation of the diagnostics on the beam experiments.

INTRODUCTION

A number of techniques have been used for diagnosing the transverse spatial and velocity distribution of heavy-ion beams in the experimental heavy-ion inertial fusion energy program [1]. These diagnostic tools include wire grids, slit scanners, Faraday cups, etc. Recently we have developed the method of imaging beams on kapton film [2]. The beam ions strike the film and degrade its polymer structure. The degradation is visibly evident as a darkening of the film, and acts as a high-resolution indicator of the time-integrated beam current density profile. A drawback of the kapton imaging technique is that the kapton film needs to be replaced for every measurement, and that the image lacks time resolution. As a result we have developed optical diagnostic techniques. These techniques are related to the previously reported gated beam imager (GBI)[3]. The GBI uses a pepper-pot to create beamlets that are imaged directly onto a gated microchannel plate (MCP) and CCD camera. The scintillator-based technique described here replaces the MCP imager with a thin sheet of scintillator material. It is simple, compact, and more flexible, because only the scintillator material is placed in the path of the beam.

Inorganic scintillators are widely used as beam profile monitors, and the mechanism and optical response to an ion beam have been studied extensively [4]. The scintillation yield increases with particle energy; it depends on the ion energy loss per unit path length dE/dx and on the ion species. For a given energy the yield is somewhat larger for an electron than for a beam ion. This behavior is in contrast to that of kapton film, which

strongly discriminates against electrons and low energy ions. But since the beam ion energy is much higher than the maximum energy expected from any stray electrons, the overall yield from beam ions is still expected to be much greater than from the same number of electrons.

OPTICAL BEAM IMAGING

We have used glass and ceramic (98% alumina) as scintillator materials. Charge neutralization is provided by a high-transparency (80-90% transmission) metallic mesh placed on or near the surface of the scintillator. Beam ions striking the mesh generate secondary electrons. Since the secondary electron yield is on the order of 10 or greater for the beams of interest, sufficient electrons are created on the mesh to charge-neutralize the insulating surface. In addition, by applying a negative bias to the mesh, stray external electrons are decelerated and deflected away from the scintillator, limiting their contribution to the optical image to negligible levels.

Images on the thin (0.1 mm) wafer of alumina are viewed from the rear. Typical time response of the optical emission, as measured by a photomultiplier tube (PMT), is shown in Figure 1. The Injector [5] extraction voltage pulse is shown in the upper trace for reference. The two lower traces show the (negative) PMT signal when the exit aperture of HCX is grounded (upper curve) and when the exit aperture of HCX is at -30 kV potential. When the exit aperture is at a large negative potential a long tail is observed in the PMT signal, associated with energetic electrons arriving at the scintillator, and as verified by the current draw on the scintillator plate. When the bias is reversed, the tail is no longer present.

The measured rise time of the scintillator is $<50 \text{ ns}$. There is no evidence for saturation or thermal quenching in the scintillator response. Linearity over the range of measured intensities was tested by imaging the same beam in horizontal and vertical slit scans. The local intensities in the two scans differed by an order of magnitude, but the summed intensities of all images in each of the two scans agreed. The lifetime of the scintillator material under intense ion beam bombardment is limited. For an HCX K^+ beam (kinetic energy = 1.0 MeV, $\tau_{\text{pulse}} = 4 \mu\text{s}$, $j = 60 \text{ mA/cm}^2$), the optical emission of the material decays with an e-folding rate of ~ 170 pulses. As a result, for very intense beams, such as HCX, for long life it is necessary to limit intensity by placing holes or slits upstream of the scintillator.

* Work performed under the auspices of the U.S. Department of Energy by the university of California, Lawrence Berkeley National Laboratory under Contract No. DE-AC03-76F00098.

[#]fbieniosek@lbl.gov

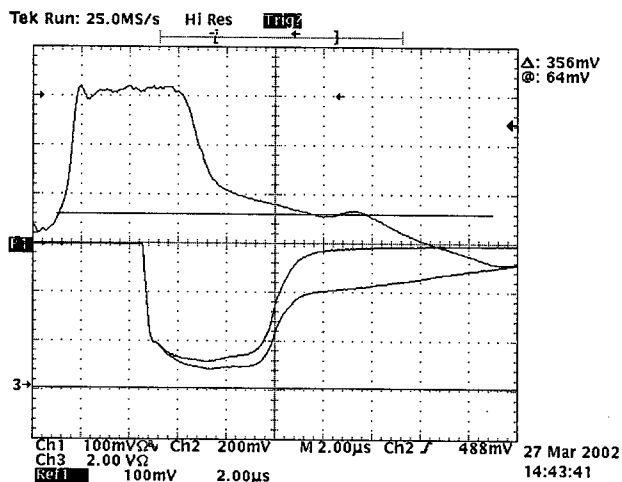


Figure 1. Top: Injector extraction voltage pulse; bottom: optical emission from scintillator at the downstream end of HCX[6] with (upper trace) and without (lower trace) electron suppression.



Figure 2. Transverse beam image taken on NTX [7]. The scale is 3 cm x 3 cm. Also shown is the color palette used to represent the images.

BEAM IMAGE DATA

Time-resolved beam-induced images on the scintillator screen are captured with a Princeton Instruments gated intensified CCD camera viewing the scintillator through a vacuum window. Figure 2 shows a typical beam image taken on NTX. The beam is a final-focus beam with a sharp spot. Images were processed in ImageJ.

In addition to the usual beam distribution in x-y space we have the ability to image the beam in other dimensions of phase space. By interposing horizontal and vertical slits, phase space distributions in $y'(x,y)$, $x'(x,y)$ are measured; and with the use of a pepper-pot array of pinholes, the distribution in $x'(y'(x,y))$ is measured. Figure 3 shows a series of beam images on the scintillator for a slit at various horizontal locations across the HCX beam. The images are for a 1- μ s gate in mid-pulse. The dark band in the images is a 0.5-mm support across the slit, located just below the vertical axis of the HCX. The images show the horizontal angular beam spread (x') as a function of y for a given slit position x . The structure in

the images represents structure in the transverse particle distribution that is not accessible in a double-slit scan.

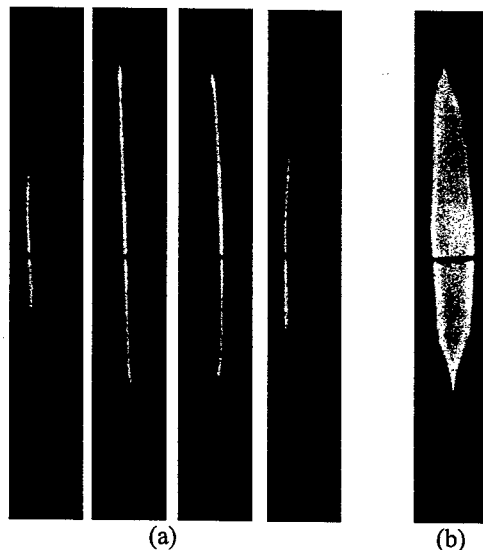


Figure 3. (a) Series of representative images of the beam passing through a slit at various horizontal locations across the beam. (b) Sum of horizontal slit images in a scan.

In a double-slit scan, the signals are summed by a second slit-cup scanned across the first slit such that a line-integrated profile of the beam results. A slit scan can be simulated in the optical data by integrating the optical signal along a vertical or horizontal line. Figure 4 shows a comparison between a line-integrated profile of the beam from the optical data, and the equivalent profile for the same beam measured by moving a slit-cup detector across the beam ("mechanical"). The two curves do not agree exactly because the two diagnostic planes differ ($\Delta z=4.1$ cm). The notch in the optical data corresponds to the location of the support seen in Figure 3.

Table 1: Measured RMS beam parameters

	Double Slit	Optical
a	12.3 mm	12.1 mm
b	20.9 mm	20.4 mm
a'	-37.9 mrad	-35.8 mrad
b'	43.3 mrad	41.6 mrad
ϵ_x	67 π mm mrad	76 π mm mrad
ϵ_y	64 π mm mrad	71 π mm mrad

The 2*RMS horizontal and vertical beam size and angle a, b, a', b', and the 4*RMS emittances ϵ_x and ϵ_y are calculated in the usual way, and summarized in Table 1 in comparison with mechanical slit scan data for the same beam. The agreement is within experimental errors in the beam size and angle. The emittance measurements are very sensitive to the noise level in the data. Increased noise or scatter in the optical image signal compared to the double-slit scanner is reflected in a higher determination of the emittance.

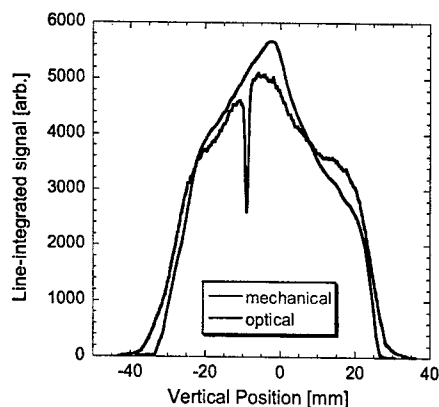


Figure 4. Comparison between a vertical mechanical scan and a simulated optical slit scan for an 80% fill-factor case on HCX.

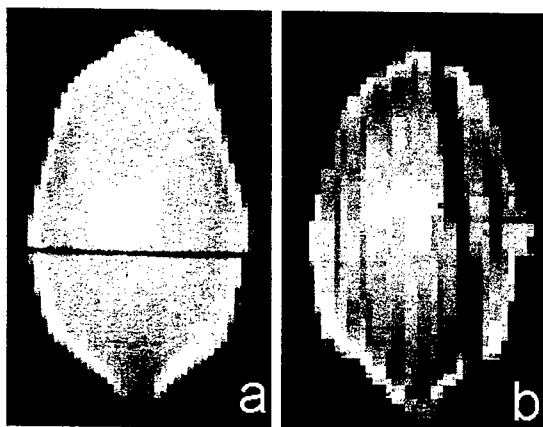


Figure 5. Constructed image of the HCX beam intensity profile based on measured (a) optical slit scan and (b) mechanical crossed-slit measurement. The scale for both images is 3.0 x 4.68 cm.

Algorithms for reconstruction of the beam profiles in all transverse dimensions have been developed [8]. A typical reconstructed image is shown in Figure 5a. This profile was developed from an optical slit scan (as in Figure 3) using 31 beam pulses. It represents the transverse beam intensity distribution referred to the horizontal slit plane. The assumption of a linear transformation of the beam between the slit and the screen is made. Figure 5b shows the equivalent profile of the beam constructed by building up an image point-by-point using a pair of crossed slits, integrated over a 1- μ s time window in mid pulse. This image required 4096 beam pulses. The sloping dark band in the crossed-slit data is caused by a support across the slit-cup detector entrance slit. Similar images of the moments of the beam distribution, such as the local mean angle, and the local RMS angle spread (which is related to

the transverse beam temperature distribution), are also constructed from the optical data.

Optical emission from beam-gas interactions

Other mechanisms for beam-induced optical emission have been observed. There is a weak optical signal from beam interaction with ambient gas. A stronger emission comes from the gas cloud that is created at a wall when bombarded by the intense ion beam. Images taken through a hole plate show optical signal attributed to this effect through the holes that can be significant for intense or tightly-focused beams. This effect can also be expected to occur at the front surface of the scintillator. The scintillator can be modified to eliminate it by depositing a thin (150 nm) aluminum layer on the front surface as an optical barrier. In addition, this mechanism provides an alternate imaging technique that is rugged and self-healing. It may prove to be a useful remote diagnostic for beam-wall interactions.

CONCLUSIONS

Imaging of the beam by optical diagnostic techniques provides a diagnostic tool of great capability and flexibility for HIF-VNL experimental beams. It provides complete, high-resolution two-dimensional images of the beam in as little as a single pulse, in contrast to thousands of beam pulses required by older diagnostic techniques such as a crossed-slit scan. It also provides full 4 dimensional beam profile information with the use of slits combined with pinholes.

REFERENCES

- [1] R. O. Bangerter, Nucl. Instrum. Methods Phys. Res. A 464, 17 (2001).
- [2] F. M. Bieniosek, et.al., Rev. Sci. Instrum. 73, 2867 (2002).
- [3] L. Ahle, H.S. Hopkins, Gated beam imager for heavy ion beams, Proc. 1998 Beam Instrumentation Workshop, SLAC, May 4-7, 1998.
- [4] R.B. Murray, and A. Meyer, Phys. Rev. 122, 815 (1961).
- [5] F. M. Bieniosek, et. al., 2-MV Injector for HCX, Proc. 2001 Particle Accelerator Conference, Paper WPAH011.
- [6] P. A. Seidl, et.al., The High Current Transport Experiment for Heavy Ion Inertial Fusion, Proc. 2003 Particle Accelerator Conference, Paper ROAC001.
- [7] S. Yu, et.al., Focusing and neutralization of intense beams, Proc. 2003 Particle Accelerator Conference, Paper TOAA001.
- [8] A. Friedman, et.al., Simulation Using Initial 4-D Beam Particle Distributions Synthesized from Experimental Data, Proc. 2003 Particle Accelerator Conference, Paper TOPB006.

A SECOND BEAM-DIAGNOSTIC BEAMLINE FOR THE ADVANCED LIGHT SOURCE*

F. Sannibale, D. Baum, N. Kelez, T. Scarvie, LBNL, Berkeley, CA 94720, USA
K. Holldack, BESSY II, Berlin, Germany

Abstract

A second beamline, BL 7.2, completely dedicated to beam diagnostics is being installed at the Advanced Light Source (ALS). The design has been optimized for the measurement of the momentum spread and emittance of the stored beam in combination with the existing diagnostic beamline, BL 3.1. A detailed analysis of the experimental error has allowed the definition of the system parameters. The obtained requirements found a good matching with a simple and reliable system based on the detection of X-ray synchrotron radiation (SR) through a pinhole system. The actual beamline, which also includes a port for visible and infrared SR as well as an X-ray beam position monitor (BPM), is mainly based on the design of two similar diagnostic beamlines at BESSY II. This approach allowed a significant saving in time, cost and engineering effort. The design criteria, including a summary of the experimental error analysis, as well as a brief description of the beamline are presented.

INTRODUCTION

Diagnostic beamlines using synchrotron radiation (SR) are a powerful tool for measuring storage ring parameters. In our case, we were particularly interested in measuring emittance and momentum spread of the ALS electron beam. The new beamline, BL 7.2, while allowing several different measurements, has been optimized for the measurement of these two quantities in combination with the existing diagnostic beam line, BL 3.1. In this paper we present a summary of the experimental error analysis that allowed defining the new system specifications, the pinhole system that we select as a best requirement matching and a general description of BL 7.3 features. The new beamline is presently under installation and will be commissioned in August this year.

THE MOMENTUM SPREAD-EMITTANCE MEASUREMENT

For a beam at equilibrium the transverse beam size is given by the combination of the emittance and momentum spread terms. For the horizontal rms size we can write:

$$x_{rms} = \left(\beta_x \varepsilon \frac{1}{1+\kappa} + \left(\eta_x \frac{\sigma_p}{p} \right)^2 \right)^{1/2} \quad (1)$$

where β_x and η_x are the horizontal beta function and dispersion at the point of observation, ε is the natural emittance, κ is the emittance ratio and σ_p/p is the rms relative momentum spread. If horizontal beam size measurements in two different points of the machine are performed and the optical functions at the observation points are known, it is straightforward by using equation (1) to extract the values of the horizontal emittance and of the momentum spread:

$$\varepsilon_x = \frac{\varepsilon}{1+\kappa} = \frac{x_{rms1}^2 \eta_{x2}^2 - x_{rms2}^2 \eta_{x1}^2}{\beta_{x1} \eta_{x2}^2 - \beta_{x2} \eta_{x1}^2} \quad (2)$$

$$(\delta p)^2 = \left(\frac{\sigma_p}{p} \right)^2 = \frac{x_{rms2}^2 \beta_{x1} - x_{rms1}^2 \beta_{x2}}{\beta_{x1} \eta_{x2}^2 - \beta_{x2} \eta_{x1}^2} \quad (3)$$

Here and throughout the paper the index $i = 1$ refers to the new BL 7.2 and $i = 2$ to the existing BL 3.1.

Experimental Error Analysis

In order to define the specifications for the new beamline a complete analysis of the experimental error has been performed [1]. As example, we report here the expression obtained by propagating the error on equation (3):

$$\begin{aligned} \frac{\sigma_{\delta p}^2}{\delta p^2} = & M_{\partial p1} \frac{\sigma_{M1}^2}{M_1^2} + M_{\partial p2} \frac{\sigma_{M2}^2}{M_2^2} + P_{\partial p1} \frac{\sigma_{px1}^2}{p_{x1}^2} + P_{\partial p2} \frac{\sigma_{px2}^2}{p_{x2}^2} + \\ & + R_{\partial p1} \frac{\sigma_{xR1}^2}{x_{R1}^2} + R_{\partial p2} \frac{\sigma_{xR2}^2}{x_{R2}^2} + \Gamma_{\partial p1} \frac{\sigma_{g1}^2}{g_1^2} + \Gamma_{\partial p2} \frac{\sigma_{g2}^2}{g_2^2} + \\ & + B_{\partial p1} \frac{\sigma_{\beta_{x1}}^2}{\beta_{x1}^2} + B_{\partial p2} \frac{\sigma_{\beta_{x2}}^2}{\beta_{x2}^2} + B_{\partial p12} \frac{\sigma_{\beta_{x1}\beta_{x2}}}{\beta_{x1}\beta_{x2}} + \Pi_{\partial p} \frac{\sigma_p^2}{p^2} \end{aligned} \quad (4)$$

Equation (4) shows the dependence of the experimental error on the errors of the single parameter of the actual measurement system: M_i is the total magnification of the i -th system, p_{xi} is the pixel size (CCD or phosphor), x_{Ri} is the system resolution and the quantity g_i defined as the 'digital amplitude' is the numerical amplitude of the signal at the ADC frame grabber at the end of the acquisition chain. For a Gaussian distribution [1]:

$$\frac{\sigma_{gi}^2}{g_i^2} = \frac{\ln[D_i(2^{bi}-1)]}{3\pi D_i^2(2^{bi}-1)^2} \quad (5)$$

*Work Supported by the Director, Office of Science, of the U.S. Department of Energy under Contract No. DE-AC03-76SF00098

where b_i is the number of bits of the ADC and $0 \leq D \leq 1$ is the 'dynamics factor', a numerical quantity indicating the percentage of the system dynamics used in the measurement. The coefficients of the error terms in equation (4) are functions of the source point and measurement system parameters. For example:

$$R_{\phi 2} = \left(\frac{x_{R2}^2}{x_{rms2}^2} \right)^2 H_{X22} \quad (6)$$

with

$$H_{X22} = \frac{\beta_{x1}^2 x_{rms2}^4}{(\beta_{x1} x_{rms2}^2 - \beta_{x2} x_{rms1}^2)^2} \quad (7)$$

Equation (4) and the similar expression for the emittance have been systematically evaluated for the ALS case (Table 1) as a function of all the measurement system parameters. Figure 1 shows some examples.

Table 1: ALS Parameters

ALS Parameter	BL 7.2	BL 3.1
β_x [m]	0.9	0.35
η_x [m]	0.07	0.03
x_{rms} [μ m]	105	57.1
Energy [GeV]	1.9	
Current [mA]	400	
Critical Energy [keV]	3.07	
Natural Emittance [nm]	6.9	
Natural Energy Spread	0.001	

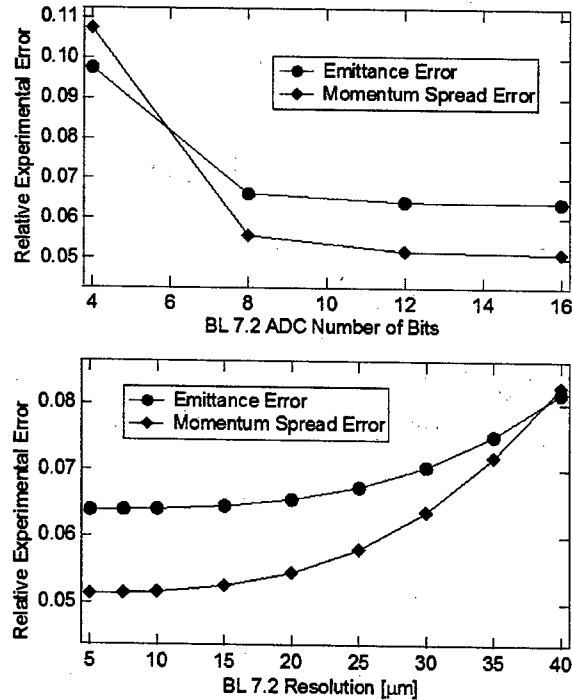


Figure 1: Experimental error as function of the BL 7.2 ADC number of bits (top) and resolution (bottom).

The complete error analysis brought to the specifications for the new system shown in Table 2.

Table 2: BL 7.2 Specifications

Parameter Specification	Value
Resolution [μ m]	≤ 25
Pixel size [μ m]	≤ 10
Total magnification	≥ 1
ADC number of bits	≥ 8
Dynamics factor	≥ 0.5

The resolution requirement finds a good matching with a very simple and reliable system based on the detection of X-ray synchrotron radiation through a pinhole system.

THE PINHOLE SYSTEM

The pinhole shown in Figure 2 is the simplest system for performing profile measurements.

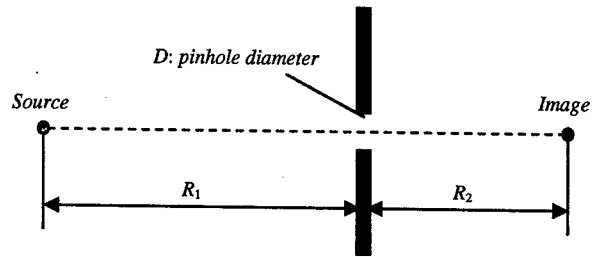


Figure 2: Pinhole System Schematics.

The magnification of the system is R_2/R_1 while the total resolution is given by [2]:

$$x_R = \sqrt{\frac{4}{25} R_1^2 \frac{\lambda^2}{D^2} + \frac{1}{16} \left(1 + \frac{R_1}{R_2}\right)^2 D^2} \quad (8)$$

where λ is the wavelength of the radiation used for the measurement and the other quantities are defined in Figure 2. The first term in the right hand side of equation (8) is due to diffraction while the second is due to the geometry of the system. For the optimum pinhole diameter:

$$D_{OPT} = \sqrt{\frac{8}{5} \frac{R_1 R_2}{R_1 + R_2} \lambda} \quad (9)$$

the two contributing terms become equal and the resolution assumes its minimum:

$$x_{R \min} = \sqrt{\frac{1}{5} R_1 \left(1 + \frac{R_1}{R_2}\right) \lambda} \quad (10)$$

BEAM LINE 7.2 DESCRIPTION

BL 7.2 was mainly based on the design of similar diagnostic beamlines at BESSY II [3] allowing a significant saving in time, cost and engineering effort. With reference to Figure 2, a variable thickness Molybdenum filter has been inserted between the pinhole and the image plane with the double role of band-pass filter for the proper selection of the radiation wavelength and as a variable attenuator. Downstream the filter at the image plane, a phosphor screen allows the conversion from X-rays to visible light. The image is then collected and digitized by a system composed by a remotely controlled zoom, a CCD camera and a frame grabber. Table 3 summarizes BL 7.2 parameters while Table 4 shows the characteristics of the five positions filter-attenuator used in the system.

Table 3: BL 7.2 Characteristics

BL 7.2 Parameter	Value
R1 [m]	6.08
R2 [m]	2.04
Pinhole Diameter [μm]	20
CCD Pixel size [μm]	8.6
Total maximum magnification	1.31
ADC number of bits	8
Dynamics factor	≥ 0.5

Table 4: BL 7.2 Filter-Attenuator Characteristics

Pos.	Mater.	Thick. [μm]	Flux [ph/s]	Attn. Factor	$\langle E \rangle$ [keV]	σ_E [keV]	x_R [μm]
1	Al	10	$2.3 \cdot 10^{11}$	1	8.5	3.6	26.7
2	Mo	5	$6.3 \cdot 10^{10}$	3.7	10.8	3.7	24.3
3	Mo	20	$1.5 \cdot 10^{10}$	15.3	13.3	3.3	22.9
4	Mo	50	$3.9 \cdot 10^9$	59.0	15.1	2.7	22.3
5	Mo	90	$1.2 \cdot 10^9$	192	16.3	2.2	21.9

The fourth column of Table 4 shows the flux of photons impinging the phosphor downstream the filter at the nominal ALS current. The intensity is large enough to allow low error profile measurements with stored currents much smaller than the nominal maintaining at the same time a reasonable integration time. The sixth and seventh columns of the table show respectively the average energy and the rms energy spread of the filtered photons. The last column indicates the system resolution obtainable with the different filters.

Table 5 summarizes the performances of the system for different measurements. It must be remarked that the minimum value for the emittance and momentum spread experimental error is mainly defined by the optical functions at the two source points and cannot be significantly reduced by a further adjustment of the BL 7.2 parameters.

Preliminary resolution studies considering the polarization of the synchrotron radiation [4] have

shown a better resolution for the pinhole system than the one calculated by using expression (8). In fact, due to the nature of the SR the photons passing through the small pinhole are naturally polarized in the machine plane. The diffraction figure for such a polarization is smaller than for the case of non-polarized light with beneficial impact on the resolution. A more precise characterization of such effect is under way.

Table 5: BL 7.2 Calculated Performances

Measurement Type	Experimental Error (rms value)
Momentum Spread	5.6 %
Horizontal Emittance	6.6 %
Horizontal Beam Size	1.3 %
Horizontal Dispersion	1.2 %
Horizontal Distribution Centroid	1.1 %

In the actual design, BL 7.2 has a matrix of 21 rows and 11 columns of pinholes instead of a single pinhole. As described in reference [3], this configuration allows the measurement of other quantities such as emission and aperture angles of the SR at the source. The remotely controlled zoom lens permits passing from the high resolution mode, where only the central pinhole is visible, to the low resolution one where the whole pinhole matrix can be viewed.

Another feature of BL 7.2 is the presence of an X-ray beam position monitor for the measurement of the electron beam orbit position and angle at BL 7.2 source point. The system, which is of the same kind of the ones in successful operation at BESSY II, is based on the differential measurement of the electron secondary emission induced on two metallic blades by the SR [3].

Finally, a special BL 7.2 port dedicated to visible and infrared SR can be used for several different electron beam measurements including longitudinal distribution profile and motion, transversal motion and coherent effects in the SR at the infrared and far-infrared wavelength.

ACKNOWLEDGEMENTS

The authors want to acknowledge A. Biocca, E. Williams and B. Bayley for their contributions and the other members of the ALS Accelerator Physics Group for the helpful discussions.

REFERENCES

- [1] F. Sannibale, "Experimental Error Analysis of a Possible Measurement of the Emittance and Momentum Spread at the ALS" ALS Note LSAP-301 (2003).
- [2] Y. Wu, private communications.
- [3] W. B. Peatman and K. Holldack, "Diagnostic front end for BESSY II", J. Synchrotron Rad. **5**, 639 (1998).
- [4] J. Byrd, private communications.

DEVELOPMENT OF A LONGITUDINAL DENSITY MONITOR FOR STORAGE RINGS*

M. Zolotarev, J.-F. Beche, J. Byrd, P. Datte, S. De Santis, P. Denes, M. Placidi, A. Ratti, V. Riot, R. Schoenlein and W. Turner, Lawrence Berkeley National Laboratory, Berkeley, CA 94720, USA

Abstract

We report on development of a new storage ring operations tool for measurement of longitudinal beam density profile. The technique mixes synchrotron light with light from a mode locked solid-state laser oscillator in a non-linear crystal and detects the up-converted radiation with a photo-multiplier. The laser is phase locked to the storage ring RF system. The laser choices available for repetition frequency, pulse length and phase modulation give a very wide range of options for matching the bunch configuration of particular storage rings. Progress in the technology of solid-state lasers ensures this system can be made robust for routine use in storage ring operations. A very large number of important applications are possible including measurement of the fraction of untrapped particles prior to acceleration, the population of particles in the nominally unfilled RF buckets in a bunch train ("ghost bunches"), longitudinal tails, the diffusion of particles into the beam abort gap and the normal bunch parameters of longitudinal shape and

intensity. We are currently investigating application to two devices: (1) the 1.9 GeV ALS electron storage ring at LBNL with 328 RF buckets, 2ns bucket spacing, 276 nominally filled bunches, 15-30ps rms bunch length and (2) the 7 TeV LHC proton collider under construction at CERN with 35,640 RF buckets, 2.5 ns bucket spacing, 2,808 nominally filled bunches, 280-620 ps rms bunch length. A proof of principle experiment is being conducted on ALS. The results of the ALS experiment and detailed analyses of the application to LHC and its requirements are described.

INTRODUCTION

The purpose of the work described in this paper is to develop a flexible beam instrument for the measurement of the longitudinal bunch distribution of beam particles in storage rings. The approach that is being developed is indicated schematically in Fig. 1 and has two parts; (1) utilization of the synchrotron and wiggler radiation

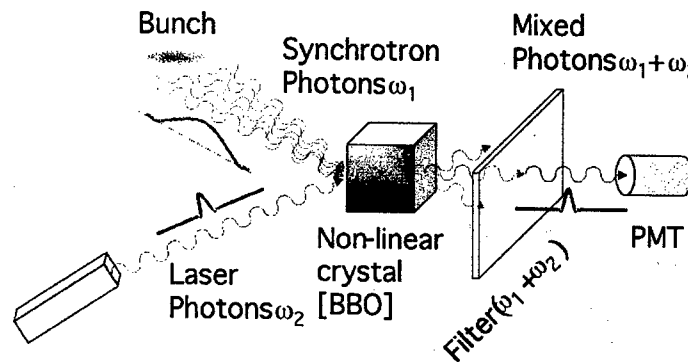


Figure 1. Schematic of the experimental technique for longitudinal beam density measurement by up-conversion of synchrotron radiation with a CW laser.

emitted by highly relativistic beam particles in strong magnetic fields and (2) cross correlation of the synchrotron or wiggler radiation with light from a solid state CW laser that is phase locked to the storage ring radio frequency system. The cross correlation is done by mixing the laser and beam radiation in a non-linear crystal and detecting the sum frequency radiation. When the synchrotron radiation is in the near infrared, this allows shifting the detection wavelength to the

optical region where quantum efficiency is high. A prototype system has been assembled and initial data taken in beamline 5.3.1 at the ALS electron storage ring at LBNL.

Owing to the large range of laser pulse lengths and repetition frequencies available it is possible to design a system that can accurately measure bunch shapes with ~1 ps to ~50 ps resolution and with rms lengths from ~10 ps to ~1 ns for any modern day storage ring;

* Work supported by the US Department of Energy under contract DE-AC03-76SF00098.

Tevatron, RHIC, ALS, LHC, APS etc. A longitudinal density monitor will find a wide range of applications that provide essential information for machine operation and longitudinal beam dynamics studies, including measurements of: (1) the untrapped beam fraction, (2) the intensity of ghost bunches, (3) the fraction of particles in the beam abort gap, (4) the longitudinal bunch shape and (5) coherent multi bunch modes. The concept was originally proposed and is being developed at LBNL for the Large Hadron Collider (LHC) under construction at CERN. In this case the stored beam energy is very high ~350 MJ/beam and can cause extensive damage to machine components if some of it diffuses into the beam abort gap. It is therefore clearly necessary for LHC operations to have a good understanding of the longitudinal distribution of protons. In addition, it is desirable to minimize the untrapped beam fraction prior to the energy ramp and to limit the beam population in the ghost bunches which cause background in the detectors. In the LHC context our goal is to develop an instrument with four orders of magnitude dynamic range so diffusion of beam particles into unwanted regions can be detected well before reaching a level that could damage equipment. The idea of building such a system on ALS was to demonstrate the quality of information available and the practicality of such a system for routine use in an accelerator control room.

EQUIPMENT

The synchrotron radiation from the bunched beam of the ALS is mixed in a non-linear crystal with a mode locked Ti:Al₂O₃ laser oscillator and the up-converted radiation is detected with a photo-multiplier tube. The laser operates at 71 MHz (14 ns) with pulse length 50 fs, wavelength 800 nm and power 100-200 mW and has been described previously [1]. The 197 m main ring of the ALS has 328 RF buckets separated by 2 ns so that after 7 revolutions each RF bucket has been sampled once ($7 \times 47 = 328 + 1$). The laser is phase locked to the ALS RF frequency. The laser is phase modulated at 10 Hz with a mirror mounted on a piezo-electric crystal and arranged to sample the profile of each RF bucket with 32 time slices separated by approximately 4.8 ps. Nominally 276 consecutive buckets are filled with ~1.2 mA per bunch and the 52 bucket gap has a single "camshaft" bunch of ~6 mA near the center of the gap.

The electronic hardware and the software necessary to measure the longitudinal density profile of the ALS was developed in 2002. A data acquisition board was designed and fabricated to accumulate the number of photon counts per time slice per bunch passage. The data acquisition board contains an address generator and bunch accumulation memory that keeps the data sorted according to position in the circumference of the ALS. Data accumulation stops and a trigger is generated for readout by a PC after a certain number of

revolutions of the ALS. The software that has so far been developed allows for display of (1) electron density profile with 4.8 ps sampling interval over the full circumference of the ALS, (2) peak and integrated intensity per RF bucket versus bucket position and (3) rms pulse length per RF bucket versus bucket position. Examples are given in the following section.

INITIAL RESULTS

The data acquisition board and software described in the previous section have been successfully tested in initial experiments on the ALS.

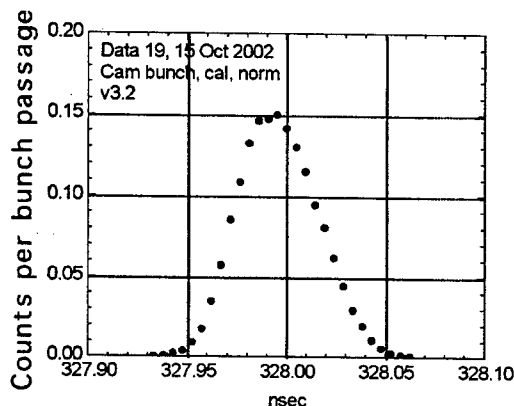


Figure 2. Beam intensity profile of a single bunch in the ALS measured by correlation of synchrotron light emission with a mode locked solid-state laser oscillator.

Fig. 2 shows the density profile of the "camshaft" pulse in photon counts per bunch passage for a typical fill of the ALS (1 count = 4.4 mA). The rms pulse length is approximately 18 ps. The 'camshaft' pulse is quite symmetric and leans forward slightly due to the inductive/resistive impedance of the ALS ring [2]. Similar density profiles of the complete RF bucket train of the ALS were obtained simultaneously.

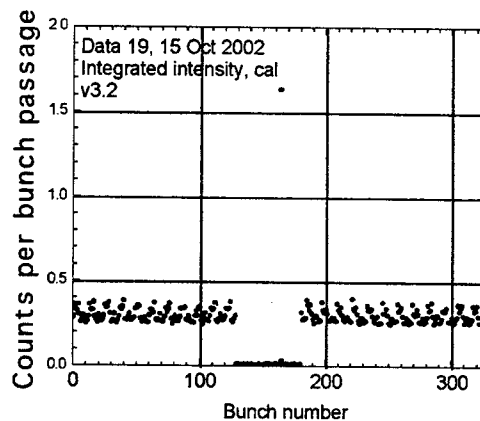


Figure 3. Integrated intensity of all 328 RF buckets in the ALS.

Fig. 3 shows the integrated bunch intensity versus RF bucket number (from 0 to 327). The gap in bunch intensity extends from buckets 129 to 180. The "camshaft" bunch is in the middle of the gap at bucket number 164 and has intensity 1.63 counts.

A low intensity 0.035 counts is visible in the trailing bucket number 165. The average background is 0.014 counts and can be further reduced by inserting a filter to reject second harmonic laser light and decreasing the ambient background radiation from room lights near the photomultiplier. Inspection of the nominally filled RF buckets reveals a nine bucket repeating pattern of bunch intensity variation at the level of $\pm 20\%$. This is traceable to intensity variation from the booster injecting into the ALS. Fig. 4 shows the rms bunch length versus bunch number. The rms bunch lengths of the nominally filled RF buckets are in the range 16 to 18 ps and show a trend of decreasing linearly from 18 ps adjacent to the gap to 16 ps on the opposite side of the ring due to transient beam loading in the harmonic RF cavities. The approximately 40 ps rms bunch length for the empty gap buckets corresponds to the rms length of a uniform distribution with full duration equal the measurement window per bucket. This can be corrected in software by subtracting the background level. The background level is also responsible for the 28 ps length attributed to the parasite bunch immediately trailing the "camshaft".

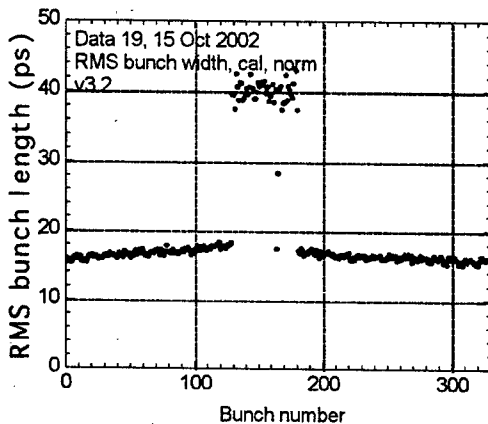


Figure 4: RMS bunch length of the 328 RF buckets in the ALS.

Fig. 5 shows in more detail the leakage from the "camshaft" bunch into the two trailing RF buckets on a logarithmic scale to emphasize the dynamic range of signal detection. The peak of the 'camshaft' bunch is 5×10^{-2} counts whereas the noise level is $\sim 2 \times 10^{-5}$, giving a signal to noise ratio of roughly 2.5×10^3 . The noise is primarily due to fluctuations in ambient background light and can be further improved so 10^4 dynamic range can be expected.

The power of the experimental method under development is clearly indicated in Figs.2-5. The time

resolution exceeds that possible by purely electromagnetic pickup devices. The dynamic range that can be expected is at least four orders of magnitude. The technique is well suited to routine digital signal analysis of a very large number of buckets (328 for ALS and 3,564 for the future LHC).

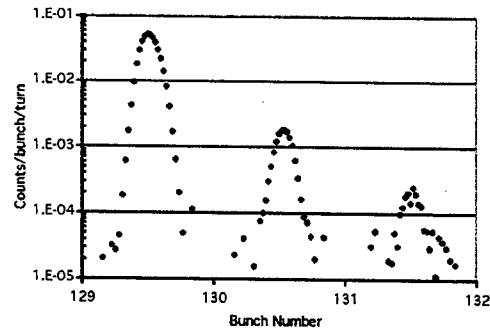


Figure 5: "Camshaft" pulse and two trailing RF buckets. Background has been subtracted.

CONCLUSIONS

In this paper we have presented a summary description of a new tool, based on non-linear mixing of the synchrotron radiation with a mode-locked laser, for measuring the longitudinal beam profile in a storage ring. The non-linear mixing technique allows to detect the beam signal in the optical range with high quantum efficiency, even when the natural synchrotron radiation has longer wavelengths (for example, in lower energy proton rings). Additionally, our instrument has very good time resolution (which depends on the laser parameters) and dynamic range.

We also present the first results of our instrument testing on Berkeley ALS main storage ring. A comparison with other diagnostics available at the ALS shows good agreement with the LDM data, for both the bunch length and phase.

REFERENCES

- [1] R.W. Schoenlein et al, Science, 287, 2237. (2000)
- [2] J.M. Byrd et. al., Proc. Microbunches Workshop, Upton, NY, Sep. 1995, AIP Conf. Proc. 367,327 (AIP Press).

DARHT-II ENERGY ANALYZER*

Arthur C. Paul, Steven Hawkins, James McCarrick, James Sullivan, James Watson, Glen Westenskow
Lawrence Livermore National Laboratory, Livermore, CA 94550, USA.

Shmuel Eylon, Thomas J. Fessenden
Lawrence Berkeley National Laboratory, Berkeley, CA 94720, USA.

William Nexsen
Johnston Controls, Livermore, CA 94550, USA.

Abstract

A energy analyzer system is being built for the DARHT-II accelerator similar to the energy analyzer used on the Astron accelerator [1]. This system consists of a scattering wire, magnetic bend, and null signal detector. The wire thickness of 40 mil carbon and the scattering angle of 11 degrees is chosen for good signal to noise ratio. The dipole bend angle is 60 degrees, with a 30 cm radius of curvature. The image-plane focal distance is chosen for the required energy resolution. The energy resolution and acceptance are 0.1% and $\pm 5\%$ with a time response of 10 nsec. The wire must survive the 2usec 2kA, 18.4 MeV DARHT-II beam. The MCNP code [2] was used to study the wire scattered properties. The scattered beam fills the available 1x2 cm dipole aperture. The dispersion normal to the beam direction is 0.43 cm/%. The detector is a PIN diode array which determines the beam position on the chip. This array consists of 40 2.5x0.1x0.25 mm bins with a gain in excess of 10000. The system will be installed in the space between the debris blocker and the cruncher solenoid up-stream from the shuttle dump [3].

1 Introduction

We have developed a energy spectrometer for DARHT-II based on an instrument developed for the Astron Accelerator some 30 years ago. We propose to locate the spectrometer downstream of the Debris Blocker in front of the Shuttle Dump, figure 1. The preliminary specifications of the analyzer are:

Energy Resolution	$\approx 0.1\%$
Energy Acceptance	$\pm 5\%$
Relative accuracy/repeatability	$\approx 0.1\%$
Absolute accuracy	$< 1\%$
Time response	$< 10\text{ ns}$

Consideration was given to minimizing perturbations of the primary DARHT beam when the analyzer is not in use.

* This work was performed under the auspices of the U.S. Department of Energy by the University of California, Lawrence Livermore National Laboratory under contract No. W-7405-ENG-48.

The instrument uses a small rod or wire placed transverse to the beam to scatter a tiny fraction of the primary beam into a secondary beam line. The secondary line is 11 degrees from the main line. The scattered beam travels one meter through an adjustable aperture located in front of an analyzing magnet that bends the scattered beam 60 degrees further from the main beam and focuses it to approximately a 1 mm wide strip at the plane of a PIN detector array ≈ 34 cm away. The image of the scattering wire at the detector plane is approximately a 1x10 mm ellipse. The detector array is 4 cm long in the bend plane and is located transverse to the scattered beam. The energy acceptance of this detector array intercepts electrons within $\pm 5\%$ of the central ray energy and amplifies the scattered beam current by a factor greater than 10,000. Calculations suggest that the energy of the scattered beam can be determined with a resolution of approximately 0.1% by electrically determining the transverse position the secondary beam strikes the detector array.

2 Scattering wire

Because of the higher DARHT beam energy, obtaining adequate signal at the detector required a scattering rod or wire that was about 1 mm in diameter if carbon or 0.5 mm diameter if titanium. However, the temperature of the carbon wire could increase by as much as 1000 degrees C and titanium would not survive a 2 cm diameter DARHT beam at full current and pulse width. As a consequence, if required we propose to expand the beam to 7 cm diameter thereby dropping the beam current density by a factor of 10 when the scattering wire is present by turning off focusing upstream of the wire, figure 2. The energy lost in the scattering wire is not negligible and can amount to as much as 1 or 2%. Fortunately, the Monte Carlo code calculations indicate that the energy spectrum is spread by only about 0.5%. When the analyzer is not in use, the scattering wire is withdrawn from the main beam line to avoid perturbing the primary beam.

3 Magnet

The bend magnet is based on the design of an existing Los Alamos magnet. The principal difference is that the gap is increased from 1 to 1.5 cm. This will permit the insertion of a separate aluminum vacuum chamber with inside dimensions of 2 cm width by 1 cm height. It also will permit the insertion of a precision Hall effect Gauss meter in the magnet gap for precise determinations of the bending magnetic field. The beam enters and exits normally to the magnet with a 30 cm radius of curvature in the magnet under nominal conditions. This provides a bend plane focusing of the beam some 30 cm past the magnet exit, figure 3.

4 The Detector

The detector was designed for operation at very low rep-rate. It consists of a 0.25 cm wide by 4 cm long strip of silicon biased to approximately 500 Volts. The strip is segmented every 0.1 cm to form 40 0.25x0.1 cm sections oriented transverse to the detected beam as indicated in figure 5. The strip is 250 μ m (0.025 cm) thick and is p-doped on front and n-doped on back to form a PIN array. Energy deposited in the detector from the scattered beam creates electron hole pairs in the silicon which are swept out by the bias voltage. Calculations suggest that a current gain greater than 10,000 should be expected. The time response of the detector is predicted [4] to be approximately 10 nsec.

5 Signal Strength

The point design has tended to maximize the amplitude of the detector signal under the philosophy that too much signal is better than too little. Calculations suggest that the signal voltage could be several hundred volts, which is much more than adequate, and more than the PIN detector could provide. An aperture in front of the magnet was included to provide a simple way of reducing the signal if required. Using a smaller scattering wire and/or switching to carbon would also be very effective in lowering signal strength. Notice that all these strategies would improve the resolution of the instrument and carbon would survive much better.

6 Shielding

The PIN detector is sensitive to both the scattered electrons and the x-ray background so shielding will be required. The detector is located just in front of the shuttle dump but its view of the dump is partially occluded by a large focus magnet. Initial scooping shielding calculations suggest that the unshielded x-ray signal will be approximately equal to the detector signal. Thus it appears that the detector must be housed in a shield-enclosure that reduces

the background x-ray intensity by 2-3 orders. Some actual measurements of the background x-ray flux on FXR have indicated that the x-ray background may not be as serious a problem as first thought.

7 Calibration

We estimate that a determination of the absolute energy the DARHT-II beam accurate to perhaps 1% can be obtained from knowledge of the parameters of the analyzer and a measurement of the bending magnetic field. If a more accurate measurement of the beam energy is required, the analyzer could be calibrated using a known beam.

The instrument will first be mounted on ETA II to test the DARHT analyzer with an actual electron beam prior to deployment on DARHT. Calculations suggest that because of the lower ETA II energy, a 10 mil carbon wire will generate approximately the same detected signal as a 40 mil wire used with DARHT II.

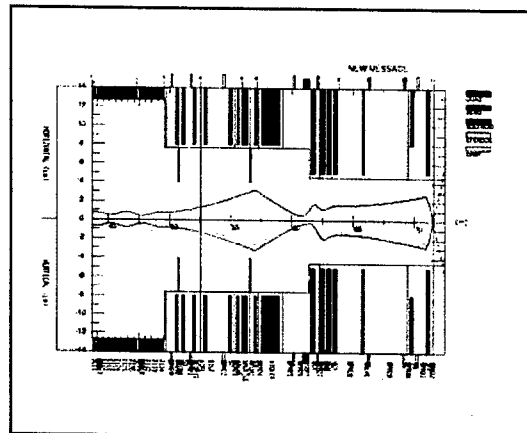


Figure 1) Nominal beamline extending from the exit of the accelerator to the x-ray target. The energy analyzer scattering wire will be located at 52.5 meters and is shown here as the line intersecting the beam.

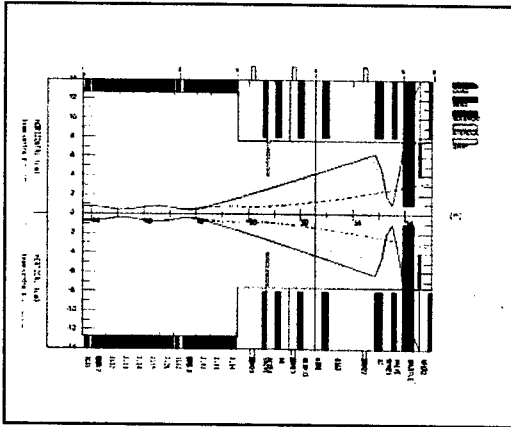


Figure 2) Magnets leading up to the scattering wire are turned off so the beam expands to reduce the current density on the wire shown here as the line intersecting the beam. Dashed line the beam profile with magnets on.

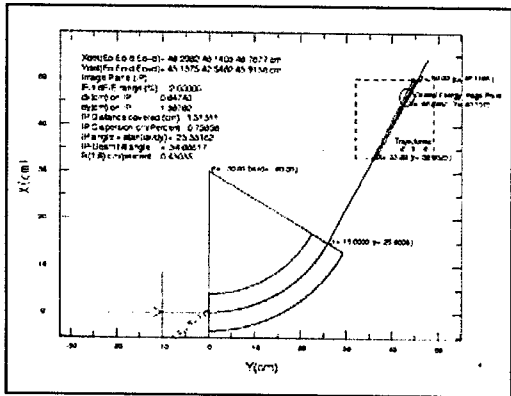


Figure 3) Overall layout of the energy analyzer components. Intensity aperture, dipole magnet, and PIN detector. The scattering wire is off scale to the left.

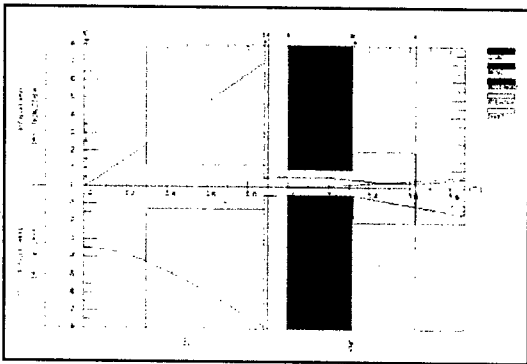


Figure 4) The available aperture varies along the path leading to the PIN detector. The scattered beam passing through the limiting aperture almost fills the available gap of the magnet.

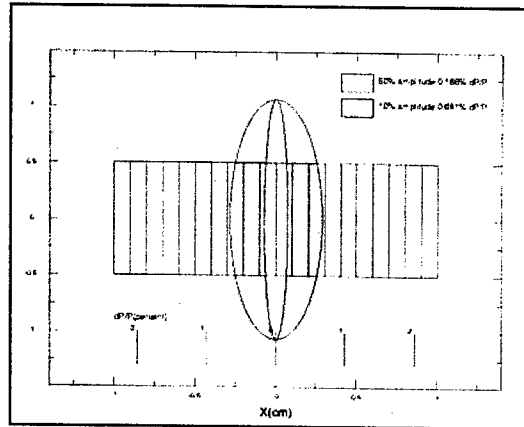


Figure 5) Beam super-imposed on the detector showing the 50% and 10% amplitude foot print. The detector has a 0.1 cm bin size and covers a 1 by 4 cm area. The beam hard edge half size is 0.287 by 1.07 cm, at the 50% amplitude the full size is approximately the detector bin size.

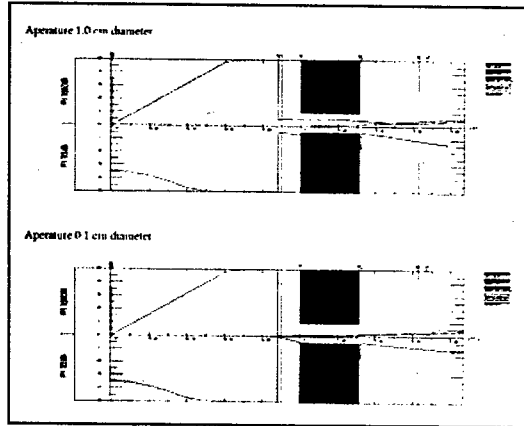


Figure 6) Effect of the collimating aperture on the beam intensity at the detector. Above, 1.0 cm diameter aperture with intensity $i/l_0 \approx 1.74 \times 10^{-5} P(\theta)$, below, 0.1 cm diameter aperture with intensity $i/l_0 \approx 1.74 \times 10^{-7} P(\theta)$.

8 References

- [1] T.J. Fessenden, "The Astron On-Line Beam Energy Analyzer", Rev. of Sci. Instruments., 43, 1090, (1972)
- [2] "MCNP - A General Monte Carlo N-Particle Transport Code", LA-12625-M, March 1997.
- [3] A.C.Paul, G.J.Caporaso, Y.J.Chen, G.Westenskow, W.M.Fawley, E.P.Lee. "The Beamline for the Second Axis of the Dual Axis Radiographic Hydodynamic Test Facility" 1999 Particle Accelerator Conference, New York.
- [4] R.W. Kuckuck, "Semiconductor Detectors for use in the Current Mode", UCRL-51011 (1971)

PROGRESS ON A SMITH-PURCELL RADIATION BUNCH LENGTH DIAGNOSTIC

S.E. Korbly, A.S. Kesar, M.A. Shapiro, and R.J. Temkin
Plasma Science and Fusion Center, MIT, Cambridge, MA 02139 USA

Abstract

A Smith-Purcell radiation diagnostic to measure the micro bunch length of a 20MeV, 17 GHz electron bunch train is being implemented at MIT. The bunch length can be determined by measuring the frequency and angular distribution of the emitted radiation. The beam is produced by a 17 GHz, 50 MeV/m traveling wave accelerator built by Haimson Research Corporation (HRC). The high operating frequency of this accelerator allows for the production of ultra-short bunches of about 180 femtoseconds. At this time we are assembling the experiment and we will present an update on the progress.

1 INTRODUCTION

The HRC accelerator system consists of a chopper-prebuncher injector, and a quasi-constant traveling wave disc loaded accelerating structure consisting of 94 cavities that operate in the $\frac{2\pi}{3}$ mode[1], [2]. The accelerator has achieved a beam energy of 17 MeV at 100mA. Simulations [1] indicate that the phase spread at the exit of the accelerator should be about 1° , or a bunch length of ~ 180 fs. Conventional methods for measuring bunch length consist of using streak cameras or RF deflecting structures. While streak cameras have been shown to work down to ~ 200 fs, the bunch length of the HRC accelerator is at the operating limit. Additionally, streak cameras are expensive and the measurement process is destructive. HRC is building an experiment, in parallel with the Smith Purcell experiment, to use an RF deflecting structure to measure the bunch length[5], however, this technique also has the disadvantage of being destructive.

Two techniques have been developed that utilize lasers to measure the bunch length: X-ray generation through Compton scattering and an electro-optic technique. The Compton scattering method requires a TeraWatt laser and a high charge electron beam in order to produce enough x-rays. The electro-optic technique requires the laser and electron bunch to be properly phased together. Both of these methods would require a substantial upgrade to the laser system currently in operation at MIT.

Several coherent radiation techniques have been employed to measure bunch lengths, including transition radiation, diffraction radiation and Smith Purcell radiation. These techniques all exhibit qualitatively similar angular distributions of radiated power and have the feature that the radiation intensity scales as the square of the number of particles. However, Smith Purcell radiation has the further

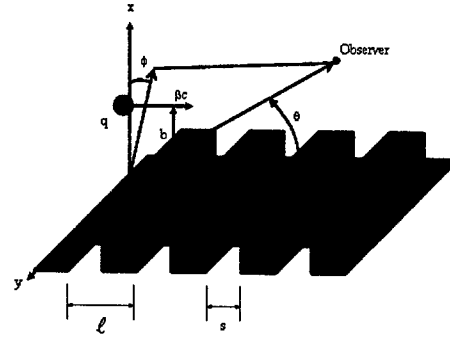


Figure 1: Schematic of an electron bunch, q , passing over a grating of period l , with an impact parameter b .

advantage over the other two coherent radiation methods in that the intensity of radiation scales as the number of grating periods. In addition, the Smith Purcell diagnostic is non-interfering and non-destructive. Using Smith Purcell radiation as a bunch length was first proposed by Nguyen[3] and demonstrated by Doucas[4]. The experiment by Doucas at Frascati was performed on a beam that was 14 ps and the wavelength of the measured radiation was 0.65 mm to 4 mm.

2 SMITH-PURCELL RADIATION DIAGNOSTIC

An electron passing close to the surface of a metal diffraction grating as in Figure 1 emits Smith-Purcell radiation at a wavelength λ_n given by

$$\lambda_n = \frac{l}{n} \left(\frac{1}{\beta} - \cos \theta \right) \quad (1)$$

where l is the grating period, θ is the emission angle with respect to the propagation direction, n is the diffraction order, and β is the velocity of the electron bunch. The angular distribution of power radiated by the electrons is given by [6]

$$\frac{dP}{d\Omega} = N_g \frac{e I n^2 \beta^3}{2 l \epsilon_0} \left(1 + N_e e^{-k^2 \sigma^2 \cos^2 \theta} \right) \times \frac{\sin^2 \theta}{(1 - \beta \cos \theta)^3} R_n^2 \exp \left(-\frac{4\pi |n| b}{\gamma l (1 - \beta \cos \theta)} \right) \quad (2)$$

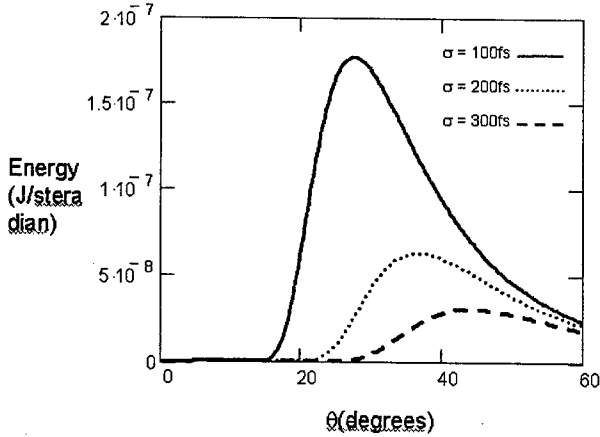


Figure 2: Plot of radiated power as a function of angle for three different bunch lengths (100 fs, 200 fs and 300fs).

where N_g is the number of grating strips, I is the beam current, N_e is the number of electrons in the bunch, ϵ_0 is the permittivity of free space, b is the height of the bunch above the grating surface, γ is the relativistic factor $(1 - \beta^2)^{-\frac{1}{2}}$, k is the wave vector, σ is the bunch length, and R_n^2 is the grating efficiency factor.

For radiation at wavelengths shorter than the bunch length the radiation is incoherent. However, at wavelengths longer than the bunch length the radiation is coherent and the temporal coherence of the electron bunch enhances the intensity of the radiation. In general, the coherence term is $(1 + N_e F)$, where F is the form factor given by the Fourier transform of the bunch distribution. For Equation 2 a Gaussian distribution has been assumed giving a coherence term $(1 + N_e e^{-k^2 \sigma^2 \cos^2 \theta})$.

The estimated bunch length for the HRC accelerator is 180 femtoseconds or $55 \mu\text{m}$. In Figure 2 equation 2 is plotted as a function of angle for three different bunch lengths (100 fs, 200 fs, and 300 fs) and for $b = 0.5 \text{ mm}$, $\gamma = 35$, $l = 2.1 \text{ mm}$, $N_e = 1.2 \cdot 10^8$, $N_g = 50$, and $|n| = 1$. The bunch length diagnostic involves measuring the angular distribution of the radiation to determine the length of the pulse.

3 EXPERIMENTAL SETUP

3.1 HRC Accelerator

The HRC accelerator is powered by a relativistic klystron which has produced powers up to 26 MW with a saturated gain of 67 dB[7]. The linac consists of a DC thermionic gun, a chopper-prebuncher injector, and a quasi-constant accelerating structure consisting of 94-cavities that operate in the $\frac{2\pi}{3}$ mode. The electron bunches produced by the injector are designed to be accelerated by the linac to energies of 25 MeV. Initial operation of the accelerator with injected RF power up to 10 MW produced

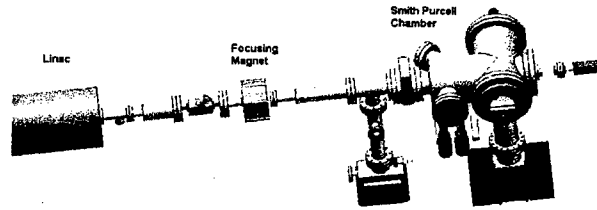


Figure 3: Schematic of the Smith Purcell experimental beamline

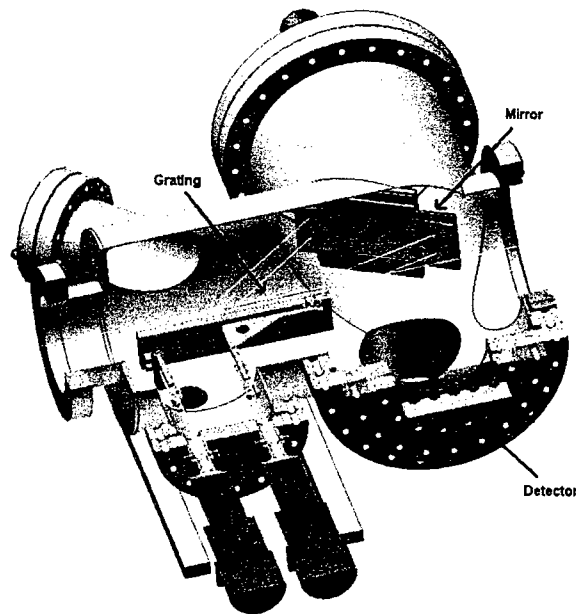


Figure 4: Schematic of the Smith Purcell experimental vacuum chamber

beam energies up to 17.5 MeV with up to 100 mA of transmitted beam current. The accelerator is currently being commissioned to full operating parameters.

A schematic of the accelerator beamline with the Smith Purcell experiment vacuum chamber is shown in Figure 3. The Smith Purcell experiment will be placed ~ 1 meter downstream from the exit of the linac to allow for the use of a focusing solenoid and steering coils.

3.2 Smith Purcell Diagnostic

A schematic of the Smith Purcell diagnostic vacuum chamber is shown in Figure 4. The essential components of the diagnostic include the grating, a mirror to capture and focus the radiation, a window through which the radiation passes out of the vacuum chamber and a detector.

The grating parameters have been optimized for the HRC electron beam using the procedure in [8] for an echelle grating. The grating parameters include: a period of 2.1 mm, a blaze angle of 10° , and a length of 10 cm ($N_g = 47$). The radiation is collected by a mirror with a radius of 48.89 cm and is designed to collect radiation emitted between the angles 15° and 40° and redirect it out a 10 cm window. Both pyroelectric and bolometer detectors will be implemented to measure the radiation. The experimental chamber has been baked out and will shortly be installed on the accelerator beamline.

4 CONCLUSIONS

The 17 GHz traveling wave disc loaded structure has demonstrated a beam energy of 17 MeV at 100 mA current. To our knowledge this is the highest frequency stand alone accelerator in the world. A Smith-Purcell radiation diagnostic to measure the bunch length of the HRC accelerator is currently being implemented. The estimated bunch length of the accelerator is ~ 180 fs which should produce coherent radiation in the THz regime. The Smith Purcell experimental chamber is currently being installed on the accelerator beamline and operation will commence shortly.

5 ACKNOWLEDGEMENTS

This research is supported by the U.S. Department of Energy. The authors would like to thank Hayden Brownell of Dartmouth College for his assistance in the design of the experiment.

6 REFERENCES

- [1] J. Haimson and B. Mecklenburg, "HV injection and phase orbit characteristics for sub-picosecond bunch operation with a high gradient 17 GHz linac", Proc. 6th Workshop on Advanced Accelerator Concepts, No. 337, pp146-59.
- [2] S.E. Korbly, W.J. Brown, M.A. Shapiro, R.J. Temkin, "Design of a Smith Purcell Radiation Bunch Length Diagnostic", Proc. 2001 Particle Accelerator Conference, 01CH37268, 2001, pp. 2347-2349.
- [3] D.C. Nguyen, "Electron Bunch Length Diagnostic With Coherent Smith-Purcell Radiation", Proc. 1997 Particle Accelerator Conference, 97CH36167, 1997, pp. 1990-1992.
- [4] G. Doucas, et.al., "Determination of longitudinal bunch shape by means of coherent Smith-Purcell Radiation", Phys. Rev. ST-AB, Vol 5, (2002) 072802.
- [5] J. Haimson, B. Mecklenburg, G. Stowell, B. Ishii, "A Circularly Polarized Beam Detector for Direct Measurement of Ultra Short Electron Bunches", Proc. 10th Workshop on Advanced Accelerator Concepts, No. 647, pp. 810-820.
- [6] K.J. Woods, J.E. Walsh, R.E. Stoner, H.G. Kirk and R.C. Fernow, "Forward Directed Smith-Purcell Radiation from Relativistic Electrons", Phys. Rev. Lett., Vol. 74, pp. 3808-3811 (1995)
- [7] J. Haimson, B. Mecklenburg, B.G. Danly, "Initial performance of a high gain, high efficiency 17 GHz traveling wave

relativistic klystron for high gradient accelerator research", Pulsed RF Sources for Linear Colliders. Montauk, NY, 1994

- [8] S. H. Trotz, J.H. Brownell, J.E. Walsh, G. Doucas, "Optimization of Smith Purcell Radiation at very high energies", Phys. Rev. E, Vol 61, (2000), pp. 7057-7064.

BEAM DIAGNOSTIC SYSTEM FOR HIGH INTENSITY PROTON LINAC AT KAERI

S. J. Park, J. H. Park, Y. S. Bae, W. H. Hwang, J. Y. Huang, and S. H. Nam,
Pohang Accelerator Laboratory, POSTECH, Pohang, Korea
and

Y. S. Cho, J. M. Han, S. H. Han, B. H. Choi
Proton Engineering Frontier Project, KAERI

Abstract

A 100-MeV high-intensity (20 mA CW) proton linac is being built in the KAERI (Korea Atomic Energy Research Institute), Korea. Beam diagnostic system for the machine require to include BCMs (Beam Current Monitors), BPPMs (Beam Position and Phase Monitors), and other devices. BCMs are of special importance for high-intensity proton linacs, since the control of beam loss is critical. They should have high stability and resolution better than $5E-4$. BPPMs are for measuring beam position and phase (w.r.t RF) simultaneously, that are crucial for the successful commissioning and operation of the accelerator. All diagnostic devices are required to operate both in CW and pulsed (several ms) modes. Pulsed mode operation is useful when machine tuning and commissioning. In this article, we report the developmental status of beam diagnostic devices for the KOMAC accelerator, with detailed description on the BPPM PU design.

1 INTRODUCTION

The KOMAC (Korea Multi-purpose Accelerator Complex) is one of HPPAs (High-Power Proton Accelerators) which are under construction at the KAERI (Korea Atomic Energy Research Institute), Korea. It aims to generate 100-MeV proton beams at the beam current of 20 mA, CW. Refer to Table 1 for the major beam parameters of the KOMAC accelerator.

Table 1: Beam parameters of KOMAC accelerator

	Operation Modes		Remark
	CW	Pulse	
Beam Energy	100 MeV		
β	0.43		
γ	1.107		
Beam Current	20 mA max.	20 mA peak	
Pulse Width	NA	2 ms	
Bunch Length	160 ps		PARMILA Simulation
Bunching Frequency	350 MHz		

The beginning parts of HPPAs includes ion sources, RFQs and DTLs which are complex and have tight installation spaces. This is especially true for diagnostic devices, and their design and installation often become designer's "nightmare." Meanwhile, diagnostics including BPMs and CTs are very important for successful commissioning and operation of the accelerators. Hence, their implementation should be considered from the early stage of the accelerator design. Successful compromise between the two conflicting side is possible when the diagnostic devices can be made compact without sacrificing their performances. Compact devices are easy to handle, economical, and generally have better high-frequency characteristics. Modern beam diagnostic devices are far more compact than their ancestors. For example, some CTs from the Bergoz Instrumentations are now integrated with CF flanges and their total length (axial) can be made as small as 30 mm. Majority of BPM PUs (Pick-Ups) for proton accelerators are still striplines that yield well defined response even for low-intensity beams. But their sizes are still too big to be installed in the narrow front-ends the accelerator. For example, the axial length of the striplines for the SNS (Spallation Neutron Source, USA) linac exceeds 100 mm, even if they are installed in the vacuum. Button-type capacitive PUs have been simple and reliable, but their application to the proton machines has been limited because of their insufficient response to low-intensity beams. Modern HPPAs such as the KOMAC are designed to have very high beam intensities, so that even the buttons could generate enough signals for precision beam position measurements. In this regards, we have chosen the button-type PU for use in the KOMAC accelerator. One of the disadvantages of the buttons is that, it is difficult to predict the PU sensitivity using analytic formulas. In fact, the PU sensitivity for low-beta beams can not be practically determined even by experimental methods, due to the difficulty of simulating electromagnetic fields from the low-beta beams. We have decided to utilize the computer code for determining the sensitivity of the button-type PU. We have chosen the MAGIC code which is a kind of the PIC (Particle-In-Cell) code and can treat the particle and electromagnetic system in the full three dimensional manner.

2 DESIGN OF BPPM PU

The theoretical estimation of the sensitivity of stripline PU was established by R. E. Shafer.^[1] It is basically 2D theory and can not be used for designing the button-type PUs which are 3D features. There are commercial electromagnetic codes that can simulate 3D geometries, including the MAFIA T3. But the MAFIA T3 can handle only ultra-relativistic particles and can not be applied to low-beta beams. (The port boundary of the MAFIA T3 can accept only TEM mode whose phase velocity is equal to that of the light. And low-beta beams generate fields that are not in the simple TEM mode.) Limitations of the Shafer's theory and the MAFIA code have led us to consider on using the MAGIC code. It is versatile and can handle arbitrary combinations of particle beams and electromagnetic structures.

Fig. 1 shows the 3D model of the button PU for the MAGIC simulation and its cross-sectional view in the transverse plane. In the left figure of Fig. 1, proton bunches travel left-to-right direction. Beam signals are coupled to the four buttons that are installed around the circumference of the beam pipe. Buttons are connected to 50-ohm coaxial lines whose dimensions are different from those of usual fabrication. This simplified the simulation geometry without sacrificing reliability of the simulation.

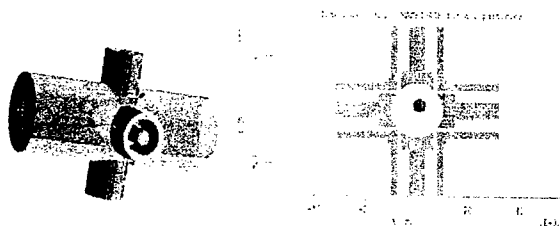


Figure 1: Modelling of button-type PU for MAGIC simulation. Left figure: 3D model, Right figure: Cross-sectional view. Dot inside beam pipe in right figure indicates proton beam. Diameter of beam pipe is 20 mm.

Default beam parameters used in the simulation are shown in Table 2. The left figure of Fig. 2 is the voltage waveform developed between the inner and outer conductors of the coaxial line. As expected, they are considerably longer than the beam bunch length, which is due to the axial extension of fields from the low-beta beams. ($\beta = 0.08$ for $E = 3$ MeV) With increasing the beam energy, beam fields concentrate in the transverse plane, and the pulse widths of signals coupled to buttons are shortened approaching that of charge distribution in the beam. This is shown in the right figure of Fig. 2 which is the signal waveform for the beam energy of 100 MeV.

Table 2: Default beam parameters used in MAGIC simulation.

Beam Energy	3 MeV
Average (Peak) Beam Current	20 (570) mA
Bunching Frequency	350 MHz
Bunch Length	43 ps rms

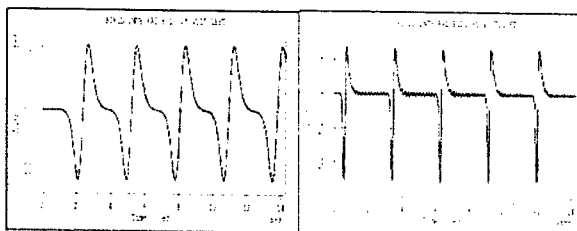


Figure 2: Waveforms of voltage signal developed at the end of one of coaxial lines for beam energies of 3 MeV (left) and 100 MeV (right).

The dependence of the PU sensitivity on the beam energy was simulated with result shown in Fig. 3. As expected from the Shafer's theory, the sensitivity increases dramatically with decreasing the beam energy. It also increases with increasing frequency at low energies but converge to the same value at high energies.

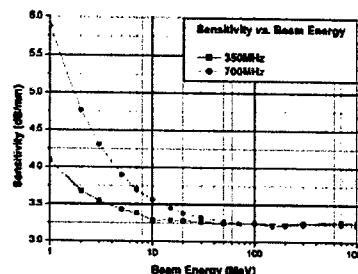


Figure 3: Dependence of PU sensitivity on beam energy.

Sensitivity of the PU to beam position change was simulated by moving the beam in the transverse plane in the step of 1 mm. The sensitivity map was obtained by plotting the delta-over-sum values of band-pass filtered voltage signals appearing at the ends of the coaxial lines. The center frequencies and bandwidth of the band-pass filter were 350 or 700 MHz and 20 MHz respectively. See Fig. 4 for the sensitivity maps for the frequencies of 350 and 700 MHz.

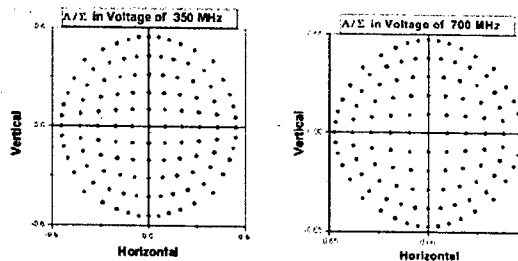


Figure 4: Sensitivity map of button PU at the frequencies of 350 and 700 MHz. Beam pipe diameter = 20 mm. Button diameter = 12 mm. Beam energy and beta are 3 MeV and 0.08 respectively.

Note that the sensitivity for 700 MHz was about 7.5% larger than that of the 350 MHz.

In order to confirm the validity of the MAGIC simulation, we have simulated the BPM PU of the PLS (Pohang Light Source). The PU consists of four buttons with 9.5-mm diameter installed in vacuum chamber that has diamond-like cross section. Table 3 compares some of simulation results with experimental measurements. Beam parameters used in the simulation are; Beam energy = 2.5 GeV, Average (Peak) current = 200 (1600) mA, Bunching frequency = 500 MHz, Bunch length = 26 ps. The measured signal amplitude may contain substantial errors due to our rough estimation of the cable attenuation for the wide-band pulses. Simulated sensitivity values needs further refinement with finer meshes.

Table 3: Comparison between MAGIC simulation and experimental measurement results of PLS BPM PU.

		Simulation	Measurement
Signal Amplitude (V)		5.5	3
On-center Sensitivity (%/mm)	X	6.6	6.15
	Y	7.7	6.13

The fabrication of the PU that consists of buttons, coaxial feedthroughs, and vacuum chamber is in progress at the Hitachi Electronics in Japan. A sample PU that is composed of one button + feedthrough and vacuum chamber will be fabricated by the company and its electrical performance will be tested in the Pohang Accelerator Laboratory.

3 BPPM ELECTRONICS

The signal processing electronics should provide both CW and pulsed measurement of beam position and phase for the beam current ranging from 0.2 to 20 mA (40-dB dynamic range). Resolution and stability are required to be better than 50 μm . For this, the LR (Log-Ratio) electronics would be the best choice since it has large acquisition bandwidth (> 5 MHz) and reasonable dynamic range (50 dB).^[2] Resolution performance is rather marginal (~50 μm at 20-mm ϕ Beam pipe) but can be improved by the averaging multiple samples. Commercial LR electronics is already available from Bergoz Instrumentation at reasonable price. Phase measurement circuit could be fabricated in house, or custom-ordered from the company to make it integrated into the existing LR electronics avoiding the necessity of expensive connectors and cables.

4 BCM DEVELOPMENT

Efforts for developing BCM hardware will be saved by collaborating with companies including the Bergoz Instrumentation. In order to make BCMs highly stable

and immune to bunch-length changes, it is recommended to limit the measurement bandwidth by tuning the current monitor to a specific frequency among various spectral contents in the beams. This can be realized by providing small capacitance, C in the winding of high-permeability core, which will oscillate at the frequency determined by the formula $f = 1/2\pi\sqrt{LC}$ where, L is the leakage inductance of the winding.^[3] By adjusting the value of C, the oscillation can be tuned to a specific harmonic (e.g., 350 MHz) among the beam spectrum. The oscillation should be made low Q to avoid excessive or erratic responses. Prototype BCMs based on the above operating principle (Tuned-CT) are under fabrication in the company and their performance will be tested at the KOMAC accelerator.

5 CONCLUSION

We conclude this article with the following summarizing remarks:

1. A button-type PU for use in the KOMAC (Korea Multi-purpose Accelerator Complex) accelerator was designed utilizing the MAGIC code.
2. Dependence of the PU sensitivity on the beam energy and the frequency well corresponded to the theoretical predictions.
3. Simulation results of the PLS (Pohang Light Source) electron BPM PU reasonably agreed to the experimental measurements.
4. "Tuned-CT" for measuring beam currents with high stability (5E-4) is under development with the collaboration with the Bergoz Instrumentation.

ACKNOWLEDGEMENTS

The authors would like to thank to Julien Bergoz, Klaus Unser in the Bergoz Instrumentation and Jim Hinkson in the GMW Associates for their numerous and enthusiastic discussions. This work was supported by the Ministry of Science and Technology, Korea.

REFERENCES

- [1] R. E. Shafer, "Sensitivity of PUs for low beta beams," Proc. of the BIW93.
- [2] A. Kalinin, "The Log-Ratio Beam Position Monitor," Proc. Of the BIW 2002, Upton, New York, 2002, p.384.
- [3] Private communication with Bergoz Instrumentation.

IMPROVED RESULTS FROM THE GAS SCATTERING ENERGY SPECTROMETER ON THE ISIS RFQ TEST STAND

J.P.Duke, D.J.S.Findlay, A.P.Letchford, J.Thomason, RAL, CCLRC, UK

Abstract

The novel Gas Scattering Energy Spectrometer on the ISIS RFQ Test Stand at the Rutherford Appleton Laboratory (Oxfordshire, UK) has been used to measure the energy spectrum of the ~ 665 keV H^- beam from a four-rod RFQ as a function of RF drive power. Since EPAC'02 changes have been made to the experimental arrangement, which markedly improve the quality of the results that can be obtained. These new results are reported.

1 THE APPARATUS

The purpose of the Gas Scattering Energy Spectrometer (GSES) is to confirm the mean energy and energy spread of the nominal 665 keV beam from the ISIS RFQ. This RFQ, after comprehensive testing, is intended to replace the existing Cockcroft-Walton pre-injector on the ISIS spallation neutron source at the Rutherford Appleton Laboratory (RAL). The four-rod RFQ performs well, and is able to transport more than its design current of 30 mA at less than its nominal design RF power of 210 kW.

A more detailed description of the design process for the apparatus used can be found at [1]. Its basis is a set of two cascaded assemblies each consisting of a 130 mm long gas scattering cell, a 0.5 m drift length and three small (~ 0.2 mm diameter) apertures, which together reduce the peak intensity of the beam current sufficiently to allow a semiconductor charged particle detector [2] to be used to detect individual H^- ions and measure their energies. The total drift length between RFQ exit and detector is ~ 6 m. Xenon gas (at low pressure) is used to scatter the H^- beam because the higher the atomic number of the scatterer the lower is the energy loss for a given mean multiple scattering angle. The energy loss caused by the xenon is calculated for the relevant scattering thicknesses used and is added back in as a small correction to the measured energies.

The particle detector used was an Ortec® BA-025-025-1500 silicon surface barrier detector with an active area of 25 mm² and a depletion depth of 1.5 mm, and was operated at a bias voltage of 186 V. Signals from the detector pass first through an EG&G Ortec® [2] Model 1421H pre-amplifier and then into a Canberra® Model 2020 spectroscopy amplifier with 1 μ s pulse shaping. The bipolar output from the amplifier is passed into a TRUMP PCI-8k multi-channel analyser PC card. Ortec® Maestro-32 spectrum analysis software is used to visualise and analyse the resultant spectra. Before taking a measurement the system is calibrated by fitting gaussians to the 624 and 656 keV lines from a 2kBq Cs-137

conversion electron source which is installed in the detector box on a movable arm. After calibration the bias voltage is never changed.

In the present measurements the X-ray background has been greatly reduced. In the previous measurements reported in [3], X-rays produced between the rods within the RFQ vessel were able to reach the surface barrier H^- particle detector by propagating down the beam pipe, and the addition of the resultant noise to the H^- pulses from the particle detector had the effect of broadening the measured energy spectrum. In the present measurements a 4mm thick tantalum disc was introduced to attenuate the X-rays (maximum photon energy 90 keV corresponding to the peak-to-peak rod-to-rod RF voltage of 90 kV). A hole of 0.5 mm diameter, the minimum diameter practicable, was drilled through the tantalum disc, and the tantalum disc was then glued to the front of the aluminium disc in the final bellows before the diagnostic box so that the hole in the tantalum disc lined up with the ~ 0.2 mm diameter hole in the aluminium disc. Although a thickness of 4 mm of tantalum is able to block effectively all the X-rays [4] some are still able to reach the detector through the central hole, but overall the X-ray flux on the detector is reduced by a factor ~ 250 .

A further improvement made in the present experimental system was the application of a 285 μ s gating pulse to the multi-channel analyser to eliminate interference spikes at the beginnings and ends of the

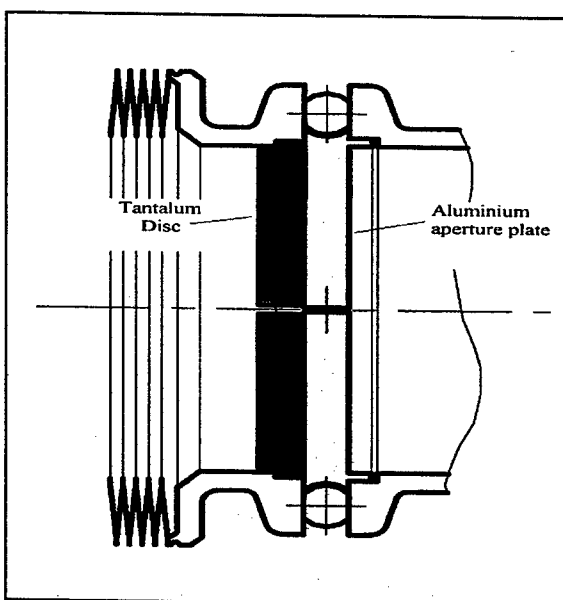


Fig. 1: The new tantalum disc attached to the aperture plate

pulses of RF driving the RFQ. Conversion electron calibration runs were performed while gating only during the RF pulse, and the standard deviations of the two caesium peaks measured as 4.7 ± 0.4 keV compared with 5.1 ± 0.1 keV gating *outside* the RF. Therefore there seems to be no significant residual widening effect from the X-rays.

2 DATA ANALYSIS

The measured spectra of energies of H^- particles from the RFQ should be corrected for the following effects: background, energy losses in the xenon gas, energy straggling in the xenon gas, and finite resolution of the surface barrier detector.

Background was first removed from the present measurements by subtracting from the H^- spectrum channels the average value of 400 channels well above the H^- peak in energy. Next, three sets of cubic splines were fitted to the data to represent plausibly smoothly the data and $\pm 2\sigma$ error limits. The resolution function of the surface barrier detector (given by the shape of the Cs-137 conversion electron lines as described above) was then deconvolved from the data by taking the best fit spline set, convoluting it with a gaussian of standard deviation 5.1 keV representing the resolution function (FWHM 12.0 keV) of the surface barrier detector, and adjusting the height of each channel until the convolution of the resolution function and the corrected spectrum function best fitted the measured spectrum data. Then the energy loss of the H^- particles in the xenon, only ~ 1.8 keV for the gas pressures typically used, was added back on the basis of polynomial interpolation amongst tabulated values of proton stopping power in xenon as a function of proton energy [5]. The energy straggling in the xenon [6] was estimated at typically only 2×10^{-2} keV, and so was neglected. Finally, from the corrected spectra of H^- particles from the RFQ were calculated mean energies and RMS widths, both for spectra truncated at energies corresponding to the full width tenth maximum points and for the entire spectra (including the asymmetric low and high energy tails). The mean energies for the whole distributions were consistently lower than those for the truncated distributions (Fig 3.). This confirms the previous finding that the low energy tail is larger than the high energy one.

The corrected measured results have been compared with computational particle tracking simulations of the RFQ. Performing this comparison is useful both to verify the RFQ codes and to confirm that the RFQ is performing as expected/predicted. Due to the long drift length between RFQ and detector, and the high space charge forces in the RFQ bunches, the beam has completely debunched by the time it reaches the detector. The high space charge also affects the energy spectrum of the beam, widening the energy spread. Therefore, in order to compare like with like, the measured and simulated energies and widths are compared at the position of the detector.

One effect not included in the calculation above is that of stripping of H^- ions in xenon. It has been previously calculated that at the pressures used in this experiment, almost all the H^- ions should be stripped to H^+ . Therefore the two electrons will carry off some small fraction of the H^- particles' energy. This fraction may be $\sim 2 \cdot m_e c^2 / m_p c^2$, i.e. $\sim 1/918$. Assuming a mean energy of 665 keV, this effect would add at most 0.72 keV to the energies quoted below for protons.

3 RESULTS AND DISCUSSION

The following graphs summarise some of the results obtained in the experiments reported above:

Figure 2 shows one example of the spectra obtained. The blue curve represents the original raw data. The red curve represents the same data after correction for energy loss in the xenon, detector resolution and background.

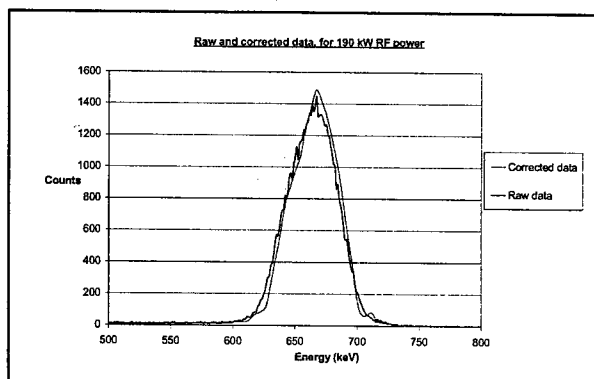


Fig. 2: Raw and corrected spectrum data, for an RF power of 190 kW

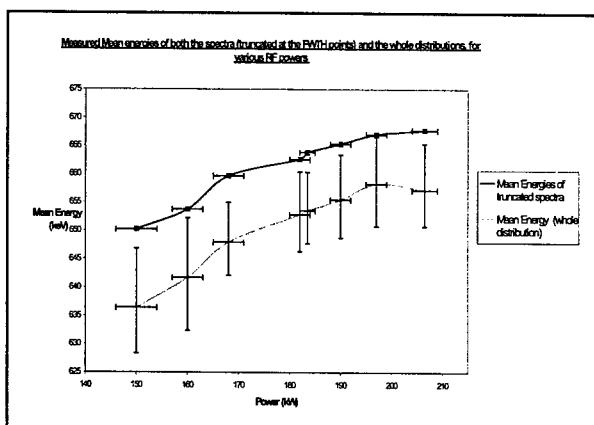


Fig. 3: Comparison of mean energies of truncated and untruncated spectra

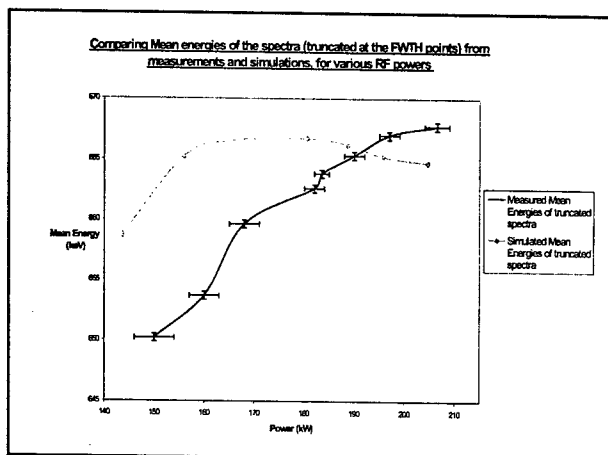


Fig. 4: Comparison of Measured and Simulated mean energies, for the truncated spectra, for various RF powers

At no RF powers do the simulated mean energies differ from the measured mean energies (for the truncated spectra) by more than 1.7% (Fig. 4). The small remaining differences between them could be partly due to the fact that the GSES by its very design selects only the central portion of the beam, whereas in order to provide sufficiently good statistics, the simulated figures are calculated by including particles with a larger range of angles. The measured mean energies generally rise with RF Power. However, the difference in RF power dependence of the mean energies between the measured and simulated results is as yet not understood.

At powers well below the design RFQ operating power, i.e. $< \sim 170$ kW, the measured distributions become more asymmetric, with the lower energy tail becoming a greater proportion of the whole, and the central peak becoming consequently narrower. This is indicative of the reduction of the size of the RF bucket and the large phase oscillations which occur at lower powers.

As can be seen from Fig. 5, the measured RMS widths for the truncated spectra are fairly constant at 16.5 keV

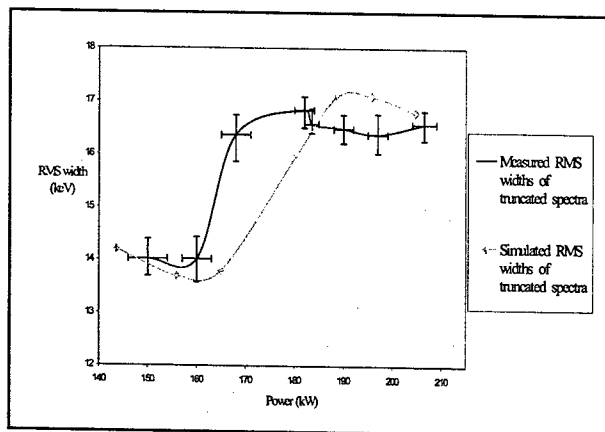


Fig. 5: Comparison of Measured and Simulated RMS widths, for the truncated spectra, for various RF powers

above about 165 kW, about 14 keV below this RF power, and compare well with the simulated values. The tracking simulations indicate that the space charge after the RFQ exit acts to increase the energy spread of the beam by several keV.

4 CONCLUSIONS

The Gas Scattering Energy Spectrometer has been used successfully to re-measure energy spectra from the ISIS RFQ. The improvements made to the experimental arrangement have substantially improved the quality of the data. The results indicate that the beam from the RFQ is consistent with the longitudinal acceptance of the 70 MeV linac intended to be fed by the RFQ.

5 REFERENCES

- [1] J.P.Duke, D.J.S.Findlay, G.R.Murdoch-'WPAH115', "Design of a Gas Scattering Energy Analyser for the ISIS RFQ Accelerator Test Stand", PAC 2001, Chicago
- [2] EG&G Ortec®; now part of the Ametek® Group: <http://www.ortec-online.com/>
- [3] J.P.Duke, D.J.S.Findlay, S.Hughes, P.Knight, G R Murdoch-'THPLE046', "Measurements of Beam Energy using the Gas Scattering System in the ISIS RFQ Test Stand", EPAC '02, Paris
- [4] "Photon Cross Sections, Attenuation Coefficients, and Energy Absorption Coefficients from 10keV to 100GeV"- by J.H.Hubbell at the Centre for Radiation Research, 'NSRDS-NBS 29', pub. 1969 by United States Department of Commerce
- [5] "Stopping-Power and Range Tables for Electrons, Protons, and Helium Ions" <http://physics.nist.gov/PhysRefData/Star/Text/contents.html>
- [6] Bruno Rossi, "High Energy Particles", pub. Prentice-Hall, 1952, pgs 14-15,31-32

VERY HIGH RESOLUTION RF CAVITY BPM*

Marc Ross[#], Joe Frisch, Linda Hendrickson, Douglas McCormick, SLAC, Stanford, CA 94025, USA,

Vladimir Vogel, Budker Institute of Nuclear Physics, Novosibirsk, Russia

Hitoshi Hayano, Junji Urakawa, KEK, Tsukuba-shi, Ibaraki-ken, Japan

Abstract

Linear collider (LC) interaction region beam sizes and component position stability requirements are expected to be a few nanometers[1]. It is important to show that the related tolerances can be achieved, with an electron beam if possible. Using recently developed component stabilization technology, very high-resolution beam position monitors (BPM's), and the ultra-low emittance beam at the KEK ATF, we plan to demonstrate the required stabilization. Our first step is to develop high-resolution RF cavity beam position monitors, using either C or X band frequencies. A C-band cavity BPM with a resolution of 25 nm has been reported in tests at FFTB [2]. By correcting for the effects of non-axial trajectories and using both position and angle BPM movers, we expect to be able to demonstrate a resolution of 2 to 3 nm over a dynamic range of +/- 20 μ m. We report on the progress of the tests here.

INTRODUCTION

Recent progress in accelerator performance has resulted in part from precision beam position monitors (BPM's). Third generation synchrotron radiation sources, such as the Swiss Light Source, are very close to achieving sub-micron beam stability over relatively long periods of many hours or even days.

Future accelerator projects, such as the linear collider, require large numbers of BPM's with 200 nm resolution and 1 μ m accuracy. Near the collision point, somewhat better resolution will be important. Given these developments, it is important to understand the limits on BPM performance and evaluate their role in the design of new machines. An RF cavity BPM, coupled with modern waveform processing, has been estimated to have resolution below one nanometer [3]. In this paper we illustrate the application of nanometer resolution BPM's and report on tests aimed at proving their performance.

NANOMETER RESOLUTION

The theory of high resolution BPM's has been reported in [4]. C-band (6426 MHz) cavity BPM's, illustrated in figure 1, have been installed in the ultra-low emittance extraction line of the KEK Accelerator Test Facility ATF for the purpose of evaluating their performance and understanding the stability of the beam. Given the state of the art of storage ring and linear collider design, this appears at first to be beyond what is needed. These

BPM's have an estimated loss factor of 3.9×10^{10} J/C²/mm² or about 10^{-12} W for a 1 nm offset with a beam of 1.6 nC, typical for the ATF. About 50% of this power is coupled out and can be mixed down to an IF waveform that is digitized. Table 1 summarizes the signal strength and the expected noise levels.

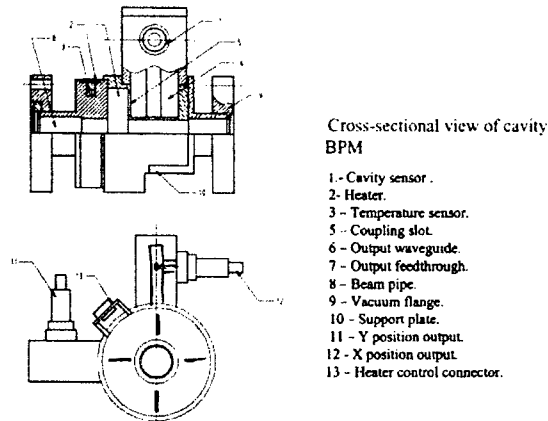


Figure 1: Schematic of the ATF extraction line C-band RF cavity BPM.

Table 1: Signals and noise in the cavity BPM system. The estimated thermal noise, at the digitizer, corresponds to less than one nanometer beam motion at 10^{10} particles per bunch (ppb).

Circuit location	Estimated signal
E_dep (10^{10} ppb, 1nm offset)	10^{-19} J
Energy coupled out	5×10^{-20} J
Output power	5×10^{-13} W (-93dBm)
Downconvert/amp (50dB)	-43dBm
Into digitizer	3mV p/p
Thermal noise in band at cavity (10MHz)	-98dBm
Thermal noise with 3dB noise figure at digitizer	-45dBm

Measurements

In [3], an experiment for proving BPM resolution is described. Using BPM's produced by the BINP group, we have reproduced that installation at the ATF. Because the signal emerging from the RF cavity BPM depends on the angle of the beam trajectory as well as its offset within the BPM, we have also included pitch and yaw movers on each BPM. Thus each BPM has 4 four independent remotely controlled degrees of motion, x, y, x', and y'.

As in [4], we orthogonalize the sine-like and cosine-like (I/Q) responses of the BPM's using the position and angle movers. Unfortunately, whereas the position motion

* Work supported by US Department of Energy under contract DE-AC03-76SF00515

[#]mccrec@slac.stanford.edu

control (x, y) does not also move the angle of the monitor, the angle control is not perfectly centered at the BPM center and also moves the BPM position, making the I/Q determination a little less accurate. Nevertheless, once the response matrix of the mover controls and the I/Q signals is known, it is straightforward to find the trajectory through the BPM which produces minimum or no power out on average.

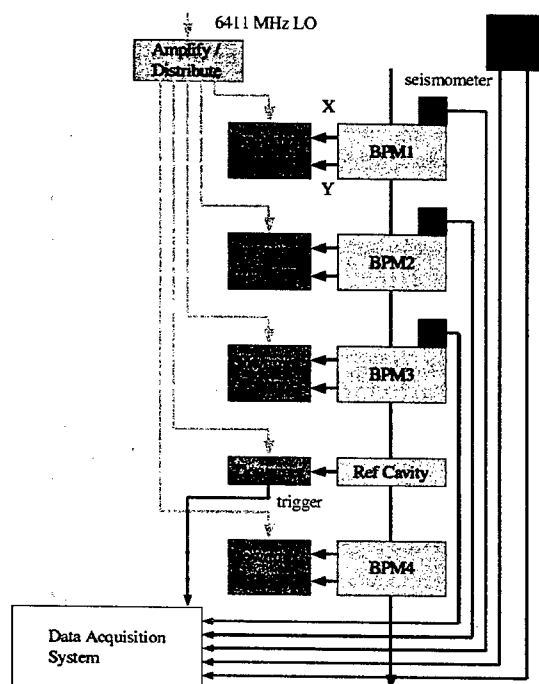


Figure 2: Schematic of the high resolution BPM test equipment, showing the BPM placement along the beamline and the signal processing electronics. In this experiment seismometer vibration monitors (shown on the right) were used to check the motion of the BPM's and BPM supports.

In the ATF extraction line, where these measurements were made, the beam repetition rate is 1.5 Hz, the beam size σ_x/σ_y is 50/5 μm , the beam energy E_b is 1.3 GeV and typical beam pulse to pulse position y variation is 3 μm .

Figure 2 shows the signal processing system used to acquire waveforms from each BPM. Care is taken to keep the noise figure low and to use a narrow band system. The final 15 MHz IF is digitized using 12 bit 100 MHz digitizers. Figure 3 shows the digitized waveforms from the beam trigger, the reference cavity, and the x, y output from one of the BPM's. Initial commissioning of the system is underway and resolution measurements will be done soon.

INTERACTION REGION STABILIZATION

The two sets of focusing magnets that are aligned with the entrance to the linear collider detector must be stabilized with respect to each other to within a few

nanometers [5]. Beam tests, using SLC and FFTB, that prove the performance of development stabilization systems have been proposed [6]. In the SLC-based proposal, for example, the key issue is to demonstrate that two beams can be kept in collision with the help of prototype active stabilization systems.

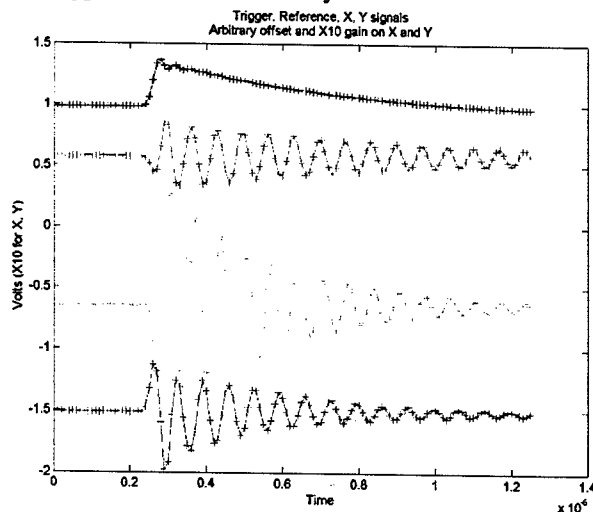


Figure 3: Digitized IF waveforms from the RF cavity BPM's. From top to bottom, the trigger, reference cavity IF and x, y IF waveforms are displayed. The time base is in μs .

In the ATF extraction line, using nanometer resolution BPM's, we will be able to validate the performance of stabilization system prototypes. One of the stabilization systems in development uses precision inertial sensors and an active 'extended object' feedback process. Other stabilization systems use a 'reference object' and 'optical anchor' to indirectly refer the two sets of focusing magnets to each other [7]. The ATF test will use two systems like the one illustrated in figure 2, with a total of 6 RF cavity BPM's with their support movers. The supports will be stabilized using prototype interaction region stabilization feedback. In this experiment, the beam and the BPM's function as a nanometer stability alignment reference.

FEEDBACK

The ATF nanometer BPM's will also be used to demonstrate the stabilization of the trajectory of a long, multi-bunch train [8]. In this experiment, broadband electronics will be coupled with the cavity BPM to provide a correction signal for a feedback kicker. It will be possible to stabilize, to within a few nanometers, the bunches in the train that follow roughly the first 60 ns.

CONCLUSIONS

Interferometers, capable of measuring distances with precision, are not able to provide nanometer resolution measurements with respect to a reference line. There is no presently available technology capable of making alignment measurements with respect to a straight-line

reference at the nanometer level. Using a high energy electron beam and nanometer resolution BPM's we expect to develop the technology to perform this sort of measurement. The beam and BPM's are then a tool used to test and validate mechanical engineering designs.

REFERENCES

- [1] "The Zeroth Order Design Report for the Next Linear Collider", <http://www-project.slac.stanford.edu/lc/ZDR/Zeroth.html>
- [2] T. Slaton *et al.*, "Development of Nanometer Resolution C Band Radio Frequency Beam Position Monitors in the Final Focus Test Beam", XIX Linac Conference, 08/1998.
- [3] Z. Li, *et al.*, "Cavity BPM with Dipole-Mode-Selective Coupler", this conference.
- [4] M. Ross, *et al.*, "RF Cavity BPM's as Beam Angle and Beam Correlation Monitors", this conference.
- [5] J. Frisch, *et al.*, 'Inertial Sensor Development for Active Vibration Stabilization', this conference.
- [6] Experiment proposal for the 'LINX' project, <http://www-project.slac.stanford.edu/lc/linx/>
- [7] Proceedings of the ICFA Nano-beam workshop, <http://icfa-nanobeam.web.cern.ch/icfa-nanobeam/>
- [8] P. Burrows, *et al.*, "Feedback on Nanosecond Timescales for Linear Colliders: Results from First Beam Tests at the NLC Test Accelerator at SLAC", this conference

RF CAVITY BPM'S AS BEAM ANGLE AND BEAM CORRELATION MONITORS*

Marc Ross[#], Josef Frisch, Douglas McCormick, SLAC, Stanford, CA 94025, USA
Hitoshi Hayano, KEK, Tsukuba-shi, Ibaraki-ken, Japan

Abstract

It has been shown that high performance cavity BPM's are capable of accurate beam trajectory angle and beam 'tilt', (x-z or y-z correlation) measurements [1],[2]. Such a device will be very useful for the optimization of a variety of beamlines, such as high current linacs, bunch rotators and storage rings. The signal from a non-axial trajectory or a tilted beam is in quadrature to that observed from a simple displacement of a very short bunch. Using in-phase / quadrature-phase (I/Q) demodulation of the cavity BPM signal, it is possible to separate position and angle/tilt. In this paper, we present results of beam angle and tilt monitor tests carried out in the KEK Accelerator Test Facility (ATF) extraction line.

INTRODUCTION

The purpose of the monitor and how it will be used in the linear collider is described in [1] and [2]. We will review only the basic signal generation here. Consider the system shown schematically in Figure 1: a beam of charge Q , composed of 2 macroparticles located at $\pm \sigma_z$, with a tilt angle θ (or projected dipole length δ), passes through a cavity BPM with frequency f and angular frequency $\omega = 2\pi f$. The particles will induce voltage signals:

$$V_+(t) = -\frac{Q}{2} \theta \sigma_z \frac{d^2 V}{dQ dy} \sin(\omega(t + \sigma_z/c)) \quad (1)$$

$$V_-(t) = -\frac{Q}{2} \theta \sigma_z \frac{d^2 V}{dQ dy} \sin(\omega(t - \sigma_z/c)) \quad (2)$$

for the two macroparticles. The sum response is:

$$V(t) = -Q \frac{d^2 V}{dQ dy} \theta \frac{\omega \sigma_z^2}{c} \cos \omega t \quad (3)$$

where we have assumed that $\omega \sigma_z/c \ll 1$. Equations 1 and 2 show that the signal is 90 degrees out of phase with the signal from a rigid offset of the beam and is proportional to the beam tilt angle.

A convenient expression is the ratio of the peak voltage, V_y , induced by a rigid offset ($y = \delta$), to the peak voltage, V_t , due to a tilted beam (total projected dipole δ).

$$\frac{V_t}{V_y} = \pi f \frac{\sigma_z}{c} \quad (4)$$

Expression 4) can be thought of as the in-phase to quadrature phase ratio and it clearly shows that, if δ is

non-zero, the device can also be used as bunch length monitor. If a displacement δ can be introduced and, independently, a tilt with projected dipole δ' can also be introduced, then the ratio of the response amplitudes in the I/Q plane gives the bunch length.

It is important to note that there is a similar signal induced by 'trajectory tilts' or non-axial trajectories. In that case, the length scale in equation 4) σ_z is replaced with the cavity active length.

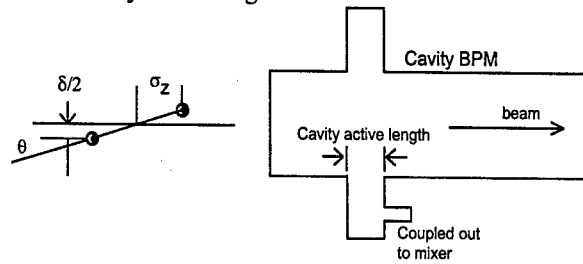


Figure 1: Schematic of the cavity BPM with an incoming 'tilted' beam.

To demonstrate the utility of a tilt monitor with resolution adequate for use in the linear collider, we installed a powered RF deflector, high performance analog and digital RF circuitry for the BPM signal processing and a set of BPM cavity movers to precisely null the BPM signal in the ATF. Both the deflection cavity and the BPM use C-band RF [3], with wavelengths of 52.5 and 46.7 mm respectively. When a 3 mA (9×10^9 e- single bunch), intensity beam is extracted from the ATF, the bunch length $\sigma_z = 9$ mm [4]. This is large compared to the nominal LC σ_z of 110 um, so we expect the I/Q signals to be easier to observe.

ELECTRONICS - DESIGN

The BPM signals were mixed down to 20MHz and then recorded and analyzed using digital down conversion. A simplified block diagram is shown in figure 2. A noise measurement gave approximately 300 microvolts RMS.

Damage of the front end of the system by mis-steered beam is a serious concern for sensitive cavity BPM's. The specified damage level for the pre-amplifiers is 15dBm. For most of our test the amplifiers had an additional 20dB attenuation on their inputs. No damage was observed to the amplifiers. The maximum levels for large mis-steering were estimated to be 30-40dBm.

RF DEFLECTION CAVITY

A 5712 MHz standing wave deflection cavity was installed in the beamline upstream of the cavity BPM system. The cavity is a rectangular pillbox operating with

* Work supported by US Department of Energy under contract DE-AC03-76SF00515

[#]mccr@slac.stanford.edu

an "accelerating" type mode. The beam trajectory far from the axis where the magnetic fields produce a transverse deflection. The cavity was driven by a TWT with output power of ~ 1 KW. The cable to the cavity had an attenuation of 3dB, for a total drive power to the cavity of ~ 500 W peak. The RF phase was not synchronized with the beam phase. The cavity kick amplitude and trajectory transfer function to the BPM were calibrated using the BPM movers.

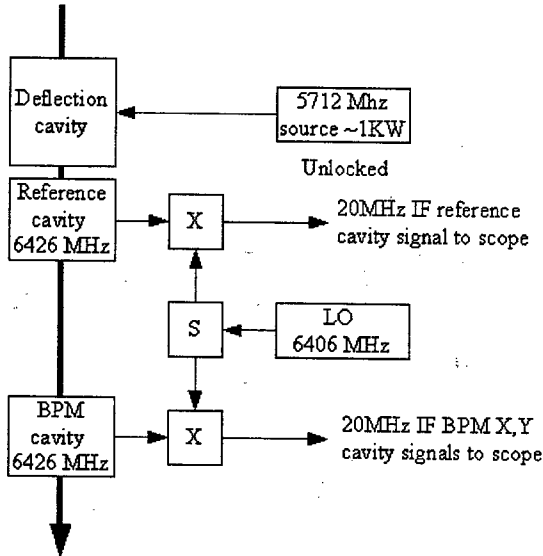


Figure 2: Block diagram of the tilt monitor beamline component layout and signal processing electronics.

DATA ANALYSIS AND CALIBRATION

The cavity and reference IF signals were fit to an assumed damped exponential of the form $V = d + Ae^{(-t/\tau)} \sin(\omega_0 t + \kappa t + \phi_0)$. The Matlab *Fminsearch* algorithm was used to fit the 5 parameters: d , τ , A , ϕ_0 , and κ . An example waveform with the superimposed fit is shown in figure 3.

An analysis window that starts after the initial transient and continues for approximately τ is used. The difference between the BPM phases and the reference cavity phase is then estimated.

The resulting BPM phase and amplitude signals are converted to I/Q vector signals. These are normalized by the amplitude of the reference cavity signal to give normalized I/Q signals. The I/Q signals are linear combinations of the beam position and tilt signals.

The RF cavity BPM calibration was done using its x , x' , y , and y' movers. At a beam current of 5mA in the ring (1.2×10^{10}), the vertical sensitivity was about 30 mV/micron. A noise of 300 microvolts corresponds to a resolution of about 10 nm.

MEASUREMENTS

In order to demonstrate the effectiveness of the monitor for measuring tilts, we used the unlocked deflection cavity and observed the I/Q response of the cavity BPM. Figures

4 and 6 show the I/Q response in internal digitizer units (where the gain of I and Q channels are roughly equal) and figure 5 shows the same in calibrated units. Since the calibration of the beam tilt response cannot be independently known, the units used in the plot were derived from the trajectory tilt calibration. The 3 lines in the figures 4 - 6 show the y and y' axes from the mover based calibration, the third line is 90 degrees from the y calibration direction.

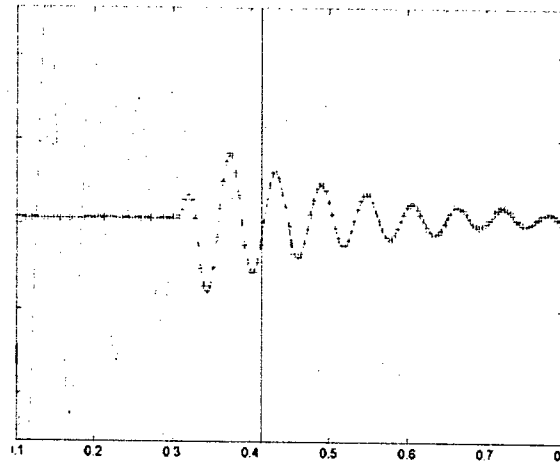


Figure 3: Example waveform with superimposed fit. The fit window is begins about 100 ns following the initial transient.

Using 4), we can estimate the bunch length from the ellipticity of the fitted curve in figure 4. Table 1 shows a comparison between the bunch length estimates from the ellipticity and those presented in [4]. The ATF beam has strong σ_z growth with current because of intra-beam scattering.

Table 1: Comparison between bunch length σ_z estimates from the cavity BPM I/Q ellipticity and streak camera measurements made with stored beam as the intensity and RF gap voltage (V_g) is varied.

Condition	ellipticity	σ_z - ellipticity	σ_z - streak camera
3.5mA	0.81	8.5 (mm)	9.0 (mm)
0.39 mA	0.64	6.9	6.3
1.7 mA	0.74	7.7	7.5
0.465 mA	0.61	6.6	6.8
0.3 mA/ V_g reduced 50%	0.79	8.3	8.8

SENSITIVITY TO ANGLED TRAJECTORIES AND TILTED BUNCHES

The ATF bunch is long compared to the cavity wavelength, so the assumption that $\omega\sigma_z/c \ll 1$ is not valid at ATF. This effect is included in the results listed in Table 1. However, for the purpose of illustration, we will use equation 4) to estimate the beam tilt sensitivity. We find that the ratio of the peak voltage, V_p , induced by a rigid offset ($y = \delta$), to the peak voltage, V_e , due to a tilted

beam (total projected dipole δ') is 0.54 for $\sigma_z = 8\text{mm}$, typical for the beam used in these tests. This means that if the sensitivity to a 1 micron displacement is V , then a beam with a total projected dipole length of $1/0.54 = 1.9\text{ }\mu\text{m}$ will produce the same signal V in quadrature to the displacement.

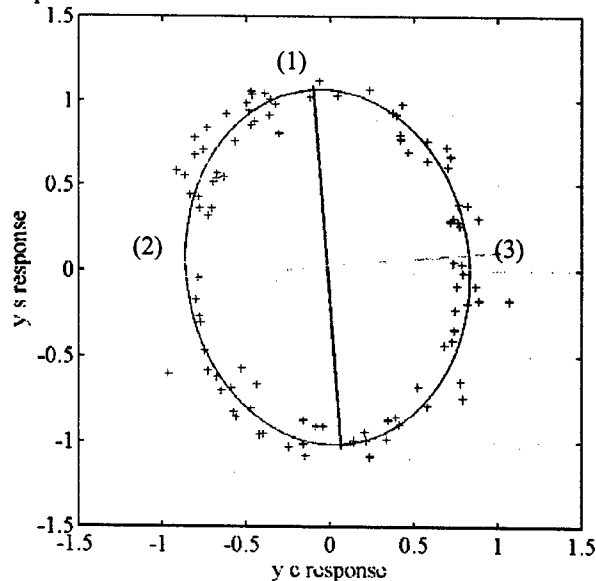


Figure 4: Cavity BPM I/Q signals from 100 beam pulses with the unlocked deflection cavity on. The scale is internal digitizer units. The near vertical line (1) corresponds to a pure displacement, the horizontal line (2) corresponds to an angular displacement (based on the y' mover) and (3) is perpendicular to (1). The fitted ellipticity is 0.8104.

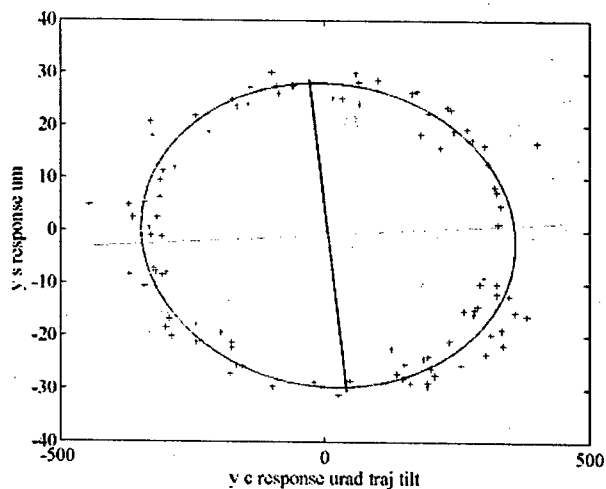


Figure 5: Scaled I/Q response from the cavity BPM, same data as figure 4. The horizontal scale is in units of trajectory angle (urad) and the vertical scale is in μm . The small angle between the plot vertical and the actual vertical I/Q direction is not corrected.

CONCLUSIONS

Initial tests show a strong tilt dependent signal, as would be expected with the long ATF beam. Further tests will use a sequence of monitors in order to determine the monitor resolution. Also, the deflector cavity will be locked to the ATF RF in order to attempt to measure the actual incoming beam tilt.

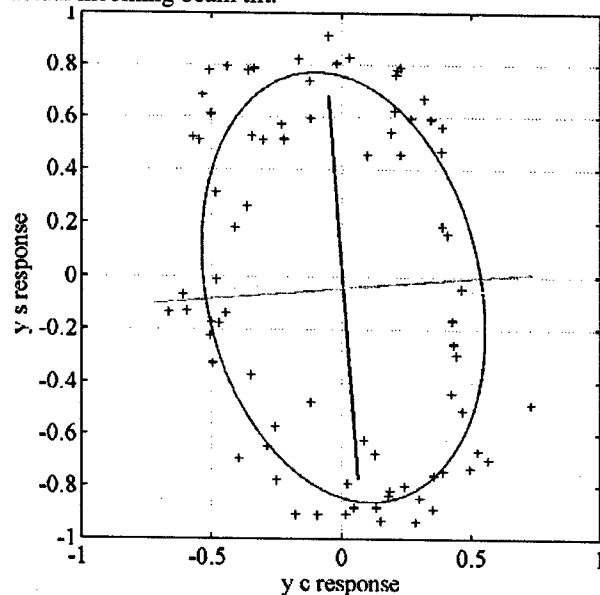


Figure 6: Cavity BPM response at lower intensity, where $\sigma_z \sim 7\text{ mm}$, showing a narrower ellipse. The figure axes units are the same as in figure 4. The fitted ellipticity is 0.6384.

ACKNOWLEDGEMENTS

We would like to acknowledge the assistance of the ATF group, especially J. Urakawa. We would also like to thank V. Vogel and S. Smith for useful discussion. The experiment would not have been possible without the loan of a high power C-band source from T. Shintake of RIKEN and H. Matsumoto of KEK.

REFERENCES

- [1] W. Wuensch, "Measurements for Adjusting BNS Damping in CLIC", CLIC - 244, 17.08.94
- [2] P. Tenenbaum *et al.*, "Beam Tilt Signals as Emittance Diagnostic in the Next Linear Collider Main Linac", EPAC 2002, 06.2002.
- [3] Vladimir Vogel and Nikolai Solyak designed and fabricated the cavity BPMs used in this test. See: V. Balakin, *et al.*, "Experimental Results from a Microwave Cavity Beam Position Monitor", PAC1999, 04.1999.
- [4] T. Naito, *et al.*, "Bunch Length Measurement in the ATF Damping Ring", ATF Internal Note, ATF-01-01.

BUNCHED BEAM CLEANING SYSTEM OF SPRING-8 BOOSTER SYNCHROTRON

T. Aoki, K. Fukami, N. Hosoda, T. Ohshima, M. Shoji, K. Tamura, H. Yonehara
JASRI/SPRING-8, Mikazuki, Sayo-gun, Hyogo 679-5198, Japan

Abstract

In order to fill an aimed radio frequency (rf) bucket with an electron beam in the storage ring at SPRING-8, the bunched beam cleaning system which we call RF knockout (RF-KO) system is installed in the booster synchrotron. The time width of the beam from the linac operated with 2856MHz rf is 1nsec for single-bunch beam operation. The beam is distributed not only in a single rf bucket of the booster synchrotron operated with 508.58MHz rf but also in other rf buckets. The energy of injected beam is increased from 1GeV to 8GeV. The RF-KO system is operated at minimum beam energy of 1GeV because the required knockout power is reduced. The bunched beam in the satellite rf buckets are coherently shaken by the electromagnetic field produced by four RF-KO electrodes in the vacuum chamber. As the amplitude of betatron oscillation increase, the beam soon begins to collide with a beam duct and is lost. The single-bunch beam injected into the targeted rf bucket is effectively kept alive on the zero-crossing point of RF-KO waveform with a precise timing system. The beam intensity of satellite rf buckets in the storage ring was measured with a photon counting method and determined to be 10^{-9} less than that of the main rf bucket.

INTRODUCTION

SPRING-8 is a synchrotron radiation facility composed of a 1GeV linac, a booster synchrotron, and an 8GeV storage ring. The booster synchrotron operated with 508.58MHz rf is designed to accelerate an electron beam from 1GeV to 8GeV with a repetition rate of 1Hz. The time width of the beam from the linac operated with 2856MHz rf can be selected as 40nsec for multi-bunch filling and as 1nsec for several-bunch filling into the storage ring. Although eight-pulse beam can be injected per one cycle from the linac, usually only one-pulse beam is injected. At the several-bunch filling mode, the beam of 1nsec is distributed not only in a single rf bucket of the booster but also in other rf buckets. Most of the beam in satellite rf buckets are dark current from the electron gun and the accelerator columns of the linac. It is necessary to suppress or to remove the beam in satellite rf buckets for high purity bunch formation in the storage ring.

At the high energy of 8GeV, it is hard to remove the satellite bunches in the storage ring. We think it is easy to remove the satellite bunches in the booster at low energy and to make any beam-filling pattern with high purity bunches into the storage ring. Beam cleaning in the booster is done by RF-knockout (RF-KO) system which kicks the beam in satellite bunches with electromagnetic force at low energy [1]. Figure 1 shows the beam energy

pattern of the booster. The pattern can be changed easily by operation window software. The flat-bottom period of 250msec is decided for eight-pulse beam injection that is the maximum number of beam-pulse accepted in the booster. To keep the beam cleaning duration more than 100msec for the latest eighth-pulse beam, the flat-bottom of 250msec is needed.

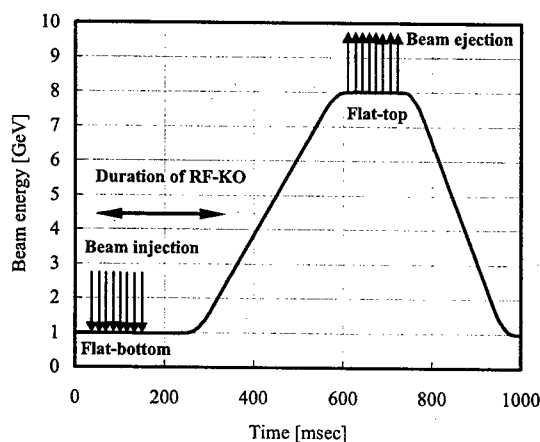


Figure 1: Beam energy pattern of booster and timing of beam injection and ejection. RF-KO system is operated at flat-bottom period.

RF-KO SYSTEM

The RF-KO system consists of a low-level system, a high-power system, and a beam-kicker. Figure 2 shows the block diagram of the RF-KO system. To remove the beam in the satellite rf buckets effectively, the sine-wave signal resonate with vertical betatron oscillation is used for beam-kick.

Not to affect the main bunch, RF-KO signal must be zero output at the instant of main bunch passing through the beam-kicker. Zero-crossing points of rectangle-wave, rise and fall of the wave-form, is adjusted to keep the main bunch alive. The rectangle-wave is generated by the arbitrary waveform generator with external clock of 508.58MHz. The frequency of the rectangle-wave is four times the revolution frequency of the booster that makes eight zero-crossing points at the rf buckets for eight-pulse beam injection. The RF-KO waveform is produced by multiplying the sine-wave and the rectangle-wave together.

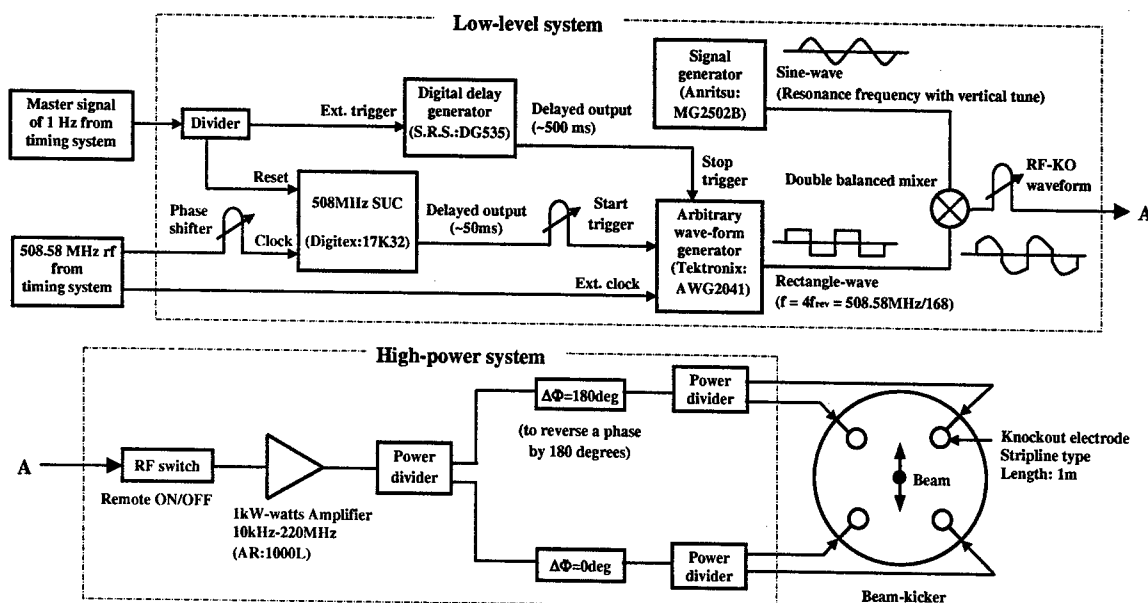


Figure 2: Block diagram of RF-KO system

The RF-KO waveform was produced only by the arbitrary wave-form generator in the old system. The vertical betatron tune was adjusted to the RF-KO signal because the variation of the RF-KO frequency was limited. We improve the system to combine the sine-wave with the rectangle-wave by using a double balanced mixer. The RF-KO frequency can be adjusted more accurately on the resonance frequency. This method also simplifies the machine tuning for the beam cleaning.

The RF-KO signal is amplified by a 1kW-output amplifier and is divided into four electrodes of the beam-kicker. The Beam-kicker is composed of four 1m-long electrodes installed in a cylindrical vacuum chamber. Arrangement of four electrodes in the vacuum chamber is rotated 45 degree from orthogonal position. Phase of the signal to the upper two electrodes are reversed 180 degree to kick the beam in vertical direction. The beam-kicker is installed in the booster where the vertical betatron function is large enough for effective beam kick. The signals passed through the electrodes are attenuated 30dB and are observed by oscilloscope for monitoring of the system condition.

BETATRON TUNE MEASUREMENT

It is important to measure the betatron tune accurately at the flat-bottom period. The RF-KO electrodes are used both as a beam-shaker for tune measurement. The low-level signal output of RF-KO is switched to random-noise generator for the beam-shake. Connection between the RF-KO high-power system and the electrodes are changed correspond with the direction of betatron tune. The time variation of the betatron frequency is measured by real-time spectrum analyzer (Tektronix: 3056). The RF-KO frequency, which

resonates with vertical tune, is determined by this measurement.

Figure 3 shows the time variation of the vertical betatron tune. The fluctuation of the tune in the flat-bottom period is about 0.015, and it is mainly caused by the current ripple of the magnet power supplies. The vertical betatron tune must be adjusted in constant value for effective beam kick. The excitation current pattern of the quadrupole magnets are corrected to fix the betatron tune in constant value.

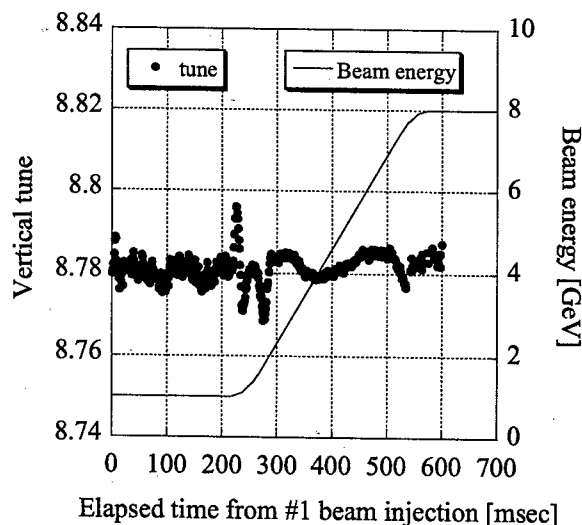


Figure 3: Time variation of vertical betatron tune.

TUNING FOR BEAM CLEANING

On the machine tuning for the beam cleaning, it is important to adjust the timing of RF-KO signal and RF-KO frequency. The zero-crossing point of the RFKO

signal is set on the main rf bucket by using phase shifter. In case that the zero-crossing point is synchronized with the main bunch, no beam loss is observed on an averaged beam current measured by DCCT.

For the fine tuning of RF-KO frequency, beam is shaken by the beam-shaker with continuous sine-wave. A frequency that grows up the beam loss is set directly as the RF-KO frequency. Due to the betatron tune dependence on beam charge density, the vertical tune of 40nsec beam is higher about 0.002 than that of 1nsec beam in the same averaged beam current. The charge density per bunch of the 40nsec beam is about 1/20 less than that of the 1nsec beam. It is hard to measure the vertical tune of the satellite bunches, so we use the tune value of 40nsec beam as the RF-KO frequency.

The single-bunch impurity is measured by using the visible synchrotron light at the accelerator diagnostics beam-line I (BL38B2) in the storage ring. Photon counting method with a fast light shutter system is used [2]. The fast light shutter system consists of Pockels cells, polarizers and a high voltage pulser. The fast light shutter extracts a light pulse from a particular bunch in the storage ring. The bunch impurity can be decided by the extinction ratio of the light shutter (typically 10^5). The latest result of the impurity measurement is less than 2×10^{-11} and less than 1×10^{-9} before and after the main rf bucket, respectively. The results of both are the measurement limit of this system.

We measure the bunch impurities of the satellite rf buckets adjacent to the main rf bucket as a function of the acceleration voltage of the booster. Figure 4 shows the dependence of the bunch impurities on the acceleration voltage at the flat-bottom period. The increase of the acceleration voltage decreases the bunch impurity exponentially. Now, we are investigating the mechanism of this relation.

CONCLUSION

To make the high purity bunches in the SPring-8 storage ring, the beam cleaning system was installed in the booster synchrotron. It was confirmed that the high purity bunched beam was formed efficiently in the booster by removing the satellite bunches at low beam energy of 1GeV. Another advantage of the beam cleaning system in the booster was the ability to make any beam-filling pattern in the storage ring with high purity bunches. Several-bunch filling pattern into the storage ring has been successfully operated, and the beam-line users are satisfying the bunch purity.

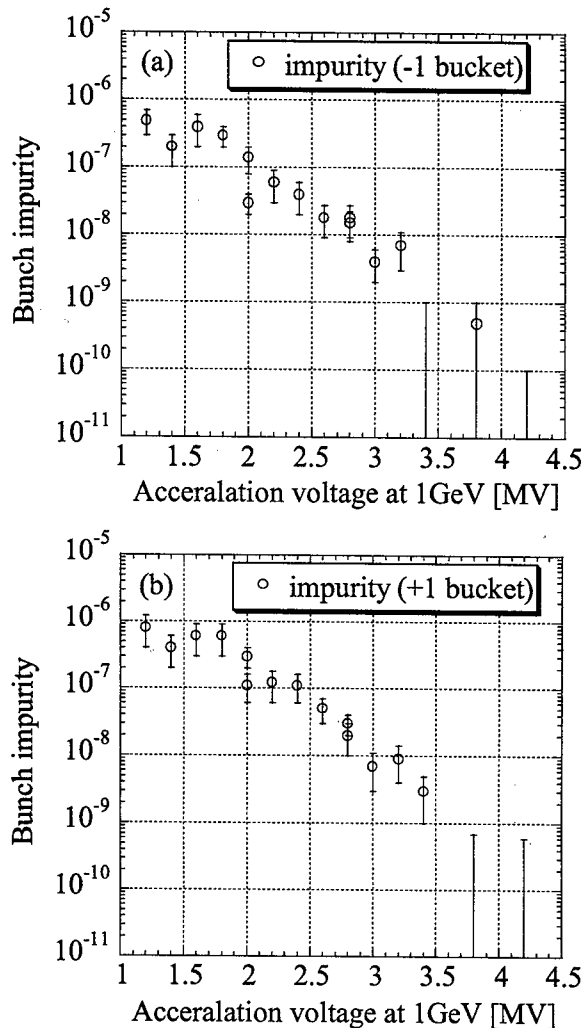


Figure 4: Relation between the acceleration voltage of the booster and the bunch impurity. Upper (a) is -1st bucket and lower (b) is +1st bucket, which are just before and after the main rf bucket, respectively. The bucket spacing is about 2nsec.

REFERENCES

- [1] H. Suzuki et al., Nucl. Instr. and Meth. A 444 (2000) 515-533
- [2] K. Tamura, Proc. of the 12th symp. on Acc. Sci. and Tech., (1999) p546-548

BEAM POSITION MONITORING SYSTEM FOR THE 1.5GeV TRANSPORT LINE OF NSRRC

K.H. Hu, Jenny Chen, C.H. Kuo, C.J. Wang, Demi Lee, K.T. Hsu

National Synchrotron Radiation Research Center

NO. 101, Shin-Ann Road, Hsinchu Science-Based Industrial Park, Hsinchu, Taiwan.

Abstract

The extracted 1.5 GeV electron beams from the booster synchrotron are transported via a transport line and injected into the storage ring. This booster-to-storage ring transport line equipped with seven stripline beam positions monitors. Commercial log-ratio BPM electronics were adopted to process the 500MHz bunch signal directly. The position of the passing beam is digitized by VME analog interface. This report addresses the system architecture, software tools, and performance of the BTS trajectory measurement. This system will provide an elegant tool for optimizing the performance of the transport line. Preliminary results and possible applications are included.

1 INTRODUCTION

The booster-to-storage ring transport line (BTS) of the NSRRC (formerly the SRRC) consists of seven stripline-type BPMs for measuring the trajectory of the beam. The BPMs are a complementary tool to fluorescence screen monitor for the operation of transport line. A logarithmic-ratio signal processing technique is commonly use for monitoring the position of the beam. It provides the advantages of a normalized real-time response, and an excellent dynamic range of intensity and position measurement. It is based on the inexpensive integrated circuit family of demodulating logarithm amplifiers, manufactured by Analog Devices, Inc. Log ratio electronics were recently adopted for use as the BPMs to provide a convenient means of operating the transport line.

2 LR-BPM

Commercially log-ratio beam position monitors (LR-BPM) [1] are used to measure the beam position in the BTS of the NSRRC. The functional block diagram of the LR-BPM is shown in Figure 1. The log ratio processor is a two-channel device. This module consists of a low-pass filter, a band-pass filter, a log-ratio amplifier, a sample & hold (S/H) circuit, a timing control circuit, and a position and intensity signal processing circuit. For details about the principles and implementation, please refer to reference [2].

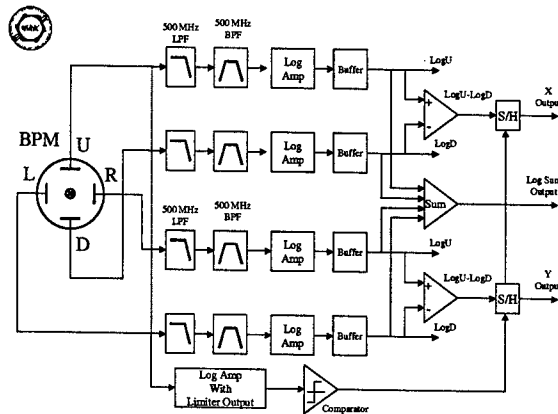


Figure 1: Functional block diagram of the LR-BPM.

3 TRANSPORT LINE LOG-RATIO BPM SYSTEM

The 1.5 GeV electron beam is extracted from the booster synchrotron and transported via a 70 m long transport line before being injected into the storage ring. Seven stripline-type BPMs are installed in the transport line, as shown in on the Figure 2. The striplines are mounted on the circular vacuum chamber with 63 mm inner diameter. The striplines is 10 mm in width and 150 mm long. The beam intercept angle is about 10 Degrees. The sensitivity of the BPM is about 1 dB/mm near the center of the chamber

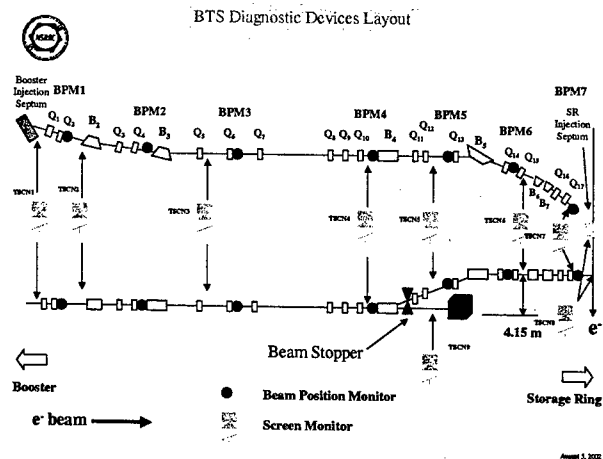


Figure 2: Transport line layout and the BPM installation.

The LR-BPM is configured in self-beam trigger mode. The electronics include a two-channel sample & hold circuit for X and Y output. A log sum output signal is also available. An in-housed made peak detector module in VME form factor is used to hold of the log sum output. In Figure 3 shows the signal processing circuitry of the log sum hole module. The input signal is firstly inverted. When the inverted log sum signal amplitude is more than the output of the peak detector, the peak detector operates in the sampling mode and the output follows the input; otherwise, the peak detector operates in the hold mode. The drop rate of the fast peak detector is rather high so a second sample & hold stage is need to keep output of the sum up to 100 msec. The timing circuit provides an S/H command for the slow S/H and to trigger the ADC modules.

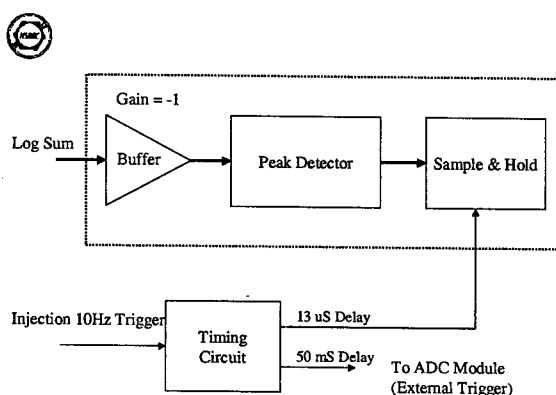


Figure 3: The peak detector circuit for log sum signal.

A 32-channel, 16-bit VME ADC module acquires the data from seven LR-BPMs. The position data are holding on the S/H on the LR-BPM module, and a peak detector holds the log sum value. A PPC CPU module running LynxOS and controls the operation of the VME crates. Collected data are sending to a control database every 100 msec to be displayed and fed to various applications. The LR-BPM in S/H mode with self-beam trigger is working correctly when the signal is sufficiently strong to activate the trigger circuitry. There is no indication whether the trigger is happen or not. To address the problem of data correctness, the log sum signals are used to check the data validation of the position data. If the log sum signal is large than some presentable level, it can ensure the LR-BPM is working properly and provide reliability data. The application software can do this check in control system easily.

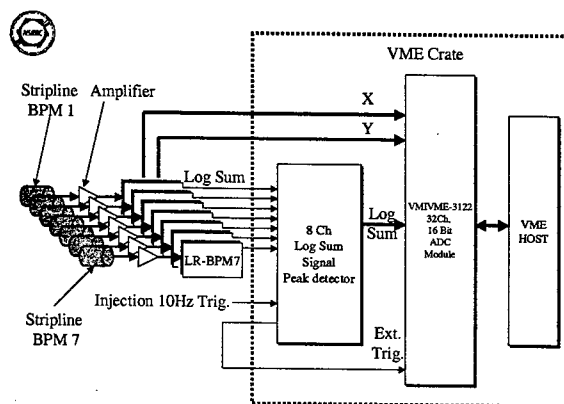


Figure 4: Data Acquisition System for the BTS LR-BPM.

4 PRELIMINARY TEST RESULTS

A preliminary beam test was recently conducted to check the functionality of the BTS LR_BPM system. Figure 5 show the log sum of LR-BPMs along the beam transport line. The data is not corrected for the attenuation of cables. The cable for BPM 1 is the longest. The drop of log sum after BPM 5 is the results of a beam stopper (for safety purpose) is close to prevent mistake injection, the location of the beam stopper is shown in Figure 2. Figure 6 shows the log sum of LR-BPMs along the beam transport line of a routine injection scenario. The trigger of electron gun will stop immediately when the storage ring stored beam accumulated to 200 mA corresponding to the machine cycle near 120. The intensity variation of the transport line will reveal the performance of the booster synchrotron. Figure 7 shows the log sum of BPM 7 during a routine injection scenario. The estimated variation in the intensity of the booster beam is less than 25%. The log sum information can complement the screening to optimize the operating conditions of the transport line and the extraction conditions of the booster synchrotron, even if is not sufficiently accurate. The information also provides the loss of the beam along of the transport line.

The input current of correct magnet power supply controls the position of the beam. HC1 is the first horizontal correct power supply; VC1 is first vertical correct power supply. The Figure 8 shows result of HC1 versus X position variation. The Figure 9 shows result of VC1 versus Y position variation.

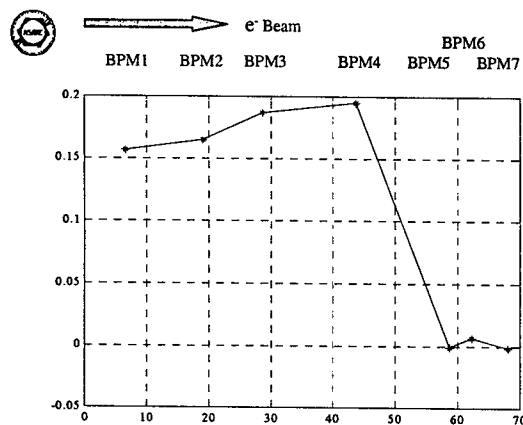


Figure 5: The snapshot of the log sum output.

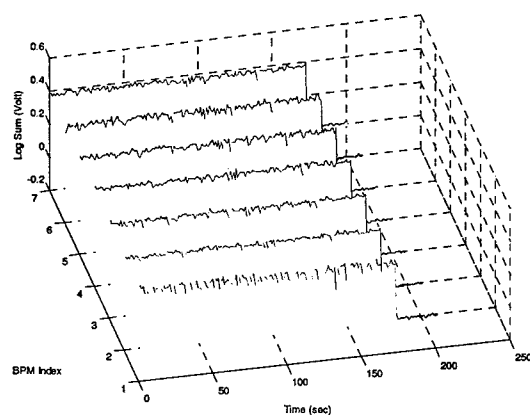


Figure 6: The BTS beam intensity (log sum) distribution as function of time in a routine injection scenario. This figure is shown the log sum output or BTS LR-BPM during injection, the stored beam current of the storage ring is started from 0 mA and accumulate to 200 mA about 170 seconds.

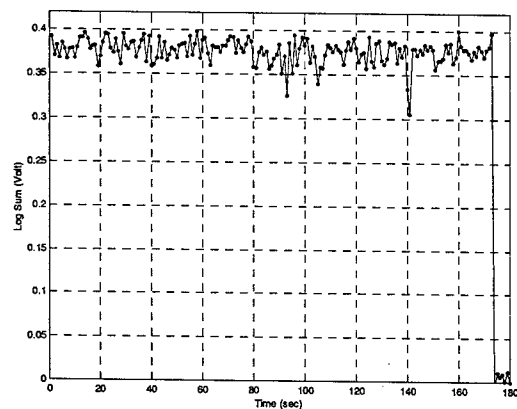


Figure 7: The log sum output of the BPM7, which installed at the upstream of the storage ring injection septum in a routine injection.

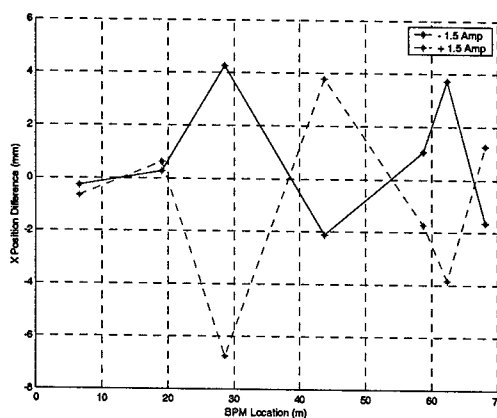


Figure 8: Horizontal trajectory difference when the first horizontal corrector (HC1) change ± 1.5 A.

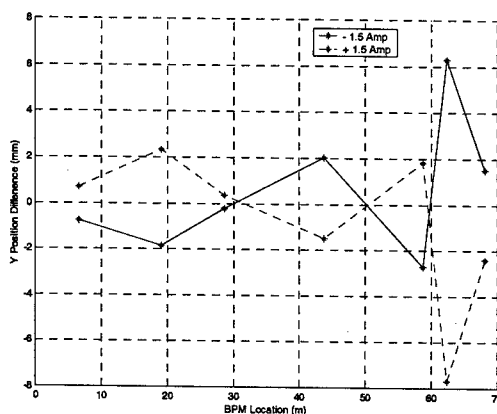


Figure 9: Vertical trajectory difference when the first vertical corrector (VC1) change ± 1.5 A.

5 SUMMARY

The LR-BPM system for the transport line non-destructively measures the trajectory of the beam. It can simultaneously measure the position and the intensity of the BTS in the injection period. The intensity information also provides the loss of the beam along of the transport line. The log sum information complements in optimizing the operating conditions of the transport line and the extraction conditions of the booster synchrotron, improving the efficiency of injection. The system was recently integrated and tested. Further improvements are ongoing. This measurement system is expected to be helpful in optimizing the transport line for routine operation and top-up mode operation in the near future.

6 REFERENCES

- [1]. Log-ratio Beam Position Monitor – User's Manual, Bergoz Instrumentation
- [2]. A. Kalinin, "The Log-Ratio Beam Position Monitor", AIP Conference Proceedings 648, Upton, New York, 2002, pp.384-392.

FUNCTIONALITY OF THE DIGITAL BEAM POSITION MONITOR TEST-BED IN NSRRC

C. H. Kuo, Jenny Chen, K. H. Hu, K. T. Hsu

National Synchrotron Radiation Research Center, Hsinchu, Taiwan, R. O. C.

Abstract

A digital beam position monitor (DBPM) test-bed was implemented recently in the NSRRC to perform functionality and performance evaluation. The programmability nature of DBPM system is essential for multi-mode high precision beam position measurement. The system will support high performance beam position, turn-by-turn beam position, tune and other diagnostic measurements. Control system interface was implemented to support the operation of DBPM system. Preliminary test results includes various aspects will be discussed and presented in this report.

INTRODUCTION

A test-bed of digital receiver based beam position monitor (DBPM) is implemented [1,2]. The purpose of this test-bed is used to evaluate and explore the potential and performance of the new technology for beam diagnostics application at the storage ring. The system composes a multi-channel coherent down-converter and a VME64x crate equip with multi quad-digital receivers boards (QDR). Preliminary results presents that the system achieved micron resolution in closed-orbit mode and high resolution in turn-by-turn mode.

The digital BPM electronics are commercial products [3]. The electronics consist of two parts, the first parts is 4 channels RF down converter that convert 500 MHz beam signal into intermediately frequency (20 MHz) coherently. Four IF signals are digitized and processed by quad-digital receiver boards. The resolution of averaged beam position measurement can be better than one micron and achieve around 10 μ m turn-by-turn resolution. The QDR consists of four symmetrical channels. The system block is shown in the figure 1. It consists of RF down convert, a band-pass filter, analog-to-digital converter (ADC), digital down converter (DDC), FIFO memory and FPGA is for the data acquisition and control purposes.

The ADC is based on AD6644/6645. It is used for the analog to digital conversion. This is a high speed, high performance, low power, and monolithic 14-bit analog-to-digital converter. All necessary functions, including track-and-hold and reference are included on chip to provide a complete conversion solution.

The programmable DDC is composed of synchronization, input, input level detector, carrier mixer, CIC decimating filter, half-band decimating Filter, 255-tap programmable FIR filter, automatic gain control, Cartesian to Polar converter.

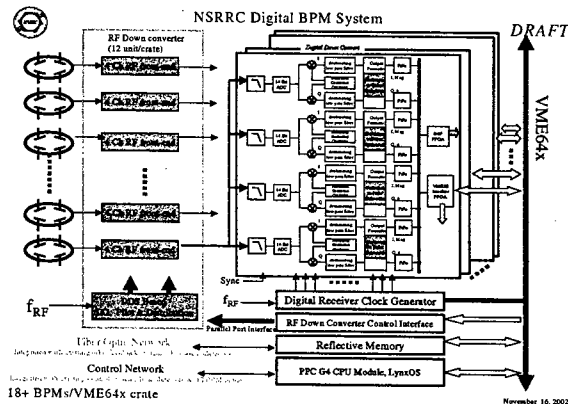


Figure 1: System block diagram of digital BPM test-bed.

CONTROL SYSTEM INTERFACE FOR DBPM TEST-BED

The control system interface is separated to two layers. The embedded layer is VME64x crate with PowerPC module running the real time operation system of LynxOS. The user interface layer is located at workstation/Unix and PC/Linux control console, support commercial software Matlab and LabVIEW. The VME host receives control parameters from user interface by Ethernet. The control parameters include that change operation mode either turn-by-turn mode or closed orbit mode, adjust FIR filter coefficient and decimation factor of system. The data of DBPM is replied to user interface after receive software trigger from Ethernet. The software environment is shown in the figure 2. The DBPM test-bed is seamless integrated with the existing system.

There are two threads in the VME host. One is setting thread that handles all parameter control, such as turn-by-turn mode and close orbit mode control parameters update. Another is reading thread that handles control status response and data access of DBPM. All data and control parameter are collected in the share memory. The closed orbit data is sent to a dedicated BPM server node by reflective memory network. The update rate of closed orbit beam position is 1 KHz in the orbit feedback reflective memory network. The VME host of the BPM server down sampled the closed orbit data to 10 Hz and update to dynamic database in all control consoles.

The data of DBPMs in turn-by-turn mode are directly served to client running on control console via control Ethernet. The input rate of DBPM is 50 MS/s. The output rate is 2.5 MS/s after CIC, half-band and FIR filter. The CIC decimation factor is 5, half-band decimation factor is 2 and FIR decimation factor is 2. BPM acquisition is started after accepts event from client. Position calculation is done after the FIFO of DBPM is full. The

maximum depth of FIFO is 8192 long words in each channel. The maximum record time is 3.2 milliseconds in the turn-by-turn mode.

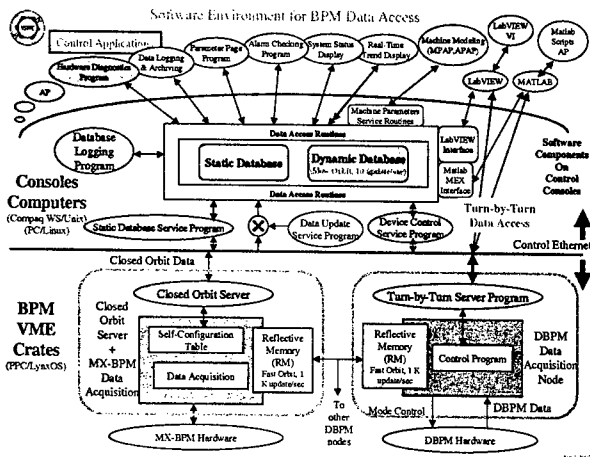


Figure 2: Software environment for BPM data access.

PRILIMINARY SYSTEM TEST RESULTS

Preliminary beam test was done recently. The installed BPMs will join the routine operation in near future. To examine the closed orbit performance, short-term and long-term test in underway. The long-term stability can be achieved $\sim \mu\text{m}$ level with 1KHz output rate that is comparative with existing orbit feedback system. The resolution can be better after optimized the parameters of digital receiver.

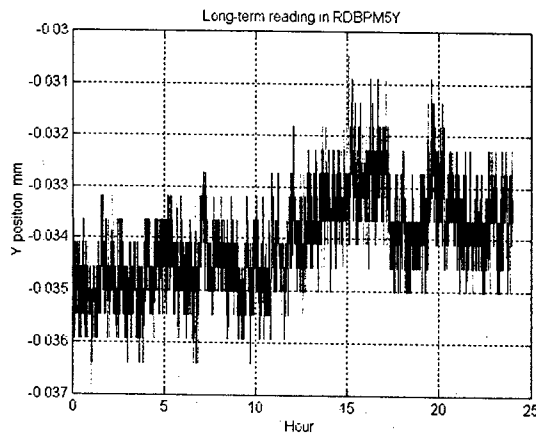


Figure 3: Long-term stability in the closed orbit mode with 1KHz output rate.

The revolution frequency of the storage ring of NSRR is 2.5 MHz. The turn-by-turn BPM electronics have 1.25 MHz bandwidth is essential in principle. However, the fractional tune of the storage ring is less than 0.33, bandwidth of 0.8 MHz is enough to support the measurement. The preliminary turn-by-turn parameter set achieves 0.8 MHz bandwidth (-3 dB) at this moment as shown in figure 4. The investigation is going how to increase bandwidth by optimize the parameters of digital

receiver. Adopt data post processing to compensate the frequency response to increase the bandwidth is another alternative solution.

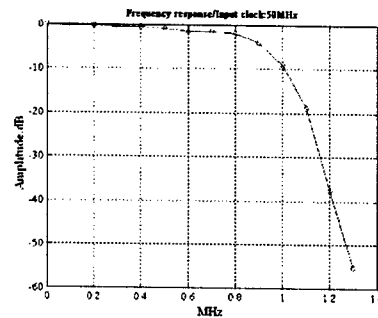


Figure 4: Bandwidth of DBPM system for turn-by-turn mode.

To demonstrate the functionality of the turn-by-turn mode, various test have been done recently. Figure 6(a) presents the data of a BPM in frequency domain with horizontal kick. Betatron oscillation is clearly observed by the output of DBPM. Figure 6(b) shows the data of a BPM in frequency domain with vertical kick. Figure 5 shows a single button reading in the time domain of DBPM with ~ 1 mrad horizontal kick by an injection kicker, the horizontal betatron oscillation is excited.

The turn-by-turn beam position in for one DBPM is shown in the figure 7 when the RF gap voltage modulation is turn on. The RF gap voltage modulation is used to remedy the strong longitudinal coupled bunch instability right now. The beam was excited by narrow band white noise, both horizontal and vertical betatron oscillation are excited. The top figure is the signal picked up by a single button. The prominent sinusoidal signal is induced by the RF gap voltage modulation. Turn-by-turn beam position is calculated by using four button signals. The horizontal position is ride on the 50 kHz of background that is shown in the middle figure. This background is due to un-calibration of the four button processing chain. Parallel processing electronics are insensitivity to the longitudinal instability in the principle. The background can be minimized after applied proper calibration correction. Bottom figure is the vertical position shown clean betatron oscillation. The phase space measurement by two BPMs with horizontal phase advance near $\pi/2$ is shown in the figure 8. The difference color dots define various groups of turns.

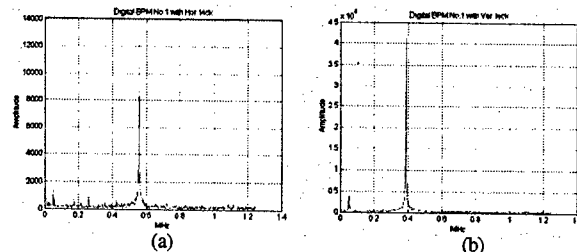


Figure 5: (a) The frequency domain of digital BPM with horizontal kick, (b) with vertical kick.

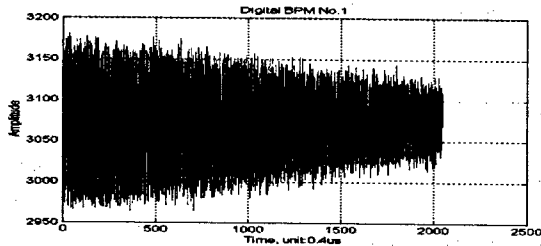


Figure 6: Damped horizontal betatron oscillation observed by a single button of BPM.

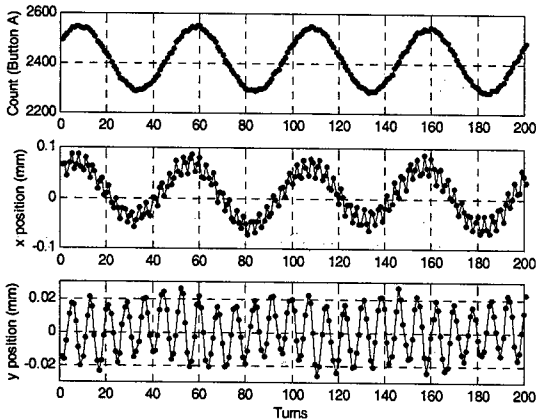


Figure 7: Preliminary results of the DBPM test bed shown that the turn-by-turn resolution is better than 10 μ m. Upper: single button signal; Middle: un-calibrated horizontal position; Bottom: un-calibrated vertical position.

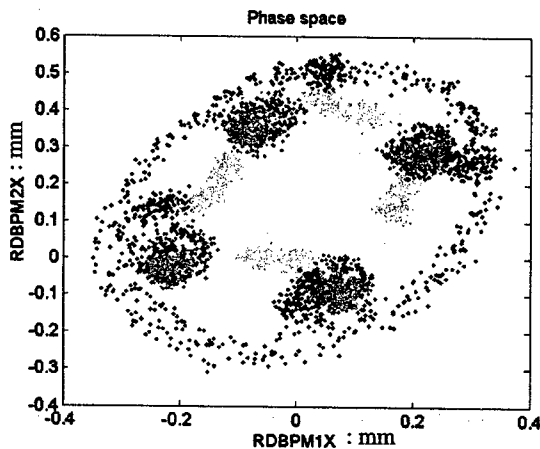


Figure 8: Phase space near 4th order resonance, blue dot: 1 to 1000 turns, green dot: 1001-2000, cyan dot: 2001-3000, red dot: 3001-4000, magenta dot: 4001-5000.

DIGITAL TUNE MONITOR

The dedicated tune monitor in implementation. It is based on a dedicated digital BPM working in turn-by-turn mode; the system block diagram is shown in figure 8. The stored beam is excited by a narrow band white noise. This level of the excitation is controlled by digital output interface to keep the level as low as possible. Fourier analysis of the beam position in the turn-by-turn mode can

extract tune. Very small beam size blowup (several percent) was observed. It may be compatible with user, which is not demanding on beam condition.

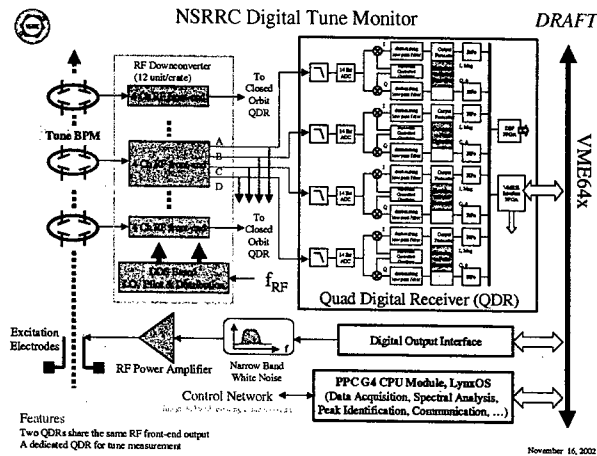


Figure 9: The block diagram of digital tune monitor.

FUTURE PROSPECTS

System integration and preliminary beam test is on going. The beam test results show that the system is working properly. Remaining work includes integrating the system to join the routine operation in closed orbit mode and develops better Matlab scripts to support data acquisition and analysis for turn-by-turn mode. Integration small number of digital BPMs accompany with existing MX-BPM is short-term goal. Intensive test of digital BPM will be stated soon.

REFERENCES

- [1] M. Dehler, et al., "Digital BPM System for the Swiss Light Source – First Operation Results", AIP Conference Proceedings 546, 572 (2000).
- [2] V. Schlott, et al., "First Operational Experience with the Digital Beam Position Monitoring System for the Swiss Light Source", Proceeding of EPAC 2000, Vienna, Austria, 1809 (2000).
- [3] <http://www.i-tech.si/products-dbpm2-p.html>.

SYNCHROTRON LIGHT INTERFEROMETER AT JEFFERSON LAB*

P. Chevtsov, A. Freyberger, R. Hicks, Jefferson Lab, Newport News, VA 23606, USA
J.-C. Denard, Synchrotron SOLEIL, 91192 CEDEX, France

Abstract

A synchrotron light interferometer has been built at Jefferson Lab in order to measure small beam sizes below the diffraction limit. The device is non-invasive and can monitor the profile of a few microampere electron beam. It follows the design pioneered by T. Mitsuhashi [1] and is a valuable instrument for the CEBAF accelerator. The structure of the interferometer, the experience gained during its installation, and first beam measurement results are presented. Future applications of this device include precise energy spread monitoring ($\sim 10^{-5}$) which is required by some Hall A nuclear physics experiments.

INTRODUCTION

By recirculating electrons through its two superconducting linacs up to five times, CEBAF provides nuclear physics experiments at Jefferson Lab with powerful (up to 0.8 MW) electron beams of high quality. Standard beam energies range from 0.8 to 5.7 GeV. The beam intensity ranges for three existing experimental end stations are: 1 to 180 μA for Hall A, 1 to 30 nA for Hall B, and 0.1 to 180 μA for Hall C. A growing number of experiments at the end stations have begun to require not only very small transverse beam size ($\sigma_{x,y} < 20 \mu\text{m}$) and low energy spread ($dE/E < 3 \cdot 10^{-5}$) but also their continuous monitoring at the critical points of the accelerator. One such critical point in the Hall A beam line is the high dispersion ($\sim 4 \text{ m}$) location 1C12 which is shown in Fig.1. This is the area downstream of the dipole magnet (the blue element at the center of Fig.1) which has the bending radius of 40 meters.

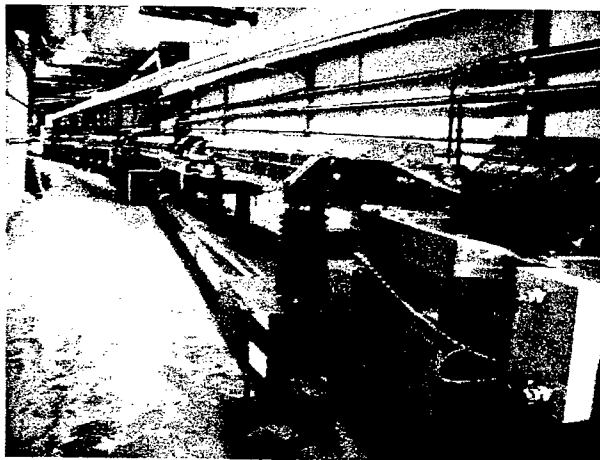


Figure 1: Location 1C12 in the Hall A beam line with the installed synchrotron light interferometer.

*Supported by DOE Contract #DE-AC05-84ER40150.

This location has two other beam profile measurement devices: a wire scanner and an optical transition radiation (OTR) monitor. The wire scanner uses 25 μm diameter tungsten wires and has a maximum beam current limit at 5 μA . Wire scans take about one minute to perform and are destructive to the beam. The OTR monitor inserts a very thin ($\sim 0.25 \mu\text{m}$) carbon foil onto the beam axis [2]. This foil introduces a small amount of halo to the beam which is acceptable to some of the experiments. The forward transition radiation is detected by a CCD camera. The resolution of the OTR monitor, limited by the used CCD camera to about two pixels, is approximately 60 μm of the RMS beam size. This is adequate to the existing but not enough for new beam requirements at Jefferson Lab.

The synchrotron light interferometer (SLI) technique that has been developed at KEK, Japan [1] for measuring very small (down to a few μm) beam sizes and successfully implemented in several electron storage rings all over the world, was very attractive for a new CEBAF beam diagnostic project. A prototype SLI has been designed and installed as a third beam profile diagnostic device at the 1C12 location. The main goals of our synchrotron light interferometer project were to determine the basic structure of the SLI for Jefferson Lab that could easily be replicated and to gain the experience during its installation in the accelerator tunnel and further operations. We also wanted to design and test software that would automate the control functions of all synchrotron light interferometer components and the calculation of the beam size with the use of the SLI data. The three different beam profile monitors at the same location would give us an excellent opportunity to use their measurement results in our work on SLI data processing and analysis models.

SLI AND ITS COMPONENTS

The SLI design at Jefferson Lab is a wave front division interferometer that uses polarized quasi-monochromatic synchrotron light. It has a 3-D structure, with major elements placed on two horizontal levels which are parallel to the ground plane (see Fig.1). Limited space and radiation levels strongly influence the SLI design and implementation.

The synchrotron light generated by the electron beam in the dipole magnet is extracted through a quartz window by the mirror installed in a vacuum chamber. After this window, external light is shielded from the SLI optical system. Two adjustable 45° mirrors guide the light through the optical system. From the first mirror light reflects downward and reaches the second mirror. This mirror is remotely controlled and sends light on the CCD

through a long (~5 m) plastic pipe and all optical components, in the direction opposite to the direction of the electron beam. The CCD and the optical components are placed in an optical box. A diffraction limited doublet lens ($f = 1$ m) is used as the camera objective. A narrow band optical filter ($\lambda_0 = 630 \pm 10$ nm) is used to obtain a quasi-monochromatic light. A polarization filter selects out the σ -polarized component of the synchrotron radiation. A double slit assembly with different distances between slits (from 5 to 20 mm) and small slit openings (1mm \times 2mm) is located right in the front of the objective lens. It is moved by a remotely controlled stepper-motor. The SLI optical box is shielded by lead blocks to avoid damage to its components from the high radiation in the accelerator tunnel.

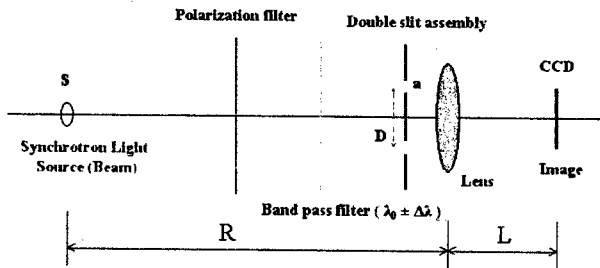


Figure 2: Synchrotron light interferometer outline.

The SLI outline is shown in Fig.2. The double slit assembly is located at the distances $R \approx 9.1$ m from the synchrotron light source point and $L \approx 1.1$ m from the CCD.

The SLI video camera is the STV digital integrating video system from the Santa Barbara Instrument Group [3]. The camera has its own control box with the RS-232 interface to an external computer. Its quantum efficiency is very high (more than 70%) for $\lambda_0 = 630$ nm and the pixel size is small (7.4 μ m \times 7.4 μ m). An electronic cooling system keeps CCD dark currents extremely low. The exposure time of the camera can gradually be changed from 0.001 seconds to 10 minutes. The CCD camera is connected to an image processor. The SLI image processor is Datacube's MaxVideo MV200 board [4] which is the basic video image processing system for beam diagnostic applications at Jefferson Lab [5]. The STV video camera and MV200 system make it possible for the SLI to measure the sizes of the CEBAF electron beams in a very wide range in energy and intensity.

INTERFEROGRAM ANALYSIS

The SLI interference pattern is captured by the CCD video camera and analyzed by the image processing software running on the MV200 and its host computer (a Motorola PowerPC based IOC) connected to the accelerator control system based on EPICS [6]. As a part

of the distributed real-time EPICS database, the digitized images from the video camera and the information about the calculated beam size are available for the accelerator control computer network and can be used for various beam diagnostic applications.

The basic parameter to calculate the beam size is the visibility V of the interference pattern. The visibility is estimated from the intensities of the first (central) maximum (I_{\max}) and minima (I_{\min}) of the interferogram:

$$V = \frac{I_{\max} - I_{\min}}{I_{\max} + I_{\min}} \quad (1)$$

Assuming a Gaussian beam shape, the RMS beam size can be calculated at the fixed separation of a double slit as [1]:

$$\sigma_{\text{beam}} = \frac{\lambda_0 \cdot R}{\pi \cdot D} \sqrt{0.5 \cdot \ln\left(\frac{1}{V}\right)}, \quad (2)$$

where D is the double slit separation (see Fig.2).

SLI image processing and data analysis are performed by new software that has been developed for this project. The MV200 continually processes a large volume of pixels corresponding to the video frames from the CCD camera using parallel pipeline technology. This technology makes it possible for the MV200 not only to routinely perform such important operations for processing as masking the pixels outside the interferogram region and subtraction of a background image but also to calculate the RMS beam size with the use of equations (1) and (2) at a high rate (up to 10 Hz in the multiplexed version of the software). In addition, the SLI data analysis software calculates corrections due to the field depth effects and imbalance between intensities of the two modes of light illuminating the double slit. The software fits the measured interference pattern using a multi-parameter, non-linear model that is based on the ideas from paper [7].

EXPERIMENTAL RESULTS

With the configuration of double slits that has been used for the last few months, the synchrotron light interferometer measured the vertical beam size. Measurements with different distances between slits have been made and the data of the three beam profile monitors at location 1C12 have been analyzed. Typical SLI interferograms are shown in Fig.3.

The measured vertical beam size was in the range from 0.12 to 0.18 mm for various CEBAF operation modes. The data of all three monitors were in very good agreement with each other.

The typical beam requirements from the Hall A users are 5 GeV energy and 100 μ A intensity. The SLI beam size measurement time for these currents and energy and

with $D=5$ mm is about 1 second. Since the amount of the emitted synchrotron light is proportional to the beam energy and intensity, the optimal video camera exposure time for each CEBAF operation mode can be calculated. Our experimental results have confirmed these calculations.

The resolution of the SLI depends on the distance between slits D and can be estimated with the use of equation (2). For example, if $D=5$ mm, then $10\text{ }\mu\text{m}$ difference at the beam size $120\text{ }\mu\text{m}$ makes more than 3 % difference in the visibility. Since the image processing system easily calculates the visibility of the CCD image with 1% accuracy, we can measure the beam size $120\text{ }\mu\text{m}$ with the resolution better than $10\text{ }\mu\text{m}$.

CONCLUSIONS

The main goals of the SLI project at Jefferson Lab have been achieved. It was demonstrated that the synchrotron light interferometer technique could successfully be used for CEBAF beam diagnostic applications. We have built an automated SLI that is easy to replicate at the other accelerator locations.

The SLI is completely non-invasive and can monitor the profile of a few microampere electron beam. Future applications of this device include precise energy spread monitoring ($dE/E < 3 \cdot 10^{-5}$) that is required by some nuclear physics experiments.

We have gained a great experience in the SLI technique and operation. The most difficult problem during the SLI installation in the accelerator tunnel was the alignment of all its optical components around the optical axis formed by the used mirrors. We are planning to implement some modifications in the synchrotron light interferometer structure that would be very helpful for the future synchrotron light interferometer projects. For example, a possibility to use a He-Ne laser as a SLI reference light source should significantly simplify the work on the SLI installation and tests.

ACKNOWLEDGMENTS

The authors are very thankful to H. Areti, G. Krafft, S. Chattopadhyay, M. Tiefenback, L. Merminiga, J. Benesch, A. Bogacz, A. Hutton, K. White, Y. Derbenev for their interest in our work and support. The authors also want to thank D. Hardy, S. Suhring, M. Spata, Z. Kursun, A. Day, all accelerator operators and technicians for their help during the SLI installation and tests.

REFERENCES

- [1] T. Mitsuhashi, "Beam Profile Measurement by SR Interferometers," Proceedings of the Joint U.S.-CERN-Japan-Russia School on Particle Accelerators, Montreux, Switzerland, 1998.
- [2] J.-C. Denard et al., "High Power Beam Profile Monitor with Optical Transition Radiation," PAC1997, Vancouver, BC, Canada, p. 2198 (1998).
- [3] Santa Barbara Instrumentation Group, www.sbig.com

- [4] Datacube Inc., www.datacube.com
- [5] D. Hardy, P. Chevtsov et al. "Multivideo Source Image Processing for Beam Profile Monitoring System," Proceedings of Beam Instrumentation Workshop 2000, Cambridge, MA USA, May 2000.
- [6] M. Kraimer et al. "Experience with EPICS in a Wide Variety of Applications," PAC1997, Vancouver, BC, Canada, p. 2403 (1998).
- [7] J. Flanagan, S. Hiramatsu, T. Mitsuhashi, "Automatic Continuous Transverse Beam-Size Measurement System for KEKB," EPAC2000, Vienna, Austria, p. 1714 (2000).

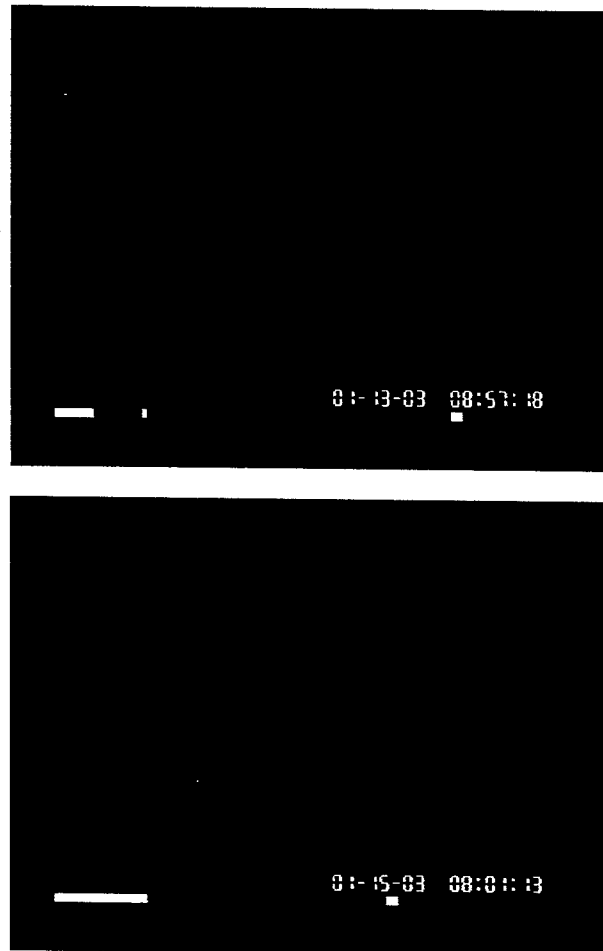


Figure 3. Typical SLI interferograms with $D=5$ mm (the upper picture) and $D=10$ mm. The calculated beam size is about 0.12 mm in both cases.

DEVELOPMENT OF A BPM LOCK-IN DIAGNOSTIC SYSTEM*

R Dickson, Jefferson Lab, Newport News, VA 23606, USA

Abstract

A system has been developed for the acquisition and analysis of high rate, time coherent BPM data across the Jefferson Lab's Continuous Electron Beam Accelerator Facility (CEBAF). This system will allow the acquisition of Beam Position Monitor (BPM) position and intensity information at a rate in excess 7 KHz for approximately 200 BPMs in a time synchronous manner. By inducing minute sinusoidal transverse beam motion in the CEBAF injector, with known phase relative to the synchronized BPM acquisition, it is possible to derive several types of useful information. Analysis of the BPM intensity data, which is proportional to beam current, by beating the signal with an in-phase sinusoidal representation of the transverse kick can localize beam scraping to a particular BPM. Similarly, real-time optics information may be deduced with an analysis of BPM position data. This paper will detail the frequency lock-in technique applied and present status.

INTRODUCTION

The CEBAF accelerator is a five pass CW recirculator, which can reach an energy of 6.067 GeV. It consists of a 67 MeV injector, two superconducting 600 MeV linacs, and 9 arcs of magnets which connect the linacs for beam recirculation. See figure 1.

The accelerator's BPM system includes more than 850 BPMs, controlled by two different types of electronics, distributed across a network of 30 Input Output Controllers (IOCs). Of interest in this discussion is one of the two types - the Switched Electrode Electronics (SEE) BPM [1] system, hereafter referred to simply as BPM.

In order to improve machine reproducibility and reduce beam tune time, a differential orbit '30 Hz' measurement system is used. This system makes it possible to track and correct machine optics by measuring the differential response generated by perturbations of the beam. By means of a small set of correctors, one can induce a beam perturbation at a frequency of 30 Hz. The effect of this perturbation is potentially apparent at any BPM point in the machine. The BPM system performs data acquisition at 60 Hz synchronized with the beam pulse. The choice of 30 Hz as the perturbation frequency enables synchronization of every other beam pulse to the positive or negative crest of the perturbation signal.

This system is limited to operation with 60 Hz pulsed beam due to the relatively large magnitude of kick applied, and is not used with continuous wave (CW) beam for machine protection reasons. Since the machine end-users are interested in delivery of continuous beam, this system is generally only used during machine set up or as

a diagnostic tool when problems arise. Obtaining a similar diagnostic tool that is usable during CW beam delivery is desirable. The development of such a tool is the focus of this paper.

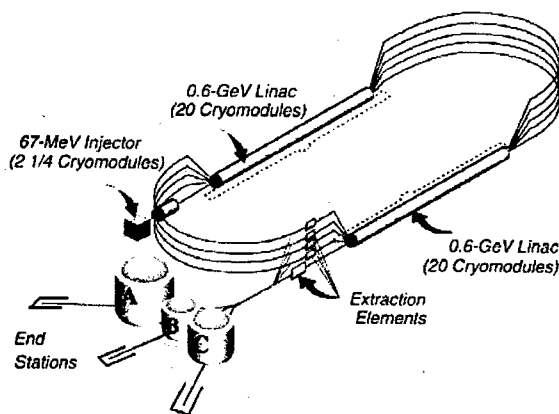


Figure 1 Machine Configuration

SYSTEM COMPONENTS

The ability to create a real-time, CW-beam, differential orbit diagnostic tool requires leveraging and integrating several existing lab diagnostic systems. These include the lab's Beam Scraping Monitor (BSM), 30 Hz Timing Synchronization System (TSS), and FastSee high speed BPM data acquisition system. Each of these systems are overviewed below.

The BSM system [2] applies a minute perturbation to the transverse beam orbit and detects resultant current fluctuations due to beam scraping. The kick is applied with air-core magnets in the machine's injector at four distinct frequencies. Two frequencies are applied to each of the horizontal and vertical axes. For each single axis, two kicks are spaced at roughly 90 degrees of relative betatron phase advance. The resultant differential orbit is of magnitude well below 100 microns. Four lock-in amplifiers are used to generate the perturbation signals and detect the beam current effect at the same frequency and phase using as input an attached beam current monitor (BCM) cavity.

The accelerator has its own 60 Hz AC line synchronized global timing reference called the Beam Sync. The BPM system uses this signal for data acquisition synchronization. The purpose of the TSS [3] is to allow the 60 Hz BPM system awareness of the polarity of the 30 Hz diagnostic's kick at each acquisition. The hardware-based TSS uses one master clock module and

*Supported by DOE Contract #DE-AC05-84ER40150

multiple slave clock modules. These 3U sized cards share the VME bus with the SEE BPM front end (IOCs). The communication flow, from master to slave boards, occurs over a single fiber optic line originating from the master. Each card has a fiber optic receiver and repeating transmitter. The last card in the chain is connected back to the master. This enables the master to perform a continuity test of the entire link. Like the beam synch, the frequency of the message passing is AC line synchronized 60 Hz. The message from the master to the slave timing modules contains status and global synchronization information. Since the sole usage of its fiber link is for this timing synchronization and there is only one source of messages, this system guarantees synchronization to a time approximately equal to the maximum round trip time for a message. Worst-case delay from received input to re-transmitted output per module is less than 1.5usec. In a complete implementation, with up to 100 IOCs participating, the total round trip time will be 150usec. This is far more accurate than needed to identify one 16.67 millisecond beam synch period from another.

The standard data acquisition mode of the BPM system digitizes position and beam current dependent intensity information at an effective rate of 60Hz. This data is further averaged to update operator displays at a 1 Hz rate. A high-speed mode exists to provide the display of position and intensity at the maximum rate possible for the BPM electronics in the form of time-domain X-Y plots and Fast Fourier Transforms (FFT). This mode is named the FastSee system. There are two flavors of SEE BPM electronics. One operates at a maximum data acquisition rate of 7.1 KHz and the other at 125 KHz. For simplicity of discussion, the 7.1 KHz version will be assumed in the following discussion.

INTERGRATING COMPONENTS TO THIS LOCK-IN SYSTEM

This lock-in system uses the differential orbit created by the BSM kick to provide a display indicative of the local relative phase advance. The four frequencies at which the BSM system modulates the transverse motion of the beam are 805.3, 867.7, 934.7, and 994.8 hertz. These frequencies were somewhat arbitrarily selected, but are spots of relatively low background noise for the machine.

In order to detect this motion, the FastSee mode of BPM data acquisition is required. The FastSee data are beat with a sinusoid matching each of the BSM drive signals in order to extract the magnitude of motion and beam current fluctuations at those frequencies. Data acquisition with common synchronization is required to provide a meaningful representation of this magnitude across the multiple BPM systems of the accelerator. The TSS system provides the mechanism for accomplishing this. Each second, a time hack is sent across the TSS fiber link from the master that correlates the next second's 59 TSS messages for all BPM IOC's. A sub-second batch of FastSee data is triggered using this one-second time hack

as a reference. This assures that all BPM's in the accelerator can gather a coincident burst of FastSee position and current intensity data.

The beating sinusoid is constructed for each FastSee data acquisition burst to match the phase and frequency of the BSM drive signal. The frequencies are fixed and known. They are simply the set points for the BSM lock-in amplifiers, as listed previously. The phase angle relative to the FastSee data is dynamic and unknown. It is measured using a VMIC-3114 analog to digital converter (ADC) triggered at the initiation of the FastSee acquisition burst. The ADC's inputs are the four BSM drive signals. This ADC is part of a dedicated system that then relays, via the site network, the phase information to all BPM IOC's for construction of the beating sinusoid.

The magnitude, at each BPM, of the current and position fluctuations due to the four perturbations are then displayed graphically for accelerator staff study.

PRESENT STATUS AND FUTURE PLANS

This system is in the process of initial testing. Problems are being addressed regarding data stability. Differential data are reasonable, if not completely stable.

In the future it will be desirable to replace the VMIC-3114 ADC with dedicated similar functionality on the TSS boards. Phase measurements of the BSM drive signals will then be possible with much greater accuracy and with less software complexity.

It will also be desirable to place perturbation sources in other locations of the accelerator in addition to the injector. At a minimum, replicating the points of excitation for the pulsed beam mode 30 Hz system is desirable. This would allow direct comparison with the two systems and a more seamless interface for accelerator staff.

By beating the FastSee intensity data with a sinusoid of twice the BSM frequency detection of aperture scraping would be possible.

REFERENCES

- [1] T. Powers, "Resolution of SEE BPMs", Proceedings Of The Beam Instrumentation Workshop, Stanford, CA, May, 1998
- [2] T. Allison, J. Sage, M. Wissman, V. Lebedev, C. Piller, "The CEBAF Beam Scraping Monitor", PAC, Chicago, IL, 2001
- [3] M. Keesee, R. Dickson, R. Flood, V. Lebedev, "The Timing Synchronization System at Jefferson Lab", ICALEPCS, San Jose, CA, 2001
- [4] R. Dickson, V. Lebedev, "Fast Feedback System For Energy And Beam Stabilization", ICALEPCS, Trieste, Italy, October, 1999

LARGE DYNAMIC RANGE BEAM PROFILE MEASUREMENTS *

A. P. Freyberger,

Thomas Jefferson National Accelerator Facility, Newport News, VA 23606, USA

Abstract

Large dynamic range ($Peak/Noise > 10^5$) beam profile measurements are routinely performed in the Hall-B beamline at Jefferson Lab. These measurements are made with a 1 to 10nA electron beam current with energies between 1 to 6 GeV. The electron beam scatters off of a thin ($25\mu\text{m}$) W or Fe wire and the scattered particle/shower is detected via scintillation or Cerenkov light several meters downstream of the wire. This light is converted to an electrical pulse via photomultiplier tubes (PMT). The PMT readout and wire motion are controlled and synchronized by VME electronics. This report describes results on increasing the dynamic range by using multiple wires of varying diameters. Profile measurements with this large dynamic range can be of use for machines with very large beam currents (e.g. energy recovering linacs) where any fractional beam loss represents a significant amount of beam power[1, 2].

INTRODUCTION

Experiments with the CLAS detector [3] in end-station B (Hall-B) at Jefferson Lab (JLAB) place strict requirements on the beam halo due to the small diameter target window (4mm). The target window frame represents a large amount of material when compared to that of the target. Halo outside of 4mm that interacts in the target frame could easily cause an event rate comparable to that of interactions in the target proper.

The beam profile is measured by correlating a wire scanner position with count rates in PMTs located downstream of the wire scanner. Due to the low operating beam current in Hall-B, typically 1 to 10nA, the PMT's can be operated in "count mode". The electron scatters from the wire via several mechanisms with bremsstrahlung, and Møller scattering dominating. The scattered electron or subsequent shower causes the PMT to respond either by Cerenkov light in the quartz window or by direct impact on the cathode of the PMT. This technique typically measures the beam profile with $Peak/Noise > 10^5$ response.

The dynamic range of 10^5 satisfies the experimenter's requirements, and often the beam profile is Gaussian over the complete dynamic range. In order to observe and measure beam halo with more sensitivity a new wire scanner with wires of multiple diameters was installed. Additionally background suppression using Møller coincidences is explored.

* This work is supported by the Southeastern Universities Research Association (SURA) which operates the Thomas Jefferson National Accelerator Facility (JLAB) for the United States Department of Energy under contract DE-AC05-84ER40150.

DESIGN

The wire scanner assembly consists of a linear actuator with 5 inches of travel. The actuator is driven by a stepper motor, which drives the wire support structure into the beam axis. The wire configuration and support frame are shown in Figure 1. The wire support is driven at a 45° with respect to the horizontal axis, which enables both the X and Y profiles to be measured with one axis of motion. The wire configuration consists of $25\mu\text{m}$ diameter X and Y wires, 1mm diameter X and Y wires and a 1mm x 10mm X plate. All wires are made out of Fe for consistency and the plate is stainless steel for convenience.

The PMTs [4] which detect the resulting scattered electron or shower are located 5m downstream of the wire scanner. The distance between the wire scanner and PMTs is optimized for symmetric Møller scattering at beam energy of 5 GeV. Four 2" diameter PMTs are installed outside of a 3" diameter beam pipe, located in the following configuration: top, bottom, beam left, and beam right. The top-bottom PMT pair uses Cerenkov light in the quartz window to detect the scattered/showering particle(s). The left-bottom PMT pair has 0.5" scintillator in addition to the quartz window for detection of the scattered/showering particle(s). The PMT signals are discriminated and counted via a VME scaler. In addition to counting the individual PMT rates, the top-bottom and left-right coincidence rates are fed to the scaler. These coincidence rates are potentially cleaner than the individual rates, however the individual rates from the quartz only PMT's are already quite clean. In addition to the PMT rates, signals proportional to the beam current are also scaled and are used to normalize the PMT rates to the beam current.

Both the stepper motor controller[5] and PMT scalers[6] are VME modules contained within the same VME crate. EPICS controls[7] are used for both devices and state code is used to synchronize the motor motion and scaler readout. During a wire scan the motor position and scaler values are written to a file for further analysis. The minimum time between scaler reads is $\sim \frac{1}{60}$ sec and is determined by the maximum update rate on the motor position. The motor speed and time between scaler reads are configurable at the beginning of each scan.

Scans were taken in Hall-B with a 1 GeV electron beam with 6 nA of beam current. Scans were taken periodically over several days, while trying to optimize the motor speed and scaler read rate. A slow motor speed results in a high number of data points that allow better matching between the $25\mu\text{m}$ and 1mm wire or plate data. However, a slow scan speed (0.125mm/sec) often resulted in an incomplete wire scan due to a beam trip. During these scans CEBAF

was delivering beam ($1 - 40\mu\text{A}$) to the other two experimental halls (Halls A & C).

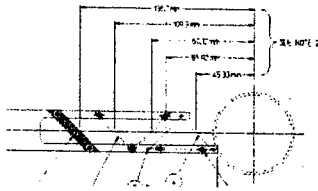


Figure 1: Mechanical schematic of the wire/plate support structure. The thin wire is $25\mu\text{m}$ in diameter. The thick wire is 1mm in diameter. The plate is 1mm by 10mm. The wire frame is moved into the beam along a 45° axis with respect to the horizontal axis.

ANALYSIS

Once a scan file has been written to disk, offline analysis must be performed to combine the $25\mu\text{m}$ wire data with the 1mm wire or plate data. The technique used is similar to that found in Ref. [8]. The beam size is small compared to the 1mm wire diameter and the X plate. Therefore this data must be differentiated before combining with the $25\mu\text{m}$ wire data. In order to determine the scale factor and position alignment a χ^2 minimization is performed to match the $25\mu\text{m}$ data with the differentiated data. Noise is suppressed on the $25\mu\text{m}$ wire data sample, by only using data with more than 10 counts.

Naively one expects a scale factor of 1600 for the 1mm wire, based on the square of the ratio of the wire diameters. The scaler factor for the match between the 1mm wire data and the $25\mu\text{m}$ wire data had a range between 1400 and 1900 for the scans that were taken. On each individual scan there are four matches that need be performed, two sides of two profiles. The minimum scale factor of the four (1400) is used to match the 1mm data with the $25\mu\text{m}$ data.

The scale factor for the X plate data will depend on the extent of the beam in the X dimension. Again a χ^2 minimization is performed and scale factor is found to be ~ 1750 .

Once the data has been combined it is fitted to the following functional form

$$F = b + G(A_{\text{core}}, \sigma_{\text{core}}, \text{mean}) + G(A_{\text{halo}}, \sigma_{\text{halo}}, \text{mean}) \quad (1)$$

where the G represents a Gaussian function and b is a constant background term. Both the core Gaussian and the halo Gaussian have the same mean.

RESULTS

Figure 2 shows the X and Y beam profile obtained using a motor speed 0.125mm/sec. A clear halo is observed with the 1mm wire data, which is too small to be observed with the $25\mu\text{m}$ wire. The parameters determined by the fit

are listed in Table 1. Figure 3 shows the X profile for the same scan using the $1 \times 10\text{mm}^2$ plate data. The parameters determined by the fit to the plate data agree with those obtained with the 1mm, see Table 1 suggesting that the scale factor is properly determined.

Figure 4 shows the X and Y beam profile obtained using a motor speed 0.250mm/sec. This scan also shows a clear halo component, slightly larger than that found in Figure 2. These parameters determined by the fit for this scan and others not shown here are tabulated in Table 1.

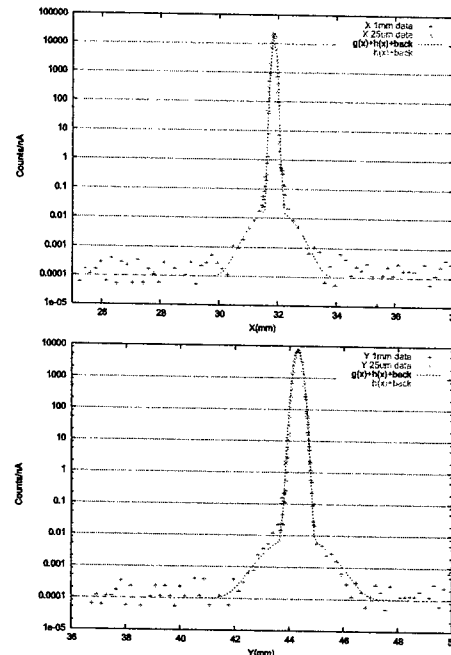


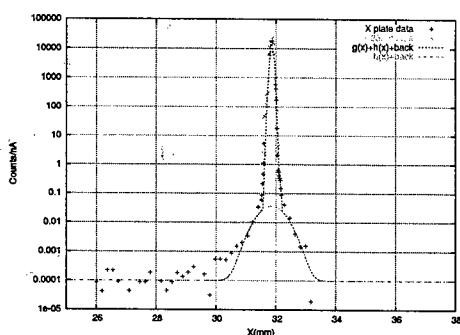
Figure 2: Beam Profile combining the $25\mu\text{m}$ and 1mm Fe wire data. The top(bottom) plot shows the X(Y) data and results of the fit to the data. The red points represent the 1mm wire data, the green points the $25\mu\text{m}$ wire data, the blue curve is the overall fit to the data and the red curve is the halo portion of the fit. The ordinate is plotted with a log-scale and the count rate is normalized to the beam current.

The figures show a signal Peak/Noise ratio of $\sim 10^8$ which is an improvement over the existing system. With this increased dynamic range small amount of beam halo has been observed in the Hall-B end-station. The source of the halo is unknown. Although the fact that the level of halo changed by several orders magnitude over several days, suggests that the source is an artifact of something changing in the accelerator.

The algorithms to merge the data sets have been developed and will continue to be improved so that the merged profiles can be obtained shortly after the scan has been completed. This will result in a quicker feedback to the operators and perhaps in isolating the source of this halo.

Table 1: Profile parameters obtained by fitting the data to the sum of two Gaussian functions with a common mean for all the scans.

	scan1	scan2	scan3	scan3-X plate	scan4
Date	Dec. 5 17:09	Dec. 9 14:45	Dec. 9 14:51	Dec. 9 14:51	Dec. 10 18:22
$\sigma_{core}[X](mm)$	0.045	0.053	0.052	0.052	0.106
$\sigma_{halo}[X](mm)$	0.380	0.470	0.494	0.476	0.656
$\sigma_{core}[Y](mm)$	0.104	0.111	0.110		0.085
$\sigma_{halo}[Y](mm)$	0.949	0.855	0.771		0.617
$\frac{A_{halo}}{A_{core}}[X]$	$4.2 * 10^{-5}$	$1.1 * 10^{-5}$	$8.0 * 10^{-6}$	$7.3 * 10^{-6}$	$3 * 10^{-4}$
$\frac{A_{halo}}{A_{core}}[Y]$	$1.3 * 10^{-5}$	$4.8 * 10^{-6}$	$5.8 * 10^{-6}$		$< 7 * 10^{-5}$
Motor Speed	0.250mm/sec	0.250mm/sec	0.125mm/sec	0.125mm/sec	1.5mm/sec
Wires	25 μ m/1mm	25 μ m/1mm	25 μ m/1mm	25 μ m/1x10mm ² plate	50 μ m

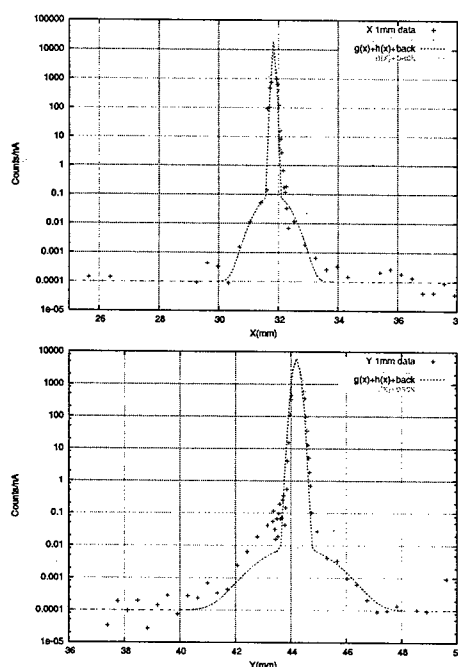

 Figure 3: X Beam Profile combining the 25 μ m and 1 \times 10mm² steel plate data. The red points represent the 1mm wire data, the green points the 25 μ m wire data, the blue curve is the overall fit to the data and the red curve is the halo portion of the fit. The ordinate is plotted with a log-scale and the count rate is normalized to the beam current.

ACKNOWLEDGMENTS

The author thanks the Hall-B staff and CLAS collaborators for beamtime to perform these measurements. Thanks also to M. Zarecky and D. Kashy for engineering and design support. The CEBAF operations staff efforts to deliver stable beam during these measurements is also greatly appreciated.

REFERENCES

- [1] A. Bogacz, *et al.*, Energy Recovery at JLAB, these proceedings.
- [2] C. Tennant, *et al.*, "Beam Characterization in the CEBAF-ER Experiment", these proceedings.
- [3] B. Mecking, *et al.*, "The CEBAF Large Acceptance Spectrometer (CLAS)", to be published in NIM-A 2003.
- [4] XP2622 photomultiplier tubes from Photonics Corporation (formerly Phillips), www.photonics.com.
- [5] VME VS4 stepper motor control from Oregon Micro Systems, www.omsmotion.com.
- [6] VME scaler, VSC16, from Joerger Electronics, www.joergerinc.com.
- [7] Experimental Physics and Industrial Control System (EPICS), <http://www.aps.anl.gov/epics>.
- [8] J.H. Kamperschroer, *et al.*, "Analysis of Data from the LEDA Wire Scanner/Halo Scraper", Proceedings of the 2001 Particle Accelerator Conference, Chicago.


 Figure 4: Beam Profile combining the 25 μ m and 1mm Fe wire data. The top(bottom) plot shows the X(Y) data and results of the fit to the data. The red points represent the 1mm wire data, the green points the 25 μ m wire data, the blue curve is the overall fit to the data and the red curve is the halo portion of the fit. The ordinate is plotted on a log-scale and the count rate is normalized to the beam current.

TUNNELING IONIZATION BUNCH LENGTH MONITOR FOR THE ULTRARELATIVISTIC COMPRESSED ELECTRON BEAMS

A. Murokh*, UCLA, CA 90095-1547, USA

Abstract

The electric field intensity of the compressed ultrarelativistic electron beams is approaching GV/m levels, which is sufficient to cause observable tunneling effect in the low band gap materials. In this article the tunneling ionization rate is estimated for the experimentally available electron beam parameters, and a proposed proof of principle experiment is outlined. Tunneling effect has exponential dependence on the electric field strength; thus being very sensitive to the electron beam peak current. This non-linear dependence opens up a possibility to construct inexpensive, single shot and non-destructive peak current diagnostics for the ultrarelativistic compressed electron beams.

INTRODUCTION

As the advanced photo-injector facilities around the world utilize bunch compression techniques to enhance brightness in the beams [1-2], the ability to measure peak currents of such beams become critical to the successful facility operations. The techniques employed for such measurements include deflecting cavities [3], streak cameras, CTR monitors (Coherent Transition/Diffraction Radiation) [4] and electro-optical systems [5]. All these techniques have been used in the past, yet they have significant limitations. Deflecting cavities are destructive to the beam, streak cameras do not have sufficient resolution for sub-picosecond beams, CTR measurements are time consuming and the data analysis requires making assumptions about the beam shape [6], and electro-optical techniques require rather sophisticated experimental apparatus.

In the same time, for the advanced facilities, such as LCLS (Linear Coherent Light Source), accurate peak current measurements are not only essential for the proper characterization of the beam, but could also provide a unique opportunity to serve as a feedback to compensate for the fast drifts in the RF phase of the injector/linacs [7]. Indeed, the peak current of the electron beam, once it is subject to bunch compression in the chicane, become most sensitive to the minor variation in the RF phase. The ability to make single shot, non-destructive, direct measurements of the peak current in a simple and easily interpretable way would be of the great value as both diagnostic technique and feedback mechanism.

Even the fastest electronic devices such as ICT or stripline monitors rely on the processes of much longer timescale than a time structure of the picosecond electron beams which are subject of the interest. As a result the measurements become integrated over the bunch length

and not sensitive to the longitudinal profile of the beam. One physical process, however, which has much shorter characteristic time is quantum tunneling, which takes place when the dielectric material is exposed to the intense electric field. The tunneling process has a time scale of the order $t \sim h/kT$ (which is about 100 femtoseconds for $T \sim 77$ K). Most importantly, the rate of quantum tunneling is extremely sensitive to the peak field, rather than the time-integrated radiation intensity flux. Hence, if one would observe the tunneling process in the material sample placed near the path of the ultrarelativistic, high current electron beam, the rate of the process will be most sensitive to the peak current in the beam, rather than the integrated charge in the bunch.

This feature makes potential quantum tunneling device an attractive alternative for the fast electron beam diagnostics. In this paper it is proposed to use quantum tunneling effect induced in the doped semiconductor materials by the bulk electric field of the ultrarelativistic compressed electron beam as a single-shot non-destructive peak current monitor.

STATIC TUNNELING MODEL

Tunneling related effects induced by the powerful laser beams have been thoroughly studied both theoretically and experimentally in the recent years [8]. The static probability of direct tunneling in the electric field has exponential dependence on the field strength [9],

$$w(t) = 4\omega_0 \left(\frac{E_i}{E_h} \right)^{5/2} \frac{E_a}{E(t)} e^{-\frac{2}{3} \left(\frac{E_i}{E_h} \right)^{3/2} \frac{E_a}{E(t)}} \quad (1)$$

where $\omega_0 = 2\pi\alpha^2 m_e c^2 / h$ is the atomic frequency unit, E_i and E_h are the ionization potentials of the sample material and hydrogen respectively, $E(t)$ is time-dependent electric field strength, and $E_a = e/4\pi\epsilon_0 r_b^2$ is an atomic unit of the electric field. In the laser induced tunneling experiments the observed ionization rate become frequency dependent below far infrared wavelength of the applied radiation. Interpolating these findings towards the electron beam induced tunneling, one would obtain the limit where static formalism applies [10],

$$E_i < U \approx \frac{e^2 E^2}{4m_e} \sigma \tau^2 \quad (2)$$

where α is the bunch length.

*murokh@physics.ucla.edu

This condition may not be satisfied, for instance in the case of the low charge bunches, or if the electron beam field is microbunched at the higher frequencies. In that case, following the analogy with the theory of the laser induced tunneling, the process deviates from the static limit (1) and become frequency dependent, being dominated by phonon-assisted ionization in solids [10], or multi-photon absorption in gases [11]. For the typical high brightness electron beam of the interest here, the condition given in (2) is satisfied; hence, below only the static tunneling ionization model will be considered. Clearly, more detailed analysis in the future should consider all the relevant processes.

Using the static tunneling model, one can calculate the physically achievable electron beam parameters, where the effect can be observed. For a typical high brightness ultrarelativistic electron beam ($\gamma > 100$) the electric field temporal profile mirrors the shape of the electron beam longitudinal distribution, as long as it is sampled sufficiently close to the beam path:

$$E(r, t) \approx \frac{I(t)}{2\pi\epsilon_0 r c} \quad (3)$$

Given post-compression electron beam peak currents values of the order $I_{\text{peak}} \sim 1$ KA, the field intensity reaches up to 100 MV/m, as far as few millimeters away from the beam path.

Such field intensities are generally not sufficient to generate observable tunneling ionization in the dielectrics at the room temperature (which typically have a band gap of around 10 eV). However, if one would use low band gap doped semiconductor materials the field of that amplitude can generate an observable tunneling ionization. Of course, the target material should be cooled under liquid nitrogen, so that the free carriers generation could be dominated by quantum tunneling effect and not the thermal noise. For instance, in doped germanium (which was used in the measurements shown

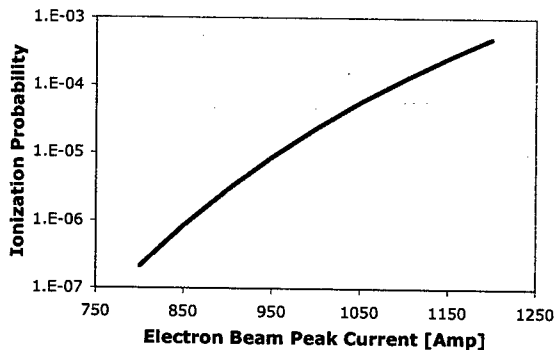


Figure 1: Static tunneling probability for the gold impurities in germanium target placed 3 mm away from the path of 1 nC ultrarelativistic electron beam.

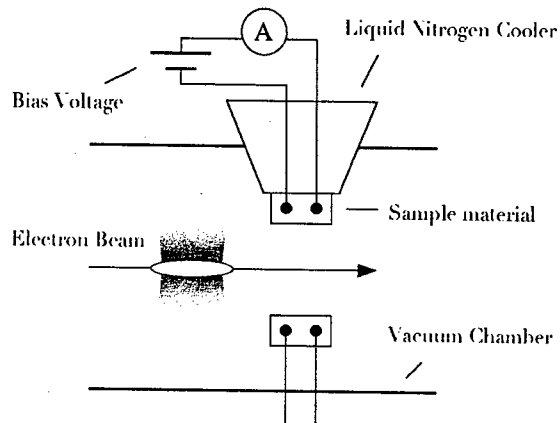


Figure 2: Experimental apparatus to measure tunneling effect in the field of the electron beam. Nitrogen cooled semiconductor sample is placed near the beam path with the bias voltage applied. Current induced by the beam passage would be mostly due to the tunneling at the dopant sites.

in [10]), the ionization energy for deep impurities is of the order of $E_i \sim 100$ meV. In such materials, deep impurities tunneling ionization has been extensively studied in the fields of the THz laser beams [12], which intensities were similar or smaller than the field values in quest.

As an example, one can consider cooled Ge:Au sample ($E_i \sim 150$ meV), and 1 nC electron beam passing 3 mm away from the target. The ionization rate calculated through time integration of the equation (1) will exhibit near exponential dependence on the electron beam peak current (Figure 1).

EXPERIMENTAL CHALLENGES

To conduct a proof of principle experiment, one has to cool the sample material down to the liquid nitrogen temperature, in order to minimize the thermal noise (Figure 2). When bias voltage (usually of the order of 5 V) is applied, and electron beam is not present, there should be no current in the circuit. However, when a high peak current electron beam passes near the biased sample, tunneling ionization at impurities sites "opens up" the circuit and the charge flow can be measured. In that case the integrated charge flux through the circuit should be a very non-linear function of the electron beam peak current. Following the model shown in Figure 1, a 10 % variation in the electron beam peak current should lead to the order of magnitude change in the measured signal area. Having such device in the beamline, would enable to observe non-destructively very small changes in the electron beam peak current and compensate for them if needed. Proper calibration against some other diagnostics may even allow the absolute measurements.

As the electron beam field strength decays radially, two identical samples should be placed symmetrically around

the path of the beam. That would allow reducing measurement errors associated with the beam position jitter. In fact, to remove the errors associated with the jitter in both planes one can consider the 4 samples system, which can also act like a BPM (Beam Position Monitor), similar to the stripline.

To improve signal to noise ratio, it is critical to prevent the target material from being irradiated by the shorter wavelength sources. Particularly problematic could be IR, optical and X-ray radiation produced by the electron beam itself upstream along the beam line. Good shielding material to reduce such problem would be silicon, which is opaque for the optical wavelengths, and yet have relatively low index of refraction for the electron beam induced field.

Another important consideration is secondary ions produced in the host material. The tunneled electrons can be accelerated by the electron beam field and reach energies above the ionization potential of the host material. Such electrons would ionize host atoms, increasing the overall ions population, and such process can generate a correction to the behaviour presented in the Figure 1; an effect somewhat similar to the one postulated in [13]. This additional ionization enhancement should be an important factor to consider, while optimizing the distance from the electron beam path to the sample for the specific electron beam parameters.

CONCLUSION

The concept of the electron beam bulk field induced quantum tunneling, introduced in this paper, can probably be expanded to a much deeper level of theoretical understanding, which at present is way beyond the author's horizon. Yet one can find it rather meaningful to conduct a pilot experiment and, if successful, use it as a reference point for further theoretical investigation of the tunneling phenomena. Such effort would not only be valuable as an electron beam diagnostics research, but also of the general interest to the material science community.

ACKNOWLEDGEMENT

The work presented in this paper was impacted by helpful discussions with C. Pellegrini, P. Krejcik, G. Travish and S. Ganichev, and also supported by the ONR Grant #N00014-02-1-0911.

REFERENCES

- [1] M. Cornacchia *et al.*, *A Sub-Picosecond Photon Pulse Facility for SLAC*, SLAC-Pub-8950, (2001).
- [2] L. Serafini and M. Ferrario, in *Physics of, and Science with, the X-ray Free-Electron Laser*, edited by S. Chattopadhyay *et al.*, AIP Conf. Proc. No. 581 (AIP, New York), 87, (2001).
- [3] R.H. Miller, R.F. Koontz, D.D. Tsang, *The SLAC Injector*, IEEE Trans. Nucl. Sci., 804, (1965).
- [4] U. Happek and A. J. Sievers, Phys. Rev. Lett. **67**, 2962 (1991).
- [5] I. Wilke *et al.*, Phys. Rev. Lett **88**, 124801, (2002).
- [6] A. Murokh *et al.*, Nucl. Instr. and Meth. A **410**, 452 (1998).
- [7] P. Emma, private communication.
- [8] S.D. Ganichev *et al.*, Phys. Rev. Lett. **80**, 2409, (1998).
- [9] P.B. Corkum, N.H. Burnett and F. Brunel, Phys. Rev. Lett. **62**, 1259, (1989).
- [10] S.D. Ganichev, W. Prettl and P.G. Huggard, Phys. Rev. Lett. **71**, 3882, (1998).
- [11] S. Augst, *et al.*, Phys. Rev. Lett. **63**, 2212, (1989).
- [12] S.D. Ganichev *et al.*, Phys. Rev. Lett. **75**, 1590, (1995).
- [13] A. Murokh *et al.*, *Limitations on Resolution of YAG:Ce Beam Profile Monitor for High Brightness Electron Beam*, Proceeds. 2nd ICFA Advanced Accelerator Workshop, edited by J. Rosenzweig and L. Serafini, (Los Angeles, 1999), World Scientific, 564, (2000).

DESIGN AND TESTING OF A FAST BEAM POSITION MONITOR*

B. Quinn[#], B. Beaudoin, S. Bernal, A. Diep, J. Harris, M. Holloway, D. Lamb, W. Lee, M. Glanzer, M. Quirus, M. Reiser, M. Walter, A. Valfells, R. Yun, P. G. O'Shea

Institute for Research in Electronics and Applied Physics,
University of Maryland, College Park, MD 20742

Abstract

The University of Maryland Electron Ring (UMER) group is currently exploring the physics of space-charge dominated beams. Seventeen Beam Position Monitors (BPMs) will be used to determine the beam centroid for steering correction purposes to within 0.5 mm. Since the pulse length is relatively long (100 ns), the BPMs can also be used for temporal beam profiling. These features are extremely useful for perturbation and longitudinal dynamics studies. For these uses the BPM needs a temporal resolution better than 2 ns. We report on the final design and testing as well as other unique features of this device.

INTRODUCTION

The University of Maryland Electron Ring (UMER) is designed as a low-energy recirculator ring for studying the physics of space-charged dominated beams [1], [2]. Since the parameters of UMER can be scaled to those of higher energy machines, it will act as a benchmark for future designs. Although UMER is compact (11.52m circumference), it is an unusually complex device. This complexity coupled with its operation in the space-charge dominated regime requires UMER to make use of multiple diagnostics and controls [3], [4], [5]. This paper will report on the final design of capacitive beam position monitors (BPMs) and the experimental results obtained using them in the areas of steering, beam profile, current and loss monitoring. For these applications, the BPM needs spatial resolution better than 0.5 mm and temporal resolution better than 2 ns.

ENGINEERING AND DESIGN

Both mechanical and electrical aspects of the BPM have been upgraded for simplification of assembly and improved data collection. Currently, UMER is utilizing ten BPMs, one in the injector and one in each of the nine ring chambers of the UMER assembly. The final UMER assembly will contain a total of seventeen BPMs. Due to space constraints; we will only discuss the changes in design since the last publication [6].

Mechanical Design

The mechanical design has been simplified. The number of individual pieces that make up the housing has been greatly reduced. This cuts the construction time in

half and results in a simple and robust frame for the BPM. Signals are collected via four striplines that are separated by grounded planes and separated from the housing by means of a ceramic encasing ring. This ring provides a consistent distance between the collecting plates and the grounded housing, ensuring that each channel of the BPM has the same capacitance. Each stripline forms an arc of 77°, an important feature held over from the old design. It can be shown that at this angle, beam displacement in the X and Y dimensions are decoupled [7].

Unlike most machines, the UMER BPMs are not a fixed part of the beam line. They can be raised out of the beam line, via a mechanical actuator, to allow an attached phosphor screen flag to intercept the beam. This enables a visual inspection of position and internal structure of the beam. When the BPM is lowered into the beam line a good electrical contact is maintained between the housing and beam line via a beryllium copper RF shielding mesh.

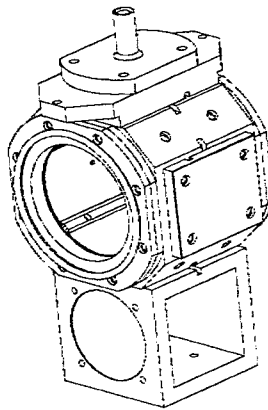


Figure 1: BPM / Phosphor Screen combination. BPM inner diameter is 2 inches.

Electrical signals from the BPMs are brought by 50Ω kapton encased transmission line to a vacuum feed through and to the electronics.

Electrical Design

The BPM buffering circuit has been redesigned with a high enough bandwidth to faithfully reproduce the beam rise and fall times. The buffer amp selected has a -3db small signal bandwidth of 750Mhz, and high AC input impedance ($C_{in} = 1.0pF$ and $R_{in} = 700k\Omega$). This input impedance is used, along with the capacitance of the collecting plate, to create the necessary time constant to accurately reproduce the beam profile. This resistance also serves to bleed off any excess charge between the 60 Hz beam pulses.

*Work supported by the United States Department of Energy

[#]bquinn@glue.umd.edu

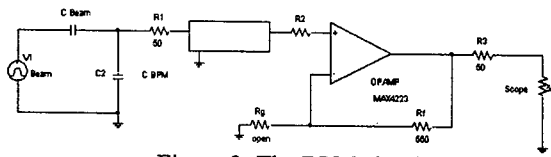


Figure 2: The BPM circuit.

Figure 2 shows the circuit where C_{Beam} is the capacitance between the beam and collecting plate. C_{BPM} is the capacitance between the collecting plate and the grounded housing. R_1 and R_2 are dampening resistance. R_1 is placed on the housing inside the vacuum chamber; R_2 is a coaxial resistor outside vacuum and can be varied as necessary. R_3 is used to match the signal input to the oscilloscope a 50Ω impedance. The downside is that R_3 also acts as a voltage divider, lowering the signal magnitude into the oscilloscope. It is preferential to have the matched signal than a larger magnitude. R_4 and R_5 set the gain of the circuit. Currently $R_6 = 0$, resulting in a unity gain.

For calibration a 100 mA, 100 ns pulse was sent through each BPM via a metal rod to simulate the beam. The rod was moved incrementally and signals were taken from each collecting plate. Calibration was achieved by taking the data from any two coplanar channels (i.e. horizontal or vertical) and plotting the difference over the sum of the signals, figure 3 shows a calibration plot.

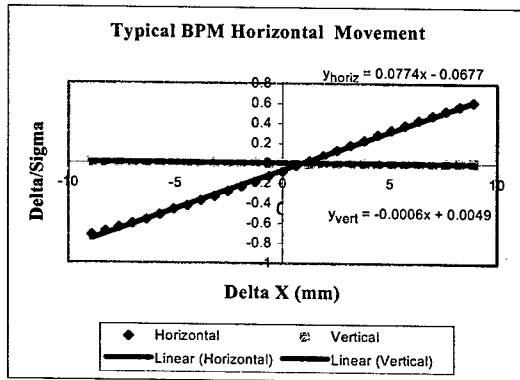


Figure 3: This graph shows the sensitivity, linearity and offset of a typical UMER BPM. Also, note that the horizontal and vertical signals are decoupled within this range.

On average the BPMs that have been calibrated using the delta over sigma method have resolution $< 0.1\text{mm}$. Results using the BPMs with actual beam confirm predicted values for linearity and resolution.

The ability to acquire an accurate beam profile is a unique feature of the UMER BPMs. In beam tests we have found the frequency response to be much better than anticipated. The experiment was conducted comparing it to a well-established diagnostic, the Bergoz current transformer model number FCT-082-20:1, in order to ascertain the relative frequency response of the BPM. Both diagnostics are located in the injector line. Two opposing channels of the BPM were summed to get total

current. The Bergoz coil is approximately 60 cm from the electron gun and the BPM is 19 cm downstream from the Bergoz coil. Hence, it is expected that the beam would have spread longitudinally and the rise and fall times would be greater at the BPM. However, as figure 4 shows, the rise time of the Bergoz coil was measured to be 2.8 ns while the rise time of the BPM was 1.7 ns for the 25 mA beam. The test was repeated with a current of 85 mA, a dampening resistance $R_2 = 200\Omega$ (see figure 2) is added to control oscillations. Even then, the BPMs' frequency response is as fast as that of the Bergoz coil.

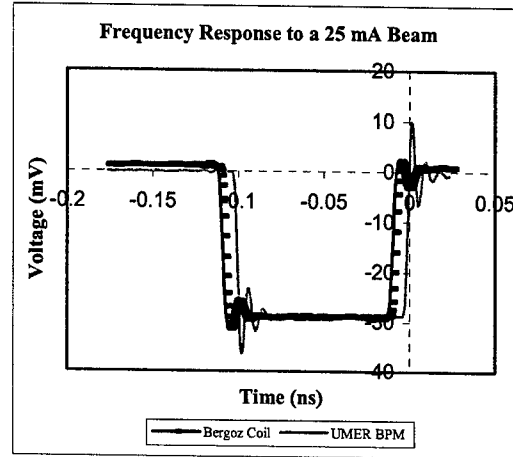


Figure 4: Frequency response of the BPM compared to the Bergoz Coil.

APPLICATIONS

The UMER BPMs have evolved into a versatile diagnostic capable of beam profiling, position and current monitoring with good resolution and high bandwidth.

Beam Position Monitoring

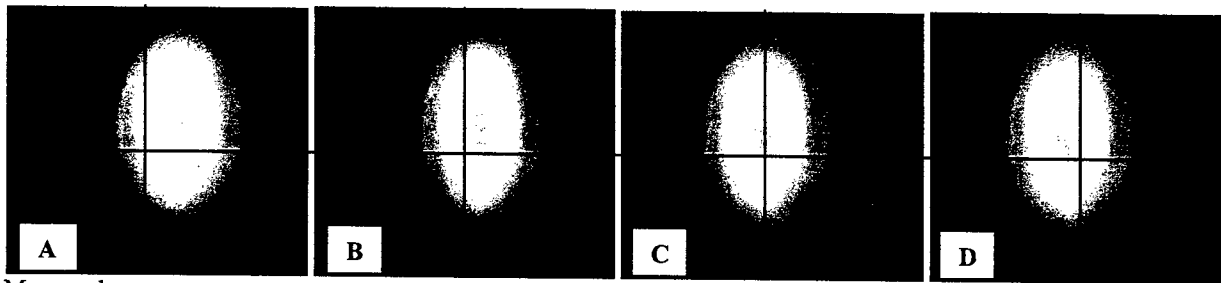
The UMER BPM is first and foremost used to determine the location of the beam centroid as a function of time. Beam position in the horizontal plane is determined by dividing the difference of the two horizontal (right and left) signals by their sum and applying the offset and resolution factors determined in calibration. Since X and Y are decoupled, repeating the process with the vertical (top and bottom) signals creates an XY pair at which the beam centroid lies. The equations are

$$X = \frac{(V_R - V_L)}{R(V_R + V_L)} - \frac{B}{R} \quad (1)$$

$$Y = \frac{(V_T - V_B)}{R(V_T + V_B)} - \frac{B}{R} \quad (2)$$

where V_X is the signal from the corresponding signal plate, R (slope) is the resolution number and B (X-intercept) is the offset number as in figure 3.

Tests were conducted with beam to confirm the accuracy of the BPMs. Varying the current on an upstream steering dipole to move the beam, position data and beam images were taken at the same location using the BPM / phosphor screen combination. The center of



Measured

A to B: X = 1.12526 mm, Y = 0.06307 mm

B to C: X = 2.33359 mm, Y = 0.18921 mm

C to D: X = 1.13526 mm, Y = 0.06307 mm

BPM Calculation:

A to B: X = 1.03819 mm, Y = 0.03904 mm

B to C: X = 2.59375 mm, Y = 0.19337 mm

C to D: X = 1.15206 mm, Y = 0.04006 mm

Figure 5: Phosphor screen images of the beam with relative center measured directly and calculated by the BPM. The crosshairs show the center of the phosphor screen.

the beam image was determined by direct measurement and converted from pixels to mm. Since the exact location of the phosphor screen is not known only a relative comparison is possible. Figure 5 shows the close agreement between direct measurement and the BPM calculations.

A user interface has been developed and is in the process of being debugged. When finished it will allow the user to select desired BPM and see a graphical representation of beam position. This is accomplished by means of a Labview BPM control program for unit selection via a multiplexer. The desired signals are fed into an oscilloscope and then into the computer. The same BPM control program then computes the beam position and displays it graphically for the user to set the proper steering to center the beam. Future upgrades will automatically control the steering magnets.

Beam Current and Loss Monitoring

Since the BPM measures charge as a function of time it may be used as a current monitor. This is achieved using a conversion factor determined from the following equation [8]

$$\frac{V_{L+R}(t)}{I_B(t)} = \frac{\phi \ell}{4\pi C_{tot} \beta_c}, \quad (3)$$

where V_{L+R} is the total voltage of two opposing plates, I_B is the beam current, ϕ is the collecting plate angle, ℓ is the plate length, C_{tot} is the total capacitance in the circuit and β_c is the relativistic factor of the beam. Solving this equation gives a conversion factor of 1.25 V/A. This number agrees with experimental observations and comparisons to the Bergoz current transformer. UMER employs a BPM every 0.64 m; therefore, the location of beam loss can be determined.

The UMER BPM has such a good frequency response that the longitudinal spread due to Coulomb forces at the head and tail of the beam can be accurately profiled. Since the UMER beam is 100 ns long and the time it will take to make its journey once around the ring is approximately 200 ns this profiling ability is of great importance. If unchecked, the longitudinal spread will

cause the head and tail of the beam to meet. UMER will employ three induction gaps to keep the beam compressed. A study of the longitudinal dynamics of the beam is currently underway to establish the specifications of the induction gaps [9]. The BPMs have become an important diagnostic for this study. Using the BPMs' ability to accurately measure the length, as well as rise and fall times, of the beam will give a better understanding of the longitudinal dynamics of space-charge dominated beams.

CONCLUSION

The UMER group has completed design and implemented a capacitive BPM for aiding the study of space-charge dominated electron beams. A spatial resolution of 0.1 mm (100 mA, 0.4 mm for 25 mA) and temporal resolution of 1.7 ns have been achieved, which exceed the design specifications. In addition to locating the centroid of the beam, the UMER BPMs are capable of high resolution beam profiling, current and loss monitoring. Ten BPMs have been constructed and are in use with the UMER beam, with seven more on the way. A user interface is being developed that will control data collection and aid in beam steering.

REFERENCES

- [1] <http://www.ireap.umd.edu/UMER>.
- [2] S. Bernal, et al., "Beam Transport Experiments over a Single Turn at the University of Maryland Electron Ring," these proceedings.
- [3] M. Walter, et al., "Alignment of Components at the University of Maryland Electron Ring," these proceedings.
- [4] M. Walter, et al., "Time Resolved Emittance Measurement in the University of Maryland Electron Ring," these proceedings.
- [5] M. Virgo, et al., "Controls and Alignment for the University of Maryland Electron Ring," PAC 2001.
- [6] J. Harris, et al., "A Fast Beam Position Monitor for UMER," PAC 2001.
- [7] Y. Zou, et al., "Development of a Prototype Capacitive BPM," Masters Thesis, University of Maryland at College Park, 1998.
- [8] R. Shafer, "Beam Position Monitoring," pg.612 AIP Conference Proceedings 249, vol.1 (1992).
- [9] J. Harris, et al., "Initial Studies of Longitudinal Dynamics on UMER," these proceedings.

TIME RESOLVED EMITTANCE MEASUREMENT IN THE UNIVERSITY OF MARYLAND ELECTRON RING*

M. Walter[#], D. Lamb, S. Bernal, I. Haber, R. A. Kishek, H. Li, B. Quinn, M. Snowel, A. Valfells, M. Reiser, P.G. O'Shea, Institute for Research in Electronics and Applied Physics, University of Maryland, College Park, MD 20742

Abstract

Initial experimental results are presented for measurements of the emittance of an electron beam in the University of Maryland Electron Ring (UMER). Two independent sets of slit-collector systems are used to measure the emittance in the vertical and horizontal directions respectively. Results are then compared to the time integrated emittance measurements obtained from a pepperpot. The UMER electron beam has an energy of 10 keV, with as much as 100 mA of current, and pulse length of 100 ns. The beam is confined by a periodic lattice of focusing/defocusing quadrupole magnets at 16 cm intervals. Beam steering is achieved with dipole magnets at 32 cm intervals and additional small steering dipoles as needed.

INTRODUCTION

The University of Maryland Electron Ring (UMER) is a low voltage (10 kV), high intensity (100 mA), recirculating electron ring designed to explore the physics of space charge dominated beams [1,2,3]. Emittance growth caused by a variety of factors, such as injection mismatch, beam steering, focusing, etc., is of keen interest to the entire accelerator community. Our key goal was to develop a method to measure the time resolved beam emittance and be able to map the phase space distribution as a function of time during the beam pulse. When combined with an energy analyser, this system will enable us to plot the full time-dependent, six dimensional, phase space of the beam [4].

PROCEDURE

Previous attempts to measure beam emittance have been unsuccessful due to tremendous amount of noise pickup from oscillatory modes within the diagnostic chamber. The wire from our previous slit-wire collector has been replaced by a shielded collector bar to reduce the noise in the data collection circuit. The collector bar is isolated from its environment by a conducting box and ceramic insulators. Mounted on the front of the box are adjustable shutter doors. The gap between the shutters may be changed to mimic a change in the wire size of a standard harp-like wire collector. The gap presented in this work was fixed at 0.5 mm. The setup is shown in Figure 1.

*This work is funded by US Dept. of Energy grant numbers DE-FG02-94ER40855 and DE-FG02-92ER54178.
#mwalter@ireap.umd.edu

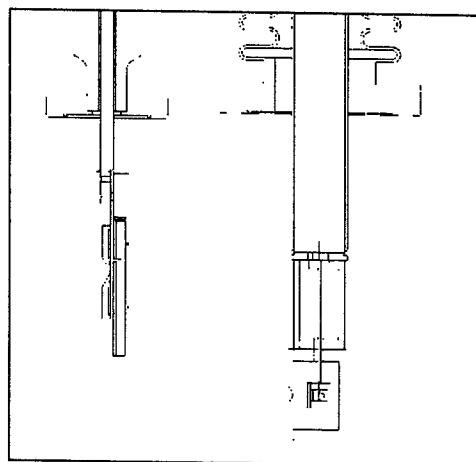


Figure 1: Slit-collector cut away view.

The overall concept of data collection remains the same as in most cases of emittance measurement with a slit-wire system [5,6]. The slit is scanned across the beam in discrete steps. At each step the collector sweeps across the portion of the beam that is not blocked by the slit. Control of the motion of both the slit and collector is achieved by use of stepper motor with position encoders. The stepper motor control and data collection have been automated through an interface with LabView software. A schematic of this setup is shown in Figure 2.

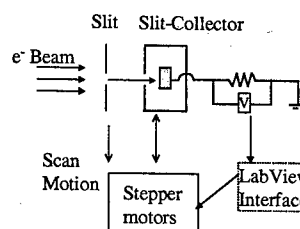


Figure 2: Slit-collector schematic.

RESULTS

A sample voltage trace for a 25 mA beam is shown in Figure 3. All data presented in this work is for a 25 mA, 10 keV beam. The low current beam was used because of the relative ease of experimental beam envelope matching as compared to the full 100 mA beam. The dotted trace is unfiltered and can be seen to contain an unacceptable amount of noise. The primary source of this noise is the fact that a majority of the beam is intercepted by the slit, which is not isolated from our electrical grounding of the ring. To eliminate this source of noise,

we simply moved the collector completely out of the beam path and recorded the noise signal for each slit position. The noise may then be subtracted from the signal. This process yields the solid trace in Figure 3.

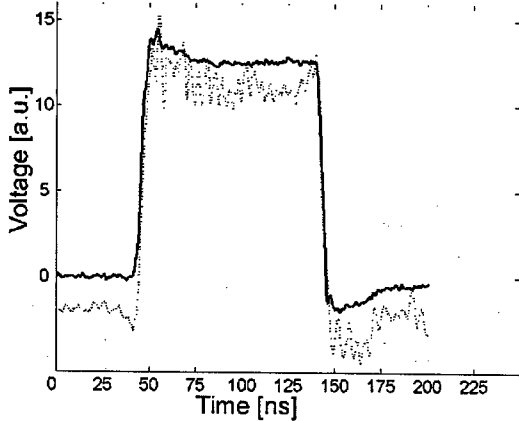


Figure 3: Current signal, raw (dotted line) and with noise subtracted (solid) at $x_{\text{slit}}=2.54$ mm and $x_{\text{coll}}=4.41$ mm.

Figure 4 shows a complete scan of the collector (x') for a fixed position of the slit ($x_{\text{slit}}=2.54$ mm). It can be seen in this figure that dynamics at the head and tail of the beam cause large uncertainty in the measurement. The higher energy head of the beam appears to have shifted toward the center of the ring (increasing x'), while the low energy tail moves to a larger radius.

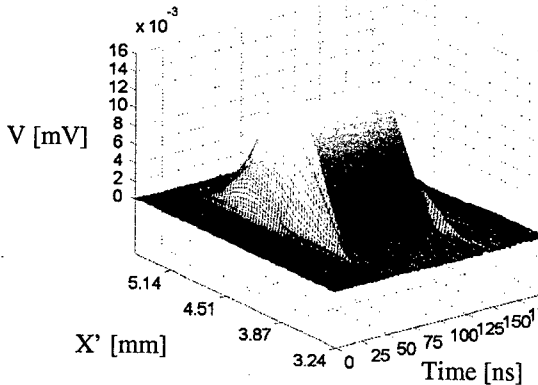


Figure 4: Filtered collector scan (x') for fixed slit position ($x_{\text{slit}}=2.54$ cm).

Figure 5 shows a full scan of the collector at $x_{\text{slit}}=7.62$ mm. The radial shear in the beam at this position is obvious. It could possibly be caused by a slight mismatch or misalignment of the beam. As these are only initial measurements, additional investigation is warranted to explain the physical mechanism of the beam dynamics. This plot is shown primarily as a demonstration of the time and spatial resolution achieved in these initial experiments.

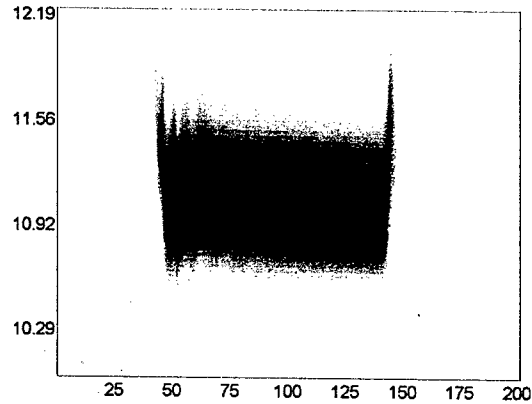


Figure 5: Collector scan for fixed slit position ($x_{\text{slit}}=7.62$ cm) showing beam shear.

Figure 6 shows a plot of the time-integrated, transverse phase space, x vs. x' (top) and y vs. y' (bottom). We also have the ability to plot the 4-dimensional velocity space as a function of time. The calculated emittance values for these plots are (presented as $4 \cdot \epsilon_{\text{rms}}$) $\epsilon_x=30 \mu\text{m}$ and $\epsilon_y=20 \mu\text{m}$. Corresponding measurements under identical beam conditions with a pepperpot yielded values of $42 \mu\text{m}$ and $28 \mu\text{m}$. Differences between the pepperpot and slit-collector may be due to a few systematic errors. The bounds of integration for the slit-collector method were fixed to avoid the head and tail of the beam, where a large contribution to the time integrated emittance may exist. Inaccuracies may also result in the pepperpot measurements because of the relatively low current beam used and resultant small spot size available for photo processing.

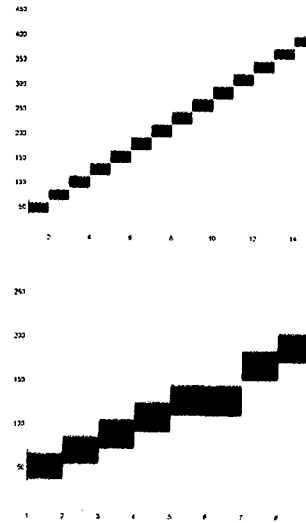


Figure 6: Time integrated phase space plot of x' vs. x (top) and y' vs. y (bottom).

CONCLUSIONS

An automated emittance measurement system has been built and successfully tested on UMER. It is fully capable of mapping time resolved transverse phase space with a resolution of 2 ns. An initial comparison of time integrated emittance measurements with those of the pepperpot give $\epsilon_x=30\text{ }\mu\text{m}$ and $\epsilon_y=20\text{ }\mu\text{m}$ for the slit-collector, and $\epsilon_x=42\text{ }\mu\text{m}$ and $\epsilon_y=28\text{ }\mu\text{m}$ from the pepperpot.

It should be noted that these are only initial results. Experiments with time-resolved measurements of the full beam have begun. Future plans include a feedback loop to modify beam steering and focusing in order to minimize emittance.

REFERENCES

- [1] <http://www.ireap.umd.edu>
- [2] P. O'Shea, et. al., "Experiments with space-charge-dominated beams for heavy ion fusion applications", *Laser and Particle Beams* (2002), 20, 599-602.
- [3] S. Bernal, et. al., "Beam Transport Experiments over a Single Turn at the University of Maryland Electron Ring", these proceedings.
- [4] Y. Zou, et. al., "Space-Charge Effects in Retarding Field Energy Analyser", these proceedings.
- [5] D. Engwall, "High brightness Electron Beams from a DC, High-Voltage, GaAs Photoemission Gun", PhD dissertation, Univ. of IL at Urbana-Champaign, 1988.
- [6] M. Zhang, "Emittance Formula for Slits and Pepperpot Measurements", FermiLab-TM-1988, Oct. 1996.

ALIGNMENT OF COMPONENTS AT THE UNIVERSITY OF MARYLAND ELECTRON RING*

M. Walter[#], S. Bernal, A. Diep, M. Glanzer, I. Haber, J. Harris, R. A. Kishek, D. Lamb, W. Lee, H. Li, B. Quinn, M. Quirus, A. Valfells, M. Reiser, P.G. O'Shea, Institute for Research in Electronics and Applied Physics, University of Maryland, College Park, MD 20742

Abstract

Alignment of experimental components is critical to operation of The University of Maryland Electron Ring (UMER). Procedures and equipment used to align components of the electron ring are presented. The compact nature of UMER (ring diameter ≈ 4 m) presents unique challenges and advantages associated with the placement of vacuum components, confinement and steering magnets, and diagnostic equipment. Alignment of all components has been accomplished with a set of two T3000 theodolites and a three-dimensional software package from the Leica Corporation. A set of fiducial monuments has been used to establish a permanent coordinate system. The position of UMER components has been measured to an accuracy of less than 100 microns in that coordinate system.

I INTRODUCTION

The University of Maryland Electron Ring (UMER) is a low energy (10 kV), high intensity (100 mA), recirculating electron ring designed to explore the physics of space charge dominated beams [1,2]. Due to its compact nature, alignment of the experimental components within the ring is critical. The UMER ring diameter is approximately 4 meters. Previous attempts to align components utilizing mechanical armatures, micrometers, and shims were found to be cumbersome and inadequate. This paper presents the methods used to solve the unique challenges associated with the placement of vacuum components, confinement and steering magnets, and diagnostic equipment. Procedures and equipment used to align components of the electron ring are presented in Sec. II. Results of our work are presented in Sec. III. In this section we also discuss possible future improvements and recommendations for further refinement of alignment issues.

II ALIGNMENT PROCEDURE

Establishment of a Coordinate System

The problem begins with the same question every experimentalist faces, "Where can we put all this stuff?"

*This work is funded by US Dept. of Energy grant numbers DE-FG02-94ER40855 and DE-FG02-92ER54178.
#mwalter@ireap.umd.edu

The experimental area assigned to UMER is shown in Fig. 1. The room is only approximately six meters wide on the left and has several obstacles in the form of steel support beams scattered throughout the area intended for setup of the ring. The problem is further complicated by the addition of approximately two meters for the injection line and two meters for extraction 140° further downstream.

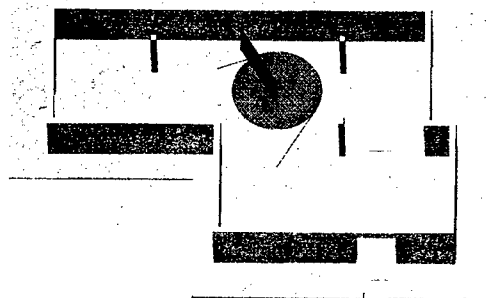


Figure 1: Experimental floor plan. Ring location (circle) and 12:00 position (plane) shown.

As seen in Fig. 1 the center of the ring was chosen to give adequate clearance to the wall and prevent interception of the corner at the lower left. To fix this location a hole was bored into the concrete and a stainless steel cylinder (monument base) was cemented in place. The cylinder has a precision 0.25 inch hole on its top side which allows a target to be inserted without error and removed when not in use. The rotational orientation of the ring was fixed with a target approximately two meters high on the wall. All angular positions are measured clockwise from the plane formed by this target and the center monument. Eight additional monuments and four wall targets have been placed around the experimental area and referenced to the ring center and angular reference plane to ensure line-of-sight from all locations.

Assembly Modeling

Next, we needed to know exactly where all the pieces of the experiment should be placed. To accomplish this, all parts and assemblies have been drawn in the three-dimensional CAD package, Pro/Engineer [3]. Those assemblies are then constrained to their ideal positions with the knowledge that the ring is divided into 18 individual sections of 20° subtended arc length each. Each section has been constructed with a central chamber and two arms, each with a 10° bend. From these

geometric constraints the exact radius to the center of each ring chamber is 1833.456 mm.

Mounted on each section are two dipole magnets to bend the beam and four quadrupole magnets for confinement [4]. The diameter of the ring is fixed by the spacing of 16 cm between quadrupoles. The dipole and quadrupole mounts are fixed in place on a cluster plate with alignment pins. The cluster plates have been machined from 0.875 inch thick aluminium plate. Figure 2 shows the detailed drawing of one of the ring sections.

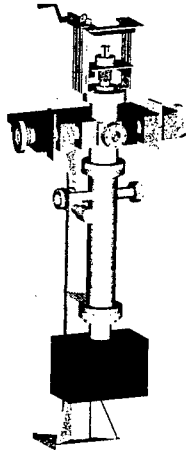


Figure 2: ProEngineer drawing of one 20° ring section.

Both the injection and extraction lines are 10° off the tangent to the ring. The diagnostic chamber has been repositioned during ring construction as sections have been installed to allow beam experiments to continue, but will be attached to the end of the extraction line upon closure. Figure 3 shows the current experimental setup with 180° of the ring installed.

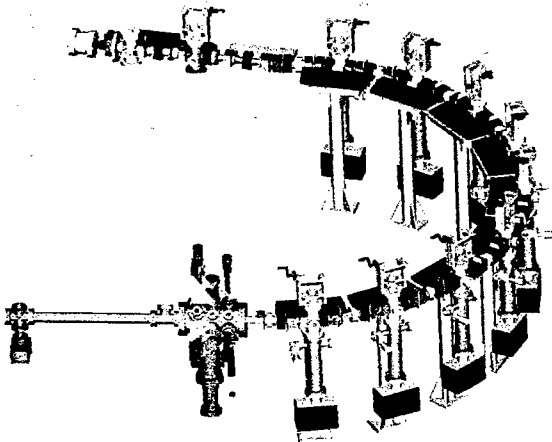


Figure 3: Current experimental setup of 180° of the complete electron ring.

Alignment Equipment

All of the previously described components have been placed in their proper positions by the use of two T3000 theodolites and their associated software package, Axyz,

from Leica AG [4]. The T3000 can measure angles with a standard deviation of 0.5 arcseconds. On the scale of distances within our lab, this translates to a few 10's of microns. The minimum focal distance is 0.51 m. Magnification varies with distance, from 13x to 43x.

The theodolites require line-of-sight not only to the component to be positioned but also to the monuments and references previously discussed. In some situations, this may require leapfrogging when only two theodolites are available. The accuracy of measurements is sensitive to the angle formed between the two theodolites and target. Ideally this angle should be kept between 60 and 120 degrees to minimize pointing error. Finally, the accuracy of measurements is highly sensitive to the ability and vision of the operator.

The software package, Axyz, records all angular measurements and calculates data points from the theodolites. It allows user defined coordinate system transformations. Simple shapes, lines, circles, etc., may be constructed to ease alignment problems. Axyz also can calculate projections, intercepts, and distances.

III RESULTS AND DISCUSSION

All the components of the electron ring may now be measured to within less than 100 microns with the theodolite alignment system. Nine ring chambers have been positioned along with all their associated magnets and diagnostics. The injection line and diagnostic chamber have been positioned. Continued refinement of positioning components within this complex system is ongoing. Beam quality has been improved by sound implementation of alignment procedures [2].

The key alignment issues in the UMER setup are the positioning of focusing magnets, component design, and manufacturing tolerances. Beam quality has been found to be extremely sensitive to offsets in the focusing lattice.

Our quadrupoles are placed within mount blocks, which are then bolted to the cluster plate with no ability to modify individual magnet positions. The cluster plate is held in position by a set of push-pull screws. It has been found that these push-pull screws cause a small deformation of the cluster plate and therefore misalignment of magnets. The machining tolerances of the mount block also affect accuracy of magnet placement.

The arms of the ring chambers also introduce error into the system. Both the accuracy of the bend angle and arm alignment during the welding process could cause misalignment. Much of that error can be compensated for with the bellows on the downstream flange of each chamber but errors normal to the ring plane are difficult to correct without tilting the chamber, which in turn would introduce errors in the pitch of the magnets.

Nearly all of the errors in alignment introduced by the magnet mount blocks and ring chambers can be corrected with a redesigned mount block or cluster plate assembly. It would be prohibitively difficult and expensive to replace the cluster plates, whereas replacement of the mount blocks is reasonably easy. The magnets are already

removed each time the system must be baked to achieve acceptable vacuum.

Figure 4 shows the prototype of the redesigned magnet mount block. The improved design allows correction in roll, pitch, and yaw with push-pull screws and a small increase in the inner bore from 2.210 to 2.335 inches. Sensitivity to the roll angle has been increased by extending the moment arm length where the block attaches to the cluster plate.



Figure 4: Current magnet mount block (left) and prototype redesign (right).

IV CONCLUSIONS

Alignment is critical to all operational aspects of UMER from injection to diagnostics at beam termination. All components of UMER can now be measured in situ, without breaking vacuum or disrupting experimental activities. A coordinate system for the experiment has been constructed and a trained team of personnel can now align and adjust components quickly and accurately. Maintenance of the ring has also been simplified because pieces may be removed and replaced easily. Alignment issues have now been incorporated throughout, from the initial design phases to finished assembly and installation.

V REFERENCES

- [1] <http://www.ireap.umd.edu>
- [2] S. Bernal, et. al., "Beam Transport Experiments over a Single Turn at the University of Maryland Electron Ring", these proceedings.
- [3] Pro/Engineer, copyright by Parametric Technology Corporation, 2001.
- [4] M. Virgo, "Controls and Alignment for the University of Maryland Electron Ring", proc. PAC, 2001.
- [5] Axyz, copyright Leica Geosystems, 2003.

EMITTANCE MEASUREMENT BY USING DUO IMAGE PATTERN OF CHERENKOV RADIATION*

Jiaer Chen, Anjia Gu, Rongli Geng, Yuantao Ding, Kui Zhao, Baocheng Zhang, Shengwen Quan
RFSC Group, Institute of Heavy Ion Physics, Peking University, Beijing 100871, P.R. China

Abstract

The emittance of the electron beam is to be measured by using Cherenkov radiation in a novel way. The image patterns of the radiation are formed both in the focal plane and image plane of an achromatic lens with long focus. Both the angular spread and radial distribution of the e-beam are obtained by processing both patterns and in this way the beam RMS emittance is directly resulted. Combining this technology with computerized tomography (CT), the actual particle density distribution in transverse phase space can be determined without any pre-assumptions. The emittance of the electron beam from the DC-SC photo-injector of Peking University is simulated and a He-Ne laser experiment is presented and discussed in this paper.

1. INTRODUCTION

For the conventional optical diagnostics using Cherenkov Radiation (CR) or Optical Transition Radiation (OTR), quadrupole-scanning techniques or "tri-gradient method" are often used to determine the e-beam emittance indirectly. The assumption of an elliptical contour in the beam phase space actually brings systematic errors.

According to parameters of the DC-SC photo-injector at Peking University^[1], the energy of the e-beam is 2-3 MeV. OTR at this level is too weak to be captured by a CCD camera. In this paper a new direct way of emittance measurement by using Duo Image Pattern of Cherenkov Radiation is introduced, which can measure the angular spread and the radial distribution of the electron beam simultaneously. Combining this method with CT, a complete phase space tomography can be made without any assumptions on the distribution of e-beam phase space and the extrapolation of angles in Radon transformation.

2. RMS EMITTANCE MEASUREMENT

As a charged particle travelling at velocity v through a dielectric medium (refractive index n), CR is emitted in a thin cone centered on the trajectory with opening angle θ_c , when $v > C/n$. In Fig. 1, θ_c , θ_i , θ_r , θ_t , and θ_f are angles corresponding to Cherenkov angle, internal incident angle, external refracted angle, tilted angle of the converter, and observation angle, respectively.

Using Snell's law, the observation angle:

$$\theta_f = \arcsin(n \sin(\theta_c - \theta_i)) \approx n(\theta_c - \theta_i)$$

where, $\theta_c = \arccos(1/\beta n)$, the CR angle.

Suppose r'_i is the divergence angle of the i^{th} particle in the beam as it passes through the converter, then:

$$\theta_{f_i} = \arcsin(n \sin(r'_i + \theta_{ci} - \theta_{ti})) = \arcsin(n \sin r'_i)$$

Setting $\theta_i = \theta_c$ approximately $\theta_f \approx nr'_i$.

Hence, the one-to-one correspondence between the observation angle of CR and the divergence angle of the e-beam is derived. According to this correspondence, Sandia Lab. devised an array of mirrors to split the CR into six

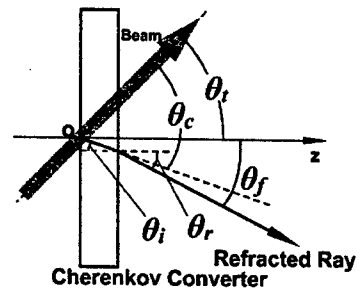


Fig.1. The angle relationship of CR

different angular slices. In order to obtain an angular resolution of a few mrad, the cameras must be placed at a distance of 30m away from the Cherenkov converter^[3].

In fact, by utilization of Fourier Transform and optical imaging technique, the information of angular spread can be obtained directly from the pattern on focal plane of the lens. For this purpose, an achromatic lens with long focus is added normally to the direction of observation (Z-axis) (as in Fig.2), and it can be shown, $y_f = f \tan \theta_f$, with small angle approximation, $y_f \approx f \theta_f = f \cdot n \cdot r'_i$, where y_f is the vertical ordinate on the focal plane of the lens, f is the focus of the lens.

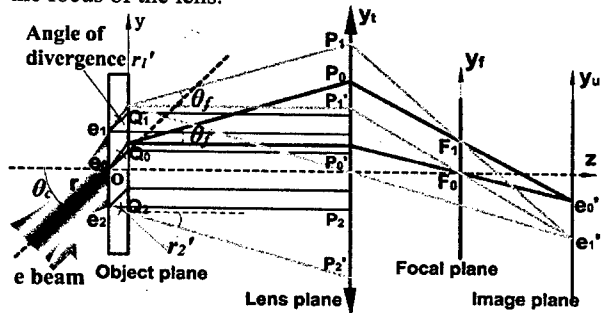


Fig.2. The optical path of "Duo Image Pattern of CR"

In principle this process can be called as "Duo Image Pattern": while the radial distribution of the e-beam is attained from the image plane of the lens (as is widely acknowledged in the conventional optical diagnostics), the additional information of the angular spread of the e-beam is obtained from the focal plane of the lens at the same time. Consequently, we can work out $\langle y \rangle$ and $\langle y' \rangle$ from these two distributions by using statistics. According to the definition, the RMS emittance can be expressed directly as^[4]:

* Supported by NSFC (10075006, 19985001)

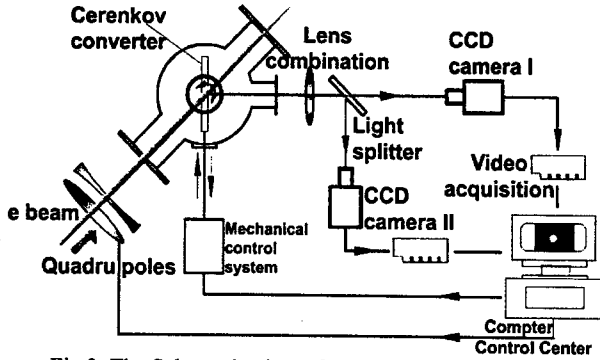


Fig.3. The Schematic view of "Duo Image Pattern" beam diagnostics of PKU-SCAF DC-SC photo injector

$$\varepsilon_{RMS} = 4[\langle (y - \langle y \rangle)^2 \rangle \langle (y' - \langle y' \rangle)^2 \rangle - \langle (y - \langle y \rangle)(y' - \langle y' \rangle) \rangle^2]^{1/2}$$

Fig.3 shows the layout of "Duo Image Pattern" beam diagnostics of the DC-SC photo-injector. Passing the combining lens, the CR is split by a light splitter. CCD cameras are placed at each branch of light, where locates the focal and image planes of the lens respectively.

Through simulation experiments, the errors derived from small angle approximation and image processing are rather low (less than 5%); yet the energy divergence of the beam takes a major part. An energy divergence of 2% at 3 MeV results in $\theta_c < 0.04\%$; while 30 MeV results in $\theta_c < 0.0007\%$. This method prefers e-beams of higher energy.

3. BEAM PHASE SPACE TOMOGRAPHY

3.1. The Difficulties in the Conventional Phase Space Tomography

CT refers to the cross-sectional imaging of an object from transmission data collected by illuminating the object from many different directions.

An object is represented by a two-dimensional function $f(x, y)$; the Radon transform of $f(x, y)$ is the line integral of f parallel to axis y , as illustrated in Fig.4:

$$p(x_1, \theta) = \int_{-\infty}^{\infty} f(x_1, y_1) dy_1 \\ = \int_{-\infty}^{\infty} f(x \cos \theta + y \sin \theta, x \sin \theta - y \cos \theta) dy_1, \theta \in [0, \pi)$$

The deficiency of rotation angle

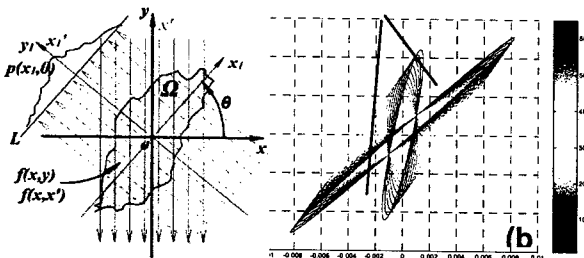


Fig.4. a. CT principles: rotation of a CT machine; b. The angle deficiency in rotation of phase-space distribution by

Changing the two-dimensional function $f(x, y)$ to $f(x, x')$, defined as the distribution function of beam phase space density, it is found that if the phase space could be rotated without distortion freely from 0 to π by some

certain transferring devices, then the CT principle can be fully applied into phase space reconstruction because of the similarity between them.

Practically, quadrupoles are used to twist the phase space^[5]. However, the whole effect includes both rotation and distortion. In addition, a considerable amount of Radon rotation angle is unavailable (shown in Fig.4). By algebra deduction and combination with CT, "Duo Image Pattern" can overcome these two difficulties successfully.

Firstly, the effect of quadrupole-scanning can be decomposed into two parts: rotation and distortion.

The transfer matrix M (consisted of quadrupole section and drift sections) is:

$$M_{BA} = \begin{pmatrix} m_{11} & m_{12} \\ m_{21} & m_{22} \end{pmatrix} = \begin{pmatrix} p_a \cos \theta_1 & p_a \sin \theta_1 \\ p_b \sin \theta_2 & p_b \cos \theta_2 \end{pmatrix} \\ = \begin{pmatrix} \frac{p_a}{\sqrt{p_a^2 p_b^2 - 1}} & 0 \\ \frac{1}{p_a} & \frac{1}{p_b} \end{pmatrix} \begin{pmatrix} \cos \theta_1 & \sin \theta_1 \\ -\sin \theta_1 & \cos \theta_1 \end{pmatrix} = M_A M_R \quad (3)$$

$$\text{Where } p_a = \sqrt{m_{11}^2 + m_{12}^2}, \quad \theta_1 = \arctan \frac{m_{12}}{m_{11}} \quad (4)$$

M_A is the affined transform matrix and M_R is the unit rotation matrix. Thus, we decompose the whole effect of quadrupole-scanning into two parts, i.e. the affined transform matrix and the unit rotation matrix, corresponding to distortion and pure rotation respectively. The affined transform results in a scaling of p_a in phase space projection over horizontal ordinate. In this way, a clearer understanding between the CT principle and phase space tomography is established.

Secondly, putting the quadrupole settings and drift section into the Eq.3,4, we find that the range of θ_1 (Radon angle) cannot cover $0-\pi$ by all means^[6]. As shown in Fig.4b, there exists considerable deficiency of Radon rotation angle, no matter how many quadrupoles are adopted. By strictly choosing the parameters of the quadrupoles settings and drift sections, Duke University FEL Laboratory (DFELL) once attained the range of θ from 0 to 0.96π , still leaving a deficiency of 7° ^[5].

Since a full π radian of the rotation angle is the basic requirement of Radon transforms, in order to extrapolate the data for this deficiency, prior assumption about phase space distribution has to be made. That yields errors in the reconstructed phase space.

3.2. Applying "Duo Image Pattern" in Phase Space Tomography

By means of "Duo Image Pattern", we obtained the angular spread and radial distribution of the e-beam simultaneously^[2], as shown in Fig.5. According to the similarity between Radon Transform and the rotation of beam phase space distribution discussed above, the Radon projection of the angular spread indicates the line integral

of $\int_{-\infty}^{\infty} f(x, x') dx$. As to the algorithm of CT image

reconstruction, this integral is equal to $\int_{-\infty}^{\infty} f(x, x') dx'$, the Radon projection of the radial distribution of e-beam.

By applying Duo Image Pattern in the phase space tomography, both of the integrals are practicable. When a deficiency appears in Radon projection of the radial distribution on the image plane of the lens, the data from the projection of the angular spread (i.e. from the pattern on the focal plane of the lens) can be used for compensation, with some linear algebra transform in advance^[6]. Therefore, a complete phase space tomography is feasible, by putting the additional information of the angular spread in the Radon Transform (shown in Fig.5).

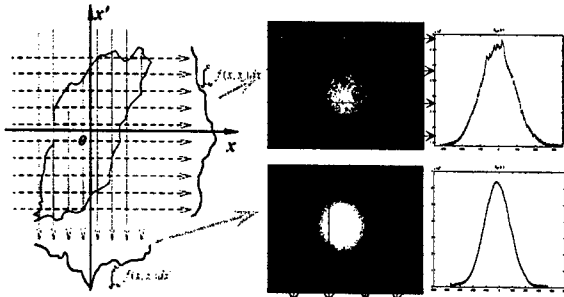


Fig.5. Phase-space tomography for the angular spread and the radial distribution by using "Duo Image Pattern".

4. SIMULATION EXPERIMENTS

4.1. Simulation Experiment with He-Ne Laser

A He-Ne Laser is used to perform the simulation experiment so as to test the Duo Image Pattern principles. The images at the focal plane and the image plane are illustrated by Fig.6a, b, respectively. Fig.6 c, d present the 3D plot of the distribution and e, f present the profiles along the centerline of a, b. The program works out:

$\langle x \rangle = \sum x_i p_i$, $\sigma = (\sum [x_i - \langle x \rangle]^2 p_i)^{1/2}$, yielding:

$\langle x \rangle$ (mm)	σ_x (mm)	$\langle x' \rangle$ (mrad)	$\sigma_{x'}$ (mrad)	$\langle (x - \langle x \rangle) * (x' - \langle x' \rangle) \rangle$ (mmmrad)	ϵ_{rms} (π mm mrad)	$\Delta \epsilon$ %
0.793	0.214	2.702	0.705	0.075	0.525	4.76

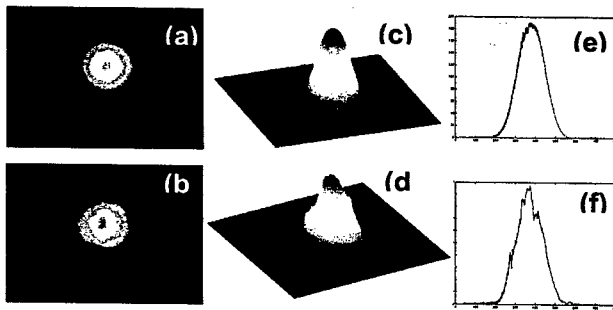


Fig.6. Simulation with He-Ne Laser and the image processing.

Via "Tri-profile Method", the emittance of the He-Ne laser results in 0.5 π mmrad. The difference in percentage between these two methods is around 5%.

4.2. Computer Simulation of Phase-space Tomography

In order to test Duo Image Pattern algorithm in beam phase space tomography, we used a computer model to simulate the measurement and reconstruction process.

First we create an initial phase space distribution in the shape of an asymmetric combined ellipse (Fig.7.a,b), considering the actual phase space distribution generally would be irregular and non-uniform. Then, the simulation transports the distribution through the initial drift section, the combined quadrupoles and the final drift section. The program generates series of images at the focal plane and the image plane of the lens respectively, and calculates the beam's spatial projection with rotation angle from 0° to 90° by integrating the final distribution over its angular spread and from 90° to 180° over its radial distribution^[6]. The process of the transform and the final reconstructed phase space are shown as Fig.7 c, d, presenting the high quality in this reconstruction.

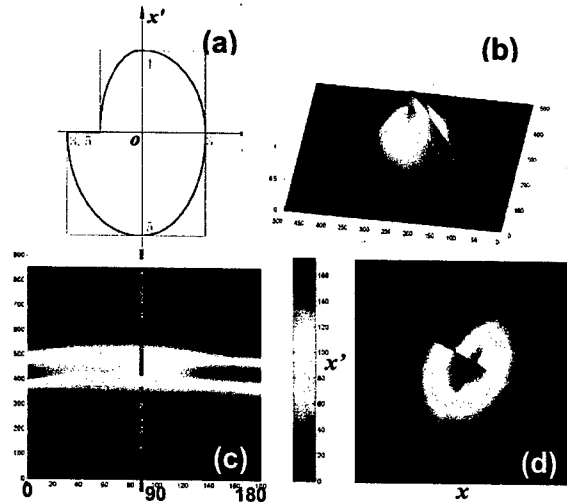


Fig.7. Phase space distribution reconstruction (colour)

a. An assumed model; b. The original distribution of the model; c. The process of Radon Transform; d. The reconstructed phase space distribution.

5. CONCLUSION

All the simulation experiments show that "Duo Image Pattern of Cherenkov Radiation" is more useful for direct measurement of e-beam RMS emittance and for more complete tomography of phase space distribution, since it can provide additional information missed by other methods and can thus realize a full π radian Radon Transform.

6. REFERENCES

- [1] Zhao Kui, Hao Jiankui, Hu Yanle, et al. Nucl. Instr. & Meth. In Phys. Res., 2001, A475:564-568
- [2] GU An-Jia, DING Yuan-Tao, ZHAO Kui, et al. HEP & NP, 2003, 27(2):163-168 (in Chinese)
- [3] Richardson R.D., Platt R.C., Crist C.E.. Particle Accelerator Conference, 1993, vol.3: 2456-2458
- [4] Stanley Humphries, Jr., Charged Particle Beams. Translated Chinese Edition: Beijing, 1999:57
- [5] McKee C B, O'Shea P G, et al. Nucl. Instr. & Meth. In Phys. Res., 1995, A358:264-267
- [6] GU An-Jia, ZHAO Kui, DING Yuan-Tao, et al. HEP & NP, 2003, 27(5):455-459 (in Chinese)

FILLING PATTERN MEASUREMENT IN THE LNLS STORAGE RING

S.R. Marques[#], H.J. Onisto, P. F. Tavares, LNLS, Campinas, Brazil, SP 13083-100

Abstract

The storage ring filling pattern affects the performance of the machine in several ways. A bunch charge meter has been developed in order to perform bunch-by-bunch charge measurement and to record the storage ring filling pattern. This instrument separates the electric pulse produced by the selected bunch from the RF signal obtained from a button pick-up. A fast switch based on a double balanced mixer (DBM) was developed to strip off all but one bunch pulse at each revolution period. A 12-bit ADC with a FIFO buffer card acquires the bunch signals. A PECL timing card performs the bunch selection. The bunch charge meter is connected to the LNLS control system through a DSP processor board, which controls the instrument through an FPGA interfacing board. The DSP software provides digital filtering. Some implementation details, performance data and operational results are presented.

INTRODUCTION

The LNLS 93-meter long 1.37-GeV electron storage ring can be filled with up to 148 bunches. The bucket spacing is 2.1 ns, and a 500-MeV booster synchrotron is the injector for the main ring. The storage ring is filled in a nearly uniform way by a system which automatically controls the phase between the booster and the storage ring, ejecting bunches to fill different buckets at each injection cycle. This system provides uniform filling as long as the LINAC beam energy stays constant along the accumulation. The bunch charge meter is supposed to be very useful for several purposes, for example: recording the filling pattern of the users' runs, machine studies about the correlations between filling patterns and instabilities, bunch lifetime measurements, etc...

SYSTEM DESCRIPTION

The instrument which contains the bunch charge meter has another RF front-end, the "bunch cleaner", which performs bunch cleaning in the booster injector (also reported in these proceedings). Figure 3 shows the block diagram of the bunch charge meter.

Back-end processor

The back-end processor is composed of a DSP C6711¹ evaluation board and a card based on an FPGA (XILINX model XC2S50E). This FPGA card was implemented in a four-layer PCB and it works integrating the DSP to the internal devices, namely: acquisition board, timing card,

programmable attenuator and the serial communication board of the LNLS control system.

The DSP accesses the FPGA through its expansion connector. The DSP software implements digital filtering and manages the communication between the instrument and the LNLS control system [1].

RF front-end

The beam signal is obtained through one button of an RF button pick-up (8.1-mm diameter). We observed that in our case using an RF combiner to sum the four signals from the pick-up is not an advantageous approach due to the RF reflections caused by the large number of connections.

This signal is applied to a programmable attenuator (Weinschel Corporation, 4206-63) and after that, it is driven to the fast switch, which separates the signal related to one electron bunch. The amplitude of the signal obtained from the button pick-up can reach several volts (peak) according to the beam current and filling pattern. It is necessary to attenuate the beam signal in order to bring it to the useful range of the fast switch.

The fast switch consists of a DBM (Minicircuits model rms-30) and a fast pulse generator (500 ps FWHM) designed on the same circuit board. Figure 1 shows the fast switch circuit.

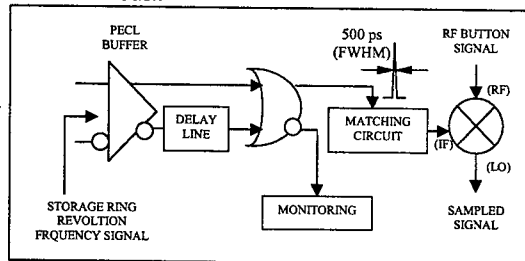


Figure 1 – Fast switch circuit.

The fast pulse is obtained through a simple PECL digital circuit by the delay introduced in one trace of a differential transmission line. When this pulse is applied to the IF input, the DBM captures the RF signal. The digital circuit is coupled with the DBM by a simple passive circuit composed of voltage dividers and matching RF capacitors. Besides RF matching, proper attenuation of the digital pulse is crucial to minimize IF-LO crosstalk.

The signal from the fast switch is analogically treated in order to allow the analog-to-digital conversion. The block diagram of the circuit that performs this treatment is shown in figure 2.

[#]sergio@lnls.br

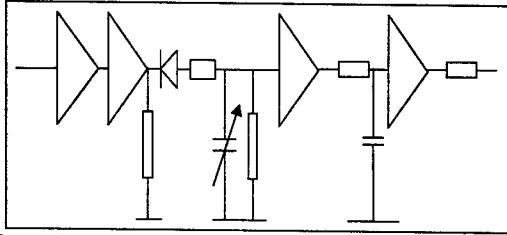


Figure 2 – Block diagram of the pulse treatment circuit.

In figure 2, the first two amplifiers are MAR-6 MMIC Minicircuits. A detector diode (Agilent Technologies, HSMS-8202) and high-frequency trimmers (Voltronics Corp. and Temex Electronics Inc.) compose the detector circuit. Afterwards the signal is amplified by a current feedback Op. Amp. and filtered. The last device is a VCA Op. Amp. (Texas Instruments, VCA610), whose gain is adjusted by the DSP through a 16-bit DAC.

Table 1: Preliminary results of the 12-bit ADC board characterization tests

SNR (Signal-to-Noise Ratio)	65.1 dB
SINAD (Signal-to-Noise And Distortion ratio)	65 dB
THD (Total Harmonic Distortion)	85.8 dB
ENOB (Effective Number Of Bits)	10.5 bits

The processor reads the data in the FIFO buffers through a digital bus (LVTTTL level, 50 ways 10 centimeters flat-cable).

Timing card

The fast switch and the ADC module are triggered by the timing card, which is a homemade PECL programmable divider. The output signals are generated through the division of the RF signal, 476.066 MHz, by

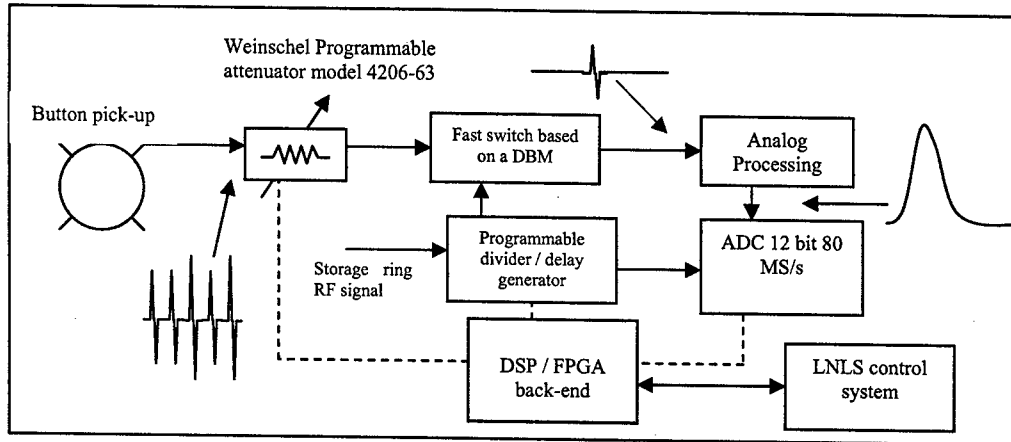


Figure 3: Block diagram of the bunch charge meter

The flexibility given by the large range of input attenuation (63 dB) and by the VCA is enough to perform filling pattern measurements in both multi-bunch and single-bunch modes.

Acquisition board

The signal after switching and analog processing has a smoothed shape and its frequency is the same as the storage ring revolution one (3.21 MHz). A 12-bit ADC board, based on the AD9432 (Analog Devices) with a FIFO buffer, was developed in order to digitize this signal.

The ADC module has 50 Ω differential input, 33 MHz analog bandwidth and maximum conversion rate of 80 MS/s (AC coupling, ECL level). We use two 8-Kbyte, 9-bit FIFO buffers (IDT, IDT72V05), but the module was designed to accept buffers with different capacities by changing them. The circuit was implemented in a four-layer PCB and several precautions [2] related to mixed-signal designs were taken in order to achieve good performance. Some results of the preliminary characterization [3] are shown in Table 1.

the storage ring harmonic number, 148, however any number between 2 and 255 can be used to divide the RF signal. This card has also a programmable delay generator with 20 ps resolution and rms jitter smaller than 5 ps. The relative phase between the two output signals can be adjusted, as well as the phase difference of these two signals to the RF signal.

The timing card was also implemented in a four-layer PCB and high speed digital routing techniques [4] were taken in order to assure signal integrity.

MEASUREMENT PROCESS

Once the bunch charge meter is on, the acquisition board acquires the beam signal without interruptions. The back-end processor controls the FIFO buffers. When the data is not required, the FIFO buffers are disabled.

Through the control system, the operator can set the desired filtering parameters, which make the acquisition slower or faster. The measurement cycle starts with the optimization of the acquisition parameters, namely: input attenuation, gain of the analog processing stage and fine phase adjusts between the fast switch and the ADC. The acquisition rate is 3.21 MHz and every complete bunch

acquisition fills the entire FIFO buffers (8 Kbytes). Once these buffers are full, which takes about 2.5 ms, the back-end processor reads these data, resets the FIFOs and changes the timing adjusts in order to measure a neighbor bunch. After acquiring the data from the 148 bunches, the filling pattern (or the average of each acquisition) is transferred to the control system.

PRACTICAL DETAILS

As we expected the process is very sensitive to timing variations. Figure 4 shows how the sampled data changes when the fine timing of the fast switch is adjusted. In this situation the ADC timing adjust was fixed.

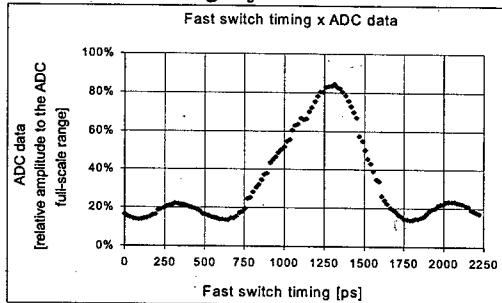


Figure 4 – Sensitivity of the ADC sampling to the timing adjusts of the fast switch.

During the testing period we observed that the variance of the measurements of the high charge bunches were bigger than the low charge bunches. By analyzing all the data (not the average result) it was possible to see a sinusoidal oscillation, which had the same frequency of the synchrotron oscillations. In some cases the amplitude of the sinusoidal oscillations observed was higher than 10% of the ADC full-scale range. The mechanism that produces this coupling is not completely understood. Figure 5 shows an 8-ksample acquisition of the signal from a 2-mA bunch. Figure 6 shows the result of one experiment in which the synchrotron frequency was measured by utilizing both a spectrum analyzer and the bunch charge meter (FFT).

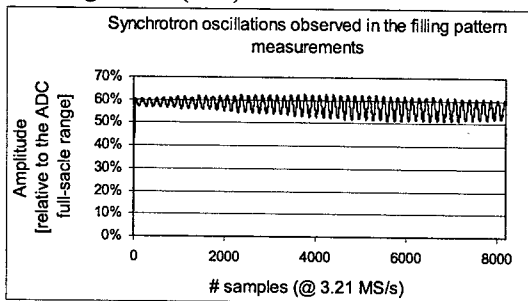


Figure 5 – 8-ksample acquisition of a signal of a 2 mA bunch.

The synchrotron oscillations observed in the bunch signals decrease the resolution of the filling pattern measurement. In order to minimize this effect the back-end processor resamples the data, in other words, the back-end processor reads a number of positions in the

buffer, waits a number of clock cycles and reads it again until reaching 8 ksamples. With this procedure a resolution better than 1% was achieved in a 3-second measurement.

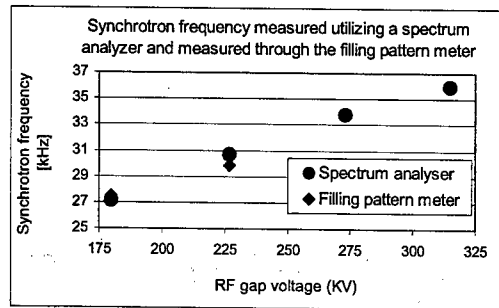


Figure 6 – Synchrotron frequency measured by utilizing a spectrum analyzer and the bunch charge meter (FFT).

A typical filling pattern of the storage ring is shown in figure 7.

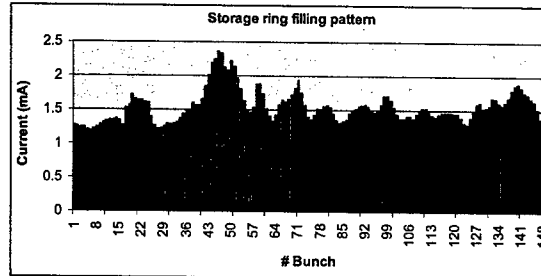


Figure 7 – Typical filling pattern of the storage ring.

We also implemented the bunch charge meter by utilizing a digitizing oscilloscope (Hewlett Packard, model 54750A) and, a measurement with similar resolution takes about 3 minutes due to the low acquisition rate.

CONCLUSIONS

The bunch charge meter has been developed and integrated to the LNLS control system. A resolution better than 1% was achieved in a 3-second measurement. The system will be calibrated by utilizing a single-bunch beam through the data obtained from both the storage ring DCCT and the HP 54750A oscilloscope.

REFERENCES

- [1] J. G. Franco, R. H. A. Farias, L. Jahnel, J. R. Piton, P.F. Tavares, "LNLS Control System", ICALEPCS 1999, Trieste, Italy, 1999, p. 651.
- [2] W. Kester, J. Bryant, "Proper grounding is critical for high-speed systems", Wireless Systems Design volume 5, number 5, (2000).
- [3] S.R. Marques, H.J. Onisto, "Chaves rápidas e módulos eletrônicos para aquisição de sinais rápidos no LNLS", internal communication.
- [4] Motorola, Inc. 1996, "High Performance ECL Data" DL140/D REV 4.

MULTICHANNEL SINGLE-SHOT TRANSIENT SIGNAL MEASUREMENTS WITH AN OPTICAL FIBER RECIRCULATING DELAY LINE LOOP*

Yan Yin, Anshi Chen, Wangsheng Zhang, Guansan Chen, Xiangzhong Wang, YY Labs, Inc., USA

Abstract

An instrument has been developed to measure single-shot electrical transient signals, in two channels, with frequency responses up to 20 GHz [1]. The instrument utilizes an optical fiber recirculating delay line loop to regenerate captured single-shot signals, and then recovers the original single-shot signals with a sampling scope. The instrument is named Single-Shot Scope.

INTRODUCTION

A real-time oscilloscope, which is useful to study beam instability of Linacs or storage rings, available commercially has frequency responses up to 6 GHz. For frequencies above 6 GHz, the only available instrument is the streak camera, which measures optical signals. Users need to convert the optical signals into electrical signals in order to perform measurements. The streak camera turns the optical signals into low-energy photoelectrons, and then uses a fast sweeping electrical field to deflect the photoelectron beam. The longitudinal intensity distribution of the beam is represented as a transverse trace displayed by a CCD camera.

YY Labs' Single-Shot Scope is based on a different principle, using fiber recirculating delay-line loop technology, which has been widely used for studying long-haul signal transmission in optical fibers [2]. The Scope captures the single-shot signals in one or two channels, and then regenerates the signals with the aid of a recirculating optical fiber delay line loop. A small portion of the signals, recirculating in the loop up to several thousand turns, is tapped out at each turn, thus forming a copy of the original signal. The energy loss is

compensated for with an optical amplifier. The original amplitudes of the signals are thus recovered. A sampling scope is utilized to obtain the original signal from the pulse train.

The instrument is assembled in two boxes. One box is labeled "Transient Signal Capture," since in it the single-shot transient signal is acquired. The other box is labeled "Pulse Train Generator," since it regenerates the two-channel single-shot signals, forming two pulse trains. The Transient Signal Capture box is located close to the source of the signal; the Pulse Train Generator box is located in the control room. The linking distance between the two boxes is limited by the signal transmission limitation of the RS232 cable.

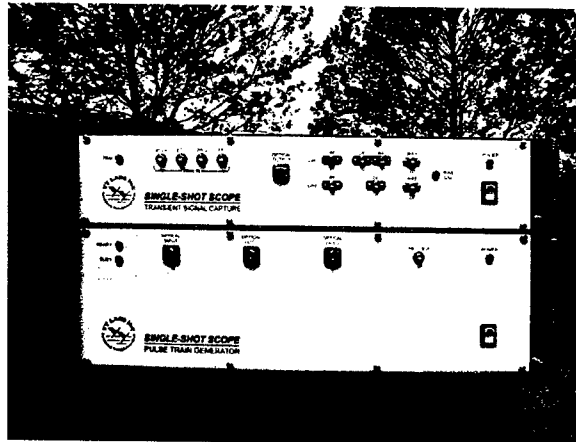


Figure 1: YY Labs' Single-Shot Scope.

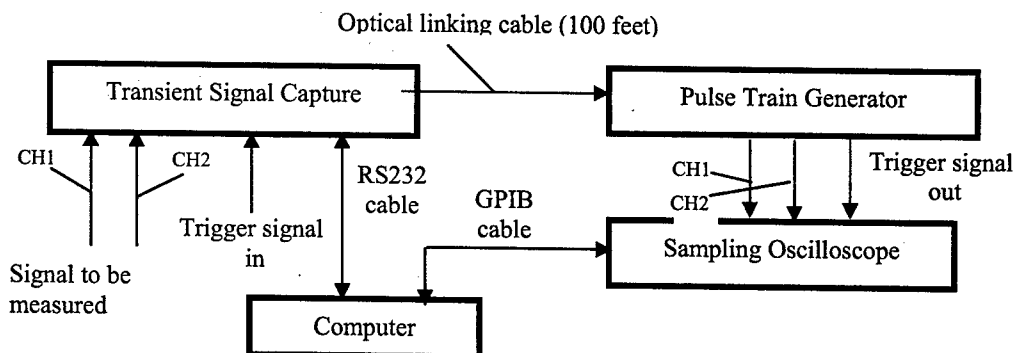


Figure 2: Single-Shot Scope Arrangement. CH, channel.

*Work supported by the U.S. Department of Energy
SBIR Contract No. DE-FG03-98ER82719

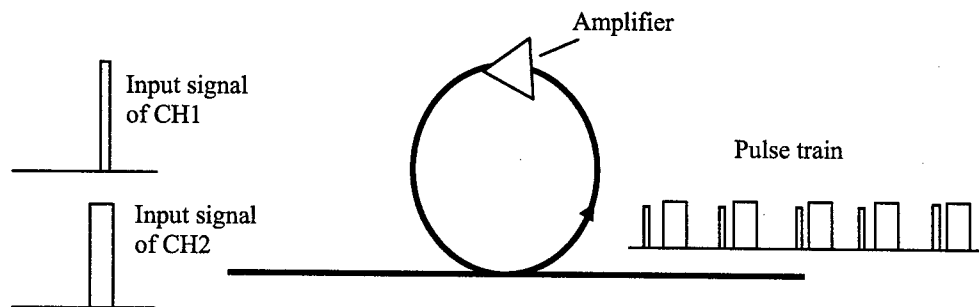


Figure 3: Principle of the Recirculating Loop.

The instrument has a gating function, which allows the instrument to select one signal from a series of signals, or gate the single-shot signal for performing measurements. The gate width is adjustable from 10 ns to 50 ns.

For the purpose of capturing the signal, the instrument has an auto-scan function. If the approximate delay time between the trigger signal and the signal to be measured is known, the delay time can be set via the computer. If the delay time of the signal is unknown, an approximation should be made, and the auto-scan function will locate and capture the signal. The scan range is 500 ns.

The instrument can measure two single-shot signals simultaneously. The two single-shot signals will be captured and injected into the fiber loop for circulation, and will form two separate pulse trains.

The number of circulations of the signal in the delay line loop is set at 1000. Each circulation takes 8 μ s. Figure 4 shows the signal circulation of 1000 turns, which is 8 ms.

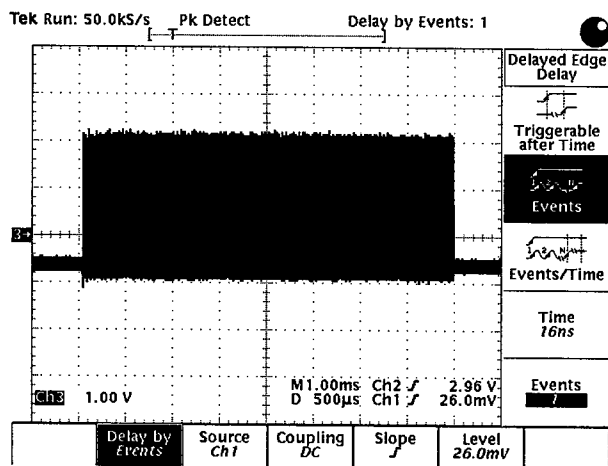


Figure 4: Circulation of 1000 Turns.

Figure 5 shows part of the circulation for a pair of pulses representing two different single-shot signals.

The advantages of using this method reside in the high-frequency response and the low loss of optical fiber, because, in this frequency range, the electrical method cannot be used due to problems of loss, dispersion, and reflection. Regarding the optical fiber, with a core diameter of only 9 μ m and attenuation of 0.2dB/km, the frequency response can easily go up to the 20-GHz range.

With the recirculating-loop method, a high-frequency instrument can be constructed with optical fiber components and low-frequency electronics. In this manner, therefore, a low-cost multichannel, high-frequency single-shot transient signal scope can be built. This PC-based, button-free instrument is easy to use.

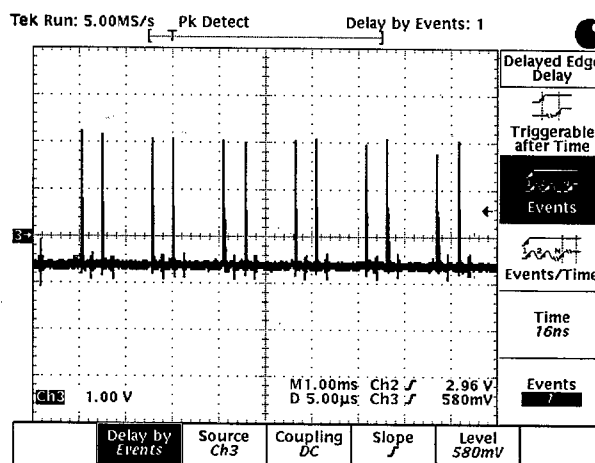


Figure 5: Circulations of Two Signals.

For the tests performed, 10-GHz photodiodes were used, which limited the frequency response to 10 GHz.

Beam tests were carried out at SLAC, as described here.

BEAM TESTS AT SLAC

The PEP-II is an $e^+ e^-$ collider with asymmetric energies in a 2200-m tunnel at the Stanford Linear Accelerator Center [3]. The PEP-II facility consists of two independent storage rings, one on top of the other, in the PEP tunnel. The high-energy ring stores a 9-GeV electron beam, and the low-energy ring stores 3.1-GeV positron beam.

The signal was taken from a button-type capacitive pick-up of 15-mm diameter, in the straight section of Region 4, 350 m from the interaction point, where the BaBar detector is located. The PEP-II was operated in multibunch mode, with e^+ and e^- circulating in the rings. The rms bunch lengths, σ , of the e^+ and e^- beams are in the range of 11 to 12 mm, which is equivalent to 40 ps, and with a FWHM of 90 ps. Without access to the tunnel,

it was not possible to place the signal capture box near the beamline, and so the signal was brought to the measurement room through an existing 35-m Helix cable (LDF2-50), nevertheless still attenuates the high frequency, the signal was somewhat stretched. For this reason, the pulse length measured was about 174 ps, with a rise time of 164 ps, and fall time of 140 ps (from peak to baseline).

Figure 6 shows the e⁺ beam signal measured by the Single-Shot Scope. Since the Single-Shot Scope gating-signal generator has a DC offset, the baseline of the signal is not at 0 volts

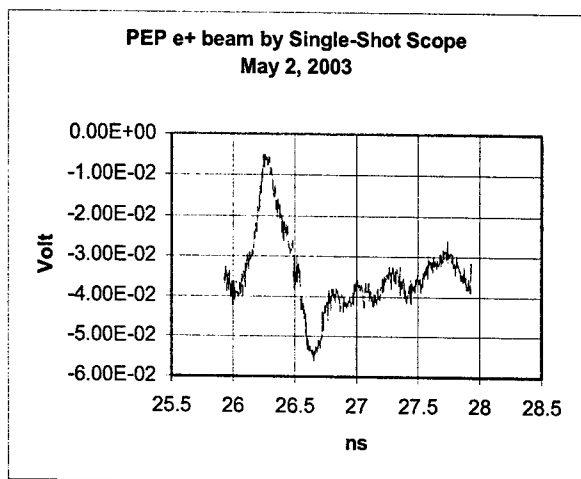


Figure 6: PEP-II e⁺ Beam Bunch Longitudinal Distribution Measured With the Single-Shot Scope

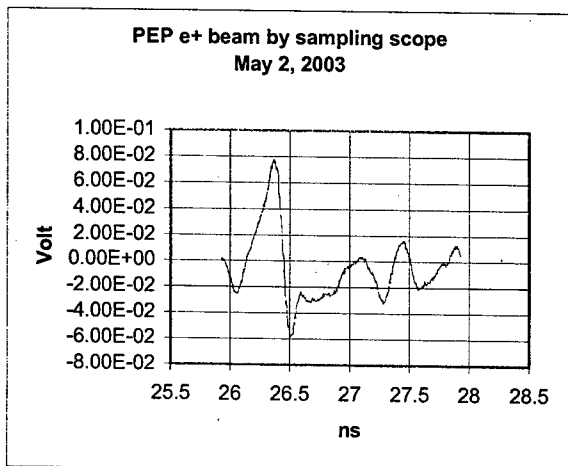


Figure 7: PEP-II e⁺ Beam Bunch Average Longitudinal Distribution Measured Directly With the TEK 11801 Sampling Scope

Figure 7 shows the e⁺ beam signal measured by the TEK11801 sampling scope. Since there were 900 bunches in the ring, the measured signal was the average over these 900 bunches, and hence differed from the single-shot measurement.

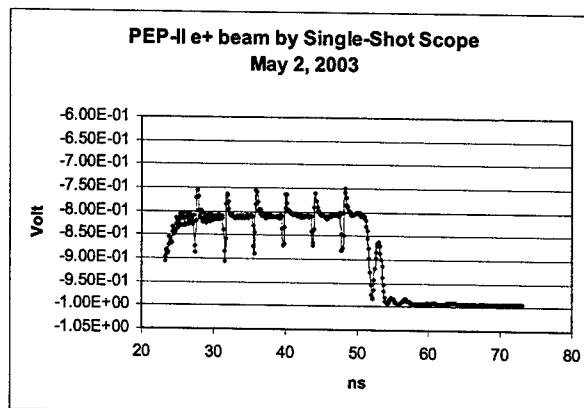


Figure 8: e⁺ Bunches Captured by the Single-Shot Scope show that multiple bunches can be measured

Figure 9 is an actual picture taken at the time of the measurement. The signal shown is negative, because the slope of the modulator, which converts the electrical signal to an optical signal, was set to negative.

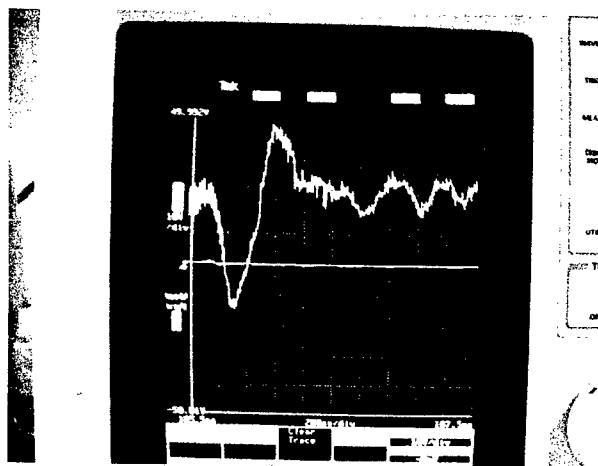


Figure 9: PEP-II e⁺ Beam Measured by the Single-Shot Scope

ACKNOWLEDGEMENT

The authors thank SLAC and SSRL for their enthusiastic support of this work by providing testing opportunities, space, and equipment for the experiments, and for the various helpful discussions with James Sebek, Bob Hettel, Alan Fisher, and others.

The authors are also grateful to Hubert Houtman for his kindness and encouragement.

REFERENCES

- [1] <http://www.YY Labs.com>.
- [2] Emmanuel Desurvire "Erbium Doped Fiber Amplifiers: Principles and Applications," John Wiley & Sons, Inc., 1994, p499
- [3] J.T. Seeman, *et al.*, "Status and Future Plans of the PEP-II B-Factory," SLAC-pub-9451, August 2002.

COMPENSATION OF NONLINEAR RESONANCES IN THE PRESENCE OF SPACE CHARGE *

A.V. Fedotov and G. Parzen
BNL, Upton, NY 11973, USA

Abstract

Imperfection non-linear resonances can lead to undesirable beam loss and thus limit the high-intensity operation. In the presence of space charge, beam response to such resonances is strongly influenced by collective beam dynamics. It is thus crucial to understand the effectiveness of the non-linear resonance compensation. We explore various procedures in the resonance correction and suggest some practical applications. Effectiveness of resonance correction for the high-intensity operation is discussed.

INTRODUCTION

A single-particle theory of nonlinear resonances and their correction is well developed. Nonlinear fields cause tune dependence on amplitude and islands to appear in the phase-space plots. When crossing the resonance, the large amplitude particles can be locked into the islands, moved to large amplitudes, and possibly be lost. Space charge introduces several aspects into resonance crossing. When the space-charge tune depression is increased, particles with the smallest amplitudes reach the resonance first as they have the largest tune shift. In addition, the space charge introduces the largest source of nonlinearity which changes the response to a resonance. For dynamic resonant response of a beam, the static description via the single-particle tune shift becomes inaccurate. A dynamic solution which includes the space-charge force and density redistribution is required [1]. All these aspects of the space charge raises very important questions: What is the role of the space charge in resonance crossing? How to account for the space-charge nonlinearity in resonance correction? Can one have a good correction of the resonances for the high-intensity operation? In an attempt to answer these question, we performed a systematic study of resonance correction issues for the high-intensity operation of the SNS ring, using the DYNA [2] and UAL [3] codes.

RESONANCE CORRECTION

The single-particle resonance condition is

$$n_x Q_x + n_y Q_y = p, \quad (1)$$

where n_x, n_y, p are the integers, with p being the driving harmonic. In the presence of the space charge it is slightly

modified [1]. In this paper we use the single-particle terminology but also make an analogy with the collective dynamics. A linear stopband can be written as

$$\Delta\epsilon = |\kappa| J_x^{N/2} J_y^{N/2} \left[\frac{n_x^2}{J_x} + \frac{n_y^2}{J_y} \right], \quad (2)$$

where J_x, J_y are actions, and $N = |n_x| + |n_y|$ is the resonance order. The excitation strength κ is

$$\kappa = \frac{1}{2\pi |n_x|! |n_y|!} \int_0^{2\pi} \beta_x^{\frac{|n_x|}{2}} \beta_y^{\frac{|n_y|}{2}} e^{i\psi} K(\theta) d\theta, \quad (3)$$

where $\psi = n_x(\mu_x - Q_x\theta) + n_y(\mu_y - Q_y\theta) + p\theta$, and $K(\theta)$ is related to the error field multipoles.

One way of correction is to minimize κ , using Eq. 3. Although this can be done in simulation when the field errors are known, in real life problems arise from the source of errors which are unknown. The measurement of the stopband has some difficulties. First, by crossing the resonance, one can measure accurately only a symmetric stopband. If there is a source of the nonlinearity, the stopband becomes asymmetric, and the loss is different depending on the direction of the resonance crossing. More importantly, the loss observed, for example, on a current monitor depends not just on the resonance strength but on the beam-pipe characteristics as well. In that sense, the measurement via the stopband is indirect and does not provide a desired accuracy.

Another way of correction is to measure the islands of the nonlinear resonance. The island width, to first order, is

$$\Delta J \sim \sqrt{\frac{\kappa}{\alpha}} J_0^{N/4}, \quad (4)$$

where α describes tune change at the island center, J_0 is action at the island center. Measurement of the island width gives a more direct information about the resonance strength since it is independent from losses on the beam pipe. Of course, one needs to answer the question what is the role of the nonlinearity α in such a measurement, especially when it will dynamically change and become large due to the space charge in the process of accumulation. A systematic study of this question was performed and findings are summarized below.

An accurate way to obtain information about the island width, is to perform tune (Q) vs amplitude (A) scan near the resonance of interest. The flat region in tune values on the Q vs A diagram gives information about the width of the island [4]. The resonance is corrected by minimizing this flat region to zero. Such a method requires a significant

* Work supported by the SNS through UT-Battelle, LLC, under contract DE-AC05-00OR22725 for the U.S. Department of Energy

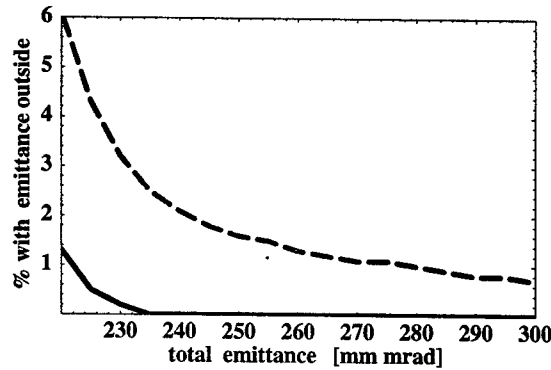


Figure 1: w.p.(6.36,6.22), $N = 0.6 \cdot 10^{14}$: sextupole errors, no correction-red (long-dash) line; correction of $3Q_x = 19$ -green (short-dash) line; no errors-blue (solid) line.

amount of time due to a required amplitude scanning. An alternative way to get similar information quickly is to kick the beam into the islands and measure the corresponding frequency spectrum. When some portion of the beam is locked into the island, one obtains the corresponding peak with the tune measurement device. The correction knobs are used to adjust the amplitude of the peak in the spectrum to zero. Such a method was recently applied for correction of nonlinear resonances at RHIC [5]. In simulations, we use the Q vs A method to find the best strength for the correctors and compare it with the stopband compensation.

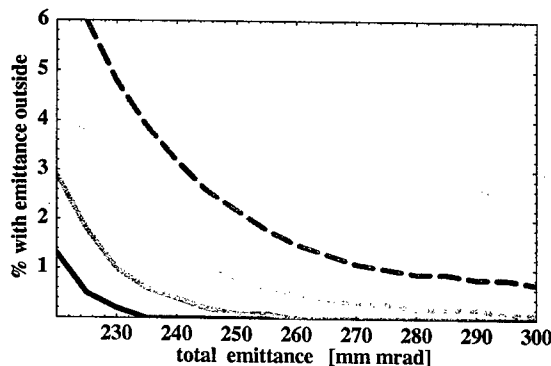


Figure 2: w.p. (6.36,6.22), $N = 2 \cdot 10^{14}$: sextupole errors without correction - red (long-dash) line; correction of $3Q_x = 19$ -green (short-dash); correction of $3Q_x = 19$, $2Q_y - Q_x = 6$ resonances - pink; no errors - blue (solid).

APPLICATION TO THE SNS

First, the strength of correctors are found for a zero space charge using the DYNA code. The nonlinearity due to the quadrupole fringe fields generate islands of a finite width. It was also found that the magnitude of the nonlinearity is not important, and that correction works nicely even for dynamic increase of the strength of the nonlinearity due to the space charge. The corresponding correctors were then

used in the UAL to simulate a dynamic accumulation process with and without the resonance correction. Various aspects of correction were studied using the sextupole resonances. The studies were then extended to include the 4th order resonances. Here, we present the studies based on a lumped source of errors, where randomly distributed errors were lumped into a single magnet. Also, for the studies of the sextupole resonances, the strength of errors was taken 5 times bigger than currently measured while for the octupole resonances - 10 times bigger. A larger strength of errors was required in order to see an appreciable emittance growth during the accumulation cycle.

Correction of 3rd order resonances

With only the sextupole errors being introduced, Fig. 1 shows the beam halo at the end of accumulation for the w.p. (6.36, 6.22) and intensity $N = 0.6 \cdot 10^{14}$ protons. Without correction, the loss due to the $3Q_x = 19$ resonances is about 2% at the acceptance of 240 π [mm mrad]. When the resonance is corrected (with two correctors at large β_x), the loss goes to zero at this acceptance. The intensity is then further increased to $2 \cdot 10^{14}$ and the loss increases to 1.6% (shown in Fig. 2). This is due to the next sextupole resonance $2Q_y - Q_x = 6$, crossed at higher intensity. We now use two other correctors at large β_y to correct this resonance. The corresponding loss with correction of both resonances decreases to 0.5%. Note, that although a good correction of $p = 6$ harmonic was possible in simulation, it will not be that good in practice, since the present location of the sextupole correctors in the SNS provides good correction only for the odd harmonics. As a result, use of other magnets with a proper phase advance (like some of chromatic sextupoles) will be needed for compensation of the resonances due to the sixth harmonic.

The fact that present location of correctors in the SNS allows a good control over the odd harmonics tempted us to explore how far in intensity we can actually go with the resonance correction, choosing, for example, the w.p. (6.4,6.3). All the working points used here, of course, should be understood as an approximate. In real life, one would be unlikely to tune the lattice exactly to a sum resonance. However, the space charge pushes the tunes away from this resonance, and a good correction is possible, as shown in simulations. Figure 3 demonstrates correction of $Q_x + 2Q_y = 19$ and $3Q_x = 19$ resonances, using two different sets of correctors. The pink (dotted) curve corresponds to $N = 3 \cdot 10^{14}$ and black (upper solid) curve corresponds to $4 \cdot 10^{14}$ with both corrections being applied. Adjusting the location of primary scraper, we can attempt to push intensity to almost $4 \cdot 10^{14}$ with relatively low losses, which was speculated before by constructing the loss curves without resonance correction [6].

Simultaneous correction of various resonances

The studies were extended to include the normal and skew octupole resonances, although the SNS does not have

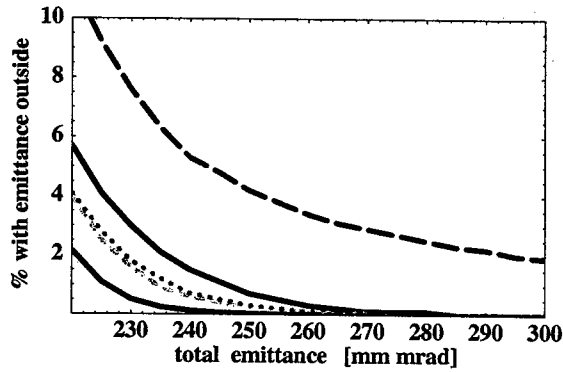


Figure 3: w.p. (6.4,6.3): $N = 2 \cdot 10^{14}$, no correction - red (long-dash line); correction of $3Q_x = 19$ and $Q_x + 2Q_y = 19$ resonances: $2 \cdot 10^{14}$ -green (short-dash), $3 \cdot 10^{14}$ -pink (dotted line), $4 \cdot 10^{14}$ -black (upper solid line).

skew-octupole correctors at the present moment. In all the cases, we were able to achieve a good correction results. For example, Fig. 4 shows high-intensity loss for the w.p. (6.36,6.22), with both sextupole and octupole errors, and correction of 3rd and 4th order resonances.

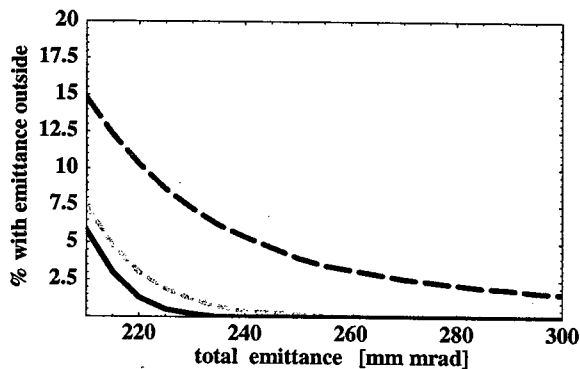


Figure 4: w.p. (6.36,6.22), $N = 2 \cdot 10^{14}$: no errors-blue (solid line); octupole and sextupole errors, no correction-red (long-dash line); correction of $3Q_x = 19$, $2Q_y - Q_x = 6$, and $2Q_x + 2Q_y = 25$ resonances-green (short-dash).

Figure 5 shows the tune space with all the 3rd and 4th order resonances which require correction for the two working points being considered. We were able to achieve very good correction with a loss at the primary scraper of about $5 \cdot 10^{-3}$. Even though, the loss is still higher than the one without resonance excitation, it should be possible to reach the uncontrolled beam loss of desired level by adjusting the aperture of the primary scraper.

SELF CONSISTENT DESCRIPTION

Although we used the terminology of a single-particle dynamics, the same description can be given using a self-consistent approach of collective dynamics. It provides a physical picture of dynamics process, including the growth

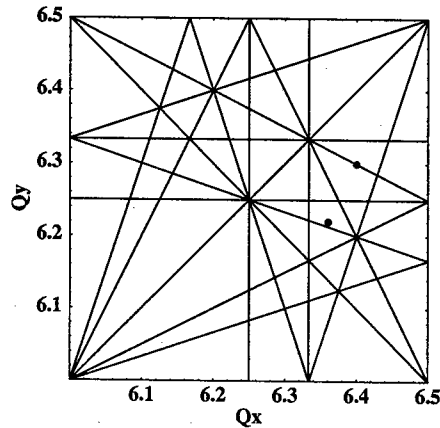


Figure 5: Tune-space with 3rd and 4th order resonances need for correction of w.p. considered.

of emittance and adiabatic increase of losses when intensity is slowly increased [1]. It also explains why the strength of the nonlinearity is not important in the resonance correction. This is because the nonlinearity determines the maximum amplitude of period- p oscillations of the corresponding collective mode (fixed point of an island), while the width of the resonance, in first order, is determined just by the resonance strength κ . As a result, if one manages to measure and correct the stopband of the resonance with a good accuracy experimentally, such a correction will give results as good as the island correction. This was confirmed in present simulations with good correction being achieved, using both the stopband and island correction methods.

SUMMARY

Correction of the nonlinear resonances with application to high-intensity operation was studied. Our findings suggest that it should be possible to correct resonances with a good accuracy and thus control beam loss at a low level.

ACKNOWLEDGMENTS

We would like to thank N. Malitsky for his assistance with the use of the UAL. We also thank the Accelerator Physics group of the SNS project.

REFERENCES

- [1] A.V. Fedotov, Resonances and beam loss in high-intensity rings, these Proceedings (2003).
- [2] G. Parzen, Phys. Rev. E 51, p.2485 (1995).
- [3] N. Malitsky and R. Talman, AIP Proc. 391 (1996).
- [4] G. Parzen, to be published (2003).
- [5] V. Ptitsyn, A.V. Fedotov, F. Pilat, EPAC'02, p. 350 (2002).
- [6] N.Malitsky, A.V. Fedotov, J. Wei, EPAC'02, p.1646 (2002).

APPLICATION OF ENVELOPE INSTABILITY TO HIGH-INTENSITY RINGS *

A.V. Fedotov, BNL, Upton, NY 11973, USA

I. Hofmann, GSI, Planckstr 1, 64291 Darmstadt, Germany

R.L. Gluckstern, University of Maryland, College Park, MD 20742, USA

H. Okamoto, Hiroshima University, Higashi-Hiroshima 739-8526, Japan

Abstract

The space-charge limit is imposed by beam response to low-order machine resonances. Here, the coherent response of the beam to such resonances is discussed, including the parametric resonance of collective beam modes with the periodic lattice, also known as the "envelope instability", when the second-order beam modes are considered. The relation of this parametric resonance to the coherent resonance condition of an integer type is explained. Practical application of such resonant responses to both structural and imperfection driven harmonics is addressed.

INTRODUCTION

When choosing the operating point in the tune space, one carefully avoids resonances driven by the lattice periodicity (structure resonances). However, unavoidable presence of errors in the magnetic field sets restrictions associated with the imperfection resonances. As a result, the condition that the individual particle tune should not be depressed by the space charge to integer or half-integer values is known as the space-charge limit. We note that such a definition of the space charge limit is different from the one used in a special class of circular machines (for example, in cooler rings) where additional efforts are undertaken to compensate for emittance growth. The maximum achievable intensity associated with crossing of the integer or half-integer tunes was first formulated using the single-particle approach. Subsequently, a more accurate treatment of collective beam dynamics gave better understanding of the beam response to such resonances [1]-[2]. Such a coherent resonance condition, corresponding to the half-integer single-particle resonance ($n/2 = \nu$, where $\nu = \nu_0 - \Delta\nu_{sc}$ and ν_0 is the zero-current tune), is

$$n = \Omega_2 = 2\nu_0 - \Delta\Omega_{2,sc}, \quad (1)$$

where Ω_2 is the frequency of the 2nd order coherent oscillation mode of the beam. The coherent resonance condition in Eq. 1 was first derived using an approximation of smooth focusing. Subsequently, it was shown that AG focusing can lead to an additional subset of collective instabilities [3]. Such an instability due to the lattice periodicity, corresponds to a coherent resonance of the parametric (half-integer) type:

$$n/2 = \Omega_2, \quad (2)$$

also known as the "envelope instability" [4]. As one can see from Eq. 2, the envelope instability limits the allowable tune space to only 0.25 and thus may have an additional impact on the performance of high-intensity machines. It is therefore extremely important to understand when such envelope instability should be taken into account, and whether it can alter the space-charge limit governed by Eq. 1. The primary goal of this paper is to explain the difference between the coherent integer and half-integer envelope responses and provide practical guidelines for consideration of the envelope instability in rings. For completeness, we also discuss coherent resonances for high-order beam modes.

GENERAL ANALYSIS

We start with the $m = 2$ modes, allowing us to employ the envelope equation:

$$a'' + K(s)a - \frac{\epsilon^2}{a^3} - \frac{\kappa}{a} = 0, \quad (3)$$

where $K(s)$ is the periodic focusing function, ϵ is the beam emittance, κ is the space charge parameter, and a is the radius of a round beam. For simplicity, we replace the periodic focusing by a time-dependent perturbation. The linearized envelope equation for small oscillations [$a \rightarrow a_0(1 + u)$] is then

$$u'' + \Omega_2^2 u + (nt) = (1 + u)\nu_0^2 \sum_n \alpha_n \cos(n\theta) + (nt), \quad (4)$$

where nt stands for "nonlinear terms". If the coefficient α_n becomes large, as in the case of periodic focusing, a more accurate treatment of the stationary state is required [5]. In Eq. 4, the term which drives matched periodic oscillation of the beam envelope and the term which describes the oscillations around such a periodic solution are both kept on the r.h.s., for comparison. In principle, these two terms should be treated separately, since the first term is just the closed orbit solution (matched solution in the presence of a time dependent perturbation). However, when only the second term is kept, as typically done to consider beam stability as a result of periodic focusing, an important implication of the first term may be overlooked. In particular, the resonant growth of such stationary solutions near the half-integer tunes, due to the first term, becomes an important effect, known as Smith/Sacherer space-charge induced coherent beam response to the imperfection resonances. Here, the

* Work supported by the SNS through UT-Battelle, LLC, under contract DE-AC05-00OR22725 for the U.S. Department of Energy.

resonant response is considered both for the case when the integer and half-integer coherent response occurs at different tunes, as well as when the driving harmonics provide a resonance condition for both resonances at the same tune.

The first term on the r.h.s. of Eq. 4 corresponds to an integer $\Omega_2 = n_1$ coherent resonance of the beam envelope with harmonic n_1 , which occurs near the half-integer single-particle tunes. The second term on the r.h.s. of Eq. 4 gives the coherent resonance of the half-integer (parametric) type: $\Omega_2 = n_2/2$, where n_2 is now another harmonic different from n_1 . The limitation due to this linear parametric resonance of the envelope modes with the periodic focusing structure suggests a design with the zero-current single-particle phase advance σ_0 per focusing period below 90° . In rings, such a condition corresponds to the structure resonance which occurs near the single-particle tunes $\nu = N/4$ with N being the structure harmonic. However, the structure resonances are typically avoided by the choice of the operating tune-box resulting in the limitation due to the imperfection resonances. Note that in a special class of rings (such as cooler rings), where additional measures are undertaken to compensate emittance growth due to the crossing of the imperfection resonances, one recovers the situation as in linear transport systems.

Resonance strength

The width of the linear parametric resonance is [5]:

$$\Delta\epsilon \approx \frac{\nu_0^2}{2\Omega} \alpha_n = \frac{\nu_0^2}{2\sqrt{2}\sqrt{1+\eta^2}} \alpha_n, \quad (5)$$

where, as an example, we substituted for Ω the frequency of the in-phase mode, with η being the tune depression defined as $\eta = \nu/\nu_0$. It depends linearly on the strength of the imperfection error α_n (to first order). Such a strength is very small for typical imperfection errors (much less than the 1% level). As a result, the corresponding resonance is expected to be very narrow and the envelope growth is detuned at a very low level due to the non-linear terms in Eq. 4, which was confirmed by numerical simulation [6]. This is, in fact, the reason why the effect of the envelope instability in rings is negligible, provided that the tune-box is chosen free of the structure resonances and only imperfection harmonics are of a concern.

On the contrary, when the source of the parametric driving term in Eq. 4 is due to the periodicity of the lattice, the width of the resonance may become significant. Strictly speaking, a perturbation approach is not applicable for very large α_n , and one needs to solve the exact equation with periodic focusing numerically. This defines the stopbands of the structure resonances which should be avoided.

Combined resonance response

If the zero-current tune is chosen in the tune-box free from the structure resonances then the effect of the parametric envelope resonance due to the imperfection harmonics at $1/4$ tunes is negligible. Also, there is no integer-type

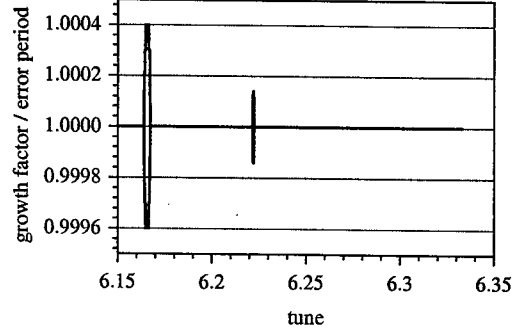


Figure 1: Growth factors for imperfection driven envelope instability with working point $\nu_{0x,y} = 6.333$ and a large error of 4% in harmonic $n = 25$.

envelope growth at such tune values with the stationary solution for periodic oscillations of the beam envelopes being well defined. When one approaches the integer or half-integer tunes, this results in a periodic growth of the beam envelopes which is described by the coherent integer response in Eq. 1. At such tunes there is also the possibility of parametric growth of the envelopes due to higher harmonics. For the parametric resonance to take place at such tunes, the stopband of the parametric resonance (due to the α_{n_2}) should be much larger than the integer stopband due to the α_{n_1} . For example, in the PSR LANL lattice with the zero-current betatron tune above $\nu = 2.5$, the parametric resonance of the beam envelope would take place at high-intensity operation. This is because the strength of the $n = 10$ harmonic (α_{10}) is much larger than that of the $n = 5$ (α_5) harmonic, since $n = 5$ is a weak imperfection harmonic while $n = 10$ is the strongest harmonic with the lattice super-periodicity $P = 10$ [8].

Extension to non-linear modes

For the case of the non-linear imperfection errors one has to consider tune values near the corresponding imperfection resonances. Similar to the $m = 2$ modes, the high-order modes can have resonant growth near

$$n = \Omega_m, \quad (6)$$

which is the coherent resonance condition for any order beam mode Ω_m derived by Sacherer [2]. To derive such a resonance condition for $m > 2$ modes one needs to use either high-order beam moment equations or the Vlasov equation. In addition, the effect of the periodic focusing adds the possibility of Ω_m resonating at the half-integers, which corresponds the parametric resonance of beam modes [7]:

$$n/2 = \Omega_m. \quad (7)$$

The practical discussion for the typical strength of an imperfection error is now similar to the discussion for the $m = 2$ modes [5].

For completeness, we note that in the absence of non-linear imperfections, the periodic oscillation of high-order

beam modes is now well defined so that the condition $n = \Omega_m$ no longer applies, and stability is now determined solely by the parametric condition $n/2 = \Omega_m$ [7]. In fact, this becomes the dominant effect in the high-current transport channel or cooler rings. With harmonic n now being the structure harmonic, the beam encounters a whole set of instabilities during the space-charge tune depression. Such instabilities were first numerically explored in connection with transport channels [3], and recently were analytically described using the terminology of resonances with an application to cooler rings [7].

When the beam has a large mismatch, the nonlinear terms ignored in the linearized approach can play an important role. In such a very general case, the condition for the non-linear parametric resonance is [5]:

$$n/k = \Omega_m, \quad (8)$$

where k now stands for the exponent of the non-linear term in the driving potential. This is similar to the non-linear envelope resonances $n/k = \Omega_2$ when the beam envelopes are mismatched [9]. Also note that in such a form, the resonance condition applies also for the coupling resonances, since the subscript m only indicates the order of the mode.

NUMERICAL ANALYSIS

Imperfection envelope instability

We used the KVXYG [4] code, which determines the growth factors of the envelope perturbations. A parametric resonance of the beam envelope may be expected in a lattice with a working point above $1/4$ tunes. We have taken a constant focusing lattice with $\nu_{0x,y} = 6.333$ and a 25-th harmonic gradient error, which implies $\sigma_0 = 91.2^\circ$ per error harmonic. For a large error of 4%, only very narrow stopbands of the out-of-phase and in-phase modes are found at $\sigma = 89.59^\circ$ and $\sigma = 88.78^\circ$ (corresponding to $\nu_{x,y} = 6.222$ and $\nu_{x,y} = 6.165$), respectively. We also confirmed that for errors of 2% and 1%, the width of these stopbands decreases linearly with the error strength, in agreement with the stopband of the parametric resonance given in Eq. 5. As a result, the instability gets detuned at a very low level. This allows the conclusion [6] that the imperfection driven envelope instability for working points above the fractional quarter-integer tunes can be ignored.

Structure envelope instability

The case of the parametric resonance of the beam envelope with the structure lattice harmonics is similar to the one studied with application to the transport channels or cooler rings. As an example, for a working point above $\nu_{0x,y} = 6$, as in the SNS, and the lattice which consists of 24 basic cells, we calculated the instability stopband for a cell with $\sigma_0 = 96^\circ$ corresponding to $\nu_{0x,y} = 6.4$ (here $\nu_0 = N\sigma_0/(2\pi)$, where N is the number of cells in the lattice). We noted that a pronounced instability stopband

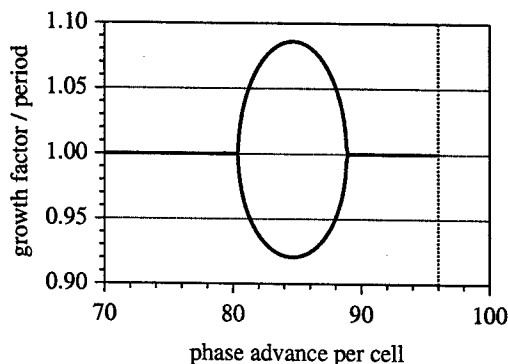


Figure 2: Growth factors for structure driven envelope instability with zero-current phase advance of $\sigma_0 = 96^\circ$, corresponding to $\nu_{0x,y} = 6.4$.

(Fig. 2) with a growth factor above unity starts for full-current phase advance $\sigma < 88.84^\circ$ (corresponding to a tune $\nu_{x,y} = 5.92$). The strong flutter of the matched FODO envelope couples the in-phase and out-of-phase eigenmodes and leads to a single stopband. In a realistic lattice one tries to avoid structure resonances by choosing the working point correspondingly.

SUMMARY

We examined the impact of integer and half-integer resonances of the collective beam modes on intensity limitation in the high-intensity rings. The imperfection driven resonance of the beam envelopes was found to be negligible. As a result, it is not expected to impose an additional restriction in the tune space.

ACKNOWLEDGMENTS

One of the authors (A.F.) is indebted to J. Holmes, S. Danilov, S. Cousineau and G. Parzen for many useful discussions on this subject. He also wishes to thank the Accelerator Physics group of the SNS project.

REFERENCES

- [1] L. Smith, Proc. Conf. on High Energy Acc. (Dubna), p. 1238; P. Lapostolle, p. 1235 (1963).
- [2] F. Sacherer, LNBL Report UCRL-18454 (1968).
- [3] I. Hofmann et al., Part. Accel. 13, p. 145 (1983).
- [4] J. Struckmeier and M. Reiser, Part. Accel. 14, p. 227 (1984).
- [5] A.V. Fedotov, I. Hofmann, R.L. Gluckstern and H. Okamoto, in preparation (2003).
- [6] A.V. Fedotov, I. Hofmann, PR STAB, V.5, 024202 (2002).
- [7] H. Okamoto, K. Yokoya, N. Inst. Meth., A482, p.51 (2002).
- [8] S. Cousineau et al., Phys. Rev. STAB, V.6, 034205 (2003).
- [9] S.Y. Lee and A. Riabko, Phys. Rev. E, V.51, p. 1609 (1995).

SPILL STRUCTURE IN INTENSE BEAMS *

M Blaskiewicz, K Brown, JW Glenn, E Raka, J Ryan,
BNL, New York 11973, USA

Abstract

Fixed target studies of small branching ratio decay processes require intense beams and smooth spills. Longitudinal structure arises through collective effects, well below the coasting beam stability threshold. These structures have been observed at the Brookhaven AGS and dependence on intensity and momentum spread measured. Measurements and amelioration techniques have been developed and will be described.

1 INTRODUCTION

The delivery of constant beam current to counter experiments at high intensities has been plagued by excessive noise like structure. Two unexpected phenomena have been noted: small clusters of protons remain as stable 'hot spots' for extended times; and the Keil-Shnell formula predicts an impedance 50 times larger than expected.

The AGS extraction relies on the chromaticity of the accelerator and an induced momentum spread in the beam. This spread is $\sim 1/2\%$ $\Delta P/P$ and the field is lowered by this amount over the two seconds of flattop to spiral the debunched beam into a third integer resonance. Spill ripple initially was dominated by correction supplies that modulated the betatron tune. This was nearly eliminated with the installation of low ripple power supplies.

With intensity increases in the AGS spill ripple again increased. This is due to collective effects in the spiraling beam awaiting extraction. Measurement of the AGS is required to understand how these bunches behave or even exist. Also this affects the limit to coasting beam intensity, which will be pushed for proton operation of the AGS.

2 SPILL MEASUREMENTS

The external beam current at the AGS is measured by a secondary emission chamber with 3 kHz electronics. The first two figures show how the structure increases disproportional with intensity. The first is at 2×10^{13} (20 TP) protons extracted from the AGS. The ripple in the current is steady and due to power supply ripple. The second shows large bursts of 'noise' in the spill. The spill bursts are fast as see in Fig 3, some only a few mSec. The average momentum swing over this period is less than the $5-7 \times 10^{-4}$ tune width of the extraction resonance times the chromaticity

The density in momentum of these 'hot spots' is of order 5 times the average density of the coasting beam.

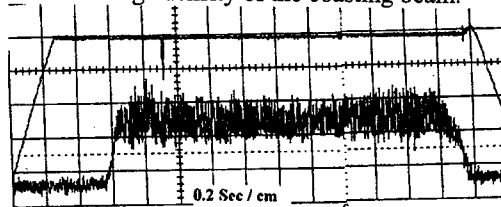


Fig 1: SEB Beam Current @ 20 TP in AGS

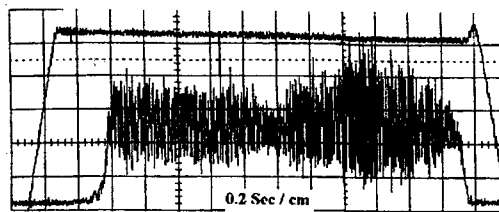


Fig 2: SEB Beam Current @ 50 TP in AGS

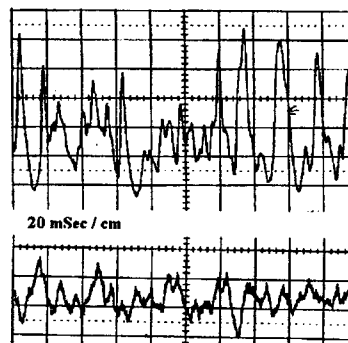


Fig 3: Fast Sweep of Spill Structure 50 & 20 TP

That these bursts are not periodic is seen in the spectra of the current, at high intensity it is mostly a noise continuum not the series of harmonics as seen at lower intensity.

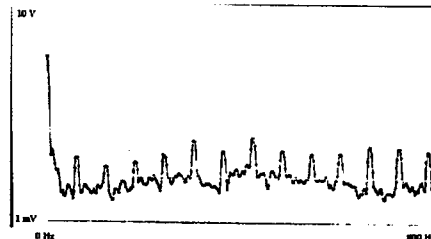


Fig 4: Spectrum of Spill Current - 20 TP / 2Sec

*Work performed under Contract Number DE-AC02-98CH10886 with the US Department of Energy

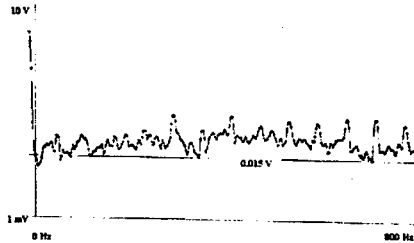


Fig 5: Spectrum of Spill Current - 50 TP / 2Sec

3 COASTING STABLE BUNCHES

These hotspots are also visible longitudinally on our fast (100 MHz) beam, or wall, current monitor. This display plots 100 sequential traces from the scope each 5 mSec later and plots them in front of the last as a contour map, 'mountain range', plot. Each trace is about one and a half AGS revolutions so the whole turn is shown. The beam is debunched on flat top by jumping the RF phase to the unstable fixed point and defocusing for a quarter synchrotron oscillation, then shutting down the RF. The plotting starts within a few mSec after this and continues into spill time. There are clusters of protons that remain stable for hundreds of mSec. The way they interact is reminiscent of the 'holes' simulated and measured in the CERN PS Booster [1]. The theory of solitons in coasting beams in this paper predicts that hot spots should be associated with a focussing impedance. However AGS extraction is well above transition and previous measurements [2] suggest an inductive broad band $|Z/n| \approx 10 \Omega$. This leads to a defocusing impedance. The actual Z/n is a function of frequency and our data suggests that the details of the frequency dependence are important. Figs 6 & 7 show that there are 'hot spots' and not 'holes' on the beam.

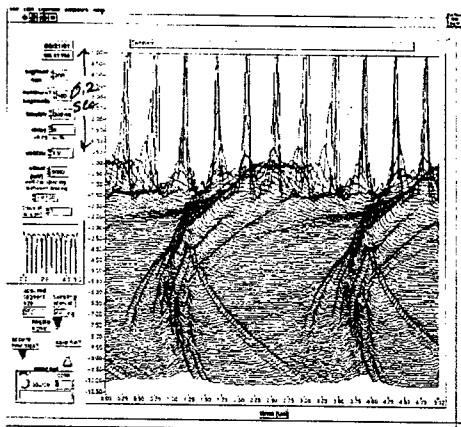


Fig 6: Lasting Bunches on Mountain Range

We studied how these bunches were effected by intensity in the AGS and the energy spread induced during RF turnoff. For a series of RF voltages at turn off, with and without the phase jump, we watched these bunches decay or not for different intensities. The current of the bunches was recorded.

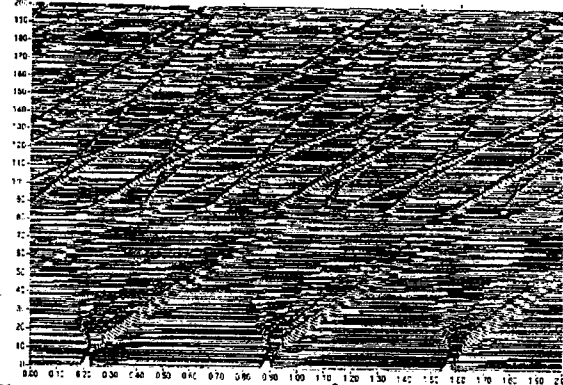


Fig 7: Mountain Range for 10^9 Gold Ions. showing a picture of solitons of gold show and that high intensity is not essential for stable isolated clusters.

Also we measured the resultant momentum spread for various RF voltages at turnoff. Two methods were used as shown in Fig 8. First the difference in rotation frequency within an accelerated beam bunch was measured by noting how much the bunch widened over 50 mSec. Note the asymmetry of debunching is similar to that modeled and seen in the CERN SPS [3]. The other method was to measure the time for the beam to be extracted with a constant rate of fall of the main magnet field. This time is determined by the tune, thus momentum, width of the beam

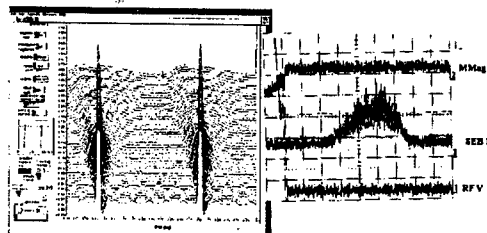


Fig 8: Debunching and Spill pictures for measurement.

Table I: Measured Momentum Spread		
RF Volt	DelP/P - %	
kV	Debunch	Spill
0	0.337	0.26
8	0.422	0.35
15	0.432	0.35
60	0.48	0.41

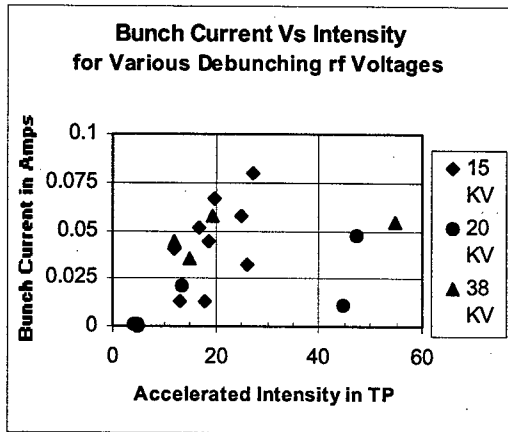


Fig 9: Beam Current of 'Hot Spots'

The results of this 'mapping' show that the primarily affector of hot spot size is the beam intensity during acceleration and the RF voltage at debunching has little effect,

$$\left(\frac{\Delta P}{P}\right)^2 = \frac{-4}{\pi} * \frac{(Z/n) \cdot \Delta I}{\eta * (E_T/q)}$$

This is an extension Koscielniak's work [1] which gives a criteria for stable solitons. For stable solitons to exist in the AGS above transition, with its $\eta = 0.0116$ and an $E_T/q = 20$ GeV and using a broad band $Z/n = 10\Omega$, for 0.1 A of protons the delP/P would be 7.4×10^{-5} ; and for the 2×10^9 Gold ions with a full delP/P of $\sim 2.5 \times 10^{-4}$ the delP/P of a soliton of 10% of the beam would have a delP/P of 10^{-5} . We currently do not have the capacity to measure this but it may be possible using the SEB. This calculation assumes a negative inductance contrary to the above mentioned measurement.

4 AGS IMPEDANCE

While mapping the effects on the stable bunches during the spill, we also raised intensity with the RF voltage held constant and noted beam losses. The intensity and momentum spread that the beam goes unstable and is lost is a function of the impedance.

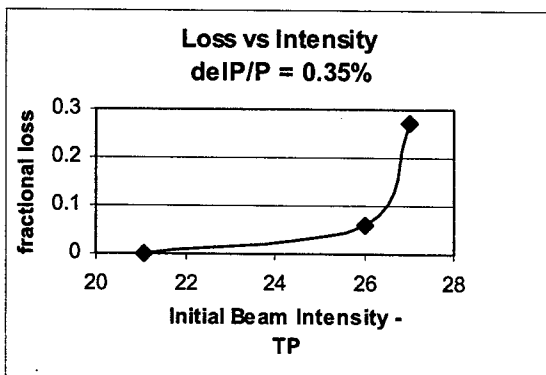


Fig 10: Beam Loss vs. Intensity, constant delP/P

Assuming that this behavior is the result of a coasting beam longitudinal instability and applying the Keil-

Schnell criteria [4], implies $[Z/n] \approx 550 \Omega$. Using this impedance, the expected limit of beam intensity vs. momentum spread and results from this test are plotted.

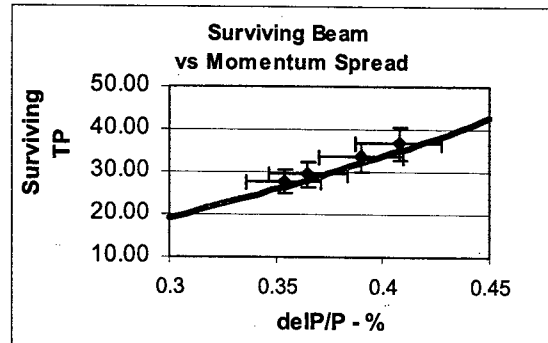


Fig 11: Surviving Beam Intensity vs. delP/P

This value is more than 50 times larger than previous estimates. We conclude that if the data in Fig 10 & 11 are due to longitudinal effects, which is reasonable considering the quantity of 'seed' solitons, these effects cannot be understood within the context of linear stability theory. To achieve 100 TP (10^{14}), a 0.7 % delP/P would be necessary to stabilize the beam.

5 AMELIORATION

The VHF cavity continues to be our main stay to prevent bunches affecting the spill [5]. Whether it will continue to be effective at higher intensities is a concern.

6 CONCLUSIONS

The high impedance measured must be better understood. This is presumably why bunches are stable above transition, while it is expected with normal inductive impedance they would be unstable and disperse. Understanding and correcting or compensating for this impedance would have a great benefit on machine performance.

7 REFERENCES

- [1] S Koscielniak, et.al, 'Longitudinal Holes ..', Phys Rev Special topics - Accels & Beams, Vol 4, 044201 (2001)
- [2] F Pedersen, E Raka 'A Measurement of Longitudinal ..' PAC79, IEEE NS-26.#3, June '79
- [3] T Bohl, et.al 'Study of a Single Bunch Instability ..' EPAC 2000, CERN-SL-2000-019 HRF
- [4] pp211, D Edwards & M Syphers 'An Introduction to the Physecs ...', J Wiley for discussion and reference.
- [5] K Brown et.al, 'Status of Slow Extraction ...', TPPE003 this conference

ELECTRON-CLOUD MITIGATION IN THE SPALLATION NEUTRON SOURCE RING*

J. Wei[†], M. Blaskiewicz, J. Brodowski, P. Cameron, D. Davino, A. Fedotov, P. He
H. Hseuh, Y.Y. Lee, H. Ludewig, W. Meng, D. Raparia, J. Tuozzolo, S.Y. Zhang, BNL
A. Aleksandrov, S. Cousineau, V. Danilov, S. Henderson, ORNL
M. Furman, LBNL; M. Pivi, SLAC; R. Macek, LANL, USA; N. Catalan-Lasheras, CERN

Abstract

The Spallation Neutron Source (SNS) accumulator ring is designed to accumulate, via H^- injection, protons of 2 MW beam power at 1 GeV kinetic energy at a repetition rate of 60 Hz [1]. At such beam intensity, electron-cloud is expected to be one of the intensity-limiting mechanisms that complicate ring operations. This paper summarizes mitigation strategy adopted in the design, both in suppressing electron-cloud formation and in enhancing Landau damping, including tapered magnetic field and monitoring system for the collection of stripped electrons at injection, TiN coated beam chamber for suppression of the secondary yield, clearing electrodes dedicated for the injection region and parasitic on BPMs around the ring, solenoid windings in the collimation region, and planning of vacuum systems for beam scrubbing upon operation.

INTRODUCTION

Electron-cloud effects are important, but incompletely understood phenomena. Effects that can severely limit the performance of high-intensity proton synchrotrons include trailing-edge tune-shift and resonance crossing, electron-proton instability, emittance growth and beam loss, increases in vacuum pressure, heating of the vacuum pipe, and interference with beam diagnostics. Similar to the Proton Storage Ring at Los Alamos (LANL), where a strong, fast transverse instability occurs when a threshold intensity is exceeded [2], the effects may limit the performance of the SNS accumulator ring [3, 4].

ELECTRON GENERATION

We classify electron production into the following categories: (1) electrons generated at the stripping foil in the injection region; (2) electrons generated at the surfaces of collimators and vacuum pipe due to the impact of lost protons; (3) electrons produced by beam-induced multipacting from the vacuum-pipe wall; and, (4) electrons produced around the ring from residual-gas ionization.

Injection stripping

During the H^- charge-exchange injection at 1 GeV beam energy, the stripped electrons with a kinetic energy

* SNS is managed by UT-Battelle, LLC, under contract DE-AC05-00OR22725, DE-AC03-76SF00098, DE-AC03-76SF00515 for the U.S. Department of Energy. SNS is a partnership of six national laboratories: Argonne, Brookhaven, Jefferson, Lawrence Berkeley, Los Alamos, and Oak Ridge.

[†] jwei@bnl.gov

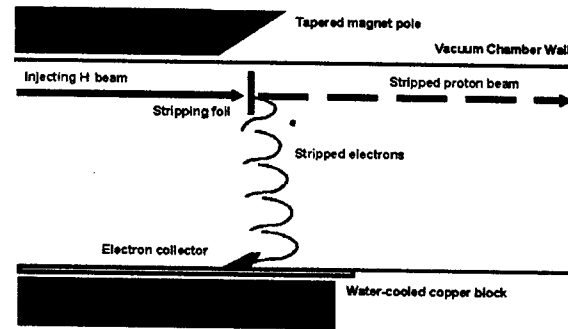


Figure 1: Injection area schematic layout.

of 545 keV and a power of 2 kW are collected by a water-cooled catcher (Fig. 1). These electrons backscatter from the catcher and the vacuum chamber, resulting in a high concentration of electrons with a broad energy spectrum. The injecting- and circulating-beams impacting on the foil produce secondary emission of electrons at tens of eV energy. The injecting- and circulating-beam also produce knock-on electrons at a high energy (up to several MeV). The stripping-foil, operating at a high temperature around 2000 K, emits thermionic electrons at low energy [5].

Collimation region

The collimators are designed to collect more than 90% of the beam loss in the ring (Table 1). Protons incident on the collimator surfaces produce secondary electrons. Depending on the energy of the beam and the incident angle, the secondary electron-to-proton yield can greatly exceed 1 when the incident beam is nearly parallel to the surface [6]. Although a serrated surface reduces the generation of secondary-emission electrons, it is practically ineffective since protons incident on the front edge of the teeth easily escape from the collimator body due to the long proton stopping-length (about one meter) at 1 GeV energy.

Table 1: Estimated beam loss in the SNS ring of a 2 MW beam.

Mechanism	Location	Fraction	Power [W/m]
ring beam halo	collimator	1.9×10^{-3}	2×10^3
excited H^0 at foil	collimator	1.3×10^{-5}	20
energy straggling at foil	collimator	3×10^{-6}	4.5
H^- magnetic strip.	inj. dipole	1.3×10^{-7}	0.3
nucl. scatt. at foil	foil	3.7×10^{-5}	2.5
collimation ineff.	all ring	10^{-4}	0.9

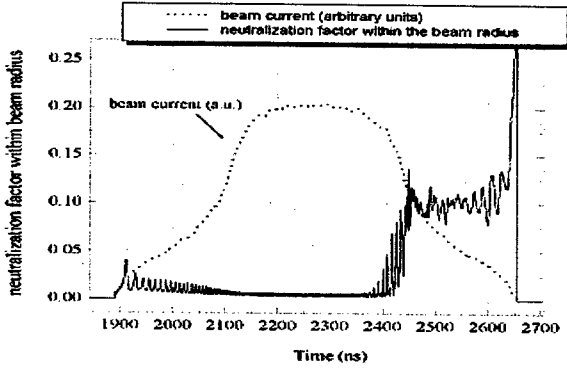


Figure 2: Computer simulation of electron generation in the SNS ring. The beam intensity is 2×10^{14} per bunch. The peak secondary-emission yield (SEY) is assumed to be 2. The peak neutralization level is about 10% within the proton rms beam radius, and about 100% on average within the beam pipe.

Beam-induced Multipacting

Beam-induced single-bunch, trailing-edge multipacting is likely to be the leading source of sustained electron-production [2, 7]. Electrons are attracted towards the rising edge of the proton bunch. At the trailing edge of the proton bunch, electrons are released and yet still accelerated by the bunch to multipact. The number of electrons grows exponentially at the trailing edge of the proton bunch. The energy gained by an electron is approximately [4]

$$\Delta E_e \approx 4m_e c^2 \beta b \sqrt{\frac{r_e N_0}{s_b^3 B_f^3}} \quad (1)$$

where N_0 is the number of protons in the bunch, s_b is the bunch separation, b is the pipe radius, and B_f is the bunching factor. For the SNS ring, $N_0 = 2 \times 10^{14}$, $s_b = 248$ m, $B_f \approx 0.5$, $b \approx 0.1$ m, and $\beta = 0.875$. The characteristic energy gain is approximately $\Delta E_e \approx 97$ eV. Single-bunch, trailing-edge multipacting is expected to occur (Fig. 2) [8].

Ionization

The rate of electron line-density increase per unit length of circumference is given by the relation

$$\frac{d^2 \lambda_e}{dt ds} = \frac{\rho_m \beta I \sigma_{ion} P}{e} \quad (2)$$

where I is the beam current, σ_{ion} is the cross-section, P is in units of Torr. At the room temperature of 300 K, the molecular density ρ_m is about $3.3 \times 10^{22} \text{ m}^{-3}$. For the SNS ring at a pressure of 10^{-8} Torr, a total number of 2.6×10^9 electrons is produced per turn when the proton intensity is 2×10^{14} . Residual gas ionization may feed these "seed" electrons to the trailing-edge multipacting process.

MITIGATION MEASURES

Control of the electron-cloud effects involves design consideration to minimize the beam loss, suppression of electron generation, and enhancement of Landau damping.

Low-loss design & operation

Minimization of beam loss is of primary importance [1]. Having a large transverse vacuum-pipe aperture and long, uninterrupted straight-sections are the two most important aspects considered. Collimators play an essential function in localizing the beam loss to controlled areas.

Landau-damping enhancement

A large vacuum-pipe aperture in high dispersion area and a large RF voltage provide sufficient momentum acceptance of $\pm 1\%$ for a $480\pi \mu\text{m}$ transverse acceptance. Longitudinal painting is used to expand the momentum spread of the injecting beam. Lattice sextupole families are used for chromatic adjustments, to either improve momentum acceptance or enhance damping. Octupoles are also available for a possible further enhancement.

Electron suppression

Injection area control Two chicane dipoles are special tapered to guide stripped electrons [9]. The electron collector is made of low charge-state C-C material with low backscattering yield.

Clearing electrodes A dedicated clearing electrode is implemented inside the stripping-foil assembly. A voltage up to 10 kV can be applied, adequate to suppress multipacting in the injection region. BPMs around the ring are designed to be also used as clearing electrodes capable of providing a voltage up to ± 1 kV, overcoming the energy gain due to the proton bunch (Eq. 1, Fig. 3).

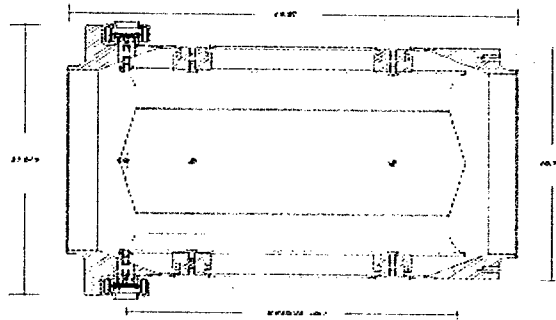


Figure 3: Floating-ground BPM for the SNS ring.

TiN surface coating The inner surface of the entire ring is coated with TiN. Coated chambers are tested for conductivity and rise-time response. With a variation within 20%, the thickness of $0.1 \mu\text{m}$ withstands the bombardment from electrons during the lifetime of the machine operation. For the ferrite of the extraction kicker inside the vacuum pipe, the coating pattern is selected to avoid Eddy-current heating and to prevent changes in material properties. Measurements of TiN-coated surfaces indicate a reduction of SEY by more than half of an unit (Fig. 4) [10]. Vacant ports are available for additional pumping if needed for the higher level of outgassing from the rougher coated surface. The

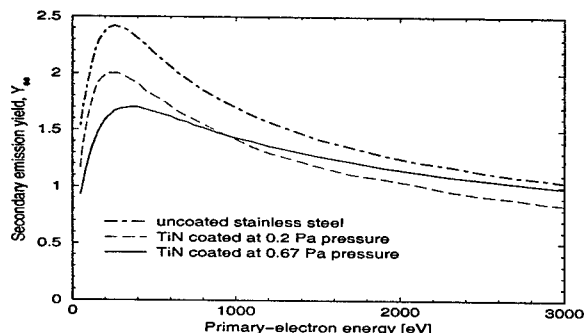


Figure 4: Secondary-electron yield for various coating conditions of the SNS ring chamber measured at CERN. Magnetron (dc) sputtering is used to coat the surfaces with $0.1 \mu\text{m}$ TiN. Surfaces coated at a pressure of 0.67 Pa, which has a lower peak Y_{se} but a higher outgassing-rate comparing with those coated at a pressure of 0.2 Pa, are adopted.

present design does not allow NEG film coating which requires in-situ baking.

Solenoids Solenoids are planned for the vacant straights (about 5 m) in the collimation region to suppress electron multipacting. The solenoid field B_ϕ of about 50 G is strong so that the radius $r_\phi = m_e e B_\phi$ (12 mm for 300 eV electrons) of electron motion is small compared with the pipe radius. Effects on the proton beam can be minimized by alternating the polarities of the solenoids according to the betatron phase. Skew quadrupoles can further be used to correct the coupling.

Beam-in-gap cleaning In order to reduce the electrons trapped by the beam in the gap, the 250 ns beam gap is cleaned by a gap-cleaning kicker for the last 100 of the 1060-turn accumulation [11]. By resonantly exciting coherent betatron oscillations, beam residuals are driven into the primary collimator, where beam loss is measured with a gated fast loss monitor. The system uses MOSFET banks to supply pulses at 30 ns rise/fall time. The burst mode frequency, greater than 1 MHz, permits turn-by-turn kicking.

Chamber & vacuum Vacuum ports are screened, and steps in the vacuum pipe are tapered at 1-to-3 ratio to reduce peaked electric fields causing electron emission. A vacuum pressure of about 10^{-8} Torr ensures low electron generation from gas ionization.

Beam scrubbing Beam scrubbing at an electron dose level of 1 mC/mm^2 can further condition the vacuum surface during operations [12]. Vacant ports can house turbo pumps to function at a vacuum pressure above 10^{-6} Torr. Extended beam storage in the ring is planned to accelerate the scrubbing process.

Active damping The possibilities of mitigating the e-p instability with wideband resistive feedback are under investigation. The e-p instability results in coherent motion in the 100-200 MHz band with growth rates in the range $30\text{-}100 \text{ ms}^{-1}$. System gain of 0.1 is necessary to damp such large growth rates. A system is envisioned with 50 cm stripline kickers for each plane to achieve the high band-

width and two pickups with flat response to 300 MHz having equivalent noise of less than 0.3 mm. The required gain is achieved with a 1.5 kW RF power amplifier driving each kicker.

Diagnostics & interference minimization

The stripping foils and the collector are monitored by the video systems. Five electron detectors are distributed at crucial locations around the ring.

Efforts are made to minimize the interference from the electron cloud. For example, the multi-channel plates for electron collection in the ring ionization profile monitors are recessed from the vacuum-chamber wall, and sweeping electrodes used to avoid superfluous signals.

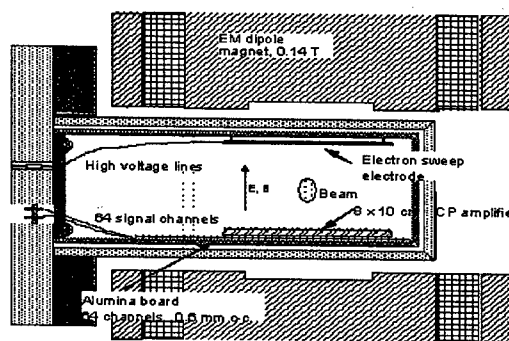


Figure 5: Ring IPM with sweeping electrodes, and with the multi-channel plates for electron collection recessed from the vacuum-chamber wall to avoid superfluous signals (courtesy R. Connolly).

SUMMARY

Present studies indicate that with preventive measures adopted to suppress electron generation and to enhance Landau damping, the impact of electron cloud can be minimized in the operation of the SNS ring.

We are indebted to the SNS team and collaborators, especially O. Gröbner, N. Hilleret, M. Plum, F. Ruggiero, N. Simos, P. Thieberger, R. Todd, F. Zimmermann.

REFERENCES

- [1] J. Wei et al, PRST-AB, **3** (1999) 080101; these proceedings; J. Wei, Rev. Mod. Phys. (Oct. 2003)
- [2] R. Macek, Workshop on Two-Stream Instab. Sante Fe (2000)
- [3] M. Blaskiewicz et al, PRST-AB, **6** (2003) 104203; these proc.
- [4] J. Wei, R. Macek, ELOUD'02, CERN-2002-001 (2002)
- [5] M. Plum et al, PAC95 (1995) 3403
- [6] P. Thieberger et al, Phys. Rev. **61** (2000) 042901
- [7] V. Danilov et al. AIP Conf. Proc. 496 (N.Y. 1999), p. 315
- [8] M. Pivi, M. Furman, PRST-AB, **6** (2003) 034201
- [9] D. Abell et al, EPAC00, p. 2107 (2000)
- [10] P. He et al, submitted to J. Vac. Sci. Tech. (2003); these proc.
- [11] R. Witkov et al, PAC99 p. 2250; N. Catalan-Lasheras et al PRST-AB **4** (2001) 010101
- [12] S.Y. Zhang et al, these proceedings

ON EMITTANCE EVOLUTION IN THE EXTRACTION SYSTEM OF HIGH-CURRENT ELECTRON AND ION SOURCES

J-M. Lagniel, P. Balleyguier, D. Guilhem, J-L. Lemaire, N. Pichoff, M. Promé
CEA/DAM, DIF/DPTA/SP2A, Bruyères-le-Châtel, France

Abstract

A simple model has been built to study the evolution of high-current electron or ion beams in axially symmetric extraction systems (electron guns or ion sources). Both electric and magnetic field components induced by a HV diode and a focusing solenoid respectively are computed using analytical formulas. The space-charge forces are computed using a ring method. In a first step, the individual effects of the 3 nonlinear forces (electric, magnetic and space charge) on the emittance evolution are presented. We then discuss how the knowledge acquired in the first step can be used to understand and optimize the emittance evolution in systems combining these effects.

INTRODUCTION

A simple model has been built to understand the behavior of high-current beams in extraction systems of electron guns or ion sources with azimuth symmetries. In a first step, the emittance evolution has been analyzed for each kind of nonlinear force present in such systems:

- nonlinear forces induced by the electric field of the diode,
- nonlinear forces induced by the magnetic field of a focusing solenoid,
- nonlinear space-charge forces.

The understanding of the individual effects has been used in a second step to optimize the emittance evolution in the case of combined effects of these forces.

DIODE

The model uses the simplest diode geometry: a flat disc as emissive area (cathode) and a thin plane with a cylindrical hole as anode. An analytical formula giving the potential distribution at any location in the (r,z) plane [1] is used to calculate the longitudinal (E_z) and radial (E_r) components of the electric field. This technique allows very fast computations of the particle trajectories. Fig. 1 gives an example for the following parameters :

Cathode : $z = 0$, $R_K = 4.5$ cm, $V = -100$ kV

Anode : $z = 10$ cm, $R_A = 5$ cm, $V = 0$

Fig. 2 shows that the rms emittance evolution in this simple system (zero current, no focusing solenoid) is already pretty complicated. In a first zone (D1), the rms emittance starting from zero at the cathode (no divergence) increases up to a maximum at $z \sim 9$ cm. In the anode area (D2, ~ 9 cm $< z < \sim 11$ cm), the emittance decreases rapidly before reaching a second maximum. After the anode area (D3), the emittance reaches another minimum before raising to a final plateau at $z \sim 30$ cm (anode position + $\sim 4 R_A$).

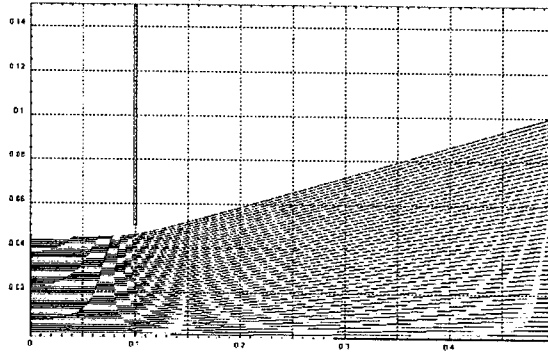


Figure 1: Particle trajectories in the diode : $R = f(z)$ (m).

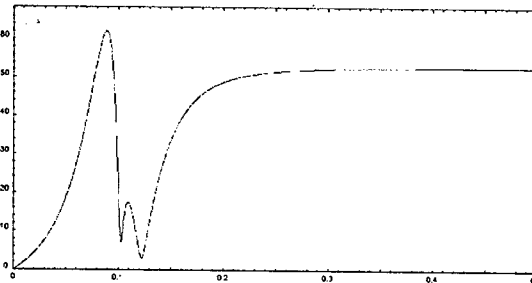


Figure 2: Evolution of the (R,R') unnormalized rms emittance value (mm.mrd) along the diode axis z (m).

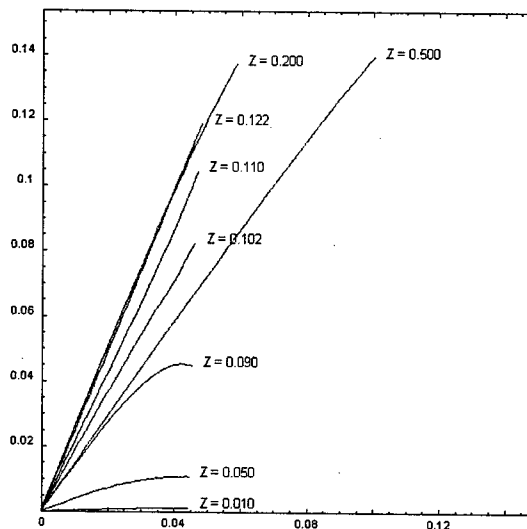


Figure 3: (R,R') emittance plot at different positions z (m) along the propagation axis of the diode.

Fig. 3 explains the rms emittance evolution. The electric field nonlinearities bend the (R,R') emittance curve - towards the R axis in zone D1, - towards the R' axis in D2 (the distribution is straightened up and the emittance reaches a minimum), - and finally again

towards the R axis in D3. The nonlinear effects become negligible at $z \sim 30$ cm where the final emittance plateau starts. In this example the final rms unnormalized emittance is ~ 50 mm.mrd; this value depends upon the ratio R_A/R_K but the emittance behavior shown on fig. 2 remains unchanged for different R_A/R_K values.

SOLENOID

Analytical formulas giving the longitudinal (B_z) and radial (B_r) components of the magnetic field generated by a coil of current at any position in the (r, z) plane can be found in [2]. They are used to compute the effect of solenoids formed by an addition of several of these coils. In a first step the particle trajectories have been analysed in such solenoids without electric field or space charge. For the results presented here a 8 cm radius 100 keV electron beam starts at $z = 0$ without divergence, a 5 coils 2 cm long 10 cm radius solenoid powered with 200 A is located at $z = 40$ cm.

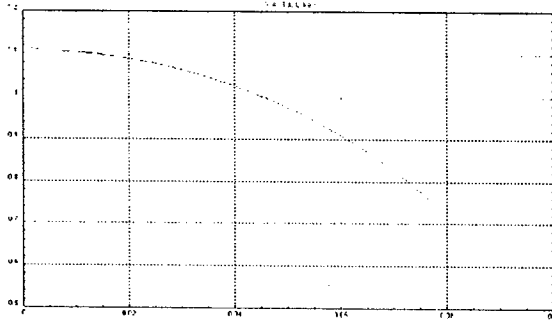


Figure 4: Solenoid focal length (m) function of r (m).

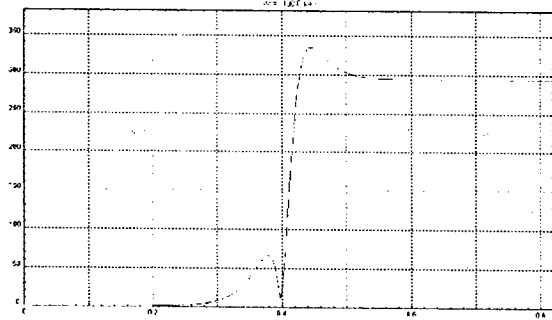


Figure 5: Evolution of the (R, R') unnormalized rms emittance value (mm.mrd) along the solenoid axis z (m).

The plot of the solenoid focal length as a function of the particle input radius (fig. 4) demonstrates the nonlinear character of this focusing element. The rms emittance evolution (Fig. 5) shows a first zone (S1) where the emittance starting from zero increases up to a maximum at $z \sim 38$ cm. After this point (S2 zone), the emittance decreases down to 0 before a big jump up to a final value of 250 mm.mrd. Fig. 6 explains this behaviour, the magnetic field nonlinearities bend the emittance curve - towards the R axis in S1, - towards the R' axis in S2 (the distribution is straighten up and the emittance reaches 0 when this effect perfectly compensates the first one).

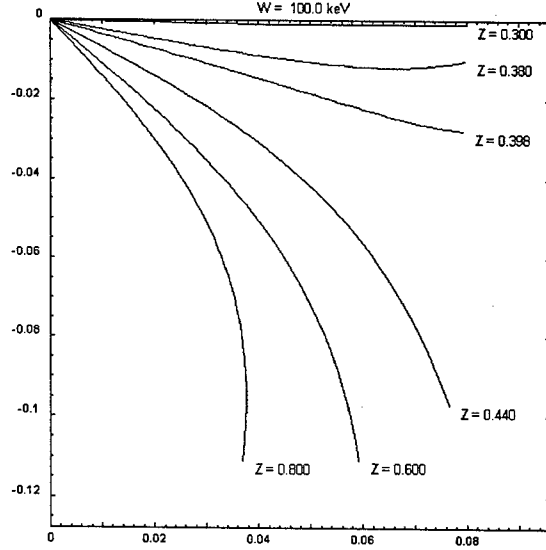


Figure 6: (R, R') emittance plot (m, rd) at different positions along the propagation axis (z) of the solenoid.

SPACE CHARGE

Since the beam is axially symmetric, each beam cross section at a particular point along the z -axis can be described by a large number of equally-charged adjacent rings. This beam description allows very fast calculations of the radial space-charge forces [3].

The examples presented here deal with the evolution in free space of 100 A - 100 keV electron beams starting with two types of current densities :

$$\rho(r) = \rho_0 \{1 - r^2/R_{\max}^2\} : \text{parabolic distribution,}$$

$$\rho(r) = \rho'_0 \{1 + r^2/R_{\max}^2\} : \text{hollow distribution,}$$

$R_{\max} = 5$ cm and no initial divergence.

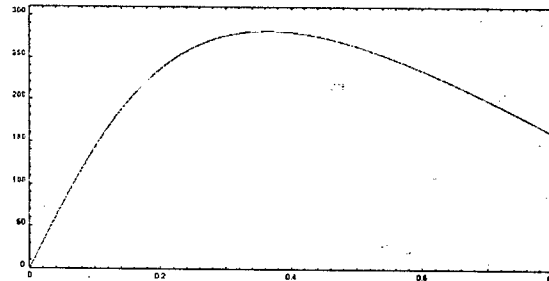


Figure 7: Evolution of the (R, R') unnormalized rms emittance value (mm.mrd) for the parabolic distribution.

Both distributions lead to very similar rms emittance evolutions (see fig. 7 for the parabolic distribution) but fig. 8 and 9 show that the space-charge nonlinearities bend the emittance curve in opposite directions : - towards the R axis for the parabolic distribution, - towards the R' axis for the hollow distribution.

MIXED SYSTEMS

Systems mixing several of these nonlinear forces have been optimized adjusting and combining opposite nonlinear effects to minimize the resulting nonlinearities.

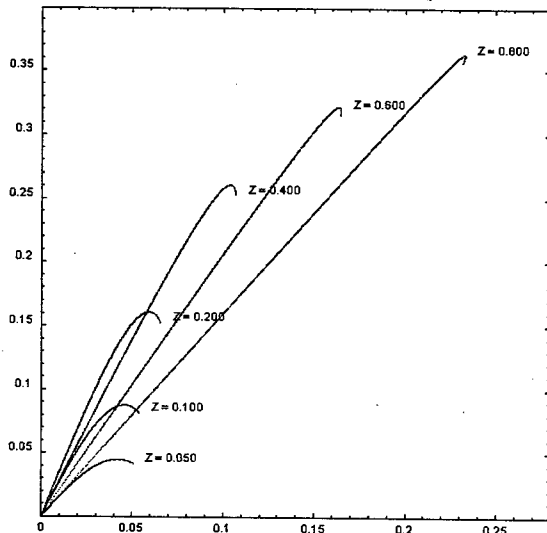


Figure 8: (R,R') emittance plot at different positions along the propagation axis for the parabolic distribution.

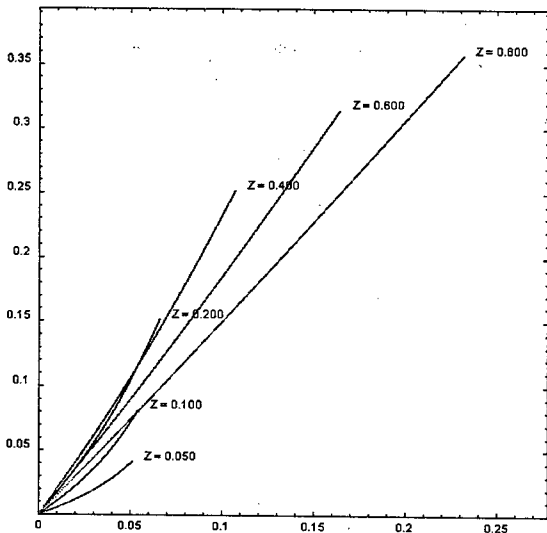


Figure 9: (R,R') emittance plot at different positions along the propagation axis for the hollow distribution.

Diode with solenoid

High emittance growth such as the one shown on fig. 5 will be also observed when a solenoid located downstream the anode of a diode is used in similar conditions. To minimize the final emittance once the diode parameters are fixed, the solenoid parameters (radius, length and strength) and position with respect to the anode must be optimized to minimize the nonlinear effects resulting from both electric and magnetic fields.

Fig. 10 gives an example for the diode parameters used previously. The optimization process on the solenoid parameters leads to a short solenoid (2 cm long) centred on the anode ($z = 9$ cm) in order to have a good overlap of the main electric and magnetic fields nonlinear zones. The solenoid radius (14 cm) and excitation current (300 A, 5 turns) have been adjusted to minimize the emittance growth keeping an efficient beam focalisation.

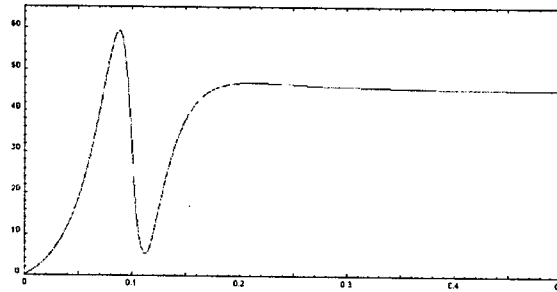


Figure 10: Evolution of the (R,R') unnormalized rms emittance value (mm.mrd) along the diode and solenoid.

Diode with solenoid and space charge

The space-charge nonlinear effects are important at low energy, i.e. in the cathode-anode area of the diode. Looking to fig. 8 and 9 with respect to fig. 3 shows that the addition of the space-charge and electric fields in this region leads to - strong nonlinear effects in the case of parabolic-type distributions, - reduced effects in the case of hollow distributions. A greater emission density at the cathode edge is then favourable to minimize the emittance growth. This is demonstrated on fig. 11 and 12 plotted for a 1 A electron beam evolving in the diode with solenoid studied previously. Calculations with the same parameters show that the ratio of the emittances with and without current at $z = 50$ cm are 1.18, 3.18 and 0.35 for uniform, parabolic and hollow density profiles respectively.

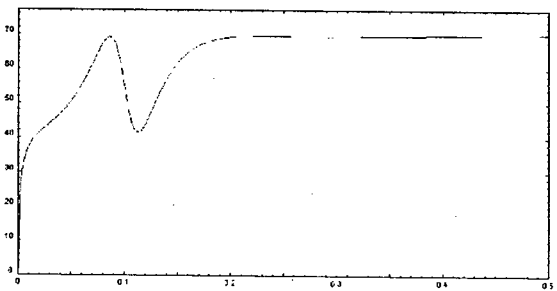


Figure 11: (R,R') unnormalized rms emittance (mm.mrd) $f(z)$ (m), diode with solenoid, 1 A beam, parabolic profile.

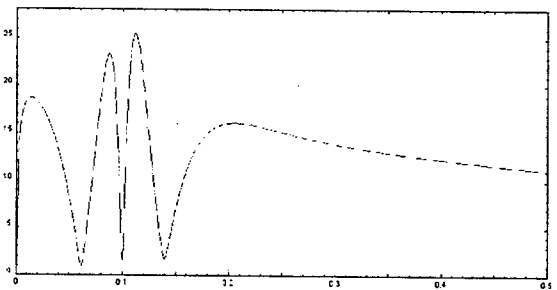


Figure 12: (R,R') unnormalized rms emittance (mm.mrd) $f(z)$ (m), diode with solenoid, 1 A beam, hollow profile.

REFERENCES

- [1] E. Durand, Electrostatique, Masson et Cie, 1966.
- [2] E. Durand, Magnétostatique, Masson et Cie, 1968.
- [3] K.R. Crandall, "A numerical experiment on space-charge effects", LINAC'66 proc., 1966, p. 233.

RESISTIVE-WALL WAKE FOR NON-ULTRARELATIVISTIC BEAMS

Frank Zimmermann, CERN, Geneva, Switzerland; Katsunobu Oide, KEK, Tsukuba, Japan

Abstract

We compute the longitudinal and transverse wake fields for velocities smaller than c , and examine under which conditions the non-relativistic terms become important.

1 INTRODUCTION

Several projects are under construction which aim to produce intense proton or ion beams at energies around 1 GeV, for example, the SNS and J-PARC. One possible performance limitations may arise from the resistive-wall impedance. The conventional treatment of the relativistic wall wake field considers an ultra-relativistic beam; see, e.g., Refs. [1, 2]. Only few papers have attempted to treat the general case. A rare and early example is Ref. [3], but in the ultrarelativistic limit its wake field does not reduce to the conventional expression. In this note we derive the non-ultrarelativistic longitudinal and transverse Green-function wake fields, through first order in the skin depth and second order in $1/\gamma$. We then apply these expressions to four examples.

2 LONGITUDINAL WAKE

We consider a beam pipe of radius b with skin depth $\delta_{\text{skin}} = \sqrt{2/(\mu_0\sigma|\omega|)}$ with conductivity σ at angular frequency ω , and assume that the charge density $\lambda \exp(iks - i\omega t)$ travels at the center of the beam pipe with $\omega = vk$ and $v < c$. Following Chao's treatment of the ultrarelativistic case [1], we introduce the new variable $z = (s - vt)$. Then all quantities have the same dependence $\exp(ikz)$ on s and t . The electric and magnetic fields are related to the scalar potential ϕ and the magnetic vector potential \vec{A} via $\vec{E} = -\nabla\phi - \partial\vec{A}/\partial t$ and $\vec{B} = \nabla \times \vec{A}$. Imposing the Lorentz condition $(\vec{\nabla} \cdot \vec{A} + (1/c^2)\partial\phi/\partial t + \mu_0\sigma\phi) = 0$, the potentials \vec{A} and ϕ fulfill the equations

$$-\Delta\vec{A} + \frac{1}{c^2}\frac{\partial^2\vec{A}}{\partial t^2} + \mu_0\sigma\frac{\partial\vec{A}}{\partial t} = \mu_0(\vec{j} - \sigma\vec{E}). \quad (1)$$

$$-\Delta\phi + \frac{1}{c^2}\frac{\partial^2\phi}{\partial t^2} + \mu_0\sigma\frac{\partial\phi}{\partial t} = \frac{\rho}{\epsilon_0}. \quad (2)$$

Inside the vacuum chamber $\sigma = 0$. The only nonzero field components are E_s , E_r and B_ϕ because of symmetry. We can thus set $A_\phi = 0$. One further degree of freedom allows us to choose $A_r = 0$ as well.

The Lorentz condition relates the two non-vanishing components as $\phi = (c^2k/\omega)A_s$. The potentials must fulfill

$$\frac{1}{r}\frac{\partial}{\partial r}\left(r\frac{\partial A_s}{\partial r}\right) - k_r^2 A_s = -\mu_0 j_s, \quad (3)$$

$$\frac{1}{r}\frac{\partial}{\partial r}\left(r\frac{\partial \phi}{\partial r}\right) - k_r^2 \phi = -\frac{\rho_0}{\epsilon_0}, \quad (4)$$

where $k_r^2 = (k^2 - k_0^2) = k_0^2/(\beta^2\gamma^2) > 0$ with $k_0 = \omega/c$. The right-hand side is zero except for inside the beam. Outside the beam, $A_s = \tilde{A}_s e^{ikz}$ is written as $\tilde{A}_s = pI_0(k_r r) + qK_0(k_r r)$, where the coefficient q is determined by the source current, and p by the surface condition at $r = b$. First we compute q . The source term j_s on the right hand side of (3) is $-\mu_0\lambda v$. The Green function for a point source is $-\ln r/(2\pi)$; the modified Bessel function K_0 expands as $-\ln z$. This yields $q = -\mu_0\lambda v/(2\pi)$. If (r, ϕ, z) are right-handed, the fields are

$$B_\phi = -pk_r I_1(k_r r) + qk_r K_1(k_r r), \quad (5)$$

$$E_s = i\omega\left(1 - \frac{k^2}{k_0^2}\right)(pI_0(k_r r) + qK_0(k_r r)). \quad (6)$$

$$E_r = -\frac{c^2 k k_r}{\omega}(pI_1(k_r r) - qK_1(k_r r)), \quad (7)$$

where we have used $I'_0 = I_1$ and $K'_0 = -K_1$. The wall is characterized by $\vec{j} = \sigma\vec{E}$ and $\rho = 0$. For $b \gg \delta_{\text{skin}}$, inside the wall we have

$$-\frac{\partial^2 E_s}{\partial r^2} \approx -\frac{1}{r}\frac{\partial}{\partial r}\left(r\frac{\partial E_s}{\partial r}\right) = (i\mu_0\sigma\omega - k_r^2)E_s, \quad (8)$$

with the solution $E_s = E_{s0} \exp(-\lambda r)$, where $\lambda^2 = -(i\mu_0\sigma\omega - k_r^2) = \lambda_0^2 + k_r^2$ and $\lambda_0 \equiv (1 - i\text{sgn}(\omega))/\delta_{\text{skin}}$, or

$$\lambda \approx \lambda_0 \left(1 + \frac{k_r^2}{2\lambda_0^2}\right) = \lambda_0 \left(1 + i\text{sgn}(\omega)\frac{k_r^2 \delta_{\text{skin}}^2}{4}\right). \quad (9)$$

The second term represents a non-relativistic effect. We will neglect it, since it is of the order δ_{skin}^2 .

The relationship between B_ϕ and E_s follows from $\vec{\nabla} \times \vec{E} = -\partial\vec{B}/\partial t$ and $\vec{\nabla} \cdot \vec{E} = 0$ as $i\omega\tilde{B}_\phi = \tilde{E}_s(1 - i\text{sgn}(\omega))/\delta_{\text{skin}}$. Inserting the expressions for B_ϕ and E_s evaluated at $r = b$ and solving for p we get

$$p = -\frac{(1 - i\text{sgn}(\omega))k_r K_0 + \delta_{\text{skin}}k_0^2 K_1}{(1 - i\text{sgn}(\omega))k_r I_0 - \delta_{\text{skin}}k_0^2 I_1}q, \quad (10)$$

where all Bessel functions have the argument $x \equiv k_r b$. The magnetic vector potential $A_s = \tilde{A}_s e^{ikz}$ becomes

$$\tilde{A}_s = -\frac{\mu_0\lambda v}{2\pi}\left[K_0(k_r r) - \frac{(1 - i\text{sgn}(\omega))K_0(x) + \delta_{\text{skin}}k_0^2 K_1(x)}{(1 - i\text{sgn}(\omega))I_0(x) - \delta_{\text{skin}}k_0^2 I_1(x)}I_0(k_r r)\right]. \quad (11)$$

Computing from this the longitudinal electric field $E_s = \tilde{E}_s e^{ikz}$ as $\tilde{E}_s = -i\omega k_r^2/k_0^2 \tilde{A}_s$, and expanding in k_r and

δ_{skin} , we obtain

$$\tilde{E}_s(k) \approx \frac{\mu_0 \lambda v c k}{2\pi} \left[\frac{(\text{sgn}(k) - i) \delta_{\text{skin}}^{(0)}}{2b} \left(1 - \frac{1}{4} \frac{k_r^2}{k^2} - \frac{k_r^2(2b^2 - r^2)}{4} \right) - i \frac{k_r^2}{k^2} \ln \frac{r}{b} \right], \quad (12)$$

where $\delta_{\text{skin}}^{(0)}$ refers to the skin depth at angular frequency ck , and we have assumed $|k| > k_r$. In the ultrarelativistic limit $k_r \rightarrow 0$, the term depending on $\delta_{\text{skin}}^{(0)}$ agrees with the result (2.77) in Ref. [1]. If $k_r \neq 0$ the electric field corresponding to the resistive-wall wake depends not only on the longitudinal distance z from the source, but also on the radial position r . The term independent of δ_{skin} describes the effect of space charge.

The longitudinal impedance per unit length is related to $\tilde{E}_s(k)$ as $\Pi(k) = -\tilde{E}_s(k)/j_s$ where $k = \sqrt{k_r^2 + \omega^2/c^2}$. From the impedance we compute the longitudinal Green function wake per unit length as $\dot{o}'(z) = -v/(2\pi j_s) \int_{-\infty}^{\infty} \tilde{E}_s(k) e^{ikz} k$, where, as before, $j_s = \lambda v$. If $\dot{o}'(z) > 0$ the wake field decelerates. Keeping only the res.-wall terms, which depend on δ_{skin} , from (12) we get

$$\dot{o}'(z) \approx -\frac{c^2 \mu_0}{4\pi^2} \sqrt{\frac{\pi}{\mu_0 \sigma c}} \frac{1}{2b} \beta (\text{sgn}(z) - 1) \left(-\frac{\gamma^2 - 5/4}{(\gamma^2 - 1)|z|^{3/2}} - \frac{15}{16} \frac{b^2}{(\gamma^2 - 1)|z|^{7/2}} \right). \quad (13)$$

In the ultra-relativistic limit this reduces to the familiar

$$\dot{o}'(z) \approx \frac{c^2 \mu_0}{4\pi^2} \sqrt{\frac{\pi}{\mu_0 \sigma c}} \frac{1}{2b} (\text{sgn}(z) - 1) \frac{1}{|z|^{3/2}}. \quad (14)$$

3 TRANSVERSE WAKE

For a transverse wake, every quantity, \sim , has the dependence $\sim \exp(i\phi + iks - i\omega t) = \sim \exp(i\phi + ikz)$ on s, ϕ and t . In addition, all field components are nonzero, and we can no longer assume that A_r and A_ϕ are zero. In cylindrical coordinates we find

$$\begin{aligned} -\frac{1}{r} \frac{\partial}{\partial r} \left[r \frac{\partial A_r}{\partial r} \right] + \frac{2i}{r^2} A_\phi + \left[\frac{1}{r^2} + k_r^2 \right] A_r &= \mu_0 j_r \\ -\frac{1}{r} \frac{\partial}{\partial r} \left[r \frac{\partial A_\phi}{\partial r} \right] + \left[\frac{1}{r^2} + k_r^2 \right] A_\phi - \frac{2i}{r^2} A_r &= \mu_0 j_\phi \\ -\frac{1}{r} \frac{\partial}{\partial r} \left[r \frac{\partial A_s}{\partial r} \right] + \left[\frac{1}{r^2} + k_r^2 \right] A_s &= \mu_0 j_s \\ -\frac{1}{r} \frac{\partial}{\partial r} \left[r \frac{\partial \phi}{\partial r} \right] + \left[\frac{1}{r^2} + k_r^2 \right] \phi &= \frac{\rho_0}{\epsilon_0}. \end{aligned}$$

The transverse components are decoupled by introducing $A_+ \equiv A_r + iA_\phi$, $A_- \equiv A_r - iA_\phi$, and $j_\pm \equiv j_r \pm j_\phi$, which yields

$$\frac{1}{r} \frac{\partial}{\partial r} \left(r \frac{\partial A_\pm}{\partial r} \right) - \left(\frac{(1 \pm)^2}{r^2} + k_r^2 \right) A_\pm = -\mu_0 j_\pm. \quad (15)$$

The original radial and azimuthal vector components are $A_r = (A_+ + A_-)/2$ and $A_\phi = (A_+ - A_-)/(2i)$.

We only consider the dipole wake, $\text{sgn}(k) = \pm 1$. Outside the beam, the solution for each component is again a superposition of two Bessel functions, i.e., for $\text{sgn}(k) = 1$,

$$\tilde{A}_+^{(1)} = p_+^{(1)} I_2(k_r r) + q_+^{(1)} K_2(k_r r) \quad (16)$$

$$\tilde{A}_-^{(1)} = p_-^{(1)} I_0(k_r r) + q_-^{(1)} K_0(k_r r) \quad (17)$$

$$\tilde{A}_s^{(1)} = p_s^{(1)} I_1(k_r r) + q_s^{(1)} K_1(k_r r) \quad (18)$$

$$\phi = p_0^{(1)} I_1(k_r r) + q_0^{(1)} K_1(k_r r). \quad (19)$$

and similarly for $\text{sgn}(k) = -1$, for which I_0 (K_0) is exchanged with I_2 (K_2). The coefficients of the Bessel functions for $\text{sgn}(k) = -1$ are called $p_+^{(-1)}$, $q_+^{(-1)}$, etc., and, by symmetry, they are equal to the corresponding coefficients for $\text{sgn}(k) = 1$, e.g., $p_0^{(-1)} = p_0^{(1)}$ and $p_+^{(-1)} = p_-^{(1)}$. Considering now a perturbation of the form $\cos \phi = (e^{i\phi} + e^{-i\phi})/2$, we obtain

$$\begin{aligned} A_r &= (p_+ I_2 + q_+ K_2 + p_- I_0 + q_- K_0) \cos \phi e^{ikz} \\ A_\phi &= (p_+ I_2 + q_+ K_2 - p_- I_0 - q_- K_0) \sin \phi e^{ikz} \\ A_s &= (p_s I_1 + q_s K_1) \cos \phi e^{ikz} \\ \phi &= (p_0 I_1 + q_0 K_1) \cos \phi e^{ikz}, \end{aligned}$$

where the argument of the Bessel functions is $(k_r r)$, and we have dropped the superindex '(1)' of all coefficients.

The Lorentz condition yields the two equations

$$\frac{k_r}{2} p_+^{(1)} + \frac{k_r}{2} p_-^{(1)} + ik p_s^{(1)} - i \frac{\omega}{c^2} p_0^{(1)} = 0 \quad (20)$$

$$-\frac{k_r}{2} q_+^{(1)} - \frac{k_r}{2} q_-^{(1)} + ik q_s^{(1)} - i \frac{\omega}{c^2} q_0^{(1)} = 0. \quad (21)$$

To determine these coefficients, we again consider the source terms. As before, $j_\phi = j_r = 0$ and $j_s = v\rho$. But the current source j_s is now displaced by a small transverse distance from the center of the pipe, so as to generate a dipole moment. The free-space Green function for the dipole current component is $(-\mu_0 \lambda v/r)/(2\pi)$, and the dipole charge source is $(-\lambda/r)/(2\pi\epsilon_0)$. In the transverse direction $j_+ = j_- = j_r = j_\phi = 0$.

By equating the source terms and their corresponding Green functions with the expansions of K_1 , K_0 or K_2 in the expressions for the vector potentials we find that $q_s = -\mu_0 \lambda v/(2\pi)(k_r)$, $q_0 = c^2 k/(\omega) q_s$, $q_+ = 0$, $q_- = 0$. Again we invoke the wall boundaries to determine the remaining coefficients. If $|\lambda_0| \gg 1/b$ and $|\lambda_0| \gg k$, we find the same condition as for $\text{sgn}(k) = 0$: $i\omega B_\phi = E_s(1 - i\text{sgn}(\omega))/\delta_{\text{skin}} = \lambda_0 E_s$. From Faraday-Maxwell's law we obtain a second boundary condition: $-i\omega B_s \approx \lambda_0 E_\phi$. The longitudinal and azimuthal field components are related to the potentials, $A_r = \tilde{A}_r \cos \phi e^{ikz}$, etc., via

$$B_\phi = \left(ik \tilde{A}_r - \frac{\partial}{\partial r} \tilde{A}_z \right) \cos \phi e^{ikz} \quad (22)$$

$$B_s = \left(\frac{1}{r} \tilde{A}_r + \frac{\partial \tilde{A}_\phi}{\partial r} + \frac{\tilde{A}_\phi}{r} \right) \sin \phi e^{ikz} \quad (23)$$

$$E_\phi = \left(\frac{1}{r} \tilde{\phi} + i\omega \tilde{A}_\phi \right) \sin \phi e^{ikz} \quad (24)$$

$$E_s = \left(-ik\tilde{\phi} + i\omega \tilde{A}_s \right) \cos \phi e^{ikz}, \quad (25)$$

so that the boundary conditions at $r = b$ become

$$-\omega k \tilde{A}_r - i\omega \partial \tilde{A}_s / \partial r = \lambda_0 (-ik\tilde{\phi} + i\omega \tilde{A}_s) \quad (26)$$

$$\lambda_0 (\tilde{\phi}/r + i\omega \tilde{A}_\phi) = -i\omega (\tilde{A}_r/r + \partial \tilde{A}_\phi / \partial r + \tilde{A}_\phi/r). \quad (27)$$

The remaining gauge freedom allows for the choice $p_0 = (c^2 k/\omega) p_s$. Using this gauge, we can solve the two equations (26) and (27) together with the Lorentz conditions (20) and (21), so as to obtain an expression relating p_s and q_s . Inserting this into the formula for $E_s = \tilde{E}_s \cos \phi e^{ikz}$ and expanding to first order in δ_{skin} and up to second order in k_r , dropping powers of order higher than 2 in r , we find

$$\begin{aligned} \tilde{E}_s(k) &= -i\omega \frac{k_r^2}{k_0^2} \frac{\mu_0 \lambda v}{2\pi} dk_r \left[K_1(k_r r) + \frac{p_s}{q_s} I_1(k_r r) \right] \\ &\approx -ckd \frac{\mu_0 \lambda v}{2\pi} \frac{1}{b^3 r} \left[\delta_{\text{skin}}^{(0)} \left(r^2 - \frac{1}{4} \frac{k_r^2}{k^2} r^2 - \frac{b^2 k_r^2}{4} r^2 \right) \right. \\ &\quad \left. (\text{sgn}(\omega) - i) + i \text{sgn}(k) b \frac{k_r^2}{k^2} (b^2 - r^2) \right]. \end{aligned} \quad (28)$$

The transverse wake is now obtained using the Panofsky-Wenzel theorem $e(E_r + (\vec{v} \times \vec{B})_r) = \int (\partial_s / \partial r) dz$, which, thanks to $\omega = vk$, is valid as in the relativistic case, and also implies $Z_\perp(k) = Z_{||}(k)/k$. This gives

$$\begin{aligned} \tilde{Z}_\perp &\approx \frac{\mu_0 i d e c \lambda v}{2\pi} \frac{1}{b^3} \left[\delta_{\text{skin}}^{(0)} \left(1 - \frac{1}{4} \frac{k_r^2}{k^2} - \frac{b^2 k_r^2}{4} \right) \right. \\ &\quad \left. (\text{sgn}(\omega) - i) - i \text{sgn}(\omega) b \frac{k_r^2}{k^2} \left(1 + \frac{b^2}{r^2} \right) \right] \end{aligned} \quad (29)$$

The transverse impedance per unit length is $Z_\perp(k) = -i \tilde{Z}_\perp / (e \lambda v d)$. In the ultrarelativistic limit, $k_r \rightarrow 0$, this agrees with the classical result of [1]. The transverse Green function wake per unit length is $W_1(z) = -1/(2\pi e \lambda d) \int_{-\infty}^{\infty} \tilde{Z}_\perp(k) e^{ikz} dk$. If $W_1(z) < 0$, the wake is defocusing. Dropping the space-charge term, from (29) the res.-wall wake function becomes

$$W_1(z) \approx \frac{\sqrt{\pi} \mu_0 c^{3/2}}{4\pi^2 b^3 \sigma^{1/2}} \beta \frac{3b^2 + 4(4\gamma^2 - 5)z^2}{8(\gamma^2 - 1)|z|^{5/2}} (\text{sgn}(z) - 1). \quad (30)$$

In the ultra-relativistic limit this reduces to

$$W_1(z) \approx \frac{\sqrt{\pi} \mu_0 c^{3/2}}{2\pi^2 b^3 \sigma^{1/2}} \frac{1}{|z|^{1/2}} (\text{sgn}(z) - 1). \quad (31)$$

4 APPLICATIONS

Typical parameters of several low-energy proton or ion accelerators are listed in Table 1. For each case we consider a stainless chamber with $\sigma = 1.4 \times 10^6 \Omega^{-1} \text{m}^{-1}$. The longitudinal wake function at the chamber wall are

shown in Fig. 1, the transverse in Fig. 2. The differences between the ultra-relativistic limit, (14) and (31), and the more accurate formulae, (13) and (30), are significant for $z > -b/\sqrt{10\gamma^2 - 7}$ or $\gamma < 3$. The energy decreases from SNS, over J-PARC and PS booster to an ECR source. The latter also illustrates the effect of a smaller pipe radius b .

Table 1: Example Parameters

	SNS	J-PARC	PS booster	ECR
γ	2.1	1.4	1.05	1.003
σ_z	25 m	12 m	26 m	100 m
σ_r	2 cm	2 cm	3 mm	4 mm
b	8 cm	12.5 cm	30 cm	3 cm
b	1.5×10^{14}	4×10^{13}	1.2×10^{12}	2×10^{13}

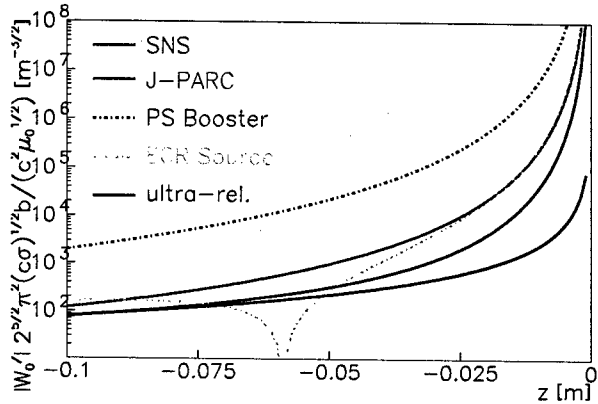


Figure 1: Longitudinal wake $|W'_0| [2^{5/2} \pi^2 b \sqrt{\sigma c} / (c^2 \mu_0)]$ at $r = b$ vs. distance z in m, according to (13) [colored] and in the ultra-relativistic limit (14) [black solid].

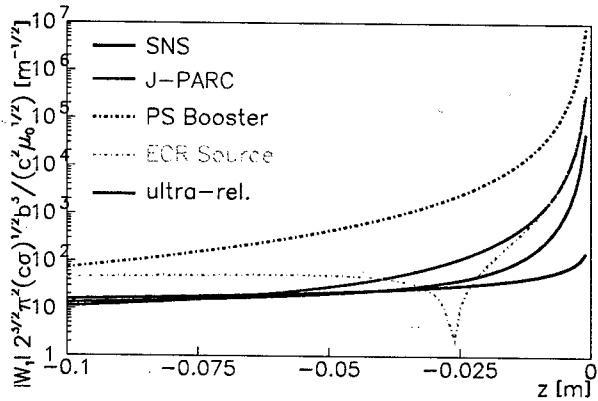


Figure 2: Transverse r. w. wake $|W_1| [2^{3/2} \pi^2 b^3 \sqrt{\sigma c} / (c^2 \mu_0)]$ vs. distance z in m, according to (30) [colored] and in the ultra-relativistic limit (31) [black solid].

5 REFERENCES

- [1] A. Chao, "Physics of Collective Beam Instabilities in High Energy Accelerators," J. Wiley (1993).
- [2] B. Zotter, S. Heifets, "Impedances and Wakes in High-Energy Particle Accelerators," World Scientific (1998).
- [3] P. Morton, V.K. Neil, A. Sessler, J. Appl. Phys. 37, 3875 (1966).

EFFECTS OF SPACE CHARGE ON DECOHERENCE IN ION BEAMS

O. Boine-Frankenheim, I. Hofmann, Y. Liu, G. Rumolo*, GSI, Darmstadt, Germany

A. Al-Khateeb, Yarmouk University, Irbid, Jordan

Abstract

This paper studies dipolar and quadrupolar decoherence of a bunch in presence of space charge. The centroid of a bunch displaced transversely or longitudinally decoheres due to nonlinearities that cause phase space filamentation and mixing. Here we show that space charge can inhibit decoherence and keep the beam centroid oscillations undamped over long times. This feature complicates the detection of echoes for diagnostics purposes. An echo requires in fact a fully decohered beam to show up as a coherent signal at later times than the excitations. Results are qualitatively compared with experiments in the GSI synchrotron SIS.

INTRODUCTION

The question of longitudinal decoherence of the collective motion of a bunch of charged particles in presence of nonlinearities due to a sinusoidal bucket and space charge is addressed in this paper.

Experimental observations are described in Section II. Section III shows a simplified calculation of decoherence due to nonlinearity and space charge. Semi-analytical expressions for the evolution of the bunch longitudinal centroid and rms-size (first two moments of the detailed longitudinal particle distribution, on which alone we assume the space charge forces to depend) with the non-linearity alone are presented in Section IV. These expressions can then be used as starting point of a recursive numerical procedure, which recalculates the single particle equation of motion with space charge and thus converges to the final profile of longitudinal centroid and rms-size evolution with space charge included after a few iterations.

OBSERVATION OF UNDAMPED CENTROID MOTION IN SIS

Longitudinal bunched beam dipole oscillations are observed during SIS operation, if there is an energy error between the injected beam from the UNILAC and the rf frequency setting in SIS. For low beam intensities the induced bunch center dipole oscillation is damped before the start of the acceleration ramp. For high beam intensities or electron cooled beams the dipole oscillation survive during ramping. For example, the waterfall plot in Fig. 1 shows the persistent dipole oscillation for $0.5 \times 10^{10} C^{6+}$ ions per bunch with an estimated equivalent coasting beam momentum spread $\Delta p/p|_{FWHM} \sim 5 \times 10^{-4}$. The estimated

frequency error is $\Delta f/f \sim 1 \times 10^{-3}$ (corresponding to $\approx 2\sigma_{z0}$ kick in the longitudinal phase space)

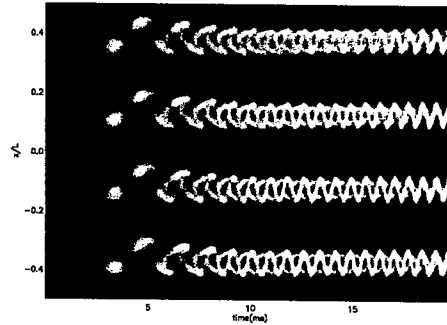


Figure 1: Observed persistent dipole oscillations of four bunches in SIS as function of time.

DECOHERENCE WITH SPACE CHARGE

A bunch with an initial longitudinally offset from the bucket center will perform synchrotron oscillations around it. If all particles have the same synchrotron tune, the centroid motion is expected to be harmonic. However, if the beam contains a spread of tunes, the motion will decohere since the individual synchrotron phases of the particles disperse. As the longitudinal phase space of the beam spreads to an annulus, the observed centroid of the beam will show a decaying oscillation and its rms-size will grow. Space charge can inhibit the centroid decoherence and thus keep the oscillations undamped by local compensation of the synchrotron detuning with amplitude.

The synchrotron frequency spread as a function of the single particle oscillation amplitude $\hat{\phi}$ in a RF bucket is (see e.g. Ref. [1])

$$\omega_s(\hat{\phi}) = \frac{\pi\omega_s(0)}{2K(\sin^2 \frac{\hat{\phi}}{2})} \approx \omega_s(0) \left(1 - \frac{\hat{\phi}^2}{16}\right), \quad (1)$$

Assuming a parabolic bunch form, space charge induces a shift $\Delta\omega$ of the incoherent frequency distribution. This shift can be related to the space charge parameter [2] $\Sigma = 2K_L z_m / \epsilon_L^2$ (longitudinal emittance ϵ_L^2 and perveance K_L , bunch half-length z_m)

$$\frac{\Delta\omega}{\omega_0} = \frac{1}{4}\Sigma \quad (2)$$

Damping of dipole modes is only possible if the coherent dipole frequency $\Omega = \omega_s(\bar{\phi})$ (amplitude of the dipole mode $\bar{\phi}$) that is not affected by space charge, lies within the incoherent frequency distribution. Persistent dipole oscillations

* G.Rumolo@gsi.de

after kicking a beam to a finite phase $\bar{\phi}$, are possible if space charge shifts the frequency distribution towards sufficiently low frequencies. Below transition energy $\Omega > \omega_0 - \Delta\omega$ yields the criterion

$$\frac{\Delta\omega}{\omega_0} > \frac{\bar{\phi}^2}{16} \Rightarrow \Sigma > \frac{\bar{\phi}^2}{4}. \quad (3)$$

This criterion is consistent with the SIS observation ($\Sigma \approx 0.4$). A similar condition was independently obtained in Ref. [3]. It is interesting to note, that above transition energy or for negative Σ (inductive impedance) one obtains

$$|\Sigma| > \frac{1}{4} (\hat{\phi}_m^2 - \bar{\phi}^2) \quad (4)$$

with the parabolic bunch half-length $\hat{\phi}_m^2$.

ITERATIVE PROCEDURE

We can express the centroid and rms-size evolutions through the integrals:

$$\bar{z}(t) = \int_{\mathbb{R}^2} z(\hat{z}, \hat{\delta}, \bar{z}, \sigma_z) \rho(\hat{z}, \hat{\delta}) d\hat{z} d\hat{\delta} \quad (5)$$

$$\sigma_z(t) = \int_{\mathbb{R}^2} z^2(\hat{z}, \hat{\delta}, \bar{z}, \sigma_z) \rho(\hat{z}, \hat{\delta}) d\hat{z} d\hat{\delta} - \bar{z}^2(t)$$

where $\rho(\hat{z}, \hat{\delta})$ is the initial particle distribution in the longitudinal phase space, $\rho(\hat{z}, \hat{\delta}) = \frac{1}{2\pi\sigma_{z0}\sigma_{\delta0}} \exp\left[-\frac{1}{2}\left(\frac{(\hat{z}-z_0)^2}{\sigma_{z0}^2} + \frac{\hat{\delta}^2}{\sigma_{\delta0}^2}\right)\right]$, and $z(\hat{z}, \hat{\delta}, \bar{z}, \sigma_z)$ is the solution of the single particle equations of motion in presence of space charge

$$\begin{cases} \dot{z} = -\eta c \delta \\ \dot{\delta} = \text{sgn}(\eta) \frac{eV_m}{p_0 2\pi R_0} \sin\left(\frac{\omega_{rf} z}{c}\right) + \mathcal{F}_{sc}(z - \bar{z}, \sigma_z) \end{cases} \quad (6)$$

The problem consists of a very complicated integro-differential set of equations having $\bar{z}(t)$ and $\sigma_z(t)$ as unknowns with initial conditions $\bar{z}(t=0) = z_0$ and $\sigma_z(t=0) = \sigma_{z0}$. We solve it by iterations following the procedure that we describe here below. As first step, we neglect space charge. Using now Eqs. (5) with the solution of the equation of motion (6) in nonlinear regime and without driving term leads us to the expressions for the bunch centroid and rms-size evolutions in absence of space charge,

$$\begin{aligned} \bar{z}(t) &= -\frac{1}{2\pi\sigma_{z0}\sigma_{\delta0}} \text{Re} \left[\frac{i \cdot e^{i\omega_s t}}{\sqrt{-\frac{1}{\pi} \left(\frac{1}{2\sigma_{\delta0}^2} + i \cdot \frac{p_0 |\eta| c k t}{2} \right)}} \cdot \right. \\ &\quad \left. \cdot \int_{\mathbb{R}} e^{-i \cdot \frac{eV_m c k}{2\pi R_0 \omega_{rf}} C(\hat{z}) t - \frac{(\hat{z}-z_0)^2}{2\sigma_{z0}^2}} d\hat{z} \right] \\ \sigma_z^2(t) + \bar{z}^2(t) &= \sigma_{z0}^2 + \frac{z_0^2}{2} - \frac{1}{4\pi\sigma_{z0}\sigma_{\delta0}} \end{aligned} \quad (7)$$

$$\begin{aligned} &\cdot \text{Re} \left[\int_{\mathbb{R}} \hat{z}^2 e^{-\frac{(\hat{z}-z_0)^2}{2\sigma_{z0}^2} - 2i \cdot \frac{keV_m c}{2\pi R_0 \omega_{rf}} C(\hat{z}) t} d\hat{z} \right. \\ &\quad \left. \cdot \frac{i \cdot e^{2i\omega_s t}}{\sqrt{-\frac{1}{\pi} \left(\frac{1}{2\sigma_{\delta0}^2} + i \cdot p_0 |\eta| c k t \right)}} + \frac{\eta^2 c^2}{\omega_s^2} \cdot \right. \\ &\quad \left. \cdot \int_{\mathbb{R}} e^{-\frac{(\hat{z}-z_0)^2}{2\sigma_{z0}^2} - 2i \cdot \frac{keV_m c}{2\pi R_0 \omega_{rf}} C(\hat{z}) t} d\hat{z} \cdot \frac{e^{2i\omega_s t}}{\frac{1}{\sigma_{\delta0}^2} + 4i \cdot p_0 |\eta| c k t} \right] \quad (8) \end{aligned}$$

where $C(\hat{z}) = 1 - \cos\left(\frac{\omega_{rf} \hat{z}}{c}\right)$.

Table 1: SIS parameters used in this study.

variable	symbol	value
Circumference	$2\pi R_0$	216 m
Revolution frequency	ω_0	8.7×10^6 rad/s
Relativistic gamma	γ	3.129
Chamber size	a, b	$10 \times \sigma_{x,y}$
Bunch population	N_b	10^{10} C ⁶⁺
Rms bunch length	σ_{z0}	2 m
Rms energy spread	$\sigma_{\delta0}$	5.9×10^{-4}
Slip factor	η	-0.0665
Synchrotron tune	Q_{s0}	6.8×10^{-4}
Initial kick amplitude	z_0	4 m
Maximum voltage	V_m	32 kV
Harmonic number	h	4

Figures 2 and 3 (blue lines) show longitudinal centroid and rms-size evolutions as resulting from the expressions (7) and (8) for SIS parameters in Table I. Due to the sinusoidal bucket the centroid oscillation, which would have survived forever undamped in the case of purely linear restoring force, significantly decoheres after a few synchrotron periods. At the same time the bunch longitudinal rms-size grows and tends to level off at the asymptotic value

$$\sigma_z(t \rightarrow \infty) = \sqrt{\sigma_{z0}^2 + \frac{z_0^2}{2}},$$

as results from Eq. (8) when taking its limit as $t \rightarrow \infty$. Our iterative procedure to evaluate the effect of space charge simply consists in using these evolutions back in the single particle equation of motion, find new solutions for a set of initial conditions and thus recalculate the integrals (5). After only two iterations the method converges to the evolutions depicted in Figs. 2 and 3 (red lines). If we evaluate the Σ factor for the parameters in Table I, we easily find out that it amounts to 0.2 compared to a kick phase of about $\pi/7$. Therefore we expect a similar evolution to that of the experiment described in Sec. I. As predicted by the above criterion (3), the damping of the centroid oscillation is no longer to be observed. The bunch longitudinal rms-size still increases even if its growth seems to stop at a lower level than without space charge.

The effect of space charge on longitudinal quadrupole oscillations can also be studied with our method. To excite

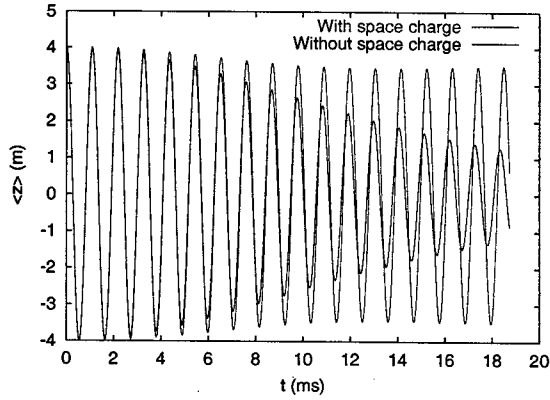


Figure 2: Decoherence of the centroid motion for a longitudinally displaced bunch due to the sinusoidal bucket nonlinearity with (red) and without (blue) space charge effects.

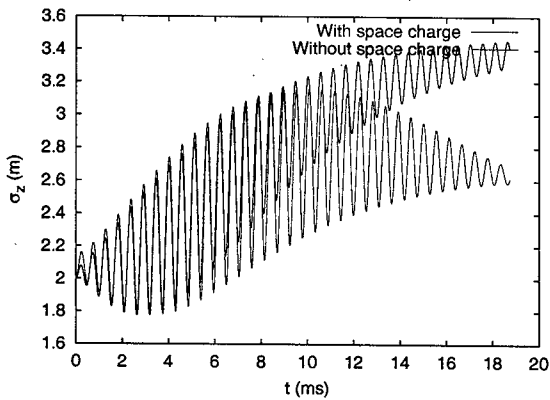


Figure 3: Bunch rms-size evolution for a longitudinally displaced bunch due to the sinusoidal bucket nonlinearity with (red) and without (blue) space charge effects.

a pure quadrupole oscillation, we only need to unmatch the bunch and set the initial longitudinal offset of the bunch, z_0 , to 0.

In this case, no centroid oscillation will be observed. The σ_z will still evolve according to Eq. (8), where this time it will be $\bar{z}(t) = 0$ and, because of the unmatched situation, σ_{z0}^2 on the first line must be replaced by $\sigma_{z0}^2/2 + \eta^2 c^2 \sigma_{\delta 0}^2 / (2\omega_{s0}^2)$. The evolution of the bunch rms-size is depicted in Fig. 4 (blue line). We have chosen to simulate an SIS bunch with a momentum spread which is scaled by a factor 0.8 with respect to the value reported in the Table I (matched value). A smaller momentum spread than the matched value would cause the bunch to shrink initially and then oscillate around the new $\sigma_z^{(match)} = \sigma_{\delta 0} |\eta| c / \omega_s = 0.8 \sigma_{z0}$ if no longitudinal detuning were included in the analysis. It is clear that, owing to the bucket nonlinearity, decoherence appears in the quadrupole oscillation, too. The asymptotic value of the bunch rms-size, which is eventually reached after the oscillation at twice the synchrotron

frequency has fully died out, will be:

$$\sigma_z(t \rightarrow \infty) = \sqrt{\frac{\sigma_{z0}^2}{2} + \frac{\eta^2 c^2 \sigma_{\delta 0}^2}{2\omega_{s0}^2}}$$

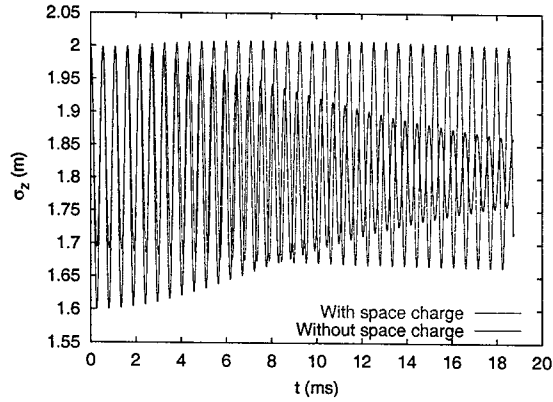


Figure 4: Bunch rms-size evolution for a longitudinally unmatched bunch due to the sinusoidal bucket nonlinearity with (red) and without (blue) space charge effects.

Just like in the case of the pure dipole oscillation, space charge causes the quadrupole oscillation to be undamped. Figure 4 (red line) shows the persistent oscillation as evaluated with the iteration method.

To cross-check the validity of the obtained analytical expressions as well as of the iterative procedure which we have used above, we have also carried out macroparticle simulations using the HEADTAIL code [4] and Vlasov simulations. The results in terms of bunch centroid and rms-size evolution agree very well with the iterative procedure.

CONCLUSIONS

Below transition even relatively low space charge suppresses the decoherence of longitudinal dipole oscillations. Therefore, in contrast to the recently described collective coasting beam echoes [5], collective bunched beam echoes might be difficult to observe.

REFERENCES

- [1] D. A Edwards, M. J. Syphers, *An Introduction to the Physics of High Energy Accelerators*, Wiley, 1993
- [2] G. Franchetti, I. Hofmann, and G. Rumolo, Phys. Rev. ST Accel. Beams 3, 084201 (2000)
- [3] A. Hofmann, F. Pedersen, IEEE Trans. Nucl. Sci. NS-26, No. 3, p.3526
- [4] G. Rumolo and F. Zimmermann, SL-Note-2002-036 (2002).
- [5] A. Al-Khateeb *et al.*, Phys. Rev. ST Accel. Beams 6, 014205 (2003)

SPACE CHARGE EFFECTS DURING THE INJECTION PERIOD OF THE KEK PS MAIN RING

S. Igarashi, T. Miura, E. Nakamura, Y. Shimosaki, M. Shirakata, K. Takayama and T. Toyama,
KEK 1-1 Oho, Tsukuba, Ibaraki 305-0801, Japan

Abstract

Space charge effects during the injection period of the 12 GeV main ring of the KEK proton synchrotron have been studied. Measurement of the transverse beam profiles using flying wires has revealed a characteristic temporal change of the beam profile within a few milliseconds after injection. Horizontal emittance growth was observed when the horizontal tune was close to the integer. The effect was more enhanced for higher beam intensity and could not be explained with the injection mismatch. Resonance created by the space charge field was the cause of the emittance growth. A multiparticle tracking simulation program, ACCSIM, taking account of space charge effects has qualitatively reproduced the beam profiles.

INTRODUCTION

The beam intensity of the KEK PS 12 GeV main ring has significantly increased since the K2K neutrino oscillation experiment started. Efforts to minimize beam loss have been continuously made. One of the issues is to reduce the loss during the injection period. Nine bunches of protons with the kinetic energy of 500 MeV are injected with the interval of 50 ms. About 30% of protons are lost during the injection period of 510 ms. The highest operating intensity of the main ring is 1.4×10^{12} protons per bunch at injection. The nominal operational tune has been optimized to be 7.15 and 5.25 for the horizontal and vertical tune respectively. The main ring has a circumference of 340 m and four-fold symmetry. A super period consists of seven FODO cells.

The incoherent tune shift is estimated to be 0.5 for the highest operating intensity without considering the effect of the image field or dispersion. The large value of the space charge tune shift is partly due to a small emittance of the injection beam. Emittance dilution and particle loss would occur under the circumstances. It is empirically known that emittance dilution observed after injection to the main ring depends on the beam intensity and tune.

PROFILE MEASUREMENTS

Flying wire transverse beam profile monitors have been operated at the main ring. An analysis procedure has recently been established to reconstruct the beam profile that quickly changes with a time scale of 1 ms or less [1].

When the injection beam intensity was set to 8.0×10^{11} protons, the beam profile 0.2 ms to 2.8 ms after injection were reconstructed as in figure 1. The horizontal tune in this case was 7.05 which was not the nominal operational

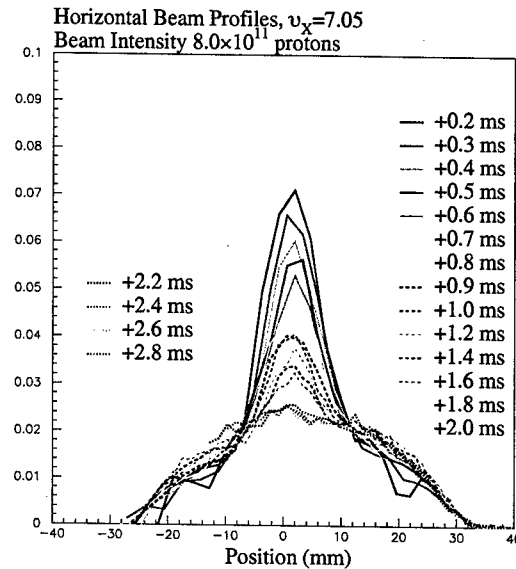


Figure 1: Horizontal beam profiles 0.2 ~ 2.8 ms after injection when the horizontal tune was 7.05 and the injection beam intensity was 8.0×10^{11} protons.

value. The vertical tune was 5.22. A significant beam loss was observed within 1 ms after injection under the condition. The reconstructed profile shows a notable change of the distribution. The profile at 0.2 ms after injection consists of a narrow peak and a broad distribution. The narrow peak diminishes in 2 ms and only the broad distribution remains.

The same procedure was applied for the horizontal tune of 7.11 and the vertical tune of 5.21 which was near the nominal operational value. The profile at 0.2 ms after injection still consists of a narrow peak and a broad distribution. The narrow peak diminishes in 1 ms, and only the broad distribution remains as in the case of the tune of 7.05. The narrow peak of this case is, however, less significant than that of the previous tune, and the beam loss is not either significant in this case.

Horizontal beam profiles after injection were measured for the injection beam intensity of 2.2, 3.9 and 8.0×10^{11} protons. The measurements were performed for a range of the horizontal tune from 7.05 to 7.26. The vertical tune was maintained to be between 5.23 and 5.32. The trigger was set to initiate the wire scanning to take beam profiles of about 4 ms after injection when the rapid change of the profile was settled. The profiles for the intensity of 8.0×10^{11} protons are shown in figure 2. It was observed to be wide

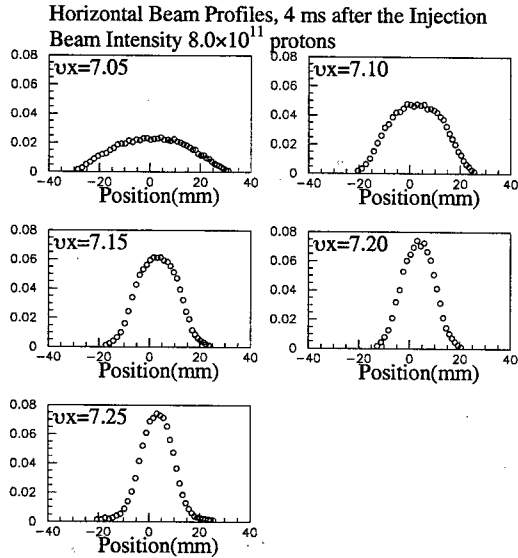


Figure 2: Horizontal beam profiles 4 ms after injection when the injection beam intensity was 8.0×10^{11} protons.

when the horizontal tune was 7.05, and became narrower as the tune was away from the integer.

The injection beam σ emittance was measured at the beam transfer line to be 3.4 and 2.7 π mmrad for the horizontal and vertical direction respectively. The emittance did not depend on the beam intensity. The measurement, however, has uncertainty from short understandings of transfer line lattice parameters.

Injection steering error, betatron function mismatch and dispersion function mismatch were measured and the effects to the injected beam to main ring were considered. The mismatch parameters were observed to show little dependence on the horizontal tune between 7.05 and 7.26. Beam emittance with the mismatch effects as a function of the horizontal tune was estimated. Little dependence on the horizontal tune was observed as in figure 3.

Each beam profile was fitted with either a Gaussian or a parabolic function and the emittance that includes the 87% fraction of the density distribution was estimated and plotted in figure 3. Emittance growth was observed when the tune is close to the integer for all the measured intensity settings. The tune dependence can not be explained only with the mismatch effects. A tune range where the emittance growth occurs depends on the intensity. It is inferred that the emittance growth is due to the space charge field.

ACCSIM SIMULATIONS

A multiparticle tracking simulation program, ACCSIM [2], taking account of space charge effects has been performed to understand the observed phenomena. Transverse space charge forces have been calculated for 10000 macro particles with a hybrid fast-multipole technique and grids of 1 mm \times 1 mm every 0.76 m step. Thin lens kicks have

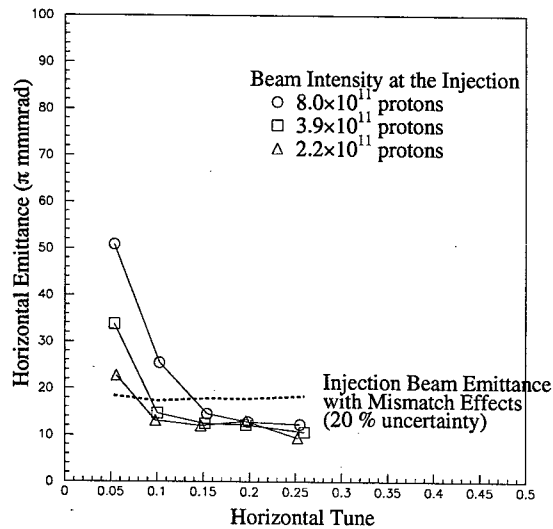


Figure 3: Horizontal 87% emittance as a function of the horizontal tune for the beam intensity of 2.2, 3.9 and 8.0×10^{11} protons.

been applied to simulate sextupole and octupole magnets. A fringing field from an injection septum magnet was suspected as one source of closed orbit distortion and included in simulations for some cases. Parameters for the injection beam emittance were based on the transfer line profile measurements. Another tracking simulation code, PATRASH [3], has also been applied and the results agreed with the ACCSIM results.

Figure 4 is the $x-p_x$ phase space plot of 20 test particles for 400 turns when the horizontal tune is 7.05. It shows patterns of fourth order resonance that was created by the space charge force. Particles having the tune of 7 by the incoherent tune shift make a resonant condition with the space charge field [4]. Octupole type space charge field creates the resonance. The resonant tune is 7/4 for a super period, because the main ring has a four-fold symmetry.

ACCSIM results of the horizontal beam profiles 0.6 ms after injection is shown in figure 5 for the beam intensity of 8×10^{11} protons. Profiles were fitted with a Gaussian plus a parabolic function for the tune of 7.05 and 7.10, and a parabolic function for the tune of 7.15 and 7.20. Only the parabolic distribution was assumed to remain in each profile after 4 ms and the emittance was evaluated to include the 87% fraction of the density distribution to compare with the measured emittance.

Figure 6 shows the comparison between the ACCSIM results and flying wire measurements for 87% emittance. The ACCSIM results reproduced the tune dependence qualitatively. The agreement is good for the intensity of 4×10^{11} protons. The ACCSIM results, however, are about 1.4 times of the measured emittance for the intensity of 8×10^{11} protons. The discrepancy may be due to uncertainty in the

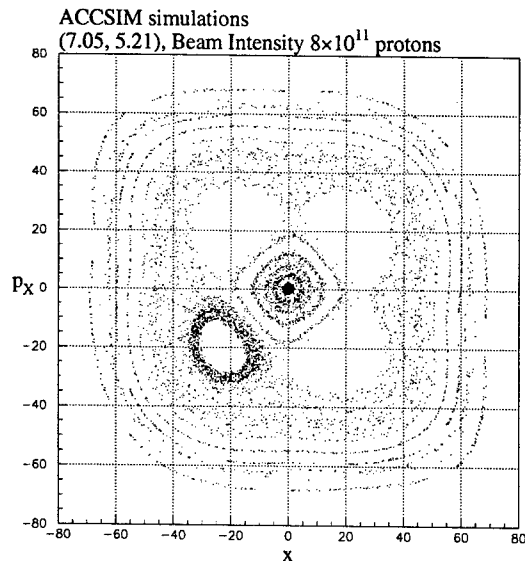


Figure 4: ACCSIM simulation of the $x - p_x$ phase space plots of 20 test particles when the horizontal tune was 7.05 and the injection beam intensity was 8×10^{11} protons.

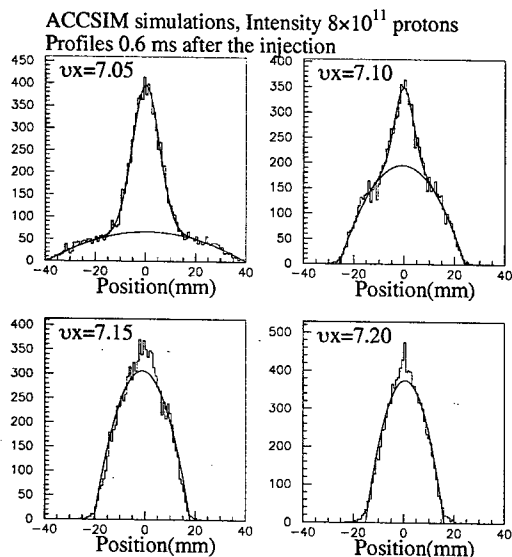


Figure 5: ACCSIM simulation of the horizontal beam profiles 0.6 ms after injection when the injection beam intensity was 8×10^{11} protons and the horizontal tune was 7.05, 7.10, 7.15 or 7.20.

measurement of the injection beam emittance. Mechanism to modify the resonance width, otherwise, has to be considered such as effects of the betatron function modulation.

CONCLUSIONS

Measurement of the transverse beam profiles using flying wires has revealed a characteristic temporal change

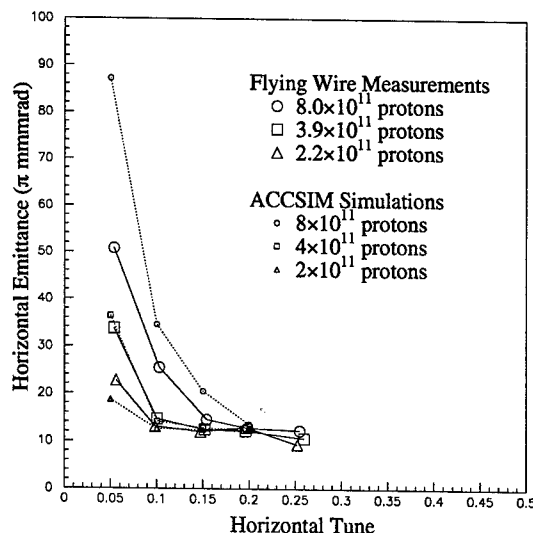


Figure 6: ACCSIM results of the horizontal 87% emittance as a function of the horizontal tune are shown in small symbols and dotted lines. Flyingwire measurement results are shown in large symbols and solid lines.

of the beam profile within a few milliseconds after injection. Horizontal emittance growth was observed when the horizontal tune was close to the integer. The effect was more enhanced for higher beam intensity. Resonance created by the space charge field was the cause of the emittance growth. A multiparticle tracking simulation program, ACCSIM, taking account of space charge effects has qualitatively reproduced the beam profiles.

ACKNOWLEDGMENTS

We thank F. Jones for valuable advices and installation of ACCSIM in our computer. We also thank H. Sato and K. Sato for useful comments.

REFERENCES

- [1] S. Igarashi, D. Arakawa, K. Koba, H. Sato, T. Toyama and M. Yoshii, "Flying wire beam profile monitor at the KEK PS", Nuclear Instruments and Methods in Physics Research A, 482/1-2,p32-41, April, 2002.
- [2] F.W. Jones, "ACCSIM Reference Guide Version 3.5s", June 1999.
- [3] Y. Shimosaki and K. Takayama, "Halo-Formation and Equilibrium in High-Intensity Hadron Rings: The Role of Non-linear Parametric Resonances Excited by the Intrinsic Beam-Core Oscillations", KEK Preprint 2001-111, September 2001.
- [4] S. Machida, "Space-charge effects in low-energy proton synchrotrons", Nuclear Instruments and Methods in Physics Research A, 309,p43-59, 1991.

CHALLENGE OF BENCHMARKING SIMULATION CODES FOR THE LANL BEAM-HALO EXPERIMENT *

W.P.Lysenko¹, J.Qiang², R.W.Garnett¹, and T. P. Wangler¹

¹Los Alamos National Laboratory

²Lawrence Berkeley National Laboratory

Abstract

We compare macroparticle simulations with beam-profile measurements from a proton beam-halo experiment in a study of beam-halo formation in mismatched beams in a 52-quadrupole periodic-focusing channel. The lack of detailed measurement of the initial distribution is an important issue for being able to make reliable predictions of the halo. We have found earlier that different initial distributions with the same Courant-Snyder parameters and emittances produce similar matched-beam profiles, but different mismatched-beam profiles in the transport system. Also, input distributions with greater population in the tails produce larger rates of emittance growth. We have concluded that using only the known Courant-Snyder parameters and emittances as input parameters is insufficient information for reliable simulations of beam halo formed in mismatched beams. The question is how to obtain the best estimate of the input beam distribution needed for more accurate simulations. In this paper, we investigate a new least squares fitting procedure, which is applied to the simulations and used to determine the injected beam distribution in an attempt to obtain a more accurate description of halo formation than from simulation alone.

1 INTRODUCTION

This paper is concerned with the comparison of self-consistent macroparticle simulations, including space-charge forces using the macroparticle simulation code IMPACT[1], with experimental measurements of the beam profiles in a high-current proton beam. The measurements were made in a beam-transport channel using a 6.7-MeV proton beam at the Low Energy Demonstration Accelerator (LEDA) facility [2] at Los Alamos National Laboratory. A major goal of the experiment was to validate the beam-dynamics simulations of beam halo. Of particular importance was the validation of the space-charge routine in IMPACT. We have observed good agreement comparing direct simulations and profile measurements for the matched beam but have been less successful in obtaining good agreement for the mismatched beams [3]. We have concluded that the beam profiles for mismatched beams are very sensitive to the initial distribution. We now investigate the use of a least squares fitting procedure applied to the RFQ simulation results to obtain an improved estimate of the initial beam distribution (at the exit of the RFQ). We suggest that this fitting procedure

may provide an improved estimate of the real beam distribution at the output of the RFQ, because it allows us to correct for unknown errors upstream of the beam-transport line that may prevent us from deducing accurately the RFQ output distribution using simulations alone. Improving our prediction of the RFQ output distribution would provide a more accurate predictive capability for the beam halo evolution in a high energy proton linac.

2 BEAM HALO EXPERIMENT

The LEDA facility consists of a 75-keV DC injector, a low-energy beam transport (LEBT) system, and a 350-MHz radiofrequency quadrupole (RFQ), which accelerates the proton beam to 6.7 MeV. A schematic diagram of the LEDA beam-halo experiment transport system that follows the RFQ is shown in Fig. 1[4]. The transport system consists of 52 magnetic quadrupoles with alternating polarity (FODO Lattice) to provide strong periodic transverse focusing. Transverse beam profiles were measured using beam-profile detectors[5] located in the middle of the drift spaces after quadrupoles 4, 20, 22, 24, 26, 45, 47, 49 and 51. The first four quadrupole gradients were independently adjusted to match the beam, by producing equal rms sizes at the beam-profile detectors. The gradients were also adjusted to produce approximately pure mismatches in either a breathing or a quadrupole mode. The beam current was varied over a range from 16 to 100 mA. In this paper we report results at 75-mA.

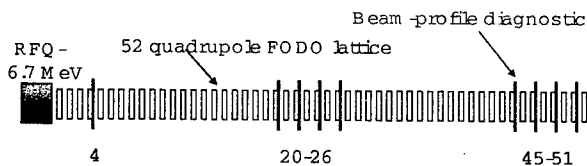


FIG. 1. Block diagram of the 52-quadrupole-magnet lattice showing the nine locations of beam-profile scanners. The first four quadrupoles upstream of scanner 4 are adjusted to match or mismatch the beam.

3 OLD SIMULATION RESULTS

We obtained rms beam widths at each of the scanners and rms emittances at scanners 20 and 45. The emittances

as well as the Courant-Snyder parameters were deduced at scanners 20 and 45 using the rms values from the four associated profile monitors (20, 22, 24, and 26, for the value at 20, and 45, 47, 49, and 51 for the value at 45). The measured results for the mismatched beams were compared with the maximum amplitude predictions of a particle-core model [6], and maximum emittance growth predictions of a free energy model [7], assuming complete transfer of the free energy. The experimental results strongly supported both analytic models [8]. We have observed good agreement between simulations and profile measurements for the matched beam, but have been less successful in obtaining good agreement for the mismatched beams. We believe that the main cause of the poor agreement for the mismatched cases lies in a lack of detailed knowledge of the initial distribution in phase space. Given that we were unable to measure the input distribution, our approach to the simulations was to generate four different initial distributions at the entrance of the beam-transport channel, all with the same Courant-Snyder ellipse parameters and emittances; these parameters were deduced from the measurements. The assumed input distributions were: 1) 6D Waterbag, 2) 6D Gaussian, 3) Double Gaussian, and 4) a distribution called LEBT/Rfq, generated from a simulation through the LEBT and Rfq, starting at the plasma surface at the exit of the ion source. All four distributions were scaled to produce the correct initial Courant-Snyder parameters and emittances. These four distributions differ qualitatively with respect to their initial halo, i.e. initial population of the outer tails of the beam. Best agreement for the observed emittance growth was obtained with the Double Gaussian, which had the largest population in the tails. This is a result that would be expected from the particle-core model [6], since most of the halo particles have initial amplitudes that lie outside the core. However, none of these initial distributions yield good agreement with measured beam profiles for the mismatched case. We have concluded that knowledge of the initial particle distribution, especially the density in the tails, is important for accurate simulations of the beam halo.

The question that remains is how to obtain reliable simulations for mismatched beams when the input distribution is not measured. A possible solution is suggested by recent results obtained from the analysis of earlier quadrupole scan measurements used to characterize the beam at the exit of the Rfq [9]. In that case the authors concluded that unknown beamline-parameter errors could lead to differences between the real and the simulation results at the output of the Rfq. The simplest assumption is that the main errors involve only the second moments, i.e. the Courant-Snyder parameters and the rms emittances. Therefore the authors modified the simulation results by adjusting the simulated Rfq output particle coordinates to change the second moments of the simulated Rfq output beam to give a best least-squares fit to all the measured profiles. This procedure produced excellent agreement between measured and simulated profiles. We would like to

investigate whether a similar method would also produce improved agreement for the beam halo experiment.

4 NEW RESULTS WITH LEAST-SQUARES FITTING

Our hypothesis is to assume that our simulation codes do contain the relevant physics. Discrepancies are most likely caused by the fact that we do not know the precise parameters for the LEBT and for the as-built Rfq, particularly the axial voltage distribution. Therefore, the real beam distribution that is injected into the beam transport channel after the Rfq is not precisely known. For this reason we have investigated whether modifications to the beam generated by Rfq simulations would improve the agreement between the simulated and measured beam profiles. We have used a modified version of the fitting code described in ref. [9] in which an IMPACT simulation of the halo channel is controlled by a nonlinear optimizer. The input beam is described by the six transverse parameters (Courant-Snyder parameters α , β , and emittances ϵ in both x and y). The optimizer varies the six parameters and attempts to minimize the differences between the simulated profiles at the wire-scanner positions and the measured profiles.

The input beams for these simulations are generated by starting with the particle distribution from our LEBT/Rfq simulation. This distribution is distorted by applying a certain linear transformation [9] to the particle phase-space coordinates that results in the beam having the six Courant-Snyder parameters requested by the nonlinear optimizer; this procedure should retain much of the higher-order structure present in the original Rfq simulation.

We fitted only to the five wire scanner profiles between 4 to 26 (10 profiles) for the matched case. Using the modified initial distribution, the simulated and measured profiles agree well for all the scanners for the matched beam. Figure 2 shows results for the matched case and the mismatched case for mismatch parameter $\mu=1.5$, where μ is defined in Ref. [8]. Rms deviations for the matched case (difference between experimental and simulated profiles) are small, about 2%. However, using this beam to simulate the mismatched cases has not yet produced as good agreement between the simulated and measured profiles.

5 CONCLUSIONS

We report on an investigation of a new least-squares fitting procedure, which is applied to the simulations in an attempt to obtain a more accurate description of the initial particle distribution. The fits were applied to a subset of the matched beam profiles. We find that the resulting profiles for the matched beam at all the scanners agree well with the measured ones, but more work is required to improve the agreement for the mismatched beams. We plan to investigate this situation further by fitting the mismatched data or fitting the matched and mismatched

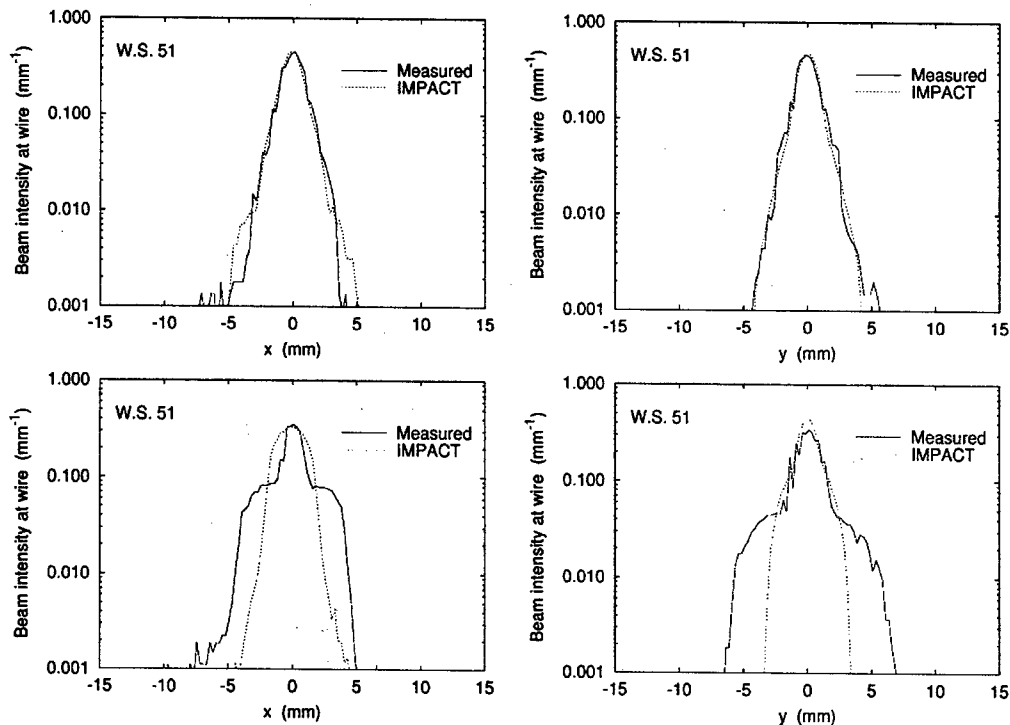


FIG. 2. Comparison of measured and simulated profiles at the final wire scanner. Top row shows the matched case and the bottom row shows the mismatched case for mismatch parameter $\mu=1.5$ as defined in Ref. 8. Both cases used an input beam determined by fitting the matched data to profiles at wire scanners 4 through 26.

data simultaneously, and comparing the initial distributions in detail. The fitting code used an older version of IMPACT. We plan to repeat the fitting using the latest version of IMPACT, which will enable us to study different boundary conditions in the space charge computations. This may lead to a better characterization of the RFQ exit beam, and an improved overall analysis of the halo experiment.

6 ACKNOWLEDGMENTS

We acknowledge the help of Dr. L. Young for providing an initial distribution from the LEPT/RFQ simulation. We acknowledge the work on the experiment by the rest of the beam-halo scientific team, C. K. Allen, K. C. D. Chan, P. L. Colestock, K. R. Crandall, J. D. Gilpatrick, J. D. Schneider, M. E. Schulze, R. L. Sheffield, and H. V. Smith. Part of the simulations were performed on the supercomputers at the National Energy Research Scientific Computing Center and the Center for Computational Sciences at Oak Ridge National Laboratory. This work was supported by the U.S. Department of Energy.

REFERENCES

- [1] J. Qiang, R.D.Ryne, S. Habib, and V. Decyk, *J. Comput. Phys.* **163**, 434 (2000).
- [2] H. Vernon Smith, J. D. Schneider, and R. Sheffield, *Proc. 2001 Part. Accel. Conf.*, IEEE Catalog No. 01CH37268, 3296-3298.
- [3] J.Qiang, et al., *Phys. Rev. ST Accel. Beams*, **5**, (124201) (2002).
- [4] T.P.Wangler et al., *Proc. 2001 Part. Accel. Conf.*, IEEE Catalog No. 01CH37268, 2923-2925; P.L.Colestock et al., *Proc. 2001 Part. Accel. Conf.*, IEEE Catalog No. 01CH37268, 170-172; M. Schulze et al, *Proc. 2001 Part. Accel. Conf.*, IEEE Catalog No. 01CH37268, 591-593.
- [5] J.D.Gilpatrick et al., *Proc. 2001 Part. Accel. Conf.*, IEEE Catalog No. 01CH37268, 525-527.
- [6] T.P.Wangler, K.R.Crandall, R. Ryne, and T.S.Wang, *Phys.Rev. ST Accel. Beams* **1**, (084201)1998.
- [7] M. Reiser, *Theory and Design of Charged Particle Beams*, (Wiley, New York, 1994), pp. 470-473.; M. Reiser, *J.Appl. Phys.* **70**, 1919 (1991).
- [8] C.K.Allen, et al., *Phys.Rev.Lett.* **89**, No.21, (214802) 2002.
- [9] W.P.Lysenko et al., presented at the Int. Comp. Accel. Phys. Conf. 2002, Michigan State University, East Lansing MI, Oct. 15-18, 2002.

HIGH BRIGHTNESS POTASSIUM ION GUN FOR THE HIF NEUTRALIZED TRANSPORT EXPERIMENT (NTX) *

S. Eylon, E. Henestroza, P. K. Roy, and S.S. Yu

Lawrence Berkeley National Laboratory, Berkeley, CA 94530, USA, and the Heavy Ion Fusion, Virtual National Laboratory

Abstract

The NTX experiment at the Heavy Ion Fusion Virtual National Laboratory is exploring the performance of neutralized final focus systems for high perveance heavy ion beams. To focus a high intensity beam to a small spot requires a high brightness beam. In the NTX experiment, a potassium ion beam of up to 400 keV and 80 mA is generated in a Pierce type diode. At the diode exit, an aperture with variable size provides the capability to vary the beam perveance and to significantly reduce the beam emittance. We shall report on the gun characterization including current density profile, phase space distributions and the control of electrons generated by the beam scraping at the aperture. Comparison with particle simulations using the EGUN code will be presented.

INTRODUCTION

The Neutralized Transport Experiment (NTX) [1-2] at Lawrence Berkeley National Laboratory is designed to study the effects of plasma neutralization for a strongly space-charge-dominated ion beam, using a 400 KeV beam of singly charged potassium ions. The experiments require variable beam current, by one order of magnitude, up to 75mA. In addition, a very high brightness source is required. One way to generate high brightness beams is to remove the edge of the beam after it is generated in the diode; but scraping the beam also generates secondary electrons that must be controlled to prevent them from perturbing the beam. We have designed a beam scraper system that includes an electron trap for the control of secondary electrons. Beam aperturing appears to be a natural match to the requirements.

The control of electrons is our first concern in this experiment, as stray electrons can introduce nonlinear space charge forces, which could lead to increase of beam emittance [3], and disruption of beam propagation. The proposed technique is to confine the electrons generated by the aperturing process to its place of birth by adjacent electron traps. These electron traps have negative potentials sufficiently large to confine the electrons even in the presence of the positive potential (a couple of kilovolts in NTX) from the self-field of the ion beam.

DESIGN

Design of the ion gun, together with the beam aperture and electron trapping device is shown in Fig. 1. The K+

beam at 400 kV and 75mA is extracted from a 2.54 cm diameter alumino-silicate source [4] across a diode with a 12 cm gap. Downstream of the exit cathode plate is a beam aperturing plate with holes of variable diameter, sandwiched between two metal tubes of 5cm length, and 6.2 cm inner diameter. The EGUN calculation in Fig. 2 shows the nominal design of -3kV on each of the metal tubes (beam scraper system), providing adequate electron trapping in the presence of the ion beam.

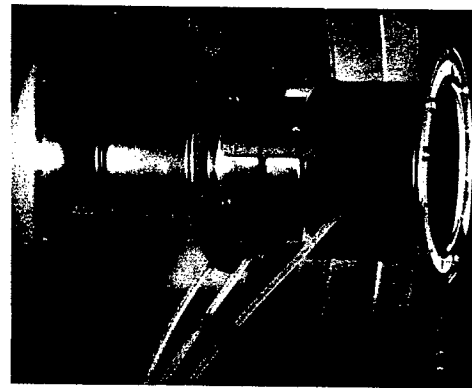


Figure 1: Beam scraper system.

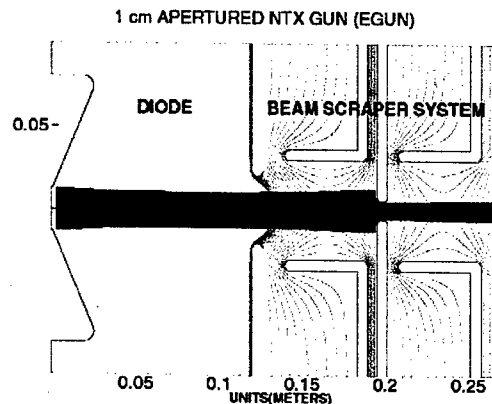


Figure 2: EGUN simulation of diode and beam aperture setup.

The primary diagnostics for this experiment consist of a Faraday cup to measure the total beam current exiting the aperture plate, and a slit/ slit-cup arrangement to measure the line-integrated beam profile (with slit cup only) and emittance (with slit and slit cup). The Faraday cup and the slit cup each consists of a collector and a guard

*Supported by the Office of Energy Research, US DOE, at LBNL & LLNL, contract numbers DE-AC03-76SF00098 and W-7405-Eng-48.

ring/grid with bias voltages that are controlled to collect beam ions only. In addition, we can also monitor the currents flowing through the aperture plate and each of the two electron traps.

EXPERIMENT

The experiment is first performed without an aperture plate. The peak current at 400 kV is 77mA, which is in agreement within the uncertainty of the measurement with the EGUN code prediction of 73 mA. The measured current follows the Child-Langmuir three-half power law as the voltage was varied over a factor of 3 in range and is shown in Fig. 3. The measured beam profile and emittance show a variation from uniformity due to known imperfections in beam optics. An aperture of 2 cm diameter was then introduced with the nominal electron trap voltages applied. The measured current is 55% of the total, again consistent with the EGUN prediction. The measured profile of the aperture beam is much more uniform, and the emittance is a factor of 2 lower (translating to an overall increase of brightness by a factor of 2).

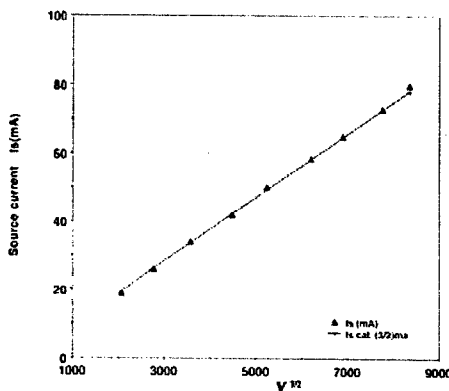


Figure 3: Extracted current from NTX follows Child-Langmuir Law.

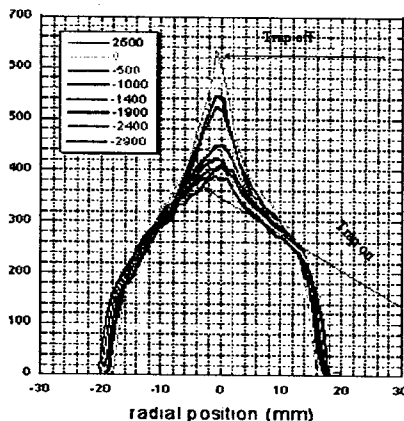


Figure 4: Beam Profile as function of trap voltage.

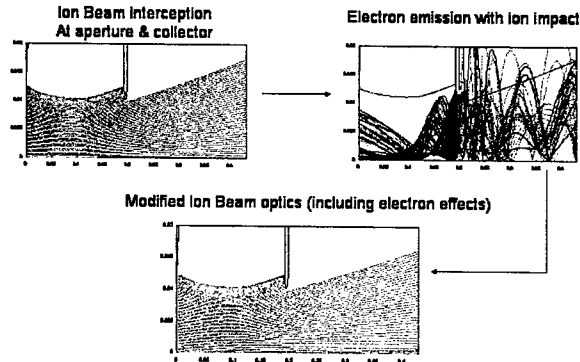


Figure 5: Beam aperturing experiments are modeled by an iterative calculation with EGUN.

To understand the effect of electrons generated by the beam on the aperture and the diagnostic plates, we vary the bias voltage on the electron trap. The total current measured in the Faraday cup increases as the magnitude of the negative bias is reduced. We also measured the change in beam profile as the bias voltage is varied. We notice that as the bias voltage moves towards zero, the on-axis current is greatly enhanced. Associated with the on-axis enhancement is a slight reduction in the overall radial dimension of the beam (Figure 4).

These observations are consistent with a picture where electrons are trapped within the beam as the electron trap voltage is reduced. To quantitatively evaluate these effects, we performed a series of simulations, using PIC codes as well as ray-tracing codes. The predicted current and beam profiles are shown in Fig 5.

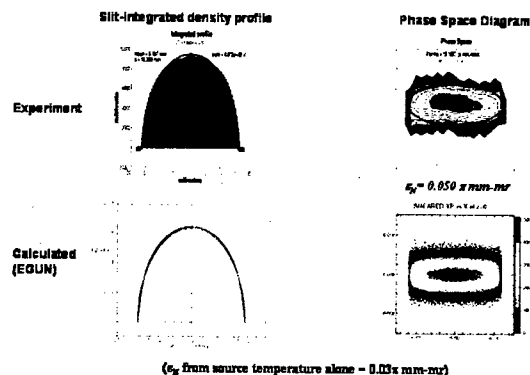


Figure 6: A High Brightness apertured beam (300kV, 25 mA, 2 cm aperture)

With the qualitative agreement of code and experiment, the following picture emerges: when the negative bias on the electron trap is sufficiently high, the electrons born on

the aperture plate and the diagnostic plates are locally trapped. Their effect on the ion beam is minimal. However, as the negative bias is reduced, the electrons are finally able to break through the electrostatic barrier, and will accumulate around the beam axis (the bottom of the potential well). The region of electron population increases with reducing bias voltage. These on-axis electrons cancel the space-charge effect of the ions, causing the overall ion beam envelope to decrease, and the on-axis ion density to increase. The total current through the aperture also increases as a result.

REFERENCES

- [1] S. S. Yu et al., "Focusing and Neutralization of Intense Ion Beams", Proc. PAC '03, TOAA001.
- [2] E. Henestroza et al., "Neutralized Transport of High Intensity Beams", Proc. PAC '03, WPPG014.
- [3] C. Lejeune et al., "Applied charged particle optics", ed. by A. Septier (1980), pt 13A, 159.
- [4] D. Baca et al., "Fabrication of Large Diameter Alumino-Silicate K^+ Sources, Proc. PAC '03 FPAB005.

FINAL FOCUS SYSTEM FOR HIGH INTENSITY BEAMS*

E. Henestroza[#], F.M. Bieniosek, S. Eylon, P.K. Roy, and S. S. Yu

Lawrence Berkeley National Laboratory, Berkeley, CA 94720, USA

Abstract

The NTX experiment at the Heavy Ion Fusion Virtual National Laboratory is exploring the performance of neutralized final focus systems for high perveance heavy ion beams. The NTX final focus system produces a converging beam at the entrance to the neutralized drift section where it focuses to a small spot. The final focus lattice consists of four pulsed quadrupole magnets. The main issues are the control of emittance growth due to high order fields from magnetic multipoles and image fields. We will present experimental results from NTX on beam envelope and phase space distributions, and compare these results with particle simulations using the particle-in-cell code WARP.

INTRODUCTION

A driver beam is transported in the final focus section through several strong magnetic quadrupoles, and is then allowed to drift ballistically through neutralizing plasma in a low-density (millitorr) gas onto the target. There are nonlinear processes both in the magnetic section as well as in the neutralized transport section. To investigate these phenomena, the Neutralized Transport Experiment (NTX) has begun at LBNL [1]. The experimental setup (Fig. 1) consists of three major sections, a low-emittance potassium gun [2], a magnetic transport section with 4 pulsed quadrupoles [3], and a one-meter long drift section with plasma neutralization [4].

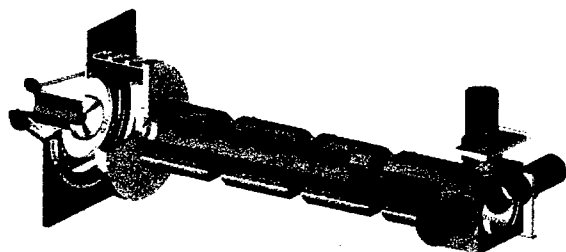


Figure 1: Final focus system for ballistically neutralized drift (cut-away view of components).

The 3-D PIC simulation code WARP3D has been used to design the gun and the magnetic lattice, and predictions

[#]EHENESTROZA@lbl.gov

*This work has been performed under the auspices of the US DOE by UC-LBNL under contract DE-AC03-76SF00098, for the Heavy Ion Fusion Virtual National Laboratory.

of nonlinear forces have been made and are compared against the NTX experiments. The MRC electromagnetic code LSP has been used to specify the requirements for the plasma source, as well as the predicted degree of neutralization as a function of the various beam and plasma parameters.

FINAL FOCUS LATTICE

The transport section is designed to correspond closely to a prototypical HIF driver final focus channel. It consists of four pulsed quadrupole magnets with short drift regions, including the drift from the source into the channel and the drift into the plasma neutralization chamber. Figure 2 shows the horizontal and vertical beam envelopes through the system, with and without beam neutralization after the final focus lattice. The quadrupole fields are chosen to obtain a beam of one-meter focal length (20 mm, -20 mr) at the entrance to the neutralization region.

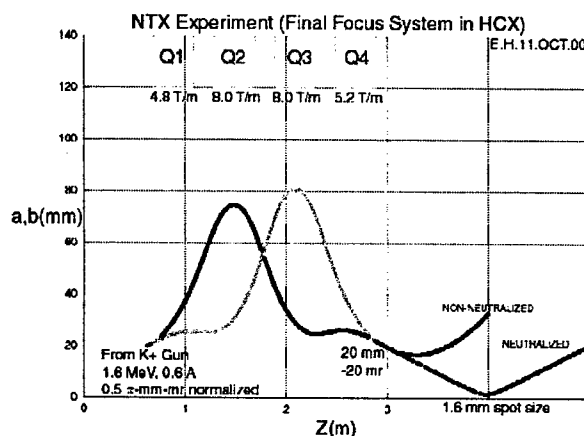


Figure 2: Final focus lattice for ballistically neutralized drift.

The heavy ion beam is space charge dominated in the final focus system, where it has a large cross section and is highly non-paraxial. The beam expands in the two center magnets, which determines the amount of nonlinear magnetic fields that the beam samples as well as the degree of non-paraxial motion. Therefore, particle tracking simulations require the knowledge of the multipole field content of the magnetic field. It can be shown that to second order [5] the main contribution to the beam dynamics come from the normal quadrupole, the normal sextupole and the pseudo-octupole components of the magnetic field. These three components are included in all the numerical simulations performed for the design of the lattice.

TRANSPORT IN FINAL FOCUS SYSTEM

A high brightness ion beam is an essential component of the Neutralized Transport Experiment (NTX). An ion beam extracted from a Pierce-type diode suffers from spherical aberrations as evidenced from phase space distortions (high emittance) and from non-uniform density profiles. Since the source of these aberrations are the high order field components, the particles at the edge of the beam are the most affected. One way to generate high brightness beams is to remove the edge of the beam after it is generated in the diode [2]. To study beam transport through the final focus system we have used a 300 keV, 25 mA, beam with a normalized emittance of $0.05 \pi\text{-mm-mr}$ and a uniform density profile. Optical scintillators imaged by CCD cameras and mechanical slit scanners [6] were used to measure the beam profiles and phase space distributions of the beam at the end of the final focus lattice. Figure 3 shows the good agreement between the measured (top) and calculated (bottom) beam profile and phase space distribution for the nominal energy (300 keV, 25 mA) and quadrupole field configuration; it also shows that the final parameters for the nominal case correspond to that of a beam of the required one-meter focal length (20 mm radius and 20 mr convergence).

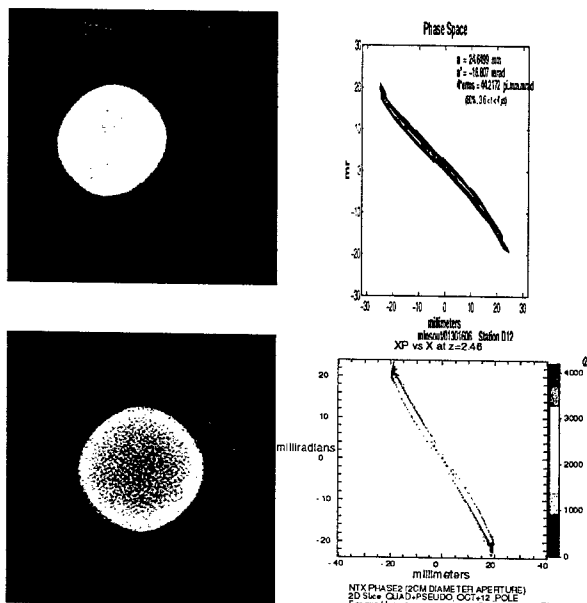


Figure 3: Experimental results and simulations of beam profile and phase space distribution at exit of channel.

The slight distortion of the beam profile was traced back to a small rotation (5 mr) of one of the quadrupoles. The beam is uniform with a narrow rim due to field aberrations and the final normalized emittance of the beam is $\sim 0.1 \pi\text{-mm-mr}$ as required by the plasma neutralization experiment [4].

The low emittance ($\sim 30 \pi\text{-mm-mr}$ unnormalized) allows for the beam to be focused to a small spot size (1–2 mm radius) at the focal point for neutralized ballistic transport. Furthermore, Faraday cup measurements of the beam current at entrance and exit of the final focus system have shown insignificant beam loss along the transport channel.

ENERGY AND QUADRUPOLE FIELD SCANS

We have also performed a complete characterization of the quadrupole lattice by comparing experimental results with particle simulations using the particle-in-cell code WARP. Figure 4 shows the good agreement between the calculated (top) and measured (bottom) beam profiles at the exit of the final focus system when the beam energy is varied in steps of 3% around the nominal energy (image at center). The numerical simulations track the beam behavior as the beam expands by a large factor when the energy changes from -9% to +9% around the nominal energy.

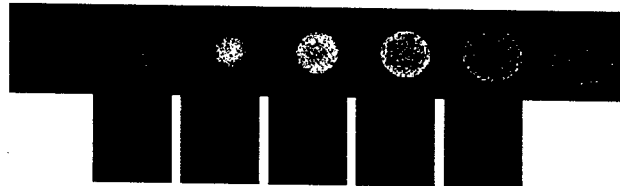


Figure 4: Numerical results and camera images of beam profiles as function of energy.

We also compared (Fig. 5) the beam profiles for several quadrupole strength configurations as calculated by WARP and as measured. For each quadrupole, the corresponding row shows the profiles for a change of -5%, 0% and +5% from the nominal quadrupole strength. This comparison shows the good agreement that we have obtained so far, between measurements and simulations.

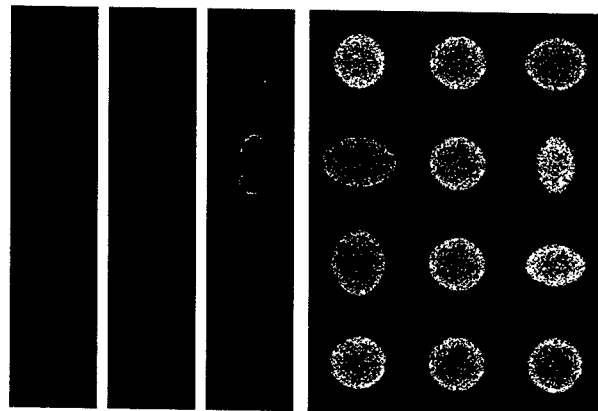


Figure 5: Numerical results and camera images of beam profiles as function of quadrupole field configuration.

4-D PHASE SPACE MEASUREMENT

We are developing a new technique to measure the 4-dimensional phase space distribution of the beam using the beam imaging diagnostics [6]. The phase space distribution $f(x,y,x',y')$ can be measured by scanning the beam with a small pinhole (20 mils in diameter) and letting the transmitted beamlet to travel a long distance (~ 1 meter) before striking the scintillator where an image is taken. The position of the pinhole defines the coordinates x and y , and from the image we can extract the density distribution of x' and y' . Due to the fact that the beam at the exit of the final focus system is prepared to focus to small spot in the absence of space charge, a standard pepperpot technique does not work since all the individual beamlets would fall on a single spot. Figure 6 shows schematically this technique along with some images of the individual beamlets that show a very detailed structure of the phase space distribution. The knowledge of the 4-dimensional phase space will be essential in order to run more realistic simulations of the beam focusing to a small spot when drifting through neutralizing plasma.

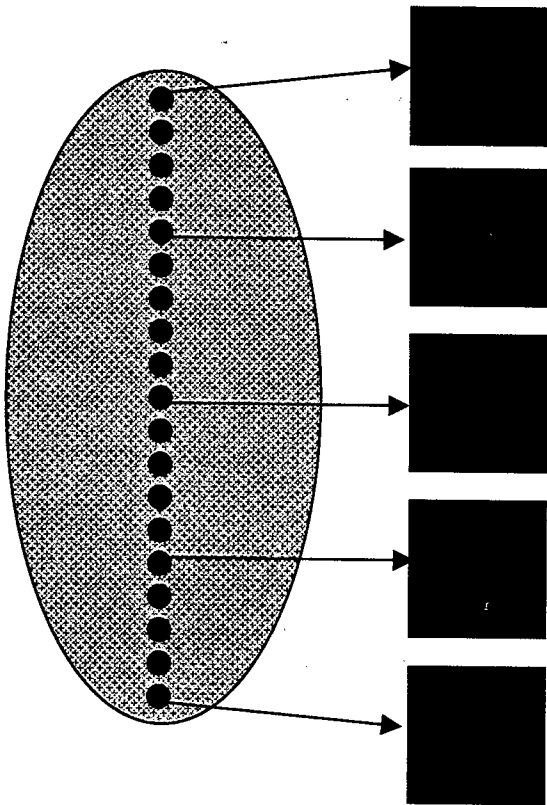


Figure 6: Beam imaging technique to measure the phase space distribution $f(x,y,x',y')$.

CONCLUSIONS

Initial experiments of beam transport through the NTX final focus systems has produced the design beam parameters required for the neutralization transport experiment. Further measurements to obtain the 4-dimensional phase space distribution at the exit of the final focus system will provide the initial condition for realistic simulation of the beam dynamics when ballistically focused through neutralizing plasma.

REFERENCES

- [1] S. S. Yu et al., "Focusing and Neutralization of Intense Ion Beams", Proc. PAC '03, TOAA001.
- [2] S. Eylon et al., "High brightness potassium source for the HIF neutralized transport experiment", Proc. PAC '03, WPPG012.
- [3] D. Shuman et al., "Magnetic lattice for the HIF neutralized transport experiment", Proc. PAC '03, WPPG017.
- [4] E. Henestroza et al., "Neutralized Transport of High Intensity Beams", Proc. PAC '03, WPPG014.
- [5] D. Neuffer, "Geometric aberrations in final focusing for heavy ion fusion", Proc. HIF Workshop, ANL, Sept. 19-26, 1978, ANL-79-41.
- [6] F.M. Bieniosek et al., "Beam imaging diagnostics for heavy ion beam fusion experiments", Proc. PAC '03, WPPB050.

NEUTRALIZED TRANSPORT OF HIGH INTENSITY BEAMS

E. Henestroza[#], S. S. Yu, S. Eylon, P.K. Roy, A. Anders, W. Sharp, LBNL, P. Efthimion, E. Gilson, PPPL, D. Welch, D. Rose, MRC

Abstract

The NTX experiment at the Heavy Ion Fusion Virtual National Laboratory is exploring the performance of neutralized final focus systems for high perveance heavy ion beams. A converging ion beam at the exit of the final focus magnetic system is injected into a neutralized drift section. The neutralization is provided by a metal arc source and an RF plasma source. Effects of a "plasma plug", where electrons are extracted from a localized plasma in the upstream end of the drift section, and are then dragged along by the ion potential, as well as the "volumetric plasma", where neutralization is provided by the plasma laid down along the ion path, are both studied and their relative effects on the beam spot size are compared. Comparisons with 3-D PIC code predictions will also be presented.

INTRODUCTION

A driver beam is transported in the final focus section through several magnetic quadrupoles, and is then allowed to drift ballistically through neutralizing plasma in a low-density (millitorr) gas onto the target. There are nonlinear processes both in the magnetic section as well as in the neutralized transport section. To investigate these phenomena, the Neutralized Transport Experiment (NTX) has begun at LBNL [1]. The experimental setup (Fig. 1) consists of three major sections, a low-emittance potassium gun [2], a magnetic transport section with 4 pulsed quadrupoles [3,4], and a one-meter long drift section with plasma neutralization.

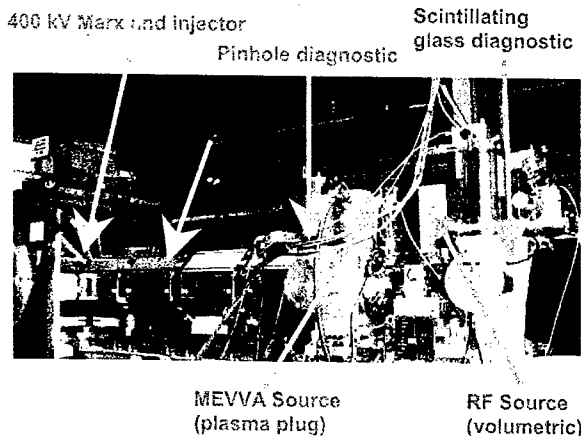


Figure 1: Neutralized Transport Experiment (NTX).

[#]EHENESTROZA@lbl.gov

*This work has been performed under the auspices of the US DOE by UC-LBNL under contract DE-AC03-76SF00098, for the Heavy Ion Fusion Virtual National Laboratory.

The MRC electromagnetic code LSP has been used to specify the requirements for the plasma source, as well as the predicted degree of neutralization as a function of the various beam and plasma parameters. The PIC simulation code WARP has also been used to simulate the beam dynamics for specific degrees of neutralization.

PLASMA NEUTRALIZATION

Neutralization is essential for focusing heavy ion beams onto target. Figure 2 shows a conceptual layout of a neutralization system. For NTX the plasma plug is a MEVVA plasma source, the volumetric plasma is supplied by an RF source and the target is a scintillator imaged by a CCD camera.

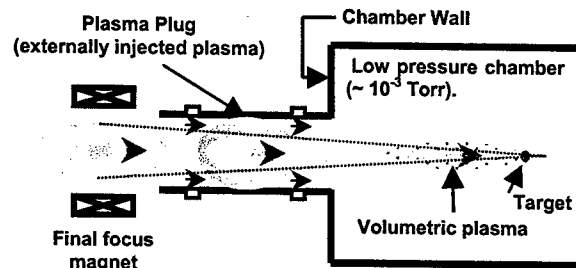


Figure 2: Neutralization system layout.

The MEVVA (Fig. 3) and the Argon plasma (Fig. 4) sources deliver reproducible plasma densities ten times greater than the beam density, sufficient for a range of plasma-plug and volumetric neutralization experiments.

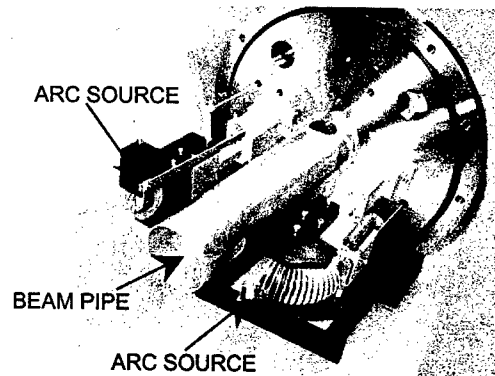


Figure 3: MEVVA plasma source.

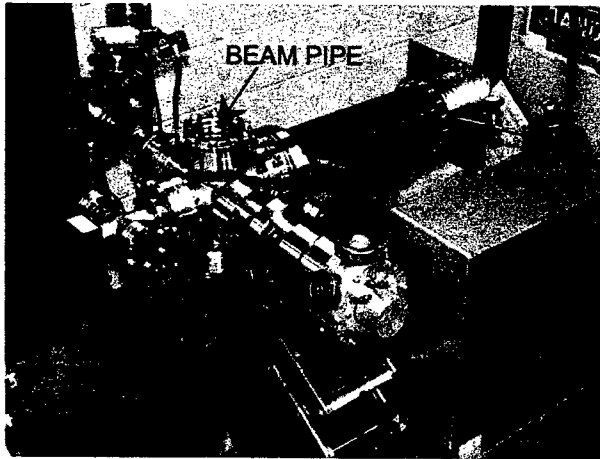


Figure 4: Argon RF plasma source.

BEAM DYNAMICS

The NTX injector can deliver high brightness beams in a range of 220–340 keV, 15–30 mA, with a normalized emittance of $\sim 0.05 \pi\text{-mm-mr}$ and a uniform density profile. The quadrupole fields in the final focus system are chosen to obtain a beam of one-meter focal length (20 mm radius and 20 mr convergence) at the entrance to the neutralization region for the nominal energy (300 keV, 25 mA). Optical scintillators imaged by CCD cameras and mechanical slit scanners [5] were used to measure the beam profiles and phase space distributions of the beam at the end of the final focus lattice. Figure 5 shows agreement between the measured and calculated beam profiles for the nominal energy and quadrupole field configuration.

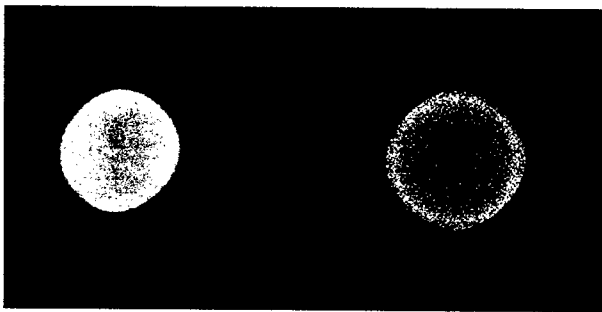


Figure 5: CCD camera image and WARP simulation results of converging beam profiles at entrance to the neutralization region.

The slight distortion of the measured beam profile is due to a small rotation (5 mr) of one of the quadrupoles. The beam is uniform with a narrow rim due to field aberrations and the final normalized emittance of the beam is $0.1 \pi\text{-mm-mr}$.

Non-neutralized drift

As a preliminary test of the NTX system, the beam was injected into a vacuum pipe without any neutralization. Figure 6 shows the measured beam profiles at 1 meter downstream from the exit of the final focus system. The energy varies from 260 to 300 keV, and the beam size is in good agreement with WARP simulations.

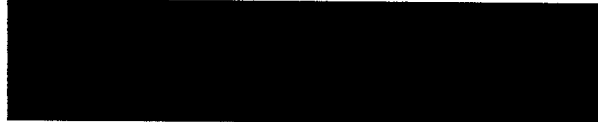


Figure 6: Beam profiles 1 meter downstream from the exit of the final focus system for non-neutralized drift.

Neutralized transport

The low emittance ($\sim 30 \pi\text{-mm-mr}$ unnormalized) of the beam at the entrance to the neutralized region allows for the beam to be focused to a small spot size (1–2 mm radius) at the focal point for neutralized ballistic transport. Figure 7 shows the measured dependence of beam spot size at the focal plane on neutralization mechanism.

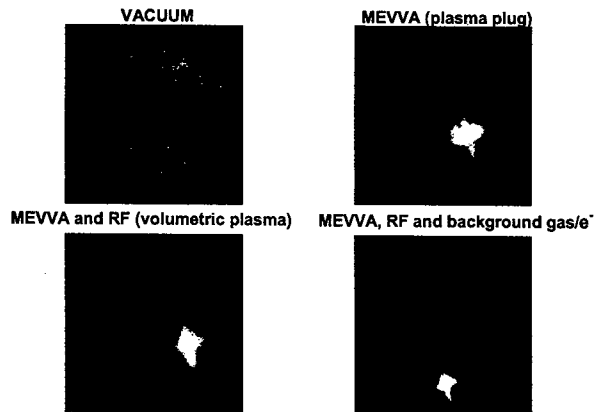


Figure 7: Spot size dependence on neutralization mechanism. Image box size is $4\text{cm} \times 4\text{cm}$ squares.

LSP simulations of NTX including plasma plug and volumetric neutralization were performed starting from beam initial conditions at the entrance to the neutralization region. In one series (Fig. 8) of LSP simulations, the initial condition is the final phase space distribution as calculated by WARP for the transport of the NTX beam from the gun to the exit of the final focus system. There is qualitative agreement with measured spot sizes. The measurement of the detailed structure of the phase space distribution in 4-dimensional phase space seems essential in order to run more realistic simulations of the beam focusing to a small spot when drifting through neutralizing plasma [4].

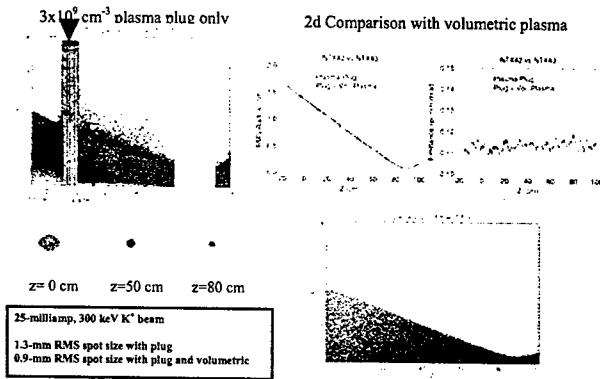


Figure 8: WARP-LSP NTX simulation with plasma plug neutralization.

ANALOG SIMULATION OF FULLY NEUTRALIZED BEAM TRANSPORT

We are developing a new technique [4] to measure the 4-dimensional phase space distribution of the beam using the beam imaging diagnostics. The phase space distribution $f(x, y, x', y')$ can be measured by scanning the beam with a small pinhole (20 mils in diameter) and letting the transmitted beamlet to travel a long distance (~ 1 meter) before striking the scintillator where an image is taken. The position of the pinhole defines the coordinates x and y , and from the image we can extract the density distribution of x' and y' . This technique will be used to measure the detailed structure of the phase space distribution.

The same diagnostics system can be used to simulate the effect of full neutralization on a beam, since each beamlet going through a pinhole only carries the information about the phase space distribution at a given location without being perturbed by the space charge of the full beam. The superposition of all the pinhole images at a given location can be compared with a beam transport calculation where the space charge is turned off at the pinhole-scan plane. Figure 9 shows a comparison between this "analog simulation" and WARP; the agreement is excellent and shows that the emittance is low enough to get a small spot (~ 1 mm radius).

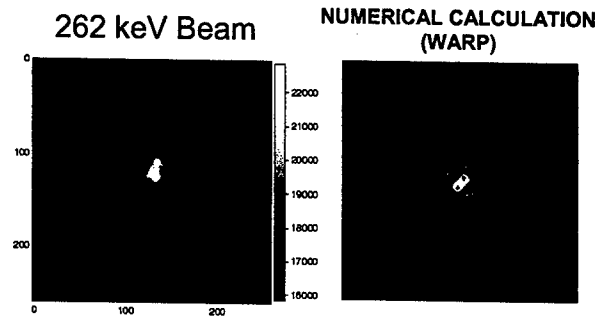


Figure 9: Analog (pinhole) simulation and WARP calculation of fully neutralized beam focused to a small spot. Image box size is 4cm \times 4 cm squares.

CONCLUSIONS

Initial experiments of beam transport through the NTX neutralization section have produced a small spot at the focal plane consistent with numerical and analog calculations. Further measurements to obtain the 4-dimensional phase space distribution at the exit of the final focus system will provide the initial condition for more realistic simulation of the beam dynamics when ballistically focused through neutralizing plasma.

REFERENCES

- [1] S. S. Yu et al., "Focusing and Neutralization of Intense Ion Beams", Proc. PAC '03, TOAA001.
- [2] S. Eylon et al., "High brightness potassium source for the HIF neutralized transport experiment", Proc. PAC '03, WPPG012.
- [3] D. Shuman et al., "Magnetic lattice for the HIF neutralized transport experiment", Proc. PAC '03, WPPG017.
- [4] E. Henestroza et al., "Final Focus System for High Intensity Beams", Proc. PAC '03, WPPG013.
- [5] F.M. Bieniosek et al., "Beam imaging diagnostics for heavy ion beam fusion experiments", Proc. PAC '03, WPPB050.

NON-INTERCEPTING DIAGNOSTIC FOR THE HIF NEUTRALIZED TRANSPORT EXPERIMENT*

P. K. Roy[#], S. Eylon, R. Hannink, E. Henestroza, J. Ludvig, D. Shuman, and S. S. Yu
Lawrence Berkeley National Laboratory (LBNL), 1 Cyclotron Road, Berkeley, CA 94720, USA

Abstract

The NTX experiment at the Heavy Ion Fusion Virtual National Laboratory is exploring the performance of neutralized final focus systems for high perveance heavy ion beams. We are developing a non-destructive beam diagnostic system to characterize the ion beam during its operation. Ion beam space charge is sensed by measuring deflection of mono energetic electron passing transversely through the ion beam. In this diagnostic system an electron beam of a submillimeter size with 1-5 μA current and 5-8 kV energy will be injected perpendicularly through the ion beam. The position and intensity of the deflected e-beam would be registered on a scintillator for optical analysis to characterize the ion beam. An electron beam of negligible space charge will be deflected at an angle that depends on the charge density and energy distribution of the ion beam along its trajectory. The e-beam current and energy are chosen such that its trajectory will be significantly perturbed without perturbing the ion beam. We present a progress report on this diagnostic system including the characterization of the electron gun, the design of the e-beam transport system, and a study of the scintillator and its associate electronics and photonic components.

INTRODUCTION

The Heavy Ion Fusion program [1] has a great demand for energy production and a series of experiments [2-4] are under way. These experiments have been considering a beam from an ion source, like k^+ [5-6]. When attempting to characterize the profile and field distribution of an ion beam, most diagnostics like a faraday cup, slit cup, pepperpot [7-8], optical scintillator are destructive to the beam line and significantly alter the properties of ion beam itself. Moreover, during the characterization process, a beam line is non-useful for its applications, and characterization is not in same sequence of time of beam application. We are interested in use of an electron beam as an electron probe within a system to develop a non intercepting diagnostic for a ion beam profile and fields measurement.

In this proceeding, overview of the diagnostic design concept will be presented first, and will follow to a description of design, construction and setup of the system. Finally the results of electron beam deflection by magnets and future plan will be presented.

*This work has been performed under the auspices of the US DOE by UC-LBNL under contract DE-AC03-76SF00098, for the Heavy Ion Fusion Virtual National Laboratory. [#]PKRoy@lbl.gov

OVERVIEW OF NON-INTERCEPTING DIAGNOSTIC

By measuring the deflections of electrons, from an e-gun, after they pass through an ion beam, we hope to work backwards and quantify how the charge varies throughout the ion beam. In order to create an array of deflections corresponding to every section of the ion beam, the electron beam's initial displacement must be varied. A chicane magnetic arrangement would provide this initial displacement. Figure 1 shows a schematic diagram of the arrangement. This arrangement consists of four dipole magnets (D1 to D4) of equal strength wired in series to produce the field directions shown.

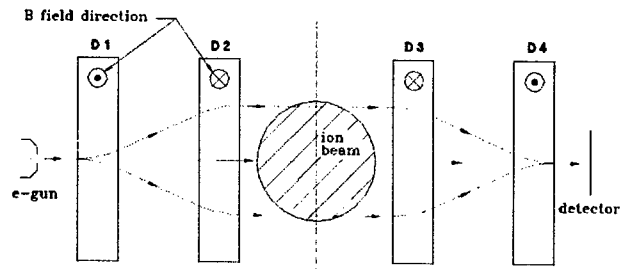


Figure 1: A sketch of non-intercepting beam diagnostic.

By varying the strength of the magnetic fields in a series of measurements, electron beam would be able to pass through every part of the ion beam, and thus a charge distribution of the cross section of the ion beam could be produced. For measurement of e-beam deflection a scintillating detector is placed at the end of the diagnostic. Deflection of an e-beam in an Ion beam charge distribution is calculated using the following formula based on a uniform cylindrical ion charge distribution.

$$\theta = \frac{2J_0 q a b}{v^2 \epsilon_0 m_e} \left(\cos^{-1} \left(\frac{b}{a} \right) \right)^{\frac{1}{2}} \quad (1)$$

where J_0 is the charge density of the ion beam, a and b are the ion beam radius, and electron beam displacement by the magnets (D1 and D2), respectively. q , m_e and v are the charge, mass and velocity of an electron, respectively. ϵ_0 is the permittivity of free space. Figure 2 shows a calculated deflection curve for a 5 keV e-beam passing through a 300 keV ion beam of 2 cm diameter and 20 mA current.

INSTRUMENTATION AND EXPERIMENTAL SETUP

Development of the diagnostic was considered in several stages. These were: selection of electron gun and electron beam imaging scintillator, design of 4 dipole magnets, installation of electron gun, magnets and scintillator in a same vacuum chamber keeping a pathway for a future ion beam line. A brief description of the devices has been presented below.

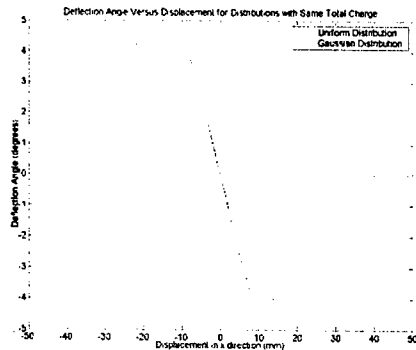


Figure 2: Deflection of electron beam by an ion beam.

Electron gun

A factory made (EGG-3101, Kimball Physics Inc.) 10 keV, and 10 μ A range LaB₆ cathode [9-10] embedded electron gun was installed in the diagnostic box to use as an electron probe. A working distance of the gun is around 1 meter with a spot of couple of hundred micron in diameter.

Chicane Magnet

The dipoles are iron dominated to minimize current requirement and provide high field uniformity. They are designed to operate in vacuum, in order to eliminate the need for a vacuum chamber that can fit between the poletips. Aluminum can be hard anodized for electrical insulation, eliminating the need for organic or fiber base inorganic insulation which are less vacuum compatible. A low current density minimizes resistive loss, allowing coil cooling by radiation only, eliminating the need for water cooling in vacuum. A small number of turns minimize voltage drop and conducting area. This place is less demand on electrical insulation and reduces out gassing. Figure 3 and 4 show the H dipole DC magnet that was designed and fabricated at LBNL. Coils are machined from a single piece of 6060-T6 aluminum, slotted to provide the desired current path, then hard anodized for electrical insulation. Leads are gold plated to minimize contact resistance. Use of annealed ultra low carbon steel was used for high permeability and low out gassing. The magnet layout (30 mm magnetic length along e-beam, 6 mm poletip gap, 60 mm drift distance (horizontal) between steel yokes, 150 mm pole-tip heights) requires a current of 6.7A @ \sim 3 mV/coil to achieve an e-beam (5 keV) height of 40 mm (32 G). This calculation includes a

PANDIRA [11] derived correction factor for the "bonus" fringe field that provides additional vertical bending beyond the pole-tip edge.

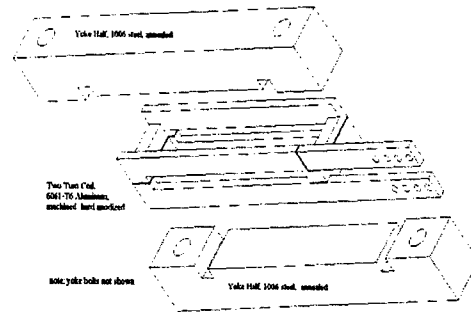


Figure 3: DC dipole magnet, exploded view.

Scintillator

An Yttrium Aluminum Perovskite Scintillator (YAP:Ce) was used with the system. Density, maximum emission length, decay time and photon emission ability of this scintillator are 5.57 g/cm³, 350 nm, 27 nsec, and 18/keV, respectively. It has negligible thermal expansion (4-11 ppm) with high melting point (1875°C). The depth or thickness of the 5 keV stopping at YAP was calculated to be 0.028 μ m using well known Bethe formula [12], where atomic density of the scintillator in atoms per cubic meter, $\rho = 3.859 \times 10^{28} \text{ m}^{-3}$ was calculated from a consideration of effective atomic number 36 of YAP:Ce scintillator. This atomic number is equal to atomic number of Krypton (Kr), therefore the atomic mass of YAP is considered to be the same as Kr (83.80). Though a calculated time constant was obtained in the femto second range, however, charge can build up on the front surface of the scintillator, if it is isolated from the ground. This charge buildup will repulse the incoming beam trajectories on or near the same landing area. To drain this charge, a 100 nm Aluminum coating on a YAP scintillator was made by evaporation. The capacitance of scintillate embedded charge relative to the aluminum layer is calculated to be 5.28×10^{-7} farad. An RC time constant 2.23×10^{-13} sec was calculated for the 100 nm coating which is sufficient for charge draining. Some input energy of the e-beam is lost in this coating. For a 100 nm coating this is calculated to be approximately 1.2keV.

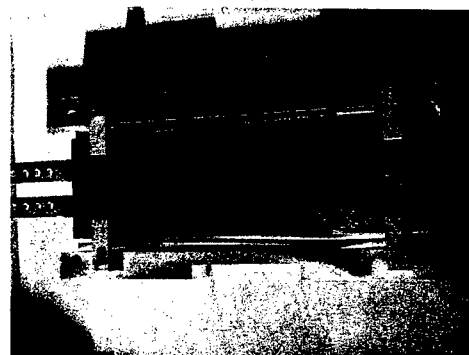


Figure 4: Mechanical Design of a DC dipole magnet.

Experimental setup

Figure 5 shows an image of the diagnostic box assembled with an electron gun, magnets and scintillator. A CCD camera is installed and focused on the scintillator. This camera was connected to a computer to record image data. During start up, the gun source is electrically heated to an emission temperature. The electron beam is focused to the scintillator using appropriate voltages for focus and grid. Pressure of the system is maintained better than 1×10^{-7} Torr using 2 turbo-molecular pumps.



Figure 5: Ion beam diagnostic.

RESULTS AND DISCUSSIONS

The electron gun operates at energy of 5 to 10 keV and delivering a beam current as our requirement of 1 to 2 μA . We are able to obtain mm size electron beam spot at a distance of 1.25m (after D4 magnet in the Fig. 1) without any magnetic steering or focusing in the drift path. Figure 6 shows images of electron beam height at an ion beam path (between D2 and D3 of Fig 1.) varying current through magnets D1 and D2 (Fig.1). A small change in electron beam location was identical by knowing a pixel

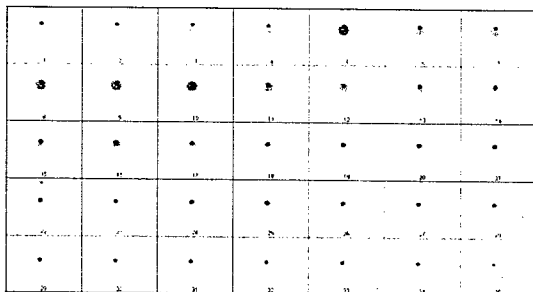


Figure 6: Electron beam deflection height through a 2 cm scintillator. Dark center spot is an e-beam spot deflected from up to down as shown by numerical numbers.

value of the center of an e-beam spot, thus beam size did not effect to any small deviation of landing, and thus were able to get a good resolution of displacement. Figure 7 shows an experimental data of e-beam displacement at the center of the diagnostic (between D2 and D3 in the Fig. 1)

by 2 magnets (D1 and D2). A displacement of 25mm for a 6keV e-beam was recorded by a gap field of 25G or a current of 6.5A through the DC magnets. We measure a height change of ± 3 cm of the e-beam that indicates that a large size (~ 6 cm diam.) ion beam scan is possible.

We are designing a time e-beam pulse system to implement the diagnostic in an ion beam.

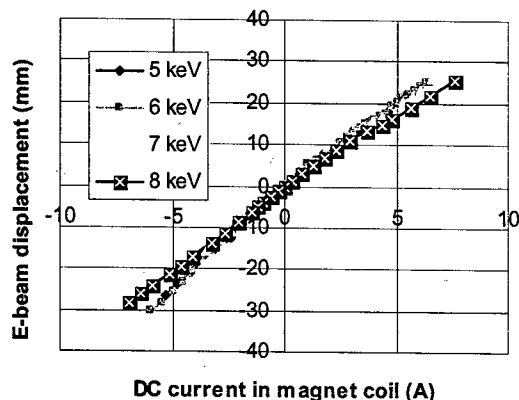


Figure 7: E-beam deflection at the center of diagnostic.

REFERENCES

- [1] R.O. Bangerter, "The heavy ion fusion program in the USA" Nucl. Instrum. and Meth. In Phys. Research A, 464 (2001) 17-23.
- [2] S. S. Yu et al., "Focusing and Neutralization of Intense Ion Beams", Proc. PAC '03, TOAA001.
- [3] E. Henestroza et al., "Neutralized Transport of High Intensity Beams", Proc. PAC '03, WPPG014.
- [4] P.A. Seidl et al., "The high current experiment: First results", Laser and Particle Beams 20 (2002),435-440.
- [5] D. Baca et al., "Fabrication of Large Diameter Alumino-Silicate K^+ Sources, Proc. PAC '03 FPAB005.
- [6] S. Eylon et al., "High brightness potassium source for the HIF neutralized transport experiment", Proc. PAC '03, WPPG012.
- [7] C. Lejeune et al., "Applied charged particle optics", ed. by A. Septier (1980), pt 13A, 159.
- [8] J. G. Wang et al. Nucl. Instrum. Methods. A307 (1991), 190
- [9] J.M. Lafferty, J. Appl. Phys. 22 (1951), 299.
- [10] P.K.Roy et al., Rev. of Sci. Instrum. 67(12) (1996), 4098.
- [11] K. Halbach et al., POISSON/ SUPERFISH, v 6.28, Los Alamos Accelerator code group, LANL.
- [12] www.aps.anl.gov/techpub/lsnotes/ls165/ls165/html

MAGNETIC LATTICE FOR THE HIF NEUTRALIZED TRANSPORT EXPERIMENT (NTX)*

D. Shuman[#], S. Eylon, E. Henestroza, P. K. Roy, W. Waldron, S. S. Yu, LBNL, T. Houck, LLNL

Abstract

The NTX experiment at the Heavy Ion Fusion Virtual National Laboratory is exploring the performance of neutralized final focus systems for high perveance heavy ion beams. A pulsed magnetic four-quadrupole transport system for a 400 keV, 80 mA space charge dominated heavy ion beam has been designed, fabricated, tested, measured, and commissioned successfully for the Neutralized Transport Experiment (NTX). We present some generalized multipole decompositions of 3-D finite element calculations, and 2-D transient finite element simulations of eddy currents in the beam tube. Beam envelope calculations along the transport line were performed using superposition of individually 3-D calculated magnetic field maps. Revised quadrupole design parameters and features, plus fabrication and testing highlights are also presented. Magnetic field measurements were made using both Hall probes (low field DC) and inductive loop coil (high field pulsed). Magnet testing consisted of repetitive full current pulsing to determine reliability.

MAGNETIC LATTICE

The transport section is designed to correspond closely to a prototypical HIF driver final focus channel. It consists of a double FODO channel with very short drift regions, including the drift from the source into the channel, and the drift into the plasma neutralization chamber. Fig. 1 shows the X and Y beam profiles through the system, with and without beam neutralization at the exit. The beam is quite large in the two center magnets, which determines the required bore size and winding radius. The magnet has a relatively short center section and a substantial portion of the magnetic field is contained in the end fringe fields, with significant axial components. The heavy ion beam is space charge dominated, having a large cross section, and being highly non-paraxial. As such, the usual method of (beam axis integrated) field quantification into normal multipoles of discrete length does not allow accurate particle tracking simulation, as these hard-edge field simplifications do not contain the axial field components and nonlinear (with radius) gradients which are a significant source of particle deflection. Thus, both normal and pseudomultipoles are important and both must be considered in lattice design, requiring 3D magnetic analysis.

[#]DBShuman@lbl.gov

*This work has been performed under the auspices of the US DOE by UC-LBNL under contract DE-AC03-76SF00098, for the Heavy Ion Fusion Virtual National Laboratory.

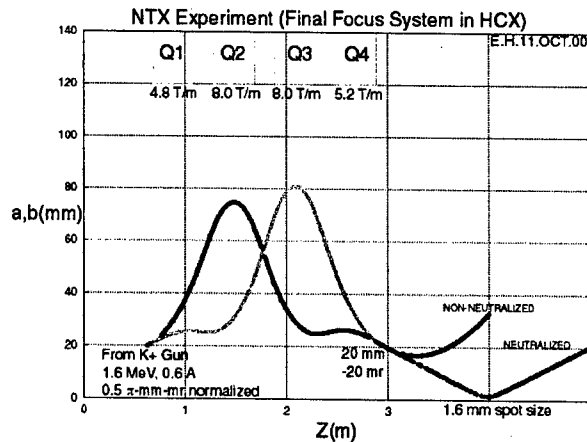


Figure 1. Magnetic Lattice

MAGNETIC FIELD MODELING

A three-dimensional finite element model of the magnet was generated, using ANSYS/EMAG and solved for the static field in 3D space. A scalar potential formulation was used, with source current elements used for the coil. The space modeled was a 1/8th section of one half the magnet. Far field (infinite boundary) elements bounded the outer radius and end, at a distance 75 cm from the magnet midplane, which extends well past the source and final focus points. A cylindrical Neumann boundary was used to simulate the steel core, in order to speed analysis for a fine mesh model. An earlier coarse mesh model with steel included (nonlinear B-H curve) showed no significant saturation.

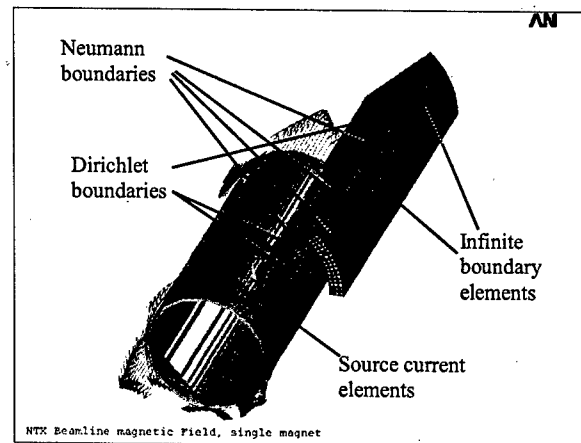
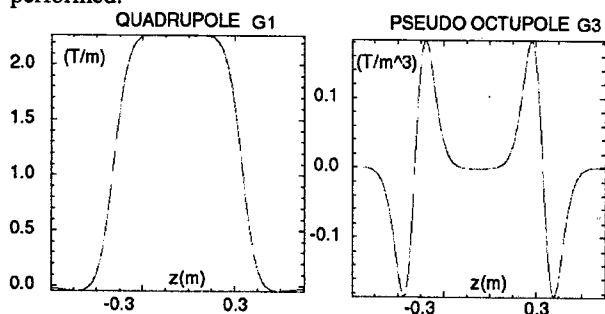


Figure 2. Symmetric Magnet Model, Half Octant

The resulting 3D field maps generated were decomposed into both normal and pseudomultipoles as a function of distance in the axial direction. Figure 3 shows these

multipoles as a function of distance in Z. Both half octant models and full magnet f.e. models, complete with spiral coil geometry and leads, were computed to determine both symmetry-allowed and full skew (normal and skew) multipoles, respectively. These are the dominant field quantities for this short but highly non-paraxial beam, with higher order normal multipoles being relatively unimportant. Finally, beam tracking simulation through a lattice of focusing elements generated by multiple superposition of these field maps was performed.



$$B_{\perp}(r, \theta, z) = G_1(z)r \cos(2\theta) + G_3(z)r^3 \cos(2\theta) + \dots$$

Fig. 3. Dominant Multipoles

MAGNET DESIGN, FAB., & TEST

Coil Design

The magnet design concept is essentially unchanged from the design presented at PAC2001¹. Subsequent changes include a larger bore and winding radius, plus a simplified coil design. Revised design and operating parameters are shown in table 1 below:

Table 1. Revised Magnet Parameters

Beam Aperture Radius, R_b	14.9	cm
Magnet Winding Radius, R_w	17.32	cm
Steel Inner Radius, R_{wi}	18.33	cm
Steel Outer Radius, R_o	25.63	cm
Mag., Total Lengths, L_m, L_o	46, 50	cm
Magnet to magnet spacing	60	cm (ctr.-ctr.)
Field Gradient, B'	2-5	T/m
Maximum Field, B	0.6	T, @12cm
Number of turns, N	8	Turns/coil
2D Field Coefficients, B_n ($\sum A_n /2A_2, n=6,10,\dots,26$)	7×10^{-4}	T/T @10cm
Conductor diameter, d_c	4.65	mm
Magnet Current, $I_{min} - I_{max}$	3.3- 8.2	kA
Magnet Resistance, R	.036	Ω
Magnet Inductance, L	232	μH
Pulse length (full half sine), t	2.2	mS
Magnet Voltage, max., V	2.7	kV
Pulse energy, max., U	7.8	kJ
Energy loss/pulse, max., Q_t	2.7	kJ
Max., Operating Pulse Rates	0.5, 0.1	Hz
Temp. Rise, Max., steady state	25	$^{\circ}C$, (0.5Hz P.R)

Fabrication

The magnet was fabricated as per ref. 1, with the following improvements:

- To simplify coil fabrication, a simplified coil design featuring a novel diagonal leadout was used. The diagonal leadout (from the inner turn) approximates a "stairway" of "missing" currents that are inherently present in any spiral coil. This allows short coils with few turns to have relatively high field symmetry. A concept is shown below in fig.3.

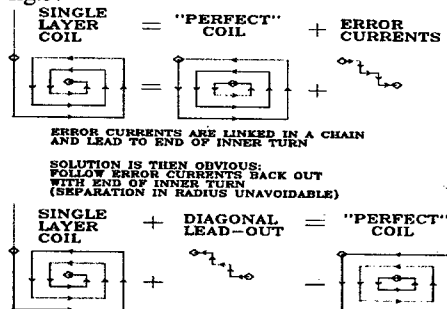


Figure 3. Diagonal Coil Leadout Concept

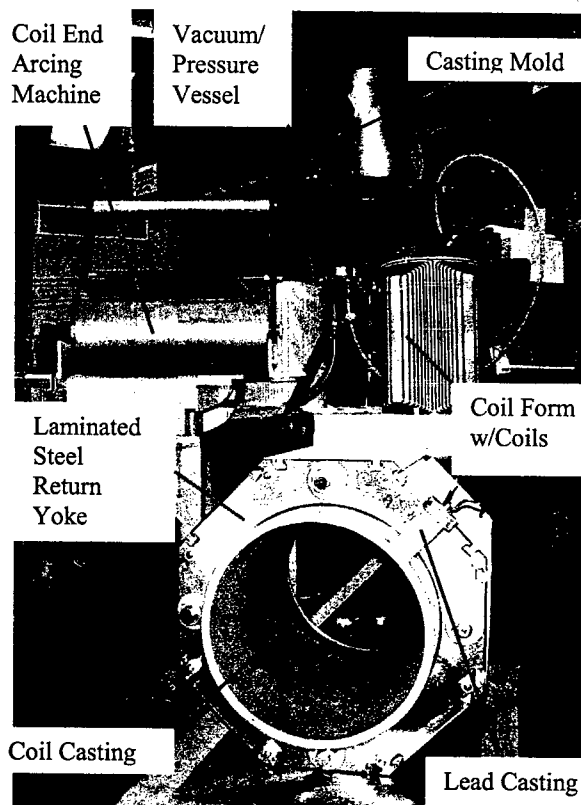


Fig. 4 Magnet Fabrication

- A lead casting section was added to provide an exit for the leads that was readily accessible on the exterior of the core for reparability. This section was designed to flare the ground surface (provided

by resistive paint) away from the leads where they exit the casting to avoid high field concentrations. This enables the leads to be kept close together in the coil area near the beam, minimizing field errors from them.

Operation

- A 2 mF pulser capacitance was chosen in order to increase the pulse length, reducing voltage and eddy currents.

Testing

- Six quadrupoles total were fabricated, to provide two spares, one of which was subjected to 10,000 full current pulses for testing reliability. All other magnets were subjected to 1,000 full current pulses for acceptance testing. No cooling, other than free air convection is necessary.
- Field was measured with a system of 12 high impedance inductive pickup coils mounted to a four arm "cross", with three three orthogonal coils mounted on each arm end. Primary goals were find the magnetic center and azimuthal axes for each magnet, though gross multipole measurements were possible. The coils are open circuit and induced voltage is measured and integrated over the magnet pulse. Figure 5 shows the axial field falloff profile compared with the computed model (peak fields normalized for comparison).

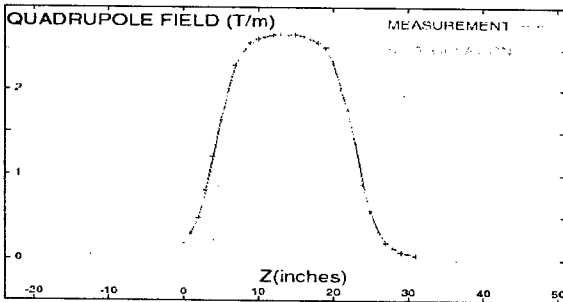


Figure 5. Calculated vs. Measured Gradient

BEAM TUBE EDDY CURRENTS

Both 2D and 3D transient magnetic modeling was performed to determine the effect of eddy currents in surrounding components such as beam tubes, flanges, diagnostics, electron traps, etc. Per ref. 1, coil and core eddy currents were calculated to be insignificant. The thin-walled stainless steel/fiberglass composite beam tube specified in ref. 1 was manufactured by an outside vendor, but the S.S. liner subsequently delaminated immediately after cure. The vendor used air pressure to hold the S.S. tube round while filament winding over it. It is thought that insufficient care was taken to balance the tensile hoop (and possibly longitudinal) stresses from air pressure against hoop compressive stresses generated from winding, to avoid residual tensile stresses in the liner. A 0.134" wall thickness standard 12" dia. S.S. vacuum tube was used instead. Eddy currents were calculated by

transient 2-D finite element analysis and found to be acceptable, with a 7.4% loss of peak field, and a 0.28 mS field peak time lag from the source current peak, as shown in figures 6 and 7.

The close magnet spacing precluded the use of core steel overhang on the coils. Such overhang, normally used to clamp off end fields, would act to couple the quadrupoles via their end fields, making them difficult to adjust and increasing eddy currents in the end laminations and plates. Similarly, vacuum flanges located in the high field regions or between the magnets could be susceptible to high eddy currents, as well.

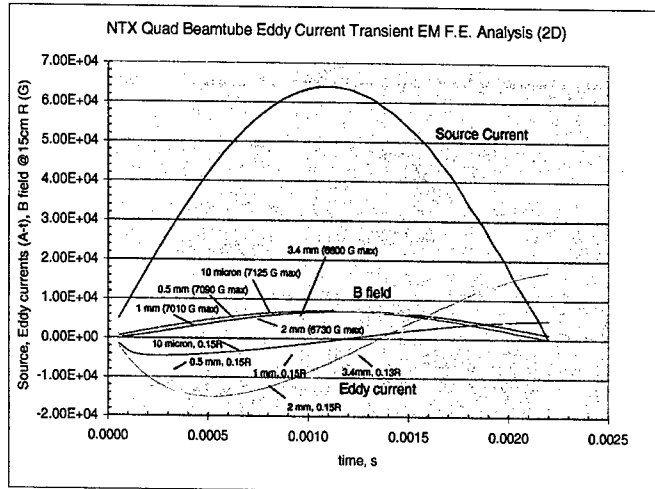


Figure 6: Beam tube Eddy Currents and B fields.

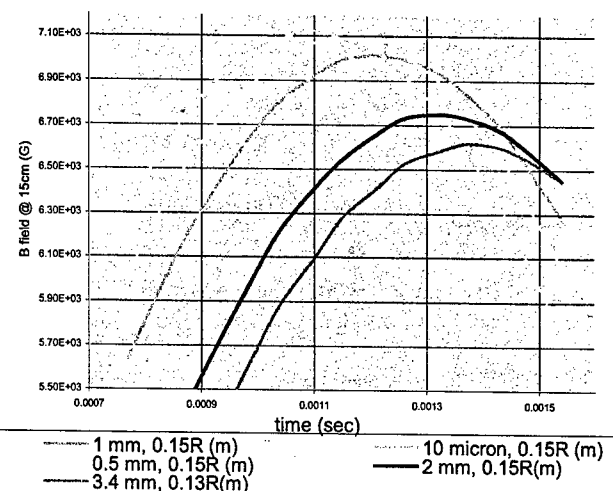


Figure 7: Peak B field vs. beam tube thickness and radius.

REFERENCES

- [1] A Large Bore Pulsed Quadrupole Magnet for Transport of High Current Beams at Low Energies, D. Shuman, et. al., PAC2001, pg. 2937

ANALYTICAL STUDY OF ENVELOPE MODES FOR A FULLY DEPRESSED BEAM IN SOLENOIDAL AND QUADRUPOLE PERIODIC TRANSPORT CHANNELS

Boris Bukh, Lawrence Berkeley National Laboratory, Berkeley, CA 94720
 Steven M. Lund, Lawrence Livermore National Laboratory, Livermore, CA 94550

Abstract

We present an analysis of envelope perturbations evolving in the limit of a fully space-charge depressed (zero emittance) beam in periodic, thin-lens focusing channels. Both periodic solenoidal and FODO quadrupole focusing channels are analyzed. The phase advance and growth rate of normal mode perturbations are analytically calculated as a function of the undepressed particle phase advance to characterize the evolution of envelope perturbations.

INTRODUCTION

The KV envelope equations are often employed to model the transverse evolution of the envelope of beam particles in intense beam transport channels[1]. For periodic focusing channels, there have been no fully analytical studies of perturbations in the beam envelope evolving about the matched beam envelope. Here we analytically calculate properties of small-amplitude elliptical envelope perturbations in the limit of full space-charge depression for several periodic thin-lens transport channels. Because the thin-lens model provides a reasonable approximation to the focusing effects of more realistic applied focusing elements, results derived provide a guide to the properties of envelope perturbations associated with space-charge-dominated beams.

ENVELOPE MODEL

The KV envelope equations for a fully depressed coasting beam with elliptical edge radii $r_x = 2\sqrt{\langle x^2 \rangle}$, $r_y = 2\sqrt{\langle y^2 \rangle}$ aligned along the transverse x and y axes are [2, 3]

$$r_j''(s) + \kappa_j(s)r_j(s) - \frac{2Q}{r_x(s) + r_y(s)} = 0, \quad (1)$$

where j ranges over x and y , Q is the dimensionless beam perveance, and s is the axial coordinate. The equations (1) apply directly to a beam in a quadrupole focusing channel with $\kappa_x = -\kappa_y$, but for solenoidal focusing one has to assume zero beam canonical angular momentum with $\kappa_x = \kappa_y$ and interpret all results in a rotating Larmor frame[2, App. A]. The equations can be written in terms of scaled sum and difference coordinates $R_{\pm} = (r_x \pm r_y)/(2\sqrt{2Q})$ as

$$\begin{aligned} 2R_+''(s) + 2\kappa_x(s)R_+(s) - \frac{1}{R_+(s)} &= 0, \\ 2R_-''(s) + 2\kappa_x(s)R_-(s) &= 0 \end{aligned} \quad (2a)$$

for solenoidal focusing, and

$$2R_+''(s) + 2\kappa_x(s)R_-(s) - \frac{1}{R_+(s)} = 0, \quad (2b)$$

$$2R_-''(s) + 2\kappa_x(s)R_+(s) = 0$$

for quadrupole focusing. In free drift regions $\kappa_x(s) = \kappa_y(s) = 0$, and the equations can be integrated by using constancy of envelope Hamiltonian

$$R_+'^2(s) - \ln R_+(s) = \text{const} \quad (3)$$

to yield[2]

$$\ln \frac{R_+(0)}{R_+(s)} = R_+'^2(0) - \left\{ \text{erfi}^{(-1)} \left[\text{erfi} R_+'(0) + \frac{e^{R_+'^2(0)} s}{\sqrt{\pi} R_+(0)} \right] \right\}^2, \quad (4a)$$

$$R_-(s) = R_-(0) + sR_-'(0), \quad (4b)$$

where $\text{erfi}(z) = \text{erf}(iz)/i$ is the imaginary error function.

Without loss of generality[2, Sec. II E], we assume that the length of the free drift interval between the two adjacent thin lenses is 2 as in Fig. 1. By symmetry we need only to consider the envelope evolution of the beam between two neighboring lenses only. We take the first lens to be at axial location $s = -1$ and the second one to be at $s = 1$. We also assume that in alternating gradient channel the second lens (at $s = 1$) is focusing in x . Then for both thin lens solenoids and quadrupoles we take near $s = 1$

$$\kappa_x(s) = \frac{1}{f} \delta(s - 1), \quad (5)$$

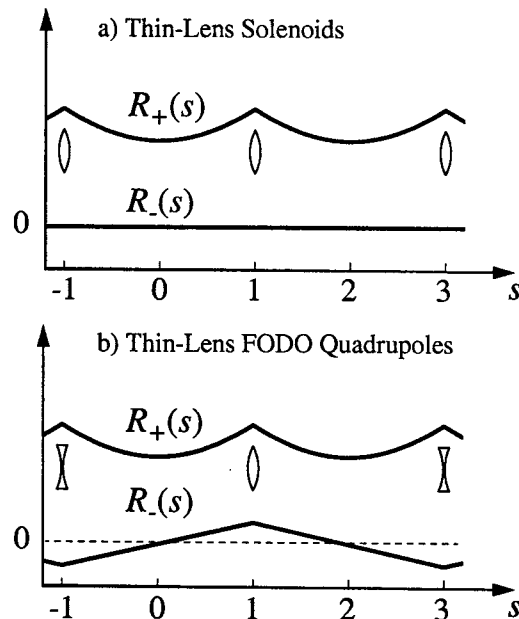


FIG. 1: Matched beam envelopes $R_{\pm}(s)$ and transport lattice for (a) solenoid, and (b) FODO quadrupole thin-lens channels.

*This research was performed at LBNL and LLNL under US DOE contact Nos. DE-AC03-76SF0098 and W-7405-Eng-48.

where $f = \text{const}$ is the thin lens focal length and $\delta(s)$ is the Dirac delta-function. The focal length f can be related to the undepressed particle phase advance over one lattice period σ_0 as [2, Sec. IID]

$$\frac{1}{f} = \begin{cases} 2 \sin^2 \frac{\sigma_0}{2}, & \text{solenoidal focusing,} \\ \sin \frac{\sigma_0}{2}, & \text{quadrupole focusing.} \end{cases} \quad (6)$$

We analyze the perturbations of the envelope coordinate vector $\mathbf{R}(s) = (R_+(s), R_+(s), \zeta(s)R_-(s), \zeta(s)R'_-(s))$ from the mid-drift at $s = 0$ to the next mid-drift at $s = 2$. Here, $\zeta(s) = 1$ when the next lens to be traversed is focusing, and $\zeta(s) = -1$ when the next lens is defocusing.

PERTURBATIVE ANALYSIS

To analyze the first-order perturbations in the coordinate vector $\mathbf{R}(s)$ we compute the Jacobian matrix $\mathbf{M}(0, 2)$ where $\mathbf{M}(s_1|s_2) = \partial \mathbf{R}(s_2)/\partial \mathbf{R}(s_1)$ and derivatives are evaluated for a matched envelope. Since $\mathbf{M}(0|2)$ is symplectic, then the first-order perturbations are stable if and only if all eigenvalues of \mathbf{M} lie on the unit circle $|z| = 1$.

In calculating $\mathbf{M}(0|2)$, we henceforth denote $\mathcal{F}(s \pm 0) \equiv \lim_{\delta \rightarrow \pm 0} \mathcal{F}(s + \delta)$ to represent the discontinuous action of the thin lenses on the beam envelope functions. To exploit lattice symmetries, we split the interval $(0, 2)$ into three parts $(0, 1-0)$, $(1-0, 1+0)$ and $(1+0, 2)$, and calculate $\mathbf{M}(0, 2)$ as $\mathbf{M}(0|2) = \mathbf{M}(1+0|2)\mathbf{M}(1-0|1+0)\mathbf{M}(0|1-0)$. By symmetry, $\mathbf{M}(1+0|2) = \mathbf{M}(0|1-0)^{-1}$. Thus,

$$\mathbf{M}(0|2) = \mathbf{M}_f(-1+0)^{-1} \mathbf{M}_s \mathbf{M}_f(1-0), \quad (7)$$

where $\mathbf{M}_s = \mathbf{M}(1-0|1+0)$ is the "singular Jacobian" associated with the thin lens focusing kick, and $\mathbf{M}_f(s) = \mathbf{M}(0|s)$ for $|s| < 1$ is the "free drift Jacobian" associated with the half-drift.

To evaluate \mathbf{M}_s , we consider the action of the thin lens according to Eqs. (2) and (5). We obtain

$$\mathbf{M}_s = \begin{bmatrix} 1 & 0 & 0 & 0 \\ -\frac{1}{f} & 1 & 0 & 0 \\ 0 & 0 & 1 & 0 \\ 0 & 0 & -\frac{1}{f} & 1 \end{bmatrix}, \quad \mathbf{M}_s = \begin{bmatrix} 1 & 0 & 0 & 0 \\ 0 & 1 & -\frac{1}{f} & 0 \\ 0 & 0 & -1 & 0 \\ \frac{1}{f} & 0 & 0 & -1 \end{bmatrix} \quad (8)$$

for solenoidal and quadrupole channels respectively.

To evaluate $\mathbf{M}_f(s)$, the free expansion solutions in Eqs. (4) and the matched beam symmetry condition $R'_+(0) = 0$ are employed to evaluate Jacobian elements:

$$\mathbf{M}_f(s) = \begin{bmatrix} \frac{R_+(s) - sR'_+(s)}{R_+(0)} & 2R_+(0)R'_+(s) & 0 & 0 \\ -\frac{s}{2R_+(0)R_+(s)} & \frac{R_+(0)}{R_+(s)} & 0 & 0 \\ 0 & 0 & 1 & s \\ 0 & 0 & 0 & 1 \end{bmatrix}. \quad (9)$$

To complete the evaluation of $\mathbf{M}_f(1-0)$, we find relations of the elements to σ_0 by deriving equations connecting $R_+(1-0) \equiv R_+(1)$, $R'_+(1-0)$, and $R_+(0)$ to these quantities for the matched beam envelope. By symmetry, for a periodic, matched envelope

$$R'_\pm(1-0) = -R'_\pm(1+0), \quad (10)$$

For solenoids, Eqs. (2a) and (5) can be integrated once about $s = 1$ to obtain

$$R'_\pm(1+0) = R'_\pm(1-0) - \frac{1}{f}R_\pm(1).$$

Combining these constraints with the matching conditions (10), we get

$$R'_\pm(1-0) = \frac{1}{2f}R_\pm(1). \quad (11)$$

Similarly, using Eqs. (2b) and (5) for alternating gradient focusing and matched beam symmetries (10), we obtain

$$R'_\pm(1-0) = \frac{1}{2f}R_\mp(1). \quad (12)$$

The solenoidal and quadrupole matching conditions in Eq. (12) for R_+ can be expressed as

$$\hat{k}R_+(1) = 2R'_+(1-0), \quad (13)$$

$$\text{where } \hat{k} = \begin{cases} \frac{1}{f} = 1 - \cos \sigma_0, & \text{solenoidal focusing,} \\ \frac{1}{2f^2} = \frac{1}{4}(1 - \cos \sigma_0), & \text{quadrupole focusing.} \end{cases}$$

Applying Eqs.(3) between $s = 0$ and $s = 1-0$ with the matched beam condition $R'_+(0) = 0$ leads to

$$R_+(1) = R_+(0)e^{R_+^2(1-0)}. \quad (14)$$

Using Eqs. (13) and (14) in Eq. (4) then yields

$$\hat{k} = 2\sqrt{\pi}e^{-R_+^2(1-0)}R'_+(1-0)\text{erfi } R'_+(1-0). \quad (15)$$

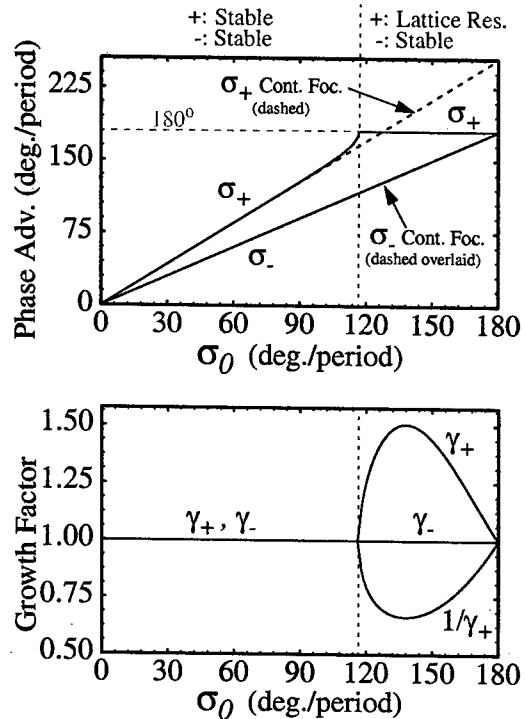


FIG. 2: Phase advances (σ_\pm) and growth factors (γ_\pm) for the breathing and quadrupole modes for a thin-lens solenoidal focusing channel and a fully depressed beam. Continuous focusing model predictions for σ_\pm are superimposed (dashed curves).

Equations (13)–(15) provide the needed constraints to relate the elements of $M_f(1-0)$ to σ_0 . Elements of $M_f(-1+0)$ can be calculated from these constraints using the matched beam symmetries

$$R_+(-1) = R_+(1), \quad R'_+(-1+0) = -R'_+(1-0). \quad (16)$$

$$\begin{aligned} M_+(0|2) &= \begin{bmatrix} \frac{R_+(-1)+R'_+(-1+0)}{R_+(0)} & 2R_+(0)R'_+(-1+0) \\ \frac{1}{2R_+(0)R_+(-1)} & \frac{R_+(0)}{R_+(-1)} \end{bmatrix}^{-1} \begin{bmatrix} 1 & 0 \\ -\frac{1}{f} & 1 \end{bmatrix} \begin{bmatrix} \frac{R_+(1)-R'_+(1-0)}{R_+(0)} & 2R_+(0)R'_+(1-0) \\ -\frac{1}{2R_+(0)R_+(1)} & \frac{R_+(0)}{R_+(1)} \end{bmatrix} \\ &= \begin{bmatrix} \cos \sigma_0 - 4R_+^2(1-0) \cos^2(\frac{\sigma_0}{2}) & 2\frac{R_+^2(0)}{f} [1 - 2R_+^2(1-0)] \\ \frac{-f}{R_+^2(0)} \cos^2(\frac{\sigma_0}{2}) [1 - \cos \sigma_0 + 4R_+^2(1-0) \cos^2(\frac{\sigma_0}{2})] & \cos \sigma_0 - 4 \cos^2(\frac{\sigma_0}{2}) R_+^2(1-0) \end{bmatrix}, \quad (17) \\ M_-(0|2) &= \begin{bmatrix} \cos \sigma_0 & 1 + \cos \sigma_0 \\ -1 - \cos \sigma_0 & \cos \sigma_0 \end{bmatrix}. \end{aligned}$$

Eigenvalues λ_{\pm} of the matrices $M_{\pm}(0|2)$ are

$$\begin{aligned} \lambda_{\pm} &= \cos \sigma_0 - 4R_+^2(1-0) \cos^2(\frac{\sigma_0}{2}) \pm 2i \cos(\frac{\sigma_0}{2}) \sqrt{[1 - 2R_+^2(1-0)] [\sin^2(\frac{\sigma_0}{2}) + 2R_+^2(1-0) \cos^2(\frac{\sigma_0}{2})]} \\ \lambda_{-} &= \cos \sigma_0 \pm i \sin \sigma_0. \end{aligned} \quad (18)$$

Real-valued mode phase advances σ_{\pm} and growth factors γ_{\pm} per lattice period satisfy $\lambda_{\pm} = \gamma_{\pm} e^{i\sigma_{\pm}}$. With proper branch selection[2] we get

$$\begin{aligned} \sigma_{+} &= \arg \lambda_{+} \text{ with } + \text{ sign in Eq. (18),} \\ \sigma_{-} &= \sigma_0, \end{aligned} \quad (19)$$

and growth factors as

$$\gamma_{+} = \begin{cases} 1, & \text{stable,} \\ \sqrt{2 [\cos \sigma_0 - 4R_+^2(1-0) \cos^2(\frac{\sigma_0}{2})]^2 - 1}, & \text{unstable,} \end{cases}$$

$$\gamma_{-} = 1.$$

These solutions are plotted in Fig. 2 as a function of σ_0 . The extent of the band of instability ($\gamma_{+} \neq 1$) in σ_0 can be calculated from γ_{+} directly as

$$\sigma_0 \in \left[\arccos \left(1 - \sqrt{\frac{2\pi}{e}} \operatorname{erfi} \frac{1}{\sqrt{2}} \right), \pi \right] \approx [116.715^\circ, 180^\circ].$$

The stability of quadrupole focusing can be investigated analogously except that we must work with the full 4×4 Jacobian matrix $M(0|2)$. After multiplying out the matrices in Eq. (7) and calculating the eigenvalues using the constraints in Eqs. (12)–(15) yields

$$\lambda = w - \frac{1}{2}\hat{k} \pm i\sqrt{w\hat{k} + [1 - \frac{1}{2}\hat{k}] [\hat{k} + 8R_+^2(1-0)]}, \quad (20)$$

where $w = \pm \sqrt{[1 - \frac{1}{2}\hat{k}] [1 - \frac{1}{2}\hat{k} - 8R_+^2(1-0)]}$ and \hat{k} is given by Eq. (13). These eigenvalues can be employed to calculate phase advances (σ_B and σ_Q) and growth factors (γ_B and γ_Q) of the breathing and quadrupole modes as

For solenoidal focusing R_{\pm} are uncoupled, and $M(0|2)$ is of block diagonal form with $M(0|2) = \begin{bmatrix} M_+(0|2) & 0 \\ 0 & M_-(0|2) \end{bmatrix}$, where $M_{\pm}(0|2)$ are 2×2 symplectic matrices that can be independently analyzed for the stability of perturbations. We compute $M_{\pm}(0|2)$ from Eq. (7):

$\sigma_{B,Q} = 2 \arg \lambda$ and $\gamma_{B,Q} = |\lambda|^2$ (see Fig. 3). Using Eqs. (15) and Eq. (20) we find numerically that the instability band is located on the interval $\sigma_0 \in (121.055^\circ, 180^\circ)$.

REFERENCES

- [1] J. Struckmeier and M. Reiser, Part. Accel. **14**, 227 (1984).
- [2] S. M. Lund and B. Bukh, *Stability of the KV envelope equations describing intense ion beam transport* (2003), preprint.
- [3] M. Reiser, *Theory and Design of Charged Particle Beams* (John Wiley & Sons, Inc., New York, 1994).

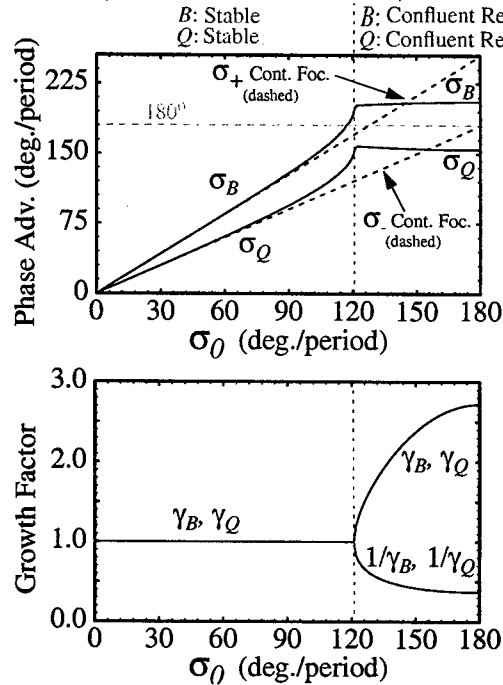


FIG. 3: Phase advance (σ_Q and σ_B) and growth factors (γ_Q and γ_B) for the breathing and quadrupole modes for a thin-lens FODO quadrupole focusing channel and a fully depressed beam. Continuous focusing model predictions for σ_{\pm} are superimposed (dashed curves).

INFLUENCE OF CONDUCTING PLATE BOUNDARY CONDITIONS ON THE RMS ENVELOPE EQUATIONS DESCRIBING INTENSE ION BEAM TRANSPORT*

Steven M. Lund, Lawrence Livermore National Laboratory, Livermore, CA 94550
Boris Bukh, Lawrence Berkeley National Laboratory, Berkeley, CA 94720

Abstract

In typical diagnostic applications, intense ion beams are intercepted by a conducting plate with slits to measure beam phase-space projections. This results in the transverse space-charge field near the plate being shorted out, rendering simple envelope models with constant space-charge strength inaccurate. Here we develop a simple corrected envelope model based on analytical calculations to account for this effect on the space-charge term of the envelope equations, enabling more accurate comparisons with experiment. Results are verified with 3D self-consistent PIC simulations.

INTRODUCTION

Low-order models of intense ion beams often employ the rms envelope equations to describe the self-consistent evolution of the beam edge in response to applied focusing, space-charge, and thermal defocusing forces.¹ Such envelope models are typically solved with constant beam emittances (phase-space area) and perveance (space-charge strength) to extrapolate experimental measurements and understand the evolution of the beam envelope away from diagnostic stations. Developing a simple model to compensate for changes in the envelope induced by plates used in diagnostics is important to enable more precise estimates of the beam envelope without the need for large simulations. Elimination of systematic errors in this process improves beam envelope control and matching — important to limit the generation of beam halo and related particle losses.

ENVELOPE MODEL

Consider a long-pulse, unbunched beam with particles of charge q and mass m moving with axial velocity $\beta_b c$ and relativistic factor $\gamma_b = 1/\sqrt{1 - \beta_b^2}$. We take the transverse orbit $x(s)$ of a beam particle to satisfy the paraxial (axial energy variation of particles neglected) equation of motion¹

$$x'' + \kappa_x x + \frac{q}{m\gamma_b^3 \beta_b^2 c^2} \frac{\partial \phi}{\partial x} = 0. \quad (1)$$

Here, s is the axial coordinate of a beam slice, $\kappa_x(s)$ is the linear applied focusing functions of the lattice, and the electrostatic potential ϕ is related to the density of beam particles n by the 3D Poisson equation $\nabla^2 \phi = -qn/\epsilon_0$

subject to $\phi = \text{const}$ on conducting boundaries. An analogous equation applies to the y -orbit $y(s)$.

Denote a transverse statistical average in a axial slice of beam particles by $\langle \dots \rangle_\perp$. RMS measures of the transverse edge radii of the beam envelope are

$$r_x(s) = 2\sqrt{\langle x^2 \rangle_\perp} \quad \text{and} \quad r_y(s) = 2\sqrt{\langle y^2 \rangle_\perp}. \quad (2)$$

Differentiating the equation for r_x and employing Eq. (1) yields the envelope equation

$$r_x'' + \kappa_x r_x - \frac{2Q}{r_x + r_y} F_x - \frac{\epsilon_x^2}{r_x^3} = 0. \quad (3)$$

Here, $Q = q\lambda/(2\pi\epsilon_0 mc^2 \gamma_b^3 \beta_b^2) = \text{const}$ is the dimensionless perveance ($\lambda = \text{const}$ is the line-charge density of the beam slice),

$$F_x = -\frac{4\pi\epsilon_0}{\lambda} \left(\frac{r_x + r_y}{r_x} \right) \left\langle x \frac{\partial \phi}{\partial x} \right\rangle_\perp, \quad (4)$$

is a form-factor, and

$$\epsilon_x = 4 \left[\langle x^2 \rangle_\perp \langle x'^2 \rangle_\perp - \langle x x' \rangle_\perp^2 \right]^{1/2} \quad (5)$$

is the rms emittance. Analogous equations to (3)–(5) apply in y . For the special case of 2D ($\partial/\partial z = 0$) transverse self-fields with constant charge density on nested elliptical surfaces with principal axis radii αr_x and αr_y aligned with the x - and y -coordinate axes, Sacherer² showed that $F_x = F_y = 1$. The Vlasov model self-consistent KV distribution satisfies this condition for a uniform density elliptical beam with $\epsilon_x = \text{const}$ and $\epsilon_y = \text{const}$. The envelope equations (3) are also often applied with $F_x = F_y = 1$ in an rms equivalent beam sense.^{1,2}

SELF-FIELD SOLUTION

We model a beam near a conducting plate as impinging on a perfectly conducting plane at $z = 0$ in free-space from $z < 0$. Then the method of images can be used to solve for ϕ in the beam region with $z < 0$ as

$$\phi(\mathbf{x}) = \frac{q}{4\pi\epsilon_0} \int_{\text{beam}} d^3 \tilde{\mathbf{x}} \left[\frac{n(\tilde{\mathbf{x}})}{|\mathbf{x} - \tilde{\mathbf{x}}|} - \frac{n(\tilde{\mathbf{x}}_I)}{|\mathbf{x} - \tilde{\mathbf{x}}_I|} \right], \quad (6)$$

where $\mathbf{x} = x\hat{\mathbf{x}} + y\hat{\mathbf{y}} + z\hat{\mathbf{z}}$ and $\mathbf{x}_I = x\hat{\mathbf{x}} + y\hat{\mathbf{y}} - z\hat{\mathbf{z}}$ are the direct and image coordinates, and we have dropped an arbitrary additive constant. We further idealize by assuming that the beam is normally incident with uniform density and a constant, round edge-radius ($r_x = r_y = R = \text{const}$). Then the beam density is

$$n(r, z) = \frac{\lambda}{\pi q R^2} \Theta(R - r) \Theta(-z), \quad (7)$$

*This research was performed at LLNL and LBNL under US DOE contract Nos. W-7405-Eng-48 and DE-AC03-76SF0098.

where $\Theta(x)$ is the Heaviside step-function [$\Theta(x) = 0$ for $x < 0$ and $\Theta(x) = 1$ for $x > 0$]. In (r, θ, z) cylindrical coordinates, $1/|\mathbf{x} - \tilde{\mathbf{x}}|$ can be expanded as³

$$\frac{1}{|\mathbf{x} - \tilde{\mathbf{x}}|} = \sum_{m=-\infty}^{\infty} \int_0^{\infty} dk e^{im(\theta - \tilde{\theta})} J_m(kr) J_m(k\tilde{r}) e^{k(z - \tilde{z})},$$

where $z_>$ and $z_<$ denote the greater and lesser of z and \tilde{z} , and $J_m(x)$ is an m th-order ordinary Bessel function. Using this expansion and Eq. (7) in Eq. (6) gives in the beam

$$\phi(r, z) = \frac{\lambda}{\pi\epsilon_0} \int_0^{\infty} \frac{dw}{w^2} (1 - e^{-w|z|/R}) J_0\left(w \frac{r}{R}\right) J_1(w),$$

and the corresponding radial and axial electric field components $E_r = -\partial\phi/\partial r$ and $E_z = -\partial\phi/\partial z$ are

$$\begin{aligned} E_r(r, z) &= \frac{\lambda}{\pi\epsilon_0 R} \int_0^{\infty} \frac{dw}{w} (1 - e^{-w|z|/R}) J_1\left(w \frac{r}{R}\right) J_1(w), \\ E_z(r, z) &= \frac{\lambda}{\pi\epsilon_0 R} \int_0^{\infty} \frac{dw}{w} e^{-w|z|/R} J_0\left(w \frac{r}{R}\right) J_1(w). \end{aligned} \quad (8)$$

These field components are plotted in Fig. 1. Note that the radial field remains nearly linear within the beam ($r < R$) until z is a fraction of a beam radius from the plate. The axial field increases near the plate because the negative image beam is closer.

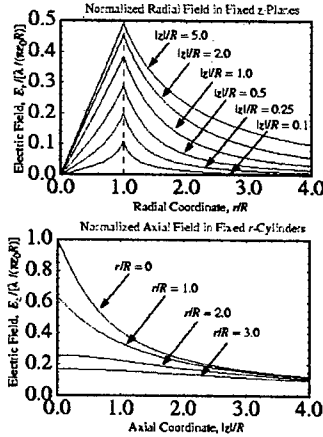


FIG. 1: Self-field components near a conducting plate.

Equations (8) are checked by calculating the limits

$$\begin{aligned} \lim_{z \rightarrow -\infty} E_r(r, z) &= \frac{\lambda}{\pi\epsilon_0 R} \int_0^{\infty} \frac{dw}{w} J_1\left(w \frac{r}{R}\right) J_1(w) \\ &= \frac{\lambda}{2\pi\epsilon_0 R} \begin{cases} \frac{r}{R}, & 0 \leq \frac{r}{R} \leq 1, \\ \frac{1}{r/R}, & 1 \leq \frac{r}{R}, \end{cases} \\ E_z(r = 0, z) &= \frac{\lambda}{\pi\epsilon_0 R} \int_0^{\infty} \frac{dw}{w} e^{-w|z|/R} J_1(w) \\ &= \frac{\lambda}{\pi\epsilon_0 R^2} (\sqrt{R^2 - z^2} - |z|). \end{aligned} \quad (9)$$

The radial field limit is the usual expression for a uniform density beam of radius R . The axial field limit shows that $\phi(r = 0, z)$ logarithmically diverges in $|z|$. This divergence is related to the 2D nature of the problem and shows that this model is inadequate for direct use in estimates of axial acceleration induced by the plate. Regularization of this divergence to model image induced self-field accelerations can be carried out by adding a grounded, cylindrical pipe to cutoff the self-field interaction range (as would be present in the laboratory).

CORRECTED AXISYMMETRIC ENVELOPE EQUATION

We apply the self-field solution above to motivate a simple, corrected envelope equation for an axisymmetric beam with a normally incident centroid impinging on a conducting plate from $z < 0$. We take $\kappa_x(s) = \kappa_y(s) \equiv \kappa(s)$, $\epsilon_x = \epsilon_y \equiv \epsilon$, and $r_x(s) = r_y(s) \equiv R(s)$. The form-factors (4) are calculated from Eq. (8) as

$$F_x = F_y = -\frac{4\pi\epsilon_0}{\lambda} \left\langle r \frac{\partial\phi}{\partial r} \right\rangle_{\perp} = F\left(\frac{|z|}{R}\right) \quad (10)$$

where,

$$F(\zeta) \equiv 8 \int_0^{\infty} \frac{dw}{w^2} (1 - e^{-w\zeta}) J_1(w) J_2(w). \quad (11)$$

We apply this form-factor to a beam with evolving radius $r_x(s) = r_y(s) = R(s)$ to obtain a corrected axisymmetric beam envelope equation

$$R'' + \kappa R - \frac{Q}{R} F\left(\frac{|s - s_p|}{R}\right) - \frac{\epsilon^2}{R^3} = 0. \quad (12)$$

Here, $|s - s_p|$ is the axial distance of the beam slice from the conducting plate.

An approximate analytical expression for the form-factor (11) can be calculated using the on-axis field $E_z(r = 0, z)$ in Eq. (9) and the Poisson equation to derive a power series solution for E_r valid within the beam. Truncating this series to radial terms of order r^3 and lower yields

$$F(\zeta) \simeq \frac{\zeta}{\sqrt{1 + \zeta^2}} \left[1 + \frac{1}{4} \frac{1}{1 + \zeta^2} \left(1 - \frac{\zeta^2}{1 + \zeta^2} \right) \right]. \quad (13)$$

The “exact” [Eq. (11)] and approximate [Eq. (13)] form-factors are plotted versus ζ in Fig. 2. For large ζ note that $F \simeq 1$ and we obtain the usual envelope equations, whereas F rapidly decreases to zero for ζ corresponding to several beam radii from the plate where the radial self-field is shorted out by the conducting plate, thereby decreasing the strength of the perveance term in the envelope equation.

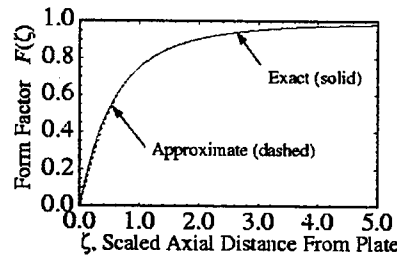


FIG. 2: Form factor and approximate form factor.

A numerical solution to the corrected envelope equation (12) is plotted in Fig. 3 together with the uncorrected solution for $F = 1$. Parameters correspond to typical diagnostic situations in the High Current Experiment (HCX) for Heavy-Ion Fusion (HIF),⁴ where a 1–1.8 MeV, 200–700 mA, K^+ ion-beam with $\epsilon_x \sim \epsilon_y \sim 50$ –100 mm-mrad is

Perveance Q	Emittance ϵ (mm-mrad)	Initial conditions		Final Conditions (R in mm, R' in mrad)					
		$R(0)$ (cm)	$R'(0)$ (mrad)	$F = 1$		$F = F(s - s_p /R)$		3D PIC Simulation	
				$R(s_p)$	$R'(s_p)$	$R(s_p)$	$R'(s_p)$	$R(s_p)$	$R'(s_p)$
$8 \cdot 10^{-4}$	100.	1.	0.	1.0220	6.2444	1.0211	5.5765	1.0223	5.5508
$8 \cdot 10^{-4}$	100.	1.	20.	1.1608	25.7757	1.1600	25.1224	1.1616	25.1150
$8 \cdot 10^{-4}$	100.	1.	40.	1.2998	45.3919	1.2990	44.7511	1.3012	44.7790
$8 \cdot 10^{-4}$	100.	1.	-20.	0.8833	-13.1644	0.8825	-13.8492	0.8836	-13.8960
$8 \cdot 10^{-4}$	100.	1.	-40.	0.7450	-32.3841	0.7442	-33.0866	0.7448	-33.1350
$10 \cdot 10^{-4}$	50.	1.	0.	1.0250	7.1132	1.0212	5.5765	1.0178	5.2704
$10 \cdot 10^{-4}$	50.	1.	20.	1.1639	26.6470	1.1600	25.1224	1.1567	24.8105
$10 \cdot 10^{-4}$	50.	1.	-20.	0.8863	-12.3204	0.8825	-13.8492	0.8791	-14.1640

TABLE I: Initial and final envelope radii and angles for uncorrected and corrected envelope models and self-consistent PIC simulations.

focused in a FODO quadrupole lattice with period 60 cm and an undepressed particle phase advance of $\sigma_0 = 60^\circ - 90^\circ$. Free-drifts to diagnostic stations are ~ 7 cm, average matched beam radii are ~ 1 cm, and maximum matched beam envelope angles are ~ 50 mrad. Final values of envelope solutions for a range of HCX-like parameters are contrasted in Table I for form-factors $F = 1$ and $F(|s - s_p|/R)$. The most significant correction for these parameters is in the envelope angle at the plate $R'(s_p)$ with typical experimentally resolvable errors ~ 1 mrad occurring. Envelope coordinate errors $R(s_p)$ are not resolvable.

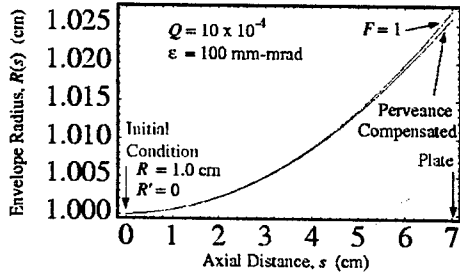


FIG. 3: Envelope for a drift solution into a plate.

PIC SIMULATIONS

Self-consistent 3D electrostatic PIC simulations were carried out to check the corrected envelope model predictions presented above for deviations due to: self-field nonlinearities, emittance growth, variation in the beam envelope near the plate [$R(s) \neq \text{const}$ in beam self-fields], energy deviations due to the beam seeing its image in the plate, and elliptical beam effects due to $r_x \neq r_y$ (simulated but not presented in this article). The WARP code developed by LLNL for simulation of intense beams for HIF applications was employed. This code is modular with an extensive hierarchy of models.⁵ We carried out simulations with: a 10 cm radial beam pipe with $\phi = 0$, boundary conditions on the left and right axial bounds with $E_z = 0$ (at injection) and $\phi = 0$ (at plate), and steady-state mid-pulse solutions iterated from uniform, semi-Gaussian beam injection conditions on the left axial boundary. Results of these simulations are included in Table I and agree well with corrected envelope model results for typical ranges of Q in the HCX experiment.⁴ The simulations showed neg-

ligible rms emittance growth ($\sim 1\%$ and less) and verified that the nonlinear space-charge fields within a fraction of a beam radius of the plate have insufficient time to cause deviations from the simple envelope model.

CONCLUSIONS

Generalized transverse envelope equations were derived to improve modeling of intense ion-beams impinging at normal incidence on a conducting plate. These equations were analyzed in an axisymmetric limit using an analytical solution form-factor to account for the plate shorting-out the space-charge field near the plate. Model results compared well with self-consistent 3D PIC simulations. Contrasting results with standard (fixed perveance term) envelope equations for usual parameters shows that small, but significant angle errors result if this effect is not corrected. Comparisons of experimental results to envelope models were improved by incorporating this systematic effect in the analysis of the HCX experiment. In this work, we employed heuristic form-factors to model the experimental beam with elliptical cross-section:

$$F_x = F_y = F \left(\frac{|s - s_p|}{\sqrt{r_x(s)r_y(s)}} \right). \quad (14)$$

Simulations verify that this replacement recovers most of the correction for elliptical beams without extreme ellipticity ($r_x/r_y \sim 3$ and less) and in continuing studies we are developing improved approximations.

ACKNOWLEDGMENTS

The authors wish to thank Edward Lee and John Barnard for useful discussions and Dave Grote and Jean-Luc Vay for help with the WARP simulations.

REFERENCES

1. M. Reiser, *Theory and Design of Charged Particle Beams*, (Wiley, 1994).
2. F.J. Sacherer, IEEE Trans. Nuc. Sci. **14**, 1105 (1971).
3. J.D. Jackson, *Classical Electrodynamics*, (Wiley, 1975).
4. P.A. Seidl et al., paper ROAC001, PAC 03.
5. D.P. Grote, et al., Nuc. Instr. Meth. A **415**, 428 (1998).

REALISTIC MODELING OF CHAMBER TRANSPORT FOR HEAVY-ION FUSION*

W. M. Sharp, D. P. Grote, D. A. Callahan, M. Tabak, LLNL, Livermore, CA 94550, USA
E. Henestroza, S. S. Yu, LBNL, Berkeley, CA 94720, USA
P. F. Peterson, U C Berkeley, Berkeley, CA 94720, USA
D. R. Welch, D. V. Rose, Mission Research Corporation, Albuquerque, NM 87110, USA

Abstract

Transport of intense heavy-ion beams to an inertial-fusion target after final focus is simulated here using a realistic computer model. It is found that passing the beam through a rarefied plasma layer before it enters the fusion chamber can largely neutralize the beam space charge and lead to a usable focal spot for a range of ion species and input conditions.

INTRODUCTION

To achieve high gain, indirect-drive targets for heavy-ion fusion must be driven by a tailored input-energy profile.[1] This profile is designed to launch a series of four shocks through the capsule that compress and accelerate the fuel on a low adiabat. The pulse shape typically consists of a long (~ 25 ns), low-power "foot" that heats the hohlraum interior to about 100 eV and launches the first shock. The power is then ramped to the peak value and held for about 8 ns as the subsequent three shocks are launched. The hohlraum geometry and the required temperature history of the capsule determine the ion-beam current profile. In addition, distributed-radiator targets [2,3] require different ion kinetic energies in the foot and main pulses to compensate for ion range shortening as the hohlraum is heated, and the beam energy must be deposited in an annular region on each end of the 5-mm-radius cylindrical target to produce the necessary radiation symmetry inside the hohlraum. These target requirements put tight constraints on the number, current, and focal radius of the drive beams.

A point design meeting these constraints has recently been worked out [4]. In this paper, we use the electromagnetic particle-in-cell code LSP [5,6] to investigate the chamber transport of the foot and main-pulse beams of this design. The single-beam simulations here include beam neutralization by plasma injected into the chamber-entry beam line, collisional ionization of the beam and background gas, and photoionization by X rays from the heated target. The results both demonstrate the viability of the point design and explore the effects of the initial emittance and convergence angle of the beam, the choice of ion species, and the spatial profile of the neutralizing plasma.

RESULTS

Parameters

The power profile required by the point-design target is built up using beams with different durations, currents, energies, and arrival times, as sketched in Fig. 1. A total of 120 beams is specified, divided into five classes. The lower-energy foot is built up by stacking three types of beam, and the main pulse is formed from two more types. The large number is needed both to keep the current in each beam manageable and to give each type of beam adequate azimuthal symmetry when deposited in the annuli on the target ends.

The point design specifies beams of singly charged bismuth ions (209 amu). However, the simulations here also model beams of xenon (131 amu) to test the sensitivity of the beam focal radius to ion mass. Since target stopping power is principally a function of ion velocity, the energy of ions is roughly proportional to atomic mass M , and beam current increases inversely with M . The beam perveance, which is a measure of the importance of space charge in transverse dynamics, increases like M^2 . To have the required stopping power, bismuth main-pulse ions require an energy of 4 GeV, while xenon ions must have 2.5 GeV. Foot pulse energies are 25% lower. Due to their higher power, the initial foot pulses and the final 48 main pulses are the most challenging to focus, so the beam parameters used here match those two types. These main-pulse beam currents

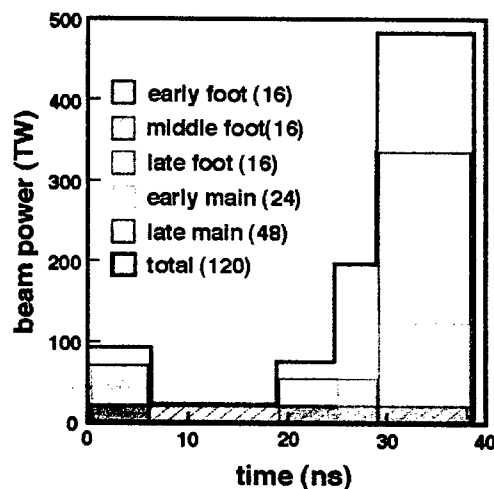


Figure 1: Power deposited on the fusion target by 120 ion beams. Numbers in parentheses give the number of beams of each type.

* This work was performed under the auspices of the U. S. Department of Energy by University of California Lawrence Livermore National Laboratory and Lawrence Berkeley National Laboratory under contracts W-7405-ENG-48 and DE-AC03-76SF00098.

are 2 kA for bismuth and 3.2 kA for xenon, and the corresponding foot-pulse currents are 1.5 kA and 2.4 kA. In all cases here, beam current falls off in the 3-ns beam ends like a normal ogive, and the radius drops from its mid-pulse value to 2 cm with a similar S-shaped pattern.

As discussed elsewhere [7] in more detail, each beam is focused on a target location six meters from the last final-focus magnet. A beam first passes through a conical 3-m pipe lined with a molten-salt vortex to protect the surface. This molten-salt layer is modeled as an insulator with a surface conductivity of 220 S/m. The beam then enters the 3-m radius fusion chamber, filled with BeF₂ and LiF vapor from the molten salt jets used to protect the chamber walls. This background gas has a vapor pressure of $7 \times 10^{12} \text{ cm}^{-3}$.

Distributed-radiator targets require that at least 90% of the beam energy be deposited in an annulus on each end of the hohlraum. For the specific target used in the point design, the main pulse must hit an annulus with a half-width of 1.8 mm, and the annulus for foot pulses has a 2.2-mm half-width. Therefore, a good criterion for evaluating the simulations is the fraction of energy deposited in a band with a half-width equal to that of the target annulus. This measure ignores the curvature of the annulus but is still a useful approximation.

Effects of Plasma Parameters

Plasma neutralization after final focus is essential for all the cases discussed here. The maximum perveance of main pulses is 7×10^{-5} for bismuth and 1.7×10^{-4} for xenon, and that of foot pulses is 2.5 times higher. Analytic work by Olson [8] indicates that the upper perveance limit for ballistic transport is about 1.6×10^{-5} , so the number of beams would have to be increased roughly ten-fold to meet this condition. Instead, as in Ref. 7, we use a rarefied plasma in the beam entry pipe to neutralize each beam before it enters the chamber. Placing a 10-cm thick layer of plasma with a density of $3 \times 10^{11} \text{ cm}^{-3}$ near each end of the 3-m entry pipe increases beam neutralization from about 30% near the target to more than 95% and decreases the rms radius of the beam focal-spot from about 2.5 cm to less than 2 mm.

While a neutralizing plasma upstream makes a dramatic improvement in beam focus, we find that increasing the plasma density has little effect, so long as there are sufficient plasma electrons in the volume swept out by the beam to fully neutralize the beam space charge. The $3 \times 10^{11} \text{ cm}^{-3}$ plasma density used here is about a factor of ten higher than this minimum, but a significant change in the beam focal radius is only seen when the plasma density is lower than about 10^{10} cm^{-3} .

Although the beam focal spot is not sensitive to the plasma density, the axial density profile of the plasma layers is found to have a pronounced effect, particularly that of the first layer encountered by the beam. When the plasma density drops abruptly to zero at the plasma edge, only about 85% of the energy of a bismuth main pulse falls within the requisite 1.8-mm half-width band, but this fraction increases to 92% when the density falls

parabolically over 3-cm and to 97% for a 6-cm parabolic or normal-ogive edge. An examination of these cases shows that a current of backstreaming electrons nearly equalling the beam current develops as the unneutralized beam approaches the square-profile plasma. This current flows near the beam axis, and the resulting nonlinear space-charge field within the beam causes a substantial emittance increase. Both the electron current and the emittance increase are less for the other plasma profiles. For example, we see only a 10% emittance increase in the entry pipe for the ogive profile, compared with nearly a doubling for a square plasma edge. For the remaining cases here, we use the more realistic ogival profile.

We have also studied the sensitivity of the beam focal spot to the length plasma. Specifically, we have compared placing a plasma layer near each end of the entry pipe against backfilling the entire entry pipe with plasma. In each case, a 6-cm ogival plasma boundary is used on each plasma edge, and the same $3 \times 10^{11} \text{ cm}^{-3}$ interior density is specified. For both bismuth and xenon main pulses, a plasma backfill increases the energy deposited on the target annulus by about 3%. Nonetheless, we use the layout with two plasma layers for other cases here because it poses fewer engineering problems.

Effect of Initial Emittance

The robust point design specifies an initial normalized edge emittance of about 2 mm-mrad, allowing less than a factor of five growth from source to target. Simulations show a marked degradation in the beam focal spot when this stringent condition is not met. When the initial emittance of a xenon main pulse is doubled, for example, the energy deposited in a 1.8-mm half-width band drops from 96% to 90%, and this fraction drops to about 85% when the emittance is tripled. Bismuth beams a somewhat less sensitive to emittance change, but a tripling of the nominal value still leads to an unusable focal spot. Since the emittance grows only about 20% in the chamber when a realistic plasma density profile is used, emittance growth in the accelerator is tightly constrained.

Effect of Convergence Angle

A smaller beam convergence angle is preferable for several reasons. The unshielded solid angle around the target through with neutrons, gamma rays, and debris can escape is proportional to the square of the beam radius, so reducing the convergence angle simplifies shielding. A second benefit is that the beam bundle converging on each end of the hohlraum can have a smaller cone angle, allowing the use of higher-gain targets as well as smaller and less costly final-focus magnets.

The robust point design specifies a maximum convergence angle of 10-mrad, corresponding to a 6-cm radius after final focus, six meters from the target. LSP simulations of both bismuth and xenon show less than a 5% drop in the energy deposited within the target annulus when a 7.5-mrad convergence angle is used. This change is substantially less than the 25% predicted from a simple ballistic-transport model, indicating that residual space

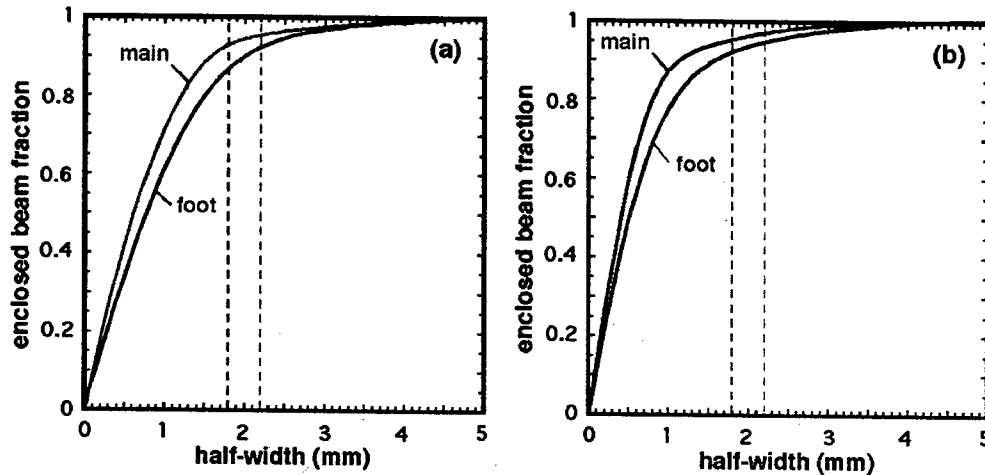


Figure 2: Fraction of beam energy deposited within a band of a specified half-width for (a) xenon and (b) bismuth main and foot pulses. Half-widths of the corresponding target annuli are shown as dashed lines.

charge still plays a role in transverse dynamics. Due to this insensitivity to convergence angle, an optimized design would likely use a smaller value, although the other simulations here use 10-mrad.

Effects of Ion Species

The choice of beam ion species has a major impact on the cost of a driver. Since the required energy of beam ions is proportional to their atomic mass, and the cost of induction accelerators increases proportionally with the beam energy, power-plant studies favor a low ion mass.

Energy deposition for main and pulses of bismuth and xenon are compared in Fig. 2. While bismuth has better focus near the center of the pulse and is therefore more robust, as expected, both species satisfy the criterion that at least 90% of beam energy fall within the appropriate target annuli. The main pulse fractions are 96% for bismuth and 93% for xenon. Due to the absence of a photoionized plasma, the foot pulses have poorer neutralization near the target, a larger halo, and lower fractional deposition. However, the deposition fractions are only about 1% less than the corresponding main-pulse values, due to the wider target annulus.

Recent work on beam sources indicates that intense beams of negatively charged halogen ions may be feasible [9]. Such beams could be photoneutralized after final focus by laser and would not need a neutralizing plasma. We have simulated chamber transport of a neutral iodine (127 amu) main pulse, using the same beam power as the point design and including ionization of the beam and background-gas due to collisions and target X rays. Near the target, the net charge of the iodine beam is less than that of a plasma-neutralized xenon beam, and the fraction of energy deposited in a 1.8-mm half-width band exceeds 98%, compared with 93% for xenon. This improved beam deposition might allow the use of higher emittance beams and permit a simpler chamber design due the absence of plasma neutralization.

CONCLUSIONS

The chamber-transport simulations here improve on those published with the "robust point design" [4] in several ways. Both the beams and the plasmas used to neutralize them are given more realistic density profiles, boundary conditions in the chamber entry pipe are closer to those expected in a driver, and a much wider range of beam parameters has been investigated. The principal finding of this work is that elements as low in atomic mass as xenon could be used as beam species. Also, both main and foot pulses could have a smaller convergence angle and somewhat higher emittance than previously considered. These changes would permit a more economical driver than is possible using bismuth. Finally, preliminary simulations of initially neutral beams show even better transport characteristics than positive ions.

REFERENCES

- [1] J. Lindl, *Phys. Plasmas* **2** (1995) 3933.
- [2] M. Tabak and D. A. Callahan, *Nucl. Instr. and Meth. in Phys. Res. A* **415** (1998) 75.
- [3] D. A. Callahan and M. Tabak, *Nucl. Fusion* **39** (1999) 1547.
- [4] S. S. Yu, *et al.*, "A Robust Point Design for a Heavy Ion Fusion Reactor," to be published *Fusion Sci. and Tech.* (2003).
- [5] T. P. Hughes, *et al.*, *Phys. Rev. ST Accel. Beams* **2** (1999) 110401.
- [6] D. R. Welch, *et al.*, *Nucl. Instrum. Meth. Phys. Res A* **464** (2001) 134.
- [7] W. M. Sharp, *et al.*, "Modeling Chamber Transport for Heavy-Ion Fusion," to be published in *Fusion Sci. and Tech.* (2003).
- [8] C. L. Olson, *AIP Conf. Proc.* **152** (1986) 215.
- [9] L. L. Grisham, "Proof-of-Concept Experiments for Negative Ion Driver Beams for Heavy Ion Fusion," in these proceedings.

REVERTED RESONANT "WAKEFIELD"

E. S. Masunov, MEPhI, Moscow, 115409, Russian Federation
A. V. Smirnov, DULY Research Inc., CA 90275, USA

Abstract

A new kind of coherent radiation induced by uniformly moving charge is introduced. It appears as a wavepacket forerunning ahead of the charge. It was derived as a complementary case of existing theory of resonant wakefield extended to include the exotic "overturned wake" affected by the leading front distortions due to dispersion. Corresponding conditions, causality and potential realizations in special types of slow-wave systems are analyzed and discussed. Those can include moving media and meta-materials, plasma and some of periodic structures.

INTRODUCTION

Resonant long-range wakefields have common nature with the Cherenkov effect and are very well studied for about half a century. Classic wakefields are generated behind the short bunch (or charge) at the following conditions: i) synchronism between the charge velocity and modal phase velocity: $v_{ph} = v$; ii) normal dispersion

of the slow-wave system (or medium): $v_{gr} \leq v_{ph}$.

In this paper we consider the situation when $v_{gr} > v = v_{ph}$. So far it was widely assumed that no any resonant propagating field could be generated in this case. From the other hand, some TWTs are operating successfully in the vicinity of the $v_{gr} \approx v_{ph}$ [1].

Theoretical analysis [2,3] predicts the resonant wave to be emitted in front of the bunch at $v_{gr} > v$ similarly as it takes place in a super-radiant single-pass FEL. We shall distinguish such a reversed "wakefield" considered here from "reversed Vavilov-Cherenkov radiation". This term was introduced originally by Veselago in 1968 [4] and refers to more trivial case of negative group velocity in a medium.

RESONANT FIELDS INDUCED IN A SLOW-WAVE SYSTEM

To find the fields induced by a charge in an arbitrary slow-wave guide it is convenient to apply the method of eigenmodes $\vec{E}_{\pm s}, \vec{H}_{\pm s}$ of variable amplitudes [5]. Along with Fourier-transformation it allows taking into account charge distribution in the bunch as well as dispersion effect for the fields in the time-domain [6,2]. Assuming point charge q of limited lifetime $\tau_0 = L/v$ propagating along a semi-infinite waveguide with transverse coordinate $\vec{\rho}_{\perp}(z)$ one can derive the following expression for the resonant modal fields induced:

$$\vec{E}_s(\vec{r}, t) = -2q \operatorname{Re} A_s^L(z, t) \frac{\vec{E}_s^0(z, \vec{r}_{\perp}) E_{-s}^0(z_1, \vec{\rho}_{\perp}(z_1))}{|N_s| \cdot |v^{-1} - v_{grs}^{-1}|}, \quad (1)$$

where $E_{\pm s}^0(z, r_{\perp}) = E_{\pm s} / \exp(\pm i h_s z)$, $h_s = h'_s + i h''_s$, $h'_s > 0$;

$$\tilde{h}_s = h'_s - i h''_s v_{grs} / (v - v_{grs});$$

$$A_s^L(z, t) = \exp(i \tilde{h}_s (z - vt)) [A_s(z_1, \tau) - A_s(z_1 - L, \tau)] \times \Pi((vt - z) / (v - v_{grs})); \quad \tau = t - z/v,$$

$\Pi(x)$ is the symmetric Heaviside function: $\Pi(0) = 1/2$;

$$N_s = \int_{\perp} dS \{ \vec{E}_s \times \vec{H}_{-s} - \vec{E}_{-s} \times \vec{H}_s \} \approx -4P_s; \quad z_1 = \frac{z - v_{grs} t}{1 - v_{grs} / v};$$

$t_1 = z_1 / v$, and, for the 2nd - order dispersion [2,7]:

$$A_s(z_1, \tau) = \frac{1}{2} \operatorname{erfc} \left(\frac{z_1 (1 - v_{grs} / v)}{-(1+i) \sqrt{|v'_{grs}| \tau}} \right), \quad v'_{grs} = \frac{d^2 \omega}{dh_s'^2}.$$

In the limit of linear dispersion (i.e., $dv_{grs}/dh \rightarrow 0$) the

field amplitude $|A_s^L(z, t)|$ at $v \neq v_{grs}$ is proportional to

the following propagating factor:

$$[\Pi(t_1) - \Pi(t_1 - \tau_0)] \Pi((vt - z) / (v - v_{grs})). \quad (2)$$

One can see from (1) that coherent propagating waves are emitted under the following conditions:

$$2Q_s |v - v_{grs}| \gg c, \quad T_1 = L |v_{grs}^{-1} - v^{-1}| \gg 2\pi / \omega_{1s}. \quad (3)$$

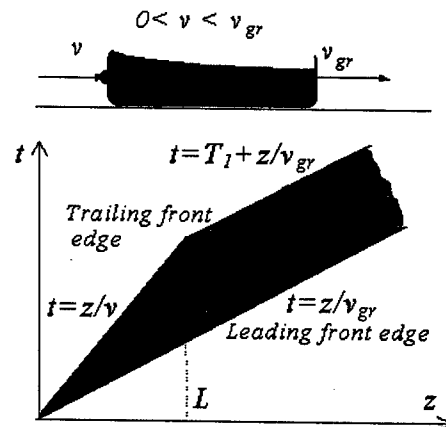


Figure 1: Space-time diagram for the resonant field radiated at anomalous dispersion.

The fields (1,2) were derived without any limitation imposed on the relationship between the group and charge velocities and have to be valid for both cases: $v_{gr} < v$ and $v_{gr} > v$. The leading (group) front of the radiated

field is subject to diffusion (1) because of non-linearity of anomalous dispersion.

Along with the conventional situation when $v_{grs} < v$, the case $v_{grs} > v$ obeys the causality principle as well.

At $v_{grs} > v$ the field surpasses the charge (see Fig. 1) and is no longer a normal wake. One can see from (1,2), in both cases the waveform is defined through the retarded argument $t_1 > 0$, which is always less than the current time t : $t - t_1 = \frac{vt - z}{v - v_{grs}} > 0$. In other words, the

fields are defined by the perturbations occurring in past time.

SYSTEMS WITH ANOMALOUS DISPERSION

Dispersive and moving medium

The condition of anomalous dispersion in an unbounded motionless medium having refraction index n_{med} is trivial:

$$1 - n_{med} < \omega \frac{dn_{med}}{d\omega} < 0. \quad (4)$$

Usually anomalous dispersion is accompanied by resonant absorption of the molecules that breaks corresponding constraint in (3). However, anisotropic "metamaterials" [8,9,10] with unusual properties due to negative dielectric macroscopic permittivity (or negative magnetic permeability) can have $dn_{med}/d\omega < 0$ [11] and, maybe, moderate losses at some frequencies.

One can obtain an anomalous dispersion in a normal medium moving with the velocity $\vec{v}_{med} = \vec{\beta}_{med}c$. If the medium flow is non-relativistic, collinear to the phase velocity, and higher order dispersion is negligible one can find directly from [12]:

$$\beta_{gr} - \beta_{ph} \approx \frac{2\beta_{med} + n_{med}(\beta_{med}n_{med} - 1)}{n_{med}^2} \frac{\omega}{n_{med}} \frac{dn_{med}}{d\omega}. \quad (5)$$

For a cold plasma formed by (relativistic) electrons moving with velocity β_{med} through a motionless neutralizing background (ions) the solution of the dispersion equation is well known:

$$\beta_{gr} - \beta_{ph} = \pm \beta_{med} / (\omega/\omega_p \pm 1), \quad (6)$$

where $\beta_{gr} = \beta_{med}$, the signs \pm correspond to slow and fast waves respectively, $\omega_p = q\sqrt{n_0/(m_0\epsilon_0\gamma_{med}^3)}$ is the plasma frequency, and $\gamma_{med} = 1/\sqrt{1 - \beta_{med}^2}$ is the relativistic factor for the moving medium.

Thus one can provide $\beta_{gr} > \beta_{ph}$ for slow-wave in drifting plasma or in a passive normal medium at $\beta_{med} > n_{med}/(n_{med}^2 + 2)$, provided high-order dispersion and dissipation effects are not significant.

Dispersive or moving medium in a conducting pipe

For a pipe filled with motionless dispersive medium ($dn_{med}/d\omega \neq 0$) one can easily obtain the following condition of anomalous dispersion ($v_{gr} > v_{ph} > 0$):

$$\frac{1}{\beta_{ph}^2 n_{med}} - 1 < \frac{\omega}{n_{med}} \frac{dn_{med}}{d\omega} < \frac{1}{\beta_{ph}^2 n_{med}^2} - 1. \quad (7)$$

Let us consider now a pipe with moving medium. Using Lorentz' transformations one can find the dispersion and the following condition of anomalous dispersion:

$$\frac{\gamma_{med} g_s}{|n_{med}|h} > \frac{1}{\sqrt{\beta_{med}^2 - n_{med}^2}}, \quad \text{where } |n_{med}| < |\beta_{med}| \quad (8)$$

where g_s is the modal transverse wavenumber

($g_s = j_{0s}/b$ for a cylindrical pipe of radius b), j_{0s} is the s -th root of the Bessel function (of the first kind of the zero-th order for monopole mode).

Relativistic plasma can be a good candidate for anomalous system to satisfy (8). But self-consistent behavior of the plasma makes the analysis more complicated than it is presented here. Along with the active character of the system it can diminish the simplified concept of group velocity.

Periodic slow-wave systems

In a long periodic slow-wave structure the group velocity does not depend on the harmonic number for the given frequency. Consequently, one can always find some n^{th} spatial harmonic for which $v_{gr} > v_{ph} > 0$ in the vicinity of the passband middle provided $N_{per} > \max\{2N_f, n\}$. Moreover, one can anticipate that ohmic losses will satisfy the condition (3) even at room temperatures.

Metal helix was the first classical metal slow-wave structure and continues to be employed successfully in numerous TWTs and BWOs for more than fifty years. Its specific dispersive properties can be applied directly to our case of interest. For instance, helical structures designed to operate at non-relativistic beam energies can have $dv_{ph}/d\omega > 0$ along with $v_{gr} > 0$ at some frequencies for the first and the second space harmonics [1,13,14].

One of such structures is four-thread helix in a pipe depicted in Figure 2. The lowest fundamental mode is quadrupole mode ($f \approx 7.3$ GHz, $Q \approx 4000$) having $\beta_{gr} = -0.61$ for the phase advance per cell $\vartheta = \pi/2$. Correspondingly, for the space harmonic at $\vartheta = 3\pi/2$ at the same frequency we have $\beta_{gr} = +0.61$ and $\beta_{ph} = 0.21$. So, ~ 12 keV electron (or ~ 7 MeV proton) bunch having substantial quadrupole component will induce this mode as a forerunning wave. Monopole mode has $\beta_{gr} = +0.57$ group velocity at $\vartheta = \pi/2$ ($f \approx 17$ GHz, $Q \approx 9000$).

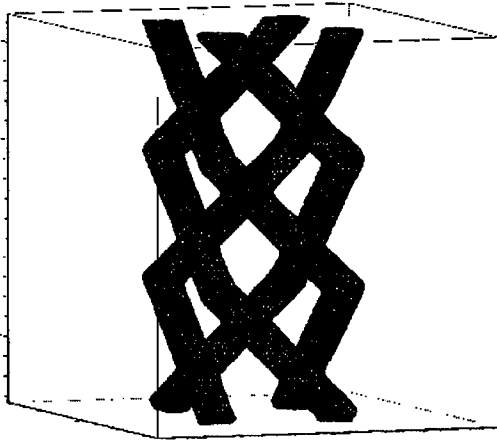


Figure 2: Example of helical slow-wave structure (metal pipe is not shown).

For the 1st spatial harmonic (at $\vartheta=5\pi/2$, monopole mode) one obtains $\beta_{ph}=0.29$ at the same group velocity and frequency. It means that $\sim 25\text{keV}$ electron (or $\sim 26\text{MeV}$ proton) bunch can radiate the reverted "wakefield".

In open waveguides [15,16,17] the group velocity is naturally high and approaches to the speed of light. However, at shorter wavelengths (infrared and optical range) we usually have $\vartheta \gg \pi$, oversized mode of operation $N_f \gg 1$, no slow waves in the system [17] or the number of slow and fast harmonics interacting with the bunch is too big [18] resulting in degradation of efficiency and length of interaction.

DISCUSSION

At longer wavelengths and low-energy bunches the simplest proof-of-principle system would be some of metal-dominated periodical structures.

Resonant wakefields can affect performance of some high intensity ion linacs (especially RFQ).

BBU effect can occur at $v_{gr} > v_{ph} > 0$. In the absence of reflections, beam break-up would appear as diffusion and shortening of the leading front of the beam pulse (instead of trailing edge shortening for conventional BBU).

Hypothetical laser acceleration scheme in the media having $v_{gr} > v_{ph} > 0$ requires the bunch to be injected *before* the driving electromagnetic (laser) pulse front edge. Analogously, in the case of collinear acceleration driven by a charged bunch in such a medium, its radiation will "push" ahead the bunch to be accelerated in front of the driving bunch.

The treatment given here is not applicable directly to the Cherenkov radiation. However, the group velocity concept could be very useful in studying this effect in more general case when $v_{gr} \neq v_{ph}$. For example, the pre-threshold short-pulse radiation [19,20,21] can be explained qualitatively as a normal wake at $v_{ph} - v_{gr} \ll v \approx v_{ph}$.

ACKNOWLEDGEMENTS

The authors are grateful to A. M. Sessler, J. S. Wurtele, and G. Stupakov for their constructive response. Discussions with G. V. Voskresenskii were very fruitful and helpful.

REFERENCES

- [1] J. Rowe. Non-linear Electron Wave Interaction Phenomena, Academic Press, New York and London (1965)
- [2] A. V. Smirnov, Ph. D. dissertation, Moscow, Moscow Engineering Physics Institute, MPhI (1985).
- [3] E. S. Masunov, Dr. Sc. dissertation, Moscow, Moscow Engineering Physics Institute, MPhI (1989).
- [4] V. G. Veselago, Sov. Phys. Usp., Vol. 10, (1968) 509.
- [5] L. A. Vainshtein, "Electromagnetic Waves", Izd. Sov. Radio, USSR, Moscow, (1957).
- [6] V.N. Gusarov, Yu.S. Serebryakov, Sov.J.-Tech.Phys., V42, N5 (1972)991
- [7] A.V. Smirnov, "Long Range Resonance Wake Fields at High Group Velocity and High Dispersion of Group Velocity", a talk given in the Accelerator Theory Club for ARDA group at SLAC. 02/09/01.
- [8] <http://www-physics.ucsd.edu/lhmedia/how.html>
- [9] D. R. Smith, W. J. Padilla, D. C. Vier, S. C. Nemat-Nasser, S. Schultz, Phys. Rev. Lett., vol. 84, no. 18 (2000) 4184
- [10] R. A. Shelby, D. R. Smith, S. Schultz, Science, vol. 292, 6 (2001) 77
- [11] <http://www.waves.utoronto.ca/prof/gelefth/metamaterials/UofTMetamaterials.html>; http://physics.ucsd.edu/~drs/left_home.htm
- [12] L. D. Landau, E. M. Lifshits. Electrodynamics of Continuous Media. Moscow, "Nauka" (1992).
- [13] L. A. Vainshtein. Electromagnetic Waves. Moscow, "Radio i svyaz" (1988).
- [14] D. A. Watkins, E. A. Ash, J. Appl. Phys., 25, N 6 (1954) 782
- [15] L.A. Vainshtein, Open resonators and waveguides, 'Sov. Radio', Moscow (1966).
- [16] A.V. Smirnov, in Proc. of the Particle Accelerators Conf. (PAC'99), NY, 1999 March 29th - April 2nd, p. 3615
- [17] M. Xie, in Proc. of the Particle Accelerators (PAC'97) Conf., Vancouver, 12-16 May, 1997, p. 660
- [18] A.V. Smirnov, D. Yu, in Proc. Particle Accelerator Conf. (PAC2001), IL, Chicago, 18-22 June (2001) 4032
- [19] P.C. Clemmow, J.P. Doudherty. Electrodynamics of Particles and Plasma. Addison-Wesley Publishing Company, The Advanced Book Program (1990)
- [20] arXiv:nucl-th/9907010 v1 5 Jul 1999
- [21] J.Ruzicka, "Theoretical and experimental investigation of the Vavilov-Cherenkov effect", Ph.D. Dissertation, JINR Dubna, 1993.

THREE-DIMENSIONAL MODELING OF INTENSE BUNCHED BEAMS IN RF ACCELERATORS AND SOURCES*

R. Bhatt, M. Hess, and C. Chen, Massachusetts Institute of Technology
Plasma Science and Fusion Center, Cambridge, MA 02139, USA

Abstract

A three-dimensional model of intense bunched beams is developed for cylindrical and corrugated conducting pipes. Updated comparisons between the current limits derived from this model and experimental data from PPM focusing klystrons are presented. An electrostatic Green's function is formulated for azimuthally symmetric slow-wave structures. Analytical and numerical results are presented for the potential of a periodic bunched pencil beam in a small-rippled waveguide approximation.

INTRODUCTION

The modeling of intense charged-particle beams is an important subject in beam physics [1,2] and to the development of rf accelerators and the high-power microwave (HPM) sources [3] driving them.

Recent analytic and semi-analytic Green's function analyses to address these issues have resulted in confinement conditions for bunched pencil beams in round cylindrical pipes [4-7]. The model predicts beam losses, which have been measured in a number of periodic permanent magnet (PPM) focusing klystrons at SLAC and KEK [8-12].

In this paper, we present updated comparisons between theory [4-7] and the PPM klystron experiments at SLAC [8,9,11] and KEK [10,12], and describe our initial efforts to generalize the previous model [4-7] to slow-wave structures. In particular, we derive an electrostatic Green's function for an azimuthally symmetric cylindrical conductor with small-amplitude axial variations of its radius. Self-consistent electrostatic potentials are computed for a periodic bunched beam propagating off-axis in the pipe.

UPDATED COMPARISONS BETWEEN THEORY AND PPM KLYSTRON DATA

The theoretical results, based on a three-dimensional bunched beam model for a perfectly conducting circular pipe with a *constant* radius, predict a current limit for PPM focusing klystrons being developed for TeV linear collider applications. For $\alpha \equiv 2\pi af / \gamma_b \beta_b c < 2$, the limiting current I_b is approximately given by [4-7]

$$\frac{8c^2 I_b}{\omega_{c,rms}^2 a^2 I_A} \cong \frac{\alpha}{\pi}, \quad (1)$$

where a is the beam tunnel radius, f is the operating

frequency of the klystron, $\beta_b c$ is the dc beam velocity, γ_b is the relativistic mass factor for the dc beam, $\omega_{c,rms}$ is the rms cyclotron frequency associated with the PPM focusing field, and $I_A = 17\text{kA} \times \gamma_b \beta_b$ is the Alfven current.

Figure 1 and Table 1 show updated comparisons between the predicted (solid line) and the experimental data points. From Table 1 and Fig. 1, it is evident that both the SLAC 50 MW X-Band XL-PPM klystron [8,9] and Toshiba/KEK 50 MW C-Band PPM klystron [10] operate below the current limit. This agrees with minimal beam losses observed in both experiments. On the other hand, the SLAC 75 MW X-Band XP-1 [8,9] and XP-3 [11] PPM klystrons and the BINP/KEK 75 MW X-Band PPM-1 klystron [12] all operate at or above the current limit, and observe significant beam losses.

ELECTROSTATIC GREEN'S FUNCTION IN A SLOW-WAVE STRUCTURE

As an initial effort to generalize the previous model [4-7] to slow-wave structures, we pose the problem of determining the electrostatic Green function in an azimuthally symmetric slow-wave structure.

Employing cylindrical coordinates (r, ϕ, z) , the conducting surface of the waveguide is specified by $r = a(z)$, where the pipe radius, a , is a function of the axial coordinate. The Green's function is then determined by the solution of

$$\begin{cases} \nabla^2 G(\mathbf{x}; \mathbf{x}') = -4\pi\delta(\mathbf{x} - \mathbf{x}') \\ G(r = a(z)) = 0. \end{cases} \quad (2)$$

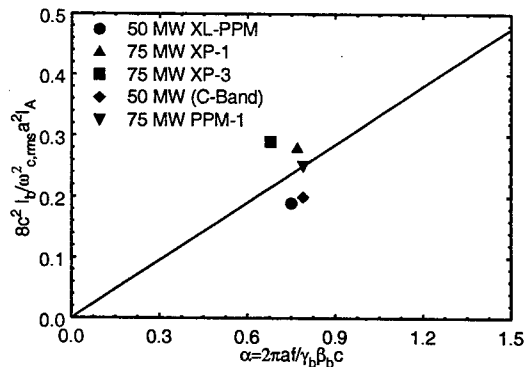


Figure 1: Comparison between theoretical current limit and experimental data for PPM klystrons.

*Research supported by DOE and AFOSR.

Table 1: Experimental parameters and theoretical current limits for PPM klystrons.

PARAMETER	50 MW XL-PPM (SLAC)	75 MW XP-1 (SLAC)	75 MW XP-3 (SLAC)	50 MW (Toshiba/KEK)	75 MW PPM-1 (BINP/KEK)
f (GHz)	11.4	11.4	11.4	5.7	11.4
I_b (A)	190	257	257	317	266
γ_b	1.83	1.96	1.96	1.69	1.94
B_{res} (T)	0.20	0.16	0.18	0.14	0.17
a (cm)	0.48	0.54	0.48	0.90	0.55
α	0.75	0.77	0.68	0.79	0.79
$\frac{8c^2 I_b}{a_c^2 m_0^2 a^2 I_{A, \text{exp}}}$	0.19	0.28	0.29	0.20	0.25
$\frac{8c^2 I_b}{a_c^2 m_0^2 a^2 I_{A, \text{th}}}$	0.238	0.244	0.216	0.251	0.251
Beam Power Loss	0.8%	significant but not measured	significant but not measured	small but not measured	30%

This is reduced to a boundary value problem for Laplace's equation by separating the singular (free-space) and regular components of the Green's function and writing $G(\mathbf{x}; \mathbf{x}') = |\mathbf{x} - \mathbf{x}'|^{-1} + G_R(\mathbf{x}; \mathbf{x}')$. This leaves

$$\begin{cases} \nabla^2 G_R(\mathbf{x}; \mathbf{x}') = 0 \\ G(r=a(z)) = f(\phi, z), \end{cases} \quad (3)$$

where the boundary function is defined by $f(\phi, z) \equiv -|\mathbf{x}(r=a) - \mathbf{x}'|^{-1}$.

The regular part of the Green's function may be expanded in the cylindrical coordinate eigenfunctions of the Laplacian as

$$G_R = \int_{-\infty}^{\infty} d\lambda \sum_{\nu=-\infty}^{\infty} e^{i\lambda z} e^{i\nu\phi} I_{\nu}(\lambda r) A_{\lambda\nu}, \quad (4)$$

where the amplitudes $A_{\lambda\nu}$ are determined by the boundary equation

$$\begin{aligned} G_R(a, \phi, z) &= f(\phi, z) \\ &= \int_{-\infty}^{\infty} d\lambda \sum_{\nu=-\infty}^{\infty} e^{i\lambda z} e^{i\nu\phi} I_{\nu}(\lambda a(z)) A_{\lambda\nu}. \end{aligned} \quad (5)$$

The standard procedure for determining the amplitudes $A_{\lambda\nu}$ involves taking the Fourier transform of Eq. (5) and utilizing the orthogonality properties of the basis functions to isolate the amplitudes. This yields

$$\tilde{f}_{\lambda\nu} = \frac{1}{2\pi} \int_{-\infty}^{\infty} dz \int_{-\infty}^{\infty} d\lambda e^{i(\lambda-\lambda')z} A_{\lambda\nu} I_{\nu}(\lambda a(z)), \quad (6)$$

where the Fourier transform of the boundary function is defined as

$$\tilde{f}_{\lambda\nu} = \frac{1}{4\pi^2} \int_{-\infty}^{\infty} dz \int_{-\pi}^{\pi} d\phi e^{-i\lambda'z} e^{-i\nu\phi} f(\phi, z). \quad (7)$$

Note that for a constant $a(z)$ in Eq. (6), the z integral reduces to a delta function, yielding the result for a straight cylinder [4]: $\tilde{f}_{\lambda\nu} = A_{\lambda\nu} I_{\nu}(\lambda a)$. For an arbitrary axial profile, Eq. (5) cannot be analytically inverted to obtain the amplitudes $A_{\lambda\nu}$.

SMALL-RIPPLE APPROXIMATION

The system does present an approximate analytic solution if the axially-varying conductor radius is approximately equal to its average value. We thus take the *small ripple approximation*, assuming that $a(z) = a_0 + a_1(z)$, where $a_1(z) \ll a_0$. Employing this approximation to Taylor expand the Bessel function appearing in Eq. (5) to first order in a_1/a_0 permits writing the transformed boundary function as $\tilde{f}_{\lambda\nu} \equiv \tilde{f}_{\lambda\nu}^0 + \tilde{f}_{\lambda\nu}^1$, where the result for the straight cylinder of constant radius a_0 is represented by $\tilde{f}_{\lambda\nu}^0 = A_{\lambda\nu} I_{\nu}(\lambda' a_0)$, and the first order correction due to the axially-varying wall radius is represented by

$$\begin{aligned} \tilde{f}_{\lambda\nu}^1 &= \frac{1}{2\pi} \int_{-\infty}^{\infty} dz \int_{-\infty}^{\infty} d\lambda e^{i(\lambda-\lambda')z} A_{\lambda\nu} \lambda a_1(z) I_{\nu}'(\lambda a_0) \\ &= \int_{-\infty}^{\infty} d\lambda A_{\lambda\nu} \lambda \tilde{a}_1(\lambda' - \lambda) I_{\nu}'(\lambda a_0), \end{aligned} \quad (8)$$

with the introduction of the Fourier transform of the wall ripple, defined by $\tilde{a}_1(\kappa) = \frac{1}{2\pi} \int_{-\infty}^{\infty} a_1(z) e^{-i\kappa z} dz$.

We shall henceforth in this paper assume a sinusoidal wall profile (see Fig. 2) given by $a_1(z) = \varepsilon a_0 \cos(2\pi z/\ell)$, with the understanding that an arbitrary (small-amplitude) wall profile may be constructed through an appropriate Fourier superposition of above modes. With this choice, the transformed boundary function becomes

$$\begin{aligned} \tilde{f}_{\lambda\nu} &= A_{\lambda\nu} I_{\nu}(\lambda a_0) + \frac{\varepsilon}{2} A_{\lambda-p, \nu} a_0 (\lambda - p) I_{\nu}'(a_0 (\lambda - p)) \\ &\quad + \frac{\varepsilon}{2} A_{\lambda+p, \nu} a_0 (\lambda + p) I_{\nu}'(a_0 (\lambda + p)). \end{aligned} \quad (9)$$

It is consistent with the *small ripple approximation* to use a first-order in ε perturbation expansion to invert Eq. (9) for the amplitudes $A_{\lambda\nu}$. Writing $A_{\lambda\nu} \equiv A_{\lambda\nu}^0 + \varepsilon A_{\lambda\nu}^1$ and separately equating the coefficients of each order of ε in Eq. (9) yields

$$\begin{aligned} A_{\lambda\nu} &\equiv A_{\lambda\nu}^0 - \frac{\varepsilon}{2} A_{\lambda-p, \nu}^0 a_0 (\lambda - p) \frac{I_{\nu}'(a_0 (\lambda - p))}{I_{\nu}(a_0 \lambda)} \\ &\quad - \frac{\varepsilon}{2} A_{\lambda+p, \nu}^0 a_0 (\lambda + p) \frac{I_{\nu}'(a_0 (\lambda + p))}{I_{\nu}(a_0 \lambda)}, \end{aligned} \quad (10)$$

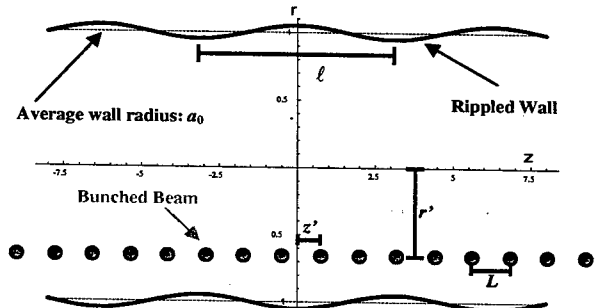


Figure 2: Bunched beam in a rippled-wall waveguide.

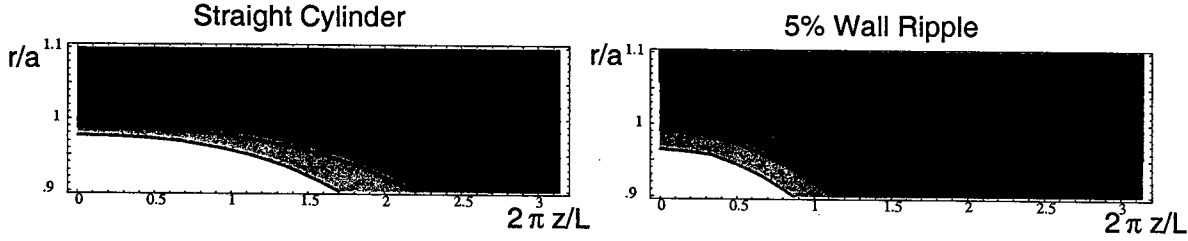


Figure 3: Equipotential curves for a bunched beam in a straight (left) and corrugated (right) cylinder.

where $A_{\lambda\nu}^0 = \tilde{f}_{\lambda\nu} [I_\nu(a_0\lambda)]^{-1}$.

All that remains is to determine the transformed boundary function, $\tilde{f}_{\lambda\nu}$. Employing a well-known Fourier-Bessel expansion [13] for the $1/R$ potential, the boundary function may be written as

$$f(\phi, z) = -[x(r=a(z)) - x']^{-1} \\ = -\frac{1}{\pi} \sum_{n=-\infty}^{\infty} \int_0^\infty e^{in(\phi-\phi')} e^{ik(z-z')} I_n(kr') K_n(ka(z)) dk, \quad (11)$$

where we've assumed $r' < a(z)$. Taking the Fourier transform as per Eq. (7) and making use of the *small ripple approximation* to expand the Bessel function yields

$$\tilde{f}_{\lambda\nu} = -\frac{1}{\pi} e^{-i\lambda z'} e^{-i\nu\phi'} \left[\begin{aligned} &I_\nu(\lambda r') K_\nu(\lambda a_0) \\ &+ \frac{\varepsilon}{2} e^{i\nu\phi'} a_0(\lambda - p) I_\nu((\lambda - p)r') K_\nu((\lambda - p)a_0) \\ &+ \frac{\varepsilon}{2} e^{-i\nu\phi'} a_0(\lambda + p) I_\nu((\lambda + p)r') K_\nu((\lambda + p)a_0) \end{aligned} \right]. \quad (12)$$

Combined with Eqs. (10) and (4), this result determines the electrostatic Green's function for an azimuthally symmetric pipe with small-amplitude axial variations in its radius, accurate to first order in ε .

Given the Green's function, the electrostatic potential may be computed for an arbitrary charge distribution. For purposes of comparison, it is useful to consider the bunched beam charge distribution of [4],

$$\rho(r, \phi, z) = \frac{1}{r} \delta(r - r') \delta(\phi - \phi') \sum_{n=-\infty}^{\infty} \delta(z - z' - nL). \quad (13)$$

This distribution (depicted in Fig. 2) represents a periodic bunched beam with bunch spacing L , displaced from the axis by a distance r' , and with one bunch offset from the $z=0$ plane by a distance z' . Integrating the Green's function over this distribution yields $\Phi(\mathbf{x}) = \Phi^0(\mathbf{x}) + \varepsilon\Phi^1(\mathbf{x})$, where the first term is the straight cylinder potential of [4],

$$\Phi^0 = \frac{2}{L} \sum_{n=-\infty}^{\infty} \sum_{\nu=-\infty}^{\infty} e^{in(z-z')} e^{i\nu(\phi-\phi')} \frac{I_\nu(n\hat{r}_c)}{I_\nu(n\alpha_0)} \left[\begin{aligned} &I_\nu(n\alpha_0) K_\nu(n\hat{r}) \\ &- I_\nu(n\hat{r}_c) K_\nu(n\alpha_0) \end{aligned} \right] \quad (14)$$

and the second term gives the correction due to a sinusoidal wall ripple,

$$\Phi^1 = \frac{1}{L} \sum_{n=-\infty}^{\infty} \sum_{\nu=-\infty}^{\infty} e^{in(z-z')} e^{i\nu(\phi-\phi')} \left[\begin{aligned} &e^{i\varepsilon\phi} \frac{I_\nu(n\hat{r}) I_\nu((n-\hat{p})\hat{r})}{I_\nu(n\alpha_0) I_\nu((n-\hat{p})\alpha_0)} \\ &+ e^{-i\varepsilon\phi} \frac{I_\nu(n\hat{r}) I_\nu((n+\hat{p})\hat{r})}{I_\nu(n\alpha_0) I_\nu((n+\hat{p})\alpha_0)} \end{aligned} \right]. \quad (15)$$

The quantities introduced above are defined as $\alpha_0 \equiv 2\pi a_0 / L$, $\hat{r} \equiv 2\pi r / L$, $\hat{r}' \equiv 2\pi r' / L$, $\hat{z} \equiv 2\pi z / L$,

$\hat{z}' \equiv 2\pi z' / L$, $\hat{p} \equiv L / \ell$, $\hat{r}_c \equiv \min(\hat{r}, \hat{r}')$, $\hat{r}_c \equiv \max(\hat{r}, \hat{r}')$, and $a_1(z) = \varepsilon a_0 \cos(2\pi z / \ell)$.

Figure 3 shows equipotential curves in the plane of the charge for a bunched beam in both a straight and corrugated cylinder. Relevant parameters are $\alpha_0 = 2$, $\hat{r}' = 0.5$, $\hat{z}' = 0$, $\hat{p} = 1$, and $\varepsilon = 0.05$. The black region (corresponding to the zero potential surface) conforms to the straight and sinusoidally rippled cylindrical walls, respectively.

REFERENCES

- [1] M. Reiser, *Theory and Design of Charged-Particle Beams* (Wiley & Sons, New York, 1994).
- [2] R.C. Davidson, *Physics of Nonneutral Plasmas* (Addison-Wesley, Reading, MA, 1990).
- [3] J. Benford and J. Swegle, *High Power Microwaves* (Artech, Boston, 1992).
- [4] M. Hess and C. Chen, *Phys. Plasmas* **7** 5206 (2000).
- [5] M. Hess and C. Chen, *Phys. Lett. A* **295**, 305 (2002).
- [6] M. Hess and C. Chen, *Phys. Plasmas* **9**, 1422 (2002).
- [7] M. Hess, MIT Ph.D. Thesis (2002).
- [8] D. Sprehn, G. Caryotakis, E. Jongewaard, R.M. Phillips, in *Proceedings of 19th International Linac Conference* (Argonne National Laboratory Report ANL-98/28), p.689.
- [9] D. Sprehn, et al., in *Intense Microwave Pulses VII*, edited by H. E. Brandt, SPIE Proc. **4301** (2000), p. 132.
- [10] Y. H. Chin, et al, in *Proceedings of the Particle Accelerator Conference 2001*, edited by P. W. Lucas and S. Webber, (2001), p. 3792.
- [11] SLAC Website <http://www-project.slac.stanford.edu/lc/local/MAC/OCT2001/Caryotakis%20NLC%20KLYSTRON%20R.pdf>
- [12] H. Matsumoto, et al, in *Proceedings of the Particle Accelerator Conference 2001*, edited by P. W. Lucas and S. Webber, (2001), p. 993.
- [13] Jackson, J., *Classical Electrodynamics* (Wiley, New York, 1962).
- [14] Gradshteyn, I.S. and Ryzhik, I.M., *Table of Integrals, Series, and Products*, 5th Edition (Academic Press, San Diego, 1994).

BEAM HALO FORMATION AND LOSS INDUCED BY IMAGE-CHARGE EFFECTS IN A SMALL-APERTURE ALTERNATING-GRADIENT FOCUSING SYSTEM*

J. Zhou, B. L. Qian and C. Chen, MIT Plasma Science and Fusion Center, Cambridge, MA 02139
E. Henestroza, S. Eylon and S. Yu, Lawrence Berkeley National Laboratory, Berkeley, CA 94720

Abstract

Effects of image charges on beam halo formation and beam loss in small-aperture alternating-gradient focusing systems are studied analytically, computationally, and experimentally. Nonlinear image-charge fields result in chaotic particle motion and the ejection of particles from the beam core into a halo. Detailed chaotic particle motion and structure of the particle phase space is studied, and the beam loss rate is computed for a long transport channel. Image-charge effects are also studied for a short transport channel, and compared with the Neutralized Transport Experiment (NTX) at LBNL.

INTRODUCTION

An important aspect in the design of periodically focused beams in such accelerators is to prevent the beams from developing halos because they may cause beam losses to the conducting walls of the accelerating structures. The problem of halo formation and beam losses is of a serious concern in the design of small-aperture focusing transport systems that are often required in order to keep accelerator costs manageable. Two key mechanisms for halo formation have been studied using analytical models [1-3] and self-consistent simulations with particle-in-cell (PIC) techniques [4-7]. Until the present analysis, however, most published analytical results [1-3] on beam halo formation have been based on free-space models in which wall effects on halo formation have been ignored.

In this paper, we report a new mechanism for chaotic particle motion and halo formation in intense charge-particle beams. In particular, use is made of a test-particle model to investigate the dynamics of root-mean-squared (rms) matched intense charged particle beams propagating through an alternating-gradient quadrupole magnetic field and a small aperture. While the present model allows for nonuniform beams with elliptic symmetry, the effects of image charges on halo formation are illustrated with a uniform (KV) beam distribution [8]. It is shown that the image-charge-induced fields are nonlinear, and that they induce chaotic particle motion and halo formation.

We consider an rms-matched continuous intense charged-particle beam propagating in the longitudinal direction through an alternating-gradient quadrupole magnetic field with axial periodicity length s in a perfectly conducting round pipe with radius R . The beam density is assumed to be $n = n(x^2/a^2 + y^2/b^2)$. An

analytical expression for the scalar potential can be obtained for the assumed density profile,

$$\phi = -\pi abq \int_0^\infty \frac{ds}{\sqrt{(a^2+s)(b^2+s)}} \int_0^T n(T) dT + \pi abq \left[\int_0^\infty \frac{ds}{\sqrt{(a^2+s)(b^2+s)}} \int_0^{T_1} n(T_1) dT_1 - 2 \ln\left(\frac{R}{r}\right) \int_0^{T_1} n(T_1) dT_1 \right] \quad (1)$$

where

$$T = x^2/(a^2+s) + y^2/(b^2+s), T_1 = x_1^2/(a^2+s) + y_1^2/(b^2+s), r = (x^2 + y^2)^{1/2}, x_1 = R^2 x/(x^2 + y^2), \text{ and } y_1 = R^2 y/(x^2 + y^2).$$

For the KV beam, the periodic beam envelope functions $a(s) = a(s+S)$ and $b(s) = b(s+S)$ can be calculated from envelope equations [9]. Furthermore, in the paraxial approximation, the transverse equations of motion for an individual test particle can be obtained [3] with the potential in Eq. (1).

It is important to specify initial conditions for the test-particle motion that are consistent with the assumed beam density, which is accomplished by the particular choice of an initial distribution function [3] at $s = s_0$, i.e.,

$$f_b(x, y, x', y', s_0) = N_b \delta(W-1) / \pi^2 \epsilon_x \epsilon_y, \text{ where } x' = dx/ds, \text{ and } W \text{ is the variable defined by } W = x^2/a^2 + (ax' - xa')^2/\epsilon_x^2 + y^2/b^2 + (by' - yb')^2/\epsilon_y^2. \text{ Here, } a, a', b, \text{ and } b' \text{ denote the "initial" values at } s = s_0.$$

IMAGE-CHARGE EFFECTS IN A LONG TRANSPORT CHANNEL

Using the model established in the previous section, we can investigate the halo formation and beam chaotic motion induced by the image-charge effects. For a long quadrupole focusing channel with the step-function lattice, the envelope functions $a(s)$ and $b(s)$ are obtained numerically and are benchmarked against the published results for the free-space case in [3]. The system parameters are chosen to be $\eta = 0.5$, $KS/\epsilon_x = 10.0$, $\epsilon_x = \epsilon_y = \epsilon$, and vacuum phase advance $\sigma_v = 80.0^\circ$, which correspond to those in the High-Current Experiment (HCX) at LBNL [10]. The mechanism of beam loss is best illustrated by the phase space structure for the test-particle motion in the (x, x') plane as shown in Fig. 1, where the Poincaré surface-of-section plots for the trajectories of test particles are demonstrated for two cases: (a) free-space ($\hat{R} \equiv R/\sqrt{\epsilon S} = \infty$) and (b) $\hat{R} = 4.5$. Forty one and twenty nine test particles are loaded

* Supported by the U. S. Department of Energy, Grant No. DE-FG02-95ER40919 and No. DE-FG02-01ER54662.

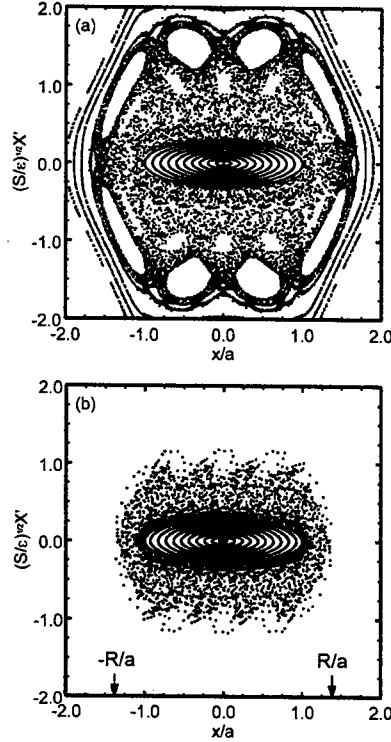


Fig.1 Poincaré surface-of-section plots of test particles propagating over 1000 lattice periods in the phase plane (x, x') for two cases: (a) free-space $\hat{R} = \infty$ and (b) $\hat{R} = 4.5$.

uniformly at $s = 0$ between the intervals $-2.0 \leq x' \leq 2.0$ and $-1.32 \leq x' \leq 1.32$ along the x' -axis in Figs. 3(a) and 3(b), respectively. Because all of the test particles have $(y(0), y'(0)) = 0$, their trajectories remain in the (x, x') plane of the phase space. As shown in Fig.1 (a), well inside the beam with $W_x \leq 1$ the motion is regular, whereas there is a chaotic sea bounded between $W_x = 1$ and an outer Kolmogorov-Arnold-Moser (KAM) surface at $x/a = 1.7$ for the free-space case with $\hat{R} = \infty$. This chaotic sea is fully connected; that is, a particle in the chaotic sea will fill out the entire region if it travels for a sufficiently long distance. As the pipe radius R decreases, the conductor wall intersects the chaotic sea as shown in Fig.1 (b), in which case the particles in the chaotic sea will eventually strike the wall.

It should be pointed out that as the pipe radius R decreases, the image effect on the dynamics of a beam with the KV distribution is subtle, as illustrated in Fig. 2. In Fig. 2 the transverse energy $W_x(s) = (x/a)^2 + (\alpha'x'/\varepsilon)^2$ is plotted as a function of the axial distance s for 50 test particles loaded at $s = 0$ on the beam boundary $W_x(0) = 1$ in the phase space with the initial phases $\phi_0 = \tan^{-1}[(S/\varepsilon)^{1/2} a(0)x'(0)/x(0)]$ uniformly distributed

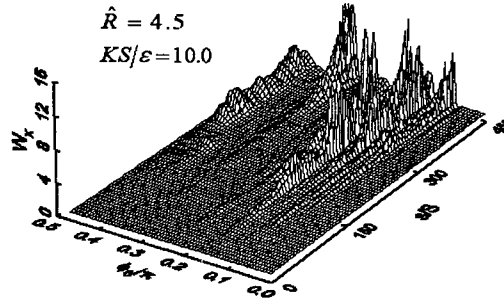


Fig. 2 Plots of W_x vs s for 50 test particles for $\hat{R} = 4.5$. The test particles are initially loaded uniformly with phase ϕ_0 ranging from 0 to $\pi/2$ on the beam boundary $(x(0)/a(0))^2 + (a(0)x'(0)/\varepsilon)^2 = 1$ in the phase space.

from 0 to $\pi/2$ for $\hat{R} = 4.5$. The system parameters are chosen to be the same as in Fig. 1. For the free-space case, the motion is stable, and the transverse energy is conserved with $W_x(s) = 1$ for all of the test particles. As R decreases to $\hat{R} = 4.5$, some test particles become chaotic due to the nonlinear force of the induced image charge on the wall, and the transverse energies of these particles are no longer constant.

Furthermore, the beam loss is computed as a function of propagation distance, and the results are shown in Fig. 3. The four curves correspond to four choices of the pipe radius with $\hat{R} = 3.8, 3.9, 4.0$, and 4.5 . The beam loss rate increases with the decreasing pipe radius, where the image effects play a more important role in the total space charge force. When the maximum beam envelope fills 86% of the pipe, the beam loss reaches 8% at $s = 1000S$. Although the results shown in Fig. 3 are based on the test-particle calculations, they provide order of magnitude estimates for the actual beam losses, which are being studied using self-consistent simulations.

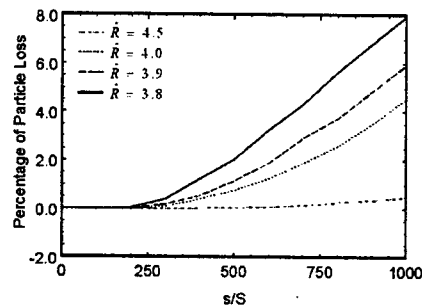


Fig. 3 Plots of the percentage of particles sticking the conductor wall as a function of propagation distance for several choices of $\hat{R} \equiv R/\sqrt{\varepsilon S}$. Here, 10,000 test particles with the KV distribution initially are used in the simulations.

Table 1. Simulation Parameters for NTX

Ion Energy:	300 KeV
Ion Current:	25 mA
Initial Beam Radius:	10 mm
Initial Beam Radius Derivative:	27 mr
Beam Velocity:	0.004 c
Magnetic Quadrupoles (T/m):	2.8,-3.62, 3.39, -1.95
Emittance ($4\pi \times rms$):	12π mm-mrad
Channel Length:	2.4 m
Final Circular Beam Radius:	20 mm
Final Beam Radius Derivative:	-20 mr
Pipe Radius:	75.8 mm

IMAGE-CHARGE EFFECTS IN NTX

We also use the theoretical model to analyze the NTX. Table 1 shows the simulation parameters for the NTX and Fig. 4 shows the beam envelopes. The focusing channel in the simulation is slight different from the experiment, and the emittance in the simulation is about 2 times the experimental value. Test-particles are put to propagating in the focusing channel of NTX to investigate image-charge effects for KV distribution beams.

Shown in Fig. 5 are the plots of the line-integrated phase plane distributions in (x, x') and (y, y') at the end of the channel, as obtained from the experimental measurements (left) and the simulation (right). The linear parts of x' and y' are subtracted in Fig. 5. There is no halo formation in the simulation for this short channel. However, the nonlinear forces induced by image charges create slight S-shaped and non-elliptic distributions in (x, x') and (y, y') , respectively, although we are still investigating the discrepancy between the experiment and theory regarding the orientation of the S-shaped distribution.

CONCLUSION

We have shown using a test-particle model that in a small-aperture alternating-gradient focusing channel, image-charge effects induce a new mechanism for chaotic particle motion and halo formation in intense charge-particle beams. The percentage of beam loss has been calculated as a function of propagating distance and aperture size. Because our results are obtained for ideal

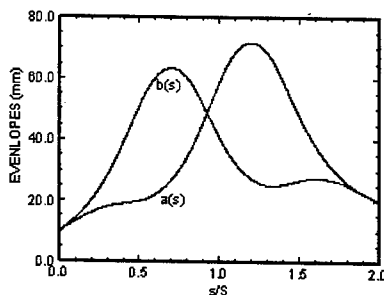


Fig. 4 Plots of the envelopes of the focusing channel of NTX.

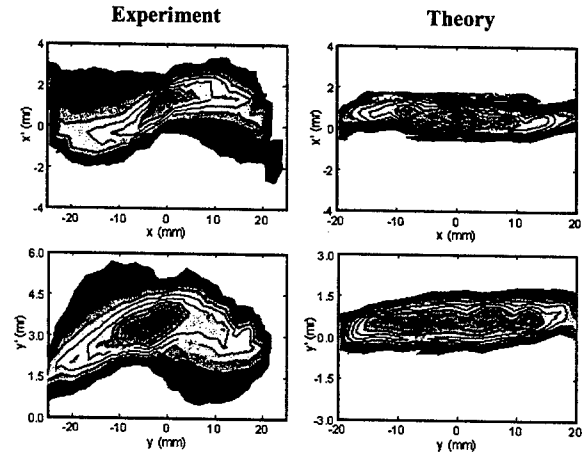


Fig. 5 Poincaré surface-of section plots of test particles at the end of NTX Channel in the phase plane (x, x') and (y, y') .

KV distribution, they represent the minimum beam loss one may achieve in a long (>100 periods) focusing system such as the planned Integrated Research Experiment (IRE) for heavy ion fusion. They also suggest that in short (2 to 30 periods) systems such as the existing Neutralized Transport Experiment (NTX) and High-Current Experiment (HCX), imperfections such as charge-density fluctuations, mismatch, and focusing field nonlinearity and error may play more important role than image charge effects on beam halo production.

REFERENCES

1. R. L. Gluckstern, Phys. Rev. Lett. **73**, 1247 (1994).
2. J. M. Lagniel, Nucl. Instrum. Methods Phys. Res. **A345**, 405 (1994).
3. Q. Qian, R. C. Davidson, and C. Chen, Phys. Plasmas **2**, 2674 (1995); Phys. Rev. **E51**, R5216 (1995).
4. I. Haber, in *Proc. 1984 INS Int. Symposium on Heavy Ion Accelerators and Their Applications to Inertial Fusion* (Inst. Nuclear Study, Tokyo, 1984), p. 451.
5. C. M. Celata, in *Proc. 1987 Part. Accel. Conf.* (IEEE, New York, 1987), p. 996.
6. R. W. Garnett, et al., *Space Charge Dominated Beams and Applications of High Brightness Beams*, edited by S. Y. Lee, AIP Conf. Proc. No. **377** (AIP, New York, 1996), p. 60.
7. T. P. Waggler and J. Qiang, *Advanced Accelerator Concepts*, edited by C. E. Clayton and P. Muggli (AIP, Mandalay Beach, CA 2002), p. 878.
8. I. Kapchinskij and V. Vladimirskij, in *Proceedings of the International Conference on High Energy Accelerators and Instrumentation* (CERN Scientific Information Service, Geneva, 1959), p.274.
9. B. L. Qian, J. Zhou, and C. Chen, Phys. Rev. ST Accel. Beams **6**, 014201 (2003).
10. P. A. Seidl, F. M. Bieniosek, C. M. Celata et al., Nucl. Instrum. Methods Phys. Res. **A464**, 369 (2001).

INITIAL EXPERIMENTAL RESULTS OF THE SMALL ISOCHRONOUS RING (SIR)*

J. Rodriguez[†], E. Pozdeyev, F. Marti, NSCL, Michigan State University, MI 48824, USA

Abstract

The Small Isochronous Ring (SIR) is under development at the National Superconducting Cyclotron Laboratory (NSCL) at Michigan State University (MSU). The ring is a small-scale experiment that simulates the dynamics of intense beams in large-scale accelerators. Its main purpose is the study of longitudinal space charge effects in the isochronous regime. A 20 to 30 keV bunch of hydrogen or deuterium ions is injected in the ring. After a variable number of turns (~ 20-30), the bunch is extracted and its longitudinal profile is studied. This paper describes the hardware already designed, manufactured and installed as well as the first preliminary experimental results.

1 INTRODUCTION

The main goal of the project is to study experimentally the effects of space charge in the isochronous regime. Using low energy, low intensity hydrogen or deuterium beams, we intend to simulate the beam dynamics of high current machines. Papers [1], [2] and [3] provide additional details on the project. Results of simulations of the beam dynamics in the injection line and in the ring can be found in [4] and [5] respectively.

The injection line of SIR and the four magnets of the

ring have been manufactured and installed. Beam has been extracted, injected in the ring and detected with a Faraday Cup after $\frac{1}{4}$ of a revolution. No systematic experiments have been performed yet since the assembly finished at the end of April 2003. Figure 1 shows a picture of room where SIR is being built. Beam has been transported through the colored segments.

2 ION PRODUCTION AND SEPARATION

A multicusp ion source is used to produce a beam composed of H^+ , H_2^+ and H_3^+ ions. Experiments with deuterium will also be performed. In this case, the ultimate pressure in the ring will be lower since its higher mass will increase the effective pumping speed giving a longer life-time of the bunches in the ring.

Biasing the source (up to 30 kV) defines the extraction energy of the beam. The puller of the ion source also acts as the first ground electrode of the Einzel lens that immediately follows. Focusing as close to extraction as possible is required due to the large angle dispersion of the extracted beam. Typically, a voltage in the Einzel lens of $\sim \frac{2}{3}$ of the extraction voltage provides a focusing length ~ 10 cm. Some non-linear effects have been observed. Simulations indicate that they are mainly

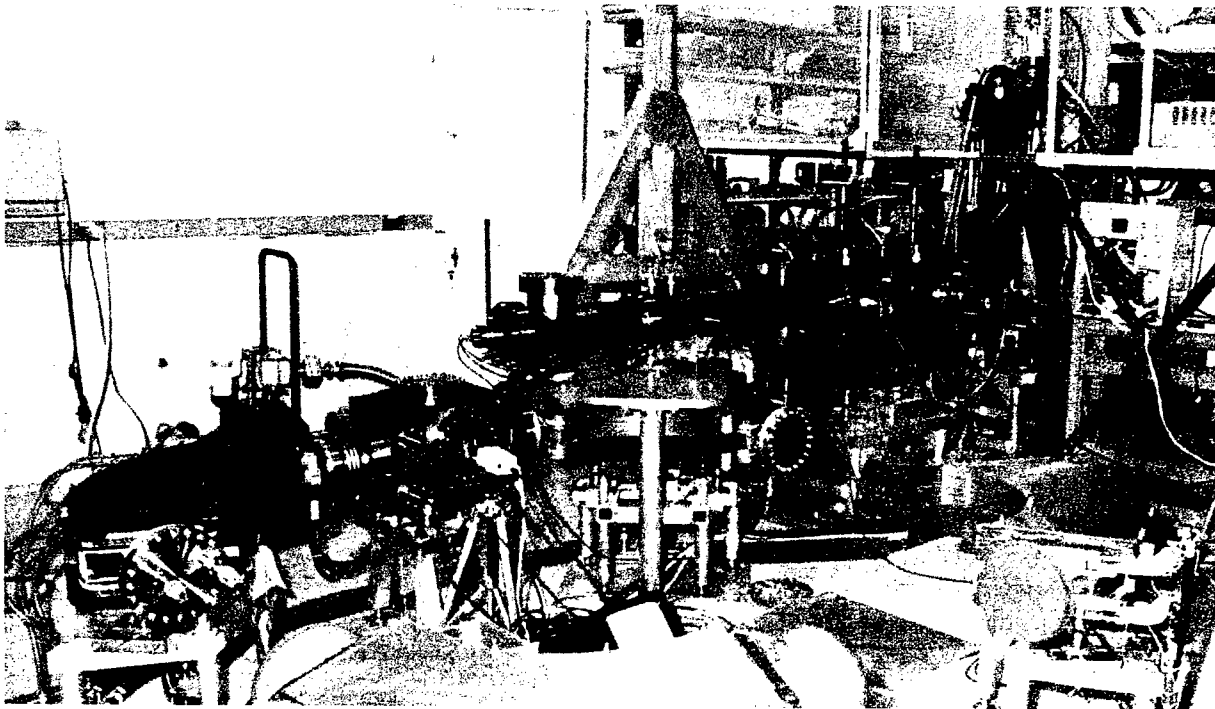


Figure 1: Room where SIR is being built.

*Work supported by NSF Grant # PHY-0110253.

[†]rodriguez@nscl.msu.edu

produced by the Einzel lens [4].

A couple of orthogonal pairs of steering plates (9 cm long, 6 cm gap, ± 1 kV voltage, up to 65 mrad kick to 30 keV H_2^+ beam) are the first mean to correct possible misalignments in the injection line.

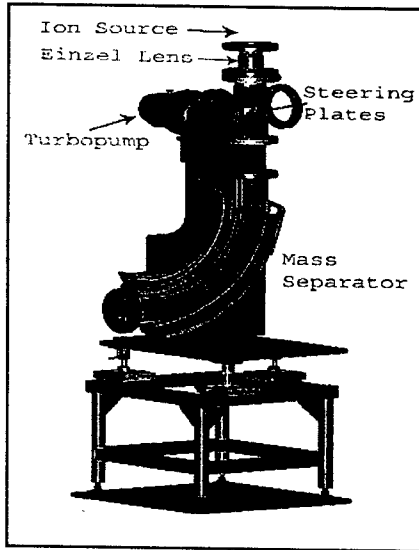


Figure 2: First section of injection line

The different mass states are separated by a dipole magnet identical to those used in the ring [2].

The first preliminary measurements show currents in the order of 10-100 μA for different ions species. This is enough to cover the desired range of peak currents in the ring. Systematic experiments to characterize the extracted beam will be conducted in the following months.

3 EMITTANCE MEASUREMENT SYSTEM

A couple of orthogonal pairs of movable slits and Faraday Cups are used to characterize the transverse beam parameters. This information is used to recalculate the

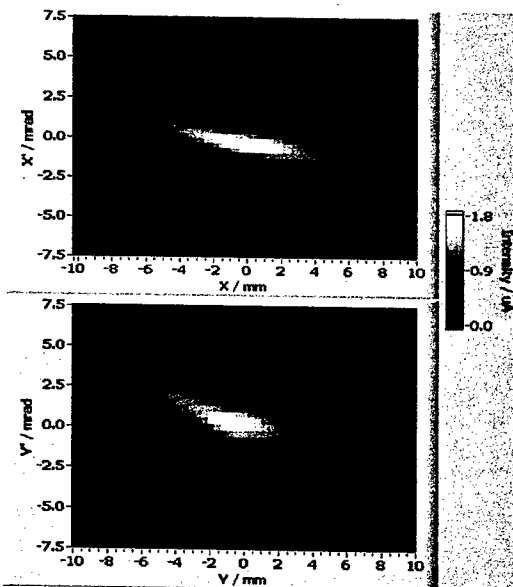


Figure 3: X-X' and Y-Y' maps (15keV H_2^+)

focusing lengths of the Einzel lens and electrical quadrupoles needed to match the injected beam to the close orbit solution in the ring.

Figure 4 shows an X-X' (medium plane of the ring) and a Y-Y' map of a 15 keV H_2^+ beam from which an emittance $\epsilon \approx 10\pi \cdot mm \cdot mrad$ (unnormalized) can be estimated. Previously, other experiments were performed where the ion source had a 2 mm diameter aperture instead of a 1 mm one. In that case an emittance $\epsilon \approx 50\pi \cdot mm \cdot mrad$ was measured.

The distance between slits (0.5 mm gap) is 47.5 cm. Another couple of orthogonal pairs of steering plates (identical to the ones right after the ion source) are located between slits. These electrodes, together with the dipole magnet and the inflector plates can be adjusted to correct for possible misalignments or residual external fields.

A beam stopper will be added in this region in the coming months. It will be covered with phosphor to be used as a fast diagnostic tool.

4 MATCHING AND CHOPPING SECTION

A triplet of electrical quadrupoles, located right after the emittance measurement box, together with the Einzel lens and the quadrupole corrector coil in the mass separator provide flexibility to match the extracted beam to the close orbit solution in the ring. Refer to [4] for more details in the capabilities of the injection line to match different initial ensembles. The lengths of the quadrupoles are 10.5 cm, 14 cm and 6 cm. The distance between them is 9 cm and the gap between electrodes is 7 cm. The shape of the electrodes is not hyperbolic but circular. 3-D calculations do not show a significant deviation from ideal case.

A pair of 5 cm long plates are pulsed up to ± 3.5 kV to provide the time structure of the bunches. Two grids next to the plates are used to limit the deflection region. Bunches as short as 30 ns are expected. At this time, no precise measurements of bunch lengths have been performed since a fast Faraday Cup has not been built yet. A regular Faraday Cup located at the end of the injection line has been used and pulses $< 5 \mu s$ have been observed.

A pair of 16.5 cm inflector plates (gap ≥ 7 cm), located right after the chopper, bend the trajectory of the beam

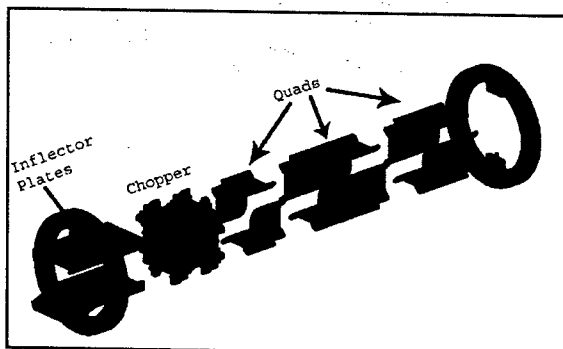


Figure 4: Quads, Chopper, Inflector Plates Section

17.5° and a second pair located in between two of the magnets of the ring, position it in its medium plane. This second pair is pulsed to avoid deflection after completion of the first turn. The geometry of plates is optimized to maximize distance between deflected beam and plates and to avoid introducing non-linear effects in the beam.

5 RING INJECTION SECTION

Besides a pair of pulsed deflector plates responsible for bending the beam trajectory back to the medium plane of the ring, there is a movable three position phosphor screen. This allows interception of the beam both when it is injected and after the first turn. Figure 5 shows the beam being intercepted when injected.

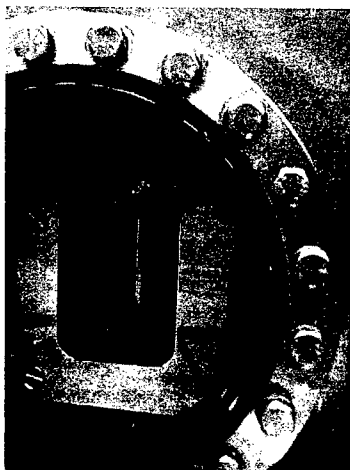


Figure 5: Beam intercepted in phosphor screen

A triangular shape in the beam can be observed. Although, no satisfactory explanation was found yet, it is believed that the ceramics holding the Einzel lens may be

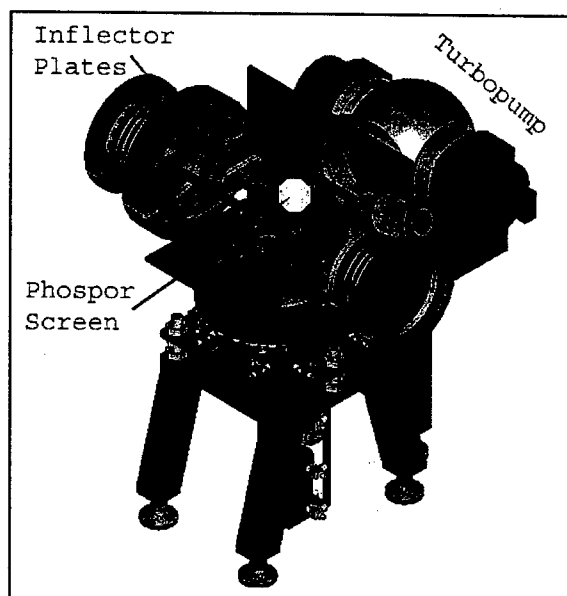


Figure 6: Straight section between magnets

the cause. They may be charging up or the perturbation they introduce in the field distribution could be disturbing the beam close to their position.

Three 500 L/s turbopumps are used to reach a pressure of $2 \cdot 10^{-7}$ torr in the ring with a few mTorr pressure in the Ion Source. One of them is located right after the ion source, a second one in the emittance measurement box and a third one in the first straight section between magnets. A fourth one will be installed in one of the other sections of the ring.

6 CONCLUSION

The injection line and the four ring magnets have been manufactured and installed. Beam completed $\frac{1}{4}$ of a revolution in the ring at the end of April 2003.

In the next few months, the other three straight sections of the ring will be designed and manufactured. A Fast Faraday Cup will be developed and tested. The control system will be enhanced. The source of the triangular shape of the beam will be studied and corrected. Systematic experiments to characterize the ion source will also be performed.

7 ACKNOWLEDGMENT

The authors are grateful to the staff of NSCL for their suggestions and support. In particular, we would like to thank R. Zink, R. Fontus, D. Sanderson, D. Pedtke, R. York, A. Zeller, D. Lawton, S. Hitchcock, D. Devereaux and A. Mond for their involvement in the design, manufacturing and/or assembling of different parts of SIR.

8 REFERENCES

- [1] E. Pozdeyev, "A Small Isochronous Ring for Experimental Study of the Longitudinal Space Charge Effect in Isochronous Cyclotrons", PAC'2001, pg. 3549.
- [2] E. Pozdeyev, F. Marti, J. Rodriguez, R. York, "Small Isochronous Ring Project at NSCL", EPAC'2002, pg. 1395.
- [3] E. Pozdeyev et al., "Report on progress of the Small Isochronous Ring project at NSCL", these proceedings.
- [4] J. Rodriguez, E. Pozdeyev, F. Marti, "Injection Line of the Small Isochronous Ring", EPAC'2002, pg. 1401.
- [5] E. Pozdeyev, J. Rodriguez, "Computer Simulations of the Beam Dynamics in the Small Isochronous Ring", EPAC'2002, pg. 1398.

SNS LINAC COMMISSIONING – TRANSVERSE MATCHING *

Dong-o Jeon[#], ORNL, Oak Ridge, TN37830, USA
J. Stovall, LANL, Los Alamos, NM87545, USA

Abstract

The Spallation Neutron Source Linac consists of a few distinct sections which require careful transverse matching. Robust techniques for transversely matching various sections of the SNS Linac have been identified and will be presented. These techniques do not require us any knowledge of machine optics, and are robust against up to 20% measurement uncertainties, beam mismatch, etc.

INTRODUCTION

The Spallation Neutron Source Linac consists of a Drift-tube Linac, a Coupled Cavity Linac followed by a Superconducting Linac [1]. We studied feasible schemes of transversely matching various sections of SNS Linac utilizing wire-scanners or emittance measurement devices. A few matching schemes are tested using the Parmila code [2]. We assume ideal longitudinal matching and concentrate only on transverse matching. The following are the assumptions and conditions under which the study is done:

- About 10% uncertainty in the initial matching quad gradient between the model and real machine is assumed.
- A certain level of measurement uncertainty (10 to 20%) in rms beam size or emittance is assumed.
- As input distribution, we use a beam distribution tracked from the DTL with the initial 30% transverse and longitudinal mismatches.
- Optimization is done with 10 000 macro-particles input distribution using the Parmila code.

The uncertainty in the initial matching condition is assumed, because actual transverse matching condition may be different from that obtained from the model (Trace3D etc) due to various reasons such as the uncertainty in longitudinal set-point of cavities, machine imperfections, and beam distributions. The 10% measurement uncertainty in rms beam size means that 3σ of Gaussian error distribution is 10%. In reality this uncertainty includes pulse-to-pulse jitter and measurement uncertainties in rms beam sizes. Also we use a beam distribution including mismatch as stated in the third bullet. 30% mismatch means that the beam distribution is transformed by $x \rightarrow 1.3x$ where $\alpha=0$ and momentum is adjusted accordingly to preserve phase space area. By doing so, we can study the effect of unknown mismatch present in the real beam and can see how reliable the matching routine is. It should be noted that these are very pessimistic assumptions.

Measurement accuracy in this note is defined by the accuracy of rms beam size converted from the wire-scanner data or emittance data. 20% measurement uncertainty means that 3σ of Gaussian uncertainty distribution is 20% of the actual value.

In simulation test, optimization is done using a minimization routine of MATLAB®. This routine uses the simplex search method [3]. This is a direct search method that does not use numerical or analytic gradients. The optimization procedure consists of 20 iterations. Simulations are carried out from DTL tank 6 (the last DTL tank) to the end of SCL (Superconducting linac) to explore the matching.

MATCHING MEBT TO DTL

Matching with wire-scanners

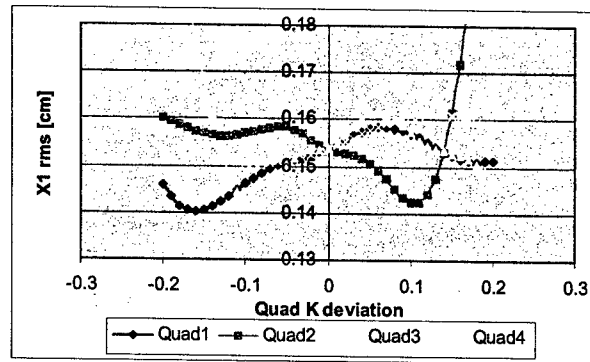


Figure 1: x rms beam size [cm] vs. quadrupole strength change. The wire scanner is located at the end of DTL tank 1. 0.1 Quad K deviation means that quadrupole gradient is 110% of design value (that is 10% more).

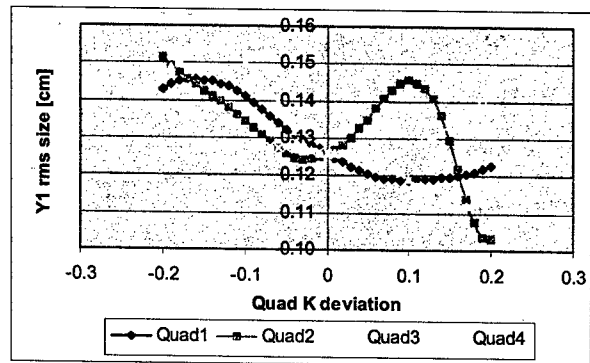


Figure 2: y rms beam size [cm] vs. quadrupole strength change. The wire scanner is located at the end of DTL tank 1.

The behavior of rms beam sizes is investigated with respect to the four matching quadrupole gradients at the end of MEBT. Figures 1 and 2 strongly indicate that

* SNS is managed by UT-Battelle, LLC, under contract DE-AC05-00OR22725 for the U.S. Department of Energy.
[#]jeond@ornl.gov

there could be more than one solution that generates the prescribed x and y rms beam sizes. And the variation of rms beam sizes is quite nonlinear. Therefore it is expected that the matching result won't be so robust. As an alternative, we try using the rms emittance.

Matching with rms emittances

The behavior of rms emittances with respect to the gradient change of the four MEBT matching quadrupoles and rf phase and amplitude offset of DTL tank 1 are studied. Figures 3 and 4 indicate that rms emittance is minimum when matching is proper and that there exists only one minimum. In the case where DTL tank 1 rf amplitude and phase are varied (see Figs 3 and 4), this alters transverse matching due to the change of transverse rf defocusing force and the design matched condition is no longer matched.

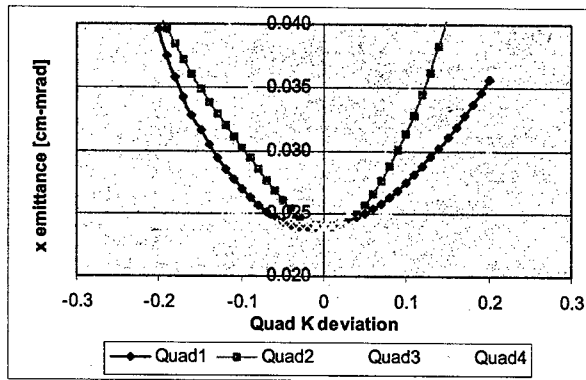


Figure 3: Plots of x emittance in cm-mrad with respect to the change of quadrupole gradient. 0.1 on x-axis means quadrupole strength is off by +10% of design value. When the gradient of quadrupole 1 is varied, the gradients of the rest three quadrupoles are set to its design values.

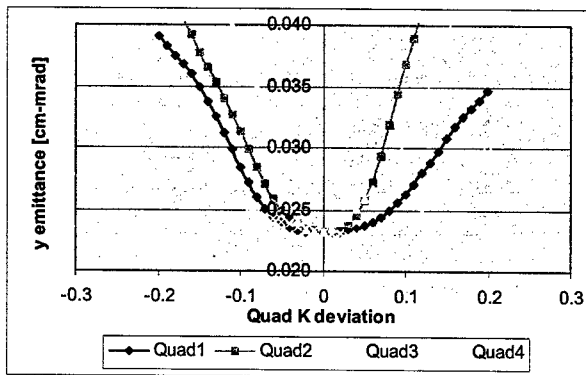


Figure 4: Plots of y emittance in cm-mrad with respect to the change of quadrupole strength. 0.1 on x-axis means quadrupole strength is off by +10% of design value. When the gradient of quadrupole 1 is varied, the gradients of the rest three quadrupoles are set to design values.

Figure 5 shows the x and y rms emittances after optimization vs. various levels of measurement error from 0% to 20%. 20% error on x-axis means 20% emittance measurement error. This means that 3σ of normal error

distribution are equal to 20% of the measured quantity. "before opt" means the rms emittances before optimization. Compared with design values, a reasonable level of transverse matching can be accomplished using rms emittances. 20% measurement error seems tolerable.

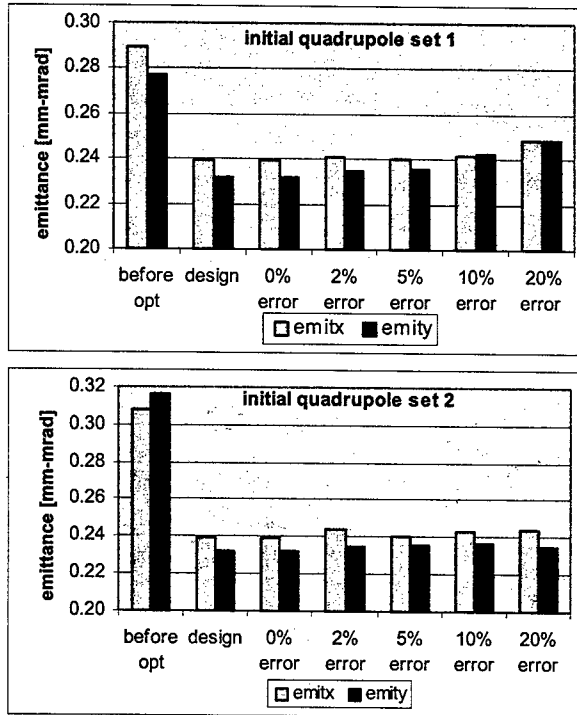


Figure 5: Plots of rms emittances vs. emittance measurement errors. 20% error means that 20% measurement error is included in rms emittance values, which means that 3σ of normal error distribution are equal to 20% of the quantity.

MATCHING DTL TO CCL AND CCL TO SCL

We study the transverse matching scheme of DTL to CCL (and CCL to SCL) by minimizing the envelope beating using multiple wire-scanners placed in series [4]. It is possible that machine may not be running smoothly enough during the commissioning stage. So it's better to do matching by a series of short optimization pieces. The 20-iteration optimization is estimated to take up to two hours.

Simulation results indicate that minimum number of wire-scanners is mainly dependent on the uncertainty between the model matching condition and the actual one. When 10% uncertainty in initial matching quad gradient is assumed, four wire-scanners are required to obtain reasonable matching and the scheme is tolerant of up to 20% (at 3σ) measurement uncertainty in the rms beam size. Plots of rms emittance from the CCL to SCL are shown in Fig. 6 for two different measurement uncertainties of rms beam sizes, namely 0% and 10%. 20% uncertainty in the initial matching condition is assumed. These are results when four wire-scanners are

used. Unlike the baseline configuration of wire-scanners, reasonable matching is obtained with 10% or more measurement uncertainty. It should be noted that the resulting match is better as there is less fluctuation in the rms emittance compare with Fig. 7. The beam envelope profiles in Fig. 7 are superior to those in Fig. 8 for the same 10% rms beam size uncertainty. Beam profiles obtained from using wire-scanners not in series for matching are shown in Fig. 8.

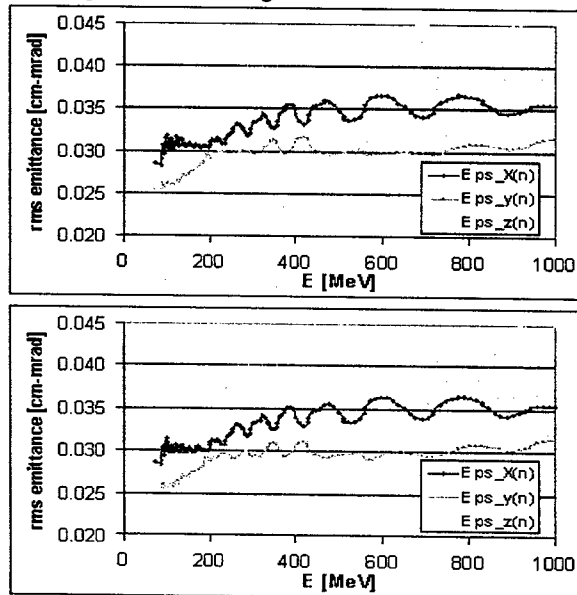


Figure 6: Plots of rms emittance for the cases with 10% (the top plot) and 20% rms beam size measurement uncertainties (the bottom plot). Four wire-scanners are used in series.

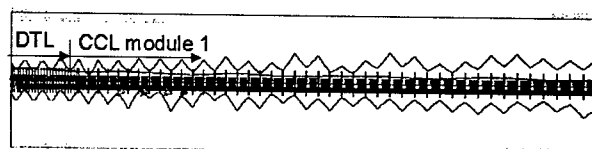


Figure 7: Trace3D [5] plots of beam envelopes after matching with 10% rms beam size uncertainty using four wire-scanners (red arrows) in series.

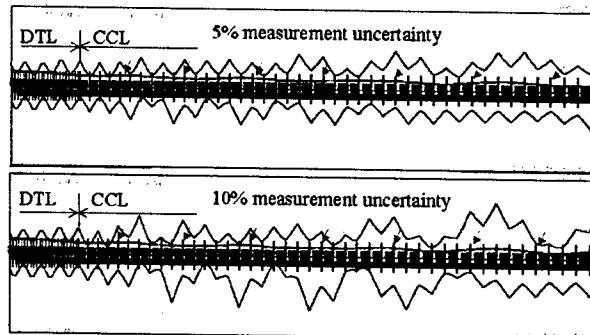


Figure 8: Trace3D plots after matching using wire-scanners (red arrows) not in series which are indicated by red arrows.

CONCLUSIONS

Most desirable ways of performing transverse matching are presented:

- Transverse matching of MEBT to DTL will be done by minimizing rms emittances.
- Transverse matching of DTL to CCL and CCL to SCL will be done using four wire-scanners in series.
- The proposed schemes are tolerant of measurement uncertainties, pulse-to-pulse jitters and beam mismatch, as well as it generates better matching.
- Measurement accuracy better than 20% is required for the proposed scheme to accomplish transverse matching.

REFERENCES

- [1] J. Stovall et al, Proc. of 2001 Particle Accelerator Conference (Chicago, 2001) p. 446.
- [2] H. Takeda, Parmila code.
- [3] Lagarias, J.C., J. A. Reeds, M.H. Wright, and P.E. Wright, "Convergence Properties of the Nelder-Mead Simplex Algorithm in Low Dimensions," May 1, 1997. To appear in the SIAM Journal of Optimization.
- [4] D. Jeon et al, Proc. of LINAC2002 conference (August 2002): MO422.
- [5] K. Crandall and D. Rusthoy, An Interactive Beam-Transport Code, Los Alamos National Laboratory report LA-10235-MS (January 1985): the Trace3D code.

RECENT RESULTS FROM THE PAUL TRAP SIMULATOR EXPERIMENT

E. P. Gilson*, R. C. Davidson, P. C. Efthimion, R. Majeski and H. Qin
 Plasma Physics Laboratory, Princeton University, Princeton, New Jersey, 08543, USA

Abstract

The Paul Trap Simulator Experiment (PTSX) is a compact laboratory facility whose purpose is to simulate the nonlinear dynamics of intense charged particle beam propagation over large distances through an alternating-gradient transport system. The simulation is possible because the quadrupole electric fields of the cylindrical Paul trap exert radial forces on the charged particles that are analogous to the radial forces that a periodic focusing quadrupole magnetic field exert on the beam particles in the beam frame. Initial experiments clearly demonstrate the loss of confinement when the vacuum phase advance σ_v of the system exceeds 90° . Recent experiments show that PTSX is able to successfully trap plasmas of moderate intensity for thousands of equivalent lattice periods.

INTRODUCTION

The Paul Trap Simulator Experiment (PTSX) is a cylindrical Paul trap whose purpose is to simulate the dynamics of charged particle beams in alternating-gradient (AG) magnetic transport systems [1]. The transverse electrostatic forces that PTSX exerts on the plasma are of the same form as the transverse forces that the quadrupole magnets exert on a beam in an AG system [1, 2]. Moreover, the self-fields can be expressed in analogous forms so that the transverse dynamics of both systems are described by a similar set of equations. Because of the long confinement times of ions in PTSX relative to the oscillation frequency of the trap voltage, PTSX is capable of simulating the beam dynamics over equivalent propagation distances of many kilometers. The waveform of the trap voltage is controlled by an arbitrary function generator so that the waveform can be varied in order to study a wide variety of beam physics topics.

The PTSX device is able to study intense beams in which the space-charge is non-negligible and the normalized intensity parameter $s = \omega_p^2/2\omega_q^2$ (where ω_p is the plasma frequency, and ω_q is the smooth focusing applied betatron frequency) approaches unity. Such intense beams are of increasing interest due to their relevance to high-energy physics, heavy ion fusion, spallation neutron sources, tritium production, and nuclear waste transmutation [3, 4]. Our goal is to study the properties of high-intensity beams where the self-field effects can significantly alter beam equilibrium, stability and transport properties.

In this paper, a brief description of the machine is presented, including several modifications to the original design. Then, the operating parameter regimes of the ion source and the trap itself are discussed. Finally, recent ex-

perimental results on the loading and trapping of emittance-dominated one-component plasmas are shown.

APPARATUS

Details of the PTSX apparatus appear in Ref. [5] and so only a brief description is given here. The PTSX device consists of three cylindrical electrodes of radius $r_w = 10$ cm that are sliced into four 90° sectors as shown in Fig. 1. The central electrode has length $2L = 2$ m while the end electrodes are each 40 cm long. The trap confines

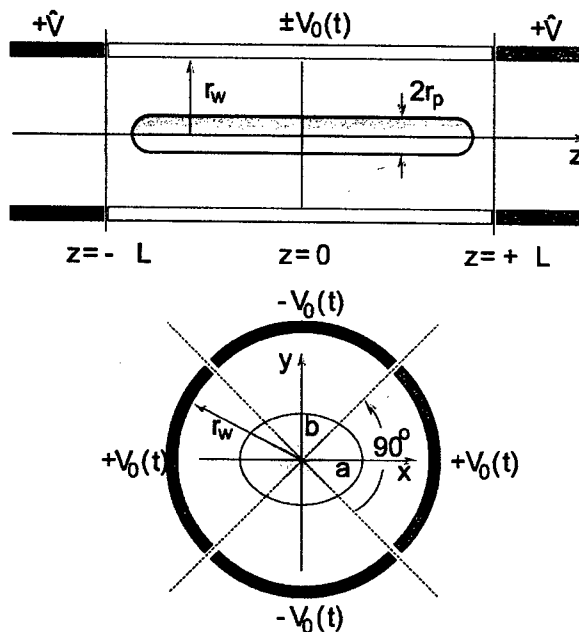


Figure 1: The PTSX device consists of three of cylindrical electrodes, each sliced into four 90° sectors. An oscillating voltage, $\pm V_0(t)$, confines the plasma radially to a radius r_p . Static voltages, $+V$, confine the ions axially.

charged particles (presently cesium ions) radially by applying a periodic voltage $\pm V_0(t)$ to the four sectors. In the limit of high frequency, this creates a ponderomotive force that points radially inwards; note, however, that the trap need not operate in this limit to effectively confine particles. A dc voltage, $+V$, applied to the end electrodes confines the ions axially. The ratio L/r_w is large in order to minimize the effects of the ions bouncing off of the dc end-potentials as these effects are outside of the analogy. If the plasma radius r_p is small compared to r_w , then the fields from the walls are almost purely quadrupolar with corrections on the order of $(r_p/r_w)^4$. For PTSX, $V_{0\max} \leq 400$ V,

*egilson@pppl.gov

$\hat{V} = 150$ V, and the frequency f of the oscillating voltage is less than 150 kHz.

For the sinusoidal oscillations used to date, $\omega_q = 4eV_{0\max}/\sqrt{2}m\pi^2r_w^2f$. Values of the vacuum phase advance ($\sigma_v = \omega_q/f$) from 0° to beyond 90° are easily accessible by the proper choice of $V_{0\max}$ and f as demonstrated in Fig. 2. For the experiments presented here, $V_{0\max} = 235$ V and $f = 75$ kHz, so that $\omega_q = 6.51 \times 10^4 \text{ s}^{-1}$ and $\sigma_v = 49.7^\circ$.

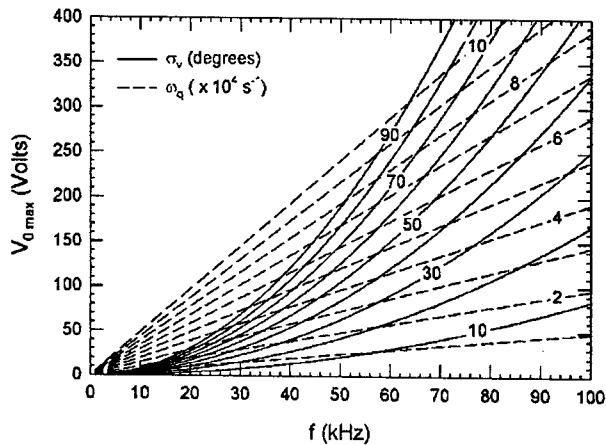


Figure 2: In the $(V_{0\max}, f)$ parameter space, curves of constant σ_v are parabolae, while the curves of constant ω_q are straight lines.

The PTSX device normally operates in a load—trap—dump cycle. During loading(dumping), the short electrodes on the source(diagnostic) end of the machine are made to oscillate with the same voltages, $\pm V_0(t)$, as the long electrodes, which allows the ions to pass. When dumped, the ions strike a Faraday cup that has a collection aperture with a diameter, $2r_{ap} = 1$ cm [Fig. 3(b)]. Either the charge or the average current can be measured with an electrometer to determine the radial plasma density profile.

There have been two modifications to PTSX since the device was described in Ref. [5]: the ion source has been improved, and the Faraday cup enclosure has been enlarged. A Pierce electrode has been added to the ion source assembly that employs an aluminosilicate cesium source, an acceleration grid, and a deceleration grid to provide the ions [Fig. 3(a)]. Adjusting the biases on the grids allows the current I_s that streams into the trap, and the ion energy E to be varied independently. The Faraday cup enclosure now shields the top, bottom, left, and right sides of the Faraday cup from stray ions [Fig. 3(b)].

EXPERIMENTAL RESULTS

We expect that I_s should follow the Child-Langmuir $V_e^{3/2}$ scaling with the extraction voltage V_e . The current I_s is measured by allowing the ions to “free stream” directly from the ion source to the Faraday cup where they are collected on the shield enclosure itself rather than through the

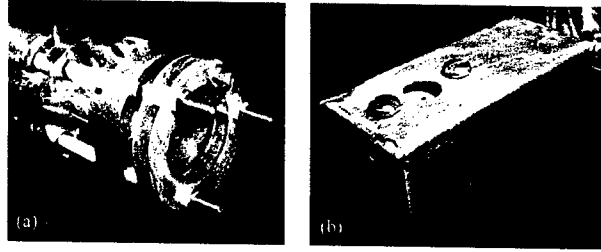


Figure 3: (a) A Pierce electrode has been added to the cesium ion source. (b) The Faraday cup shield has been extended to more completely block stray ions.

aperture. There is no axial trapping in this mode of operation. The data in Fig. 4 shows that I_s is linear for small V_e and even sub-linear at larger V_e . Despite the departure from Child-Langmuir, this control gives us a wide range of currents to use for loading the trap.

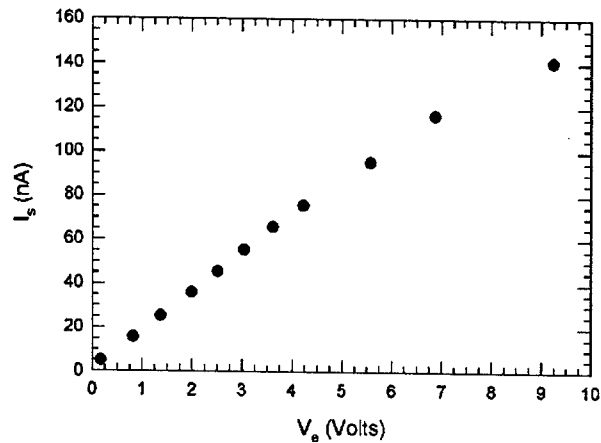


Figure 4: Rather than the $V_e^{3/2}$ scaling of the Child-Langmuir law, the current extracted from the ion source depends linearly on the extraction voltage.

Initial PTSX results confirmed the existence of the envelope instability and loss of confinement for $\sigma_v = 90^\circ$ [6]. This measurement was made with the ions “free streaming”. In the absence of space-charge effects, the transverse orbits are governed by Mathieu’s equation, and the system parameters must be chosen so that the single-particle orbits are stable. Indeed, if system parameters are chosen so that the vacuum phase advance is greater than 90° , no ions survive the 2.6 m transit from the ion source to the Faraday cup.

Subsequent experiments investigated properties of trapped plasmas, such as loading time effects, radial profiles, and lifetimes. A radial profile is shown in Fig. 5 for which the ions were loaded for 5 ms, trapped for 1 ms, and then dumped. This trapped plasma corresponds to parameters for which $I_s = 5$ nA. Because the transit time of an ion along the PTSX device is on the order of milliseconds, a loading time of 1 ms is inadequate to fully

load the trap. We observe that the amplitude of the radial profile nearly doubles if we allow loading to occur for more than two transit times. The profile is Gaussian in shape, consistent with one-component plasmas that are relatively hot, or emittance-dominated. In thermal equilibrium, the average density profile is proportional to $\exp[(-e\phi - m\omega_p^2 r^2/2)/kT]$. Therefore, if the space charge is negligible, so that ϕ can be ignored, then the radial profile will be nearly Gaussian. For a space-charge-dominated beam, the radial profile will approach a flat-top distribution [3]. It is not known whether the 0.7 cm offset is due to electrode asymmetries, distortion of the ion trajectories due to the Faraday cup, or to misalignment of the Faraday cup.

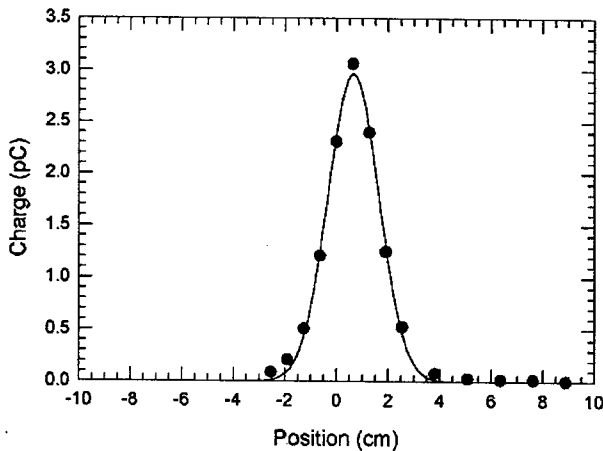


Figure 5: The charge collected in the Faraday cup through the 1 cm aperture. The trap walls are at $r_w = \pm 10$ cm.

It is assumed that the number density $n(r)$ is given by the total charge $Q(r)$ collected through the 1 cm aperture divided by the volume $\pi r_{ap}^2 2L$. The line density, $N = \int n(r) 2\pi r dr$, can be measured in two complementary ways: by using I_s and E , or by using $n(r)$. Having measured I_s and E previously, the line density is given by $N = 2 \times 5.2 \times 10^7 I(\mu A) / \sqrt{E(\text{eV})} \text{ cm}^{-1}$. The factor of two is a phenomenological factor that accounts for the ions that bounce and travel back towards the ions source during a loading that is longer than twice the transit time. Alternatively, $n(r)$ can be integrated numerically. In the present case, where $n(r)$ is Gaussian, the fit parameters of the Gaussian fit are used. These methods agree to within a factor of 3. The difference could arise because the ultimate energy of the injected ions may not be given simply by the grid biases, but rather influenced by space-charge effects such as the formation of a virtual cathode, or perhaps because the influence of the trapping voltage \hat{V} causes the plasma to have a length shorter than $2L$. For the data in Fig. 5, the Gaussian fit gives $n(0) = 1.2 \times 10^5 \text{ cm}^{-3}$, which implies that $s = 0.18$ and $N = 7.1 \times 10^5 \text{ cm}^{-1}$.

The reproducibility of the system allows us to measure the time evolution of the plasma by measuring the radial profiles of plasmas held for different times. Figure 6 shows that for a plasma corresponding to an initial intensity pa-

rameter $s = 0.13$, N decays slowly with time. As 1 s is the approximate timescale for ion-ion and ion-neutral collisions, it suggests that confinement is otherwise quite good until collisions cause transport and plasma loss. Even so, a plasma lifetime of one second allows for approximately 10^5 oscillation periods, and this would correspond to an AG system that is 100 km long if the magnet period is 1 m.

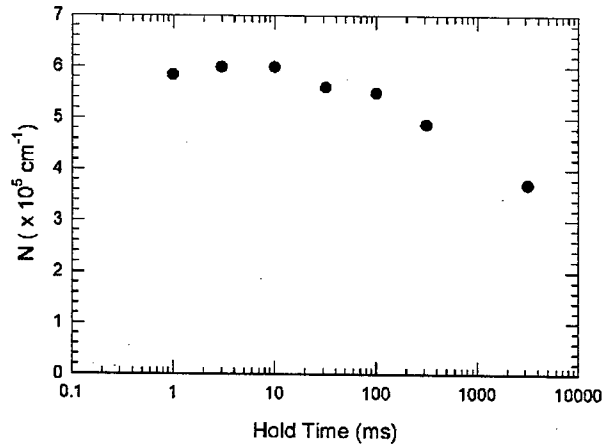


Figure 6: The line density, N , stays relatively steady for several hundred milliseconds before charge is gradually lost from the trap.

CONCLUSIONS

By demonstrating that PTSX can create and trap plasmas that are well-behaved for hundreds of milliseconds, even for $s = 0.13$, the opportunity exists to perform experiments in which the intensity parameter s is extended towards unity, and in which the oscillating voltage waveform on the trap walls is varied in order to simulate various beam physics phenomena.

This research was supported by the U.S. Department of Energy.

REFERENCES

- [1] R. C. Davidson, H. Qin, and G. Shvets, *Phys. Plasmas* **7**, 1020 (2000).
- [2] H. Okamoto and H. Tanaka, *Nucl. Instrum. Methods Phys. Res. A*, **437**, 178 (1999).
- [3] R. C. Davidson and H. Qin, *Physics of Intense Charged Particle Beams in High Energy Accelerators* (World Scientific, Singapore, 2001).
- [4] M. Reiser, *Theory and Design of Charged Particle Beams* (Wiley, New York, 1998).
- [5] E. P. Gilson, R. C. Davidson, P. C. Efthimion, R. Majeski and H. Qin, *Laser and Particle Beams* **21**, to be published (2003).
- [6] C. M. Celata, et al., *Phys. Plasmas* **10**, 2064 (2003).

DRIFT COMPRESSION AND FINAL FOCUS OF INTENSE HEAVY ION BEAM*

Hong Qin¹, Ronald C. Davidson¹, John J. Barnard² and Edward P. Lee³

¹ Princeton Plasma Physics Laboratory, Princeton University, Princeton, New Jersey 08543

² Lawrence Livermore National Laboratory, Livermore, California 94550

³ Lawrence Berkeley National Laboratory, Berkeley, California 94720

Abstract

The longitudinal and transverse dynamics of a heavy ion fusion beam during the drift compression and final focus phase is studied. A lattice design with four time-dependent magnets is described that focuses the entire beam pulse onto a single focal point with the same spot size.

LONGITUDINAL DRIFT COMPRESSION

In the currently envisioned configurations for heavy ion fusion, it is necessary to longitudinally compress the beam bunches by a large factor after the acceleration phase and before the beam particles are focused onto the fusion target. The objective of drift compression is to compress a long beam bunch by imposing a negative longitudinal velocity tilt over the length of the beam in the beam frame. Because the space-charge force increases as the beam is compressed, either a larger focusing force is needed to confine the beam in the transverse direction or the beam radius will grow. It is advantageous to have a non-periodic quadrupole lattice along the beam path when the beam is undergoing longitudinal compression. In this paper, we describe the design of such a lattice with four final focusing magnets that focus the beam onto the target. The designed lattice is expected to apply for the entire beam pulse. In particular, different slices should be focused onto the same focal point at the target. This is difficult with a fixed lattice if the beam current or velocity varies during the pulse. One solution is to use a time-dependent lattice which provides a different focusing strength for different slices of the beam pulse. We demonstrate that the entire pulse can be compressed and focused onto the same focal point on the target by using four time-varying quadrupole magnets at the very beginning of drift compression. The following set of beam parameters typical of heavy ion fusion is used in the present study. We consider a CS^+ beam with rest mass $m = 132.9$ amu, kinetic energy $(\gamma - 1)mc^2 = 2.43$ GeV, and initial beam half-length $z_{b0} = 5.85$ m. The goal is to compress the beam by a factor of 21.8. The final average current is taken to be $\langle I_f \rangle = 2254$ A.

We use a one-dimensional warm-fluid model [1, 2] to describe the longitudinal dynamics of drift compression. For the longitudinal electric field, the conventional g -factor model is adopted, with $eE_z = -(ge^2/\gamma^2) \partial\lambda/\partial z$ and $g = 2 \ln(r_w/r_b)$. Here, e is the charge, $\lambda(t, z)$ is the line density, r_w is the wall radius, and r_b is the average beam radius. We also allow for an externally applied axial focus-

ing force $F_z = -\kappa_z z$. In the beam frame, the warm-fluid equations for the line density $\lambda(t, z)$, longitudinal velocity $v_z(t, z)$, and longitudinal pressure $p_z(t, z)$ are given by

$$\begin{aligned} \frac{\partial\lambda}{\partial t} + \frac{\partial}{\partial z}(\lambda v_z) &= 0, \\ \frac{\partial v_z}{\partial t} + v_z \frac{\partial v_z}{\partial z} + \frac{e^2 g}{m\gamma^5} \frac{\partial\lambda}{\partial z} + \frac{\kappa_z z}{m\gamma^3} + \frac{r_b^2}{m\gamma^3 \lambda} \frac{\partial p_z}{\partial z} &= 0, \\ \frac{\partial p_z}{\partial t} + v_z \frac{\partial p_z}{\partial z} + 3p_z \frac{\partial v_z}{\partial z} &= 0. \end{aligned} \quad (1)$$

We treat g and r_b as constants for present purposes. Among all of the self-similar solutions [1] admitted by the nonlinear hyperbolic partial differential equation system (1), the parabolic self-similar solution is the most suitable for the purpose of drift compression, and has the form of [1]

$$\begin{aligned} \lambda(t, z) &= \lambda_b(t) \left(1 - \frac{z^2}{z_b^2(t)}\right), \quad v_z(t, z) = -v_{zb}(t) \frac{z}{z_b(t)}, \\ p_z(t, z) &= p_{zb}(t) \left(1 - \frac{z^2}{z_b^2(t)}\right)^2, \quad \frac{dz_b(t)}{dt} = -v_{zb}(t). \end{aligned} \quad (2)$$

Following the derivation in [1], we obtain the familiar longitudinal envelope equation

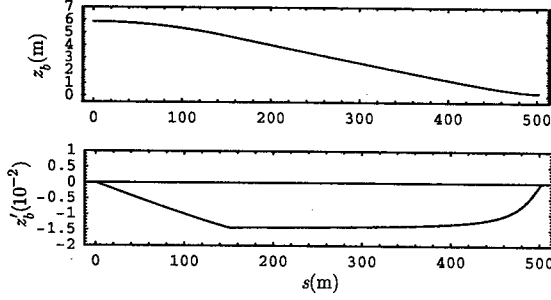
$$\frac{d^2 z_b}{ds^2} + \kappa_z z_b - K_z \frac{1}{z_b^3} - \varepsilon_l^2 \frac{1}{z_b^3} = 0, \quad (3)$$

where $s = \beta ct$ is the normalized time variable, $K_z \equiv 3N_b e^2 g / 2m\gamma^5 \beta^2 c^2$ is the effective longitudinal self-field permeance, N_b is the total number of particles in the bunch, and $\varepsilon_l \equiv (4r_b^2 W / m\gamma^3 \beta^2 c^2)^{1/2}$ is the longitudinal emittance. In the drift compression scheme considered in this paper, the longitudinal emittance is taken to be $\varepsilon_l = 1.0 \times 10^{-5}$ m, where $K_z = 2.88 \times 10^{-5}$ m, corresponding to an average final current $\langle I_f \rangle = 2254$ A, $z_{bf} = 0.268$ m, and $g = 0.81$. An initial longitudinal focusing force is imposed for $s < 150$ m so that the beam acquires a velocity tilt $z'_b = -0.0143$ at $s_b = 150$ m. The axial beam size $z_b(s)$, obtained numerically from the Eq. (3), is plotted together with the velocity tilt $z'_b(s)$ in Fig. 1. A pulse shaping technique has also been demonstrated so that any initial pulse shape can be shaped into a parabolic one which can then be self-similarly compressed [1, 2].

LATTICE AND TRANSVERSE DYNAMICS

For each slice in a bunched beam, the transverse dynamics in a quadrupole lattice is described approximately by

* Research supported by the U.S. Department of Energy.


 Figure 1: Dynamics of the beam half-length $z_b(s)$.

the transverse envelope equations:

$$\begin{aligned} \frac{d^2 a(s, z)}{ds^2} + \kappa_q a(s, z) - \frac{2K(s, z)}{a(s, z) + b(s, z)} - \frac{\epsilon_x^2}{a(s, z)^3} &= 0, \\ \frac{d^2 b(s, z)}{ds^2} - \kappa_q b(s, z) - \frac{2K(s, z)}{a(s, z) + b(s, z)} - \frac{\epsilon_y^2}{b(s, z)^3} &= 0, \end{aligned} \quad (4)$$

where $K(s, z) \equiv 2e^2 \lambda_b(s) [1 - z^2/z_b^2(s)] / m\gamma^3 \beta^2 c^2 z_b(s)$ is the transverse perveance. Here, z is the longitudinal coordinate for different slices, which enters the equations only parametrically. Because $K(s, z)$ is an increasing function of s , it is advantageous to increase the strength of $\kappa_q(s)$ to reduce the expansion of the beam radius. Since the quadrupole lattice is not periodic, the concept of a “matched beam” is not well defined. However, if the non-periodicity is small, we can seek an “adiabatically-matched” beam [1]. We describe here the design of a non-periodic lattice which provides the required control of beam radius when the beam is compressed. The drift compression and final focus lattice should apply for all slices in a bunched beam. In particular, each slice of the beam should be focused onto the same focal point at the target. A fixed lattice designed for one slice of the beam will not focus other slices onto the same focal point. Actually, most of the other slices cannot be focused at all due to their different perveance and emittance. Our goal can be achieved by designing a drift compression and final focus lattice for the central slice ($z = 0$), and then replacing four quadrupole magnets at the beginning of the drift compression by four time-dependent magnets whose strength varies about the design values for the central slice. The time-dependent magnets, which provide a slightly different focusing lattice for different slices, are placed at the beginning of the drift compression because the engineering constraints of time dependent magnets are generally easier at the 100 ns timescale than they are at the 10 ns timescale.

First, we design the drift compression and final focus lattice for the central slice at $z = 0$. It is intuitive that a lattice, which keeps both the vacuum phase advance and the depressed phase advance constant, is less likely to induce beam mismatch [3]. Constant vacuum phase advance and constant depressed phase advance requires (when $\eta \ll 1$)

$$\eta^2 \left(\frac{B'}{[B\rho]} \right)^2 L^4 = \text{const.}, \quad K \left(\frac{2L}{\langle a \rangle} \right)^2 = \text{const.}, \quad (5)$$

where η is the filling factor, L is the lattice period, B' is field gradient of the magnets, and $\langle a \rangle$ is the average beam radius. For the drift compression scheme considered here, $K_f/K_0 = 21.8$. If we allow $\langle a \rangle$ to increase by a factor of 2.33, i.e., $\langle a \rangle_f / \langle a \rangle_0 = 2.33$, we obtain $L_f/L_0 = 1/2$, and $(\eta B')_f / (\eta B')_0 = 4$. We also need to specify η , B' , and L . If we choose $L_i = L_0 \exp[-(\ln 2) s_i/s_f]$, and $B'_i = \text{const.}$, then from Eq. (5), $\eta_i = \eta_0 \exp[(\ln 4) s_i/s_f]$, where $s_i = \sum_{j=0}^{i-1} L_j$. We also choose self-consistently the following system parameters: $\sigma_v = 72^\circ$, $B'_i = 31.70 \text{ T/m}$, $L_0 = 6.72 \text{ m}$, and $\eta_0 = 0.0725$. The focusing strength of each magnet is $\hat{\kappa} = 0.38 \text{ m}^{-2}$. Let N denote the total number of quadrupole magnet sets. From $s_f = \sum_{j=0}^{N-1} L_j$, we obtain $N = 53$.

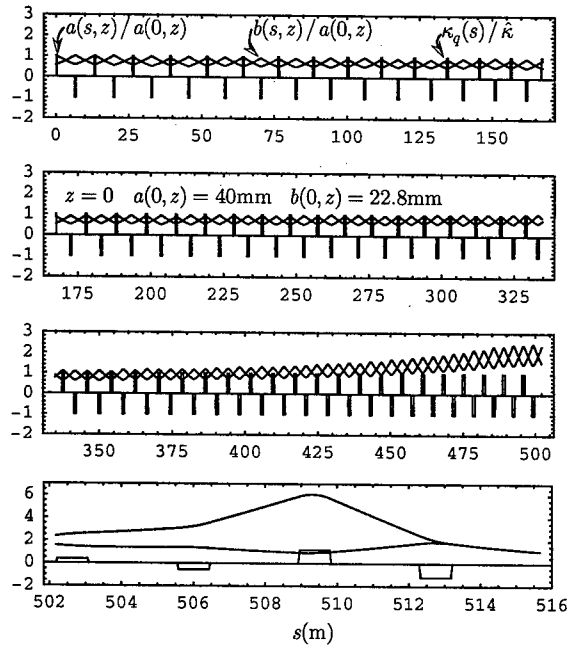


Figure 2: Envelope dynamics for the central slice.

The resulting lattice design is illustrated in Fig.2 together with the solutions to the transverse envelope equations. After determining the non-periodic lattice layout, we search iteratively for the adiabatically-matched solutions. The solutions plotted in Fig.2 are adiabatically-matched because the envelope is locally matched and contains no oscillations other than the local envelope oscillations. On the global scale, the beam radius increases monotonically. From the numerical solution shown in Fig. 2, the average beam size increases by a factor of 2.33, which agrees with the design assumption. The final focus magnets, consisting of four quadrupole magnets with different strength, will assure that the envelope converge in both directions at the exit of the last focusing magnet (both a' and b' are negative). Right after the last focusing magnet, the beam enters the neutralization chamber where the space-charge force is neutralized and the beam is focused onto a focal point at

$$z_{fol} = - \frac{a}{\partial a / \partial s} \Big|_{s=s_{ff}} = - \frac{b}{\partial b / \partial s} \Big|_{s=s_{ff}}, \quad (6)$$

where z_{fol} is the distance between the focal point and the exit from the last final focus magnet, and s_{ff} is the distance from the beginning of the drift compression to the exit from the last final focus magnet. It is necessary that $a/(\partial a/\partial s)$ and $b/(\partial b/\partial s)$ have the same value at $s = s_{ff}$ for a focal point to exist. The transverse spot size measured by the envelope amplitudes at the focal point a_{fol} and b_{fol} is determined by the emittance and incident angle at $s = s_{ff}$,

$$a_{fol} = \frac{\varepsilon_x}{\partial a/\partial s} \Big|_{s=s_{ff}}, \quad b_{fol} = \frac{\varepsilon_y}{\partial b/\partial s} \Big|_{s=s_{ff}}. \quad (7)$$

For the central slice at $z = 0$, we obtain $z_{fol} = 5.276$ m, and $a_{fol} = b_{fol} = 1.22$ mm.

For other slices ($z \neq 0$), the objective is to manipulate the beam and magnet configuration so that the beam particles can be focused onto a focal region with the same or smaller spot size,

$$z_{fol} = 5.276 \text{ m}, \quad a_{fol} \approx b_{fol} \lesssim 1.22 \text{ mm}. \quad (8)$$

We observe, for the line density profile $\lambda(s, z) = \lambda_b(s)[1 - z^2/z_b^2(s)]$, that the solution to the transverse envelope equations for all of the slices can be scaled down from that of the central slice according to

$$\begin{pmatrix} a(s, z) \\ b(s, z) \\ \partial a(s, z)/\partial s \\ \partial b(s, z)/\partial s \end{pmatrix} = \sqrt{1 - z^2/z_b^2(s)} \begin{pmatrix} a(s, 0) \\ b(s, 0) \\ \partial a(s, 0)/\partial s \\ \partial b(s, 0)/\partial s \end{pmatrix}, \quad (9)$$

provided the emittance is negligibly small or scales with the perveance according to $(\varepsilon_x, \varepsilon_y) \propto 1 - z^2/z_b^2(s)$. However, the emittance in general is small but not negligible, and does not scale with the perveance. In fact, during adiabatic drift compression or pulse shaping, the emittance scales with the beam size, i.e., $\varepsilon_x \propto a$ and $\varepsilon_y \propto b$. In this paper, we assume that the initial emittance scales with beam size, and that for each longitudinal slice the normalized emittance is conserved. This implies that the scaling in Eq. (9) and the requirement in Eq. (8) can't be satisfied.

One solution to this difficulty is to vary the strength of four magnets in the very beginning of the drift compression for different value of z such that the desired scaling in Eq. (9) holds at $s = s_{ff}$. Combined with Eqs. (6) and (7), this will guarantee the satisfaction of the requirement in Eq. (8). This is a viable solution because the emittance, and therefore the departure from the desired scaling, are small. Numerically, the necessary variation of the strength of the magnets is found by a 4D root-searching algorithm. Shown in Fig. 3 is the dynamics of $a(s, z)$ and $b(s, z)$ for $z/z_b(s) = 0.968$, when the strength of the 3rd, 5th, 7th and 9th magnets are modified to satisfy Eq. (9) at $s = s_{ff}$. The initial conditions are taken to be those satisfying Eq. (9) at $s = 0$. As evident for Fig. 3, a small perturbation in the strength of the magnets introduces a small envelope mismatch in such a way that Eq. (9) is satisfied at $s = s_{ff}$. We note that a similar scaling does not exist for $0 < s < s_{ff}$.

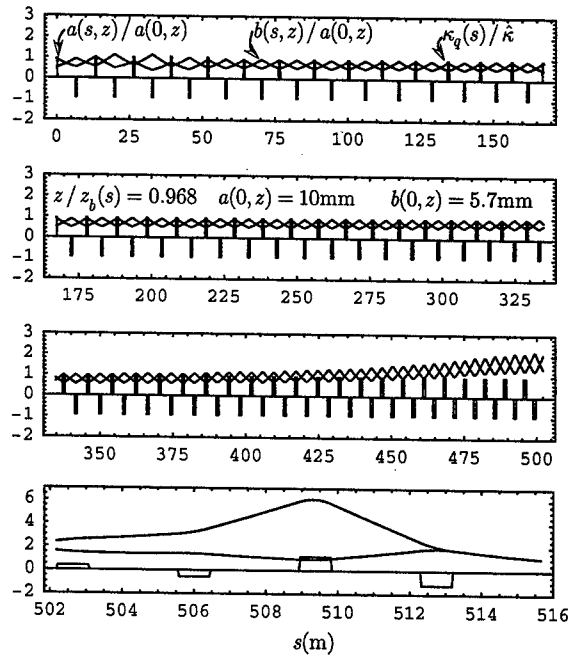


Figure 3: Envelope dynamics for the slice near the front of the beam pulse with $z/z_b(s) = 0.968$.

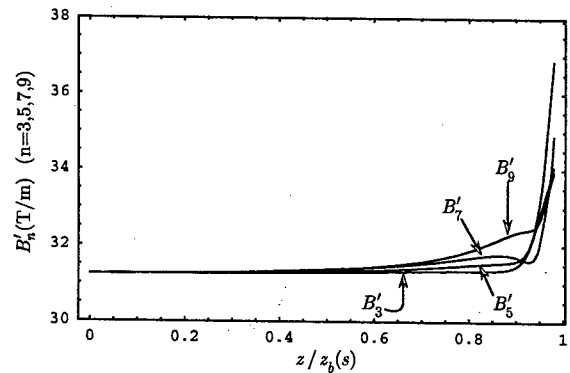


Figure 4: Strengths of the 3rd, 5th, 7th, and 9th magnets as functions of $z/z_b(s)$.

Plotted in Fig. 4 are the strengths of the 3rd, 5th, 7th and 9th magnets as functions of z which are able to focus the entire beam onto a focal region with the same spot size. It is also possible to choose other sets of four magnets as time dependent ones to achieve the same objective. In principle, we can use this method to correct any deviation from requirement (8) due to other possible mechanisms, such as momentum spread and magnet imperfections.

REFERENCES

- [1] H. Qin and R. C. Davidson, Phys. Rev. ST Accel. Beams **5**, 03441 (2002).
- [2] H. Qin and R. C. Davidson, Laser and Particle Beams **20**, 565 (2002).
- [3] E. P. Lee and J. J. Barnard, Laser and Particle Beams **20**, 581 (2002).

RF PLASMA SOURCE FOR HEAVY ION BEAM CHARGE NEUTRALIZATION

Philip C. Efthimion, Erik Gilson, Larry Grisham, Ronald C. Davidson, Plasma Physics Laboratory, Princeton University, Princeton, NJ 08543

Simon S. Yu and B. Grant Logan, Lawrence Berkeley National Laboratory, Berkeley, CA 94720

Abstract

Highly ionized plasmas are being used as a medium for charge neutralizing heavy ion beams in order to focus the ion beam to a small spot size. A radio frequency (RF) plasma source has been built at the Princeton Plasma Physics Laboratory (PPPL) in support of the joint Neutralized Transport Experiment (NTX) at the Lawrence Berkeley National Laboratory (LBNL) to study ion beam neutralization with plasma. The goal is to operate the source at pressures $\sim 10^{-5}$ Torr at full ionization. The initial operation of the source has been at pressures of 10^{-4} - 10^{-1} Torr and electron densities in the range of 10^8 - 10^{11} cm^{-3} . Recently, pulsed operation of the source has enabled operation at pressures in the 10^{-6} Torr range with densities of 10^{11} cm^{-3} . Near 100% ionization has been achieved. The source has been integrated with the NTX facility and experiments have begun.

INTRODUCTION

HIBALL-II is a possible heavy ion fusion reactor design [1]. The final focusing magnets must focus multiple heavy ion beams to a small spot size in the target chamber. This will require a deliberate charge neutralization of the ion beams. The plasma will be created or injected into the drift section between the last magnetic lens and the reactor chamber. The Neutralized Transport Experiment (NTX) [2] has been configured to investigate the most promising neutralization methods. One charge neutralization concept employs a heavy ion beam propagating through a highly ionized plasma column [3]. The cold plasma ion motion is neglected, and electrons from the cylindrical plasma move into the beam channel, reducing the net positive beam charge over the larger volume of the plasma channel. For NTX, ion beam densities are in the range of 10^8 - 10^9 cm^{-3} . Present calculations require the plasma to be in the range of 0.1- 2 meters in length with an electron density comparable to 1-100 times the beam density. The operating pressure for the plasma needs to be in the range of 10^{-6} - 10^{-5} Torr to prevent neutrals from stripping the beam ions to higher charge states. Previous plasma sources tested operated continuously, but were limited to pressures greater than 0.5 mTorr. The heavy ion beams for fusion will have pulse lengths in the sub-microsecond range. Consequently, operating the plasma source in a pulsed mode has been investigated. Both the gas feed to the source and the RF power are pulsed to achieve near full ionization at pressures in the range of 10^{-6} - 10^{-5} Torr during the first few milliseconds of source operation.

This operation results in plasma densities and operating pressures acceptable for charge neutralization experiments in NTX. The source has now been installed on NTX, and initial experiments have commenced. Here, the new pulsed source is described and its operating characteristics are compared to continuous sources previously investigated.

CONTINUOUS ECR SOLENOID SOURCE

The continuous plasma source is a simple electron cyclotron resonance (ECR) solenoid source. It is a 4" diameter cylinder and is approximately 12" long. Simple 16-gauge wire is wound around the cylinder to create a solenoid field. Up to 15 amperes of current can be applied to the coil to create a 30 gauss field. A radio frequency (RF) antenna couples power into the cylinder through a quartz window mounted at one end of the cylinder. The antenna is a simple 3-turn spiral. The spiral antenna is cooled with water and mounted in an enclosure against the window to prevent wave leakage. The source operates at 13 MHz frequency and at nominal power levels of 1 kW. The spiral antenna is impedance matched to the 13 MHz radio frequency source with a pair of tunable capacitors arranged in series and parallel to the antenna. The source operation near 0.5 mTorr exhibits an electron cyclotron resonance. When varying the field, the plasma density is a maximum when $\omega \sim \omega_{ce}$ at 6.2 gauss, and indicates cyclotron wave damping. Here, ω_{ce} is the electron cyclotron frequency. The operation of this source behaves like similar sources studied in the literature. It has an operating range down to 0.5 mTorr. Below this pressure the source extinguishes.

PULSED PLASMA SOURCE

The pulsed plasma source (Fig. 1) has a 6-way cross at the center of its design. A turbo-pump attached to one face maintains the vacuum while the gas inlet and the RF quartz window are attached to the opposite face. A three-turn copper spiral antenna is situated inside a shielded box and faces the window. The RF matching network is directly connected to the antenna enclosure and is tuned to match the low impedance antenna to the 50 Ohm transmission cable. Perpendicular to the turbo-pump and antenna, and directed into the page, are two flanges to the 6-way cross where the drift tube for the ion beam is connected. The plasma drifts into the center of the cross, and intersects the propagating ion beam. The source operates by applying a puff of argon gas and a pulse of RF power to the antenna. The potential advantages of

pulsed operation are that it can easily operate at high peak RF power levels, and the amount of gas can be limited. The plasma density and the neutral gas pressure are issues primarily during the 100 μ s the ion beam passes through the plasma. Consequently plasma parameters and neutral gas pressure are dynamic quantities and need to be measured as a function of time in order to evaluate source operation.

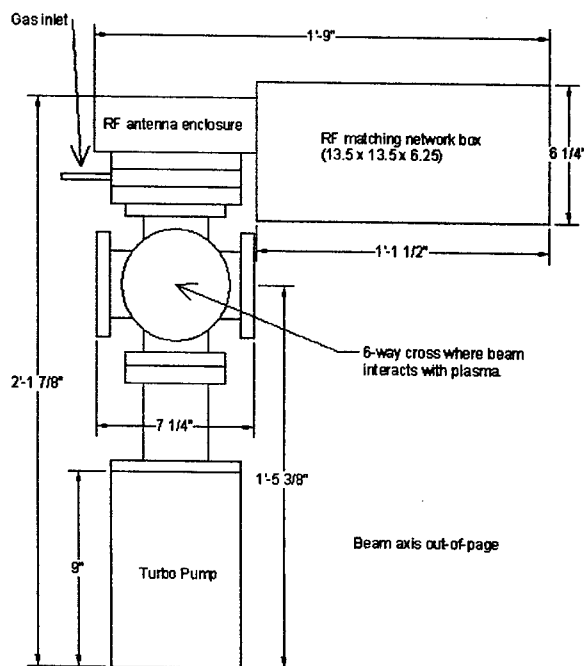


Figure 1: Schematic of pulsed plasma source.

PULSED PLASMA DIAGNOSTICS

A typical ion gauge controller does not have the time response to measure the quick pressure bursts when a gas puff is applied to the system. However, by measuring the voltage across a resistor placed in series with the ion gauge's collector current, the dynamic absolute pressure in the plasma source can be ascertained. The dynamic pressure measurement is calibrated at a fixed pressure while the pressure gauge is read, and the voltage across the resistor is recorded. To insure that the observed rise time is indicative of the rising gas pressure and not the RC time response of the circuit, the pressure measurement for a given plasma condition was repeated with two different resistors with an order-of-magnitude difference in resistance. The pressure evolutions for the two resistors were in agreement. Applying a 5 ms gas puff to the plasma source, the pressure sharply rises to 2 mTorr and pumps away in 1 second. This is expected to be compatible with NTX because it produces 100 μ s ion beams every 15 seconds.

The plasma electron density was measured with a Smart Soft Langmuir probe. It compensates for measurements in RF fields and can make high time-resolved measurements with reproducible plasmas. The

pulsed plasma source was observed to be very reproducible in parameters and breakdown time. Furthermore, the Langmuir probe is mechanically stepped through the plasma source for spatial measurements.

PULSED PLASMA SOURCE OPERATION

To operate the plasma source, the gas valve and the RF power are triggered at the same time ($t = 0$). In this mode it is easy to deliver more than 2 kW of RF power to the source, compared to only 1 kW for continuous plasma source operation. The power is measured with a directional coupler and calibrated diode. The source characteristics for a net forward power of ~ 3.5 kW versus time are shown in Fig. 2. Before $t = 3.75$ ms, the plasma density is less than the sensitivity of the Langmuir probe ($\sim 10^7$ cm $^{-3}$), and the neutral pressure is below the sensitivity of the dynamic pressure measurement (10^{-6} Torr). The onset of breakdown is clearly observed in the forward and reflected RF power versus time. The RF matching network is adjusted so that there is a maximum net power delivered to the plasma. At $t = 3.75$ ms the electron density is 10^{11} cm $^{-3}$ and simultaneous low neutral pressure. The ionization fraction for $t = 3.75 - 4$ ms is in the range of 50-100%. At later times the power density is not sufficient to sustain the ionization fraction, and the neutral density rises faster than the electron density.

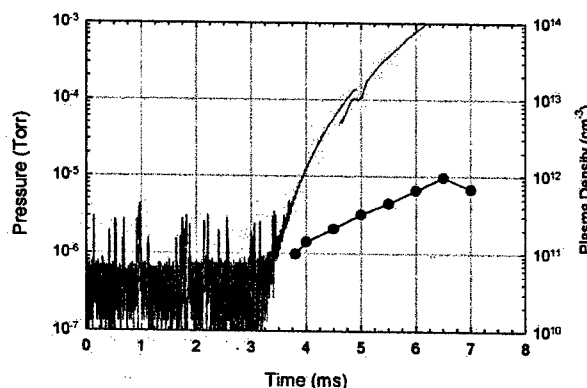


Figure 2: Time evolution of neutral gas pressure and plasma electron density (solid circles) in the pulsed plasma source.

One upgrade under consideration is to replace the gas valve with a faster one to reduce the length of the gas puff and the total amount of gas into the system. Another upgrade would be to increase the RF power level with a pulsed RF supply.

MEASUREMENTS AT LBNL

The pulsed plasma source was shipped to Lawrence Berkeley Laboratory (LBNL) and set up for initial testing. One difference between the source tests at Princeton and those at LBNL was that the RF generator was not able to provide 3.5 kW of power at LBNL and was limited to 2.5 kW. This limited the maximum plasma density achieved.

A number of density measurements were made in the 6-way cross with the Langmuir probe. A profile measurement was made transverse to the axis of the plasma source and turbo-pump (Fig. 3). The density is peaked on axis. There is a factor of 2 drop near the plasma source wall radius of 5 cm. Distances greater than 5 cm from the center of the cross is hidden from the straight-line path of the plasma out of the source. There the density decreases by an order-of-magnitude at a distance 5 cm from the wall radius of the plasma source.

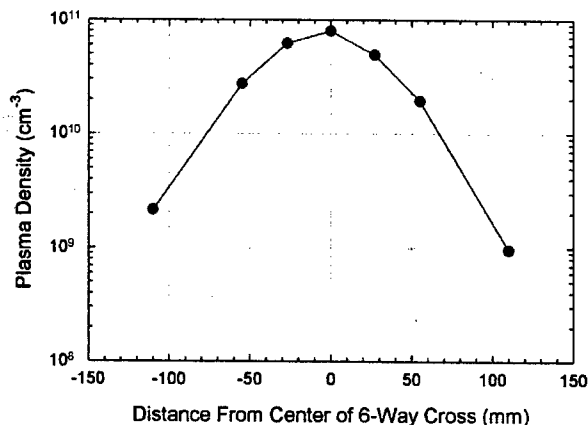


Figure 3: Plasma density profile in the cross transverse to the plasma source.

Another profile measurement was made in the 6-way cross, but along the axis of the plasma source. In this direction the plasma has a steep gradient away from the antenna because of the short plasma skin depth (~1 cm). This has also been seen in our previous steady-state ECR plasma sources. Consequently, the plasma density drops by 2 orders-of-magnitude across the cross diameter in this direction. In the ECR source, a weak magnetic field was used to reduce this, but is not used in the pulsed source.

Lastly, a density measurement at the center of the cross as a function of RF power was completed (Fig. 4). The electron density increases exponentially as a function of power. The data point near 3.5 kW was obtained at Princeton, but not at LBNL. Consequently, the source is limited to $5 \times 10^{10} \text{ cm}^{-3}$ density for the NTX experiments until the RF generator can produce the higher power levels.

The pulsed plasma source has been mounted on NTX and neutralization experiments have begun.

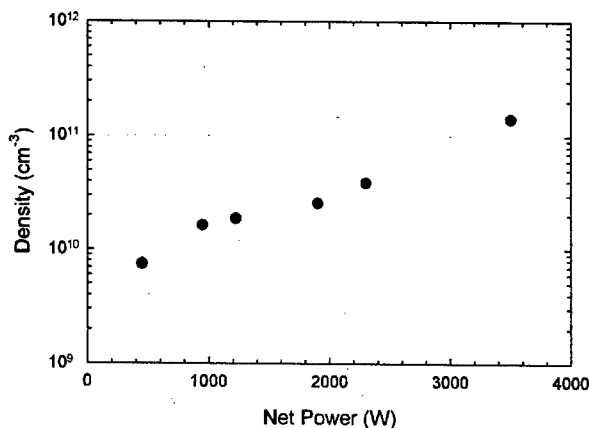


Figure 4: Electron density in the center of the cross as a function of RF power.

FUTURE PLANS

The RF generator will be brought back to its 4 kW power capability in order to achieve the densities observed at Princeton. Furthermore, the gas valve will be replaced with a faster one to limit the gas introduced to the NTX vacuum system. Lastly, modified versions of the pulsed plasma source may be examined at Princeton to achieve larger plasmas along the ion beam path. This research was supported by DOE Contract No. DE-AC02-76-CH-03073.

REFERENCE

- [1] B. Badger, et al. (1984), "HIBALL-II, An Improved Conceptual Heavy Ion Beam Driven Fusion Reactor Study", KfK-3480, Kernforschungszentrum Karlsruhe Report.
- [2] S. Yu, et al., Bull. of Am. Phys. Soc. **46**, 195 (2001).
- [3] B. G. Logan and D. A. Callahan, Nucl. Instr. and Meth. In Phys. A **415**, 468 (1998).
- [4] P. C. Efthimion, et al., Laser and Particle Beams **21**, 1 (2003).

SIMULATING ACCELERATOR STRUCTURE OPERATION AT HIGH POWER*

V. Ivanov[#], C. Adolphsen, N. Folwell, L. Ge, A. Guetz, Z. Li, C.-K. Ng, J. W. Wang, M. Wolf, K. Ko, SLAC, Menlo Park, CA 94025, USA

G. Schussmann, UC Davis, CA 95616, USA

M. Weiner, Harvey Mudd College, Claremont, CA 91711, USA

Abstract

The important limiting factors in high-gradient accelerator structure operation are dark current capture, RF breakdown and electron multipacting. These processes involve both primary and secondary electron field emission and produce plasma and X-rays. To better understand these phenomena, we have simulated dark current generation and transport in a linac structure and a square-bend waveguide, both high power tested at SLAC. For these simulations, we use the parallel, time-domain, unstructured-grid code Tau3P and the particle tracking module Track3P. In this paper, we present numerical results and their comparison with measurements on energy spectrum of electrons transmitted in a 30-cell structure and of X-rays emitted from the square-bend waveguide.

INTRODUCTION

The X-Band linac R&D for the NLC focuses on developing high gradient accelerating structures to increase linac efficiency and thereby lower the machine cost. In high power tests however, it was found that RF breakdown and dark current generation have prevented the structures from reaching their design gradients. These limiting factors are complex processes for which theoretical understanding is lacking especially when they occur in complicated 3D geometries. Recent advances in parallel code development made by the Advanced Computations Department (ACD) at SLAC have led to a simulation capability for studying dark current and RF breakdown in realistic structures under experimental conditions. A particle tracking module in 3D - **Track3P** has been developed with complete surface physics included, which is interoperable with fields generated either by the parallel eigensolver **Omega3P** for standing wave structures, or by the time-domain field solver **Tau3P** for traveling wave structures. We present simulation results from **Track3P/Tau3P** to two applications with measured data.

SIMULATION CODES

Tau3p

This code is a time-domain parallel solver [1], which solve the Maxwell system

$$\begin{aligned}\frac{\partial \vec{B}}{\partial t} &= -\nabla \times \vec{E}, \\ \frac{\partial \vec{D}}{\partial t} &= \nabla \times \vec{H} - \vec{J}.\end{aligned}$$

Here \vec{E} and \vec{H} - electric and magnetic fields, $\vec{D} = \epsilon \vec{E}$, $\vec{B} = \mu \vec{H}$ - induction vectors, ϵ , μ - permittivity and permeability of the media, \vec{J} - excitation current

The numerical algorithm uses explicit scheme of finite volume integration on unstructured grid.

Track3p

Particle tracking module [2] uses \vec{E} and \vec{B} fields from Tau3p to push particles using the Boris scheme for the motion equations:

$$\frac{d\vec{p}}{dt} = e(\vec{E} + \frac{1}{c}[\vec{v} \times \vec{B}]), \quad \vec{p} = m\gamma\vec{v}, \quad \gamma = \frac{1}{\sqrt{1-v^2/c^2}}$$

with particle injection given by

$$I(t) = \frac{I_{\max}}{1 + \left(\frac{v_0}{a} \left(t - \frac{\phi_0}{\omega} - iD_i \right) \right)^2}$$

where I_{\max} - amplitude of the injection current, α - half-width of the bunch, e and m - charge and mass of particle, Δt - repetition period, E_i - injection energy, c - speed of light, ϕ - phase of injection, ω - circular frequency of the fields, i - number of bunch, and

$$v_0 = \frac{c}{\sqrt{1 + \left(\frac{mc^2}{2|e|E_i} \right)^2}}$$

SURFACE PHYSICS

Thermal emission is described by the Child-Langmuir law

$$J(\vec{r}, t) = \frac{4}{9} \epsilon_0 \sqrt{\frac{2|e|E^2(\vec{r}, t)}{m d}}$$

where ϵ_0 - vacuum permittivity, d - distance from the emitter surface where electric field is evaluated.

Field emission in high-gradient field is described by the Fowler-Nordheim formula

$$J(r,t) = 1.54 \times 10^{\left(-6 + \frac{4.52}{\sqrt{\phi}}\right)} \frac{(\beta E)^2}{\phi} e^{\left(\frac{-6.53 \times 10^9 \phi^{1.5}}{\beta E}\right)}$$

where ϕ - work function, β - field enhancement factor.

The model of secondary emission is characterized by the ratio $\sigma = I_{\text{secondary}}/I_{\text{primary}} = \delta + \eta + r$, which is a function of the energy of incident primary particles e_{pri} . It includes the following components (Fig.1):

- δ - true secondary emission (0-50 eV); maximum $e_m \sim 2-4.5$ eV; width $\Delta e \sim 12-15$ eV;
- η - non elastic reflection (50 eV- e_{pri});
- r - elastic reflection ($r = 0.05-0.5$ for metals).

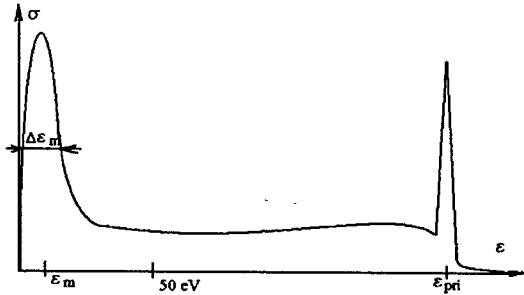


Figure 1: Components of secondary emission.

We use the Lye-Dekker's model [3] for true secondary emission

$$\delta = \frac{\delta_m}{g_m} g\left(z_m \frac{\epsilon}{\epsilon_m}\right), \quad g(z) = z^{-n} \left[1 - e^{-z^{n+1}}\right],$$

where $\delta_m = 1.4$, $\epsilon_m = 2.5$ eV, $z_m = 1.84$, $n = 0.35$.

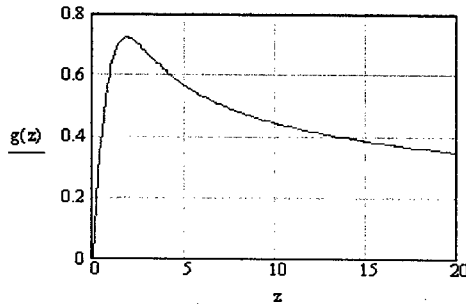


Figure 2. Normalized curve by Lye-Dekker.

SQUARE BEND SIMULATION

Square bend waveguide (Fig. 3a) used at NLCTA to transport SLED II output power to structures. Electric and magnetic fields are shown at Fig. 3b.

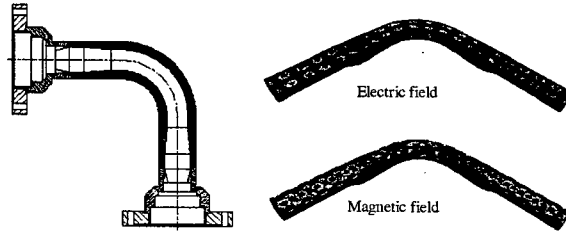


Figure 3. Square Bend Waveguide a) and EM fields b).

High power test on a 90 degree square bend provided measured X-ray data to allow the secondary emission model in Track3P be Benchmarked on a simple geometry

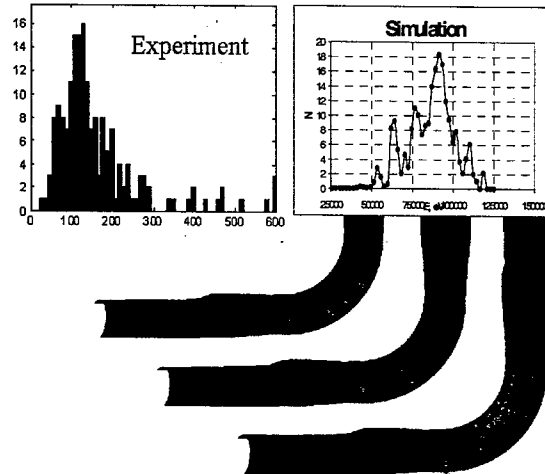


Figure 4. Experimental and numerical data for square bend waveguide. Red colour shows primary particles, green - secondaries.

Good agreement between Track3P simulation and measurement indicates high energy X-Rays seen in experiments are due to elastically scattered secondary electrons.

30-CELLS HIGH-GRADIENT STRUCTURE

NLC X-band structure showing damage after high power test [2].

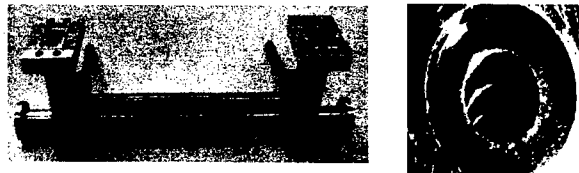


Figure 5. Damage in X-band structure.

Realistic simulations needed to understand underlying processes in the structure. Distributed model on a mesh of half million hexahedral elements (Fig.6) for Tau3P simulation of field evolution. Field distribution shown at Fig.8, and dark current evolution at Fig.8.



Figure 6. Discrete partitioned model of 30-cell structure with two couplers.



Figure 7. Field distribution in travelling wave structure.

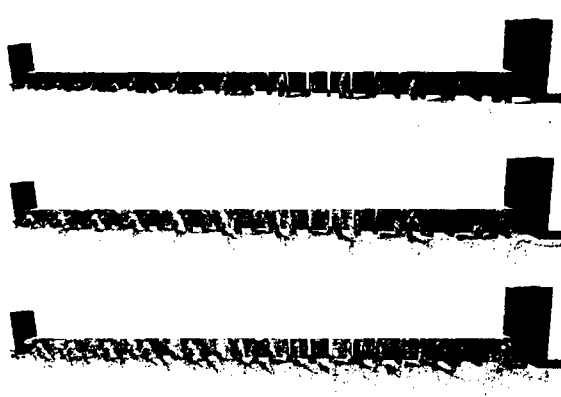


Figure 8. Evolution of dark current process.

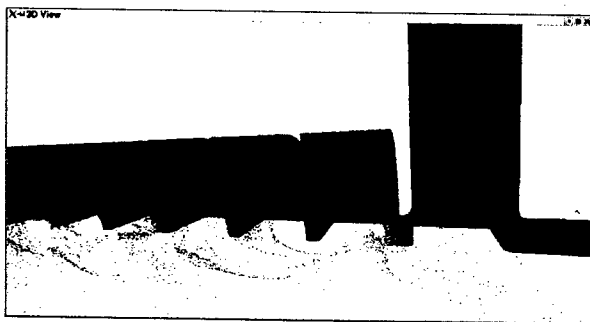


Figure 9. Emission in the coupler area

Numerical simulation demonstrates good agreement between experimental [4] and numerical data presented at Fig.10. Next Fig.11 shows total current in output cross-section which is about 5% of all emitted current in the structure.

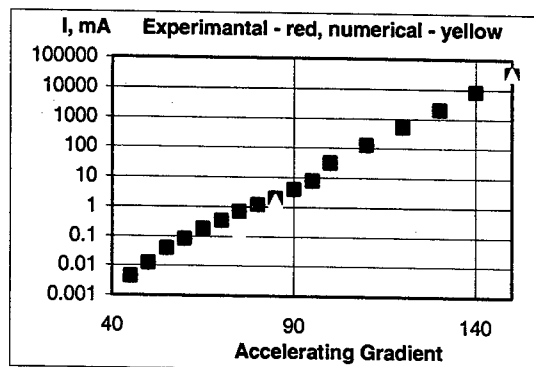


Figure 10. Experimental and numerical data for 30-cells structure

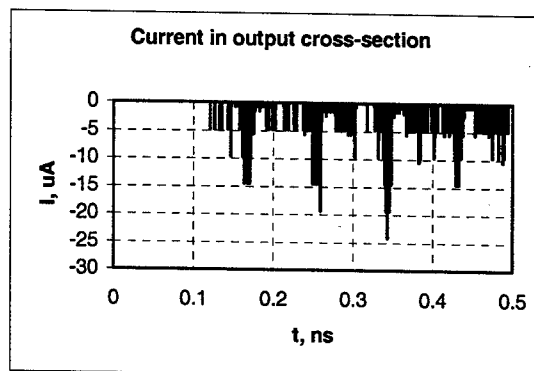


Figure 11. Total Current in Output Cross-Section.

CONCLUSIONS

Numerical simulations of Dark Current problem in high-gradient accelerating structure help for better understanding the physical phenomena in high power. It will be useful for design of rf-components of future Linacs.

ACKNOWLEDGEMENTS

This work supported by Department of Energy under contract DE-AC03-76SF000515.

REFERENCES

- [1] N. Folwell, K. Ko, Z. Li, B. McCandless, C. Ng, M. Wolf et al., *LINAC-2000* Conference, Monterey, CA, USA, August 21-25, 2000.
- [2] V. Ivanov, G. Schussmann, M. Weiner, *ACES-2002*, March 18-22, 2002, Monterey, CA.
- [3] S. Yamaguchi, Report LAL/RT- 92-18, Orsay, France, December 1992.
- [4] J. Wang, R. Curry et al., Proc. of the *LINAC-92* Conference, Ottawa, Canada, August 24-28, 1992.

A MODIFIED QUADSCAN TECHNIQUE FOR EMITTANCE MEASUREMENT OF SPACE CHARGE DOMINATED BEAMS *

C.Limborg*, S.Gierman*, J.Power*

*MS 69, SLAC 2575 Sand Hill Road, Menlo Park CA, USA

*ANL, 9700 S. Cass Avenue, Argonne, IL 60439 USA

Abstract

The quad-scan technique is one of the most commonly used methods for measuring emittances in photo-injectors at medium range energy in which the beam is not primarily space charge dominated. The space charge can nevertheless contribute strongly to the beam size evolution along the drift from the scanning quadrupole to the measurement screen. To take the space charge into account, we fit the beam sizes while solving the envelope equation for each quadrupole value. This algorithm is first applied to round beams and then extended to asymmetric beams. The benchmarking of this solver with the envelope equation tracker with PARMELA simulations is presented. The quadrupole scan algorithm including space charge correction for the round and not round beams is presented.

1 MOTIVATION

The beam trace emittance in a single plane is given by $(\langle x^2 \rangle \langle x'^2 \rangle - \langle x x' \rangle^2)^{1/2}$ where the average $\langle \rangle$ is taken over the whole beam distribution of particles with position x and angle x' . It corresponds to the square root of the determinant of the beam matrix. To measure the emittance, one of the techniques commonly used is the quadrupole scan. We consider a beam with beam matrix σ_{P_0} at point P_0 .

$$\sigma_{P_0} = \begin{bmatrix} \langle x_o^2 \rangle & \langle x_o x_o' \rangle \\ \langle x_o x_o' \rangle & \langle x_o'^2 \rangle \end{bmatrix} \quad (1)$$

This beam is transported through a quadrupole of strength kL and a drift of length l , represented by the transport matrix M and striking a screen at P . The beam matrix at P is given by σ_P . The term $\sigma_P(1,1)$ writes

$M_{11}^2 \sigma_{P_0}(1,1) + M_{12} M_{11} \sigma_{P_0}(1,2) + M_{22}^2 \sigma_{P_0}(2,2)$ (2)
In the quadrupole scan technique, the strength k of the quadrupole is varied. With three k values, one can deduce the three unknowns and compute the beam emittance. To get rid of the systematic errors one usually uses many more points. This over-determined system also contains information about the two other emittances.

With this linear analysis, one ignores the strong space charge effects. For this reason, at low energy, it is standard to use the pepper pot emittance measurement

technique instead of the quadrupole scan.

In this paper, we describe a method to take space charge into account in any quadrupole scan measurement. Also we extend the method to deduce the two transverse emittances and the longitudinal emittance.

2 ENVELOPE EQUATION

The envelope equation [1] describes the evolution of a beam in the presence of space charge forces. With the assumption that the space charge force can be linearized the envelope equation can be written as three coupled equations describing the evolution of an ellipsoidal beam as described very thoroughly in [2].

$$\begin{aligned} X'' + k_x^2(s)X - \frac{3K}{2} \frac{1 - \xi(Z/\sqrt{XY})}{Z(X+Y)} - \frac{\epsilon_x^2}{X^3} &= 0 \\ Y'' + k_y^2(s)Y - \frac{3K}{2} \frac{1 - \xi(Z/\sqrt{XY})}{Z(X+Y)} - \frac{\epsilon_y^2}{Y^3} &= 0 \\ Z'' + k_z^2(s)Z - \frac{3K}{2} \frac{1 - \xi(Z/\sqrt{XY})}{XY} - \frac{\epsilon_z^2}{Z^3} &= 0 \end{aligned} \quad (3)$$

$$X^2 = 5 \langle x^2 \rangle, Y^2 = 5 \langle y^2 \rangle, Z^2 = 5 \langle z^2 \rangle$$

With the beam perveance K

$$K = \frac{qN}{2\pi\epsilon_0} \frac{1}{\gamma^3 \beta^2} \frac{q}{mc^2} \text{ and } qN \text{ is the charge} \quad (4)$$

$$\xi(s) = \frac{s}{2} \int_0^\infty \frac{dt}{(t+1)(t+s^2)^{3/2}} \quad (5)$$

3 COMPARISON WITH PARMELA

1D result

We compared the evolution of beam sizes R and its conjugate variable R' for a round beam from PARMELA with those obtained when transporting the 1D envelope equation (first equation of (3) with $X = Y = R$). We assumed a constant peak current and a constant emittance. For a bunch with Gaussian profile, one usually uses 2.355 times the rms bunch length to compute the peak current. It appears that using $\sqrt{12}$ time the rms bunch length to compute the peak current was giving better agreement as shown in figure 1. The 3D envelope equation tracker includes the variation in bunch length along the drift and thus automatically makes the appropriate correction.

Those differences come from the fact that individual slices have in fact a different peak current. When applying the same algorithm to the individual slices using the correct slice peak current and initial R and R' , we obtained a satisfying agreement as shown in figure 2.

(*) Contact: C.Limborg

e-mail: limborg@slac.stanford.edu

SLAC is operated by Stanford University for the Department of Energy under contract number DE-AC03-76SF00515

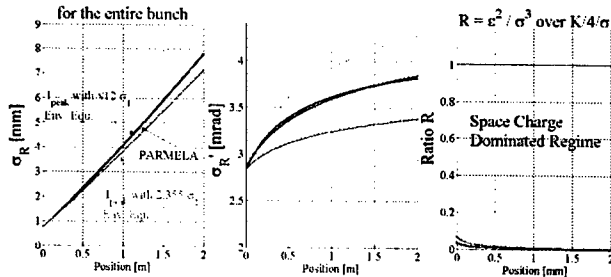


Figure 1- Evolution of beam size and divergence for a 5.7 MeV beam along a drift; the peak current has been computed 3 different ways (1) with $2.355 \sigma_1$ (2) with $\sqrt{12} \sigma_1$ and (3) using the total bunch length

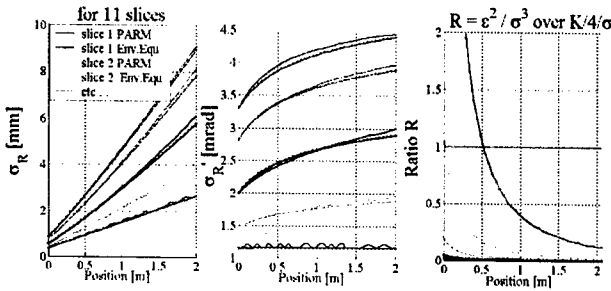


Figure 2 – Evolution of beam size and divergence for a 5.7 MeV beam along a drift, for the 6 first slices out of 11; Comparison between PARMELA (PARM.) data and Envelope Equation (Env. Equ.) solver

A square pulse was also studied. In this case, the number of particles varies strongly inside the slices close to the head and tail since the longitudinal space charge force is stronger on the steep edges. So particles drift from slice to slice and the peak current varies. Accordingly, the agreement with PARMELA is not as good. This type of behavior also occurs for bunches with longitudinal asymmetric profiles.

2D result

We then solved numerically the 2 first equations of (3) for non-round beams. Those two equations are coupled through the rms horizontal and vertical beam sizes. The agreement is satisfying as shown in figure 3. The calculation was done here with PARMELA using the 3D algorithm. But it does not differ much from the 2D result as the beam aspect ratio does not exceed 2 to 1.

The discrepancies are justified in the next paragraph.

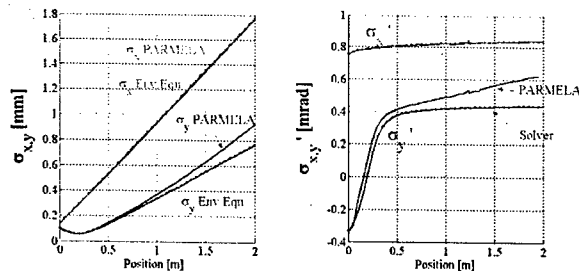


Figure 3- Evolution of beam size and divergence along a drift for a non-round beam. The solver agrees well with

the simulation over 1.5 m. The beam was here at 30 MeV but in the space charge dominated regime.

3D result

We solve numerically the 3 equations of (3). The peak current is then automatically computed correctly. Figure 4 shows that in case of a strong bunch lengthening along the drift, the 3D solver gives some very good results.

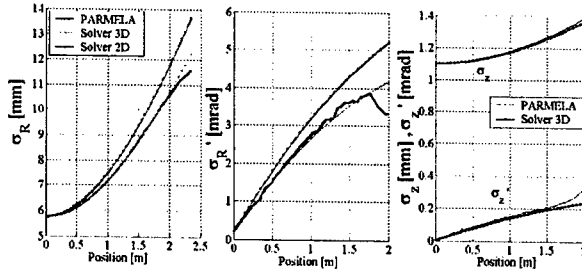


Figure 4- Evolution of beam transverse size (1), divergence (2) and bunch length and its derivative (energy spread) (3) along a drift for a 8.5 MeV beam;

The 3D envelope equation tracker was applied for various beam of low energy 5MeV and 8.5 MeV and to higher energy beams such as 30 MeV. It gave some very satisfying agreement with PARMELA. Beams with asymmetric longitudinal profiles cannot correctly be represented by the rms quantities.

4 QUADRUPOLE SCANS

For typical emittance measurements based on quadrupole scans, two quadrupoles Q1 and Q2, are used. The scan is done by varying the strength of the second quadrupole. The first one is chosen such that the beam on the screen has good dimensions and provides a fair intensity. One can choose the settings such that both the horizontal and vertical beam sizes will go through a waist during the scan.

The three coupled equations of (3) can be transformed into six first order differential equations. The transfer matrix approach can then be used. It is equivalent to that of the envelope equation but easier to manipulate. This formalism has been described thoroughly in [2] and it is also that developed for Trace 3D [3,4].

$$\sigma = \begin{pmatrix} \langle x^2 \rangle & \langle x x' \rangle & \langle x y \rangle & \langle x y' \rangle & \langle x z \rangle & \langle x z' \rangle \\ \langle x x' \rangle & \langle x'^2 \rangle & \langle x' y \rangle & \langle x' y' \rangle & \langle x' z \rangle & \langle x' z' \rangle \\ \langle x y \rangle & \langle x' y \rangle & \langle y^2 \rangle & \langle y y' \rangle & \langle y z \rangle & \langle y z' \rangle \\ \langle x y' \rangle & \langle x' y' \rangle & \langle y y' \rangle & \langle y'^2 \rangle & \langle y' z \rangle & \langle y' z' \rangle \\ \langle x z \rangle & \langle x' z \rangle & \langle y z \rangle & \langle y' z \rangle & \langle z^2 \rangle & \langle z z' \rangle \\ \langle x z' \rangle & \langle x' z' \rangle & \langle y z' \rangle & \langle y' z' \rangle & \langle z z' \rangle & \langle z'^2 \rangle \end{pmatrix}$$

$$\sigma_{i+1} = M \sigma_i M \text{ and } X^2 = \langle x^2 \rangle, Y^2 = \langle y^2 \rangle, Z^2 = \langle z^2 \rangle$$

$$M_{sc} = \begin{pmatrix} 1 & 0 & 0 & 0 & 0 & 0 \\ \Delta s/f_{sc,x} & 1 & 0 & 0 & 0 & 0 \\ 0 & 0 & 1 & 0 & 0 & 0 \\ 0 & 0 & \Delta s/f_{sc,y} & 1 & 0 & 0 \\ 0 & 0 & 0 & 0 & 1 & 0 \\ 0 & 0 & 0 & 0 & \Delta s/f_{sc,z} & 1 \end{pmatrix}$$

$$1/f_{sc,x} = K/2 \left[\frac{1}{5} \frac{1}{X^2} \right]^{3/2} R_d \left[\frac{Y^2}{X^2}, \frac{Z^2}{X^2}, 1 \right]$$

$$1/f_{sc,y} = K/2 \left[\frac{1}{5} \frac{1}{Y^2} \right]^{3/2} R_d \left[\frac{Z^2}{Y^2}, \frac{X^2}{Y^2}, 1 \right]$$

$$1/f_{sc,z} = K/2 \left[\frac{1}{5} \frac{1}{Z^2} \right]^{3/2} R_d \left[\frac{X^2}{Z^2}, \frac{Y^2}{Z^2}, 1 \right]$$

The transport matrix used for drifts and quadrupoles are standard. But they are fragmented in N pieces. For instance, the drift of length L is fragmented into N pieces to apply the space charge kicks every N/L.

$$M_{d,L} = M_{sc} M_{d,L/N} M_{sc} M_{d,L/N} M_{sc} M_{d,L/N} \text{ etc ...}$$

We checked that the coupling terms in the σ matrix can be neglected. We thus only kept the terms $\sigma_{i,i}$ and $\sigma_{i,i+1}$ for $i = 1$ to 6. They constitute the 9 unknowns we want to determine.

Round beam result

To reduce the number of unknowns, we first solve for the round beam at the entrance of Q1. That reduces the number of unknowns to 6. The transformations are

For a point with the 6D coordinates

$$X_o = (x, x', y, y', z, z')$$

$$X = M_{Q2} M_{d,1} M_{Q1} M_{d,2} X_o$$

The beam matrix is then given by

$$\sigma_p = M_{Q2} M_{d,1} M_{Q1} M_{d,2} \sigma_{p0} M_{d,2}^t M_{Q1}^t M_{d,1}^t M_{Q2}^t$$

with $M_{Q1}(k)$

and M_d is function of $(\sigma_{i,local})$

The data to fit are

$\sigma_p(1,1)$ as a function of k

and $\sigma_p(3,3)$ as a function of k

As shown in figure 5, the solver without space charge matches well the horizontal beam size but does not fit the vertical one correctly. It gives a 71.4 mm.mrad horizontally and 69 mm.mrad vertically. The solver which includes the space charge fits well both horizontal and vertical beam sizes and gives the correct emittance of 60 mm.mrad. The longitudinal emittance, not represented here, given by the solver with space charge is also determined accurately to be 6.4 mm.mrad.

To solve this problem numerically, an internal MATLAB solver is used[5]. It consists of a constrained non-linear least-square fit algorithm based on the Levenberg-Marquardt method. This algorithm is also described in [6].

The robustness of the algorithm needs to be assured. In particular, this algorithm should work for noisy data, such as experimental data.

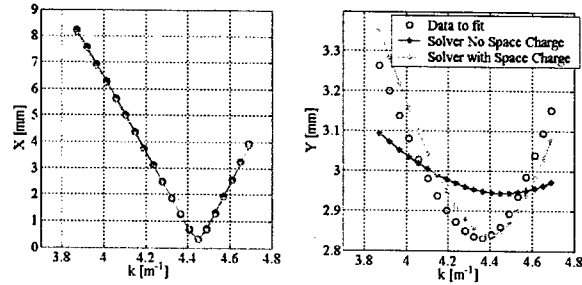


Figure 5 – Beam Size (1) horizontal and (2) vertical on measurement screen. The beam has a 8.5 MeV and is space charge dominated

Consideration for Elliptic BEAMS

To fit the beam at Q2 entrance, where it is elliptical, we can use the results of the round beam at the entrance of Q1 and transport them to Q2. However, a general algorithm which solves for the 9 unknowns has also been developed as it is useful for flat beam injectors. This algorithm fails for the case described in figure 5 when we look for a solution at Q2 entrance at which the beam is elliptical. The solution found corresponds to a local minimum of the least square function and does not lead to the solution.

5 CONCLUSION

We have demonstrated by comparing PARMELA simulations with the tracking of the envelope equation that the 3D envelope equation tracking can be applied very accurately for low energy beams. Even if the envelope equation represents the evolution of rms quantities, it also applies to non-Gaussian beams as long as they have ellipsoidal symmetry. If the longitudinal profile is asymmetric, the envelope equation is not appropriate. The space charge correction to a quadrupole scan fitting algorithm works fine for a round beam. The longitudinal emittance can be successfully deduced. Improvement of the solver for the 9 parameters of a non-round beam requires more sophisticated algorithms than the internal Matlab solvers.

REFERENCES

- [1] F.R. Sacherer, "RMS Envelope Equations with Space Charge", IEEE Trans. Nucl. Sci., Vol. NS-18(1971), pp. 1105-1107
- [2] C.K. Allen "Theory and Technique of Beam Envelope Simulation", LANL, LA-UR-02-4979 August 2002
- [3] TRACE 3D, LANL Codes, laacg1.lanl.gov/laacg/services/Trace3D.html
- [4] TRACE 3D, User Manual, AccelSoft, <http://www.ghga.com/accelsoft/home.html>
- [5] MATLAB, User's Manual, <http://www.mathworks.com/access/helpdesk/help/toolbox/curvefit/curvefit.shtml>
- [6] "Numerical Recipes in C, The Art of Scientific Computing" 2nd edition, Cambridge University Press W.Press, S.Teulosky, W.Vetterling, B.Flannery

CALCULATION OF THE MAXIMUM STORED BEAM CURRENT CONSIDERING THE PHASE NOISE OF A GENERATOR RF SIGNAL

L.H. Chang, Ch. Wang, M.C. Lin, G.H. Luo
National Synchrotron Radiation Research Center

Abstract

Synchrotron motion was numerically simulated to examine the maximum stored beam current, which is limited by beam loading. In addition to the machine operating parameters, the simulation considers the influence of the phase noise of a generator voltage on the maximum stored beam current. The computed result shows that increasing the phase noise level can reduce the maximum stored beam current and the reducing of the maximum stored current, due to an increase in the noise level, escalates with increasing the cavity voltage.

INTRODUCTION

To meet the requirement of users, we will replace two existed conventional cavities with one CESR-III 500 MHz SRF module to increase the stored electron beam from 200 mA to 500 mA and to improve the beam stability. When machine is upgraded, the beam loading ratio will increase from the current value 1.3 to 6.9 [1]. To insure the beam current can reach the design goal, it is necessary for us to examine the influence of the phase noises on the beam current when the machine is operated under such heavy beam loading conditions.

The current theoretical computation of the maximum stored beam current is based on the study of Robison in 1964 [2]. The study indicated that the beam current reaches its maximum limit when the generator rf voltage is pushed to the opposite phase of the beam current by the detuned cavity. The cavity is detuned to compensate for the change, caused by the beam loading, in the cavity matching impedance.

In the theoretical computation, the beam-induced voltage and the generator voltage are treated as a purely sinusoid signals, without noise. In reality, the generator voltage is always accompanied with different kinds of noise, such as harmonic, amplitude and phase noises.

In this paper, the phase noise of a generator voltage is included in the numerical simulation. From the simulation, we can investigate the synchrotron motion of each beam bunch turn by turn. Whether the beam current is above or below the limitation can then be determined from the behavior of each beam bunch in the simulated motion. The maximum beam currents computed for different phase noise levels are demonstrated by an example, which is also used to compare the theoretical and simulated results.

FORMALISM FOR CALCULATION

Difference Equations for Synchrotron Motion

In the study we assume that the electrons in a bunch bucket act as a single rigid macro-particle. The energy and time deviations of a beam bunch, ε and τ , during the synchrotron motion can then be described by the following equations:

$$\frac{d\varepsilon}{dt} = \frac{e}{T_0} V_{acc}(t_s + \tau) - eU_{rad}(\varepsilon) \quad (1)$$

$$\frac{d\tau}{dt} = \alpha \frac{\varepsilon}{E_s} \quad (2)$$

where T_0 is the revolution period of the synchronous particle, e is the electron charge in a bunch, V_{acc} is the accelerating voltage, α is the momentum compaction factor, E is the electron energy, the subscript s presents the quantity for the synchronous bunch. U_{rad} is the radiation loss. The radiation loss in a single turn is given by

$$U_{rad} [KeV] = 88.46 \frac{E [GeV]^4}{\rho} [m] \quad (3)$$

$$= 26.520308 E [GeV]^3 B [T] \quad (4)$$

where ρ is the radius of curvature of the orbit in the bending magnet and B is the bending magnetic field. Rewriting (1) and (2) for a single turn period and imposing the symplectic condition [3], we can obtain the particle tracking equations for the synchrotron motion:

$$\varepsilon_{j+1} = \varepsilon_j + eV_{acc}(t_s + \tau_j) - eU_{rad}(\varepsilon_j) \quad (5)$$

$$\tau_{j+1} = \tau_j + \alpha T_0 \frac{\varepsilon_{j+1}}{E_s} \quad (6)$$

where the subscript j represents the number of revolutions of a beam bunch. In synchrotron motion, the radiation loss for a synchronous beam bunch is exactly compensated by the accelerating voltage:

$$V_{acc}(t_s) = |\vec{V}_c| \cos(\phi_s) = U_{rad}(\varepsilon = 0) \quad (7)$$

where ϕ_s is the synchrotron phase and \vec{V}_c is the cavity voltage.

Tuning Angle for Beam Loading Compensation

The tuning angle is a measure of the phase difference between the excited rf signal and its generator current for a cavity. From microwave circuit theory, it can be expressed

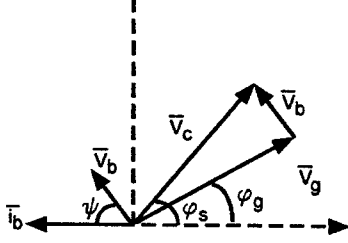


Figure 1: Phasor diagram for beam loading compensation when the cavity is detuned to ψ .

by the cavity loaded quality factor Q_L , the rf signal frequency ω_{rf} and the cavity resonance frequency ω_c as follows:

$$\tan(\psi) = -2Q_L \frac{\omega_{rf} - \omega_c}{\omega_c} \quad (8)$$

When there is beam current in a storage ring, the change in cavity matching impedance, which is changed by beam loading, can be compensated for, to minimize the reflected rf power by tuning the cavity tuning angle ψ to [4]:

$$\tan(\psi) = -\frac{2I_a R_s}{V_c(1+\beta)} \sin \phi_s + \tan \theta \left[\frac{2I_a R_s}{V_c(1+\beta)} \cos \phi_s + 1 \right] \quad (9)$$

where I_a is the average beam current, R_s is the shunt impedance of the cavity, β is the coupling factor of the cavity and θ is the tuning angle offset when the beam current is zero. The offset is usually set to a negative value to reduce the Robinson instability. Notably in following discussion, the tuning angle is supposed to be tuned to minimize the reflected rf power.

Beam-Induced Voltage and Generator Voltage

The simulation assumes that the initial beam-induced voltage is induced by the beam bunch which is synchronous with the oscillating rf field. The bunch, compared to the rf wavelength, is considered to be zero-dimensional. Based on both assumptions, the initial beam-induced voltage can be expressed as [5],

$$\vec{V}_{b0} = -\frac{2I_a R_s}{1+\beta} \cos(\psi) \exp(i\psi) \quad (10)$$

From the tuning angle expressed in (9), the initial beam-induced voltage in (10) and the phasor diagram shown in Fig.1, the initial generator voltage can be obtained:

$$\vec{V}_{g0} = \vec{V}_c - \vec{V}_{b0} \quad (11)$$

As we start to simulate the synchrotron motion of each beam bunch with (5) and (6) from a small initial phase deviation, the initial beam-induced voltage, expressed in (10),

begins to decay with time and to be superimposed by the induced voltage of the bunches passed and passing through the cavity. The beam-induced voltage seen by a bunch passing through the cavity can be obtained by adding up the voltages induced by the passed and the passing bunches [6]:

$$\vec{V}_b(t_m) = -\frac{\omega_c R_s}{Q_0} \left\{ \sum_{n=-\infty}^{n < m} q_n \exp[i\omega_c(t_m - t_n)] \cdot \exp\left(-\frac{t_m - t_n}{T_d}\right) \right\} - \frac{\omega_c R_s}{2Q_0} q_m \quad (12)$$

where Q_0 is the unloaded quality factor of the cavity, T_d is the field decay time constant, and is equal to

$$T_d = 2 \frac{Q_L}{\omega_c} \quad (13)$$

Notably according to the fundamental theorem of beam loading [7], only half of the induced voltage acts back on the beam bunch itself, so the last term of (12) contains a factor 1/2.

Here we express the generator voltage as a regular sinusoid signal which has noise sidebands:

$$\vec{V}_g(t_m) = |\vec{V}_{g0}| [1 + \delta_A \cos(\omega_a t_m)] \cdot \exp\{i[(\omega_{rf} t_m) + \delta_p \cos(\omega_p t_m) + \phi_g]\} \quad (14)$$

where ω_a and ω_p are the amplitude and phase modulation frequency respectively, δ_A and δ_p are the magnitudes of the amplitude and phase modulations respectively.

The time period between two near bunches is too short for the feedback circuit to respond for correcting the cavity voltage, so (14) assumes that the variation of the beam-induced voltage during the synchrotron motion can not affect the generator voltage via the feedback circuit. Therefore, the generator voltage in (14) is independent of the beam-induced voltage.

LIMITATION OF STORED BEAM CURRENT

From (5) and (6), we can obtain the synchrotron motion of each beam bunch turn-by-turn. The effect of the beam loading and the phase noise on beam motion acts through the beam-induced voltage in (12) and the generator voltage in (14).

If the beam current is below the maximum limitation, the phase and energy deviations of the beam bunch will be bounded within a limited area as in the simulation of motion, as shown in Fig. (2.a). In contrast, if the beam current is above the limitation, as in Fig. (2.b), both deviations move away from the synchronous point until the beam bunch is lost.

From the calculation shown in Fig. (3), we can find that for a constant cavity voltage, the maximum stored beam

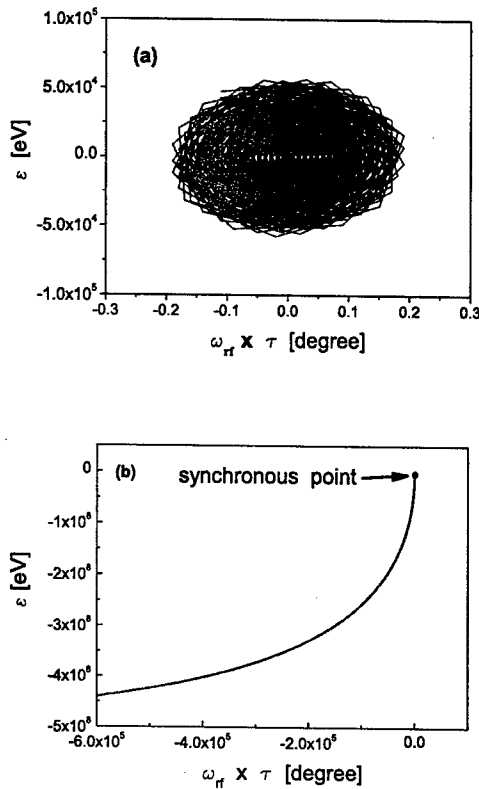


Figure 2: Simulated beam motion described by phase and energy deviations as beam current is (a) under or (b) above the maximum limite

current can be reduced by an increase in the phase noise level of a generator rf signal. The reduction is obvious, particularly when the cavity voltage is high. The theoretical maximum stored beam current,

$$I_{max} = \frac{\sin \Phi_s}{\sin 2(\Phi_s - \theta)} \cdot \frac{V_c}{R_s} (1 + \beta) \quad (15)$$

is compared with the numerically simulated value, shown in figure (3), in the case of no noise. The comparison indicates that the maximum limitation predicted from the theoretical computation is always higher than that from the numerically simulated value. A possible reason for the discrepancy is the phases of the passing beam bunch and its induced voltage. The last term in (12) has only a real part, which means that the passing beam bunch and its induced voltage are always in phase regardless of the time deviation of the beam bunch in the motion simulation. The beam bunch will transfer more energy to its induced voltage if we consider this in-phase phenomenon in the energy transfer process. More energy transferred from beam bunches means greater beam loading. This in-phase relationship is not considered in the theoretical computation.

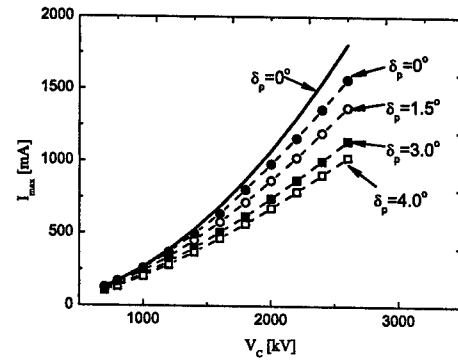


Figure 3: simulated maximum stored beam current versus gap voltage for the generator rf signal with different phase noise levels (symbol-dashed curves), and that predicted from (15) in the case of no noise (solid curve). The parameters used are $E_s = 1.5 \text{ GeV}$, $\omega_{rf} = 500 \text{ MHz}$, $Q_0 = 1.0 \times 10^9$, $R_s/Q_0 = 44.5$, $\beta = 4000$, $T_0 = 200/\omega_{rf}$, $\alpha = 6.768 \times 10^{-3}$, $\omega_p = 720 \text{ Hz}$, $U_{rad}(\epsilon = 0) = 168 \text{ keV}$, $P_{loss} \equiv V^2/2R_s$.

CONCLUSIONS

This paper has presented a way to calculate the maximum stored beam current, including the influence of the phase noise of the generator rf signal, and has demonstrated that the maximum stored beam current can be reduced by an increase in the phase noise level. The calculation in Fig. (3) suggests that our rf generator must maintain its phase noise of 720 Hz below 3 degrees, if we plan to store the beam current up to 500 mA at the cavity voltage of 1600 kV.

That (15) does not consider the in-phase of the passing beam bunch and its induced voltage may cause the predicted maximum beam current higher than that predicted by the numerical simulation.

REFERENCES

- [1] Ch. Wang, "A decade of operational experience with the 500 MHz rf system at SRRS and the next era of superconducting rf," EPAC2002, Paris, June 2002, PP 769-771.
- [2] K.W. Robinson, "Stability of beams in Radio frequency systems," CEAL-1010. Feb. 1964.
- [3] S.Y. Lee, *Accelerator Physics*. Singapore: World Scientific publishing Co. Pte. Ltd. 1999, pp 221-222.
- [4] Mathew Sands, "Beam Cavity Interaction-II, Maximum Beam current", RT/3-76, Laboratoire de 1 Accelérateur Linéaire, Orsay 1976, Eq.(18).
- [5] P.B. Wilson, "Beam loading in high-energy storage ring", SLAC-PUB-1456, June 1974.
- [6] H. Padamsee, J. Knobloch and T. Hays, *RF superconductivity for accelerators*. New York: Wiley series in beam physics and accelerator technology, 1998, p.335.
- [7] P.B. Wilson, 9th Int. Conf. On High Energy Acc. (1974) p.57.

SPACE-CHARGE-DOMINATED PHENOMENA IN THE UMER SOURCE REGION*

I. Haber, S. Bernal, R. A. Kishek, P. G. O'Shea, B. Quinn, M. Reiser, Y. Zou
University of Maryland, College Park, MD 20742-3511 USA

A. Friedman^{1,2}, D. P. Grote^{1,2}, J. -L. Vay^{1,3}
¹HIF-VNL; ²LLNL, Livermore, CA; ³LBNL Berkeley, CA

Abstract

For space-charge-dominated beams, details of the beam distribution as it emerges from the source region can strongly influence beam evolution well downstream. This occurs because collective space-charge modes, excited as the beam is born, can remain undamped for many focusing periods. Nevertheless, traditional studies of the source region in particle beam systems have emphasized the behavior of averaged beam characteristics such as total current, rms beam size, or emittance, rather than the details of the full beam distribution function that are necessary to predict the excitation of any collective space-charge modes. Simulations of the source region using the particle-in-cell WARP code along with detailed comparisons to experimental measurements of the beam in the University of Maryland Electron Ring (UMER) are therefore being employed to understand the complex behavior that has been observed in the source region, including a surprising sensitivity of the beam evolution to details of the transverse velocity distribution.

INTRODUCTION

In many accelerator systems space-charge-dominated behavior, including the excitation of space-charge collective modes, can be significant in the source region even when the downstream characteristics are not space-charge-dominated. Furthermore, if the transverse evolution is viewed in a frame moving with the beam, it can be seen that these modes can remain relevant as the beam is accelerated, and it has been observed in simulations that they remain undamped for many focusing periods. Traditional studies of the source region in particle beam systems have emphasized the behavior of averaged beam characteristics, such as total current, rms beam size, or emittance, rather than the details of the full beam distribution function that are necessary to predict the excitation of collective modes. Because of the comprehensive diagnostics on the University of Maryland Electron Ring (UMER) experiment, extensive detailed observations of the evolution of these modes have been possible.

A primary tool for understanding the detailed evolution of a space-charge-dominated beam in the source region in general, and the UMER ring in particular, has been the use of simulation in concert with detailed experimental measurement. However, "first principle" simulations beginning from the emitter surface have often displayed sensitivity to details in the numerical model that appear to

reflect similar sensitivities to details of the actual gun geometry. Since accurate prediction of the beam evolution in the UMER ring requires comparable accuracy in specifying the injected beam distribution, a systematic program is underway to compare particle-in-cell WARP code simulations of the beam with experimental measurement in the source region. The sections below will describe some of the complexity in beam evolution that has been observed as a result, including the surprising sensitivity of the evolution of the beam profile to details of the transverse velocity distribution

THE UMER SOURCE

The UMER source is a variable perveance Pierce geometry electron gun modified by a gridded cathode used to control the current pulse, and an anode grid used to impose a uniform potential at the anode plane. The perveance can be varied by changing the cathode-to-anode spacing. The gun is normally operated to provide approximately 118 mA in the anode-to-cathode region, so that the nominal ring injection current of 100 mA current is obtained after interception by the anode grid.

Unlike the anode grid, which appears to have a relatively minor influence on the exiting distribution function, the cathode grid that is used to rapidly switch the current has been observed to strongly influence the beam characteristics. While study of the effect of the cathode grid in a triode has an extensive history, the work that was done has generally concentrated on the parameter regime appropriate to using the beam as an amplifier tube rather than the as a beam switch. In addition, emphasis in early studies was primarily on the behavior of the total current at the anode, and not on the detailed characterization of the beam distribution function important to UMER ring operation. As will be discussed below, examination of the beam distribution that emerges from the cathode has uncovered a degree of complexity not previously appreciated.

EXPERIMENTAL DIAGNOSTICS

The primary experimental diagnostic tool employed here is a phosphor screen mounted on a plunger-like apparatus so the screen can be translated along the injector transport line to measure the variation of the beam profile as it propagates. An additional feature of the apparatus used to measure characteristics of the beam distribution function is the capability to insert various beam masks approximately 1 cm downstream from the

anode grid location. One of these masks is a "pepper pot" consisting of an array of small holes that can be used to sample the beam velocity distribution.

A less straightforward use of the masks is to split the beam into five beamlets in a pattern resembling the five face of a die. It has previously been determined that the beam evolution after traversing such a mask depends on the temperature of the beam emerging from the mask. This evolution therefore provides an independent estimate of the beam emittance without relying on the fairly complex slit-slit measurements that were not operational in the early stages of the beam experiments. Two additional measurements which were performed that provide a consistency check on the beam characteristics are the degradation of the shadow of the anode grid with distance and the evolution of the Bernal[1] ring patterns as a single beam propagates.

GUN SIMULATION

Many of the observed UMER gun characteristics described below appear to result from details of the beam evolution in the region between the cathode and the cathode grid. However, with available computer resources it is difficult to resolve the grid region in the same calculation that represents the entire gun structure. This is because the grid wire diameter is 0.0254 mm and the distance from cathode to grid, as well as is the spacing between grid wires, are 0.15 mm. These distance are much less than the 3 mm cathode radius and the approximately 25 mm separation between the cathode grid and the anode grid. In addition, unlike the gun structure itself, the grid geometry is not axisymmetric, so that modeling the grid structure requires full three-dimensional simulation.

The first WARP code simulations were therefore performed assuming axisymmetry. Sensitivities to various experimental and simulation parameters were examined, and comparisons between available measurements and the code predictions were used to infer information about the beam distribution function. More recently high-resolution simulations have been undertaken to examine the influence of the cathode grid on the gun characteristics. These simulations examine only a small transverse central portion of the beam.

COMPARISON TO EXPERIMENT

The set of gun operating parameters used for the UMER injector were determined by experimentally adjusting the anode-cathode spacing and the grid voltage to achieve an output current of 100 mA, which is the value desired for nominal ring operation. The cathode-to-grid potential during the pulse is set by varying a bias voltage added to the voltage pulse applied across the cathode-to-grid gap, so that the negative bias voltage prevents any current from being drawn except during the approximately 100 ns beam pulse. It should be noted that the actual pulse voltage applied to the cathode-to-grid gap

is difficult to measure in the existing apparatus and is difficult to calculate because the loading on the pulser as a function of bias voltage is not known. Many of the beam characteristics must therefore be inferred from a combination of simulation and other measurements of the beam characteristics.

Simulation of the gun geometry that assumes self-consistent Child-Langmuir emission from a cathode placed at the location of the cathode grid predicts a current of 125mA. This is close to the actually obtained current of approximately 118mA, as inferred from the 100mA measured downstream of the approximately 87% transparent anode grid. The prediction by this simulation of a current approximating actual observation appears to be evidence that the current enhancement expected from injection into gun with a substantial initial energy approximately counteracts the 66% transparency of the cathode grid.

The Child-Langmuir simulation predicts a hollowed beam with current density at the outer edge of approximately 1.5 times the central value. Because of the difficulty of realistically modeling the emission characteristic of the gridded cathode, a simulation assuming transversely uniform emission from the grid surface was used to test the importance of self-consistently modeling the transverse variation of the emission. The transverse characteristics at the anode plane were very close to those obtained from the self-consistent calculation. On the other hand, sensitivity of the profile to total current was observed, since a reduction of the injected current by approximately 10% resulted in a substantial modification of the profile at the anode plane.

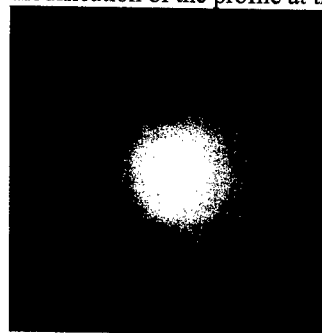


Fig. 1. Phosphor screen image of the beam approximately 60 mm from the anode plane. A weak shadow of the anode grid is observable.

Direct measurements of the beam profile were obtained using a phosphor screen placed approximately 60 mm downstream of the anode grid. Figure 1 is a typical phosphor screen image of the beam. Note that the grid bias voltage is set at a low enough value that the cathode-to-grid potential is into the "saturation" region where the current is weakly dependent on this voltage, in contrast to the rapid variation in current with bias voltage observed in the region near current cut-off by the bias potential.

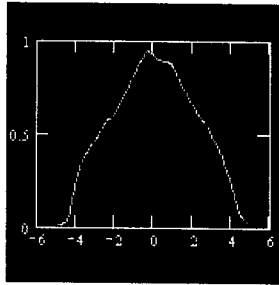


Fig. 2. Current density plotted along a diameter of phosphor image in Fig. 1.

Figure 2 is a plot the light intensity along a diameter cut through the plot in Fig. 1. Unlike the hollowed simulation profiles, it is peaked at the beam center. Furthermore, only when the transverse temperature of the injected distribution is increased by something between a factor of 25 and 100 times the intrinsic value of the 0.1 eV emitter temperature, does the simulated profile begin to match the peaked behavior observed. Such a large assumed transverse injection temperature is inconsistent with the five-beamlet patterns observed[2] as well as to the measured degradation of the anode mask shadow.



Fig. 3. Phosphor screen image downstream of the pepper pot showing a hollowed velocity space distribution.

The discrepancy between the observed radial variation in current density and that predicted by simulation can be resolved by injecting an initial hollowed transverse velocity distribution such as shown in Fig. 3, which is the image formed by passing the beam through the pepper pot mask. The peaked distribution shown in Fig. 2, including the small depression in beam density at the beam center that can be seen in Fig. 1, are then observed in the simulation. The total transverse energy contained in the hollowed velocity distribution is also consistent with the beam downstream evolution of the beam passed through the five-beamlet mask. The hollowed initial velocity distribution also improves agreement between simulation and phosphor screen measurements of the evolution of the shadow of the anode grid, as well as the downstream evolution of the full beam density patterns.

Because of the uniformity across the beam profile of the hollowed distribution observed in Fig. 3, it is likely that this hollowing is caused by the influence of the cathode grid. Since the grid physics is seen to be

important to prediction of the downstream evolution, simulations are underway to examine the influence of the cathode grid on the gun beam characteristics for parameters in the range of interest to the UMER gun.

In order to perform simulations with resolution sufficient to examine the physics of the very small region between the cathode and the cathode grid, only a small transverse region, corresponding to a single cell of the cathode grid is examined. The transverse boundary conditions are assumed periodic, and the computational requirements are further reduced by assuming fourfold transverse symmetry. A typical simulation of such a long thin region, as might be appropriate to examining the beam behavior near the gun center employs 16 by 16 transverse grid cells and 1024 cells in the longitudinal direction.

Analytic calculations of the cathode grid region [3] predict that under typical operating conditions a virtual cathode will form downstream of the cathode grid at a distance somewhat greater than the cathode-to-grid spacing. It is therefore necessary to perform the simulation for a distance much greater than the 0.15 mm cathode-to-grid spacing. It was, in fact, observed that simulating a longitudinal region much shorter than the full gun length would result in sufficient ambiguity in specifying the downstream potential that it was simpler to include the entire 25 mm region.

The simulations were performed with a potential between cathode grid in the range around 20V independently measured by the energy analyzer.[4] Preliminary observation of the parametric behavior, which includes complex current rise waveforms, including virtual cathode oscillations for sufficiently large cathode-to-grid potential is too complex to describe here, however many of the features observed experimentally are reproduced in the model.

CONCLUSIONS

A combination of simulation and measurement has revealed considerable complexity in the behavior of the UMER gridded gun. Furthermore, understanding this complexity appears to be important to predicting the injected beam characteristics for injection into the UMER ring. A continuing program that combines simulation and measurement is therefore underway to develop the level of predicative capability desired for interpretation of the detailed beam characteristics in the ring.

REFERENCES

- [1] S. Bernal, R. A. Kishek, M. Reiser and I. Haber, Phys. Rev. Lett. Vol. 82, (May, 1999).
- [2] I. Haber, S. Bernal, C. M. Celata, A. Friedman, D. P. Grote, R. A. Kishek, B. Quinn, P. G. O'Shea, M. Reiser, submitted to Nucl. Instr & Methods A
- [3] Y. Zou, H. Li, M. Reiser, P. G. O'Shea, submitted to Nucl. Instr & Methods A
- [4] Y. Cui, Y. Zou, A. Valfells, I. Haber, R. A. Kishek, M. Reiser, P. G. O'Shea, Proc of 2003 PAC.

LARGE DIFFUSE HALOS IN TIME-DEPENDENT SPACE-CHARGE POTENTIALS WITH COLORED NOISE*

C. L. Bohn[#], Northern Illinois University, DeKalb, IL 60115 and Fermilab, Batavia, IL 60510, USA
I. V. Sideris, Northern Illinois University, DeKalb, IL 60115, USA

Abstract

We explore the potential impact of colored noise on space-charge-induced halo formation. By coupling particle orbits to parametric resonance, colored noise due to space-charge fluctuations and/or imperfections in the beamline can eject particles to much larger amplitudes than would be inferred from parametric resonance alone.

INTRODUCTION

The pursuit of high-current light-ion accelerators such as are needed to drive high-intensity spallation neutron sources has brought the realization that, albeit necessary, the ability to control root-mean-square beam properties is not sufficient. Perhaps the most prominent example concerns beam halos, *i.e.*, particles that reach large orbital amplitudes due to time dependence in the space-charge potential. The concern is that impingement of beam particles on the beamline could generate radioactivation that would preclude routine, hands-on maintenance. Just a tiny impingement (~ 1 nA/m/GeV) is troublesome. For a 100 mA, 1 GeV light-ion beam, this criterion translates to just 1 in 10^8 particles lost per meter [1].

Early efforts to identify the fundamental mechanisms of halo formation centered on the use of a 'particle-core' model [2,3]. The basic recognition was that if a uniform-density core is made to pulsate, particles that initially lie outside the core and that resonate with its pulsations can reach large amplitudes and form a 'halo'. This led to the identification of parametric resonance as the essential mechanism of halo formation.

The key feature of parametric resonance in the context of the particle-core model is a hard upper bound to the amplitude that a halo particle can reach [4]. The particle's orbital frequency is a function of its amplitude. At large amplitude the particle falls out of resonance with the core, thereby preventing the amplitude from growing further. This lends hope to the possibility of computing an aperture requirement for beamline components; smaller aperture requirements are preferred in that, for example, they mitigate concerns about shunt impedance in the accelerating cavities.

An important question is whether there is any physics not included in the particle-core model that could significantly influence the maximum particle amplitude. Herein we show that the answer is yes; *the presence of colored noise can potentially boost a statistically rare particle to much larger amplitudes by continually kicking it back into phase with the core oscillation.*

METHODOLOGY

Following the ground-breaking work that introduced the particle-core model [2,3], we consider radial orbits governed by the dimensionless equation of motion

$$\ddot{x} + x[(1-x^2)\Theta(|x|-1) + 2(M-1)\cos\omega t\Theta(1-|x|)] = 0, \quad (1)$$

where x is normalized to the matched core radius a , time is multiplied by the external focusing frequency Ω , ω is the core-oscillation frequency, $M=a(0)/a$ is the mismatch, *i.e.*, the ratio of initial-to-matched core radii, and $\Theta(u)$ is the Heaviside step function. The first and second terms in square brackets govern the motion of the particle when it is outside and inside the core, respectively.

We add to Eq. (1) fluctuations in the form of Gaussian colored noise such that $\omega \rightarrow \omega(t) = \omega_0 + \delta\omega(t)$, with

$$\langle \delta\omega(t) \rangle = 0 \text{ and } \langle \delta\omega(t)\delta\omega(t_1) \rangle \propto \exp(-|t-t_1|/\tau_c), \quad (2)$$

in which τ_c is the autocorrelation time. Upon generating a colored-noise signal, we calculate $\langle |\delta\omega| \rangle$ which becomes a measure of the noise strength. Colored noise is a realistic phenomenon that will arise self-consistently from charge-density variations and from irregularities in the beamline; in the former case the autocorrelation time could be short, say of the order of a plasma period, and in the latter case it could be long, say several betatron (orbital) periods [5].

We fix the mismatch parameter at $M=1.5$, and the initial conditions of the orbit at $x(0)=1.2$, $\dot{x}(0)=0$. The orbit is computed from Eq. (1) first without, then with, the noise of Eq. (2) using a variable-time-step integrator. For zero colored noise, the maximum amplitude $|x_{\max}|$ depends on the core-oscillation frequency ω_0 ; Fig. 1 shows this dependence. The particle can reach relatively large amplitudes for a wide range of frequencies ω_0 . We present results for $\omega_0=3.53$ because the associated power spectra of the orbits are especially clear; different choices of ω_0 do not change the essential findings.

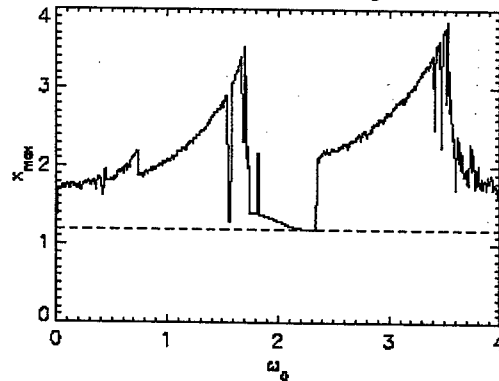


Fig. 1. Maximum orbital amplitude $|x_{\max}|$ vs. frequency ω_0 with zero noise. The horizontal line is at $x(0)=1.2$.

*Work supported by DoEd Grant G1A62056.

[#]clbohn@fnal.gov

We consider the colored noise to be a random process, which means each individual particle will see a different manifestation of the noise. Thus, in an 'axisymmetric' model, such as that of Eq. (1), each particle initially occupying a thin annulus centered at radius $x(0)$ will experience noise that differs from that seen by each of the other particles. Accordingly, we adopted a 'survey strategy'. For the given initial conditions and a specific choice of noise parameters, we sequentially computed 10,000 orbits, each experiencing its own random manifestation of the colored noise, and we catalogued the maximum amplitudes of these orbits. As is shown and explained below, the colored noise will keep a statistically rare particle in phase with the core oscillation such that this particle reaches much larger amplitudes than without colored noise. Moreover, as time progresses, its maximum amplitude will grow indefinitely. We shall demonstrate that there is in principle no hard upper bound to the halo amplitude in the presence of colored noise.

RESULTS

Without Colored Noise

The case of zero noise constitutes the baseline against which to assess the influence of colored noise. The corresponding orbit $x(t)$ and its power spectrum appear in Fig. 2. The orbit, which we integrated to high precision, reaches a maximum radius $x_{max}=3.9$; it goes no further regardless how long the orbit is integrated. Parametric resonance indeed establishes a hard upper bound to the orbital amplitude in the absence of noise.

The power spectrum, however, is complicated, and stays complicated. As Fig. 2 suggests, there is interplay between harmonics of the external frequency Ω and core-oscillation frequency ω_0 (since time is measured in the unit of the inverse external frequency, $\Omega = 1$ here). The interplay results in the formation of not only several prominent spectral lines, but also continua, signifying that the orbit is chaotic.

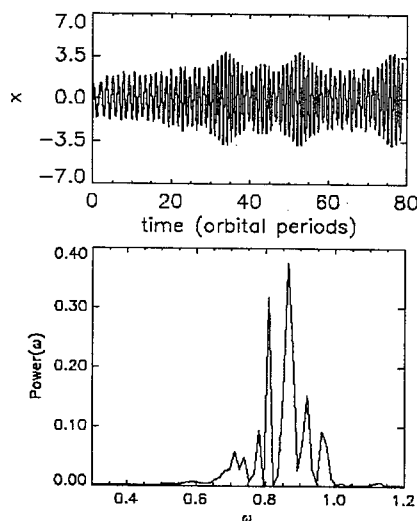


Fig. 2. (top) Orbit without noise; (bottom) power spectrum (Fourier transform of the orbit).

With Colored Noise

The influence of noise on halo formation depends on its strength $\langle |\delta\omega| \rangle$ and its autocorrelation time. For two choices of autocorrelation time, $t_c = 1\tau$ and $t_c = 12\tau$, with τ denoting the representative orbital period of the particle, we investigated a broad range of strengths, specifically $10^{-5} \leq \langle |\delta\omega| \rangle \leq 1$, with the goal of ascertaining to what extent the results may be regarded as generic. All of the results presented herein derive from sequential computations of 10,000 orbits with noise randomly generated for each orbit separately.

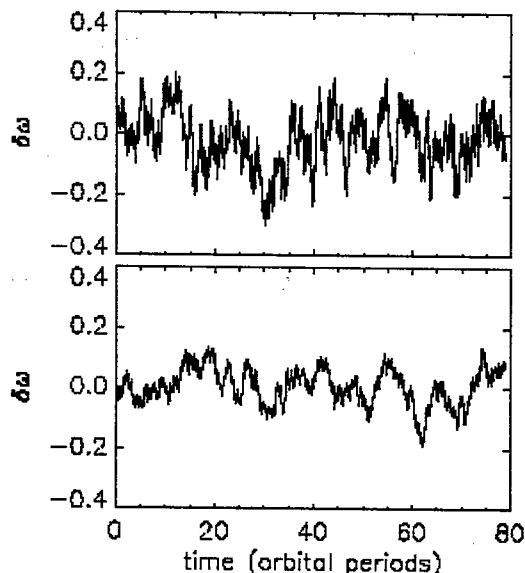


Fig. 3. Example manifestations of colored noise along an orbit for $\langle |\delta\omega| \rangle = 0.09$ and $t_c = 1.5\tau$ (top), 12τ (bottom).

Manifestations of colored noise that a particle might see are illustrated in Fig. 3, which is provided as an aid toward conceptualizing the physical meaning of the noise parameters. Shown there are manifestations of noise for $t_c = 1.5\tau$ and 12τ for a fixed range $\langle |\delta\omega| \rangle = 0.09$.

Next, we consider the one particle out of the sample of 10,000 that reaches to the largest amplitude $|x_{max}|$ during the integration time of 80τ , which is representative of the length of a 1 GeV proton linac. Results for fixed $t_c = 12\tau$ and $\langle |\delta\omega| \rangle = 0.09$ are provided in Fig. 4, which shows this special orbit. Figure 4 also shows the distribution of $|x_{max}|$ for the entire 10,000-orbit sample. Notice that for this case $|x_{max}|$ averaged over the sample is less than 3.9, the value pertaining to the bare parametric resonance. This means the noise kicks 'typical' particles out of phase with the core oscillation while it simultaneously kicks rare particles into phase. Also plotted is $|x_{max}|$ versus $\langle |\delta\omega| \rangle$, from which one sees that even much weaker noise can suffice to eject rare particles to larger amplitudes relative to the parametric resonance alone. This is due to the chaoticity of the orbits in that their inherent continuum of frequencies enhances the coupling of the noise to the orbit even when $\langle |\delta\omega| \rangle$ is small. The power spectrum of these rare orbits eventually becomes sharply peaked at the

particle's orbital frequency. Interestingly, we find for $t_c = 1\tau$ that there is no substantial difference in the results; they are qualitatively the same.

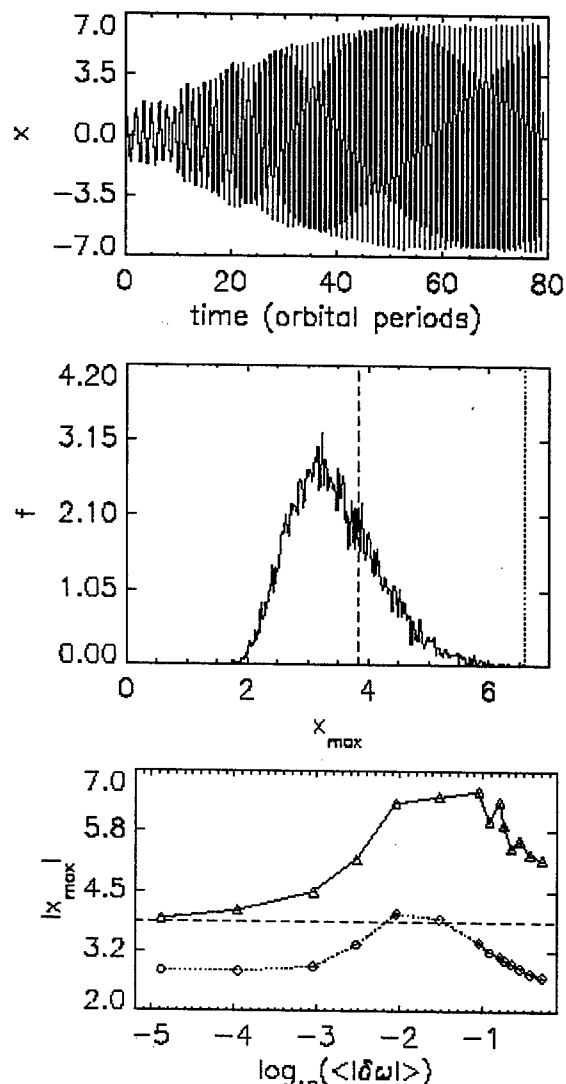


Fig. 4. (top) Orbit of the one particle reaching the largest $|x_{\max}|$ given noise with $\langle|\delta\omega|\rangle=0.09$, $t_c = 12\tau$. (middle) Distribution of $|x_{\max}|$ of all 10,000 particles in the sample; the lines show largest $|x_{\max}|$ with no noise (dashed) and with this noise (dotted). (bottom) Largest $|x_{\max}|$ reached by any particle vs. $\langle|\delta\omega|\rangle$ with $t_c = 12\tau$ (triangles); mean $|x_{\max}|$ of the 10,000-particle sample (diamonds).

If the integration time is extended indefinitely, then there are orbits that continue to grow to seemingly unlimited amplitude. The orbit of one such particle appears in Fig. 5. This long-time orbit exemplifies that *there is in principle no upper bound to the halo amplitude in the presence of colored noise.*

DISCUSSION

The influence of colored noise on particle orbits, and in particular its role in generating large diffuse halos in time-dependent potentials, appears to be generic, i.e., not

restricted to the simple particle-core model of Eq. (1). For example, we did the same numerical experiments using a model of a beam bunch in which the unperturbed potential is a spherically symmetric configuration in thermal equilibrium [6] and the perturbation has prolate spheroidal symmetry with a single driving frequency. In this potential the vast majority of the orbits quickly became chaotic and coupled to the perturbation. The net effect as concerns halo production was qualitatively the same as described above, though the dynamical details were richer, reflecting the more complicated potential. The collection of findings suggests that formation of large diffuse halos is not particularly sensitive to details in either the governing potential or the noise.

It remains, of course, to explore the extent to which this phenomenology applies in a real machine. Doing so will involve simulations of beams in real beamlines. One possibly fruitful approach is to extract the smooth, time-dependent potential from the simulations and then pursue a statistical analysis in parallel to what we have done here. Alternatively, the colored noise may be built into the simulation itself. A realistic manifestation of the colored noise would need to reflect the machine design, i.e., by incorporating imperfections in the fields and hardware alignment, and/or by including details of the evolving space-charge potential such as a sufficiently detailed mode spectrum. Of course, as the beam is accelerated and becomes relativistic, space charge will become decreasingly important, and growth of the halo will thereby be mitigated.

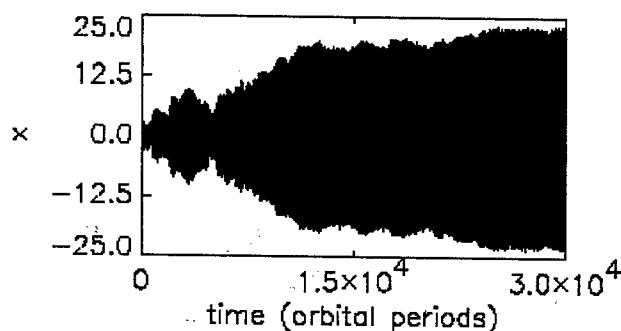


Fig. 5. Long-time evolution of a large-amplitude orbit given noise with $\langle|\delta\omega|\rangle=0.09$, $t_c = 12\tau$.

REFERENCES

- [1] R. A. Jameson, *Fus. Eng. Design* **32 - 33**, 149 (1996).
- [2] J.S. O'Connell, T.P. Wangler, R.S. Mills, K.R. Crandell, *Proc. PAC93*, 3657 (1993).
- [3] R. Gluckstern, *Phys. Rev. Lett.* **73**, 1247 (1994).
- [4] T.P. Wangler, K.R. Crandall, R. Ryne, T.S. Wang, *Phys. Rev. ST-AB* **1**, 084201 (1998).
- [5] We have confirmed that also adding colored noise to the external focusing frequency does not change our results, so we choose to present the simplest model.
- [6] C.L. Bohn, I.V. Sideris, *Phys. Rev. ST Accel. Beams* **6**, 034203 (2003).

MAIN REGULARITIES OF PARTICLE REDISTRIBUTION IN SPACE CHARGE DOMINATED BEAM TRANSPORT AND BUNCHING

Boris Bondarev, Alexander Durkin

Moscow Radiotechnical Institute

113519, Russia, Moscow, Warshawskoe shosse 132, lidos@aha.ru

INTRODUCTION

Space charge effects are one of the main factors that can cause beam losses. When focusing and phasing forces are comparable to Coulomb ones summary beam field contains considerable much nonlinear component of proper field that leads to effective phase volume growth. During high-current beam motion a low-density extent beam part (so called "halo") appears. Two problems must be solved in order beam losses not exceed the given value:

1) input beam parameters must be chosen in such manner that beam size in the channel was minimal;

2) channel bore radius must be chosen with reserves to ensure full transmission of halo particles.

The main features of charge redistribution in high-current beam during bunching, accelerating and transporting must be revealed in order to solve above-mentioned problems. Experience leads us to use results obtained by many scientists. Below we summarize results of the work on this problem that were got by the authors.

BEAM CHARGE REDISTRIBUTION DURING HIGH-CURRENT BEAM TRANSPORTING

The main feature of the process is formation of core (area near axis with high charge density) and halo (peripheral domain with low charge density) with intense particle interchange between these two domains. It is common knowledge that core-halo formation takes place during high-current beam transporting. Nevertheless nobody gives strong mathematical definitions for core or halo sizes. We suppose to consider plot of Coulomb force versus radius and Coulomb force maximum E_r (see Fig. 1) can be defined as core boundary.

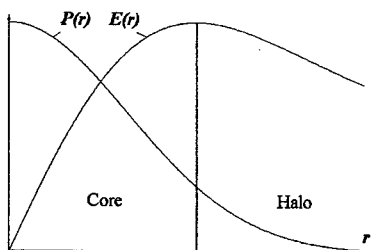


Fig.1.

Beam core definition.

$P(r)$ – beam density, $E(r)$ Coulomb force

If we use quadruple focusing, core has form of ellipse in (x,y) -plane. Ellipse semi-axes are defined as distances between origin and points of maximum for Coulomb force projections on each of transverse axes E_x, E_y .

The studies were conducted in order to establish that charge distribution inside core becomes uniform during the motion. For this fact confirmation charge distribution inside core was replaced by uniform one after some time. Result comparison shows that charge distributions core sizes, *rms*-emittances and so on have only a weak difference.

The conducted studies show that in steady state beam can be nominated as matched one if core oscillation frequency coincides with focusing period frequency. In such cases RMS and full emittances growth will be minimal.

Among infinity number of phase space distributions that give uniform projections on (x,y) -plane there is well-known KV-distribution. So we can use well-known analytical results for obtaining of matched beam initial parameters.

The main laws of mismatched SCD-beam charge redistribution during its transport can be stated on the base of performed investigations:

1) The main futures of charge redistribution both for matched and mismatched SCD-beams are the same in any focusing channel. A beam core-halo formation with active particle interchange is viewed as well as establishment of core uniform charge distribution.

The vast majorities of core particles are ex-halo ones or will be halo ones in coming.

2) SCD beam core oscillations are damping and halo oscillation amplitudes are growth.

3) limited oscillation amplitudes are observed for considered parameters (*rms*-emittance, core radius, beam boundary radius and so on).

4) As expected the relative *rms*-emittance growth was increased with mismatching increasing.

5) The relative *rms*-emittance growth was practically the same for Gauss and uniform input distributions.

6) In the case of mismatching more than 1.5 *rms*-emittance growth is bigger and faster for beam which core radius exceeds matching value in comparison with beam which core radius is the same times smaller.

7) In a transition regime *rms*-emittance growth takes place in points where core radius growth.

8) Comparison of results with uniform and Gauss input charge distributions in beam transporting in periodical channel shows that in the both cases final core

mismatching is much smaller than input one. In the versions with Gauss input distributions only one frequency coincide with frequency of external focusing force stays clearly defined. It can be said that core automatically matched with periodical focusing channel. In the versions with uniform input distributions core oscillation frequency does not coincide with external force frequency. It can be concluded that when potential energy of input (Gauss) beam noticeable bigger than the same one of final beam charge redistribution leads to beam matching and accompanies by noticeable kinetic energy growth. In another case potential energies of output and input beams slightly differs and full matching does takes place but core oscillations in this case also noticeable reduced.

9) *rms*-emittance growth with the same input mismatching is less if input beam density is bigger.

10) Transition process study shows that a mechanism of core density equalization takes place during core oscillations. This process is connected with oscillations of charge amount inside core and is in anti-phase with core oscillations. When core size is reduced number of particles that lost core exceeds number of particles that enters core, i.e. core charge reduced and core density aligning. The opposite process takes place when core size increased. Kinematics effect explains the process partly: halo particles catch up with beam boundary when core is reduced and halo particles move towards beam boundary when core is increased.

Conclusion can be made that the state with matched core is energetically best suited to beam transporting in the focusing channel (it is a state with beam minimal internal energy).

THE BUNCHING PROCESS MAIN FEATURES FOR HIGH-CURRENT BEAM

In the previous part SCD-beam transporting was considered when beam density in equal manner was changed in each transverse cross-section and it had remained intact in longitudinal direction. In present division we try to elucidate the main features of SCD-beam bunching. As usual we will consider the simplest model of the process. In the frame of the model we proposed that particle transverse motion is absent and we observe only Coulomb force reaction on bunching in longitudinal direction. In considered case charge distribution in transverse directions will be the same for all beam cross-sections (we suppose that it is uniform) and charge density modulation take place only in longitudinal direction. Synchronous phase -90° corresponds to beam center that moves with constant velocity. Because initial beam is continuous and non-modulated so modulation always will be periodical.

In given case we have a possibility to deduce and analyze several relations for proper field of beam flow with periodic charge distribution.

Let us consider axial symmetrical charge flow along Z-axis with velocity v and radius R_b inside cylindrical channel with radius R_a . Let us consider that beam current $I(r, z)$ periodically varies along Z with period L .

If density $\rho(r, z)$ is periodical one it can be presented as Fourier series

$$\rho(r, z) = \sum_{k=0}^{\infty} \rho_k \cos \omega k z$$

Then we obtain potential U in the form of series

$$U(r, z) = -\sum \rho_k \left(\frac{1}{\omega k R_b} \right)^2 \left(1 - \frac{I_0(\omega k R_a)}{I_0(\omega k R_b)} \cdot C(\omega k R_a, \omega k R_b) \right) \cos \omega k z,$$

where $\omega = 2\pi/L$, function $C(x, y)$ defines as

$$C(x, y) = \frac{I_1(y)K_0(x) + K_1(y)I_0(x)}{I_1(y)K_0(y) + K_1(y)I_0(y)} = y \cdot (I_1(y)K_0(x) + K_1(y)I_0(x))$$

Correspondingly

$$E_z = -\frac{\partial U}{\partial z} = \frac{2I}{\epsilon_0 v L} \sum_{k=0}^{\infty} q_k F_k(\omega k r, \omega k R_a, \omega k R_b) \sin \omega k z,$$

where q_k are decomposition harmonics for $\frac{\partial}{\partial z} \rho(r, z)$.

Let us consider the axis field and suppose that $x = \omega k R_a$, $\gamma = R_b / R_a$. Then

$$F_k(0, x, \gamma) = F_{k0}(x, \gamma) = \frac{1}{(\gamma x)^2} \cdot \left(1 - \frac{C(x, \gamma)}{I_0(x)} \right)$$

Herewith

$$\lim_{x \rightarrow \infty} F_{k0}(x, \gamma) = \frac{1}{4} (1 - \ln \gamma^2) = D_0,$$

Below $F_{k0}(x, \gamma)$ -functions will be called as harmonic factors.

Let us consider ion bunching in the field of traveling wave with amplitude E_m and frequency ω . We suppose that particles are moving along channel axis and particle velocities are non-relativistic

$$m \frac{dV}{dt} = -eE_m \sin(kz - \omega t) + eE_c$$

where $\omega = \frac{2\pi c}{\lambda}$, $k = \frac{2\pi}{L}$, $L = \beta_c \lambda$, $\beta_c = v_c / c$, E_c is Coulomb field intensity. Jumping from variable t to variable $v_s t = z_s$ we obtain

$$m \frac{dV}{dz_s} = -\frac{eE_m}{v_s} \sin(k(z - z_s)) + eE_c$$

Choosing $\Psi = k(z - z_s)$ as non-independent variable

and jumping to bunching phase $\tau = \Omega z_s$, $\Omega^2 = \frac{keE_m}{mv_s^2}$

we obtain the main equation of bunching

$$\frac{d^2 \Psi}{d\tau^2} = -\sin \Psi + \frac{2ID_0}{\epsilon_0 c \beta_s^2 \lambda E_m} \sum_{n=0}^{\infty} q_n \frac{F_{n0}(x, \gamma)}{D_0} \sin n\Psi$$

Bunching equation general view shows that with given relations between geometrical sizes R_d/L and R_b/R_d bunching process is defined by unique parameter

$$\alpha = 2ID_0 / \varepsilon_0 c \beta^2 E_m \lambda$$

It means that in the frame of the same geometrical relations bunching process does not changed if $I/(WE_m\lambda)$ -value is kept, where W is particle energy. If maximal allowable value of α_{max} , is defined then ultimate beam current is directly proportional to particle energy and external RF field amplitude and is in inverse proportion to operating frequency f

Remark 1. It can be shown oneself that ultimate permissible beam current will be growth with increasing of R_d/L because all Coulomb field harmonics are reduced. However external field intensity at the axis E_m also reduced as $1/I_0(2\pi R_d/L)$, that gives more upstanding effect towards reducing the beam current limit.

Remark 2. The above research differs slowly from universally accepted. It is usual to suppose that ratio of phase force to Coulomb one does not depend on beam energy and Coulomb force reduced with beam energy growth due geometrical factor R_d/L reducing. In the present work coulomb parameter α reduces with opposite proportionality when beam energy growth though Coulomb field harmonics increase when L growth. We can calculate that first harmonic coefficients are growth only 2-2.5 times during unlimited growth of L . As beam mean velocity β increases effect of α reducing is prevailed. If in the relation for Coulomb field intensity factor $1/(2\pi R_b/L)^2$ will be included into α , an universally accepted result will be achieved.

It is evident that particles positioned near bunching center during their moving towards center form potential barrier for following particles. During the first quarter of period the barrier is growth and each next particle feels bigger resistance from Coulomb field then previous one. So during the first quarter of period a hard core was generated in the central domain.

Starting from some value of α particle energy loss needed the barrier get over is comparable with particle kinetic energy derivable from external RF field. Starting from this value of α beam can be nominated as SCD-beam.

With further α increase additional pulse derived by particle after exit from core leads to essential increase of its phase oscillation amplitude. Starting from some value of α fraction of particles that overflow period boundary (which amplitude exceeds π) sharply increased. We will call such particles as "lost" ones.

Increasing α more and more we will come to situation when particles are fully decelerated by core field and they cannot pass throughout bunch center. However bunching will be possible in this case also. It is necessary to match rate of potential barrier growth with particle

kinetic energy. The rate of external RF field growth can be used as matching instrument.

Computer investigation results give a possibility to make several conclusions about SCD-beam bunching:

1. During bunching in the field with increment amplitude beam can be considered as SCD-beam for $\alpha > 0.07$. For $\alpha > 1.2$ beam losses are appeared and beam bunching without losses is impossible in principle.

2. For effective SCD-beam bunching it is principal to have beginning part with increment field and with length 1 - 1.5 periods of phase oscillations.

3. With beam current growth ($\alpha > 0.8$) Coulomb field harmonic spectrum defined by the first harmonic that essentially exceeds the other ones.

Specification and main result of analysis for charge redistribution inside SCD-beam are contained in reports [1-6].

REFERENCES

- [1] B.I.Bondarev, A.P.Durkin, R.A.Jameson, Space Charge-Dominated Beam Bunching, *Proceedings of the Second International Conference on "Accelerator-Driven Technologies and Applications"*, June 3-7, 1996, Kalmar, Sweden, Uppsala University, pp.1071-1077.
- [2] B.I.Bondarev, A.P.Durkin, B.P.Murin, Intense Ion Beam Transport and Space Charge Redistribution, *Proceedings of the XVIII International Linear Accelerator Conference*, 26-30 August 1996, Geneva, Switzerland, CERN 96-07, v.1, pp.210-212.
- [3] A.P.Durkin, B.I.Bondarev, B.P.Murin. Study of Space Charge-Dominated Beam Bunching, *Proceedings of the XVIII International Linear Accelerator Conference*, 26-30 August 1996, Geneva, Switzerland, CERN 96-07, v.1, pp.208-209.
- [4] Bondarev B.I., Durkin A.P., Murin B.P., Jameson R.A. Emittance Grows and Halo Formation in Charge-Dominated Beams. *International Conference on Accelerator-Driven Transmutation Technologies and Applications*, July 25-29 1994, MGM Hotel, Las Vegas, Nevada, AIP Conference Proceedings 346, p.377-382.
- [5] Bondarev B.I., Durkin A.P. SCD-Beam Main Regularities in Beginning Part of High-Current Proton Linac, *Computational Accelerator Physics Conference, AIP Conference Proceedings 391*, pp.173-178, (Virginia, USA, September 1996).
- [6] Bondarev B.I., Durkin A.P., Korenev I.L., Shumakov I.V., Vinogradov S.V. The Main Regularities Of Core-Halo Formation In Space Charge-Dominated Ion Beam, *Proceedings of the 1999 Particle Accelerator Conference*, New York City, March 29th - April 2nd, 1999, pp.1764-1766.

ANGULAR MOMENTUM MEASUREMENT OF THE FNPL ELECTRON BEAM

Y. Sun*, K.-J. Kim†, University of Chicago, Chicago, IL 60637, USA

P. Piot, K. Desler‡, D. Edwards, H. Edwards, M. Huening, J. Santucci, FNAL, Batavia, IL 60510, USA

N. Barov, D. Mihalcea, Northern Illinois University, DeKalb, IL 60115, USA

R. Tikhoplav, University of Rochester, Rochester, NY 14627, USA

S. Lidia, LBNL, Berkeley, CA 94720, USA

S.-H. Wang, Indiana University, IN 47405, USA

Abstract

In the flat beam experiment at Fermilab/NICADD Photoinjector Laboratory(FNPL)[1], it is essential to have a non-vanishing longitudinal magnetic field on the photocathode. The canonical angular momentum of the electron beam generated by this magnetic field is an important parameter in understanding the round to flat beam transformation. In this paper, we report our measurements of the canonical angular momentum, which is directly related to the skew diagonal elements of the beam matrix before beam is made flat. The measurements of the other elements of the beam matrix are also reported.

THEORY

The round-to-flat beam transformation was proposed by Brinkmann, Derbenev, and K. Flöttmann[2] based on the idea of flat-to-round transformation by Derbenev[3]. An extensive theoretical treatment of the transformation was given by Burov, Nagaitsev and Derbenev[4]. Here we summarize the main results obtained in these papers by using an approach based on the rotational symmetry and two associated invariants of the beam matrix[5].

Rotationally Invariant Beam Matrix

The coordinates of a particle in transverse phase space can be denoted by two vectors:

$$X \equiv \begin{bmatrix} x \\ x' \end{bmatrix} \text{ and } Y \equiv \begin{bmatrix} y \\ y' \end{bmatrix}. \quad (1)$$

The corresponding 4×4 beam matrix is then defined by

$$\Sigma = \begin{bmatrix} \langle XX^T \rangle & \langle XY^T \rangle \\ \langle YX^T \rangle & \langle YY^T \rangle \end{bmatrix}. \quad (2)$$

Let R be the 4×4 rotation matrix :

$$R = \begin{bmatrix} I \cdot \cos \theta & I \cdot \sin \theta \\ -I \cdot \sin \theta & I \cdot \cos \theta \end{bmatrix}, \quad (3)$$

with I standing for the 2×2 identity matrix. The beam matrix is rotationally invariant if:

$$\Sigma = R \cdot \Sigma \cdot R^{-1}. \quad (4)$$

* yinesun@uchicago.edu

† Also APS, ANL, Argonne, IL 60439, USA

‡ Also DESY, 22603 Hamburg, Germany

The most general form of a rotationally invariant beam matrix is given by:

$$\Sigma = M_d \cdot \Sigma_0 \cdot M_d^T, \text{ with } \Sigma_0 = \begin{bmatrix} \varepsilon_x T & \mathcal{L} J \\ -\mathcal{L} J & \varepsilon_x T \end{bmatrix}. \quad (5)$$

where M_d is the 4×4 transfer matrix of a drift space, T and J are 2×2 matrices defined in Eq. 6, and the quantities ε_x , β and \mathcal{L} are constants.

$$T \equiv \begin{bmatrix} \beta & 0 \\ 0 & \frac{1}{\beta} \end{bmatrix}, \text{ and } J \equiv \begin{bmatrix} 0 & 1 \\ -1 & 0 \end{bmatrix}. \quad (6)$$

If the beam matrix is diagonalized through some symplectic transformations, it takes the following form in the diagonalizing base:

$$\Sigma_{diag} = \begin{bmatrix} (\varepsilon_x - \mathcal{L})T_- & 0 \\ 0 & (\varepsilon_x + \mathcal{L})T_+ \end{bmatrix}, \quad (7)$$

where T_- and T_+ are diagonal matrices similar to T in Eq. 6. The beam matrix in Eq. 7 represents a flat beam which is completely decoupled in the two transverse planes with (orthogonal) transverse emittances given by:

$$\varepsilon_1 = \varepsilon_x - \mathcal{L}; \quad \varepsilon_2 = \varepsilon_x + \mathcal{L}. \quad (8)$$

The fact that rotationally invariant beam matrix has eigenvalues ε_1 and ε_2 is a general consequence of the two associated invariants: $\text{Det}(\Sigma)$ and $\text{Tr}(\Sigma J_4 \Sigma J_4)$, where J_4 is the four dimensional unit symplectic matrix.

In the flat beam experiment at FNAL, the photocathode is immersed in a solenoidal magnetic field. Consider an electron at the photocathode surface with coordinates given by Eq. 1. The electron coordinates downstream of the solenoidal field are then given by:

$$X = \begin{bmatrix} x \\ x' - \kappa y \end{bmatrix}, \quad Y = \begin{bmatrix} y \\ y' + \kappa x \end{bmatrix}, \quad (9)$$

where $\kappa = \frac{eB_z}{2P}$, B_z is the longitudinal magnetic field on the photocathode, P is the particle momentum. From Eq. 9 and assuming there is no correlated moment at the photocathode surface (i.e. $\langle xx' \rangle = \langle xy \rangle = \dots = 0$), the beam matrix downstream of the solenoid takes the form:

$$\Sigma_{sol} = \begin{bmatrix} A & \kappa \sigma^2 J \\ -\kappa \sigma^2 J & A \end{bmatrix}, \quad (10)$$

where $\sigma^2 = \langle x^2 \rangle = \langle y^2 \rangle$, $\sigma'^2 = \langle x'^2 \rangle = \langle y'^2 \rangle$, and

$$A \equiv \begin{bmatrix} \sigma^2 & 0 \\ 0 & \kappa^2 \sigma^2 + \sigma'^2 \end{bmatrix}. \quad (11)$$

The beam matrix Eq. 10 is of the form Σ_0 in Eq. 5, with the following identifications:

$$\mathcal{L} = \kappa \sigma^2, \quad \varepsilon_x^2 = \varepsilon_{th}^2 + \mathcal{L}^2, \quad \beta^2 = \frac{\sigma^2}{\sigma'^2 + \kappa^2 \sigma^2}. \quad (12)$$

where $\varepsilon_{th} \equiv \sigma \sigma'$ is the "thermal" emittance¹. For an angular momentum dominated beam ($\kappa \sigma \gg \sigma'$), $\beta \approx 1/\kappa$.

The beam matrix after acceleration in a rotationally symmetric structure would also be of the form given by Eq. 10, with the thermal emittance in general larger than the one on the cathode due to the space charge effect.

Conservation of Canonical Angular Momentum

The cylindrical symmetry of the system (both of the photo-emitted beam and of the externally applied fields) leads to the conservation of canonical angular momentum.

On the photocathode, the electron beam does not have any mechanical angular momentum. Thus the averaged canonical angular momentum is:

$$\langle L \rangle = e B_z \sigma^2 = 2 P \mathcal{L}. \quad (13)$$

As beam propagates outside the solenoidal field, the mechanical angular momentum equals to the canonical angular momentum.

EXPERIMENTAL MEASUREMENTS

Measurement of \mathcal{L}

Assuming a laminar beam (i.e., neglecting the terms x' and y' in Eq. 9), the canonical angular momentum of an electron can be inferred from the observation of the beam transverse density at several locations. Indeed a measurement of the beam radii r_1 and r_2 at two locations along the beam line z_1 and z_2 , together with a measurement of the shearing angle θ of the beam as it drifts between the two considered locations provides the canonical angular momentum via:

$$L = P \frac{r_1 r_2 \sin \theta}{D}, \quad (14)$$

wherein $D = z_2 - z_1$. The method is illustrated in Fig. 1.

To measure the shearing angle we intercept the beam at location z_1 with a multi-slit mask consisting of horizontal slit apertures. The thereby generated "beamlets" are then observed at the location z_2 . All the beam transverse density measurements are performed using optical transition radiation (OTR) screens. An example of such measurement is illustrated in Fig. 2.

¹Our definition of thermal emittance includes both the thermal emittance induced by the photo-emission process together with other thermalizing effects that occurs later in the transport line.

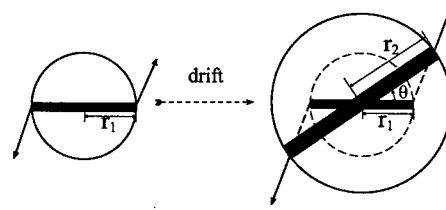


Figure 1: Beam with canonical angular momentum-induced shearing while drifting. The dark narrow rectangular can be a slit inserted into the beam line in order to measure the shearing angle.

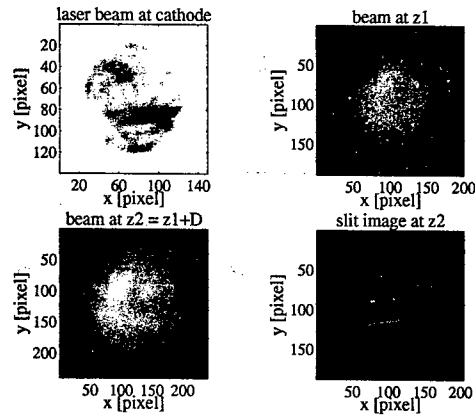


Figure 2: One set of images needed to calculate canonical angular momentum.

By observing the slit images on different OTR screens downstream, the evolution of L along the beam line can be measured. Such a measurement is plotted in Fig. 3. Within experimental error, the canonical angular momentum of an electron calculated from different screens agrees with each other. On another hand, one can measure the photocathode drive-laser beam size on the photocathode surface, this together with the knowledge of B_z , provide a measurement

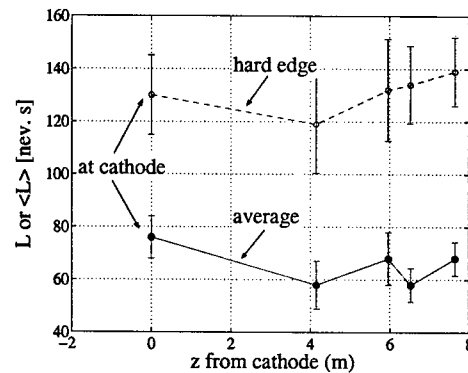


Figure 3: The canonical angular momentum of an electron: on the hard-edge of beam spot and averaged over the whole beam.

of L at $z = 0$, which is in good agreement with the canonical angular momentum computed along the beamline. In Fig. 3 we have also plotted the averaged canonical angular momentum computed from $\langle L \rangle = P\sigma_1\sigma_2 \sin \theta/D$.

Figure 3 demonstrates the canonical angular momentum is conserved for each electron in a laminar beam, thus $\langle L \rangle$ for the beam is also conserved. Given the beam energy ~ 15 MeV in the experiment, we have $\mathcal{L} = \frac{\langle L \rangle}{2P} \approx 0.62 \pm 0.04$ mm mrad.

In a separate experiment (with a different laser spot radius), we have explored the dependence of canonical angular momentum on B_z . Our results, see Fig. 4, confirm the expected linear dependence. A linear regression of the data gives $d\langle L \rangle/dB_z = 0.08 \pm 0.02$ neV·s/G, to be compared to $d\langle L \rangle/dB_z = 0.08 \pm 0.03$ neV·s/G as evaluated from Eq. 13.

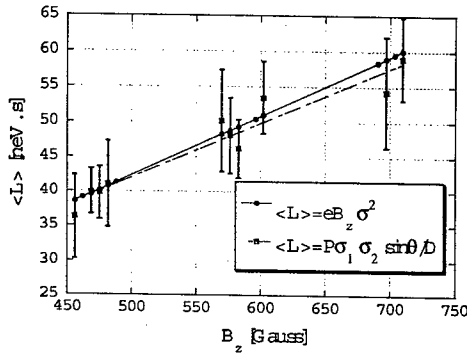


Figure 4: The averaged canonical angular momentum of an electron with different magnetic fields on the cathode.

Measurement of ε_x and β

From Eq. 5, the RMS beam envelope at location z in a drift space is given by:

$$\sigma(z) = \sqrt{\varepsilon_x \beta \left[1 + \left(\frac{z - z_0}{\beta} \right)^2 \right]}. \quad (15)$$

where z_0 is the beam waist location.

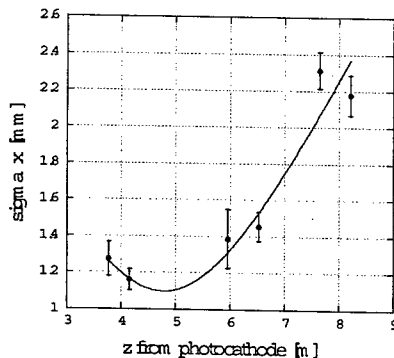


Figure 5: RMS beam envelope in a drift space.

We can measure the RMS beam size $\sigma(z)$ at different locations z in a drift space, and fit the thereby measured beam envelope to Eq. 15. From Fig. 5, we have at the beam waist location ($z_0 = 4.79 \pm 0.20$ m), $\varepsilon_x = 0.67 \pm 0.04$ mm mrad, $\beta = 1.79 \pm 0.28$ m.

Prediction of Best Possible Flat Beam Emittances

Now that \mathcal{L} , ε_x and β are measured, we can predict the best possible flat beam emittances one could get downstream of the round-to-flat beam transformer. From Eq. 8 we find: $\varepsilon_1 = 0.05 \pm 0.04$ mm mrad; $\varepsilon_2 = 1.29 \pm 0.04$ mm mrad. Notice that for ε_1 , the error is comparable to the emittance itself.

Measurement of Flat Beam Emittances

The cylindrically symmetric beam discussed above is made flat through a skew quadrupole channel. The experimental setup is detailed in Ref. [1, 6, 7]. Our experimental conditions here differ from those in previous references, where the emphasis was put on achieving the best transverse emittance ratio. In the present experiment, however, no attempt was made to optimize the beam emittance by adjusting B_z or σ . These latter values were kept identical to those used for the measurement of L reported in Fig. 3. Note also the bunch charge (~ 1 nC) was twice as large as in Ref. [1]. The results for the *normalized* emittances are: $\varepsilon_1^n = 1.5 \pm 0.3$ mm mrad; $\varepsilon_2^n = 59 \pm 9$ mm mrad. The aforementioned errors only include the statistical errors arising from the calculation of the RMS beam or beamlet sizes.

CONCLUSIONS

The measurement of rotationally invariant beam matrix upstream of the skew quadrupole channel gives the upper limit of the achievable flat beam emittances. This allows one to do parametric studies to prepare a beam with potential to be manipulated into a flat beam with high emittance ratio, without having to actually go through the skew quadrupole channel.

REFERENCES

- [1] D. Edwards *et al.*, in *Proceedings of the XX International Linac Conference*, 122 - 124 (2000).
- [2] R. Brinkmann *et al.*, *Phys. Rev. ST Accel. Beams* 4, 053501 (2001).
- [3] Ya. Derbenev, report UM-HE-98-04, University of Michigan (1998).
- [4] A. Burov *et al.*, *Phys. Rev. E* 66, 016503 (2002).
- [5] K.-J. Kim, "Notes on angular momentum dominated beam", to be published.
- [6] D. Edwards *et al.*, in *Proceedings of IEEE Particle Accelerator Conference 2001*, 73 - 75 (2001).
- [7] E. Thrane *et al.*, "Photoinjector Production of a Flat Electron Beam", *Proceedings of XXI International Linac Conference*, (2002).

MULTIPLE BEAM INTERACTION STUDIES IN HEAVY ION FUSION

D. R. Welch, D. V. Rose, Mission Research Corp., Albuquerque, NM,
S. S. Yu, Lawrence Berkeley National Laboratory, Berkeley, CA,
C. L. Olson, Sandia National Laboratories, Albuquerque, NM

Abstract

Beam combining and compression in a neutralized plasma is simulated with a three-dimensional particle-in-cell code. The sensitivity of these processes to perveance and plasma conditions is studied.

INTRODUCTION

Heavy ion fusion (HIF) requires the acceleration, transport, and focusing of many individual ion beams. Drift compression and beam combining prior to focusing results in 10--100 individual ion beams with 10^{-5} -- 10^{-4} C/m line-charge densities. A focusing force is applied to the individual ion beams outside of the chamber. For neutralized-ballistic transport (NBT), these beams enter the chamber with a large radius (relative to the target spot size) and must overlap inside the chamber at small radius (~ 3 mm) prior to striking the target. In this paper, we consider the combining of many beams in the presence of a neutralizing plasma over roughly 10 m just upstream of a preformed discharge channel specifically for pinched transport modes. Shown schematically in Fig. 1, the individual ion beams combine, drift, and possibly compress before being captured in an adiabatic discharge lens still outside of the chamber and injected at small radius into the chamber. Recent work for assisted-pinched transport (APT) has shown that a discharge channel can efficiently capture and transport a very high current ion beam to a 5-mm spot on the fusion target[1]. The target is actually heated on two sides requiring two beam-guiding discharge channels and two return-current channels to maintain symmetry. In the APT scenario, possible deleterious effects of beam overlap and combining may include instabilities and increased emittance growth. Implicit particle-in-cell (PIC) simulations indicate there are perveance limits above which beam filamentation can prevent good coupling to the discharge channel. The goal of these calculations is to elucidate the basic physics issues of plasma-neutralized beam combining.

The calculations are performed with the 3-D parallel LSP[2] PIC code to address the issues concerning high plasma densities. In particular, an energy-conserving implicit algorithm is used for dense plasma where the details of electron plasma oscillations can be ignored. We initially treat both plasma electron macroparticles with fluid equations, and ion species are treated with kinetic equations. This algorithm has also been employed in modeling heavy ion beam propagation in the 1--100-mtorr pressure regime.[3,4] In order to initialize a reasonable beam-plasma equilibrium, a neutral beam is injected at the $z = 0$ plane that was stripped to charge state +1 in the first 10 cm of transport in the plasma. Previous attempts to

initialize an ion beam resulted in large electromagnetic fields in the sheath at the injection plane that increased beam emittance.

SIMULATIONS OF BEAM TRANSPORT

We first examine the 2-D propagation of already combined beams in a 10-m length conical drift section filled with a plasma of density roughly that of the focused beam. The outer wall radius is set at 1.5 times that of the ballistically focusing beam and provides a space-charge-limited supply of electrons. The goal is to strike the adiabatic channel with a spot radius of 1 cm. The channel radius decreases from 2 cm to 0.5 cm, compressing the beam to a 5-mm radius. We examine several beam ions: Ne^+ , K^+ , Xe^+ , and Pb^+ . The total energy on target is fixed at 6 MJ (3 MJ on each side). The beam velocity is also held constant with a tilt from 0.125--0.165 c . Over the 14.5-m drift length to the target, the 100-ns beam pulse will compress to 8 ns. This configuration tests the concept of plasma-neutralized drift and compression and is not an actual design. The large velocity tilt obviously requires an achromatic final focusing lens. The combined beam is injected with uniform density as an annulus with 5-cm inner radius and 10-cm outer radius. For a Ne^+ beam, the ion average energy is 210 MeV with a 150-kA initial current. As the ion mass increases, its energy increases and the beam current decreases to maintain the total 3-MJ energy. The density of the Ne^+ beam is shown in Fig. 2. By 240 ns (the beam pulse has already compressed by a factor of 2), the ion density is compressed preferentially at the beam edges. The ensemble emittance grows from an initial 50π -mm-mrad to 75π -mm-mrad resulting in a fairly large spot at 10 m. The bulk of the beam actually strikes the outer wall of the tube near $z = 10$ m. The radial filamentation is a result of imperfect current neutralization at the beam edges with roughly 10--20 kA of net current (beam + plasma current). These currents are in rough agreement with analytic models of beam plasma neutralization that predict a 97% current neutralization for this case.[5] The propagation gets progressively better with increasing ion mass. The Xe^+ beam focused to the required 1-cm radius with only 30% emittance growth over the initial 13π -mm-mrad. This beam and the Pb^+ beam produced a sufficiently small beam spot to couple to the discharge channel and, ultimately, the target. We also tried applying a 1--4 kG solenoidal magnetic field to reduce the growth of the filamentation for the Ne^+ beam. Preliminary calculations

show the transport was more stable with a 4-kG applied field.

Simulations of actual 3-D beam combining were performed in Cartesian coordinates with $\frac{1}{4}$ the actual volume. Symmetry boundary conditions were employed at the $x = 0$ and $y = 0$ planes to speed the calculations but maintain beam-beam interaction. As before, the beams are transported in a 10-m conical tube. We injected two uniform-density beams of 3-cm radius centered at $x = 6.50$ cm and $y = 3.75$ cm, and $x = 3.75$ cm and $y = 6.50$ cm. Their edges just touch at the injection plane. This configuration of two beams per quadrant represents eight beams in the full volume, however, only interactions between nearest neighbors is modeled. As observed in the 2-D simulations, the lighter beam ions exhibit filamentary structure. Shown

in Fig. 3, the Ne^+ beams quickly develop five distinct filaments. The combined beam emittance grows to $86 \pi\text{-mm-mrad}$ —15% larger than the 2-D case. The most interesting case was the K^+ beam which exhibited both 2-D and 3-D structures. The individual beams develop an annular structure before combining and eventually filamenting in azimuth. The filamentation then saturates at a modest level and relaxes to a more 2-D state. As before, the Xe^+ beams combined quiescently with an adequate 1-cm spot at 10 m with a combined beam emittance of $15 \pi\text{-mm-mrad}$. The final emittance of the combined Xe^+ beams grew to $15 \pi\text{-mm-mrad}$ only 10% more than the sum of the injected emittances of the eight individual beams.

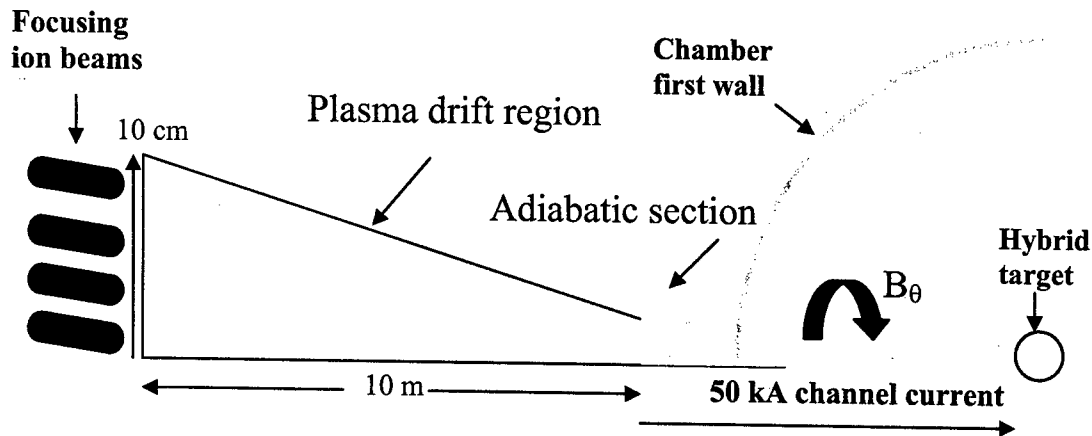


Figure 1. A schematic of the final focus and transport of ion beams for assisted-pinch transport is shown. The focusing beams enter at the left.

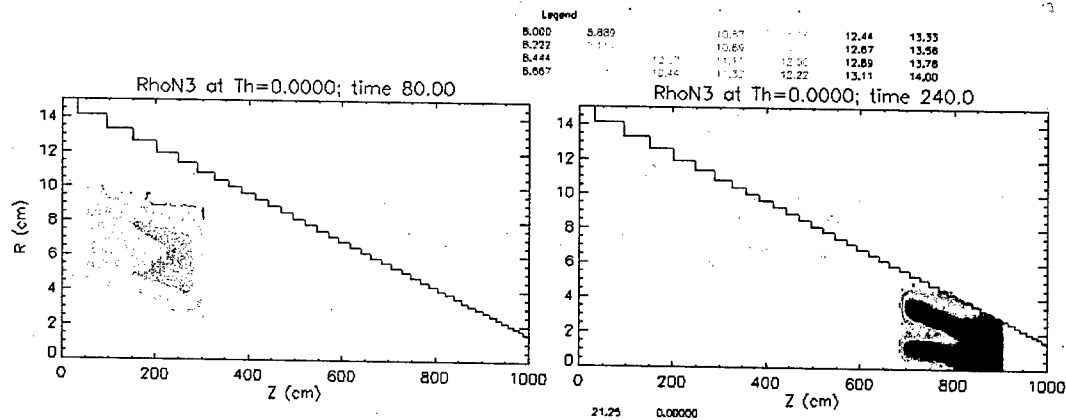


Figure 2. The Ne^+ beam density (log with legend above) after 80-ns (left) and 240-ns (right) transport in $4 \times 10^{14}\text{-cm}^{-3}$ plasma is shown. Note the radial filamentation.

SUMMARY

We have simulated the drift, combining, and compression of HIF beams in two and three dimensions with the LSP code. The implicit simulations were designed to model the drift section prior to beam capture in the adiabatic discharge channels envisioned for APT. Maintaining a constant ion beam energy of 3 MJ, the simulations identified the consequences of a few percent of unneutralized beam current. The 10--20 kA of net current for the Ne^+ beams was sufficient to filament and disrupt focusing to the desired 1-cm spot after 10 m drift. The Xe^+ ions exhibited much less severe behavior than the Ne^+ beams producing an adequate spot for APT with only 10% emittance growth. Using an extreme 30% beam velocity tilt, the compression of the beams from 100 ns to 8 ns on target did not appear to cause additional problems beyond the effect of increasing the combined beam current (and net current).

A sufficiently large solenoidal field has the potential to reduce magnetic pinch effects by forcing purely axial electron neutralization. The effect of a solenoidal magnetic field on the 2-D transport of the Ne^+ did reduce the instability growth in 2-D simulations. Future work must include larger (> 1 Tesla) and fields that are tailored to the beam trajectory. Simulations in the full 3-D volume are required to study the evolution of dipole instabilities.

ACKNOWLEDGEMENTS

We express our appreciation for useful discussions and support to Grant Logan, Alex Friedman, William Sharp, Christine Celata, Igor Kaganovich, and the ARIES Team. Work supported by ARIES, the Virtual National Laboratory for HIF, the Department of Energy through Princeton Plasma Physics Laboratory, and Lawrence Berkeley National Laboratory.

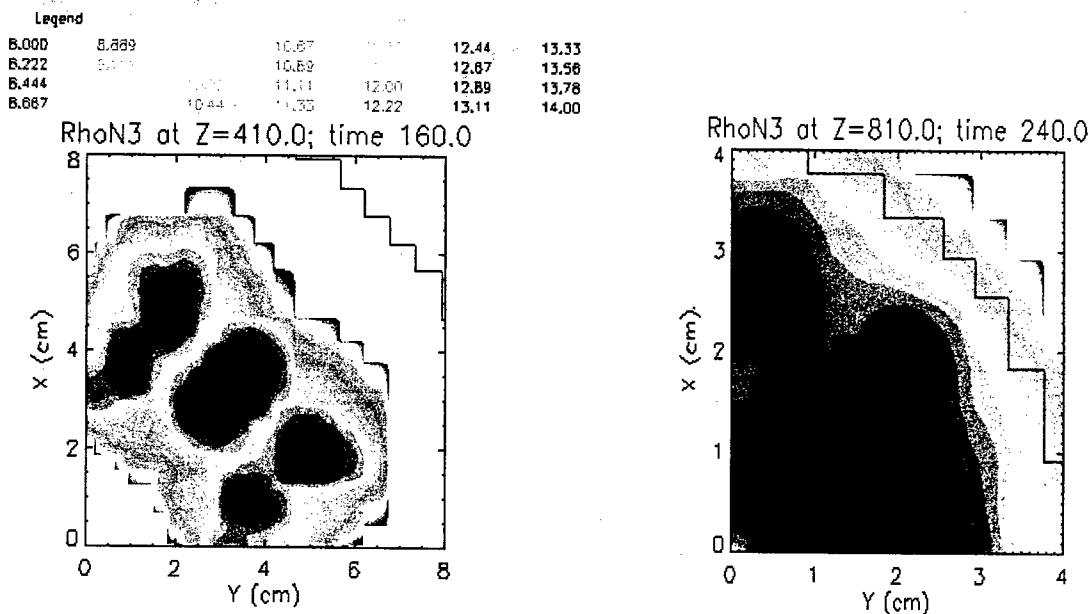


Figure 3. For the 3-D LSP simulation, the Ne^+ beam density (log with legend above) after 160-ns (left) and 240-ns (right) transport in $4 \times 10^{14}\text{-cm}^{-3}$ plasma is shown at the $z = 410\text{-cm}$ and 810-cm planes, respectively. Note the azimuthal filamentation.

REFERENCES

- [1] D.A. Callahan, M.C. Herrmann, and M. Tabak, *Laser and Particle Beams* **20**, 405-410 (2002).
- [2] LSP is a software product of Mission Research Corporation (<http://www.mrcabq.com>).
- [3] D.R. Welch and C.L. Olson, *Fusion Eng. Des.* **32--33**, 477 (1996).
- [4] D.V. Rose, P.F. Ottinger, D.R. Welch, B.V. Oliver, and C.L. Olson, *Phys. Plasmas* **6**, 4094 (1999).
- [5] D.R. Welch, D.V. Rose, B.V. Oliver, T.C. Genoni, R.E. Clark, C.L. Olson, and S.S. Yu, *Phys. Plasmas* **9**, 2344 (2002).

OBSERVATION OF COHERENT MICROWAVE TRANSITION RADIATION IN THE APS LINAC*

G. Decker, X. Sun
Argonne National Laboratory
Argonne, IL 60439, USA

Abstract

The APS injector includes a conventional S-band linear accelerator with three separate electron sources. Two electron guns are used as primary and secondary sources for injection into the APS 7-GeV storage ring, while a separate laser photocathode gun is available for free-electron laser (FEL) research. We report here the results of the dependence of 30-GHz coherent microwave transition radiation on electron bunch length. Sensitivity to pulses as short as 200 to 300 femtoseconds has been demonstrated.

BACKGROUND

As part of upgrade efforts to generate very short (< 1 ps) bunches in the APS linac to support FEL research, a bunch compressor was installed in CY2000-2001. The APS linac is used 75% of the time for routine top-up injection to the storage ring every two minutes, with the balance of 25% of the time reserved for injector studies, operator training, and FEL studies. A bunch compressor is installed in linac sector three, where the electron beam energy is approximately 150 MeV.

A diagnostic station including an infrared Michelson interferometer [1,2] is located immediately downstream of the bunch compressor. It consists of a vacuum cube with two ports in-line with the electron beam and one port devoted to an actuator with an insertable mirror inclined at a 45 degree angle. A separate port has a commercial-grade fused silica window providing the optical path to the interferometer. This interferometer is sensitive to coherent transition radiation generated by the electron beam striking the mirror.

For the duration of the summer 2002 APS operating period, a Ka-band microwave detector, shown in Figure 1, was installed in the optical path of this diagnostic station, "looking" directly into the aforementioned window. For this measurement, the waveguide H-plane was oriented vertically, and the mirror orientation was such as to deflect the radiation in the horizontal plane. Figure 2 represents a plan view of the measurement geometry.

SIMULATION RESULTS

Simulation results [3] showed the potential for the generation of electron bunches as short as 10 to 20 fs rms, provided that reasonable improvements in linac rf system

stability were made. In actual fact, recent experiments indicate that the minimum attainable bunch length using the present linac hardware is somewhere in the range of 200 to 250 fs rms using the laser photocathode gun (PC gun) [4], and 250 to 300 fs using thermionic rf gun 2.

The PC gun emits a single pulse of electrons at up to a 6-Hz duty cycle, with the temporal profile defined by the laser pulse. In contrast, rf gun 2 emits an 8-nanosecond-long train of pulses separated by 350 ps, with the pulse train duty cycle being as high as 30 Hz.

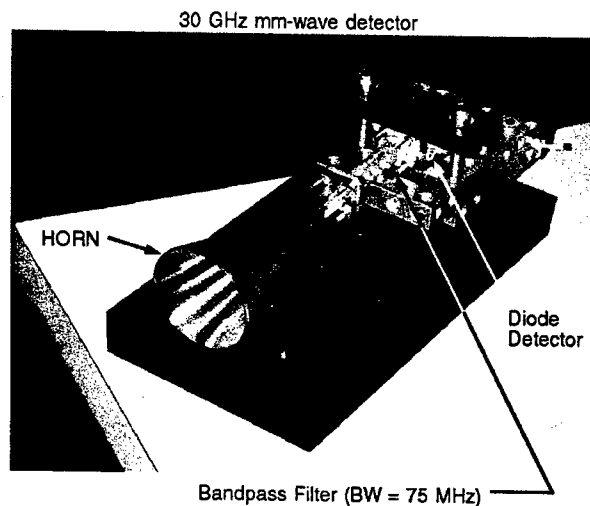


Figure 1: Microwave horn / detector assembly used to detect coherent transition radiation.

Experimental Arrangement for Detection of 30 GHz Coherent Transition Radiation (L3 CTR Diagnostic)

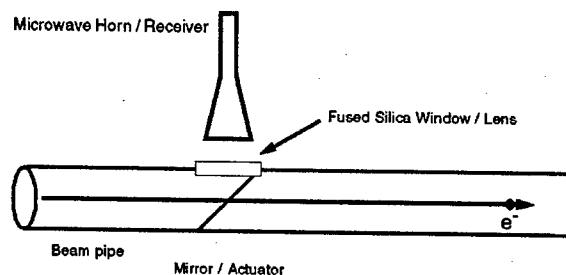


Figure 2: Microwave horn / detector arrangement used to detect coherent transition radiation. Plan view.

Shown in Figure 3 is the geometry used in a MAFIA simulation to determine the output of the microwave horn resulting from the collision of a Gaussian line charge with the mirror. Here, the beam is traveling in the positive Z

*Work supported by U.S. Department of Energy, Office of Basic Energy Sciences, under Contract No. W-31-109-ENG-38.

direction, with the Y axis corresponding to the vertical coordinate—the H-plane of the WR-28 waveguide. The circular beam openings upstream and downstream of the mirror, and the waveguide horn output were constrained by waveguide boundary conditions in the MAFIA simulation.

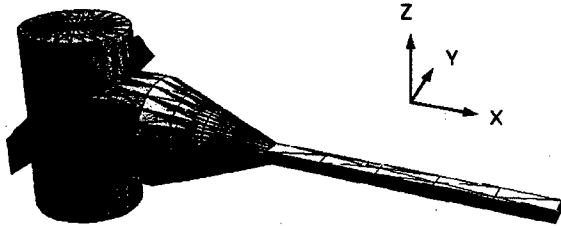


Figure 3: Microwave horn geometry used in MAFIA simulation.

Results of the simulation at the waveguide output are shown in Figure 4.

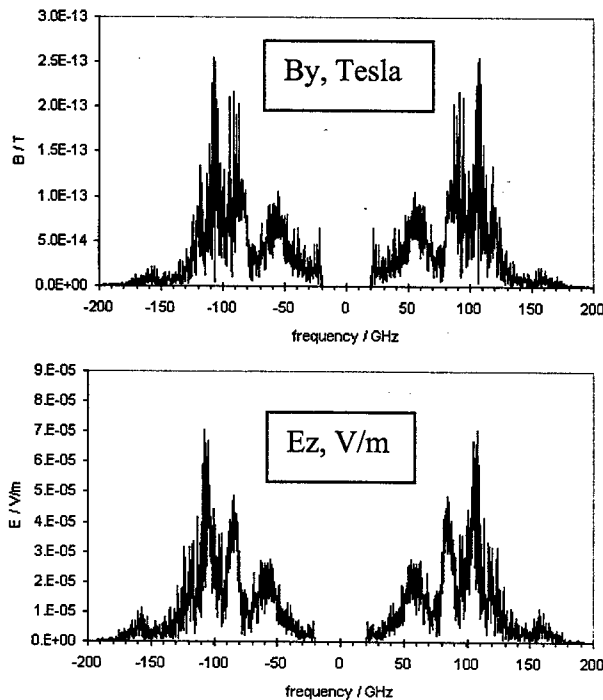


Figure 4: Magnetic and electric field vs. frequency for 0.7-ps rms, 0.75-nC line charge striking a mirror inclined at 45 degrees.

While all six components of the electromagnetic field were calculated, only those corresponding to the lowest propagating waveguide mode (WR-28) are displayed. This mode has a cutoff frequency of 21.1 GHz, consistent with the MAFIA result.

The MAFIA simulation was performed after actual experimental results using the detector of Figure 1 were in hand, so it was somewhat of a surprise to see relatively little predicted signal strength near 30 GHz, where the detector was designed to be most sensitive. The remaining electromagnetic field components had strengths

comparable to those shown in Figure 3; however, E_x shows a cutoff near 45 GHz, and E_y shows cutoff-type behavior near 70 GHz. Since the bunch spectrum extends out to a few hundred GHz, it should be no surprise that these higher-order waveguide modes are excited.

In fact, you can do a simple calculation using the method of images to convince yourself that you ought to have seen no signal in the 26.5-40 GHz waveguide passband, by symmetry. Shown in Figure 5 is a contour plot showing the scalar potential shortly after a 150-MeV point charge has passed through a mirror inclined at 45 degrees relative to the direction of motion.

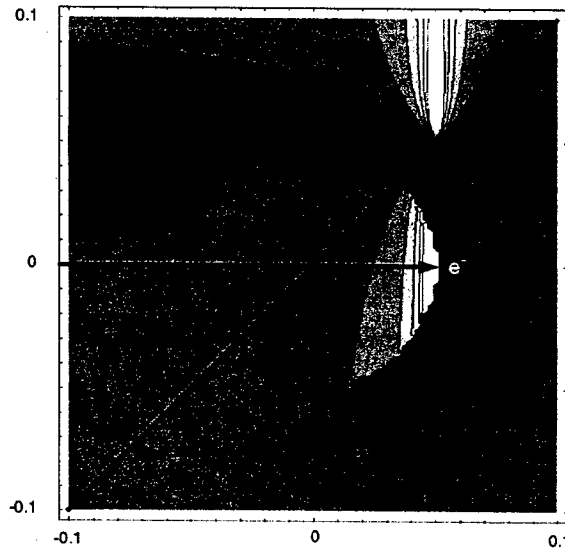


Figure 5: Scalar potential of an electron passing through an infinite mirror, indicated by the diagonal line. The arrow indicates the trajectory of the electron.

It is interesting to see the Coulomb field of the particle and its image annihilate each other at the instant that they strike the mirror. On the other side, you can see the Coulomb field reassembling itself. The sphere centered on the point of impact is the light cone. Points inside of it above the mirror think there aren't any charges anywhere, and similarly points outside the sphere below the mirror also think there are no charges anywhere, i.e., the scalar potential is zero. Given that one part of the electric field can be written as the gradient of the scalar potential, the step change in potential at the light cone will contribute a large, radially polarized electric field, consistent with known properties of transition radiation [1].

It appears that, by symmetry, we expect that the lowest TE_{10} waveguide mode would not be excited at all. Being good experimentalists, and prior to realizing this, we installed a 30-GHz microwave horn anyway, as described above, basically to "see what happens."

EXPERIMENTAL RESULTS

Lo and behold, using the device shown in Figure 1 with its passive, nonlinear detector (i.e., a diode) driving a

50-ohm line (Andrews FSJ1-50), the oscilloscope traces of Figure 6 were collected.

First Results June 2, 2002
30 GHz detector driving 50 Ohm line

Alpha Magnet Current

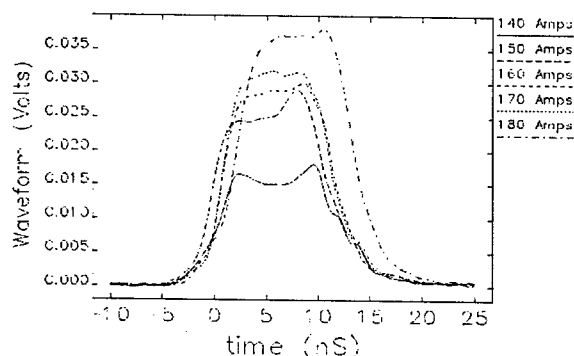
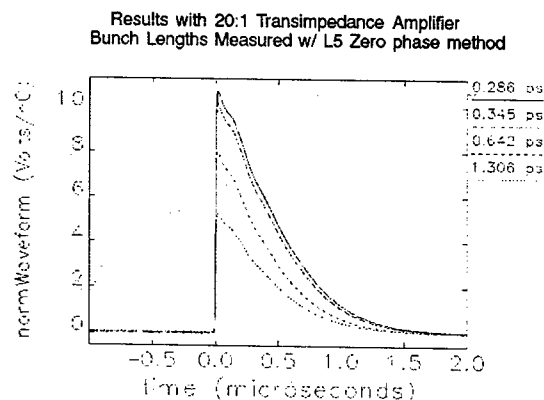


Figure 6: Microwave horn / detector signal from 8-ns, S-band-modulated, 150-MeV beam striking a mirror.

The different traces correspond to changes in the rf gun 2 alpha-magnet setting, which had the effect of changing the bunch length. An attempt was made to keep the macropulse charge constant at approximately 0.5 nC. In fact, at the extreme of short bunch length, the transmitted charge actually decreased, but this resulted in the largest signal from the detector.

Shown in Figure 7 are data collected with the addition of an in-tunnel transimpedance amplifier, since the microwave detector was never designed to drive a 50-ohm line. The tradeoff is signal strength vs. speed, as can be seen from the long signal decay time.



RF gun 2, 0.25 nC / 8 ns macropulse; Charge normalization "by eye"

Figure 7: Normalized detector signal vs. bunch length.

The data are roughly normalized by noting the beam current reading from a nearby current monitor. In this case, a careful rms bunch length measurement at each alpha-magnet setting was performed [4], as indicated in the legend.

One last data set (Figure 8) was collected prior to removal of the device, but this time a careful charge normalization was performed by collecting a nearby BPM's intensity signal using the same oscilloscope. In this case, the linac wasn't behaving itself very well, and we

were unable to get the rms bunch length much below 500 femtoseconds. The data set does fill in the gaps for longer bunch length, and shows some peculiar differences in decay time that are not well understood.

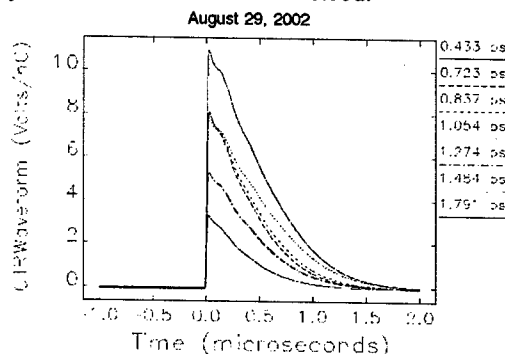


Figure 8: Accurately normalized signal vs. bunch length.

CONCLUSIONS

One final observation was that the 30-GHz center frequency, 75-MHz bandwidth bandpass filter shown in Figure 1 is not a very good filter for frequencies above about 45 GHz. Using the APS Diagnostics Group's 50-GHz network analyzer, it is clear that things are going awry as we push to higher frequencies. It is reasonable to suppose that the really high frequency junk seen in Figure 4 is bleeding through to the detector. This is a likely explanation as to why this device is such a good bunch length detector, even down below 300 femtoseconds (that's 3 degrees of phase at 30 GHz).

A second possibility is simply that alignment is critical, and the nulling effect described earlier only applies to the condition where the waveguide is accurately aligned on the image charge trajectory as it approaches the mirror. In any case, it was very gratifying that it was so easy to build a bunch-length monitor that is sensitive to short bunches appropriate for free-electron lasers in spite of not understanding what we were doing at the time.

ACKNOWLEDGEMENTS

Michael Borland's assistance in performing the careful independent bunch-length measurements was absolutely crucial to this work.

REFERENCES

- [1] U. Happek, E.B. Blum, A.J. Sievers, Phys. Rev. Lett. **67** (1991) 2962.
- [2] A.H. Lumpkin et al., Nucl. Instrum. Meth. A **475** (2001), 476.
- [3] M. Borland, "Potential Production of Ultrashort Electron Bunches with the Advanced Photon Source Linac," PAC'01, Chicago, IL, p. 2209 (2001).
- [4] M. Borland, J. Lewellen, "Initial Characterization of Coherent Synchrotron Radiation Effects in the APS Bunch Compressor," PAC'01, Chicago, IL, p. 2839 (2001).

RHIC TRANSVERSE INJECTION DAMPING*

A. Drees†, R. Michnoff, M. Wilinski, C. Montag, P. Cameron
BNL, Upton, NY 11973

Abstract

Since the beginning of the currently ongoing RHIC run a transverse injection damper is available. The damper is based on a fast kicker module in combination with a HV power supply and fast HV switches. This system can damp one injected bunch at the time with a given kick amplitude ("bang-bang mode") for several hundred turns. This report gives an overview of the injection damping system and summarizes its performance and our experience during the first months of usage.

INTRODUCTION

The damper module used for the RHIC injection damper is based on a VME board originally designed for the AGS damping system with a programmable FPGA (Field Programmable Gate Array) [1]. The existing fast transverse kickers [2], which are currently used for the RHIC tune measurement system [3] serve also for the injection damper. Since only used at injection, the kicker hardware including power supply and fast HV switches is shared. With this system one single bunch can be damped at the time only.

KICKER AND BPM

Each ring has two kicker modules with four 2m-long stainless steel striplines mounted on ceramic stand-offs spaced 1m apart allowing both, horizontal and vertical kicks. The two kickers are connected in series to provide 4m of stripline kickers. Each stripline subtends an angle of 70° at an aperture of 7 cm. The assembly is designed to give 50Ω impedance when opposing lines are driven in the difference mode. Each of the four planes can be powered independently. So far only pulsed power has been used. The kick pulses are generated by fast FET switches[4] producing an approximately 140 ns long pulse. By centering this pulse on the measured bunch single bunch excitation is possible with 60 (RHIC design) and even up to 120 bunches (RHIC upgrade) per ring where the bunch spacing is about 110 ns. Only one out of the 60 or 120 bunches respectively is kicked. All switches for all striplines in both rings are charged by one 5kV/2A power supply. Most BPMs used in RHIC are realized by short circuited transmission lines of 23 cm length, with a design impedance of 50Ω, and an aperture of 7 cm [5]. The selection of BPMs listed in [6] is based on devices with analog signals available in the 1002

service building, close to the 2 o'clock interaction region (IR2).

KICKER LOCATION

Figure 1 shows the vertical and horizontal beam profiles in terms of σ around IR2 for beams at 100 GeV with a normalized emittance of 40 π mm mrad. In order to avoid

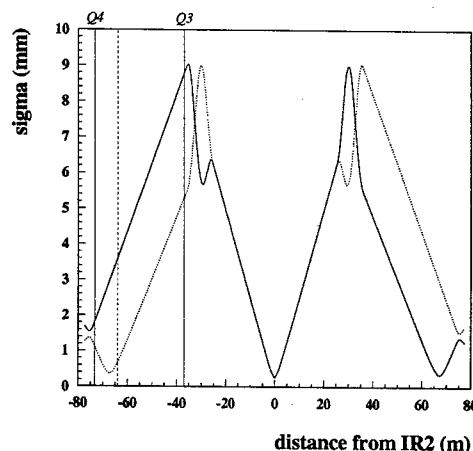


Figure 1: Horizontal (solid line) and vertical beam profile (dotted line) in units of sigma around IR2. The dashed line indicates the old kicker location from where it was moved to -52 m.

the kickers being the limiting aperture, they have to be at $\geq 6\sigma$, allowing them to move as close as -52 m from the IR. The required kick strength g for a linear amplifying system can be defined as:

$$\frac{2}{tf} = g = \sqrt{\beta_{s0}\beta_s} \frac{\Delta x'}{x} \quad (1)$$

with $f = 78$ kHz being the revolution frequency, t being the required damping time and β_{s0} , β_s being the β -functions at the location of the kicker and at the location of the BPM respectively. Equation 1 can be used as a conservative estimate for the required bang-bang kick strength. After a certain number of turns, however, the bang-bang damper would become counter-productive. Therefore the injection damper will be limited to a few hundred turns for damping. For linear damping, a given amplitude should generate a kick $\Delta x'$ of:

$$\Delta x' = \frac{2x}{t\sqrt{\beta_{s0}\beta_s}f} \quad \text{and} \quad (2)$$

$$x = \frac{\Delta x'}{2} tf \sqrt{\beta_{s0}\beta_s}. \quad (3)$$

The achievable kick angle for a single 3 kV pulse is about 11 μ rad at injection for Au and p [7]. Using the β -functions

* Work performed under Contract Number DE-AC02-98CH10886 with the auspices of the US Department of Energy.

† drees@bnl.gov

at the kicker and the chosen Q3/Q1 BPMs (see table 1) and a damping time of 200 turns, i.e. 2.5 msec, results in an approximate orbit amplitude of 32 mm vertically (Q1) and 75 mm horizontally (Q3). The largest observed amplitudes at injection in the straight sections were ≤ 25 mm in both planes. Therefore, the existing kick strength should be sufficient to antagonize injection oscillations in both planes.

The typical phase advance in one turn in RHIC is approximately $0.21/2\pi$ to $0.23/2\pi$ for both planes, corresponding to about 80° . In general, the tunes are fairly close and separated by some 0.01 to 0.02 only. Therefore, after one full turn, a local phase advance of close to 0° or 180° between BPM and kicker is most suitable for the damper. With this configuration a total shift of close to 90° will be kept. The neighboring Q3 BPMs offer 0° relative to the new position in the horizontal plane. The Q1 BPMs on the other side of the IR provide an approximate phase advance of close to 180° relative to the new kicker location in the vertical planes.

Table 1: Approximate β functions at the location of the blue and yellow kicker and damper BPMs around IR2 for the injection lattice.

device name	plane	s(m)	$\beta_x \cdot 10$ β_x (m)	β_y (m)
blue kicker	HV	2503	67	12
bi1-bh3	H	2519	141	48
bo2-bv1	V	2581	73	73
yellow kicker	HV	2609	67	12
yi2-bh3	H	2593	141	48
yo1-bv1	V	2531	73	73

TRIGGER AND DATA ACQUISITION

Figure 2 sketches the signal processing and triggering of both, the BPMs and the kickers, for a bang-bang injection damping system. The damper module is based on the existing AGS module and needs adjustments for the RHIC damper in the I/O area. The V124 module [8] receives and

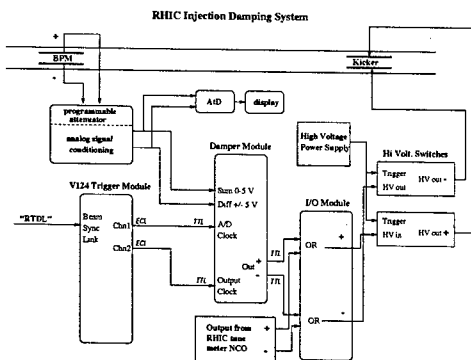


Figure 2: Block diagram for the RHIC injection damper.

decodes the beam synchronous event link [9]. The raw data acquisition from the two BPM planes is triggered by two channels of the V124 board where a total of 8 channels is available. Each channel for BPM readout and the kicker trigger has the appropriate delay so, on turn-by-turn acquisition, the same bunch will be observed on the BPM and then kicked. Start turn number, total number of turns for acquisition and damping as well as time delays are all parameters which can be remotely set from a console level computer. In general, the V124 allows the system to be triggered by any event broadcasted on the beam synchronous link such as the injection-event, start-acceleration-event or on demand. However, to damp injection oscillations only the injection-event is used.

EXPERIENCE

The RHIC transverse damper, although only working in "bang-bang" mode, could reduce injection oscillations significantly for all particles used in the RHIC run 2002/2003: deuterons(d), Gold (Au) and protons (p). Figure 3 shows a typical injection oscillation (beam position as a function of turn number) in the blue vertical plane on Dec. 27 02. The oscillation amplitude of the incoming beam is about 2 mm in this example and about 1 mm when the amplitude gets bigger again at about turn number 650. Figure 4 demon-

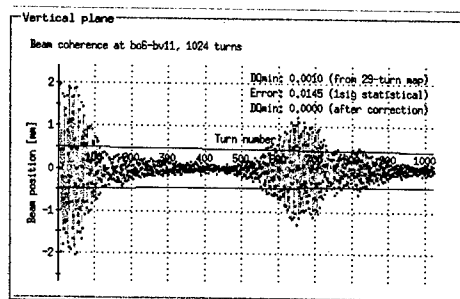


Figure 3: Injection oscillation without transverse damper in the blue ring, vertical plane, with deuterons.

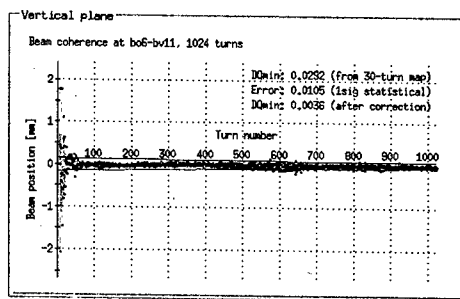


Figure 4: Injection oscillation with transverse damp ON for the same plane as above.

strates the damper performance in the same plane with the damper turned ON. The damper is kicking for 20 turns and the oscillation amplitude is reduced to 0.1 mm. There is no

visible reoccurrence of the oscillation around turn 650. In general, the damper efficiency is between 70% and 90% for the various beam species and planes and the default number of turns for the damper to kick was set to 50.

Using the Ionization profile monitor [10] we measured the beam profile and emittance of the incoming beam at injection with the damper on and off. Figure 5 shows the beam profile in the yellow horizontal plane (Au) with damper off (left) and damper on (right). The normalized emittance in the first case was 10π and in the latter 8.5π . This decrease of emittance by about 10-15% was reproducible.

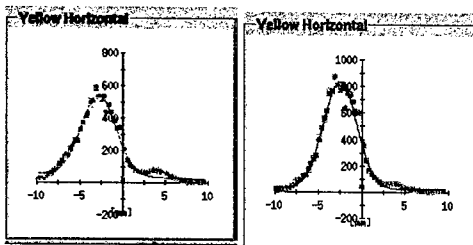


Figure 5: Horizontal beam profile at injection for Au particles with transverse damper off (left) and transverse damper on (right).

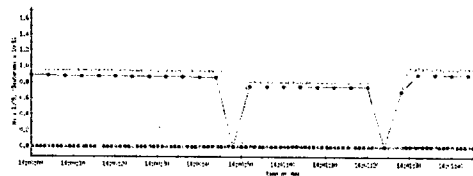


Figure 6: Bunch intensity for one injected Au-bunch with (left), without (center) and again with (right) transverse damper.

Figure 6 demonstrates the effect of the reduced emittance on the bunch intensity of the incoming beam. When the transverse damper was used the intensity could be increased by about 10% compared to beam injected with the damper off.

CONCLUSION

The existing tune meter kicker modules are suitable to act as a transverse injection dampers in "bang-bang" mode. Relative to the kicker location, the existing Q3 and Q1 BPMs provide a suitable phase advance after one turn of about 90° and 270° respectively. The high β -function at the BPMs of 140 m and 71 m respectively eases an amplitude measurement with good signal to noise ratio in both planes. The transverse dampers provided reliable injection oscillation reduction of 70-90% in all planes and with all species. At the same time it could reduce the normalized emittance of the incoming beam by about 10-15% and increase the intensity per bunch by an equivalent amount of 10%.

ACKNOWLEDGEMENT

We would like to thank the following people (in arbitrary order) for their support: Siegfried Naase, Gary Smith, Tom Russo, Mike Brennan, Ed Koropsak, Frank Dusek, Tony Curcio, Thomas Roser, Brent Gingrich, Vincent Lo Destro Vivek Ponnaiyan, Larry Hoff, Yuke Tian, Heather Hartmann, Roger Connolly and Freddy Severino. Their hard work was absolutely essential for the timely completion of the damper project.

REFERENCES

- [1] Michelle Wilinski et al., "Enhancements to the Digital Transverse Dampers at the Brookhaven AGS", Proceedings of the BIW2002, Brookhaven, 2002.
- [2] J. Xu et al., "The Transverse Damper System for RHIC", Proceedings of the Particle Accelerator Conference (PAC) in San Francisco, 1991.
- [3] A. Drees, R. Michnoff, M. Brennan, J. DeLong, "ARTUS: The Tune Measurement System at RHIC", Proceedings BIW2000, Boston, 2000.
- [4] Behlke Electronic GmbH, <http://www.euretek.com/>
- [5] P. Cameron et al., "RHIC Beam Position Monitor Assemblies", IEEE Proc., 1995 PAC.
- [6] A. Drees et al., "A Transverse Injection Damper at RHIC", Proceedings of the BIW2002, Brookhaven, 2002.
- [7] P. Cameron, R. Connolly, A. Drees, W. Ryan, H. Schmickler, T. Shea, D. Trbojevic, "ARTUS: A Rhic TUNE Measurement System", RHIC/AP/98-125, internal note.
- [8] H. Hartmann, T. Kerner, "RHIC beam synchronous trigger module", Proc. PAC 1999 (p. 696).
- [9] T. Kerner, C. R. Conkling Jr., B. Oerter, "V123 Beam Synchronous Encoder Module", Proc. PAC 1999 (p. 699).
- [10] R. Connolly, P. Cameron, W. Ryan, T.J. Shea, R. Sikora, N. Tsoupas, "The RHIC Ionization Beam Profile Monitor", Proc. 99 Particle Accel. Conf., 1999, p. 2114, IEEE Cat. No. 99CH36366.

RHIC ELECTRON DETECTOR SIGNAL PROCESSING DESIGN*

J. Gullotta[†], D. Gassner, D. Trbojevic, S. Zhang
Brookhaven National Laboratory, Upton, NY 11973, USA

Abstract

The RHIC gold beam intensity is presently limited by pressure rise at some warm sections, and the main cause is thought to be the electron cloud. For the FY2003 RHIC run, a system has been installed to characterize the electron cloud, if it exists. The system is comprised of electron detectors, high voltage bias supplies, signal amplifiers, and data acquisition electronics, all integrated into the Controls system. The 11 detectors are grouped into four locations, one in an interaction region and three in single beam straight sections. This paper describes the signal processing design of the detector system, and includes data collected from the FY2003 run.

INTRODUCTION

The Relativistic Heavy Ion Collider (RHIC) at Brookhaven National Laboratory has eleven electron detectors installed for measuring the electron cloud density in the beam pipe. This paper will describe the construction, specifications, and tolerances of the RHIC electron detector system. Actual results are presented and discussed as a verification of the system's usefulness as a tool to measure the electron cloud.

OPERATIONS

During the FY2002 RHIC Au-Au run, intensity was limited to 5×10^8 ions/bunch while running 110 bunches/fill. The limiting factor was vacuum pressure rises which caused the beam to abort. These pressure rises were linked to beam intensity and thought to be caused by the beam interacting with electron clouds in the beam pipe. Design intensity of RHIC is 10^9 ions/bunch at 110 bunches/fill. This limitation caused the machine to run at just over 50% of design intensity.

We are currently running deuteron on gold(d-Au) collisions in the FY2003 run. For the FY2003 d-Au run, intensity has been lowered to avoid electron cloud limitations, so there have been considerably less pressure rise events. However, during a dedicated beam studies period, intensity was maximized to induce pressure rises. A single event that resembled electron cloud multipacting occurred coincidentally with a major pressure rise.

Machine Timing

At 100 GeV, RHIC has a revolution period of $12.789 \mu\text{sec}$ and therefore a revolution frequency of

78.193 kHz . There are 360 RF buckets around the whole ring. While we are running 110 bunches we fill every third bucket, and leave ten consecutive spaces (30 buckets) empty for the abort gap. The length of one RF bucket is 35.53 nsec . The time from the head of one bunch to the head of the next is 106.575 nsec , with a periodicity of 9.383 MHz . The abort gap is $1.066 \mu\text{sec}$ long.

Electron Cloud Structure

Figure 1 shows RHIC electron detector signal corresponding to a vacuum pressure rise during fill 3107. Figure 2 is a wall current monitor trace showing the bunch structure for fill 3107. Notice the two groups of low intensity bunches which cause a weaker electron cloud signal. The wall current monitor signal is acquired by a scope sampling at 4 GS/sec. Therefore the x-axis of figure 2 is $1/4 \text{ nsec}$ counts. The y-axis of figure 2 is an arbitrary scale used for relative bunch-to-bunch measurements. The electron cloud signal is sampled at 1 GS/sec, so the x-axis in figure 1 has units of nanoseconds. The units of the y-axis of figure 1 are millivolts, with an arbitrary DC offset.

The data in figure 1 shows the only time that electron multipacting is thought to have occurred during the FY2003 d-Au run. The beam was lost due to a vacuum pressure rise about 20 seconds after the data in figure 1 was taken. Evidently, the scope was set to too high of a resolution because saturation occurs before the end of a single turn. In subsequent samplings (not shown) during this fill, the scope is saturated as soon as sampling begins. However, the structure of the signal in figure 1 closely resembles previous research on this topic [4].

According to the physical models and simulation results, we were expecting to collect electron cloud current on the order of $50 \mu\text{A}$ during electron multipacting. The detector drives an amplifier input with an impedance of 50Ω . Therefore, the expected voltage to be seen on the output of our 32 dB amplifier is 100 mV minus cable losses.

During fill 3107, the scope saturated during the first turn in which data was logged, corresponding to at least 80 mV of collected signal. We can only hypothesize that the maximum signal collected was much larger than 80 mV before the beam was aborted 20 seconds later.

SYSTEM LAYOUT

The detectors are located in the ring at four major locations. One group, having two detectors, is at the 12 o'clock interaction region. The other three groups are located in straight sections in 12, 1, and 2 o'clock and are constituted of the other nine detectors. The signal amplifiers are all located in the ring within 5 feet of each detector. The

* Work performed under the auspices of the U.S. Department of Energy

[†] Email: gullotta@bnl.gov

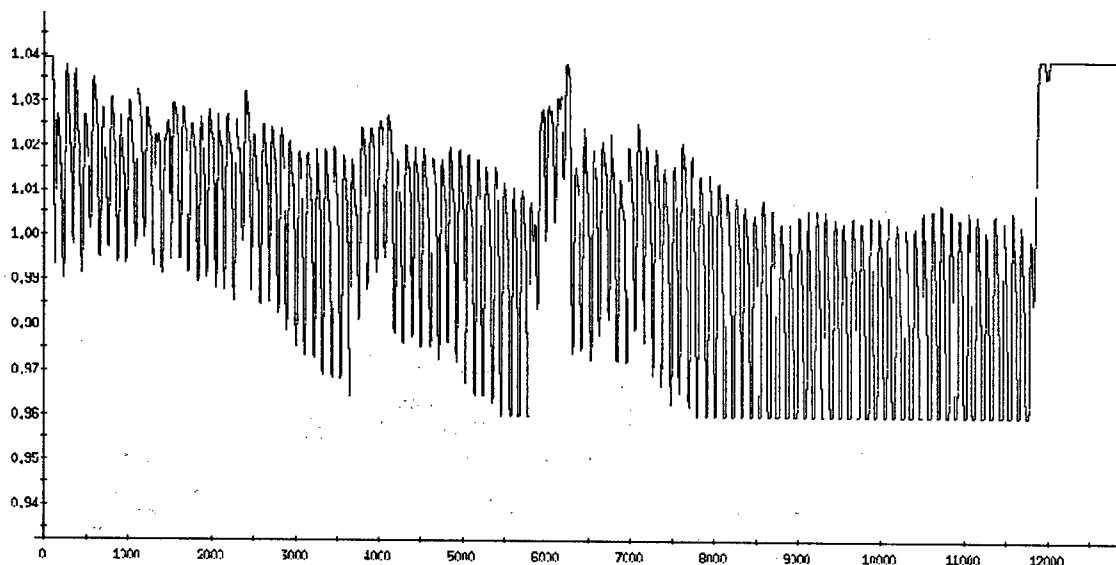


Figure 1: Electron detector signal for one turn during electron multipacting. FY2003 d-Au run, fill 3107

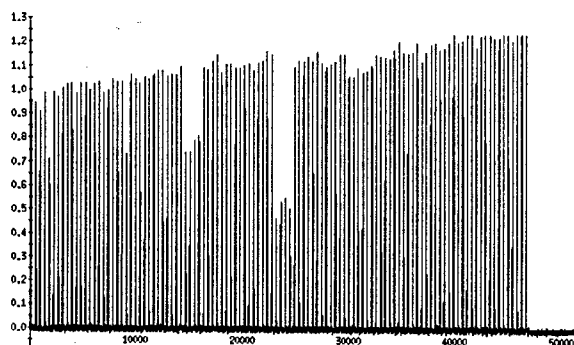


Figure 2: Wall current monitor for fill 3107, 110 bunches

high voltage power supplies, oscilloscopes, RF multiplexors, and trigger sources are all located in the service building. The signal is carried on 3/8" foam core Heliax, and the bias voltage is carried to the ring via RG-59 red 75 Ω high voltage coaxial cable.

Scope and Trigger

To acquire the signal read back from the detectors, an ethernet ready scope is used. This scope is the LeCroy Waverunner LM354 2GS/s 4 channel scope. The scope is triggered on beam events using our VME trigger card, the V124.

Detector Design

The detectors are installed in a vacuum tee in the beampipe on a 6.75" conflat flange. The signal is collected on a single collector anode, which is a flat metal plate that has a surface area of 78.5c². There are two suppression

grids on the beam side of the anode which each have a transmittance of 80%. To attempt to shield the detector from RF noise and image current effects, the port is covered with a perforated steel sheet that has a transmittance of 23%. Therefore, the effective surface area of the collector anode is 11.75c². The two suppression grids and the collector anode are electrically connected to external electronics via feed-thrus in the flange[5].

Controls Architecture

Our "Controls System" consists of many VME chassis and the ethernet network that connects them. Included in the VME chassis are device cards which may be data acquisition devices, trigger sources, muxes, etc. The controls system allows for the remote control of these device cards and the logging and display of the data that is read back.

Biasing

The suppression grids and the anode need to have their electric potentials specified with respect to ground. Usually we desire these potentials to be variable. ISEG VHQ-202M VME based high voltage power supplies were used when a variable bias was needed. However, in the case that a fixed voltage is suitable, batteries were used to reduce the complexity and cost of the system. For nearly all measurements, we used 45VDC to bias the collector anodes, and grounded all of the suppression grids.

Signal Amplifier

Much work was done to choose the correct amplifier for the signal path. The signal is very small, and must traverse a large distance(~ 175 e e s) to our data acquisition electronics. Currently, and since the system was in-

stalled, the signal is amplified in the ring using an AC coupled amplifier. This amplifier is a wideband amplifier, the Sonoma Instruments 310-N. This is the amplifier that was used to collect the data in figure 1.

The 310 has a bandwidth of 10kHz-1GHz, and a gain of 32dB. It was thought that an AC coupled amplifier would be well suited for the task, but it seems now that lower frequency signals are present and are shrouded by the low frequency cutoff of the 310. Therefore, we are developing a new amplifier that is DC coupled, and can withstand a large input bias voltage. The details of this design follow.

DC AMPLIFIER DESIGN

The application specific amplifier is a DC coupled trans-impedance amplifier which can withstand a relatively large input bias voltage, and has a bandwidth of 25 MHz(see Table 1). Since we assume there is a DC component of the electron cloud, we desire that the amplifier is DC coupled. However, we want to continue to monitor the high frequency components of the signal. Based on the structure of the electron cloud, 20 MHz is the lowest acceptable bandwidth.

Table 1: Amplifier specifications

Specification	Value
Bandwidth	DC-25MHz
Input Impedance	1k Ω
Voltage Gain	0dB
Max Bias Voltage	65VDC
Bias Volt. Rejection	103dB min
Output Impedance	50 Ω
Noise Figure	10mV
Power Supply	± 12 VDC, 120mA

Electrical Design

To allow the front-end to withstand large bias voltages, an amplifier circuit that has active common-mode rejection was chosen. The circuit used is similar to the one in the literature [1], but has a few modifications to compensate for sensitivity on the output to bias voltages caused by currents induced in the input load. This was not a problem in the literature, but our application is slightly different. By using this amplifier, we are able to bias the detector up to 65 VDC, while DC coupling our signal path to the data acquisition electronics. The amplifier removes the DC bias from the output in a very robust way.

Frequency Domain Design

To attempt to extend the bandwidth of the amplifier, a dynamic model of the system was developed [3] [6]. The actual response of the system rolls off at lower frequency

than the modeled system, but has a similar shape. A network analyzer was used to obtain the actual frequency response. The lower bandwidth of the actual system is most definitely the result of unmodeled parasitic elements on the prototype board. A compensation scheme was developed to increase the bandwidth[2]. For simplicity, a zero was added to the transfer function of the amplifier at about 10 MHz.

Testing

One of our spare detectors resides in an evacuated test chamber. Also in this chamber is an electron gun that we use to test our detector and amplifier electronics. We use a Kimball Physics fast pulsed electron gun, model EFG-7/EGPS-7. We pulse the gun at 1MHz between 1% and 20% duty cycle to test the high frequency characteristics of the amplifier. Tests were also conducted to verify the DC nature of the amplifier using constant electron current from the gun [5].

FUTURE WORK

At the time of this paper, the DC coupled amplifier had not yet been used in the ring. We plan to install one of our DC coupled amplifiers in the ring during our polarized proton operations this spring.

ACKNOWLEDGEMENTS

The authors would like to thank M. Blaskiewicz, A. Curcio, D. Gullotta, P. He, H. Hseuh, U. Iriso-Ariz, S. Jao, S. Polizzo, T. Russo, P. Sampson, R. Schroeder, G. Smith, A. Weston, and P. Ziminski. Your help was indispensable in completing the work documented here.

REFERENCES

- [1] P.Horowitz, W.Hill, "The Art of Electronics", Cambridge, 1989 [p.423]
- [2] G.Franklin, J.Powell, A.Emami-Naeini, "Feedback Control of Dynamic Systems", 3e, Addison Wesley, 1994.
- [3] "Effect of Parasitic Capacitance in Op Amp Circuits", Texas Instruments Application Report, Feb. 1999.
- [4] G.Arduini, J.Jiminez, K.Weiss, "The SPS as a Vacuum Test Bench for the Electron Cloud Studies with LHC Type Beams", Proc. 2001 PAC, Chicago.
- [5] P. He, H.C. Hseuh, D. Gassner, J. Gullotta, D. Trbojevic, S.Y. Zhang, "Calibration of RHIC Electron Detectors", Proc. 2003 PAC, Portland.
- [6] C.Close, D.Frederick, "Modeling and Analysis of Dynamic Systems", 2e, J.Wiley, 1995.

MULTI-MILLION-TURN BEAM POSITION MONITORS FOR RHIC

T. Satogata *, P. Cameron, P. Cerniglia, J. Cupolo, C. Dawson, C. Degen, J. Mead, K. Vetter
Brookhaven National Laboratory, Upton, NY 11973-5000, USA

Abstract

During the RHIC 2003 run, two beam position monitors (BPMs) in each transverse plane in the RHIC blue ring were upgraded with high-capacity mezzanine cards. This upgrade provided these planes with the capability to digitize up to 128 million consecutive turns of RHIC beam, or almost 30 minutes of continuous beam centroid phase space evolution for a single RHIC bunch. This paper describes necessary hardware and software changes and initial system performance. We discuss early uses and results for diagnosis of coherent beam oscillations, turn-by-turn (TBT) acquisition through a RHIC acceleration ramp, and ac-dipole nonlinear dynamics studies.

INTRODUCTION AND ARCHITECTURE

The RHIC BPM system[1, 2, 3] consists of 160 23-cm cryogenically-stable striplines per plane per ring: 72 dual-plane BPMs are distributed through the interaction regions (IRs), and 176 single-plane BPMs are located at each arc β_{\max} . Signals are cabled through 6 dB reflection attenuators and 20 MHz lowpass filters to analog/digital integrated front ends (IFEs). Each IFE contains independent electronics boards for two measurement planes, including active 20 and 40 dB gain stages, 16-bit digitizers for 1 μ m resolution over a ± 32 mm measurement range, and Motorola 56301 fixed-point digital signal processors (DSPs) for data reduction and acquisition control. Arc IFEs are in the tunnel, 2 m above the cryostat, or in tunnel alcoves for radiation protection; IR IFEs are located in equipment buildings.

During data acquisition, each IFE calculates the trigger and digitizer status, digitized raw signals, and beam position once per turn for a single RHIC bunch. Upon receipt of a beam-synchronous trigger, all RHIC BPMs can digitize up to 1024 consecutive turns and stream them to the local DSP buffer. This data is then passed along an IEEE 1394 connection to VME memory and the RHIC control system. This upgrade extends the on-board memory space of selected RHIC BPMs to provide much longer buffers for purposes of beam studies, energy-ramp beam instability study, and analysis of well-established slow coherent oscillations of RHIC beams. With average orbit data available only as fast as 1/2 Hz and 1024-turn TBT acquisition covering only 13 ms, this upgrade provides TBT data capability that easily spans the BPM system's former frequency-domain blind spot of 1-100 Hz.

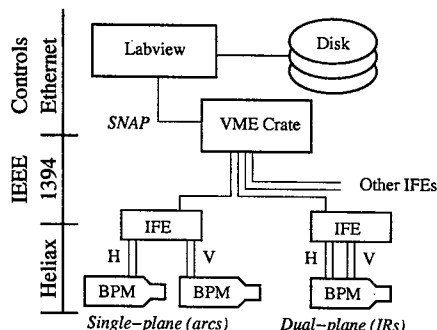


Figure 1: Architecture of the BPM million-turn upgrade

UPGRADE CHANGES

Hardware

The existing RHIC BPM digital electronics has a PCI mezzanine carrier (PMC) slot available, which made the hardware upgrade straightforward. The Motorola 56301 DSP has a built-in PCI interface, allowing a glueless interface to the PMC memory card. A commercially available PMC memory Card from RAMIX (model 551) was purchased and installed. This memory card provides 512 Mbytes of SDRAM, which is used to buffer the TBT data until readout. A special million-turn event was defined on the global event link to provide a start trigger for data acquisition; once data acquisition is started, the DSP ignores interrupts until the full acquisition is complete and data is read out.

The RAMIX 551 PMC memory card consumes 600 mA at 3.3 V. The existing voltage regulator on the BPM electronics is an On Semiconductor CS5203A-3GT3 LDO. The power dissipated from this regulator increased by $(5.0V - 3.3V) \times 600mA = 1$ W, requiring an additional heat sink.

Four BPM planes with IFEs located in the 2 o'clock instrumentation building were modified in late April 2003, during RHIC polarized proton run. In the RHIC sitewide nomenclature, they are bo2-bh8 and bh10 (horizontal) and bo2-bv7 and bv9 (vertical). Typical phase advances between these BPMs in all RHIC optics are 70 to 80 degrees, providing orthogonality for phase space reconstruction.

Software

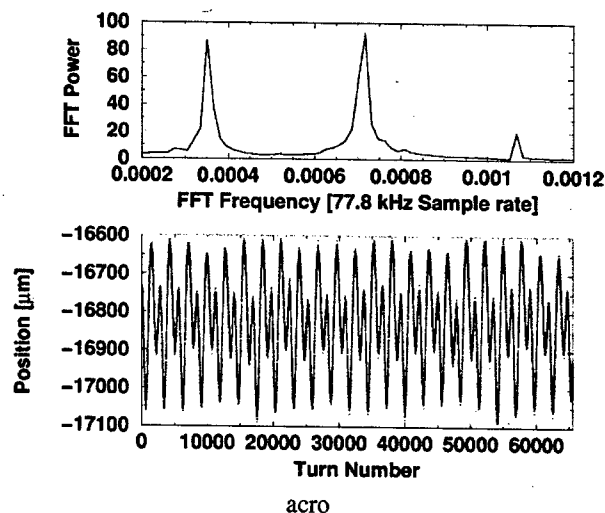
The DSP software was modified to add a new special million-turn mode of operation, preserving the full base functionality (average orbit and 1024-turn TBT acquisition) of the upgraded BPMs. Each TBT data point includes raw digitizer values, calculated beam position, and a status word, requiring 4 words of storage per turn. This allows

*Work performed under Contract Number DE-AC02-98CH10886 with the auspices of the US Department of Energy; author email satogata@bnl.gov

The handshake protocol makes the data transfer time very long, and it can take a few hours to read out the full 128 million turns for a *single* plane. Upgrades will con-

EXPERIENCE AND APPLICATIONS

The limited 1024-turn buffer size of the RHIC BPM system hampered their use during RHIC ac dipole optics and nonlinear dynamics studies[5], since the ac dipole excitation ramp time is several hundred milliseconds to adja-



2698

batically excite coherent oscillations and avoid emittance blowup. The million-turn BPMs will enable acquisition of TBT data and full phase space reconstruction during a full cycle of ac dipole ramp-up, flattop, and ramp-down. This permits fine-tuning and of the ac dipole excitation, as well as explorations of phase space smear and other topics in nonlinear beam dynamics[6].

When the full system is commissioned, a provocative planned use is the acquisition of an entire RHIC acceleration and squeeze ramp. These ramps typically take 5-10 minutes, easily within the acquisition time of the million-turn BPM system. With tunemeter kicks occurring every two seconds, acquisition of all million-turn BPM planes will provide full beam centroid phase space on the acceleration ramp. This system will also permit detailed study of intensity-dependent transverse instabilities, particularly through transition energy, as observed and corrected during the 2003 RHIC deuteron-gold run[7, 8].

REFERENCES

- [1] T.J. Shea and R.L. Witkover, "RHIC Instrumentation", Beam Instrumentation Workshop 1998 (Stanford).
- [2] T. Satogata *et al.*, "RHIC Instrumentation", Nucl Instr Meth in Phys Res A 499 (2003) pp. 372-387.
- [3] T. Satogata *et al.*, "RHIC BPM System Performance, Upgrades, and Tools", EPAC2002 (Paris, France).
- [4] C. Montag *et al.*, "Measurements of Mechanical Triplet Vibrations in RHIC", EPAC2002 (Paris, France).
- [5] M. Bai *et al.*, "Measurement of Betatron Functions and Phase Advances in RHIC with AC Dipoles", WPAB072, these proceedings (May 2003).
- [6] S. Peggs, "Nonlinear Diagnostics Using AC Dipoles", PAC 1999 (New York, New York).
- [7] T. Satogata *et al.*, "Commissioning of RHIC Deuteron-Gold Collisions", TPPB043, these proceedings (May 2003).
- [8] M. Blaskiewicz *et al.*, "Transverse Instabilities in RHIC", RPPB007, these proceedings (May 2003).

WAVEGUIDE MODE REFLECTOMETRY FOR OBSTACLE DETECTION IN THE LHC BEAM PIPE INCLUDING SIGNAL ATTENUATION

F. Caspers, T. Kroyer, CERN, Geneva, Switzerland

Abstract

Unexpected obstacle formation in the LHC beam-pipe during assembly, cool down and operation may lead to major disturbances. Thus a fast, precise, sensitive and reliable means to detect and characterize such a fault is highly desirable, preferably without the need to break the vacuum. Waveguide mode time domain reflectometry using the synthetic pulse technique has been selected for this purpose. The system will use a modern vector network analyzer operating using essentially the fundamental TM mode on the LHC beam-screen. The objective is to measure over a full arc (2.5 km) with access from either side both in reflection (≈ 1.25 km range) and transmission mode. If the proposed system is implemented a total of 32 couplers will be permanently installed, which may be used in normal operation for beam diagnostics and other applications.

The attenuation of several short beam-screen sections has been measured both for TE and TM modes by means of a resonator method and these data are compared with theoretical results. Waveguide calibration on the beam-pipe and digital signal processing to compensate dispersion are studied. Finally, using a 44m test track the performance of the proposed methods is examined.

INTRODUCTION

For proper operation of CERN's Large Hadron Collider, it is of utmost importance that the beam-screen, fig. 1, is free from any obstacle larger than a pinhead. During the installation procedure however, there is a non-negligible probability that a permanent deformation or simply some forgotten screw remains inside. In this case it would be advantageous to have a means to detect such obstacles during assembly and possibly in situ without having to open the vacuum.

Any intruding device such as a little robot is out of question for vacuum reasons, regardless of the possibility that it could get stuck inside. Optical lasers and ultrasonic pulse-echo detection are too limited in dynamic range. However the beam-pipe can be considered as a waveguide with modes propagating above a certain cut-off frequency. Since the beam-pipe is covered with axial pumping slots, TE modes will radiate considerably, while TM modes are hardly influenced, given that their wall currents are parallel to the slots.

In this approach synthetic pulse reflectometry was preferred over a FMCW¹ method and real time pulse reflectometry for the simple reason that the latter methods would require the development of much of the front-end measure-

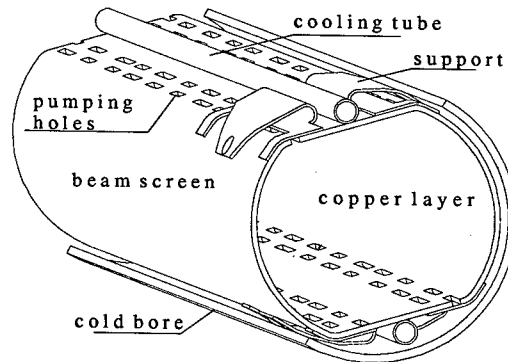


Figure 1: The LHC beam-screen with the surrounding cold bore, the pumping slots and the cooling tubes

ment equipment. For synthetic pulse reflectometry a state-of-the-art vector network analyser (VNA) has been used to measure the frequency response of s_{11} , the time domain profile of s_{11} is obtained by Fourier transform. In addition, high dynamic range (>120 dB) and good reproducibility have been obtained this way. This method has already been successfully applied over much shorter ranges (13m) at ESRF² [1].

Two plans for the realization are proposed:

- **The baseline programme:** During assembly, sections of say 100m length are checked before sealing the beam-pipe. The measurement would be done at room temperature by branching some kind of adaptor directly on one end of the beam-pipe.
- **The full scale version** should allow in-situ measurements in the LHC. Coupling to the beam-pipe should utilize a button type pick-up installed at the end of each arc (32 in total), requiring detection ranges up to 1250m at low temperature.

RESONATOR MEASUREMENTS

The attenuation in the beam-pipe constitutes a major limiting factor. We used a resonator method to determine the attenuation and the cut-off frequencies of the first TE and TM modes. The resonator was built by soldering brass plates on the ends of a sample of beam-pipe. A measurement in transmission mode reveals the characteristic pattern of peaks as shown in fig. 2.

Cut-off frequencies

Given this data, the cut-off frequency of the respective mode can be determined with very good accuracy using

¹Frequency Modulated Continuous Wave

²European Synchrotron Radiation Facility, based at Grenoble, France

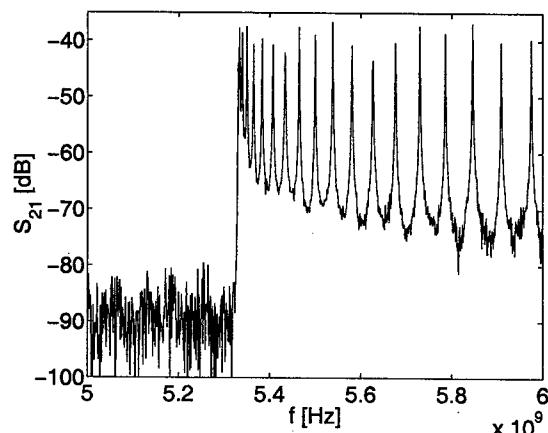


Figure 2: Pattern of resonance peaks for the first TM mode on a 100 cm long beam-pipe resonator in transmission

the method presented in [2]. The cut-off of the first TE and TM modes are given in the table below.

Mode ³	TE_{c11}	TE_{s11}	TM_{01}	TM_{11}
f_c [GHz]	3.61	4.32	5.33	7.99

Table 1: The measured cut-off frequencies for the first modes on the slotted beam-pipe

Attenuation

The relation between a peak's quality factor and the attenuation at this frequency is given in [3] by

$$Q_L = \frac{\pi \lambda_H}{\lambda_0^2 \alpha} \quad (1)$$

with Q_L , λ_H , λ_0 and α representing the measured loaded quality factor, the guided wavelength, the free wavelength and the attenuation in [dB/m], respectively. By appropriate choice of the mode launchers the coupling was kept sufficiently small that the unloaded quality factor Q_0 could be approximated by Q_L .

In figure 3 the attenuation α for the fundamental TM mode is compared to the theoretical curve for a circular waveguide having the same cut-off frequency f_c , as given in [4]. The measured values are larger by around 40%, which could be due to the properties of the beam-pipe, especially the longitudinal welding strip, the saw-teeth like corrugations, the general surface roughness and to a minor degree, the radiation through the slots.

For the TE modes³ things look different. The TE_{s11} mode is much affected by the slots, since its current maximum is at the location of the slots. The radiation losses make the attenuation increase by nearly a factor 2. For the fundamental TE mode (TE_{c11}) this is not the case, however its attenuation curve flattens above 4.5GHz, which indicates

³The indices c and s of the stand for the sine (vertical) and cosine (horizontal) polarization of the TE_{11} mode

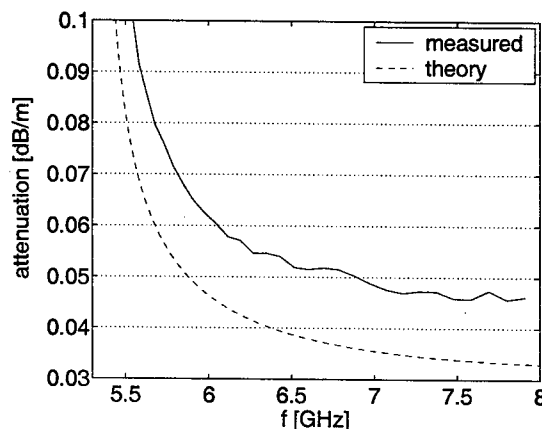


Figure 3: Attenuation of the fundamental TM mode on the beam-pipe, compared to calculated values for a circumscribed circular waveguide

that radiation losses (which increase with f^2 as a first approximation) begin to prevail. At low temperature (20K) this effect will become more significant, since the resistive losses are estimated to decrease by a factor 4 to 5. This observation indicates that the TM_{01} mode should be a better choice than the fundamental TE mode.

MEASUREMENTS ON THE TEST TRACK

After some preliminary tests a straight section of nearly 44m of beam-pipe with two interconnects was made available for measurements. The coupling to the beam-pipe consisted of a non-optimized adapter available from previous tests that was fitted to the end of the beam-pipe. Inserting an appropriate mode launcher excited the desired mode. On this line the performance of waveguide calibration and signal processing was tested.

Waveguide calibration

When doing measurements involving transitions between different types of lines and on electrically long devices calibration is highly recommended. For such a non-standard waveguide profile as the beam-pipe however no calibration standards are commercially available. Therefore we had to make them on our own. As for an ordinary waveguide calibration, three standards were used: two offset shorts of lengths $l_1 \approx 7mm$ and $l_2 \approx 20mm$ and one load. The shorts were realized by soldering a brass plate at the given position into a sample of beam-pipe and to get a load, some absorbing material was inserted into another piece (fig. 4).

The major advantage of waveguide calibration on the beam-pipe was found to be that initial reflections from the beam-pipe adapter could be avoided. However, due to the fragile contacts of the adapter and changing properties of cables, the calibration deteriorated every time some mechanical intervention was done. In particular in the time

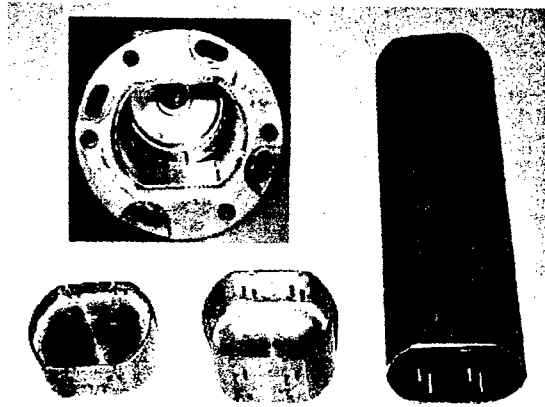


Figure 4: The coax-to-beam-pipe adapter and the three standards for waveguide calibration

domain it was noticed that calibrated measurements have a smaller dynamic range⁴ than uncalibrated ones.

Signal processing

It soon became clear that some serious signal processing had to be done. This is mainly due to two reasons:

- The **maximum number of points** available on our VNA is limited to 1601. Since this is insufficient to get both good spatial resolution (large frequency range) and good spatial range (closely spaced frequency points), measurements in adjacent frequency ranges have to be combined externally before doing the FFT.
- **Waveguide dispersion** on the beam-pipe will cause considerable smear-out on the emitted (synthetic) pulses. A numerical correction of this effect is called for.

For the implementation of these tasks MATLAB[®] was chosen.

Dispersion compensation. After having run down z meters on a waveguide with guided wavelength λ_H and cut-off frequency f_c the phase change can be expressed by

$$\phi(f) = -\frac{2\pi}{\lambda_H} z = -\frac{2\pi f \sqrt{1 - \left(\frac{f_c}{f}\right)^2}}{c_0} z = -2\pi \tau \sqrt{f^2 - f_c^2}, \quad (2)$$

introducing the free space delay $\tau = \frac{z}{c_0}$. By subtracting the part of this phase term that goes with higher than linear order of f from the phase of measured data, the dispersion can be compensated for *one* distance z . By repeatedly doing this procedure for increasing foci z , each time cutting out the focused region a dispersion compensated trace can be made up. The actual performance of this method is illustrated in figure 5.

⁴ difference between maximum amplitude and RMS noise level in *one* time domain trace

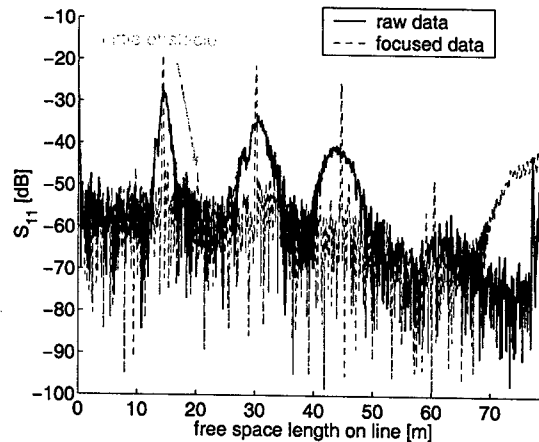


Figure 5: Dispersion compensation for the first TM mode on the test track

Other implemented features, such as analysis of mode mixing and multiple reflections by the interconnects are presented in detail in [5].

CONCLUSION

The feasibility of an obstacle-locating reflectometer for the LHC beam-pipe was studied. First the crucial characteristics of the beam-pipe were determined in a resonator measurement. With the attenuation obtained, a range of 600m for the detection of a M4 nut size obstacle seems possible at room temperature, with a substantial gain expected for low temperature operation (20K). In a measurement on a 44m long test track, waveguide calibration on the beam-pipe was examined and the data was processed to correct smear-out provoked by dispersion.

ACKNOWLEDGEMENTS

The authors would like to thank F. Peterson, T. Linnecar and R. Garoby for their support and N. Hilleret, J. Knaster, E. and H. Kos for their help.

REFERENCES

- [1] Caspers, F., Jacob, J., Gautier, G. et alias, *Wireless Impedance Measurements and Fault Location on ESRF Vacuum Chamber Assemblies*, CERN/PS, 1992
- [2] Caspers, Fritz and Scholz, T., *Measurement of Trapped Modes in Perforated Waveguides*, CERN-PS-RF, 2000
- [3] Matthaei, George, Young, Leo and Jones, E. M. T., *Microwave Filters, Impedance-Matching Networks, and Coupling Structures*, Artech House, Dedham, 1980
- [4] Meinke, H. and Gundlach, F. W., *Taschenbuch der Hochfrequenztechnik*, Dritte Auflage, Springer-Verlag, Berlin, 1968
- [5] Kroyer, Thomas, *A Waveguide High Order Mode Reflectometer for the Large Hadron Collider Beam-pipe*, Wien, 2003 (to be published)

TUNE MEASUREMENT METHODS OF THE TEVATRON

C.Y. Tan, X.L. Zhang, P. Lebrun
FNAL, Batavia, IL 60510, USA*

Abstract

We will discuss several methods for measuring the tunes in the Tevatron. These methods can be separated into three classes: active, passive and hybrid. In the active method, the beam is tickled in order to obtain a frequency response. In the passive method, a Schottky detector which uses a resonant stripline is used to measure the Schottky spectrum of the beam. In the hybrid method, we tickle the beam using kickers, or the Tevatron Electron Lens (TEL) in order to bring the tune signal above the noise floor of the Schottky detectors. An automatic tune fitting algorithm is also under development which allows us to measure the tune without human intervention.

INTRODUCTION

There are several tune measurement methods used in the operation of the Tevatron. These methods are developed in part because the antiproton tune is difficult to measure when there are protons in the Tevatron. In high energy physics conditions, the proton beam current is about 10 times higher than the antiproton beam current and thus the proton signal swamps the Schottky detectors despite their directivity. The preferred method for measuring proton tunes is to use the Schottky detectors which are passive and thus do not influence the beam in any way. For measuring antiproton tunes, we have to gently excite the beam transversely either with stripline kickers or with the Tevatron Electron Lens (TEL). Finally, a tune fitting method is also under development which will allow us to read the proton tune without human intervention. This method when fully operational will allow us to quickly measure chromaticities and also track the evolution of the proton tunes during collisions.

SCHOTTKY DETECTORS

The Schottky detectors [1] are 1 m in length with a square cross section shown in Figure 1. The stripline consists of two copper bars which can be moved by stepper motors to change the sensitivity. Its resonant frequency can also be tuned by using the variable capacitor C_v . Presently these detectors are tuned to resonate around 21.4 MHz with a loaded $Q_L = 370$.

Four of these detectors have been built to allow us to look at the horizontal and vertical tunes of both the protons and pbars. However in practice, only the proton tunes are monitored during high energy physics (HEP). Although

these detectors are directional, the pbar tunes are not normally monitored because a lot of the proton signal still leaks through which swamps the pbar signals. In order to overcome this, we have to gently kick — tickle the pbars in order to see their tunes.

Tickling

The process of gently kicking the beam is what we call *tickling*. We have two tickling methods which we use to observe pbar tunes using the Schottky detectors

- Tevatron Electron Lens (TEL).
- Gated noise on a stripline kicker.

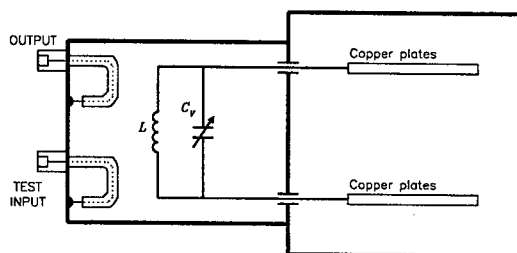


Figure 1: Transverse geometry of the Schottky pickup reproduced from [1]

Tevatron Electron Lens

The TEL, is built for the Tevatron Beam-Beam Compensation R&D Project, can also be used as a beam exciter for beam tune measurements [2]. To do this, the electron beam of the TEL is placed very near the bunch to be measured by timing the electron beam pulse to a specific bunch or bunches.

The electron beam used for this purpose is round with a diameter of about 3.5 mm and is modulated with gated white noise whose modulation depth is also adjustable. Every time the selected bunch passes by the electron beam, it receives a kick from the electron beam (this is just like the stripline beam tickler discussed below). Therefore, beam dipole oscillations are excited and thus Schottky signals which were originally too weak to be seen by a spectrum analyzer is excited above the noise floor. Besides using the white noise modulation, a chirp or a modulation sweep can also be applied. One caveat is that the beam-beam kick can be very strong, and so the peak electron current and modulation depth must be well controlled to avoid fast beam blowups or even beam loss.

* Work supported by the U.S. Department of Energy under contract No. DE-AC02-76CH03000.

In practice, the electron beam is gated to a specific antiproton bunch and then set to about 1 to 2 mm from it. This allows us to tickle it and measure its tune. As a comparison, the nearest proton bunch is about 7 mm away from the electron beam.

Gated Noise Tickling

In gated noise tickling, a bandwidth limited white noise is applied to one selected pbar bunch with a stripline kicker. Figure 2, shows what happens when we do this to pbar bunch 24. Before applying the tickle, we see a proton signal which leaks through. After we apply a vertical tickle, we can clearly see the pbar vertical tune.

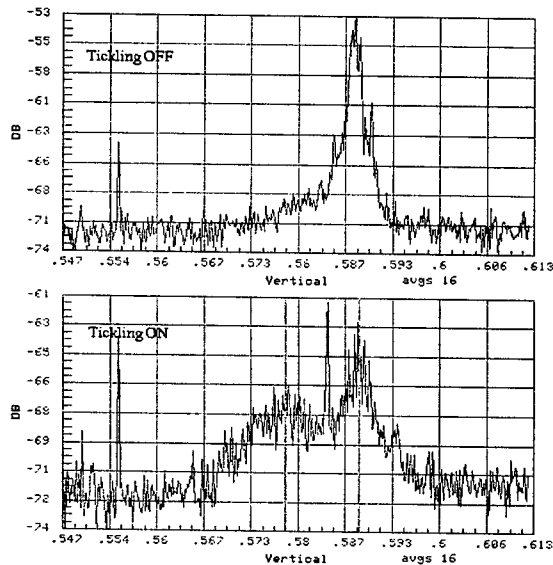


Figure 2: Pbar tune of bunch 24 with gated tickling ON and OFF

FREQUENCY RESPONSE MEASUREMENT

We measure the frequency response of each pbar bunch by tickling the beam with a stripline kicker and then measuring the frequency response with a stripline pickup. See Figure 3. A critical part of the setup is the autozero box [3] which centres the beam virtually between the stripline pickups. The sample and hold circuit allows us to measure the pbar tune of individual bunches. Figure 4 shows the frequency response of one pbar bunch.

TUNE FITTING

In order to automate the tunes, decoupling and chromaticity measurements, we have written a tune fitting software package. Frequency spectra similar to the one shown in Figure 2 are read out at a frequency of approximately 0.5 Hz into a conventional computer running SUNOS.

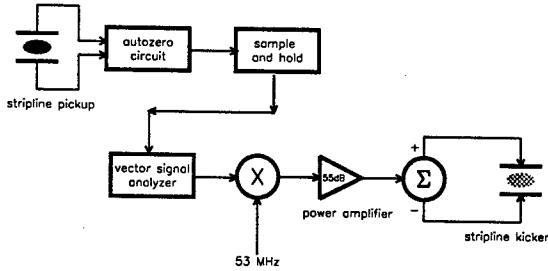


Figure 3: Frequency response measurement setup

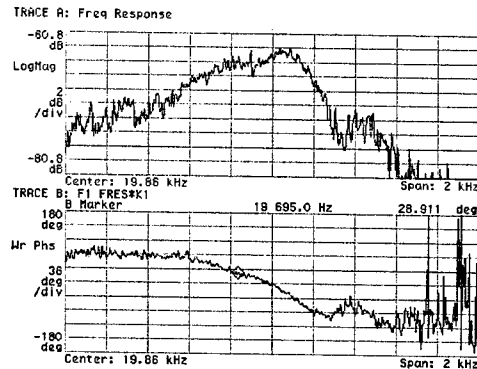


Figure 4: Frequency response of pbar bunch 1

First, such spectra are Gaussian-smeared¹ to smooth out the data and to select the location of the broad components of the spectrum. Only two such peaks are crudely located, corresponding to the vertical and horizontal tunes from the proton beam. Second, each of these regions are analyzed separately, based on the original data. We look for the characteristic pattern corresponding to the excitation of the synchrotron-betatron (SB) sidelines, separated from the main line frequency by ≈ 85 Hz and ≈ 31 Hz at 150 and 980 GeV, respectively. We fit the data with an incoherent sum of five resonant "Breit-Wigner" functions:

$$A(f) = B + \sum_{i=1}^5 (A_i \Gamma / ((f - f_{0,i})^2 + \Gamma^2/4)) \quad (1)$$

where f_0 is the frequency of the main line, $f_{0,(i+1)} - f_{0,i}$ is the SB tune split, Γ is the width of the resonance. The strength of each individual line A_i and B the noise floor are free parameters. The tune is located at the line closest to the position of the broad, smoothed-out, peak. Such fits are done on a linear scale to enhance such features.

Figure 5 summarizes these operations. It should be noted that the software often fails to properly assign the correct plane (X vs Y) for a given set of tunes lines. This is because the Tevatron is strongly coupled (with a typical mini-

¹The value of a given bin in the frequency domain is replaced by the sum of the neighboring bins, weighted by a Gaussian centered in that given bin.

imum tune split of ~ 0.004 to ~ 0.008) and we are running with tune differences in the X and Y planes close to this minimum tune split. Maybe a closer look at the relative signal strength on the X and Y pick will help sort this out. However, this does not prevent us from measuring tunes or chromaticities for a given plane when we run close to the minimum tune split, because we can keep track of the tunes for each individual plane with past measurement which are taken away from the minimum tune split region.

This method works very well when we tickle the “un-coalesced” (53 MHz bunched beam, with a longitudinal emittance of a fraction of an eV-sec) proton beam. It allows us to accurately measured the betatron coupling by simply sweeping the vertical base tune setting and recording these tunes, as shown in Figure 6. These frequency spectra are more difficult to analyze when relatively large emittance, coalesced (396 ns bunch spacing), and quiescent beam circulates in the Tevatron during HEP operation. Consequently, the fit often fails to locate the SB features. Yet, based on a large number of such fits, stable tunes can be assigned to the proton beam for both planes.

This tune fitter reports results continuously at about 0.5 to 1 Hz, with a delay time of about 5 seconds. This delay is due to the scanning and averaging in the HP3561a spectrum analyzer, about a second or so for Data Acquisition via the GPIB and various computers, and sending the output to the datalogger nodes, and finally about a second for doing the fits. We are currently working on faster algorithms, relying solely on the smoothed out spectra, to speedup this procedures. In addition, we can merge this software with the control software regulating the tickling of specific bunches allowing us to systematically explore qualitatively the beam-beam tune-shift phenomenon in the Tevatron.

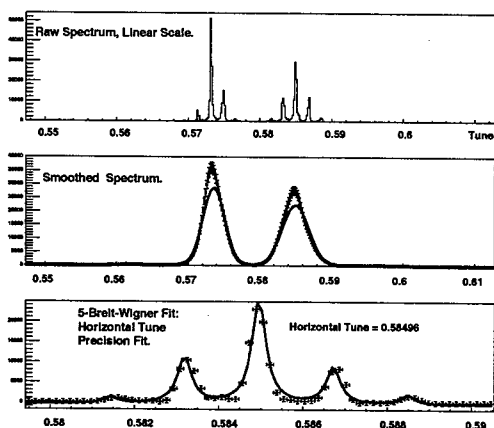


Figure 5: Tune fitter spectra. The vertical scale is related to power, in arbitrary units. The horizontal tune scale is fixed by the known revolution frequency and the analyzer scan settings. Fits are described in the text.

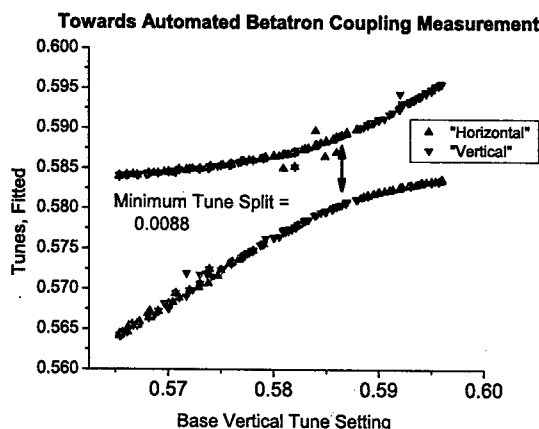


Figure 6: A measurement of the betatron Tune coupling based on the fits discussed above.

CONCLUSION

We have discussed the various methods which we use to measure the proton and antiproton tunes in the Tevatron. None of the methods for measuring the antiproton tunes are completely satisfactory at this time. A new set of Schottky detectors operating at 1.6 GHz is being commissioned which will allow us to measure bunch by bunch antiproton tunes passively. Unfortunately, the tune resolution of this system will be ~ 0.005 rather than ~ 0.0001 of the 21.4 MHz Schottky system discussed above. The tune fitting programme also shows promise in providing us with a way of automatically reading and tracking the evolution of the tune during a high energy physics operations.

ACKNOWLEDGMENTS

We thank John Marraffino for his technical expertise and advices on the fitting software. We also are thankful to members of the Accelerator Controls Department for their data acquisition work and dedicated support.

REFERENCES

- [1] D. Martin, *et al*, “A Resonant Beam Detector for Tevatron Tune Monitoring”, Accelerator Science and Technology Proceedings, vol 3 1486-1488, 1989.
- [2] X.Zhang, K.Bishofberger, V.Shiltsev, F.Zimmermann, The Special Applications of Tevatron Electron Lens in Collider Operation, this conference.
- [3] C.Y. Tan, “Theory of the Autozero Box and the Transverse Tune Measurement System”, Fermilab, TM-2078, Oct 1999.

THE SNS LASER PROFILE MONITOR DESIGN AND IMPLEMENTATION*

S.Assadi, A. Aleksandrov, W.Blokland, A. DeCarlo, C. Deibele, P. Gibson, W. Grice, M. Hechler, T. Hunter, J. Kelly, P. Ladd, G. Murdoch, M. Plum, J. Pogge, K. Potter, D. Purcell, T. Shea, D. Stout

ORNL, Oak Ridge, TN 37830 USA

Abstract

After a successful demonstration of a non-intercepting beam profile monitor for the H^- beams at the 750 KeV and the 200 MeV LINAC at Brookhaven National Laboratory, the SNS project approved using a Nd:YAG laser rather than the traditional carbon wire for transverse profile monitors in the SNS super-conducting LINAC. Experiments have also been performed on SNS 2.5 MeV medium energy beam transport line at LBNL. The design and the implementation of a multi-station profile monitoring system using a single laser will be presented. The laser beam is scanned across the H^- beam to photo-neutralize narrow slices. The liberated electrons are collected to provide a measurement of the transverse beam profile. The prototype system has been tested; the measurement and performance results will be presented.

INTRODUCTION

The SNS accelerator systems are described in details elsewhere [1]. The Spallation Neutron Source now being built in Oak Ridge, Tennessee, USA, accelerates an H^- ion beam to 1000 MeV with an average power of 1.4 MW. The H^- beam is then stripped to H^+ , compressed in a storage ring to a pulse length of 695 ns, and then directed onto a liquid-mercury neutron spallation target. Most of the acceleration in the LINAC is accomplished with super-conducting RF cavities. These eleven medium beta ($\beta=0.61$) and twelve ($\beta=0.81$) cavities are separated by warm sections (Fig.1). The profile monitor system for the SCL was originally envisioned to be a carbon wire scanner system. However, LINAC designers were concerned about the possibility that carbon wire ablation, or broken wire fragments, could find their way into the super-conducting cavities and cause them to fail. The SNS based-line carbon profile monitors developed [2] at Los Alamos National Laboratory in conjunction with search for alternatives such as laser profile monitors to minimize the above risks. Experiments at Brookhaven National Laboratory (BNL) using Nd-Yag laser to measure profiles of H^- beams proved to be promising. Once the laser profile monitor concept was proven by experiments at BNL, and subsequently on the SNS MEBT at Lawrence Berkeley National Laboratory [3,4], the decision was made to replace the carbon wire scanner system with the laser profile measurement system in the Super-Conducting LINAC (SCL). The advantages that the laser profile monitor system has over the wire scanner system are: 1) profiles can be measured during normal operations, as opposed to the 100 μ s, 10 Hz duty factor restriction

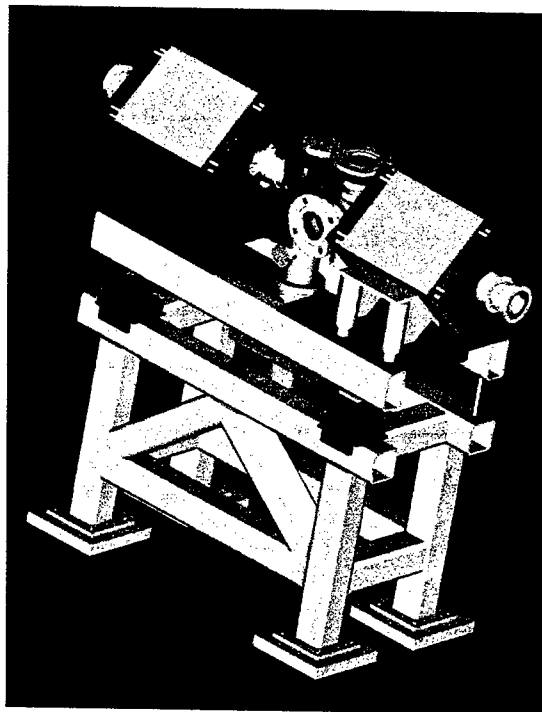


Fig.1. SNS "warm section" is a two quadrupole and diagnostic beam-box located between two super-conducting cavity modules.

needed to prevent damage to carbon wires; and 2) there are no moving parts inside the vacuum system, thus reducing the possibility of a vacuum system failure.

A disadvantage is that the laser is not as radiation hardens as a wire scanner actuator, but we have overcome this issue by placing the laser far away from the beam line in the Klystron Gallery and use optical transport line to transfer the laser beam to each station.

Dynamic range

The laser profile monitor concept is straightforward: a tightly focused laser beam is directed transversely through the H^- beam, causing photo-neutralization. The released electrons are either swept away by magnetic fields normally present in the LINAC lattice, or directed by a special dipole magnet to an electron collector that may or may not be part of the laser profile monitor system. The beam profile is measured by scanning the laser beam across the H^- beam and measuring the resultant deficit in the H^- beam current and/or, if the released electrons are collected, by measuring their current. A simple 3D drawing of the concept is shown in Fig. 2.

The advantage of collecting electrons vs. measuring the deficit in beam current are: 1) the signal to noise ratio is better because of the large numbers of released electrons; and 2) the simplicity of the electron collector, since the electron energy is well defined and the electrons are well collimated. The disadvantages are: 1) an external magnetic field is required, 2) an in-vacuum electron collector is required, and 3) the electron collector signal may suffer from interference caused by beam loss. At the SNS LINAC we will use both methods. Every laser station will have an electron collector, and there will be beam current measurements at the entrance and exit of the super-conducting LINAC.

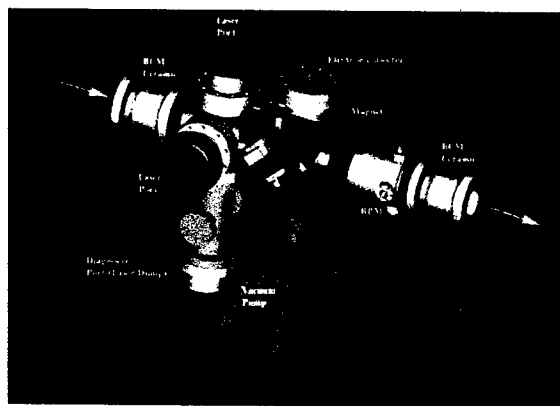


Fig. 2. Stripped electrons are bent into the collector via the dipole magnet (magenta color).

LASER AND OPTICS CONSIDERATIONS

General

A number of considerations guided the design of the optical system for the SNS laser profile monitor. First and foremost, the system must be capable of delivering high peak-power optical pulses to the ion beam. In order to provide adequate spatial resolution, the laser beam must be brought to a focus smaller than the ion beam and must be scanned in both transverse directions across the ion beam. Finally, the design must include a distribution system to accommodate multiple diagnostic stations.

The pulses are provided by a Q-switched Nd:YAG laser that runs at a repetition rate of 60 Hz and emits 9-ns pulses with energies up to 650 mW. The laser operates at a wavelength of 1064 nm, which is near the peak of the photo-neutralization response for H⁺. Because the 9-ns laser pulses are significantly longer than the ion pulses, a narrowband injection seeder is also included in the system to provide a smoother temporal profile. The prototype experiments were performed in low radiation areas and so the laser could be placed in close proximity to the diagnostic station. In the final implementation, however, the radiation levels will be much higher, thus necessitating removal of the laser to a remote location. The proposed location for the laser is in an adjacent building near the end of the LINAC tunnel and over 200 meters from the diagnostic stations. For propagation over

a distance this large, the beam must be expanded to a size of one inch or more. After being directed to the tunnel by a series of mirrors, the beam will travel down the tunnel in a beam tube mounted near the tunnel ceiling. Removable mirrors will be placed at each diagnostic station to direct the laser beam to the focusing and scanning optics. A second removable mirror switches the beam between the horizontal and vertical scans.

Because the laser beam must propagate so far from source to target, and because the source and target are in different buildings, mechanical vibrations are a concern. Of course, it is difficult to estimate the magnitude of these vibrations until the full system is implemented. A number of measures have been taken, however, to minimize and control beam jitter. The first comes in the optical design, itself. As described below, a lens is used to focus the laser beam onto the target. Mechanical vibrations in any of the upstream optics are expected to result in variations in both the position and incidence angle of the incoming beam. Because a lens maps the direction of an incoming beam to a single position in the focal plane, changes in the beam position alone have no effect on the focal position. Thus, it is only the angle of incidence that is of concern. The geometry of the system helps here. Nearly all of the downstream optics for each diagnostic station are mounted on a custom optical table. Most of the mechanical instabilities, then, are expected in the upstream optics where the beam is sent from one building to another. Because the upstream optics are over 200 meters from the target, large angular deviations in the beam will cause it to miss the downstream optics altogether. If the beam pointing is stable enough to keep the laser beam on the downstream optics, therefore, the angular variations from the upstream optics will be too small to significantly affect the profile measurement.

The challenge, then, is to keep the beam jitter small enough so that the beam is not steered off the downstream mirrors. The current design includes active stabilization to help in this regard. A beam position sensor will be placed near the diagnostic stations and will provide an error signal to piezo-electric actuators controlling one of the upstream mirrors. The feedback will be used to lock an auxiliary beam, rather than the primary beam, since it pulses at a rate of only 60 Hz. This method should make it possible to correct for much of the mechanical instability in the system.

The laser pulses arrive at each diagnostic station in the form of a one-inch beam and are then focused into the ion beam by a single lens. The lens is located approximately 20 cm from the beam center and is placed as close as possible to the vacuum windows. This design serves a number of purposes. First, it ensures that the beam is large when it passes through the vacuum window, thus reducing the chances of laser damage. Second, the relatively short focal length yields a convergent beam. By changing the position of the focusing lens, it is possible to change by a small amount the size of the laser beam as it crosses the ion beam. This function is accommodated in our set-up by a translation stage that moves the lens

parallel to the laser beam. For the ion beam profile, itself, the laser beam is translated across the ion beam. This is accomplished by translating the final steering mirror. Since the light passes through the focusing lens after striking the mirror, the two are mounted and translated together. Thus, the effect of the lens upon the beam is unchanged throughout the scan.

An additional benefit afforded by the optical design described above is that it minimizes the effects of unwanted reflections. As the beam exits the vacuum chamber, a small fraction of the light is reflected back toward the ion beam. Even with uncoated windows, the amount reflected is only a few percent of the primary beam. But the signal level from this unwanted reflection can be significant if the light is concentrated near the center of the ion beam. Using a lens to couple the light into the vacuum chamber ensures that the beam is diverging as it leaves the target. It continues to diverge as it is reflected back toward the ion beam so that the reflected energy is spread out over an area much larger than that occupied by the ion beam. Thus, the signal contribution from unwanted reflections is quite small and is fairly constant throughout the scan.

Data acquisition system

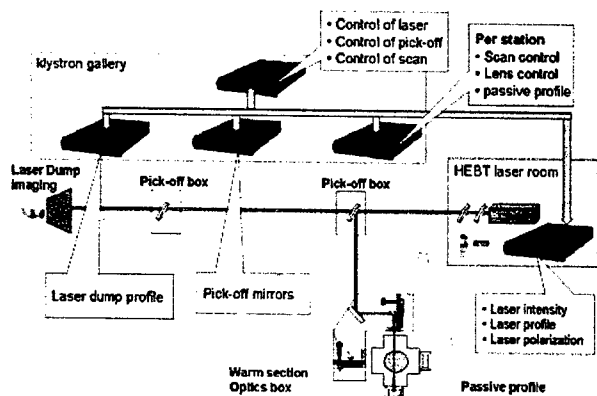


Fig. 3. Distributed PC systems and LabView data acquisition is used to collect and analyze data.

EXPERIMENTAL RESULTS AND CONCLUSION

We have successfully tested the SNS laser profile monitor. Figure (4) shows the completely stripped off electrons from the portion of the H^- beam intercepted by the laser.

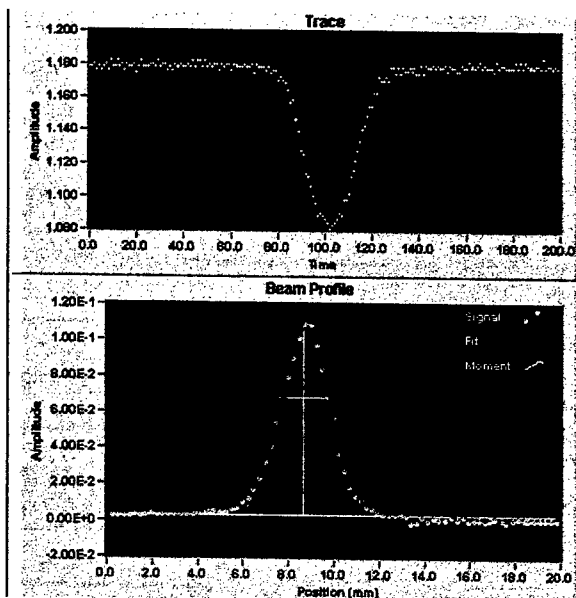


Fig.4. Horizontal beam profile in the SNS MEFT, measured in January 2003. Top: The electron collector signal at the center of the H-minus beam. Bottom: the results of the measurement, with a Gaussian fit plotted out to 2.5 σ .

REFERENCES

- [1] N. Holtkamp, "these conference proceedings, PAC2003, Portland
- [2] R. Hardekopf et al, "Wire Scanner Design for the SNS Superconducting-RF Linac," proceedings of the 2001 Particle Accelerator Conference, Chicago, Ill, USA, June 18 - 22, 2001.
- [3] R. Connolly et al., "Laser Profile Measurements of an H^- Beam," proceedings of the 2001 Particle Accelerator Conference, Chicago, Ill, USA, June 18 - 22, 2001.
- [4] R. Connolly et al., "Laser Beam-Profile Monitor Development at BNL for SNS," proceedings of the 2002 Beam Instrumentation Workshop, Upton, NY, USA, 6 - 9 May 2002.
- [5] A. Aleksandrov, SNS-NOTE-AP-44

* SNS is managed by UT-Battelle, LLC, under contract DE-AC05-00OR22725 for the U.S. Department of Energy. SNS is a partnership of six national laboratories: Argonne, Brookhaven, Jefferson, Lawrence Berkeley, Los Alamos and Oak Ridge.

DESIGN OF AN OPTICAL DIFFRACTION RADIATION BEAM SIZE MONITOR AT SLAC FFTB

Y. Fukui*, D.B. Cline, F. Zhou, University of California at Los Angeles

M. Ross, P. Bolton, Stanford Linear Accelerator Center

J. Urakawa, M. Tobiyama, KEK, High Energy Accelerator Research Organization, Japan

R. Hamatsu, T. Muto, P.V. Karataev, Tokyo Metropolitan University, Japan

A. P. Potylitsyn, G.A. Naumenko, A.S. Aryshev, Tomsk Polytechnic University, Russia

Abstract

We design a single bunch transverse beam size monitor which will be tested to measure the 28.5 GeV electron/positron beam at the SLAC FFTB beam line. The beam size monitor uses the CCD images of the interference pattern of the optical diffraction radiation from two slit edges which are placed close to the beam path. In this method, destruction of the accelerated electron/positron beam bunches due to the beam size monitoring is negligible, which is vital to the operation of the Linear Collider project.

OVERVIEW

The Optical Diffraction Radiation(ODR) is generated when a charged particle bunch passes by inhomogeneous boundaries, and is considered as the wake field of a beam bunch. By using a tilted conducting slit where a beam bunch passes through the center of the slit aperture, we can observe the interference pattern of the backward scattered ODR from two edges of the conductive slit. The ratio of the photon intensity at the peak of the interference pattern of the ODR and that at the valley of the photon intensity gives the information of the transverse beam size. [1, 2, 3, 4] Because the distances of the edges of the slit from the beam central trajectory is typically 10 times or more larger than the transverse beam size, this beam size monitor is non-invasive, which is essential to minimize the beam loss in beam size monitor. This beam size monitor measures the beam size of a single bunch, and the fraction of the sampling of the beam bunches depends on the speed of the readout system of the interference pattern of the ODR. Most of the experiments on the use of the ODR for a beam size monitor has been done only recently with electron beams up to around 1 GeV at TTF(Tesla), and at ATF(KEK). With the 28.5 GeV e^-/e^+ beam at the SLAC FFTB (Final Focus Test Beam), the γ factor of 5.8×10^4 allows us to use much larger aperture size than those with lower beam energy, which contributes to reduce the background photons significantly. The test of the beam size monitor by using ODR at the SLAC FFTB provides a unique condition for a non-invasive beam size monitor with the highest beam energy electron and positron beam. The transverse RMS beam size of electron and positron beam at

a focal point of the SLAC FFTB are 2 -10 μm in horizontal and vertical. The FWHM bunch length is 0.7 mm. The intensity of electron and positron beam is $(1 - 3) \times 10^{10}$ particles/pulse. The normalized transverse emittance are $(30 - 50) \times 10^{-6}$ m-rad in horizontal and $(3 - 6) \times 10^{-6}$ m-rad in vertical. The international collaboration, with researchers at KEK, Tokyo Metropolitan University, and at Tomsk Polytechnic University who have done significant R&D on the beam size monitoring with the ODR at the KEK ATF in Japan with the 1.3 GeV electron beam [5], allows us to understand the dependence of the beam size measurement with the ODR on the beam energy and on the level of the background radiation.

DESIGN OF THE BEAM TEST EXPERIMENT

A schematic diagram of the beam size monitor with the ODR interference pattern measurement and a conventional wire scanner for a cross calibration is shown in Fig. 1.

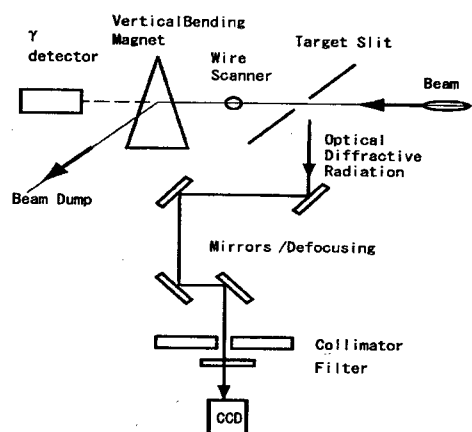


Figure 1: A schematic diagram of an ODR beam size monitor

Because the wavelength of the diffracted optical photon, around 0.5 μm , is much shorter than the beam bunch length, 0.7 mm, the observed optical diffraction radiation is incoherent, and the optical wavelength allows us to use a simple CCD. The CCD camera is trigger-able with 1000×1000 pixels with 14-16 bits resolution in each pixel. The size of the CCD is $16 \times 16 \text{ mm}^2$. The target slit is made

* fukui@slac.stanford.edu

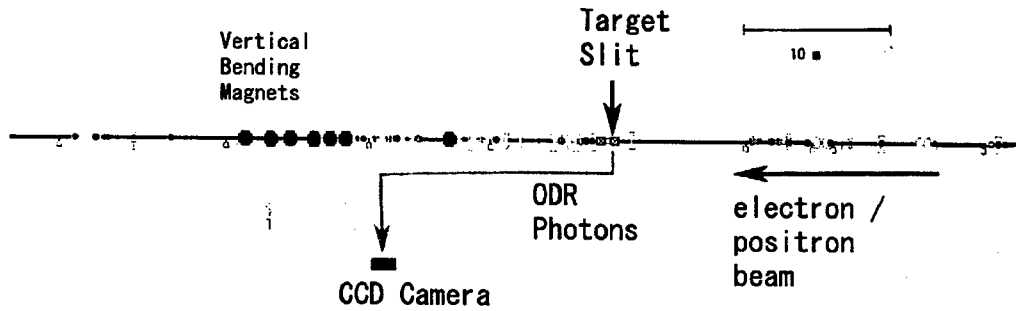


Figure 2: Top view of the experiment layout at the SLAC FFTB

of crystalline wafer/block with 3-5 μm thick Au conductor coating on the top plane. The slit aperture is around 0.2 mm.

Assuming the typical transverse beam size of 5 μm (horizontal) \times 5 μm (vertical), at the SLAC FFTB focal point, the measurement error of the transverse beam size is expected to be around 0.06 μm in an ideal case by using the interference pattern of the optical diffraction radiation with a bandwidth of 480 - 520 nm. The size of the error of the transverse beam size measurement depends on the level of the background photons into the CCD camera and the stability of the transverse beam size and shape and the location of the transverse center of gravity of the beam. The transverse tail part of the beam interacts with the target slit which generates the optical transition radiation (OTR). Scattered synchrotron radiation of the target slit can also contribute to the background optical photons. [6] The downstream end of the closest dipole and quadrupole magnets are 20 m and 1 m away from the target slit respectively. The total path length of the ODR photons between the target slit and the CCD camera is around 30 m where the CCD camera is located in a measurement room located outside of the FFTB tunnel shield wall. Fig. 2 shows the top view of the experiment area at the FFTB test beam line.

We obtained the simple estimation of the ODR photon yield by using the exact Maxwell equation solution on the infinitely thin ideally conductive semi-plane with the optimal gap width of the target slit at 0.2γ . The part of the ODR yield within the optimal angular width of $0.1/\gamma$, is estimated as:

$$= 5 \times 10^{-5} \gamma^2 \left(\frac{\sigma}{\gamma \lambda} \right)^2,$$

where γ is the Lorenz-factor, λ is the radiation wavelength, σ is the transverse beam size with the Gaussian approximation. For λ at 10 μm , σ at 0.5 μm , and γ at 60,000 this value is smaller by a factor of 4×10^4 than the ODR yield in the same angular width at the maximum of the ODR angular distribution, and it is smaller by a factor of 10^5 than the optical transition radiation (OTR) yield in the same angular width at the maximum of the OTR angular distribution. The angular distribution of parallel polarization of an ordinary ODR (in the far field zone) is presented

in Fig. 3.

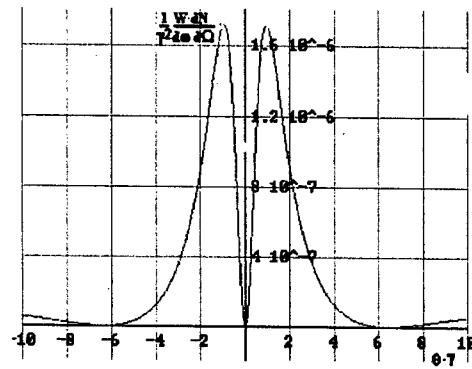


Figure 3: Parallel polarization component of backward ODR intensity from a slit of 0.1 γ width for γ at 60000. Angular distribution in polarization plane, calculated without accounting of the pre-wave zone effect.

The expected number of the optical diffraction radiation photons in the 1 dimensional angle range of $10/\gamma$ rad within the bandwidth of 480 - 520 nm is around $1 \times 10^6 / (10^{10} \text{ electron/positron bunch})$ which is roughly the same as that of the optical transition radiation, if the conducting plate is placed directly in the beam. The number of ODR photons in the bandwidth has weak dependence on the beam energy. Study is underway to investigate the possibility of using the polarization of the optical diffraction radiation in order to suppress the background optical photons into the CCD camera with a polarization filter.

The effect of the total wake field of a beam bunch to the subsequent beam bunches must be calculated with a typical target slit parameters. And the 'pre-wave' zone effect must be taken into account in the calculation of the yield of the ODR photons from the target slit.

The nature of the 'pre-wave zone' effect for a backward transition (diffraction) radiation may be explained as follows: if a detector is placed at a distance less than γ^2 from a target, then measured radiation characteristics will be distorted in comparison with ones for far field zone. Model of this effect was developed for transition radiation [7, 8]

and this one was observed experimentally in the OTR for electron energy at 0.9 GeV. [9] We developed a simpler model of radiation in pre-wave zone which allows us to calculate the transition and diffraction radiation properties for different geometries. Fig. 4 shows the preliminary angular distribution of parallel polarization component of backward ODR intensity from a slit of $0.1\lambda\gamma$ gap width for γ at 60000 with the distance of the detector at 5.4m from the target with the pre-wave zone effect.

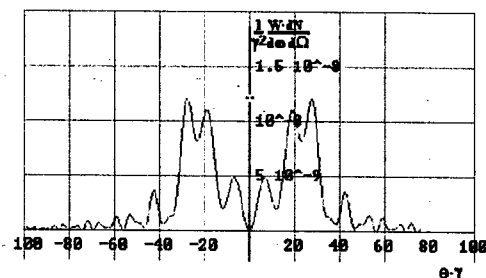


Figure 4: Parallel polarization component of backward ODR intensity from a slit of $0.1\lambda\gamma$ width for γ at 60,000. Angular distribution in polarization plane, calculated with the pre-wave zone effect.

The goals of the beam test for the beam size monitor with optical diffraction radiation at the SLAC FFTB are :

1. establish the measurement system of the transverse size of the 28.5 GeV electron and positron beam with the optical diffraction radiation,
2. obtain the size of the systematic error of the transverse beam size measurement by using the conventional wire scanner with multiple beam bunches, or by using the optical transition radiation from a single beam bunch off a slant target plate directly placed in the beam path,
3. optimize the slit plate angle, gap size, and the bandwidth of the optical diffraction radiation for a precise non-invasive beam size monitor,
4. study on the measurement error of the transverse beam size due to the background photons into the CCD camera by:
 - i) optical transition radiation off the target slit which is generated by the transverse beam tail particles,
 - ii) scattered optical photons off the target slit material associated with the beam halo, and
 - iii) synchrotron radiation at the upstream dipole magnets and quadrupole magnets.

The key issues are to use conventional wire scanners and the optical transition radiation for cross-calibration of the beam size measurement, and to understand the background optical photons at the SLAC FFTB. The challenges of this beam test are to achieve the required flatness of the conductive slit surface, and to resolve the small opening angle between the interference pattern peaks within a reasonable distance without distortion.

SUMMARY

We design a single bunch transverse beam size monitor which will be tested to measure the 28.5 GeV electron/positron beam at the SLAC FFTB beam line. The beam size information is given by the ratio of the ODR photon yield in the valley and that in the peak. But the information is distorted by the pre-wave zone effect of the ODR photons, and it is smeared and offsetted by the background photons by the optical transition radiation by the transverse beam tail particles, the synchrotron radiations through the magnetic elements, and the beam halo. Work is in progress in finding the optimum parameters of the ODR beam size monitor which gives the maximum information on the transverse beam size with those distortion effects and backgrounds.

REFERENCES

- [1] M. Castellano, A new non-intercepting beam size diagnostics using diffraction radiation from a slit. Nucl. Inst. And Meth. A 394(1997) 275-280
- [2] Y. Dnestrovskii, et al., "Radiation from Charged Particles Passing Near a Perfect Conductor" Sov., Phys., Dokl. 4(1959)132.
- [3] A. P. Kazantsev, et al., "Radiation of a Charged Particle Passing Close to a Metal Screen" Sov., Phys., Dokl. 7(1963)990.
- [4] A.P. Potylitsyn "transition radiation and diffraction radiation. Similarities and differences." Nucl. Inst. and Meth. B 145(1998) 169-179
- [5] T. Muto, et al., "First Stage Experiment on Optical Diffraction Radiation at KEK-ATF" ICFA Laser Beam Interaction Workshop, NY, Stony Brook, June 2001
- [6] G.A. Naumenko. "Synchrotron radiation contribution to optical diffraction radiation measurements." Nucl. Inst. and Meth. B 201(2003) 184-190
- [7] V.A. Verzilov. "Transition radiation in the pre-wave zone." Phys. Let. A 273 2000 135-140
- [8] S.N. Dobrovolsky, N.F. Shul'ga. "Transition and Diffraction Radiation by Relativistic Electrons in a Pre-Wave Zone." Proceedings of EPAC 2002, Paris, France
- [9] M. Castellano et al., "Search for the pre-wave zone effect in transition radiation." Phys. Rev. E 67, 015501(2003)

MEASUREMENT OF ELECTRON BEAM DIVERGENCE USING OTR-ODR INTERFEROMETRY

R. B. Fiorito*, A. G. Shkvarunets and P. G. O'Shea, Institute for Research in Electronics and Applied Physics, University of Maryland, College Park, MD. 20742, USA

Abstract

Optical transition radiation (OTR) interferometry has been shown to be a useful diagnostic for measuring the divergence of electron beams over a wide range of beam energies (15 MeV - 230MeV) [1]. However, beam scattering in the first foil of the interferometer ultimately limits the useful range of such a device. To overcome this effect we have designed and tested a perforated front foil interferometer to measure divergence of electron beams in the range of 100-1000 micro radians. Unscattered beam electrons passing through the holes in the screen produce optical diffraction radiation (ODR), while those passing through the solid portion produce OTR. For the proper hole size, number and screen thickness, the ODR-OTR interferences are readily observable above an incoherent background produced by the scattered electrons. The fringe visibility provides a measurement of beam divergence. The results of proof of principle measurements are presented. In addition, we introduce a novel design for an interferometer useful for the diagnosis of low energy, low emittance beams.

INTRODUCTION

Conventional OTRI cannot be used for lower energy beams ($E \leq 10$ MeV) or high energy beams with very low divergence because scattering in the first foil of the OTR interferometer dominates and obscures the beam divergence. To overcome this problem we have devised a perforated foil (mesh) - solid foil interferometer, which produces a combination of ODR from the holes and OTR from the solid portion of the mesh. These radiations interfere with backward reflected OTR produced from the second mirrored foil as shown in Figure 1.

The presence of the perforations produces a complication as far as analysis is concerned since no analytic theory for diffraction radiation from a matrix of holes in a metallic foil exists. To overcome this difficulty we have devised a simulation code (BEAMDR), which calculates the electric and magnetic fields at any distance from a radiating foil for any geometry of single or multiple holes. The results of BEAMDR are combined with analytic calculations of OTR from the mirror to produce far field ODR-OTR interference patterns.

A second code is used to convolve the ODR-OTR interference pattern with a given distribution of particle trajectory angles (usually a Gaussian distribution of angles) and a given optical band pass function. The latter is needed to produce distinct visible fringes for a given range of divergence. Divergence measurements are obtained by fitting the final code results for various rms

divergences with measured interference patterns. A complete description of these codes is given in [2].

In Section I. of this paper we present a detailed comparison of theoretical predictions and experimental data taken with both conventional OTR and ODR-OTR interferometry to demonstrate its viability as a diagnostic method.

In Section II. we describe a new type of interferometer, useful for low energy beams, which uses forward directed radiation from a metal mesh and a *dielectric* foil. The design, operation and predicted performance of this novel device are discussed in detail.

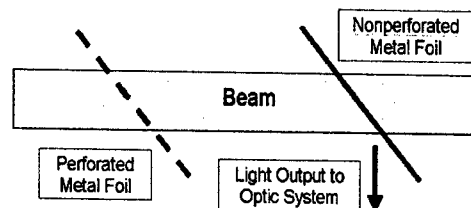


Figure 1: ODR-OTR interferometer; interferences between forward directed ODR from a mesh inclined at 45° and backward reflected OTR from a parallel mirror are observed at 90° with respect to the beam direction.

PROOF OF PRINCIPLE EXPERIMENT

Both ODR-OTR and conventional OTR-OTR interferometers were used to measure the divergence of the Naval Postgraduate School's 95 MeV electron beam linac. The average current of this machine is about 0.1 μ A, and the macropulse repetition rate is 60 Hz.

A detailed description of the ODR-OTR and OTR interferometers used in our proof of principle experiment and the optical layout is fully described in [3], so that we will only briefly mention the relevant details of the interferometers.

A 5 μ m thick, rectangular aperture copper micromesh (750 lines per inch, 33 micron period) is used as the first foil for the ODR-OTR interferometer, and a 0.7 micron aluminum foil is used as the first foil in the conventional OTR interferometer. The latter produces a calculated rms scattering angle of about 0.1 mrad, which is much less than the expected rms beam divergence, $\theta_{rms} \sim 1$ mrad. An aluminized silicon mirror serves as the second foil for both systems. The foil spacing $L = 25.4$ mm. A 650nm X 70 nm band pass filter was used to observe the interferences.

* rfiorito@umd.edu

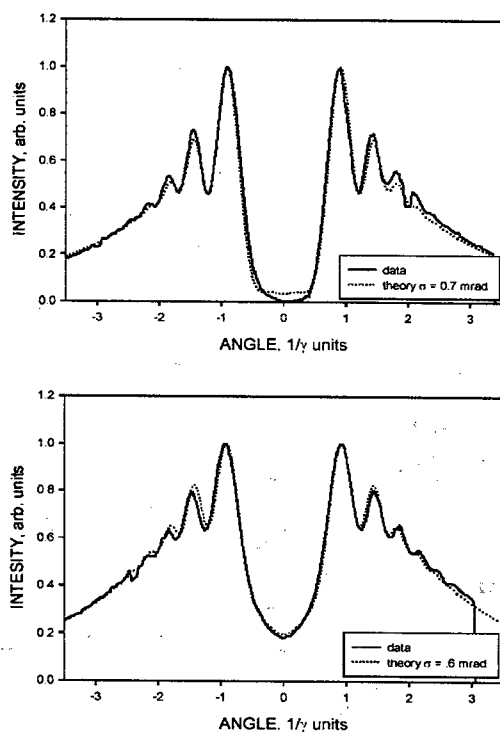


Figure 2: (top): fit of a vertical scan of OTR-OTR interference pattern to computer generated simulation; (bottom): similar fit to vertical scan of ODR-OTR interference pattern with theoretical calculation.

Figure 2. (top) shows a vertical (y) scan of an OTR interferogram taken at a vertical (y) beam waist condition together with a fitted theoretical scan. The fitted value of the rms (y) divergence of the beam, $\sigma_y = 0.7 \pm 0.05$ mrad. Figure 2. (bottom) shows a similar scan of an ODR-OTR interferogram taken under the same beam conditions. The fit to the data is obtained from a simulation code that we developed to analyze ODTRI [2]. The divergence measured with ODTRI, $\sigma_y = 0.6 \pm 0.05$ is in good agreement with that obtained using OTRI. Note the increased filling in and reduced visibility of the fringe pattern due to the presence of the incoherent background from scattered electrons in the solid portion of the mesh.

NEW, LOW ENERGY INTERFEROMETER CONCEPT

For low energy beams the inter foil spacing ($L \sim \gamma^2 \lambda$) is too small to directly observe backward reflected OTR and reflected ODR from an inclined mesh - foil interferometer. For example, at beam energy $E = 10$ MeV and $\lambda = 650$ nm, $L < 1$ mm.

We introduce a new type of interferometer to solve this problem which observes interference between forward directed ODR from a mesh and forward directed radiation from a thin dielectric foil as shown in Figure 3.

We refer to the radiation produced in the dielectric as dielectric optical radiation or DOR. The interferences are

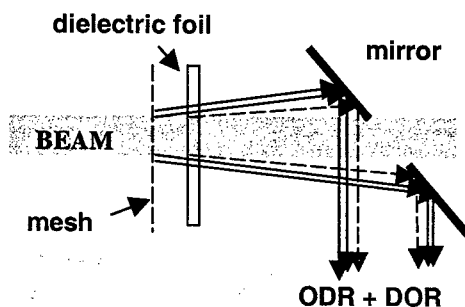


Figure 3: Mesh-dielectric foil interferometer.

collected by a downstream mirror which has a circular hole to allow the beam to pass through. The size of the hole, $a \gg (\gamma \lambda / 2\pi)$ the impact parameter for the generation of ODR from the mirror, but is small enough so that most of the angular interference pattern will be observed.

There are two important questions that immediately arise regarding the performance and design of this device, namely: (a) what are the properties of dielectric optical radiation and (b) what is the effect of multiple scattering of electrons in the dielectric on this radiation?

To answer (a) we have taken three approaches to calculate DOR at observation angles in the range of $(1 - 4)/\gamma$, the angular region of interest.

(1) An *analytic solution due to Pafomov* [4], in which all components of the radiation are calculated including multiple reflections within the dielectric.

(2) A *polarization current model* in which radiation is generated from each of a series of infinitesimal layers produced by the electron as it passes through the dielectric material. This radiation has an component in the vicinity of $1/\gamma$ as well as at the Cherenkov angle. OTR from the boundaries and refraction effects are included.

(3) A *transparent "metal" model* in which each surface produces radiation with an intensity equal to that of OTR from a metal-vacuum interface. Again the refraction of OTR from the first boundary is included as in model (2).

Our calculations show that the angular distributions obtained from these three different calculations give nearly identical results in the angular region of interest. This means that we can safely employ the simplest, i.e. the two metal OTR model, to calculate the response of either a solid metal foil - dielectric interferometer or a perforated foil - dielectric interferometer.

Figure 4. shows a comparison between the Pafomov solution for DOR and the two metal OTR model for two wavelengths. Apart for small differences near the maxima, the results are the same. We see that the intensity of DOR can be controlled by proper choice of thickness and wavelength. In particular, it can be adjusted to equal that of OTR from a single metal foil. Once this is done, the ODR-DOR interferometer will have the same

properties as the ODR-OTR interferometer described above in Section I.

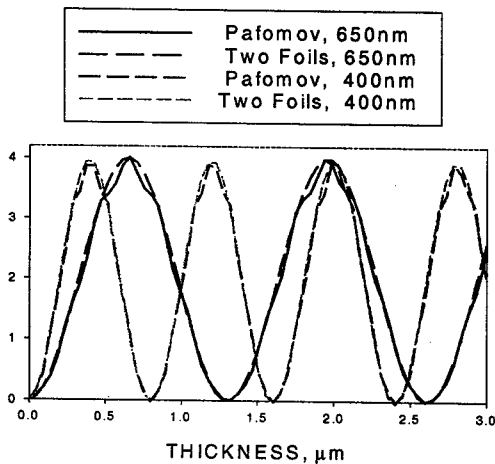


Figure 4: The Pafomov and two metal foil model of dielectric foil radiation for two different wavelengths.

Effect of Scattering in the Dielectric

Code calculations have been performed using the two metal surface model for a beam energy $E=10$ MeV, dielectric thickness $d=5.438$ μm , dielectric constant $\epsilon = 2.25$, inter foil spacing $L = 5\text{mm}$, observation wavelength $\lambda=650\text{nm}$ and band pass $\Delta\lambda=0$. This set of parameters produces a net intensity of DOR equal to unity in metal - vacuum OTR intensity units. When electrons are scattered in the dielectric with the same scattering angle considered above for a mesh - solid foil interferometer ($\sigma_{\text{foil}} = 10$ mrad), the intensity distribution of DOR is only mildly affected by this heavy scattering. Thus we conclude that scattering in the dielectric does not significantly affect the angular distribution and intensity of DOR.

Figure 5. shows the effect of beam divergence on the interferences of an OTR-DOR interferometer with a scattering $\sigma_{\text{foil}} = 10$ mrad in the dielectric.

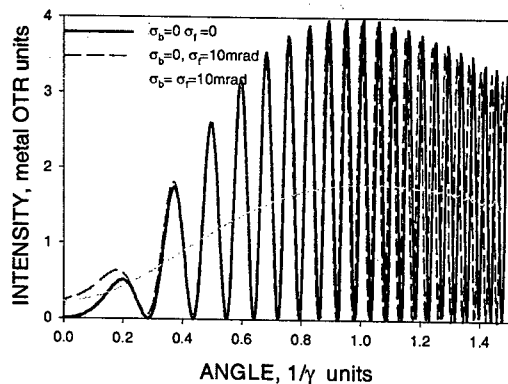


Figure 5: Effect of beam divergence on OTR-DOR interferences.

The dashed (red) and solid (black) curves are nearly indistinguishable except for small observable angles. Thus

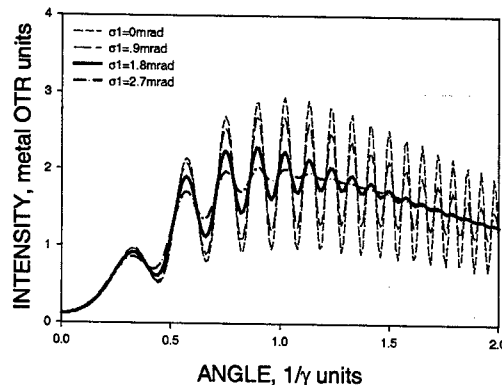


Figure 6: Effect of beam divergence on OTR-DOR interferences

scattering in the dielectric has a negligible effect on the vast majority of the observed interferences.

The reason for this result is that the path length between the foils primarily determines the difference in phase of the photons generated at the first and second foils. This difference is negligibly affected by the optical path length and scattering introduced by a thin dielectric foil. However, the relative phase is still strongly affected by *scattering in the first foil*. For this reason a mesh or perforated foil must be used in combination with a dielectric foil to measure the beam divergence for low energy beams.

Figure 6. shows the effect of beam divergence on ODR-DOR interferences in the presence of scattering in the dielectric foil, $\sigma_{\text{foil}}=10\text{mrad}$. In this case $E=8$ MeV, $L=1.5$ mm, $d=5.449\mu\text{m}$, $\lambda=650\text{nm}$ and $\Delta\lambda=0$.

CONCLUSIONS

Experiments have verified that ODR-OTR interferometry is a viable diagnostic method to measure beam divergence for moderate energy beams. We have demonstrated computationally that ODR - DOR interferometry is an new, effective divergence diagnostic for low energy, low emittance electron beams.

ACKNOWLEDGEMENT: Research sponsored by ONR and the DOD Joint Technology Office.

REFERENCES

- [1] R.B. Fiorito and D.W. Rule, AIP Conf. Proc. No. 319, R. Shafer ed., 187 (1994).
- [2] A.G. Shkvarunets, R.B. Fiorito and P.G. O'Shea, Nuc. Instrum. and Methods B 203, 153 (2003).
- [3] R.B. Fiorito, A.G. Shkvarunets, and P.G. O'Shea, AIP Conf. Proc. No. 648, G. Smith and T. Russo eds., (2002).
- [4] V.E. Pafomov, JETP, 33, 1074, (1957).

A NEW TOOL FOR BEAM-LIFE RESEARCH AT HLS STORAGE RING

Yuxiong Li[#], Juexin Li, Zuping Liu, Weimin Li

National Synchrotron Radiation Laboratory, University of Science and Technology of China
Hefei, Anhui 230029, P.R.China

Abstract

A beam loss monitoring system was set up for HLS (Hefei Light Source) last year. The beam loss message includes some beam life related factors. So, besides detecting vacuum failures in the storage ring, this system may serve as a useful tool in beam life research.

The beam life is composed of three parts: Touschek life, quantum life and vacuum life. The exact loss position of the corresponding stored electrons can be concluded if we detect shower electrons, which give a distinct clue of loss location, but not to detect bremsstrahlung photos or neutrons. So it is important to analyze the positions where beam losses take place and qualitatively distinguish them.

With the help of this system, the researchers have found and resolved following problems: A 20-40 mA beam loss frequently observed during ramping process; vacuum dead area near the front ends of beam lines; a beam life decline when a 6-Tesla superconducting wigglers was powered; etc.

PREFACE

We completed a beam loss monitoring (BLM) system for HLS (Hefei Light Source) last year. The original purpose was detecting vacuum failures in the storage ring. During the design stage, by calculation we found that the beam loss message includes some beam life related factors and it is possible to expend BLM system's function. It may serve as a useful tool in beam life research. This idea has been proved.

THEORETICAL ANALYSIS

Part of the beam loss component ΔI is measured by this system. For HLS, the total electron amount is about 10^{13} when the stored current is 100 mA and the loss rate is about $10^7/s$ if the $1/e$ beam life is 10 hours. There are about 10^4 records of lost electrons per second even if only 1/1000 of them can be detected. So it is easy to get high measurement sensitivity by this system.

The main points for designing and applying such a system in beam life research are as following: beam loss mechanisms, different components of the lost beam and how to distinguish them, suitable and cheap measurement devices, the best positions to install the devices along the storage ring.

The beam life can be roughly explained by following formula:

$$\frac{1}{\tau} = \frac{1}{\tau_T} + \frac{1}{\tau_q} + \frac{1}{\tau_v}$$

τ -beam life time τ_T -Touschek life time

τ_q -Quantum life time τ_v -Vacuum life time

Here τ_q can usually be omitted since it is much longer than τ_T and τ_v when the machine operates well. The collision among inner-bunch electrons is an elastic one and may bring about large momentum deviations and hence electron loss, that determines Touschek life τ_T . This kind of loss always involves a pair of electrons, for which the chances to hit inner or outer wall of the vacuum chamber are equal. The electron colliding with residual gas molecule may lose energy, and then hit the inward wall of the chamber during or after passing dipoles, if the energy loss exceeds a certain amount. By calculating we know the critical value of energy loss is about 2.4% and learn how the loss rate is distributed along the ring. [1]

Shower occurs when the electron hits the vacuum chamber wall. Among this process, shower electrons carry more distinct position information of lost electron than photos and neutrons do. To understand their distribution we tracked the shower electrons, whose energy down to 1.5 MeV, outside the vacuum chamber wall by EGS4 method. We use the detector which is very sensitive to shower electrons (the detection efficiency is over 30% to the shower electron whose energy higher than MIP) but nearly no response to photos and neutrons (its sensitivity to gamma is lower than 0.06%). Therefore where the electrons are lost can be determined.

The important thing is to analyze the different positions where various beam loss components take place. To qualitatively distinguish them, we will select corresponding measure points.

APPLICATION

Based on the theoretical analysis we completed this new beam loss monitoring (BLM) system.[2] In addition to the high sensitivity to vacuum failures, we have applied it in beam life research successfully. Different from the similar systems we use the detectors in pairs along the storage ring. Twelve pairs are fixed on 12 dipole exits separately and another one is fixed on the linear section. We think the sum of count rate coming from half of all the detectors, which are fixed on the outward chamber wall, may be more or less related with Touschek life time. The difference between the count rate sums from the detectors, which are fixed on the inward

[#] lyx@ustc.edu.cn

and outward wall separately, reflects the vacuum life time. This BLM system has made an important contribution to machine study.

EXPERIMENTAL RESULTS

The system runs well after completed. The primary results we got are indicated below:

Additional beam loss during ramping process

The 200 MeV electrons will be ramped to 800 MeV after injected to the storage ring. There often existed 20-40 mA beam loss at the beginning of the ramping process.

See Figure 1.

With the help of the BLM system we found this part of the beam loss took place at the downstream of the first dipole B01, the inner wall of the storage ring. We think this is because of the delay from the kicker closed to total stopped. Therefore the orbit keeps moving after ramping begins. We resolved this problem by locking the time between injection stops and ramping begins with a MCU. The beam loss at B01 decreased two orders of magnitude. The total beam loss is only several mA's during the ramping process. See Figure 2.

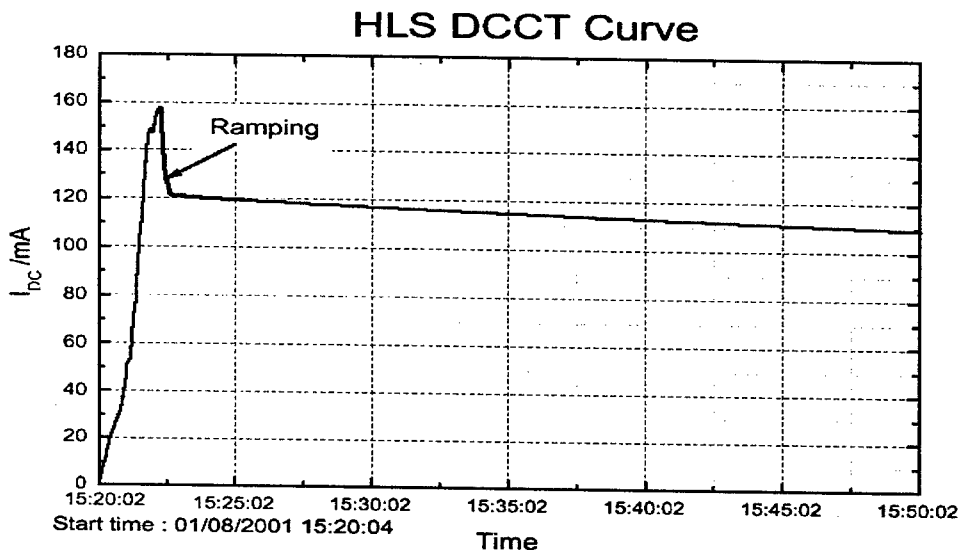


Figure1: The beam loss during ramping process before improvement

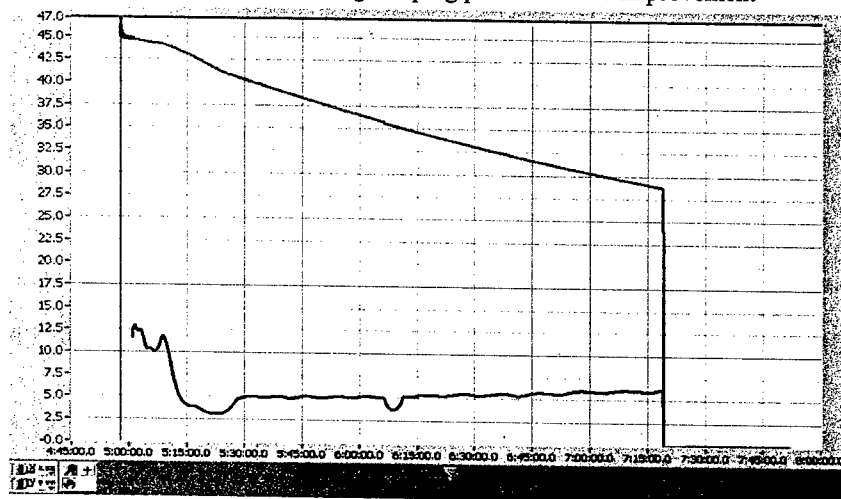


Figure2: The beam loss during ramping process after improvement

Beam loss caused by the accumulated gas at the front ends

Due to lack of vacuum pumps near the water-cooling masks at the front ends of photon beam lines, some gas was accumulated there and would impact the electron

beam strongly later, when the gate valve was opened. This phenomenon was clearly recorded by the BLM system. We can see this phenomenon clearly in Figure 3. So the local vacuum system should be improved. Less beam loss will be propitious to beam life.

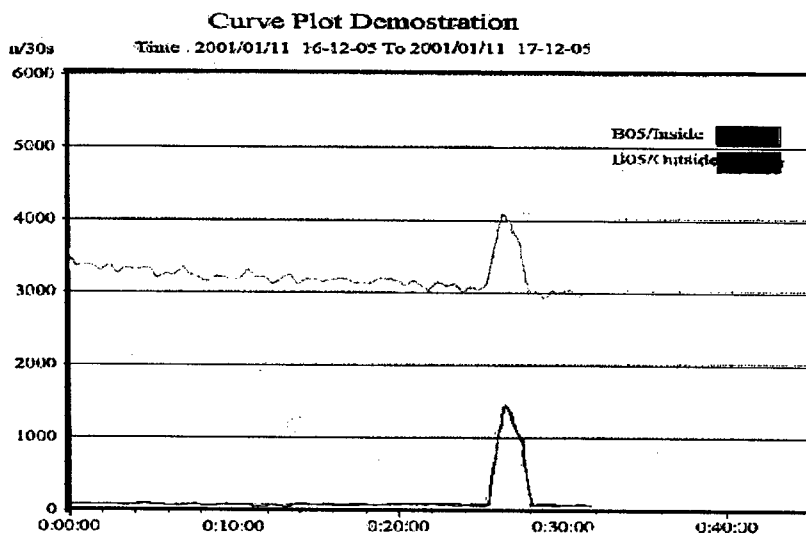


Figure 3: Beam loss caused by the accumulated gas at the front ends

The Influence comes from the superconducting wiggler

The beam lifetime decreased seriously when a 6-Tesla superconducting wiggler was powered if the machine operation parameters were not properly chosen. It once declined from 9.7 hours to 2.9 hours because of this, as a result of beta function distortion and quantum lifetime reduction. After calculations, a quadrupole strengths

global compensation was carried out and led to a great success. Figure 4 is the beam loss before-and-after the global compensation. In Figure 2, the lower line is the beam life curve. The beam life suffered from a small drop caused by wiggler powering and it recovered after the compensation. The machine runs well after the parameters were readjusted.

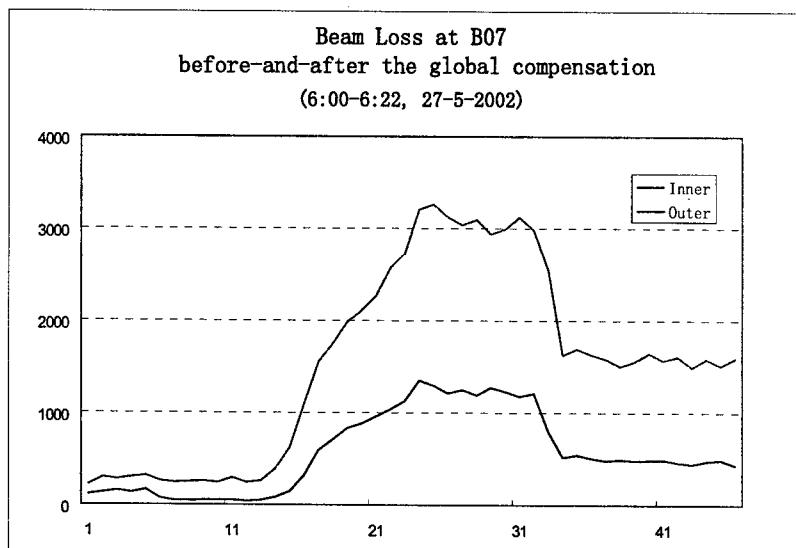


Figure 4: The beam loss before-and-after the global compensation

The BLM system for storage ring is outside the vacuum chamber, does not influence the machine operation and is reliable and cheap. It is really a useful new tool for beam life research.

REFERENCES

- [1] Cui Yonggang etc. Nuclear Techniques, Vol.25(2002), No.2, p. 95-98,
- [2] Li Yuxiong etc. NIMA 467-468(2001) p.80-83

NEW DESIGN OF THE TESLA INTERACTION REGION WITH $L^* = 5$ M

O.Napoly, J.Payet, CEA/DSM/DAPNIA, Saclay, France

Abstract

We study the main implications of increasing the last drift length l^* from 3 to 5 meters, in the TESLA interaction region: namely, the design of a new final focus system with a better chromatic correction, the extraction of the beam after the collision through the opposite doublet, and the new collimation requirements.

INTRODUCTION

Increasing the distance l^* between the final doublet and the interaction point (IP) to $l^* = 5$ m would be beneficial for the TESLA Interaction Region (IR) design. From the accelerator point of view, the superconducting final quadrupoles would move out of the large field (4 T) region of the detector solenoid, thus reducing the need for an optical correction of the solenoid effect on the beam. From the detector point of view, the forward acceptance would increase at low angles, the TPC (Time Projection Chamber) and calorimeter background created in the quadrupole cold mass would reduce, and it would offer the possibility of a lighter mask with a simpler support system.

In counterpart, a longer l^* raises three problems, mainly:

- the correction of the chromaticity created by the last doublet, which is proportional to l^*
- the extraction of the spent beam
- the extraction of the synchrotron radiation generated in the last doublet.

We successively discuss these three points.

THE FINAL FOCUS SYSTEM

By adopting the central idea of the NLC final focus system [1,2,3] – non-zero dispersion in the final quadrupole doublet to correct its chromaticity locally by inserting one sextupole between the quadrupoles – the performance of the chromatic correction can be greatly improved. However the NLC layout as such is not compatible with the TESLA head-on collision scheme. Indeed, a magnet free drift space of about 240 m is necessary to let the beamstrahlung cone be intercepted at the position of the beam dump [4].

Taking advantage of the superior chromatic correction, a new TESLA final focus system with $l^* = 5$ m has been designed, as displayed in Figure 1. Chromo-geometric aberrations are compensated at the second order by two pairs of interleaved sextupoles, each pair acting essentially in one plane. Within each pair, the transfer matrix R in the xy -plane between the sextupole located at the first (x -pair) or second (y -pair) maximum of the beta-functions, and the sextupole located in the last doublet has the form:

$$R = \begin{vmatrix} M & 0 & 0 & 0 \\ R_{21} & 1/M & 0 & 0 \\ 0 & 0 & M & 0 \\ 0 & 0 & R_{43} & 1/M \end{vmatrix},$$

where the non-zero terms are arbitrary. The second order geometric aberrations produced by the two vertical sextupoles are thus cancelled [2]. The dispersion in the doublet results in an angular dispersion $D'_x = 10$ mrad at the IP, to be compared with the $37 \mu\text{rad}$ beam angular spread. It also creates a sizeable the 2nd order dispersion which is cancelled by including a fifth sextupole at the upstream maximum of the dispersion function.

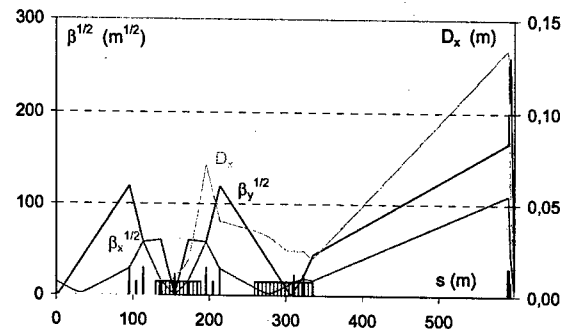


Figure 1: Optics of TESLA final focus with $l^* = 5$ m (NLC-like solution).

By optimizing the beta-waist position at the first dipole family, the horizontal emittance growth generated by synchrotron radiation is minimized to small fraction of the 10^{-11} m nominal emittance for the 400 GeV beam energy (Figure 2).

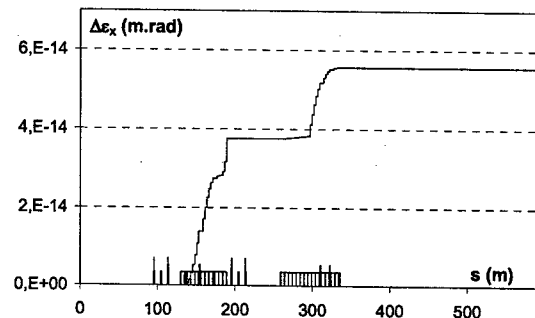


Figure 2: Horizontal emittance growth for the 400 GeV beam energy. Nominal emittance is 10^{-11} m.

An alternative optics solution (Figure 3) has also been studied where the smaller horizontal chromaticity is compensated in an upstream correction section like in the

TESLA TDR[4] design. In this 'hybrid' system, the two sextupole pairs are not interleaved. The IP second-order dispersion is cancelled by an intermediate dispersion bump which also reduces the angular dispersion at the IP to $D'_x = 2.6$ mrad.

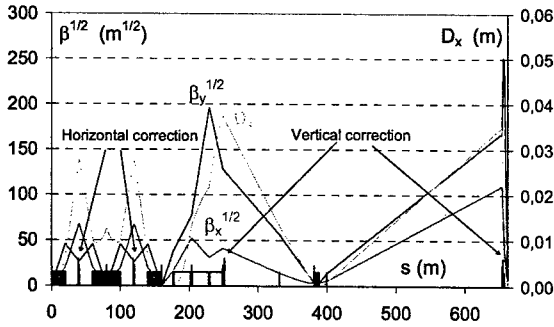


Figure 3: Optics of TESLA final focus with $l^* = 5$ m (hybrid solution).

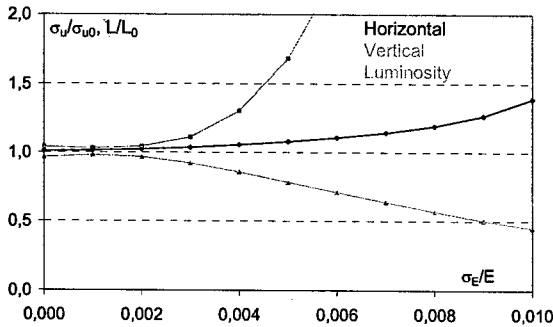


Figure 4: IP bandwidths of the $l^* = 5$ m final focus (NLC-like solution).

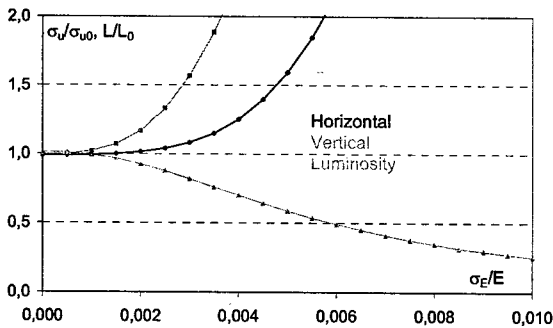


Figure 5: IP bandwidths of the $l^* = 5$ m final focus (hybrid solution).

The performance of the NLC-like and hybrid final focus systems are plotted in Figs.4,5 in terms of normalized beam sizes and luminosity (without beam-beam effect) as functions of the beam RMS energy spread σ_E/E . While both systems prevail over the TDR $l^* = 3$ m design, the NLC-like system is definitely superior. It is also the shortest and its only drawback is the larger IP angular dispersion D'_x .

THE SPENT BEAM EXTRACTION

The acceptance of the outgoing final doublet to particles originating from the point-like collision at a given angle can be defined by calculating the maximum angle θ_{\max} with respect to the beam axis for a particle to hit the doublet aperture as a function of its energy. Due to the doublet polarity, the tightest acceptance occurs when the IP emission is in the horizontal plane. These acceptances are compared in Figure 6 in the cases where $l^* = 3$ and 5 m assuming a doublet aperture diameter of 48 mm and a 4 T solenoid field applied over the first 4.5 m distance. The difference between the two curves is small and the $l^* = 5$ m weaker doublet is actually more efficient in extracting the low energy particles like the e^+e^- pairs and the e^\pm bremsstrahlung. Tracking simulations must be done to confirm this analysis.

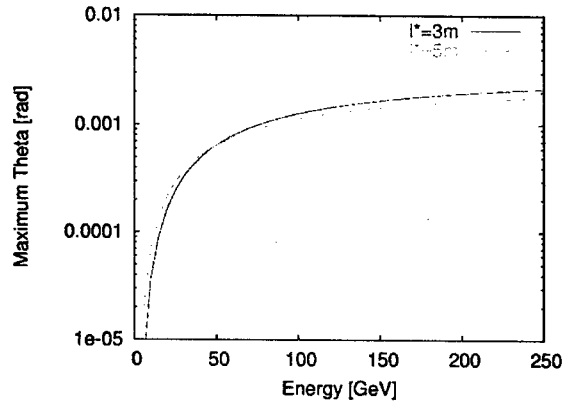


Figure 6: Angular acceptance in the horizontal plane of the outgoing final doublet as a function of particle energy.

THE COLLIMATION REQUIREMENTS

Extraction of the synchrotron radiation from the doublet regions for an incoming beam with a transverse extension of $8.6 \sigma_x \times 47.5 \sigma_y$ is shown in Figure 7.

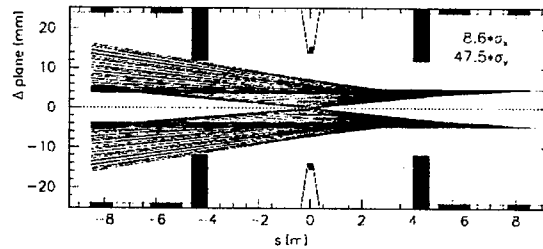


Figure 7: Diagonal stretch of the synchrotron radiation emitted by the final doublet through the opposite inner mask (black) and doublet apertures (hatched).

The collimation depths are set by the aperture and the position of the inner mask. A diameter of 24 mm at most is required to properly shield the vertex detector of 15 mm radius. Moving the mask away from the IP by 2 m along with the doublet is favourable for the detector point-of-view because it increases the low-angle coverage

and minimizes the weight of the overall detector mask. But, as shown by Table 1, the collimation requirements are indeed much tighter than in the TDR design. These tight collimation requirements should be met by an improved collimation optics using tail folding by non-linear elements (octupoles) [5].

Table 1: Beam collimation requirements for synchrotron radiation extraction.

	l^*	IP to Mask distance	Number of σ_x	Number of σ_y
TDR design	3 m	2 m	13	81
New design	5 m	4 m	8.6	47.5

The above collimation depths are derived from an analysis [6] which assumes nominal beam phase-space distributions at the IP and ignores the energy dimension. Taking the energy dependence into account is necessary, especially with a non-zero dispersion function in the doublet, but it should rely on realistic rather than ideal beam distributions. Therefore, once the TESLA-TDR collimation section has been matched to the entrance of the NLC-like final focus optics (figure 8), the 5D beam phase-space enclosed by the apertures of the energy and betatron spoilers is transported to the final doublet for on-momentum (figure 9) as well as off-momentum energies.

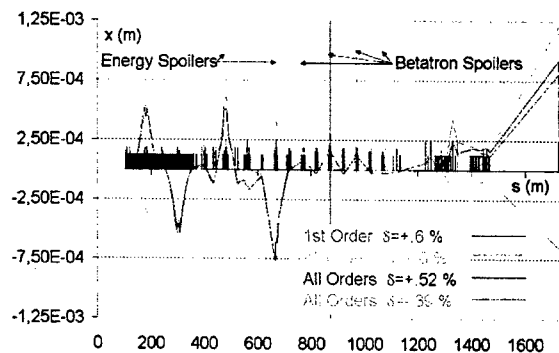


Figure 8: Off-momentum central trajectories through the TESLA beam delivery system.

The importance of doing the off-momentum transport to all orders by scaling the magnet strengths, rather than at the 1st order only, is highlighted by Fig.8 which shows that the higher order dispersion is large in particular in the betatron collimation section. Once the energy collimation depths are set for given apertures of the two energy spoilers, in the present case $[-0.52\%, +0.39\%]$, the extreme photon rays originating from the phase-space corners (red dots in Fig.9) are plotted through the IR apertures for a dense enough set of energy deviations within the energy window, and the betatron spoiler apertures are fine-tuned until the synchrotron ray pattern reproduces that of figure 7. In the present case, it ended

up in closing the one horizontal betatron spoiler in phase with the final doublet by about 30%. A wider energy collimation could result into more sizeable changes of the betatron spoilers.

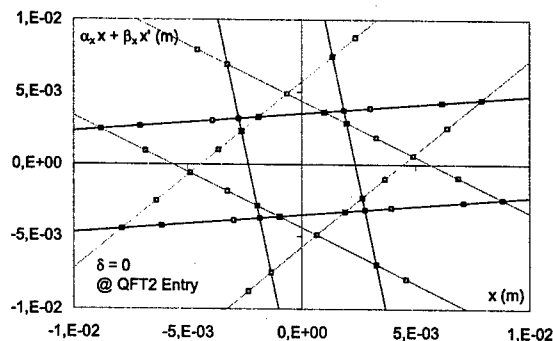


Figure 9: On-momentum horizontal phase-space enclosed by the collimation spoilers. Colours of the slits match those in Fig.8.

CONCLUSIONS

In order to upgrade the IR design of TESLA, the optics of a final focus system with $l^* = 5$ m has been studied. Two chromatic correction optics inspired by the new NLC final focus have been derived and their performance have been compared and found already superior to the previous $l^* = 3$ m design. The spent beam extraction of the new systems seems more favourable for low energy particles. The collimation depths are more stringent, as expected, and they might require adapting an octupole tail-folding optics into the collimation section. Using the collimation section designed for the TESLA TDR, the impact of energy deviations on the on-momentum aperture settings of the betatron spoilers has been studied by propagating the energy-dependent un-collimated phase-space to the final doublet and checking the synchrotron radiation stay-clear.

REFERENCES

- [1] P. Raimondi, A. Seryi, "Final Focus Design", SLAC, October 5, 2000.
- [2] P. Raimondi, A. Seryi, "Novel Final Focus Design for Future Linear Colliders", Physical Review Letters Vol. 86 Num.17 p 3779, April 2001.
- [3] P. Raimondi, "Chromatic Aberrations and their Corrections", Snowmass, July 2001.
- [4] "TESLA Technical Design Report", DESY 2001-011, March 2001.
- [5] R. Brinkmann, P. Raimondi, A. Seryi, "Halo Reduction by Means of Non Linear Optical Elements in the NLC Final Focus System", 2001 Particle Accelerator Conference, Chicago.
- [6] O. Napoly, "Collimation Depth Requirements for the TESLA IR", Saclay Preprint, DAPNIA/SEA-01-02 and TESLA Note 2001-18, 2001.

OPTIMUM CHOICE OF RF FREQUENCY FOR TWO BEAM LINEAR COLLIDERS

H.H. Braun and D. Schulte
CERN, Geneva, Switzerland

Abstract

Recent experimental results on normal conducting RF structures indicate that the scaling of the gradient limit with frequency is less favourable than was believed. We therefore reconsider the optimum choice of RF frequency and iris aperture for a normal conducting, two-beam linear collider with $E_{\text{CMS}}=3$ TeV, a loaded accelerating gradient of 150 MV/m and a luminosity of $8 \cdot 10^{34} \text{ cm}^{-2} \text{ s}^{-1}$. The optimisation criterion is minimizing RF costs for investment and operation with constraints put on peak surface electric fields and pulsed heating of accelerating structures. Analytical models are employed where applicable, while interpolation of simulation program results is used for the calculation of luminosity and RF structure properties.

INTRODUCTION

The rationale for the use of high frequency, normal conducting linac technology for linear colliders in the multi-TeV regime like CLIC [1] has been discussed in [2] and earlier by [3]. However, there it is assumed that the increase of obtainable accelerating fields with frequency as observed in the 3-12 GHz range [4] continues for even higher frequencies. This assumption was not confirmed by recent experiments [5], which indicate rather a saturation of the attainable field for an electric surface field-strength E_s of about 300 MV/m independent of frequency. Another important limitation comes from cavity surface damage due to pulsed surface heating ΔT by the magnetic RF surface field H_s . Recent measurements indicate that the pulsed heating must be limited somewhere in the range of 40 to 120 K for copper cavities [6]. Based on these informations the optimum RF frequency and accelerating structure iris opening a/λ in terms of costs is computed for a two beam linear collider like CLIC. The

center of mass energy E_{CMS} , mean accelerating gradient G and effective luminosity L_1 in a 1% energy bin are assumed to be those of the present CLIC design, i.e. 3 TeV, 150 MV/m and $3.3 \cdot 10^{34} \text{ cm}^{-2} \text{ s}^{-1}$.

ASSUMPTIONS

The assumptions below are used for the optimisation:

RF- structures

The structure geometry parameters are determined by the condition that for a given a/λ the cell geometry giving the highest shunt impedance R_s' for a surface to accelerating field ratio $E_s/G \leq 2$ should be chosen. To determine these geometries a large number of cases have been computed with the code URMEL. The results are compiled in table 1 with the definition of the geometry parameters in fig. 1. It is apparent that for larger apertures the cell-to-cell phase advance has to be decreased to keep the surface field small at the expense of reduced Q values. The cell parameters of table 1 are applied to the middle cell of the structure and the variation of R_s' and Q along the structure is neglected. Although the URMEL calculations as listed in table 1 are performed for cells without higher order mode damping, the effect of the damping is taken into account by applying a fudge factor of 0.8 to Q and a factor of 1.41 to H_s/G . These are typical values for the CLIC accelerating structures presently under consideration [7]. The length of the RF structure is determined by the requirements that the group velocity varies linearly along the structure, fulfilling the constant gradient condition for half the nominal beam current. The ratio of group velocity at the structure input to output is fixed to 3. These choices of parameters seem to be a good compromise for RF to beam efficiency, maximum field at zero beam current and technical feasibility.

Table 1 Travelling wave structure cell parameters, which give highest R_s' for $E_s/G \leq 2$. The parameters are given for a synchronous frequency of 30 GHz. The scaling behaviour with frequency is indicated in the 2nd row.

a mm	ϕ deg.	d mm	ϵ	B mm	E_s/G	H_s/G 1/k Ω	R_s' M Ω /m	R_s'/Q k Ω /m	Q	v_g/c %	$\sqrt{\langle W_r \rangle}$ kV/C/m ²	v_1 GHz
$1/\nu$	1	$1/\nu$	1	$1/\nu$	1	1	$\nu^{1/2}$	ν	$\nu^{-1/2}$	1	ν^3	ν
1.00	144	0.6	1.2	3.91	1.96	2.55	192.8	40.9	4714	0.6	1.85	46.03
1.25	144	0.7	1.4	3.98	1.97	2.75	165.0	35.3	4675	1.3	1.39	43.79
1.50	144	0.9	1.4	4.08	1.98	3.03	137.7	30.1	4574	2.0	1.05	41.68
1.75	135	1.0	1.4	4.22	2.00	3.24	115.2	26.7	4322	3.8	0.85	39.75
2.00	108	0.9	1.4	4.38	2.00	3.34	93.0	25.3	3681	7.6	0.76	38.13
2.25	90	0.9	1.4	4.57	1.97	3.62	69.2	22.2	3117	10.5	0.63	36.93
2.50	72	0.8	1.4	4.76	1.98	3.86	50.5	19.6	2582	13.3	0.52	36.12
2.75	72	0.9	1.8	5.00	2.00	4.21	41.2	16.4	2514	16.2	0.38	35.28
3.00	60	0.9	1.8	5.30	2.00	4.84	26.3	13.5	1945	17.9	0.29	34.48

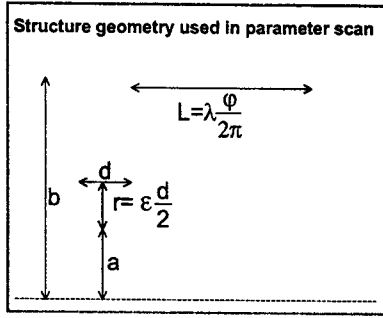


Fig. 1 Definition of geometry parameters for table 1.

Bunch charge and spacing

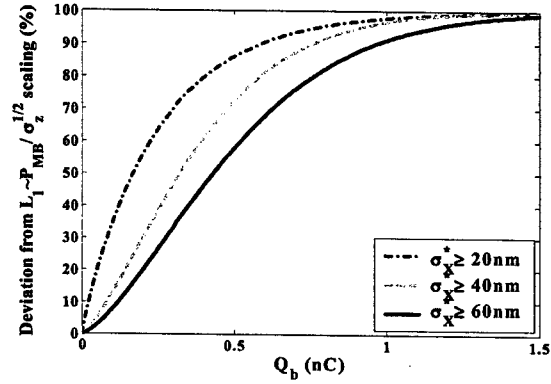
The bunch charge Q_B and bunch-length σ_z are optimised according to the criteria described in [8] with the constraints that the total energy spread is kept $\leq 1\%$ and the transverse short-range wakefield at a distance σ_z behind the bunch center is kept at a constant value taken from the present CLIC design. A gaussian bunch shape is assumed and the longitudinal and transverse short-range wakefields are computed with the formulae given in [9]. The RF phase is fixed at 12° off crest.

The bunch spacing is obtained by the requirement that the long-range wakefield strength should be kept constant. The rationale for this is, that for given linac length and alignment tolerance the emittance growth due to transverse wakefields should be approximately constant if the wakefield strength is kept constant. Since the bunch charge is already determined as described above, only the bunch spacing can be adjusted to fulfil this condition. This spacing is worked out by computing for each geometry of table 1 the rms strength $\sqrt{\langle W_T'^2 \rangle}$ and the 1st synchronous dipole mode frequency of the transverse long-range wakefield ν_1 with the code ABCI. These values are listed in the two last columns of table 1. Assuming an exponential damping in time with a damping time of $\tau = Q/\pi\nu_1$, where the quality factor of the first dipole pass-band Q is assumed to be 20, the bunch distance needed to keep the long-range wakefield strength constant at a reference value W_{REF} given by the present CLIC design can be estimated as:

$$\Delta t_B \approx \frac{\tau}{2} \log \left(\frac{\langle W_T'^2 \rangle}{W_{REF}^2} + 1 \right)$$

Luminosity

The effective luminosity L_I scales in the multi TeV regime like $\sim P_{MB}/\sigma_z^{1/2}$ if the vertical beam size at the IP σ_Y^* is kept constant and the horizontal beam size σ_X^* is adjusted to an optimum value [2]. P_{MB} is the mean power of the main beam. However, as pointed out in [8] this optimum value cannot be reached for all possible combinations of bunch charge and length due to limitations of the damping ring and the beam delivery system. Fig. 2 shows the deviation from this scaling as a function of bunch charge computed with the program GUINEA-PIG.


 Fig. 2 Deviation from $L_I \sim P_{MB}/\sigma_z^{1/2}$ scaling due to constraints on σ_X^* for $\sigma_Y^* = 0.7$ nm.

Pulse length and repetition rate

The pulse length is determined by the condition that the maximum pulsed surface heating is kept constant at $\Delta T = 80$ K and the repetition rate is adjusted in a manner to keep the effective luminosity L_I constant.

Costing

To estimate the dependence of overall costs on ν_{RF} and a/λ we assume that the dependency of main linac and tunnel costs on these quantities is small, since G and therefore the total linac length is kept constant. Implicitly it is also assumed that the strength of focusing systems and alignment tolerances are kept constant. Therefore the main cost dependence comes from the RF power source and here more specifically from the drive beam accelerator. The two main contributions are the costs for electricity and the investment costs for the RF source needed to power the drive beam accelerator. Supposing that the drive beam scheme is sufficiently flexible to have constant wall plug to (high frequency) RF efficiency $\eta_{plug-RF}$ of 40% [1], we compute the electricity costs for a ten-year period with 5000h of running a year as

$$C_E = P_{MB} / (\eta_{plug-RF} \cdot \eta_{RF-MB}) \cdot 5000h \cdot 10y \cdot 0.06 \text{ SFr/kWh}$$

With η_{RF-MB} the RF to main beam power transfer efficiency computed for each combination of ν and a/λ . For the power source investment it is assumed that the source can be broken up in klystron/modulator units delivering 4 kJ RF energy per pulse each, with a unit cost estimated from past experience [10] of

$$C_U = 1.725 \text{ MSFr} + 0.012 \text{ MSFr} \cdot \nu_R [\text{Hz}]$$

where ν_R is the repetition frequency. Hence the total investment cost for this power source is given by

$$C_I = C_U \cdot E_{CMS} \cdot Q_B \cdot N_B / (\eta_{RF-MB} \cdot \eta_{RFDM}) / 4 \text{ kJ}$$

With N_B the number of bunches per pulse and η_{RFDM} the drive beam RF to main beam RF power transfer efficiency. The present CLIC value of $\eta_{RFDM} = 68\%$ has been assumed. The total cost of the drive beam power source is given by

$$C_{\text{Total}} = C_E + C_I$$

RESULTS

Putting all together we get the drive beam power source cost as shown in fig. 3 and fig. 4. The curves in fig. 3 are computed without constraints on σ_x^* , while $\sigma_x^* \geq 60$ nm is imposed for the case shown in fig. 4. At the present status of the damping ring and beam delivery system design this latter case is the more realistic assumption. For each frequency the a/λ that minimises total costs has been chosen. In the unconstrained case this leads to a constant a/λ of 0.15. In the constrained case a/λ increases almost linearly from 0.15 at 14 GHz to 0.275 at 42 GHz. For the unconstrained case C_E is almost constant and C_I decreases monotonically with frequency. For the more realistic constrained case a flat cost minimum is achieved for the frequency range 22-26 GHz. Table 2 compares parameters that correspond to the cost minimum of fig. 4 with the present CLIC parameters*. The improvement in RF source cost is not dramatic, however, the optimised case has the additional advantage of reduced electric surface field and pulsed surface heating for the main linacs in comparison with the present CLIC reference design.

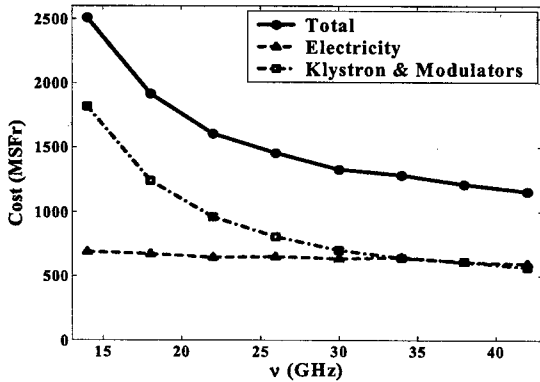


Fig. 3 Costs of power source with unconstrained σ_x^* .

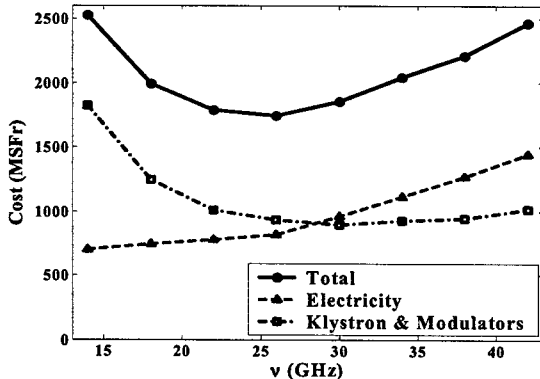


Fig. 4 Costs of power source with $\sigma_x^* \geq 60$ nm.

CONCLUSION

Although the faith that higher frequencies automatically lead to higher achievable accelerating fields has vanished in recent years, the argument that high frequencies are fa-

vourable for TeV class linear colliders is still valid for budget reasons. The optimum frequency depends on the limitations on the achievable IP beam size. In the CLIC case this optimum is at the present design state at about 22-26 GHz with an a/λ of 0.175-0.2. If progress in the design of the damping ring and beam delivery system allows for smaller IP beam size, this optimum will shift to higher frequencies. Further studies are necessary to investigate the impact of parameters on the other components of the drive beam complex, the injector chain, damping rings, main linacs and beam delivery system.

Table 2 Present CLIC and optimised parameters

	present	optimised
E_{CMS} (TeV)	3	3
G (MV/m)	150	150
σ_y^* / σ_x^* (nm)	0.7 / 60	0.7 / 60
L_1 (10^{34} cm 2 s $^{-1}$)	3.3	3.3
v_{RF} (GHz)	30	26
a/λ (averaged)	0.2	0.2
Q_B (nC)	0.64	0.92
σ_z (μ m)	35	44
Δt_B (ns)	0.66	0.77
T_{Puls} (ns)	103 ns	49 ns
v_{rep} (Hz)	100	150
P_{AC} (MW)	319	280
η_{RF-MB} (%)	23.1	24.6
C_E (MSFr)	890	820
C_I (MSFr)	1270	930
C_{Total} RF source (MSFr)	2160	1750

REFERENCES

- [1] The CLIC Study Team (edited by G. Guignard), "A 3 TeV e $^+$ e $^-$ Linear Collider Based on CLIC Technology," CERN rep. 2000-008
- [2] J.P. Delahaye, G. Guignard, T. Raubenheimer, I. Wilson, "Scaling Laws for e $^+$ e $^-$ Linear Colliders," CLIC Note 333, 1997 and Proc. 19th Int. Linac Conf., Chicago, 1998
- [3] R.B. Palmer, "The Interdependence of Parameters for TeV Linear Colliders," SLAC-Pub-4295, 1987
- [4] J. W. Wang, G. A. Loew, "Field Emission and RF breakdown in high-gradient room-temperature linac structures," Proc. Part. Acc. Conf, Chicago, 1989
- [5] S. Döbert, "Status of Very High-Gradient Cavity Tests," Proc. 21st Int. Linac Conf., Kyongju, 2000
- [6] D. P. Pritzkau and R. H. Siemann, "Results of an RF Pulsed Heating Experiment at SLAC," Proc. of 20th Int. Linac Conf., Monterey, 2000
- [7] W. Wuensch, private communication
- [8] D. Schulte, "Luminosity Limitations at the Multi TeV Linear Collider Energy Frontier," Proc. 8th Europ. Part. Acc. Conf., Paris, 2002
- [9] K. Bane, "Short-range Dipole Wakefields in Acc. Structures for the NLC," SLAC-PUB-9663, 2003
- [10] H. Frischholz and G. McMonagle, priv. comm.

* Same power source cost model has been applied for both cases.

PROGRESS IN THE DESIGN OF A DAMPED AND TAPERED ACCELERATING STRUCTURE FOR CLIC

J.-Y. Raguin*, I. Wilson and W. Wuensch
CERN, Geneva, Switzerland

Abstract

Two of the main requirements for CLIC 30 GHz accelerating structures are an average accelerating gradient of 150 MV/m and features which suppress long-range transverse and longitudinal wakefields. The main effects that constrain the design of a copper structure are a surface electric field limit of about 300 MV/m, from evidence produced by the CLIC high-gradient testing program, and a pulsed surface heating temperature rise limit estimated to be of the order of 100 K. The interplay between maximum surface electric field, maximum surface magnetic field, transverse-wakefield suppression and RF-to-beam efficiency has been studied in detail. Several structures with a 110° phase advance and rather constant peak surface electric field distributions have been designed. Different damping-waveguide geometries and waveguide-to-cavity couplings are compared.

1 INTRODUCTION

The choice of an average loaded gradient of 150 MV/m for the CLIC 30 GHz main linac accelerating structure and the necessity to suppress the wakefields result in large surface electric fields and pulsed surface heating temperatures. Minimizing these values has been chosen as key design criteria based on experimental observation of erosion due to RF breakdown [1] and calculation and observation of cracking due to pulsed surface heating [2, 3].

In our previous studies [4], a $2\pi/3$ -quasi-constant gradient 84-cell copper structure called XDS (conveX Damped Structure) was designed with an elliptical cross-section for the cell-to-cell irises. For a given iris thickness and radius, such a profile allowed to reduce the ratio of the peak surface electric field to the accelerating gradient E_{peak}/E_{acc} . Heavy damping of the higher-order modes to provide wakefields suppression was achieved by coupling each cell to a set of four identical radial T-cross waveguides. The convex outer-wall profile of the cells was optimized to reduce the ratio of the peak surface magnetic field to the accelerating gradient H_{peak}/E_{acc} (see Figure 1 for the topology of the cells). The maximum unloaded surface electric field decreased from 400 MV/m at the head of the structure to 320 MV/m at the end whereas the maximum unloaded temperature rise increased from 120 K to 154 K (with a 121 ns pulse length and assuming that the thermal and electrical conductivity as well as the thermal diffusivity is constant during the pulse length). These values present a substan-

tial improvement compared to the one of an older design [5] but are still too high for copper. The amplitude of the transverse wakefields at the second bunch was also too high (90 V/pC/mm/m).

To reduce further the peak surface electric and magnetic fields, a phase advance of 110° was selected along with a suitable tapering of the iris thickness and radius. Several geometries of the damping waveguide and of the waveguide-to-cavity coupling were jointly studied aiming at rather constant unloaded peak electric field and maximum temperature rise distributions along the structure as well as reduced amplitudes of the transverse wakefields. The main outcome of these studies is a 77-cell structure with a peak surface unloaded electric field of about 350 MV/m, a constant pulsed heating temperature rise of about 120 K, an RF-to-beam efficiency of 24 % and an amplitude of the transverse wakefields of 45 V/pC/mm/m at the second bunch.

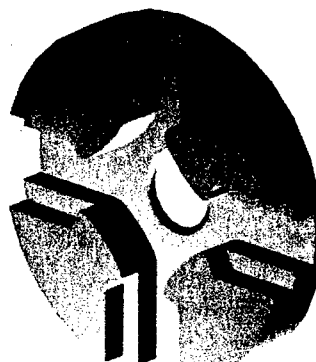


Figure 1: Topology of the XDSs cell and damping waveguides.

2 SOME DESIGN CONSIDERATIONS

The parametric studies performed on constant-impedance classical accelerating structures (no damping waveguides) [6] showed that, for a fixed iris radius and thickness, E_{peak}/E_{acc} is reduced when the phase advance is lowered. However, the shunt impedance also decreases, which has the adverse effect of reducing the RF-to-beam efficiency. A 110° phase advance is therefore considered as a good compromise between a $\pi/2$ phase advance, which would lead to a structure requiring a higher input power, and the $2\pi/3$ phase advance adopted in [4]. The 110° phase advance is also advantageous since, for an

* now with Paul Scherrer Institute, CH-5232 Villigen PSI, Switzerland.

iris thickness ranging from 0.8 mm to 0.55 mm and an iris radius varying between 1.5 mm and 2.0 mm, the H_{peak}/E_{acc} ratios do not vary too much from their $2\pi/3$ phase advance values.

Unlike the studies reported in [4], the new XDSs have iris thicknesses that are kept constant or decrease linearly along the structure. However, the iris radius is still tapered linearly from 2.0 to 1.5 mm. In the absence of damping waveguides, H_{peak}/E_{acc} decreases then strongly along the structure. The waveguide-to-cell couplings can therefore be increased along the structures while maintaining H_{peak}/E_{acc} within acceptable values. Consequently, the cell Qs of the lowest dipole band also decrease along the structure.

3 DESIGN STUDIES

The first 110° phase advance structure (XDSa) design has a cell-to-cell iris radius varying linearly from 2.0 mm to 1.5 mm, as in [4], and a constant iris thickness of 0.8 mm. The cross-section of the tip of the irises is elliptical and has an eccentricity of 1.8. The damping T-cross waveguides are dimensioned so that the cutoff frequency of the first propagating mode is 32.3 GHz, above the 29.985 GHz fundamental but below all the higher order modes. The waveguide-to-cell coupling irises are identical all along the structure and are 3.0 mm wide. E_{peak}/E_{acc} varies from 2.21 for the first cell to 1.80 for the last cell. The optimization of the convex outer-wall shape, a combination of straight and elliptical sections, gives a ratio H_{peak}/E_{acc} which decreases from 4.50 mA/V to 4.21 mA/V for the first and last cells, respectively. The variation of Q , R'/Q and v_g/c is summarized in Table 1.

Table 1: Fundamental mode parameters of the first, middle and last cell – XDSa

	Q	R'/Q (k Ω /m)	v_g/c (%)
First cell	3387	24.1	7.66
Middle cell	3342	27.9	5.24
Last cell	3292	32.1	3.25

The unloaded peak surface electric fields of the first and last cells are equal when the structure consists of 65 cells whereas the unloaded maximum temperature rises are similar for 90 cells (see Figure 2). The variation of the RF-to-beam efficiency with the number of cells shows a maximum of 26 % for 122 cells. For an 83-cell structure, the peak surface electric field decreases from 349 (first cell) to 316 MV/m (last cell), the pulsed temperature rise increases from 121 to 130 K and the RF-to-beam efficiency is 25 %. The dipole Qs computed with GdfidL [7] for the lowest dipole band are 53, 45 and 40 for the first, middle and last cell, respectively, giving an amplitude of the transverse wakes at the second bunch of 65 V/pC/mm/m.

To improve the damping of the transverse dipole modes, a 110° phase advance structure (XDSb) has been designed such that the width of the waveguide-to-cell coupling iris increases from 3.0 mm for the first cell to 3.2 mm for the

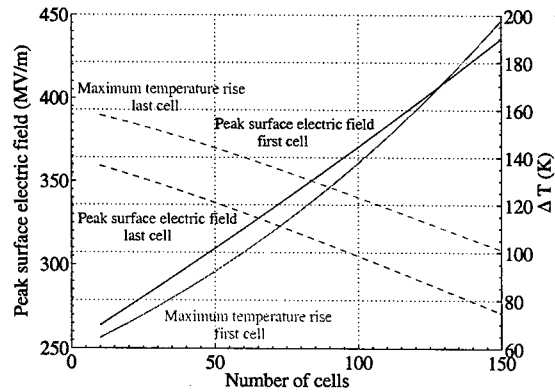


Figure 2: Unloaded peak surface electric field and maximum temperature rises for the first (—) and last cells (---) vs. number of cells – XDSa.

last one. With a variation of the iris thickness from 0.8 mm to 0.55 mm, the minimum thickness that ensures mechanical rigidity, the ratio H_{peak}/E_{acc} is equal to 4.17 mA/V for the last cell, slightly lower than in XDSa. E_{peak}/E_{acc} of the last cell increases to 2.00. Due to the tapering of the cell-to-cell iris thickness, the T-cross damping waveguides have to be designed for each cell. The dimensions were chosen so that the cutoff frequency of the their fundamental mode is 32.3 GHz. Table 2 shows the Q , R'/Q and v_g/c for the middle and last cells, the first cell being identical to the one of the XDSa.

Table 2: Fundamental mode parameters of the first, middle and last cells – XDSb

	Q	R'/Q (k Ω /m)	v_g/c (%)
First cell	3387	24.1	7.66
Middle cell	3379	28.4	5.61
Last cell	3365	33.2	3.84

Compared with the XDSa, the slower decrease of the ratio E_{peak}/E_{acc} combined with a similar variation of the ratio H_{peak}/E_{acc} presents the advantage that there is a range of number of cells for which both the unloaded peak surface electric field and the maximum temperature rise are rather constant along the structure (see Figure 3). For an 83-cell structure, the peak surface electric field is about 355 MV/m and the maximum temperature rise is 122 K. The RF-to-beam efficiency is about 25 % whereas a 130-cell structure would have the maximum efficiency of 27 %.

Due to the increase of the waveguide-to-cell iris width, the Qs associated with the lowest dipole band are now 31 and 24 for the middle and last cells. The amplitude of the transverse wakefields at the second bunch is reduced to 58 V/pC/mm/m.

A better damping of the transverse dipole modes can be achieved by increasing further the coupling between the cells and their damping waveguides. An increase of the waveguide-to-cell coupling iris width would however lead to higher H_{peak}/E_{acc} ratios. A second approach consists in suppressing the rounded transition between the coupling

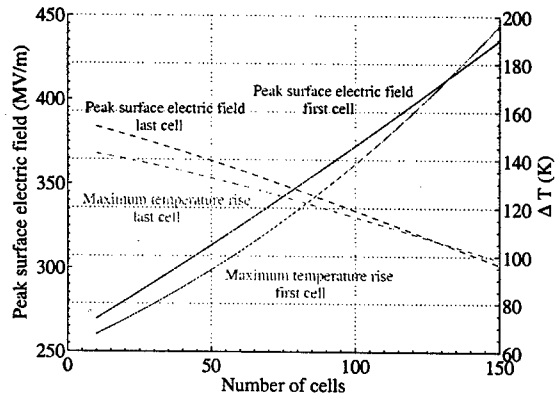


Figure 3: Unloaded peak surface electric field and maximum temperature rises for the first (---) and last cell (—) vs. number of cells – XDSc.

iris and the waveguide. A structure (XDSc) based on this later consideration (see Figure 4) has been designed, the variation of the cell-to-cell iris thickness and of the width of the waveguide-to-cell-coupling iris along the structure being the same than for the XDSc.

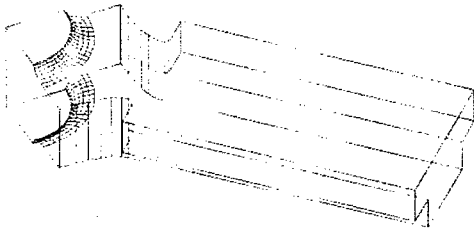


Figure 4: Geometry of the XDSc first cell and damping waveguide.

With a more realistic copper conductivity of 5.51×10^6 , a reduction of 5 % compared to the conductivity used in the design of the previous structures, the ratios E_{peak}/E_{acc} are 2.20 and 1.95 for the first and last cells whereas H_{peak}/E_{acc} decreases from 4.51 mA/V to 4.10 mA/V. The Q , R'/Q and v_g/c for the first, middle and last cells are presented in Table 3.

Table 3: Fundamental mode parameters of the first, middle and last cell – XDSc

	Q	R'/Q (kΩ/m)	v_g/c (%)
First cell	3266	24.0	7.61
Middle cell	3260	28.4	5.58
Last cell	3252	33.0	3.83

The unloaded and loaded accelerating gradient and peak surface electric field profiles for a 77-cell structure are shown in Figure 5. The distributions of the peak unloaded surface electric fields and temperature rises are still rather constant, the maxima being 347 MV/m and 122 K, respectively. The RF-to-beam efficiency is 24 % and the required input power per section is 125 MW.

The dipole Qs associated with the lowest dipole band are now 43, 27 and 21 for the first, middle and last cells, and the

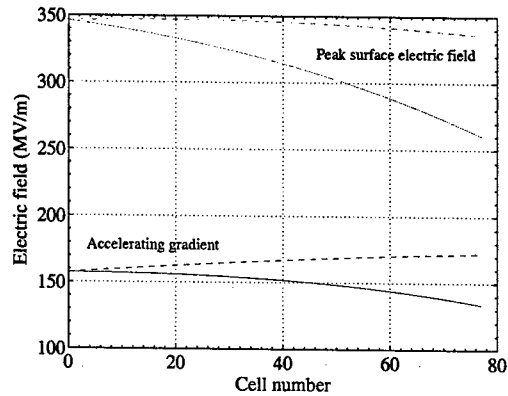


Figure 5: Unloaded (---) and loaded (—) accelerating gradients and peak surface electric fields – XDSc.

amplitude of the transverse wakefields at the second bunch is 45 V/pC/mm/m.

The computed peak surface electric fields are still above the tolerable limit for copper (of the order of 300 MV/m [1]) but seem acceptable for molybdenum [8]. The design of a new structure with cell-to-cell molybdenum irises shows RF performances [9] similar to the one given above. The high pulsed temperature rises are still however an unresolved issue.

4 ACKNOWLEDGEMENTS

The authors are indebted to W. Bruns for having performed computations of the structures with the code GdfidL.

5 REFERENCES

- [1] H. H. Braun, S. Döbert, I. Syratchev, M. Taborelli, I. Wilson and W. Wuensch, "CLIC High-Gradient Test Results", to be published in Proc. LINAC 2002, Gyeongju, and CLIC-Note 535, CERN, 2002.
- [2] I. Wilson, "Surface Heating of the CLIC Main Linac Structure", CLIC-Note 52, CERN, 1987.
- [3] D. P. Pritzkau and R. H. Siemann, "Experimental study of rf pulsed heating on oxygen free electronic copper", *Phys. Rev. ST Accel. Beams*, vol. 5, 112002, 2002.
- [4] J.-Y. Raguin, D. Schulte, I. Syratchev, I. Wilson and W. Wuensch, "A New Damped and Tapered Accelerating Structure for CLIC", to be published in Proc. LINAC 2002, Gyeongju, and CLIC-Note 536, CERN, 2002.
- [5] I. Wilson and W. Wuensch, "The CLIC Main Linac Accelerating Structure", Proc. LINAC 2000, pp. 419-421, Monterey, 2000.
- [6] H. H. Braun, <http://ps-div.web.cern.ch/ps-div/CLIC/>, CLIC Structures Working Group, Meeting of 5-3-2001.
- [7] W. Bruns, "The GdfidL Electromagnetic Field Simulator", www.gdfidl.de.
- [8] W. Wuensch, H. Braun, S. Döbert, I. Syratchev and I. Wilson, "A Demonstration of High-Gradient Acceleration", these proceedings.
- [9] A. Grudiev, private communication.

MAIN LINAC EMITTANCE GROWTH AND LUMINOSITY IN FUTURE LINEAR COLLIDERS

D. Schulte, CERN, Geneva, Switzerland

Abstract

Wakefield and dispersive effects in the main linac of a future linear collider can strongly affect the beam-beam interaction at the collision point [1]. For a static situation, this paper investigates the luminosity for realistic bunches in the case of the TESLA, NLC and CLIC projects assuming different degrees of collision optimisation. A part of this work was performed for the International Linear Collider Technical Review Committee [2].

INTRODUCTION

Future linear colliders require very small beam sizes at the interaction point (IP) in order to achieve high luminosity. The high density of each beam at collision leads to the creation of a strong electro-magnetic field which focuses the oncoming beam. The beam-beam interaction is strong enough to actually change the beam size during the collision, which results in an increase of the luminosity by a factor of typically 1.5–2 compared to the case without beam-beam forces. However, the deflection of the beam particles leads to the emission of beamstrahlung, which is similar to synchrotron radiation. Many of the electron-positron collisions will thus take place with a centre-of-mass energy lower than the nominal value. To minimise this effect but still obtain high luminosity flat beams are used in which the horizontal RMS beam size σ_x is much larger than the vertical σ_y , see the parameters in Table 1.

The strength of the beam-beam interaction can be conveniently described using the disruption parameters $D_{x,y}$:

$$D_{x,y} = \frac{2Nr_e\sigma_z}{\gamma\sigma_{x,y}(\sigma_x + \sigma_y)} \quad (1)$$

Here, N is the number of particles per bunch, σ_z the RMS bunch length and r_e the classical electron radius. For large D the beam-beam effects are important while for $D \ll 1$ the each beam acts as a thin lens. In the proposed machines one finds $D_x \ll 1$ and $D_y \gg 1$, so we will concentrate on the vertical plane.

For large D , it has been found that taking into account the full 6-dimensional correlation of the beam distribution for the simulation of the beam-beam collision is very important [1]. In the case of TESLA (with an older parameter set) a very small emittance increase of about 1% could lead to 20% luminosity reduction, if the beam-beam collision is not optimised.

In the following, the possibility to restore the luminosity by optimising collision offset and angle of the two beams is

investigated. Also the effect on the beamstrahlung is considered. Since in many physics experiments only the fraction of the luminosity with a centre-of-mass energy close to the nominal value $E_{cm,0}$ is of interest, the luminosity \mathcal{L}_{peak} , which contains all collisions with $\Delta E_{cm}/E_{cm,0} < 0.01$ is introduced as a figure of merit. Of particular interest are TESLA because of its high disruption parameter and CLIC at $E_{cm} = 3$ TeV because in this machine the beam-beam effect is so strong that many particles loose the major part of their energy through beamstrahlung and hence experience a much larger effective disruption than indicated in table 1.

SIMULATION PROCEDURE

All projects foresee a certain budget for the emittance growth due to imperfections from the damping ring to the IP (from the beginning of the linac to its end, in case of CLIC). As a simplification, it is assumed in the following that all emittance growth is due to the main linac. Relatively complex beam-based alignment techniques are foreseen to minimise this effect. In the simulation we replace these techniques by a simple one-to-one steering and scale the imperfections such that we achieve an aver-

Table 1: Some beam parameters at the interaction point of the different machines. In the case of CLIC the transverse sizes are obtained by fits, since the beam distribution is not very Gaussian. The beam consists of trains of n_b bunches, which are delivered with a repetition frequency f_r . In case of NLC and CLIC the luminosities \mathcal{L}_0 differ slightly from those in [2] because the latter allow for some other effects. The disruption parameters D_x and D_y are calculated using the nominal emittance at the IP, these are in case that the emittance growth is completely uncorrelated.

	unit	TESLA	NLC	CLIC	CLIC
N	$[10^9]$	20	7.5	4	4
σ_z	$[\mu\text{m}]$	300	110	35	35
σ_x	$[\text{nm}]$	554	243	204	60
σ_y	$[\text{nm}]$	5.0	3.0	1.2	0.7
E	$[\text{GeV}]$	250	250	250	1500
f_r	$[\text{Hz}]$	5	120	200	100
n_b		2820	195	154	154
\mathcal{L}_0	$[10^{34}\text{m}^{-2}\text{s}^{-1}]$	3.4	2.1	2.3	8.0
P_b	MW	11.3	7.0	4.9	7.4
D_x		0.22	0.16	0.04	0.07
D_y		24.8	12.8	6.6	6.3

Table 2: The emittances used (initial and final in the vertical plane) and the misalignments used to mimic the static errors of the machines. After application of the errors only a one-to-one correction was performed. If more sophisticated beam-based alignment schemes were used, much larger errors would be permitted.

	unit	TESLA	NLC	CLIC	CLIC
ϵ_x	[μm]	10	3.6	2	0.68
$\epsilon_{y,i}/\epsilon_{y,f}$	[nm]	20/30	20/40	5/10	5/10
σ_{BPM}	[μm]	25	5.0	0.72	0.4
σ_{cav}	[μm]	500	12.5	8.0	4.5
σ'_{cav}	[μrad]	300	100	8.0	4.5

Table 3: Luminosities found for all machines, before correction (\mathcal{L}_0), after offset optimisation (\mathcal{L}_{off}) and after further angle optimisation (\mathcal{L}_{angle}).

	unit	TESLA	NLC	CLIC	CLIC
\mathcal{L}_0	[$10^{34}\text{m}^{-2}\text{s}^{-1}$]	3.4	2.1	2.3	8.0
\mathcal{L}_1	[$10^{34}\text{m}^{-2}\text{s}^{-1}$]	2.2	1.8	2.2	7.4
\mathcal{L}_{off}	[$10^{34}\text{m}^{-2}\text{s}^{-1}$]	2.5	2.1	2.5	7.9
\mathcal{L}_{ang}	[$10^{34}\text{m}^{-2}\text{s}^{-1}$]	3.3	2.2	2.6	8.1

age emittance growth equivalent to the budget. The relative sizes of the imperfections—misalignment of the beam-position monitors (BPMs) and the structures and tilt of the structures—are chosen to represent the performance of the more complex alignment algorithm. Table 2 lists the initial and final emittances and the alignment errors used. It should be noted that the emittance varies from machine to machine and that only the average of the machines simulated is consistent with the budget.

The emittance growth in the main linac is simulated using PLACET [3]. Then the mean beam angle and offset are corrected before the beam is transported through the beam delivery system, also using PLACET. A number of machines with different seeds for the random number generators are simulated and their angle and offset at the IP are corrected. Pairs of these beams are fed into the beam-beam simulation code GUINEA-PIG [4].

In the optimisation, first the relative offset of the two colliding beam is varied as to maximise luminosity. Then the vertical crossing angle is modified, this certainly can change the projected emittance. Several options exist to achieve such a modification; here we just modify position and crossing angle at the IP without worrying about the actual implementation.

Since the beam-beam collision is not very stable, in particular in the case of TESLA, the convergence of the beam-beam simulation has to be carefully checked, details can be found in [5].

AVERAGE TOTAL LUMINOSITY

The luminosities found in the simulation are compared to the target values in table 3. In case of NLC and CLIC

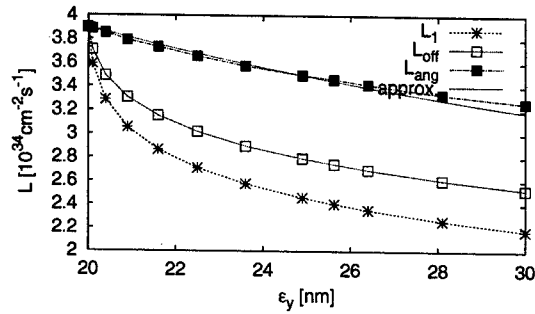


Figure 1: The luminosity as a function of the emittance at the end of the linac in the case of TESLA. For comparison, the expected luminosity using the simple scaling $\mathcal{L} \propto \sqrt{\epsilon_y}$ is also shown.

the achieved values are not far from the goal even without performing an offset and angle optimisation. In the case of TESLA the optimisation is essential. In all cases the achieved luminosity is consistent with the design value. A second iteration of the very simplistic optimisation procedure leads to a very small further improvement. The two parameters offset and angle seem thus quite orthogonal.

In TESLA it was foreseen to longitudinally move the beam waist slightly before the collision point, since this yields higher luminosity [6]. A further optimisation was therefore attempted for TESLA. First the waists of both beams were longitudinally moved in a symmetric fashion, then in an asymmetric way. The improvement was tiny, about 2%, without correlation it raised the luminosity by about 15% from $3.0 \times 10^{34}\text{cm}^{-2}\text{s}^{-1}$ to $3.4 \times 10^{34}\text{cm}^{-2}\text{s}^{-1}$. It remains to be investigated if a better procedure could yield better performance.

One can conclude that all projects can on average about achieve the target luminosity if the design emittance goal can be met. Within limits, the emittance can serve as a reasonable measure to predict the luminosity after performing the optimisation. This is exemplified in Fig. 1, which shows the luminosity in the most interesting case of TESLA as a function of the emittance at the IP. Before optimisation, a small growth leads to large reduction in luminosity. After full optimisation the luminosity seems to scale as $\mathcal{L} \propto \sqrt{\epsilon_y}^1$.

MACHINE-TO-MACHINE VARIATIONS

The luminosity of an individual beam-beam collision can be predicted from the emittances of the two beams with a limited precision. The dependence $\mathcal{L} \propto 1/\sqrt{\epsilon_{y,1} + \epsilon_{y,2}}$ is only approximately valid, see Fig. 2 for TESLA. Here the actual distribution needs to be taken into account.

The realistic beam distributions not only affects the to-

¹It should be noted that for larger variations of the vertical emittance the beam-beam interaction is also affected and the simple $\mathcal{L} \propto \sqrt{\epsilon_y}$ does not hold true, this is independent of whether the correlations are taken into account or not.

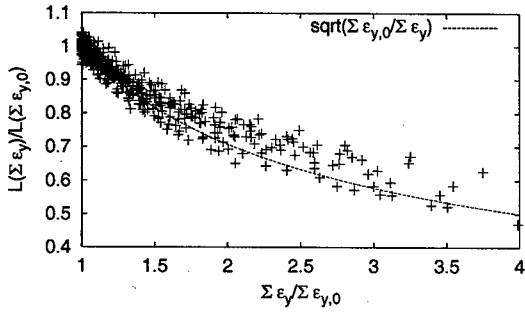


Figure 2: The luminosity of the individual collisions as a function of the sum of the two vertical emittances (TESLA).

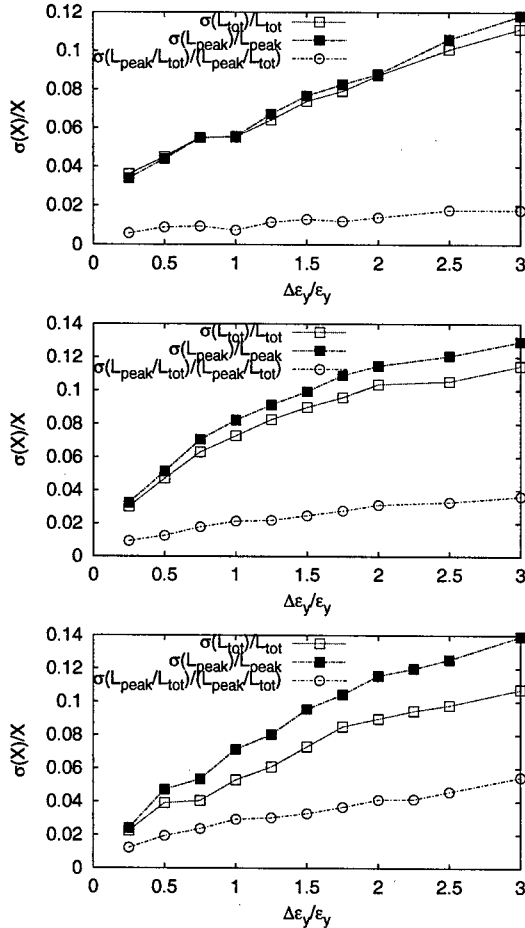


Figure 3: RMS-fluctuations of the luminosity as a function of the emittance growth in the main linac for TESLA, NLC and CLIC (at $E_{cm} = 3$ TeV), respectively.

tal luminosity but also the amount of beamstrahlung radiated by the beams and thus the luminosity spectrum. If two beams collide with a small vertical offset they emit more beamstrahlung. In the case of realistic beams, fractions of them will actually collide with an offset which might yield more beamstrahlung and affect the luminosity \mathcal{L}_{peak} close to the nominal centre-of-mass energy.

Above, the alignment errors in the main linac were chosen to yield an average emittance growth equal to the budget. In the following, the sizes of these errors are determined for each individual machine to yield exactly the target emittance. This allows to determine the RMS fluctuation of the luminosity for machines with the same emittance.

For the average total luminosity the results are similar to the previous ones, the emittance budgets are consistent with the target luminosities. The change of the ratio $\mathcal{L}_{peak}/\mathcal{L}_{tot}$ due to the emittance growth is small, less than 1% in all machines. But, as can be seen in Fig. 3, the RMS luminosity variations of the individual machines increases with the emittance growth; in the case of CLIC at $E_{cm} = 3$ TeV the beamstrahlung adds significantly to the variations of \mathcal{L}_{peak} .

CONCLUSION

In the strong beam-beam interaction regime a very small emittance increase can lead to a large luminosity reduction. It has been shown that this strong reduction can be cured by optimising the collision offset and angle. This requires a luminosity monitor and sufficiently stable beam conditions. In this case one can first optimise the collision offset and then the angle to recover most of the lost luminosity. Dynamic imperfections may be too fast to allow the use of a luminosity monitor and can therefore stay problematic, see also [7]. After optimisation, the ratio of the luminosity close the nominal centre-of-mass energy to the total one $\mathcal{L}_{peak}/\mathcal{L}_{tot}$ does on average not depend strongly on the correlated emittance growth, but the RMS fluctuation from machine to machine do.

REFERENCES

- [1] R. Brinkmann, O. Napoly and D. Schulte. CLIC-Note 505 (2001).
- [2] The International Linear Collider Technical Review Committee is headed by G. Loew. SLAC-R-606 (2003).
- [3] E. D'Amico, G. Guignard, N. Leros, D. Schulte. CERN/PS 2001-028 (AE).
- [4] D. Schulte. CERN/PS 99-014 (LP).
- [5] D. Schulte. CLIC-Note 544 (2002).
- [6] D. Schulte. PhD. thesis. TESLA 97-08 (1996).
- [7] A. Seryi et al. This conference.

BUNCH-TO-BUNCH ENERGY STABILITY TEST OF THE NB PROTOTYPES OF THE TESLA SUPERSTRUCTURE

V. Ayvazyan, P. Castro, R. Kammering, H. Schlarb*, S. Schreiber, J. Sekutowicz, S. Simrock, M. Wendt, (DESY), M. Hüning (FNAL), M. Ferrario (INFN)

Abstract

Two 2x7-cell Nb superstructures have been tested with beam during the last TESLA Test Facility (TTF) linac run in summer 2002. The structures have been operated at 2 K in the standard TTF cryomodule and have been installed in the linac after the injector. We report on the bunch-to-bunch energy stability test which showed that energy stored in the superstructure could be refilled in the time between two passing bunches. The goal to keep the bunch-to-bunch energy stability below $5 \cdot 10^{-4}$ has been achieved.

INTRODUCTION

An alternative layout of the TESLA linear collider [1, 2, 3], is based on weakly coupled multi-cell superconducting structures, called the superstructures (SST). The weak coupling of 0.04% between the multi-cell structures, the subunits, is achieved by connecting the cavities with $\lambda/2$ tubes. This has two advantages: it reduces significantly the investment cost due to a simplification the RF system and secondly increases the filling factor of the main accelerator. The fundamental power coupler (FPC) supplying the entire chain of subunits with 1.3 GHz RF is mounted at one end of the SST. The energy flow through the superstructure is controlled by means of cold tuners allowing to balance the stored energy and thus the accelerating gradient in each subunit. Unlike a standard multi-cell cavity, the accelerating mode in a SST is the π -0 mode – π cell-to-cell phase advance and 0 subunit-to-subunit phase advance – which is below cut-off in the interconnecting tubes. This allows to attach higher order mode (HOM) couplers at the interconnection, in the middle of the multi-cell structure. In this way, good damping of parasitic modes can be maintained, avoiding extensive heating of the HOM couplers.

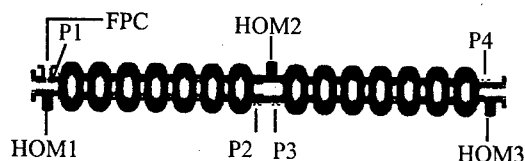


Figure 1: Scheme of a 2x7-cell Nb superstructures.

After several RF test on warm copper models of the superstructure [3] the next step was to study the performance of niobium SST's at 2 K with beam. In summer 2002, two 2x7-cell superstructures, sketched in Fig. 1, have been in-

stalled in the TESLA Test Facility linac to address the following questions:

- balancing the acceleration field in subunits,
- damping of the higher order modes,
- achievable energy stability of the electron beam.

In this paper, we address the third item the refilling process in cavities with high beam loading. A detailed description of the mechanical layout, the cavity tuning, and the HOM damping in a superstructure can be found elsewhere [4, 5]. Numerical simulations of the transient state and the bunch-to-bunch energy spread predict that there is enough time to refill the cells energy before the next bunch arrives. The computed bunch-to-bunch energy deviation for a 2x7-cell and a 2x9-cell (preferred design in TESLA TDR) are shown in Fig. 2. For all bunches in the train the computed

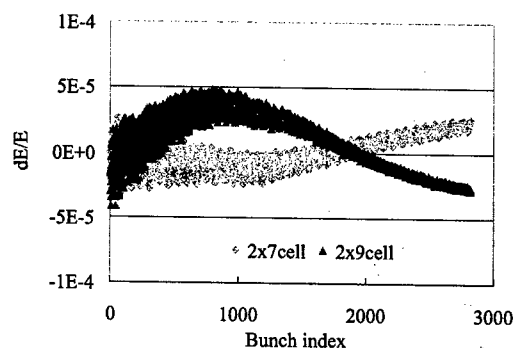


Figure 2: Computed energy deviation for the TESLA beam: 2820 bunches, 3.2 nC/bunch, spacing 337 ns.

variation for both versions of the SST was very small, less than $\pm 5 \cdot 10^{-5}$. The difference in shape of the two curves is due to the different mode beating.

EXPERIMENTAL SETUP

The TTF photo injector is based on a normal conducting laser driven L-band RF gun and a single superconducting 9-cell cavity boosting the beam energy to 15.3 MeV. The beam is then accelerated by two acceleration modules. High resolution energy spectrometer are situated at the injector and the end of the linac (see Fig. 3). For this experiment, two 2x7-cell superstructures (SST-1 and SST-2) have been installed after the photo-injector. They have an active length of 3.26 m. Unfortunately, the second acceleration module with eight standard 9-cell super-

*schlarb@desy.de

conducting cavities has been installed after the superstructures but before the spectrometer. For the energy stability measurements, the SST's have been operated at a gradient of 14.3 MV/m, while the cavities in the second cryomodule were detuned to reduce their influence. This results in a total energy E_{tot} of 62 MeV at end of the linac. The bunch spacing was 1 μ s to meet the highest possible data acquisition rate of the front-end electronics allowing to sample parameters for each bunch in a pulse train. Bunch charges of typically 4 nC (nominal 8 nC) and beam durations between 530 μ s and 760 μ s (nominal 800 μ s) at 1 Hz repetition rate have been chosen to achieve the required operation stability for this experiment.

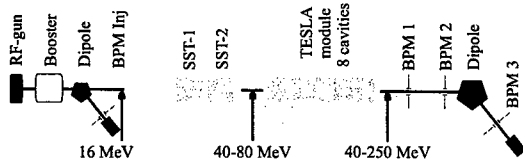


Figure 3: Scheme of TTF linac for the SST test.

MEASUREMENT OF FIELD PROBES

A flat energy distribution of the bunches in a macro-pulse train does not necessarily prove a proper refilling of the weakly coupled subunit. A reduced gradient in one subunit may have been compensated by overfilling the other. This would have been possible, since the low level RF system (LLRF) controls the phase and amplitude of the vectors sum of all cavities and not of each cavity individually. Using the signals of all four field probe (P1-P4 in Fig. 1) the gradients can be monitored at the entrance and the exit cells of both cavities. An example recorded with 4 mA beam current and 530 μ s pulse duration is shown in Fig. 4. Without the energy refilling the beam would take almost 70% of the energy stored in cells and the voltage would drop by 45%. No such phenomenon was observed. All probes show noise fluctuations mainly caused by the down-converters of

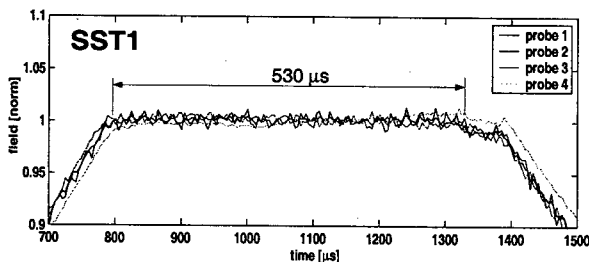


Figure 4: Signals from field probes P1-P4 measured during acceleration of 530 bunches ($I = 4$ mA, $g = 14.3$ MV/m).

the LLRF-system (250 kHz oscillations).

BEAM ENERGY STABILITY

The TTF linac layout does not provide the possibility to measure the beam energy spread before and behind the SST simultaneously. Therefore the energy stability of the beam exiting the injector had to be carefully studied. The goal was to measure bunch to bunch energy variations with a resolution well below 0.01%. It was also necessary to examine effects of the second acceleration module even through their cavities have been detuned.

Energy jitter from the photo-injector

Because the energy gain in the SST is set to be 47 MeV only, phase and amplitude jitter of the laser, the RF gun or the booster cavity might seriously spoil the energy measurement for the SST. After tuning the injector parameters properly, a beam energy spread of 0.09% during a time period of 30 min has been achieved. The bunch to bunch energy variation for 100 macro-pulses are plotted in Fig. 5. The energy $E_{i,m}$ of the i^{th} bunch in the m^{th} train can be

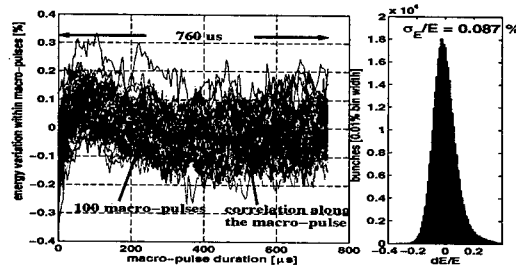


Figure 5: Left: Injector bunch-to-bunch energy variation of 100 macro-pulses (color curved). Right: Energy spread of for all bunches ($E = 15.3$ MeV).

decomposed as

$$E_{i,m} = E_{inj} + \Delta E_m + \Delta E_{corr,i} + \delta E_{i,m} \quad (1)$$

with E_{inj} the average energy of all bunches, ΔE_m the energy deviation of the m^{th} macro-pulse train, $\Delta E_{corr,i}$ the energy time correlation common in all macro-pulses (black curve in Fig. 5) and $\delta E_{i,m}$ a residual fast bunch-to-bunch energy jitter. Only the later contribution is critical for our purpose. The rms widths of $\delta E_{i,m}$ amounts to 6.7 keV (see Tab.1) and sets the lower limit on the σ_E/E_{tot} measurement at the end of the linac to $1.1 \cdot 10^{-4}$.

Accuracy of the energy measurement

The energy variation of the bunches is calculated by means of two strip-line BPMs upstream the spectrometer dipole to correct for the incoming orbit jitter (see Fig.3) and BPM3 located in the spectrometer line with large dispersion ($\eta_x = -1.48$ m). All BPMs have been calibrated by steering the transverse position of the beam in the BPMs with well known dipole corrector. The control software

calculates online the energy of all bunches in the entire bunch train and compensates for the non-linear response of the BPMs for large beam offsets [8]. The accuracy of the BPMs has been determined to be $60 \mu\text{m rms}$ [9] resulting in a relative energy resolution of $\sigma_{E, \text{res}}/E_{\text{tot}} = 1.2 \cdot 10^{-4}$.

Influence of the second acceleration module

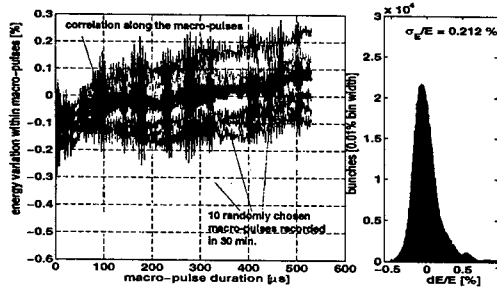


Figure 6: Energy deviation along a pulse train measured in the spectrometer ($I = 3.8\text{mA}$, $t = 530\mu\text{s}$).

Fig. 6 shows typical energy distributions of pulse trains recorded in 30 minutes. The overall energy spread of the beam amounts to 0.2%. The contributions split according to Eq. 1 are listed in Tab. 1. The dominating contribution of the energy spread comes from the macro-pulse to macro-pulse energy jitter. Unlike the smooth energy distribution observed in the injector, very fast oscillations are superimposed to slow low frequency drifts across the pulse trains. A careful analysis of the energy spectrum obtained by Fourier, shown in Fig. 7, states that the largest part of the fast oscillations are induced by the eight detuned cavity. The resonance at 250 kHz is identified as an uncompleted removal of the down-converter noise perturbing the LLRF-regulation. A couple of other smaller resonances are related to the feedback gain of the LLRF feedback loop. Some of the resonances are strongly enhanced if high gains between 50 and 100 are adjusted. This increases the energy spread within the macro-pulse but reduce the energy jitter from pulse train to pulse train. The presented data are taken at a loop gain of 30 (small). If the influence of 2nd acc. module is removed by using an approximation depicted by the dashed lines in Fig. 7, a relative rms energy spread within the 1800 macro-pulses of $4.2 \cdot 10^{-4}$ is calculated. If only 100 macro-pulses with the smallest drifts are taken into ac-

Table 1: Contributions of energy spread at the injector ($E_{\text{inj}} = 15.3\text{MeV}$) and at the end of the linac ($E_{\text{tot}} = 61.5\text{MeV}$)

	$\sigma(\Delta E_m)$	$\sigma(\Delta E_{\text{corr},i})$	$\sigma(\delta E_{m,i})$	σ_E
inj	10.1 keV	5.5 keV	6.7 keV	13.4 keV
tot	122.9 keV	32.9 keV	25.4 keV	130 keV

count one finds $2.2 \cdot 10^{-4}$ as the lowest achieved value for the intra macro-pulse energy deviation of the bunches.

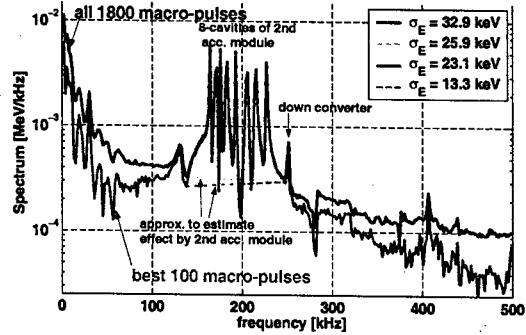


Figure 7: Spectrum of the energy modulation.

SUMMARY

In this experiment with 2×7 -cell superstructures we achieved a bunch-to-bunch energy stability in macro-pulses of 0.064% for more than 30 minutes. Significant influences of the second acceleration module and the LLRF on the measurement have been found, while investigation on the incoming energy jitter from the injector states that these influences can be neglected. The upper limit for the bunch-to-bunch energy deviation caused by the cavities of the superstructures only has been estimated to be $\sigma_E/E = 2.2 \cdot 10^{-4}$, well below the TESLA specification of 0.05%.

REFERENCES

- [1] "TESLA Technical Design Report, Part II: The Accelerator", DESY 2001-011, Hamburg; March 2001.
- [2] J. Sekutowicz et al., "Superconducting Superstructure", Proc. of LC97, Zvenigorod, Sep. 29-Oct. 3, 1997.
- [3] J. Sekutowicz et al., "Superconducting superstructure for the TESLA collider; A concept", PR-ST A.B, 1999.
- [4] J. Sekutowicz et al., "Active HOMs Excitation in the First Prototype of Superstructure", Proc. of PAC03, Portland, May 12-16, 2003.
- [5] P. Castro et al., "Analysis of the HOM damping with Modulated Beam in the First Prototype Superstructure", Proc. of PAC03, Portland, May 12-16, 2003.
- [6] J. Sekutowicz et al., "A Superstructure for High Current FEL Application", Proc. of PAC03, Portland, May 12-16, 2003.
- [7] M. Ferrario et al., "Multi-Bunch Energy Spread Induced by Beam Loading in a Standing Wave Structure", Par. Accel., Vol. 52, 1996.
- [8] N. Sturm, "Energie-Stabilisierung für den Freien Elektronenlaser an der TESLA-Test-Anlage" Diploma Thesis, DESY 2002, Hamburg.
- [9] H. Schlarb, "Collimation System for a VUV Free-Electron Laser at the TESLA Test Facility", DESY-THESIS-2001-055.

SIMULATIONS OF THE TESLA LINEAR COLLIDER WITH A FAST FEEDBACK SYSTEM

D.Schulte, CERN; N.Walker, DESY; G.White, Queen Mary, University of London

Abstract

The tolerances on the beams as they collide at the interaction point of the TESLA linear collider are very tight due to the nano-metre scale final vertical bunch spot sizes. Ground motion causes the beam to increase in emittance and drift out of collision leading to dramatic degradation of luminosity performance. To combat this, both slow orbit and fast intra-train feedback systems will be used. The design of these feedback systems depends critically on how component misalignment effects the beam throughout the whole accelerator. A simulation has been set up to study in detail the accelerator performance under such conditions by merging the codes of PLACET, MERLIN and GUINEA-PIG, together with Simulink code to model feedback systems, all under a Matlab environment.

INTRODUCTION

All of the proposals for the future Linear Collider (LC) require similarly challenging final beam spot sizes: TESLA [1] 5nm, NLC/JLC [2] 2.7nm and CLIC [3] 1nm, are the proposed vertical bunch spot sizes at the IP. This places very rigorous stability requirements on all three designs. The most severe tolerance is for the final focusing quadrupole magnets. To keep the luminosity loss to within a few percent at TESLA, the beams need to be kept in collision to within about 10% of the vertical beam spot size. This implies a tolerance on the final quadrupoles of 0.1nm. The limiting factor for stability along the beamline of TESLA is that of ground motion. There has been a considerable effort undertaken into the study of the magnitudes and effects of ground motion at different possible sites for the LC which are covered in detail elsewhere[4]. If uncorrected, ground motion causes a total loss of luminosity within seconds through beam misalignment and emittance growth[4]. To combat this, a program of passive and active support systems to stabilise the beamline elements, together with different levels of beam-based feedback systems, is being pursued.

Three levels of beam-based feedback system are being developed. A slow orbit correction feedback will adjust the beam trajectory periodically to compensate for low frequency ground motion. An inter-pulse feedback acts in a few locations to correct accumulated errors that occur in between the action of the slow system, and also to provide the possibility of straightening the beam. Finally, a fast intra-train feedback system acting at the IP keeps the beam in alignment, correcting for high frequency cultural ground motion moving the final quadrupoles. For TESLA, a second intra-train system will be used further upstream to additionally remove any incoming angle jitter which also

leads to a loss in luminosity. Fig. 1a shows the results of a GUINEA-PIG [6] simulation of the expected luminosity loss for gaussian bunches as a function of vertical beam offset at the IP.

BEAM SIMULATIONS INCORPORATING FAST-FEEDBACK SYSTEMS

The fast feedback systems are designed to remove beam jitter that occurs at frequencies comparable with the repetition rate of the machine by measuring the first few bunches in the train and correcting the following bunches within that train. The bunch structure thus dictates the operating requirements for the system. For NLC/CLIC designs there are 192/154 bunches per train separated by 1.4/0.7 ns. TESLA will have 2820 bunches separated by 337 ns. The NLC/CLIC case requires a much more aggressive design requiring, at present, a purely analogue electronic approach. The TESLA scheme allows for a more complex digital based algorithm to be employed. Simulations of the fast feedback systems are written in the Matlab/Simulink environment. The feedback system for TESLA is implemented as per the TESLA TDR [5]. This consists of an IP feedback operating within the TESLA interaction region, consisting of a BPM approximately 3m downstream of the IP and a fast stripline kicker downstream of the final focusing quadrupole doublet. The system relies on the beam-beam kick behaviour shown in fig.1b, where the nm scale offsets give rise to a large angular kick leading to a measurable BPM signal of many $\mu\text{m.s}$. TESLA also requires a fast angle feedback system to counter incoming angle jitter at the IP. The system uses fast stripline kickers placed at the IP phase 850m upstream of the IP to cancel the orbit offset in a BPM 450m downstream with a 90° phase advance. Three kickers are used to give a maximum correction of $10\sigma_y$ at the IP to the $0.1\sigma_y$ level assuming a BPM resolution of $2\mu\text{m}$.

SIMULATION OF THE TESLA FAST FEEDBACK SYSTEM

For TESLA, a simulation has been put together under Matlab of the TESLA collider from the exit of the damping rings through to the IP, including the beam-beam interaction and the fast feedback systems. This brings together the codes of PLACET [7], MERLIN [8] and GUINEA-PIG together with the purpose written feedback code. This allows the effect of 'banana' bunches caused by short-range wake-field effects in the accelerating structures to be accounted for. This has been found to be an important effect- the vertical emittance growth of just 1-2% naively would give a

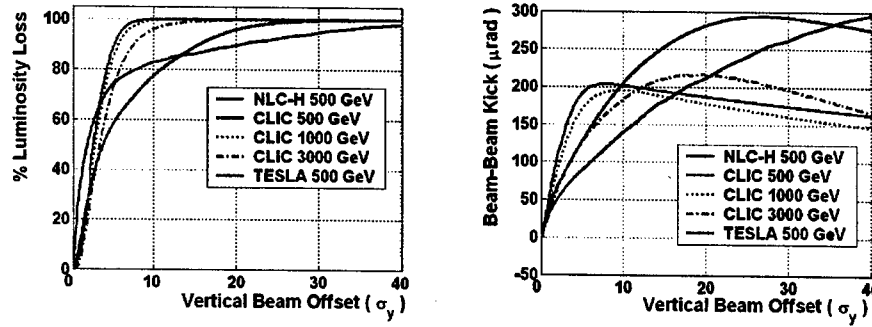


Figure 1: (a) Luminosity loss as a function of vertical beam offset with gaussian beams for TESLA, NLC and CLIC. (b) The beam-beam kick angle as a function of beam offset.

luminosity loss of just a few percent. However, due to the strong beam-beam effect, simulations with GUINEA-PIG have shown that the banana bunch effect can lead to a much larger degradation in luminosity, factors of 2-3 down on the nominal luminosity have been simulated [9]. In addition to a large drop in luminosity, the beam-beam dynamics are also altered with the banana shaped bunches. Fig. 2 shows the expected luminosity of colliding 2 'banana' bunches with offsets in y and y' in the $[-2 : 2]\sigma_{y,y'}$ range. With gaussian beams, the optimal collision parameter is with a zero y, y' offset. With the banana bunches this changes, so that a non-zero offset is now optimal. The blue region shaded in fig. 2 shows where the feedback system will settle by default. The angle system still settles at zero, but the IP feedback system will settle with a small non-zero y offset which, desirably, is always slightly in the direction of optimal luminosity. To optimise the luminosity, it is required that the feedback system now have an additional luminosity feedback element which locates the optimal collision parameters in y and y' . Previous studies [5] have indicated that by using the first layer of the TESLA LCAL system to count the coherent e^+e^- pairs created in the beam-beam interaction, a signal proportional to luminosity could be made available to the feedback system on a bunch by bunch basis.

There is huge parameter space to be explored with such simulations, and it is desirable to compare different parameter sets with as much statistics as possible. Each run of the full simulation takes tens of hours on a single modern CPU. In order to make maximum possible use of each simulation run, all data is stored each time. Summary data is stored of the run, e.g. luminosity, dE/dL , beam parameters at the IP as a function of bunch number and so on. Also, the entire incoming and outgoing beam particles at the IP are kept along with 4-vectors of background particle species formed in the beam-beam collision. Namely, the e^+e^- coherent pairs, photons, hadronic background and mini-jets. An on-going project is to deploy the simulation on a dedicated multi-cpu cluster at QMUL which exists as part of the UK Particle Physics GRID project.

A SAMPLE SIMULATION RUN

Described here is a single seed from an example run of 500 bunches, showing the operation of the feedback system in the presence of banana bunches. The parameters of this run are:

PLACET: This code simulates the passage of the beam through the TESLA Linac. It is set up to give, on average, the design TESLA luminosity after beam-based alignment has been performed. 500 bunch seeds are then generated with an injection error of RMS $0.2\sigma_y, \sigma_{y'}$ in the vertical axis. To simulate fast ground motion that occurred between trains, the quadrupoles are also randomly offset in the vertical plane with an RMS of 70nm representing a worse-case high frequency ground motion component from measured data at the DESY site[4].

MERLIN: This is responsible for transporting the representation of the beam through the TESLA Beam Delivery System. Vertical Random jitter on quads of 70nm RMS are added. A 0.14% RMS energy jitter was added to the electron bunches to simulate their passage through the positron source undulator. There were 80,000 macro particles per bunch tracked through MERLIN and passed on to GUINEA-PIG which calculates the beam kicks and backgrounds as well as the luminosity data.

Feedback: BPM resolutions of $2\mu\text{m}$ for the angle feedback and $5\mu\text{m}$ for the IP feedback system were assumed, and kicker errors of 0.1% RMS bunch-bunch were also assumed. An algorithm simulating the PI control system was tuned on 2 test bunches to provide stable rejection of noise at the $0.1\sigma_{y,y'}$ level. The PI controller is modelled as the discrete transfer function: $\frac{a_0 z + a_1}{z - 1}$ where the controller coefficients for the IP feedback are 0.135 and -0.001664 for a_0 and a_1 respectively. This is obtained from the PI algorithm,

$$u_{PI}(k) = K_P e(k) + K_I \sum_{j=0}^{k-1} e(j),$$

where e is the incoming error (beam kick) signal to be nulled, K_I is a constant which defines the steady-state response, and K_P provides the fast initial response to the error signal. These are tuned to provide the fastest possible error correction whilst keeping the fast jitter to below the

0.1 σ level. The angle feedback controller coefficients are set to 0.168 and -0.1256 guided by similar constraints as the IP feedback system. This system has a naturally slower response due to the 10 bunch latency arising from the large kicker-BPM separation.

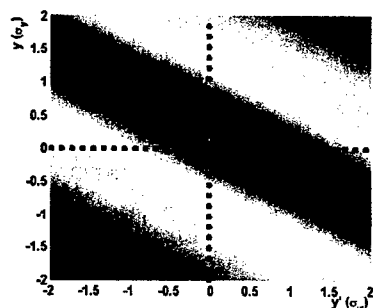


Figure 2: Luminosity as a function of vertical position and angle beam offset at the IP. The blue shaded area depicts the area that the feedback system automatically corrects to.

Fig. 3 shows the feedback systems bringing the beams into angular alignment over the first 150 bunches. The beam fluctuates substantially for about the first 100 bunches until the HOM's are damped in the LINAC. Feedback is performed by steering the positron beam only. This reduces bunch-bunch noise enhancement by the feedback system. In the inset to fig. 3 it can be seen how the feedback system enhances high frequency uncorrelated jitter in the beam. There is a 10 bunch latency of the angle feedback system due to the kicker-BPM separation. The system is assumed to then settle down to its 'zero' position after the 150 bunch mark. The simulation then uses a luminosity monitor signal corresponding to the first LCAL layer to optimise the collision parameters- this is simulated as the number of e^+e^- pairs passing through an annulus, radius of between 1.2 and 6.2cm at a distance of 220cm after being tracked through a 4T solenoid field. It was found to be optimal to integrate the luminosity signal over 10 bunches to avoid statistical luminosity fluctuations. Fig. 4 shows the operation of the luminosity feedback system in conjunction with the IP feedback system. One beam is ramped past the other in 0.1 σ_y steps and the corresponding LCAL signal is found, the BPM input signal corresponding to this maximum signal is then passed to the PI feedback controller as a set-point allowing this optimal collision parameter to be held. The same procedure is applied to the angle system after the y-position is re-established. The luminosity as a function of bunch number is shown in fig. 5.

REFERENCES

- [1] R. Brinkmann. Proc. EPAC 1998
- [2] T. Raubenheimer (ed.). SLAC Report 474.
- [3] J. P. Delahaye et al. Act.Phys.Polon.B30(2029-2039).

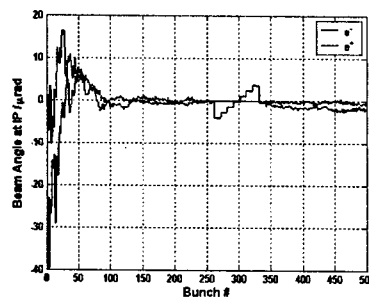


Figure 3: Beam vertical angle at the IP for the first 500 bunches at TESLA with fast feedback.

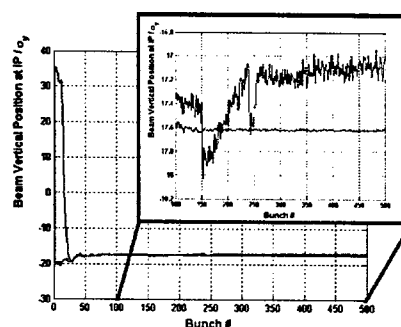


Figure 4: Beam vertical position at the IP for the first 500 bunches at TESLA with fast feedback.

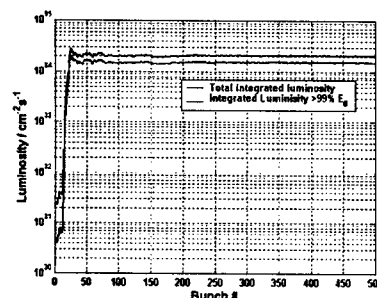


Figure 5: Total integrated luminosity and luminosity within 1% of 500GeV energy peak.

- [4] N. Walker, A. Walski, 'Luminosity stability issues for the TESLA Beam Delivery System.' TESLA 2000-22 Oct. 2000.
- [5] http://tesla.desy.de/new_pages/TDR_CD/PartII/accel.html
- [6] D. Schulte, DESY-TESLA-97-08, 1997.
- [7] <http://dschulte.home.cern.ch/dschulte/placet.html>
- [8] <http://www.desy.de/merlin/>
- [9] D. Schulte, Nanobeams Workshop 2002 "Update on banana simulations".

SIMULATIONS OF THE STATIC TUNING FOR THE TESLA LINEAR COLLIDER

D. Schulte, CERN, Geneva, Switzerland
N. Walker, DESY, Hamburg, Germany

Abstract

At the heart of the TESLA linear collider are the two 10 km long superconducting linacs. A linac is constructed from 858 cryomodules each containing 12 nine-cell 1.3 GHz superconducting cavities. 355 quadrupoles provide the necessary beam focusing. The advantages of low-frequency superconducting RF in terms of wakefield behaviour are well known, and the TESLA alignment tolerances are relatively loose. However, the effects of cavity tilts and their impact of the linac beam-based alignment algorithms have until recently not been fully investigated. In addition, the strong sensitivity to correlated emittance growth due to the high beam-beam disruption parameter makes it desirable to control the linac emittance down to a few percent. In this report we discuss various static tuning algorithms and present new simulation results. Discussions of the relative merits and applicability of the methods is also discussed.

INTRODUCTION

TESLA is a proposal for a e^+e^- linear collider with an initial centre of mass energy range up to 500 GeV, with a possible upgrade to 800 GeV, and a design luminosity of $3 \times 10^{34} \text{ cm}^{-2} \text{ s}^{-1}$ (at 500 GeV) [1]. The linac technology is based on 1.3 GHz superconducting RF. Each 10 km linac is constructed from 858 cryomodules containing 12 nine-cell niobium cavities. The focusing (beam transport) is provided by a regular 60° FODO lattice with 355

quadrupoles. As within any of the proposed future linear colliders, a major challenge is the preservation of the tiny vertical emittance ($\gamma\epsilon_y \sim 2 \times 10^{-8} \text{ m}$ for TESLA) from the damping ring to the interaction point (IP), and in particular in the main linac. Table 1 lists the *luminosity* tolerances and the expected achievable *installation* tolerances. The luminosity tolerances indicate the level of alignment precision required to achieve (on average) the goal luminosity. The installation tolerances represent those believed achievable in the real machine. The relatively low frequency superconducting RF has the advantage of relatively weak wakefields, which is reflected in the corresponding cavity luminosity tolerance which can be achieved during construction and installation. The luminosity tolerances for the cavities are based on the TDR transverse wakefield [1] which has since been superseded by a more accurate calculation [2], indicating a transverse wakefield 30% weaker than previously thought; this should lead to a reduction of the wakefield induced* emittance growth by 60%.

Chromatic (dispersive) effects from offset quadrupoles and orbit deviation are the dominant source of emittance growth in TESLA; this is particularly true at the entrance of the linac where there is a large uncorrelated energy spread of ~3% resulting from the bunch compressor. The strength of the effect is reflected in the BPM offset luminosity tolerance of 25 μm (table 1); this should be compared to the expected installation tolerance of ~360 μm^\dagger .

In the past, so-called dispersion free steering (DFS) [4] has been extensively studied as the primary beam-based alignment method. However, in the results reported in [1] and [2], the effects of the cavity tilts were not included, as well as other 'realistic' errors such as beam jitter. A more complete study of the TESLA linac performance has since been made [5], where a complete set of realistic errors (including the cavity tilts) have been modelled using the LIAR code [6]: the average emittance growth was ~140% after DFS, which is several factors more than the previously reported results.

In this paper we will review new simulation results of beam-based alignment for the TESLA linac, including the new transverse wakefield potential, with specific emphasis on the ballistic alignment technique [7], where the average emittance growth is observed to be ~30%.

* It is actually misleading to talk about emittance growth from wakefields and dispersion separately, since the two are coupled.

$\dagger \sqrt{200^2 + 300^2} \approx 360 \mu\text{m}$

Table 1: Component tolerances for the TESLA main linac. The *luminosity tolerances* are those random RMS values which result (on average) in the budgeted emittance growth after one-to-one linac steering. The *installation tolerances* are those accuracies to which the components are expected to be installed; these numbers are used in the simulations. Units are μm and μrad .

		reference axis	RMS tolerance
<i>Luminosity tolerance</i>			
BPM	offset	ref. line	25
cavities	offset	ref. line	500
	tilt	ref. line	300
<i>Installation tolerance</i>			
quadrupole	offset	cryomodule	300
structure	offset	cryomodule	300
	tilt	cryomodule	300
BPM	offset	cryomodule	200
	resolution	-	10
cryomodule	offsets	ref. line	200

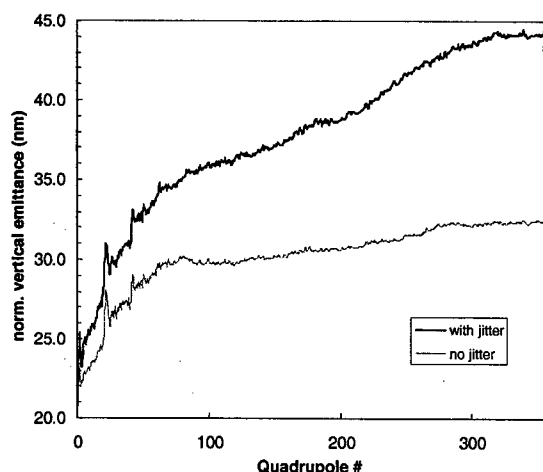


Figure 1: Results of simulating DFS on the TESLA linac (average over 100 seeds). The black line shows results with a stable; the magenta line shows the effects of $\sim 1\sigma$ beam jitter. In both cases BPM noise was included ($10 \mu\text{m RMS}$).

BEAM-BASED ALIGNMENT METHODS

Dispersion Free Steering (DFS)

As its name implies, DFS attempts to find a trajectory which minimises the dispersion generated. This is achieved by finding an orbit which minimises the difference orbit when either the beam energy or the lattice strength is modified. In the absence of cavity misalignments or other 'external fields' which can kick the orbit between the quadrupoles, there is no conceptual difference between changing the quadrupole strengths and modifying the beam energy. However, when we consider the effects of cavity steering, then it is important to use the energy method in order to get a 'true' dispersion measurement (merely changing the quadrupole strengths does not 'measure' the dispersive kicks from the cavities).

The method adopted in [5] divided the linac into a number of overlapping sections or *bins* (typically 20 quadrupoles with an overlap of 10). DFS is then applied to each bin in turn. For each bin, the upstream energy was varied by $\sim 20\%$ and the difference orbit measured. With the additional knowledge of the optics an orbit can be found which minimises the measured difference.

DFS suffers from several problems:

- In the presence of BPM noise, the exact solutions typically result in an absolute orbit which exhibits a long wavelength bowing with very large unrealistic amplitudes. This tendency must be compensated by constraining the resulting orbit to be within the expected absolute alignment error of the BPMs.
- The upstream energy is modified by changing either phase or amplitude of the upstream cavities. In the presence of cavity alignment errors (particularly tilts), this causes a steering of the

beam which – if not corrected for – will confuse the measurement of the 'dispersive' orbit.

- Similarly incoming random beam jitter must be compensated, or averaged away.

Figure 1 shows the results of applying DFS to the TESLA linac using the simulation code PLACET [7]. Specifically, the plot shows the effects of upstream beam jitter on the results (upper curve); in this case two BPMs at the entrance to each bin were used to fit out the incoming oscillation. The degree to which this can be achieved depends on the BPM resolution assumed ($10 \mu\text{m RMS}$). The results indicate that the jitter is responsible for a factor $\sim 3/2$ in emittance growth, and would appear to explain some of the discrepancy between the TDR results and those reported in [5].

Ballistic Alignment (BA)

In ballistic alignment [8], a reference line is established by first turning off all the components (quadrupoles, cavities, correctors) within a given section, and then allowing the beam to 'coast' through that section. Assuming that there are no other fields which can influence the beam, the BPM readings define a straight line (to within the BPM resolution) to which the beam is re-steered after components are restored to their original values. As with DFS the linac is divided into bins, but unlike DFS they are not overlapped. To prevent the corrected orbit 'walking away', the ballistic BPM readings are first linearly corrected to arbitrarily zero the last BPM in the current bin; this BPM acts as a pivot location or node, where the straight ballistic reference lines are allowed to have an angle. Figure 2 shows schematically a section of linac after ballistic alignment. For the case of perfect BPMs (zero resolution), the remaining dispersive kicks are simply given by the angles at the section boundaries (α_i). The effect of BPM noise is indicated by the red dotted line in figure 1.

The main advantages of BA over DFS are:

- since a single pulse can be used to determine the ballistic trajectory, the method is relatively insensitive to upstream beam jitter;
- there is no 'fit' in the process which may be numerically unstable (as is the tendency in DFS);
- notwithstanding remnant fields, the components are either off, or at their nominal settings, so the motion of the magnetic centres (for example) with excitation is not a problem.

The main disadvantage is the control of the beam during the ballistic measurement. Turning off 7 FODO cells and the associated RF causes a large β -beat, and a large energy error ($\Delta E \sim 7 \text{ GeV}$, corresponding to $\sim 300\%$ in the worst case at the beginning of the linac). If left uncorrected, the downstream orbit would also perform large amplitude oscillations which could damage the linac. TESLA does have the advantage of relative large apertures (70 mm diameter), and in practise, the alignment would probably start with all the RF off and the entire lattice scaled to the initial energy of 4.6 GeV . As

each section is ballistically aligned (and the RF in that section turned on), the remaining downstream linac will be scaled to the new energy. In addition feedback will be used to maintain the downstream orbit. Further simulations of the control of the beam are needed to determine the maximum allowed length of ballistic section – particularly in the first linac sections where the effects are likely to be most dramatic.

Another possible issue which also affects DFS performance is that of BPM resolution. Initial beam-based alignment is likely to be at reduced beam power to protect the linac from possible damage; this means either a significant reduction in the number of bunches or a reduction in single bunch charge or (most likely) both. This may have a significant impact on the BPM performance. Reduction of the bunch charge will also affect the wakefields, although in TESLA this is probably not an issue.

In principle, the transverse wakefields will define the 'straightness' of the ballistic trajectory. In CLIC simulations [8] the ballistic process is generally iterated to converge to the final desired orbit. The current simulations suggest that no such iteration is required for TESLA, as the wakefield effects on the ballistic orbit are small.

The performance of the ballistic method depends on:

- The size of the node angles α_i , the typical size of which depend on the expected BPM offsets, and the length of the ballistic sections (L_b);
- The resolution of the BPMs.

For the current simulations, bins of 14 quadrupoles were taken (7 cells, or a total phase advance[†] of $7\pi/3$) corresponding to a length of ~ 410 m in the low energy section of the linac. A BPM single-shot resolution of $10 \mu\text{m}$ was also used.

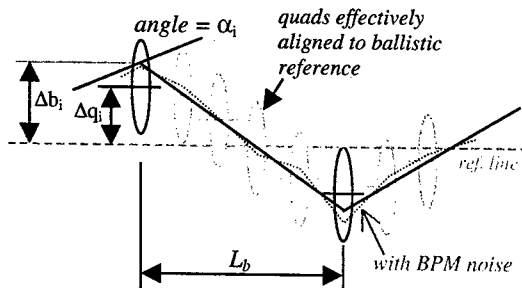


Figure 2: The result of ballistic alignment: the quadrupoles are aligned on straight line segments between bin boundaries (nodes). The RMS offset of the nodes is simply given by the RMS BPM offset with respect to the reference line ($\sim 360 \mu\text{m}$ for TESLA). The solid lines represent the best case for perfect BPMs (no noise); the red dotted line indicates the effect of finite BPM resolution.

Figure 3 shows the results of applying ballistic alignment to the TESLA linac, with all the installation

[†] care must be taken to avoid multiples of π .

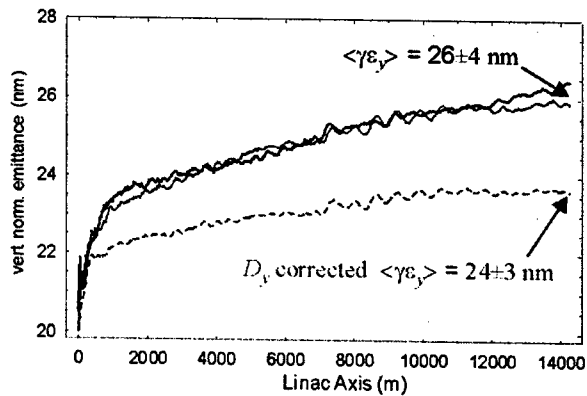


Figure 3: Results of simulations of ballistic alignment for the TESLA linac (averaged over 100 seeds). The two solid lines show independent results from the simulation codes MERLIN [9] (red) and PLACET [7] (blue). The red dotted line shows the emittance after the linear energy correlations are removed.

errors in table 1, including $10 \mu\text{m}$ RMS random BPM noise and an initial random beam jitter of $\sim 5 \mu\text{m}$ ($\sigma_y/2$) RMS. The average emittance achieved as $26 \pm 4 \text{ nm}$, corresponding to an emittance growth of 30%; $\sim 85\%$ of the machines produced an emittance growth of 50% or less. Note that half of this emittance growth comes from the first ~ 750 m or $\sim 12 \text{ GeV}$ of the linac where the energy spread is large due to bunch compression.

A large fraction of the 'projected' emittance shown in the solid lines in figure 3 is correlated with energy. In principle, the linear correlations $\langle y\delta \rangle$ and $\langle y'\delta \rangle$ can be removed with use of orbit bumps in the linac, or the dispersion correction available in the beam delivery system (BDS). The green dotted lines in figures 3 and 4 show the emittance after this correction: the average linac exit (dispersion corrected) emittance is now $\sim 18\%$. Applying two such corrections (for example, two bumps at the correct phase as suggested in [2]) may improve performance since some fraction of the correlation corrected at the first bump would otherwise filament (decohere) by the end of the linac. The study of realistic bumps has still to be made.

REFERENCES

- [1] TESLA Technical Design Report, TESLA-Report 2001-13 (2001)
- [2] V. Tsakanov, TESLA-99-21 (1999).
- [3] I. Zagorodnov and T. Weiland, these proceedings (2003).
- [4] T. Raubenheimer and R. D. Ruth, NIM A302:191 (1991).
- [5] P. Tenenbaum, R. Brinkmann, V. Tsakanov, Proc. EPAC 02 (2002).
- [6] R. Assmann *et al*, SLAC/AP-103 (1991)
- [7] <http://dschulte.home.cern.ch/dschulte/placet.html>
- [8] T. Raubenheimer and D. Schulte, PAC 99 (1999)
- [9] <http://www.desy.de/~merlin>

COMPARISON OF THE TESLA, NLC AND CLIC BEAM-COLLIMATION SYSTEM PERFORMANCE*

A. Drozhdin⁴, G. Blair⁶, L. Keller⁵, W. Kozanecki², T. Markiewicz⁵, T. Maruyama⁵, N. Mokhov⁴, O. Napoly², T. Raubenheimer⁵, D. Schulte³, A. Seryi⁵, P. Tenenbaum⁵, N. Walker¹, M. Woodley⁵, F. Zimmermann³. ¹DESY, Hamburg, Germany; ²DSM/DAPNIA, CEA-Saclay, France; ³CERN, Switzerland; ⁴FNAL, Batavia, USA; ⁵SLAC, Stanford, USA; ⁶Royal Holloway College, UK

Abstract

This report describes studies performed in the framework of the Collimation Task Force organized to support the work of the second International Linear Collider Technical Review Committee. The post-linac beam-collimation systems in the TESLA, JLC/NLC and CLIC linear-collider designs are compared using the same computer code under the same assumptions. Their performance is quantified in terms of beam-halo and synchrotron-radiation collimation efficiency. The performance of the current designs varies across projects, and does not always meet the original design goals. But these comparisons suggest that achieving the required performance in a future linear collider is feasible.

INTRODUCTION

We present a summary of comparisons of the collimation-system performance for the three main candidate linear-collider designs: JLC/NLC, CLIC and TESLA. The essence of these results is included in Ref. [1] and more details can be found in Ref. [2].

For the next generation e^+e^- linear colliders (see [1] and Table 1), small fractional beam losses along the transport line, or the presence of particles far from the beam core in the IP region, may strongly affect the background conditions in the detector, as well as cause irradiation and heating of collider components.

Table 1: LC parameters for 500 GeV c.m.energy.

parameter	TESLA	NLC	CLIC
Bunch population, $E + 10$	2	0.75	0.4
Number of bunches per train	2820	192	154
Separation between bunches, ns	337	1.4	0.67
Repetition frequency, Hz	5	120	200
Average current (each beam), μ A	45.1	27.6	19.7
Beam power (each beam), MW	11.3	6.9	4.9
Normalized emitt. x,y, mm-mrad	10, 0.03	3.6, 0.04	2.0, 0.01
Beta function at IP, x,y, mm	15.2, 0.41	8, 0.11	10, 0.05
Beam size at IP, x,y, (σ), nm	553, 5	243, 3	202, 1.5

All machine designs need to remove this halo to a certain "collimation depth", which is generally set by the synchrotron-radiation fan generated by the halo particles in the last few magnets close to the IP: by definition, all particles within the collimation depth generate photons that should pass cleanly through the IR. Halo particles outside this collimation depth are removed by physically intercepting them with "collimators", which are formed by a thick absorber of many radiation lengths placed in the optical shadow of a thin spoiler, the thickness of which is generally less than one radiation length.

* Work supported in part by US DOE, Contract DE-AC03-76SF00515.

Analytic estimates predict halo of the order of 10^{-6} of the LC beam current. However, given the SLC experience, designers of collimation systems have taken the conservative approach to build a collimation system that would be able to intercept a fractional halo of 10^{-3} of the beam – the number we assumed for the present study.

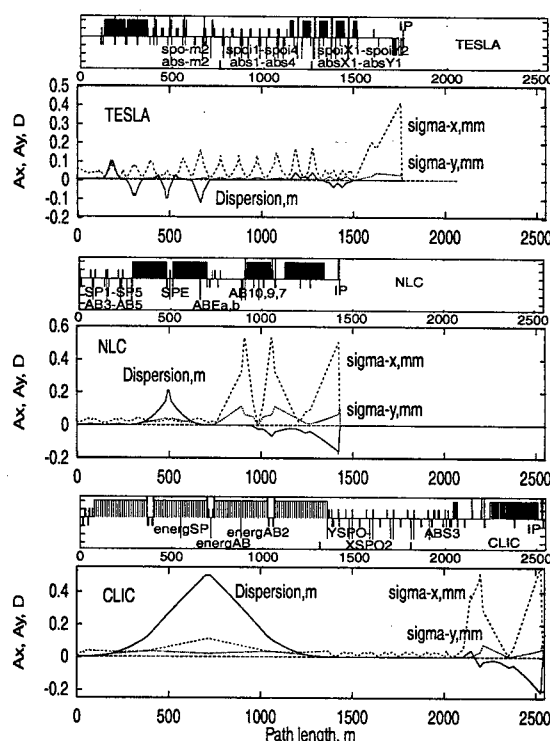


Figure 1: Collimator locations in TESLA, NLC and CLIC.

The comparative studies were carried out using the program STRUCT [3]. This package performs particle tracking, taking into account aperture restrictions, interaction of primary beam particles with collimators, beam losses, synchrotron radiation and transport of the photons along the beamline.

COLLIMATION IN LINEAR COLLIDERS

All designs have a dedicated primary collimation system (betatron and off-energy) located upstream of the final focus system (FFS). Additional secondary or "clean-up" collimators are located in the FFS. The maximum number of halo particles that may be intercepted in this secondary system is limited by the muon flux the detector can tolerate. The primary system — which intercepts most of the halo — should have high enough an "efficiency" to reduce the

losses in the secondary system to acceptable levels. At the same time, the combination of primary and secondary collimation must bring the halo population outside the collimation depth in the final doublets within tolerance.

Collimation of the beam requires putting material close to a beam with a high energy density, which in turn creates a risk that a missteered beam might destroy the collimator. In practice, in order to limit the betatron functions in the collimation region, the design relies on thin (0.5-1 radiation length) spoilers which scrape the halo with minimal heating and enlarge the spot size of a missteered beam via multiple Coulomb scattering and energy loss. The enlarged beam is then absorbed in thick (30 radiation lengths) copper absorbers. Absorbers in the primary collimation section should lie in the shadow of their spoiler partner to reduce the probability of being hit directly by a missteered beam.

Table 2 lists the physical properties of the spoilers and absorbers for the three machines. Fig. 1 shows collimator locations, horizontal dispersion and beam sizes in the BDS.

Table 2: Parameters and achieved performance of the post-linac primary collimation systems. $\sigma_{x,y}$ are the beam sizes at the primary spoiler (including the dispersive contribution); $\sigma_{x,y}^{\beta}$ refer to the betatron contributions alone. The spoiler settings are tighter than the effective collimation depth at the FD due to dispersive and higher-order effects.

		TESLA	JLC-X/NLC	CLIC
Nominal collimation depth (at spoiler)	# $\sigma_{x,y}^{\beta}$	12, 74	10, 31	9, 65
Energy collimator	x gap, mm	3.0	6.4	3.2
	$\sigma_{x,y}$, μm	154, 4.5	534, 29	814, 38
Betatron collimator	x, y gaps, mm	3.0, 1.0	0.6, 0.4	0.68, 0.4
	$\sigma_{x,y}$, μm	129, 7	28, 6.5	38, 3
IP phase	x, y gaps, mm	3.0, 1.0	0.6, 0.5	0.6, 0.4
	$\sigma_{x,y}$, μm	128, 7	16, 0.8	22, 3
Effective collimation depth (at FD)	# $\sigma_{x,y}^{\beta}$	13, 80	15, 31	11, 100
Spoiler material		Ti	Cu + Be	
Spoiler length	mm (rad.length)	35 (1)	117 (0.5 C_u + 0.3 Be)	
Absorber length	mm (rad.length)	500 (35)	429 (30)	
Achieved primary-collim. efficiency		0.01	$< 1 \cdot 10^{-5}$	$< 3 \cdot 10^{-4}$
Losses in secondary collimation section	part./bunch	$2.4 \cdot 10^5$	50	1000

RESULTS

Methodology

The effectiveness of the collimation system can be quantified in terms of: a) the fraction of initial halo particles that survive (or are rescattered out of) the primary collimation system and hit secondary collimators or other aperture limitations closer to the IP (this is relevant when estimating muon backgrounds); b) the number of halo particles that lie outside the collimation depth when they reach the final doublet (this is relevant when estimating synchrotron-radiation backgrounds).

For simulations of the effectiveness of the three collimation systems and of background conditions at the IP, the beam halo was represented by a large number of rays (typically 5×10^5) distributed in phase space with $1/r$ amplitude distributions and with a Gaussian momentum distribution of $\sigma(dP/P) = 1\%$.

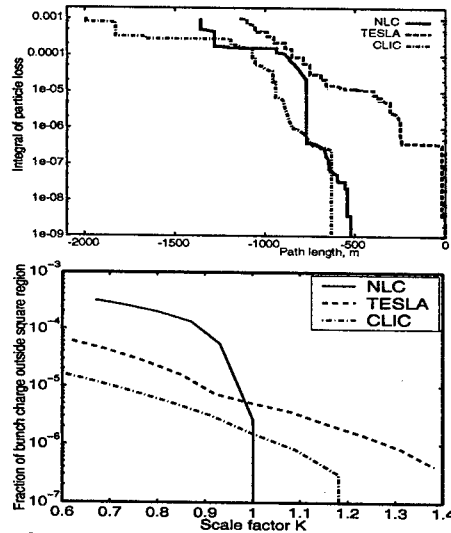


Figure 2: Collimation-system performance assuming an incident fractional halo of 10^{-3} . Top: fractional loss of charged-halo particles, integrating back, starting at the IP. The horizontal scale shows the distance from the IP. Bottom: number of charged-halo particles per bunch, normalized to the nominal bunch charge, in a rectangular $x - y$ window at the entrance to the final doublet, as a function of the collimation depth. The scale factor K defines the window dimension: for $K=1$, the window size corresponds to the effective collimation depth listed in Table 2.

Primary-collimation Efficiency

Figure 2 (top) displays, for each machine, the cumulative particle loss, starting at the IP and integrating back to the entrance of the collimation system.

- The NLC design achieves a primary-collimation efficiency significantly better than 10^{-5} , resulting in less than 10^4 particles per train being lost in the secondary system.

- In TESLA, with the primary collimation as currently designed, the loss rate in the secondary system amounts to about 1% of the initial halo population. Because the TESLA bunch spacing is longer than the entire bunch train for the warm machines, TESLA generally quotes background rates per bunch crossing. However the subdetector most sensitive to muon background, the time projection chamber (TPC), integrates over 150 bunches, so that for the same assumed incident halo fraction of 10^{-3} , the effective halo population becomes similar to that of NLC and the effective loss in the secondary collimation system amounts to $3 \cdot 10^7$ particles per sensitivity window.

- The CLIC collimation system achieves a primary-collimation efficiency of about 3×10^{-4} .

Halo Photons

The collimation-system performance achieved at the entrance to the final doublet, and the resulting level of halo-induced SR backgrounds, are summarized in Tables 3 and 4. They can be characterized as follows.

In NLC, the edge of the collimation depth is sharply defined (Fig. 2 bottom); but for no halo photons to hit

Table 3: Synchrotron radiation from the beam halo near the IP. The number of bunches per 'effective' train reflects the sensitivity window of the time projection chamber (TPC).

	TESLA	JLC-X/NLC	CLIC
# bunches/effective train	150	192	154
Losses on SR mask upstream of FD			
Mean photon energy (MeV)	0.474	0.031	0.032
# photons/bunch	$1.4 \cdot 10^6$	$4.5 \cdot 10^6$	$8.5 \cdot 10^8$
# photons/eff. train	$2.1 \cdot 10^8$	$8.7 \cdot 10^7$	$1.3 \cdot 10^6$
Total photon energy (GeV)	670 (100000)	14 (2700)	0.28 (43)
/bunch			
/eff. train			
Charged halo (part./bunch)	7440	(none)	(none)
Losses on upstream detector mask			
Radius, mm	12	10 (QD0)	13
Photon losses, mW	0.03	0	$1.8 \cdot 10^{-6}$
Photon losses, GeV/bunch	13	0	$3.8 \cdot 10^{-4}$
Losses on vertex detector			
Radius, mm	-	10	13
Photon losses, mW	-	$< 10^{-7}$	$1.6 \cdot 10^{-3}$
Photon losses, GeV/bunch	-	$< 2.7 \cdot 10^{-5}$	0.33
Losses on downstream detector mask			
Radius, mm	12	13 (lum. monitor)	13
Photon losses, mW (GeV/bunch)	0.36 (158)	0	0.011 (2.2)
Losses on SR mask downstream of outgoing-side FD			
Mean photon energy (MeV)	10.1	-	-
# photons/bunch	$1.2 \cdot 10^7$	-	-
# photons/eff. train	$1.8 \cdot 10^9$	-	-
Total photon energy (GeV)			
/bunch	$1.2 \cdot 10^5$	-	-
/eff. train	$1.8 \cdot 10^7$	-	-
Charged halo (part./bunch)	246	-	-

the beam pipe near the IP, rather tight collimator settings (± 0.2 – 0.3 mm) are needed¹. The halo photon flux hitting the FD SR mask on the incoming-side (Table 3) is low enough; in addition, these photons are rather soft ($\langle E_\gamma \rangle \sim 31$ KeV). The halo hitting the detector masks and the vertex detector is negligible. Photon losses in the outgoing beam line were not calculated for NLC or CLIC because it was assumed that the crossing-angle geometry provides enough flexibility for an ample stay-clear on the spent-beam side.

In TESLA, the boundary of the collimated halo is barely visible. Charged-halo losses on the SR mask amount to about 7400 particles/bunch on the upstream side, and about 250 particles/bunch on the downstream mask. Simulations also indicate that some SR photons from the halo ($> 10^5$ photons/bunch) hit the detector mask located 3 m downstream of IP; their total energy (158 GeV/bunch) is however small compared to that of beam-beam induced pairs. More importantly, one observes a sizeable outgoing photon halo ($\sim 1.2 \times 10^5$ GeV/bunch, corresponding to about 1.2×10^7 photons) hitting the downstream SR mask 18 m from the IP: the total energy of the halo photons intercepted by this mask is about half of that deposited by outgoing SR photons from the beam core hitting the same mask (Table 4). Both the mean energy (Table 3) and the number of halo photons per pulse is an order of magnitude larger in TESLA than in NLC, because of significantly stronger bending fields. This remark also applies to SR photons radiated by the core of the incoming e^\pm beam.

The halo in CLIC-500 appears reasonably well-behaved, and the number of photons hitting the SR and IR masks is

of no concern. This promising performance was however obtained with rather tight collimator settings. Detailed simulations of the 500 GeV CLIC system are only beginning, and its collimator configuration is still in flux.

Synchrotron Radiation from the Beam Core

A sizeable flux of SR photons produced by the beam core (primarily in the last dipole) hits the SR masks on either side of the IP (Table 4). In NLC, when integrated over the entire bunch train, the flux of SR photons from the core reaches a level that may deserve attention. In TESLA, about 10^{10} core photons/bunch hit the SR mask upstream of the IP, depositing 10^9 GeV/effective bunch train. While it is plausible that the effectiveness of the TESLA collimation system may be further improved, these results underscore the urgent need for more detailed studies. In CLIC, the flux of intercepted core SR photons is slightly lower than in NLC, presumably due to the fact that the CLIC IR has been optimized for 3 TeV c.m. energy.

Table 4: SR from the beam core hitting IR masks.

	TESLA	NLC	CLIC-500
Losses upstream of FD			
Mean photon energy (MeV)	0.450	0.032	0.034
# photons/bunch	$1.4 \cdot 10^{10}$	$0.9 \cdot 10^9$	$5.9 \cdot 10^8$
# photons/eff. train	$2.1 \cdot 10^{12}$	$1.7 \cdot 10^{11}$	$9.1 \cdot 10^{10}$
Total photon energy (GeV)			
/bunch	$6.2 \cdot 10^6$	$3.0 \cdot 10^4$	$2.0 \cdot 10^4$
/eff. train	$9.3 \cdot 10^8$	$5.8 \cdot 10^6$	$3.1 \cdot 10^6$
Losses downstream of outgoing FD			
Mean photon energy (MeV)	0.467	-	-
# photons/bunch	$4.7 \cdot 10^8$	-	-
# photons/eff. train	$7.1 \cdot 10^{10}$	-	-
Total photon energy (GeV)			
/bunch	$2.2 \cdot 10^5$	-	-
/eff. train	$3.3 \cdot 10^7$	-	-

Further plans include continuing studies of muon backgrounds, evaluation of performance in a non-ideally tuned BDS with both static and dynamic errors, etc. [6].

SUMMARY

Comparative studies of the performance of the post-linac beam-collimation systems in the TESLA, NLC and CLIC designs have shown that the performance of the systems as currently designed is not uniform across projects, and that it does not always meet all the design goals. As of this writing, the CLIC and NLC collimation schemes appear the most promising. Improvements of the TESLA collimation system are expected to result from the ongoing overhaul of their BDS design [5]. Overall, the very existence of an acceptable solution suggests that achieving the required performance in future linear colliders is feasible.

REFERENCES

- [1] Second ILC-TRC Report, SLAC-R-606, 2003.
- [2] A. Drozhdin, *et al.*, FERMILAB-TM-2200, 2003.
- [3] A. Drozhdin, *et al.*, 'STRUCT Program User's Reference Manual', <http://www-ap.fnal.gov/~drozhdin/>
- [4] A. Drozhdin, *et al.*, LCC-118, SLAC, to be published.
- [5] J. Payet, O. Napoly, N. Walker, these proceedings.
- [6] Collimation Task Force Workshop, SLAC, Dec. 2002, <http://www-project.slac.stanford.edu/lc/wkshp/colltf2002/>

¹Here we present only the more pessimistic case, i.e. without tail folding octupoles, included in NLC BDS, which allow widening the spoiler gaps by a factor of 3 to 4. NLC collimation performance with these octupoles is discussed in Ref. [4]

CTF3 PROTOTYPES: DESIGN, TESTS AND MEASUREMENTS

A. Ghigo, D. Alesini, C. Biscari, R. Boni, A. Clozza, G. Delle Monache, A. Drago, A. Gallo, F. Marcellini, C. Milardi, C. Sanelli, M. Serio, F. Sgammà A. Stecchi, A. Stella, M. Zobov, INFN-LNF, Frascati, Italy.

R. Corsini, L. Rinolfi, CERN, Geneva, Switzerland.

Abstract

The high efficiency in the 30 GHz power production is maintained if the beam quality is preserved along the rings and the transfer lines of the CLIC Test Facility (CTF3) compressor system [1,2]. The energy loss and energy spread, caused by vacuum chamber components coupling impedance and by coherent synchrotron radiation (CSR) emission, must be minimized.

The magnetic layouts of the first ring of the compressor system, called Delay Loop (DL) and of the transfer line between the Linac and DL are presented. Tests and measurements on several vacuum chamber components prototypes are reported. The 3 GHz RF deflectors, that will provide the injection in the Combiner Ring, have been studied, realized, tested, installed and successfully used in the first interlaced bunch trains injection in the CTF3 preliminary phase. A standing wave 1.5 GHz RF deflector for injection into the Delay Loop is proposed.

INTRODUCTION

The 30 GHz RF power production, needed in the CLIC project, depends on the drive beam structure; after the recombination system very short bunches with regular spacing are required. To preserve the beam quality in the CTF3 compressor system the ring lattices are isochronous and the R_{56} of the transfer lines is kept very small.

The study of rings and transfer lines optics has been reported in the CTF3 Design Report [1] and in several articles [2,3]. The coherent synchrotron radiation effect for short bunches as well as the vacuum chamber coupling impedance become important issues, leading to an energy loss and to an increase in energy spread. In fact, the energy losses give rise to relative phase errors

between bunches through non perfect isochronicity, which results in deterioration of the timing between individual bunches and merging trains; the energy spread leads to bunch lengthening and phase space distortion.

The INFN Frascati laboratories will provide the first of the two rings of the compressor system called Delay Loop (DL). At the exit of this ring the frequency of the bunches coming from the Linac (1.5GHz) will be doubled with an increment of the current by a factor two. A magnetic bunch stretcher chicane is part of the transfer line that join the Linac with the DL; it is used to increase the bunch length in order to reduce CSR and impedance effects.

Therefore the magnetic stretcher/compressor chicane was designed with an R_{56} tunable in the range of +50, -30 cm that allows to vary the bunch length in a very wide range.

Systematic experimental studies of the CSR effect in the compressor are also foreseen with an energy analyser and an emittance measurement system at the chicane exit. In this paper the study and the prototype realization of several components of the vacuum chamber are described. The tests of the RF deflectors realized by LNF, and successfully used in the CTF3 preliminary phase [5], are also reported.

MAGNETIC LAYOUT

The optics of Delay Loop and Transfer lines have been well studied including multiparticle tracking [3]. The magnetic layout of the Delay Loop and transfer lines has been completed using existing dipole and quadrupole magnets of the EPA complex in CERN together with the injection extraction septa magnet. In Fig. 1 the layout of the magnetic elements is shown.

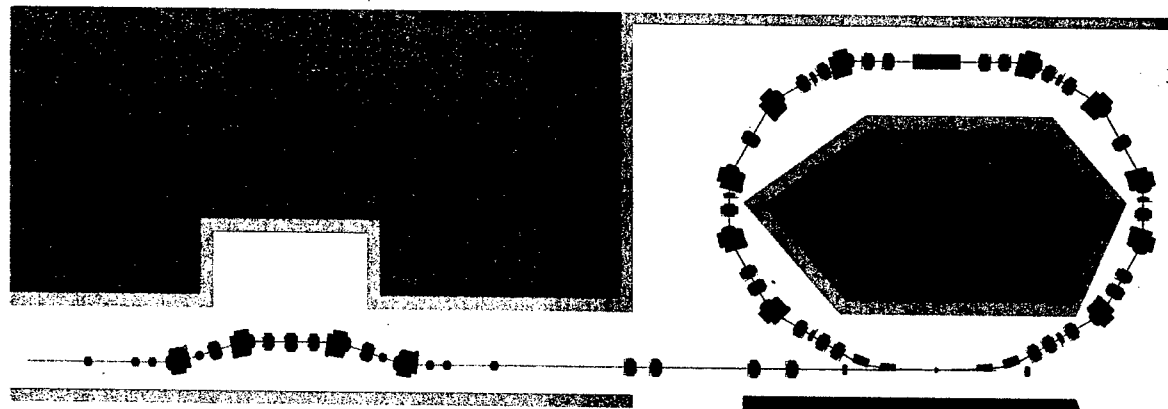


Figure 1: Layout of the Delay Loop and Transfer Line magnetic elements.

PROTOTYPES

The first prototypes vacuum chamber components studied and realized are the pump ports, shielded bellows and beam position monitors. The longitudinal impedance measurements of these devices have been done because their large number along the rings and transfer lines can contribute in significant way to the impedance. The Combiner Ring RF deflectors have been also tested and installed in the CTF3 preliminary phase [5]. The Delay Loop RF deflector has been studied.

Vacuum Pump Port

In the design of vacuum pump ports RF screen the hidden slots idea, applied successfully for PEP II, has been adopted. This allows to reduce by some orders of magnitude the coupling impedance and to prevent radiation into the pump chamber. The realized RF screen consists of 38 grooves 72 mm long, 2 mm wide and 2 mm deep in the rectangular vacuum chamber pipe with 4 mm thickness; these grooves are used to decrease the coupling impedance. Along each groove 25 circular holes of 1 mm (smaller than the bunch longitudinal size) are drilled for pumping purpose; these holes prevent penetration of the RF fields outside of the beam pipe. To decrease further the impedance in the rectangular geometry of the beam pipe, the grooves are placed closer to the chamber corners and there are no grooves on the lower and upper desks of the chamber near the symmetry axis.

The impedance of the prototype section, 8 cm long, that provides a vacuum conductance of 60 l/s, has been measured with the wire methods with resistive matching. The measurements, extended up to 4.5 GHz (maximum allowable range with resistive matching), have shown that the impedance values are too small to be detected by the measurement apparatus. The calculated impedance of these pumping screen is $Z/n=j\ 4.3 \cdot 10^{-6}\ \Omega$. No resonant mode seems to appear.

Shielded Bellows

A prototype of the shielded bellows that provides the vacuum chamber flexibility has been developed. The RF shielding is a sliding finger structure, similar to that used in the KEKB rings, with the same inner shape of the rectangular vacuum chamber. The number and the shape of the sliding contact have been chosen in order to reduce the coupling of the bunch field to the bellows structure; the thickness and position of the spring finger have been chosen to maximize the electrical contact. The bellows impedance, predominantly inductive, has been evaluated to be about $10^{-6}\ \Omega$.

Beam Position Monitor

The CTF3 BPM works in principle as a transformer excited by the beam. The beam image current is diverted to four metallic strips placed outside the vacuum chamber ceramic gap and short-circuited to the two ends of the metallic vacuum chamber. Small ferrite core

transformers, placed at the end of each strip, provide signals whose amplitude depends on the beam position [1].

The striplines are surrounded by ferrite tiles to improve the low frequency response. Such ferrites, at high frequency, have high RF losses and damp unwanted resonances of the external metallic shield.

Measurements based on the coaxial wire method have been performed to estimate the transfer impedance of the device and showed a low frequency cut-off at 400kHz [3].

To investigate position sensitivities of the device, a series of measurements with a movable wire has been performed at the calibration bench shown in Fig.2.

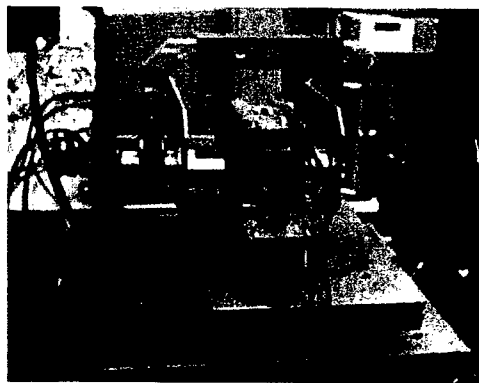
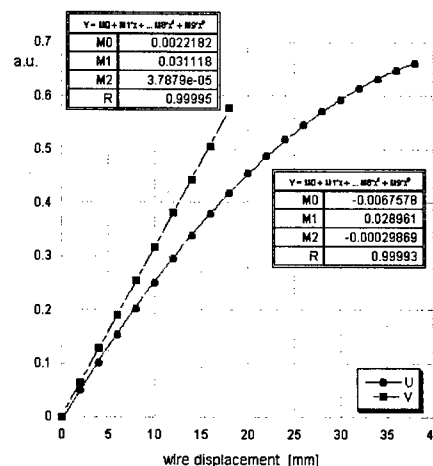


Figure 2: BPM calibration bench

Beam position is derived from the ratios U, V (pseudo-positions) between the peak intensities v_i of the signals from the windings by using a non linear fit:

$$x = k_x \cdot U + f(U, V) \quad y = k_y \cdot V + g(U, V)$$

where k_x and k_y are the inverse sensitivities to beam displacement and $f(U, V)$ and $g(U, V)$ are polynomial functions.



Figures 3: Position sensitivities along the horizontal and vertical axis

The outputs v_i at a fixed frequency from each secondary winding have been acquired for several transverse wire positions to derive coefficients of the polynomial functions (f and g) used to correct non linearities of the BPM for large beam offsets (see Fig. 3).

Data from these measurements showed 20dB maximum amplitude excursion between the four signals V_i for a beam offset by 70% of the vacuum chamber dimensions.

In order to reduce the beam coupling impedance, the internal wall of the ceramic gap will be coated with a conductive film whit thickness that allows only lower frequency components of beam fields to propagate outside to be picked up by the secondary windings.

RF DEFLECTORS

Combiner Ring RF Deflectors

The bunch trains interlacing scheme of CTF3 is based on the use of RF deflectors as injection kickers. The Combiner Ring RF deflector design has been based on an already optimized TW deflecting structure. The interaction between the beam and the deflector operating mode (beam loading) has been studied to evaluate the impact on the quality of the extracted beam. We came to the conclusion that the beam loading in a pair of 10-cells TW deflectors does not produce a significant degradation of the beam quality, provided that the betatron phase advance between the two devices is properly chosen [1]. Following these results, two deflectors used in CTF3 preliminary and nominal phases have been built in collaboration with the Soltan Institute for Nuclear Studies (Swierk, Poland).

The INFN-LNF CTF3 group collaborated in the CTF3 preliminary phase (which started in autumn 2001 and has been completed during year 2002) having a goal to demonstrate the "funneling" injection scheme and bunch train compression in an isochronous lattice. The main difference between these preliminary experiments and the nominal CTF3 is the limited beam current available from CERN LEP Injector Linac.

In CTF3 preliminary phase the concept of bunch train combination by means of RF deflectors has been demonstrated experimentally [5].

Delay Loop RF Deflector

The Linac bunch train, 1.4 μ s long, is composed by sequence of 140 ns bunch trains, with 1.5 GHz repetition rate, phase shifted by one 3 GHz RF cycle. The odd trains are injected into the Delay Loop and recombined at the extraction after one turn with the pair incoming trains. This scheme is used to double the current in the 140 ns train increasing to 3 GHz the bunch repetition rate. An RF deflector, working at 1.5 GHz RF frequency, placed at the conjunction point of transfer line and Delay Loop, provides the injection/extraction in/from the Delay Loop.

The pulsed RF source is a 1.5 GHz Klystron, custom developed for this purpose, with maximum RF delivered power of 20 MW with 5 μ s pulse length. The requested deflection angle is 15 mrad at the maximum energy of

300 MeV (nominal energy of the full current beam is 150 MeV).

Different design solutions for this device have been investigated. A standing wave cavity, that has more compact design with respect to the multicell travelling wave structure and provides better kick efficiency, has been chosen. In Table 1 the characteristics of two different standing wave single-cell deflectors with different Q value are presented. Because of the filling time and finite RF pulselength, there are different deflection angles from head to tail of the bunch train coming from the Linac. The cavity with lower Q is less efficient but minimizes these kick differences that produce a transverse emittance growth.

Table 1. Different Q value cavities comparison

Q	4200	5800
P (15mrad@300MeV)	18 MW	14 MW
ΔV start to end	1.5 %	4.0 %

Figure 4 shows the HFSS model of the developed single cell standing wave deflecting cavity. The cavity is fed by two waveguide placed on opposite sides in the horizontal plane.

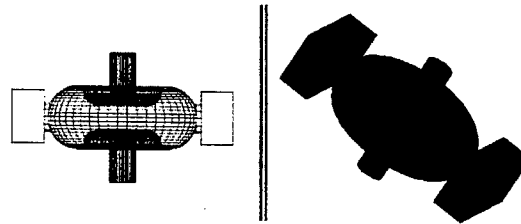


Figure 4: 1.5 GHz RF deflector model

ACKNOWLEDGMENTS

The authors wish to thank G. Fontana, V. Lollo, and A. Zolla for the machine layout and the mechanical project of the presented prototypes; S. Pella for the technical support during measurements; the CTF3 CERN technical staff for the RF deflectors installation and power test.

REFERENCES

- [1] G. Geschonke, A. Ghigo et al., "CTF3 Design Report" CERN/PS 2002-008 (RF), LNF-02/008 (IR)
- [2] C. Biscari et al., "CTF3: Design of Driving Beam Combiner Ring", EPAC'2000, Vienna, p.450.
- [3] D. Alesini et al., "CTF3 Compressor System", Proceedings of EPAC 2002, Paris, France, p.416.
- [4] D. Alesini et al., "RF Beam Deflector for CTF3 Combiner Ring", Proceedings of EPAC 2002, Paris, p.2115.
- [5] F. Tecker et al. "Bunch Frequency Multiplication in the CLIC Test Facility CTF3" PAC 2003, these proceedings.

HARMONIC CAVITIES FOR THE NLC DAMPING RINGS*

S. de Santis[#], A. Wolski, LBNL, Berkeley, CA 94720, USA

Abstract

To achieve high luminosity, a linear collider needs damping rings to produce beams with very small transverse emittances. In the NLC, design constraints place the Main Damping Rings in a parameter regime where intrabeam scattering (IBS) is likely to be a limitation on the emittance, and hence on the final luminosity. It is possible to mitigate the effects of IBS by lengthening the bunch: this may be achieved by redesigning the lattice with higher momentum compaction, or by use of higher harmonic cavities. Here, we consider the latter approach. We estimate the required bunch lengthening that might be needed, outline some appropriate parameters for the harmonic cavities, and discuss some of the effects that might be introduced or exacerbated by the cavities, such as synchronous phase variation along the bunch train.

THE NLC MAIN DAMPING RINGS

A lattice design for the NLC Main Damping Rings (MDRs) was produced in April 2001 [1]. Some relevant parameters are given in Table 1. This design met the specifications for damping rate and emittance at low current, but studies of a variety of collective effects motivated a new design [2] with a longer bunch. Among the effects causing concern was intrabeam scattering, which was estimated to increase the extracted horizontal emittance some way above the specified value.

Table 1: Lattice Parameters for the 2001 NLC MDR

Energy	1.98 GeV
Circumference	299.792 m
Natural emittance (normalized)	2.2 μm
Equilibrium vertical emittance	0.014 μm
Mean beta functions (x,y)	3.6 m, 7.1 m
Mean horizontal H functions	1.9 mm
Expected rms vertical dispersion	1.5 mm
Transverse damping times (x,y)	4.8, 5.0 ms
Longitudinal damping time	2.6 ms
Momentum compaction	2.95×10^{-4}
Natural bunch length	3.7 mm
Natural energy spread	0.091%
Bunch charge	7.5×10^9
Bunch store time	25 ms

Before attempting a new lattice design, the possibility of increasing the bunch length using harmonic cavities was considered. Here, we report on the results of the study of the effects of the harmonic cavities, and discuss the reasons for choosing a new lattice as the preferred approach to reducing the severity of the collective effects.

*Work supported by the US DOE contract DE-AC03-76SF00098.
[#]SDeSantis@lbl.gov

IBS ESTIMATES

IBS is not generally a significant effect in electron storage rings, since the growth rates are usually much smaller than the radiation damping rates. Observations have been made at the KEK ATF [3] and the ALS at LBNL [4], both operating in regimes where the coupling is very small. There is some uncertainty as to whether the measurements made at the ATF are fully explained by the IBS model [3,5]; however, since the issue is presently unresolved, we base our estimates on this model, using approximations that are valid in the relevant regime [6]. Using the method described in [3], we can calculate the evolution of the transverse and longitudinal emittances as functions of time after the injection of the beam into the damping ring, including the effects of IBS and radiation damping.

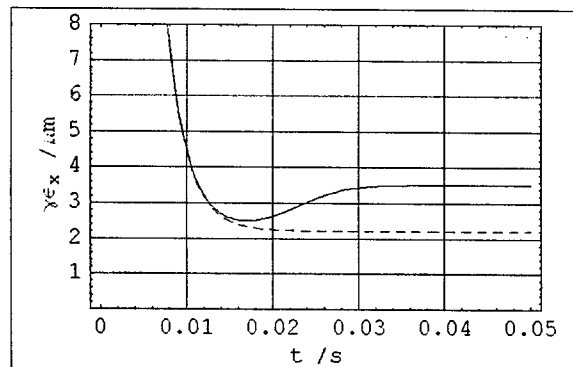


Figure 1: Evolution of horizontal emittance with IBS (solid line) and with radiation only (broken line)

Figure 1 shows the evolution of the horizontal emittance following injection into the ring with a normalized emittance of 150 μm . IBS also leads to an increase (though less severe) in the vertical and longitudinal emittances. In the horizontal plane, we observe the characteristic minimum associated with IBS, which becomes strong enough to increase significantly the horizontal emittance only when the vertical emittance has damped to a certain value. At equilibrium, the horizontal emittance is increased to 3.51 μm . The specified extracted emittance is 3.0 μm .

Increasing the bunch length reduces the charge density and thus reduces the IBS growth rates. However the extracted horizontal emittance is a relatively weak function of the natural bunch length (Figure 2): in order to achieve 3 μm extracted emittance, the bunch length needs to be increased to between 4.5 mm and 5.0 mm, depending on the equilibrium vertical emittance. Note that the equilibrium vertical emittance needs to be reduced close to 0.01 μm in order to achieve 0.02 μm extracted, with IBS.

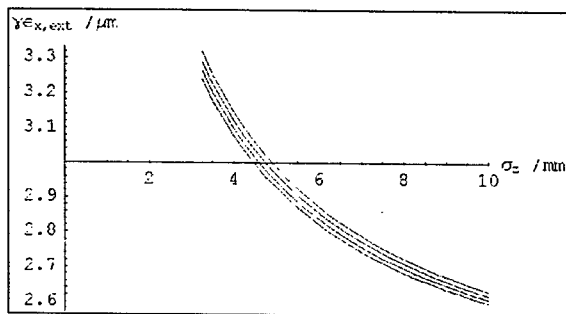


Figure 2: Extracted horizontal emittance as a function of natural bunch length, for equilibrium vertical emittances from 0.013 μm to 0.010 μm (from left to right).

LENGTHENING THE BUNCH WITH A HIGHER HARMONIC VOLTAGE

The fundamental theory of a higher harmonic RF system is described in [7]. In our case we are interested in bunch lengthening of around 30%, which allows the possibility of using a somewhat simplified theory and rather relaxed requirements for the cavity parameters.

Higher harmonic RF systems are already in use, or are being designed, in a number of electron storage rings and have been the object of recent studies [8]. The main problem connected with the use of harmonic cavities, in either passive or active mode, is the transient beam loading induced on the bunch train. The difference in the bunch phases, relative to the RF voltage, can assume very high values, which make obtaining a uniform bunch lengthening difficult. As an additional problem in the NLC damping rings, the systems downstream of the damping ring accept a limited variation (less than 10 mm) of the bunch phase at input. It should be noted that simulations indicate a 6 mm phase variation from just the main RF system.

In first approximation, we can say that the bunch lengthening is proportional to the inverse of the derivative of the total RF voltage. Hence:

$$\frac{V'_{RF}}{V'_{Tot}} = \frac{\sigma_{zh}}{\sigma_z} \quad (2)$$

where σ_{zh} is the bunch length, when the harmonic voltage $V_h(t)$ is applied and

$$V'_{Tot} = V_{RF} + V_h \quad (3)$$

With our parameters, Eq.(3) yields a value for the required peak harmonic voltage of about 80 kV.

Common beam loading models are not adequate to describe the effects with harmonic cavities. For this reason we use a simple tracking code, developed by J. Byrd at the Advanced Light Source, in which we compute the transient voltages, induced by the uneven fill, in the main and harmonic RF system. This code is also used for determining the fundamental parameters of the harmonic cavities, based on the target harmonic voltage and the MDR parameters (Table 2). At this first stage, the bunches are treated as point-like charges and it is possible to include the effects of the main RF cavities high-order

modes and random non-uniformities in the bunch charges (which turn out finally to be negligible).

Table 2: Parameters for the 2001 NLC MDR RF system

Main RF frequency	714 MHz
Shunt impedance	3.744 M Ω
R/Q	117
Coupling factor	12.33
Peak RF voltage	1.07 MV
Energy loss/turn	792 keV
DC beam current	729 mA
Number of bunches	3 \times 192

The total voltage (main RF voltage plus harmonic voltage) is then used for calculating the length of each individual bunch.

SIMULATION RESULTS

Table 3 reports the main parameters for the third harmonic RF system used in the tracking code. These parameters were chosen to obtain a harmonic voltage higher than the 80 kV reported in the previous paragraph: equations 2 and 3 underestimate the required voltage, since they do not include the additional energy loss due to the harmonic cavity and the phase relation between fundamental and harmonic voltage.

Table 3: RF Parameters for the 2001 NLC MDR third harmonic RF system

Harmonic RF frequency	2142.4 MHz
Shunt impedance	0.7 M Ω
R/Q	35

As previously stated, such parameters for the harmonic cavity can be easily obtained with a traditional single cell copper cavity. The harmonic cavity is tuned 0.4 MHz above the third RF harmonic because of stability considerations.

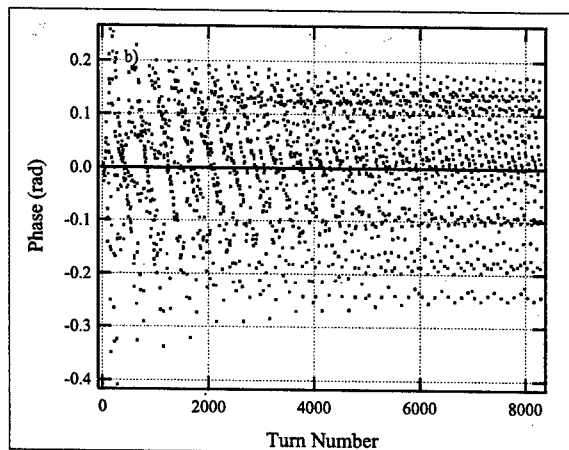


Figure 3: Turn-by-turn phase of bunches in the NLC MDR.

Our simulation code tracks the three trains of 192 bunches each and calculates their phases (referred to the main RF frequency) turn by turn. Figure 3 shows the

evolution in the bunch phases from an arbitrary initial distribution, for the first 8300 turns, which corresponds to the MDR injection/extraction cycle. It can be seen that the first 3000 turns are enough to damp the bunch phases to their regime values.

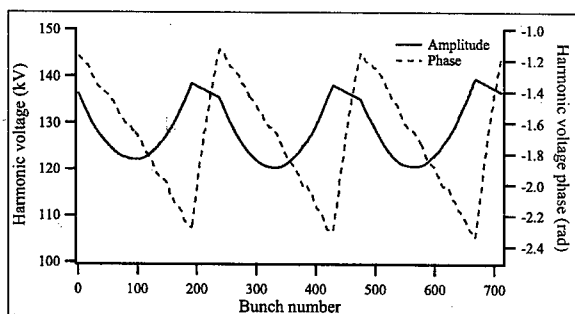
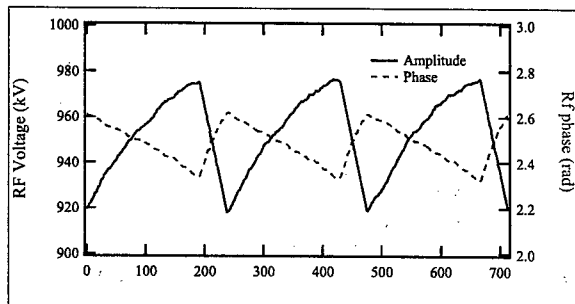


Figure 4: Fundamental (upper) and harmonic (lower) RF voltages and phases.

The fundamental and harmonic RF voltages and phases along the bunch trains are shown in Figure 4. These results include the high-order modes of the main cavities and a 10% random fluctuation in the bunch charges. The gaps are included in the calculation, since from the point of view of the tracking code, these are simply bunches with zero charge.

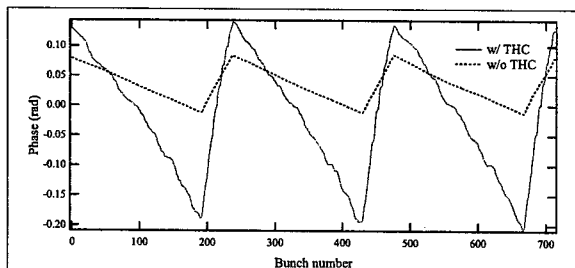


Figure 5: Bunch phase transients with and without the harmonic RF system.

Figure 5 shows the resulting variation of the bunch phases. As a reference, we report also the same variation calculated without the third harmonic cavity, which turns out to be substantially smaller. The phase transient with the harmonic cavity is far larger than the maximum specified for the bunch compressor.

As a final check, the new bunch lengths, after the harmonic voltage is applied, are calculated and reported in

Fig.6, showing that the applied voltage is indeed necessary for obtaining the 30% required lengthening.

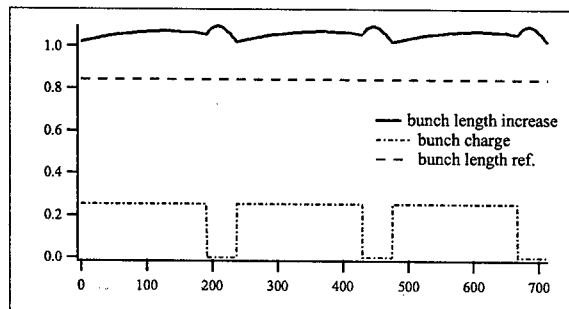


Figure 6: Bunch lengthening.

CONCLUSIONS

Our calculations show that a simple higher harmonic RF system could be easily designed to obtain the bunch lengthening required to overcome the IBS related emittance increase in the NLC MDR. Because of the intrinsic characteristics of such systems, the effect on the bunch phase distribution would be substantially larger than the maximum specified for the bunch compressor.

Though it might be possible to design a more complex system (with energy storage cavities, for instance) able to reduce the phase transient, it was decided to investigate a lattice redesign, which could give a longer bunch without the need for a higher harmonic RF system.

ACKNOWLEDGMENT

The authors wish to thank Dr. J. M. Byrd for his invaluable advice.

REFERENCES

- [1] A. Wolski and J. Corlett, "The Next Linear Collider Damping Ring Lattices", PAC'01, p.3795.
- [2] A. Wolski et al, "A Lattice with Larger Momentum Compaction for the NLC Main Damping Rings", these proceedings.
- [3] K.L.F. Bane et al, "Intrabeam Scattering Analysis of ATF Beam Measurements", SLAC-PUB-8875, 2001.
- [4] J. Corlett et al, "Measurements of Intrabeam Scattering at Low Emittance in the Advanced Light Source", HEACC'01.
- [5] J.D. Bjorken and S.K. Mtingwa, "Intrabeam Scattering", Particle Accelerators 13 p.115, 1983.
- [6] T.O. Raubenheimer, "The Generation and Acceleration of Low Emittance Flat Beams for Future Linear Colliders", SLAC report 387, 1991.
- [7] J.M. Byrd, et al. "Design of a Higher Harmonic RF System for the Advanced Light Source", Nucl. Instr. Meth. A 439, 15, 2000.
- [8] J.M. Byrd, et al. "Transient Beam loading Effects in Harmonic RF Systems for light Sources", Phys. Rev. ST-AB 5, 092001, 2002.

STUDY OF NEAR-FIELD VIBRATION SOURCES FOR THE NLC LINAC COMPONENTS

F. Asiri, F. Le Pimpec, A. Seryi SLAC, CA USA *

Abstract

The vibration stability requirements for the Next Linear Collider (NLC) are far more stringent than for the previous generation of Colliders. To meet these goals, it is imperative that the effects of vibration on NLC Linac components from near-field sources (e.g. compressors, high vacuum equipment, klystrons, modulators, pumps, fans, etc) be well understood. The civil construction method, whether cut-and-cover or parallel bored tunnels, can determine the proximity and possible isolation of noise sources. This paper presents a brief summary and analysis of recently completed and planned studies for characterization of near-field vibration sources under either construction method. The results of in-situ vibration measurements will also be included.

INTRODUCTION

To maintain the desired luminosity of the NLC, the focusing components on the main Linac must be kept at a few nanometers above a few Hz. These components can be affected by far-field (natural) and near-field (man-made) vibration sources. This paper is concerned only with near-field sources (e.g. mechanical and electrical equipment, RF generating equipment, etc). These sources are mainly located either in the Support tunnel, Fig.1, or far away (> 100 m) from the Beam tunnel. The characterization of near-field vibration sources and its effects on the main Linac components is part of an ongoing R&D program at NLC that is presented in this paper. The first part of the paper will present the influence of the vibration induced by RF power generating elements and by the RF itself. The second part will deal with the transfer of vibration from surface to the tunnel invert.

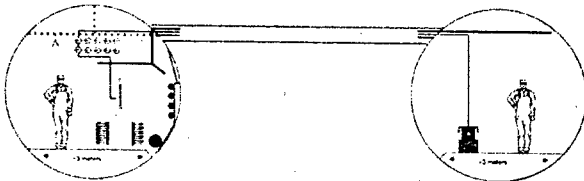


Figure 1: Cross-section of support and beam tunnels.

RF VIBRATION CHARACTERIZATION

At first, we will focus on the vibration contribution of high power generating RF components. The study was carried out near the supporting structure of the 8 pack project [1]. The 8 pack project is the test bench of klystrons and their modulator to produce high power RF for the Next Linear Collider Test Accelerator (NLCTA). One of the ge-

phone sensors was placed at the base of the modulator at 76 cm above the concrete floor and the second one was located on the concrete floor at ~ 1.2 m away from the base of the modulator support, or at its base (0 m). The signals of the Mark-4 geophones were measured simultaneously.

We performed tests in two different conditions of the modulator. In the first case, the water cooled modulator was under a 20 kV voltage and was running at 30 Hz or 10 Hz (at this voltage the klystrons was not conducting, thus did not deliver RF power). In the second case the modulator was running at 10 Hz and was under 400 kV (the klystron was delivering ~ 40 MW of RF power at $1.6 \mu s$).

Fig.2 shows the response of the sensors vs times for the modulator under a 20 kV. In this case the modulator was running at different frequencies. The seismometer located at the base of the modulator clearly shows vibrations due to modulator pulsed operation, while the geophone located on the concrete floor does not indicate any change due to the modulator running conditions.

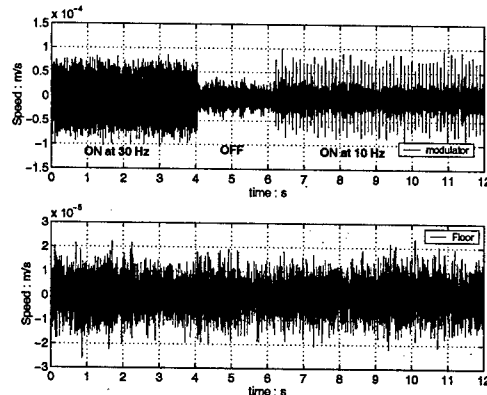


Figure 2: Response of the geophones when the modulator was running at different frequencies or was switched off. Note the difference of the scales.

Fourier analysis also does not reveal any additional noises due to modulator on the floor. Fig.3 and Fig.4 show the average integrated displacement (AID) of the two seismometers. The blue lines are the response of the sensor placed at the base of the modulator, where the difference between the modulator on and off cases is clearly seen. The green lines are the response of the sensor placed on the concrete floor either at ~ 1.2 m or at the base of the stand (0 m), and the on and off cases overlap.

Interesting that, when the modulator is under 400 kV and delivering power to the klystron, its vibration is slightly less than for a 20 kV running modulator. One can also note that background noise was different in the conditions of Fig.3 and Fig.4 (see green curves below 60 Hz) which was due to different level of activity of the construction crew working at NLCTA.

* Work supported by the U.S. Department of Energy, Contract DE-AC03-76SF00515.

The main conclusion of the modulator vibration study is that the transmission of vibration from the modulator to the concrete floor is not significant, and, on the level of background noise at NLCTA, not noticeable.

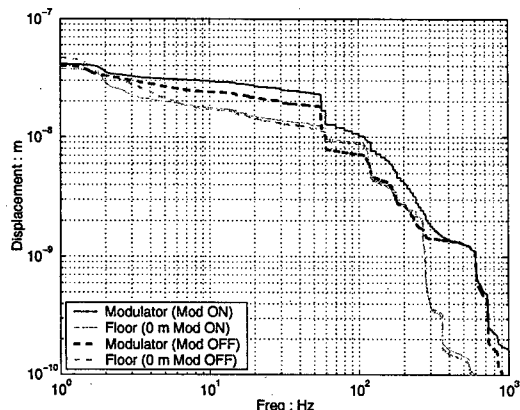


Figure 3: Average Integrated Displacement (AID) of the seismometers when located at the base of the modulator and on the floor at ~ 1.2 m of the supporting structure. The modulator is under 20 kV.

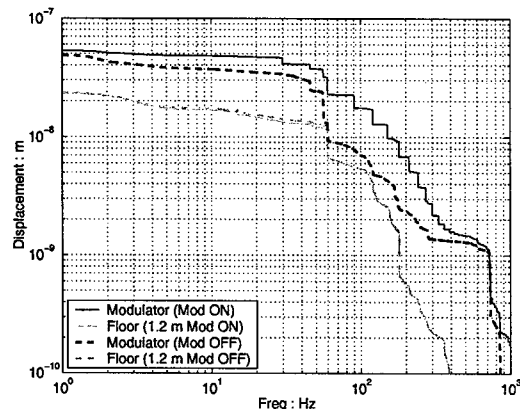


Figure 4: AID of the seismometers when located at the base of the modulator and on the floor 0 m of the supporting structure. The modulator is under 400 kV.

We also studied vibrations of accelerating structures due to cooling water (reported earlier, see [2]), and due to RF pulse (presented below). When the klystrons are delivering power, the RF heating produces acoustical vibration in the accelerating structure. Possible vibration produced by the RF were measured by 3 piezo-accelerometers placed on the accelerating travelling wave structure bolted on its support or girder, placed on the girder, and placed on the waveguide. The X-rays coming out from the structure when filled by the RF did not affect the measurements of our accelerometers.

These measurements, Fig.5, show that feeding a structure (60 cm long travelling wave structure H60Vg3R), via its waveguide, with 100 MW at 400 ns of RF power at 60 Hz (corresponded to about 70 MV/m accelerating gradient) does not lead to any significant increase of vibration in

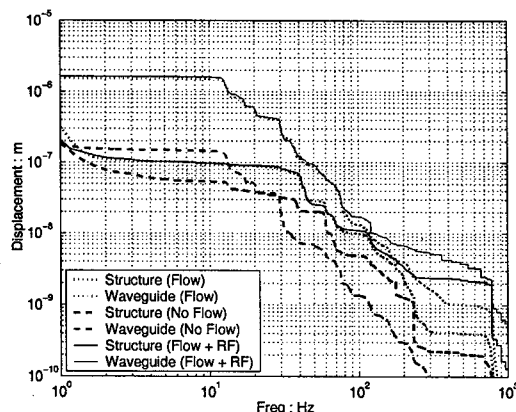


Figure 5: AID for the structure and its connected waveguide when cooled or not with water (dot and dashed line) then when cooled and fed with RF.

comparison to vibrations produced by cooling water. The water induced vibrations dominate, but they are tolerable, since, with an appropriate design, the vibration transmission to the linac quadrupoles is rather small [2]. Vibration of the loosely supported RF waveguide is higher than of the RF structure, but apparently this does not significantly increase vibration of either structure or the quadrupoles.

VIBRATION TRANSFER FROM SURFACE TO BEAM TUNNEL

One of the questions to be addressed is whether there is a significant difference in the vibration attenuation characteristics between a tunnel bored at great depth (in bedrock) or excavated in cut-and-cover construction at lesser depth, with regard to vibrations generated at the surface. A study was carried out at SLAC [3], representing the vibration attenuation characteristics of the soil, assuming the SLAC beam line housing to be representative of a cut-and-cover construction. The second vibration measurement study is currently underway in the Red Line tunnels in Los Angeles. This study will establish the vibration characteristics between two tunnels, along the tunnel as well as from surface to the tunnel. The following is a brief presentation of data from the study carried out at SLAC.

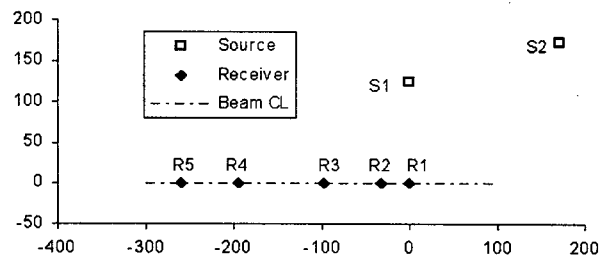


Figure 6: Relative locations of sources and receptors (scale in feet).

Fig.6 shows the relative locations of sources and the receivers. The receivers locations were on the floor along the

centerline of the beam. The sources were on the ground surface. Drive location S1 was at the same approximate elevation as of the Klystron gallery floor, which lies about 36 ft (11 m) above the elevation of the receiver locations. Drive location S2 was about 10 ft (3 m) uphill from S1.

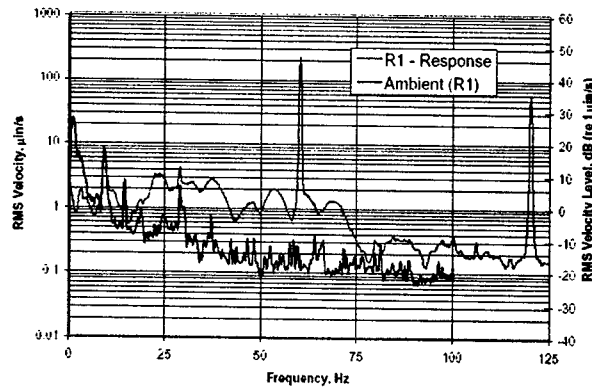


Figure 7: Typical response at R1 to hammer blow at S1, with ambient at R1.

Fig.7 shows two spectra. One is the ambient measured at the receiver location R1. The other is a fast Fourier transform of the response to several hammer blows. Several observations may be made. The peaks at 60 Hz and 120 Hz are electronic artefacts. The peaks centered at ~ 8.75 Hz and at ~ 14.25 Hz in both ambient and response have a nearly identical amplitudes. The peak at 18.75 Hz has a slightly different amplitude. At these frequencies, the "response" (red line) is being governed more by ambient than by the input force, so the transfer functions derived from the "response" will be invalid. The "ambient" (blue line) at frequencies less than 7 Hz (in this case) lies above the "response". This suggests that there is some variability to the ambient environment at these low frequencies, and these will degrade the accuracy of transmission function at lower frequencies.

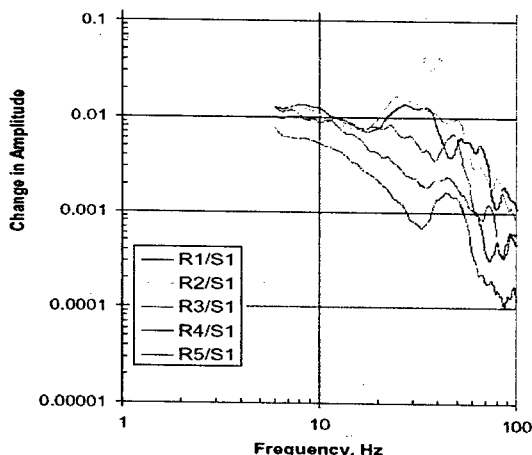


Figure 8: Log-mean ground transmission from the drive point S1 – heavily smoothed.

Fig.8 shows a smoothed spectra which were calculated by log averaging the amplitudes over a 10 Hz interval centered on the plotted point. It provides the transfer function (showing change of amplitude) measured at R1 to R5 using S1 as a drive point, Fig.6.

Source (S1) to Receiver(m)	Attenuation at Given Frequency			
	10 Hz	20 Hz	30 Hz	60 Hz
R1(39)	0.024	0.0084	0.012	0.005
R2(40.2)	0.012	0.012	0.014	0.004
R3(48.6)	0.011	0.0084	0.006	0.001
R4(69.9)	0.010	0.004	0.002	0.001
R5(86.7)	0.005	0.002	0.0009	0.0003

Table 1: Attenuation factor, referring to Fig.6.

The Table 1 summarizes the apparent attenuation at several frequencies at which mechanical equipment usually operates. The figures in Table 1 represent the attenuation factor A for a vibration with its source near S1 propagating along the same path. Let us give an example how such data can be used. Suppose a pump is installed at S1, and it produces vibrations at 30 Hz of amplitude X. The amplitude at 30 Hz that we would measure at R5 would be the greater of either ambient or $0.0009X$. Suppose we take the ambient measured shown for the tunnel in (Fig.7) as representative of the tunnel in general. The amplitude at 30 Hz is about $1.5 \mu\text{m/s}$. If we were to place a pump at S1 and be sure to avoid having its vibrations exceed ambient at R5, we would need to impose a limit on the resulting vibration at S1 of $1.5/0.0009 = 1.7 \text{ mm/s}$.

CONCLUSION

It has been shown that the vibration transmitted by the RF generating equipment to the floor is insignificant. Hence, klystrons and or modulators running in the Support tunnel of the NLC should not effect alignment of the Linac. Vibration contribution of an RF pulse to an accelerating structure has also been found negligible relative to water-cooling. Thus, it leaves electrical and mechanical rotating equipment as possibly a dominating source of vibration. The attenuation factors presented in the paper can be used in planning stage of the NLC project for specifying and locating the mechanical rotating equipment, as well as to assess their vibration effects on the focusing components on the Main Linac and provide a means for establishing the vibration budgeting scheme for the project.

REFERENCES

- [1] <http://www-project.slac.stanford.edu/lc/local/Projects/8Pack/8Pack.html>.
- [2] F. Le Pimpec et al. In *Nanobeam, Lausanne (CH)*, 2002. SLAC-PUB-9558.
- [3] <http://www-project.slac.stanford.edu/lc/ilc/TechNotes/LCCNotes/PDF/LCC-0115.pdf>.

CAPTURE AND POLARIZATION OF POSITRONS IN A PROPOSED NLC POLARIZED POSITRON SOURCE*

Y.K.Batygin and J.C.Sheppard, SLAC, Stanford, CA 94309, USA

Abstract

A proposed NLC polarized positron source utilizes a 150 GeV electron beam passing through a helical undulator. The resulting flux of polarized photons is converted in a thin positron production target. Spin polarized positrons are captured using a high field flux concentrator followed by an accelerator section immersed in a solenoidal field. Positron tracking through the accelerating and focusing systems is done together with integration of spin precession. Optimization of the collection system is performed to insure high positron yield into the 6-dimensional acceptance of the subsequent pre-damping ring while keeping the high value of positron beam polarization.

INTRODUCTION

The original proposal on polarized positron production specifically for linear colliders was made in Ref. [1]. It incorporates an idea to utilize a helical undulator to produce circularly polarized photons which, being directed onto the target, create polarized positron-electron pairs. A proposed NLC polarized positron source includes a helical undulator, a production target followed by a short solenoid with a strong magnetic field (flux concentrator), a 250 MeV linac with 0.5 Tesla focusing solenoids and a 1.76 GeV booster linac with quadrupole focusing. Parameters of the positron injector are summarized in Table 1. Collected positrons are cut by a 6-dimensional acceptance of the positron pre-damping ring (PPDR). At the injection point into pre-damping ring, the positron beam is cut transversely by the transverse acceptance of 0.03π m-rad and in energy spectrum to 2%, which corresponds to energy interval of 40 MeV. The ultimate goal of the collector system is to provide the highest number of positrons within the 6-dimensional acceptance of the pre-damping ring keeping longitudinal polarization of the beam as high as possible.

Table 1. NLC polarized positron injector parameters.

Parameter	Value
Electron beam energy	150 GeV
Electrons/Bunch	$8 \cdot 10^9$
Bunches / pulse	192
Pulses/sec	120
Undulator type	Helical
Undulator Parameter, K	1
Undulator Period	1 cm
First Harmonic Cutoff En.	10.7 MeV
$dN\gamma/dL$	2.6 photons/m/e ⁻
Undulator Length	132 m †
Photon Collimator Trans.	0.5
Target Material	Ti-alloy
Target Thickness	0.5 R.L.
Yield (N_+/N_e)	$2.9 \cdot 10^{-2}$ ‡
Capture Efficiency	0.2
Positrons/Pulse	$1.5 \cdot 10^{12}$
Positrons/Bunch	$8 \cdot 10^9$
Positron Polarization	0.6

† Length for unity gain e⁻/e⁻; ‡ Yield for cut spectrum

POLARIZED POSITRON TRACKING

Positron tracking from the target to end of 1.9 GeV linac is performed using BEAMPATH [2]. The initial positron distribution after interaction of photon beam with a 0.5 RL Ti target was calculated using the EGS4 program [3], adapted for polarized beams [4, 5]. Particle tracking was accompanied with integration of the Thomas-BMT equation [6], describing the precession of the spin vector \vec{S} :

$$\frac{d\vec{S}}{dt} = \frac{e\vec{S}}{m\gamma} \times [(1 + g\gamma)\vec{B}_\perp + (1 + g)\vec{B}_\parallel + (g\gamma + \frac{\gamma}{1 + \gamma})\frac{\vec{E} \times \vec{\beta}}{c}], (1)$$

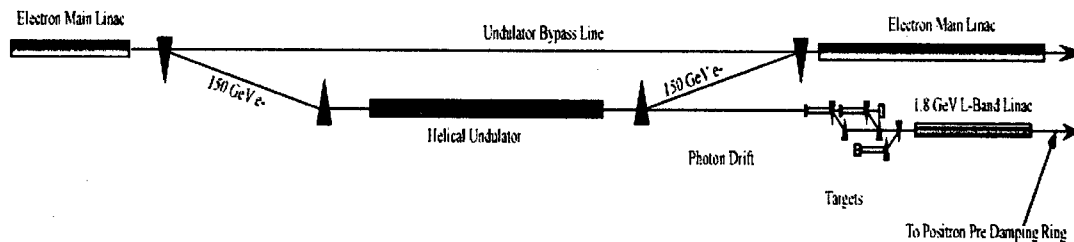
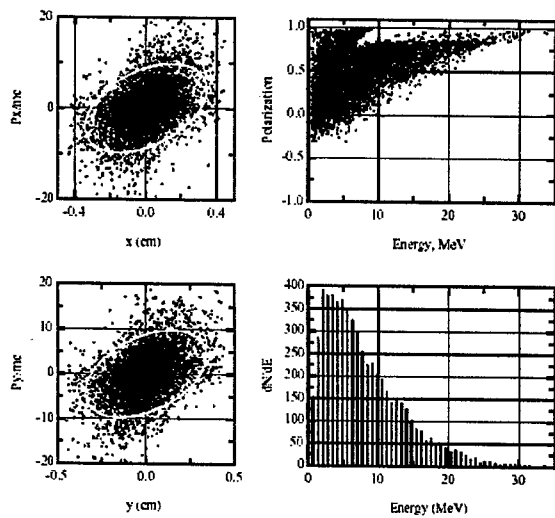
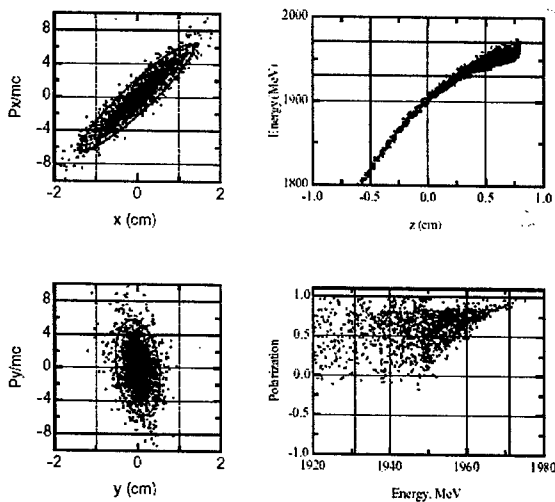


Fig. 1. NLC polarized positron injector layout.

Table 2. Yield of positrons with respect to incident γ -flux.

Energy of 1 st harm. cutoff, MeV	Positron yield at the target, $N_{e^+, \text{target}}/N_\gamma$	Positron capture at 1.9 GeV, $N_{e^+, 1.9\text{GeV}}/N_{e^+, \text{target}}$	Positron yield at 1.9 GeV, $N_{e^+, 1.9\text{GeV}}/N_\gamma$	Positron polarization, $\langle P_z \rangle$
10.7	0.029	0.20	$5.8 \cdot 10^{-3}$	0.59
30	0.11	0.058	$6.4 \cdot 10^{-3}$	0.59
60	0.17	0.026	$4.4 \cdot 10^{-3}$	0.59


 Fig. 2. (Blue) initial distribution of positron generated by 10.7 MeV γ -flux, (red) positron accepted at 1.9 GeV, (green) area of 0.03π m rad.

 Fig. 3. (Blue) distribution of positrons at 1.9 GeV, (red) emittance area of 0.03π m rad and $\Delta E/E=2\%$.

where g is the anomalous magnetic moment of the positron, \vec{E} is the electrical field, and \vec{B}_\perp and \vec{B}_\parallel are components of the magnetic field perpendicular and parallel to particle velocity. Initially the spin vector of each positron is pointed along the momentum vector. During beam transport, the spin vector precesses, resulting in the depolarization of the beam. We define the longitudinal polarization as an average of the product of the longitudinal component S_z and the value of polarization, P , over all positrons:

$$\langle P_z \rangle = \frac{1}{N} \sum_{i=1}^N S_z^{(i)} P^{(i)}. \quad (2)$$

The initial value of longitudinal polarization is $\langle P_z \rangle = 0.43$. Polarization of the final beam depends strongly on the energy of accepted particles and is typically in contradiction with the value of positron capture. Below, several different schemes of positron injection are considered.

POSITRON BEAM DYNAMICS

Figs. 2, 3 illustrate dynamics of the positron beam created by a $K=1$, helical undulator spectrum of photons with a first harmonic cutoff energy of 10.7 MeV (note: only the first 4 undulator radiation harmonics are included) [7]. Initial beam after the target has an energy spread of 0-30 MeV and normalized, rms emittance of 0.0095π m-rad (see Fig. 2). The target is followed by a flux concentrator [8], which is a solenoid with a sharp increase in magnetic field up to peak value of 5.8 Tesla at a distance of 5 mm from the target and an adiabatic decrease of the field over a distance of 15 cm. An additional magnetic field of 1.2 Tesla at the target is required to confine the emitted positron beam with its large momentum spread.

The flux concentrator is followed by a 250 MeV linac with an effective accelerating gradient of 25 MeV/m and transverse focusing by a 0.5 Tesla solenoid field. After acceleration to 250 MeV, positrons are accelerated in a linac with quadrupole focusing and an accelerating gradient of 15 MeV/m. During acceleration, high energy particles are placed on the top of accelerating field.

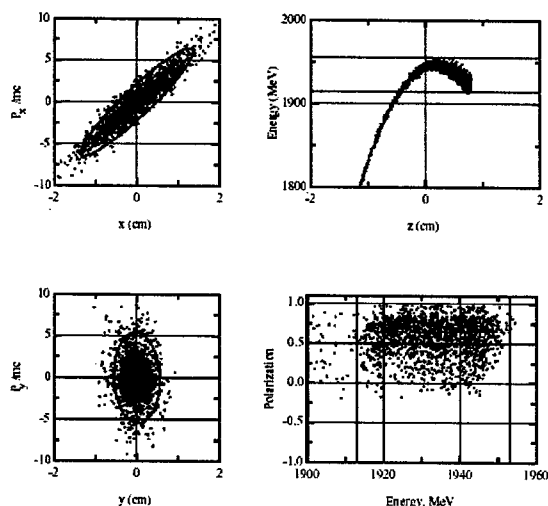


Fig. 4. (Blue) 1.9 GeV distribution of positrons at RF phase in linac $\phi = -11.5^\circ$, (red) emittance of 0.03π m rad and $\Delta E/E = 2\%$.

This gives the possibility to retain the original particle energy distribution and not to mix high energy, high polarized positrons with low energy, low polarized positrons. At the energy of 1.9 GeV, 20% of the initial positrons are within the 6-dimensional phase space acceptance with an average polarization of $\langle P_z \rangle = 0.59$.

To provide higher positron transmission, the high-energy positrons might be shifted in RF phase with respect to peak of RF voltage. Fig. 4 illustrates results of positron capture simulation in case the RF phase shift in 1.76 GeV linac is selected to be $\phi = -11.5^\circ$. The value of RF phase shift is adjusted in such a way that the energy difference in head particles and top-energy particles is within the interval of $\Delta E/E = 2\%$. It provides the value of positron capture of 26% while beam polarization is kept as high as $\langle P_z \rangle = 0.56$.

Increasing of the energy of incoming photons results in wider energy spectrum of outgoing photons. Table 2 contains results of capture of positrons created by the K=1, helical undulator spectrum with first harmonic cutoff energies of 10.7 MeV, 30 MeV and 60 MeV. According to EGS4 simulations, the distribution of positron polarization as a function of energy remains qualitatively the same, but is scaled to a wider energy interval. The fraction of captured positrons is 0.058 for positrons generated by the 30 MeV cutoff γ -flux, and 0.026 for that generated by the 60 MeV cutoff γ -flux. These values are substantially smaller than the value of capture of positrons created by 10.7 MeV γ -flux. However, the target conversion rate from photons to positrons increases with the energy of incoming photons. From Table 2 it follows that the value of position yield at 1.9 GeV is of the order of $(4...6) \cdot 10^{-3}$ and is a weak function of energy of γ -flux.

Table 3. Capture and polarization of positrons obtained from 10.7 MeV γ -flux.

	After target	End of 1.9 GeV linac, $B_{\text{target}}=1.2\text{T}$	End of 1.9 GeV linac, $B_{\text{target}}=6.4\text{T}$
Fraction of positrons within $\varepsilon_x, \varepsilon_y < 0.03 \pi$ m rad, $\Delta E = \pm 20\text{MeV}$	0.72	0.20	0.29
Positron polarization, $\langle P_z \rangle$	0.43	0.59	0.55

OPTIMIZATION OF POSITRON TRANSMISSION

According to design, the positron production target is surrounded by tapered solenoidal magnetic field of $B_t = 1.2$ Tesla followed by a strong magnetic field of flux concentrator with a total peak field of $B_{FC} = 6.4$ Tesla. The sharp change in magnetic field at the injection is a barrier for low-energy positrons. Transverse momentum of the particle after injection is

$$p_\phi = p_{\phi 0} + \frac{er}{2}(B_{FC} - B_t). \quad (3)$$

Assuming an initial value of azimuthal momentum is $p_{\phi 0} = 0$ and beam radius of $r = 2$ mm, the value of azimuthal momentum after injection is $p_\phi = 3.1$ MeV/c.

Total particle momentum in magnetic field is conserved, which means that low-energy particles with smaller energy are reflected from the target. This gives the idea that if target is placed inside magnetic field of flux concentrator, this barrier is removed and more positrons can be captured. Simulations indicate that it results in significant increase (up to 29%) of the value of positron capture (see Table 3).

REFERENCES

- [1] V.E.Balakin and A.A.Mikhailichenko, Preprint BINP 79-85 (1979).
- [2] Y.Batygin, RIKEN-AF-AC-17, ISSN 1344-3877 (2000).
- [3] W.Nelson, H.Hirayama and D.Rogers, SLAC-Report-265 (1985).
- [4] K.Flottmann, Ph.D. Thesis, DESY-93-161A (1993).
- [5] J.C.Liu, T.Kotseroglou, W.R.Nelson, D.Schultz, SLAC-PUB-8477 (2000).
- [6] V.Bargmann, L.Michel, V.L.Telegdi, Phys. Rev. Lett. 2, p.435 (1959).
- [7] J. C. Sheppard, SLAC LCC-095 (2002).
- [8] A.V.Kulikov, S.D.Ecklund and E.M.Reuter, Proc. of the 1991 Particle Accelerator Conference, p. 2005 (1991).

*Work supported by the US Department of Energy under Contract No D-AC03-76SF00515.

A TEST OF NLC-TYPE BEAM LOADING IN THE SLAC LINAC*

F.-J. Decker, T.O. Raubenheimer, A. Seryi, J.L. Turner, M. Woods, J. Yocky,
SLAC, Stanford, CA 94309, USA

Abstract

The linac at the Stanford Linear Accelerator (SLAC) runs routinely with a beam loading of around 12% for the fixed target experiment E-158. Typical energy spread and energy jitter are 0.1% and 0.05%. To explore the conditions for the Next Linear Collider (NLC) the linac was operated with 20% beam loading. This was attained by increasing the beam charge from $5 \cdot 10^{11}$ to $9 \cdot 10^{11}$ particles and increasing the pulse length from 250 ns to 320ns. Although the beam loading compensation was more difficult to achieve, a reliable operating point was found with a similar energy spread and energy jitter as at the lower loading. Furthermore, using the sub-harmonic buncher (SHB), the beam was bunched at 178.5 MHz instead of the nominal 2.8 GHz so that the charge from 16 adjacent buckets was combined into one. Increased transverse instability and beam losses along the linac were observed indicating the possible onset of beam break-up.

1 INTRODUCTION

The fixed target experiment E-158 has similar parameters (not including the emittance) to the NLC (Tab.1). The main differences are total charge and the bunch spacing. Two different experiments were done at the end of E-158 Run II in the fall of 2002.

Parameter	E-158	NLC-500
Charge/Train	6×10^{11}	14.4×10^{11}
Repetition Rate	120 Hz	120 Hz
Energy	45 GeV	250 GeV
e ⁻ Polarization	-80%	80%
Train Length	270ns	267ns
Microbunch spacing	0.3ns	1.4ns
Beam Loading	13%	22%
Energy Spread	0.15%	0.16%
Intensity Jitter	0.5% rms	0.5% rms
Energy Jitter	0.03% rms	0.3% rms
Transverse Jitter	5% of spotsize (x or y)	22% of x spotsize, 50% of y spotsize

Table 1: Comparison of E-158 and NLC parameter.

First the charge and pulse length was raised at a lower energy to accommodate the additional beam loading. Then the sub-harmonic buncher was switched on which puts the charge in every 16th S-band bucket resulting in a

bunch spacing of 5.6 ns. These two setups had quite some different difficulties, the first one getting the beam through the injector chicane (160 MeV point), the second one had signs of beam losses in the linac (beam break up).

2 INJECTOR

2.1 Phase Loading

The beam loading in the injector region is especially tricky, since the beam is not at the crest of the RF curve and therefore creates in general amplitude and phase variations along the beam. The phase loading is strongest in the capture region where the velocity is still far below the speed of light. A pulsed phase shifter, which quickly reverts the phase by 180° is installed at the klystron, which feeds the first acceleration section. A problem arises from the fact that it also feeds via a high power splitter a 4-cell S-band buncher just in front of this section. So any necessary adjustments cannot be optimized independently. Another problem is also the fixed 180° phase flip. Here a slower change of the order of the pulse length and with a variable amount in phase would help the high charge setup.

At the chicane a beam energy spread along the pulse would create different phases along the main linac. A 4° variation is normally already observed in E-158 with $6 \cdot 10^{11}$ particles. Higher currents make this more difficult to compensate. This compensation can have different setups, first with energy and phase all the same, or phase and energy in such a way that together with the following linac the end energy variation is compensated. A special scenario exists when a charge-induced phase offset can reduce the energy jitter at the end [1].

2.2 Diagnostics

Behind the capture section is a toroid and a gap monitor. Figure 2 shows the toroid signal with and without the sub-harmonic buncher (SHB). The sloped down distribution is necessary to achieve the best beam loading compensation and a small energy spread. The individual bunches which are 5.6 ns apart can be better resolved by a gap monitor, where the RF coming out of a ceramic gap is measured by a crystal detector. This device is also sensitive to the bunch length (Fig. 3).

3 LINAC

3.1 Beam Break-Up

The long pulse current of about 450 mA ($9 \cdot 10^{11}$ particles or nearly 150 nC in 320 ns) is much higher than was achieved many decades ago in the SLAC linac.

*Work supported by Department of Energy contract DE-AC03-76SF00515.



Figure 1: The current signal of a fast toroid shows the sloped distribution (50 ns/div). Individual bunches have more charge and can nearly be resolved with the SHB on.

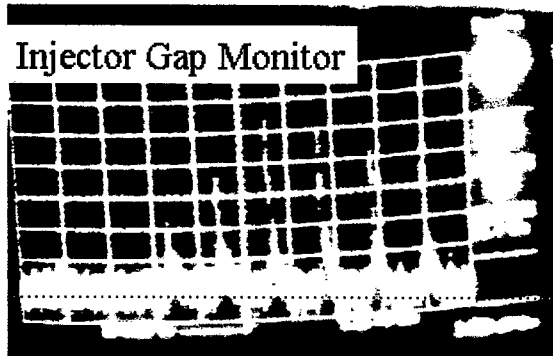


Figure 2: Gap monitor showing the beginning of the bunch train (5 ns/div).

$$I_{breakup} (mA) \propto \frac{\phi \epsilon}{Z \tau}$$

ϕ	focusing strength of quad lattice
ϵ	energy gradient
Z	length of Linac
τ	pulse length

The reasons are the higher RF gradient due to SLED, a stronger quadrupole focusing introduced for the SLC, the shorter beam pulse (<500 ns instead of 1.5 μ s), and the early dimpling of cell 3, 4, and 5 in some accelerator sections, which changed the 4140 MHz transverse deflecting mode.

No beam break-up [2,3,4] was observed when the sub-harmonic buncher was turned off and each consecutive bucket was filled. As soon as the SHB was turned on the injector had actually less problems, but there was beam loss observed in the linac when the pulse was lengthened above 90 ns. Figure 3 shows the beam spot of a synchrotron light monitor (SLM) in the following A-Line at a high dispersion in x . The top shows a long pulse (320 ns) where the energy spread is not totally compensated, while the bottom shows a shorter pulse (and therefore less energy variation) with a blow-up in y . This is an indication of beam break-up, which should be first visible in y , since the RF couplers are in x and therefore the x transverse mode can better decay.

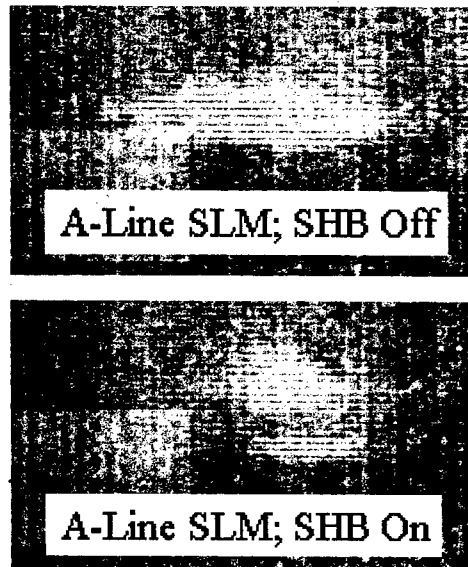


Figure 3: Beam spot on Synchrotron Light Monitor.

3.2 BPM at End of Linac

A quick check to look at the raw BPM signal is shown in Fig. 4. The signal didn't show any instability, but it was in x and the pulse was reduced just to 80 ns to minimize losses in the linac.

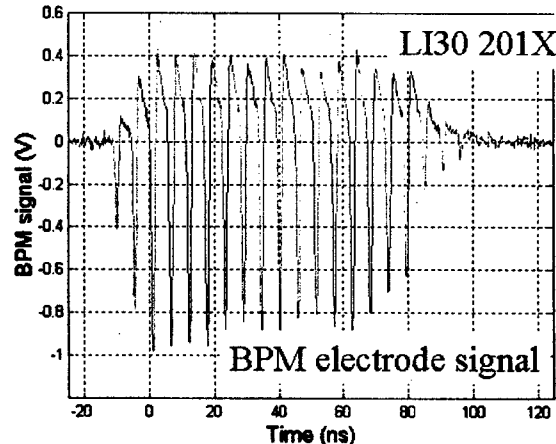


Figure 4: BPM raw signal at the end of linac.

4 A-LINE

4.1 Gated Camera

The A-Line bends the beam to the fixed target experiment E-158 in Endstation A. The bending creates synchrotron radiation, which is monitored by a gated camera. The gate was fully open for Fig. 3, but can be reduced down to 60 ns, so the energy and energy spread along the pulse can be measured (Fig. 5). This measurement is normally used to fine-tune the charge distribution so that there is no energy variation along the pulse. This was not done in this case leaving about a 100 MeV slope. The energy spread also shows some increased values near the tail end of the pulse. This can be the case if the tail shifts in phase and therefore is further off the crest of the RF.

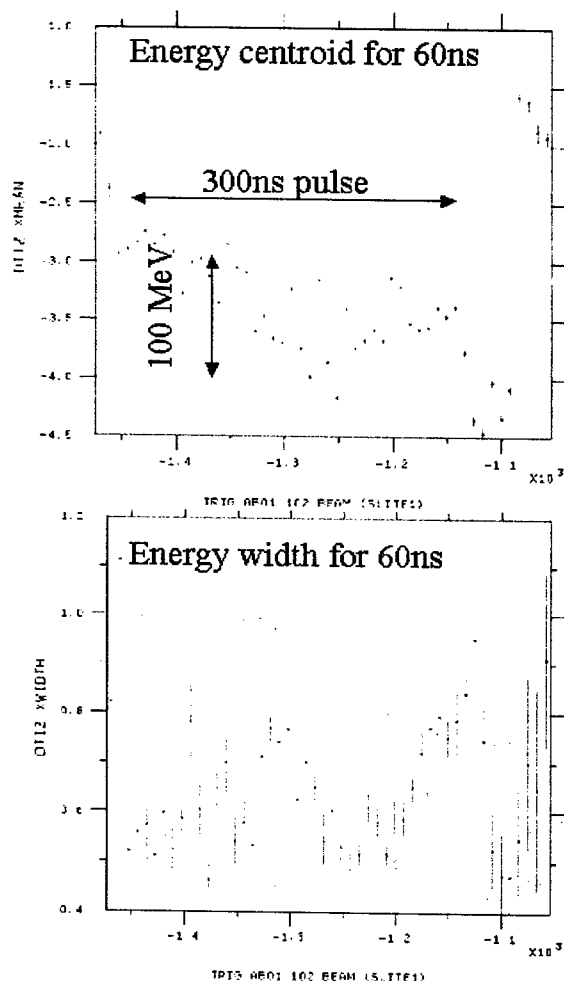


Figure 5: Energy and energy spread along the beam pulse.

4.2 Toroids

The toroids in the injector and linac were all saturating and only A-Line toroids were measuring the transported charge up to $9 \cdot 10^{11}$ particles per pulse. So it was difficult

to check or quantify any possible beam loss. On the other hand any substantial loss in the main linac would have triggered the Machine Protection System, which would have caused the beam to rate limit or trip off.

4.3 Beam Loading and Jitter

The beam energy of the A-line was lower to 40 GeV to accommodate a beam loading up to 25% or $1.4 \cdot 10^{12}$ particles in a 450 ns pulse [5]. About 20% loading with $9 \cdot 10^{11}$ particles in 320 ns was achieved. With the bigger loading the energy jitter of the tail of the pulse also increase since the intensity jitter was about constant. Figure 6 shows the beam tail moving up to ± 10 mm at the highest dispersion point of $\eta_x = 5$ m for charge variation between 7.6 and $7.7 \cdot 10^{11}$ particles per pulse.

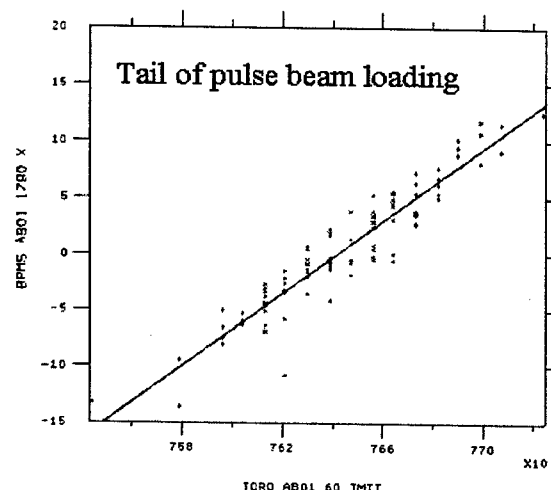


Figure 6: Beam loading measured for the tail of the pulse.

5 SUMMARY

Although this test was done with not much time in the last shift of the E-158 experiment before Thanksgiving of 2002, it accomplished quite some results. A peak charge of $9 \cdot 10^{11}$ particles in 320 ns at 40 GeV in a stable condition, with problems near the 160 MeV chicane. And beam break-up effects in the linac for pulse length over 90 ns. Analytical and simulation efforts were not done yet to check whether these results are within the expectations.

6 REFERENCES

- [1] F.-J. Decker et al., "High Power Beams at SLAC", PAC01, Chicago, June 2001.
- [2] R. Neal et al., "The Stanford Two-Mile Accelerator," W.A. Benjamin, Inc., New York, 1968, p. 203-237.
- [3] G. Loew et al., SLAC-PUB-0659.
- [4] R. Helm, G. Loew, SLAC-PUB-083.4
- [5] F.-J. Decker, Z.D. Farkas, J. Turner, "High Current, Long Beam Pulse with SLED, SLAC-PUB-8113, Apr 1999, or PAC 99, New York, Mar 1999, p 774-776.

IMPLEMENTATION OF DYNAMIC MISALIGNMENTS AND LUMINOSITY STABILIZATION*

L. Hendrickson, T. Himel, T.O. Raubenheimer, A. Seryi, P. Tenenbaum, M. Woodley
SLAC, Stanford, USA
D. Schulte CERN, Geneva, Switzerland

Abstract

To fully characterize the luminosity performance of a linear collider, it is important to simulate the effects of ground motion as well as the beam-beam feedback and other stabilization systems planned to compensate for that motion. The linear collider simulation codes have recently been extended to include both ground motion models and stabilization systems to support the work of the International Linear Collider Technical Review Committee (TRC) [1]. This paper discusses the implementation details and the optimization strategies for interpulse beam-beam feedback.

INTRODUCTION

One of the TRC tasks was to evaluate strategies for keeping the beams in collision. Although simplified assumptions were used, the studies provide an initial look at operation of a linear collider and a basis for more detailed future work. For NLC, CLIC and TESLA, simulations included initial imperfections, realistic ground motion models, stabilization of the beam collisions at the interaction point (IP), and vibration of the final doublet. Results of these simulations are reported separately [2].

Simulation Platform

Many of the simulations were performed using Matlab-LIAR [3], interfaced to Guinea-Pig [4] to simulate the beam-beam effects. MATLAB provides a flexible simulation platform, LIAR incorporates fast wakefield tracking with emittance dilution effects, and the DIMAD tracking engine is used for regions with nonlinear focusing elements, including the beam delivery, where wakefields are not a concern. A full ground motion simulation [5] is included, with diffusive ("ATL") motion as well as cultural noise. There are optional transfer functions at specified locations. In particular, vibration of the final doublet has a significant effect on the collisions at the IP, and it is important to include effects of additional vibration and any active stabilization [6].

In other simulations, the code PLACET [7] was used with Guinea-Pig. The code, which uses Tcl-Tk as an interface language, was extended to perform tracking in nonlinear elements and to allow the simulation of ground motion. A simplified modeling of the effect of slow feedbacks on the fast motion was incorporated.

* Work supported in part by US DOE, contract DE-AC03-76SF00515.

Initialization of Imperfect Machine States

In all proposed linear colliders, the beam emittance will increase during transport from damping rings to IP even after all means of emittance preservation have been implemented. Although details of the simulation strategy are described elsewhere [8], it is important to note that the characteristics of the beam-beam deflection are affected by the initial state of the machine and thus the optimal strategies for feedback design must include consideration of these effects. For these simulations, only the main linac and beam delivery system (BDS) were considered. The BDS was treated as perfect (i.e. with no initial static errors). To streamline the calculations, alignment procedures were modeled with a simplified method which should mimic the behavior of the complex algorithms. The simulation included RMS position errors of the BPMs and the accelerating structures and tilts of the structures. Structure misalignments create emittance growth mainly due to wakefields, while misalignment of the BPMs leads to dispersive emittance growth. A simple one-to-one trajectory correction was applied throughout the linac. Before entering the BDS, the mean offset and angle of the bunch were corrected.

DESIGN CONSIDERATIONS FOR BEAM-BEAM FEEDBACK

An IP feedback system is required to keep the beams in collision at the interaction point. Such a system will use the beam-beam deflection as a very precise measurement of the beam separation. The TRC design used the SLC feedback system [9] as a model, but some choices were re-evaluated in view of the likely operating regime of a future collider. Three considerations were:

- Modeling the beam-beam deflection curve.
- Optimizing the feedback deflection setpoint
- Designing the time response characteristics of the feedback controller.

Modeling the Deflection Curve

The beam-beam deflection curve in Figure 1 is a plot of the deflection of one of the beams, as a function of the beam-beam separation at the IP. The separation is controlled by an upstream kicker or dipole corrector. The deflection curve is a nonlinear function. It may be measured by using the kicker or corrector to sweep one beam across the other, while measuring the beam-beam deflection with BPMs on either side of the IP.

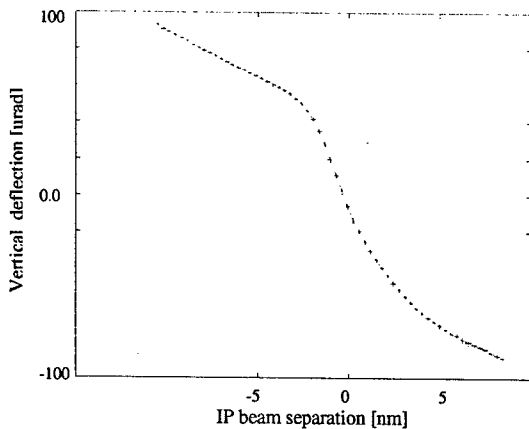


Figure 1: Beam-beam deflection curve for NLC.

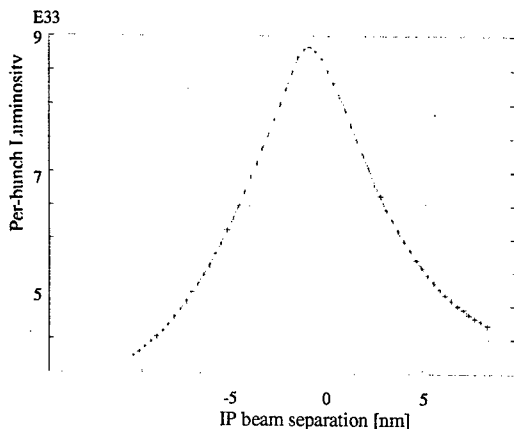


Figure 2: Luminosity as a function of beam separation for NLC

For SLC IP feedback, a linear fit was used based on the steepest slope in the central region. This resulted in a feedback response which would be conservatively slow for large beam-beam separations. For the LIAR TRC simulations, the deflection curve was modeled with a piecewise linear fit. This assumes that very good data may be available in a real collider even in the presence of beam jitter. This kind of "clean" beam-beam scan may be obtained if the scan can be performed over a single bunch train with very fast kickers. In PLACET the feedback assumed a linear deflection curve. Simulations indicate that the piecewise linear fit may not be necessary and that the simpler linear algorithm may be equally effective (see "Optimization of Feedback" and [8]).

Optimizing the Deflection Setpoint

Because the bunch shape may be asymmetric, the maximum luminosity may not be achieved when the beams are colliding head-on, as shown in Figure 2. It is preferable to find a feedback deflection setpoint which maximizes the luminosity. In the SLC, the

deflection setpoint was obtained from head-on collisions as determined by the beam-beam deflection fit, regardless of luminosity. In PLACET an optimization routine used local quadratic approximations. In the LIAR TRC simulations, an asymmetric Gaussian was fit to the luminosity versus position. This might assume the existence of a fast and accurate luminosity monitor that is proportional to luminosity or is at least maximized with maximum luminosity, see [8]. However, in operation, it is possible to average many pulses to reduce the effects of monitor noise and beam jitter, or the setpoint itself may be optimized in real-time as described later.

Time Response for Feedback

In addition to optimal time response, there are other considerations in designing a beam-based feedback controller. Response speed must be faster than or comparable to what a typical operator might be able to stabilize manually, or the operator will simply take control. Robustness during changing machine conditions is also important. The SLC system [9] was designed using modern optimal control theory. This method minimized the RMS of the beam state under given assumptions, but was tuned to also give a good response for a step function. The feedback exhibited an exponential response with a time constant of about 6 feedback iterations (figure 3, --). For the SLC IP feedback, the controller had a faster time response (figure 3, --), with additional complexities. The control system included latency in BPM processing, computing and actuation, so that the feedback was unable to implement any response to a change within the next 120-Hz pulse. This was modeled using Predictor-Corrector formalism, but the feedback response function was adversely affected. For future colliders, it is assumed that actuation would be effective on the next machine pulse, resulting in an improved feedback response function (figures 3,4, -o).

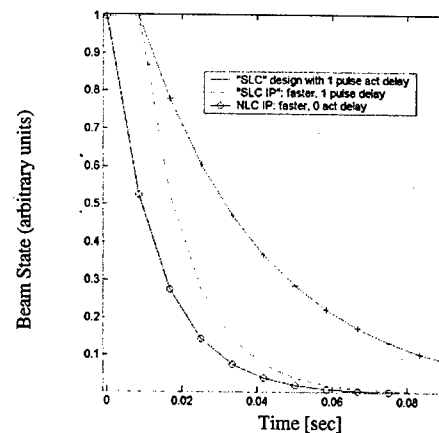


Figure 3: Step response for different feedback assumptions.

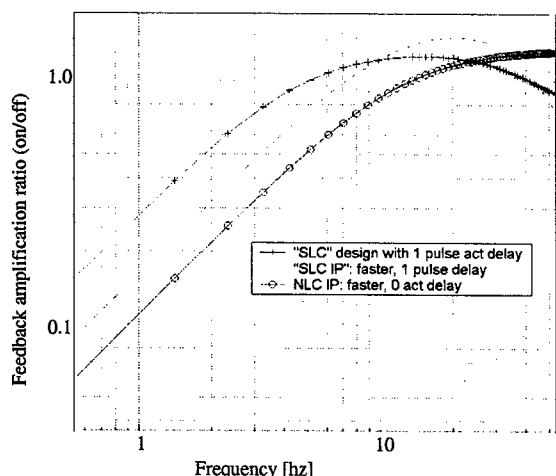


Figure 4: Feedback frequency response function for different assumptions (120-Hz pulse rate). The "NLC" design (-o), with low latency and faster response, has good response without excessive amplification.

OPTIMIZATION OF FEEDBACK

In addition to the TRC simulations, a separate effort was made to understand the sensitivity of the NLC IP feedback performance to different parameters and to implement a design which could maximize luminosity in the presence of beam jitter and other imperfections. Three parameters were adjusted in simulated-realtime:

- Slope for linear deflection approximation
- Deflection Setpoint
- Exponential time constant for feedback response.

The approach was to simulate operation over many pulses with ground motion while adjusting values of these parameters, to achieve maximum luminosity. The first two parameters were readily optimized within the framework of the TRC simulations. However the "real-time" optimization process can produce a different result from the scan procedure. The LIAR-based TRC simulations assumed a perfect "instant" measure of the beam-beam deflection curve and luminosity curve. With very large ground motion, the beam shape itself can change on short timescales. Furthermore, for linear approximation of the deflection curve, the ideal slope depends upon the beam jitter. One might guess that a detailed piecewise linear fit could be optimal, but in simulations thus far, it was not found to be helpful. For smaller ground motion, the feedback response was not very sensitive to the deflection slope and a non-optimal feedback was easily able to keep the beams in collision. For very large ground motion, the shape of the deflection curve changed from pulse to pulse, and a linear fit based on the current average beam conditions worked as well or better than the detailed nonlinear fit. Adjusting both the linear slope and the deflection setpoint using time-averaged luminosity is particularly suitable when beam jitter and measurement errors are an issue, because

appropriate averaging of many pulses can be adjusted as needed.

Optimizing the exponential time constant presented additional complexities in the SLC framework because a number of matrices incorporated the time response. Therefore the algorithm was converted to an equivalent exponential form, in which the time response could be optimized by adjusting just one parameter: exponential weight. The response was nearly identical, with one exception: the SLC feedback had a small DC offset by design, and in the exponential form the DC offset was gone - a beneficial side-effect. The equations are:

```
state_vec = expected_change +
weight * (state_vec - raw_state_vec) + raw_state_vec
delta_act = - nmpt * state_vec
act_vec = act_vec + delta_act
expected_change = bmpt * delta_act
Where: weight = the exponential gain: exp(-1/npulses)
state_vec = estimated state vector
raw_state_vec = measured deflections, converted to
corrector units
act_vec = actuator vector (correctors)
nmpt,bmpt are transport matrices
```

In the PLACET simulations a linear deflection curve was assumed and the gain was optimized for a set of 25 different machines. With these more pessimistic but also more robust assumptions the feedback performance was still very comparable to the LIAR-based TRC results.

FUTURE WORK

The NLC feedback optimization studies did not include the effects of final doublet vibration and stabilization, and these are likely to affect the results. Future work will incorporate IP feedback systems with linac and BDS stabilization and steering systems, with more realistic and detailed operational scenarios.

REFERENCES

- [1] "Second ILC-TRC Report", SLAC-R-606,2003.
- [2] A. Seryi, et al., "Effects of Dynamic Misalignments and Feedback Performance on Luminosity Stability in Linear Colliders", in these proceedings.
- [3] P. Tenenbaum, et al., "Recent Developments in the LIAR Simulation Code", SLAC-PUB-9263 (2002).
- [4] D. Schulte, "Beam-Beam Simulations with Guinea-Pig", CERN-PS-99-014; ICAP 1998.
- [5] <http://www.slac.stanford.edu/~seryi/gm/model>
- [6] J. Frisch, et al., "Active Vibration R+D for the Next Linear Collider", SLAC-PUB-9419, PAC 2001.
- [7] D. Schulte, et al., "Simulation Package based on PLACET. CLIC-Note 482 (2001).
- [8] D. Schulte, "Luminosity in Future Linear Colliders in the Presence of Static Wakefield Effects in the Main Linac", CLIC Note 544, CERN, 2003.
- [9] L. Hendrickson, et al., "Feedback Systems for Linear Colliders", SLAC-PUB-8055; PAC 1999.

OPTIMIZED WAKEFIELD SUPPRESSION & EMITTANCE DILUTION-IMPOSED ALIGNMENT TOLERANCES IN X-BAND ACCELERATING STRUCTURES FOR THE JLC/NLC¹

R.M. Jones, Z. Li, R.H. Miller and T.O. Raubenheimer; SLAC, USA

Abstract

In order to prevent electrical breakdown occurring in the JLC/NLC (Japanese Linear Collider/Next Linear Collider) X-band structures several new structures are under investigation. These accelerating structures represent an evolutionary design of the DDS series of structures [1]. The phase advance per cell has been varied and the detailed elliptical shape of the cell has been varied in order to simultaneously minimize the group velocity, the surface electromagnetic fields and the pulse temperature rise on the copper surface [2]. It is also important to ensure that the wakefield induced by multiple bunches traversing the accelerating structures does not disrupt trailing bunches. The long-range wakefield must be decreased adequately in order to prevent a BBU (Beam Break Up) instability occurring and to ensure that emittance dilution due to the higher order modes is kept to acceptable levels. The long-range wakefield is forced to de-cohere by detuning all of the frequencies such that the mode density of frequencies is approximately Gaussian. In order to minimize the impact of the wakefield on the beam dynamics we change the bandwidth and the standard deviation of the Gaussian distribution of frequencies such that a "cost function" is minimized. Interleaving of cell frequencies of adjacent structures is required to adequately damp the wakefield of each particular structure under consideration. The resulting alignment tolerances imposed on the cells and structures is significantly looser alignment tolerances with the use of the code.

1 INTRODUCTION

We report on manifold damping and detuning of the wakefield in the X-band accelerating structure known as H60VG3S17 which forms the baseline design for the JLC/NLC [3]. In particular we discuss damping of the long-range wakefield which, if left unchecked, will result in severe emittance dilution of the beam.

The 55 cells of the 60 cm structure, H60VG3S17, incorporate a $5\pi/6$ phase advance per cell and four manifold are attached to couple out the wakefield. It is an evolutionary design from the original R/DDS series using the same method to detune and damp the wakefield. The average group velocity of the accelerating structure is $0.02c$ and the a/λ (iris radius to free space wavelength) has an average value of 0.17 . The value of a/λ has been reduced from 0.18 in H60VG3S18 order to reduce the pulse temperature heating that occurs on the surface of the copper structures. Reducing the iris radius increases

the shunt impedance of the accelerating mode and also increases the short range wakefield ($\sim a^{-3.8}$) and requires slightly tighter tolerances on the structure-to-structure alignments and also a slightly larger BNS energy compensation requirement [2]. These effects do not put severe constraints on the overall design of the linac as they are relatively small changes.

Interleaving of the frequencies of neighbouring structures is discussed in section 2 as a means to damp the wakefield to levels that do not appreciably dilute the emittance of the beam. Beam dynamics issues are discussed in section 3 in which the progress of the charged particle bunch train is monitored in phase space throughout the linac using the particle tracking simulation code LIAR [4]. The 4th section addresses the cell and structure alignment tolerances that are imposed on the accelerator for a specified emittance dilution

2 WAKEFIELD OPTIMIZATION

The dominant dipole deflecting mode in H60VG3S17 is confined to the first frequency band. As we have a limited number of cells, namely 55, for each H60VG3S17 structure then the mode separation is larger by a factor of approximately four compared to that of the DDS series (which consisted of 206 cells). Thus, we interleave the frequencies of the modes of adjacent structures in order to

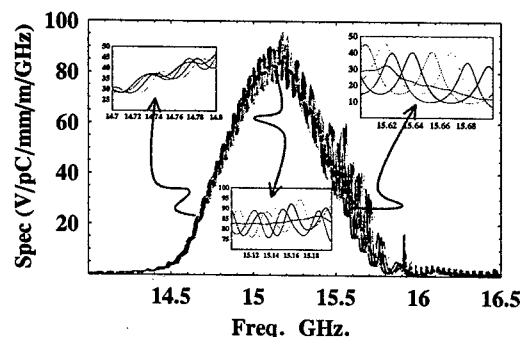


Figure 1: Spectral function of interleaved H60VG3S17. Reflections from the HOM (Higher Order Mode) coupler are not included in the simulation. The spectral functions of the individual structures oscillate about the interleaved overall distribution (shown in black and dashed). The middle and ends of the band are shown inset for clarity.

¹ Work supported by the U.S. DOE Contract No. DE-AC03-76SF00515.

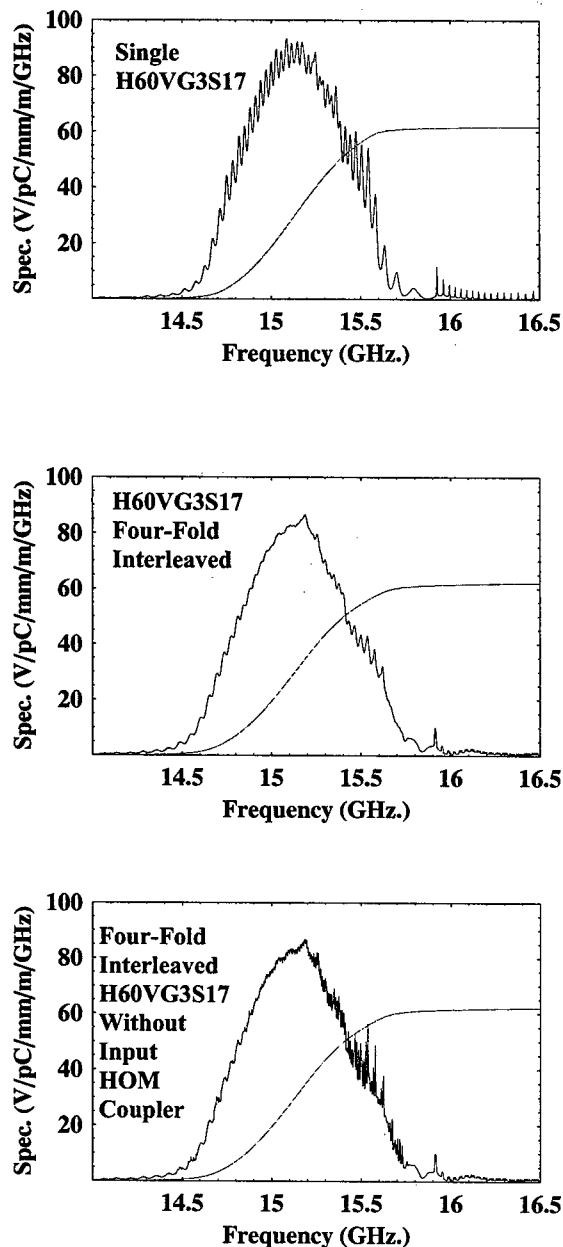


Figure 2. Spectral function for HDDS under three different conditions. Shown uppermost is a single structure in which the cost function has been minimized when all the cells are coupled to the manifold. The bandwidth is 7.80% and the total frequency width is 3.71σ . Four-fold interleaving of the frequencies of adjacent structures is shown in the middle figure. The re-optimised bandwidth for the middle fig. is 9.88% and 4.68 units of σ . The spectral function which results when the input HOM coupler is removed is shown as the lowermost fig.

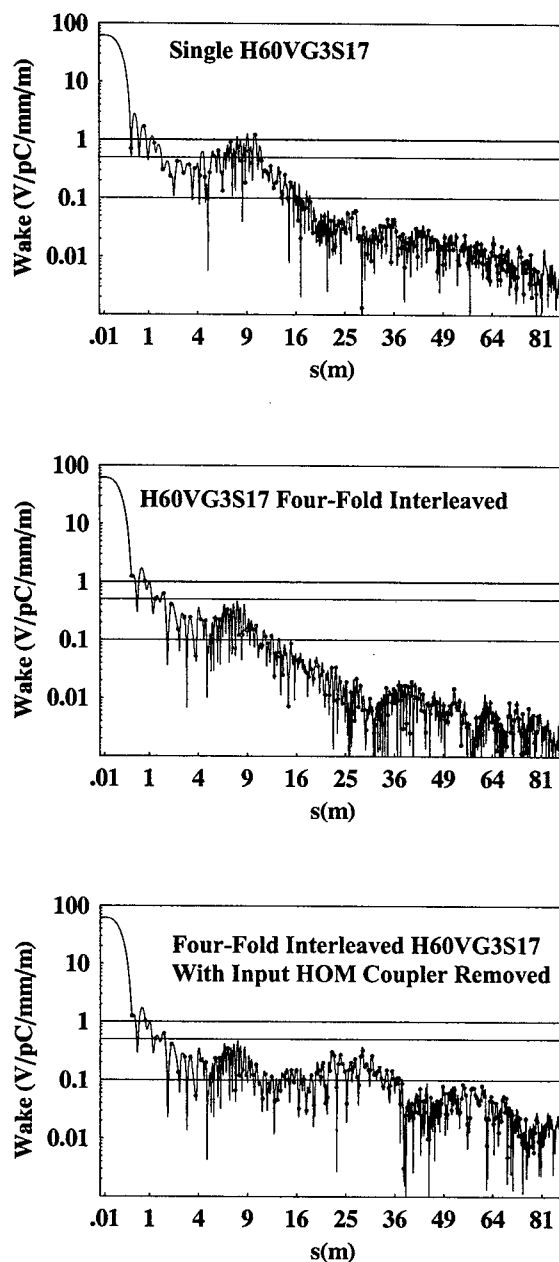


Figure 3. Envelope of wake function for the conditions given in the adjacent figure. The points are at the location of the bunches. Each bunch is separated from its neighbour by 42cm and there are 192 of them in each bunch train. The wake which incorporates 4-fold interleaving of structures is below 1V/pC/mm/m for all bunches apart from the first.

damp the wakefield to an acceptable level. The frequency separation of three of the four structures is based on the separation of the maxima in the oscillatory function of one of the four spectral functions. The individual spectral functions, together with the overall, interleaved function, are illustrated in fig 1. The uncoupled kick factor density function is a Gaussian function and its bandwidth is determined with a computer code that automatically minimizes the "cost function" [5]. The optimised non-interleaved versus four-fold interleaved spectral function and wakefield are compared in fig 2. Also indicated is the effect of removing the input HOM coupler on the wakefield. It is clearly a small effect and thus it may be feasible in future structures to dispense with the upstream HOM coupler entirely.

3 BEAM DYNAMICS

The sum wakefield is defined as the wake evaluated at the location of the bunch summed over all bunches that have proceeded that bunch. The RMS value of the sum wakefield serves as a guide as to whether or not BBU will occur and provided it is less than unity BBU has been found to be suppressed. The RMS of the sum wakefield, S_{RMS} , for the three cases corresponding to the wakes of fig 3 is evaluated as a function of fractional change in the bunch spacing. A change in the bunch spacing corresponds to a systematic error in the frequencies of all cells. The emittance growth as the beam traverses the

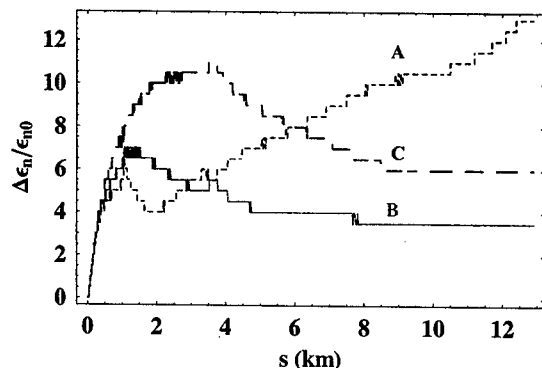


Figure 4. Simulation of $\Delta\epsilon/\epsilon_0$, the percentage emittance growth for a single accelerating structure (A), four-fold interleaving of adjacent structures with (B) and without input HOM couplers attached (C)

linac is shown in fig 4 for identical offsets of 25% of σ_y . Each of these curves is obtained for systematic errors in the cell frequencies of 7.5MHz, 33.5MHz and -10.5MHz for A, B, C respectively and are chosen such that a local maxima in S_{RMS} is achieved. The non-interleaved structure is not desirable. However, both four-fold interleaved structures show no more than a 6% dilution of the beam emittance. Also, the emittance dilution at the nominal bunch spacing (42cm, and no frequency errors) shows no more than 4% in all cases, including the non-

interleaved case. However small systematic errors strongly influence the sum wakefield and hence the emittance would readily grow in this situation. Four-fold interleaving of structures is planned for the NLC with considerably relaxed tolerances in frequency errors and also in alignments as will be seen in the next section.

4 ALIGNMENT TOLERANCES

The transverse long-range and short-range wakefield dilute the final emittance of the beam and it imposes a tolerance requirement on the alignment of groups of cells. The tolerance due to the transverse long-range wakefield is calculated both with an analytical method [6] and by numerically tracking the beam down the linac and moving groups of cells transversely in a random manner (for a specified rms offset) with the computer code LIAR [4]. The tolerances that result from this procedure for a maximum emittance dilution of 10% are shown in Fig 5 for the linac parameters given in [7], modified to take into account 4-fold interleaving of structures. Excellent agreement between the analytical model and the tracking method is obtained. The long-range wake imposes a cell-to-cell and structure-to-structure alignment tolerance of 33 μ m and 160 μ m, respectively.

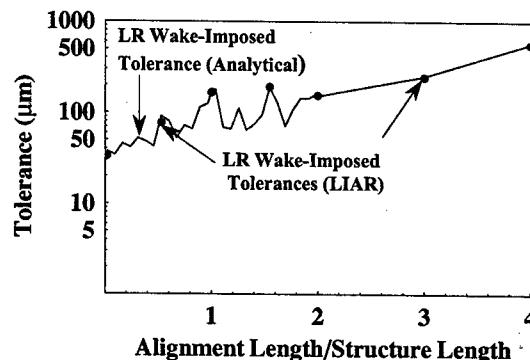


Figure 5. Alignment tolerances for H60VG3S17.

5 ACKNOWLEDGMENTS

These results were first presented at the SLAC structures group meeting and we thank all members of the group for stimulating discussions. We are pleased to acknowledge particularly useful comments from Dr. David Burke

6 REFERENCES

- [1] R.M. Jones et al, PAC97, also SLAC-PUB 7537
- [2] Z. Li et al, WPAG027, these proceedings.
- [3] P. Tenenbaum, private communication
- [4] R. Assman et al, LIAR, SLAC-PUB AP-103
- [5] R.M. Jones et al, LINAC2002, also SLAC-PUB 9407
- [6] K.L.F. Bane et al, EPAC94, also SLAC-PUB 6581
- [7] R.M. Jones et al, LINAC2000, also SLAC-PUB-8610

ENERGY DISPERSION COMPENSATION AND BEAM LOADING IN X-BAND LINACS FOR THE JLC/NLC¹

R.M. Jones, V.A. Dolgashev, R.H. Miller, C. Adolphsen and J.W. Wang; SLAC, USA

Abstract

The shape of an RF pulse is distorted upon propagating through an X-band accelerator structure due to dispersive effects. This distortion together with beam loading introduce energy spread between 192 bunches. In order to minimize this energy spread we modify the input RF pulse shape. The pulse propagation, energy gain, and beam loading are modelled with a mode-matching computer code and a circuit model. A 2D model and a circuit model of a complete 60 cm structure, consisting of 55 cells and input and output couplers is analyzed. This structure operates with a $5\pi/6$ phase advance per cell. Dispersive effects for this structure are more significant than for previously studied $2\pi/3$ phase advance accelerating structures. Experimental results are compared with the theoretical model and excellent agreement is obtained for the propagation of an RF pulse through the structure.

1 INTRODUCTION

The NLC/JLC (Next Linear Collider/Japanese Linear Collider) baseline design now consists of eight 60cm accelerating structures attached to a girder (of which there are several thousand). Each cell in the structure has a phase advance of $5\pi/6$. Previously $2\pi/3$ was the phase advance of choice, but a higher phase advance was chosen in order to reduce the group velocity of the fundamental mode wave, which was thought to reduce any electrical breakdown occurring in the structures [1]. A CAD view of several cells in H60VG3 is shown in fig. 1. This accelerating structure consists of 55 cells and has been carefully designed to reduce the electromagnetic fields on the surface of the copper, to minimize the pulse temperature heating effects (by shaping the cavity-manifold slots into a "pie" shape).



Figure 1: Cross-sectional view of a CAD drawing of the H60VG3 accelerating structure. Sending an rf pulse down the accelerator resulted in a noticeable distortion in the shape of the pulse output from

55 cells and this is discussed in section 2. Section 3 delineates the effect of beam loading on the overall pulse shape and means to overcome the energy deviation over the pulse train caused by this dispersive effect.

2 DISPERSION IN TW STRUCTURES

Shown in fig 2 is the result of an experiment to measure the pulse shape after transiting through all 55 cells of the TW (Travelling Wave) structure H60VG3. Distortion is evident at both the trailing and leading edge of the pulse.

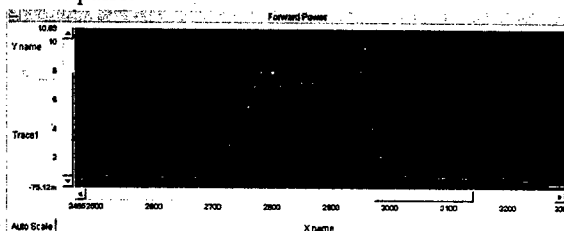


Figure 2: Oscilloscope measurement of the output pulse for a 240ns input rectangular pulse with a 10ns rise and fall time injected into H60VG3

To simulate the propagation of the pulse we utilize the 0 and π frequencies from 5 cells in a 3D simulation of cells with boundary conditions corresponding to an infinitely periodic structure. From these points we obtain the corresponding dispersion curves for these cells and additional cells are obtained by interpolation. We use a circuit model [2] to simulate the propagation of a pulse through this structure and also through constant impedance structures.

Prior to obtaining the pulse shape the accelerator must be matched to the attached couplers and this is simulated by varying the end cell frequencies and Q values. Fig. 3 illustrates the frequency behaviour of the reflection coefficients after the structure has been matched. In all cases to achieve this reflection coefficient we utilize [3] and apply it to the circuit model to obtain minimize the internal reflection coefficient of the accelerator. The pulse shape after propagating through all 55 cells is shown in fig 4 for three phase advances: $2\pi/3$, $3\pi/4$ and $5\pi/6$. Before electrical breakdown and the consequent damage to the structures was discovered [4], all DDS (Damped and Detuned Structures) were fabricated with a $2\pi/3$ phase advance per cell. Little pulse distortion is

¹ Work supported by the U.S. DOE Contract No. DE-AC03-76SF00515.

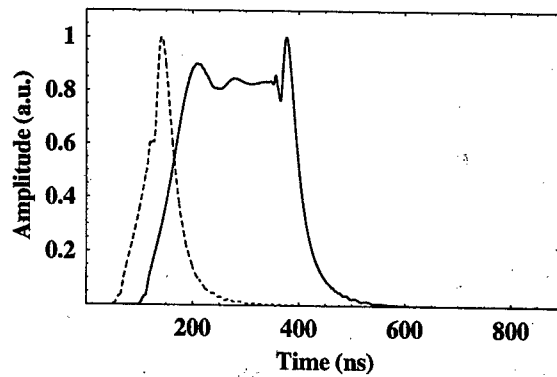
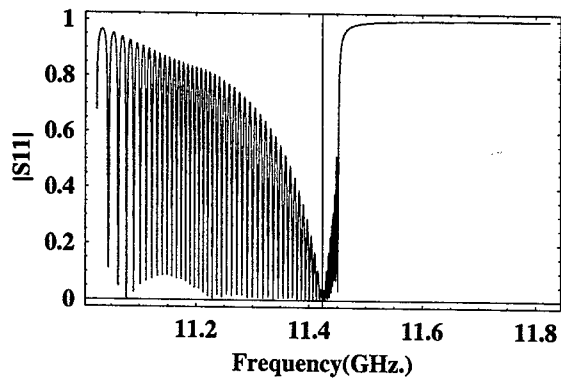
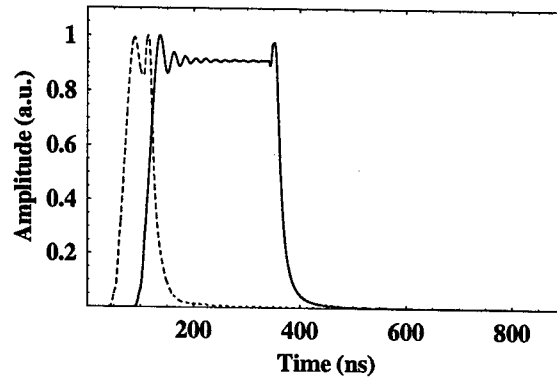
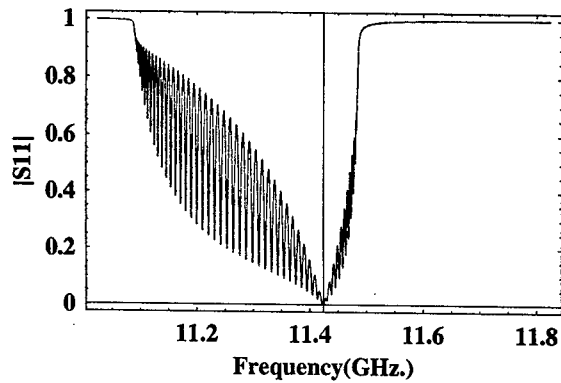
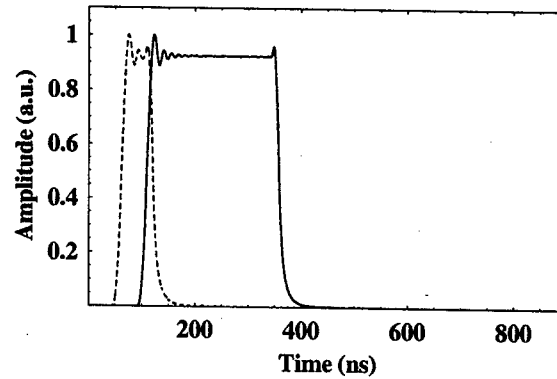
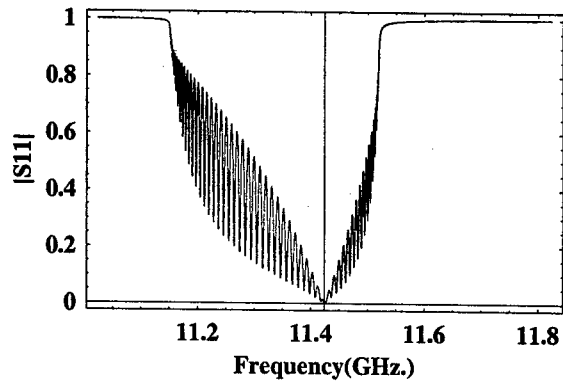


Figure 3: Reflection coefficient of the input to several travelling wave accelerator structures each of which consists of 55 cells. The uppermost consists of a constant impedance structure with a phase advance per cell of 120 degrees, the middle to a constant impedance with 135 degrees phase advance and, the lowermost to H60VG3 in which the phase advance is 150 degrees and the cell parameters vary smoothly along the accelerator structure.

Figure 4: A rectangular pulse with a fall and rise time of 10ns and a flat-top of 240ns and 50ns is propagated through the accelerating structures described in fig 3. The final output pulse for each structure is illustrated above (blue and dashed for the shorter input pulse).

seen for this case. The reduced group velocity structure that was measured experimentally (fig 2.) corresponds to the simulation in fig 4 with a $5\pi/6$ phase advance per cell. The distortion recorded in the experiment is well represented by the simulation and it is clear that the pulse distortion occurs due to dispersion in the structure. The intermediate phase advance of $3\pi/4$ gives rise to very little distortion in the pulse shape and it is shown because it corresponds to another potential structure that has been under consideration for the NLC. In all cases shown in figs. 3 and 4 a circuit model has been used. However, a mode matching method [5] applied to the $5\pi/6$ case shows very similar pulse distortion. We utilize this mode matching method to calculate energy gained by 192 electron bunches traversing the structure and this is described in the following section

3 BEAM LOADING AND ENERGY DISPERSION COMPENSATION

Multiple bunches of electrons passing through an accelerating structure load down the accelerating field and consequently the field is reduced. In order to reduce this droop in the field the initial RF pulse is ramped up as the structure is filled with electromagnetic field. Here we calculate the effect of beam loading from the impedance

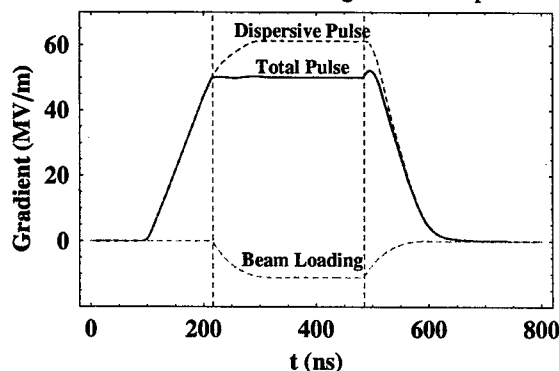


Figure 5: Individual components of a beam-loaded pulse that reaches cell 55 of H60VG3. The dashed vertical (blue) lines indicate the region in which all bunches are accelerated.

of the beam [5] and the beam loading, together with the total pulse are shown in fig 5. Over all bunches the energy deviation from bunch-to-bunch is quite small. However, the energy deviation at the final focus of the collider is required to be very small, namely 0.25% RMS [6]. For this reason we show the energy deviation along the pulse train on an expanded scale in fig 6. The set of points labelled 0 corresponds to this energy deviation and the maximum deviation is approximately 0.75%.

To compensate for this deviation in the energy over the bunch train we investigated reshaping the input RF pulse to the structure. A fraction of the derivative of the energy deviation over train of bunches is added to the original input pulse and this fraction is varied until the energy

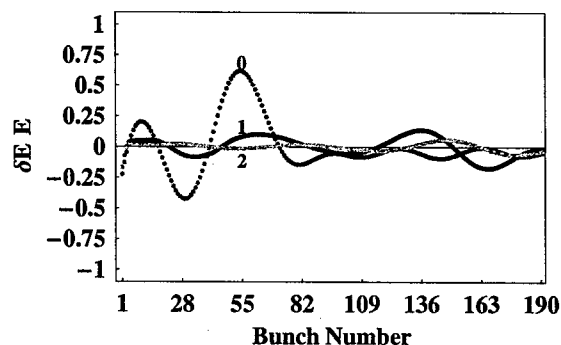


Figure 6: Percentage energy deviation along the train of electron bunches for each stage of the iteration

deviation is minimized. The set of points (in blue) labelled with "1" in fig 6 corresponds to the new energy deviation along the bunch train; the maximum deviation is below 0.2%. Application of the same iterative method again gives the set of points "2" (magenta) and this reduces the energy deviation still further, to less than 0.1%. Further application of this technique allows the energy deviation to be reduced to less than 0.05%. The input pulse prescribed from this process is shown in fig 7.

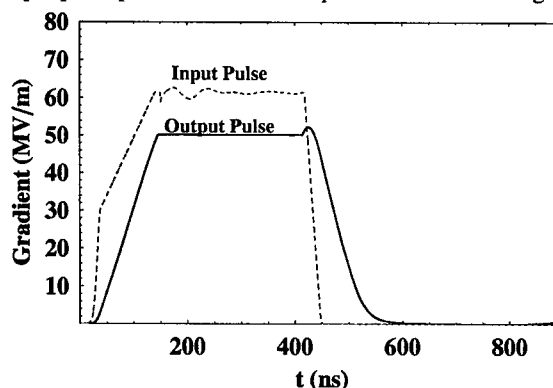


Figure 7: Input pulse to compensate for energy deviation over the pulse train together with final output pulse

Manipulating the phase of the klystrons that feed the structure will allow this pulse shape to be obtained [7].

This energy compensation method results in a small loss of energy as the pulse is compensated over the course of the bunch train. We are also investigating applying a similar compensation scheme over the initial ramp of the pulse and this will minimize the loss in overall efficiency.

4 REFERENCES

- [1] R.M. Jones et al, PAC2001, also SLAC-PUB-8887
- [2] R.M. Jones, to be published
- [3] N.M. Kroll et al, LINAC2000, also SLAC-PUB-8614
- [4] C. Adolphsen et al, PAC2001, also SLAC-PUB-8901
- [5] V. Dolgashev, Proc. ICAP98, California, 1998.
- [6] P. Tenenbaum, private communication
- [7] S. Tantawi, private communication

A RECIPE FOR LINEAR COLLIDER FINAL FOCUS SYSTEM DESIGN

Andrei Seryi, Mark Woodley SLAC, USA*
Pantaleo Raimondi INFN, Italy

Abstract

The design of Final Focus systems for linear colliders is challenging because of the large demagnifications needed to produce nanometer-sized beams at the interaction point. Simple first- and second-order matrix matching have proven insufficient for this task, and minimization of third- and higher-order aberrations is essential. An appropriate strategy is required for the latter to be successful. A recipe for Final Focus design, and a set of computational tools used to implement this approach, are described herein. An example of the use of this procedure is given.

INTRODUCTION

The new compact final focus system [1], based on local chromaticity correction in the final doublet, is now being adopted for all of the linear collider designs because of its superior performance over the traditional final focus design. At the same time, we are receiving an increasing number of requests for a more detailed recipe for the optical design of such a system. A brief, spontaneously written recipe was discussed at the recent Nanobeam workshop [2]. A more detailed treatment is given here.

Some traditional FF systems have been designed using the FFADA (Final Focus Automatic Design and Analysis) program [3]. Although FFADA automates the generation of different solutions for the final telescope, the most tedious part of the design process, minimization of the third-order U3466 aberration (the notation of TRANSPORT [4] is used here and below) still required a trick - one needed to use FFADA to generate a system with certain demagnifications M_x and M_y , check U3466, change M_x and/or M_y , recheck U3466, and iterate until the aberration vanished.

This process can be expressed as a recipe: while preserving the desired linear and second-order properties of the system under consideration, scan possible solutions along particular degrees of freedom (M_x or M_y in this case), find the optimum, scan along other degrees of freedom, and continue iterating until a proper solution is found. Sometimes no satisfactory solution can be found, either because you are stuck in a local minimum or because the requested performance cannot be achieved. In these cases you must use your intuition to know when you need to go back and change something.

A similar approach can be used for designing a compact FF system. In this case, there are many more free parameters that can be changed, but the basic procedure is the same.

* Work supported in part by US DOE, Contract DE-AC03-76SF00515.

A TUNING RECIPE

The following steps were used to design a compact FF system, which will be presented in the next section. The procedure has been implemented as a semi-automatic design tool based on Matlab. As with any recipe, this one should be considered a guide more than a detailed map. It may be necessary to change the strategy or add more steps, depending on the situation (e.g. how far you are from a solution) or depending on the tools being used. The FF system presented in [1] was designed entirely using TRANSPORT. In the following, it is assumed that the basic matching is done with MAD [5]. The element names correspond to those shown in Figure 1. Only those steps of the design which involve variables (*knobs*) important for aberration tuning are highlighted.

0) Design the betatron and energy collimation systems.

1) Work backwards from the IP starting with design values for β^* , η^* , and L^* . Choose reasonable lengths for the Final Doublet (FD) quadrupoles QD0 and QF1 and the separation between them. At a later stage the quadrupole lengths and their separation can be varied to trade synchrotron radiation in the FD against FD vibration tolerances. Make a linear match, varying the strengths of QD0 and QF1, to obtain certain values for α_x and α_y at the exit of QF1 (going away from the IP). These values will later be used to optimize 3rd order aberrations (such as U3246, U1226, etc.).

2) Make a linear match, varying the strength of QD2A, QF3, QD2B, QD4, QF5, QD6, and QF7, to obtain the following conditions: a) "pseudo -I" transform between SD0 and SD4 (all $R_{ii}=-1$, $R_{12}=V_1$, and $R_{34}=V_2$); b) "pseudo +I" transform between SF1 and SF6 (all $R_{ii}=1$, $R_{12}=V_3$, and $R_{34}=V_4$); c) horizontal and vertical waists ($\alpha_{x,y}=0$) at the center of QF7. These V_i are knobs to be used for further aberration tuning (usually for geometric terms such as U1222, U3224, U3444, etc.).

3) Make a linear match, varying the bending angles of B1, B2, and B5, to obtain zero dispersion ($\eta=0$ and $\eta'=0$) at the end of the system, with a certain nonzero value of dispersion at SF5. This dispersion value becomes another tuning knob (affects geometric and chromogeometric terms).

4) Make a linear match, varying the strengths of six beta-matching quadrupoles (labelled "QM" in Figure 1) to obtain a telescopic transformer (diagonal) matrix for the system with certain demagnifications M_x and M_y .

5) Reverse the system and start from the FF entrance. Make a second-order match, varying the strengths of all sextupoles, to zero the T126, T122, T166, T346, and T324 aberrations. At a later stage, when one is close to a solution, SF5 or SF6 can be excluded from the match and left for

later hand/automated tuning.

Further minimization of higher-order aberrations involves both computation of the higher-order transfer matrices for the system and manipulation of beam properties determined by tracking. Implementation will depend on the available tools. In our example, we use the complementary programs TRANSPORT and TURTLE [6] to minimize higher-order aberrations. TRANSPORT calculates matrices up to third-order, while TURTLE is a six-dimensional particle tracking code. Note that it is important to do the tracking and higher-order matrix calculation with codes that are consistent with one another. Using DIMAD [7] for the tracking is also a good choice.

6) Convert the matched optics from MAD to a TRANSPORT/TURTLE deck (using a conversion program developed at SLAC). For convenience of further evaluation of aberrations, calculate the inverse of the total first-order matrix of the FF system and insert this matrix at the beginning of the beamline, so that the overall first-order matrix becomes the identity matrix.

7) Run TRANSPORT to calculate the second- and third-order matrices, as well as the beam matrix with energy offset $+\Delta$ and $-\Delta$. The higher-order chromatic aberrations can be determined from the off-energy matrices.

8) Using the same TRANSPORT beamline, track the beam to the IP using TURTLE. Either the aberrations or the tracked beam sizes could be used as criteria for automatic minimization. In addition the bandwidth of the system, or the variation of the tracked IP beam sizes with energy, is an important quantity to optimize.

Remember this state, then return to the beginning and change the value of some knob. In essence you are computing numerical derivatives of the important aberrations and beam properties with respect to each knob and with respect to energy. Do this for all the knobs. Some knobs affect several aberrations, but differently, eventually allowing all of the major aberrations to be minimized (if in principle a solution exists for the requested parameters). In general all lengths, especially the lengths of the bends B1 and B2 and the drifts surrounding them, are additional knobs (in particular for U3466). Select the best set of knob values, keeping in mind that iteration of this process will be required due to the nonlinearity of the response of the aberrations to knob changes.

Repeat until an acceptable solution is found. Use knobs appropriate to the situation. Most of the steps in this procedure can be performed automatically. For example, Matlab-based scripts are used in our example to generate the TRANSPORT/TURTLE files, run these programs, read, analyze, and present the results, and then to search for an optimal solution using Matlab's optimization routines.

When a solution is close to optimum, and most of aberrations are small, use octupoles OC10 and OC1 near QD10 and the FD, respectively, for fine tuning of U3246 and U3244.

Typically the third-order aberrations can be made small and the bandwidth of the system is limited by fourth or-

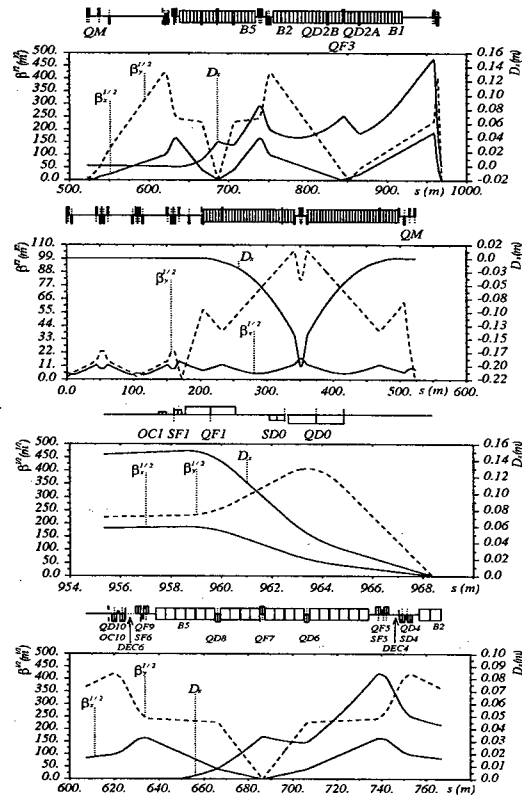


Figure 1: Preliminary optics for the NLC low energy BDS, $L^* = 3.51$ m, $\eta'^* = 0.009$. Final focus proper, collimation section, final doublet region, aberration correction region.

der terms, in particular V32246 (observed in the way that U3224 changes with energy). Use decapoles DEC6 and DEC4 (see Figure 1) with equal strengths to cancel this aberration. For better cancellation of V32446, use a sum of aberrations as a minimization criterion, constraining $U3244_{+\Delta E}$ and $U3244_{-\Delta E}$ to be asymmetric (as in Figure 4). In our case, since TRANSPORT and TURTLE do not handle decapoles, it was necessary to use DIMAD tracking to optimize the strength of these elements.

The authors wish to note here that we do not know of a single optics code that can do all that we need, e.g. TURTLE/TRANSPORT do not handle decapoles or synchrotron radiation, while MAD does not calculate or allow matching of higher-order aberrations. Clearly, there is a need for a more complete beam optics design code.

BDS FOR THE SECOND IR OF NLC

The methods and tools described above have been used to design a Beam Delivery System (BDS) for a second, low energy, Interaction Region (IR) for NLC. This BDS must be somewhat shorter than the primary, high energy, IR BDS (which is 1.4 km long), to allow space for the transport lines that provide the necessary separation between the two IRs (see [8] for more discussion of this configuration). The optics for this preliminary design are shown in Fig-

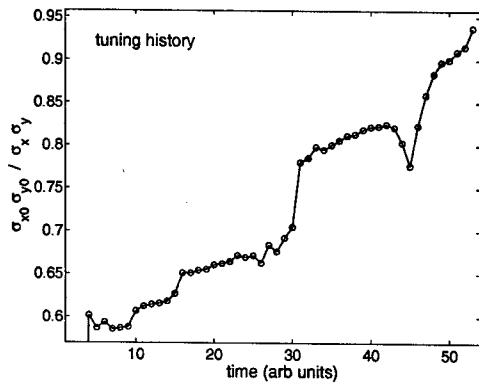


Figure 2: Tuning history for the low energy NLC BDS design. σ_{x0} and σ_{y0} are the nominal linear IP spot sizes.

ure 1. The nominal input beam parameters are: energy $E = 250$ GeV/beam, emittances $\gamma\epsilon_{x,y} = (3.6, 0.04) \cdot 10^{-6}$ m, energy spread $\sigma_E = 0.25\%$, bunch length $\sigma_z = 0.11$ mm. At the IP $\beta_{x,y}^* = (8, 0.11)$ mm and $\sigma_{x,y}^* = (243, 3)$ nm.

The optics shown is optimized for 250 GeV/beam. For the 500 GeV/beam case (and for 650 GeV/beam, available with reduced beam current), the final doublet will be replaced with a longer version in order to reduce synchrotron radiation in the FD ("long doublet" version), and the angle of the B1, B2, and B5 bends will be reduced by approximately a factor of two (with simultaneous adjustment of the bends in the energy collimation section to keep the IP location fixed) to reduce synchrotron radiation in the bends.

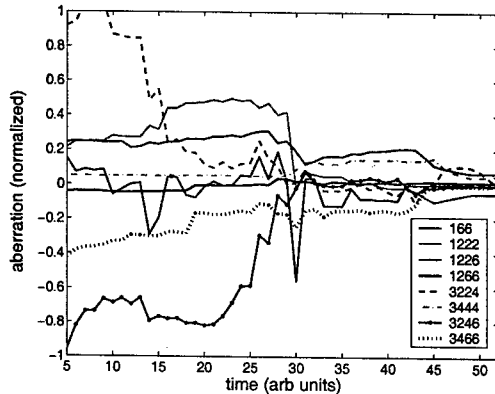


Figure 3: Predominant second and third order aberrations during tuning (normalized to the nominal beam sizes).

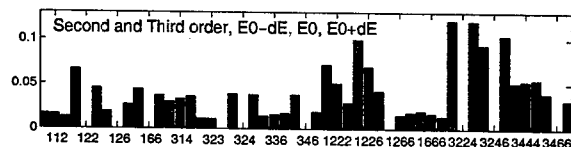


Figure 4: Predominant second and third order aberrations (for the on-energy beam and for $+\Delta E$ and $-\Delta E$) at the final stage of tuning (absolute values, normalized to the nominal beam sizes). Note the symmetry of $U3244_{+\Delta E}$ and $U3244_{-\Delta E}$ terms.

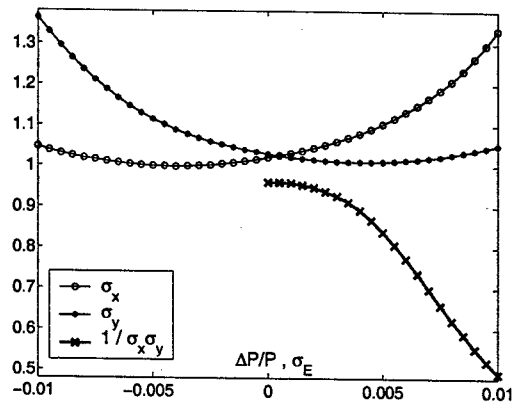


Figure 5: DIMAD tracking results for the final system. Luminosity equivalent IP beam sizes versus energy offset, and $1/\sigma_x\sigma_y$ (normalized) versus energy spread. Hour-glass, beam-beam effects, and synchrotron radiation are not included.

Figures 2 and 3 show the history of the tuning process. The quantity plotted in Figure 2 is equivalent to fractional luminosity. Note that not all intermediate steps are shown. Both hand tuning and automatic optimization with Matlab were used during this process.

Figure 4 shows the predominant second- and third-order aberrations remaining after tuning (absolute values, normalized to the nominal IP beam parameters) for both the on-energy beam and for beams with $\pm 0.2\%$ energy offset. Observation of these aberrations can aid in the creation of additional tuning knobs. Matrix elements for the off-energy beams and their asymmetry give information about fourth- and fifth-order chromatic aberrations. Figure 5 shows the resulting bandwidth of the system, obtained by tracking.

Finally, we note that in spite of the seeming tediousness of this approach to FF design, this method is almost directly applicable for tuning a real final focus during commissioning and operation.

CONCLUSION

A recipe for the optical design of a compact final focus system is presented and illustrated with an example of a preliminary design for the low energy NLC beam delivery system.

REFERENCES

- [1] P. Raimondi and A. Seryi, Phys. Rev. Lett. **86**, 3779 (2001).
- [2] A. Seryi, SLAC-PUB-9648, 2003.
- [3] O. Napoly, B. Dunham, CEA-DAPNIA-SEA-94-12.
- [4] D. Carey, K. Brown, F. Rothacker, SLAC-R-530, 1998.
- [5] H. Grote, F. C. Iselin, Nucl. Instr. Meth. A **293**, 464 (1990).
- [6] D. Carey, K. Brown, F. C. Iselin, SLAC-R-544, 1999.
- [7] R. Servranckx, et al., SLAC-0285, 1990.
- [8] T. Markiewicz, et al., in these proceedings.

LONG TERM STABILITY STUDY AT FNAL AND SLAC USING BINP DEVELOPED HYDROSTATIC LEVEL SYSTEM*

A. Seryi, R. Ruland SLAC, Stanford, CA, USA

V. Shiltsev, J. Lach, D. Plant FNAL, Batavia, IL, USA

A. Chuprya, A. Erokhin, M. Kondaurov, A. Medvedko,

V. Parkhomchuk, E. Shubin, S. Singatulin BINP, Novosibirsk, Russia

A. Kuznetsov Novosibirsk State University, Russia

Abstract

Long term ground stability is essential for achieving the performance goals of the Next Linear Collider. To characterize ground motion on relevant time scales, measurements have been performed at three geologically different locations using a hydrostatic level system developed specifically for these studies. Comparative results from the different sites are presented in this paper.

INTRODUCTION

Small emittances and nanometer size beams of the Next Linear Collider set tight requirements on alignment and motion of its components. While fast motion affects beam separation in the interaction point, slow ground motion may cause beam emittance growth, as its short wavelength components result in accumulated misalignments and deviation of the beam trajectory from a smooth line.

This article summarizes two-years studies performed in collaboration of BINP, FNAL and SLAC to investigate slow ground motion in three different geological conditions: in the shallow Main Injector tunnel in glacial till (Fig. 1), in the deep Aurora mine in dolomite, and in shallow SLAC linac tunnel in sandstone.

For these studies, BINP has developed a special Hydrostatic Level Measuring System (HLM System). The HLM System is based on principle of communicating vessels and capacitive measurements of the water level. Each sensor is equipped with a temperature sensor. The capacitance - to - frequency converter has specially clocked calibration procedure that allows avoiding influence of many factors on measurements accuracy. As a result, the accuracy of sensors is better than a micron and resolution is better than 0.1 micron with 5 mm dynamic range. The SAS-1 sensor model has separate pipes for connecting the water and air tubes. The SAS-2 sensor model (used for these studies) is built to use in a system with "half-filled" single tubes. A principle advantage of a single tube system (with continuous free water surface) is that the relative water level does not depend on temperature variations, as it is defined only by gravity, in contrast to a double tube system, where temperature difference cause change of water density and change of water height in the sensors. The sensors have digital output via the standard RS-485 interface. A special atmospheric air pressure monitor is an integral part of the system. A test device (TD), to programmably vary the

water level (e.g. for tests of water dynamics or tests of calibration), is a part of HLM System as well.

RESULTS OF STUDIES

The slow motion most worrisome for a linear collider is believed to be the diffusive ATL motion, because of its short "wavelength" character. The variance of the relative misalignment for ATL is proportional to elapsed time and spatial separation $\Delta X^2 = A \cdot T \cdot L$. The coefficient A depends strongly on geology, and its clarification, for the chosen geologies, was one of the main goals of the study.

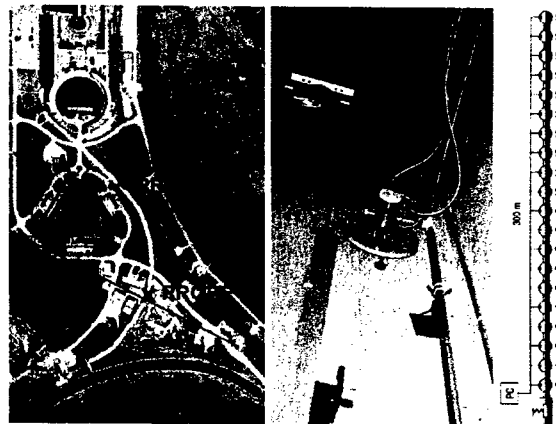


Figure 1: FNAL areal photo with marked locations of the first and the last SAS sensor and location of the water well – cause of the "2-hours puzzle"; photo of HLM system installed in MI8 tunnel; system layout.

For study at FNAL Main Injector tunnel, 20 SAS-2 sensors were installed over 300 m distance in the MI8 transfer line. The very first measurements immediately gave a surprise dubbed "2-hours puzzle" – the motion looks quasi-periodic with amplitude of about $10 \mu\text{m}$ near one end of the system, smoothly vanishing to the other end of the system. The period was not constant, but slowly varied by about 30% (see Fig.2 where one can also see a spike due to earthquake in Alaska, which caused quench of the Tevatron and was also detected by a seismometer at Northern Illinois University). Sudden disappearance of the motion on January 3, 2002, for about one day, hinted to the man-made character of the phenomenon. After extensive search, in August 2002, Duane Plant found the cause – domestic water well located 219 ft deep and several hundred feet away which slowly and periodically change ground water level

* Work supported in part by US DOE, Contract DE-AC03-76SF00515.

and pressure and caused ground to move, see Fig.3. (We appreciate suggestion by Rainer Pitthan who proposed that a sump pump may be a cause – a very close hit).

The “2-hours puzzle” is probably the first observation of cultural ground motion on such a low frequency scale. (Traditionally, cultural noise is man-made vibrations above 1Hz). Such cultural slow motion is worrisome, because it has poor spatial correlation. This underlines importance of more careful attention to shallow tunnels in sedimentary or glacial geology in populated areas.

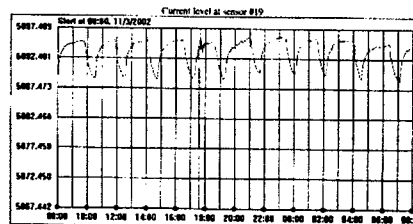


Figure 2: Level at sensor 19 in MI8. The periodic motion is due to 2-hours puzzle. The spike is earthquake in Alaska.

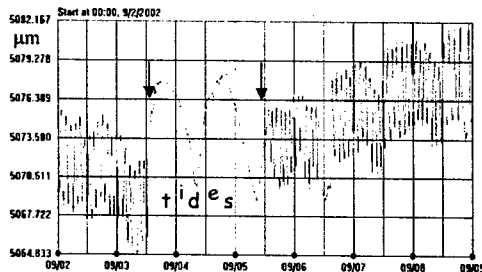


Figure 3: The “2-hours puzzle” is switched off and on.

As the “2-hours puzzle” could not be turned off for sufficiently long time, analysis of natural ground motion was hampered. The sufficiently long puzzle-free data came only from the month of February 2003. Diffusion coefficient A , calculated for this month, is shown in Fig.4 (calculated using three sensors, to remove the irrelevant common change of ground tilt). One can see that the envelope of A corresponds to previously found values (from the PW on surface tunnel [1]) and roughly constant with ΔL from 15 m to 90 m. The mean value of A however appears to decrease with L , as if it shows not $\Delta X^2 \propto L$ but rather $\Delta X^2 \propto 1$ behavior. To find if it is a reality, one would need more 2 hrs puzzle-free data and also better understanding of the effects of viscous damping in the HLM System pipes (see further discussion below).

For further study of slow ground motion in Aurora mine, the existing HLM System [1] was augmented with four new BINP sensors on May 2002 (see Fig.5). Though with less statistics (both in time and space), the SAS sensors appear to show about twice smaller diffusion: about $(6 \pm 3) \cdot 10^{-7} \mu\text{m}^2/(\text{m}\cdot\text{s})$ is observed with Fogale-based system and about $3 \cdot 10^{-7} \mu\text{m}^2/(\text{m}\cdot\text{s})$ is observed with new SAS sensors. This underlines the importance of low electronic drift in a measuring system – well known headache of instrumentation developers.

Hydro-dynamics of water motion in long half filled tubes

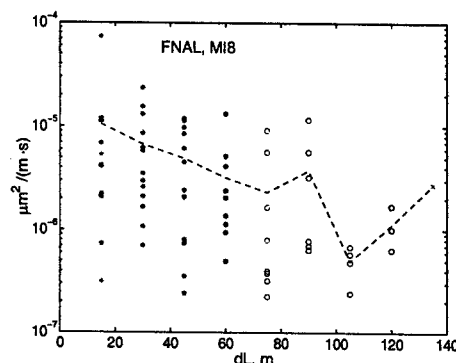


Figure 4: Diffusion found on three sensors for 2 hrs motion-free data from the MI8 tunnel.

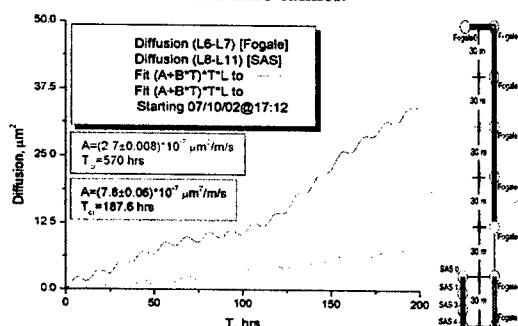


Figure 5: Example of diffusion found in Aurora mine with Fogale and new SAS sensors, and location of sensors.

plays important role in measurements with HLM System and should be taken into consideration. Neglecting, for a moment, viscosity, the phase velocity of propagation of long gravity waves in half-filled round pipes is $V = (\pi g R/4)^{1/2}$, see [4]. For our case of 1” pipes, it is $V \approx 0.3 \text{ m/s}$ and for a periodic 15 minutes motion excited by a test device, a 0.4π phase shift would be observed after 50 m, corresponding well with observation, see Fig. 6.

Note that these long gravity waves in tubes have no dispersion. However, if viscous damping is taken into account, dispersion appears. The viscous damping affects dynamics strongly: the damping coefficient is $\gamma = 1/R(\nu\omega/2)^{1/2}$ (for water $\nu \approx 0.01 \text{ cm}^2/\text{s}$) [4]. For example, for 15 min period, we have $\gamma/\omega \approx 0.7$, i.e. the motion is strongly damped! We do not have an exact solution for

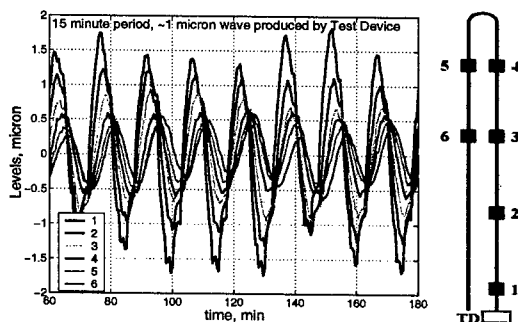


Figure 6: One micron wave excited by test device in 2x30m HLM System at Sector 10 lab in SLAC linac tunnel.

water dynamics in large damping case, but it appears that in many cases the motion would exhibit aperiodic damped flow, as observed in Fig. 7, where equilibrium is reached several hours after a TD step change, in a 300 m system.

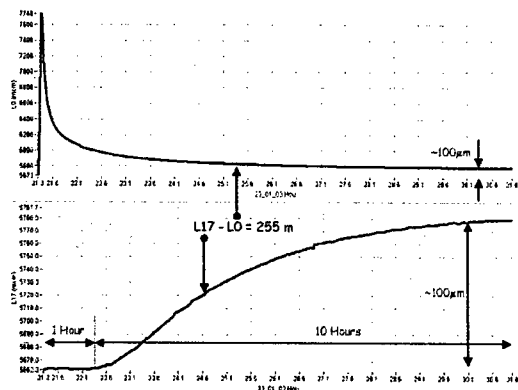


Figure 7: Reaction of sensors #0 and #17 to a level step change by a test device in MI8 HLM System.

It is very important to stress, that though the viscous water dynamics may affect measurements by HLM System of the long wavelength ground motion, measurement of the important (for linear collider) ground motion with wavelength of tens of meters is still accurate, as it involves only one sensor and water redistributes only near this sensor. Tests performed with MI8 system have shown that if one sensor is displaced, it reacts within about one minute. For this reason, application of HLM system for ground motion study, and for machine alignment, is appropriate.

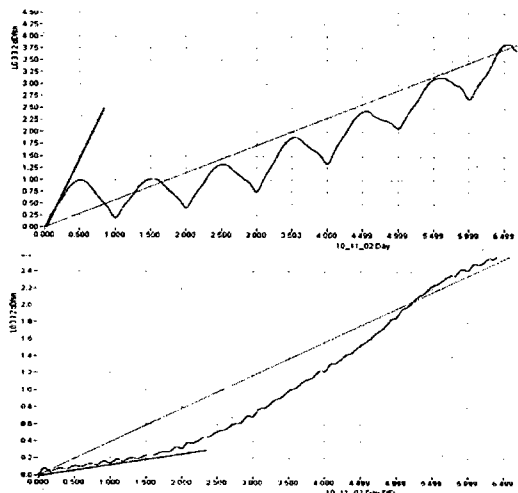


Figure 8: Diffusion found on three sensors without (top) and with (bottom) filtering out the components with period equals one day. Sector 10 HLM System.

The 2x30 m HLM System in Sector 10 alignment lab in SLAC linac tunnel is configured in such a way, that two pairs of sensors are located together, for cross check of their stability, see sensor location in Fig. 6. It is also planned to later install hydrostatic sensors of alternative design, and also install a stretched-wire system, for triple cross-check.

The two sensors located close together follow each other with about 3 μm for 4 month (within $\sim 1 \mu\text{m}$ if one compensates for temperature correlation). The rms of difference of this two sensors was found to be about 55 nm (for time difference less than one day), corresponding to resolution of about 40 nm.

Details of installations of water tubes were found to be very important and may allow for further improvements. At MI8 the tubes are installed loosely. Variation of temperature do not cause transverse variation of tube position, and so there is no observed significant correlation of temperature and mean level at FNAL MI8 HLM System. However, studying motion with Sector 10 HLM System, we found unexpectedly large correlation of the mean water level with mean temperature – about 33 $\mu\text{m}/^\circ\text{C}$. We explain this by the fact that, at Sector 10, tubes are rigidly fixed to the floor, and so the variation of temperature may cause large transverse deflection of tubes (as $\Delta h \approx \ell(\alpha\Delta T)^{1/2}$), and as a result, large correlation of temperature and mean level. And though we use relative levels (w.r.to the mean) for ground motion analysis, this temperature sensitivity may be suppressed mostly but not entirely.

The mentioned temperature sensitivity is clearly seen as daily variation in diffusion analysis plots from Sector 10 HLM, see Fig. 8, where apparently the motion of the tubes, and not ground, artificially dominates the picture (see Fig 8, top, where the red fit line corresponds to $3.3 \cdot 10^{-7} \mu\text{m}^2/(\text{m}\cdot\text{s})$). Fourier suppression of daily harmonic, produces, we believe, more accurate estimation of about $2.3 \cdot 10^{-7}$ for the red line fit and about $0.7 \cdot 10^{-7}$ for the small time part (see Fig 8, bottom plot).

As a summary, the diffusion coefficients A (in units of $10^{-7} \mu\text{m}^2/(\text{m}\cdot\text{s})$) are: (10-100) for MI8 shallow tunnel in glacial till (in absence of dominating cultural motion); about 3 or below in deep Aurora mine in dolomite and in Sector 10 shallow tunnel in sandstone (irrelevant motion of the tube may still be a large contribution in the Sector 10 A value). Previous studies for FNAL surface and at SLAC tunnel are confirmed, and new measurements in Aurora mine are about factor of two below the previously found values.

CONCLUSION

The study performed have confirmed the strong dependence of slow ground motion on geological conditions – a competent geology is beneficial for NLC.

Hydrostatic Level Measuring System, as a slow ground motion and alignment monitoring tool, has been studied and several important factors affecting its performance have been found and investigated.

REFERENCES

- [1] V. Shiltsev, et al., in Proc. of PAC2001.
- [2] A. Seryi, et al., in Proc. of PAC2001.
- [3] V. Shiltsev, FERMILAB-FN-0717, March 2002.
- [4] L. Landau, E. Lifshitz, Fluid Mechanics, 1959.

WIGGLERS AND SINGLE-PARTICLE DYNAMICS IN THE NLC DAMPING RINGS

M. Venturini* and A. Wolski, LBNL, Berkeley CA 94720, USA
A. Dragt, U. of Maryland, College Park MD 20742, USA

Abstract

Wiggler insertions are expected to occupy a significant portion of the lattice of the Next Linear Collider (NLC) Main Damping Rings (MDR) and have a noticeable impact on the single-particle beam dynamics. Starting from a realistic 3D representation of the magnetic fields we calculate the transfer maps for the wigglers, accounting for linear and nonlinear effects, and we study the beam dynamics with particular attention paid to the Dynamic Aperture (DA). A DA reduction is observed but appears to remain within acceptable limits.

INTRODUCTION

The need for a larger momentum compaction in order to tame the effects of collective instabilities has motivated a redesign of the current NLC MDR lattice [1]. The strength of the magnetic field in the dipoles was decreased causing a reduction of radiation loss and therefore requiring longer wiggler insertions to maintain the desired damping. The wiggler insertions now occupy about 61.6 m of the 300 m ring circumference (up from 46.2 m) adding further linear and nonlinear perturbations to the lattice. An accurate assessment of these effects is desirable in order to obtain a proper tuning of the linear lattice and determine the impact on the Dynamic Aperture (DA). A sufficiently large DA is required for a good injection efficiency (at injection the NLC MDR's should be capable of accommodating a beam with 150 mm-mrad normalized emittance in both transverse planes and a full width $\pm 1\%$ energy spread).

A previous study [2] showed that the effects of the wiggler nonlinearities in the earlier design of the NLC MDR lattice while noticeable did not introduce unacceptable degradation of the DA. The study made use of a suitable fitting of the magnetic field in the wiggler midplane and a simplified symplectic integrator for tracking the orbits of individual particles. A similar conclusion was reached after a first investigation of the new lattice [1] that was carried out with the wigglers modelled as sequences of standard elements (combined function dipoles, thin octupoles, and drifts). The parameters for these standard elements were tuned in such a way as to reproduce the same horizontal and vertical kicks through a wiggler period as obtained from the more accurate symplectic integrator technique employed earlier.

In this paper we report on a further study on the new lattice using a method that makes some improvements on the field representation and avoids some of the simplifications in the integrator mentioned above. The method requires

one component of the magnetic field (for instance obtained with the aid of a magnet design code) on the surface of a cylinder coaxial to and contained within the wiggler aperture. This is sufficient information to determine the field in the interior of the cylindrical surface in the form of a full 3D multipole expansions, properly accounting for the longitudinal dependence of the fields. Upon suitable truncation of this series expansion we determine the corresponding transfer map through third order in the dynamical variables using the code MARYLIE3.0 [4].

WIGGLER FIELD ANALYSIS

In a current-free region the magnetic field can be expressed in terms of a scalar potential ψ , which solves the Laplace equation. For a periodic structure of period λ_w the most general such scalar potential can be written in cylindrical coordinates as $\psi = \sum_{m=0}^{\infty} \psi_m(\rho, z) \sin m\phi + \text{term proportional to } \cos m\phi$, where $\psi_m(\rho, z) = \sum_{p=-\infty}^{\infty} e^{2\pi i p z / \lambda_w} I_m(2\pi p / \lambda_w) b_{m,p}$, I_m are the modified Bessel functions, and $b_{m,p}$ arbitrary coefficients. The terms proportional to $\cos m\phi$ correspond to the 'skew' components of the fields, are absent in a error-free planar wiggler and will be neglected here. The azimuthal number $m = 1, 2, 3, \dots$ corresponds to the dipole, quadrupole, sextupole, ... components (the $m = 0$ solenoidal term is also absent in an ideally built wiggler). Alternatively, one can express ψ_m as a power series in the radial variable ρ in the form: $\psi_m(\rho, z) = \sum_{\ell=0}^{\infty} (-1)^{\ell} \frac{m!}{2^{2\ell} \ell! (\ell+m)!} C_m^{[2\ell]}(z) \rho^{2\ell+m}$, where $C_m^{[2\ell]}(z)$, defined by $C_m^{[2\ell]}(z) = \frac{(-1)^{\ell}}{\sqrt{2\pi}} \frac{1}{2^m m!} \sum_{p=-\infty}^{\infty} e^{2\pi i p z / \lambda_w} \left(\frac{2\pi p}{\lambda_w} \right)^{2\ell+m} b_{m,p}$, is the 2ℓ derivative of $C_m^{[0]}(z) \equiv C_m(z)$. We will refer to the functions $C_m(z)$ as 'generalized gradients'. A field expansion in the current-free region is uniquely determined by specification of the generalized gradients.

Suppose the radial component of the magnetic field is given on the surface of a cylinder of radius R in terms of the Fourier series $B_{\rho} = \sum_{m=0}^{\infty} B_m(R, z) \sin(m\phi)$. Then, it can be easily shown that the coefficients $b_{m,p}$ are related to the Fourier integral $\tilde{B}_{m,p} = \frac{1}{\lambda_w} \int_0^{\lambda_w} dz e^{-i2\pi p z / \lambda_w} B_m(R, z)$ of the field data B_m by $b_{m,p} = \tilde{B}_{m,p} \lambda_w / [2\pi p I'_m(2\pi p R / \lambda_w)]$. Notice that because of its exponential behavior the Bessel function I'_m in the denominator of the above expression has a filtering effect on high frequency noise possibly present in the field data [3].

A full 3D field map for a MDR wiggler period is available based on the preliminary design discussed in [5]. The wiggler period is $\lambda_w = 27$ cm, the magnetic field peak

*mventurini@lbl.gov

value 2.1 T. Because the (anti-)symmetry of the fields under a 180° rotation is enforced exactly only the $2(2n+1)$ harmonics are present (dipole, sextupole, decapole, ...). Analysis of the radial component of this field at $R = 9$ mm results in the profiles of the generalized gradients shown in Fig. 1.

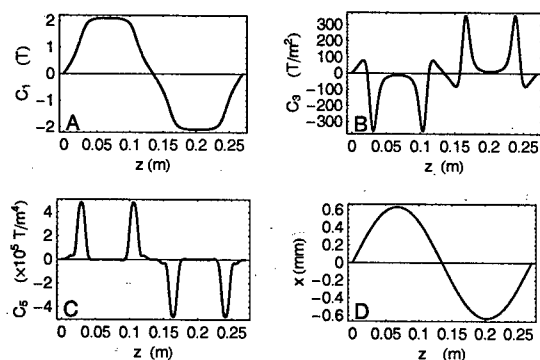


Figure 1: Generalized gradients $C_m(z)$ for one period of the MDR wigglers corresponding to the dipole $m = 1$ (A), sextupole $m = 3$ (B), and decapole $m = 5$ (C) field components. The reference orbit is also reported (D).

MAP COMPUTATION

As an alternative to integrating the equations of motion for the individual particles we use knowledge of the magnetic fields for a wiggler period to determine the corresponding transfer map. We carry out the calculation in a canonical framework using the deviations coordinates from the reference orbit. This requires going through the following steps: determination of the vector potential associated with the field 3D multipole expansion, calculation of the reference orbit, re-expansion of the vector potential (and Hamiltonian) as Taylor series with respect to the deviation coordinates. The Hamiltonian in the latter form is then suitable for calculating the transfer map upon solving the equation of motion - a task carried out by MARYLIE3.0 built-in routines. The resulting map through third order has the Lie representation $\mathcal{M} = \cdots M \exp(:f_3:) \exp(:f_4:)$, where M is the 6×6 matrix describing the linear part of the dynamics, while the f_ℓ 's are homogeneous polynomial of degree ℓ in the dynamical variables. The matrix M depends only on the quadratic part of the Hamiltonian; f_3 depends also on the cubic part; f_4 also on the quartic part. These two generators are connected to quadratic (and higher), cubic (and higher) terms of the map in Taylor form respectively. For straight magnetic elements (in which the reference orbit follows the magnet axis) each individual $2n$ -pole component of the magnetic field contributes only to the f_ℓ generator with $\ell \geq n$ (the main contribution is absorbed by the generator with $\ell = n$ while the contribution to the generators with $\ell > n$ is related to the z -varying part of the generalized gradient - a fringe effect). However,

because in wigglers the reference orbit deviates from the z -axis, expressing the field in the deviation coordinates (from the magnet frame coordinates) produces a cascade of feed-down terms affecting the generators with $\ell < n$ as well. For example, a sextupole component introduces a correction to the linear part of the dynamics (one can think of this term as a quadrupole-like component); a decapole component affects f_4 (octupole-like), f_3 , (sextupole-like), etc. These feed-down terms are weighted by increasing powers of the deviation $x_r(z)$ of the reference orbit from the wiggler axis. Because for wigglers in high energy machines this amplitude is fairly small ($x_r(z) \leq 0.6$ mm in our case), in practice for each multipole component only the first feed-down term, which is proportional to $x_r(z)$, is significant. For this reason not including higher order multipoles above the decapole in the field representation (as we do) does not affect the calculation of the 3^{rd} order map substantially.

An insight into the relevant terms of the map can be obtained from a simplified analytical calculation under the assumption that the particle orbits (in the deviation variables) do not deviate considerably from straight lines. In such a model the sextupole and decapole components of the field contribute to the dynamics only through feed-down terms. In particular, integrals of the sextupole feed-down term (proportional to $x_r(z)C_3(z)$) contribute to the linear part of the map introducing defocusing horizontally and focusing vertically, while integrals of the decapole feed-down term (proportional to $x_r(z)C_5(z)$) represent the main contribution to the cubic part of the map. No quadratic or quartic terms appear (as would be case for ordinary sextupole or decapole magnets) because the integrals of the $C_3(z)$ and $C_5(z)$ vanish over a wiggler period. As for the dipole field component, its main effect is to add linear focusing in both transverse planes through the integrals of terms like $x_r(z)C_1^{[2]}(z)$ - essentially a fringe-effect. The net result on the linear dynamics is significant focusing in the vertical plane (the sextupole feed-down and dipole fringe-field terms add up) and relatively small defocusing in the horizontal plane where the dipole fringe-field and the sextupole feed-down terms have opposite sign (with the latter prevailing slightly). In spite of the approximation involved this simple model appears to be in good quantitative agreement with the MARYLIE numerical calculation for the linear part of the map and reasonable qualitative agreement for the nonlinear part. In particular, the MARYLIE calculation confirms that the dominant nonlinearities are of third order (octupole-like).

In the absence of a detailed design for the ends of the wiggler insertions we used a model consisting of bending magnets and two thin octupole and sextupole lenses.

DA STUDY

The new MDR lattice is discussed in detail in [1]. For this study we switched off the rf cavities and did not include any errors in the magnets or wigglers. Tracking was

carried out element by element using the MARYLIE symplectic integrator. In particular, tracking through the wiggler insertions (consisting of 6 full periods in addition to entry and exit ends) was done by propagating the particle orbits through each individual period, using the maps determined from the field data - as discussed in the previous Section. All the other elements were modelled using the MARYLIE standard element library with the inclusion of the MARYLIE built-in modelling of fringe-field effects in the hard-edge limit. In this study the physical aperture of the vacuum chamber (8 mm radius in the wigglers, 20 mm everywhere else) was not accounted for. The DA of the MDR lattice is affected by both the sextupole magnet and wiggler nonlinearities. An assessment of the relative impact of the two sources of nonlinearities is obtained by comparison of the two pictures of Fig. 2. These and the following figures show the DA through 500 turns in the $x-y$ plane located in the middle of the first quadrupole magnet downstream the injection point (the beta-functions are about $\beta_x = 16$ m and $\beta_y = 1.6$ m). The particles are launched at this location with vanishing transverse momenta. The half-ellipse corresponding to 15σ the injected beam size - a plausible DA target - is also shown. Fig. 2A is relative to a lattice in which the wiggler nonlinearities are artificially masked away (sextupoles dominate); Fig. 2B refers to a lattice with the sextupoles turned off (wigglers nonlinearities dominate).

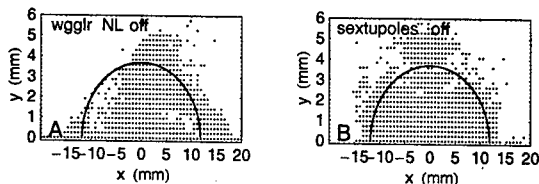


Figure 2: On momentum DA with wiggler nonlinearities turned off (A) and chromatic sextupoles turned-off (B)

The combined effect of chromatic sextupoles and wiggler nonlinearities on the dynamic aperture are shown in Fig. 3A for on-momentum particles and Fig.'s 3B and 3C for off-momentum particles (+1% and -1% respectively). The 15σ boundary appears to be mostly respected by on-momentum particles while a somewhat larger degradation of the DA is observed for off-momentum particles.

Finally, Fig. 3D shows the on-momentum DA for a representation of the wiggler periods constructed using combined function dipoles of length $\lambda_w/4$ and thin octupoles. The peak field in the dipoles was set to 2.28 T, so as to give the design integrated squared field strength while the field gradient (-1.66 T/m, defocusing horizontally) was adjusted to give a linear transfer map for one wiggler period close to the map calculated by numerical integration through the wiggler field (the individual entries of the linear matrix entries deviate less than 1%); the strength of the octupole lens was tuned to fit the x^4 Lie generator of the same map. Both maps result in similar horizontal and vertical

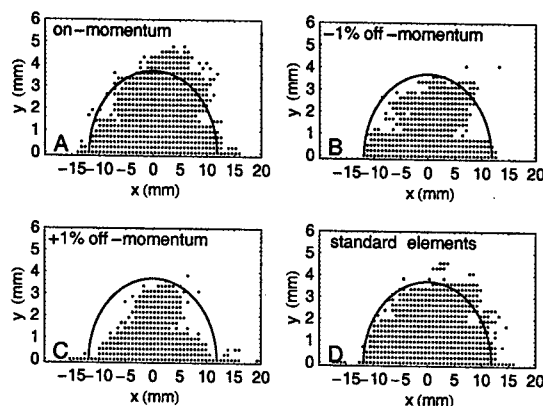


Figure 3: Dynamic aperture for model with wiggler map integrated through fields (A,B,C) and model using standard elements (D) - on momentum.

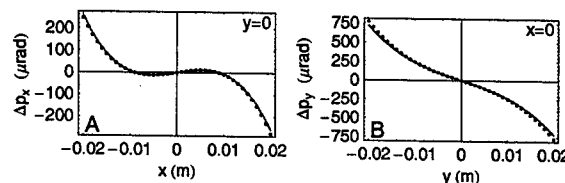


Figure 4: Horizontal (A) and vertical (B) kicks through one wiggler period from map calculated by integration through actual fields (dots) and map constructed from standard elements (line).

kicks through a wiggler period (Fig. 4) - with some noticeable discrepancies emerging (not shown) when both $x \neq 0$ and $y \neq 0$ - a reflection of the fact that the nonlinear generators of the two maps (in particular those related to $x-y$ coupling) are not identical. Nevertheless, on-momentum the DA aperture resulting from using the standard element model for the wiggler (Fig. 3D) does not appear very different from that resulting from the more accurate modelling (Fig. 3A). However, a larger discrepancy can be noted in the off-momentum cases (not shown) with the calculation done using the standard-element model giving a somewhat more pessimistic estimate of the DA.

Work supported by the US DOE under Contract DE-AC03-76SF00098.

REFERENCES

- [1] M. Woodley and A. Wolski, NLC Tech Note LCC-0113 (2003); A. Wolski *et al.*, (these Proceedings).
- [2] A. Wolski *et al.*, PAC01, Proceedings, p. 3798 (2001).
- [3] M. Venturini and A. Dragt, NIM-A 415 417 (1998).
- [4] A. Dragt *et al.*, MARYLIE3.0, Users' Manual, Univ. of Maryland Dept. of Physics Technical Report (May 2003).
- [5] J. Corlett *et al.*, CBP Tech. Note 199, LBNL, Berkeley (1999), (also NLC Tech Note LCC-0031).

A LATTICE WITH LARGER MOMENTUM COMPACTION FOR THE NLC MAIN DAMPING RINGS*

A. Wolski[#], LBNL, Berkeley, CA 94720, USA

T.O. Raubenheimer, M. Woodley, J. Wu, SLAC, Menlo Park, CA 94025, USA

Abstract

Previous lattice designs for the Next Linear Collider Main Damping Rings [1] have met the specifications for equilibrium emittance, damping rate and dynamic aperture. Concerns about the effects of the damping wiggler on the beam dynamics [2] led to the aim of reducing the total length of the wiggler to a minimum consistent with the required damping rate, so high-field dipoles were used to provide a significant energy loss in the arcs. However, recent work has shown that the wiggler effects may not be as bad as previously feared. Furthermore, other studies have suggested the need for an increased momentum compaction (by roughly a factor of four) to raise the thresholds of various collective effects. We have therefore developed a new lattice design in which we increase the momentum compaction by reducing the field strength in the arc dipoles, compensating the loss in damping rate by increasing the length of the wiggler. The new lattice again meets the specifications for emittance, damping rate and dynamic aperture, while having the benefit of significantly higher thresholds for a number of instabilities.

DESIGN OBJECTIVES

Some of the parameters specifying the performance of the Main Damping Rings (MDRs) for the NLC are shown in Table 1. In addition, since the average injected beam power into the ring in operation will be 55 kW, the injection efficiency will have to be close to 100%, and this places demanding requirements on the acceptance.

Table1: NLC Damping Ring Specifications

Bunches per train	192
Bunch-to-bunch spacing	1.4 ns
Kicker rise/fall time	65 ns
Collider repetition rate	120 Hz
Injected horizontal/vertical emittance	150 μm
Extracted horizontal emittance	3 μm
Extracted vertical emittance	0.02 μm
Extracted energy spread	10^{-3}

The circumference of the lattice is constrained by the need to accommodate a number of bunch trains, with sufficient spacing to allow the kickers to turn on and off between the trains. The number of trains stored, and the injected and extracted emittances specify the damping rates. Note that the normalized emittances are given in Table 1. As with the previous design, a circumference of 300 m has been chosen. This provides sufficient room for

the necessary number of arc cells to achieve the natural emittance, the damping wiggler, injection and extraction systems and other components. Three bunch trains are stored at any given time.

LATTICE PARAMETERS

Some of the principal lattice parameters for the new design are given in Table 2.

Table 2: Principal Lattice Parameters

Beam energy	1.98 GeV
Circumference	299.792 m
Arc cells	32 TME
Wiggler length	61.6 m
Betatron tunes (x,y)	21.150, 10.347
Natural chromaticity (x,y)	-30.74, -28.76
Natural emittance (normalized)	2.37 μm
Natural energy spread	9.75×10^{-4}
Harmonic number	714
RF voltage	2.0 MV
RF acceptance	1.52 %
Natural bunch length	5.49 mm
Synchrotron tune	0.0118
Momentum compaction	1.39×10^{-3}
Energy loss/turn	970 keV
Damping times (x,y,t)	3.6, 4.1, 2.2 ms

Compared to the previous lattice, the momentum compaction has been increased by more than a factor of four. This was one of the main aims of the design, since this gives an increase of roughly two in the bunch length and reduces the impact of a number of collective effects. The increase in momentum compaction has been achieved by reducing the dipole field by a factor of two. Since this leads to a lower energy loss per turn, and hence longer damping times, it is necessary to increase the length of the wiggler to compensate. In fact, we have somewhat overcompensated by increasing the wiggler from 46 m to nearly 62 m, which reduces the vertical damping time from 5 ms in the previous lattice to 4.1 ms in the present version. This will provide some safety margin against possible effects (such as a mismatch of the injected phase space) tending to reduce the effective damping period.

One concern with the increased length of the wiggler is the effect on the beam dynamics. The dynamic aperture of the lattice is of importance because of the need for a large acceptance, and it is possible that intrinsic nonlinearities in the wiggler field could reduce the dynamic aperture. However, recent detailed studies based on a magnetic design for the NLC damping wiggler suggest that the wiggler length in the present design is acceptable [3].

*Work supported by the US DOE, under contract numbers DE-AC03-76SF00098 and DE-AC03-76SF00515.

[#]awolski@lbl.gov

LATTICE DESIGN

The overall layout of the electron MDR, with associated injection and extraction lines, is shown in Figure 1. The positron and electron MDRs are identical, but the positron complex includes a pre-damping ring to accept the large emittance beam from the positron source, and reduce its dimensions so that it can be accepted cleanly by the MDR. The four arcs in the MDR are composed of detuned Theoretical Minimum Emittance (TME) cells. The detuning from the strict minimum emittance conditions is necessary to optimize the dynamic stability with the given space constraints. Two long straights, each containing approximately 30 m of wiggler are located opposite each other. The remaining two straights contain all other systems.

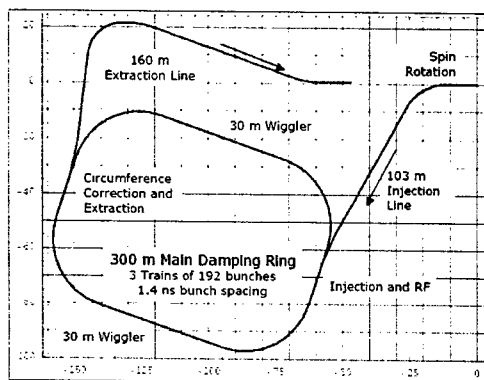


Figure 1: Overall Layout of the Electron MDR

The lattice functions in one TME cell are shown in Figure 2.

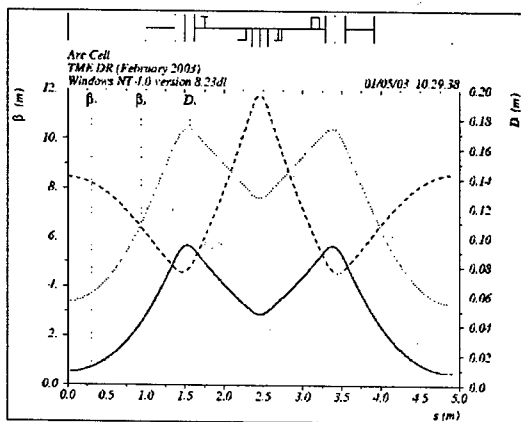


Figure 2: Lattice Functions in One Arc Cell

The arc dipoles have a main field of 0.6 T, and a vertically focusing gradient of 2.0 T/m. The horizontally focusing quadrupoles in the cell are offset with respect to the nominal straight path between the dipoles, to provide some bending of their own. This helps to allow more independent control of the dispersion and horizontal beta function, to reduce the natural emittance of the lattice while allowing flexibility for optimizing the nonlinear dynamics. The quadrupoles have a pole-tip radius of 24

mm, and the beam is offset horizontally from the quadrupole center by 2.6 mm.

The lattice functions in the injection straight are shown in Figure 3.

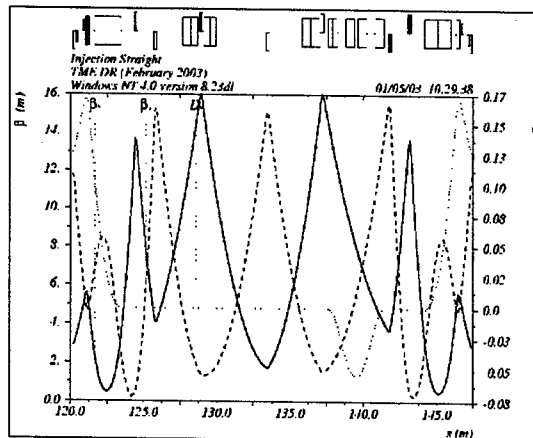


Figure 3: Lattice Functions in the Injection Straight

The injection septum is in two parts with a quadrupole sandwiched in between. Following the injection kicker is a four-magnet chicane, which provides control of the circumference over a range ± 2 mm (since the RF frequency is locked to other parts of the collider, small changes in beam energy must be effected by direct variation in the circumference). The extraction straight is similar to the injection, except that five RF cavities are located immediately before the extraction kicker. The cavities allow variation of the RF voltage up to 2.5 MV, so the bunch length may be reduced (and RF acceptance increased) if allowed by collective effects. The location of the RF cavities ensures that trains can be extracted and injected into the ring without inducing any transient effects from changes in the beam loading in the cavities.

CHROMATIC PROPERTIES AND DYNAMIC APERTURE

The linear lattice has been designed to keep the natural chromaticities as small as possible, and to provide locations for the chromatic sextupoles with large dispersion and good separation of the beta functions. This allows the strengths of the sextupoles needed to correct the chromaticity to be kept low, so that it is possible to obtain a reasonable dynamic aperture. There remains some significant higher order chromaticity: the variation in tune with momentum deviations up to $\pm 1.5\%$ are shown in Figure 4. Resonance lines up to fifth order are also shown.

The dynamic aperture of the lattice for on-momentum particles is shown in Figure 5. The half-ellipse in the plot shows fifteen times the injected beam size at the observation point. No errors are included, except for a systematic octupole component of integrated normalized strength $k_3l = 100 \text{ m}^{-3}$ per period. A more detailed study of the effect of the wiggler on the beam dynamics is reported elsewhere in these proceedings [3].

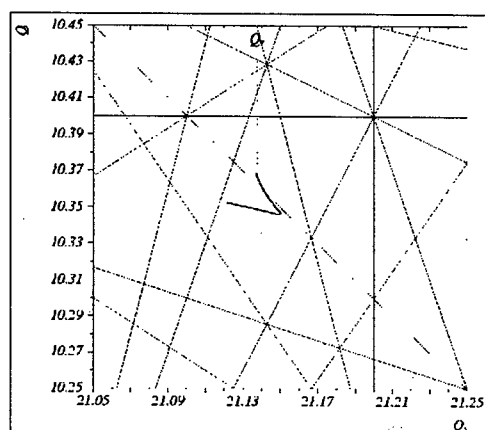


Figure 4: Tune Variation with $\pm 1.5\%$ Energy Deviation

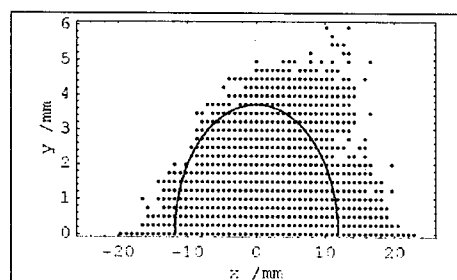


Figure 5: Dynamic Aperture for On-Momentum Particles

For particles with momentum deviations of $\pm 1\%$, the dynamic aperture falls somewhat below the target of fifteen times the injected beam size. The dynamic aperture of the lattice is probably sufficient, although further optimization is desirable. Studies of the effects of systematic and random field errors and magnet misalignments are planned.

ALIGNMENT SENSITIVITIES

The luminosity of the collider depends critically on the vertical emittance from the damping rings, and the specifications are demanding. The 2001 design was very sensitive to misalignments, mainly because the vertical tune was too close to an integer value. This has been corrected in the present design. The sensitivities may be quantified by giving the rms sextupole misalignment, or quadrupole roll, that would, without any other errors, generate the specified vertical emittance [4]. These values are given in Table 3, with values for the Advanced Light Source (ALS) at LBNL for comparison.

Table 3: Misalignments Generating $0.02 \mu\text{m}$ Vertical Emittance

	NLC MDR	ALS
Sextupole Alignment [μm]	53	30
Quadrupole Roll [μrad]	511	200

Note that a vertical emittance of $0.02 \mu\text{m}$ has recently been achieved in the ALS [5]. We therefore have some confidence that the specified vertical emittance for the NLC MDRs is achievable.

INSTABILITY THRESHOLDS

To estimate the effect of the larger momentum compaction, we consider the microwave threshold estimated by the Boussard criterion, and the threshold for a microwave-type instability driven by the radiation impedance (CSR instability) [6,7,8]. These effects are of concern because of the increase in the longitudinal emittance and, more importantly, because of the transients introduced if these instabilities appear in a bursting mode as has been frequently observed. For the nominal bunch charge of 0.75×10^{10} , the microwave impedance (Z/n) threshold has increased from $100 \text{ m}\Omega$ to $630 \text{ m}\Omega$. The thresholds for the CSR instability as a function of radiation wavelength are shown in Figure 6. The vacuum chamber will cut off wavelengths above values around 3 mm (which is less than the bunch length). The increased momentum compaction has significantly raised the microwave and CSR instability thresholds, as expected.

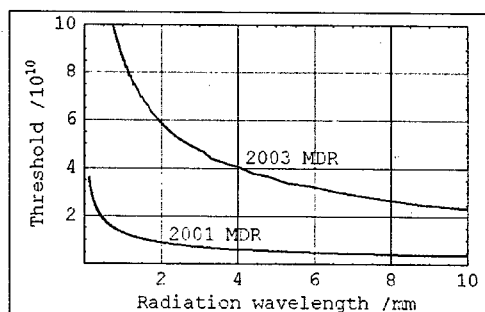


Figure 6: CSR Instability Thresholds

REFERENCES

- [1] A. Wolski and J. Corlett, "The Next Linear Collider Damping Ring Lattices", PAC'01, p.3795.
- [2] A. Wolski and Y. Wu, "Effects of Damping Wigglers on Beam Dynamics in the NLC Damping Rings", PAC'01, p.3798.
- [3] M. Venturini, "Wigglers and Single-Particle Dynamics in the NLC Damping Rings", these proceedings.
- [4] T. Raubenheimer and A. Wolski, "Comparison of Alignment Tolerances in LC Damping Rings with those in Operating Rings", Nanobeams'02.
- [5] C. Steier et al, "Coupling Correction and Beam Dynamics at Ultralow Vertical Emittance in the ALS", these proceedings.
- [6] S. Heifets and G. Stupakov, "Beam Instability and Microbunching due to Coherent Synchrotron Radiation", PAC'01, p.1856.
- [7] J. Wu, T. Raubenheimer and G. Stupakov, "Calculation of the Coherent Synchrotron Radiation Impedance from a Wiggler", Phys. Rev. ST Accel. Beams, 6, 040701 (2003).
- [8] J. Wu, T. Raubenheimer and G. Stupakov, "Impact of the Wiggler Coherent Synchrotron Radiation Impedance on the Beam Instability", these proceedings.

FEEDBACK ON NANO-SECOND TIMESCALES: FAST FEEDBACK SIMULATIONS

G.R. White, Dept. of Physics, Queen Mary, University of London

Abstract

The FONT group (based at QMUL and Oxford Universities) are responsible for the design of the IP fast intra-train feedback system to be implemented in the IR of the future linear collider. This system is intended to correct for luminosity loss due to high frequency ground motion. The work presented here was carried out to test the feasibility of such a feedback system and to investigate, through simulation, the optimum design and operating parameters.

INTRODUCTION

All of the proposals for the future linear collider require similarly challenging final beam spot sizes: TESLA [1] 5nm, NLC/JLC [2] 2.7nm and CLIC [3] 1nm, are the proposed vertical bunch spot sizes at the Interaction Point (IP). This places very rigorous stability requirements on all three designs. The most severe tolerance is for the final focusing quadrupole magnets. To keep the luminosity loss to within 2 percent, the beams need to be kept in collision to within 40% and 60% of the final beam spot size for NLC and CLIC respectively. This implies a tolerance on the final quadrupoles of about 1nm and 0.6nm for NLC/JLC and CLIC respectively.

The limiting factor for stability along the beamline for the linear collider is that of ground motion. There has been a considerable effort undertaken into the study of the magnitudes and effects of ground motion at different possible sites for the linear collider which are covered in detail elsewhere[4]. If uncorrected, ground motion causes a total loss of luminosity at the linear collider within seconds through beam misalignment and emittance growth. To combat this, a program of passive and active support systems to stabilise the beamline elements, together with different levels of beam-based feedback systems, is being pursued.

Three levels of beam-based feedback system are being developed. A slow feedback will move quadrupoles and structures onto the beam trajectory about every 30 minutes to compensate for low frequency ground motion. An inter-pulse feedback acts in a few locations to correct accumulated errors that occur in between the action of the slow system, and also to provide the possibility of straightening the beam. Finally, a fast intra-train feedback system acting at the IP keeps the beam in alignment, correcting for high frequency cultural ground motion moving the final quadrupoles. For TESLA, a second intra-train system will be used further upstream to additionally remove any incoming angle jitter which also leads to a loss in luminosity.

BEAM SIMULATIONS INCORPORATING FAST-FEEDBACK SYSTEMS

The fast feedback systems are designed to remove beam jitter that occurs at frequencies comparable with the repetition rate of the machine by measuring the first few bunches in the train and correcting the following bunches within that train. The bunch structure thus dictates the operating requirements for the system. For NLC/CLIC designs there are 192/154 bunches per train separated by 1.4/0.7 ns. TESLA will have 2820 bunches separated by 337 ns. The NLC/CLIC case requires a much more aggressive design requiring, at present, a purely analogue electronic approach. The TESLA scheme allows for a more complex digital based algorithm to be employed. Simulations of the fast feedback systems are written in the Matlab/Simulink environment. The feedback system for NLC and CLIC is based on the system designed by S. Smith at SLAC [5].

SIMULATION RESULTS

NLC

The effect of vertical beam offsets at the IP of the NLC-H 500GeV machine was studied with different variants of the feedback design implemented in the Simulink model, using the GUINEA-PIG [6] modelling package to calculate the beam-beam kick effects and luminosities. In the simulation, the BPM and kicker are assumed to be positioned at a distance of 4.3m from the IP at the same side of the IP, where the beam deflection is measured on one beam, and the other incoming beam is then kicked. This is possible at NLC (and CLIC) due to the non-zero crossing angle. Although, at the NLC, with mechanical stabilisation systems active, the IP offsets are expected to be small ($\Delta y < 5\sigma$) the effect of offsets of up to 40 times the vertical IP beam spot size were investigated to see the full capabilities of the system. Fig. 1a shows the results of running the simulation over one full bunch train (192 bunches) with different initial offsets. Shown in the filled-in region is the case with no feedback, where the luminosity quickly drops off as the beams are offset, with 60% luminosity loss for a $5\sigma_y$ offset. The top two curves show the effect of the standard feedback algorithm with a single gain stage set at 2 different levels ('low' and 'high'). Low gain is better at low offset, high at larger offsets due to the non-linearity of the beam-beam kick vs. beam offset function. In an attempt to remove this effect, a linearisation step is included in the simulation where the gain is chosen based on the incoming BPM signal. The third curve shows the effect of a 3-stage linearisation to the predicted beam-beam kick curve. The last curve shows the effects of incorporating a further gain

stage in the feedback loop to damp down the oscillatory effects arising from having a too high gain for the given offset.

Being closely integrated into the Interaction Region (IR) close to the IP, the feedback system is forced to operate in an environment of background particles generated at the IP during beam collisions. This could potentially lead to damaging effects to the system itself, and also, through secondary production and scattering of background particles, to the sensitive particle detectors (principally the vertex and central tracking systems). To model the potential impact of the feedback system in the IR, GEANT3 [7] and FLUKA99 [8] models of the IR were taken and the material making up the feedback system was added. Fig. 2 shows the positioning of the BPM and kicker of the feedback system within the IR of the NLC as implemented in the models. The source of background modeled was that of the coherent e^+e^- pairs which were generated with the GUINEA-PIG model and then tracked through the GEANT and FLUKA models. Fig. 3 shows just a few e^+e^- pairs and the associated scattered secondaries tracked on one side of the IP. Fig. 4 shows the intercepted electromagnetic background in the strips of the feedback BPM strips. According to S. Smith[5], the feedback system will be sensitive to intercepted EM radiation at the level of 3pm of Δy^* (at the IP) resolution per electron knocked off the BPM strips. The background radiation would thus present a significant source of noise in the feedback system if an intercepted spray of particles at the BPM at the level of 10^5 per bunch crossing existed. As can be seen in Fig. 4, the expected level is much less than this. Fig. 5 shows the rate of secondary EM particles hitting the layers of the vertex and central tracking detectors with and without the BPM and kicker of the feedback system included in the GEANT model. As can be seen, the inclusion of the system has very little impact on the background levels. This is due to the positioning of the system behind the masks and LCAL system which are designed to shield the IP from scattered secondaries. Modeling of the system forward of this mask where the system is clearly within the field of pairs confined by the solenoid field seen in fig. 3 shows a large increase in detector backgrounds. Fig. 6 shows the neutron flux in the vertex tracking layers, again- this positioning of the feedback system has little impact on the background levels. The integrated flux with the FB system included is $6.6 \pm 1.3 \times 10^9$ 1 MeV equivalent neutrons per cm^2 per year. The default value without the FB system in is $5.5 \pm 0.8 \times 10^9$.

CLIC

For the CLIC simulation, the same system is used as in NLC. The curves in fig. 1b show the effect of offset beams on luminosity for the cases of no feedback, and the system as described in the above section with the 3-stage linearisation, placed at a distance of 4.3m as in NLC and closer, 1.5m as maybe possible with the CLIC IR design. As can

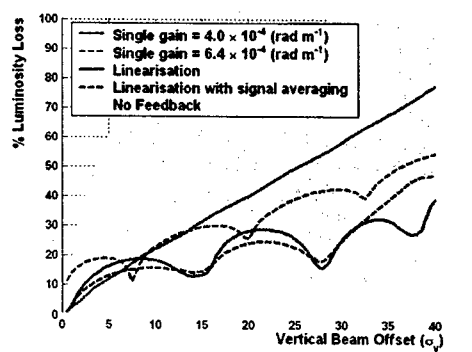


Figure 1: Simulation of luminosity loss at NLC-H (left) (500 GeV) with varying initial beam offsets at the IP.

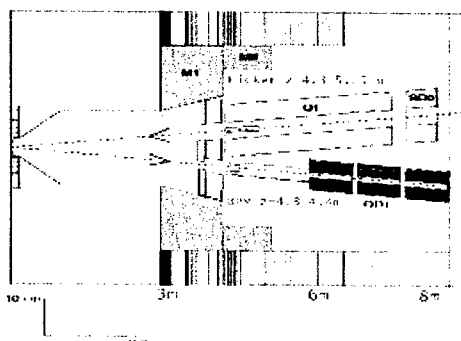


Figure 2: GEANT model of NLC IR showing the positioning of the IP feedback kicker and BPM components.

be seen, the CLIC luminosity is very dependent on highly aligned beams, the smaller train length and shorter bunch spacing gives the feedback system less tries at correcting the offsets. The latency of the system is dominated by the time of flight of the beams between IP and feedback components.

As in the NLC case, G. Myatt at Oxford has begun to look at the backgrounds for the CLIC case in a GEANT CLIC IR model. Fig. 8 shows the CLIC interaction region with the feedback system placed in a 'near' position inside the mask, and a 'far' position outside of the protective mask. A

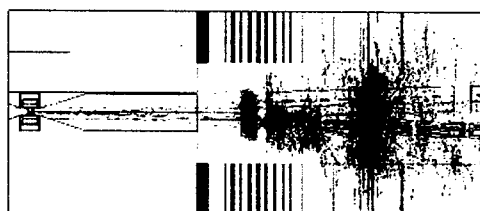


Figure 3: GEANT model of NLC IR with 20 tracked e^+e^- background pairs. Charged particles are shown in red and photons in blue.

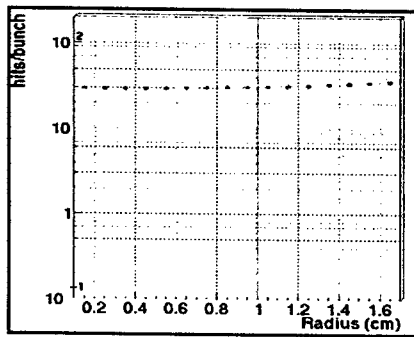


Figure 4: EM background flux at the z location of the feed-back BPM. The stripline radius is shown as 1cm in the plot.

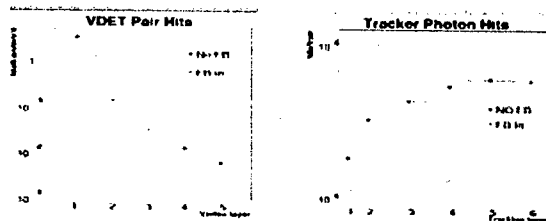


Figure 5: Background particle flux in the vertex (left) and central (right) trackers. The predominant backgrounds of charged particles in the vertex tracker and photons in the TPC are plotted for the IR with and without the feedback material included.

sample train of CLIC background e^+e^- pairs were fed into the GEANT model and tracked. Initial studies show that the far position gives about 2 extra hits per mm^2 per train in the vertex detector (compared with no feedback system present). The near position produces negligible extra hits in the vertex detector but produces considerable extra neutral background radiation in the end of the unprotected TPC. Further studies will continue for the CLIC case.

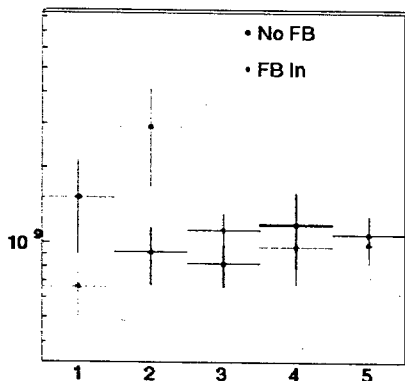


Figure 6: The neutron flux in the 5 layers of the vertex tracker with and without the feedback system included in the IR FLUKA99 model.

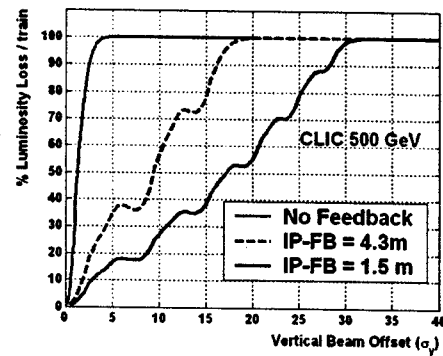


Figure 7: Simulation of luminosity loss at CLIC 500 GeV machine with varying initial beam offsets at the IP.

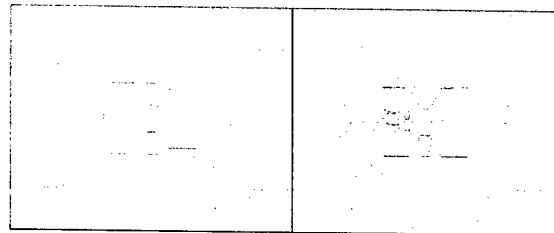


Figure 8: Two positions for the CLIC feedback system- 'near' and 'far', inside and outside the mask region.

REFERENCES

- [1] R. Brinkmann. Proc. EPAC 1998
- [2] T. Raubenheimer (ed.). SLAC Report 474.
- [3] J. P. Delahaye et al. Act.Phys.Polon.B30(2029-2039).
- [4] <http://www-project.slac.stanford.edu/lc/local/AccelPhysics/GroundMotion/>
- [5] S. Smith LCC-0056 2001.
- [6] D. Schulte, DESY-TESLA-97-08, 1997.
- [7] http://wwwinfo.cern.ch/asdoc/geant_html3/geantall.html
- [8] <http://fluka.web.cern.ch/fluka/material/Fluka/head.html>

FORM-FACTOR FOR A TARGET USED FOR POSITRON GENERATION WITH UNDULATOR RADIATION CONVERSION¹

A.Mikhailichenko, Cornell University, LEPP, Ithaca NY 14853, USA

Abstract

It is shown here that the needle type target gives advantages in conversion of gammas from helical undulator into positrons. This is not possible with usual electron to positron production method.

INTRODUCTION

In all operational electron-positron colliders, positrons created by primary electrons in a heavy material target. This primary electron beam with energy E_0 , when hits the target, develops a cascade, what is a mixture of electrons, positrons and gammas. Namely these gammas are responsible for positron creation in electric field of nucleus of target material. This cascade develops along the target starting from the points of penetration of initial beam. The cascade propagates inside matter until energy of particles reaches the critical value, $E_c \approx 610/(Z+1.24)$, MeV, Z stands for atomic number. Transverse size of the cascade in maximum is of the order of Molière radius $R_M \approx X_0 E_s / E_c$, where X_0 is a radiation length, $E_s = \sqrt{4\pi\alpha} \cdot mc^2 \approx 21.2 \text{ MeV}$ —is a scale energy. For W $R_M^W \approx 2.57 X_0$, ($l_M^W = 0.9 \text{ cm}$). For Ti, $R_M^{Ti} \approx 0.7 X_0$, ($l_M^{Ti} = 2.45 \text{ cm}$).

In many laboratories, including BINP Novosibirsk, there were carried investigations on how shape of the target can increase the yield of positrons. Desire was to let positrons, created inside initial parts of volume, escape from the target through the sides without experience of multiple scattering.

Result for W in traditional conversion scheme was negative, however—targets are relatively short and there is no much room for manifestation of angular escape. So, now all operational targets are wider, than the width of a cascade at maximum, $R_s \geq R_M$.

POSITRONS GENERATION WITH UNDULATOR

Method of polarized positron generation was proposed in [1]. In this new method, at first stage, circularly polarized gammas obtained from primary high-energy ($>100 \text{ GeV}$) electron/positron beam by beamstrahlung in a helical undulator/wiggler. At second stage these circularly polarized gammas converted into positrons/electrons into thin, $\sim 0.5 X_0$, target. Just selecting the positrons or electrons with highest possible energy, one can obtain a

beam of *longitudinally polarized* secondary particles. For the wiggling by primary beam it was suggested to use electromagnetic waves, fields of helical crystals and static helical fields [1]. Static helical magnetic fields were found as the only practical ones, however.

Laser radiation as a kind of electromagnetic wave was specially mentioned in 1992 [2] as an example. Formulas and the method are the same, naturally. Later, in 1995, the way with laser radiation was manifested as a direct line for JLC [3,4].

For successful operation, the number of periods in undulator must be around $M \approx 10^4$, what defines the total length of undulator $L = M \lambda_u \geq 100 \text{ m}$ with period $\lambda_u \approx 1 \text{ cm}$. This covers the losses associated with energy selection of particles. It was found (see [7, 9] for details) that optimal value of undulatority factor $K = e H \lambda_u / 2 \pi m c^2$ is $K \sim 0.4$. Polarization $\geq 65\%$ can be obtained with such long undulator.

So one can see, that any percentage in increase of positron production allows the same percentage in cut of 100 m undulator.

Size of the gamma beam and angular spread can be estimated as

$$\sigma_r \approx \sqrt{\gamma \epsilon \beta / \gamma + D \sqrt{\langle \theta^2 \rangle}} \approx L \sqrt{\langle \theta^2 \rangle} \approx 5 \cdot 10^{-4} \text{ m},$$

$$\sigma_r' \approx \sqrt{\langle \theta^2 \rangle} \approx 5 \cdot 10^{-6} \quad (1)$$

where the distance from the target to the undulator D estimated as $D \sim L$ and the size of primary electron/positron beam included too. These numbers used for numerical modeling of conversion.

DESCRIPTION OF PROCEDURE

For calculations the code CONVER [5] operating on PC was used. The code, in its turn, uses results of calculations done by other code- UNIMOD2 [6]. The last one, EGS-like code, calculates the cascade processes in semi-infinite media, keeping the individual history of every particle in cascade since the first appearance. Calculations in CONVER arranged so that the files obtained from UNIMOD2 are transferred to PC and user can easily assemble a target of any shape as a sum of isles, each of them is a body of revolution with polygonal cross section. If trajectory of any particle in cascade meets empty space, its trajectory just continued linearly by CONVER up to the next isle with material. Individual parameters of every particle in cascade at the out of target

¹ Extended version is available at http://www.lns.cornell.edu/public/CBN/2003/CBN03-2/CBN03_2.pdf. Work supported by NSF.

region allow to calculate efficiency as well as to prepare the files for further tracking.

With help of these codes numerous parameters were calculated, such as, for example, polarization, energy deposition and efficiency as function of thickness [7].

TI TARGET

Although utilization of undulator/wiggler conversion decreases average power deposition in target $>10^2$ times, it is still not enough for TESLA. Utilization of Ti for target was suggested in [8]; namely this publication initiated work with Ti in [7]. In addition to bigger volume of cascade developing in this material, it has higher heat capacity. This is a sequence of Dulong-Petit law.

Now, as the cascade process is no longer involved in conversion with undulator, result of shape optimization might indicate some significant improvements. First results were quite positive. This was mentioned for the first time in [9].

As all the files with Ti from UNIMOD2 were preserved since the [7] done, it was easy to make calculations for the form-factor now. Example of graphical presentation of output coordinates is shown in Fig.1. Here the shape of cylinder is clearly visible. Each point represents coordinates, when particle (positron) leaves the target.

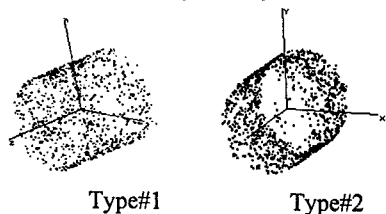


Figure 1: Different type of arrays of output coordinates. Type#1 for relatively short target. Type #2-for the long target. Lengths of cylinders are not in scale with diameter.

In Fig.2 the efficiency represented as functions of thickness for different target diameter. Energy of photons $E_\gamma = 30$ MeV, positrons selected in interval 15-30 MeV within capturing polar angle $\Delta\theta \leq 0.5$ rad. After $R_t > 4\sigma_\gamma$ the graphs began decline as functions of thickness –positrons cannot escape freely though the sides. One can see, that efficiency of positron conversion for infinitely wide target has maximum around 1.25 cm long-target. Accuracy of calculation was $\leq 10\%$. Same data, as in Fig.8, but transposed, are represented in Fig.8. Typically parameters of targets considered for DESY so far located behind the right edge of this Fig.8-wide targets. It is clearly seen from this figure, that optimum target diameter is somewhere between 0.75-1.0 mm. Even for target having length ~ 1 cm it is better to have its diameter small, something about 1 mm. This is a new result.

So the strategy in obtaining maximum yield is now to increase the length of the target simultaneously decreasing its radius to about $R_t \approx 2\sigma_\gamma$.

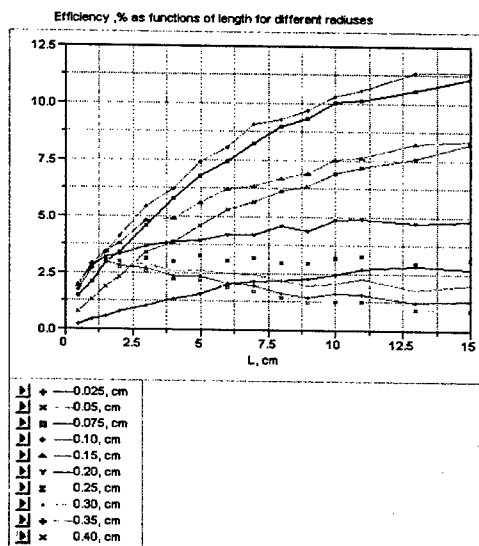


Figure 2: (Color) Efficiency as functions of target length for different values of radius.

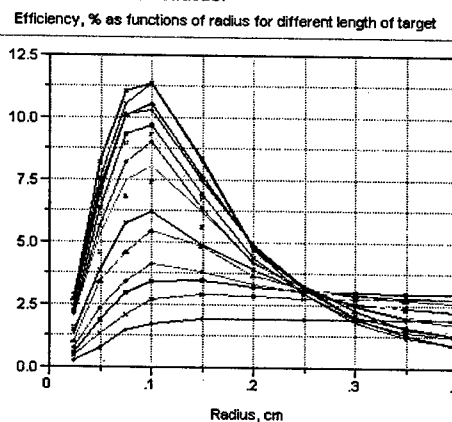


Figure 3: (Color) Efficiency as functions of target radius for fixed length. Curves are running for lengths 0.5, 1.0, 1.5, 2.0, 3.0, ..., 11, 13, 15 cm.

TECHNICAL REALIZATION OF COLLECTION SYSTEM

First scheme, Fig.4, uses short target with reduced diameter. Here Ti needles pressed is Be wheel. All assembly located in vacuum. Rotation of wheel synchronized with repetition rate of machine.

Total power deposited in the target system is few hundreds Watts only, so the cooling is not a problem here. Other technical solution is shown in Fig.5. Here the target of 2-6 cm long enclosed into a Ti cylinder with a coolant running inside. For coolant it is naturally to use liquid Lithium. For pumping of liquid Lithium a well-developed technique can be used [10].

Some of positrons can hit the target again, but as the target is thin in transverse direction, the scattering is small. Scheme with flux concentrator of this type was successfully implemented into CESR [11].

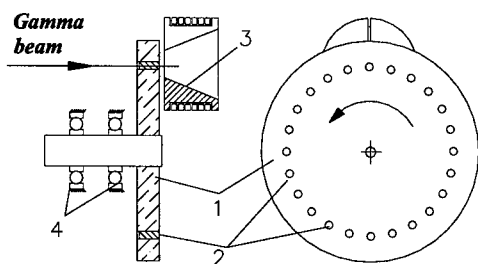


Figure 4: Realization of multi-target assembly. Ti needles pressed into Beryllium wheel. Here 1 is Beryllium wheel, 2 are Ti needles, 3—is a flux concentrator, and 4—bearings.

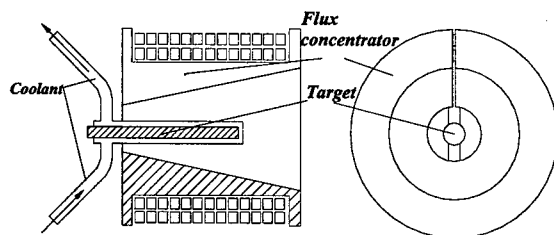


Figure 5: Another technical realization of target assembly. Ti target enclosed in Ti container with Li coolant.

Other way to increase cooling of target is shown in Fig. 6. Coolant flowing between discs effectively working because the distance from coolant edge to the point inside the target defined by thickness of the disc, not a diameter.

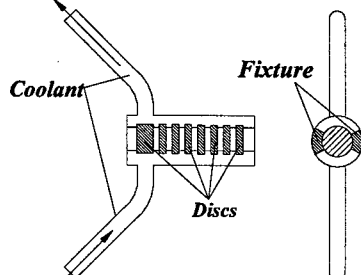


Figure 6: Sandwich-type high power target. W or Ti target discs enclosed in Ti container with coolant.

One other way to increase positron production –utilization of few targets and combining positrons into longitudinal phase-space is among guaranteed ones [1], [7], [9], [12]. This is also some kind of form-factor problem.

CONCLUSION

Increase in positron production allows proportional shortage of ~100-meter undulator and/or a source of additional operational margins for conversion system.

It is shown here for the first time, that needle-like Ti target with radius ~1mm ($R, \cong 2\sigma_r$) can give yield ~11.4%, which needs to be compared with ~2.7% yield for infinitely wide target and the same capturing angle ~0.5rad and for $E_\gamma = 30\text{MeV}$. This is two times bigger than for W target. Of course final numbers will depend on

capturing system, however indication, that form-factor can improve the yield so much, gives the basis for target optimization for real LC conversion unit. Decreasing diameter of the target also helps in cooling, even if the target is short.

Optimistically speaking, one can expect shortage of undulator length at least in half if the optimal target shape is used. If the length kept the same, this optimization will give wider operational margins or higher polarization, as one can select among much more positrons now.

In conclusion Author thanks A.D. Bukin for permission to use his code, which made this job possible.

REFERENCES

- [1] V.E. Balakin, A.A. Mikhailichenko, "Conversion system for obtaining highly polarized electrons and positrons", Preprint INP 79-85, Novosibirsk 1979.
- [2] E.G. Bessonov, "Some aspects of the theory and technology of the conversion systems of linear Colliders", 15th International Conference on High Energy Accelerators, Hamburg, 1992, p.138.
- [3] T. Hirose, in "Proceedings of International Workshop on Physics and experiments with Linear Collider's, Morioka, Iwate, Japan, September 8-12, 1995, World Science, Singapore, 1996, pp.748-756.
- [4] T. Okugi, et al., Jpn. J. Apl. Phys. 35 (1996) 3677.
- [5] A.D. Bukin, "Search of the optimum form of positron converter", Preprint INP 90-100, Novosibirsk 1990.
- [6] A.D. Bukin, N.A. Grozina, M.S. Dubrovin e.a., UNIMOD2-Universal Simulating program for e^+e^- experiments, Manual, Preprint BINP 90-93, Novosibirsk 1990.
- [7] A.D. Bukin, A.A. Mikhailichenko, "Optimized Target Strategy for Polarized Electrons and Positrons Production for Linear Collider", Budker INP 92-76, Novosibirsk, 1992.
- [8] J.Rossbach, K. Floetmann, "A High Intensity Positron source for Linear Collider", DESY M-91-11.
- [9] A.A. Mikhailichenko, "Use of undulators at High Energy to Produce Polarized Positrons and Electrons", Workshop on New Kinds of Positron Sources for Linear Colliders, SLAC, March 4-7, 1997, SLAC-R-502, pp. 229-284.
- [10] G.I. Silvestrov, "Liquid metal Targets for Intensive High-Energy Physics Beams", *ibid*, p.376-407.
- [11] J. Barley, V. Medjidzade, A. Mikhailichenko, "New Positron source for CESR", CBN 01-19, Cornell, 2001, 16 pp.
- [12] A. Mikhailichenko, "Conversion System for obtaining Polarized Electrons and Positrons at High Energy", Translation of Dissertation, CBN 02-13, Cornell, 2002.

PULSED UNDULATOR TO TEST POLARIZED POSITRON PRODUCTION AT SLAC

A.Mikhailichenko, Cornell University, LEPP, Ithaca NY 14853, USA

Abstract¹

We represent technical details and results of testing pulsed undulator with ~ 2 -mm period, $K \sim 0.1$, manufactured by Cornell LEPP for test of polarized positron production at SLAC.

INTRODUCTION

Conversion system for polarized positron production [1] contains ~ 130 m-long helical undulator followed by thin target. Helical gammas radiated by primary high-energy beam in undulator transfer their polarization to the positrons and electrons at the high edge of energy spectrum. Selecting secondary positrons/electrons by energy, one can at the same time select their polarization (higher energy—higher polarization). Right now there is a proposal for E-166 experiment at SLAC [2] to test this idea, initiated by publication [3].

Experiment requires, that undulator ~ 1 -long, must be installed in FFTB channel. Here ~ 50 GeV SLAC beam will generate ~ 10 MeV gammas [2]. General descriptions were done in [4], [5], and model with period 2.4mm was manufactured, Fig.1. This model was tested for 1 kV of static voltage. In this publication we describe more engineering details of undulator design.

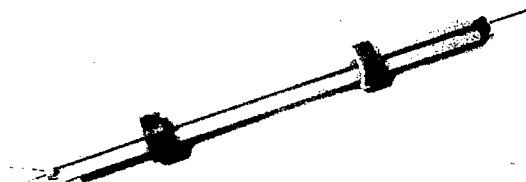


Figure 1: Model of pulsed undulator with period of 2.42 mm and 231.5 mm long [4]. Three G-10 rods squeezed with help of short rings having cylindrical grooves. This arrangement serves as a positioning system

One meter long pulsed undulator having 6 mm period and the axis field $\sim 6kG$ ($K \approx 0.35^2$) was successfully tested many years ago [6]. The feeding current in a wire with 1×1 mm² cross section was ~ 10 kA. Pulse duration was ~ 50 μ sec, feeding voltage ~ 1.19 kV required by inductance ~ 1.3 μ H allowed operation with repetition rate of 25Hz³. Such high current (and inductance) was forced by the aperture clearance of 4mm in diameter

¹ Extended version is available at http://www.lns.cornell.edu/public/CBN/2003/CBN03-5/CBN03_5.pdf

² This value is optimal for 150 GeV primary beams.

³ Required by VLEPP parameters at that time.

required. Intensive cooling of this device was a main engineering achievement.

Namely this technology was used for short period undulator suitable for test at SLAC.

GENERAL DESCRIPTIONS

Undulator has two helixes shifted in longitudinal direction by half-period [7], Fig.2. Technology for manufacturing of double helix with period 2.4 mm was tested successfully [4]. There was not found any limitation to make the windings with period 2 mm. Small period required for generation of gammas with appropriate energy ~ 10 MeV, forcing shrinkage of aperture. Fortunately this drastically reduces inductance of undulator. In its turn this yields proportional reduction of voltage required for excitation of necessary current ~ 1.6 kA. The helixes immersed in coolant liquid avoiding overheating.

Basically the helixes will be wound on the StSt tube of gage size 19 with nominal OD 0.042" (1.0668 mm). Kapton insulation 0.003" - thick will serve for electrical insulation. This tube has the wall thickness of 0.0035" (0.0889mm)⁴. This tube allows the ID diameter 0.889 mm available for the beam.

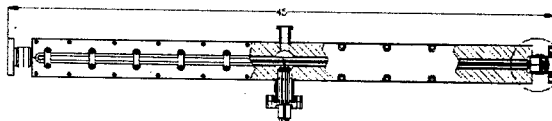


Figure 3: General view of undulator. Length is shown in inches. The current feed-throughs (four in total) located at the central part. Circled region scaled in Fig.6. StSteel flanges are the parts of transitions welded to Al corps.

General view of undulator represented in Fig. 5. Total length of undulator is 45" (≈ 114) cm allowing pure helical winding occupy 2×50 cm of each helicity. Corps made from Aluminum alloy. We used here the same scheme for fixation core with helixes as in [6]. StSteel flanges are welded to the corps using commercially made transitions⁵. Cross section of undulator in regular part is represented in Fig. 6. Basically the body of undulator is an 3" \times 3" \times 41" Aluminum block with groove in the middle. Inside this groove two roads 5 located in corners, giving the basis by theirs surfaces. These roads made from G10 cylindrical rods of 0.375" in diameter. After making cut with 60° upper surfaces of these roads coincide with axes of undulator. This axis located ≈ 1.5 " from the bottom surface. The third road presses the helical windings to the basement lodgment arranged by

⁴ New England Small Tube Catalog, tube GS#19, XTW.

⁵ Thermionics Northwest, Inc.

other two by springing bars seeing if Fig.4, and marked as 4 in Fig.6.

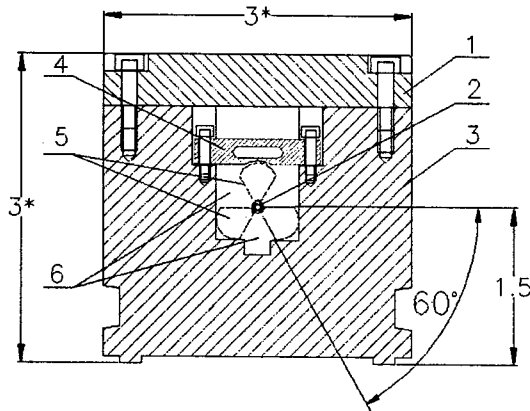


Figure 4: Cross-section of undulator, Fig.5. Two G10 rods are based in corners of long groove. Third rod with help of springing bars 4 compresses the windings to the other two ones. 1 – is a cover, 2 – is bi-helix. 3 – is a corps, 5 – are G10 rods, 6 – is filled with coolant. Parts 1, 3 made from Aluminum.

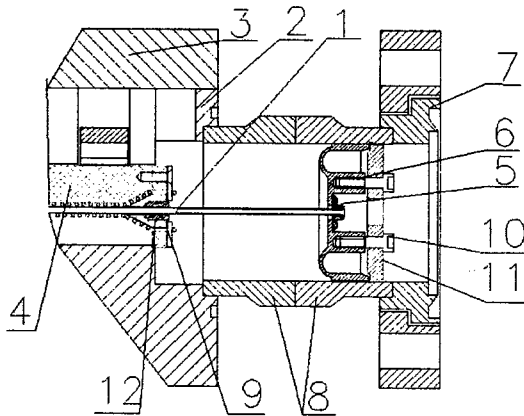


Figure 5: Scaled view of circled parts in Fig.3. 1 – is the helices, wound on StSteel tube. 2 – is the corps, 3 – is a cover, 4 – is the upper rod, 5 – is end cup, 6 – is intermediate cup, 7 – is a standard 2 1/4 flange, 8 – is a StSteel-Aluminum transition, 9 – is the end commutation, 10 – are screws, 11 – is a springing washer, 12 – is a trimming conducting cylinder (flux attenuator). Inner volume filled by coolant.

End part of undulator circled in Fig. 5 is shown scaled in Fig.7. Here helices 1 with tube based on the surface of two rods. It is clearly seen the end commutation 9 made with ring. Conically expanded helices can be seen here too. Conical expansion made for proper adjustment of integrals along edge region. For the same purposes the conducting cylinders (See Fig.8) serve too. For high-energy particles the radius of space helix of trajectory is very small, $\rho \approx \lambda_u K / 2\pi\gamma$, where K – is undulatority factor. For 50GeV beam $\gamma \approx 10^5$ and for our parameters $\rho \approx 3 \cdot 10^{-7} \text{ mm}$ allows to treat trajectory as a

straight line when calculating integrals along trajectory.

Intermediate cap 6 made from St Steel welded to the transition. In this design standard transition Al/StSteel with rotatable flange used at both ends. StSteel tube (vacuum chamber) caring the helices brazed to the cap 6 with end cap 5. This end cap 5 allows small transverse movements, accommodating the transverse position of the end cap on the orifice of intermediate cap 6. With the help of threads 10 and washer 11 the vacuum tube can be stretched in longitudinal direction. That is why the intermediate cap 6 made with developed surface. Copper cylinder 12 serves as trimming flux attenuator.

Upper rod has grooves with period of helix, fixing longitudinal positions of the wires.

FIELDS IN UNDULATOR

Fields in undulator calculated analytically and numerically with 3D code MERMAID. We used both ways for the field evaluation. Both gave the same result [4]. Field attenuation defined by skin-depth in StSteel, what is of the order $\sim 3.6 \text{ mm}$ for such duty times. So attenuation is going to be 2.4%.

For our case the only first longitudinal harmonic is important. For the axis field of undulator with thin wires, one can obtain expression as [4]

$$H(0,0,z) = \frac{I}{\pi a} \times \left(\frac{2\pi a}{\lambda_u} \right)^2 \times \cos \left(\frac{2\pi z}{\lambda_u} \right) \times K_1' \left(\frac{2\pi a}{\lambda_u} \right). \quad (2)$$

This formula is illustrated in Fig.6. One can see from there, that for $\lambda_u \approx 2a$ the field is only $\sim 17\%$ less, than asymptotical value for infinitely long two-wire line. Longitudinal profile at the end of helices is represented in Fig.7. This type of field mapping used for modeling end field effects. Fig. 8 explains what type of corrections used to trim end fields.

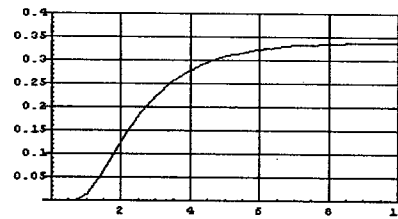


Figure 6: Field at the axis, G , for radius $a=1$ as a function of λ_u , Current $I=1 \text{ A}$. Saturation indicates that the field can be calculated as for two parallel infinitely long wires.

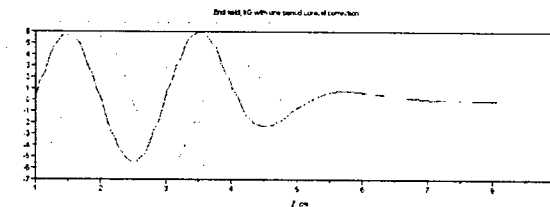


Figure 7: (Color) Longitudinal field profile, kG along undulator aperture near the end, cm. End correction.

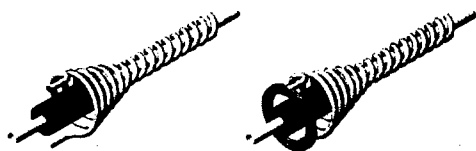


Figure 8: (Color) End correction made for input, left and conductor jumper, right. Copper cylinder serves as a flux attenuator.

Integrals calculated from fixed point inside the undulator to the point far out from the end and the integral for central (axes) line subtracted from every one, calculated for off-axis position. The difference after correction remains within 0.0025 kGcm . Even not corrected end commutation gives integral deviation $\sim 0.035 \text{ kG}\cdot\text{cm}$, what yields the angular kick $x' \approx 2 \cdot 10^{-7} \text{ rad}$ only for 50 GeV beam. Nevertheless this commutation correction is a useful tool.

PARAMETERS

Parameters of undulator are represented in Table 1 below. Voltage required based on the calculation of inductance done at the same time with field calculations. Number of quanta radiated, radiation losses and polarization value are taken from [4] and [9]. Factor Power supply described in detail in [5]. It is pretty much the same type used in [8], see Fig. 9.

Table 1.

Parameter	Value	Value
Length	$2 \times 50 \text{ cm}$	$2 \times 50 \text{ cm}$
Period	2.0 mm	2.4 mm
Axis field	5.6 kG	7.62 kG
K	~ 0.1	~ 0.17
$\hbar\omega$	11.7 MeV 9.94	$10 \text{ MeV} (50 \text{ GeV})$ $8.5 \text{ MeV} (46 \text{ GeV})$
Losses/part.	$1.15 \times 10^{-12} \text{ J/m}$	$0.31 \times 10^{-12} \text{ J/m}$
Losses		1.902 MeV/m
Quanta/particle	$0.16/\text{m}$	$0.36/\text{m}$
Current	1.6 kA	2.3 kA
Pulse duration	$30 \mu\text{s}$	$30 \mu\text{s}$
Heating/pulse	$\sim 3 \text{ degC}$	$\sim 2.7 \text{ degC}$
Inductance	$\sim 9.9 \times 10^{-9} \text{ H/cm}$	$\sim 8.6 \times 10^{-9} \text{ H/cm}$
Resistance	$\sim 0.0035 \text{ Ohm/cm}$	$\sim 0.0011 \text{ Ohm/cm}$
Inductive Voltage/length	1.65 V/cm	$\sim 1.54 \text{ V/cm}$
Resistive Voltage/length	5.6 V/cm	$\sim 2.5 \text{ V/cm}$
Average polarization	90%	$\sim 90\%$

Radiation in the undulator is typical for quantum regime: the amount of energy radiated by particle is less, than energy of quanta. This brings the radiation process in statistical regime.

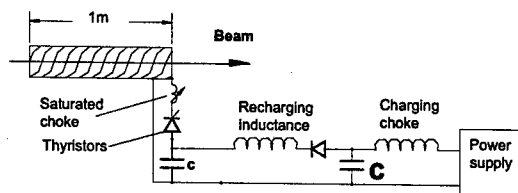


Figure 9: Scheme of pulser for undulator.

CONCLUSIONS

Pulsed undulator developed for E-166 experiment at SLAC itself despite its unique parameters looks also a pretty guaranteed from the engineering point of view. Real test with designed pulsed current is under preparation. Static test of insulation done at the Air for 1 kV DC voltage applied to the chamber and wires.

We believe however, that for future linear collider a SC undulator with large ($\sim 6 \text{ mm}$ in dia) aperture and $\sim 8 \text{ mm}$ period is more suitable from the exploitation point of view.

REFERENCES

- [1] V.Balakin, A. Mikhailichenko, "Conversion System for Obtaining Highly Polarized Electrons and Positrons at High Energy", Budker INP 79-85, September 13, 1979.
- [2] E-166, see: <http://www-project.slac.stanford.edu/lc/local/PolarizedPositrons/pdfs/E-166TLD.pdf>
- [3] R.Pitthan, J.Sheppard, "Use of Microundulators to Study Positron Production", LC02, Proceedings, SLAC-WP-21.
- [4] A.A. Mikhailichenko, "Pulsed Helical Undulator for test at SLAC the Polarized Positron Production Scheme, Basic Description", CBN 02-10, September 16, 2002, Cornell University, LEPP.
- [5] A.Mikhailichenko, "SLAC test pulsed undulator concept", Cornell LEPP CBN 02-7, Aug.16, 2002.
- [6] A.A. Mikhailichenko, "Dissertation", BINP, Novosibirsk, 1986, Translation: CBN 02-13, Cornell LEPP, 2002. Electronic version is available at: <http://www.lns.cornell.edu/public/CBN/2002/CBN02-13/DISSERT.pdf>.
- [7] R.C. Wingerson, "Corkscrew" -a Device for Changing the Magnetic Moment of Charged Particles in a Magnetic Field", Phys. Rev. Lett., 1961, Vol. 6, No. 9, pp. 446-449.
- [8] J.Barley, V.Medjidzade, A. Mikhailichenko, "New Positron Source for CESR", CBN 02-8, Cornell LEPP, 2002.
- [9] A.A.Mikhailichenko, "Optimized parameters of the Helical Undulator for test at SLAC", LC02, Proceedings, SLAC-WP-21.

THE TECHNICAL REALISATION OF RF KICKERS FOR CLIC TEST FACILITY CTF3

E.Plawski, S.Kulinski, A.Kucharczyk, INS, Swierk, Poland

Abstract

The bunch train compression scheme in CLIC Test Facility CTF3 includes two fast RF kickers operating in deflecting mode on 3 GHz frequency. The kickers designed by common INFN-Frascati/INS-Swierk effort were produced in Institute for Nuclear Studies in Swierk and are successfully operated at full power in CTF3 experiment in CERN. The details of fabrication procedure and low power RF measurements are presented in this paper.

INTRODUCTION

In CTF3, 30 GHz high power generation experiment, two fast kickers are needed [1] for injection of electron beam bunches to combiner ring.

The kickers [2] are disk-loaded, backward type waveguides working in the $2/3$, EH_{11} hybrid mode. They are essentially based on formerly optimised at CERN waveguide for beam deflection[3].

BASIC PARAMETERS OF DEFLECTOR

Type: Travelling wave RF structure working in EH_{11} deflecting mode,	$f = 2998.55$ [MHz]
No of active rf cells	$N = 10$
Phase shift/cell	$2/3$
Length including 2 coupling cells	46cm
I/O ports	SLAC type flanges, WR -284
RF power	in pulse $P = 8$ [MW]
	average less than 5kW

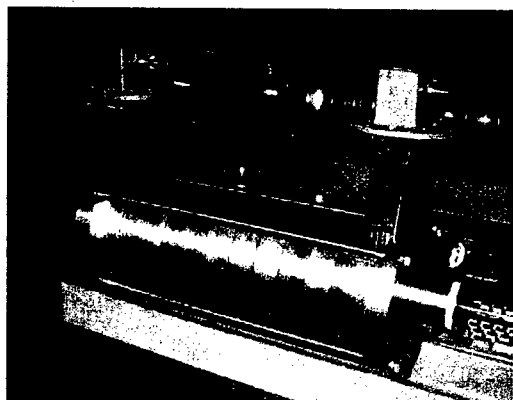


Fig.1 Full scale aluminium model of TW, 2998.5MHz deflecting structure

On the basis of 3D calculations performed in LNF-INFN Frascati, the full scale, n-cell ($n=2...10$) aluminium model shown in Fig.1 was build and measured

in INS in order to acquire the necessary experimental knowledge on deflecting mode. The influence of mode polarisation rods as well as frequency dependence on coupling measuring antennas size and structure temperature were verified. Also the size of matching iris apertures in coupling cells was experimentally verified.

The results of calculations, MAFIA and HFSS simulations and model measurements, were reported at EPAC 2002 Conference [3]. Also the phase shift per cell method of measurements to be used in ready made RF copper deflectors was mastered on this model (detuning plunger method).

FABRICATION OF COPPER DEFLECTORS

The components of deflector are fabricated from certified OFHC copper delivered by Outukumpu Enterprise*. The measured Cu content was 99.998% and oxygen content below 1.0 ppm. This last number is extremely important when technology of hard soldering (brazing) in hydrogen atmosphere is used, which was the case of our RF deflectors manufacture in 2002. Unlike in the old CERN procedure, the single cells of deflector were designed in the form of cups (Fig.2).

The cups are brazed together to form a disk-loaded circular waveguide structure of deflector. Such solution is a little more difficult in machining but

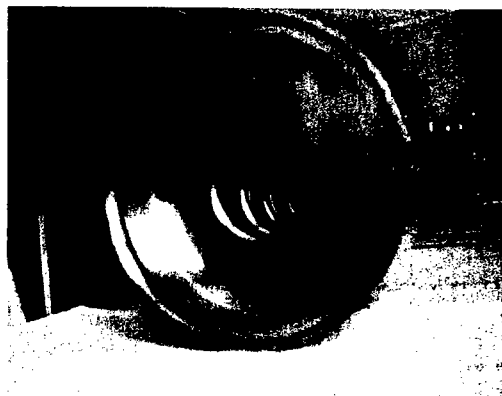


Fig. 2 The pilot series of 4 cells after hydrogen furnace brazing with 880°C LV30P filler alloy.

reduces by factor 2 the number of brazed joints. Pilot series of cells was produced to check the repeatability of machining (numerical lathe and milling

* Outukumpu Poricopper, Pori, Finland

machines with typical tolerance of $\pm 0.01\text{mm}$). This series was used next, to experiment the brazing procedure in hydrogen furnace.

All along the deflectors manufacture process, the procedure of lubrication, chemical cleaning and vacuum out-gassing at elevated temperature was chosen such as to reach in ready made deflectors, the vacuum better than 10^{-9} Torr after few hours of pumping.

During machining, MOBIL-SOLVAC 1535GD lubricant (liquid containing sodium sulfonate and boric acid esters)[†] was used.

The chemical cleaning before brazing involved following steps:

- washing in trichloroetylen(before rf checks of cylinders),
- etching (orthophosphoric acid or mixture of sulphur and nitric acids),
- washing in alkaline detergent liquid followed by hot tap water,
- washing in hot distilled water and drying in vacuum oven.

The brazing was made in several steps with three brazing alloys: LV30P(30%Cu,60%Ag,10%Pd) at 880°C , copper silver eutectic LV28(28%Cu,72%Ag) at 780°C , and Incusil-15 at 700° . Intermediate measurements of frequencies (single cells, dispersion curves before and after soldering) are executed in order to have full control of prototype production. The measured dispersion curve of soldered 8 internal cells is shown in Fig.3. Side half-cells were attached at both ends of the set to enable the excitation of 2 /3 mode. As it is seen from the measurement ,the rod splitters shift the lowest frequency of vertical polarity by 38.9MHz above the 2 /3 working horizontal polarity of mode .

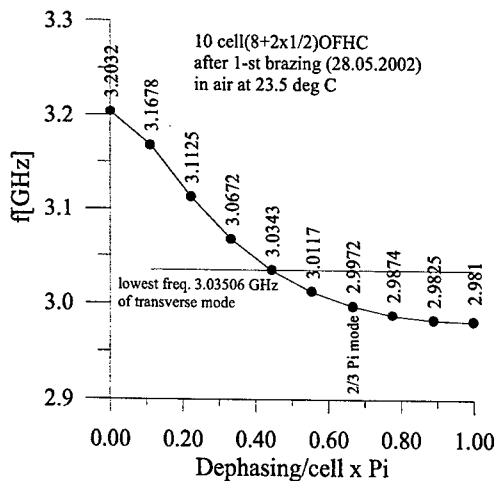


Fig.3 Dispersion curve of dipole mode measured in 8 brazed internal cells with added side half-cells.

The choice of hydrogen atmosphere brazing was forced by the lack of vacuum furnace of sufficiently large

[†] Producer: MOBIL OIL Corporation,Princeton,N.J.,USA

diameter. Biggest hydrogen furnace can accommodate the whole deflector including coupling waveguide chimneys.

After the last brazing operation the whole deflector is pumped and heated in vacuum chamber to the temperature 180°C limited by aluminium vacuum seals used (the beam input/output tubes are sealed with aluminium vacuum gaskets). The last operation of fabrication procedure is the check of leak rate using helium leak detector after which the deflector is closed under the high vacuum till the RF final measurements. The helium leak detector ASM-181f / ALCATEL with the sensitivity better than 10^{-10} Torr l/s was used for that purpose and no leaks were found in both deflectors. The deflector ready for safe transportation is shown in Fig.4.

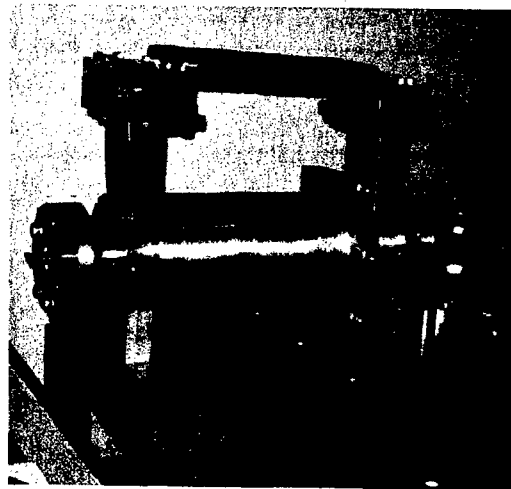


Fig. 4 3 GHz deflecting structure after fabrication

Appropriate cooling in moderate average power rf cavities is provided by either water cooled tubes directly soldered to cavity body outside surface, or by special demountable cooling panels attached tightly to cavity body after high temperature out-gassing. As the cavity side wall is thick (inner diameter 11.2cm, outer diameter 12.4cm) the last solution was adopted. It consists of eight attachable mechanically (not soldered!) copper heat radiators, each made of 38mm wide rectangular pipes assuring good thermal contact on side surface of deflector.

MEASUREMENTS

During the fabrication procedure and after completion of each deflector thorough RF measurements were made in order to guarantee the designed parameters. After machining, the frequencies of all single cups were controlled in the known design frequencies test set. The test set consists of standard cell having exact internal dimensions of deflector cell coupled to measured cup, in aim to form two cell resonator. The dispersion curves of

string of internal cells were measured before and after first brazing operation (vide Fig.3).

The last measurement was the control of phase advance per cell of ready made deflector. The method of "detaining short" developed at SLAC [4] was applied. The HP 8753C/85047A vector network analyzer was used to trace the phase advance corresponding to sliding short jump from cell to cell.

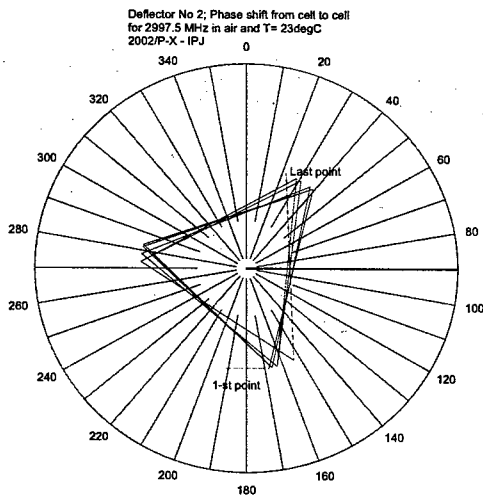


Fig.5 The measured phase advance per cell in second deflecting structure of CTF3

The measured result for deflector No.2 is shown in Fig. 5 , where in the polar co-ordinate the deviation of the phase shift per cell is illustrated. The VSWR for both deflectors was within 1.1 at the working frequency 2.9975GHz in air . The low power measurements finished, the deflectors were vacuum leak tested and next filled with dry nitrogen.

CONCLUSIONS AND ACKNOWLEDGEMENTS

Two deflectors produced in INS Swierk underwent the additional vacuum tests in LNF-INFN Frascati and rf power tests at CERN. The tests were very satisfactory. The vacuum obtained was better than 10^{-10} Torr and RF power in excess of 10 MW can be fed without breakdowns. Actually deflectors are used in CTF3 experiment program. The authors wish to express their gratitude to the team of Dr E. Nietubyc of LAMINA Establishment for their deep interest and important help in successful realisation of deflectors.

REFERENCES

- [1] Gallo et al. "Studies On the RF Deflectors for CTF3", EPAC 2000 Proc.
- [2] D. Alesini et al., "RF Beam Deflectors for CTF3 Combiner Ring", EPAC 2002 Proc.
- [3] Ph. Bernard et al., CERN Yellow Report 70-26.
- [4] A.L.Eldredge et al. , p.293 in "Linear Accelerators" edited by P.Lapostolle and A. Septier

DEVELOPMENT OF ROOM TEMPERATURE ACCELERATING STRUCTURES FOR THE RIA*

N.E. Vinogradov, P.N. Ostroumov, E. Rotela, S.I. Sharamentov, S. Sharma, G.P. Zinkann, ANL, Argonne, IL 60439, USA

J.W. Rathke, T.J. Schultheiss, Advanced Energy Systems, Inc., Medford, NY 11763, USA

D.L. Schrage, Los Alamos National Laboratory, MS H817, Los Alamos, NM 87545

Abstract

The proposed Rare-Isotope Accelerator Facility (RIA) [1] includes a driver linac and a post-accelerator based on superconducting cavity technology. The exceptional sections of the RIA accelerators are front ends that comprise normal-conducting continuous wave accelerating structures to obtain particle velocities acceptable for further acceleration by superconducting cavities. The front ends for both accelerators are based on RFQ technology. An engineering design of a 57.5 MHz RFQ for the driver linac has been developed. A cold model of the 57.5 MHz RFQ has been fabricated.

The post-accelerator consists of a conventional RFQ operating at 12 MHz and two sections of a hybrid RFQ (H-RFQ) operating at 12 and 24 MHz. A 1:2 scale cold model of the 12 MHz H-RFQ has been built and studied to determine the final specifications for the full power hybrid RFQ. This paper reports on the present development status of these accelerating structures.

INTRODUCTION

The primary scope of the driver linac RFQ is the acceleration of low longitudinal emittance dual charge state uranium beams up to energies acceptable by the superconducting linac. In order to simplify the front end of the multi-beam driver linac and accommodate different ion species from the ECR ion source the RFQ must be capable of operating at a wide range of power levels. The physics design of the RFQ beam dynamics and accelerating structure was established earlier [2]. Several types of resonant structures have been analyzed in order to satisfy all specifications. As a result an original RFQ structure that combines the advantages of the four-vane and split-coaxial structures has been proposed in collaboration with ITEP team, Moscow [2]. The structure provides high shunt-impedances, has extremely good mode separation and moderate transverse dimensions ~50 cm at 57.5 MHz operating frequency.

The concept of the RIA post accelerator suitable to produce high-quality beams of radioactive ions over the full mass range, including uranium, at energies above the Coulomb barrier was presented in ref. [3]. The most efficient generation of rare isotope beams requires singly-charged ions at initial injection. Very-low-charge-state ions can most efficiently be bunched and accelerated by using three sections of a cw, normal-conducting RFQ for

the first ~9 MV of the post-accelerator. The first two sections of the RFQ should operate at as low a frequency as is practicable to maximize the transverse focusing strength. At ANL the acceleration of $^{132}\text{Xe}^{1+}$ ions in the split-coaxial RFQ geometry operating at 12 MHz [4] has been demonstrated. An RFQ for acceleration of heavy ions with a minimum charge to mass ratio of 1/240 will have similar design. The last two sections of the RFQ will be based on a more effective accelerating structure, a hybrid RFQ [5].

DRIVER LINAC RFQ

Table 1 presents basic parameters of the cw RFQ accelerator that is being designed for the RIA driver linac. The design addresses the requirements for efficient cooling throughout the structure, precise alignment, reliable RF contacts, and fine tuning capability. The RF, thermal and structural analyses have been completed in response to these requirements. Results of these analyses show that the thermal and structural design of this RFQ is very robust [6,7].

Table 1. Basic parameters of the RFQ

Operating frequency	57.5 MHz
Length	4 m
Duty cycle	100%
Transverse dimensions	0.51 m
Peak surface field	140 kV/cm
Input&output particle velocity	0.00507/0.02 c
Design charge-to-mass ratio	1- 28.5/238
Normalized transverse emittance	0.5 π mm-mrad
Longitudinal emittance at the exit of RFQ for 99.9% of particles,	$\leq 2\pi$ keV/u-nsec

A typical segment with cutaway sections to show the cooling passages is shown in Fig. 1. Several different approaches to fabrication of the RIA RFQ were discussed during the conceptual design phase. Ultimately we have chosen a fully brazed assembly using step brazing to fabricate the vanes and quadrant details and finally a complete segment with end flanges. An octagonal cross section of the RFQ tank was accepted as the most appropriate to apply the step brazing technique. This approach borrows heavily from the techniques used successfully on the LEDA RFQ at Los Alamos [8]. The RFQ is designed as a 100% OFE copper structure with GLIDCOP® dispersion strengthened copper end flanges. Six longitudinal segments will be mechanically assembled to form the complete 4-meter RFQ structure.

* Work is supported by the U.S. Department of Energy under contract W-31-109-ENG-38.

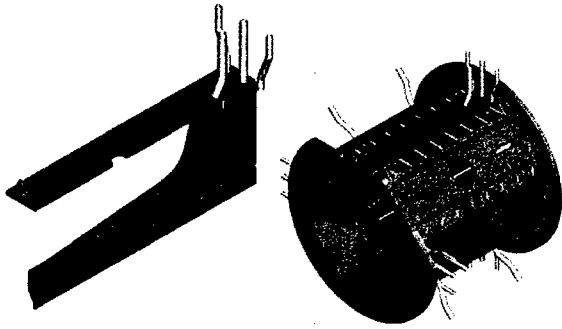


Figure 1. Segment details with cooling channels. The vane assembly is shown separately on the left.

The full-scale aluminum cold model of the RFQ segment was designed and constructed. This model is necessary to verify final internal dimensions of the RFQ prior to the fabrication of full copper structure, and testing of machining and final assembly tolerances. Precise measurements for the gravity deflection of horizontal vane show acceptable deviations of the vane's profile. The final assembly of the model was completed and the specified tolerances on the vane tip location of less than 50 μm were achieved. A photograph of the one-segment aluminum cold model is shown in Fig. 2.

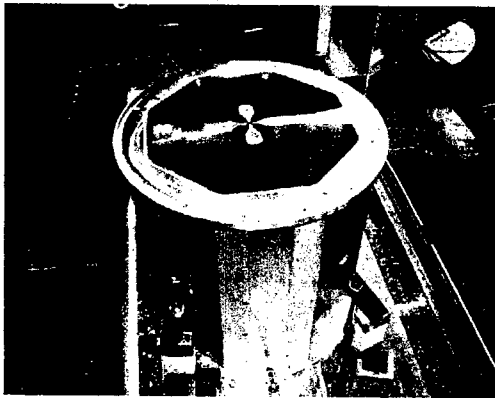


Figure 2. Photograph of the aluminum model.

A full power engineering prototype of a single segment of the 57.5 MHz RFQ is being developed and fabricated. The main reasons to proceed with fabrication and testing of the engineering model are: a) the transverse dimensions of the RFQ are significantly larger than those in 4-vane high-frequency RFQs built using the brazing technique; b) due to the large cut-out in the vane it is prudent to demonstrate mechanical stability during high temperature brazing. Once the fabrication is complete, testing of the RFQ prototype over the wide range of input power is necessary. Successful testing of the RFQ over the wide range of RF power level will simplify the design and minimize the cost of the RIA Driver Front End because the same RFQ will be able to accelerate the full range of ions from proton to uranium.

Recently, we have performed tests of major brazed junctions of the RFQ engineering prototype that demonstrated machining and brazing of the copper vane assembly within specified tolerances. Fabrication of the full-power copper prototype of a single segment of the 57.5 MHz RFQ will be pursued as soon as funds become available..

HYBRID RFQ FOR THE POST-ACCELERATOR

The Hybrid Radio Frequency Quadrupole (H-RFQ) is an accelerating structure designed to accelerate low-velocity heavy ions with a q/A ratio = 1/240 [5]. The assembly drawing of the H-RFQ is shown in Fig. 3. The H-RFQ structure consists of three sections of drift tubes and two RFQ sections. In the drift tube sections the beam is accelerated and defocused transversely. Transverse focusing is provided by the RFQ sections. Each of the RFQ sections consists of two sets of non-modulated vanes with a length of $\beta\lambda$ separated by a drift space of $\beta\lambda/2$. The appropriate focusing strength is achieved by adjusting the distance between the vanes. Using the combination of the drift tube and RFQ structures a factor of two higher output beam energy is achieved when compared to a conventional RFQ accelerator.

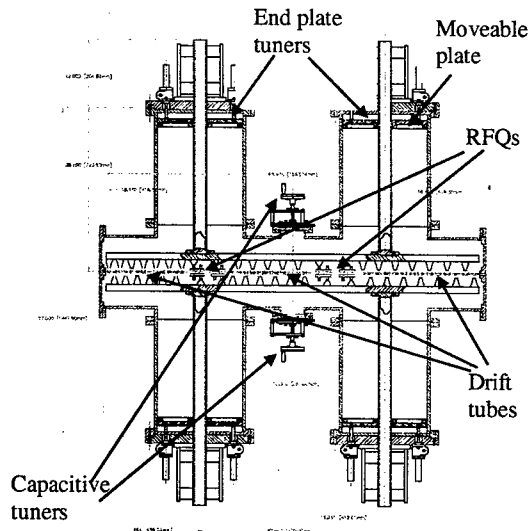


Figure 3. Assembly drawing of the H-RFQ cold model.

A half-scale (24.25 MHz) aluminum cold model of the Hybrid RFQ has been designed, built and tested. The goals were to determine the final resonator dimensions, accelerating and focusing field distribution, quality factor and coupling to the external power supply.

First, a numerical simulation of the cold model's electrodynamic parameters was done using the MWS code. The numerical simulation of this complicated structure had some difficulties. The size of the drift tube gaps and the RFQ vane spacing is very small compared to

the overall dimensions of the cavity. This difference required a very large number of mesh cells for the simulation which resulted in unacceptable calculation time and the solution was non-convergent. To rectify this, some simplification of the shape of the structure had to be implemented. With this simplification a frequency error in the simulation was expected. Therefore, the designed resonator dimensions needed experimental testing and the aluminum cold model of the H-RFQ (Fig. 4) was built.

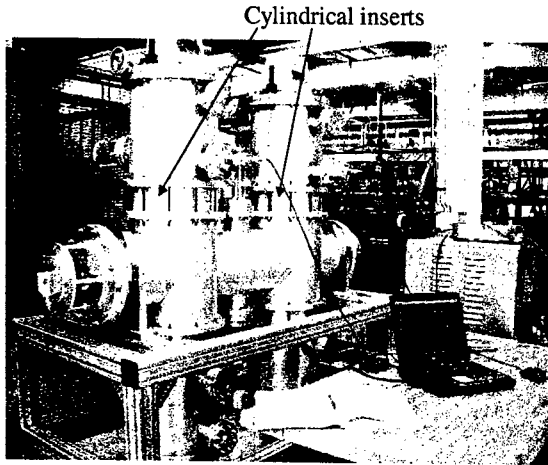


Figure 4. 24.25 MHz Hybrid RFQ aluminum cold model.

The experimental investigation of the 24.25 MHz H-RFQ cold model was carried out using both an HP Network Analyzer and a standard bead-pull technique using a phase-locked loop. The first measurements of the electrodynamic parameters of the cavity revealed three important shortcomings of the cold model. These are: the measured quality factor turned out to be 3.5 times lower than the calculated value, the frequency was approximately 2 MHz high, and there was a tilt in the field amplitude distribution of the third drift tube section.

To address the low Q , a stiffer spring material from Bal Seal Engineering was used to improve the RF contacts. In addition, we used special conductive silver grease supplied by Tecknit. After these modifications were made the measured quality factor was stable and was about 70% of the calculated value. Table 2 summarizes these results.

Table 2. H-RFQ electrodynamic parameters.

	MWS simulation	Measurement before the modification	Measurement after the modification
Q	4700	1350-2300	3150
f (MHz)	24.65	26.5	24.25

To improve the resonant frequency the dimensions of the H-RFQ model have been changed. Cylindrical inserts to lengthen the vertical stubs of the cavity were designed and installed to lower the eigen frequency (see Fig. 4). After this modification the resonant frequency was close to the expected value as is seen from Table 2.

To improve the final problem of the field tilt, capacitive tuners were installed at appropriate locations. These tuners removed the field tilt in the end of the third drift tube section. The final distribution of electric field along the structure is shown in Fig. 5. The amplitude of the field in the accelerating gaps is uniform within $\pm 1.5\%$ that is fully acceptable from the beam dynamics point of view [5].

The designed resonant frequency, uniform field amplitude distribution and high quality factor in the resonator were obtained after slight modifications of the model designed by the MWS code. Complete specifications for the final design of the 12 MHz hybrid RFQ have been established and detailed drawings of the full-power 12.125 MHz H-RFQ are being prepared.

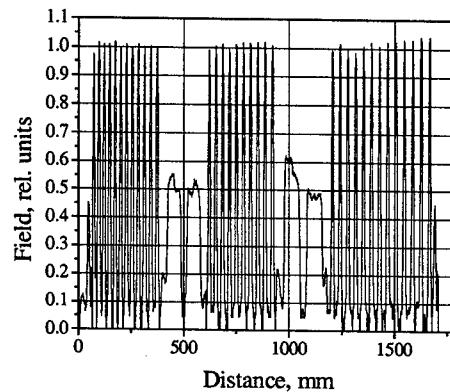


Figure 5. Field distribution along the H-RFQ.

ACKNOWLEDGEMENTS

We would like to address our thanks to A. Barcikowski and B. Rusthoven, TD-ANL, H. Friedsam's alignment group at ASD-ANL and A. Deriy, ATLAS Operations Group.

REFERENCES

- [1] K. Shepard. Proc. of the XXI LINAC conference, Gyeongju, Korea, August 19 - 23, 2002.
- [2] P.N. Ostroumov, A.A. Kolomiets, D.A. Kashinsky, S.A. Minaev, V.I. Pershin, T.E. Tretyakova, S.G. Yaramishev. Phys. Rev. STAB 5, 060101, 2002.
- [3] P.N. Ostroumov et al, Proc. of the EMIS-14, Victoria, Canada, May 6-10, 2002, Abstract Number 79.
- [4] M Kelly et al Proc. of the 2001 PAC conference, Chicago, IL, June 18-22, 2001, p. 506.
- [5] P.N. Ostroumov and A.A. Kolomiets. Proc. of the 2001 PAC conference. Chicago, IL, June 18-22, 2001, p. 4077.
- [6] J. Rathke et al. Proc. of the XXI LINAC conference, Gyeongju, Korea, August 19 - 23, 2002.
- [7] T.J. Schultheiss et al. Proc. of the XXI LINAC conference, Gyeongju, Korea, August 19 - 23, 2002.
- [8] D. Schrage, et al., Proc. of the XIX LINAC Conf., Chicago, IL, August 1998, p. 679.

AGS UPGRADE TO 1-MW WITH A SUPER-CONDUCTING LINAC INJECTOR*

A.G. Ruggiero, J. Alessi, D. Raparia, T. Roser, W. Weng, BNL, Upton, NY 11973, USA

Abstract

It has been proposed to upgrade the Alternating Gradient Synchrotron (AGS) accelerator complex at the Brookhaven National Laboratory (BNL) to provide an average proton beam power of 1 MW at the energy of 28 GeV. The facility is to be primarily used as a proton driver for the production of intense neutrino beams [1]. This paper reports on the feasibility study of a proton Super-Conducting Linac (SCL) as a new injector to the AGS. The Linac beam energy is 1.2 GeV. The beam intensity is adjusted to provide the required average beam power of 1 MW at 28 GeV. The repetition rate of the SCL-AGS facility is 2.5 beam pulses per second.

INTRODUCTION

The AGS upgrade requires operation of the accelerator at the rate of 2.5 cycles per second, and a new injector capable to follow the operation at 2.5 Hz. The present injector made of the 200-MeV room-temperature Linac and of the 1.5-GeV AGS-Booster will not be able to achieve the goals of the upgrade.

The proposed new injector is a 1.2 GeV Super-Conducting Linac (SCL) with an average output beam power of 45 kW. The choice of the energy value is determined in part by the capability to limit beam losses due to stripping of the negative ions that are used for multi-turn injection into the synchrotron, and in part to fit the entire SCL on a straight line between the exit of the 200-MeV room-temperature Linac and the injection point selected into the AGS.

The SCL is composed of three parts: (i) a Front-End, that is the present 100-mA negative-ion source, followed by the 0.75-MeV RFQ, (ii) the room-temperature Linac that accelerates protons to 200 MeV, and (iii) the SCL proper. This in turn is made of three sections, each with its own energy range, excitation RF frequency, and different cavity-cryostat arrangement. The three sections are labeled: Low-Energy (LE), Medium-Energy (ME), and High-Energy (HE). The beam leaves the present room-temperature Linac at the energy of 200 MeV, and, after a bend of 17.5°, enters a straight tunnel, where the SCL proper is located, about 120 meter long, to join the AGS tunnel. A schematic view of the new injector is given in Figure 1. The main injector and AGS parameters are given in Table 1.

THE NEW INJECTOR

The project described corresponds to an average SCL beam current of 37.6 μ A, that yields the required average beam power of 1 MW at the top energy of 28 GeV, including also a controlled beam loss of about 5% during multi-turn injection into the AGS. The average beam power in exit is 45 kW, considerably less than the 1-MW level of the equivalent 1.0-GeV SCL for the Spallation Neutron Source (SNS) [2]. Thus the concern about component activation by the induced radiation from uncontrolled beam losses is greatly reduced. The repetition rate of 2.5 beam pulses per second gives a beam intensity of 0.94×10^{14} protons accelerated per AGS cycle; that is about 30% higher than the intensity routinely obtained with the present injector. At the end of injection, that takes about 240 turns, the space-charge tune depression is $\Delta\nu = 0.2$, assuming a bunching factor (the ratio of beam peak current to average current), during the early part of the acceleration cycle, of 4. Also, with the normalized beam emittance of 100π mm-mrad, the actual beam emittance at 1.2 GeV is $\epsilon = 50 \pi$ mm-mrad. The SCL beam pulse length is 0.72 ms, and the beam duty cycle 0.18%.

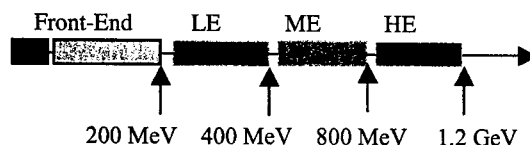


Figure 1. Schematic of the new AGS Injector.

The front-end of the Linac is made of the present ion source with minor power supply modifications to operate with a longer pulse width. The ion source is located on a platform at 35 kV, and is followed by the 0.75-MeV RFQ that works at 201.25 MHz. The beam is to be periodically chopped by a chopper located downstream the RFQ. The beam chopping extends over 75% of the beam extension, at a frequency matching the AGS accelerating rf (8.0 MHz, harmonic number = 24) at injection into the AGS. Moreover, the transmission efficiency through the RFQ and the DTL is low, so that at present a beam current of 35 mA can be achieved at 200 MeV. Thus we assume that the average current of the beam pulse in the SCL, where we assume no further beam loss, is conservatively 21 mA.

The combination of the RFQ and of the subsequent bunchers bunches the beam with a sufficiently small longitudinal extension so that each of the beam bunches at 201.25 MHz can be reasonably fitted in the accelerating rf buckets of the following room-temperature Linac that

* Work performed under Contract Number DE-AC02-98CH10886 with the auspices of the US Department of Energy.

operates also at 201.25 MHz. The required modifications and cost of the Front-End and the 200-MeV room-temperature Linac are described elsewhere [3]. The design of the transfer of the beam from the exit of the SCL to the injection location into the AGS is given in [4], whereas the process of injection proper into the AGS is described in [5].

Table 1. Injector and AGS Parameters for 1-MW Upgrade

Increment. Linac Ave. Power, kW	37.5
Kinetic Energy, GeV	1.2
β	0.8986
Momentum, GeV/c	1.92
Magnetic Rigidity, T-m	6.41
Repetition Rate, Hz	2.5
Linac Average Current, μ A	37.6
Linac No. of Protons / pulse	9.38×10^{13}
AGS Circumference, m	807.076
Revol. Frequency, MHz	0.3338
Revolution Period, μ s	2.996
Bending Radius, m	85.378
Injection Field, kG	0.7507
Chopping Ratio, %	75
Peak Current, mA	28
Average Current, mA	21
Injection Loss, %	5.0
Injected Protons per Turn	3.74×10^{11}
Number of injected Turns	239
Linac Pulse Length, ms	0.716
Linac Duty Cycle, %	0.179
Bunching Factor	4
Norm. Emitt., π mm-mrad	100
Emittance, π mm-mrad	48.8
Space-Charge Δv	0.187

THE SUPER-CONDUCTING LINAC (SCL)

The SCL accelerates the proton beam from 200 MeV to 1.2 GeV. The configuration and the design procedure of the SCL is described in detail in [6]. It is typically a sequence of a number of identical periods as shown in Figure 2. Each period is made of a cryo-module of length L_{cryo} and of an insertion of length L_{ins} . The insertion is needed for the placement of focusing quadrupoles, vacuum pumps and valves, steering magnets, beam diagnostic devices, bellows, and flanges. It can be either at room temperature or in a cryostat as well. Here we assume that the insertions are at room temperature. The cryo-module includes M identical cavities, each of N identical cells, and each having a length NL_{cell} , where L_{cell} is the length of a cell. To avoid coupling by the leakage of the field, cavities are separated from each other by a sufficiently long drift space d . An extra drift of length L_w may be added internally on both sides of the cryo-module to provide a transition between cold and warm regions. Thus, the length of a cryo-module is

$$L_{\text{cryo}} = MNL_{\text{cell}} + (M - 1)d + 2L_w$$

The choice of cryo-modules with identical geometry, and with the same cavity/cell configuration, is economical and convenient for construction. But there is, nonetheless, a penalty due to the reduced transit-time-factors when a particle crosses cavity cells, with length adjusted to a common central value β_0 that does not correspond to the particle instantaneous velocity. To minimize this effect, the SCL is divided in three sections, each designed around a different central value β_0 , and, therefore, with different cavity/cell configuration. The cell length in a section is fixed to be

$$L_{\text{cell}} = \lambda\beta_0 / 2$$

where λ is the RF wavelength. We adopted an operating frequency of 805 MHz for the LE-section of the SCL, and 1,610 MHz for the subsequent two sections, ME and HE. The choice of the large RF frequency in the last two sections has been dictated by the need to achieve as a large accelerating gradient as possible so the SCL would fit entirely within the available space. The major parameters of the three sections of the SCL are given in Tables 2 and 3. The total expected cost is around 100 M\$ for the SCL alone, excluding modifications of the Front-End, the room-temperature 200-MeV Linac, and of the transport and injection into the AGS.

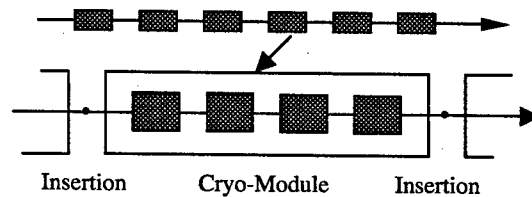


Figure 2. Configuration of a Proton Super-Conducting Linear Accelerator

The length of the SCL depends on the average accelerating gradient. The local gradient has a maximum value that is limited by three causes: (1) For a realistic cell shape, we set a limit on the average axial electric field to 15 MV/m at 805 MHz, and 30 MV/m at 1,610 MHz. (2) There is a limit on the peak power provided by rf couplers that we take here not to exceed 400 kW, including a contingency of 50% to avoid saturation effects. (3) To make the longitudinal motion stable, we can only apply an energy gain per cryo-module that is a relatively small fraction of the beam energy in exit. The conditions for stability of motion have been derived in [6].

The number of cells and cavities may vary in principle from section to section, but we have found it convenient here to adopt the same distribution in all sections. There is one klystron feeding a single coupler to a single cavity. The total length of the SCL injector proper from end to end is about 130 meter, including a 4.5-m long matching section between LE and ME sections. When averaged

over the real estate, the actual acceleration rate is about 5 MeV/m in the LE section and 10 MeV/m in the ME and HE sections. Efficiencies, defined as the ratio of beam power to required total AC power, is relatively high for a pulsed Linac, ranging between 9 and 15%.

Table 2. General Parameters of the SCL

Linac Section	LE	ME	HE
Ave. <i>inrem.</i> Power, kW	7.52	15.0	15.0
Average Beam Current, μ A	37.6	37.6	37.6
Initial Kinetic Energy, MeV	200	400	800
Final Kinetic Energy, MeV	400	800	1200
Frequency, MHz	805	1610	1610
Protons / Bunch $\times 10^8$	8.70	8.70	8.70
Temperature, °K	2.1	2.1	2.1
Cells / Cavity	8	8	8
Cavities / Cryo-Module	4	4	4
Cavity Separation, cm	32.0	16.0	16.0
Cold-Warm Transition, cm	30	30	30
Cavity Internal Diameter, cm	10	5	5
Length of Warm Insertion, m	1.079	1.379	1.379
Accelerat. Gradient, MeV/m	10.5	22.9	22.8
Ave. Gradient, MeV/m	5.29	9.44	10.01
Cavities / Klystron	1	1	1
No. of rf Couplers / Cavity	1	1	1
Rf Phase Angle	30°	30°	30°
Transverse Focussing	FODO	Doubl.	Doubl.
Phase Advance / FODO cell	90°	90°	90°
Norm. rms Emitt., π mm-mrad	2.0	2.0	2.0
Rms Bunch Area, π °MeV	0.5	0.5	0.5

A Super-Conducting Linac is most advantageous for a continuous mode of operation (CW). There are two problems in the case of the pulsed-mode of operation. First, the pulsed thermal cycle introduces Lorentz forces that deform the cavity cells out of resonance. This can be controlled with a thick cavity wall strengthened to the outside by supports. The actual design of a cavity cell is described in detail in [7]. Second, there is an appreciable period of time to fill the cavities with RF power before the maximum gradient is reached [6]. During the filling time, extra power is dissipated also before the beam is injected into the Linac. The extra amount of power required is the ratio of the filling time to the beam pulse length. The filling times are also shown in Table 3.

TRANSVERSE FOCUSING

The upgrade makes use of the present 200-MeV room-temperature Linac, with proper power supply modifications for larger pulse width. This Linac provides a negative ion beam with an emittance of 2.0π mm-mrad. To avoid uncontrolled beam losses that may cause radiation activation, one requires that the ratio of inner cavity radius to rms beam size is at least a factor of 6 all over the length of the SCL. This is difficult to achieve in the ME and HE section where the inner aperture is of only

5 cm because of the larger RF frequency. We have thus adopted in these two sections transverse focusing with doublets of quadrupoles, whereas a FODO singlet sequence was found adequate in the LE section.

Table 3. Summary of the SCL Design

Linac Section	LE	ME	HE
Velocity, β : In	0.5662	0.7131	0.8418
Out	0.7131	0.8418	0.8986
Cell Reference β_0	0.615	0.755	0.851
Cell Length, cm	11.45	7.03	7.92
Total No. of Periods	6	9	8
Length of a period, m	6.304	4.708	4.994
FODO-Cell ampl. func., β_Q , m	21.52	8.855	8.518
Total Length, m	37.82	42.38	39.96
Coupler rf Power, kW (*)	263	351	395
Energy Gain/Period, MeV	33.33	44.57	50.10
Total No. of Klystrons	24	36	32
Klystron Power, kW (*)	263	351	395
$Z_0 T_0^2$, ohm/m	378.2	570.0	724.2
$Q_0 \times 10^{10}$	0.97	0.57	0.64
Transit Time Factor, T_0	0.785	0.785	0.785
Ave. Axial Field, E_a , MV/m	13.4	29.1	29.0
Filling Time, ms	0.337	0.273	0.239
Ave. Dissipated Power, W	2	11	8
Ave. HOM-Power, W	0.2	0.5	0.4
Ave. Cryogenic Power, W	65	42	38
Ave. Beam Power, kW	7.52	15	15
Total Ave. rf Power, kW (*)	17	31	30
Ave. AC Power for rf, kW (*)	37	69	67
Ave. AC Power for Cryo., kW	46	30	27
Total Ave. AC Power, kW (*)	83	99	94
Efficiency, % (*)	9.05	15.21	16.08

(*) Including 50% rf power contingency.

CONCLUSION

The proposed SCL for the 1-MW AGS upgrade is not much different in size and scope from the equivalent accelerator of the SNS project. Though the average values of beam and RF power are considerably lower, because of the smaller duty cycle, nonetheless peak values are comparable to the SNS SCL, since we use similar pulse width and current.

REFERENCES

- [1] Report of the BNL Neutrino Working Group, BNL-69395. 28 October, 2002.
- [2] SNS Design Report, 1.0-GeV SCL
- [3] <http://raparia.sns.bnl.gov/nwg.ad>
- [4] D. Raparia, *private communication*, 2003.
- [5] N. Tsoupas, *contribution to this conference*, 2003.
- [6] A. G. Ruggiero, "Design Considerations on a Proton Superconducting Linac". BNL-Internal Report 62312. August 1995.
- [7] D. Raparia, *private communication*, 2003.

STUDY OF A 10-MW CONTINUOUS SPALLATION NEUTRON SOURCE*

A.G. Ruggiero, H. Ludewig, S. Shapiro, BNL, Upton, NY 11973, USA

Abstract

This paper reports on the feasibility study of a proton Super-Conducting Linac as the driver for an Accelerator-based Continuous Neutron Source (ACNS) [1] to be located at Brookhaven National Laboratory (BNL). The Linac is to be operated in the Continuous Wave (CW) mode to produce an average 10 MW of beam power. The Linac beam energy is taken to be 1.25 GeV. The required average proton beam intensity in exit is then 8 mA.

INTRODUCTION

It is commonly agreed that a Super-Conducting Linac (SCL) is the most effective choice for a continuous high-power proton beam in the GeV range. Other devices, like Cyclotrons or Fixed-Field Alternating-Gradient accelerators, should also be considered, but they are less efficient and are more prone to uncontrolled beam losses.

A SCL is also most suitable for a continuous mode of operation (CW), where average and peak performance are equal, as opposed to a pulsed mode where the peak performance determines the design and requirements. The design of SCL is simplified with the CW mode of operation, since it avoids large excursion between average and peak values, and related fatigue effects. In the CW mode the concern with cavity *Filling Time* and *Lorentz Forces* are removed.

Though the feasibility of SCL is within present mechanical, cryogenic, and RF technology, it has nonetheless not been proven entirely yet. One SCL is presently being build for the Spallation Neutron Source (SNS) [2] project; and another has been proposed and conceptually designed for the AGS Upgrade at Brookhaven [3]. The Accelerator-based Continuous Neutron Source (ACNS) can also make use of a similar SCL. Despite the larger average beam power required, it compares favorably with the other two projects, as it can be seen from the comparison in Table 1.

The proposed SCL driver for the ACNS accelerates protons to 1.25 GeV, operates in the CW mode, and generates an average beam power of 10 MWatt. The average beam current is 8 mA, and the total length of the superconducting section about 160 m. The Linac is made of three parts: a Front-End, that is a 10 mA ion source followed by a 2-MeV RFQ, a room temperature 200-MeV Drift-Tube Linac (DTL), and the Super-Conducting Linac (SCL) proper. This in turn is made of three sections: the low-energy (LE) section that accelerates protons to 400 MeV, the medium-energy (ME) section for further acceleration to 800 MeV, and the high-energy (HE) section that accelerates to the final energy of 1.25 GeV.

* Work performed under the Contract Number DE-AC02-98CH10886 with the auspices of the U.S. Department of Energy.

The selected operating frequency of the room temperature components, RFQ and DTL, is 350 MHz; the LE section of the SCL captures and accelerates the beam at 700 MHz, whereas the last two sections can either operate also at 700 MHz or at 1,400 MHz. In the first case we rely on available industrial RF power sources, in the latter case the RF power sources, at twice the frequency, need to be demonstrated and developed, but could allow a shorter length of the accelerator and be more economical. In any case, the study has shown that the accelerator is feasible, can be built in a relatively short period of few years, and has an estimated total cost for the superconducting sections of about 100 M\$.

REQUIREMENTS OF THE PROTON DRIVER

The accelerator driver of the ACSN facility is schematically shown in Figure 1. The proton beam aims directly to the core, and can be placed either underneath or above the target, with Figure 1 showing the former case. The actual location of the accelerator with respect to the target and the interface with final transport, bend and the target itself remain to be investigated.

Acceleration of positive-ions (protons) is assumed, since there is no requirement for the injection in a subsequent circular storage device as in the SNS project. For the same reason, the beam in exit of the RFQ does not need to be pre-chopped.

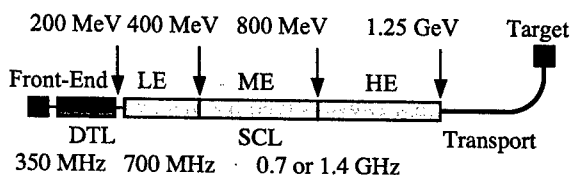


Figure 1. Layout of the 1.25-GeV, 10-MW SCL

The Front-End is made of an Ion Source placed on a platform at 35-50 kV. It has a continuous beam output of 10 mA. It is followed by a 350-MHz RFQ which focus, bunch and accelerate the beam to about 2 MeV. At the exit, the beam bunches are compressed sufficiently to be squeezed within the rf buckets of the Drift-Tube Linac (DTL) which operates also at 350 MHz. Because of the relatively low beam current, and the absence of stringent requirements on the beam emittance and momentum spread, space-charge effects are not expected to play a relevant role. As a consequence, no major beam losses are expected in the RFQ. A transmission of 80% is conservatively assumed, and the beam intensity at the exit

of the RFQ is 8 mA. We assume that there are no further losses during the transfer of the beam through the rest of the accelerator, all the way down to the Target. At the exit of the SCL, and on the Target, the beam intensity is then 8 mA.

Table 1. Comparison of three SCL Projects

	SNS	AGS	ACNS
Kinetic Energy, GeV	1.0	1.2	1.25
Ave. Power, MW	1.0	0.045	10
Duty Factor, %	6.0	0.18	100
Repetition Rate, Hz	60	2.5	--
Pulse Length, ms	1.0	0.72	--
Peak Power, MW	16.7	25	10
Ion Source Current, mA	35	35	10
Ave. Beam Current, mA	1.0	0.035	8
Peak Beam Current, mA	26	21	8
Protons / Bunch, $\times 10^8$	4.3	8.7	1.43
RF, GHz	0.805	0.805-1.61	0.7 - 1.4
Coupler RF Power, MW	170-350	260 - 400	80 - 155
Length, m	158	120	163
Inj. Energy, MeV	185.6	200	200
Cryo. Power (2.1°K), kW	0.5	0.15	5.3
Ave. AC Power, MW	3.1	0.28	23
Ave. Gradient, MV/m	3.1 - 6.5	5.3-10.0	3.3 - 8.7
Efficiency, %	26 - 30	9 - 16	35 - 40
Capital Cost, M\$	110	97	85
Operation Cost, M\$ / yr	2.0	0.18	15.2

Blue - Positive Features

Red - Negative Features

LINAC DESIGN

In a proton linac there is a large variation of beam velocity, in our case from $\beta = 0.08$ at 2 MeV to $\beta = 0.90$ at 1.25 GeV. The first accelerating section cannot be made of half-wavelength super-conducting RF cavities, though quarter-wavelength super-conducting linear accelerators do exist and are successfully operational. We prefer to assume here a room-temperature conventional Drift-Tube Linac (DTL) operating in a continuous mode. We shall also assume an energy of 200 MeV for this section to ease the design and manufacturing of the RF cavities in the early part of the SCL proper. Also, the RFQ, if desired, can be made super-conducting to ease the concern with the thermal load. Other solutions are of course possible, and they should be examined with a more careful and detailed design.

Thus, the SCL proper starts at 200 MeV and ends at 1.25 GeV. The corresponding variation of velocity is from $\beta = 0.5662$ to $\beta = 0.9034$. Since the length of the rf cavity cells is $L = \beta\lambda/2$, it should in principle vary between 12.2 and 19.4 cm, with $\lambda = 42.83$ cm, the RF wavelength at 700 MHz, the chosen operating RF frequency of the SCL. To optimize the accelerating gradient it would be desirable to manufacture cavities with cells varying in length as the beam accelerates. This may not be economical, and we prefer to manufacture RF cavities all with the same cell length. This simplifies the design, and reduces the cost, at the expense of a modest reduction of

the transit time factor. Here we assume that the SCL is divided in three sections each operating at three intermediate values of velocity. The super-conducting LE section, from 200 to 400 MeV, has the cavity cell length adjusted to the intermediate value $\beta = 0.616$, the ME section, from 400 to 800 MeV, to $\beta = 0.755$, and the HE section, from 800 MeV to 1.25 GeV, is designed with the intermediate value $\beta = 0.852$.

The layout of the Super-Conducting Linac is described in [4]. For more details see also the contribution to this Conference [3], where a SCL in pulsed mode is described. It is made of a sequence of identical periods each consisting of a Warm-Insertion for the location of focussing quadrupoles, steering magnets, vacuum pumps, and instrumentation, and of a Cryo-Module including a number of cavities all with the same number of individual cells. Each cavity is powered by a single RF coupler connected directly to one Klystron, the RF power source.

The parameters of the SCL are given in Tables 2 to 4. Table 3 shows the RF for the ME and HE sections to be 1.4 GHz, this gives a compact super-conducting structure with a total length of 160 m that may cost about 100 M\$ to be build. When the RF of 700 MHz is chosen also for the last two sections, we found that the length and the expected cost have increased by about 20%.

Table 2. SCL Parameters for 10-MW ACNS

Increm. Linac Ave. Power	8.4 MW
Type of Particles	Protons (H^+)
Kinetic Energy in entrance	200 MeV
Kinetic Energy in exit	1.25 GeV
β	0.9034
Momentum, GeV/c	1.9769
Magnetic Rigidity, T-m	6.594
Repetition Rate	CW
Linac Duty Cycle, %	100
Ion Source Current	10 mA
RFQ Transmission, %	80
Chopping Ratio, %	100
Linac Average Current, mA	8.0

CONCLUSION

When compared to a pulsed mode of operation, a CW SCL requires considerably much more cryogenic power and, despite a higher efficiency, more electrical AC power. In our case the AC power requirement needed just for the operation of the SCL exceeds 20 MW that cannot be easily acquired on the BNL site. An energy recovery is thus desirable, as it can be obtained for example from the spallation target itself when this is operated in a hybrid configuration [5]. But on the other end, the performance of the accelerator in CW mode is expected to be more stable than that in pulsed mode when the peak performance values are even larger and pose a significant operational concern. Moreover, a non small feature is the lower intensity per bunch, as seen in Table 1, that

removes some of the concern with beam halo formation and consequent latent, uncontrolled beam loss.

It should be reminded that the first proposal for a high-power proton SCL in the GeV energy range was the Accelerator-based Production of Tritium (APT) [6]. This also was to be operated in the CW mode, and the beam power required had an ambitious figure of hundreds of MW. Yet the design of the project was found to be entirely feasible, and removed several concerns for the application of superconductivity to a proton linear accelerator. We have all learned considerably from this earlier project of which the same design criteria still apply.

- [2] SNS Design Report, 1.0-GeV SCL
- [3] A.G. Ruggiero et al., contribution to this Conference, Portland, Oregon. May 2003.
- [4] A. G. Ruggiero, "Design Considerations on a Proton Superconducting Linac". BNL-Internal Report 62312. August 1995.
- [5] A.G. Ruggiero, "A Superconducting Linac as the Driver of the Energy Amplifier". Informal Report, BNL 63527, UC-414 AGS/AD/97-1. October 1996.
- [6] A Feasibility Study of the APT Superconducting Linac. Edited by K.C.D. Chan. April 1996. Los Alamos National Laboratory, LA-UR-95-4045.

Table 3. General Parameters of the SCL

Linac Section	LE	ME	HE
<i>Ave. increm. Power, MW</i>	1.60	3.20	3.60
Average Beam Current, mA	8.0	8.0	8.0
Initial Kinetic Energy, MeV	200	400	800
Final Kinetic Energy, MeV	400	800	1250
Frequency, MHz	700	1400	1400
Protons / Bunch $\times 10^8$	1.43	1.43	1.43
Temperature, °K	2.1	2.1	2.1
Cells / Cavity	8	8	8
Cavities / Cryo-Module	4	4	4
Cavity Separation, cm	60.0	30.0	30.0
Cold-Warm Transition, cm	70	30	30
Cavity Internal Diameter, cm	12	6	6
Length of Warm Insertion, m	1.30	1.30	1.30
Acceler. Gradient, MeV/m	8.21	22.3	22.7
<i>Average Gradient, MeV/m</i>	3.28	8.08	8.63
Cavities / Klystron	1	1	1
RF Couplers / Cavity	1	1	1
Rf Phase Angle	30°	30°	30°
Transverse Focussing	FODO	FODO	FODO
Phase Advance / FODO cell	90°	90°	90°
Norm. rms Emitt., π mm-mrad	0.3	0.3	0.3
Rms Bunch Area, π °MeV	0.5	0.5	0.5

REFERENCES

- [1] S. Shapiro et al., "Accelerator Based Continuous Neutron Source (ACNS)". BNL-Formal Report 71184. April 2003.

Table 4. Summary of the SCL Design

Linac Section	LE	ME	HE
Velocity, β : In	0.5662	0.7131	0.8418
Out	0.7131	0.8418	0.9034
Cell Reference β_0	0.616	0.755	0.852
Cell Length, cm	13.19	8.08	9.12
Total No. of Periods	7	8	8
Length of a period, m	8.721	6.187	6.519
FODO-Cell ampl. func., β_0 , m	29.78	21.12	22.26
Total Length, m	<i>61.05</i>	<i>49.49</i>	<i>52.15</i>
Coupler rf Power, kW (*)	81	135	155
Energy Gain/Period, MeV	30.00	50.00	57.50
Total No. of Klystrons	28	32	32
Klystron Power, kW (*)	81	135	155
$Z_0 T_0^2$, ohm/m	379.5	570.0	725.9
$Q_0 \times 10^{10}$	1.07	0.68	0.77
Transit Time Factor, T_0	0.785	0.785	0.785
Ave. Axial Field, E_a , MV/m	10.4	28.4	29.0
Filling Time, ms	0.778	0.802	0.714
Ave. Dissipated Power, kW	0.385	2.369	2.149
Ave. HOM-Power, W	17.2	39.3	39.3
Ave. Cryogenic Power, kW	0.506	2.486	2.272
Ave. Beam Power, MW	1.60	3.20	3.60
Total Ave. rf Power, MW (*)	2.16	4.32	4.86
Ave. AC Power for rf, MW (*)	3.69	7.39	8.31
Ave. AC Power for Cryo., MW	0.359	1.763	1.612
Total Ave. AC Power, MW (*)	4.052	9.152	9.923
Efficiency, % (*)	39.49	34.96	36.28

(*) Including 35% rf power contingency.

RESULTS OF THE IPHI DRIFT TUBE LINAC'S HOT MODEL CW TESTS

P.-E. Bernaudin*, G. Congretel, DSM/DAPNIA/SACM, CEA Saclay, France

A. Fontenille, E. Froidefond, M. Fruneau, D. Marchand, M. Planet, J.-C. Ravel, IN2P3/LPSC, CNRS, Grenoble, France

P. Balleyguier, DIF/DPTA, CEA DIF, France

Abstract

In the course of the IPHI project (high intensity, cw proton injector), a Drift Tube Linac hot model has been built and tested. The main difficulty associated with these machines is the high RF thermal losses inducing significant heating and deformations if not kept under strict control. Therefore the hot model has been tested under nominal RF conditions (40 kW cw for an accelerating field of 1.75 MV/m) to verify the suitability of the technical choices made: materials, mechanical designs, construction techniques, vacuum... This prototype includes four accelerating cells, three full drift tubes, two of which enclose a quadrupole electromagnet. Results show that a stainless steel envelope can be used even at these high power densities, provided that it is copper plated both inside and outside to enhance its thermal conductivity and lower the temperature gradients. This solution leads to a cheap and reliable machine. The new kind of drift tube / magnet assembly tested in this DTL model ("flooded drift tube"), where the whole drift tube is filled with water cooling simultaneously the magnet leads and the drift tube walls, is also a suitable solution, cheap and more efficient than the usual ones. With the successful tests of this hot model, one more step has been made towards a cw Drift Tube Linac for high intensity light ions accelerators.

INTRODUCTION

The IPHI project [1] included in its original version, after the RFQ accelerating section, a 1 MW DTL (Drift Tube Linac) intended to accelerate the 100 mA protons beam from 5 to about 11 MeV. To pave the way for this machine, a 4 cells full scale model has been designed, built and tested under full RF power conditions (but without beam).

DESIGN OF THE DTL HOT MODEL [2]

The DTL hot model is made of four symmetrical and identical cells, similar to the full DTL's first one. It therefore includes three full drift tubes plus two half ones fitted on the end caps of the model. Two of the drift tubes enclose an electromagnet designed to provide the maximum strength required by the DTL (4.70 T). The accelerating field is 1.75 MV/m, corresponding to 40 kW of RF power.

Drift tubes and magnets' design

Two different drift tube / quadrupole assemblies have

been designed and built.

The first, most conservative one was designed by AES. It includes a standard, hollow conductor, iron-cobalt electromagnet. Cooling of the drift tube is on the outer radius of the drift tube only. The major weakness of this design is the complexity of its structure, including a difficult transparent welding, which makes it costly. On the other hand, it is a well established design.

The second, more innovative drift tube / magnet design is called "flooded" because the whole drift tube is filled with the cooling water [3]. The magnet's leads are cooled externally by this flow. Its iron pole and yokes are protected from corrosion by electrolytic copper plating. The main advantage of this design is that it is more efficient (cooling is better and the better optimisation of the drift tube's internal space allow to use a bigger magnet) and far more simple to manufacture (and therefore cheaper). On the other hand, corrosion should be considered carefully for long lifetime accelerators.

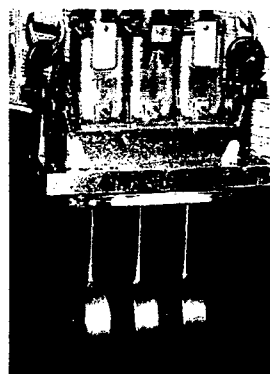


Figure 1: The hot model's girder with all three drift tubes fitted.

Tank's design [4]

The tank is made of a stainless steel envelope, copper plated both inside and outside. The inner plating is obviously for RF conductivity purposes whereas the outer plating allows decreasing significantly thermal gradients and stresses by artificially enhancing the stainless steel conductivity. Nevertheless, all massive, non welded parts like the girder and the end caps are made of copper.

All drift tubes are fitted on a single girder (figure 1) on which they can be aligned outside of the tank. Each drift tube is fitted with a mechanical tuning device allowing precise positioning of the drift tube at any moment. Copper bellows are used as a flexible link between the drift tubes' stems and the girder. Combined RF and

*pebernaudin@cea.fr

thermal simulations have been made to ensure that the troubles encountered with such a project in the past were not to happen again [5].

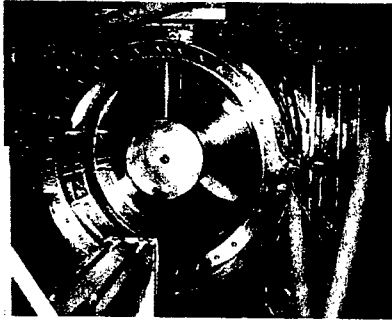


Figure 2: Inside view of the hot model tank with drift tubes fitted.

The full tank was thermally baked during manufacturing process to outgas the hydrogen. Pumping block includes a turbo molecular, titanium sublimation and ionic pumps. Helicoflex seals are used for mechanical reference faces; otherwise standard conflat copper seals are used.

RF power is coupled through an iris whose length is optimised. Two small shutters allow tuning of the coupling factor.

RF seals (silver plated copper-beryllium springs) are used on the end caps and on the girder flanges. RF computations indicated that these are not necessary for the stem-girder link.

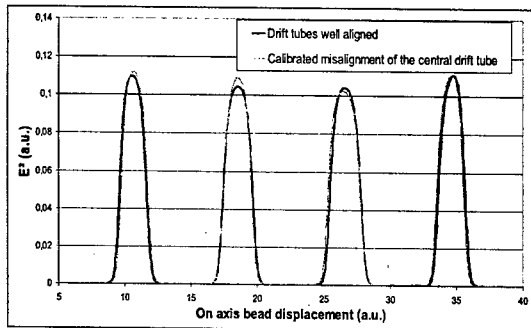


Figure 3: Low power measurement of the accelerating field using the bead perturbation technique. Blue curve: all drift tubes well aligned. Rose curve: central drift tube displaced.

HOT MODEL TESTS

RF measurements

Low power measurements performed indicated that the Q factor was only 2/3 of the *SUPERFISH* value. It was even lower without using the RF seals, which is a strong indication of their efficiency. The relatively low Q value can be explained by the very strong end effects (the model is very short) and by the size of the various ports (vacuum, RF coupling) with respect to the model size.

The absence of RF seals around the stems is certainly another factor of explanation, as underlined by the bellows heating phenomenon (see below).

Accelerating field aspect has been checked using the bead perturbation technique. The influence of a drift tube misalignment has been verified (figure 3).

At high power, the accelerating field has been measured using the bremsstrahlung spectra of the electrons in the cavity (figure 4). By measuring the maximum energy (100-150 keV) of the spectrum one can get the accelerating field value. Results show that the accelerating field is lower than expected, with a very good agreement with the Q factor measurements (better than 3%).

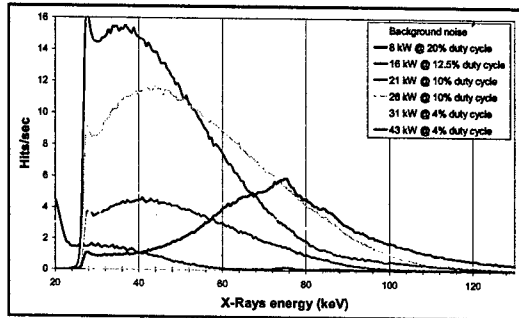


Figure 4: Measurement of the accelerating field using X-ray spectrometry method for different power levels.

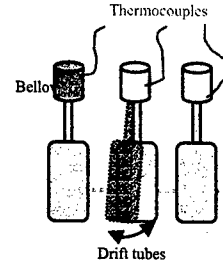
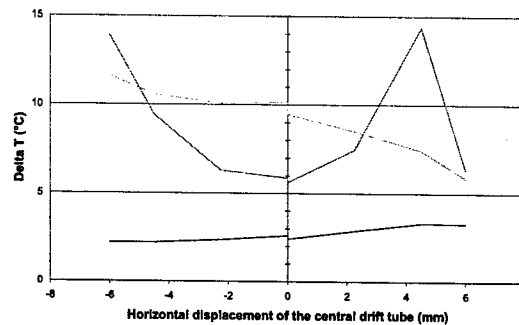


Figure 5: Measurement of the drift tube's misalignment influence on the bellows heating. Top: principle of the test; the central drift tube is shifted left or right and the temperature is measured on all three bellows (at different altitudes). Bottom: heating on all three bellows. The central bellow (rose curve) is the hotter, and the influence on adjacent bellow is sensible but smaller. Tests are performed at 25% of the nominal power.



Thermo mechanical aspects

Several thermocouples have been placed in points where heating should have been the strongest according to computations, and in several other representative or sensible points (by example inside the empty drift tube). The temperature on the stem has also been checked using a pyrometer.

All heating are adequate with expectations but for two points: RF coupling iris and the copper bellows linking the stem to the girder.

The heating of the RF coupling slot is caused by the fact that the iris is not copper plated outside.

The heating of the copper bellows is ten times higher than expected (some 30 to 50°C to be compared with 4 or 5°C). The lower part of the bellow is the hotter one, indicating than the power deposit is strongly non linear along its length. It has been verified that a dissymmetry of the cells have a strong influence on the temperature of the bellows, as shown by the *MAFIA* computations (figure 5). Nevertheless, even in this case power deposits remain strongly higher than expected for still unknown reasons. Anyway, the copper bellows system is adequate. This phenomenon plays undoubtedly a significant part in the Q factor decrease. The use of RF seals to shelter the bellows would probably help to raise somewhat the Q factor and to decrease heating as well.

The displacement of the drift tube's axis has been measured. A thin slot has been placed in the drift tube aperture and a laser has been diffracted by this slot. The light intensity of the diffraction figure's central fringe varies linearly with the displacement of the slot. The precision of this measurement is around 5 microns. The measured values are of some 180 microns, which is in good agreement with computations. The major contribution (around 150 microns) of this displacement is caused by the tank's dilatation and can be compensated by supporting the tank at the girder's level.

A mechanical problem related with the flooded drift tube has been discovered. If the water pressure is too high, the drift tube's thin wall is deformed and leads to a frequency shift of several dozens kilohertz (depending on the pressure). If the water pressure is unstable (which happened during the first part of the tests) the RF system becomes unstable (as the resonance frequency itself changes with pressure). This problem can easily be solved by strengthening the drift tube's structure; several solutions are considered.

Other tests

Several other tests have been performed on this prototype. Before the high power tests, the efficiency of the flooded drift tube's cooling system has been verified. The magnets gradient has also been measured. In both cases results were as good as expected.

Vacuum was constantly checked during operations. Conditioning proved fast, indicating that surfaces were reasonably clean: very few sparks were observed. Multipactoring happened only at very low power (below

2 kW). Outgasing proved higher than expected at first, but decreased quickly. Nevertheless, baking of the cavity after the copper plating process would certainly be useful. The replacement of all Helicoflex seals by Viton ones led to an increase of the pressure by a factor of 2.

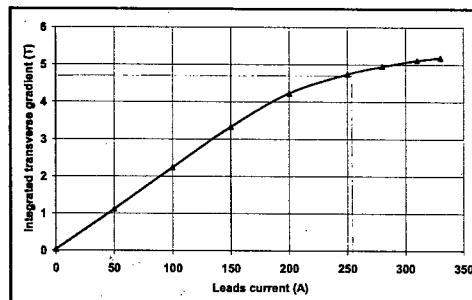


Figure 6: Integrated gradient measurement of the flooded quadrupole magnet for various currents. Effect of saturation is clearly shown.

CONCLUSION

The feasibility of a cw, 352 MHz DTL is well established, using reliable and relatively cheap technologies. Several design improvements have been identified: the mechanical structure of the flooded drift tube should be strengthened, the tank should be supported at the girder level, but these remain minor changes. The next step should take into account all problems related with a long structure, like the number of girders to be used or the length of the tank sections.

ACKNOWLEDGMENTS

The authors would like to thank the CERN PS and SPS people who provided all the needed help to perform these tests successfully, especially MM. Vretenar, Hajdas, Montesinos, Marques and Mrs. Bunaciu.

REFERENCES

- [1] P.-Y. Beauvais, "Status report on the construction of the French high intensity proton injector (IPHI)", EPAC 2002.
- [2] P.-E. Bernaudin, "Etude et optimisation d'un linac à tubes de glissement pour accélération de forts courants de protons en continu" (2002), CEA thesis ref. DAPNIA-02-05-T.
- [3] P.-E. Bernaudin & al., "Technical innovations for a High-Gradient Quadrupole Electromagnet Intended for High Power Proton Drift Tube Linacs", IEEE Trans. App. Sup., Vol.12, No.1, March 2002.
- [4] M. Painchault & P.-E. Bernaudin, "Conception thermo-mécanique d'un tank de DTL", CEA report DAPNIA/SEA/01-33.
- [5] B.G. Chidley, "Conditioning experiments on the 100% duty factor 3 MeV Alvarez linac", Linac 1979.

BEAM DYNAMICS STUDIES IN SPIRAL 2 LINAC

R. Duperrier, D. Uriot, CEA Saclay, 91191 Gif sur Yvette; N. Pichoff, CEA Bruyères le Châtel, BP 12, 91680 Bruyères le Châtel; P. Bertrand, B. Bru, A. Savalle, F. Varenne, GANIL, BP 55027, 14076 Caen; J.-M. De Conto, E. Froidefond, LPSC, 38026 Grenoble; J.L. Biarotte, IPN, 91406 Orsay, France.

Abstract

The proposed LINAG driver for the SPIRAL 2 project aims to accelerate a 5-mA D^+ beam up to 20 A.MeV and a 1-mA beam for $q/A=1/3$ up to 14.5 A.MeV. It is a continuous wave regime (cw), designed for maximum efficiency in the transmission of intense beams. It consists of an injector (two ECR sources + a Radio Frequency Quadrupole) followed by a superconducting section based on an array of independently phased cavities. This paper presents beams dynamics studies associated to the LINAG driver. End-to-end simulations (low-energy beam lines, RFQ, medium-energy beam line, SC linac) are shown.

INTRODUCTION

The possibility of a high-intensity accelerator at GANIL, producing secondary beams of unprecedented intensity, is considered. A project named SPIRAL 2 [1] is being under way presently in order to add medium-mass nuclei to those available with SPIRAL. In this project, fission induced by deuterons is proposed for the production of the radioactive ions, with the aim of at least 10^{13} fissions per second at least, with and without a converter. With the same linac, the SPIRAL 2 project aims to accelerate ions with $q/A=1/3$.

The linac consists of a double injector (two ECRs sources + a Radio Frequency Quadrupole) and a superconducting linac with independent resonators (QWRs and/or HWRs). The accelerating optimisation has to be performed for ions with $q/A=1/3$ (optimum β for the superconducting part). The input energy is 20 A.keV. This allows an extraction voltage of 60 kV (no platform). The output energy is set to 14.5 A.MeV for the 1-mA ions beam and to 20 A.MeV for the 5-mA deuterons beam. The input normalised rms emittances are 0.2 and $0.4 \pi \cdot \text{mm} \cdot \text{mrad}$ for deuterons and $q/A=1/3$ ion respectively. It is assumed that this choice would give comfortable margins for such beam currents.

THE LEBT LINES

The LEBT for the D^+ beam is mainly based on the use of 2 conventional solenoids and a quadrupole triplet, to transport and match the beam at the RFQ entrance. For this design, we need to take into account the installation of a LEBT that transports $q/A=1/3$ ions to the same RFQ. Figure 1 shows the beam line architecture.

A possible transfer line has been studied considering a D^+ beam for the over-estimated normalised RMS emittance of $0.2 \pi \cdot \text{mm} \cdot \text{mrad}$. Figure 2 shows a possible

tuning for this line. A scheme for the heavier ion transport has also been studied and figure 3 presents the structure of the line and ion envelopes.

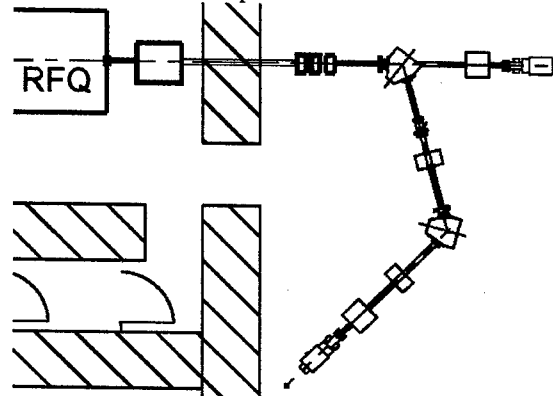


Figure 1: LEBT architecture.

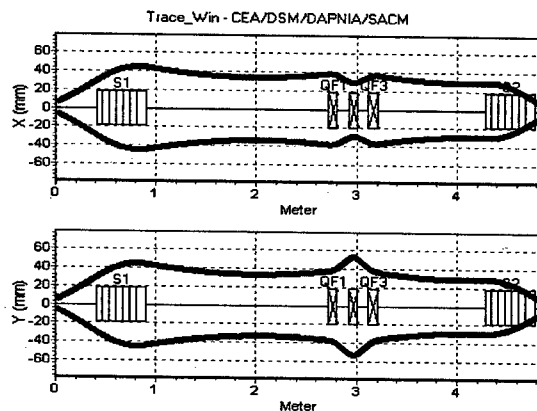


Figure 2: Deuteron envelopes in the LEBT.

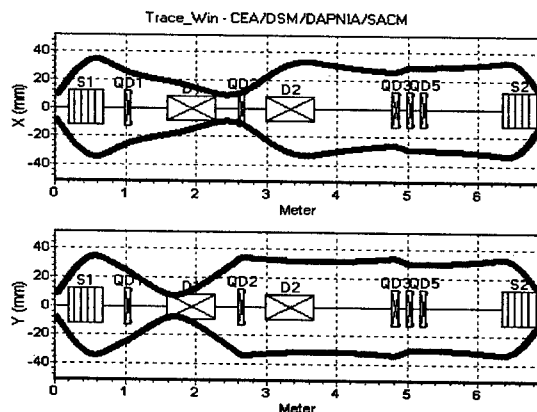


Figure 3: Ion envelopes in the LEBT.

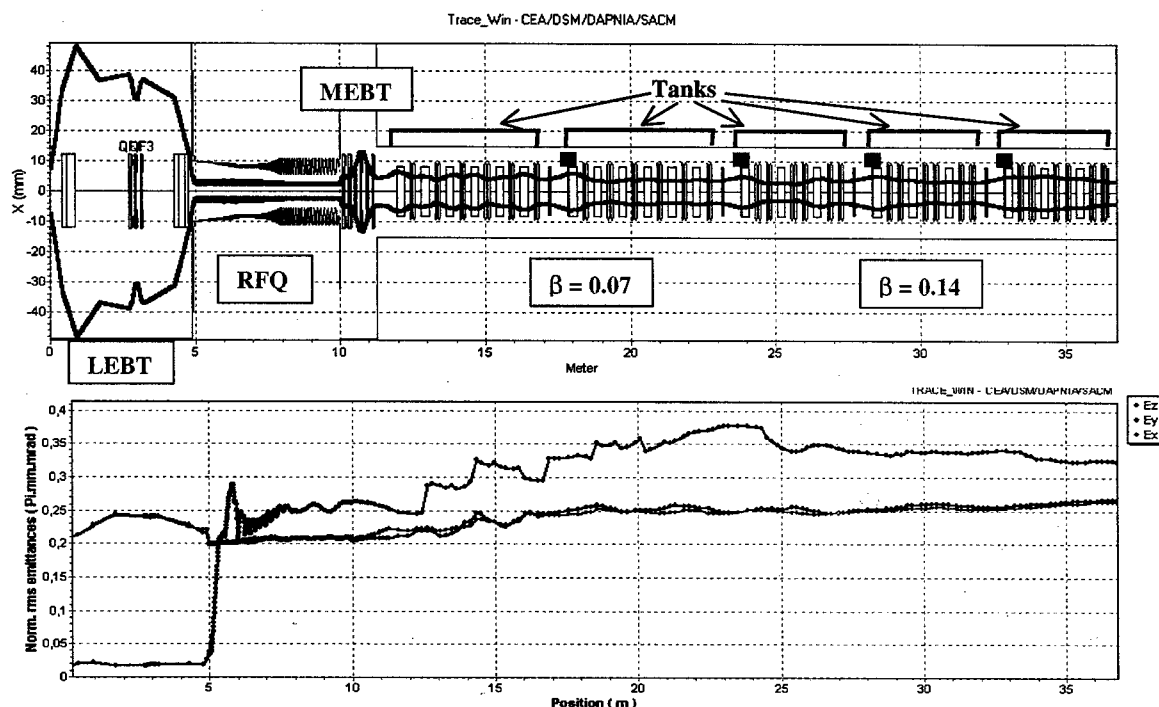


Figure 4 : Deuteron beam envelope and emittances behavior in the SPIRAL 2 linac

THE RFQ

The RFQ must operate in cw mode. Its frequency has been chosen to be 88 MHz, a sub-harmonic of 352 MHz. This rather low value has been determined for the following reasons: the RF power density is quite low at this frequency and allows a solution based on a formed-metal technology, leading to a cheap mechanical solution; at low frequencies, the inter-electrode distance is larger and permits a higher margin for the mechanical tolerances; power sources are readily available. The RFQ output energy, 0.75 A.MeV, has been determined by the fact that the first cavities of the SC linac must permit a possible evolution of the machine to ions with $q/A = 1/6$, which means that their β -values have to remain quite low (~ 0.07). The main RFQ parameters are described in the following table. The maximum peak field value is kept at a conservative level of 1.65 Kilpatrick [2], lower than LEDA [3] which also works in cw mode. The transverse curvature of the pole, ρ , has been maintained constant to simplify the machining (with a 2D tool).

Table 1: Main RFQ parameters

Parameters	Values
Length	5.077 m
Minimum aperture (a)	1 cm \rightarrow 0.55 cm
Mean aperture (R_0)	1 cm \rightarrow 0.82 cm
Pole curvature (ρ)	0.75 cm
Modulation (m)	1 - 2
Voltage	100 \rightarrow 113 kV
Peak field	1.65 Kp; 17.88 MV/m
Synchronous phase	- 90 deg \rightarrow - 30 deg

Beam dynamics calculations have been performed with the code TOUTATIS [4]. The transmissions are better than 99.9% for the ion beam and the deuteron beam. No transverse emittance growth is observed in the simulation. The longitudinal rms emittances are equal to 0.05 and 0.13 deg.MeV for the deuterons and the ions, respectively.

Monte Carlo simulations have been performed assuming mechanical tolerance of ± 0.1 mm on machining of the electrodes and ± 0.2 mm on misalignment. The results confirm that the deuteron beam transmission remains very close to 100% (only 5.10^{-5} loss rate). This gives quite a comfortable safety margin: losses of up to 3% have been considered for radioprotection purposes.

THE SC LINAC

The superconducting linac is linked to the RFQ by a Medium Energy Beam Transport line (MEBT). Figure 4 shows the deuteron beam envelope and emittance behavior in the SPIRAL 2 linac. The MEBT includes the possibility to inject heavy ions coming from another RFQ. It contains two quadrupole triplets and two buncher cavities at 88 MHz. The linac must have the ability to accelerate with a maximum energy gain and must also be capable of being extended to accelerate heavy ions in future. It is based on independently phased superconducting resonators (QWR and/or HWR). Two families of β are used with a frequency of 88 MHz for the first one to ensure an efficient transition to the 88 MHz RFQ. The frequency of the second family is equal to 176 MHz to get a smooth transition to a possible future 352 MHz linac [5].

The linac design is optimised with a routine that iterates through on possible geometrical β and transition β for the two families. The criterion to define the optimum β is the shortest linac with a minimum number of resonators. This process is performed with an (01) period for the first family and an (011) period for the second family where 0 is a solenoid and 1 a cavity. This lattice ensures a good efficiency of the cavities for this range of β . The resultant β are 0.07 and 0.14 and the transition β is equal to 0.08 for an accelerating field, E_{acc} , equal to 8 MV/m. The first family requires 12 cavities (2 tanks) and the second one 18 cavities (3 tanks). A fallback solution has also been studied if it would turn out that this E_{acc} is too optimistic. An additional tank at the end of the linac would allow to decrease E_{acc} to 6.5 MV/m. The number of resonators then becomes 24 for the second family.

The beams dynamics have been performed with the codes TraceWin, PARTRAN [6] and LIONS_LINAC [7]. Emittance behaviour in the linac is shown in figure 4. All these codes are capable to use 3D field maps [8]. However, it is important to notice that the steering effect, induced by QWRs, is not included in the simulation shown by the figure 4. This problem is studied at present time using maps computed by SOPRANO [9]. The first studies show that vertical displacements are sufficient to reduce the emittance growth induced by the dependent phase deflection for the first family. For the second family, HWR may be used as a fallback solution if steering of 176 MHz QWR is too serious.

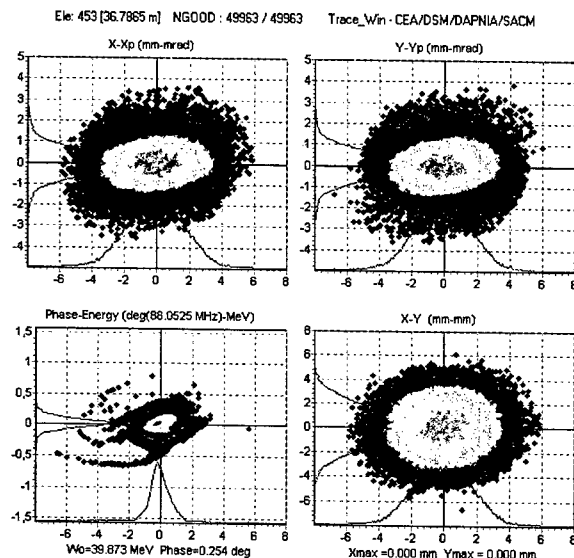


Figure 5: Deuterons beam in phase space at linac end.

The transmission of the superconducting part is 100%. For simulation of figure 4, the longitudinal emittance growth is around 30%. For the transverse plane, the emittance growth is 25%. Figure 5 shows the phase space portrait of the deuteron beam at the exit of the linac. It is clear that the longitudinal plane is the critical point at this stage of the study.

CONCLUSION

In the present paper, we have studied in detail technical aspects of the SPIRAL 2 linac. We have shown that a possible architecture can be found to reach the SPIRAL 2 goal. Meanwhile, several supplementary studies are required: use of 3D maps, correction of the steering effect induced by QWRs, correction scheme for the linac errors (BPMs and steerers), and definitions of the tolerances for construction.

REFERENCES

- [1] A. Mosnier for the SPIRAL2 project team, "SPIRAL 2: A high intensity deuteron and ion linear accelerator for exotic beam production", this conference.
- [2] T.P. Wangler, "RF linear accelerator", Wiley publishers.
- [3] H. V. Smith and D. Schneider, "Status update on the Low Energy Demonstration Accelerator (LEDA)", LINAC 98 conference, Chicago, p. 418.
- [4] R. Duperrier, "TOUTATIS: a RFQ code", Physical Review Special Topics Accelerators and Beams, December 2000.
- [5] LINAG Phase I, a technical report, version 1.3, GANIL, june 27, 2002.
- [6] N. Pichoff and D. Uriot, "CEA Saclay codes review for high intensity linac", ICCS conference, Amsterdam, 2002.
- [7] P. Bertrand, "LIONS_LINAC: a new particle-in-cell code for linac", this conference.
- [8] D. Uriot and N. Pichoff, "New implement in TraceWin/PARTRAN codes: integration in external fields map", this conference.
- [9] www.vectorfields.com

INSTABILITIES STUDY AND IMPLICATIONS FOR THE RIA PROJECT

R. Duperrier, CEA Saclay, 91191 Gif sur Yvette cedex, France,
D. Gorelov NSCL-MSU, East Lansing, MI 48824, USA

Abstract

The Rare Isotope Accelerator (RIA) [1] requires a high power linac capable of accelerating all ions up to uranium to energies of 400 MeV/u with a beam power of 100 to 400 kW in a CW regime. One of the most challenging features of the proposed RIA driver linac is the simultaneous acceleration of different charge states in order to increase the final beam power. The acceleration in the last part of the accelerator is provided by elliptical cavities. Three geometrical β are used: 0.47, 0.61 and 0.81. To minimize the cost, one option is to reduce the number of cryostats. This implies a maximal number of cavities per cryostat. Assuming a lattice composed by one doublet and one cryostat, this option leads to an increase of the longitudinal phase advance if each cavity is used at the maximum field. The transverse phase advance, has to be set correctly in order to ensure stable motion. This report aims to evaluate the sensitivity to instabilities induced by the transverse to longitudinal coupling in the elliptical cavities of the RIA linac for an 88^+ uranium beam.

THEORY

This section is a brief summary of the theory developed by I.M. Kapchinsky in Reference [2]. The transverse electric and magnetic field components produce a defocusing effect. The defocusing is a function of the phase of each particle and induces a coupling term in the equations of motion. The equations of motion for the transverse plane may be reduced to

$$\frac{d^2 x}{dt^2} = -\frac{ev}{m_0 \gamma} G(t) - \frac{e}{2m_0 \gamma} \left\{ \left(\frac{\partial E_z}{\partial z} \right) (t) + \frac{v}{c^2} \left(\frac{\partial E_z}{\partial t} \right) (t) \right\} x \quad (1),$$

where $G(t)$ is a periodic function which represents the focusing, γ is the Lorentz factor, v the speed, m_0 the mass, and the terms in the braces represent periodic functions for the defocusing induced by the accelerating gaps. After simplification, this equation may be reduced to the canonical form of the Mathieu equation:

$$\frac{d^2 x}{d\tau^2} + \pi^2 [a^2 + 2q \sin(2\pi\tau)] x = 0 \quad (2),$$

with $a = 4\sigma_{0T}^2 / \sigma_{0L}^2$, $q = \Phi |\cot(\phi_s)|$, τ is a new dimensionless variable, Φ is the phase amplitude of the particle, and ϕ_s is the synchronous phase. The parameters σ_{0T} and σ_{0L} are the transverse and longitudinal phase advance per period at zero current, respectively. It can be

shown that the unstable part of the general solution of equation 2 has the form

$$x(\tau) \propto [C e^{k\tau} \cos(\phi(\tau)) + D e^{-k\tau} \sin(\phi(\tau))] \quad (3),$$

where $\phi(\tau)$ is the betatron phase. The parameter k can be calculated using the diagram of Figure 1 where $k = \mu\pi$.

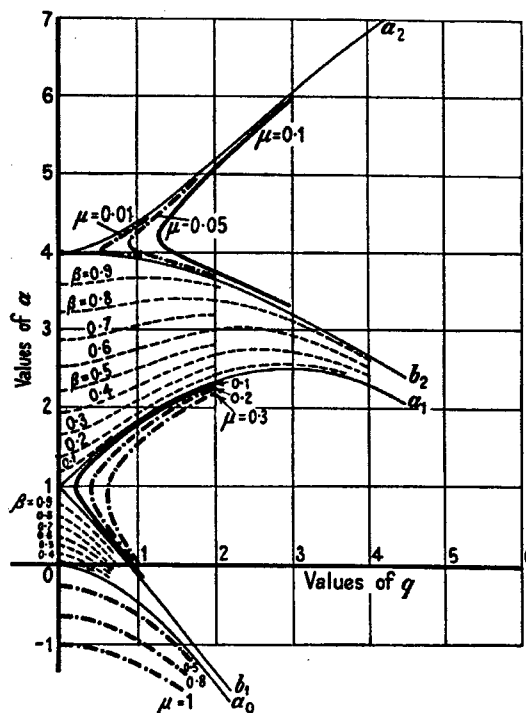


Figure 1: Stability diagram of the Mathieu equation from N.W. McLachlan, Theory and applications of Mathieu functions, Dover Publisher, 1964.

A FEW EXAMPLES

To illustrate this theory in the RIA case, let us test several configurations of the low β section of the elliptical cavities part of the linac. As was pointed out in [3], only this part is relevant, because as the velocity increases, the longitudinal phase advance decreases and pushes the beam to a stable area in the Mathieu diagram (a increases). The recommendation of this previous work [3] was that no more than three cavities per period should be included due to parametric resonance.

To explore a different part of the diagram and test our code PARTRAN [4], we use a test design with a geometrical $\beta = 0.47$, 14 periods (typical for this part of the linac), a constant synchronous phase of -30° , a constant longitudinal phase advance equal to 90° per

period, a phase amplitude Φ equal to 15° , and rms normalized emittances $\varepsilon_T = \varepsilon_L/2 = 0.6 \pi \text{ mm mrad}$. We take ε_L a factor of two larger than ε_T to maximize the effect. A higher amount of energy is then available for the instabilities. The radial dependence of the field in a gap is represented by a Bessel function in PARTRAN, following Reference [5]. With this set of parameters, q is equal to 0.45. Figure 2 shows a classical beam envelope behavior for this linac.

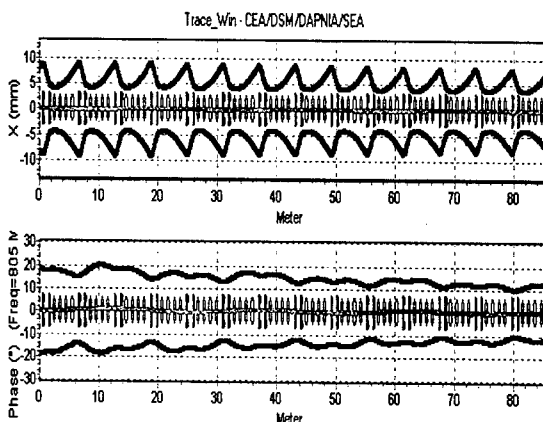


Figure 2: Beam envelope behavior in the test case.

If we set the doublets to get a constant transverse phase advance per period equal to 50° , the parameter a is equal to 1.23. The theory predicts unstable motion. Figure 3 shows the emittance behavior for this case.

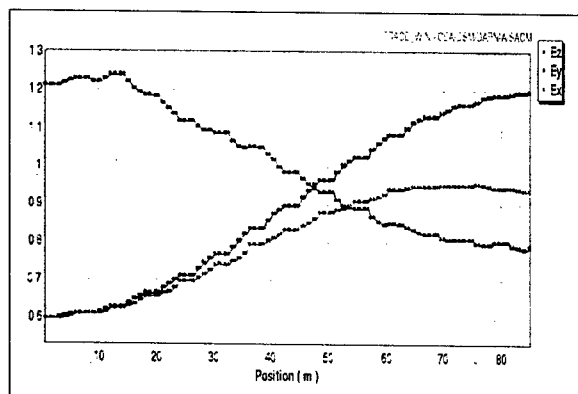


Figure 3: Rms norm. emittances for the 50° case.

This simulation shows an unstable motion that is damped at the end of the section. A transfer of energy occurs between the transverse planes and the longitudinal plane. This transfer is damped when the equipartitioning condition is met [5].

To continue this illustration of the theory with the PARTRAN code, two supplementary cases are tested. For the first one, we set the transverse channel to a constant 80° phase advance. This is equivalent to $a = 3.16$. With q still equal to 0.45, the theory predicts stable motion.

Again, a simulation with PARTRAN shows a very good agreement for this case (see Figure 4).

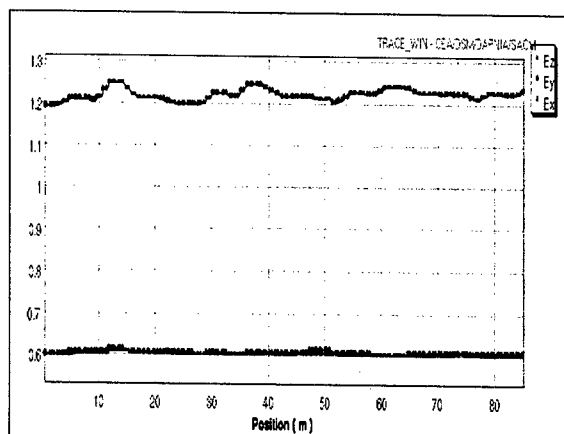


Figure 4: Rms norm. emittances for the 80° case.

For the next case, we set the transverse phase advance to 90° ($a=4$). The results are shown in Figure 5. The motion for this case should be unstable due to a second-order resonance.

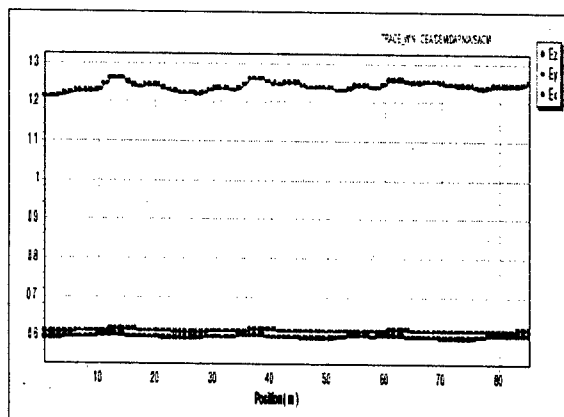


Figure 5: Rms norm. emittances for the 90° case.

Figure 5 shows that there is no significant effect on the halo and the rms emittance. This is still in agreement with the theory. Indeed, the strength of the instability may be reduced to the value of the coefficient k in the exponential (see Equation 3). In Figure 1, it can be seen that, for the same q , k is almost 20 times weaker for a second-order resonance than for a first-order one. This diagram shows that it is possible to increase the strength of the instability if q is increased. Taking into account that Φ must be lower than ϕ_s , the maximum value for q that we can get, decreasing ϕ_s , is 1, according to the q definition above. To display this resonance, a new design with a constant synchronous phase equal to -10° is studied. The number of periods is 20 in order to have enough time for the instability to occur. The phase amplitude Φ is maximum and equal to 10° . The rms normalized emittances are

$\varepsilon_T = \varepsilon_L/2 = 0.3 \pi \text{ mm mrad}$. Parameter a is still equal to 4 and $q = 0.99$. Figure 6 shows the behavior of the emittances for this set of parameters.

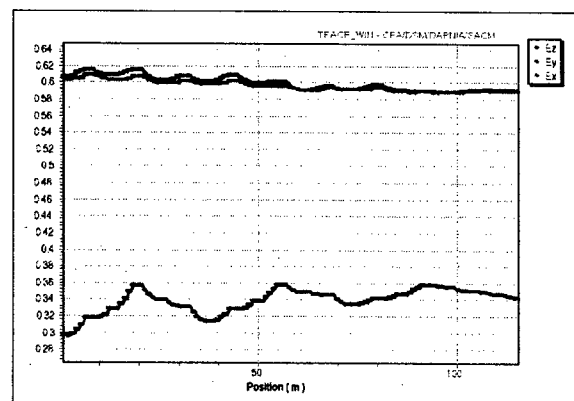


Figure 6: Rms norm. emittances for $a=4$ and $q=0.99$.

A clear exchange occurs. The transverse rms emittances lose 2% compared to their initial values. The effect is weak, but can be simulated with PARTRAN. All these results show that the code is capable of correctly illustrating the theory.

FOCUS ON RIA DESIGN

The problem of parametric resonance is more important at geometrical β equal to 0.47 than at $\beta_g = 0.61$ or 0.81 if we take into account that the longitudinal phase advance decreases with $1/\beta^2$. The $\beta_g = 0.47$ section of the RIA linac uses four cavities per cryostats, a constant synchronous phase of about -30° and 14 periods [6]. Figure 7 shows the behavior of the transverse and longitudinal phase advance for this section.

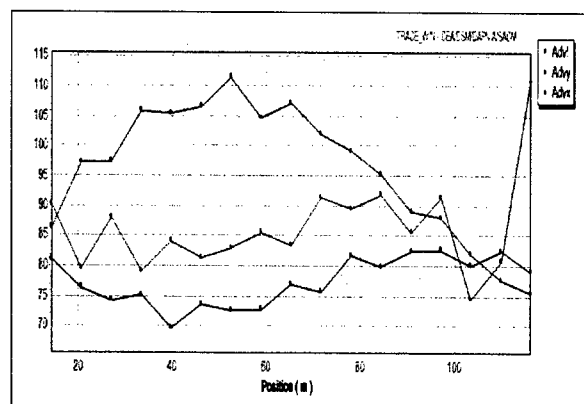


Figure 7: Behavior of phase advances for transverse and longitudinal planes.

Computing the parameters a and q according to the equations described above, it appears that 1-2 periods at the beginning and 3-4 periods at the end of this section are in the second-order resonance part of Figure 1. But the

main part is located in the stable area of this diagram. A simulation of this section of the linac shows no emittance growth [6].

This result is in agreement with the above study. The second order resonance is so weak in this case, that it cannot be observed in the simulation. Although our code is able to simulate a 2% emittance growth, that is in any case negligible for this linac.

CONCLUSION

This study shows that there is no reason to decrease the number of cavities per cryostat from 4 to 3 in order to avoid instabilities due to the defocusing effect in accelerating gaps. Indeed, the number of cavities is not the issue. The phase advance per period is the relevant parameter. With the present accelerating field, the choice of 4 cavities is safe. If it is possible to increase the field due to new technological progress, it is necessary to increase the transverse phase advance via higher gradient in the quadrupoles to keep the motion stable. A new limit will then appear. If the transverse phase advance per lattice is higher than 180° , an unstable motion occurs [5]. One could think that this limitation would be lower if we take into account the coupling induced by the space charge and would become 90° . In Reference [7], it is clearly shown that it is relevant only for high tune depression, which is clearly not the case for the RIA driver linac. These results and the theory of parametric resonances are not in agreement with Reference [3], which shows emittances growth of 20% with 4 cavities. In this study, the author assumes that a second order resonance is responsible for this effect. We find here that it is not possible to get such emittance growth with a second order resonance for this part of the linac.

REFERENCES

- [1] C.W. Leemann, "RIA Facility Project", proc. of LINAC 2000, Monterey, CA, 2000.
- [2] I.M. Kapchinsky, "Theory of resonance linear accelerator", Harwood academic publishers.
- [3] P.N. Ostroumov, "Design Features of high-intensity medium-energy superconducting heavy-ion linac", Linac 2002, Korea.
- [4] N. Pichoff et al., "CEA Saclay Codes review for high intensity linac", ICCS conference, Amsterdam, 2002.
- [5] T.P. Wangler, "RF linear accelerator", Wiley publishers.
- [6] D. Gorelov, T. Grimm, W. Hartung, F. Marti, X. Wu, R.C. York and H.J. Podlech, "Beam Dynamics Studies at NSCL of the RIA Superconducting Driver Linac", Proc. of EPAC'2002, Paris, France, June 2002.
- [7] M. Reiser, "Theory and design of charged particles beams", Wiley publishers.

A SCRF LINAC AS A FEL DRIVER AND STORAGE RING INJECTOR

J. Rose, B. Podobedov, J. Murphy, T. Shaftan, B. Sheehy, X.J. Wang, L.H Yu

BNL, Upton, NY 119733, USA

Abstract

A 5 GeV Super-conducting Radio Frequency (SCRF) linac for the dual application of FEL driver and top-off injector for a storage ring is described. Starting from the FEL drive beam requirements of sub-picosecond bunch lengths and kiloamp peak current the choice of frequency, gradient and operating modes of the linac are presented. Magnetic optics and RF system descriptions follow to provide the specified beam parameters. Accelerator design issues are identified for future studies.

INTRODUCTION

Next generation light sources may include or be based on Free Electron Lasers (FEL) driven by super-conducting radio frequency (SCRF) linacs. The NSLS at BNL undertook a design study of a linac driven FEL in which we looked at the trade-offs in the of choice linac cavity frequency, pulsed vs. CW operation and bunch repetition rates. We then present the conceptual design of a pulsed 1300 MHz SCRF linac that provides ultra-short bunch length and high peak current while preserving the low emittance required by the FEL. In addition, a method of performing top-off injection into a storage ring in the same macro-pulse as the FEL bunch train is described. This method allows the frequency of the linac and ring to be independent over hundreds of kHz bandwidth.

FEL BEAM REQUIREMENTS

As part of the conceptual design of a FEL user facility at NSLS [1] a cascaded High Gain Harmonic Generation (HGHG) FEL was produced, utilizing the so-called "fresh bunch" technique [2]. This technique uses a short ~100 fs electron pulse seeded with a ~20 fs laser pulse overlaid at the front of the electron bunch to produce HGHG FEL laser pulse. A magnetic chicane is used to delay the electron bunch and a harmonic of the HGHG is used to seed a fresh portion of the bunch. This process is repeated several times and can produce very short wavelength FEL light at relatively low electron energies. The electron beam requirements to produce 4.5 Angstrom FEL light are given in Table 1.

Table 1: Electron bunch parameters for 4.5 Angstrom cascaded HGHG FEL.

Electron Energy	4.75 GeV
Electron bunch length	100 fs rms
Energy Spread	0.01% rms

CHOICE OF LINAC FREQUENCY

Design studies incorporating 700 MHz and 1300 MHz cavities were compared. Three cases were considered: TESLA like cavities [3] at 1300 MHz and 20 MV/m, the same cavity shape scaled to 700 MHz at 16 MV/m and the case with 700 MHz and 20 MV/m. The lower gradient was included due to the realization that the larger cavities may not be able to operate at as high a gradient due to the larger surface area and corresponding higher statistical defect probabilities, and susceptibility to microphonics. Identical cavity designs were used in each case to preserve the integrity of the frequency scaling, changes in one case could in most cases be made in the other, increasing iris diameter for instance, with the same effect in both cases. Beam loading can be neglected if either the average current is low or if the time between bunches is long enough to allow the rf generator to replace the energy in the cavity before the subsequent bunch arrives. In this case the power required by the rf system is dominated by the microphonics and is approximated by the product of the stored energy of the cavity and the maximum frequency deviation bandwidth of the cavity resonance. Since the 700 MHz cavities have nearly four times the stored energy they require four times the installed rf power for equal microphonics bandwidth.

Clearly the lower frequency favours very high current machines due to the lower loss factor translating into higher single and coupled bunch instability thresholds. However, the lowered frequency results in higher cost, driven by higher rf power requirements, greater material costs (primarily the high purity niobium), and higher civil construction costs (longer linac). This, coupled with the lower technical risk associated with the well-developed TESLA design leads us to the choice of 1300MHz.

A cost benefit analysis was performed for CW vs. pulsed operation of the linac. It was clear that the pulsed linac could deliver more electron bunches at a lower installation and operating cost than the CW linac. The cryogenic and RF costs dominate the scaling, and the lack of a CW electron gun to meet the FEL requirements today or in the foreseeable future led us to choose pulsed operation. The recent successes of SCRF Electron Recirculating Linacs [4] may change this economics if a CW electron gun can be developed. Relevant parameters of the pulsed mode of operation are given in Table 2.

Table 2: Pulsed linac operation. The AC power estimates were made assuming a 50% AC to RF efficiency and 500:1 ratio of AC watts to 2°K W.

5GeV Linac	1.3 ms pulse/10 Hz
Gradient	25 MV/m
# Cavities	192
# of Klystrons	6 (10 MW)
Average rf power	780 kW
Cryo load @2°K	~350 W +static losses
Linac Length	288 m
Bunch Rate	100 kHz (10 MHz for 1 ms x 10 Hz)
AC Power (Cryo + rf only)	~2 MW

LONGITUDINAL DYNAMICS

The conceptual design of a SCRF linac with two magnetic chicanes to provide the FEL bunch requirements is shown schematically in Figure 1, and the parameters of the linac in Table 3.

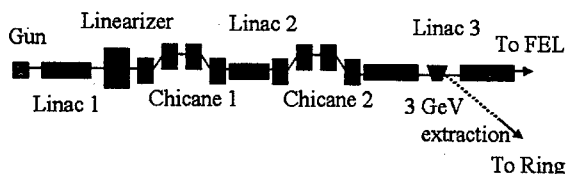


Fig. 1: Layout of 4.75 GeV FEL driver linac.

Table 3: 4.75 GeV SCRF linac parameters.

Parameter	Unit	Value
Injector energy	MeV	10
Bunch length	ps	2
Energy spread (rms)	%	0.2
1 st linac maximum energy gain	MeV	150
1 st linac phase	Deg	28.7
Beam energy after 1 st linac	MeV	141.6
3 rd harm. linearizer max energy gain	MeV	25
1 st Chicane R56	mm	50
Bunch length (rms)	ps	0.32
Energy spread (rms)	%	0.83
2 nd Linac maximum energy gain	MeV	600
2 nd linac phase	Deg	41
Beam energy after 2 nd linac	MeV	716.0
2 nd Chicane R56	mm	41
3 rd linac maximum linac gain	MeV	4241.1
3 rd linac phase	Deg	-18
Final beam energy	MeV	4750
Final bunch length (rms)	ps	0.1
Final energy spread (rms)	%	0.0085

The photo-injector is pulsed at 10 Hz with 1 ms macropulses with a bunch frequency of 10MHz. These are accelerated in the first linac to a high enough energy to avoid space charge blow-up of the bunch in subsequent beam manipulations. The beam passes through a linearizer to take out the RF induced curvature in

longitudinal phase space before going through the first chicane. Two chicanes are used to compress the beam in stages separated by an energy gain in the second linac. This allows for the natural reduction in rms energy spread due to the energy gain. Finally the beam is accelerated to the final energy of 4.75 GeV for the FEL. Since the beam is not always on crest in order to chirp the beam for compression, the installed linac energy gain has to be 5 GeV.

RF SYSTEMS

The proposed photocathode gun is a 3.5 cell gun operating at 1300 MHz. With the combination of proper cell shaping to increase the shunt impedance and over-coupling the cavity to decrease the fill time at the expense of installed RF power a preliminary design with 60 MV/m gradient on the cathode and 60 W/cm² has been achieved.

The SCRF linac is powered by eight high-power klystrons. There is one each for the first two linac sections, consisting of 6 and 24 9-cell cavities respectively. The final linac section consists of 170 cavities and requires 6 klystrons. The first 150 MeV linac section before the linearizer could in principle have a 2.5 MW klystron. The remaining klystrons are 10MW klystrons.

RING INJECTION

Electron bunch quality of the linac greatly exceeds the requirements of a ring injector, and injected bunch will filament in the storage ring to an equilibrium emittance determined by the ring lattice.

The electron bunch is extracted from the linac at the 3 GeV of the beam energy, where a fast extraction kicker is placed in a gap between cryostats. The 1.75 GeV of linac beyond this point in the FEL line is sufficient to vary the FEL linac energy from 1.25 to 4.75 GeV without affecting ring energy or phase. The ring extraction energy can be varied over a small range and likewise compensated by the remaining FEL linac tanks.

The proposed storage ring RF system would utilize CESR II SCRF cavities at 500 MHz. This produces a somewhat awkward frequency ratio of 2.6. Although it is possible to lock the frequency of the ring by providing a variable path length chicane, and cogging by adjusting phase to fill different ring buckets the following novel approach has been adopted.

The ring RF system would be designed to be several hundred kHz from 500 MHz, in fact the first NSLS upgrade lattice resulted in an RF frequency of 499.97 MHz. The resulting frequency ratio instead of being rational is now irrational and there arises a beat frequency between the respective RF systems of 300 kHz. This allows the ring buckets to "precess" past the linac rf system. In 3.3 μ s any given ring bucket will precess 2π radians, and line up with an injected bunch. This is shown in Fig. 2.

A separate photo-cathode laser locked to the linac RF and triggered at a zero of the phase error between the linac and ring creates a bunch at the tail end of the FEL beam macro-pulse (Fig. 3). This bunch is separated from the FEL bunches by a minimum of the extraction kicker rise time and by up to 3.3 microseconds which is the time it takes any given bucket to precess past the injection point.

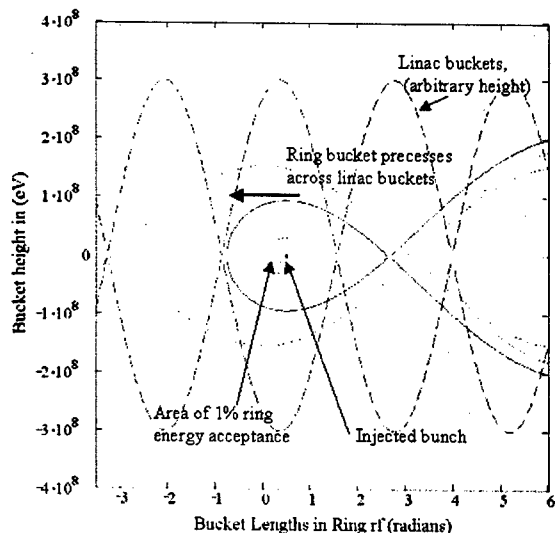


Fig. 2: Bunch and bucket traces for 499.97 MHz ring buckets and 1300 MHz linac bucket.

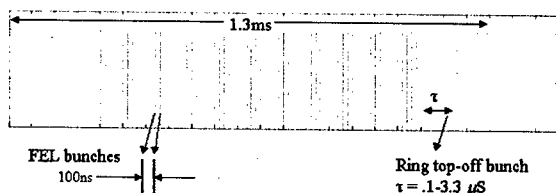


Fig. 3: Bunch pattern in macro-pulse showing the creation of the ring pulse on the tail end of the FEL bunch train.

CONCLUSION

Next generation light sources, which may include short-wavelength FEL's as well as storage rings with top-off injection, can use the same SCRF linac for both purposes. The linac has to be optimised for the FEL beam, but easily meets the requirements for the ring. Bunch "stealing" at the end of the FEL macro-pulse with asynchronous linac and ring frequencies insures independent operation of the two machines.

REFERENCES

- [1] B. Podobedov et al, NSLS Upgrade Concept, these proceedings
- [2] J. Wu and L.H. Yu, Cascading stages of High Gain Harmonic Generation to produce coherent hard X-ray, NIM A 475 (2001), 104-111
- [3] K. Floettmann, The TESLA linear collider and X-ray FEL, proceedings of LINAC 2002
- [4] J.B. Murphy, Energy Recovery Linacs Light Sources: an Overview, these proceedings

BEAM DYNAMIC CALCULATIONS FOR THE SUPERCONDUCTING COSY INJECTOR LINAC

A. Lehrach, H. Jungwirth*, R. Maier, R. Tölle, Forschungszentrum Jülich, Germany

Abstract

A superconducting injector linac for the Cooler-Synchrotron COSY is under investigation to increase the intensity of polarized proton and deuteron beams [1]. In this report the layout and magnet requirements of the matching and linac section are discussed and sensitivity studies of the lattice performed to find the requirements for an orbit correction system. A 6-dimensional multi-particle tracking code [2] was used to simulate the beam in the transverse and longitudinal phase space.

INTRODUCTION

The Institut für Kernphysik of the Forschungszentrum Jülich is investigating a new injector (COSY-SCL) for the cooler-synchrotron COSY, which will replace the more than 30 years old cyclotron JULIC. Our aim is to increase the intensity of polarized proton and deuteron beams in COSY typically by a factor of 10 compared to what can be delivered to experiments at present. The conceptual design of COSY-SCL has been described previously [1]. It makes use of a superconducting linac, together with advanced ion sources and interchangeable 160 MHz RF-quadrupole (RFQ) pre-accelerators including booster cavities for H^- and D^- beams, respectively. The linac design is based on a 44 single-cell half-wave resonator (HWR) acceleration structure, of which the first 20 resonators operate at 160 MHz and the remaining 24 at 320 MHz, for delivering both polarized and unpolarized pulsed H^- and D^- beams at a kinetic energy between 50 and 60 MeV for charge exchange (stripping) injection into COSY. The beam current will be limited to 2 mA (peak) in pulses lasting up to 500 μ s at a maximum repetition rate of 2 Hz.

Beam dynamic simulations have been carried out to investigate the transversal optics and orbit deviations in the matching and linac sections due to misalignments of optical and accelerating elements.

BEAM MATCHING SECTION

The layout of the matching section including the first two unit cells of the linac can be seen in Fig. 1 (upper part). The whole matching section has only a length of about 1 m, 78 cm for the focusing magnets including drift spaces and 21 cm for a 160 MHz rebuncher. Quadrupole doublets are used for transverse focusing. This simple type of focusing structure fits the requirements for the matching section, because it automatically creates a circular transverse beam profile between the two quadrupoles as well as in the middle of the rebuncher,

where the beam size is of the order of 13 mm in diameter. The two quadrupole doublets located upstream and downstream of the rebuncher are also sufficient to match the orientation and size of the transverse phase space distribution from the exit of the RFQ section to the entrance of the first cryostat. The second quadrupole doublet is already part of the first linac unit cell. To reduce construction costs, the same quadrupole type like in the linac section can be utilized. Such quadrupoles have an effective length of 8.5 cm, an aperture of 38 mm and a maximum gradient of 45 T/m [3]. The following transverse beam properties at the end of the RFQ section are expected for D^- : $\epsilon=5\pi$ mm.mrad (1σ , geometric), $\alpha_{x,y}=-1.5$; 0.6, and $\beta_{x,y}=0.4$ m/radian; 0.2 m/radian [4]. In Figure 1 (lower part) the transverse beam envelopes are shown. The maximum focusing gradient for this layout is less than 20 T/m for D^- and less than 10 T/m for H^- . The diagnostic devices will be placed between the quadrupoles, following the same adjustment procedure like in the linac section itself [1].

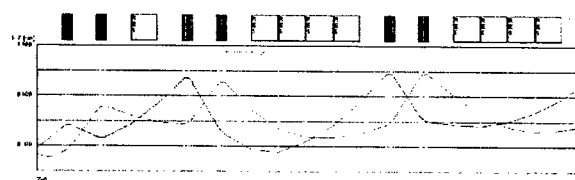


Figure 1: Matching section including the first two unit cells of the linac (upper part) and transverse 4σ beam envelopes in the matching section and at the entrance of the linac (lower part).

For longitudinal beam matching, a 2-gap-spiral resonator with approximately 100 kV maximum voltage and a length of 15 cm is proposed [4]. Since the RFQ sections for H^- and D^- are nearly the same, except for a few periods in the first part of the two RFQs, roughly the same particle distribution is expected for H^- and D^- at the exit of the RFQ section. The bunch length is about $\pm 15^\circ$ with a full energy spread of 75 keV/nucleon (Figure 2). In the drift between RFQ and rebuncher, the longitudinal phase space distribution diverges, leading to a bunch length of more than $\pm 20^\circ$. The rebuncher inverts the energy deviation of the beam, leading to a converging beam in longitudinal phase space. This requires a peak voltage of 45 kV for D^- and 22.5 kV for H^- with the present rebuncher design. Thus the beam motion from the exit of the RFQ section to the entrance of the first cryostat corresponds to a 180° image of the beam in longitudinal phase space. The longitudinal phase space distribution continues to converge in the first cryostat to a very small

*Present address: Accel Instruments, Bergisch Gladbach, Germany

bunch length of less than $\pm 5^\circ$ in the middle. Simulations show, that the presented layout is capable to accept 5 % variation of the initial beam parameters without beam losses. It also clarifies, that the rebuncher doesn't need any transverse beam focusing properties.

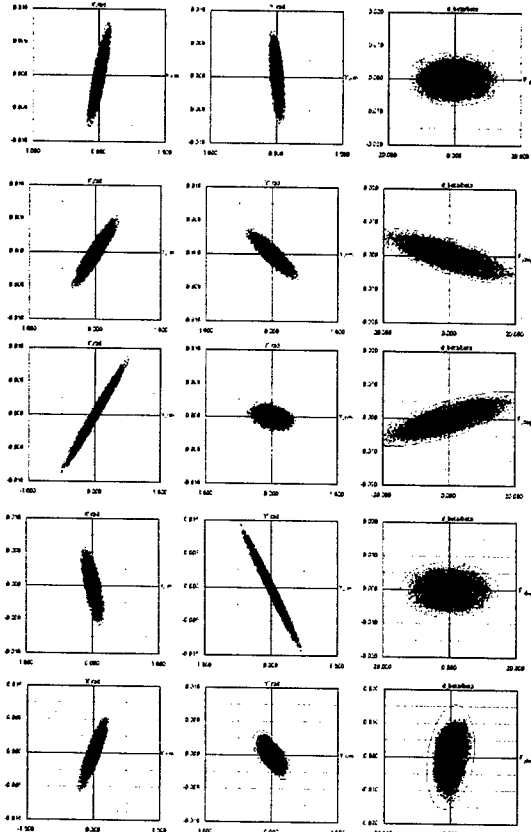


Figure 2: Transverse and longitudinal phase space distribution of the beam (from the top) at the exit of the RFQ section, the entrance of the rebuncher, the exit of the rebuncher, the entrance of the first cryostat, and in the middle of the first cryostat.

LINAC SECTION

Four resonators will be mounted in each cryostat. Quadrupole magnets and also diagnostic devices will be placed between the cryostats. Transverse beam focusing in the linac is based on a doublet like structure outside the cryostats, utilizing two conventional quadrupole magnets in each unit cell with a diagnostic box in between. Since we are limited in length of the unit cells due to beam dynamical requirements for the longitudinal phase space [1], the design of the quadrupoles is critical in terms of physical length and maximum gradient. We tried to optimize the drift space between the quadrupoles and the length of the magnets by two criteria, moderate quadrupole gradients with acceptable beam envelopes. After several iterations, we came to the conclusion that the best compromise is to use a unit-cell length of 1.7 m and an effective quadrupole length of 8.5 cm with

theoretical gradients of less than 40 T/m. This corresponds to a physical magnet length of 12.5 cm and a drift space of 13 cm in between the two quadrupoles of a doublet. Identical arrangements can be used for all unit cells.

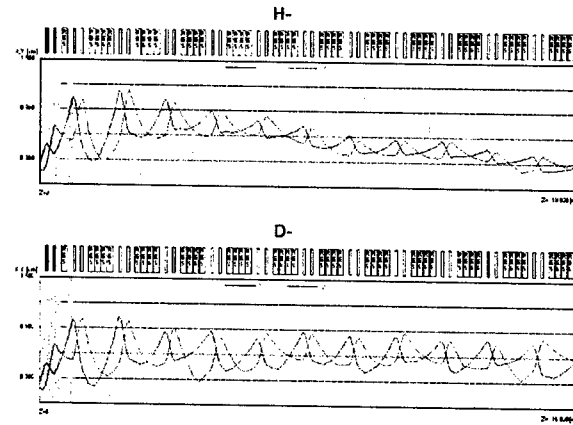


Figure 3: Lattice of the linac including the matching section. 4σ beam envelopes computed for accelerating H^- (upper plot) and D^- periodically constant throughout the linac and can be optimized further.

Figure 3 shows the beam envelopes computed for H^- and D^- using 10000 particles. The quadrupole settings are chosen for keeping the beam envelopes periodically constant throughout the linac and can be optimized further. The betatron amplitudes and thus also the beam envelopes have a periodic structure. The minimum of the betatron amplitude in each unit cell is slightly increasing with the rigidity of the beam, depending on the focusing strength applied. The 4σ beam envelope is expected to be less than 12 mm. The maximum gradient needed for this lattice is about 25 T/m for 50 MeV H^- and 38 T/m for 56 MeV D^- . Figure 4 shows the results obtained for the 6-dimensional phase space of the H^- and D^- beams at the linac exit.

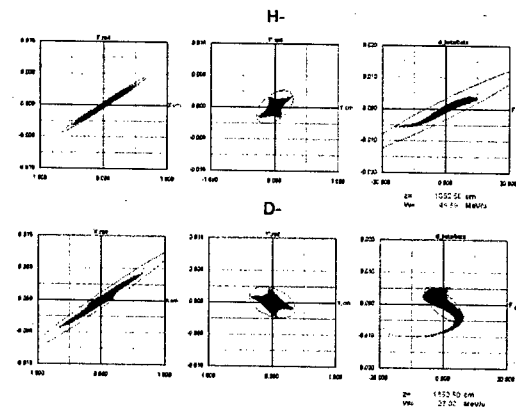


Figure 4: The 6-dimensional phase space computed by tracking simulations for 50 MeV H^- (upper plots) and 56 MeV D^- (lower plots) beams at the linac exit.

These results indicate that in such a lattice we would have to expect a transverse geometric beam emittance ($4\sigma_{rms}$) of less than 4π mm.mrad for H^- and about 5π mm.mrad for D^- at the linac exit (see table 1).

Table 1: Geometric beam emittance ($4\sigma_{rms}$ and max.) at the exit of the linac section.

	Horizontal (geom.)	Vertikal (geom.)
H^-		
$4\sigma_{rms}$	2.6π mm.mrad	3.6π mm.mrad
Max.	8.9π mm.mrad	16.7π mm.mrad
D^-		
$4\sigma_{rms}$	4.6π mm.mrad	4.7π mm.mrad
Max.	36.2π mm.mrad	20.5π mm.mrad

For the longitudinal phase space at extraction one finds minimum $\Delta p/p$ values of $\pm 2 \times 10^{-3}$ and $\pm 8 \times 10^{-3}$, respectively, depending on the orientation of the longitudinal phase space distribution of the beam.

SENSITIVITY OF THE LATTICE

Orbit deviations in the linac are mainly caused by misalignments of magnets and resonators. To determine such effects, magnets and resonators are randomly shifted in all three dimensions by maximum values of ± 0.1 mm and ± 0.75 mm, respectively [5]. In addition the phase and amplitudes of the resonators are also randomly changed by up to $\pm 0.5^\circ$ and $\pm 0.5\%$. For each case ten samples of 1000 particles were tracked through the matching and linac section. Figure 5 shows the resulting orbit deviations and associated divergences of the beam center for H^- in the horizontal and vertical plane.

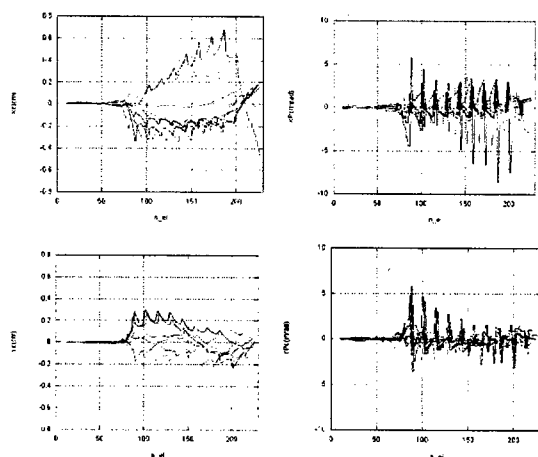


Figure 5: Orbit deviations (left) and divergences (right) of the beam center in the horizontal (upper plots) and vertical (lower plots) planes for H^- versus element number for ten different cases of randomly distributed errors.

The orbit deviation of the beam center for H^- is less than 8 mm with a orbit divergence up to 10 mrad. For D^- this effect is smaller. The maximum orbit deviation of the beam center in both planes is only about 4 mm and the maximum orbit divergence about 8 mrad. Taking maximum beam envelopes of about 11 mm and maximum orbit deviations of about 8 mm into account, the acceptance of the machine is too small without orbit corrections, leading to significant beam losses.

CONCLUSION

For 50 MeV H^- and 56 MeV D^- , quadrupoles with an effective length of 8.5 cm and a maximum gradient of 45 T/m are sufficient to focus the beam in the given lattice with a unit cell length of 1.7 m. Without correction, significant beam losses are expected. To reduce beam losses, typical correcting angles of up to a few milliradian for H^- and D^- are required, if one would place correcting dipoles between the quadrupoles of the doublets or use extra dipole windings on the quadrupoles. A correction system or beam based alignment is certainly needed under these circumstances, and a steering concept will have to be developed.

ACKNOWLEDGMENT

The authors would like to thank P.N. Ostroumov (ANL), K.W. Shepard (ANL), S.O. Schriber (MSU), A. Schempp (Univ. Frankfurt), R. Eichhorn (FZJ), and Y. Senichev (FZJ) for fruitful discussions.

REFERENCES

- [1] COSY-SCL Design Update, Internal Report, Forschungszentrum Jülich, March 2002 (<http://www.fz-juelich.de/ikp/linac-public/>); R. Tölle et al., COSY-SCL, the Superconducting Injector Linac for COSY, this conference.
- [2] P.N. Ostroumov, Technical Internal Note, Argonne National Laboratory, August 2001.
- [3] U. Bechstedt (Forschungszentrum Jülich), private communication.
- [4] A. Schempp (Universität Frankfurt), private communication.
- [5] R. Eichhorn (Forschungszentrum Jülich), private communication.

DEBUNCHER DEVELOPING FOR H AND D BEAMS INJECTION INTO COSY RING

N. Vasyukhin, R.Maier,Y. Senichev, R. Stassen, R.Toelle, FZJ, Germany

Abstract

In case of super-conducting injector in synchrotron due to high accelerating gradient the energy spread of beam after linac exceeds the longitudinal acceptance of ring. The problem becomes even more difficult, when we need to inject two beams with different charge/ mass ratio. We consider the problem, when H^- and D^- particles are injected and ratio of mass to charge differs by a factor of two. Both beams will be injected into ring at an approximately similar energy 50 MeV. To fulfill the monochromatization requirement the momentum spread of H and D beams has to be decreased from $\Delta p/p = \pm(5 \div 8) \cdot 10^{-3}$ [1] to $\Delta p/p = \pm 1.5 \cdot 10^{-3}$, or in special case $\Delta p/p = \pm 7.5 \cdot 10^{-4}$ by the debuncher system optimized for both sorts of particle simultaneously. For this purpose the E and H debuncher types are considered.

PHASE ADVANCE ADJUSTMENT.

The first and obvious possibility is to adjust the advanced phase $\Phi \sim \sqrt{E_s} \sin \phi_s$ in the longitudinal plane of whole linear accelerator and rotate the phase portrait to get

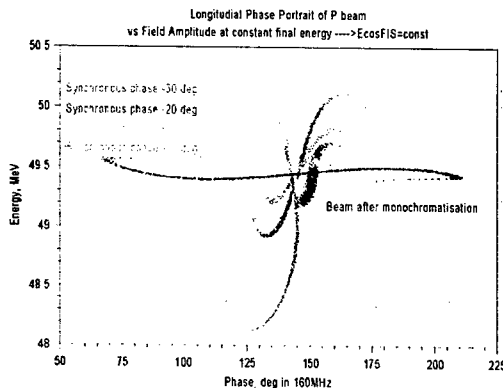


Figure1: H-beam phase portrait on linac exit vs synchronous phase

smaller momentum spread. Definitely using this method, we should conserve the final energy of linac, what is possible in case $E_a \cos \phi_s = const$. From Figure 1 you can see that minimum momentum spread of H beam can be reached at $\phi_s = -25^\circ$, when 85% of particles will be in the frame of required momentum spread. However, for D beam the optimum phase advance is another value (see figure 2). The best case is $\phi_s = -22^\circ$, when we can save about 80% of particles.

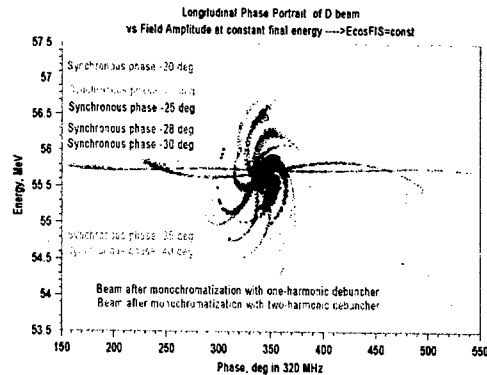


Figure 2: D-beam phase portrait on linac exit vs synchronous phase

BEAM DEBUNCHERING.

Another method of monochromatization is connected with using the debuncher for H and D beams after linac. The type and construction of debuncher is determined by required generator power. We study two options: one short (single gaps) and two long (six gaps) cavities. Both options are for 160 MHz frequency, since in case 320 MHz it is not enough large linear phase oscillation region. In second option we optimized geometry of cavity for solid-state generator ≤ 10 kW. Beam parameters have been taken for synchronous phase in linac $\phi_s = -30^\circ$, since for this value the separatrix is optimized. H and D-beams parameters on linac exit are placed in table 1. You can see momentum spread is very different for H and D.

Table 1

	H	D
Frequency, MHz	160	160
Beam velocity/c	0.313	0.238
Beam kinetic energy, MeV	49.4	55.7
Beam chamber aperture diameter, mm	20	20
Duty cycle	1%	1%
Beam $\pm \Delta p/p$	$5.73 \cdot 10^{-3}$	$8.9 \cdot 10^{-3}$
Bunch length in 160 MHz	$\pm 19^\circ$	$\pm 7^\circ$

One single-gap debuncher

It based on conventional omega-structure. After drift of 12 m D-bunch phase length increases up to $\pm 85^\circ$ (in 160 MHz) and H-bunch up to $\pm 30^\circ$. The beam dynamic calculation shows that in order to decrease momentum spread up to required value we need RF pulse power around 110 kW for proton and 60 kW for deuteron, and

the peak electric field is 25 MV/m (1.9 Kilpatrick). Thus, the option of single-gap debuncher requires high power RF generator with enough high peak electric field.

Two multi-gaps debuncher

In this option we investigated another solution: two different multi-gaps debunchers for proton and deuteron, and both optimized for maximum power generator limited by 10 kW. One of the most appropriate structures is drift tube resonator. We considered TM and TE types. After analyzing we took the TE rectangular cavity with cross-section $\sim 50 \times 50$ cm. The TM type has almost the same shunt impedance but 2 times bigger sizes. In multi-gaps case the main criterion is the required generator power (or shunt impedance). Peak electric field is much less than Kilpatrick limit. Different variants have been calculated on MAFIA with variation of gap coefficient $\alpha_1 = \frac{b_1}{\beta\lambda}$ for

regular cells and $\alpha_2 = \frac{b_2}{\beta\lambda}$ for extremes. Here b_1 and b_2 - gaps length. Figures 3, 4 show the 3D diagram plotted to define optimal α_1 and α_2 for D and H debuncher.

Further calculations were fulfilled with optimal parameters for each case. The number of gaps in H debuncher is taken 4 and 6 in D debuncher. The stem radius of drift tube is $R_{stem} = 1$ cm and length of cavity

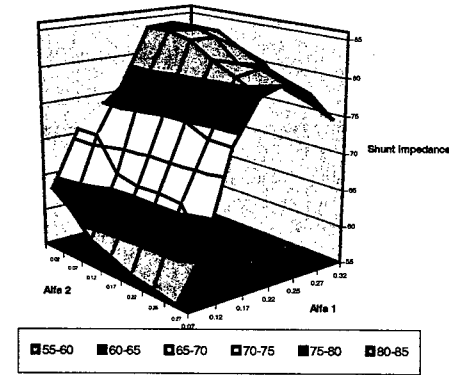


Figure 3: Shunt impedance vs gap ratio for 6 gap debuncher, Deuterons

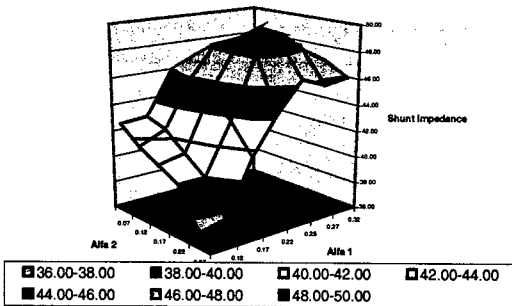


Figure 4: Shunt impedance vs gap ratio for 4 gap debuncher, Protons

$$Z_{length} = N_{gaps} \cdot \frac{\beta\lambda}{2}$$

To estimate the required power of generator the beam dynamics code was used. The real electric field distribution was obtained from MAFIA.

The final momentum compression depends on bunch length increasing in drift space and rotation angle in debuncher. However, in the optimized drift the bunch length has not to exceed the value, when head-tail particles appear in non-linear sin-wave region of debuncher electrical field. So, we should trade off both factors. For our bunch shape from linac the optimum drift between linac and debuncher is 9m and 20m for D and H beams accordingly. Coming in buncher, D-bunch has the phase length $\pm 67^\circ$ and H-bunch $\pm 63^\circ$ (both in 160 MHz). The final phase portrait after monochromatization is shown on figures 1 and 2. Table 2 gives the parameters of debuncher cavity for proton and deuteron calculated for aperture radius $R_a = 1$ cm, outer radius of drift tube

$$R_{outer} = 1.5 \text{ cm}, \text{ stem radius } R_{stem} = 1 \text{ cm}.$$

Table 2

Num. Gaps	L_{cavity} (m)	R_{sh} (M Ω)	R_{sh}/L_s (M Ω /m)	$\frac{E_{peak}}{E_{Kilpatrick}}$	Power of generator P_{gen} kW
Protons					
2	0.58	10.2	17.5	0.78	51.1
3	0.86	28.8	33.0	0.47	16.4
4	1.15	49.8	43.3	0.36	9.5
5	1.46	67.5	46.2	0.24	7.3
Deuterons					
2	0.42	14.6	34.7	0.80	57
3	0.65	30.1	46.8	0.59	35
4	0.87	48.8	56.1	0.53	19.3
5	1.1	67.1	60.1	0.46	16.5
6	1.3	85.2	65.5	0.62	11.7
7	1.56	103	66.1	0.45	9.2

Adding second resonator with doubled frequency, we can improve momentum spread (see figure 2). Usually the second harmonic cavity is used to linearize the sin-wave field. In our case it is supposed to correct bunch shape and compensate nonlinearity of whole linear accelerator, which one allows to have on exit for single deuterons bunch $\Delta p/p = \pm 4.5 \cdot 10^{-4}$. Second resonator can be based on conventional one gap omega structure. In this case required power for second generator is 5.5kW. The drift length for deuterons should be increased up to 14 m.

RF field errors

All above stated calculations consider bunch after ideal linear accelerator. In reality due to RF field amplitude and phase instabilities ($\sim 1\%$, 1°) the effective bunch has larger sizes. Figure 5 shows the effective bunch portrait after linac for the different instability value. Obviously, the optimised debuncher system has to take into account this circumstance.

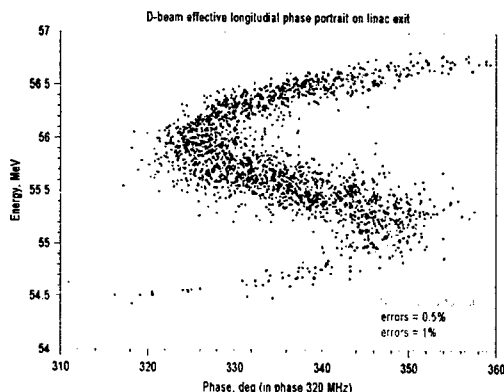


Figure 5: D-beam effective phase portrait on linac exit vs errors.

Table 3 shows the percentage of accepted particles and the required power of generator in case of 5 gaps cavity for proton and 6 gaps cavity for deuterons with various drift length.

Table 3

Drift length, m	Percentage of particles in region $\Delta p / p = \pm 1.5 \cdot 10^{-3}$ consider errors=1%	Percentage of particles in region $\Delta p / p = \pm 1.5 \cdot 10^{-3}$ consider errors=0.5%	P, kW
Protons			
16	98.38	99.64	10.2
17	99.01	99.73	9.7
18	99.19	99.73	8.2
19	99.19	99.82	7.3
20	99.37	99.82	6.8
21	99.55	99.91	6.5
Deuterons			
5	88.95	95.96	27.3
6	92.45	97.66	20.9
7	94.07	98.11	16.6
8	95.6	98.47	14.1
9	95.6	98.11	11.7
10	95.6	97.66	10.1
11	95.24	97.3	8.6
12	95.23	97.3	8.2
13	95.15	97.39	7.7
14	94.7	97.21	7.2

The percentage of accepted particles depends on drift length weakly, but the required power grows with drift significantly. From table we can see 9 m drift space gives the best captures of D-particle, but the power little bit exceeds 10 kW. Therefore 12 m drift space option is more preferable.

Two harmonic debuncher

Almost the same estimations have been done in case of two-harmonic debuncher. Two-harmonic debuncher consists of two cavity – cavity with normal frequency (160MHz) and cavity with doubled frequency (320MHz). First cavity is 5 gaps cavity for protons and 6 gaps cavity for deuterons. Second harmonic cavity is based on conventional one-gap omega structure. Due to larger linear region in two-harmonic debuncher, the optimized drift space has another value. Table 4 shows percentage of accepted D-beam and required power of generator for first (P_1) and second (P_2) cavity in case of two-harmonic debuncher.

Table 4

drift	Percentage of particles in region $\Delta p / p = \pm 1.5 \cdot 10^{-3}$ consider errors=1%	Percentage of particles in region $\Delta p / p = \pm 1.5 \cdot 10^{-3}$ consider errors=0.5%	P_1 , kW	P_2 , kW
12	95.69	97.66	9.6	1.4
13	96.41	98.56	9.6	3.1
14	97.21	99.28	9.6	4.5
15	97.12	99.01	9.1	5.5
16	96.68	98.29	8.5	5
17	95.87	97.84	7.5	5

You can see actually H-beam does not need the second harmonic cavity. However, for special requirements, when we need $\Delta p / p = \pm 7.5 \cdot 10^{-4}$ the second harmonic cavity is needed for H beam as well, and the capture efficiency will be 95% for RF errors 1% and 97.5% for errors 0.5%.

CONCLUSIONS.

So, we analyzed: 4 possibilities of H and D beams monochromatization simultaneously:

1. Phase advance adjustment: it has the momentum spread reduction limitation.
2. One single-gap debuncher: it specifies high peak electric field and high power RF generator.
3. Two multi-gaps debunchers: the solid-state generator can be used.
4. Two-harmonic debuncher: it improves monochromatization and allows to get the effective momentum spread $\sim 7.5 \cdot 10^{-4}$

REFERENCES

- [1] Yu.Senichev, et al., SOME FEATURES of BEAM dynamics in super-conducting linac based on quarter- and half-wave cavities, EPAC 2002.

THE RFQ-INJECTOR FOR COSY-SCL*

K.-U. Kühnel, A. Schempp, IAP, Goethe University, Frankfurt
C. P. Welsch, MPI-K, Heidelberg
A. Schnase, R. Tölle, Forschungszentrum Jülich
Germany

Abstract

For the new sc-linac for COSY at FZ Jülich [1], a combination of an RFQ and a spiral loaded cavity will accelerate H,D- beams up to 2.5 MeV/u for injection into the sc-linac.

The RFQ is a 3.8 m long four-rod design which accelerates deuterons with an initial energy of 25 keV/u up to 2 MeV/u. Behind the RFQ a compact booster cavity of 300 mm length is mounted. This spiral loaded cavity accelerates the beam to a final energy of 2.5 MeV/u. It uses four accelerating gaps with an effective voltage of 1 MV. An alternative design has gaps with additional electrodes in an rf-quadrupole configuration to add a focussing field in this DTL structure.

The status of the work on this new injector is presented.

1 INTRODUCTION

At the Forschungszentrum Jülich a new injector for the cooler synchrotron COSY is developed. COSY-SCL will be a superconducting linac operating at a frequency of 160 MHz [2]. The low energy part of the injector consists of a conventional room temperature RFQ in combination with a short booster cavity. The ion source delivers polarized protons and deuterons at 25 keV. To accelerate both types of ions ensuring equal beam characteristics, two RFQs with einzellenses and booster cavities are mounted on a rail system. An overview of the beamline is given in figure 1.

2 RFQ DESIGN

The design of the RFQ electrodes has been done under consideration of the beam parameters listed in Table 1:

Input energy	25 keV/u
Input emittance	0.14π mm mrad
Current	1.5 mA
Output energy	2 MeV/u
Max. beam angle at the exit	± 15 mrad in both planes
Phase width at the exit	$\Delta\phi \leq \pm 15^\circ$

Table 1: RFQ beam parameters

In figure 2 the design parameters of the RFQ are shown.

RFQJuel, F=160 MHz, U=110 KV

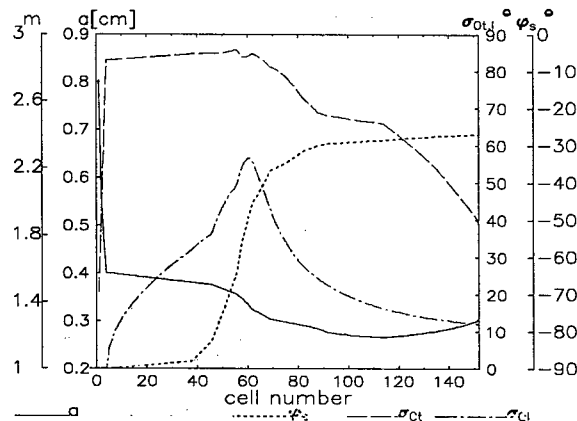


Figure 2: Design parameters of the RFQ

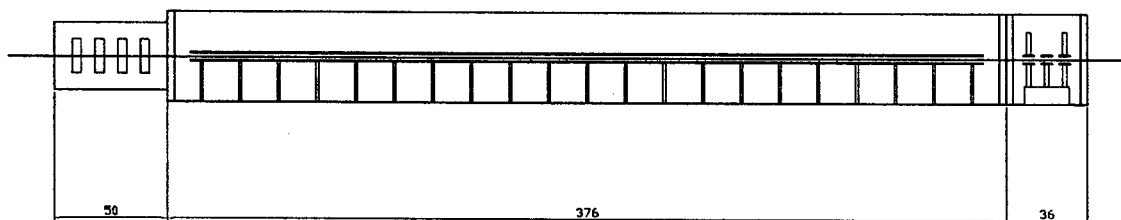


Figure 1: Overview of RFQ and Booster

In the first few cells the aperture decreases from 0.8 cm to 0.4 cm to match the beam radially. After the bunching section the ideal phase is raised to -27° and the aperture decreases furthermore to a minimum of 0.27 cm. The aperture is growing at the end of the electrodes which leads to a decrease of the focusing strength. This is necessary to maintain the beam angle of 15 mrad at the exit of the RFQ.

For the acceleration of the deuteron beam an electrode voltage of 110 kV is necessary. To gain that voltage the power consumption of the RFQ will be about 500 kW at a duty cycle of 1%. To study the thermal evolution in the RFQ the program ISAFEM was used. Figure 3 shows the temperatur distribution in one RFQ stem without cooling.

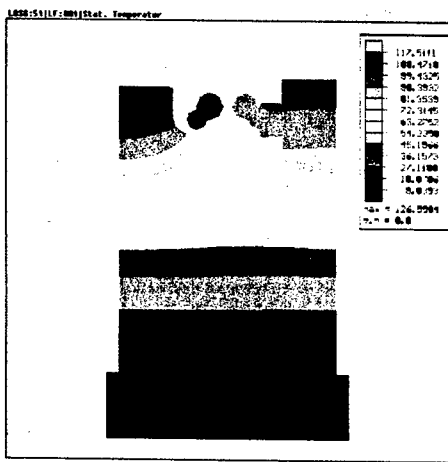


Figure 3: Temperature distribution in an RFQ stem without cooling calculated with ISAFEM.

3 BEAM DYNAMICS

The input distribution has been generated according to the expected beam emmitances at the RFQ entrance. They fit well into the acceptance of the RFQ as shown in figure 4.

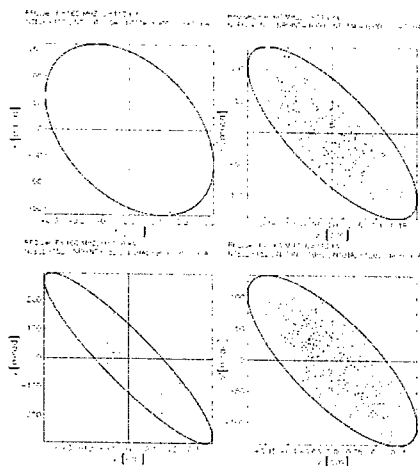


Figure 4: Input distribution and acceptance of the RFQ.

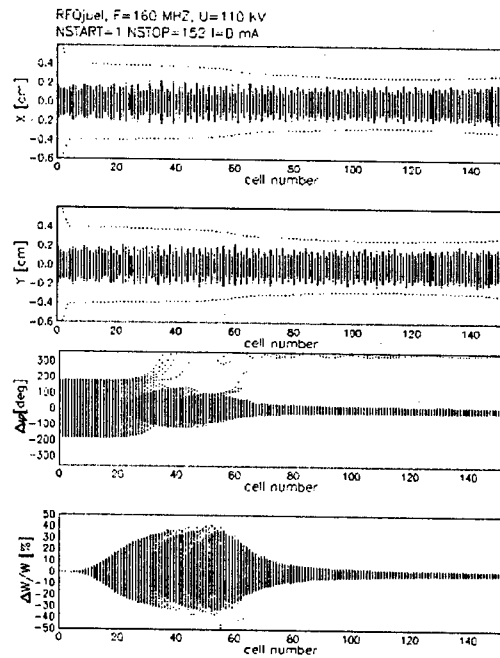


Figure 5: PARMTEQ simulation of the RFQ. The upper two graphs display the transverse beam envelope. The longitudinal evolution of the beam is shown in graphs three and four.

The propagation of the beam through the 152 RFQ cells is displayed in figure 5. The aperture growth at the end of the electrodes corresponds to a decrease of the focusing strength. Therefore the beam radius is rising slightly, but the angular spread is small and meets the requirements listed in table 1. The energy spread of the beam reaches its minimum at the end of the structure. The output distribution of the RFQ is shown in figure 6.

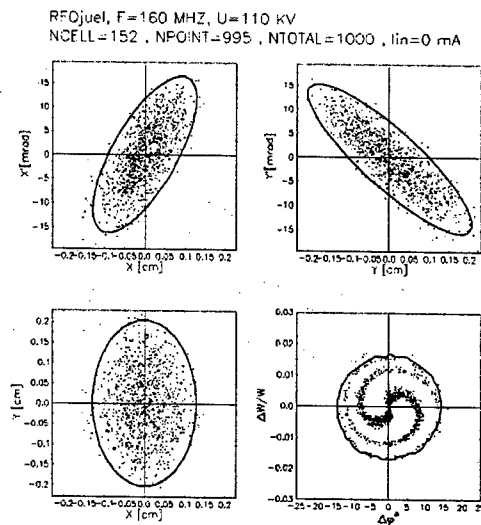


Figure 6: Output distribution of the RFQ.

To reach the overall energy of 2.5 MeV/u a booster cavity is mounted directly at the end of the RFQ. Because

RFQs get less effective at higher energies and the length of the RFQ shouldn't exceed 4 m to ease manufacturing, a spiral loaded cavity with 30 cm length and four accelerating gaps is used. The parameters of the cavity are listed in table 2.

Length:	300 mm
Diameter:	280 mm
Aperture:	20 mm
Gap voltage:	250 kV
Power consumption:	150 KW

Table 2: Parameters of the booster cavity.

DTL cavities thus short feature a high energy acceptance and flexibility [3]. They can be used both as booster or buncher cavities. A drawing of the spiral loaded cavity is pictured in figure 7.

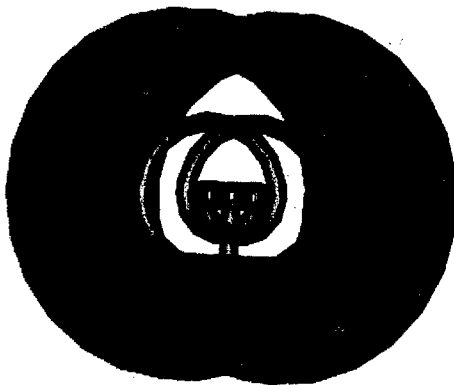


Figure 7: drawing of the spiral loaded cavity.

To match the beam to the following SC linac a matching line consisting of quadrupoles and a buncher is used. The beam distribution after the matching section is pictured in figure 8.

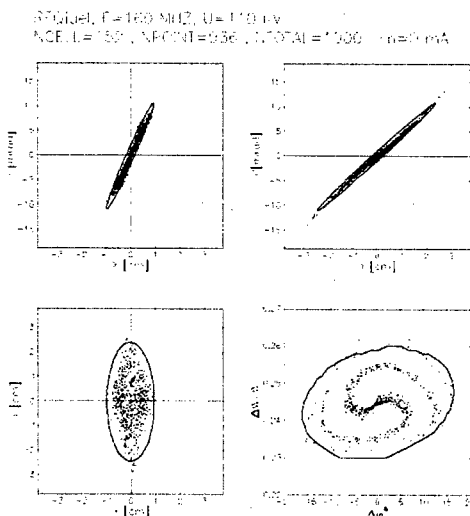


Figure 8: Beam distribution after the matching section.

Optional to the classical DTL booster a DTL cavity with additional quadrupole electrodes could be used to achieve a better focussing a higher energies. This type of cavity is being examined at IAP. Figure 9 shows a schematic drawing of an accelerating gap with quadrupoles. To describe this kind of structure PARMTEQ was used introducing a new transport element which allows to transform the beam through an arbitrary three dimensional potential distribution [5].

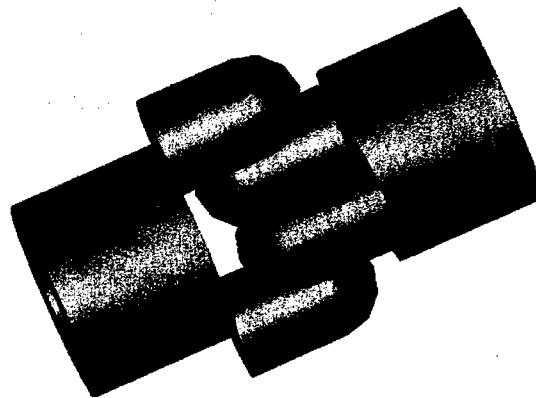


Figure 9: Schematic drawing of an accelerating gap with quadrupoles

4 CURRENT STATUS

At present the vacuum vessel as well as the resonating structure for the RFQ are built at NTG in Gelnhausen. All components for the booster cavity are under construction in Frankfurt

The machining of the vacuum vessels will be finished soon. The alignment of the electrodes as well as RF tuning of both cavities will take place at IAP in Frankfurt.

REFERENCES

- [1] R. Tölle et al., "A new superconducting injector for COSY", Proc. EPAC 2002
- [2] R. Tölle et al., "COSY-SCL, the Superconducting Injector Linac for COSY", this conference
- [3] C. P. Welsch et al., "Development of Rebunching Cavities at IAP", Proc. LINAC 2000
- [4] K.-U. Kühnel et al., "Development of a FDT Cavity", Proc. EPAC 2002
- [5] A. Bechtold et al., "Erweiterung von PARMTEQ um ein Modul zur Berechnung der Teilchendynamik in einer frei wählbaren Potentialverteilung", Int. Rep. Okt. 2000

DESIGN OF A SUPERCONDUCTING CH-CAVITY FOR LOW- AND MEDIUM BETA ION AND PROTON ACCELERATION*

H. Liebermann, H. Podlech, U. Ratzinger, A. Sauer, Institut für Angewandte Physik,
Frankfurt, Germany

Abstract

The cross-bar H-type (CH) cavity is a multi-gap drift tube structure based on the H-210 mode currently under development at IAP Frankfurt and in collaboration with GSI. By use of the KONUS beam dynamics long lens free sections can be realized, making the design of a superconducting multi-cell CH resonator possible. Numerical simulations and rf model measurements showed that the CH-type cavity is an excellent candidate to realize s.c. multi-cell structures ranging from the RFQ exit energy up to the injection energy into elliptical multi-cell cavities. The reasonable frequency range is from about 150 MHz up to 800 MHz. A 19-cell, $\beta=0.1$, bulk niobium prototype cavity is under construction at the ACCEL-Company, Bergisch-Gladbach. This paper will present detailed MicroWave Studio simulations of the superconducting CH cavity.

INTRODUCTION

Linacs based on room temperature (rt) H-mode cavities (RFQ and drift tube structures) have become a standard solution in the velocity range from $\beta=0.002$ up to $\beta=0.1$ [1]. RF power tests show the capability of IH-cavities to stand about 25 MV/m on-axis field [2]. Moreover H-type cavities allow for the acceleration of intense beams [3]. One new aspect of investigations started at GSI and IAP Frankfurt was to extend the velocity range of the H-mode cavities up to $\beta=0.5$ by developing the CH-DTL [4]. Many future projects (Accelerator Driven Transmutation Project ADTP [5], European Spallation Source ESS [6], Experimental Accelerator-Driven System XADS, the International Fusion Materials Irradiation Facility (IFMIF) or the Radioactive Ion beam Accelerator RIA [7]) are based on the availability of efficient accelerating cavities with properties like mentioned above, which additionally can be operated in cw mode. It is commonly accepted that above an energy of 100 A · MeV super-conducting elliptical cavities are superior to rt structures. Up to 20 A · MeV, super-conducting (splitring and quarter wave) cavities were used in heavy ion accelerators. In the energy range in between, the development of spoke-type resonators started just some years ago [8, 9]. These cavities usually provide only a few accelerating gaps. By combining the advantages of H-mode cavities with the benefits of superconductivity, effective ion acceleration with multi-gap structures will become possible. Our investigations show that for high current proton beams the injection energy will be around 5 MeV, while

for heavy ions the injection energy may become as low as 1 A · MeV. The CH-structure is efficient for beam energies up to 150 A · MeV.

SUPERCONDUCTING (SC) STRUCTURES

The sc CH-structure could be an excellent choice for a cw operated ion linac. In sc cavities there is no cooling problem like in cw operated rt linacs. In general, sc linacs can be operated at higher voltage gradients above a certain duty factor. On the other hand, at low duty factors and high beam currents rt structures are very favourable because they are cheaper and can tolerate dark current contributions. To demonstrate the capabilities of the CH-DTL, it is foreseen to test a sc CH cavity prototype. A design and engineering study has been performed in close cooperation with industry¹. This study shows the feasibility of the production of superconducting CH cavities. After a call for tenders the CH prototype has been ordered. The cavity is expected to be delivered in January 2004. To test the cavity a new cryogenic lab has been established at the IAP in Frankfurt. This includes a vertical 600 l cryostat, two 250 l transport dewars for liquid helium, a laminar flow box (class 100) and a magnetic shielding to avoid trapped flux from the earth magnetic field in the cavity surface during cool down.

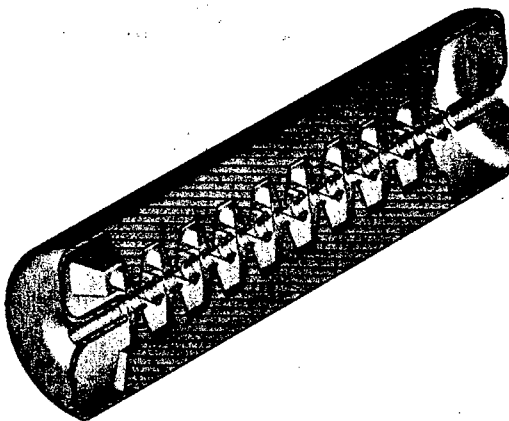


Figure 1: The sc 352 MHz CH prototype with matched end cell geometry

The CH prototype with 19 gaps will be made of bulk ni-

* Supported by GSI Darmstadt, EU and by BMBF, contr. no. 06F134I

¹ ACCEL Company, Bergisch Gladbach, Germany

bium, the diameter is 28 cm, the length is 105 cm. At an operation frequency of 352 MHz, this corresponds to a particle β of 0.1. One important issue during the design phase was the minimization of the electric and magnetic peak fields to reduce the risk of field emission and of thermal break down. An accelerating gradient of 5 MV/m results in an electric peak field of 26.4 MV/m and in a magnetic peak field of 30 mT which is a very moderate value.

CH CAVITY DESIGN

The CH-cavity exceeds the mechanical rigidity of other multi cell structures at similar β and operation frequencies, and it exceeds by far the rigidity of IH-tanks (110-mode). Together with the application of the KONUS beam dynamics [10], resulting in long, lens free beta graded accelerating sections housed in individual cavities, this opens the possibility to develop a super-conducting multi-cell cavity [11]. The RF behavior of the resonators was studied with an analytical model first, allowing a rough evaluation of the fundamental cavity parameters.

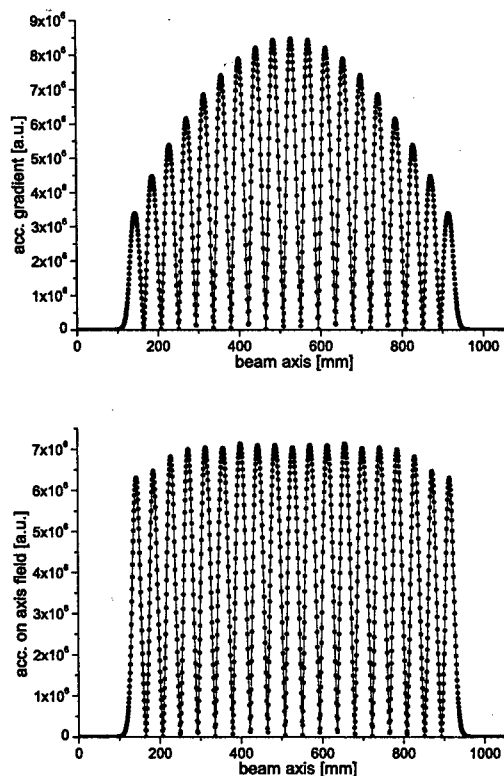


Figure 2: Accelerating on axis field distribution of the 352 MHz CH cavity without (top) and with (bottom) gap length variation

The consequent numerical simulations of the resonators

were done using CST-MWS[®][12]. One of the calculated resonator geometries is shown in fig.1. The results of these calculations are shown in tab.1. Fig.2 shows the accelerating on axis field distribution of the 352 MHz CH cavity before and after field optimization.

To get a flat field distribution, the length of each gap along the CH cavity was optimized. Fig.3 shows the resulting gap length distribution.

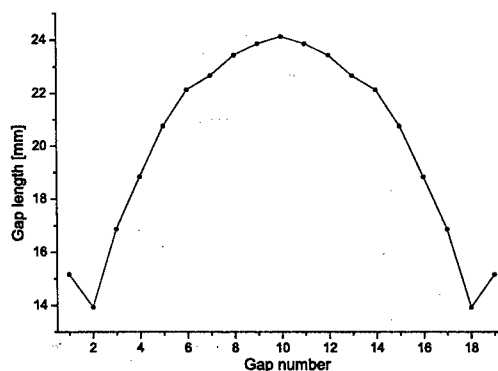


Figure 3: Gap length distribution along the CH cavity at a constant periodical length of 42.857 mm

frequency [MHz]	351.628
beta	0.1
R_a/Q [k Ω]	1.61
E_{peak}/E_a	6.59
B_{peak}/E_a [mT/MV/m]	7.29
cavity length [m]	1.048
gaps	19
aperture diameter [mm]	25
tank diameter [m]	0.28
at $E_a=5$ MV/m :	
E_{peak} [MV/m]	32.95
B_{peak} [mT]	36.45

Table 1: Parameters of the prototype cavity

A small B_{peak}/E_a ratio indicates, that the achievable accelerating gradient limit will be higher. For example with a gradient of 5 MV/m the maximum magnetic field on the resonator surface will be as low as 36.45 mT (352 MHz, $\beta=0.1$ resonator), giving a comfortable safety margin with respect to the BCS-limit of 210 mT. At an $E_a = E_0 \cdot T$ of 5 MV/m, the corresponding stored field energy is 4 J.

Fig.4 shows the magnetic field on the surface of the CH cavity.

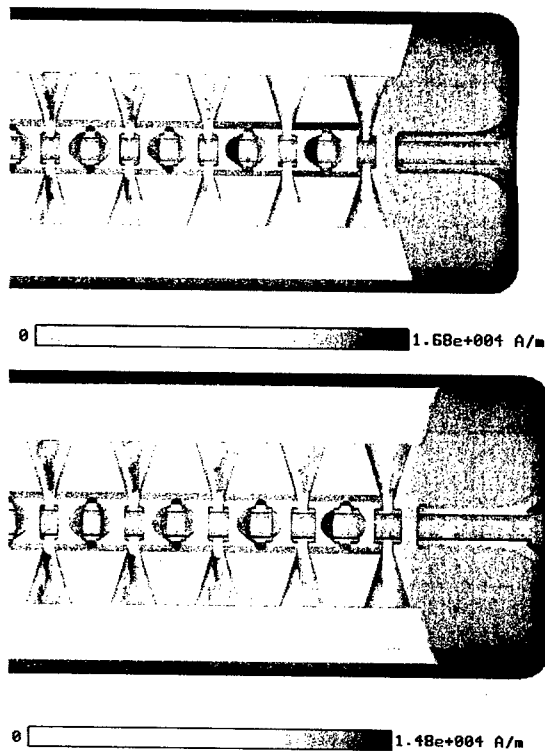


Figure 4: Magnetic field on the surface of the 352 MHz CH cavity without (top) and with (bottom) gap length variation. The stored field energy of 1 J is identical in both simulations

CH CAVITY TUNING

For tuning the frequency as well as the voltage distribution during the fabrication process it is planned to incorporate cylindrical blocks on the girders between adjacent stems (fig.5).

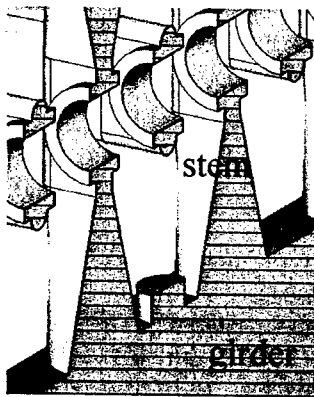


Figure 5: Tuning the 352 MHz CH cavity with cylindrical niobium blocks along the girders

Fig.6 shows that up to a height of about 3 mm the tuner acts inductively while longer cylinders act capacitively. The total tuning range $\Delta f/f$ at a cylinder diameter of 20 mm and at a maximum height of 10 mm corresponds to $2.5 \cdot 10^{-4}$.

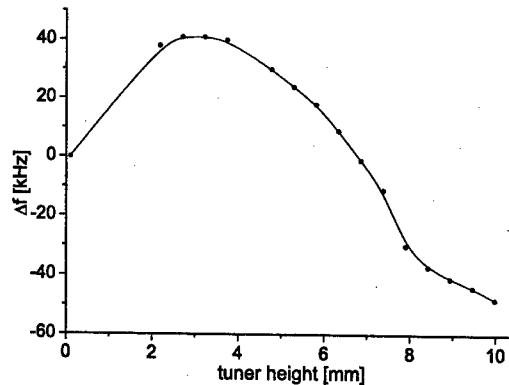


Figure 6: Frequency tuning of the CH cavity by a cylinder as shown in Fig.5 with variable height

OUTLOOK

Using the rt model cavity, further investigations will start soon. A mechanism for tuning the cavity (fast und slow) has to be developed. This can be done either by deforming the re-entrant shape geometry or by deviating from the round tank cross section. In a next step, possible high power input coupler geometries have to be studied. The aim is to design a coupler, which should provide a variable coupling factor even in the cold state.

REFERENCES

- [1] U. Ratzinger, Nucl. Physics, A 701 (2002) 641c
- [2] J. Broere et al., Proc. LINAC98, Chicago, ANL-98/28, p.771
- [3] W. Barth, Proc. of the Lin. Acc. Conf., Monterey, SLAC-R-561, (2000) 1033.
- [4] U. Ratzinger, Proc. EPAC 2000, Vienna, p.98
- [5] R.A. Jameson et al., Proc. Europ. Part. Acc. Conf., Berlin, (1992) 230.
- [6] ESS-CDR, eds.: I. Gardener, H. Lengeler and G. Rees, ESS-Report 95-30-M (1995).
- [7] J.A. Nolen, Proc. of the Lin. Acc. Conf., Geneva (1996) 32.
- [8] K.W. Shepard et al., Proc. of the Lin. Acc. Conf., Monterey, SLAC-R-561, (2000) 920.
- [9] D.L. Schrage et al., Proc of the Part. Acc. Conf., Chicago (2001) 906.
- [10] U. Ratzinger, Nucl. Intr. Meth., A 415 (1998) 229.
- [11] R. Eichhorn et al., Proc. of the LINAC 2002, Korea
- [12] CST MICROWAVE STUDIO, CST Computer Simulation Technology.

THE FRANKFURT FUNNELING EXPERIMENT*

H. Zimmermann, J. Thibus, N. Müller, I. Müller, A. Schempp
Institut für Angewandte Physik, Johann Wolfgang Goethe-Universität,
Robert-Mayer-Straße 2-4, D-60325 Frankfurt am Main, Germany

Abstract

Funneling is a procedure to multiply beam currents at low energies which is necessary for the proposed new high current accelerator facilities like HIDIF or ESS. Funneling can be done by several stages. The beams of several LEBT's are merged in multiple stages to any kind of energy and beam current by funneling. The main goal is to keep the emittance nearly unchanged.

The Frankfurt Funneling Experiment consists of two ion sources, a Two-Beam RFQ accelerator, two different funneling deflectors and a beam diagnostic equipment system. The whole set-up is scaled in He^+ instead of Bi^+ of the first funneling stage of a HIIF driver. The progress of our experiment and the results of the simulations will be presented.

1 INTRODUCTION

At low energies the beam currents of linacs are limited by space charge effects, focusing and transport capability of the accelerator.

Funneling is doubling the beam current by combination of two bunched beams preaccelerated at a frequency f_0 with an r.f. deflector to a common axis and injecting into another r.f. accelerator at frequency $2f_0$ as indicated in figure 1.

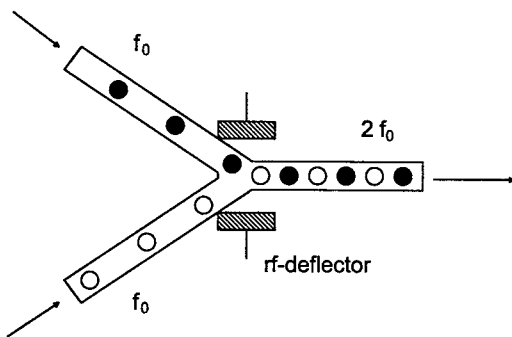


Fig. 1: Principle of funneling.

By the use of the Two-Beam RFQ the two beams are brought very close together while they are still radially and longitudinally focused. Additional discrete elements like quadrupole-doublets and -triplets, debunchers and bending magnets, as they have been proposed in first funneling studies, might not be necessary [1,2,3]. A short r.f. funneling deflector is placed at the beam crossing position behind the RFQ [4].

*Work supported by the BMBF

2 EXPERIMENTAL SETUP

Beam experiments with our Two-Beam RFQ were done with He^+ -ions at low energies to facilitate ion source operation and beam diagnostics (fig. 2). Two small multicusp ion sources and electrostatic lenses, built by LBNL [5,6], are used. The LEBT's are attached directly on the front of the RFQ with an angle of 75 mrad, the angle of the beam axis of the Two-Beam RFQ.

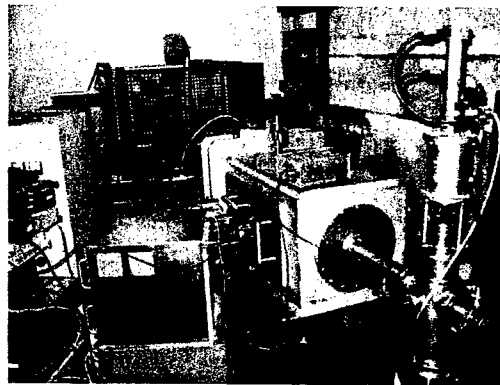


Fig. 2: Picture of the experimental set-up.

The Two-Beam RFQ consists of two sets of quadrupole electrodes, where the beams are bunched and accelerated with a phase shift of 180° between each bunch, driven by one resonant structure. The RFQ is divided in two sections. The first section, which is about two thirds of the total length of 2 meters, accelerates the beam to a final energy of 160 keV. The last section has to match the beam to the funnel deflector to optimize beam radius and phase width.

At present one beam axis consists of the old unmodulated electrodes whereas the other beam axis consists of the new modulated electrode endpart. This will allow to compare directly both beams. Within a short time the second beam line will be upgraded too.

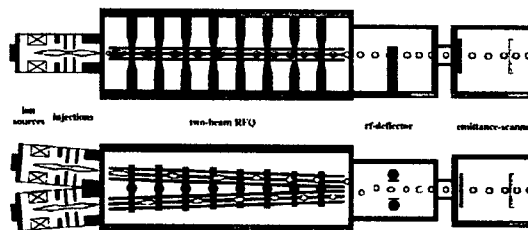


Fig. 3: Scheme of the experimental set-up.

Figure 4 shows the Parmteq simulations with the new RFQ electrode endpart. The new electrode design reduces beam radius and phase spread at the funneling deflector corresponding to the old electrode design (figure 5).

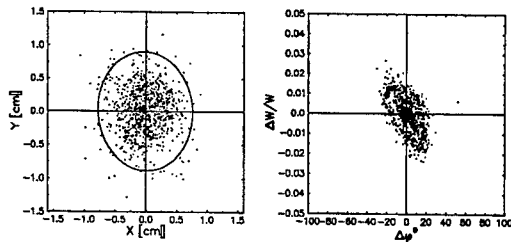


Fig. 4: Beam data with the new design of the RFQ electrode endpart.

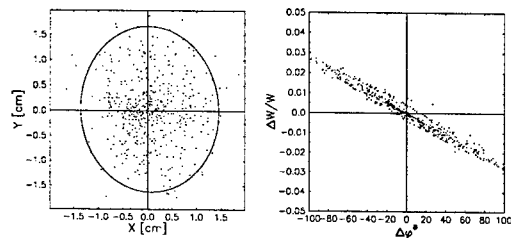


Fig. 5: Beam data with unmodulated electrode endpart.

3 FUNNELING DEFLECTOR

For beam bending to a common axis we have investigated several schemes of deflectors [7]. We have done experiments with the one cell and the multi cell deflector. The crossing point of the two beams is right in the middle of the deflector, which is 52 cm behind the RFQ.

The angle between the two beam axes is 75 mrad. The one cell funnel deflector bends this angle down to zero by an r.f. voltage of 25 kV.

Figure 6 shows a simulated beam bending with the one cell funnel deflector. The deflector bends the beam from an average angle of 37.5 mrad down to zero.

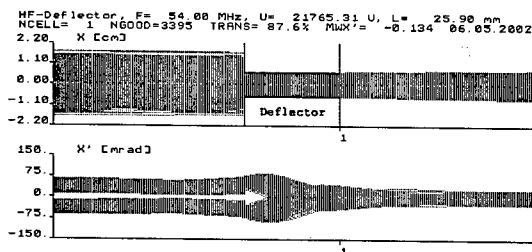


Fig. 6: Simulation of the beam bending in the one cell funnel deflector from $\langle x' \rangle = 37.5$ mrad to $\langle x' \rangle = 0$ mrad.

Figure 7 displays a result of a simulation for the funneling with two beams with the new electrode design.

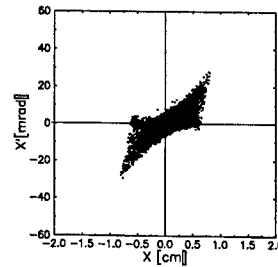


Fig. 7: Simulated funneling with new RFQ electrode design.

At the moment a new software for field calculations and particle transport (completely in 3D) for the deflector module in Parmteq is being developed. This will allow us to improve the existing deflector structures and design new structures for future funneling deflectors.

4 THE NEW RFQ ELECTRODES

The new RFQ electrode endpart has been manufactured and installed in the RFQ for first experiments.

Figure 8 shows one beam line with transfer to the new modulated electrode endpart.

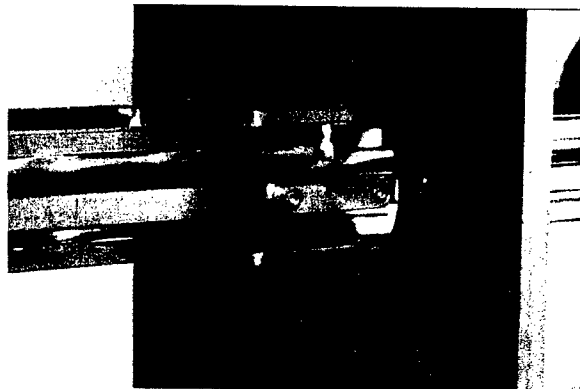


Fig. 8: The mounted electrodes at the stem.

The old design uses unmodulated electrodes at constant aperture after the acceleration part until the end. In the new design the bunch drifts for 12 cells with increasing aperture. The last 8 cells have a modulation up to $m = 1.4$ to bunch the beam with the time focus at the funneling deflector. At the same time the focusing is made stronger to avoid a diverging beam and get more beam into the aperture of the deflector. Thus the RFQ provides a longitudinal and radial focus at the deflector.

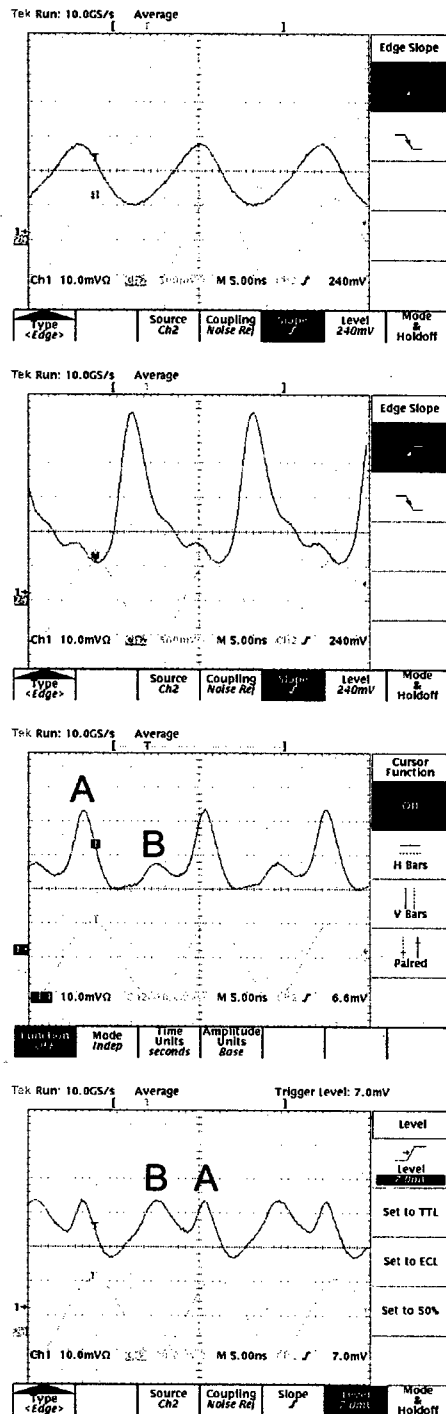


Fig. 9 a-d: Beam pulse measurements with a faraday cup.
a: Unmodulated electrode endpart
b: Modulated electrode endpart
c: Both beams
d: Same current at faraday cup

Figure 9a displays the beam pulses of the old design with unmodulated electrodes at the end. In Figure 9b shorter beam pulses with the modulated endpart is shown. Figure 9c shows the interlaced beam pulses now with $2f_0$. Both beams have the same current at the faraday cup (figure 9d).

The used faraday cup has a restricted bandwidth and cannot resolve the pulses at high resolution. But the results clearly indicates the improvements of the matching to the funnel deflector.

5 CONCLUSIONS

Funneling has been demonstrated with both kind of funnel deflectors [7]. To achieve a proper funneling the beam radius and phase width at the point of the funneling deflector has to be as small as possible.

The manufacturing of the last electrode section is done. The installation of the new electrode endpart at one beam line and the retuning of the RFQ accelerator was completed. First beam tests have been done.

Next step will be bending and diagnostics with the new beam. The installation of the new electrodes at the second beam line will follow. Then we will measure emittance growth during funneling with our beam diagnostic device.

REFERENCES

- [1] K. Bongardt and D. Sanitz, "Funneling of Heavy Ion Beams", Primary Report, Kernforschungszentrum Karlsruhe, 11 04 02P14C (September 1982).
- [2] J.F. Stovall, F.W. Guy, R.H. Stokes and T.P. Wangler, "Beam Funneling Studies at Los Alamos", Nucl. Instr. and Meth. A278 (1989) p.143.
- [3] K.F. Johnson, O.R. Sander, G.O. Bolmer, J.D. Gilpatrick, F.W. Guy, J.H. Marquardt, K. Saadatmand, D. Dandoval and V. Yuan, "A Beam Funnel Demonstration: Experiment and Simulation", Particle Accelerators, Vols. 37-38 (1992) p. 261
- [4] A. Schempp, "Design of Compact RFQs", Proc. Linear Accelerator Conference 1996, CERN 96-07, p. 53.
- [5] K.N. Leung, "Multicusp Ion Sources", Rev. Sci. Instrum. 65(4) (1994) p. 1165.
- [6] R. Keller in: The Physics and Technology of Ion Sources, Edited by I. G. Brown, Wiley-Interscience Publication, New York.
- [7] H. Zimmermann, A. Bechtold, A. Schempp, J. Thibus, "Funneling with the Two-Beam RFQ", Proceedings EPAC 2002, Paris, p. 972-974

COLD-MODEL TESTS OF AN ANNULAR COUPLED STRUCTURE FOR UPGRADE OF A J-PARC LINAC

H. Ao*, JAERI, Ibaraki, 319-1195, Japan

N. Hayashizaki, TITech, Tokyo, 152-8550, Japan, V. Paramonov, INR, Moscow, Russia

Abstract

An Annular Coupled Structure (ACS) has been developed for upgrade of a J-PARC (Japan Proton Accelerator Research Complex) linac from 180 MeV to 400 MeV. Although install area is prepared for the ACS cavities at an initial construction, it will be used as a beam-transport line temporarily. Aluminum and copper models were fabricated for RF properties confirmation based on an initial design, and for final optimization. RF measurement procedure of the ACS structure was also studied thorough the R&D process. Many items should be considered for mass production; schedule, handling parts, utilities, and so on. The measurement results of models and some fabrication status are presented.

INTRODUCTION

The phase-1 construction of High Intensity Proton Accelerator Facility (JAERI/KEK joint project) has been started. A nickname for this facility has been decided to be "J-PARC" (Japan Proton Accelerator Research Complex)[1]. The plan has been discussed and proposed jointly by the High Energy Accelerator Research Organization (KEK) and the Japan Atomic Energy Research Institute (JAERI).

The following are the complete design of the linac. The linac uses normal-conducting cavities up to 400MeV. An RFQ linac accelerates the beam up to 3MeV, a DTL up to 50MeV, an SDTL up to 190MeV, and an ACS up to 400MeV. An acceleration frequency from the RFQ to the SDTL is 324MHz, and the ACS is 972MHz. For the detail design of the ACS, refer to the references [2, 3].

The beam energy of the linac is planned for 180 MeV at present temporarily, which is restricted from a total budget. Although the ACS is not sure to be installed at an initial operation of the phase-1, R&D for a cavity fabrication and a mass production should be finished as soon as possible. Since April 2002, the fabrication of first 972 MHz prototype module was started. This is first buncher module, consisting of two 5-cells accelerating cavities and a 5-cells bridge cavity. And then, at the last of fiscal year 2002, second buncher module and three accelerating module were ordered. Fabrication of these modules will be active from April 2004 mainly. Two 17-cells accelerating cavities and a 9-cells bridge cavity were chosen for the accelerating module. The total number of accelerating modules were reduced from 23 to 21 at present design to save a

total fabrication cost. (The former design was 15-cells and 23-modules.)

ALUMINUM MODEL TEST AND COUPLING IRIS ANALYSIS

A wave guide and a bridge cavity are coupled with an iris for matching condition of RF power. A coupling factor β was analyzed for this region and discussed.

Review of JHF L-band ACS coupling

An ACS prototype module for JHF was developed at KEK. This module was installed high power RF and confirmed the cavity is performance. Based on the this module, a coupling β was analyzed for the iris part dimensions of the JHF module with an HFSS. Figure 1 shows an analyzed model and a calculated S11 parameter. The analyzed model in Fig. 1 includes 1-cell (0.5-cell + 0.5-cell) cavity. The upper boundary plane is a magnetic boundary for a $\pi/2$ mode excitation, and the rear plane is a magnetic boundary and the bottom plane is an electric boundary because of a symmetry. Evaluated from this results, a coupling value is $\beta = 37.5$. The designed value is $\beta = 43$, supposing that a Q-value and a coupling factor are ideal between a bridge cavity and an accelerating cavity. Measured value is $\beta = 0.99$ for whole cavities [4]. This is one sample of comparing an analysis and a measurement.

For another case, 2.5-cell (2-cell + 0.5-cell) cavities case was analyzed. This analysis concludes $\beta = 12.8$. It is considered reasonable. This is because that a ratio of two cases are $37.5/12.8 = 2.93$; it is almost equal to a ratio of a stored energy. These results will be checked by model and module measurements in a fabrication process.

Half-scale model test for J-PARC

In advance of the practical ACS cavity production, a half scale aluminum model was fabricated; the frequency is 1944 MHz. This model aims at the evaluation of the cavity properties with low power RF and the examination of the measuring method required for the RF measurements [5].

As mentioned in above section, a coupling β was also analyzed for a half-scale model. Several size of iris and connecting dimensions are fabricated and these measurement is underway. (See Fig. 2) For a regular accelerating section, accelerating and coupling cells have a margin for frequency tuning at initial dimensions, so that these cells have been tuned by several times of machining.

* aohi@linac.tokai.jaeri.go.jp

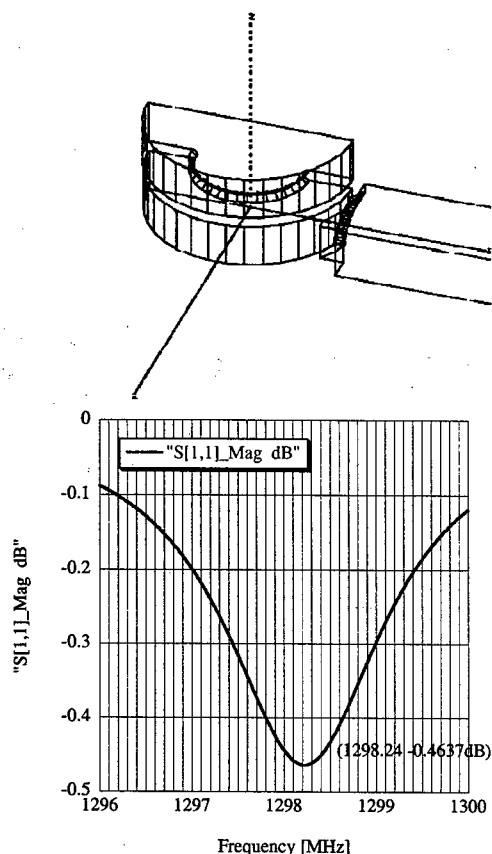


Figure 1: The analyzed model shape and the calculated S11 parameter with an HFSS

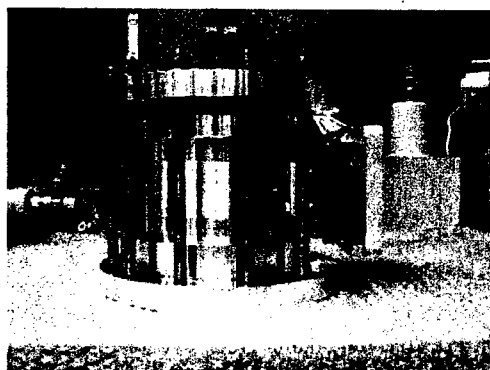


Figure 2: Half-scale aluminum model of connection part between a bridge cell and a wave guide

PROTOTYPE MODULE

Machining of half-cell disks

Many half-cell disks are layered and brazed for assembling an ACS cavity. Figure 3 shows the configuration of a half-cell disk. Flatness of a composition surface is important for brazing. An OFC half-cell disk is machined as

follows:

- 1) machined with 5-10 millimeter margin at a material factory,
- 2) machined with 1 mm margin and then annealed,
- 3) machined with 0.5 mm, 0.18 mm, 0.08 mm margin step by step,
- 4) four coupling slots are drilled on a machining-centre,
- 5) finished with ultraprecision machining for the design shape.

It is better to minimize the margin for ultraprecision machining. This is because that small volume of machining saves damage for a cutting tool, thus it brings stable quality of machining. It is slightly difficult to keep the accuracy of flatness less than $10\mu\text{m}$ in the normal machining of the large diameter (460mm). Therefore, the final margin for diamond machining is depend on an error of normal machining.

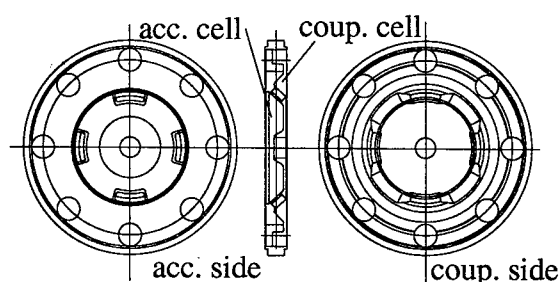


Figure 3: Configuration of the half-cell disk

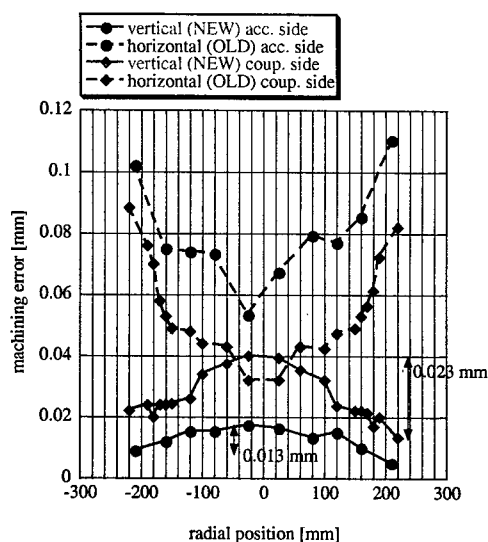


Figure 4: Machining error of a horizontal turning machine vs. a vertical turning machine

Figure 4 shows An example of a machining error with a normal turning machine is showed in Fig. 4 which compares a horizontal type turning machine (a rotating axis is

horizontal) and a vertical type turning machine (a rotating axis is vertical). Some reasons of the machining error are:

- 1) temperature control of a turning machine,
- 2) temperature control of machined object,
- 3) heat effect caused by machining.

Especially, it is considered that the error between a center and a circumference part are caused from the increase of the object temperature. The new vertical turning machine takes care of all above points; placed air conditioned area, temperature controlled cutting oil, and high-rotating speed reduces heating effect. Therefore, the new vertical turning machine can reduce a machining error drastically.

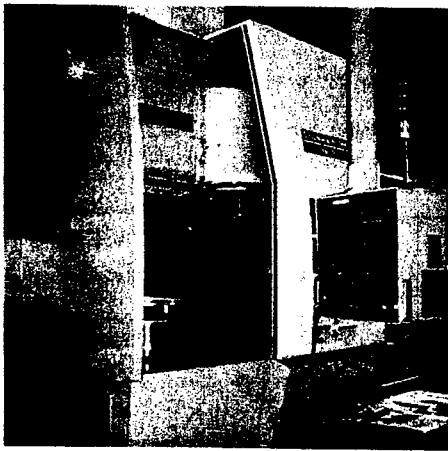


Figure 5: Vertical turning machine

Wave guide flange and RF window

An wave guide flange for a vacuum region and RF window have been developed. The wave guide is WR975. A rectangular flanges were fabricated and tested with several thicknesses of gaskets. (See Fig 6) These flanges are vacuum tight and they are adopt for ACS modules and RF windows.

The RF window is a pillbox type and a diameter of a ceramic window is 285mm. First prototype window is under fabrication. Although it is ensured 0.4 MPa of resist pressure for cooling water, a water cooling system of the linac recommends up to 1MPa strongly. A sleeve design around a ceramic for an accelerating modules will be revised to keep toughness up to 1MPa. This prototype window will be used for measurement of RF properties and a high-power test at a test stand.

SUMMARY

The half and full-cell models are corrected and measured continuously. The fundamental measurement procedure and accuracy requirements for measurement tools have been developed.

The technical problems have been solved for the machining of half-cell disk. The real-scale RF measurement con-

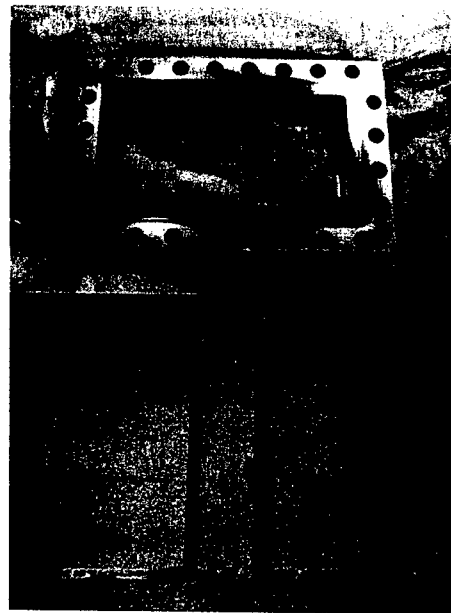


Figure 6: Rectangular flange and gaskets for vacuum waveguide WR975

tinues for improving a tuning process. We are planning the measurement procedure through the assembling of the buncher cavity.

Fabrications and R&D schedule are as follows. The first buncher fabrication is scheduled to finish in February 2004. An high-power test of this buncher is planned for a next step. From April 2004, the second buncher and accelerating modules are started. The second buncher has the same design as first one. Trial machining and tuning R&D are proceeded to next β energy of modules.

REFERENCES

- [1] Y. Yamazaki, "The JAERI-KEK Joint Project (the J-PARC Project) for the High Intensity Proton Accelerator", in these proceedings
- [2] V. V. Paromonov, "The Annular Coupled Structure Optimization for JAERI/KEK Joint Project for High Intensity Proton Accelerators", KEK Report 2001-14, 2001
- [3] N. Hayashizaki et al. "Structure Design of the Annular Coupled Structure Linac for the JAERI/KEK Joint Project", Proc. of the 2002 Linac Conf., August 2002
- [4] Y. Morozumi et al., "Multi-cell Bridge Coupler", Proc. of the 1990 Linac Conf., p.153, 1990.
- [5] H. Ao et al. "R&D Status of the Annular Coupled Structure Linac for the JAERI/KEK Joint Project", Proc. of the 2002 Linac Conf., August 2002

LOW POWER TEST OF RFQ MOCK-UP MODULES AT 175MHz FOR IFMIF PROJECT

S. Maebara[†], T. Morishita, M. Sugimoto, T. Imai, H. Takeuchi, JAERI, Ibaraki-ken, Japan
S. Sazawa, M. Saigusa, Ibaraki University, Ibaraki-ken, Japan

Abstract

The 175MHz RFQ mock-up modules which consist of end-plate modules and central modules, have been designed by MAFIA code, and the mock-up modules have been fabricated for a low power test. By the low power test results and the analysis of higher modes, it was found that the resonant frequency of operation mode (TE_{210}) is not affected by higher modes in the RFQ length of 4.1m. This result showed one of feasibility for the application technique using two coupling plates in the 12m-long IFMIF RFQ.

1 INTRODUCTION

International Fusion Materials Irradiation Facility (IFMIF) is an accelerator-based neutron irradiation facility to develop materials for fusion reactor[1-3]. In the system, 40MeV deuteron beam with a current of 250 mA is injected into liquid lithium flow with a speed of 20 m/s, neutron field similar to the D-T Fusion reactor (2MW/m², 20 dpa/year for Fe) is produced by the Deuteron-Lithium (D-Li) stripping reaction. The required current of 250 mA is realized by two beam lines of 125 mA, and the output energies at injector, radio-frequency quadrupole (RFQ) linac and drift tube linac (DTL) are designed to be 0.1, 5.0 and 40 MeV, respectively [4].

In the 175 MHz IFMIF RFQ system, the RFQ total length is needed to be 12 m to accelerate ions up to 5 MeV, and hence suppression of higher modes is indispensable. For this purpose, a coupling plates are used, central modules which have a short longitudinal length, are connected through the coupling plates. This coupled cavity technique is developed for 350 MHz RFQ system in APT/LEDA project of LANL[5-8], will be used in IFMIF RFQ system. In order to apply this technique, it is indispensable to verify resonant frequencies of operation mode and higher modes in the short central module. In case that two coupling plates are applied for the IFMIF RFQ, the short central module length is 4 m, operation mode and higher modes in the length were verified by the low power test and the analysis of higher modes.

2 DESIGN OF RFQ MODULES

A four-vane RFQ modules were designed by MAFIA code. The RFQ modules consist of two end-plate modules and central modules, two end-plate modules are connected to both sides of the central modules. A coupling plates are not included in, to evaluate operation mode (TE_{210}) and higher modes (TE_{21n} and TE_{11n}) up to a longitudinal [†]maebaras@fusion.naka.jaeri.go.jp

length of 4.1 m. For both modules, the vane tip has no modulation, the cavity shapes have no curved lines excepting for the vane tips. The bore diameter and the vane radius are required by Ion Beam Transport Simulation, the diameter and the radius are $\phi 8$ mm and 4 mm, respectively. The resonant frequency was analyzed by changing each cavity dimension. For the resonant frequency of 175MHz, mock-up modules were fabricated. The material of aluminum was used. Photograph of central module and end-plate module are shown in Fig.1. The gap between end-plate and undercut vane edge is 40 mm, the longitudinal length and the radial length for the undercut vane is 50 mm and 70mm, respectively. In this dimension, electric field strength at the vane edge which is 1% lower than one at the central module center, is suppressed, electric field uniformity around the tip of vane for a longitudinal length is kept.

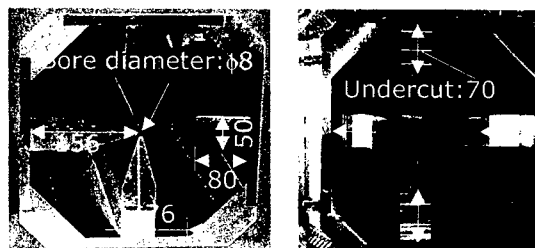


Fig.1 Photograph of Central and End-plate module

3 LOW POWER TEST

In Fig.2, photograph of the 4.1m-Long RFQ module is indicated. The RFQ module consist of four central modules and two end plate modules, each central module length is 1m. In the end-plate modules, the central module length of 50mm is including. In this system, the resonant frequency and the mode number for operation mode and higher modes were measured Network Analyzer. The two loop coils of $\phi 60$ mm and $\phi 25$ mm were used for an RF input coupler and a pick-up coil, respectively. For the resonant frequency, a peak values of a transmission coefficient factor (S_{21}) were measured, the mode number was evaluated by phase difference in each cavity and the calculation results by MAFIA code.

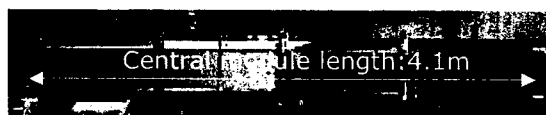


Fig.2 Photograph of the 4.1m-Long RF module

The measured result is shown in Fig.3. Six peaks are observed, it was found that TE_{110} , TE_{210} , TE_{111} , TE_{211} , TE_{112} and TE_{212} mode from a low frequency side are excited. The resonant frequency of 187 MHz for the operation mode (TE_{210}) was measured, but the designed value was 175 MHz. The order of mode number and the number of higher modes, however, are in agreement with calculation results. The frequency difference between TE_{210} and TE_{110} , and between TE_{210} and TE_{111} are more than 1.6 MHz, the operation mode of TE_{210} was not affected by these higher modes. It was found that the operation mode is not affected by higher modes if the frequency of operation mode is far from higher modes more than 1MHz.

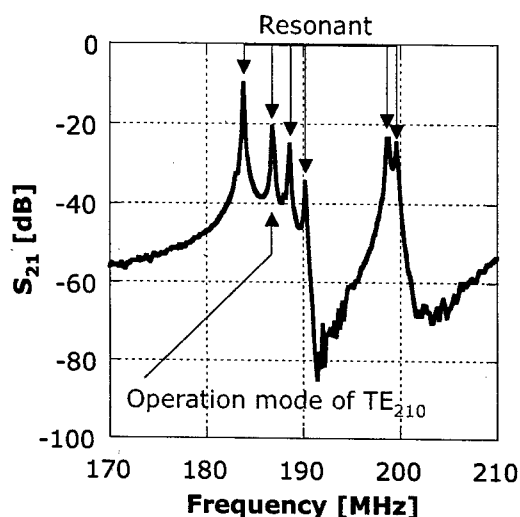


Fig.3 Measured resonant frequency

In order to agree with these measured resonant frequencies, mesh sizes of MAFIA code were optimized. In this result, it was found that the mesh size not in excess of 5mm/mesh is needed at the end-plate module part in z-axial direction, but the mesh size of 27.5mm/mesh or less is needed at central module part. The difference between measured values and calculated values was caused by the roughness of mesh sizes. Because the boundary condition are complicated configuration by undercut vane parts and the gap between the end-plate and undercut vane edge, the mesh size has to be cut fine at the end-plate parts. The measured resonant frequencies were in agreement with the calculated values using the optimized mesh sizes, within 200kHz ~1.13MHz. For the frequency difference between each modes, it were in agreement within -0.18 ~ +0.471 MHz.

4 IMPROVEMENT OF RFQ MODULE

The central module and the end-pate modes were redesigned by the optimized mesh sizes so as to obtain the resonant frequency of 174 MHz in the RFQ module length of 4.1m. The improved cavity dimensions are

shown in Fig.4. The values with arrow are indicated for the improved dimension, blue and red values are previous and improved dimension, respectively.

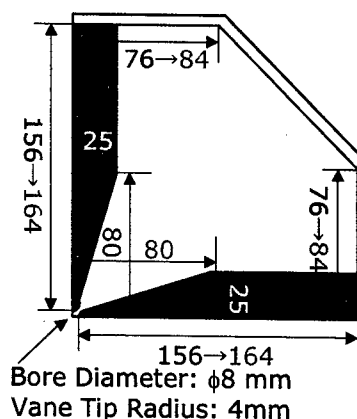


Fig.4 Improved cavity dimension

One central module and two end-plate modules were improved, the resonant frequency in the RFQ module length of 1.1m was measured. The measured result is shown in Fig.5. The resonant frequency of 175.65 MHz for operation mode was obtained, the frequency was in a good agreement with the calculated one of 174.36 MHz. The difference was less than 1% of operation frequency. This difference is supposed to be caused by misalignment at the connection between central module and end-plate module, but the analysis in details has not been done yet.

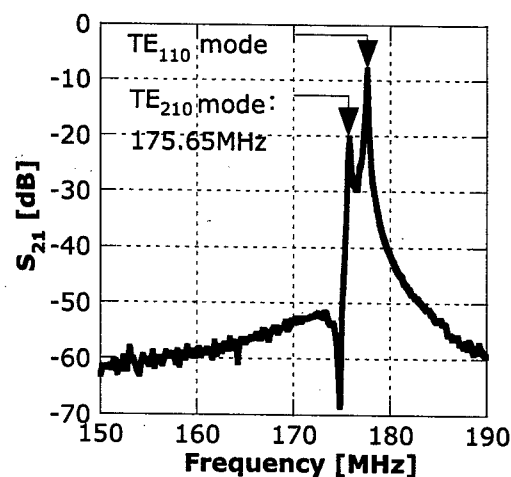


Fig.5 Measured resonant frequency of Improved RFQ

5 HIGHER MODES ANALYSIS

Higher modes analysis as a function of a longitudinal length up to 4.1 has been done by MAFIA code using the optimized mesh sizes. The result is shown in Fig.6. In the case of RFQ length of 4.1 m, the resonant frequencies of TE_{210} and TE_{111} modes are 173.91 MHz and 176.18 MHz,

respectively. The difference is 2.27 MHz, it is assessed that the operation mode is not affected by TE₁₁₀ mode. It is also found that the difference of more than 1.54 MHz is obtained by the RFQ length of more than 2.1m, operation mode is not affected. But the RFQ system design using 2, 3 and 5 coupling plates is considerable in this result, the RFQ design using two coupling plates will a good candidate from a low cost-effectiveness point of views.

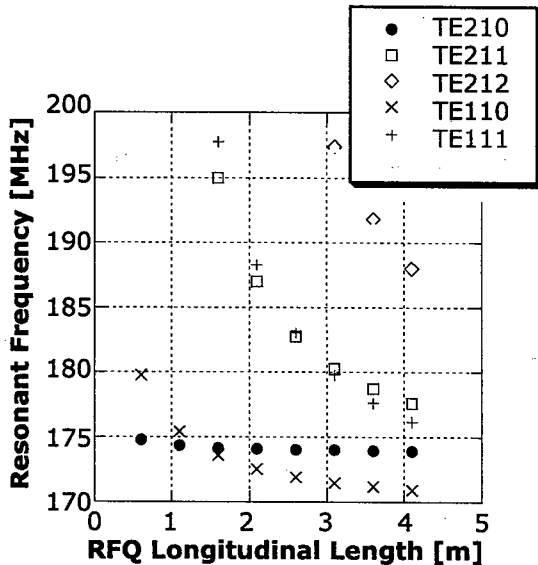


Fig.6 Higher modes analysis

5 FUTURE PLANS

In this works, the cavity's dimension for 175 MHz RFQ is obtained, the ridged coaxial waveguide of 1 5/8" is suitable for RF Power lead. From the withstanding voltage points of view, water cooling for the inner conductor is indispensable, R&D of multi RF input couplers are needed to lead the RF power of 700kW level per one RFQ module length of 4.1 m. In the nest step, a high power RF input couplers using this ridged coaxial waveguide are installed into RFQ modules, the evaluation for the resonant frequency and the power balance in each cavity by a low power test is planning.

6 SUMMARY

The RFQ modules which consist of end-plate modules and central module, were designed by MAFIA code, the modules were fabricated for a low power test. In the tests, the resonant frequencies of operation mode and higher modes were measured in the RFQ length of 4.1m, it was found that the operation mode will not be affected by TE₁₁₁ mode. The mesh sizes of MAFIA code, moreover, were optimized so as to agree with the measured resonant frequency, it was found that the mesh size of 5mm/mesh in a longitudinal direction is needed for end-plate parts.

The RFQ modules were redesigned by the optimized mesh sizes, and the RFQ modules were improved. The resonant frequency of 175.65 MHz in the RFQ length was obtained by the improved RFQ modules, the measured frequency was in a good agreement with the calculated one of 174.39 MHz. By this result, MAFIA code has made it possible to analyze accurately for 175 MHz RFQ. In the higher mode analysis by this MAFIA code, it was found that the operation mode is not be affected by TE₁₁₁ mode in the RFQ length of 4.1 m, it was indicated that one of feasibility for the application technique using two coupling plates in the 12m-Long IFMIF RFQ.

REFERENCE

- [1] IFMIF-CDA Team (Ed.) M.Martone, "IFMIF, International Fusion materials Irradiation Facility Conceptual Design Activity, Final Report", ENEA Frascati Report, RT/ERG/FUS/96/17 (1996).
<http://www.frascati.enea.it/ifmif/>
- [2] T.Kondo, J.of Nucl.Mater., 258-263,47(1998).
- [3] T.E.Shannon, et.al., J.of Nucl.Mater., 106, 47(1998).
- [4] IFMIF International Team, "IFMIF-KEP Report", JAERI,JAERI-Tech 2003-005, March 2003.
- [5] D.Schrage, et al., "CW RFQ Fabrication and Engineering", Proc. LINAC98 (Chicago,24-28 August 1998), pp679-683.
- [6] L. M. Young, et al., " High-Power Operation of LEDA", Proc. LINAC2000 (Monterey, 21-25 August 2000), pp336-340.
- [7] L. M. Young, et al., "Operations of the LEDA Resonantly Coupled RFQ", Proc. PAC2001 (Chicago, 18-22 June 2001), pp309-313.
- [8] H. V. Smith, Jr. et al., "Low-Energy Demonstration Accelerator (LEDA) Test Results and Plans", Proc. PAC2001 (Chicago, 18-22 June 2001), pp3296-3298.

DEVELOPMENT OF A LOW-ENERGY PROTON ACCELERATOR SYSTEM FOR THE PROTON ENGINEERING FRONTIER PROJECT (PEFP)

J.M. Han, Y.S. Cho, H.J. Kwon, J.H. Jang, K. K. Jeong, Y.J. Kim, S. H. Han, K.T. Seol, M.Y. Park,
J. H. Na, H.H. Lee, B.H. Choi, KAERI, Daejeon, Korea

Abstract

The development of a low-energy proton accelerator has started as the first phase of the Proton Engineering Frontier Project (PEFP). The low-energy proton accelerator system consists of a 50keV proton injector, low-energy beam transport (LEBT), 350MHz, 3MeV radio-frequency quadrupole (RFQ), 350MHz, 20MeV drift-tube linac (DTL), and rf system. The proton injector is under operation, RFQ is testing rf power, and a design of DTL has finished.

1 INTRODUCTION

The Proton Engineering Frontier Project (PEFP) that consists a construction of a 100 MeV proton linac and its application in the industries and the basic science areas is developing in Korea Atomic Energy Research Institute (KAERI) as Korean national research facility. In the first phase, an engineering design and construction for the low-energy proton accelerator system that includes injector, LEBT, RFQ[1], DTL[2] and RF system[3] are underway. In parallel, an applications of keV and MeV proton beams are being developed such as ion irradiators, surface modification of materials. In the second phase, a 100 MeV linac and several beam lines of 20 MeV and 100 MeV will be constructed, and several applications with high current proton beams, and an user program for future extension of the program are planned.

The development of a low-energy proton accelerator has started from September, 2002 at Daejeon. After a 20MeV beam commissioning is finished, we will move a new site.

Subsequent sections of this paper describe the present status of the low-energy linac system.

2 LINAC SYSTEM

2.1 Injector

A dc injector capable of 50keV, 50mA proton beam operation constructed. It uses a dc duoplasmatron proton source. Injector includes proton source, power system, chamber, and diagnostics



Figure 1. Constructed Injector.

2.2 LEBT System

LEBT system was designed with the codes, TRACE 3D, POISON, PARMTEQM, and ANSYS. 2.2m-long test Low Energy Beam Transport (LEBT) system which match between the ion source and the RFQ linac was assembled. LEBT consists of two solenoid magnets, two steering magnets, and a beam line, as shown in Fig. 2.

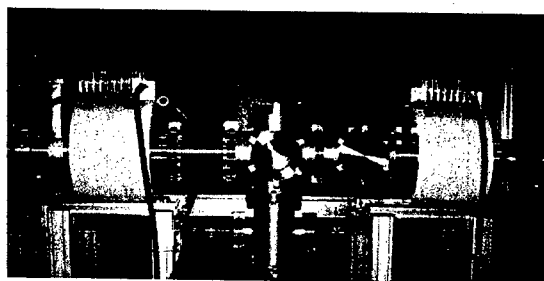


Figure 2. Assembled LEBT System.

The 16cm-i.d, 20cm-long solenoid lenses with polar cores have 72000A/turns, maximum power loss, 8.1kW, and dc fields 5000Gauss at a beam axis. In order to control of X and Y motions, two steering magnets are placed in the LEBT. These can correct 1.7cm horizontal offset on the beam axis.

2.3 RFQ System

The design of the 3MeV RFQ cavity was performed by the beam dynamics codes, PARMTEQM [4], the thermal and stress analysis code, ANSYS, and the cavity design codes, SUPERFISH and MAFIA. The main parameters given in table 1.

Table 1. 3.0MeV RFQ Parameters.

PARAMETER	VALUE
Operating frequency	350 MHz
Particles	Proton
Input / Output Current	21 / 20 mA
Input / Output Energy	0.05 / 3.0 MeV
Input / Output Emittance, Transverse/norm.	0.02 / 0.023 π -cm-mrad rms
Output Emittance, Longitudinal	0.246 MeV-deg
Transmission	95 %
Structure Type	4-vanes
Peak Surface Field	1.8 Kilpatrick
Structure Power	350 kW
Beam Power	68 kW
Total Power	418 kw
Length	324 cm

The RFQ cavity was machined into OFH-Copper and was integrated from four separate 81cm-long sections which was fabricated by vacuum furnace brazing. Fig.3 shows the assembled RFQ system.

The average RFQ cavity structure power by rf thermal loads is 350kW and the peak surface heat flux on the cavity wall is 0.13 MW/m². In the operation of the RFQ, a key issue is to remove this heat. To do it, we constructed 24 longitudinal coolant passages in each of the sections. Total flow designed is 1500l/min with more than 1M Ω -m. In the design of the coolant passages, we considered the thermal behaviour of the vane during an operation, the efficiency of cooling and fabricating cost. Cooling system constructed consisted of 38 flow meters, 38 thermocouples and 19 pressure gauges

In the RFQ, a beam loss designed is about 1mA of proton. Vacuum system[5] constructed to pump beam loss, LEBT gas load and out-gassing from the RFQ cavity and vacuum plumbing. Vacuum pumps which consists of a 600l/min roughing pump and two 3000l/s cryopumps are completely oil-free.

RF feed is in the third section. In order to supply the RF power in the RFQ, we studied an iris-type for 3.0MeV RFQ. The input coupler designed is the tapered ridge-loaded waveguide which is interesting from an electromagnetic point of view since the cutoff frequency is lowered because of the capacitive effect center, and could in principle be made as low as desired by decreasing the gap width sufficiently. The RF vacuum window section consists of a straight WR2300 waveguide which includes a vacuum window and a port for vacuum pumping the waveguide.

Low level RF (LLRF) system constructed include the RF reference, resonance control of the RFQ cavity, klystron control, interlocks, and feedback loop. The main function of the LLRF system is to control RF fields in the RFQ cavity and maintain field stability in the range of $\pm 1.0\%$ peak to peak amplitude and $\pm 1.0^\circ$ peak to peak phase. All RF feedbacks loops will use baseband In-phase and Quadrature techniques. Maximum output power of the LLRF system is 200W. The software control of the LLRF system performs with EPICS.

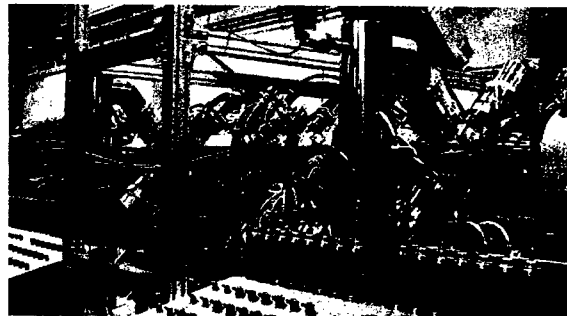


Figure 3. Assembled 3.0MeV RFQ system.

2.4 DTL System

The available structures for the 20 MeV proton accelerator are a coupled cavity DTL (CCDTL), a super-conducting cavity linac, and a conventional DTL. The CCDTL has a merit that the QM can be located at the outside of cavity. Since the high shunt impedance structure should be operated at the higher frequency than that of RFQ, a matching section is necessary to compensate the structure/frequency change and the cavity becomes longer. For the super-conducting cavity, more R&D is necessary for lower beta region. Therefore the most suitable choice is the conventional DTL in spite

of its disadvantage that the QM has to be installed even inside the short first drift tube in the first tank.

The operating frequency of RFQ is 350 MHz and the conventional DTL is also working at the same frequency in order to make the matching easy between RFQ and DTL.

The 20 MeV accelerator should be constructed within next 2 years, and should deliver the proton beam to users. With this schedule, the RF system for 20 MeV DTL should be separated from the other parts of the 100 MeV accelerator. From the construction cost estimate, one RF system for the DTL is preferred. The RF power is limited to 900 kW.

Table 2. DTL design parameters

Parameter	Value
Tank diameter	54.44 cm
Drift-tube diameter	13 cm
Bore radius	0.7 cm
Drift-tube face angle	10 degrees
Drift-tube flat length	0.3 cm
Corner radius	0.5 cm
Inner nose radius	0.2 cm
Outer nose radius	0.2 cm
Stem diameter	2.6 cm
Frequency tolerance	0.001 MHz

The required RF power for the 20MeV DTL is described in Table 3, which is an output results of the PARMILA code considering 25% power margin from the SUPERFISH code input data. The total required power is about 900kW which can be covered with one 1MW klystron.

Table 3: Required RF power for 20MeV DTL

Tank #	Cu power (kW)	Beam power (kW)	Total power (kW)
1	141.6	83.4	225.0
2	138.8	86.2	225.0
3	138.3	85.7	224.0
4	137.1	83.9	221.0
Total (kW)	555.8	339.2	895.0

The power distribution in each tank is within $\pm 1\%$. The schematics of RF power delivery system is shown in Fig. 4. The RF power from one 1MW klystron is split into four legs by magic tee to drive four DTL tanks respectively. Each leg has a phase shifter to adjust the phase of the RF field in each tank. With this type of power distribution, the amplitude of the RF field in each tank can be maintained within $\pm 1\%$ of the design value in spite of feeding equal power into each tank.

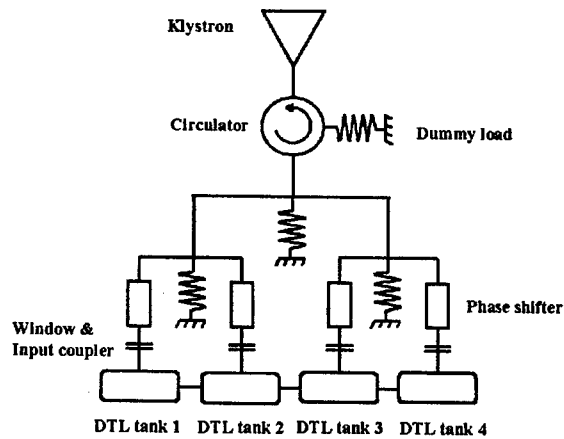


Figure 4. Schematics of RF power delivery system for 20MeV DTL

3 SUMMARY

Injetor and LEBT system has been constructed. The fabrication, electrical test, and vacuum leak test of the RFQ cavity has been completed. The low-energy linac system will be constructed in May, 2005 and the beam commissioning up to 20MeV will be finished. In 2007.

4 ACKNOWLEDGMENT

We are grateful to Dr. L. Young, Dr. R. Valdiviez at LANL, I.S. Ko and Y.S. Bae at PAL, D.S. Lim at DUE Co. Ltd., B.H. Lee and L.H. Whang at Vitzrotech Co. Ltd., C.S. Kim at KumRyung Tec. Co., S.S. Yang at Vectron Co. Ltd. and H.J. Kim at Radionix Co. This work has been supported by the Korean Ministry of Science and Technology (MOST).

REFERENCES

- [1] J.M. Han et al., "3.0MeV KTF RFQ Linac", Proc. of the 2002 Linear Accel. Conf., Gyeongju, Korea.
- [2] Y.S. Cho et al., "Design of 20MeV DTL for PEPF", these proceedings.
- [3] H.J. Kwon et al., "The RF Power Delivery System Design and Its Component Characterization for PEPF DTL", these proceedings.
- [4] K.R. Crandall et al., "RFQ Design Codes", LA-UR-96-1836, (Revised February, 1997).
- [5] M.I. Park et al., "The Vacuum Systems for PEPF LINAC", these proceedings.

- Abbott, S.R. 86
 Abell, D. 1059
 Aberle, O. 45, 878
 Abeyta, E.O. 558
 Ablett, J.M. 241
 Abo-Bakr, M. 3020, 3023
 Abrahamyan, K. 2114
 Achard, C. 495
 Ackermann, W. 3551, 3566
 Adachi, T. 1679
 Adams, D.J. 1527
 Adelman, A. 3524
 Adolphsen, C. 668, 678,
 1264, 2664, 2763
 af Ugglas, M. 1590
 Agarwal, D. 278
 Agustsson, R. 944
 Ahle, L. 989
 Ahrens, L. 51, 405, 1542,
 1545, 1640, 1685, 1697,
 1706, 1715, 2441
 Aiba, M. 1679, 3413, 3452
 Aizatsky, N.I. 1107, 3303
 Ajima, Y. 1978
 Akai, K. 356
 Akiyama, A. 2351
 Akre, R. 235, 2107, 2285,
 3141
 Aladwan, A. 238
 Alber, R. 983
 Albrecht, C. 467
 Al-Dmour, E. 238
 Alduino, J. 2138, 2156
 Aleksandrov, A. 65, 1524,
 2598, 2706, 3536
 Alekseev, I. 51
 Alesini, D. 366, 2080, 2279,
 2500, 2742, 3285
 Alessandria, F. 2080, 3285
 Alessi, J. 51, 89, 1637, 1715,
 2793, 3282
 Alexahin, Y. 1757
 Alexandrov, V. 3536
 Al-Khateeb, A. 2607
 Allen, C.K. 2360, 3527
 Allison, S. 235
 Allison, T. 1485, 2379
 Alsharo'a, M. 1792
 Altmark, A. 1891, 1894,
 1897
 Alton, G.D. 995, 998, 1001
 Ambrosio, G. 1966
 Amemiya, Y. 530
 Ames, F. 2869
 Ammigan, K. 1452
 Amundson, J. 2939, 3195
 Anami, S. 1509
 Anderberg, B. 2318, 2321
 Anders, A. 98, 2622
 Anders, W. 1186, 3020
 Anderson, D. 3141
 Anderson, D.E. 553
 Anderson Jr., J. 1652
 Anderson, R. 2390
 Anderson, S.G. 95, 2957
 Anderson, T.G. 1649, 3437
 Andersson, A. 2318, 2321
 Andler, G. 1590
 Ando, L. 81
 Andonian, G. 944, 947,
 2110, 2112, 3321
 Andreev, N. 1966
 Andreoli, S. 470
 Andresen, N. 869
 Anerella, M. 164, 1939,
 2162
 Anferov, V. 699, 1563
 Ang, Z. 1285
 Anghel, A. 878
 Angoletta, M.E. 2461
 Ankenbrandt, C. 1792,
 2936
 Annala, G. 1730, 1972,
 3062, 3359
 Antokhin, E. 2198
 Anzalone, E. 2382
 Ao, H. 2826
 Aoki, M. 1993, 2198
 Aoki, N. 530, 713
 Aoki, T. 2551
 Apgar, S.E. 553
 Arai, S. 1509
 Arakida, Y. 568, 1512,
 1784, 1807
 Arduini, G. 307, 1718,
 1727, 2240, 3038
 Arkan, T. 1210
 Arnold, N.D. 2327
 Artoos, K. 1434
 Aryshev, A.S. 2709
 Asano, H. 1338
 Asano, Y. 782
 Aseev, V.N. 2875
 Ashmanskas, W. 323
 Asiri, F. 2748
 Aspart, A. 1303
 Assadi, S. 498, 1524, 1569,
 2444, 2706
 Assmann, R. 45, 665, 3494
 Attal, M. 238
 Autin, B. 444
 Averboukh, I.I. 1074
 Avilov, A. 1619
 Ayvazyan, V. 467, 2342,
 2730
 Ayzatsky, M.I. 1605, 2098,
 2878, 2969
 Baartman, R. 1578, 1584
 Baba, H. 3332
 Baba, Y.H. 487
 Baboi, N. 467, 1086, 1261,
 1270
 Babzien, M. 944, 1909
 Baca, D. 312, 536, 553,
 3294
 Bacci, A. 2080, 3285, 3512
 B  cker, H.-J. 836
 Badea, S.V. 2138, 2156
 Bae, Y.S. 2539
 Bagge, L. 1590
 Baggett, K. 2183, 2186,
 2189
 Baglin, V. 307, 1727
 B  hr, J. 2114
 Bahrdt, J. 836
 Bai, M. 51, 54, 405, 1697,
 1706, 2204, 2207
 Baichev, I. 3494
 Bailey, C.P. 1527
 Baishev, I. 45
 Bajko, M. 1942
 Bak, P. 3318
 Bakker, R.J. 214

- Balbekov, V.** 1751, 2014, 2017
Balkcum, A. 1144
Ball, M.J. 1996
Balleyguier, P. 2053, 2458, 2601, 2799
Bandelmann, R. 467
Bandura, L. 1999
Bane, K. 126, 3126, 3252
Banna, S. 722, 1879
Bao, X. 2357
Baptiste, K. 869, 1240, 1252
Bär, R. 694
Barber, D.P. 372
Barletta, W.A. 186, 923
Barlow, D. 702, 1664
Barnard, J.J. 1521, 1990, 2658
Barnes, B. 1736
Barnes, C.D. 1530, 1933, 2101
Barnes, M.J. 1162
Barnes, P. 1309, 1323
Barni, D. 1341, 1506
Barov, N. 1870, 2682
Barr, D. 2512
Barr, G. 1987
Barstow, B. 192, 1317, 1320
Barsz, T. 2029
Bartolini, R. 914, 2077, 3285
Barton, D. 1637
Barty, C.P.J. 95
Baskiewicz, M. 302
Batchelor, K. 541
Batrakov, A. 250
Batygin, Y.K. 2751, 3548
Baudrenghien, P. 1718, 3050
Bauer, P. 1730, 1972, 3359
Bauer, S. 1410, 2887
Baum, D. 2527
Baynham, D.E. 1987
Bazarov, I. 192, 842, 848, 1201, 1317, 1323, 2062
Beard, K. 195, 332, 1104, 1575
Beaudoin, B. 426, 2312, 2571
Beche, J.-F. 2530
Bechstedt, U. 598, 3428
Bechtold, A. 1062
Beck, M. 2189
Beckert, K. 434
Beckman, L. 3389
Beczek, K. 2038
Beebe, E. 89
Beebe-Wang, J. 51, 1706
Beinhauer, W. 3551
Belgroune, M. 896
Bellavia, S. 1542
Bellenger, D.W.J. 1527
Beller, P. 434
Bellodi, G. 1527
Bellomo, P. 235
Bellucci, S. 917, 986
Beloglasov, V.I. 2878
Belohrad, D. 2461
Belomestnykh, S. 192, 1198, 1201, 1306, 1317, 1323, 1326, 1329, 1410, 1437, 2059, 3347
Beltran, C. 326, 3086
Bender, H. 558
Benedetti, G. 366, 2279, 2945
Benedetto, E. 1727, 3053
Benedikt, M. 1548
Bengtsson, J. 195
Benjamin, J. 1715
Bennett, J.R.J. 1527
Bennett, S.L. 189
Ben-Zvi, I. 39, 92, 944, 1300, 1909, 2005, 3186
Berden, G. 519
Berenc, T. 1736, 3362
Berg, J.S. 1804, 1816, 2002, 2210, 2213, 2216, 2219, 3413, 3485
Berg, S. 1416, 1422, 2029, 2038
Berg, W.J. 2417, 2420
Bergqvist, M. 2321
Berio, R. 989
Berkaev, D.E. 372
Berkvens, P. 854
Berman, L. 241
Bernal, S. 426, 1673, 1676, 2312, 2571, 2574, 2577, 2673
Bernard, A. 195
Bernardin, J. 1461
Bernaudin, P.-E. 2799
Bernstein, L. 989
Bertolucci, S. 3285
Bertrand, P. 2802, 3488
Bessonov, E. 1963
Bhashyam, S. 1966
Bhat, C.M. 514, 1769, 2345, 2348, 3180
Bhatt, R. 2643
Biagini, M. 366, 914, 2077, 2279, 2297, 2300, 2945, 3285
Biallas, G. 2123, 2135, 2183, 2186, 2189
Biarrotte, J.L. 1303, 2802
Biasci, J.C. 854
Bieler, T.R. 1359
Bieniosek, F.M. 98, 275, 312, 536, 1518, 2524, 2619, 3297
Bierwagen, J. 1353
Bilderback, D. 192
Bilheux, H. 998
Billen, J. 1461, 1515, 2844, 3518, 3521
Biller, E.Z. 1605, 2878
Billing, M. 3059
Binello, S. 1542, 1703
Bini, S. 917
Binkley, M.E. 2497
Biocca, A. 3374
Birkel, I. 893, 3273, 3276
Biryukov, V.M. 917, 986, 1655, 1691
Biscardi, R. 241
Biscari, C. 335, 366, 684, 2279, 2742, 2945, 3285
Bishofberger, K. 57, 1778, 1781
Bisognano, J.J. 3147
Bizen, T. 487
Björkhage, M. 1590

- Bjorklund, E.** 2354
Black, E. 983, 1792, 1834, 1999
Blair, G. 2739
Blanco-Vinuela, E. 1945
Blasche, K. 589
Blaskiewicz, M. 54, 135, 272, 394, 476, 797, 1195, 1569, 1706, 1715, 1816, 2595, 2598, 3026, 3029, 3035, 3344, 3419
Blind, B. 702, 1664, 2948
Bliss, N. 189, 1029
Blivet, S. 1303
Blokland, W. 1524, 2444, 2491, 2706
Blom, M. 1590
Blomqvist, I. 220
Blue, B.E. 731, 1530, 1864
Bluem, H. 92, 977
Bocchetta, C.J. 214
Boege, M. 3386
Boffo, C. 1210
Bogacz, A. 195
Böge, M. 291
Boggia, A. 3318
Bohl, T. 1718, 3050
Bohlen, H. 1144
Bohn, C.L. 2676
Bohnet, I. 2114
Boilot, D. 1332
Boimelshtein, Y. 3318
Boine-Frankenheim, O. 589, 2607
Bojtar, L. 2461
Boller, K.-J. 1900, 1903
Bolton, P.R. 2104, 2709, 3216
Bondarenco, N. 3329
Bondarev, B.I. 2679, 3002, 3530
Bongers, H. 2872
Bongers, N. 598
Boni, R. 366, 2279, 2742, 3285
Bookwalter, V. 1494
Borburgh, J. 1643
Borchard, P. 1113, 1116
Borden, M. 508, 2521, 3089, 3455
Bordry, F. 1945
Boriskin, V.N. 1107, 2878, 3303
Borissov, E. 1210
Borland, M. 247, 256, 283, 2330, 2417, 2420, 3138, 3461, 3470, 3473, 3476
Borovina, D.L. 553, 1168
Borrion, H. 2458
Bosch, R.A. 887, 929, 932, 935, 2373, 3147
Boscolo, I. 3285
Boscolo, M. 366, 914, 2077, 2279, 2945, 3285, 3548
Bosland, P. 878, 1332
Bosotti, A. 1341
Bossert, R. 1969
Bottura, L. 173, 1730, 1945
Bourcey, N. 1434
Bousson, S. 1303
Bowden, G. 1261, 1264
Bowler, M.A. 189
Boyce, J.R. 938, 941
Boyce, R. 235, 2174
Bozzini, D. 1945
Bradley III, J. 553, 1095, 1168, 1458
Brajuskovic, B. 830, 1017
Brarvar, S. 51
Braud, D. 1303
Braun, H. 495, 1156, 2721
Brautti, G. 3318
Bravin, E. 2464
Bredy, P. 878, 1332
Brelsford, B. 1542
Brenger, A. 2476
Brennan, J.M. 39, 51, 135, 394, 476, 1195, 1545, 1706, 1715, 3026, 3029, 3338, 3341, 3344
Bricault, P. 439, 1584, 1670
Bricker, S. 1353
Briddick, D. 2029, 2038
Bridges, F. 1092
Briggs, R. 3098
Brinkmann, A. 1374, 1395
Briscoe, B. 3282
Britvich, G.I. 917
Brodowski, J. 1195, 2156, 2444, 2598
Broemmelsiek, D. 3431
Broggi, F. 3285
Bromberek, D. 1416
Bross, A. 983, 1183
Broste, W. 558
Browdowski, J. 1428
Browman, A. 326, 508, 2521, 3086, 3089, 3455
Brown, B.C. 2165
Brown, C. 1446
Brown, K.A. 51, 405, 746, 1542, 1545, 1706, 1715, 2441, 2595, 3422
Brown, W. 95, 938, 2192, 2957
Browne, M. 2297
Bru, B. 2802
Brugger, M. 45, 3494
Bruhweiler, D.L. 719, 734
Brumwell, F.R. 592
Brunelle, P. 229, 896
Brunner, O. 473
Bruno, D. 743, 1700, 1706
Bruno, L. 45
Brüning, O.S. 42, 1748
Bui, T. 3560
Bukh, B. 2631, 2634
Bulfone, D. 3395
Bullard, D. 2183
Bultman, N. 1461, 2844
Bunce, G. 51
Burgazzi, L. 1506
Burgmer, R. 1948
Burke, D.L. 1264
Burkhardt, H. 45, 1721, 3041, 3044
Burns, M. 2354
Burov, A. 2020, 3062
Burrill, A. 39, 92
Burrows, P.N. 687
Busch, M. 2273
Bussmann, M. 112
Butler, C. 195

- Butler, J. 1195
 Büttner, T. 467
 Byer, R. 722, 728, 1858
 Bylinsky, I. 1285, 1584
 Byrd, J. 863, 869, 1240, 2530
 Cacciotti, L. 2476
 Cadapan, L. 235
 Cadorna, A. 2348
 Cai, Y. 350, 2288, 2291, 2297, 2300, 3542
 Calaga, R. 39, 272, 2207
 Calatroni, S. 1309
 Callahan, D.A. 2637
 Calvet, O. 1434
 Calzas-Rodriguez, C. 1945
 Cameron, P. 54, 135, 394, 524, 1703, 1706, 2444, 2447, 2598, 2691, 2697, 3026, 3029
 Campbell, L.P. 1909
 Campisi, I. 457, 977, 1104, 1377
 Cao, L. 2852
 Capatina, O. 1434
 Capista, D.P. 2165
 Caporaso, G. 563
 Cappi, R. 388, 2910, 2913
 Carcagno, R. 1969, 1972
 Cardona, J. 1059, 1706, 2901
 Carey, D. 1446
 Carli, W. 2872
 Carlier, E. 1945
 Carlson, C. (Bechtel) 558
 Carlson, C. (BNL) 1715
 Carlson, K. 2020
 Carneiro, J.-P. 2065, 2068, 2114, 3548
 Carr, G. 2354
 Carr, G.L. 241, 1497
 Carr, L. 329
 Carroll, A. 1709, 3255
 Carron, G. 1156
 Carson, J. 1969
 Carter, H. 1210, 1813
 Cary, J.R. 719, 734, 1536, 1885, 1918, 2026
 Casarin, K. 2309
 Casey, B. 241
 Casey, J.A. 547, 1500
 Caspers, F. 1801, 2470, 2700, 3479
 Caspi, S. 42, 170, 1984
 Cassel, R. 235
 Castellano, M. 2476, 3285
 Castro, P. 198, 467, 1086, 2730
 Catalan-Lasheras, N. 1428, 2144, 2225, 2598, 3026
 Catani, L. 2476, 3285
 Cattelino, M. 1144
 Caudill, L. 558
 Cederkell, J. 2869
 Cee, R. 2114
 Celata, C.M. 275, 536, 1518, 1521
 Celona, L. 81
 Cerniglia, P. 2444, 2697
 Chacon-Golcher, E. 73, 3291, 3294
 Chae, Y.-C. 3008, 3011, 3014, 3017
 Chambers, F. 563, 2960
 Champion, M. 1464, 3371, 3377
 Chan, K.C.D. 558, 3210
 Chang, C.H. 1041, 1044, 1047
 Chang, C.K. 2376
 Chang, H.P. 890, 1044
 Chang, J.C. 1476, 1479, 1482, 2402, 2405
 Chang, L.H. 1371, 2670
 Chang, S.H. 2402, 2405
 Chang, X. 39, 1300, 2005, 3186
 Chao, A. 126
 Chao, Y. 195, 294, 3243
 Chao, Z. 487
 Chapman, S. 167
 Chaput, R. 229
 Charrier, J.P. 1303
 Chase, B. 1736, 1769
 Chattopadhyay, S. 195
 Chavanne, J. 253, 854
 Chazot, G. 851
 Cheever, D. 2324
 Chel, S. 878, 1332
 Chen, A. (FNAL) 623
 Chen, A. (YY Labs) 2586
 Chen, C. 1255, 1258, 2643, 2646, 2966
 Chen, C.I. 3234
 Chen, D. 1560, 3506, 3509
 Chen, G. 2586
 Chen, H. 467
 Chen, J. 1044, 2376, 2554, 2557, 2580, 3237, 3392
 Chen, J.R. 821, 1476, 1479, 1482, 2402, 2405
 Chen, L. 2357
 Chen, S. 1921
 Chen, Y.-J. 558, 563, 2960, 3210
 Chen, Z. 2844
 Chen-Yao, L. 764
 Cherbak, E. 1177
 Chesnokov, Y. 917, 986, 1655, 1691
 Cheung, H.W.K. 2488
 Chevtsov, P. 2560
 Chiadroni, E. 914, 3285
 Chiaveri, E. 45, 878, 1309, 1332
 Chiba, J. 1509
 Chichili, D. 1969
 Chien, Y.-C. 764, 767
 Chiesa, L. 170, 1984
 Chin, M. 869
 Chin, Y.H. 479
 Chiou, J. 764
 Chishiro, E. 1338
 Cho, Y.S. 1219, 1222, 2539, 2832, 2857, 2884
 Choi, B. 235
 Choi, B.H. 1219, 1222, 1602, 2539, 2832
 Choi, J. 875, 3383
 Choroba, S. 467
 Chou, P.J. 1368, 3150
 Chou, W. 604, 623, 1551, 1554, 1557, 2922, 2925, 2936

- Chouhan, S.** 899
Chrin, J. 291
Christensen, W. 2485
Christina, V. 920, 977, 2186
Christoph, M. 39
Chu, C. 2360, 2363, 3527
Chu, P. 2366
Chun, M.H. 1470, 2857
Chung, Y.C. 1479
Chupyra, A. 2769
Cialdi, S. 3285
Cianchi, A. 2476, 3285
Ciavola, G. 81
Cimino, R. 1727
Ciocci, F. 3285
Ciovati, G. 1362, 1374, 1395
Citver, G. 39, 92
Clark, G. 601
Clarke, D.G. 1029
Clarke, J.A. 189, 1029
Clarke-Gayther, M.A. 1473
Clauser, T. 3318
Clayton, C. 731, 1530, 1864, 1873, 1933
Clendenin, J. 2104, 2126, 2129, 3216
Cliff, B.E. 2426
Cline, D. 1787, 1876, 1909, 2008, 2709
Clozza, A. 366, 2279, 2742, 3285
Cobb, J.H. 1834
Codner, G. 2399
Cohen, R. 132, 312, 536
Colby, E. 722, 1858, 2101
Cole, J.M. 998
Cole, M. 92, 977, 2047, 2050
Coleman, J. 1485
Colestock, P. 977, 3086
Collier, M. 2844
Collier, P. 307, 1718, 1727
Collins, I. 1727
Collins, J. 699
Collins, S. 1661
Colocho, W. 2297
Compton, C. 1353, 1359, 1362
Conde, M.E. 2032
Coney, L. 1587
Congretel, G. 2799
Connolly, R. 135, 1706, 2444
Cook, E.G. 544
Coosemans, W. 665
Corbett, J. 2369, 2372
Corbett, W. 235
Corlett, J. 186, 812, 866, 923, 1246, 1249, 2086, 2408, 3198
Cornelis, K. 1718, 1727, 3038
Cornelis, M. 1942
Corniani, G. 1341
Corsini, R. 684, 2742
Courant, E.D. 405, 1697, 1816, 3485
Cousineau, S. 117, 259, 1428, 1569, 1572, 2598
Cowan, B. 722, 1855
Cox, L. 1144
Craddock, M.K. 1581
Craft, B. 1053, 2382
Craievich, P. 214, 878
Crandall, K. 1515, 2855
Crandall, K.R. 2889
Crane, J.K. 95
Crappell, A. 2382
Crawford, A. 1312
Crisp, J. 1781, 2348, 2491
Crittenden, J. 1023, 1954, 3425
Crofford, M. 3377
Cross, R.R. 95
Cui, Y. 426, 511, 3156
Cullerton, E. 3068
Cummings, K. 1095, 1237
Cummings, M.A. 1834
Cummings, M.A.C. 983, 1798, 1999
Cupolo, J. 524, 2444, 2697
Cusick, M. 1144
Cutler, R. 550, 617
Czyz, W.S. 592
Dal, A. 229
Dail, J. 2183
D'Alessio, C. 2500
Dallin, L. 220, 2195
Dalmas, D. 558
Daly, E. 457, 977, 1377, 2866
Danailov, M. 214, 2306
Danared, H. 1590
D'Angelo, A. 3285
Danilov, V. 117, 1569, 1572, 2598, 3032
Danilova, E. 2363
Daté, S. 250, 881
Datta, D. 3560
Datte, P. 2530
Dattoli, G. 914, 3285
D'Auria, G. 214
Davidson, R.C. 1667, 2655, 2658, 2661, 2975, 2978, 3117, 3120, 3123
Davino, D. 1428, 2147, 2598, 3035
Davis, G.K. 457, 1383
Davis, H. 120
Dawson, C. 2444, 2453, 2697, 3026
Dawson, W. 524
Day, L. 2429
De Baca, J.M. 1237
DeBarger, S. 3141
DeCarlo, A. 1467, 2706
De Conto, J.-M. 2802
Decker, F.-J. 423, 731, 1530, 1864, 1933, 2282, 2285, 2297, 2300, 2754, 3126, 3129
Decker, G. 833, 2688
Decking, W. 652
Decyk, V. 3174
DeFord, J.F. 3554
Degen, C. 524, 2444, 2697, 3026
Dehler, M. 3395
Dehning, B. 45, 2470
Deibele, C. 1524, 2706
Deitinghoff, H. 1335, 2942
de Jong, M. 220

- Dejus, R.J. 1020
 DeKamp, J.C. 161
 Delaney, T. 690
 Delayen, J. 92, 457, 992,
 1098, 1291, 1380, 1383,
 2379, 2860
 DellaPenna, A. 524, 2444
 Delle Monache, G. 366,
 2279, 2742
 Dell'Orco, D. 235, 2174
 DeLong, J. 476, 1715, 3338,
 3341, 3344
 De Martinis, C. 2080, 3285
 Demidov, N.V. 2878
 Demirkan, M. 2318
 Demma, Th. 2993, 2996,
 2999
 Demske, D. 1497
 Denard, J.-C. 229, 2560
 Denes, P. 2530
 Deng, S. 1530, 1933
 Den Hartog, P. 824, 830,
 833, 1017
 De Ninno, G. 214, 2306,
 2309
 Denz, R. 1945
 Derbenev, Y. 941
 Derenchuk, V.P. 1563
 De Rijk, G. 1942
 Deriy, B. 2261
 Deryuga, V. 1619
 De Santis, S. 186, 866,
 2530, 2745, 3377
 Deslandes, D. 2458
 Desler, K. 2682
 Devanz, G. 878, 1086
 DeVoy, J. 2934
 Devred, A. 42, 146, 173
 Dewan, S. 770
 Dey, J. 1204, 1769, 3353,
 3356
 Diao, C.Z. 968
 Dickson, R. 2563
 Diebele, C. 2444
 Diep, A. 2312, 2571, 2577
 Dierker, S. 241
 Dietderich, D.R. 170, 1032,
 1984
 Dietrich, J. 598, 3428
 Dilley, C.E. 1909
 DiMarco, J. 1730, 1969,
 1972
 DiMauro, L. 217
 Di Mitri, S. 214, 1050
 Dimitrov, D.A. 734
 Ding, Y. 2580
 Di Pirro, G. 366, 2279,
 2476, 3285
 Di Salvo, R. 3285
 Diviacco, B. 214, 1050,
 2306
 Diwan, M. 429, 1709, 3255
 Dobbins, J. 2473, 3347
 DÅbert, S. 495, 1156
 Dodson, G. 1569
 Doelling, D. 899
 Dohan, D.A. 2327
 Doleans, M. 1599
 Dolgashev, V.A. 1264,
 1267, 1276, 2763
 Dolinskii, A. 434, 694
 Dombisky, M. 439, 1584
 Domning, E. 3374
 Donald, M. 2288, 2297
 Dong, H. 195
 Dong, S. 758
 Donley, L.I. 1159
 Dooling, J.C. 592, 1159
 Doolittle, L. 186, 1464,
 2408, 3371, 3377
 Doose, C. 1020
 Doria, A. 3285
 Dormiani, M. 3141
 Dortwegt, R. 630, 2038
 Doss, J.D. 553
 D'Ottavio, T. 1715
 Douglas, D. 195, 938, 977,
 2183, 2186, 2189, 3243
 Dovbnya, A.N. 1107, 2878,
 3303
 Dowell, D. 2104, 3216
 Dowling, A. 439
 Doyle, E. 644
 Doyuran, A. 217, 241,
 1192, 2455
 Drago, A. 366, 2279, 2742,
 3285
 Dragt, A. 2772
 Drees, A. 51, 54, 794, 797,
 1685, 1688, 1691, 1706,
 2691, 2904
 Drees, K. 3026
 Dris, S. 1204
 Drozdoff, J. 638
 Drozhdin, A. 1503, 1557,
 1733, 1742, 2739, 2925,
 2936
 Drury, M. 457
 Ducar, R. 1652
 Ducimetiere, L. 1162
 Dugan, G. 737
 Duke, J.P. 2542
 Du Mont, D. 1542
 Dunkel, K. 2887
 Duperrier, R. 2802, 2805
 Durante, M. 1948
 Durkin, A.P. 2679, 3002,
 3530
 DËrr, H.A. 836
 DËrr, V. 836
 Durtschi, G. 558
 Duru, P. 854
 Dutto, G. 601, 638, 1584
 Dwinell, R.D. 86
 Dykes, D.M. 189
 Eberhardt, W. 836
 Ebihara, K. 860, 1228
 Ecklund, S. 2297, 2300
 Edwards, D. 2068, 2682
 Edwards, H. 447, 1213,
 2682
 Edwards, R.L. 1341, 1344
 Efthimion, P. 98, 2622,
 2655, 2661
 Egawa, K. 1071, 1074
 Ego, H. 250, 487
 Ehrlich, R.D. 2399
 Eichhorn, R. 598
 Eickhoff, H. 694
 Einfeld, D. 238
 Eisen, E. 1122
 Eisert, D.E. 887, 2373
 Ekdahl, C. 558, 3210

- Elioff, T. 235
 Elleaume, P. 854
 Ellis, S. 2841
 Emamian, M. 2273
 Emery, L. 256, 283, 833, 2261, 2330, 2423, 2438, 3461, 3464, 3470, 3473, 3476
 Emhofer, S. 2869, 2872
 Emma, P. 211, 423, 914, 926, 965, 1530, 1933, 3126, 3129, 3138
 Endo, K. 1071, 1074
 Eng, W. 743, 770, 1542, 2144
 England, R.J. 3258
 Enomoto, A. 2838
 Erdelyi, B. 1760, 1772, 3542
 Erdem, O. 1933
 Ereameev, G. 1312
 Erickson, R. 2297
 Eriksson, L. 644
 Eriksson, M. 2318, 2321
 Ernst, D. 2174
 Erokhin, A. 2769
 Errede, D. 983, 1999
 Esarey, E. 719, 734, 1885
 Escallier, J. 164
 Eschke, J. 467
 Espinoza, C. 1664
 Esposito, A. 3285
 Esser, F.M. 598
 Estrada, J. 1763
 Evangelakis, G. 1709
 Evans, I. 235
 Evans, L.R. 19
 Evans, R. 1485
 Eversole, S. 558
 Eylon, S. 98, 558, 1171, 2533, 2616, 2619, 2622, 2625, 2628, 2646, 3098
 Ezura, E. 860, 1228
 Faatz, B. 467
 Fabbriatore, P. 1987
 Fabris, A. 878
 Facco, A. 470
 Falabella, S. 563
 Falce, L. 1113, 1116
 Faltens, A. 536, 1990
 Fan, L. 815
 Fan, M. 1560, 3506, 3509
 Fan, T.C. 1041, 1047
 Fang, J.-M. 1882, 1924
 Fang, S. 1285, 1404
 Fang, Z. 1071, 1074
 Fann, C.-S. 767
 Fantini, A. 3285
 Farinon, S. 1987
 Farkhondeh, M. 956, 959, 980, 2324
 Farrell, J.P. 541
 Farrow, R.C. 189
 Fartoukh, S. 2225
 Farvacque, L. 854, 3189
 Faucett, J. 2354
 Faure, J. 1840
 Faus-Golfe, A. 2240
 Favale, A. 92
 Fawley, W. 186, 558, 923, 959, 3098
 Fedotov, A. 39, 117, 383, 1572, 2589, 2592, 2598, 3032
 Fedurin, M. 1053, 2382, 2892
 Feher, S. 1969
 Feigerle, C.S. 617
 Feikes, J. 845, 3023
 Felden, O. 598
 Feldman, D. 426, 3323
 Feldman, R. 426
 Fellenz, B. 2348, 2491
 Ferguson, P. 1110
 Ferianis, M. 214
 Ferioli, G. 307
 Fernow, R.C. 2002
 Ferracin, P. 170, 1984
 Ferrari, A. 45, 684
 Ferrario, M. 467, 914, 2077, 2080, 2730, 3285, 3548
 Fessenden, T.J. 2533
 Fessia, P. 1942
 Filhol, J.-M. 229, 1332
 Filip, C.V. 1873
 Findlay, A. 2461
 Findlay, D.J.S. 2542
 Finley, D. 1207, 1210, 1813
 Fiorito, R. 1497, 2712
 Fischer, R. 2476
 Fischer, W. 51, 54, 135, 476, 794, 797, 1625, 1697, 1706, 1754, 2222, 2228, 3026, 3029
 Fisher, A. 2285, 2297, 2300
 Fisher, M. 887, 2303
 Fittinghoff, D.N. 95
 Fitzgerald, D. 508, 2521, 3089, 3455
 Fitzgerald, J. 1781
 Flanagan, J.W. 2503
 Flanz, J. 690
 Fliflet, A.W. 1128
 Fliller III, R. 272, 1685, 1691, 1706, 2904
 Floettmann, K. 965, 2114, 3500, 3548
 Flora, F. 3285
 Flora, R. 2491
 Foley, M. 983, 1213
 Folwell, N. 2664
 Fong, K. 601, 1285, 1404, 1488
 Fontenille, A. 2799
 Fontus, R. 138
 Forchi', V. 3395
 Ford, R. 1652
 Forest, E. 397, 1023, 2249
 Foster, G.W. 323, 1649, 1766
 Fox, B. 1688
 Fox, J. 2297, 2300, 3141, 3389
 Fox, W. 1461, 2841
 Frak, B. 1715
 Franchetti, G. 129, 589
 Francis, V. 1029
 Franczak, B. 589
 Franklin, W.A. 2324
 Franzke, B. 434
 Frawczyk, F.L. 2083
 Frayer, D. 558

- Freyberger, A. 195, 2560, 2565, 3243
 Friedlander, F. 1144
 Friedman, A. 132, 275, 312, 536, 1518, 2673
 Friesel, D.L. 699, 1065, 1563
 Frigola, P. 947, 2110, 2112, 2192, 3321
 Frisch, J. 644, 1279, 2545, 2548
 Frischholz, H. 473
 Froidefond, E. 2799, 2802
 Fruneau, M. 2799
 Fu, S. 1455, 1509
 Fu, W. 1685
 Fubiani, G. 719, 1885
 Fuerst, J.D. 1291, 1294, 1297
 Fujii, T. 1978
 Fujita, T. 860, 3077, 3080, 3261
 Fukami, K. 2551
 Fukuda, S. 1509
 Fukui, T. 250
 Fukui, Y. (KEK) 1509
 Fukui, Y. (UCLA) 1787, 1790, 2008, 2709
 Fukuma, H. 860, 3056
 Fuller, R. 235
 Furman, M. 132, 297, 312, 350, 2598, 3219, 3222, 3524
 Furukawa, K. (KEK) 533, 3368
 Furukawa, K. (Osaka U) 755
 Fusco, V. 914, 2077, 3285, 3548
 Gagliano, J. 1416
 Gai, W. 492, 1156, 1810, 1813, 1819, 1888, 1894, 2032
 Galambos, J. 1569, 2360, 2363, 2366, 3527
 Gallagher, R. 167
 Gallardo, J.C. 1909, 2002, 3255
 Gallegos, F. 2515, 2518
 Gallegos, R. 558
 Gallerano, G.P. 3285
 Gallo, A. 366, 2080, 2279, 2742, 3285
 Gamma, F.S. 3285
 Gammino, S. 81
 Ganetis, G. 164, 743, 1431, 1637, 1700, 1706, 2162
 Gao, J. 3264, 3267
 Gardner, C. 51, 1542, 1706, 1715
 Gardner, I.S.K. 1527
 Garnett, R.W. 2613
 Garoby, R. 1724, 2336
 Garrel, N. 1162
 Garren, A.A. 1557, 1787, 1804, 1816, 2008, 2213, 2219, 3485
 Gasser, Y. 1303
 Gassner, D. 54, 794, 1425, 1542, 1691, 2444, 2447, 2450, 2694, 2904
 Gattuso, C. 1649, 1766, 2931
 Gaudreau, M.P.J. 547, 1500
 Gaupp, A. 836
 Gavrilov, N. 2273
 Ge, L. 2664
 Gebel, R. 598, 3428
 Geddes, C.G.R. 1840
 Geer, S. 983, 1183
 Geisler, A. 899
 Gelfand, N. 1557
 Geng, R. 2580
 Geng, R.L. 264, 1309, 1312, 1314, 1317, 1323, 2059
 Genoni, T.C. 3165
 Gensch, U. 2114
 Genser, K. 1763
 Gentzlinger, R. 1341, 2841
 Gerigk, F. 1527
 Geros, E. 73
 Gerth, C. 189
 Gerth, Ch. 911
 Ghalam, A.Z. 3174
 Ghigo, A. 366, 684, 1658, 2279, 2742, 3285
 Ghiorso, W. 2524
 Ghosh, A. 164, 2162
 Giaccone, R. 719, 1885
 Giannessi, L. 914, 2077, 3285, 3548
 Giannini, G. 917
 Gibson, D.J. 95
 Gibson, P. 2706
 Gierman, S. 2104, 2667, 3216
 Gillespie, W.A. 519
 Gilpatrick, J.D. 2512, 3086
 Gilson, E. 98, 2622, 2655, 2661
 Giovannozzi, M. 129, 388, 2910, 2913, 2916
 Giove, D. 2080, 3285
 Giovenale, E. 3285
 Girard, A. 81
 Givens, M. 2029, 2038
 Gjonaj, E. 3563
 Glanzer, M. 426, 2571, 2577
 Glass, H. 1766, 1969, 1972, 2168
 Glöner, C. 1622
 Glenn, J. 51, 405, 746, 1542, 1545, 1706, 1715, 2595, 3422
 Gloor, W. 878
 Gluckstern, R.L. 2592
 Goddard, B. 45, 1646, 1721
 Godlove, T. 426, 1673, 1676
 Goeppner, G. 1416, 2029
 Gold, S.H. 492, 1128, 1147
 Goldin, F. 563
 Golovko, N.G. 1605
 Golub, Yu.Ya. 3101, 3103
 Gomez, J. 1664
 Gonin, I. 48, 1207, 1210, 1213, 2068
 Gonzales, J.M. 553
 Gonzalez, R. 2444
 Goodzeit, C.L. 1996
 Gopych, M. 3569
 Gorbachev, A.M. 1147
 Gordon, D.F. 716, 1846
 Gordon, J. 2860

- Gorelov, D. 2805, 2849, 2972
 Gössel, A. 467, 1086, 1392
 Gottschalk, S.C. 1909
 Gould, H. 1837
 Gould, O. 794, 3282
 Gounder, K. 2928, 3434, 3437
 Gourlay, S.A. 42, 170, 1032, 1984
 Grabosch, H.J. 2114
 Graef, H.-D. 3551, 3569
 Graham, D. 89
 Granata, V. 1945
 Granatstein, V. 1140
 Grau, M. 2444
 Graves, W.S. 217, 329, 956, 959, 980, 1192
 Gray, J.W. 1527
 Green, M.A. (LBNL) 186, 1834, 1987
 Green, M.A. (SRC) 887, 929
 Greenwald, Z. 2056
 Greenway, W. 1171
 Grelick, A. 1416, 1422, 2029, 2038
 Grenoble, C. 457
 Gribble, R.F. 553
 Grice, W. 1524, 2706
 Griep, B. 2887
 Grier, D. 1724
 Griffin, J. 1554, 2922
 Grimm, T. 1350, 1353, 1356, 1359, 1362, 1407, 2849, 2972
 Grippo, A. 1485
 Grisham, L. 2661, 3309
 Grishin, V. 1007, 1010
 Grote, D.P. 70, 275, 1518, 2637, 2673
 Grote, H. 3497
 Gruber, P. 1183, 1413
 Gruner, S. 192
 Gu, A. 2580
 Guan, C.Y. 815
 Guenzel, T. 854
 Guerra, A. 195
 Guethlein, G. 563
 Guetz, A. 2664
 Guidi, V. 917, 986, 1655
 Guiducci, S. 366, 914, 2077, 2279, 2945, 3285
 Guignard, G. 665
 Guilhem, D. 2601
 Guimbal, Ph. 2053, 2458
 Gullotta, J. 54, 794, 1425, 2444, 2694
 Gung, C. 1990
 Gunther, K. 1113, 1116
 Gupta, R. 42, 164, 1748, 1936, 1939
 Guy, F.W. 2889
 Gyr, M. 1646
 Ha, K.M. 2857
 Ha, W. 1861
 Haase, M. 1724
 Haber, I. 426, 511, 536, 1673, 2312, 2574, 2577, 2673, 3156, 3297
 Haberer, Th. 694
 Habs, D. 112, 2869, 2872
 Hacker, K. 423
 Hafalia, R.R. 170, 1984
 Hafizi, B. 716, 1846
 Hafz, N. 1849
 Haga, K. 860
 Hahn, A. 2488, 2491
 Hahn, H. 39, 1625, 1706, 2147, 3035
 Hahto, S.K. 3309
 Hahto, S.T. 3309
 Haimson, J. 2095
 Hajima, R. 3443, 3446, 3449
 Halaxa, E. 3297, 3300
 Halbritter, J. 1374
 Hall, R.P. 3300
 Hamatsu, R. 2709
 Hamm, R.W. 1563
 Hammons, L. 1542, 1691
 Han, J.H. 2114
 Han, J.M. 1222, 2539, 2832, 2857, 2884
 Han, S.H. 2539, 2832
 Han, Y.J. 1470, 2857, 3114, 3383
 Hanaki, H. 2838
 Hanft, R. 1730, 1972
 Hanna, B.M. 2497
 Hanna, S.M. 1077
 Hannink, R. 2625
 Hannon, F.E. 1029
 Hansen, R.W.C. 929
 Hansen, S. 323
 Hara, M. 250
 Hara, T. 487
 Harada, K. 857, 860, 3201
 Hardek, T. 553, 1095, 1168, 1458, 1461
 Hardekopf, R. 1461, 1661
 Harding, D. 1730, 2168
 Hardy, L. 854
 Harkay, K. 508, 592, 2438, 3008, 3011, 3014, 3183
 Harris, J. 426, 2312, 2571, 2577
 Harrison, J. 558, 1237
 Harrison, M. 39, 42, 164, 1748
 Hartemann, F. 95, 938
 Hartill, D. 1309, 2339
 Hartline, R.E. 1792
 Hartman, S. 752, 2270, 2273, 2482
 Hartouni, E. 1446
 Hartrott, M.v. 2114
 Hartung, W. 1350, 1353, 1356, 1362, 1395, 2849, 2972
 Harvey, M. 1715
 Harwood, L. 586, 992, 1098
 Hasegawa, K. 1509
 Hashemi, H. 238
 Hashiguchi, E. 1978
 Hashiguchi, Y. 902, 3270
 Hassanein, A. 1180
 Hassanpour, N. 3389
 Hassanzadegan, H. 238
 Hassenzahl, W. 2162
 Hatano, T. 1165
 Hauviller, C. 1434
 Hawkey, T. 547, 1500

- Hawkins, S. 2533
 Hayano, H. 530, 2545, 2548
 Hayashizaki, N. 2826
 Hayden, D. 2354
 Hayes, M. 2231, 3494
 Hayes, T. 476, 1706, 1715, 3338, 3341
 He, D.H. 968
 He, P. 54, 785, 788, 791, 1425, 2598
 He, Y. 167, 2399
 Hechler, M. 2706
 Heese, R. 217, 241
 Heidenreich, D.A. 553
 Heifets, S. 2297, 2300, 3132, 3135
 Heimann, P. 186, 1032
 Heistermann, F. 3344
 Held, B. 3554
 Hemmer, M. 2390
 Henderson, S. 117, 1467, 1569, 1572, 2598, 3416
 Hendrickson, L. 423, 644, 662, 2545, 2757, 3126
 Henestroza, E. 98, 558, 1171, 2616, 2619, 2622, 2625, 2628, 2637, 2646
 Henn, K. 598, 3428
 Henning, W. 16
 Henrist, B. 1727
 Henrist, H. 307
 Henry, J. 1377, 2866
 Heo, H. 3108
 Heppner, G. 1685
 Herbeaux, C. 229
 Herr, A.D. 617
 Herr, W. 3404
 Herscovitch, A. 39, 92
 Hertel, I. 836
 Herzog, R. 1945
 Hess, M. 2643
 Hettel, R. 235, 761
 Hiatt, T. 2183, 2186, 2189
 Hicks, J.D. 553
 Hicks, R. 195, 2560
 Hicks, W.R. 1377
 Higashi, N. 1978
 Higashi, Y. 2393, 2838
 Hill, A. 235, 1273
 Hill, C. 1029
 Hilleret, N. 307, 788, 1727
 Himel, T. 644, 2757
 Hiramatsu, S. 2503
 Hirashima, T. 1074
 Hirata, K. 2996
 Hirshfield, J.L. 725, 1128, 1131, 1147, 1150, 1882, 1924, 1927, 1930, 2881
 Hitz, D. 81
 Ho, D. 563
 Ho, H.K. 1876
 Ho, S. 620
 Hobl, A. 899
 Hock, J. 1542, 3422
 Hoff, L. 1542, 2444
 Hoffstaetter, G.H. 192, 369, 375, 842, 848
 Höfle, W. 1718, 3038
 Hofler, A. 195
 Hofmann, I. 129, 589, 2592, 2607, 2954
 Hogan, B. 1119
 Hogan, G. 702
 Hogan, J. 457, 1377, 2866
 Hogan, M.J. 731, 1530, 1864, 1933
 Holder, D.J. 189
 Holldack, K. 836, 839, 2527, 3023
 Holloway, M. 426, 2571
 Holmes, J. 117, 1569, 1572, 3503
 Holmes, R. 770
 Holtkamp, N. 11
 Holzscheiter, M. 558
 Honkavaara, K. 467, 911, 2476
 Hopkins, S. 1461
 Horan, D. 1177
 Hori, Y. 809, 860
 Horioka, K. 1807
 Horst, B. 467
 Hosoda, N. 250, 2551
 Hosokai, T. 2258
 Houck, T. 558, 2628
 Hourican, M. 1643
 Hovater, C. 195, 1098, 2379
 Howe, S. 705
 Hseuh, H. 54, 785, 788, 791, 1425, 1715, 2144, 2147, 2390, 2598, 3419
 Hsiao, F.Z. 2402, 2405
 Hsiung, G.Y. 821
 Hsu, K.T. 890, 1044, 2376, 2554, 2557, 3237, 3392
 Hsu, S.-Y. 2376
 Hsu, S.N. 821
 Hu, K.H. 2376, 2554, 2557, 3237, 3392
 Hu, M. 1649
 Huang, C. 1530, 1864, 1933, 3174
 Huang, H. (BNL) 51, 54, 405, 1697, 1706, 1712
 Huang, H. (Yale U) 1688
 Huang, J.Y. 875, 2539
 Huang, M.H. 1047
 Huang, Z. (ANL) 905
 Huang, Z. (SLAC) 329, 3138, 3231
 Hubbard, R.F. 716, 1846
 Hubers, H.-W. 839
 Huelsmann, P. 589
 Huening, M. 467, 2074, 2682, 2730
 Hughes, T. 120, 558, 3210
 Huhn, A. 2444
 Hulbert, S. 241
 Hülsmann, P. 434
 Humphries, S. 3557
 Hung, D.S. 3234
 Hunter, T. 2706
 Huo, Y. 426, 2312
 Hurh, P. 641, 1440, 1443, 1449, 1452
 Hutchinson, E. 1542
 Huttel, E. 893, 3273, 3276
 Hutton, A. 195
 Hwang, C.S. 821, 1041, 1044, 1047, 2376
 Hwang, W.H. 2539, 2857
 Iarocci, M. 1631
 Iazzourene, F. 2306, 2309
 Ieiri, T. 860, 3077, 3080

- Igarashi, S. 568, 755, 1165,
 1807, 2610
 Igarashi, Y. 2838
 Igarashi, Z. 1509
 Igo, G. 51
 Ihee, H. 420
 Ihloff, E. 2324
 Iida, K. 530
 Iida, M. 1978
 Iida, N. 2240
 Ikeda, H. 2503
 Ikeda, M. 3326
 Ikegami, K. 1509
 Ikegami, M. 1455, 1509,
 2393, 2835
 Ilg, T. 2841
 Imai, T. 2829
 Inagaki, S. 568, 1784
 Inagaki, T. 487
 Incurvati, M. 2279, 3285
 Ingrassia, P. 1715
 Irie, Y. 1512, 2509
 Iriso-Ariz, U. 54, 794, 797,
 1706, 1801, 3479
 Isaev, V.A. 1147
 Isagawa, S. 860, 1228
 Ise, T. 755
 Ishi, Y. 1512
 Ishibashi, K. 1784
 Ishikawa, T. 487
 Ishimoto, S. 1834
 Ishizuka, T. 3332
 Ito, T. 1509, 2835
 Ivanov, O. A. 1147
 Ivanov, P.M. 3062
 Ivanov, V. 1137, 2664,
 3312, 3315
 Ivanov, Yu.D. 3530
 Ivanov, Yu.M. 917
 Iversen, J. 467
 Iverson, P. 1530
 Iverson, R. 731, 1864, 1933,
 2285, 2297
 Ives, L. 269, 1110, 1113,
 1116, 1119, 1125, 1127,
 1137, 1140, 1142, 3312,
 3560
 Iwasaki, Y. 902, 2387, 3270
 Iwashita, D. 1807
 Iwashita, Y. 1993, 2198
 Izawa, M. 3201
 Jackson, A. 244
 Jackson, G. 705, 3159, 3162
 Jackson, J. 2153, 2159,
 2390
 Jacob, J. 854, 1332, 3192
 Jacobs, K.D. 887, 929,
 2303, 2373
 Jacobson, E.G. 73
 Jacobson, S. 3374
 Jacques, E. 1303
 Jacquez, E. 558
 Jaeschke, E. 836, 2114
 Jain, A. 39, 164, 1637,
 2159, 2390
 Jamilkowski, J. 1542
 Jamison, S.P. 519
 Jang, J.H. 1219, 2832, 2884
 Jansma, W. 2029
 Jansson, A. 1751, 1763
 Jason, A. 702, 1664, 1966,
 2948
 Javanmard, M. 722, 1855
 Jeanneret, J.-B. 45, 1682,
 3494
 Jennings, B. 307, 1727
 Jensch, K. 467
 Jensen, A. 3315
 Jensen, E. 2467, 2470
 Jensen, J.-P. 749
 Jensen, K.L. 3323
 Jensen, L. 307
 Jeon, D. 107, 1515, 2652,
 2855
 Jeong, K.K. 1222, 2832,
 2884
 Jeong, S.-H. 3114
 Jia, L. 1431
 Jia, Q.K. 968
 Jian, X. 3506, 3509
 Jiang, D. 2852
 Jiang, H. 1359
 Jimenez, J.M. 45, 307, 1727
 Jin, L. 369
 Jines, P. 2382, 2892
 Jing, C. 492, 1810, 2032
 Jing, D.M. 815
 Jinnochi, O. 51
 Jobe, K. 1279, 3141
 Johnson, D. (Bechtel) 558
 Johnson, D. (FNAL) 1649,
 1766, 2931
 Johnson, D. (UCLA) 1530,
 1933
 Johnson, E. 217, 241
 Johnson, G. 2841
 Johnson, J. 558
 Johnson, M. 1350
 Johnson, R.P. 1792
 Johnstone, C. 983, 1446,
 1557, 1649, 1831, 2216,
 2931, 3413
 Jones, F.W. 3404
 Jones, J.K. 2243
 Jones, K. 558
 Jones, R.M. 1261, 1264,
 1270, 2760, 2763
 Jones, T. 716, 1846
 Jones, W.P. 699, 1065, 1563
 Jordan, K. 1485
 Joshi, C. 731, 1530, 1858,
 1864, 1873, 1933
 Joshi, C.H. 1407
 Joshi, P. 2162
 Jowett, J.M. 1682
 Julian, J. 1240
 Julian, R.L. 929
 Jung, J.Y. 3458
 Jungwirth, H. 598, 2811
 Junquera, T. 1303
 Kabel, A.C. 2252, 3539,
 3542, 3545
 Kadokura, E. 1509
 Kaertner, F.X. 959, 980
 Kaganovich, D. 716
 Kaganovich, I.D. 1667,
 2975
 Kageyama, T. 800, 803
 Kahn, S.A. 1709, 3255,
 3413
 Kain, V. 45, 1685
 Kaiser, H. 467
 Kakiyama, K. 2838
 Kako, E. 1338

- Kalantari, B. 238
 Kalinichenko, A.I. 1080
 Källberg, A. 1590
 Kalnins, J.G. 1837, 2951
 Kaltchev, D. 45, 1581, 3494
 Kamikubota, N. 1509
 Kamitani, T. 1225, 3288
 Kamiya, Y. 530
 Kammering, R. 467, 2730
 Kanahara, T. 1978
 Kanareykin, A. 1888, 1891, 1894, 1897
 Kanazawa, K. 806, 2503
 Kandaswamy, J. 167
 Kaneko, N. 3326
 Kang, H. 3180
 Kang, H.S. 1470, 2857, 3383
 Kao, C.C. 241
 Kaplan, D.M. 1183, 1792, 1798, 1834
 Kaplan, R. 1306, 1437, 3347
 Karantzoulis, E. 2306, 2309
 Karataev, P.V. 2709
 Karl, F. 2390
 Karmanenko, S. 1888
 Karpov, G. 250
 Kasemir, K. 3371, 3377
 Kashikhin, V.S. 1966
 Kashikhin, V.V. 1748, 1966, 1969, 1975
 Kashiwagi, S. 3288
 Kashtanov, E. 1781
 Kaspar, K. 589
 Kasper, P.H. 1503, 2936
 Kasuga, T. 860, 1228, 3077, 3080, 3261
 Kato, T. 1455, 1509, 2393, 2835
 Katoh, T. 860, 2351
 Katsouleas, T.C. 731, 1530, 1858, 1864, 1933, 3174
 Katuin, J. 699, 1068
 Kaugerts, J. 2162
 Kawakubo, T. 1165, 1512
 Kawamoto, T. 2351
 Kawamura, M. 1509
 Kawashima, Y. 250, 487
 Kawata, H. 860
 Kedzie, M. 1291, 1294, 1297
 Keeley, D. 235, 2372
 Keil, B. 3386
 Keil, E. 414, 3413
 Keil, R.G. 887
 Kelez, N. 2527
 Keller, L. 2739
 Keller, R. 527, 3306
 Kelley, J.P. 977, 1966
 Kelly, J. 2706
 Kelly, M.P. 1291, 1294, 1297
 Kempkes, M.A. 547, 1500
 Kephart, R. 1972
 Kerby, J.S. 1745, 1969
 Kersevan, R. 854
 Kesar, A.S. 2095, 2536
 Kesselman, M. 524, 2444, 2453
 Kester, O. 2869, 2872
 Kewisch, J. 39, 372, 1300, 1694, 1700, 2005, 2011, 3186
 Khabiboulline, T. 48, 1207, 1210, 1213
 Khachatryan, A.G. 1900, 1903
 Khan, S. 836
 Khodak, I.V. 2098
 Kikuchi, M. 860, 3368
 Kikuzawa, N. 3443, 3446, 3449
 Kim, C. 1849, 1852, 1906, 1912, 2987
 Kim, D.T. 1470, 2857
 Kim, E.-S. 3105, 3108, 3111, 3114
 Kim, G.H. 1849, 1852, 1906, 1912, 2987
 Kim, J.B. 2984, 2987
 Kim, J.U. 1849, 1852, 1906, 1912, 2987
 Kim, K.-J. 905, 1813, 2682, 3138
 Kim, K.R. 1602
 Kim, M.G. 875, 3114
 Kim, S.C. 2857, 3114
 Kim, S.H. (ANL) 1020
 Kim, S.-H. (ORNL) 1365, 1467, 1599
 Kim, T.H. 1539
 Kim, Y. (CHEP) 962, 965
 Kim, Y. (DESY) 962, 965
 Kim, Y.J. 2832, 2884
 Kimura, N. 1978
 Kimura, W.D. 1909
 King, L. 457
 King, Q. 1945
 King, T.C. 2402, 2405
 Kinkead, A.K. 492, 1128, 1147
 Kinoshita, K. 2258
 Kirchgessner, J. 1314
 Kirk, H. 1628, 1631, 1634, 1709, 1787, 2008, 2213, 2219, 3255
 Kishek, R.A. 426, 1673, 1676, 2574, 2577, 2673, 3156
 Kishiro, J. 568, 1509, 1784, 1807
 Kitamura, H. 487, 962, 965
 Kitsuka, T. 902, 3270
 Klein, H. 1335, 2942
 Klein, H.-U. 1948
 Klein, S.B. 699
 Kleman, K.J. 887, 929, 2373, 3147
 Klenov, V. 3282
 Kling, N. 1542
 Klotz, W.-D. 2360, 2363, 3527
 Knapic, C. 1050
 Kneisel, P. 92, 457, 1350, 1362, 1374, 1377, 1395, 1575, 2863
 Knippels, G. 519
 Knobloch, J. 1323
 Ko, I.S. 1852, 2984
 Ko, K. 2664
 Koba, K. 1679, 1736
 Kobayashi, H. 1509
 Kobayashi, M. 860
 Kobayashi, N. 713

- Kobayashi, T.** 1509
Kobayashi, Y. 857, 860, 2171, 3201, 3204
Kobilarcik, T. 1652, 2934
Koch, J.M. 851
Koda, S. 902, 2387, 3270
Kodera, M. 250
Koiso, H. 3368
Kokhanovski, S. 3282
Kolomiets, A.A. 2875
Komada, I. 2351
Kondaurov, M. 2769
Kondo, Y. 1509
Konecny, R. 492, 1156, 1810, 2032
Konkashbaev, I. 1180
Koop, I.A. 372, 2898
Koopman, J. 2470
Kooy, H. 690
Korbly, S. 2095, 2536
Korenev, I. 1013, 1611
Korenev, S. 1013, 1015, 1608, 1611, 1614
Koropsak, E. 3026
Korostelev, M. 2315
Koschik, A. 3044
Koscielniak, S. 1488, 1831, 3413
Koseki, K. 568, 1784, 1807
Koseki, T. 530, 857
Kostin, D. 467
Kostin, M. 1446
Kotlyar, Y. 1542
Kotov, V.I. 917, 1655
Kou, C.H. 1044
Kourbanis, I. 1736, 3353, 3356
Koutchouk, J.P. 2225
Kovach, P. 1939
Kozanecki, W. (CE Saclay) 2739
Kozanecki, W. (SLAC) 2297
Kozub, S. 1781
Kozyrev, E.V. 1128
Kponou, A. 89, 3282
Kraft, G.A. 192
Kramarenko, K. 1605, 2969
Krämer, A. 589
Krämer, D. 836, 1083, 2114
Kramer, S.L. 241
Kramper, B. 2020
Krasilnikov, M. 2114, 3551, 3566
Krasnogolovets, M.A. 1107, 3303
Krasnykh, A. 1137, 3312, 3315
Krause, S. 2324
Krawczyk, F.L. 1341, 1344
Krejcik, P. 423, 1530, 1933, 2297, 3126, 3129
Kreps, G. 467, 1392
Krinsky, S. 217, 3225
Krischel, D. 1948
Krishock, A. 1542
Kroc, T. 2020
Kroll, N.M. 1270
Kroyer, T. 2700
Krusche, A. 1724
Kuan, K.C. 821
Kuba, J. 95
Kubicki, T. 1204
Kubota, C. 1509
Kubota, T. 3335
Kubsky, S. 899
Kucharczyk, A. 2787
Kuchnir, M. 1792
Kudo, K. (AIST) 2387
Kudo, K. (KEK) 860, 2351
Kudo, T. 487
Kuehnel, K.-U. 1622, 2817
Kulikov, A. 2282, 2297
Kulinski, S. 2787
Kulipanov, G. 250
Kumada, M. 1993, 2198
Kumagai, N. 250, 782, 881, 884
Kumaran, R. 1285
Kuo, C.C. 890, 1044
Kuo, C.H. 764, 2376, 2554, 2557, 3234, 3237, 3392
Kuo, K.C. 1476
Kurennoy, S. 920, 977, 1661, 2083, 3515
Kurita, N. 235
Kusche, K.P. 1909
Kushnir, V.A. 1107, 1605, 2098, 2878, 3303
Kuske, P. 839, 1186, 3020, 3023
Kustom, R.L. 1020
Kuzikov, S. V. 1147
Kuzin, M. 250
Kuznetsov, A. 2769
Kuznetsov, G. 57, 1781
Kwan, J. 70, 3291, 3294, 3297, 3300, 3309
Kwiatkowski, S. 1240
Kwon, H.J. 1219, 1222, 2832, 2857, 2884
Kwon, S. 3371, 3377
Lach, J. 2769
Lackey, J.R. 1503, 2168, 2936
Ladd, P. 2706
Ladran, A. 1243, 2023
Lagniel, J.-M. 2601
Lai, S. 1763
Laier, U. 3569
Lamb, D. 426, 2571, 2574, 2577
Lambertson, G.R. 410, 1837
Lambiase, R.F. 550, 743, 770, 2144
Lamm, M. 42, 1730, 1969, 1972
Lamont, M. 45
Lange, R. 467
Langton, J. 235
LaPointe, M.A. 1131
Larbalestier, David C. 151
Larsson, JÅrgen 2321
Laskar, J. 378, 3189
Lau, T. 3563
Lau, W. 1243, 1834
Laurent, J.M. 307
Lauze, R. 195
Laverty, M. 1404
Lawson, Greg S. 288

- Lawson, W. 1119, 1140
 Lawton, D. 138
 Laxdal, R.E. 601, 1488, 1584
 Lazurik, V.M. 1616
 Lazurik, V.T. 1080, 1616
 Le, Tuong N. 3338, 3341
 Lebedev, V.A. 29, 48, 1733, 1739, 1751, 2497, 3062
 LeBlanc, G. 2318, 2321
 Lebrun, P. 1739, 1754, 1763, 2703
 Ledford, J.E. 1341
 Lee, Demi 2376, 2554
 Lee, E.P. 312, 1521, 2658, 2975
 Lee, H.H. 2832
 Lee, H.J. 1849, 1852, 1906, 1912, 2984, 2987
 Lee, H.R. 1602
 Lee, Jinhyung 2026
 Lee, Peter J. 151
 Lee, R.C. 54, 785, 794
 Lee, S.Y. 1065, 3150, 3240
 Lee, Soon-Hong 824
 Lee, W.-T. 426, 2571, 2577
 Lee, Y.-Y. 550, 571, 617, 1569, 1572, 1637, 2144, 2147, 2150, 2153, 2159, 2390, 2598, 3416
 Leemans, W.P. 719, 734, 1840, 1885
 Lefevre, T. 2464
 Legg, R.A. 887
 Lehrach, A. 598, 2811, 3428
 Lei, S.C. 1476
 Leibfritz, J. 2020
 Leitner, D. 86
 Leitner, M.A. 86, 1521, 1990
 Lemaire, J.-L. 2601
 Lemuet, F. 444
 Lenci, S. 1122
 Lenkszus, F. 283, 2435
 Leone, S. 186
 Leontiev, V.N. 553
 Le Pimpec, F. 1279, 2748
 LeSage, G.P. 95
 Lessner, Eliane S. 3467
 Letchford, A.P. 2542
 Leung, K.N. 3309
 Level, M.-P. 229, 1332
 Leveling, A. 1440
 Levi, D. 3285
 Lewandowski, J.R. 1261, 1264
 Lewellen, J.W. 905, 1813, 2029, 2035, 2038, 2132, 2333, 2417, 2420
 Leyh, G.E. 235, 761, 1174
 Li, C. 2357
 Li, D. 186, 1183, 1243, 1246, 1249, 1389, 2023
 Li, G. 968
 Li, H. 426, 1673, 1676, 2574, 2577
 Li, H.C. 2402, 2405
 Li, J. 391, 2270, 2357, 2479
 Li, Juexin 2715
 Li, N. 2174
 Li, R. 208, 941
 Li, Shaoqing 2852
 Li, Shiqui 1560
 Li, W. 2357, 2715
 Li, Xiaoguang 2852
 Li, Y. (ANL) 905
 Li, Y. (Cornell) 620, 2264, 2399
 Li, Yuxiong 2715
 Li, Z. 1264, 2664, 2760
 Liaw, C.J. 617, 2444
 Lidia, S.M. 186, 2086, 2089, 2092, 2682, 3198, 3500
 Liebermann, H. 1335, 2820, 2942
 Lien, M.K. 592
 Liepe, M. 192, 467, 1201, 1317, 1320, 1323, 1326, 1329, 2059, 3347
 Lietzke, A.F. 170, 1984, 1990
 Ligi, C. 2279, 3285
 Likhachev, S. 1010
 Lill, Robert M. 2435
 Lim, J. 2192
 Lima, R.R. 2201
 Limborg, C.G. 235, 329, 2077, 2104, 2667, 3216, 3548
 Limon, P. 42
 Lin, F.Y. 1047
 Lin, M.C. 1371, 2402, 2670
 Lin, Y.C. 1476
 Lindgren, L.-J. 2318, 2321
 Linnecar, T. 1718, 3050
 Lipka, D. 2114
 Litvinenko, V. 391, 752, 2273, 2479
 Liu, C.Y. 1479, 1482
 Liu, G. 2357
 Liu, J.-F. 1341, 1344, 2083
 Liu, J.Y. 968
 Liu, Kuo-Bin 767
 Liu, P. 1452
 Liu, W. 492, 1156, 1810, 2032
 Liu, Y. 998, 2607
 Liu, Zuping 2715
 Lo, Y.C. 3234
 Lockey, R. 550, 1542
 LoDestro, Vincent 3282
 Loew, G.A. 647
 Loewen, R. 1264
 LÅfgren, P. 1590
 Loftsdottir, A. 863
 Logan, B.G. 1521, 2661
 Logatchov, P. 3318
 Loiacono, L. 3183
 Longcoy, L. 2324
 Longo, C. 1428
 Lonza, M. 3395
 Loos, H. 217, 241, 329, 908, 1192, 1497, 2455
 Lopes, M.L. 1596, 2201
 Lopez, A. 2029
 Lorentz, B. 3428
 Lorkiewicz, J. 467
 Lorman, E. 2494, 3062
 Losito, R. 878, 1309, 1332
 Lou, G.H. 1044
 Louie, W. 743, 1431, 1700
 Loulergue, A. 229

- Low, R. 1240
 Lowe, D. 220, 2195
 Lowenstein, D. 1715
 Lu, J. 1285
 Lu, W. 1870, 1933
 Lucas, P. 2925
 Luccio, A.U. 51, 272, 405, 1697, 1936
 Ludewig, H. 1428, 1628, 1709, 2598, 2796
 Ludvig, J. 2625
 Ludwig, M. 2461
 Lumpkin, A.H. 2411, 2414, 2417, 2420, 2423
 Lund, S.M. 132, 312, 536, 1990, 2631, 2634
 Luo, G.H. 890, 1041, 1371, 2670
 Luo, Y. 2123, 2126, 2129, 2132, 2135, 2186
 Luque, A. 3029
 Lusk, M. 2354
 Lyles, J.T.M. 1092
 Lyn, L. 1240
 Lynch, M.T. 553, 1095, 1168, 1458
 Lyneis, C.M. 86
 Lysenko, W.P. 2613
 Ma, H. 1464, 3377
 MacDonald, M.A. 189
 Macek, R.J. 326, 508, 2521, 2598, 3086, 3089, 3419, 3455
 MacGill, R. 1246
 Machida, S. 1512, 1679, 3413, 3452
 Machie, D. 1377, 2866
 Macina, D. 1742
 MacKay, W.W. 39, 51, 54, 164, 405, 1697, 1706, 1712, 1715, 1936
 MacLachlan, J.A. 1554, 1736, 1769, 3180
 MacLean, E.J. 708
 MacLeod, A.M. 519
 MacNair, D. 235
 Madre, B. 1494
 Maebara, S. 2829
 Maesen, P. 1724
 Magome, T. 250, 782
 Mahler, G. 2156
 Maier, R. 598, 2811, 2814, 3428
 Maishev, V.A. 917
 Majeski, R. 2655
 Makarov, O. 2261
 Makita, Y. 1539
 Malafronte, A.A. 2201
 Malagu, C. 917, 1655
 Malitsky, N. 272, 2919, 3482
 Malm, K. 2150
 Malmgren, L. 2321
 Malo, J.F. 2470
 Mammarella, F. 638
 Mammosser, J. 457, 1104, 1386, 2860
 Mansell, J. 1861
 Mao, S. 779
 Mapes, M. 785, 788, 1542, 2141
 Marcellini, F. 366, 2080, 2279, 2742, 3141, 3285
 Marchand, D. 2799
 Marchand, P. 229, 878, 1332
 Marchionni, A. 1649, 3440
 Marcouill, O. 229
 Marechal, X. 487
 Marhauser, F. 1189
 Markiewicz, T. 644, 2739
 Marks, S. 1032, 3458
 Marlats, J.L. 229
 Marneris, I. 746, 1542, 1637
 Maroli, C. 3285, 3512
 Marone, A. 164, 1939, 2162
 Marque, S. 878
 Marques, S.R. 2583, 3279
 Marqversen, O. 2461
 Marr, G. 1542, 1715
 Marriner, J.P. 514, 2928, 3180, 3434, 3437
 Marsden, D. 1110, 1119
 Marsh, K.A. 731, 1530, 1864, 1873, 1933
 Marshall, T.C. 1882, 1924, 1930
 Marsi, M. 2306
 Martens, M. (ANL) 2029
 Martens, M. (FNAL) 1730, 1972, 3359
 Marti, F. 138, 1353, 2649, 2849, 2972
 Martin, D. 235
 Martin, M.C. 863, 869
 Martineau, R. 2841
 Martinelli, G. 917, 1655
 Martinez, D. 2512
 Martini, M. 129, 388, 2913, 2916
 Martins, M.N. 1593, 1596, 2201
 Martovetsky, N. 1990
 Marusic, A. 524, 1706
 Maruyama, A. 1539
 Maruyama, T. 2739
 Masaki, M. 250, 881
 Mastovsky, I. 2095
 Masuda, T. 250
 Masunov, E.S. 2640, 2963
 Matheisen, A. 467
 Matoba, M. 1679, 3452
 Matsui, S. 250, 487, 884
 Matsumoto, H. 487
 Matsuoka, M. 1338
 Mattioli, M. 3285
 Matveev, Yu. 2273
 Mauri, M. 2080
 Mausner, L. 1628
 Mavanur, A. 1407
 Mazzitelli, G. 366, 1658, 2279
 McCarrick, J. 563, 2533, 3557
 McChesney, C.A. 2360, 3527
 McCormick, D. 1279, 2545, 2548
 McCrady, R. 2521, 3086, 3089, 3455
 McCrea, M. 2183
 McCuistian, B.T. 558
 McDonald, J.L. 2385

- McDonald, K.T.** 1628, 1631, 1634, 1709
McGahern, W. 2390
McGee, M. 2020
McIntosh, P. 235, 1273, 3141
McInturff, A.D. 170, 1984
McIntyre, G. 39, 1691, 2904
McKinney, W. 869
McManamy, T. 1572
McMichael, G.E. 592, 1159
McNeil, B.W.J. 189, 950, 953
Mc Nerney, A. 746, 1542
Mead, J. 524, 2444, 2697
Mecklenburg, B. 2095
Medici, G. 3285
Medjidzade, V. 167, 2399
Medvedko, A. 2769
Medvedko, E. 235, 761
Meidinger, A. 558
Meinke, R.B. 1990, 1996
Meisner, K. 1736, 1769
Melin, G. 81
Meller, R.E. 2339
Meng, W. 1637, 2144, 2147, 2159, 2598
Meot, F. 444
Merl, R. 2354, 2515, 2518
Merminga, L. 192, 195, 332
Merrill, F. 702
Mertens, V. 1721
Mertins, H.-C. 836
Merz, W. 749
Messina, G. 3285
Meth, M. 1195
Métral, E. 129, 388, 2913, 2916, 3047
Métral, G. 388, 2913, 2916
Meyer, A. 1542
Meyer, B.J. 73
Meyer, F.W. 998
Meyer, T.S. 2491
Meyer Sr., R.E. 2485
Mezentsev, N. 250
Mezi, L. 914, 3285
Mi, C. 2447
Mi, J. 550, 1640, 2147
Michalek, W. 2029
Michelato, P. 1506, 2071, 2114
Michelotti, L. 1557
Michnoff, R. 1706, 2691, 3026
Miglionico, G. 2150
Migliorati, M. 2077, 3285
Mihalcea, D. 2682
Mihara, T. 2198
Mikado, T. 713, 971, 974
Mikhailichenko, A. 167, 1822, 1825, 1828, 1954, 1957, 1960, 1963, 2399, 2781, 2784, 3350
Mikhailov, S.F. 391, 752, 2273, 2276, 2482
Milani, D. 1945
Milardi, C. 366, 2279, 2742, 2945, 3285
Miles, J. 1942
Miller, R.H. 1264, 2760, 2763
Miller, T. 2382, 2892
Mills, G.D. 998
Milner, R. 956, 959, 980
Miltchev, V. 2114
Milton, S.V. 905, 1813
Minagawa, Y. 860, 3077, 3080, 3261
Minehara, E.J. 3443, 3446, 3449
Minervini, J. 1990
Miram, G. 1110, 1113, 1116, 1137, 1140, 1142, 3312
Mishra, C.S. 1, 1649, 1766, 2928, 3434, 3437, 3440
Mistry, N.B. 167, 2399
Mitchell, D. 1213
Mitra, A. 601
Mitrochenko, V.A. 1107, 3303
Mitrochenko, V.V. 1605, 2098, 2878
Mitsubishi, T. 860, 2503, 2506, 3204, 3207
Miura, T. 2509, 2610
Miyajima, T. 860, 2171
Mizobata, M. 1071
Mizrahi, A. 722, 728
Mizuhara, A. 1142
Mizuhara, M. 1110, 1113, 1116, 1119
Modena, M. 1942
Moffitt, J.R. 2473
Mokhov, N.V. 42, 983, 1503, 1733, 1742, 1745, 1748, 2739, 2936
Möller, W.-D. 467
Molvik, A.W. 132, 312, 536
Monaco, L. 1506, 2071
Moncton, D.E. 959, 980
Monroe, J. 1587, 1652
Monroy, M. 1464, 3377
Montag, C. 51, 135, 1300, 1431, 1694, 1697, 1700, 1706, 2005, 2011, 2691, 2907, 3026, 3186
Montoya, D.I. 1341
Montoya, N. 558
Moog, E.R. 156, 1020
Moore, C. 1652, 2934
Moore, R. 1751, 1754, 2497
Moore, T. 167
Moraes, J.S. 2990
Morcombe, P. 752
Moretti, A. 1183, 1246, 1792, 2023
Morgan, G. 1936
Morgan, J. 641, 1443
Mori, W.B. 731, 1530, 1858, 1864, 1870, 1933, 3174
Mori, Y. 1231, 1234, 1679, 3413, 3452
Moricciani, D. 3285
Morishita, T. 2829
Moritz, G. 589, 2162
Moritz, L. 638
Morley, K. 702
Morris, C. 702
Morris, J. 746, 1542, 1715
Morris, W.A. 1527
Morse, E.C. 3291

- Morvillo, M. 1724
 Mosnier, A. 595
 Mostacci, A. 1801, 2500, 3479
 Mostrom, C. 558
 Mottershead, T. 702, 1664
 Mouat, M. 638
 Moy, K. 558
 Mueller, I. 2823
 Mueller, N. 2823
 Mueller, P.E. 1004
 Muggli, P. 731, 1530, 1864, 1915, 1933
 Muir, A.A. 1029
 Mulholland, G. 1631
 Mullany, B. 1428
 Müller, A.-S. 388, 893, 2913, 3273, 3276
 Mulvaney, J.M. 547, 1500
 Murai, S. 1978
 Murasugi, S. 1165
 Muratore, J. 164, 2162
 Muratori, B. 189
 Murdoch, G. 1467, 2706
 Murokh, A. 944, 2568
 Murphy, B.F. 2104, 3216
 Murphy, J.B. 176, 217, 241, 2455, 2808
 Murray, S.N. 3306
 Musser, S.E. 1356
 Mustafin, E. 589
 Musumeci, P. 1867, 1873, 2117, 2957, 3258
 Muto, A. 1679, 3452
 Muto, M. 755
 Muto, T. 2709
 Myakushko, L.K. 2878
 Myneni, G. 1374
 Na, J.H. 2832
 Nadji, A. 229, 896
 Nadolski, L. 229, 397, 896
 Nagahashi, S. 860, 2171, 2351
 Nagai, R. 3443, 3446, 3449
 Nagaitsev, S. 2020
 Nagaoka, R. 229
 Naito, F. 1509, 2835
 Nakai, H. 3326
 Nakamoto, T. 1978
 Nakamura, E. 568, 1165, 1784, 1807, 2610
 Nakamura, N. 530, 857
 Nakamura, S. 1539
 Nakamura, T. 250, 881
 Nakamura, T.T. 860, 2351
 Nakanishi, H. 860, 1228
 Nakanishi, T. 1539
 Nakano, J. 1231, 1679, 3452
 Nakashizu, T. 3326
 Nakayama, K. 530
 Nam, K.Y. 1602
 Nam, S.H. 1470, 2539, 2857, 3108
 Nantista, C.D. 482, 1276
 Napoly, O. 2718, 2739
 Narang, R. 1873
 Nash, B. 126
 Nassiri, A. 1416, 2038
 Nath, S. 1461, 1515
 Naumenko, G.A. 2709
 Naylor, C. 1542
 Naylor, G. 854
 Nehring, T. 550
 Neil, G.R. 181, 977
 Neilson, J. 269, 1119, 1125, 1127
 Nelson, J. 1279
 Nelson, R. 1098
 Nemesure, S. 1542
 Nenaseva, E. 1888, 1894
 Neri, F. 3086
 Neumann, J. 1497
 Newsham, D. 1153, 1156, 2123, 2126, 2129, 2132, 2135, 2186
 Nexsen, W. 2533
 Nezhevenko, O.A. 1128, 1131, 1147, 1150, 2881
 Ng, C.-K. 235, 1264, 2664
 Ng, K.Y. 1751, 2922, 3065
 Nguyen, D. 977
 Nicklaus, D. 323
 Nicol, T. 1969
 Nicolas, L.Y. 1733
 Nielsen, K. 558
 Nieter, C. 719, 1885, 1918
 Nigorikawa, K. 1509
 Nikitina, T.F. 2878
 Nishimori, N. 3443, 3446, 3449
 Nishimura, H. 244, 397, 1837, 2249, 2385
 Noack, F. 836
 Noble, R.J. 722, 1858
 Noda, F. 1512
 Noda, T. 250
 Nogami, T. 809, 860
 Noguchi, S. 1338, 1509
 Nolden, F. 434
 NÅlle, D. 2476
 Nomura, M. 530
 Norbrega, A. 1969
 Nordberg, E. 2399
 Norem, J. 1180, 1183, 1246, 1999
 Norris, B. 983
 Nosochkov, Y. 2288, 2291, 2300
 Novati, M. 1506
 Novokhatski, A. 315, 2294, 2297, 2300, 2981
 Nusinovich, G. 1140
 Nzeadibe, I. 235
 Oakeley, O. 752
 Obina, T. 860, 2351, 3077, 3080, 3201, 3207, 3261, 3365
 Ochiai, Y. 902, 3270
 O'Connell, C.L. 423, 731, 1530, 1864, 1933, 3126, 3129
 Odagiri, J. 2351
 Odajima, W. 1978
 Oepts, D. 519
 Oerter, B. 54, 1640
 Ogata, A. 3335
 Ogawa, H. 713, 971, 974
 Ogawa, Y. 3368
 Ogitsu, T. 1978, 3413
 O'Hara, J.F. 2512
 Ohashi, Y. 250

- Ohgaki, H. 713, 902, 2387, 3270
 Ohhata, H. 1978
 Ohishi, M. 884
 Ohkuma, H. 881
 Ohmi, K. 345, 353, 3053, 3056, 3083, 3398
 Ohmori, C. 1216, 1234, 1679, 3413, 3452
 Ohnishi, Y. 3056, 3288
 Ohnuma, S. 1557
 Ohsawa, S. 2838, 3326
 Ohsawa, Y. 860
 Ohshima, T. 250, 782, 881, 2551
 Ohuchi, N. 1978
 Oide, K. 353, 2604
 Oishi, M. 250, 782
 Okada, M. 1509
 Okamoto, H. 2592
 Okamura, M. 164, 1936
 Oleck, A.R. 1649
 Olsen, J. 235, 761
 Olson, C.L. 2685, 3165
 Olson, M. 1781
 Onishi, Y. 860
 Onisto, H.J. 2583, 3279
 Ono, M. 860, 1228
 Onoe, K. 487, 3332
 Oogoe, T. 2838
 Oothoudt, M. 2354
 Oppelt, A. 2114
 Orikasa, T. 1978
 Oro, D. 558
 O'Rourke, S. 2975
 Orris, D. 1969
 Ortega, M. 235
 Orzechowski, T. 3557
 O'Shea, P.G. 426, 511, 1497, 1673, 1676, 2312, 2571, 2574, 2577, 2673, 2712, 3156, 3323
 Österdahl, F. 1590
 Ostiguy, J.-F. 2168, 2925, 3503
 Ostojic, R. 42
 Ostroumov, P.N. 400, 2426, 2790, 2875, 2963, 3467
 Otboev, A.V. 372, 2898
 Ott, K. 773, 776
 Ottaviani, P.L. 3285
 Ottavio, D. 2360
 Owen, H.L. 189
 Owens, T.L. 3344, 3380
 Oz, E. 1530
 Ozaki, T. 860
 Ozelis, J.P. 1491, 1494
 Paál, A. 1590
 Padamsee, H. 192, 1201, 1309, 1312, 1314, 1317, 1320, 1323, 1410, 2059
 Pagani, C. 467, 1300, 1341, 1506, 2114
 Page, T. 1969
 Pai, C. 550, 2144, 2147
 Pakter, R. 1134, 2990
 Palmer, D.T. 1858, 2107
 Palmer, M.A. 2267, 2473
 Palmer, R. 1816
 Palmer, R.B. 1804, 1834, 1987, 2002, 3413
 Palumbo, L. 944, 2500, 3285
 Pantell, R.H. 1909
 Paoluzzi, M. 1724
 Papaphilippou, Y. 123, 851, 854, 1569, 2159, 3053, 3189
 Paparella, R. 470
 Pappas, C. 235
 Paramonov, V. 2826
 Pardo, R.C. 2426, 2875
 Park, B.R. 1470
 Park, B.S. 1602
 Park, E.S. 875
 Park, H.J. 3383
 Park, J.H. 2539
 Park, M.Y. 1219, 2832, 2884
 Park, S. 235
 Park, S.-S. 3114
 Park, S.J. 2539
 Parker, B. 372
 Parkhomchuk, V. 2769
 Parmigiani, F. 186
 Parodi, R. 1395
 Parsa, Z. 3005
 Partridge, R. 644
 Parzen, G. 2589
 Pasky, S. 1419, 2038, 2333
 Pasotti, C. 878
 Pasquinelli, R.J. 3068, 3431
 Pate, D. 39, 92
 Pattengale, N. 2360
 Pattengale, N.D. 3527
 Patton, J. 2363
 Paul, A.C. 2533, 2960
 Paul, K. 2931
 Paulon, R. 1506
 Payet, J. 2718
 Pearson, C. 1264
 Peatman, W.B. 836
 Pedersen, F. 2461
 Pedrozzi, M. 878
 Peggs, S. 39, 42, 135, 278, 372, 797, 1059, 1691, 2204, 2901, 2904
 Pei, Y.J. 818, 2852
 Peiniger, M. 1410
 Pekeler, M. 1410, 2887
 Pelaia, T.A. 2360, 2363, 2366, 3527
 Pellegrini, C. 211, 944, 1867, 1873
 Pellegrino, L. 366, 2279, 3285
 Pellico, W.A. 1587, 2936, 3177
 Peñano, J.R. 716
 Penco, G. 878
 Penel, C. 253
 Peng, Z.H. 601
 Perevedentsev, E.A. 2898, 3398
 Perez, F. 893, 3273, 3276
 Perezhogin, S.A. 1605
 Peschke, C. 434
 Peters, H.-B. 467
 Peterson, D. 3068
 Peterson, E. 1294
 Peterson, P.F. 2637
 Peterson, T. 1966, 1969
 Petra, M. 1020

- Petracca, S. 2993, 2996, 2999
- Petrillo, V. 3285, 3512
- Petrossyan, B. 2114
- Petrosyan, G. 470
- Petrinin, A.A. 917
- Petry, J.E. 1500
- Peyrot, M. 1948
- Pfeffer, H. 1781
- Pfister, U. 598
- Phillips, D. 1542
- Phillips, L. 1401, 2860
- Phinney, N. 678
- Picardi, L. 3285
- Pichoff, N. 2601, 2802, 3491
- Pieck, M. 1168
- Piekarz, H. 1649, 1981
- Piel, C. 2887
- Pierini, P. 1300, 1506
- Pikalov, V.A. 917
- Pikin, A. 89
- Pilat, F. 42, 51, 1697, 1703, 1706, 1712, 2207
- Pillai, C. 2515, 2518
- Piller, M. 3377
- Pinayev, I. 752, 2273
- Pindak, R. 241
- Piot, P. 911, 2682, 3500
- Pirkl, W. 186
- Pivi, M. 350, 2598, 3219, 3222
- Pjerov, S. 241
- Placidi, M. 186, 2530
- Plan, B. 253
- Planet, M. 2799
- Plant, D. 2769
- Plate, D. 1240
- Plate, S. 164, 1939
- Platz, M. 3569
- Plawski, E. 467, 2787
- Plawski, T. 195, 2379
- Plettner, T. 722, 1861
- Plouviez, E. 851, 854
- Plum, M.A. 2429, 2444, 2485
- Podlech, H. 1335, 2820, 2942
- Podobedov, B. 241, 2808
- Pogge, J. 1524, 2706
- Pogorelsky, I.V. 1909
- Poirier, R. 601, 1285, 1584
- Polozov, S.M. 2963
- Ponnaiyan, V. 54, 794
- Pont, M. 893, 3273, 3276
- Poole, M.W. 189, 950, 953
- Popenko, V.A. 2878
- Popov, G.F. 1080, 1616, 1619
- Popov, V.G. 752, 2273
- Popova, N. 1619
- Popovic, M. 983, 1792
- Pordes, S. 2491
- Portmann, G. 890, 2369, 2372, 3213, 3374
- Potter, J. 2354
- Potter, K. 1467, 2706
- Potylitsyn, A.P. 2709
- Poupeau, J.P. 1303
- Power, J. 1661, 2429, 3371, 3377
- Power, J.G. 492, 1810, 1813, 1888, 1894, 2032, 2432, 2667
- Power, K. 1936, 1939
- Powers, T. 457, 2379
- Pozdeyev, E. 138, 2649
- Prasuhn, D. 598, 3428
- Preble, J. 457, 977, 1104
- Prebys, E.J. 1503, 1587, 1652, 2936
- Preger, M.A. 366, 684, 1658, 2279, 2945, 3285
- Preis, H. 1309
- Prelec, K. 89
- Prestemon, S. 1032
- Prichard Jr., B.A. 73
- Prior, C.R. 1527
- Proch, D. 467
- Prochnow, J. 2467
- Prokop, M. 3371, 3377
- Prom, M. 2601
- Prost, A. 1643
- Prost, L.R. 275, 312, 536, 1518, 2524
- Przeklasa, R.S. 1168
- Ptitsyn, V. 51, 54, 135, 372, 405, 1697, 1703, 1706, 1712
- Pu, Y. 1539
- Puccio, B. 1945
- Pugachev, G.D. 2878
- Pugnat, P. 1942
- Purcell, D. 2444, 2706
- Pusina, J. 2086
- Qian, B.L. 2646, 2966
- Qian, Z. 1183, 1246
- Qiang, J. 1509, 2613, 2954, 3401
- Qin, B. 3506, 3509
- Qin, H. 2655, 2658, 3117, 3120, 3123
- Quan, S. 2580
- Quast, T. 836
- Quattromini, M. 914, 2077, 3285, 3548
- Quigley, P. 1410, 1437
- Quimby, D.C. 1909
- Quinn, B. 426, 1673, 2312, 2571, 2574, 2577, 2673
- Quinn, F.M. 189
- Quirus, M. 2571, 2577
- Rabedeau, T. 235
- Rabehl, R. 1969
- Radovinsky, A. 1990
- Raguin, J.-Y. 2724
- Raimondi, P. 366, 731, 2279, 2766, 2945, 3285
- Raino, A. 3318
- Raja, R. 1446
- Raka, E. 2595
- Rakhno, I.L. 983, 1742, 1745, 1748
- Rakowsky, G. 217
- Ranjbar, V. 3062
- Rank, J. 39, 1467, 2150
- Rao, Y.-N. 1578, 1584
- Raparelli, M. 2476
- Raparia, D. 571, 1428, 1467, 1569, 1572, 1637, 1709, 2150, 2153, 2156,

- 2390, 2598, 2793, 3282, 3416
- Rarback, H.** 235
- Rathke, J.W.** 92, 920, 977, 2186, 2790
- Ratti, A.** 186, 1464, 2530, 3371, 3377
- Ratzinger, U.** 1062, 1335, 2820, 2942
- Raubenheimer, T.O.** 662, 1038, 2739, 2754, 2757, 2760, 2775, 3219, 3231
- Ravel, J.-C.** 2799
- Rawnsley, W.** 601
- Read, M.E.** 1113, 1116, 1119, 1137, 1140, 1142
- Reass, W.A.** 553, 1168
- Redaelli, S.** 665
- Redlin, H.** 2114
- Reece, C.** 1377, 1398, 1494
- Reece, K.** 1569
- Reed, C.A.** 998
- Rees, D.E.** 553, 1095, 1168, 1458
- Rees, G.H.** 1527, 1557
- Regan, A.** 3371, 3377
- Rehlich, K.** 467, 2342, 2476
- Reichardt, G.** 836
- Reiche, S.** 211, 944, 947, 2110, 2112, 3153, 3321
- Reich-Sprenger, H.** 589
- Reid, J.** 48, 1204, 1213, 1769, 3353
- Reilly, J.** 1306
- Reiser, M.** 426, 511, 1673, 1676, 2312, 2571, 2574, 2577, 2673, 3156
- Rej, D.** 1461
- Remondino, V.** 173
- Renieri, A.** 3285
- Rensfelt, K.-G.** 1590
- Repikhov, G.D.** 2878
- Reprintzev, L.V.** 2878
- Reschke, D.** 467
- Resende, X.R.** 1056
- Reshetnyak, N.G.** 1107, 3303
- Reuter, A.** 92
- Revol, F.** 253
- Revol, J.L.** 851, 854
- Rey, J.M.** 1987
- Reynolds, J.** 2354
- Rhee, S.J.** 2177
- Ricci, R.** 366, 2279, 3285
- Rice, D.** 167, 278, 2399, 3425
- Richards, D.** 2844
- Richardson, R.** 563
- Reiche, S.** 203
- Richichi, S.** 167
- Richter, A.** 3551, 3569
- Ries, T.** 601, 1488
- Rifflet, J.-M.** 1948
- Rimmer, R.A.** 186, 977, 1104, 1183, 1243, 1246, 1389, 2023, 2092
- Ringwall, A.** 235
- Rinn, J.** 1942
- Rinolfi, L.** 684, 2742
- Rios, P.B.** 1593, 1596
- Riot, V.** 2530
- Ritson, D.** 1557
- Ritter, J.** 89, 3282
- Rivetta, C.** 3362
- Rizzato, F.B.** 2990
- Robb, G.R.M.** 950, 953
- Robin, D.** 224, 397, 2246, 2249, 3213
- Robinson, K.** 186
- Robinson, T.** 1119
- Roblin, Y.** 195
- Robothom, W.** 2168
- Rock, B.Y.** 2473
- Rockford, J.H.** 1987
- Rode, C.H.** 977, 2863
- Rodriguez, M.** 1237
- Rodriguez, J.** 138, 2649
- Rodriguez, L.** 558
- Rodriguez, P. (LANL)** 558
- Rodriguez, P. (SLAC)** 235
- Rodriguez-Mateos, F.** 1945
- Rogers, G.** 2303
- Rogers, J.T.** 375
- Rogov, Yu.V.** 1616
- Rohlev, A.** 2336
- Rom, M.** 3285
- Romanov, G.** 48, 1210
- Romas'ko, V.G.** 1107
- Romè, M.** 3285
- Romero, D.** 2354
- Roncarolo, F.** 2470
- Ronsivalle, C.** 914, 2077, 3285, 3548
- Root, L.** 1584
- Ropert, A.** 851, 854, 3189
- Rose, C.R.** 2485
- Rose, D.V.** 98, 2622, 2637, 2685, 3165
- Rose, J.** 217, 241, 1192, 2455, 2808
- Roseberry, T.** 1467
- Rosenberg, R.A.** 508, 3183
- Rosenthal, S.** 690
- Rosenzweig, J.B.** 95, 914, 944, 947, 1533, 1858, 1867, 1870, 1873, 2110, 2112, 2117, 2192, 2957, 3153, 3258, 3285, 3321
- Roser, R.** 1706
- Roser, T.** 24, 39, 51, 54, 405, 1545, 1637, 1697, 1715, 1936, 2204, 2793, 3026
- Ross, I.N.** 189
- Ross, M.C.** 503, 678, 1279, 2494, 2545, 2548, 2709
- Roszbach, J.** 2114
- Rossen, P.v.** 598
- Rossi, A.** 307, 1727
- Rossi, C.** 1724
- Rossi, L.** 42, 141
- Rossmannith, R.** 899, 3273
- Rotela, E.** 2790
- Roth, I.S.** 547, 1500
- Rothgeb, T.** 1377, 1386
- Roudier, D.** 1303
- Rouleau, G.** 73
- Rowley, L.** 2303
- Rowton, L.** 2841
- Roy, P.K.** 98, 2616, 2619, 2622, 2625, 2628
- Roybal, R.J.** 1341, 1661
- Roybal, W.** 1095, 1458
- Royer, P.** 684

- Rubin, D.L. 1023, 2056,
 2267, 3425
 Rudolph, K. 2869, 2872
 Rudychev, V. 1619
 Ruegg, R. 638, 1584
 Ruggiero, A.G. 1637, 2793,
 2796
 Ruggiero, F. 42, 45, 123,
 1727
 Ruggiero, R. 1748
 Ruggles, S.C. 1168
 Ruland, R. 2769
 Rumolo, G. 123, 1727,
 2234, 2607, 3038, 3041,
 3044, 3053
 Rusek, A. 1542
 Rusnak, B. 989, 1347
 Russell, A. 1652
 Russell, S. 977
 Russo, T. 1545, 3422
 Rust, K. 550, 770
 Rust, W.W. 635
 Ruth, R.D. 1264
 Ryan, J. 1542, 2595
 Rybarcyk, L.J. 1092, 1566,
 3086
 Ryne, R.D. 1509, 2954,
 3401
 Saban, R. 1945
 Sabbi, G. 42, 170, 536,
 1032, 1521, 1984, 1990
 Sabol, D. 2399
 Saeki, H. 250
 Saewert, G. 1781, 2020
 Safranek, J. 235, 890, 3213
 Sagan, D. 192, 848, 1023,
 2267
 Sahuquet, P. 1303
 Saigusa, M. 2829
 Saino, K. 487
 Saito, K. 462
 Sajaev, V. 417, 905
 Sakai, H.R. 530, 857
 Sakai, I. 1512, 1679, 3452
 Sakamoto, Y. 860
 Sakanaka, S. 860, 1228,
 3207, 3365
 Sakuda, M. 1807
 Sakumi, A. 312
 Saleh, N. 1921
 Sanchez, B.J. 2515
 Sanchez, M. 558
 Sandberg, J. 550, 571, 743,
 746, 770, 1640, 2144, 2147
 Sanderson, D. 138
 Sandner, W. 836, 2114
 Sanelli, C. 366, 2279, 2742,
 3285
 Sanfilippo, S. 173
 Sannibale, F. 863, 1658,
 2527
 Santucci, J. 2682
 Sapozhnikov, L. 3389
 Sarraf, R.H. 238
 Sasaki, S. (ANL) 2261
 Sasaki, S. (SPRING-8) 250,
 782
 Sato, H. 568, 755, 1165,
 1807, 1981
 Sato, M. 860
 Sato, Y. (IU) 3240
 Sato, Y. (KEK) 1679, 2509,
 3452
 Satogata, T. 51, 54, 272,
 278, 405, 1697, 1706,
 1712, 1715, 2204, 2207,
 2697, 2901, 3026, 3482
 Satoh, M. 533, 860, 3368
 Sauer, A. 1335, 2820, 2942
 Saugnac, H. 1303
 Saunders, A. 702
 Saunders, J. 2860
 Savage, R. 2390
 Savalle, A. 2802
 Savary, F. 1942
 Savatteri, S. 746
 Sawamura, M. 3443, 3446,
 3449
 Sazawa, S. 2829
 Scaduto, J. 39, 92, 1631
 Scandale, W. 173, 986,
 1655
 Scanlan, R.M. 170, 1032,
 1984
 Scarlett, C. 3255
 Scarpine, V. 2414, 2494,
 3062
 Scarvie, T. 869, 2527, 3374
 Schächter, L. 722, 728,
 1879
 Schaerf, C. 3285
 Schaetz, T. 112
 Schaller, S. 2354
 Schamel, H. 3029
 Schappert, W. 323, 2494
 Schauer, M. 558
 Scheer, M. 836
 Scheidt, K. 854
 Scheitrum, G. 3312, 3315
 Schellong, B. 1948
 Schempp, A. 598, 1062,
 1622, 2817, 2823
 Schilcher, T. 3386
 Shimizu, J. 250
 Schindl, K. 1682
 Schirm, K.-M. 1948
 Schlabach, P. 1730, 1969,
 1972
 Schlarb, H. 423, 467, 2074,
 2730, 3126, 3129
 Schlitt, B. 694, 1062
 Schlott, V. 3386
 Schlueter, R. 1032, 3458
 Schmalzle, J. 1939, 2162
 Schmekel, B.S. 375
 Schmerge, J.F. 2104, 3216
 Schmidt, C.W. 2020
 Schmidt, F. 1754, 1757,
 2207, 2228, 2231, 3494,
 3497
 Schmidt, P. 1948
 Schmidt, R. 45, 1945
 Schmidt-Bäcking, H. 1622
 Schmidts, F. 1775
 Schmor, P. 6, 439, 1584
 Schnase, A. 598, 1216,
 1234, 2817, 3428
 Schneider, H. 598, 3428
 Schneider, W.J. 2863
 Schnitter, U. 2201
 Schoenlein, R. 186, 2408,
 2530
 Schrage, D.L. 920, 977,
 1341, 1344, 1661, 2083,
 2790

- Schramm, U. 112
 Schreiber, S. 467, 911, 1086, 2068, 2071, 2114, 2730
 Schreuder, A.N. 699
 Schroeder, C.B. 1885
 Schuett, P. 589
 Schuh, P. 2297
 Schulte, D. 657, 662, 665, 1727, 2721, 2727, 2733, 2736, 2739, 2757, 3053
 Schultheiss, C. 524, 743
 Schultheiss, T.J. 92, 920, 977, 2186, 2790
 Schultz, D. 2129
 Schultz, J. 1990
 Schultz, R. 1443, 1449, 1452
 Schulze, M. 3086
 Schumann, R. 2114
 Schussmann, G. 2664
 Schwartz, H. 235
 Schwarz, H. 1273, 2297, 3141
 Scott, B. 235
 Scott, D.J. 1029
 Sears, C.M. 2101
 Sears, J. 1309, 1312, 1314, 1323, 1410
 Sebek, J. 235, 2494
 Seberg, S. 2156
 Seddon, E.A. 189
 Seeman, J. 315, 2294, 2297, 2300
 Sei, N. 713, 971, 974
 Seidl, P.A. 275, 312, 536, 1518, 1990
 Seifrid, P. 3068
 Seike, T. 487
 Sekachev, I. 601
 Sekutowicz, J. 467, 977, 1086, 1300, 1374, 1377, 1392, 1395, 1575, 2730, 2866
 Seletsky, S. 2020
 Semenov, A. 323, 1781
 Semertzidis, Y.K. 1625
 Sen, T. 34, 42, 1754, 1757, 1760, 1772, 1775, 3401, 3542
 Senf, F. 836
 Senichev, Y. 598, 2814
 Seo, J.-H. 3114
 Seol, K.T. 2832, 2857
 Serafini, L. 914, 2077, 2080, 3285, 3512
 Serdobintsev, G.V. 2881
 Sereno, N.S. 247, 827, 2420, 2435
 Serio, L. 1945
 Serio, M. 366, 2279, 2742, 3285
 Serrano, J. 2336
 Serriere, V. 3192
 Sertore, D. 1506, 2071, 2114
 Seryi, A. 657, 662, 2739, 2748, 2754, 2757, 2766, 2769
 Sessler, A.M. 414, 3413
 Setzer, S. 2114, 3566, 3569
 Severino, F. 1195, 2441
 Sezaki, K. 487
 Sgamma, F. 366, 2279, 2742
 Shaftan, T. 217, 241, 329, 908, 1192, 1497, 2455, 2808
 Shang, H. 247, 283, 2330, 3461, 3470, 3473, 3476
 Shang, J. 1452
 Shao, L. 1876
 Shapiro, A.H. 1341, 1344, 2083
 Shapiro, M.A. 1255, 1258, 2536
 Shapiro, S. 2796
 Shaposhnikova, E. 1718, 3050
 Sharamentov, S.I. 1291, 2426, 2790
 Sharma, S. 2790
 Sharp, W. 2622
 Sharp, W.M. 98, 2637
 Shatunov, P.Yu. 2898
 Shatunov, Yu.M. 372, 2898
 Shaw, R.W. 617
 Shchelkunov, S.V. 1924
 Shea, T.J. 1569, 2444, 2706
 Sheehy, B. 217, 241, 329, 1192, 1497, 1819, 2455, 2808
 Sheinman, I. 1888, 1891, 1897
 Shelley, F. 2515, 2518
 Shelley, Jr., F. 2354
 Shemelin, V. 192, 1201, 1314, 1317, 2059
 Shemyakin, A. 2020
 Shen, J.L. 519
 Shen, L. 2852
 Shen, S. 1347
 Shen, Y. 217, 2455
 Shendrik, V.A. 2878
 Shepard, K.W. 581, 1291, 1294, 1297
 Shephard, M. 3560
 Sheppard, J.C. 2751
 Sherman, J. 73
 Sherwood, R. 1661
 Shi, J. 369
 Shibata, K. 800, 803, 806
 Shigaki, K. 1512
 Shiho, M. 1807
 Shiltsev, V. 48, 57, 1739, 1751, 1754, 1757, 1778, 1781, 2497, 2769, 3062
 Shimada, T. 1512
 Shimizu, N. 1165
 Shimosaki, Y. 568, 1807, 2610
 Shinoue, K. 530
 Shintake, T. 487, 962, 965, 3332
 Shintomi, T. 755, 1978
 Shioya, T. 860
 Shirakata, M. 568, 1807, 2610
 Shishido, T. 1338
 Shishlo, A. 117, 2360, 2363, 2366, 3527
 Shkaruba, V. 250
 Shkvarunets, A.G. 2712
 Shoaee, H. 3371, 3377

- Shoji, M. 250, 782, 2551
Shrey, T. 1542
Shubin, E. 2769
Shul'ga, N. 3329
Shumakov, I.V. 3530
Shuman, D. 98, 2625, 2628
Shurter, R.B. 2512
Shvedov, D. 2273
Shvets, G. 3117
Sibley, C. 607
Siddons, P. 241
Sideris, I.V. 2676
Sieber, T. 2869, 2872
Siemann, R.H. 722, 728, 731, 1530, 1855, 1858, 1864, 1879, 1933
Siemko, A. 1942
Sievers, P. 45
Sigler, F. 1664
Sikora, J. 1306, 3059
Sikora, R. 524, 2444
Silzer, M. 220
Simmons, D. 558
Simmons, L. 1213
Simoens, F. 1303
Simon, F. 1948
Simonsson, A. 1590
Simos, N. 1428, 1628, 1709, 3255
Simpson, J. 1813
Simrock, S. 467, 470, 2342, 2730
Sims, J. 2841
Sinclair, C.K. 76, 192, 1317, 2062
Singatulin, S. 2769
Singer, W. 467, 1374
Singer, X. 467
Singh, O. 283
Skarbo, B. 3318
Skaritka, J. 217, 1909, 2455
Skorobogatov, V.V. 917
Skrinsky, A. 250
Slaughter, D.R. 95
Slaughter, J. 1739, 1763
Smaluk, V. 214
Smart, L. 54, 785
Smedley, J. 541, 2132
Smirnov, A.V. 1153, 1156, 2123, 2129, 2132, 2135, 2186, 2640, 3171
Smirnova, E.I. 1255, 1258
Smith, B. 1210
Smith, E.N. 2399
Smith, G. 1715, 2444, 2453
Smith, H. 423
Smith, H.V. 558
Smith, J.C. 2267
Smith, K. 1377
Smith, K.S. 476, 1195, 1545, 1706, 1715, 2441, 3338, 3341, 3344, 3380
Smith, M. 2382
Smith, S. 235, 761
Smith, S.L. 189
Smith, T. 1279
Smith, T.L. 1416, 1422, 2038
Smolenski, K. 167, 1317, 2399
Snowel, M. 2574
Snydstrup, L. 1542
Soika, R. 2162
Soliday, R. 283, 1419, 2261, 3461, 3470, 3473, 3476
Solyak, N. 1207, 1210, 1213, 1781
Someya, H. 2509
Son, D. 962, 965
Song, L. 1110, 1142
Sonnad, K.G. 1536
Sorchetti, R. 2476
Soutome, K. 250, 782, 881
Spata, M. 195
Spataro, B. 914, 2500, 3285
Spataro, C. 2159
Spencer, C.M. 779, 2177
Spencer, J. 779, 1861, 2180
Spentzouris, P. 2939, 3195
Spickermann, T. 2521, 3086, 3089, 3455
Spiller, P. 589, 694
Spinka, H. 51
Spitz, R. 1195
Sprangle, P. 716, 1846
Sprehn, D. 3312
Springer, P.T. 95
Srinivasan-Rao, T. 39, 92, 541, 2047, 2132
Stanek, M. 423, 2297
Stanford, G. 601, 1488
Staples, J. 186, 1243, 1563, 2023, 2086, 2092, 2408, 3198
Starling, W.J. 2889
Startsev, E.A. 1667, 2975, 2978, 3120, 3123
Stascheck, A. 3569
Stassen, R. 598, 2814, 3428
Stecchi, A. 366, 2279, 2742, 3285
Steck, A. 2515
Steck, M. 434
Steerenberg, R. 388, 2913, 2916
Stefancich, M. 917, 1655
Stefanski, R. 1652
Steier, C. 397, 869, 2246, 2249, 3213, 3374
Steimel, J. 48, 1736, 3068, 3071, 3074, 3353, 3356, 3362
Stein, H.J. 3428
Stein, W. 2847
Steinhauer, L.C. 1909
Stella, A. 366, 2279, 2742, 3285
Stelzer, J.E. 73
Stenning, M. 1584
Stephan, F. 2114
Stephani, T. 1948
Stepin, D.L. 2878
Steski, D. 1715
Stettler, M. 2429, 2512, 3371, 3377
Stevens Jr., R.R. 73
Still, D. 1730
Stinson, G. 1584, 1670
Stirbet, M. 457
Stockhorst, H. 598, 3428
Stockli, M.P. 527, 3306
Stockwell, B. 1122, 1144
Stoltz, P. 132

- Stott, J.P. 887, 2373
 Stout, D. 2706
 Stovall, J. 1515, 2652, 2855
 Strait, J.B. 42, 1745, 1748, 1969, 1975
 Straumann, T. 235, 761, 2494
 Striganov, S.I. 1733
 Strohman, C.R. 2473, 3347
 Strohmer, S. 899
 Studebaker, J. 558
 Stulle, F. 3129
 Stupakov, G.V. 102, 926, 1038, 3132, 3135, 3225, 3231
 Sturgess, R. 558
 Suetake, M. 860, 1228
 Suetsugu, Y. 612, 800, 803, 806
 Sugahara, R. 860
 Sugai, I. 1512
 Sugawara, S. 1978
 Sugaya, M. 1231, 1679, 3452
 Sugimoto, M. 2829
 Sugimura, T. 3326
 Sugita, K. 1978
 Sugiyama, E. 1993
 Suhring, S. 625
 Suk, H. 1849, 1852, 1906, 1912, 2984, 2987
 Suller, V.P. 189
 Sullivan, G. 558
 Sullivan, J. 2533
 Sullivan, K. 2189
 Sullivan, M. 340, 2282, 2294, 2297, 2300
 Summers, D.J. 1804
 Sun, D. 3068
 Sun, X. 2688, 3008, 3011, 3014
 Sun, Y. 2682
 Sundelin, R. 1398, 1401
 Suwada, T. 533, 1225, 3368
 Suzuki, H. 1338
 Svandrlik, M. 878
 Svirida, D. 51
 Swanson, C. 3371
 Swenson, D.A. 2889
 Swift, G. 2273
 Swinney, C. 558
 Swirsky, J. 2195
 Sylvester, C. 1969
 Symon, K.R. 452
 Syphers, M. 1649, 1754, 2931
 Syratcev, I. 495
 Sytnik, V. 1781
 Szott, Ph. 1303
 Tabak, M. 2637
 Taborelli, M. 495
 Tada, J. 782
 Tadano, M. 860, 2506
 Tai, C.-Y. 1407
 Tajima, T. 1341, 1344, 2083
 Takagi, A. 1216, 1231, 1234, 1679, 2922, 3452
 Takagi, T. 782
 Takahashi, J. 1593, 1596, 2201
 Takahashi, S. 487
 Takahashi, T. 860, 1228
 Takaki, H. 530, 857
 Takala, B.E. 1168
 Takano, S. 250, 881
 Takao, M. 250, 782, 881
 Takasaki, E. 1509, 2835
 Takasaki, S. 860
 Takashima, T. 250, 487
 Takasu, Y. 487
 Takayama, K. 568, 1784, 1807, 1981, 2610
 Takayanagi, T. 1512
 Takebe, H. 250
 Takeda, H. 1515, 2855, 3518
 Takeda, S. 487
 Takeda, Y. 1512
 Takeshita, K. 487
 Takeuchi, H. 2829
 Takeuchi, Y. 803, 860, 2351
 Talerico, P.J. 553, 1095, 1168, 1458, 1461
 Talman, R. 192, 272, 848, 2919, 3482, 3485
 Tamasaku, K. 487
 Tamura, F. 1216, 1234
 Tamura, K. 250, 881, 2551
 Tan, C.Y. 1751, 2703, 3071, 3074
 Tanabe, J. 2174
 Tanabe, T. 235
 Tanaka, H. (KEK) 1509, 2393, 2835
 Tanaka, H. (Mitsubishi) 1539
 Tanaka, H. (SPRING-8) 250, 881
 Tanaka, K. 1978
 Tanaka, T. 487
 Tang, C. 467
 Tang, Z. 623
 Tanimoto, Y. 809, 860
 Taniuchi, T. 2838
 Taniuchi, Y. 250
 Tantawi, S.G. 482, 1125, 1127, 1261, 1264, 1270, 1276
 Tarakanov, V.P. 1882
 Tarasov, G.E. 2878
 Tarawneh, H. 238, 2318, 2321
 Tariq, S. 641, 1452
 Tartaglia, M. 1730, 1969, 1972
 Tateishi, T. 884
 Tatum, B.A. 995
 Tavakoli, K. 238
 Tavares, P.F. 2583, 3279
 Tawada, M. 353
 Taylor, C. 86
 Taylor, T. 42
 Tazzari, S. 3285
 Tazzioli, F. 3285
 Tecker, F. 684
 Tegenfeldt, F. 1945
 Tejima, M. 860
 Telfer, S. 947, 2110, 2112, 2120, 2192, 3321
 Temkin, R.J. 1255, 1258, 2095, 2536
 Temnykh, A. 167, 1026, 1954, 3425

- Temple, R. 558
 Tenenbaum, P. 657, 662, 681, 2739, 2757
 Teng, L.C. 2895
 ten Kate, H. 42
 Tennant, C. 195, 2189, 3243
 Tepikian, S. 51, 135, 405, 1706, 1712, 2144, 2159, 2390
 Teramoto, A. 1071
 Terashima, A. 1978
 Terebilo, A. 235, 2255, 2369, 2372
 Terekov, V. 1691
 Terremoto, L.A.A. 1593
 Tesarek, R. 2497
 Teytelman, D. 318, 2297, 2300, 3141, 3389
 Theobald, W. 1921
 Thibus, J. 2823
 Thieberger, P. 1628, 1634, 1715
 Thiesen, H. 1945
 Thikim, M. 2303
 Thomas, C. 1575
 Thomas, R. 164, 2162
 Thomas-Madec, C. 1104, 1332
 Thomason, J. 2542
 Thompson, K.M. 1020
 Thompson, M.C. 1870
 Thompson, N.R. 189
 Thomson, D. 3377
 Thorndahl, L. 1156
 Tiede, R. 2942
 Tiefenback, M. 195, 3243
 Tigner, M. 192, 1317
 Tikhoplav, R. 2682
 Timossi, C. 2385
 Ting, A. 716, 1819, 1846
 Tinsley, D. 3068
 Titt, U. 690
 Titus, P. 1631
 Tiunov, M. 1781, 3318
 Tkachenko, L. 1781
 Tobiyama, M. 2709, 3141
 Tochitsky, S.Ya. 1873
 Todd, A. 977
 Todd, R. 788, 791
 Todesco, E. 173, 1942
 Toelle, R. 598, 2811, 2814, 2817, 3428
 Toellner, T. 2411
 Togawa, K. 487, 3332
 Tokuchi, A. 1165
 Tollestrup, A.V. 48, 1733, 2491, 2497
 Tolmachev, S. 1867
 Tom, C.Y. 558
 Tomàs, R. 2207, 2228, 2231, 2234, 2240, 2901
 Tombolini, F. 917
 Tomimasu, T. 902, 2387, 3270
 Tomizawa, H. 2838
 Tomizawa, M. 3083
 Tomlin, R. 2936
 Tompkins, J. 1730, 1966, 1969, 1972
 Tordeux, M.A. 229
 Torii, Y. 884
 Torikai, K. 568, 1784, 1807
 Torrez, P.A. 1237
 Tortschanoff, T. 1948
 Torun, Y. 1183, 1246, 1413, 1795
 Tosi, L. 214, 1050, 2306, 2309
 Totchisky, S. 1867
 Toth, C. 1840
 Touzzolo, J. 1428
 Tovstiak, V.V. 1080
 Towne, N. 241, 3168
 Towns-Andrews, E. 708
 Toyama, T. 568, 1784, 1807, 2610, 3083
 Toyokawa, H. 195, 713, 902, 938, 974, 2387, 3270
 Trakhtenberg, E. 824, 830, 1017
 Trask, W. 167
 Trautwein, A. 235
 Travish, G. 944, 947, 1867, 1870, 2110, 2112, 2192, 3321
 Trbojevic, D. 39, 51, 54, 135, 372, 794, 797, 1425, 1691, 1697, 1706, 1712, 1816, 2204, 2694, 2904, 3413, 3485
 Tremaine, A.M. 95, 2192, 2957
 Tromba, G. 2309
 Trotman, J.V. 1527
 Trovò, M. 2306
 Trujillo, P.G. 553
 Trzeciak, W. 887, 2303
 Tsai, H.J. 890
 Tsai, Z.D. 1479
 Tsakov, I. 2114
 Tsang, T. 541
 Tschalaer, C. 372, 956, 959, 980, 2324
 Tsentalovich, E. 2324
 Tsoupas, N. 51, 405, 550, 1542, 1545, 1637, 1706, 1715, 2138, 2141, 2147, 2150, 2153, 2159
 Tsuchiya, K. 860, 1978
 Tsukishima, C. 1539
 Tsumaki, K. 250, 782, 884
 Tuckmantel, J. 1718, 3050
 Tuozzolo, J. 550, 571, 1637, 2138, 2144, 2147, 2150, 2156, 2390, 2598
 Tupikov, V. 2020
 Tur, Yu.D. 2878
 Turlington, L. 1350
 Turner, J.L. 2297, 2754
 Turner, W. 2530
 Twarowski, K. 467
 Uchiyama, T. 809, 860
 Ueda, A. 860, 3201, 3204
 Ueng, T.S. 3237
 Ueno, A. 1509
 Ueno, R. 1679
 Uesaka, M. 2258
 Uesugi, T. 1216, 1231, 1234, 1679, 3452
 Ullrich, J. 1622
 Umemori, K. 860, 1228
 Umstadter, D. 1921
 Underwood, D. 51
 Urakawa, J. 2545, 2709

- Uriot, D. 2802, 3491
Uvarov, V.L. 2878
Uythoven, J. 45, 1646
Vaccarezza, C. 366, 914, 2077, 2279, 2500, 2945, 3285
Valdiviez, R. 702, 1664
Valente, A.-M. 1401, 2860
Valente, P. 1658
Valentino, V. 3318
Valfells, A. 426, 1673, 2312, 2571, 2574, 2577, 3156
Valishev, A. 3398
Valuch, D. 473, 1089
van der Laan, J.B. 372, 956, 959, 980, 2324
van der Meer, A.F.G. 519
Vanenkov, I. 1951
van Goor, F.A. 1900, 1903
VanKuik, B. 1542
van Tilborg, J. 1840
van Weelderen, R. 1945
van Zeijts, J. 51, 135, 524, 1697, 1706, 1712
Varenne, F. 2802
Varfolomeev, A. 1867
Varfolomeev, Jr., A. 1867
Variale, V. 3318
Varnasery, S. 238
Vascotto, A. 2309
Vasserman, I. 2261
Vasyukhin, N. 2814
Vay, J.-L. 132, 312, 2673, 3297
Vaziri, K. 983
Velev, G. 1730, 1969, 1972
Veness, R. 1646
Venturini, M. 863, 2772, 3144
Venturini-Delsolaro, W. 1948
Verdier, A. 444, 2237
Vermare, C. 2464
Verzilov, V. 214
Vescovi, M. 366, 2279, 3285
Veshcherevich, V. 192, 1198, 1201, 1306, 1317
Vetter, K. 524, 2444, 2697
Vicario, C. 944, 3285
Vidal, R. 2497
Vignola, G. 1053, 1658
Vikharev, A.L. 1147
Vincenzi, D. 917, 1655
Vinogradov, N.E. 2790, 2963
Vinogradov, S.V. 3530
Vinokurov, N. 2273
Viren, B. 3255
Virgo, M. 3323
Virostek, S. 1243, 2023, 2092
Visentin, B. 1303
Vlachoudis, V. 45
Vlogaert, J. 1942
Vobly, P. 2273
Vogel, H. 1410, 2887
Vogel, V. 2545
Vogler, W. 269, 3560
Volk, J.T. 1766, 2180
Volkolupov, Yu.Ya. 1107, 3303
Volkov, V.N. 2041, 2044
Vollinger, C. 173, 1951
vom Stein, P. 1410, 2887
Vorobiev, L.G. 3533
Vos, L. 45, 1801
Wada, Y. 3335
Wahrer, B. 1032
Wait, G.D. 1162
Wake, M. 568, 1784, 1807, 1981
Waldron, W. 98, 536, 1171, 1521, 2628
Waldschmidt, G. 1422
Walker, N. 657, 2396, 2733, 2736, 2739
Walker, R.P. 232
Wallace, D.J. 2303
Wallace, P. 752, 2273
Wall_n, E. 2321
Wallig, J. 1246
Walstrom, P. 544, 1966
Walter, M. 426, 1673, 1676, 2312, 2571, 2574, 2577
Walz, D. 731, 1530, 1858, 1864, 1933
Wan, W. 186, 397, 2246, 2249
Wanderer, P. 164, 1637, 2159, 2162, 2390
Wang, B. 1032
Wang, C. 1927, 1930
Wang, C.J. 2554
Wang, C.X. 3407, 3410
Wang, Ch. 1041, 1371, 2402, 2670
Wang, D. 39, 1300, 2005, 3186, 3228
Wang, D.J. 890
Wang, F. 372, 956, 959, 980, 2324
Wang, H. (ANL) 1813, 2032
Wang, H. (TJNAF) 457, 1098, 1101, 1104, 1389
Wang, J.M. 241
Wang, J.P. 815, 2357
Wang, J.W. 1264, 2664, 2763
Wang, M.H. 890, 3150, 3240
Wang, P. 752, 2479
Wang, S. 1455, 1509
Wang, S.-H. 186, 2682, 3198
Wang, T. 1386, 1398, 2860
Wang, T.S. 508, 3092, 3095
Wang, X. 2174
Wang, X.J. 217, 241, 420, 1819, 2455, 2808
Wang, X.Z. 2586
Wang, Y. (CAMD) 2382, 2892
Wang, Y. (NSRL) 815
Wangler, T.P. 2613
Warburton, D. 550, 1625, 1640, 2147
Warner, A. 2020
Warner, D.K. 1237
Warnock, R. 3144
Warsop, C.M. 1527
Watanabe, Y. 1512
Watson, J.A. 2533, 2960
Wazlawik, S. 3569
Weathersby, S. 2981

- Weaver, M. 2285
 Webber, R.C. 1503, 2936
 Weber, C. 1189
 Weggel, R.J. 1628, 1631, 1634
 Wei, J. 272, 394, 550, 571, 1569, 1572, 2153, 2159, 2390, 2598, 3029, 3032, 3416, 3419
 Wei, W. 815
 Weichert, G. 467
 Weihreter, E. 1189
 Weiland, T. 2114, 3249, 3252, 3551, 3563, 3566, 3569
 Weiner, M. 2664
 Weinrich, U. 694
 Weir, J. 563, 2960
 Weise, H. 673
 Weiss, D. 785
 Weiss, K. 307
 Welch, D.R. 98, 2622, 2637, 2685, 3165
 Welch, J. 3126
 Wells, R.P. 186, 812
 Welsch, C.P. 1622, 2817
 Welton, R.F. 527, 3306
 Wender, S.A. 1168
 Wendt, M. 467, 1086, 2730
 Weng, W.T. 429, 571, 1637, 1709, 2793
 Wenhui, H. 467
 Wenninger, J. 45, 1718
 Werin, S. 2318, 2321
 Werkema, S. 1554
 Wermelskirchen, C. 235, 761
 Wesling, S. 2029
 Westenskow, G. 2533, 3297, 3300
 Weterings, W. 1646
 White, G.R. 2733, 2778
 Whitlatch, T. 457, 977, 1377, 2866
 Widger, D. 2399
 Widjaja, C. 1921
 Widmeyer, M. 235
 Wiemerslage, G. 830
 Wienands, U. 2297, 2300, 3141
 Wilcox, R. 2408
 Wildman, D. 323, 1781, 2922, 3177
 Wildner, E. 173
 Wilinski, M. 2441, 2444, 2691
 Wilke, I. 519
 Will, I. 836, 2114
 Willen, E. 164, 1936, 1939
 Williams, C.L. 998
 Williams, E. 3374
 Williams Jr., E.L. 288
 Wilson, I. 495, 665, 1156, 2724
 Wilson, K.M. 1377, 2866
 Wilson, M. 426
 Wilson, M.N. 2162
 Wilson, P. 1264, 1282
 Win, S.S. 3056
 Wines, R. 2135, 2186
 Wisdom, J. 1861
 Wiseman, M. 457, 977, 1377
 Witkover, R.L. 2444, 2447, 2450
 Wittmer, W. 2237
 Wojtkiewicz, G. 467
 Wolf, M. 2664
 Wolski, A. 186, 652, 657, 866, 2246, 2396, 2745, 2772, 2775, 3213
 Wood, J. 51
 Wood, R.L. 920, 977, 2083
 Woodley, M. 657, 662, 2739, 2757, 2766, 2775, 3126, 3129
 Woods, M. 2754
 Wright, E. 1144
 Wu, A.T. 1386, 2860
 Wu, G. (NSRL) 815
 Wu, G. (TJNAF) 1389, 1395, 1401, 1575
 Wu, J. 126, 1035, 1038, 2775, 3228, 3231
 Wu, J.K. 3294
 Wu, K.C. 164
 Wu, V. 1246, 1769
 Wu, X. 2849, 2972
 Wu, Y. 397
 Wu, Y.K. 391, 752, 2249, 2270, 2273, 2479, 2482
 Wu, Z. 217, 420, 1192, 1497, 1819, 2455
 Wuensch, W. 495, 1156, 2467, 2724
 Wüestefeld, G. 836, 839, 845, 3020, 3023
 Xiao, A. 2488
 Xiao, M. 1730, 1757, 1760, 1772, 1775, 3401, 3542
 Xie, M. 1843
 Xiong, Y. 1560, 3506, 3509
 Xu, H.L. 968
 Xu, N. 2174
 Xu, Z. (BNL) 1688
 Xu, Z. (IMP) 1288
 Yadav, S. 1748, 1969
 Yakimenko, V. 944, 1909
 Yakovlev, V.P. 1128, 1131, 1150, 1927, 2881
 Yamada, K. 713, 971, 974
 Yamada, R. 1981
 Yamaguchi, S. 1509, 2838
 Yamamoto, A. (IHI) 3326
 Yamamoto, A. (KEK) 1978
 Yamamoto, K. 1512
 Yamamoto, M. 1216, 1234
 Yamamoto, N. 860, 2351
 Yamamoto, S. (KEK) 860
 Yamamoto, S. (Mitsubishi) 1539
 Yamanaka, S. 1165
 Yamatsu, Y. 902, 3270
 Yamazaki, A. 1679, 3452
 Yamazaki, M. 1338
 Yamazaki, Y. 576, 1509
 Yan, X. (IAP) 1335
 Yan, X. (UAD) 519
 Yan, Y. 2297, 2300
 Yang, B.X. 2411, 2423
 Yang, J.S. 1470, 2857
 Yang, M.J. 1649, 1766, 3440
 Yang, S. 1243, 1834
 Yang, X. 1288

- Yanovsky, V. 1921
 Yao, C. 758
 Yao, C.Y. 2411, 2423, 2438
 Yao, J. 2852
 Yarovoi, T. 1867
 Yasumoto, M. 713, 902, 971, 974, 3270
 Yeh, M.K. 1371
 Yin, Y. 2586
 Yocky, J. 2297, 2754
 Yoder, R. 1533, 1867, 1873, 2117, 3258
 Yokoi, T. 1679, 3452
 Yonehara, H. 250, 782, 884, 2551
 Yonemura, Y. 1679, 3452
 Yorita, T. 250, 782
 York, R. 138, 1350, 1353, 1362, 2849, 2972, 3533
 Yoshida, M. 487
 Yoshii, M. 1216, 1234, 3452
 Yoshikawa, H. 1509
 Yoshimoto, M. 1679, 3452
 Yoshimoto, S. 860, 1228
 Yoshino, K. 1509, 2393
 Yoshioka, M. 860
 Yotam, R. 235
 Young, A. 3141
 Young, L.M. 60, 920, 977, 1461, 1515, 2844, 3515, 3521
 Yu, D. 1153, 1156, 2123, 2126, 2129, 2132, 2135, 2186, 3171
 Yu, I.H. 2857
 Yu, J. 2132
 Yu, L.H. 217, 241, 2455, 2808
 Yu, S.S. 98, 558, 1171, 2616, 2619, 2622, 2625, 2628, 2637, 2646, 2661, 2685
 Yu, T. 1560, 3506, 3509
 Yuasa, Y. 1679, 3452
 Yun, J.C. 1763
 Yun, R. 426, 2571
 Yunn, B. 332, 3246
 Yusof, Z. 2032
 Zadorozhny, V. 3005
 Zagorodnov, I. 3249, 3252
 Zahariou-Cohen, S. 1542
 Zajic, V. 89
 Zakutin, V.V. 1107, 3303
 Zaltsman, A. 39, 476, 1195, 3344, 3380
 Zambon, L. 3395
 Zangrando, D. 1050
 Zapfe, K. 467
 Zaplatin, E. 598
 Zaugg, T. 508, 2521, 3089, 3455
 Zelenski, A. 51, 405, 3282
 Zeller, A. 138, 161
 Zeng, J. 770
 Zeno, K. 51, 54, 794, 1542, 1545, 1715
 Zhan, W. 1288
 Zhang, B. 2580
 Zhang, C. 250
 Zhang, H. 818
 Zhang, P. 1921
 Zhang, P.F. 968
 Zhang, S.C. 968
 Zhang, S.Y. 51, 54, 785, 794, 1425, 1706, 1715, 2598, 2694, 3419
 Zhang, W. (BNL) 550, 1640, 2147, 3255
 Zhang, W. (IMP) 1288
 Zhang, W. (YY Labs) 2586
 Zhang, X.L. 57, 1754, 1757, 1778, 1781, 2703
 Zhang, Y. (NSRL) 758
 Zhang, Y. (ORNL) 995, 1001, 1004
 Zhang, Y. (TJNAF) 941
 Zhao, F.Y. 815
 Zhao, H. 1288
 Zhao, K. 2580
 Zhao, Q. 92, 2047
 Zhao, T. 2382, 2892
 Zhao, Y. 39, 92, 1300, 2050
 Zhavoronkov, N. 836
 Zheng, H. 2922
 Zheng, Q. 1404
 Zheng, S. 467, 1392, 1395, 1575
 Zhidkov, A. 2258
 Zhiglo, V.F. 2098
 Zholents, A. 186, 397, 812, 866, 872, 923, 2086, 2132, 2408, 3198
 Zhou, F. 1876, 1909, 2709, 3186, 3228
 Zhou, J. 2646, 2966
 Zigler, A. 716
 Zimmermann, F. 123, 307, 665, 1727, 1730, 1754, 1757, 1778, 2237, 2240, 2315, 2604, 2739, 3038, 3041, 3044, 3053, 3056
 Zimmermann, H. 2823
 Zink, R. 138
 Zinkann, G.P. 2426, 2790
 Zisman, M. 361, 1183, 1243, 1246, 2023, 2297
 Zitelli, L. 1144
 Zlobin, A.V. 42, 1748, 1966, 1969, 1975
 Zobov, M. 366, 914, 2279, 2742, 2945, 3285
 Zolfaghari, A. 956, 959, 980, 2324
 Zolotarev, M. 2530
 Zotter, B. 3044
 Zou, Y. 426, 511, 1673, 2673, 3156
 Zubets, V. 3282
 Zuo, K. 235
 Zviagintsev, V. 470
 Zwart, T. 956, 959, 980, 2324